Macromolecules

Perspective

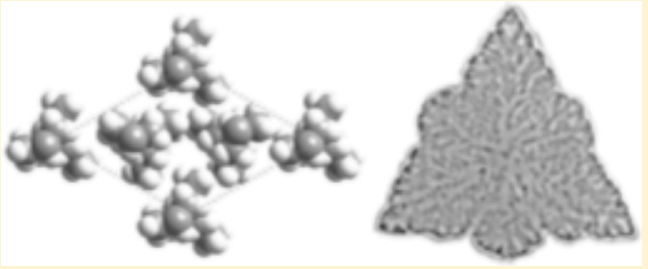
pubs.acs.org/Macromolecules

Frustration and Frustrated Crystal Structures of Polymers and Biopolymers

Bernard Lotz*

Institut Charles Sadron (CNRS − Université de Strasbourg), 23, Rue du Lœss, 67034 Strasbourg, France

ABSTRACT: The manifestations of frustration are widespread in materials science. The more specific geometrical frustration in crystalline materials is created when physical interactions between nearest neighbors induce packing modes (e.g., the slight twist between neighboring DNA strands) that cannot propagate indefinitely throughout space. The structure is made of small domains separated by dislocation lines or other less ordered walls (e.g., in DNA blue phases). A second type of *geometrical* frustration, compatible with crystallographic symmetry, may arise in hexagonal close-packed crystals of helices with 3-fold symmetry. If favorable pair−pair interactions exist between helices, they can propagate only in a honeycomb pattern. The resulting unit cell is trigonal and contains three independent helices, one of which interacts less favorably with its neighbors—thus the frustration. Recognition of this type of geometrical frustration in polymer crystallography is relatively recent, although some crystal structures determined long ago displayed what amounts to frustration. This frustration is widespread: a number of chiral crystal structures of polymers and biopolymers conform to, and probably many more will fit in, this packing scheme. Frustration in polymers manifests itself by specific diffraction and morphological features (e.g., triangular single crystals) and, in one case, could be imaged by AFM. The frustrated structures provide, in view of their unusual characteristics, an exceptional investigation material to further elucidate the finer details of polymer crystallography and polymer crystallization processes.



■ INTRODUCTION

The concept of frustration was introduced by Toulouse in 1977.[1] It dealt first with disorder in the structure of ferromagnetic and antiferromagnetic systems and was applied to spin glasses. In this analysis, the interactions between nearest neighbors dominate the structure of the material. This analysis has permeated many aspects of materials research.

In a more specific meaning, and referring to the structure of crystals (or more generally periodic structures), geometrical frustration exists when the local organization of molecules or atoms cannot be repeated indefinitely throughout space. This impossibility leads to two different "compensating" mechanisms, leaving a trace at different lengths scales: mesoscopic and crystallographic. (1) When no local mechanism relieving the induced stresses exists, the local departures from crystallographic symmetry add up, to a point where the stresses generated can no longer be handled. Relatively small crystalline clusters are formed, commensurate with the local stress generated by the departure from crystallographic symmetry. The clusters are separated by disclinations and disordered boundaries. (2) A local compensation may exist, in the form of some defective site that has a less privileged interaction with its environment. Crystallographic order is preserved, but its periodicity corresponds to that of the network of defects. The unit cell is thus typically a "large cell" that contains both ingredients of frustration: its original cause and its remedy.

In the polymer field, most of the earlier work dealt with the first type, that is, with frustration manifested at a mesoscopic scale. This frustration has been analyzed in quite detail by the French school of metallurgy, condensed and soft matter physics located in Orsay, although it did not have much echo in the standard polymer literature. The slight twist between neighbor DNA double helices axes is an archetype frustrating local organization that leads to the formation of liquid-crystalline phases.

The second type of geometrical frustration exists also in polymer crystals. It results characteristically in a honeycomb lattice that is compatible with crystallographic symmetry and can be described by a three-chain trigonal unit cell. Such structures have been observed in the late 1970s−early 1980s, but the generality of the packing scheme had not been recognized.

The present contribution presents these manifestations of frustration, since they are not very familiar in our polymer community. The concept of frustration as initially proposed by Toulouse is presented. The mesoscopic manifestations of frustration are only briefly recalled, since they have been the topic of many papers, reviews, and even books. The major emphasis is put on the geometrically frustrating trigonal lattice and on the manifestations and experimental evidence, indicating frustration in polymer crystal structures. Finally, the opportunities offered by these unusual crystal structures as fundamental research tools are presented and discussed. They have already helped elucidate finer details of molecular−molecular interactions in polymer crystallography and of the selection processes taking

Received: October 17, 2011
Revised: January 8, 2012
Published: February 21, 2012

 © 2012 American Chemical Society dx.doi.org/10.1021/ma202326t | *Macromolecules* 2012, 45, 2175−2189

place during crystal growth, but they may well be useful in other domains.

THE CONCEPT OF FRUSTRATION AND GEOMETRICAL FRUSTRATION

The Concept of Frustration. *The concept of frustration* was first introduced by the French physicist Toulouse in relation with the structure disorder in spin glasses.[1] As defined by Schiffer and Ramirez,[2] frustration is "a system's inability to simultaneously minimize the competing interaction energies between its components". Toulouse dealt initially with disorder in spin orientation in two-dimensional ferromagnetic and antiferromagnetic square lattices with Ising spins (i.e., either parallel or antiparallel). Disordered systems can exist in which "there is no way of choosing the orientations of the site spins without frustrating at least one bond". In its initial approach, frustration was thus used to describe disordered systems and has extensively been used by solid-state physicists working in this field (Figure 1a, top).

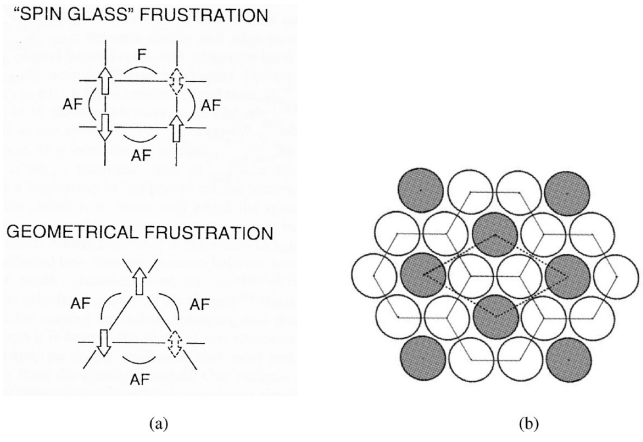


Figure 1. (a) Toulouse's original proposal of frustration generating disordered systems in spin glasses on a square lattice (top) and the concept of geometrical frustration in a triangular crystal lattice (bottom) as illustrated and discussed by Ramirez. Reproduced with permission from ref 2b. Copyright 1994 Annual Reviews Inc. (b) Geometrical frustration in a two-dimensional triangular lattice (hexagonal close packed). The two conditions (close packing and neighbor balls of different color) cannot be met simultaneously. The resulting lattice generates a trigonal cell with three elements. Reproduced from ref 16.

Geometrical Frustration. *Geometrical frustration* exists in systems where the competition originates in the spatial arrangement of the components.[2] This frustration may generate manifestations on large and on more local scales. The *large-scale manifestations* have been investigated in quite detail. To quote Sadoc and Mosseri, "Geometrical frustration (exists) when the local order cannot be propagated freely throughout the space", which leads "to describe the final structure as a mixture of ordered regions... with defects arising from the embedding. Among the defects, disclinations will play an important role".[3] Along a similar line, in a paper devoted to the "effect of frustration in liquid crystals and polymers", Kleman "assigns the term frustration to the general case in which the interactions which compete on short distances in the stability of some material lead to local configurations of molecules which are incompatible on large scales"[4] and are relieved by interdomain defect lines (disclinations). This type of geometrical frustration has a local structural origin, but its manifestations take place on a larger, mesoscopic length scale; the mutual organization of these defects frequently results in certain types of liquid crystalline textures. As indicated, a better packing of DNA double helices is obtained when their axes are slightly twisted and not parallel. This local twisted arrangement cannot be repeated indefinitely throughout space. It leads to blue and cholesteric liquid-crystalline phases (cf. Figure 9).

The impact of a slight twist between neighbor chains finds an echo in the well-known twisted lamellar morphology of crystalline polymers, more familiar in our field. Kleman, referring to the twisted single crystals of *Bombyx mori* silk fibroin[5] and drawing an analogy with the twisted layers of DNA strands in the dino-flagellate chromosome, points out that the lateral stacking of twisted β sheets (actually a double twist) is only possible for limited lamellar thicknesses and limited crystal widths. Further, the stacking of the lamellae throughout space is also inherently limited by their twisted geometry. Following this approach, the packing of twisted lamellae in optically banded polymer spherulites is yet another manifestation of a frustration scheme that, not being relieved locally, induces "long range" interdomain defects.

Geometrical frustration can exist also, in a more specific meaning, in regular, crystallographic lattices. This characteristic was actually underlined by Toulouse in his seminal paper. He points out indeed "The frustration effect... *may also exist on perfectly regular lattices* (example: the two-dimensional *triangular lattice* with all bonds negative" (i.e., antiparallel spins).[1] Frustration is *ineluctable* when considering a triangular lattice in which the entities located at the tips of the triangle interact but have only two possible "states" (e.g., in the frustrated magnets, Ising spins) (Figure 1a, bottom). This triangular lattice or, in other words, the hexagonal close packed lattice is the only lattice we will be concerned with when dealing with polymers.

A simple illustration of the 3D frustration considered in the present context is provided by a 2D analogue, namely the packing of black and white balls on a hexagonal close packed lattice. Addition of one further condition—every ball must be surrounded by balls of the opposite color—introduces a condition that cannot be met together with the close-packing condition: if a black ball is surrounded by six white balls, the latter have neighbors of the same color. Relaxing the color condition, and maintaining the physically more stringent close-packing condition, it is possible to create a relatively simple lattice in which the "unit cell" is made of three balls: two white ones and one black one (this is actually the diced lattice). The unit cell is trigonal and comprises three structural units *that are not equivalent*—they have different colors (Figure 1b). In this model the black balls *only* enjoy the two conditions set initially: close packing and white neighbors. The two white balls are in a less favorable environment—they have neighbors of their own color and are therefore frustrated. The white balls generate a *honeycomb lattice* in which every white ball connects with three like (white) neighbors out of its six neighbors.

The load of frustration may be reversed. If the balls stand for helices with 3-fold symmetry and these helices build up favorable interactions among themselves, it is clear that these favorable pairwise interactions propagate throughout the crystal lattice but involve only part of this lattice, namely the helices that are part of the "white" honeycomb. The "lone" element is frustrated. This simple scheme sets the whole framework for geometrically frustrated crystal structures of polymers: favorable or highly favorable pair–pair (i.e., helix–helix) interactions overwhelm the less favorable interactions of the

dx.doi.org/10.1021/ma202326t | *Macromolecules* 2012, 45, 2175–2189

frustrated helix with its neighbors, but the structure as a whole is stable (or metastable).

Frustration in its generic sense thus amounts to "discomfort" of a system ("a system's inability to simultaneously minimize the competing interaction energies between its components"). Frustration is a situation in which the discomfort cannot be overcome. It can lead to long-range defects, when the accumulation of small local stresses becomes unmanageable, as e.g. in some liquid crystals. The discomfort can be handled on a more local scale. In that case, although the total energy is minimized *within the unit-cell*, the *a priori* equal protagonists do not share equally the discomfort: the frustrated ones take a heavier load whereas others enjoy a more comfortable situation or environment. This latter accepted meaning of *geometrical frustration is compatible with crystallographic symmetry*—albeit of a special one, which is the central theme of the present contribution.

STRUCTURAL ORIGIN OF FRUSTRATED POLYMER CRYSTAL PHASES AND MARKERS OF POLYMER FRUSTRATION

Is the Standard $P3_1$ Unit-Cell Symmetry a Stable Crystal Packing for 3-fold Helices? The 2D analogy used to introduce the frustrating lattice mentioned and emphasized the 3-fold symmetry of the constituent helices. Polymers with 3-fold helical symmetry are frequent among isotactic polyolefins: polypropylene (iPP),[6] poly(1-butene) (iPBu1) in its Form I,[7] isotactic polystyrene (iPS),[8] etc. All of these polymers are "conformationally racemic"; i.e., the left- and right-handed helices are isoenergetic. Their stable crystal structures associate enantiomeric helical hands, but some of these polymers form also chiral phases, which are frequently metastable (e.g., the β phase of iPP, to be described next). Some chiral polymers and biopolymers have also helical conformations with 3-fold symmetry (poly(L-lactide) (PLLA), poly(L-proline), etc.). The standard crystal structure of these 3-fold helices is a one-chain trigonal unit cell with $P3_1$ (or $P3_2$ for left-handed helices) symmetry, space group number 144 (or 145) of the International Tables.[9] This unit cell contains *three* 3-fold screw axes, but the cell contains only one chain. The two other screw axes are thus merely extra elements of symmetry that are "unnecessary".

Logical as it may look, the "simple" one-chain unit cell with $P3_1$ symmetry may not be that attractive a packing mode, at least for some 3-fold helices. Consider a lattice made of 3-fold helices, with the simple $P3_1$ cell symmetry considered so far (Figure 2). For simplicity, the polymer may be isotactic polypropylene, with methyl side groups, i.e., simple round "spheres" ≈4 Å in diameter directly attached to the backbone. For the helices seen in *c*-axis projection as triangles, the methyls are located at their tips (Figure 2a). Two neighbor helices interact via the tip of one helix facing the flat surface (the "base") of another helix. The $P3_1$ symmetry imposes that the facing methyl group of the first helix is located exactly *halfway* between two methyl groups of the next face, i.e., on the path between two hills. This is an unlikely interaction (Figure 2b, left). Rotation of the helices on their axes (the only degree of freedom allowed for the $P3_1$ unit-cell symmetry) relieves only partly the situation. A more logical interaction implies both a rotation and a shift (up or down by $c/6$) of the first helix so that the methyl group nests in a "*tripod*" of three methyl groups (Figure 2b, right). The helix rotation and shift generates a *preferred* type of interaction between *two* neighbor 3-fold

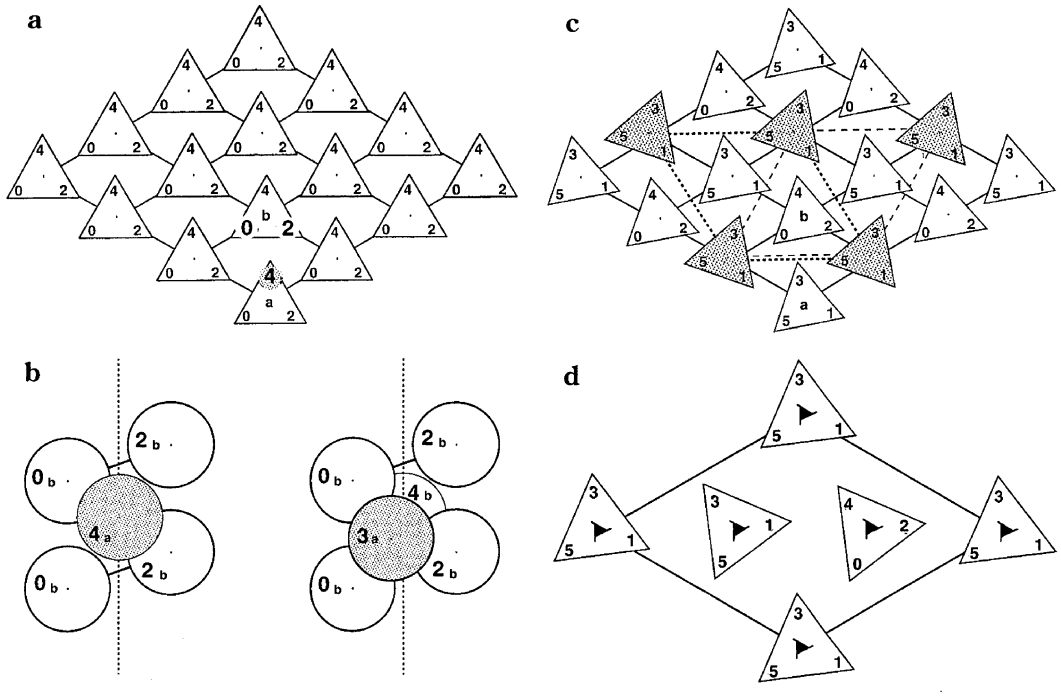


Figure 2. Derivation of a frustrated arrangement for hexagonally close packed 3-fold helices (in a trigonal lattice with $P3_1$ symmetry). (a) The side groups (round balls, representative of e.g. methyl groups in isotactic polypropylene) are identified by their height along *c* and are indicated in $c/6$ fractions. Interactions between the bottom helix a and the facing helix b are evaluated. (b) Left: the standard $P3_1$ cell symmetry imposes that the side group at level 4 in helix a is halfway between side groups at levels 2 and 6 (or 0) of helix b. Right: a better interaction is realized when chain a is shifted along *c* and rotated: the methyl group, now at level 3, is nested in a "tripod" of methyl groups. (c) This interaction propagates throughout the lattice in a honeycomb pattern, which excludes one helix out of three. The third, frustrated helix adjusts to its environment via different azimuthal setting and/or shift along *c*. (d) The final trigonal unit cell has the same $P3_1$ cell symmetry as the initial cell, but the three 3-fold axes are used to generate the three helices, which are not therefore linked by any element of symmetry. Reproduced from ref 15.

dx.doi.org/10.1021/ma202326t | *Macromolecules* 2012, 45, 2175–2189

helices: the *equivalence* principle between identical structural units (helices) in the crystal lattice has been abandoned.

In view of the 3-fold helix symmetry, similar interactions can be repeated with only three out of the initial six neighbor helices. Further, the three neighbors involved can interact in a similar way with two helices further away, etc. This creates a *honeycomb lattice* of favorable pair−pair (here helix−helix) interactions. This honeycomb lattice leaves aside one helix out of three of the initial hexagonal lattice (shaded in Figure 2c) that cannot be involved in interactions of similar "quality". It becomes the frustrated chain and by extension generates the frustrated crystal structure (Figure 2c). This "lone" helix adapts to its less favorable environment by a rotation on its axis and/or shift along the *c*-axis, but *different* from those that generated the favorable interactions between its two neighbors. Since, in addition, the relative azimuthal orientations of the various helix pairs are different, further adjustments of the settings (shift along *c*, rotation, possible positional but in any case small adjustments in the *ab* plane) are likely. In the end, and although the structure derives from favorable interactions between two helices, the final structure is made of three crystallographically independent helices (Figure 2d).

The above derivation leads to a frustrated packing mode of 3-fold helices that was described as a "North−East−East" (NEE) packing mode.[10] A second packing scheme is better described as a "North−South−South" (NSS) one (illustrated later, cf. Figure 4c and abstract). Its derivation using a similar very simple reasoning is equally straightforward.[11] (These schemes are, however, of course, simple representations of a more complex situation, with many variants.)

The frustrated structure has thus, typically, a trigonal unit cell that contains the unusual number of three chains per cell, which must be thought of as a "2 + 1" or more adequately as a "2 *versus* 1" situation. When describing the frustrated lattice, it is convenient to locate the "lone" helix at the origin of the unit cell, thus emphasizing the fact that the two central chains play similar roles (frequently, but not always). The unit cell is trigonal with, again, $P3_1$ symmetry (or, of course, $P3_2$ for left-handed helices), but *all three 3-fold helical symmetry axes are used up to build the three helices starting from their structural (monomer) repeat units*. Therefore, *no symmetry element is left* that would "link" (in a crystallographic sense) the three helices (Figure 2d): they are crystallographically "independent". The azimuthal orientation and/or relative shifts must be determined for each one of them. Note also that the up or down orientation of the helices does not feature in the above analysis. Since anticline helices are nearly isosteric, statistical substitution of up- and down-pointing helices is likely. It does not change the cell symmetry (it remains $P3_1$ or $P3_2$) but requires defining an "up" and a "down" structural unit for each helix site.

It should be mentioned that the trigonal $P3_121$ space group is a (is the only) space group that generates "spontaneously" three helices in a cell (as well as antiparallel helices) and has therefore been used frequently to describe what ultimately turned out to be frustrated structures. However, the up and down helices are related by a 2-fold axis that appears as an "unnatural" element of symmetry in these frustrated structures.[12]

Crystallographic and Morphological Manifestations of Frustration. As a consequence of their large unit cell and original packing mode, frustrated crystal structures can be identified by highly specific and tale-telling crystallographic, diffraction, and, sometimes, morphological features.

The unit cell is trigonal ($a = b$, $\gamma = 120°$) and contains the unusual number of three helices. Both single crystal (*hk*0) (Figure 3a′) and fiber patterns (Figure 3b′) display many more reflections than would be expected for a simple one-chain unit cell (Figure 3a,b). Some of these reflections are very characteristic and are easy "markers" of frustration: the presence of the extra 210 and 120 spots located between the 300 and 030 reflections,[12] (Figure 3a), the meridional 003 reflection weaker than the 103 reflection (Figure 3b′) because two of the helices are shifted by $c/2$, which cancels their contributions to this reflection (in the trigonal $P3_1$ cell symmetry, the 003 reflection is strong since all chains are "at the same height" on the *c*-axis).[13]

The *morphological indicators* are linked with the lack of symmetry of frustrated structures. Although the cell uses the symmetry elements of the trigonal $P3_1$ lattice, the cell content *as a whole* lacks any symmetry. As a result, any one crystallographic plane has *dissimilar topographies* on its front and back faces. If these planes are growth faces, this dissymmetry may lead to significantly different growth rates. The latter are primarily due to different deposition rates of the initial stem of a new layer (the so-called secondary nucleation or primary surface nucleation step).

For a NSS packing of chains, one of the sides of the (110) plane is relatively "flat", whereas the other side of the layer displays a distinctive notch between the two helices that have a "South" orientation. Initiation of a new growth layer via deposition of an initial stem on the "notched" side of the layer is energetically less costly than on the "flat" side, and this preference is repeated layer after layer. Since crystals are bounded by growth faces with the slowest growth rates, the flat surfaces will ultimately bound the crystal. In essence, differences in *growth layer topography* reduce the actual *growth* symmetry from 6-fold to 3-fold, and *triangular single crystals* (or at least crystals with 3-fold symmetry) may be formed.[14] Figure 4a,b illustrates this highly original crystal morphology for two polymers the structure of which was reexamined and found to be frustrated: poly(*tert*-butylethylene sulfide) (PTBES)[15] and a polypeptide, poly(L-hydroxyproline).[16]

Single crystals of isotacic poly(2-vinylpyridine) (iP2VP) grown in thin films display even more complex asymmetries (Figure 4d).[17] Three of the six growth sectors are thicker than the opposite ones, and their growth faces are tilted relative to the expected, "normal" (110) crystal plane. The thickening is a postcrystallization process, as indicated by the presence of conspicuous ridges curved inward, toward the crystal center (the edges of the ridges are pinned to the thinner crystal sector boundaries). Clearly, the "longitudinal" chain mobility (along the *c*-axis) varies for one and the same crystal structure and even fold plane. The thickening process indicates that the associated chain-sliding rate depends critically on the layer topography. In addition, the growth faces of the thicker sectors are not parallel to, but are tilted to, the "crystallographic" (110) growth face. The asymmetry of the growth front topography results in different rates of lateral spread and/or reorganization rate in different directions along the (110) growth layer.[17] Note that a similar asymmetry of lateral spread on the growth face has been considered recently by Shcherbina and Ungar[18] to analyze the lenticular or rounded crystal shape of polyethylene and poly(ethylene oxide). This asymmetric growth appears to be a general phenomenon, illustrated in its clearest form with the shape of these iP2VP single crystals. The latter provide an extreme morphological illustration of the lack of symmetry of frustrated polymer structures: both the growth and the thickening processes differ on the front and back sides of one and the same (110) crystallographic growth face with in addition differences in the lateral growth/thickening rates.

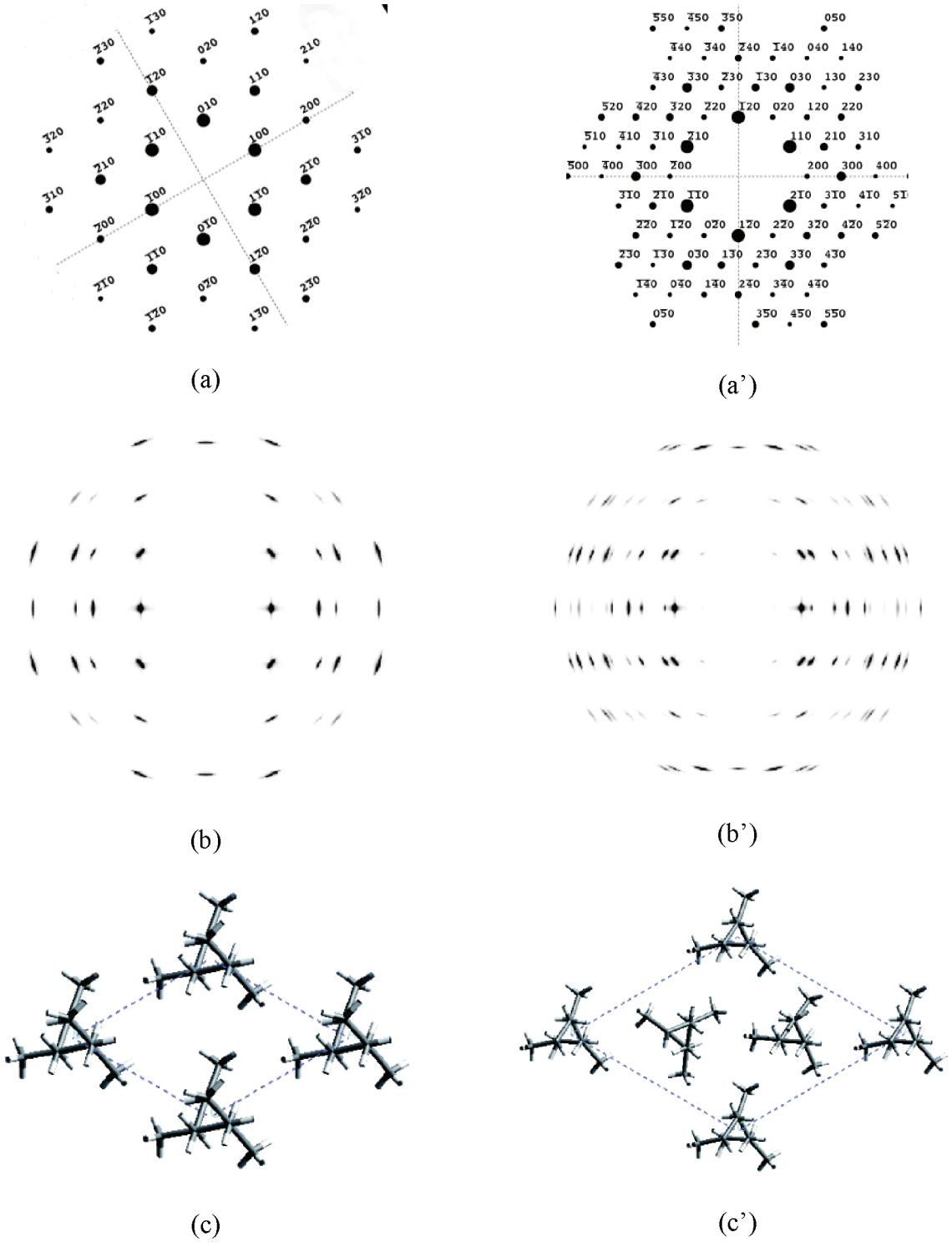


Figure 3. Comparison of one-chain and frustrated structures diffraction characteristics: calculated *hk*0 (single crystal) and fiber diffraction patterns. Left: a hypothetical one-chain unit cell of isotactic polypropylene (not observed) (c). The *hk*0 pattern (a) has been rotated by 30° in order to highlight the analogies and differences with the frustrated structure's one (a′). Right: the frustrated structure of isotactic polypropylene, β phase (c′). In the *hk*0 pattern, note the two reflections between 300 and 030, indexed 210 and 120. These reflections are an easy indicator of the frustrated character of the structure. Note also in (b′) the weakness of the meridional 003 reflection compared to its neighbor 103 (see text).

SELECTED EXAMPLES OF FRUSTRATED CRYSTAL STRUCTURES FOR 3-FOLD HELICAL POLYMERS

Frustrated structures are most frequent for crystalline polymers, either chiral or not, that have a "simple" 3-fold helical symmetry. The first *complete structure determination* was performed on isotactic poly(2-vinylpyridine) (iP2VP),[19] nearly at the same time Toulouse introduced the concept of frustration. *All* the crystallographic and original packing features of frustrated polymer structures presented above were described, including the less favorable interactions of the "frustrated" helix in the unit cell, although the word (that had barely been coined at that time) was not used. Only much later work, performed in

dx.doi.org/10.1021/ma202326t | *Macromolecules* 2012, 45, 2175−2189

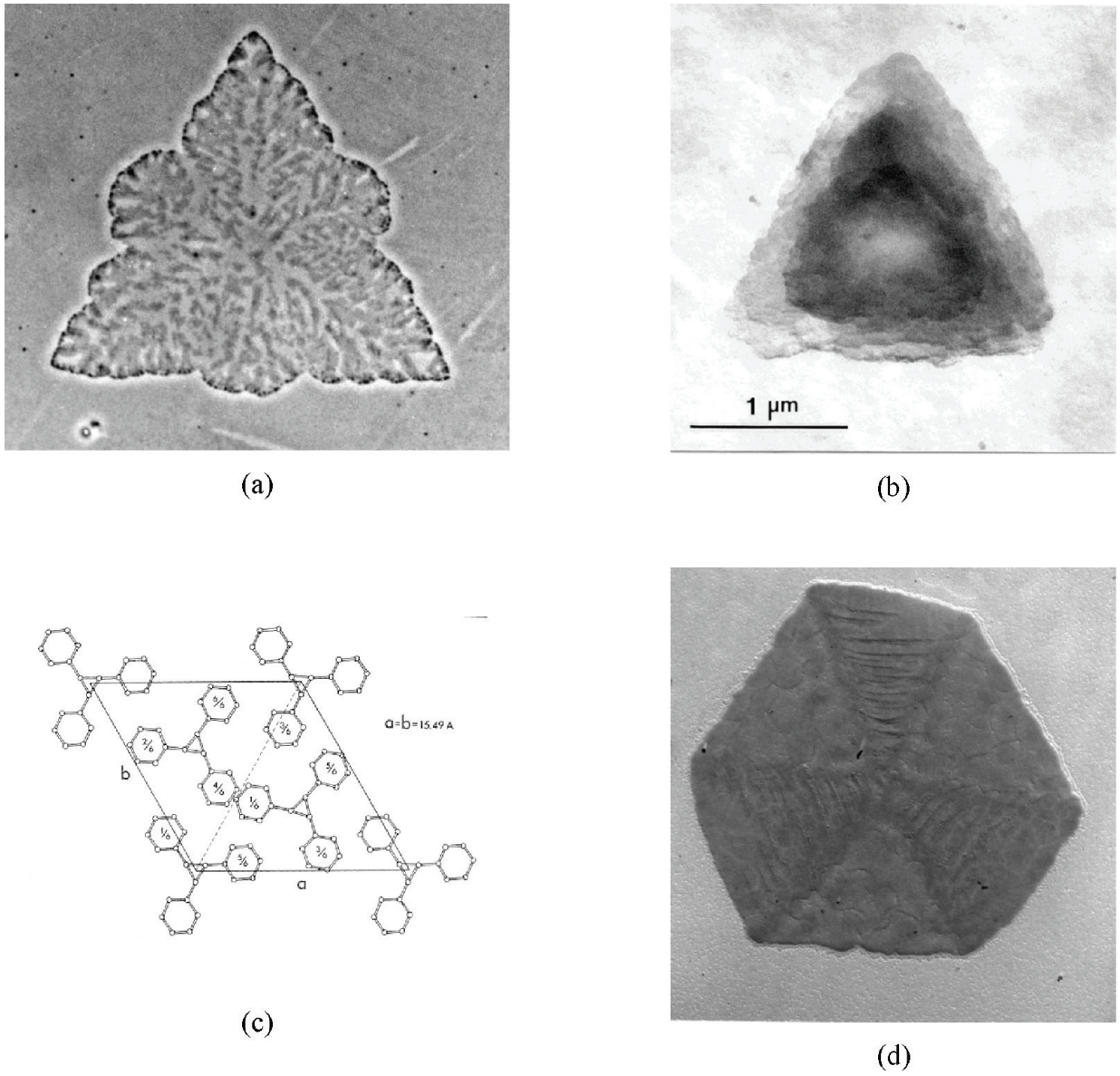


Figure 4. (a) Triangular single crystal of PTBES optical micrograph in phase contrast. Crystal edge size: ≈100 μm. Reproduced from ref 15. (b) Triangular single crystal of poly(L-hydroxyproline). Electron micrograph. Reproduced from ref 16. (c) The original crystal structure of isotactic poly(2-vinylpyridine) determined by Puterman et al., of the North−South−South type. Reproduced with permission from ref 19. Copyright 1977 Wiley. (d) Single crystal of iP2VP grown in thin film at 200 °C. Note the different features of the growth sectors. Three of them have thickened, and their growth front is tilted from the "normal" (110) crystallographic plane (see text). Reproduced with permission from ref 17. Copyright 1999 Elsevier.

connection with the elucidation of the structure of *β*iPP, helped understand that this packing mode is quite widespread in polymers and biopolymers crystallography. Frustrated structures of polymers have been found as the stable crystal phase or metastable polymorph of a number of polymers and biopolymers: different polyolefins, polyesters, a polythioester, a cellulose derivative. Frustration has also been established in a more complex structure of syndiotactic polystyrene, in which three extended chains pack together and form triplets. Finally, frustrated structures do exist for helical polymers that depart significantly from the 3-fold symmetry considered so far. Most representative examples in this area deal with a family of alkyl derivatives of poly(glutamic acid) investigated in the late 1970s and possibly, as developed later, with concentrated liquid-crystalline phases of DNA.

The detailed analysis of all these structures is beyond the scope of this contribution. Only the *β* phase of iPP and the *α*″ "superstructure" of syndiotactic polystyrene (*α*″sPS) are briefly presented. *β*iPP made it possible to *illustrate* by AFM its frustrated structure. *α*″sPS provides a very telling origin of frustration, namely via the interdigitation of notches, as in crankshafts.

Structure of Isotactic Polypropylene, *β* Modification. Although the original characteristics of the structure of iP2VP were established early on, the underlying principles were not extended to other polymer crystal structures, especially to the unsolved ones also based on 3-fold helices. Such an approach might have solved, among others, a "long-standing structural puzzle",[20] namely, the crystal structure of the metastable *β* phase of isotactic polypropylene (*β*iPP), first observed back in 1959.[21] An excellent account of the problems raised by the *β*iPP

dx.doi.org/10.1021/ma202326t | *Macromolecules* 2012, 45, 2175−2189

structure is given in the review of Brückner et al.[22] that was written prior to the analysis of this phase. βiPP cannot be oriented in fiber form by mechanical means, as it converts to the more stable αiPP. The chain conformation was known to be the "standard" 3-fold helix of αiPP. Single crystals of βiPP and their *hk*0 diffraction patterns indicated some form of hexagonal or related unit cell. These patterns helped Turner Jones[23] to discard various unit cells that had been considered in earlier[24] and in her initial works. Different available models of βiPP have been used in an analysis of the mesomorphic phase of iPP,[25] but the detailed packing of the helices in the unit cell eluded analysis for 35 years(!).

Two teams proposed independently the correct answer. In the model of Meille et al.[26] frustration is implicit, whereas the model initially outlined by Lotz et al.,[27] and later refined,[28] was introduced within the more general concept of frustration. The experimental approaches are different. Meille et al. combined electron diffraction patterns of single crystals and powder X-ray diffraction patterns; in addition, an oriented X-ray pattern was obtained from the outer part of a βiPP spherulite grown in a temperature gradient (the radial *a**-axis is the "fiber" axis). The approach of Lotz, Dorset, and collaborators relies mostly on electron diffraction of single crystals and of epitaxially crystallized films of βiPP (Figures 5a and 5b, respectively). The electron density map derived from the resulting complete set of 3D diffraction data illustrates the possibilities of single crystal electron crystallography. It highlights the different azimuthal chain settings, thus confirming the novelty of the structure (Figure 5c).

βiPP, as many other frustrated polymers, displays structural disorder, as indicated by the conspicuous streaks in the *hk*0 electron diffraction pattern, leading to a spectacular "David star" pattern (Figure 5a). The structural disorder has different origins: the usual possibility of statistical presence of up and down pointing helices at any helix site affects the interactions with neighbor helices and thus the azimuthal setting(s). This issue has been explored by packing energy analysis by Ferro et al.,[29] who also established that the frustrated structure is more stable than the standard, nonfrustrated trigonal unit cell. Such an analysis is important since a more or less random arrangement of up and down oriented stems (anticline stems) is imposed by chain folding and by a conformational restriction on possible folds specific to isotactic polyolefins.[30] Chain folding imposes a binary rhythm (up−down−up−down) in a crystal structure that is based on a unit cell with three chains, which precludes regular alternation of up−down chains at crystallographically equivalent sites. In effect, chain folding introduces an extra frustration to the structure (of the "disorder" type in Toulouse's analysis) independent of the one considered so far. In addition, since isotactic polypropylene is a chiral but racemic polyolefin, "mixed" crystals made of domains with left- or right-handed helices separated by twin/antiphase boundaries are most likely.[31] They introduce an additional symmetry, resulting in a hexagonal rather than a triangular crystal shape.

βiPP provides also an unusual opportunity to *image* the frustrated nature of its chain packing.[32] In epitaxially crystallized films, the contact plane is (110): the sequence of three helices with different azimuthal settings characteristic of frustration lies parallel to the substrate. Dissolution of the substrate exposes these helices, the surface of which can be probed by AFM. For e.g. a NSS setting of the chains, one row of methyl groups of the N chain sticks more out of the contact plane and should be better imaged than the lower methyl groups of the helices oriented SS. AFM imaging shows indeed rows of methyl groups

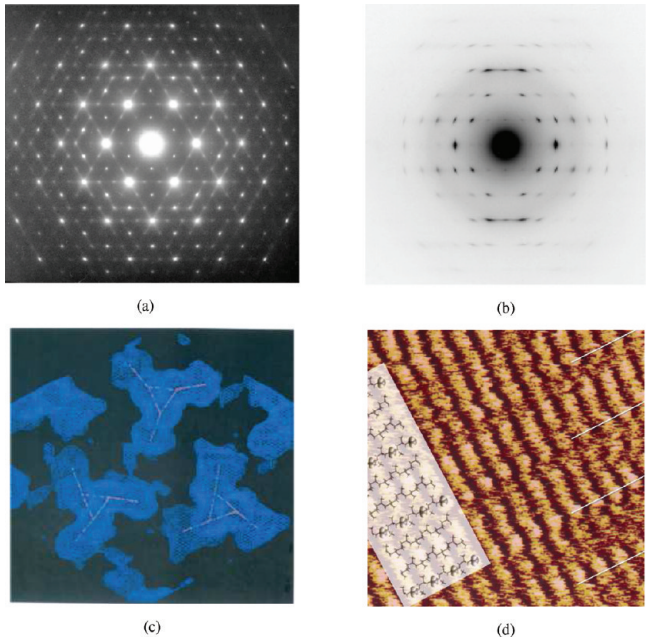


Figure 5. Frustrated crystal structure of isotactic polypropylene (βiPP). (a) Single crystal electron diffraction pattern. Note the conspicuous streaking, indicating structural disorder. The pattern has been digitally processed to enhance these weaker streaks. (b) Electron diffraction pattern of βiPP epitaxially crystallized on a βiPP-specific nucleating agent (dicyclohexylterephthalamide, DCHT). The contact plane is (110), chain axis vertical. Note the weakness of the meridional 003 reflection compared to its neighbor 103 ones (see text). (c) Electron density map as seen down the *c*-axis. (b, c) Reproduced with permission from ref 28. Copyright 1998 Elsevier. (d) Atomic force microscopy imaging (*un*filtered image) of the (110) contact plane of isotactic polypropylene in its β phase (best seen at grazing incidence, along the helix axes). The sample was epitaxially crystallized on a β phase-specific nucleating agent, di(cyclohexylterephthalamide). After washing away the substrate, the βiPP (110) contact face is exposed. The helix axes are oriented at 2 o'clock (underlined), with methyl groups 6.5 Å apart (*c*-axis repeat of βiPP) (the molecular model is inserted). Prominent rows of methyl groups (best seen at grazing incidence parallel to the chain axis) are separated by 19 Å, indicating that one helix out of three has a different azimuthal setting, a mark of frustrated structures. Image area size: 75 Å × 75 Å.

6.5 Å apart along the chain axis, with these prominent rows of methyl groups separated by the expected 19 Å characteristic of frustration (i.e., three 6.35 Å interchain distances) (Figure 5d).

Syndiotactic Polystyrene (sPS), α″ "Superstructure". The α″ "superstructure" of syndiotactic polystyrene (α″sPS) of interest in the present context is based on all-trans TTTT chain conformations. As initially established in the early 1990s,[33] it has a very large trigonal unit cell ($a = b = 26.26$ Å, $c = 5.04$ Å) that houses nine(!) chains organized in three "triplets": three chains are aligned parallel to each other, with the backbone oriented inward, and the benzene rings oriented outward. The triplet is not a 3-fold helix but has 3-fold symmetry. Formed at low T_c, an α′sPS form with only one triplet per cell may well be a disordered form of the α″sPS.

Determination of the azimuthal orientation of these triplets in the α″sPS unit cell has been a progressive process. In all cases, the crystal structures were based on a scheme of 2 + 1 (in chain axis projection, one triplet is antipolar to the two others). The initial high symmetry of the model[33] was progressively reduced,[34] leading ultimately to a frustrated packing mode that accounts for the very detailed single crystal electron diffraction data (Figure 6a,b).[35]

dx.doi.org/10.1021/ma202326t | *Macromolecules* 2012, 45, 2175−2189

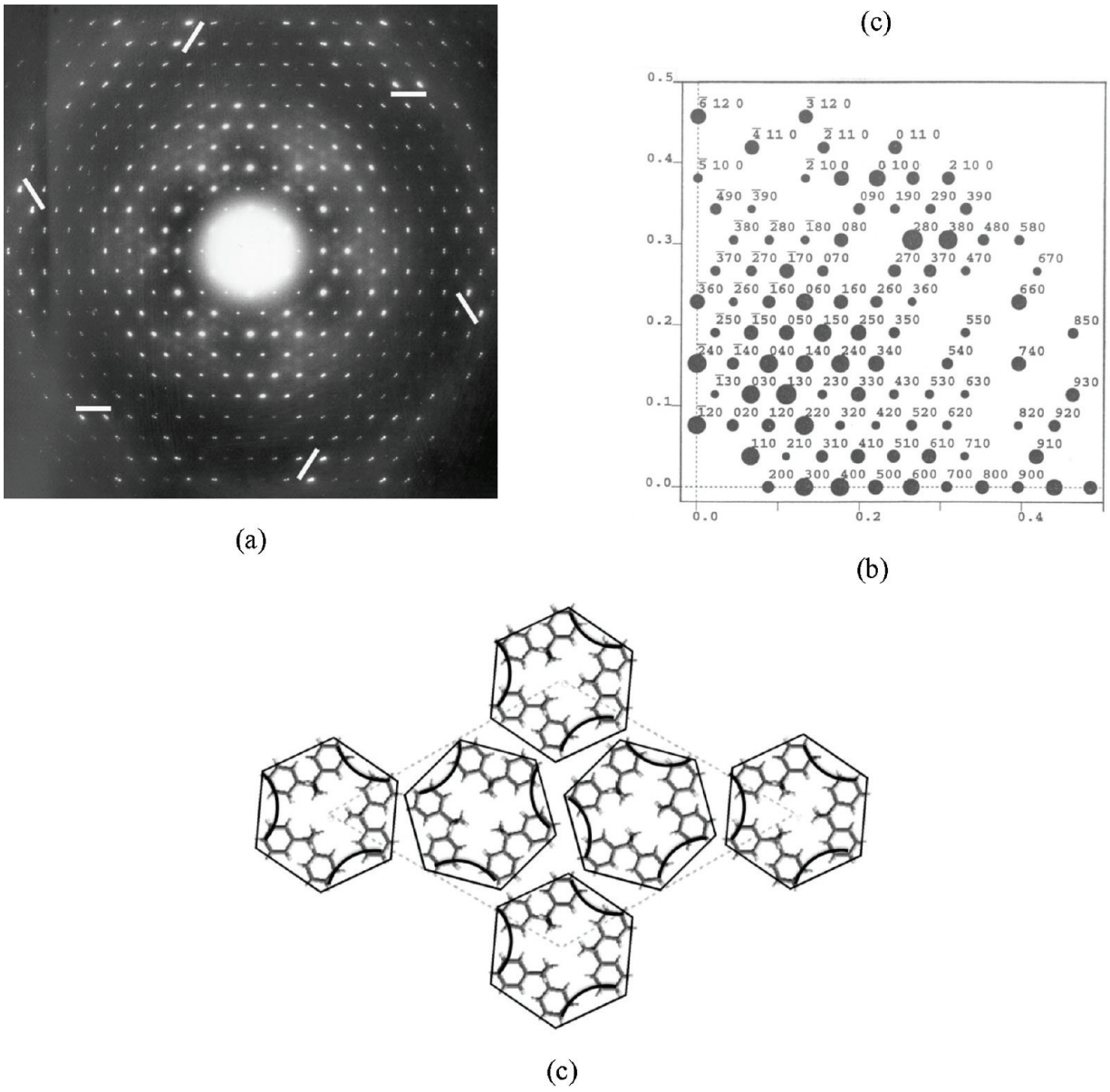


Figure 6. Frustrated structure of syndiotactic polystyrene, α'' form (α''sPS). (a) Electron diffraction pattern of an α''sPS single crystal. Two strong reflections indexed as 280 and 380 (cf. part b) are underlined. They highlight the fact that the diffraction pattern lacks 2-fold symmetry. (b) Calculated $hk0$ single crystal pattern of α''sPS using the model of frustrated structure shown in part c. Note the overall agreement with the experimental pattern, as illustrated by the strength of the 280 and 380 reflections. (c) Frustrated crystal structure of α''sPS. Note the interdigitation of notches of the two central triplets of helices (at the center of this cell) and the different azimuthal setting of the "frustrated" triplet (located at the corner of the cell). (a, b) Reproduced from ref 35.

The unit-cell structure (Figure 6c) is determined by the fact that the six benzene rings lining the outside of the triplet form a near-hexagonal, but not exactly a hexagonal pattern. Indeed, neighbor benzene rings are either linked to different backbones or linked to the same backbone. The triplet faces are thus alternating notches and more flat sides. An efficient packing mode implies optimized interdigitation of the notches, much as in crankshafts. Given the 3-fold symmetry of the triplet, this generates a honeycomb web of favorable notch−notch interdigitations, which leaves aside the corner triplet(s) in Figure 6c. No notches face it, with which it could interact. It must therefore adjust to a less favorable environment, reflected by its different azimuthal setting. Note that in view of the notch−notch interactions all the triplets of the honeycomb lattice are rotated in the same direction, either clockwise or counterclockwise. This is consistent with the asymmetric diffraction pattern of the single crystals produced at high T_c (Figure 6a). For lower T_cs, this asymmetry is lost, which suggests the existence of small domains separated by twin/antiphase boundaries. In an elegant electron microscopy study, Pradere and Thomas[36] imaged these domains, only a few to ten nanometers in size, and associated their presence with that of streaks and diffuse spots in the diffraction pattern.

MOLECULAR AND STRUCTURAL FEATURES COMPATIBLE WITH FRUSTRATION

The resolution of the βiPP structure within the frame of the frustration concept opened the way to a reanalysis of many

dx.doi.org/10.1021/ma202326t | *Macromolecules* 2012, 45, 2175−2189

earlier structures. It also triggered further studies on poorly understood systems. Some of these structures have been analyzed in detail. For others, only their frustrated nature has been established so far, on the basis of their characteristic diffraction features. Representative examples are provided in Figure 7. More need to be investigated. However, the variety of

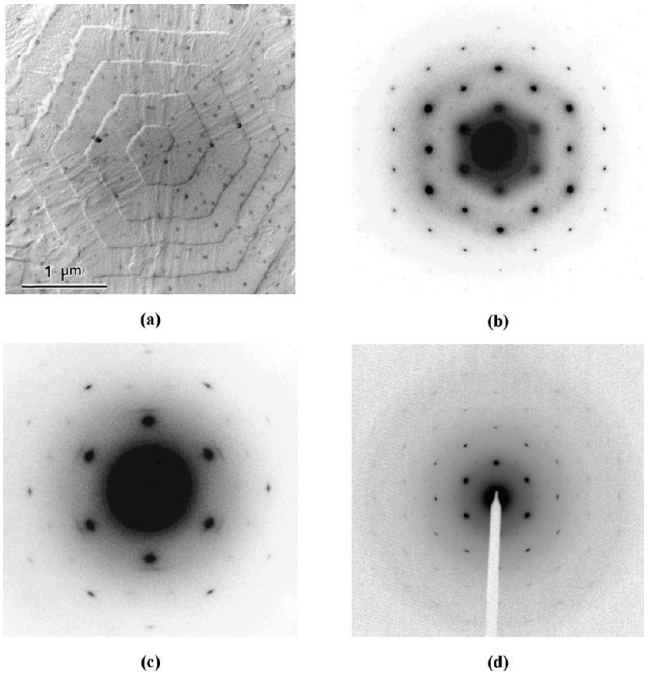


Figure 7. Evidence for frustrated structures. (a) Single crystal (screw dislocation) and (b) electron diffraction pattern of a single crystal of triethylcellulose. Cell parameters: $a = b = 15.64$ Å, $c = 15$ Å. (c) Diffraction pattern of a single crystal of poly(propylene−carbon monoxide) (Pro-CO). Note the characteristic set of reflections indicating frustration. The arced outer "satellites" of the inner 110 reflections are indexed 111. They show up because the crystal is bowl-like and help determine the *c*-axis repeat distance. (Cell parameters: $a = b = 10.74$ Å, $c = 9.17$ Å) Note that a similar pattern (without the 111 reflections) has been published recently by Yoshioka et al.[37] (d) Electron diffraction pattern of a single crystal of the frustrated β phase of poly(1,3-dioxolane). Cell parameters: $a = b = 8.07$ Å, $c = 29.55$ Å.

polymers that display frustrated structures should make it possible to assess the molecular and/or conformational features that are compatible with or induce frustrated packing schemes. As will be seen, this is not so: at this stage, there appears to be no clear rule emerging from the set of available data. This applies to the molecular features to be analyzed first, but also, less expectedly, to the 3-fold helical conformation.

Considering first the 3-fold helices and their molecular features, the *compactness and rounded shape of the side chains* were emphasized in the derivation of the frustrated structure of Figure 2. βiPP and poly(*tert*-butylethylene sulfide) (PTBES) (Figure 4a) fit in this scheme. They both have a short helix axis repeat distance ($c = 6.5$ Å) and "round" methyl groups (diameter 4 Å) or *tert*-butyl groups attached directly to the backbone (i.e., no conformational freedom except for rotation around that bond).

However, *polymers with longer side chains* adopt frustrated packings. Most illustrative is a work in progress on isotactic poly(5-methylhexene-1) (P5MHex1). This polymer adopts the classical 3-fold helix of polyolefins ($c = 6.5$ Å) and crystallizes in a unit cell that was described[38] as orthorhombic with two 3-fold helices per cell. However, the *a*- and *b*-axes are in the characteristic $\sqrt{3}$ ratio which suggests some form of trigonal packing. We have synthesized again this polymer, grown single crystals, and obtained the characteristic *hk*0 diffraction pattern of frustrated structures.[39] Moreover, the next member of this series, isotactic poly(6-methylheptene-1) (P6MHep1), crystallizes in a unit cell essentially similar to that of P5MHex1[38] that may well, also, be reinterpreted as a frustrated structure. The length of the side chains is not therefore a decisive (or a prohibitive!) feature that can favor or discard frustrated structures.

The density of favorable pair−pair interactions along the helix axis appears also *not* to be a major criterion. Frustrated structures are observed for polymers with very long *c*-axis repeat distances. Two examples may be cited: (1) Triethylcellulose (but not the other cellulose derivatives) crystallizes in a frustrated structure. Solution grown single crystals display again the tale-telling *hk*0 diffraction pattern (Figure 7a,b). The chain axis repeat distance is quite large (15 Å), whereas the interhelix distance is only ≈9 Å (no detailed crystal structure analysis yet) (2) In collaboration with Pr. Prudhomme,[40] we analyze an elusive crystal structure of polydioxolane, known to exist for 50 years, but not yet determined.[41] Poly(1,3-dioxolane) $(CH_2-CH_2-O-CH_2-O)_n$ crystallizes in its stable orthorhombic form ($a = 9.07$ Å, $b = 7.79$ Å) as a very "loose" helix with two monomer units and a *c*-axis repeat distance of 9.85 Å.[42] Strikingly, X-ray fiber patterns of these same authors indicate that the elusive form has a chain axis repeat distance *exactly triple* that of the stable form (29.53 Å). The corresponding single crystals display "frustrated" *hk*0 diffraction patterns (Figure 7d). It seems that the stable form structural/conformational unit is repeated three times in the frustrated structure. Nevertheless, and given the flexibility of the chain, it appears surprising that some shorter conformational repeat unit is not selected.

The 3-fold symmetry has so far been considered as a prerequisite in the formation of frustrated structures, even if this feature may appear released when dealing with very "loose" helices (e.g., poly(1,3-dioxolane)). However, this condition may not even be relevant.

The extensive work of Japanese colleagues on poly(glutamic acid) (PLG) γ-alkyl ester derivatives started in the late 1970s provides by far the most detailed structural study available on frustrated polymer structures (even though reference to frustration was not made).[43−46] Moreover, and this is unusual in this context, a series of alkyl derivatives display the frustrated structures: the alkyl chains range from methyl to lauryl (1 to 6 carbon atoms). Most of these PLG esters have an "anomalously disordered" structure at low temperature. At a higher temperature T_2 an "anomalous, thermally reversible crystal transition" takes place.[47] T_2 decreases with the alkyl length: 115, 64, 23, and −5 °C for the ethyl, propyl, butyl, and allyl, respectively. The diffraction pattern is sharper; three chains are in a trigonal unit cell that is "peculiar in the normal crystallographic sense". The associated activation energies are much smaller than the energies of the β relaxation (glass-like transition temperature of the side chains): 80−315 J/mol vs 95 kJ/mol, respectively. This crystal phase becomes more disordered at some higher temperature T_3, which leaves a narrow window of stability for the methyl ester (from 170 to 180 °C) but a much wider temperature range (≥100 °C) for the longer alkyl esters. The structure possesses all the features of frustrated structures: trigonal unit cells with three helices per cell "not interrelated by a crystallographic symmetry

dx.doi.org/10.1021/ma202326t | *Macromolecules* 2012, 45, 2175−2189

element" (e.g., for PPLG: $a = b = 24.3$ Å, space group $P3_2$) (Figure 9a). The c-axis shifts, and azimuthal rotations of the two central helices relative to the corner one are relatively constant: ±2 Å and ±11°−12°, respectively.

The helix conformations depart slightly from the standard 18_5 α helical geometry (3.60 residues per turn); they may be either 40_{11} or 69_{19} (3.636 and 3.6315 residues per turn). As pointed out by Sasaki et al., only the latter would be compatible with trigonal symmetry (23 residues in the asymmetric unit).[47] If this symmetry is an important ingredient/trigger of frustration, the repetition of like "frustrated" interactions in these irrational helices would be spread over about 100 Å c-axis lengths! For the "simpler" α helix with 18 residues in 5 turns, they would be distributed over five helical turns (or 27 Å). Sasaki notes also that the ordered trigonal frustrated phase is favored at higher temperature by side chain flexibility and the enlarged main chain motion "that smear the side chains interactions".[47] Relatively simple structural models (by present standards) were explored that indeed suggest that the frustrated packing is (marginally however) favored over other, hexagonal or orthorhombic, packing modes.

These early studies on PLG esters show that (1) frustrated structures can be formed with irrational helices even though the helix−helix interactions involved are spread over very large distances along the helix axis. On this basis, some irrational helices may reach via minor adjustments, 3-fold symmetry (in the present case: 18_5, 69_{19}). (2) The formation of frustrated structures is triggered by relatively small differences in interhelical interactions and results in a limited gain in overall free energy of the system. Smeared out and weakened interhelical interactions (due to chain flexibility and/or temperature) generate a smooth energy landscape and thus allow chain mobility and reorganization in a complex frustrated structure. In the present systems, as summarized by Ungar,[48] "the periodic potential of the rigid helical backbone is apparently screened off at sufficiently high temperatures by the molten aliphatic sheath; hence the chains effectively act as smooth cylinders and pack on a hexagonal lattice"—but here with the added feature of frustration.

We will return to this theme in a next section, when suggesting probable frustrated structures of concentrated phases of DNA.

FRUSTRATED STRUCTURES OF POLYMERS: BACKGROUND AND POSSIBLE FURTHER CONSEQUENCES

Recognition of frustrated polymer crystal structures provides a useful, common structral ingredient to analyze results that were at times considered as puzzling or as mere oddities. Admittedly, establishing the necessary correlations among earlier works, sometimes on different materials (e.g., polypeptides vs polyolefins), was not immediate. Insufficient awareness of past works delayed the resolution of e.g. the β structure of isotacic polypropylene and left to later authors (including the present one) the burden of reinventing or rediscovering "original" packing schemes—that had already been described in detail for iP2VP and PLG esters. The major purpose of this contribution is therefore to raise this awareness. In doing so, we discuss the filiation between these frustrated polymer crystal structures and the considerable body of knowledge available on metallic materials, point out the link with structural studies of DNA columnar assemblies and examine to what extent the present frustrated structures can help gain original insights into polymer crystal structure and crystal growth process.

Frustrated Polymer Structures: An Example of "Large Cell Crystals". Frustrated polymer crystal structures are characterized by cells larger than would be needed, were only simple crystallographic symmetry elements involved. Such a situation is not new. It has many analogues in simple metallic systems. As summarized by Sadoc and Mosseri,[3] these systems have in common to include "a periodic network of defects", leading to large cells that include and encode the defects. Curiously, the paradigmatic examples of this type of frustration are found in close-packed metallic systems for which, given the round shape of metal atoms, mostly "simple" base- or face-centered-cubic unit cells would be expected. In these large cells, frustration is manifested in the three-dimensional organization by the existence of two or even several different interatomic distances and/or atomic coordination numbers. The "disclination networks" (networks linking the unusually coordinated, "frustrated" sites) are complex polyhedra, sometimes intertwined.

Examples of complex structures are found for cubic phases (sometimes slightly distorted) of pure metals that bear some relationship with the quasi-crystals discovered later. The cell of β-tungsten is a classical example of a Frank and Kasper, tetrahedrally close-packed phase. It contains eight atoms, six of which have a different coordination number than the two remaining ones (the six atoms are arranged in pairs on the faces of the body-centered-cubic cell). The β-uranium tetragonal cell contains 30 atoms, with five different types of sites. The α-manganese cubic cell contains 58 atoms, with four different atomic positions and coordination numbers. Whereas such complex structures are more frequent in metallic alloys (with different atomic radii), their occurrence in pure monatomic metals made of "round" atoms still remains a puzzle and may derive from "subtle electronic properties".[3] In metals also, the physical origin of frustration remains a perplexing issue.

The frustration schemes in these metallic systems are thus much more varied than for polymers. By comparison, the "large cells" of the latter appear as modest illustrations of the impact of frustration. In polymers, the frustration involves mostly the azimuthal setting and c-axis shifts of the chains and thus can be analyzed via their 2D c-axis projections; the honeycomb is the only "disclination network" geometry observed so far. However, by analogy with the metals, one may ask whether synthetic polymers can also provide examples of cells with ingredients of frustration that would generate larger cells. No clear example is available yet. One possible candidate could be the structure of β poly(p-xylylene) examined by Isoda et al.[49] The trigonal cell contains 16 chains with, in the model considered so far, one site only to which no definite azimuthal chain setting can or has been assigned. This "disclination network" implying a single chain defect site every four chain sites apart in every direction appears difficult to explain on the basis of "simple" crystallographic symmetry and stem−stem interactions. A more complex structural pattern, possibly involving some form of frustration (suggested by the trigonal cell geometry, but admittedly hardly compatible with the 16 chains cell content), might possibly overcome this difficulty.

Reevaluation of Crystal Structures in the Light of Frustration: Concentrated Aqueous Phases of DNA. The recognition of frustrated structures in polymers has led to a fruitful reexamination of several earlier crystal structure determinations based on crystallographic and in some cases on morphological indicators (Figures 4 and 7). This process is not yet over. There are probably several or many more crystal structures that fit in this scheme. The prime targets are of

course chiral polymers or biopolymers with known three chains trigonal unit cells. Besides the synthetic polymers, and among other examples, some polysaccharides structures should be reexamined.[50]

A further example is provided by some *concentrated aqueous phases of DNA*. As summarized by Livolant and Leforestier,[51] DNA forms a number of liquid-crystalline and crystalline phases in concentrated aqueous solutions. They result from the fact that the best packing of DNA isochiral double helices implies a slight angular twist α. The nature of the high-density phases depends on the DNA concentration c_{DNA}, which can be translated in interhelical distances d_{DNA} (Figure 9). For d_{DNA}< 31.5 Å, DNA "refuses to twist":[52] the strands are parallel (α = 0°), and the structure becomes a columnar liquid-crystalline phase. In a small, more dilute part of that domain (31.5 Å < d_{DNA} < 29 Å), the order is only two-dimensional but becomes three-dimensional in a wider, higher concentration range (29 Å < d_{DNA} < 23.7 Å). At still higher concentrations (for 670 mg/mL < c_{DNA}< 1055 mg/mL), the 3D structure converts via a nucleation and growth process of small domains to an orthorhombic unit cell, with different interhelix distances. The 3D phase, analyzed by Durand et al. by X-ray fiber diffraction,[53] has a hexagonal/trigonal unit cell with three double-stranded DNA helices; the two central helices are shifted by ±c/6 relative to the corner one (Figure 8b). The authors take the pitch P of the helix as the c-axis parameter, even though the helix is irrational, and treat it as a continuous helix. With increasing concentration, this helix pitch decreases continuously from some 35 to 30 Å, although DNA remains in the B form, which supposes a constant axial translation per residue of 3.36 Å. The number of nucleotides per helix turn thus decreases continuously from 10.3 to 9.0 base pairs per turn.

Strey et al.[52] have reported on a similar structure. They describe it as a line hexatic phase characterized by "long-range hexagonal bond-orientational order, long range nematic order, but liquid-like, i.e. short-range, positional order". "Chiral angular frustration in a hexagonal lattice" is thought to be responsible for the formation of this different phase. However, this phase is analyzed on the basis of a distorted hexagonal unit cell perpendicular to the long axes, i.e., as for an orthorhombic cell geometry (Figure 8c). Lorman et al.[54] further develop this scheme when analyzing "positional, reorientational and bond orientational order in DNA mesophases" by considering their transverse polarization vectors (Figure 8d). They propose "various scenarios for going from the hexatic phase through the distorted hexatic phase to the crystalline phase with orthorhombic unit-cell".[54]

The structural features of the 3D phase of DNA as characterized by Durand et al. (trigonal cell geometry, three DNA double helices, symmetrical ±c/6 axis shift of the central helices) strongly suggest a frustrated packing. In this analysis, the only missing feature is the different azimuthal settings of the helices, which results from the continuous helix approximation

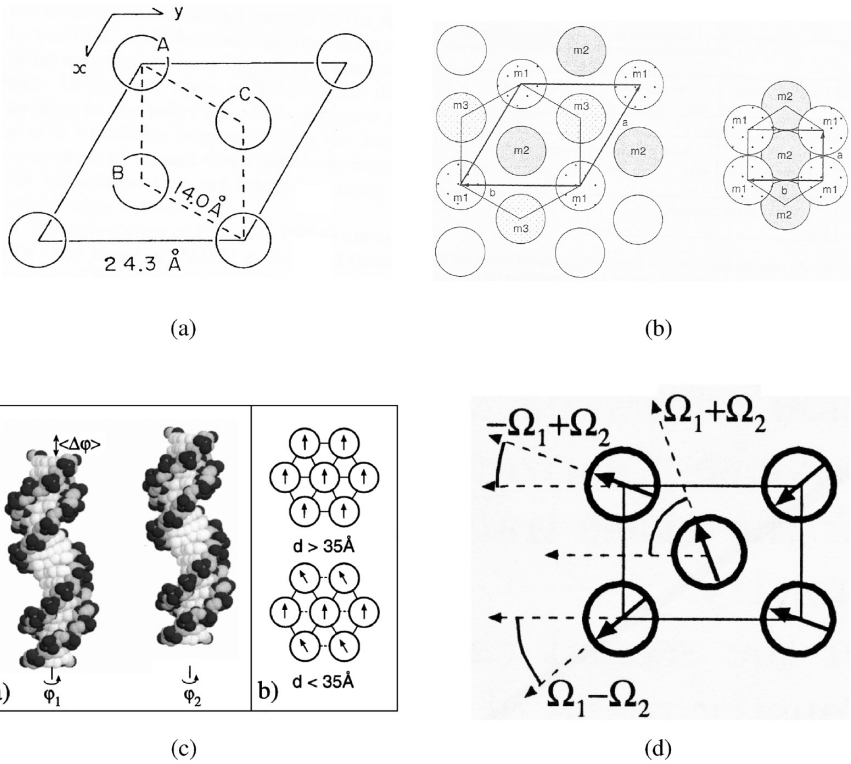


Figure 8. Models of polypeptides and DNA phases. (a) Structure of poly(propyl-L-glutamate) as determined by Sasaki. A, B, and C are α helices. B and C are shifted by 2 Å along the c-axis and rotated by ±12° relative to A. Reproduced with permission from ref 45b. Copyright 1991 John Wiley and Sons. (b) Schematic representation of the 3D trigonal (left) and orthorhombic phases of concentrated solutions of DNA in water. In the trigonal cell, helices m2 and m3 are shifted along the c-axis by c/6 (c = pitch of the double helix). Reproduced with permission from ref 51. Copyright 1996 Elsevier. (c) Illustration of the packing and azimuthal settings of DNA double helices for the cholesteric phase (d > 35 Å) and the 3D trigonal phase (d < 35 Å) considered by Frey et al. Note, in the latter case, the differing azimuthal orientations in the three densely packed planes. Reproduced with permission from ref 52. Copyright 2000 the American Physical Society. (d) Azimuthal settings considered by Lorman et al. for the orthorhombic phase of more concentrated DNA phase (illustrated in part c for d < 35 Å). Only two orientations of helices alternate in any dense plane. This scheme would not be suitable to describe the trigonal unit-cell. Reproduced with permission from ref 54. Copyright 2001 the American Physical Society.

dx.doi.org/10.1021/ma202326t | *Macromolecules* 2012, 45, 2175−2189

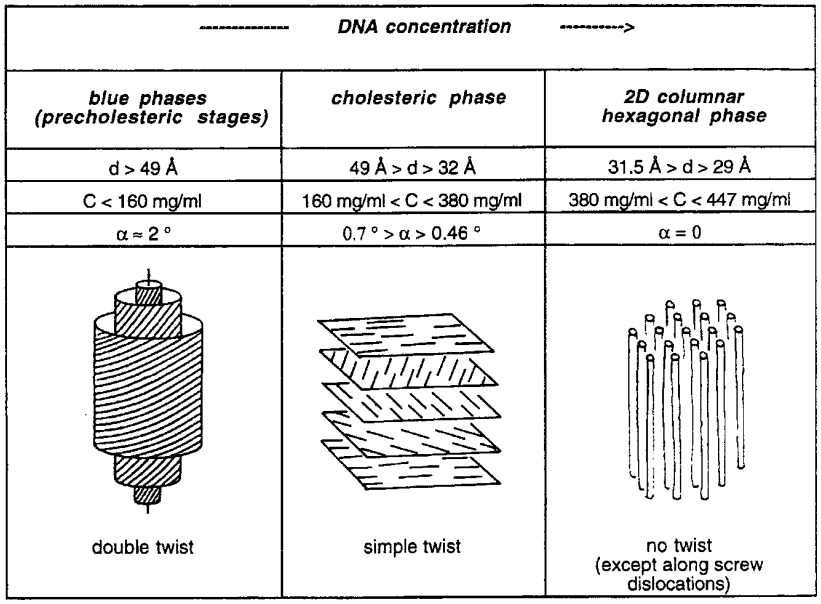


Figure 9. "Phase diagram" of aqueous DNA solutions as a function of DNA concentration. Reproduced with permission from ref 51. Copyright 1996 Elsevier.

used by these authors. The models proposed by Strey et al. and Lorman et al. do emphasize the possible impact of different azimuthal settings—in the latter case, applied to the orthorhombic unit cell. However, even if transferred to the 3D hexagonal packing, the suggested set of orientations does not account properly for the three-sites unit cell. For both structures, in any row of close-packed helices, only two azimuthal orientations of the polarization vector (or DNA helices) alternate (in one set of rows, they are even parallel) (Figure 9c,d). This feature is at odds with one of the unit cell's major characteristics, namely the presence of three DNA helices in the cell. A sequence of *three* different azimuthal orientations in any one row of close-packed helices, one of the trademarks of frustrated crystal phases, appears more logical and strongly suggests that this 3D phase of DNA displays geometrical frustration. Further X-ray diffraction investigations on better oriented samples appear necessary. In particular, the transition from the columnar hexagonal phase generates a waviness of the final 3D structure. Similar transitions produced on DNA solutions spread on orienting polymer substrates (e.g., rubbed PTFE or polycarbonate) may limit or even overcome this undesirable disorientation. It is clear however that for such irrational helices the discrimination between rotations and shifts of helices (to stick with the derivation shown in Figure 2) is difficult: in the limit of continuous helices (as assumed by Durand et al.), shifts along and rotations about the helices axes are equivalent.

A similar analysis may be held for a crystal structure of a reovirus double-helical ribonucleic acid analyzed by Arnott et al.[55] Form B (at 75% relative humidity) has a trigonal unit cell with three helices per cell, possibly organized in "triplets". However, the exact helical conformation raises a problem. A meridional reflection strongly suggests a 10-fold helix symmetry, but geometrical and packing considerations would privilege 11-fold symmetry "if one accepts the idea that RNA molecules should crystallize with only one intermolecular stereochemical relation".[55] Relaxing the latter condition as is observed in frustrated structures may be a possible way to relieve this apparent conflict and also to consider a more logical hexagonal packing of the helices.

For these hydrated phases, the DNA helix conformation is clearly not the trigger of the suggested frustrated packing. Nowhere is the 3-fold helix symmetry involved; the progressive shortening of the helical pitch indicates even a continuous change in helix symmetry. Other causes and/or contributing factors must be at play. In this respect, the specificity of the water concentration window and of the transition region suggests that a network of relatively weak intercolumnar interactions, possibly mediated by the hexagonal environment, may contribute to generate a frustrated packing: at such interhelical distances "the details of the chiral double-helical structure come to be sensed in molecular interactions".[56] At this stage, and as already suggested, the formation of "water-mediated structural forces"[57] is probable. In this analysis, the network of hydrogen bonds in the water jackets would impact (and/or be impacted by) the "frustrated" DNA azimuthal settings (see also the Note Added in Proof).

Frustration as a Probe To Evaluate Crystallization Processes: Crystal Growth, Crystal Transformations. *Crystal Growth.* In view of their striking lack of symmetry, frustrated crystal structures are very effective probes in the analysis of crystallization processes. Crystal growth involves by necessity some form of interaction of an incoming stem with growth faces. For frustrated structures, the latter have highly unconventional surface topographies. The impact of this lack of symmetry has been illustrated with the triangular shape of PTBES and poly(hydroxyproline) single cystals and even more strikingly with iP2VP (Figure 4). These crystal morphologies have been used as evidence in an ongoing debate over different possible crystallization schemes in polymers (formation of an intermediate loosely ordered phase followed by crystal reorganization versus a more traditional "nucleation and growth" process). The crystal shapes of frustrated structures appear to support the latter process. They indicate that very short-range interactions are involved not only in the initial deposition (the so-called secondary nucleation) but also in the lateral spread: the stem probes its future environment, and as a result, the rate of deposition depends on the crystal face topography. Further examples of crystal growth asymmetries with different materials should be obtained, which will either support or limit

the impact of these analyses. Whatever the outcome, the lack of symmetry characteristic of frustrated polymer structures provides a very local probe to evaluate crystal growth processes.

Crystal–Crystal Transformations. Frustrated crystal structures are frequently metastable phases and as such may be intermediate, transient phases in the crystallization process. As illustrated with poly(L-glutamate) esters and DNA, for "rigid" polymers the domain of stability may be quite large and the formation of these phases easily established. They may also intervene in the crystallization process of more flexible polymers.

The metastable, frustrated phase of poly(1,3-dioxolane) is produced first and transforms into the orthorhombic stable form by two different processes: during growth via a growth transition and in a delayed ("a few weeks" at room temperature) crystal–crystal transformation.[41,42] A similar process could remain unnoticed if the transformation times are shorter and are "merged" in the overall crystallization process. It would however leave a structural trace: conversion from a trigonal to, say, an orthorhombic unit cell is likely to result in a more disordered phase and to generate three different orthorhombic unit cell orientations.

The frustrated structure of PLLA may be involved in such a crystallization process. At low crystallization temperatures (T_c < 95–110 °C), the growth rate versus T_c curve shows a distinctive hump, suggesting that some different crystal form is produced. Also, the crystal structure, although of the stable α form, is distinctly disordered (thus its different name, α'). Yasuniva et al.[59] suggest that crystallization takes place first in the transient frustrated β phase, before conversion to the α' phase. Our own results favor such a mechanism: the diffraction pattern of the outer part of a spherulite produced at 90 °C indicates no clear radial growth direction, but rather is fairly symmetric, as would be expected after such a hexagonal to orthorhombic transformation. Along a similar line, the Raman spectroscopic analysis reported recently by Kalish et al.[60] suggests that the disordered α' phase contains some 80% of the 10_3 α helical conformation, "with randomly distributed tg′t-3_1 units" that, in the present analysis, could represent remnants of the transient frustrated β phase.

Other examples of such processes may well have remained unnoticed. They would in any case involve only chiral polymers: preservation of the helix chirality is essential in the transformation. Similar processes cannot take place for frustrated chiral phases of conformationally racemic polymers: transformation from a chiral βiPP to a racemic αiPP phase must imply (at least local) melting–recrystallization. This condition is relaxed for polydioxolane, since the final form, after the transformation, is based on a 2_1 "helix" symmetry that can be reached from either a right- or a left-handed helix.

■ CONCLUSION

Frustration is a fairly widespread phenomenon in polymers and biopolymers crystallization. It refers however to two different structural and length scales.

For years, frustration in connection with polymers has remained in the context of disclinations between single crystalline domains. In this case, "the interactions which compete on short distances in the stability of some material lead to local configurations of molecules which are incompatible on large scales".[4] The slight angular twist of DNA helices cannot be relieved locally but cannot also extend over all space because the bend energy becomes prohibitive—thus the formation of blue phases and cholesteric phases with dislocation networks and defective boundary layers.

On the opposite, the frustration mostly considered in this contribution is definitely a local, *crystallographic feature* and must be analyzed at the *unit cell* level. It is a simple case of *geometrical frustration*, compatible with the formation of single crystals. Privileged interactions are established between two neighboring, frequently 3-fold helices that are arranged in a hexagonal close packed lattice. These privileged interactions can extend over all space, in a honeycomb lattice *but they are compensated locally* by an added discomfort of one other neighboring stem. The network of "dislocations" matches and is included in the crystallographic network. The crystal structure is described as a trigonal cell with three chains, space group $P3_1$ or $P3_2$. The three *isochiral* chains are not related by any element of symmetry, which allows for different azimuthal settings and/or relative shifts along the chain axis. Since the frustrated packing implies isochirality of the helices, it applies to biopolymers with 3-fold helical conformations (poly(L-lactic acid) or poly(L-hydroxyproline)) or a cellulose derivative (triethylcellulose). More surprisingly, frustrated structures are also observed in a family of α-helical poly(L-glutamic acid) esters and, probably, concentrated phases of DNA in water, i.e., for helical conformations that are only remotely connected or plainly differ from 3-fold symmetry.

In view of the diversity of molecular and conformational characteristics of polymers that form frustrated structures, frustration appears as a rather broad possibility. It indicates that the "standard" packing of 3-fold helices in a one chain trigonal cell with $P3_1$ or $P3_2$ symmetry is not necessarily a stable one: interactions between side chains may favor specific rotations and shifts of helices, i.e., may favor frustration. Frustrated structures have been reported or observed for tight and compact helices, for more extended and flexible helices, for short and long side chains, and for loosely packed systems (e.g., solvated systems, or structures with flexible, or molten side chains) in which minor packing energy differences may be sufficient to induce deviations from "standard" crystallographic symmetry. For PLG alkyl esters and hydrated DNA phases with no 3-fold helical symmetry, the helix rigidity seems to be an important component: it induces an extra domain of stability intermediate between the melt (or dilute solution) and the standard crystal structure. As such, these frustrated structures might appear as variants of liquid-crystalline phases ("columnar hexagonal", hexatic) if their specific 3D characteristics are overlooked.

The frustrated structure is, for some polymers, the stable crystal form. In case of polymorphism, it is the lower density metastable phase. Growth transitions and/or crystal–crystal transformations to the stable forms have been documented. The frustrated structures may well act as intermediate, kinetically favored metastable phases in the crystallization process of polymers, as indicated for poly(1,3-dioxolane) and possibly (if on a shorter time scale) for PLLA at low T_c. They are however expected to leave a structural trace and therefore be diagnosed: the transformed crystal would keep a memory of the initial 3/6-fold symmetry of the parent crystal.

In hindsight, it appears surprising that the impact of this specific type of geometrical frustration has been overlooked for so long in polymer crystallography, in spite of earlier, published examples in the field and its widespread occurrence in materials science (e.g., "large unit-cells" in some metals phases). Its belated use as a screening procedure has helped solve or correct several earlier structural analyses of polymers. The list is likely

not exhausted, and further work will assess the full impact of geometrical frustration. The reevaluations completed up to now reveal interesting variants and original features in the structural and morphological details associated with frustration. In turn, the latter provide better insights into the principles governing polymer crystal packing and growth processes.

AUTHOR INFORMATION

Corresponding Author

*E-mail: bernard.lotz@ics-cnrs.unistra.fr.

Biography



Bernard Lotz is Director of Research (Emeritus) at the Centre National de la Recherche Scientifique (CNRS), the french academic organization devoted to fundamental research. He spent his career at the Institut Charles Sadron (formerly Centre de Recherches sur les Macromolecules) in Strasbourg, a laboratory owned and run by the CNRS. He has held a number of positions as a visiting scientist and invited professor in Universities and Research Centers in the USA (ATT-Bell Laboratories, Case Westen Reserve University, University of Akron, MIT), Canada (Université de Montréal), the Far East (Laboratory of Agroenvironmental Sciences, Tsukuba, Japan), and in several European Universities and Institutes. He received the 1973 Prize of the French Polymer Group and the 1989 Fraser P. Prize from the University of Amherst. He has been elected a Fellow of the American Physical Society in 1986 and is a member of the advisory editorial board of several scientific journals. His major research interests include the phase transitions (glass transition, crystallization, and melting) and the structure and morphology of crystalline polymers and biopolymers at different length scales, ranging from the chain conformation and the structure at the unit-cell level to the spherulite and bulk morphology both in their spontaneous state or as modified by appropriate additives. He is the author or coauthor of nearly 300 research papers and book chapters.

ACKNOWLEDGMENTS

I am deeply indebted to the students, collaborators, and many colleagues and friends whose contributions and inputs helped shape the above analyses.

REFERENCES

(1) Toulouse, G. *Commun. Phys.* **1977**, *3*, 115.

(2) (a) Schiffer, P.; Ramirez, A. P. *Comments Condens. Matter Phys.* **1996**, *18*, 21. (b) Ramirez, A. P. *Annu. Rev. Mater. Sci.* **1994**, *24*, 453.

(3) Sadoc, J.-F.; Mosseri, R. *Geometrical Frustration*; Cambridge University Press: New York, 1999; ISBN 0 521 44198.

(4) (a) Kleman, M. *Phys. Scr.* **1987**, *T19*, 565. (b) Kleman, M. In *Liquid Crystallinity in Polymers. Principles and Fundamental Properties*; Ciferi, A., Ed.; VCH: Weinheim, 1991; Chapter 10, pp 365−394. (c) Kleman, M. *J. Phys., Lett.* **1985**, *46*, L-723.

(5) Lotz, B.; Gonthier-Vassal, A.; Brack, A.; Magoshi, J. *J. Mol. Biol.* **1982**, *156*, 345.

(6) Natta, G.; Corradini, P. *Nuovo Cimento Suppl.* **1960**, *15*, 40.

(7) Corradini, P.; Natta, G.; Ganis, P.; Temussi, P. *J. Polym. Sci., Polym. Symp.* **1967**, *16*, 2477.

(8) Corradini, P. *The Stereochemistry of Macromolecules*; Keitley, A. D., Ed.; Marcel Dekker: New York, 1968.

(9) *International Tables of X-ray Crystallography*, 2nd ed.; Hahn, T., Ed.; Kluwer Academic Publishers: Amsterdam, 1989; Vol. *A*.

(10) The terminology describes the azimuthal orientation of the helices in the unit cell by considering the orientation of one of the side chains on a compass.

(11) Lotz, B. *J. Macromol. Sci., Phys.* **2002**, *B41*, 685.

(12) The trigonal cell with $P3_121$ symmetry was also adopted in our initial proposal of the β phase of iPP (ref 27).

(13) Since however 003 and 103 are very close to each other, they are frequently merged in fiber patterns and were indexed in earlier works as 003, which leads to a slight underestimation of the true *c*-axis repeat distance. At this stage a tribute should be paid to Turner-Jones for her work on the β phase of isotactic polypropylene. She indexed correctly the 003 and 103 reflections in the powder pattern (no oriented pattern was available at that time). Noting that the 003 reflection was weaker than the 103 one, she pointed out that the crystal structure must differ from the then known, "classical" hexagonal and trigonal packings of 3-fold helices. Although the structure could not be solved at that time, the diagnosis was correct and supported by later analyses.

(14) It should be noted however that the 3-fold morphological symmetry is not *per se* a property of frustrated crystal structures. Indeed, one chain unit cells with $P3_1$ symmetry also have very different topographies of opposite growth faces. We are not aware however of similar 3-fold or triangular growth features observed in crystals with this symmetry.

(15) Cartier, L.; Spassky, N.; Lotz, B. *Macromolecules* **1998**, *31*, 3040.

(16) Cartier, L.; Lotz, B. *Macromolecules* **1998**, *31*, 3049.

(17) Okihara, T.; Cartier, L.; Alberda van Ekenstein, G. O. R.; Lotz, B. *Polymer* **1999**, *40*, 1.

(18) Shcherbina, M. A.; Ungar, G. *Polymer* **2007**, *48*, 2087.

(19) Puterman, M.; Kolpak, F. J.; Blackwell, J.; Lando, J. B. *J. Polym. Sci., Polym. Phys. Ed.* **1977**, *15*, 805.

(20) Meille, S. V.; Ferro, D. R.; Brückner, S.; Lovinger, A. J.; Padden, F. J. Jr. *Macromolecules* **1994**, *27*, 2615.

(21) Keith, H. D.; Padden, F. J.; Walter, N. M.; Wickoff, H. W. *J. Appl. Phys.* **1959**, *47*, 1485.

(22) Brückner, S.; Meille, S. V.; Petraccone, V.; Pirozzi, B. *Prog. Polym. Sci.* **1991**, *16*, 361.

(23) Turner-Jones, A.; Cobbold, A. J. *J. Polym. Sci., Polym. Lett.* **1968**, *6*, 539.

(24) Addink, E. J.; Beintema, J. *Polymer* **1961**, *2*, 185.

(25) Corradini, P.; De Rosa, C.; Guerra, G.; Petraccone, V. *Polym. Commun.* **1989**, *30*, 281.

(26) Meille, S. V.; Ferro, D. R.; Brückner, S.; Lovinger, A. J.; Padden, F. J. *Macromolecules* **1994**, *27*, 2615.

(27) Lotz, B.; Kopp, S.; Dorset, D. L. *C. R. Acad. Sci. Paris* **1994**, *319*, 187.

(28) Dorset, D. L.; McCourt, M.; Kopp, S.; Schumacher, M.; Okihara, T.; Lotz, B. *Polymer* **1998**, *39*, 6331.

(29) Ferro, D. R.; Meille, S. V.; Brückner, S. *Macromolecules* **1998**, *31*, 6926.

(30) (a) Petraccone, V.; Pirozzi, B.; Meille, S. V. *Polymer* **1986**, *27*, 1665. (b) Sadler, D. M.; Spells, S. J.; Keller, A.; Guenet, J. M. *Polym. Commun.* **1984**, *25*, 290.

(31) The orientation of the streaks in the diffraction pattern suggests that the twin boundaries are parallel to the (110) plane, horizontal in Figure 3c.

(32) Stocker, W.; Schumacher, M.; Graff, S.; Thierry, A.; Wittmann, J. C.; Lotz, B. *Macromolecules* **1998**, *31*, 807.
(33) Greis, O.; Xu, J.; Asano, T.; Petermann, J. *Polymer* **1989**, *30*, 590.
(34) (a) De Rosa, C.; Guerra, G.; Petraccone, V.; Corradini, P. *Polym. J.* **1991**, *23*, 1435. (b) De Rosa, C.; Rapacciuolo, M.; Guerra, G.; Petraccone, V.; Corradini, P. *Polymer* **1992**, *33*, 1423. (c) Corradini, P.; De Rosa, C.; Guerra, G.; Napolitano, R.; Petraccone, V.; Pirozzi, B. *Eur. Polym. J.* **1994**, *30*, 1173. (d) De Rosa, C. *Macromolecules* **1996**, *29*, 8460.
(35) Cartier, L.; Okihara, T.; Lotz, B. *Macromolecules* **1998**, *31*, 3303.
(36) Pradère, P.; Thomas, E. L. *Macromolecules* **1990**, *23*, 4954.
(37) Yoshioka, T.; Kosoka, N.; Hiyama, T.; Nakayama, A.; Nozaki, K.; Dersch, R. Paper P2-166 presented at the international meeting "Frontiers in Polymer Science", Mainz, 7−9 June, 2009.
(38) Corradini, P.; Martuscelli, E.; Montaglioli, G.; Petraccone, V. *Eur. Polym. J.* **1970**, *6*, 1201.
(39) Buono, A. M.; et al., to be published.
(40) Prudhomme, R.; Lotz, B.; et al., to be published.
(41) Geil, P. H. *Polymer Single Crystals*; John Wiley & Sons: New York, 1963; Chapter IV, p 287.
(42) Sasaki, S.; Takahashi, Y.; Tadokoro, H. *J. Polym. Sci., Polym. Phys. Ed.* **1972**, *10*, 2363.
(43) Watanabe, J.; Ono, H.; Uematsu, I.; Abe, A. *Macromolecules* **1985**, *18*, 2141.
(44) Watanabe, J.; Takashina, Y. *Macromolecules* **1991**, *24*, 3423.
(45) (a) Sasaki, S. *J. Polym. Sci., Part B: Polym. Phys.* **1991**, *29*, 523. (b) Sasaki, S. *J. Polym. Sci., Part B: Polym. Phys.* **1991**, *29*, 527.
(46) Sasaki, S.; Uematsu, I. *J. Polym. Sci., Polym. Phys. Ed.* **1985**, *23*, 263.
(47) Sasaki, S.; Nakamura, T.; Uematsu, I. *J. Polym. Sci., Polym. Phys. Ed.* **1979**, *17*, 825.
(48) Ungar, G. *Prog. Colloid Polym. Sci.* **1992**, *87*, 53.
(49) Isoda, S.; Tsuji, M.; Ohara, M.; Kawaguchi, A.; Katayama, K.-i. *Polymer* **1982**, *23*, 1568.
(50) Nieduszynski, I. A.; Marchessault, R. H. *Biopolymers* **1972**, *11*, 1335.
(51) Livolant, F.; Leforestier, A. *Prog. Polym. Sci.* **1996**, *21*, 1115.
(52) Strey, H. H.; Wang, J.; Podgornik, R.; Rupprecht, A.; Yu, L.; Pargesian, V. A.; Sirota, E. B. *Phys. Rev. Lett.* **2000**, *84*, 3105.
(53) Durand, D.; Doucet, J.; Livolant, F. *J. Phys. II* **1992**, *2*, 1769.
(54) Lorman, V.; Podgornik, R.; Zeks. *Phys. Rev. Lett.* **2001**, *87*, 218101.
(55) Arnott, S.; Hutchinson, F.; Spencer, F.; Wilkins, M. H. F.; Fuller, W.; Langridge, R. *Nature* **1966**, *211*, 227.
(56) Podgornik, R.; Strey, H. H.; Gawrisch, K.; Rau, D. C.; Rupprecht, A.; Parsegian, V. A. *Proc. Natl. Acad. Sci. U. S. A.* **1996**, *93*, 4261.
(57) Rau, D. C.; Lee, B. K.; Parsegian, V. A. *Proc. Natl. Acad. Sci. U. S. A.* **1984**, *81*, 2615.
(58) Geil, P. H. *Polymer Single Crystals*; John Wiley & Sons: New York, 1963; Chapter IV, p 287.
(59) Yasuniva, M.; Tsubakihara, S.; Iura, K.; Ono, Y.; Dan, Y.; Takahashi, K. *Polymer* **2006**, *47*, 7554.
(60) Kalish, J. P.; Zeng, X.; Yang, X.; Hsu, S. L. *Polymer* **2011**, *52*, 3431.

■ NOTE ADDED IN PROOF

The relevance of frustrated structures to DNA mesophases presented in this paper, starting from their analogy with the examples provided by synthetic polymers, was introduced in one of our earlier papers (Puiggali, J. et al. *Polymer* **2000**, *41*, 8921). It has been further developed in a more elaborate form through a considerable body of work by, among others, Kornyshev and collaborators. After the development of a theory of interaction between two helical molecules (Kornyshev, A. A.; Leikin, S. *J. Chem. Phys.* **1997**, *107*, 3656), the phase behavior (Harreis, H. M.; Kornyshev, A. A.; Likos, C. N.; Löven, H.; Sutmann, G. *Phys. Rev. Letters* **2002**, *89*, 018303−1) and the statistical mechanics (Wynveen, A.; Lee, D. J.; Kornyshev, A. A. *Eur. Phys. J. E* **2005**, *16*, 303) of columnar DNA assemblies were considered. The analysis of interactions between helices shows that when the molecules come closer than a critical interaxial separation, the helix-specific forces may induce a spontaneous symmetry loss: the helices rotate around their long axis. A recent paper extends this approach to the structure and interactions in assemblies of other biological helices (including e.g. collagen). (Kornyshev, A. A.; Lee, D. J.; Leikin, S.; Wynveen, A. *Rev. Modern Phys.* **2007**, *79*, 943). Although mostly electrostatic pair potentials, and distribution and/or pattern of adsorbed counterions are considered, the analysis has of course general validity. In columnar DNA assemblies, sets of azimuthal orientations were considered that, in the magnetic terminology, correspond to antiferromagnetic Potts and Heisenberg phases. These phases are characterized by three sublattices with different spins orientations (here azimuthal settings) that generate typical "frustrated" cells as considered above. These phases have however specific relative spin orientations (0°, ± φ, and 0°, ±120°, respectively), a constraint that is definitely relaxed in the polymer frustrated structures investigated so far. The biological systems offer the possiblity to study the impact of different physical variables on the structure phase diagram. A finer analysis of their impact on the detailed helix-helix organization (relative azimuthal setting and helix shift, in particular of DNA, considering their relevance in biology) will require further studies, as well as much more detailed X-ray diffraction patterns. As indicated by D. Durand (personal communication) the frustrated model was imposed by the presence of one additional reflection only on the second layer line of the fiber pattern − which leaves much room for improvement. As a concluding remark, it is unfortunate that the almost parallel investigations on synthetic polymers and DNA mesophases did not cross-fertilize each other over the years - this note added in proof only provides yet another illustration. Since in all cases assemblies of helices are considered and the packing of three-fold helices of synthetic polymers provides easy conceptual guidelines on frustrated structures, further interactions should help analyze the more complex features of the double stranded DNA columnar phases.

Macromolecules

Article

pubs.acs.org/Macromolecules

An ADMET Route to Low-Band-Gap Poly(3-hexadecylthienylene vinylene): A Systematic Study of Molecular Weight on Photovoltaic Performance

Joshua C. Speros,[†] Bryan D. Paulsen,[‡] Scott P. White,[§] Yanfei Wu,[‡] Elizabeth A. Jackson,[†] Bradley S. Slowinski,[‡] C. Daniel Frisbie,*[,‡] and Marc A. Hillmyer*[,†]

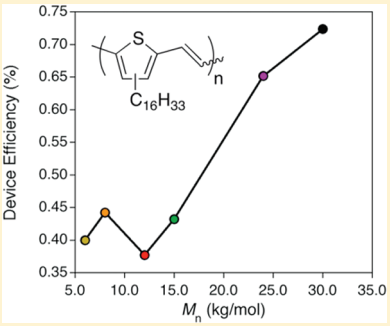
[†]Department of Chemistry, University of Minnesota, 207 Pleasant St. SE, Minneapolis, Minnesota 55455-0431, United States

[‡]Department of Chemical Engineering and Materials Science, University of Minnesota, 421Washington Ave. SE, Minneapolis, Minnesota 55455-0132, United States

[§]Department of Chemical and Biochemical Engineering, University of Iowa, 4133 Seamans Center, Iowa City, Iowa 52242, United States

Supporting Information

ABSTRACT: The effect of molecular weight on organic photovoltaic device performance is investigated for a series of low-band-gap (ca. 1.65 eV) poly(3-hexadecylthienylene vinylene)s (C16-PTVs) prepared by acyclic diene metathesis (ADMET) polymerization. By utilizing monomers of varying cis:trans (*Z*:*E*) content, seven C16-PTVs were prepared with a number-average molecular weight range of 6−30 kg/mol. Polymers were characterized by size-exclusion chromatography, ^{1}H NMR spectroscopy, ultraviolet−visible spectroscopy, thermogravimetric analysis, wide-angle X-ray scattering, and differential scanning calorimetry. C16-PTVs were integrated into bulk-heterojunction (BHJ) solar cells with [6,6]-phenyl-C_{61}-butyric acid methyl ester (PCBM), and conversion efficiency was found to increase with increasing molecular weight. This observation is attributable to an increase in polymer aggregation in the solid state and a corresponding increase in hole mobility. Finally, phase behavior and morphology of the C16-PTV:PCBM active layers were investigated by differential scanning calorimetry and atomic force microscopy, respectively.



INTRODUCTION

The promise of low-cost, solution-processable solar cells continues to motivate significant academic[1−3] and industrial research[4] in organic photovoltaics (OPVs). Optimization of both photoactive conjugated polymers and OPV architectures has led to efficiency increases from 2.5% in 2001[5] to greater than 7% in the present day.[6−10]Although contemporary devices are approaching practical maximum efficiencies of 11% theoretically predicted by Veldman et al.,[11] fundamental understanding of OPV operation and the connection to molecular parameters of the active layer components is an ongoing challenge. A particularly important parameter for OPV performance is the molecular weight of the conjugated polymer. Prior molecular weight studies have focused on OPVs utilizing poly(alkylthiophene)s (P3ATs)[12−16] and a handful of alternating donor−acceptor (D−A) polymer chain architectures.[17−19] These examples demonstrate an improvement in device efficiency, hole mobility, optical properties, and film morphology with increasing molecular weight. Expanding the scope of materials for which molecular weight influences are observed and understood is desirable.

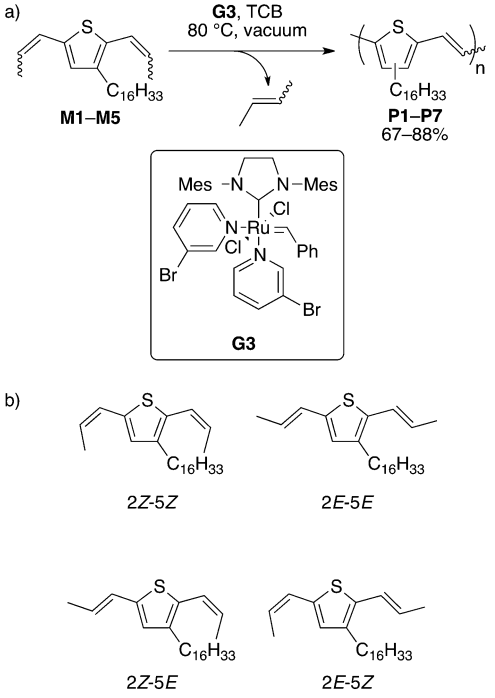
Acyclic diene metathesis (ADMET) polymerization has been employed to prepare a wide variety of materials ranging from polyethylene derivatives[20] to conjugated polymers.[21−26] Poly(thienylene vinylene)s (PTVs) are a particularly interesting class of low-band-gap conjugated polymers for OPVs.[27−30] A variety of synthetic methodologies have been exploited to prepare PTVs,[31−38] with maximum OPV efficiencies reaching 2%.[39] Recently, Qin and Hillmyer detailed the synthesis of poly(3-hexylthienylene vinylene) using ADMET polymerization in conjunction with functional group tolerant Grubbs catalysts.[40] Appreciable molecular weights (ca. 10 kg/mol) were reported, but these were only achieved after sequential catalyst additions. Realization of higher molecular weights was likely prevented by poor polymer solubility and catalyst decomposition.

Herein, we describe the ADMET preparation of seven poly(3-hexadecylthienylene vinylene) (C16-PTV) samples over a range of molecular weights (Scheme 1a). The use of a longer alkyl chain allowed for enhanced solubility at increased chain length. In addition, a more active Grubbs catalyst was utilized to reach high molecular weight at lower catalyst loadings. By addressing deficiencies in the ADMET synthesis of PTVs, we report one of the highest PTV molecular weights to date. The

Received: January 6, 2012
Revised: February 16, 2012
Published: February 28, 2012

 © 2012 American Chemical Society dx.doi.org/10.1021/ma3000434 | *Macromolecules* 2012, 45, 2190−2199

Scheme 1. Synthesis of C16-PTVs (a) and the Four Isomers of M (b)



dependence of PTV molecular weight on charge mobility was assessed in a field effect transistor (FET) structure. These materials were then integrated into bulk-heterojunction (BHJ) OPVs with [6,6]-phenyl-C_{61}-butyric acid methyl ester (PCBM) to elucidate the impact of molecular weight on performance. Finally, a temperature–composition morphology map for C16-PTV:PCBM was constructed using differential scanning calorimetry (DSC), and blend morphology was investigated with atomic force microscopy (AFM).

RESULTS AND DISCUSSION

Synthesis and Characterization. The C16-PTV monomer and corresponding polymer syntheses (Scheme 1a) were accomplished following a previous literature report (see Scheme S1 in Supporting Information).[40] En route to optimizing the Wittig reaction for a high cis double bond content, five monomers (**M1–M5**) having varying distributions of the four potential isomers (Scheme 1b) were generated. Isomer distributions were assessed by ^{1}H NMR (see Figure S5 in Supporting Information), and the percentages of these isomers and overall cis:trans (*Z*:*E*) ratios are summarized in Table 1. **M1–M5** were prepared in three steps with overall yields as high as 67% (see Supporting Information) and no detectable impurities as determined by ^{1}H NMR and GC-MS. High yields coupled with synthetic simplicity make this monomer amenable to multigram preparation.

To effectively study the impact of molecular weight on device performance, a series of C16-PTVs (**P1–P7**) were prepared by ADMET polymerization using the highly active ruthenium metathesis catalyst having an N-heterocyclic carbene and 3-bromopyridine ligands (**G3**) developed by Grubbs.[41] **P1–P7** were prepared by treating **M1–M5** with 1 mol % **G3** in 1,2,4-trichlorobenzene (TCB). The equilibrium nature of ADMET was exploited by performing the reaction under reduced pressure to remove the 2-butene byproduct. This technique is necessary to achieve high conversion.[42,43] As stated, a small library of molecular weights was obtained by utilizing monomers having different overall *Z*:*E* ratios and by varying reaction times (Table 1). Given the asymmetric nature of the monomer, **P1–P7** are obtained as essentially regiorandom polymers. This is supported by ^{1}H NMR analysis where the α-methylene protons on the alkyl chain appear as a broad singlet (2.6 ppm, Figure S6) rather than the triplet observed for regioregular thiophene polymers.[36] Additionally, Zhang et al. demonstrated the transition from four well-resolved to two broad olefinic resonances with decreasing PTV regioregularity.[44] These two broad peaks were observed in our C16-PTV samples (6.9 ppm, Figure S6), further supporting a regiorandom structure, and thus the olefin *Z*:*E* ratio could not be accurately determined. PTV regiochemistry has been shown to have little effect on OPV performance.[44]

The C16-PTV samples were slightly soluble in THF and toluene (ca. 5 mg/mL) and highly soluble in chloroform, *o*-dichlorobenzene, and TCB (>15 mg/mL). Initial molecular weight estimates were determined using size-exclusion chromatography (SEC) in chloroform versus polystyrene standards (Figure 1). The polydispersity index (PDI) values trended toward 2 with increasing molecular weight as expected for ADMET polymerization. SEC overestimates molecular weight for rodlike conjugated polymers,[45,46] making alternative molecular weight characterization necessary.

Number-average molecular weight (M_n) values were also determined by ^{1}H NMR analysis (Table 1). ADMET represents a step polymerization technique where appreciable molecular weights are only observed at high conversions. Using propenyl and aldehyde[40] end groups, it was possible to estimate monomer conversion by comparing to polymer repeat unit resonances. Additionally, treating **G3** as a monofunctional impurity that limits polymer molecular weight, the number-

Table 1. Monomer Isomer Ratios and Polymer Molecular Weight Values

polymer (monomer)	Z:E[a]	A:B:C:D[b]	*t* (h)	M_n[c] (kg/mol)	PDI[c]	X_n[d]	M_n[d] (kg/mol)
P1 (**M1**)	47:53	21:27:22:30	16	6	1.5	18	6
P2 (**M1**)	47:53	21:27:22:30	24	8	1.6	24	8
P3 (**M2**)	67:33	39:20:23:18	20	12	2.0	36	12
P4 (**M3**)	82:18	68:10:18:4	24	17	1.8	45	15
P5 (**M4**)	81:19	62:10:19:9	27	24	2.3	72	24
P6 (**M5**)	83:17	68:10:20:2	48	29	2.4	81	27
P7 (**M5**)	83:17	68:10:20:2	96[e]	33	2.2	90	30

[a]Overall monomer cis:trans ratio calculated from the relative integration of *Z* and *E* protons in the ^{1}H NMR spectrum. [b]*A* = 2*Z*-5*Z*, *B* = 2*Z*-5*E*, *C* = 2*E*-5*Z*, and *D* = 2*E*-5*E* as determined from integration of the ^{1}H NMR spectrum. [c]Determined by SEC in $CHCl_3$ with a refractive index detector and polystyrene standards. [d]Determined by ^{1}H NMR analysis. [e]Reaction was determined to be complete after 48 h by SEC.

dx.doi.org/10.1021/ma3000434 | *Macromolecules* 2012, 45, 2190–2199

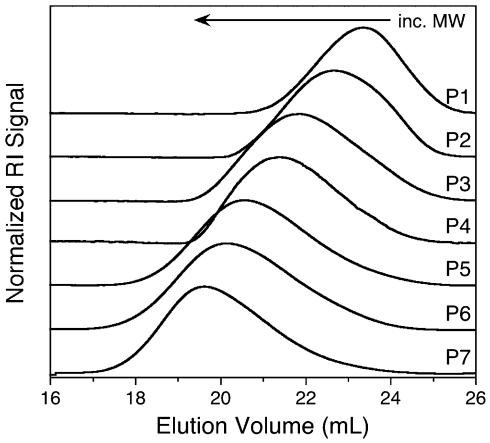


Figure 1. SEC chromatograms of **P1**−**P7**.

average degree of polymerization (X_n) and M_n was determined (see Figure S7 in Supporting Information for detailed analysis). The molecular weights calculated using ^{1}H NMR are comparable to those from SEC but are almost certainly overestimates. Given the removal of 2-butene, some fraction of polymer chains was likely terminated on one or both ends with ruthenium. However, ruthenium ends were neither observed nor quantified, leading to conversion and, ultimately, molecular weight overestimates. Also, polymer purification by Soxhlet extraction removes residual monomer and low-molecular-weight oligomers, leading to artificially high estimates of monomer conversion.

Selected ^{1}H NMR spectral regions of monomer and two representative C16-PTVs are shown in Figure 2. The absence

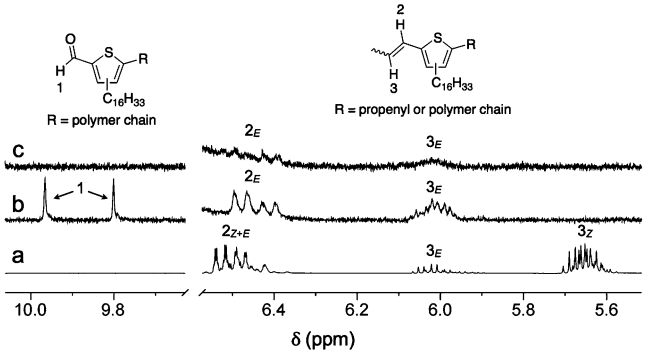


Figure 2. ^{1}H NMR spectra of (a) monomer, (b) polymer without freeze−pump−thaw (FPT), and (c) polymer with FPT.

of *Z* propenyl end groups in both polymers is indicative of their increased reactivity with **G3**. Conversely, *E* propenyl end groups persist even after 96 h of polymerization. We previously demonstrated that aldehydes residing on one or both of the polymer chain ends are the result of adventitious oxygen in the reaction solution.[40] Two aldehyde resonances, also highlighted in Figure 2b, occur due to monomer asymmetry. In this work, we demonstrate that a simple freeze−pump−thaw (FPT) cycle prior to catalyst loading effectively prevents aldehyde formation (Figure 2c). However, this additional manipulation did not lead to increased molecular weight for a given reaction time.

Biagini et al. demonstrated the deliberate end group conversion of ruthenium carbenes to aldehydes during metathesis polymerization.[47] Aldehyde end groups provide a useful synthetic handle for further reaction and functionalization. To demonstrate this, a C16-PTV partially terminated with aldehydes was treated under McMurry coupling conditions with titanium tetrachloride and zinc in THF. Following work-up, the polymer molecular weight was markedly increased (9 → 12 kg/mol). This is illustrated by the disappearance of aldehyde peaks in the product polymer ^{1}H NMR spectrum and a shift to lower elution volume in the SEC chromatogram (see Figure S8 in Supporting Information). Upon further investigation and optimization this method of chain extension could prove suitable for a variety of aldehyde-terminated conjugated polymers and make block polymerization or polymer functionalization strategies synthetically accessible.

Optical Properties. To understand the role that molecular weight plays on C16-PTV photophysical behavior, **P1**−**P7** were investigated by ultraviolet−visible (UV−vis) absorption spectroscopy in dilute chloroform solutions and as thin films on glass substrates. Figure 3a summarizes the solution data for **P1**−**P7**. As molecular weight increased the absorption maximum ($\lambda_{max,1}$) red-shifted (Table 2) indicative of an increased conjugation length. A second peak ($\lambda_{max,2}$) also appeared with increasing molecular weight. While the first peak is attributed to the $\pi-\pi^*$ transition, the second is indicative of vibronic structure that results from polymer aggregation. This phenomenon is well documented for conjugated polymers.[48,49] To confirm aggregation-induced absorption, solution spectra of **P5** were collected in chlorobenzene at room temperature, at ca. 130 °C, and upon returning to room temperature (Figure 3b). Owing to the general thermochromic nature of conjugated polymers,[50,51] there was a blue shift (14 nm) in **P5** absorption at elevated temperature. Also, the second absorption peak nearly disappeared (i.e., reduced to shoulder), indicating the breakup of polymer aggregates. Upon cooling, the original absorptive features returned, suggesting the loss of aggregation-induced absorption was not a product of polymer degradation at elevated temperatures.

Indicative of increased ordering in the solid state, a significant red shift (21−51 nm) was observed in going from solution to thin film spectra (Figure 3c). Vibronic structure was also apparent for **P1**−**P7**, and the associated absorption intensity increased with increasing molecular weight. The optical band gap (E_g^{opt}) of these materials was calculated by converting the onset absorption (λ_{onset}) to energy ($E_g^{opt} = 1240/\lambda_{onset}$) and ranged from 1.65 to 1.68 eV (Table 2). Cyclic voltammetry was also used to calculate the C16-PTV HOMO level (−4.9 eV) from the oxidation onset (see Figure S9 in Supporting Information).

Thermal Behavior. Thermogravimetric analysis (TGA) was employed to evaluate polymer thermal stability. Molecular weight was found to have no impact on decomposition temperature (T_d) as all polymers displayed 5% weight loss at 379 °C under a nitrogen atmosphere. **P7** was also analyzed in air (see Figure S10 in Supporting Information). Although the presence of oxygen reduced the T_d to 324 °C, these C16-PTVs exhibited good thermal stability regardless of molecular weight.

Temperature-dependent wide-angle X-ray scattering (TWAXS) was employed in conjunction with differential scanning calorimetry (DSC) to elucidate the solid state behavior of C16-PTVs as a function of molecular weight (Figure 4). Peak assignments in the TWAXS data (Figure 4a,b) were made based on WAXS analysis of polymer thin films at 25 °C (see Figure S11 in Supporting Information). The reflection at 0.58 Å^{-1} was ascribed to the second-order lamellar spacing (L_2) as a result of alkyl side chain interdigitation. Although the

dx.doi.org/10.1021/ma3000434 | *Macromolecules* 2012, 45, 2190−2199

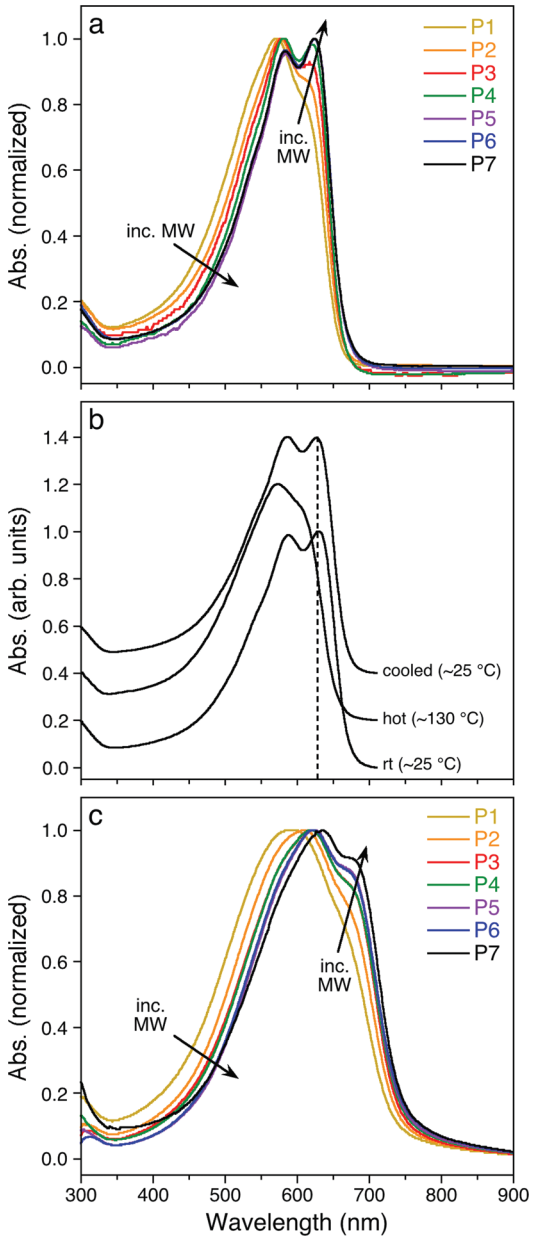


Figure 3. UV−vis spectra of (a) **P1**−**P7** in $CHCl_3$ (see Table 2 for concentrations), (b) **P5** in chlorobenzene (1×10^{-5} M per repeat unit), and (c) **P1**−**P7** as unannealed thin films on glass. Spectra are offset and a dashed vertical line is added in (b) to make the noted changes more evident.

primary lamellar reflection (L_1) was outside the measurable *q*-range for the TWAXS instrument, it was observed by thin film analysis (Figure S11). The position of the L_1 reflection gave a spacing of 22.0 Å (Figure 4c) that was generally consistent with WAXS of PTVs[30,44] and crystalline hexadecane.[52] The reflections at 0.83 $Å^{-1}$ (7.6 Å) and 1.64 $Å^{-1}$ (3.8 Å) were attributed to the intra- and intermolecular side chain-to-side chain spacings (C), respectively. The somewhat broad nature of these reflections was expected given the regiorandom nature of the polymer backbone. Finally, the reflection at 1.47 $Å^{-1}$ (4.3 Å) was assigned to the π-stack spacing (π) consistent with PTV literature.[34]

On heating **P7** to 120 °C, the L_2 and C reflections were significantly suppressed (Figure 4a), and at 200 °C the π-stack reflections were very weak. Three thermal transitions were evident in the DSC thermogram of **P7** (Figure 4d). The first, a broad transition centered on ca. 90 °C was ascribed to the melting of alkyl side chains in non-π-stacked (disordered) polymer regions. The breadth of this transition suggested a large distribution in the degree of chain order (interdigitation).[53] The second sharper transition at 110 °C was ascribed to side chain melting in π-stacked (ordered) polymer regions. The absence of L_2 and C reflections at 120 °C supports these DSC assignments. Figure 4e shows a schematic representation of the two types of side chain environments. The transition at ca. 175 °C was assigned to the melting of polymer π-stacks and is consistent with the diminished π-stack reflection at 200 °C. On the basis of literature precedent, we posit that the polymer is in a liquid crystalline state at temperatures above complete side chain melting (>110 °C) and below melting of the π-stacks (ca. 175 °C).[54]

Table 2. UV−vis Data for C16-PTVs

	UV−vis (solution)[a]		UV−vis (film)[b]	
entry	$\lambda_{max,1}$ (nm)	$\lambda_{max,2}$ (nm)	$\lambda_{max,1}$ (nm)	E_g^{opt} (eV)
P1	571	616[c]	592	1.68
P2	576	617[c]	609	1.66
P3	579	617	619 (675[c])	1.66
P4	581	621	619 (675[c])	1.66
P5	584	624	623 (680[c])	1.66
P6	584	624	623 (680[c])	1.66
P7	584	624	635 (684[c])	1.65

[a]**P1** = 2.5×10^{-5} M (repeat unit basis) in $CHCl_3$ and **P2**−**P7** = 1.0×10^{-5} M (repeat unit basis) in $CHCl_3$. [b]Films prepared by spin-coating a 10 mg/mL polymer solution in $CHCl_3$ at 1500 rpm for 40 s. [c]Absorption shoulder.

TWAXS (Figure 4b) and DSC (Figure 4d) data for the low-molecular-weight **P1** were distinct from the corresponding data acquired for **P7**. L_2 and C reflections for **P1** were absent at 100 °C and near complete loss of the π-stack reflections was evident at 120 °C. From the DSC data, the broad transition attributed to side chain melting in more disordered regions of the polymer was centered at about 60 °C as compared to 90 °C for **P7**. Furthermore, in **P1** there was no sharp transition corresponding to side chain melting in well-organized regions as observed at 110 °C for **P7**. Finally, the π-stack melting was about 65 °C lower than the corresponding melting transition in **P7**. Taken together, the higher transition temperatures for the higher molecular weight **P7** suggest that increased molecular weight enhances the overall thermal stability of polymer crystallites (see Figure S13 for polymers **P2**−**P6**). This enhancement in polymer ordering with molecular weight is consistent with observations from UV−vis spectroscopy (Figure 3c).

Hole Transport Properties. Field effect transistor measurements were employed to study the influence of molecular weight on the hole transport of neat polymer films. **P1**−**P6** exhibited transistor behavior with output curves (Figure 5a,b) displaying clear saturation behavior and very low hysteresis and transfer curves (Figure 5c) showing ON/OFF ratios of 10^3 or greater and modest hysteresis. Hole mobility values were extracted from transfer curves of devices operated in the linear regime (i.e., transistor is "on" and gate bias exceeds

dx.doi.org/10.1021/ma3000434 | *Macromolecules* 2012, 45, 2190−2199

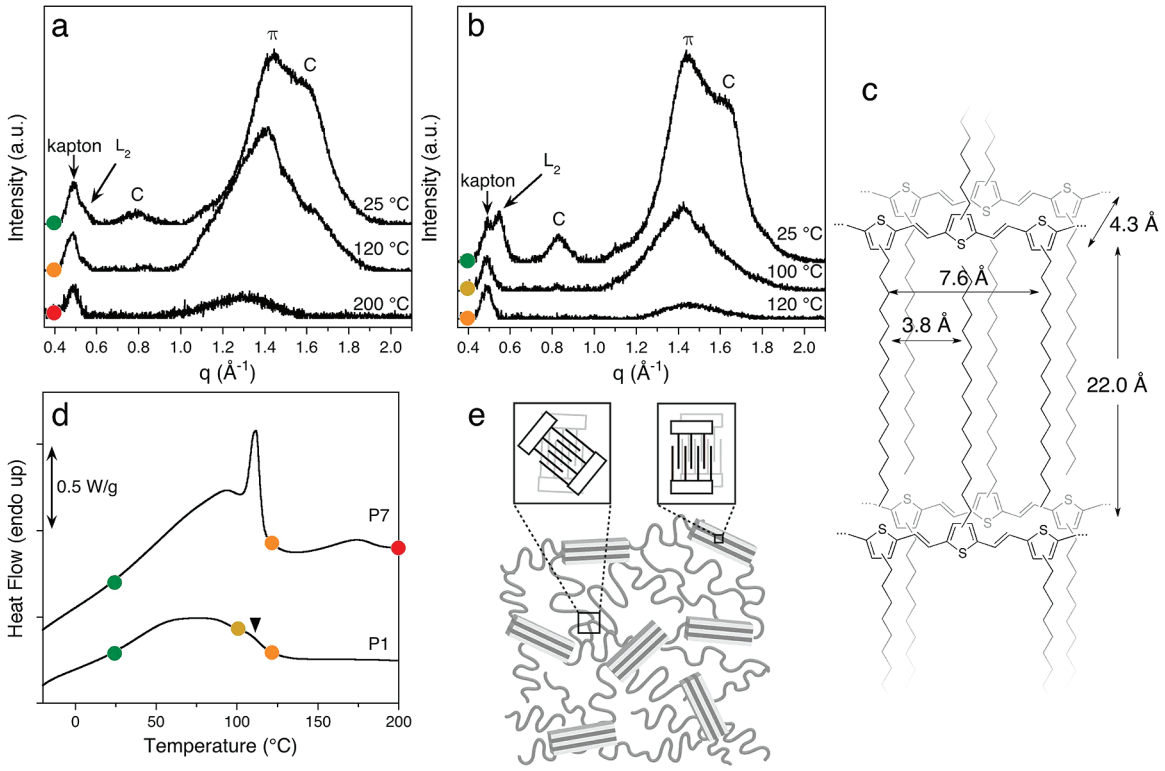


Figure 4. TWAXS patterns at various temperatures for (a) **P7** and (b) **P1**. L_2 is the second-order lamellar reflection, C is both intra- and intermolecular chain-to-chain spacing, and π is the π-spacing. (c) Schematic illustration of C16-PTV crystalline domain with lamellar (22.0 Å), chain-to-chain (7.6, 3.8 Å), and π-stack spacings (4.3 Å) determined from WAXS. (d) DSC thermograms (heating, 10 °C/min) of **P1** and **P7**. The arrowhead on **P1** marks the shoulder due to π-stack melting. The colored circles indicate the TWAXS temperatures shown in (a) and (b). (e) Schematic illustration of C16-PTV microstructure with insets highlighting interdigitation in non-π-stacked (left) and π-stacked domains (right).

the drain bias). In this regime the hole mobility may be calculated as follows:

$$\mu = \frac{L}{WC_{OX}V_D}\frac{\partial I_D}{\partial V_G}$$

where L and W are the respective length and width of the conducting channel, C_{OX} is the capacitance of the gate dielectric, V_D is the applied drain bias, V_G is the swept gate bias, and I_D is the measured drain current.

Figure 5d plots FET hole mobilities against molecular weight, clearly showing that higher molecular weight facilitates much more efficient hole transport. **P1** (M_n = 6.0 kg/mol) exhibited a low FET mobility of only 3.1 × 10^{-5} $cm^2/(V\ s)$, while **P6** (M_n = 27.0 kg/mol), having a number-average molecular weight over 4 times that of **P1**, showed well over a 2 orders of magnitude increase in FET mobility (8.0 × 10^{-3} $cm^2/(V\ s)$). This improvement in carrier mobility and transistor performance with increasing polymer molecular weight has been previously established.[14,55,56] **P2** exhibited a hole mobility of 5.5 × 10^{-4} $cm^2/(V\ s)$, consistent with the report of Kim et al. for hexyl substituted PTVs with a similar number of repeat units.[30]

In addition to hole mobility dependence on molecular weight, FET measurements also revealed a molecular weight dependence on threshold voltage (V_T). Generally, increasing molecular weight leads to a less negative V_T, although this trend appeared to plateau for higher molecular weight (>10 kg/mol). A large negative V_T is commonly attributed to an increased trap density, implying that the low molecular weight samples have a higher trap density than the high molecular weight samples, which is also consistent with the mobility trend. Both the hole mobility and threshold voltage dependence on molecular weight are attributed to preferential ordering and increased electronic coupling, which is evident in the aggregation-induced vibronic structure in the solution and film UV−vis spectra (Figure 3).

Solar Cell Performance. **PX**:fullerene BHJ devices were fabricated in a basic ITO/PEDOT:PSS/**PX**:PCBM/Al structure (inset Figure 6a). Employing **P7**, the devices were optimized for maximum power conversion efficiencies (PCE) by varying thickness and active layer composition. Highest efficiencies were found for a **P7**:PCBM ratio of 1:4 and an active layer thickness of 100−150 nm. Seventeen devices incorporating ~150 nm thick 1:4 **P7**:PCBM blends gave a PCE of 0.80 ± 0.06%, short-circuit current density (J_{sc}) of 3.32 ± 0.28 mA/cm^2, and open-circuit voltage (V_{oc}) of 0.40 ± 0.05 V under 100 mW/cm^2 simulated AM 1.5 spectrum. A high fill factor (FF) of 0.60 ± 0.03 implies good diode-like behavior. A device schematic and representative $J-V$ curve are shown in Figure 6a. Likewise, $J-V$ measurements carried out in the dark revealed good diode behavior with a rectification ratio of 1600 between +1 and −1 V shown in Figure 6b.

To investigate the polymer molecular weight effect on solar cell performance, a series of devices with ca. 100 nm thick 1:4 **PX**:PCBM active layers were tested. Figure 7a shows representative $J-V$ curves for each of the polymers investigated, with the clearest feature being the increase in photocurrent densities when going from **P1** to **P7**. V_{oc} and FF (Figure 7b,c) showed weak molecular weight dependence, with V_{oc} decreasing slightly and FF increasing slightly with molecular

dx.doi.org/10.1021/ma3000434 | *Macromolecules* 2012, 45, 2190−2199

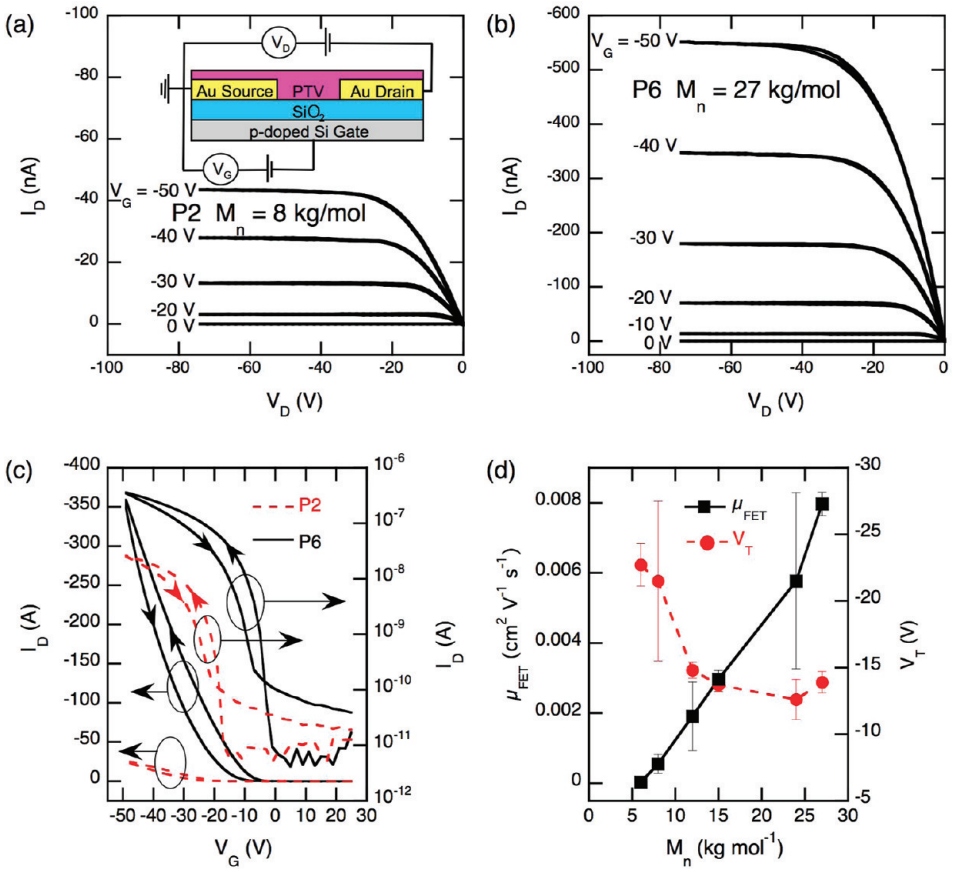


Figure 5. Output curves of (a) **P2** and (b) **P6** FETs with V_G varied from 0 to −50 V. Inset (a): device schematic. (c) Linear and semilog transfer curves of **P2** and **P6** FETs with V_D held at −10 V. (d) M_n dependence of FET hole mobility and threshold voltage of **P1**−**P6** (error bars one standard deviation).

weight. J_{sc} was strongly dependent on molecular weight (Figure 7b), with highest molecular weight devices showing roughly twice the J_{sc} of the lowest molecular weight devices. The strong J_{sc} dependence on molecular weight dominates overall device performance; thus, the PCE dependence on molecular weight mirrors the J_{sc} dependence. The shunt and series resistance extracted from the dark diode curves did not display a clear dependence on PTV molecular weight.

The PCE variation with molecular weight correlated well with the hole mobility observations, suggesting that the transport of dissociated holes is a limiting factor in device performance. The PCE and mobility trends with molecular weight are also correlated with the thin film structure as assessed by UV−vis (see Figures S14 and S15 in Supporting Information). That is, even in composite films containing 80 wt % PCBM, there is still systematic evidence of increased aggregation at high molecular weight that should favor enhanced hole mobility and thus higher J_{sc}.

One disadvantage of C16-PTV is its relatively weak light absorption, having an absorption coefficient of ca. 3.0×10^4 cm^{-1} at peak absorption (630 nm) (see Figure S16 Supporting Information). This value is considerably lower than that of the benchmark polymer regioregular P3HT,[57] which at peak absorption exceeds 1×10^5 cm^{-1}.[58,59] This low absorption of C16-PTV results in most absorption and exciton formation occurring on the PCBM, at optimum device compositions, and undermines the benefits of employing a low-band-gap material. This is borne out in low incident photon current efficiency at wavelengths of polymer absorption (see Figure S17 in Supporting Information) and illustrates the need for PTV derivatives that absorb more light to achieve higher PCE. For example, PTVs incorporating carboxylate groups have shown photoluminescent behavior, resulting in higher PCE ascribed to increased excited state lifetime.[39] Our work would suggest that increasing the molecular weight of such substituted PTVs would lead to significant increases in device performance.

Phase Behavior and Morphology. In BHJ solar cells, the active layer phase behavior and morphology are of utmost importance, but only recently have polymer:PCBM temperature−composition phase diagrams been proposed.[60,61] Several groups have since investigated the phase behavior of a variety of polymer:fullerene systems using thermal, microscopy, and spectroscopy techniques.[62−66] While not strict equilibrium phase diagrams, these studies have provided practical morphology maps pertinent to the device fabrication and testing time scale. To assess the phase behavior of our active layer blends, DSC thermograms were collected for PTV:PCBM blends with varying composition and polymer molecular weight.

The effect of PCBM composition on thermal behavior was investigated using **P7**. Figure 8a shows second heating sweeps (0−300 °C) of **P7**:PCBM blends as a function of composition after initially heating the samples to 300 °C and cooling to 0 °C. At PCBM concentrations ≥30 wt % PCBM cold crystallization (150−200 °C) and melting transitions (250−290 °C) were observed. **P7**:PCBM blends displayed consistent PCBM melting transition temperatures independent of PTV concentration (Figure 8). These data indicate the presence of a

dx.doi.org/10.1021/ma3000434 | Macromolecules 2012, 45, 2190−2199

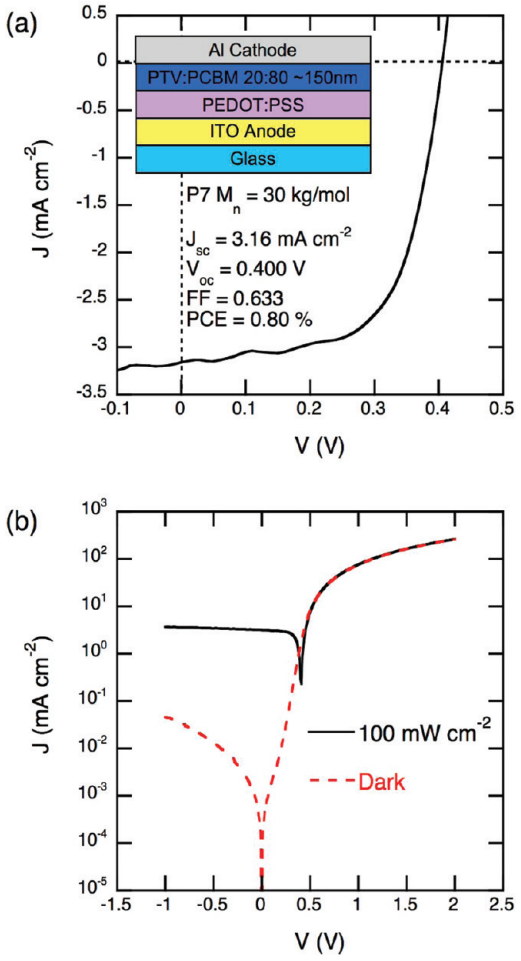


Figure 6. Optimized **P7** PTV:PCBM 20:80 solar cell *J*–*V* characteristics under simulated AM 1.5 spectrum plotted on (a) a linear scale and (b) a semilog scale with corresponding dark diode curve.

pure crystalline PCBM phase in blends containing more than 30 wt % PCBM and dissolved PCBM in blends containing less than 30 wt % PCBM. The integrated area of the PCBM crystal melting peaks for each blend, relative to the peak areas of pure PCBM, gave the fraction of crystalline PCBM present. The fraction of a pure crystalline PCBM phase was determined at each composition by applying the lever rule.[58] By this analysis, PCBM was found to have a solubility limit of 27.5 ± 3.8 wt % in **P7**.

When blends containing more than 30 wt % PCBM were heated to 300 °C, no PCBM recrystallization was evident upon cooling at 10 °C/min. This lack of recrystallization was attributed to a quenching of the **P7**:PCBM blends in a glassy phase upon cooling. This is further supported by the suppression (in enthalpy) of all (i.e., recrystallization and melting) PTV transitions. Cold crystallization (150–200 °C) of PCBM was observed during the second heating from 0 at 10 °C/min. This PCBM cold crystallization has been observed previously.[61–63,65] To substantiate the kinetic trapping of the blends in a glassy state, **P7**:PCBM blends were first cycled from 0 to 300 °C to 0 at 10 °C/min. The blends were then heated to 225 at 10 °C/min, above the temperature of PCBM cold crystallization. The following cooling to 0 °C and heating to 225 °C (both at 10 °C/min) demonstrated the recovery of PTV transitions.

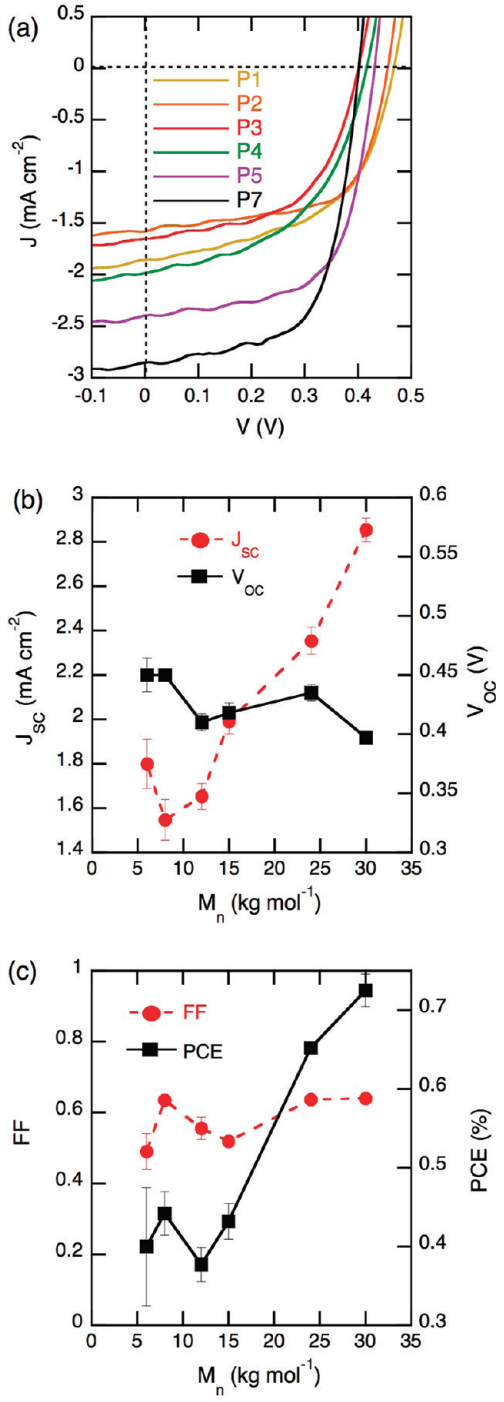


Figure 7. M_n dependence of ca. 100 nm thick PTV:PCBM 20:80 solar cells: (a) *J*–*V* characteristics, (b) J_{sc}, V_{oc}, (c) FF, and PCE of **P1**–**P7** under the simulated AM 1.5 spectrum.

To assess the polymer thermal behavior in the **P7**:PCBM blends, DSC thermograms were collected between 0 and 200 °C (Figure 8b), well below the PCBM melting transition. As shown, the polymer side chain melting (ca. 90 and 114 °C) and crystallization (90 °C) transitions characteristic of neat **P7** were observed even at excessive polymer dilution. Similar behavior was observed at all polymer molecular weights (see Figure S18 in Supporting Information). The lack of **P7** melting point depression suggests the persistent presence of pure π-stacked domains regardless of PCBM composition, with any dissolved PCBM residing in non-π-stacked PTV domains. Because of the

dx.doi.org/10.1021/ma3000434 | *Macromolecules* 2012, 45, 2190–2199

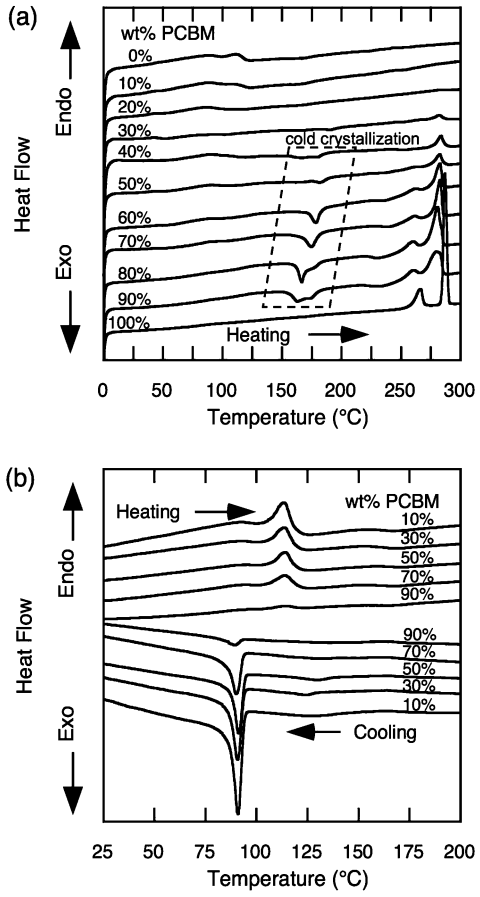


Figure 8. DSC thermograms of **P7**:PCBM at a scan rate of 10 °C/min: (a) second heating of blends up to 300 °C (above PCBM melting transition); (b) first cooling and second heating of blends heated to 225 °C (below PCBM melting transition).

large overlap of the PCBM cold crystallization (ca. 150–200 °C) with the PTV π-stack melting (ca. 175 °C), the temperature of the π-stack transition in the **P7**:PCBM blends was not strictly assigned.

The thermal and crystallographic data revealed the existence of several distinct regions of phase coexistence depending on temperature and composition (Figure 9 illustrations). Using the assigned polymer and PCBM melting transitions, in combination with neat PTV TWAXS and PCBM solubility calculations, a temperature–composition morphology map was generated (Figure 9). This morphology map represents the phase behavior that is stable over time scales related to fabrication and characterization of these BHJ devices. Below the polymer side chain melting transitions and the PCBM solubility limit, there exists two phases: non-π-stacked polymer/PCBM and π-stacked polymer crystallites, denoted as region 1 in Figure 9. Above the PCBM solubility limit, excess PCBM crystallizes creating a third phase of crystalline PCBM in addition to non-π-stacked polymer/PCBM and π-stacked polymer crystals, region 2. Above 114 °C and at PCBM compositions exceeding the solubility limit, the polymer side chains are completely melted resulting in liquid crystalline polymer, in equilibrium with a polymer/PCBM melt and crystalline PCBM, region 3. Above 114 °C and below the PCBM solubility limit there exists only liquid crystalline polymer and the polymer/PCBM melt, region 4. As evidenced by TWAXS, above 200 °C polymer π-stacking is disrupted, resulting in a single melt for PCBM compositions below the solubility limit (labeled "melt"). Above the PCBM solubility limit, PCBM crystallites are present in a polymer/PCBM melt, region 5. Finally, above ca. 280 °C, all components form a melt.

To assess the length scale of the phase separation, the morphology of active layer blends was investigated using AFM. Height and phase images of 20:80, 35:65, and 50:50 **P7**:PCBM samples prior to Al deposition were collected (Figure 10), with

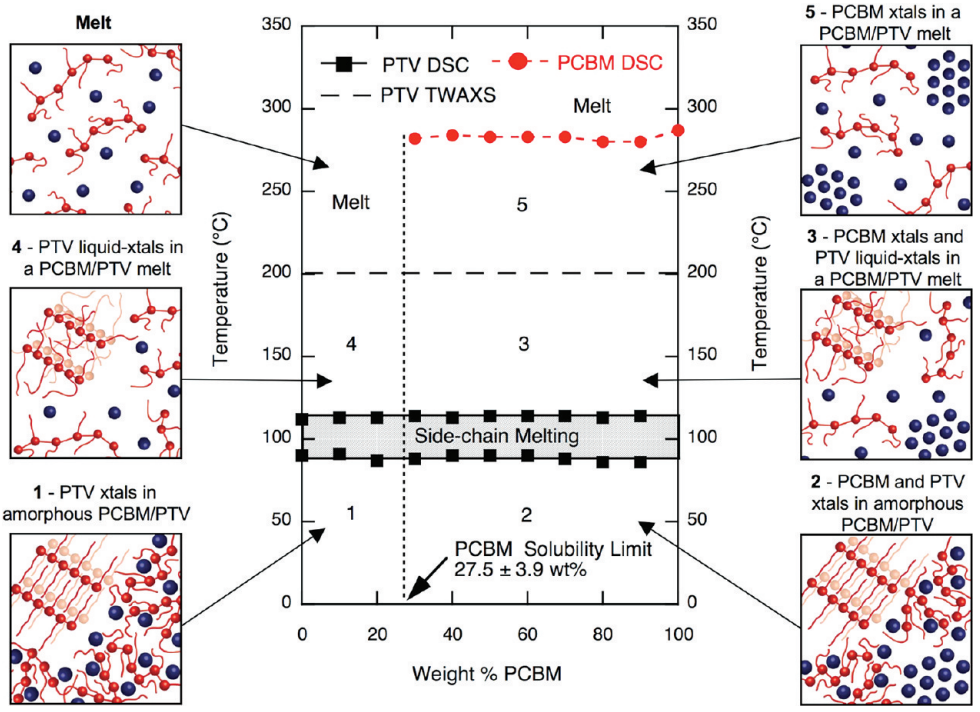


Figure 9. Temperature–composition morphology map for the **P7**:PCBM system with illustrations of the various regions of phase coexistence.

dx.doi.org/10.1021/ma3000434 | *Macromolecules* 2012, 45, 2190–2199

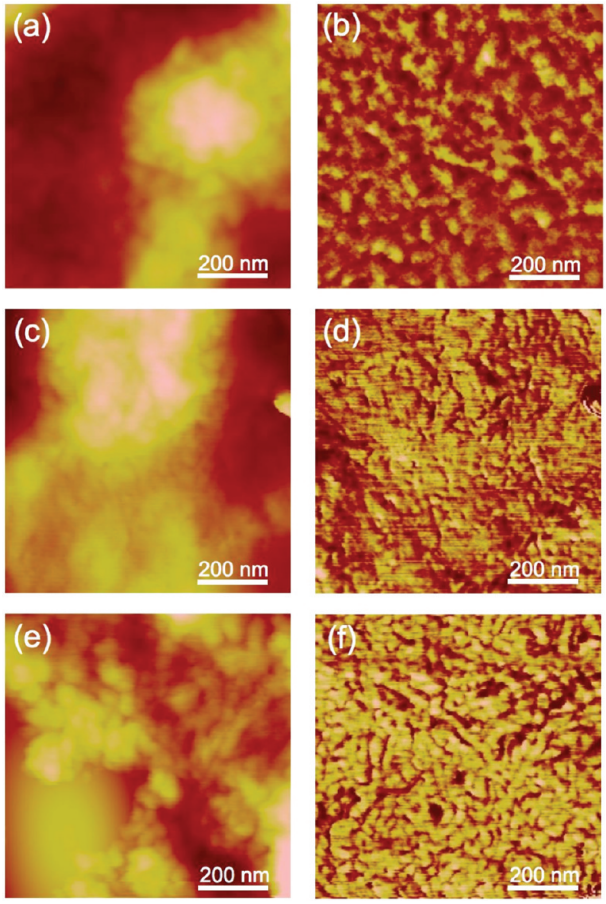


Figure 10. AFM (height, phase) images of **P7**:PCBM 20:80 (a, b), 35:65 (c, d), and 50:50 (e, f) blends.

the phase images revealing the nanoscale segregation. A fast Fourier transform (FFT) analysis of the phase images was employed to estimate the length scale of the PTV/PCBM phase separation (see Figure S19 in Supporting Information).[67,68] The FFT analysis revealed characteristic domain spacings on the order of several tens of nanometers, with the minimum domain spacing of ca. 50 nm in the 20:80 **P7**:PCBM sample decreasing to ca. 40 nm in the 35:65 sample, and further decreasing to ca. 30 nm in the 50:50 sample. Likewise, images were collected on a similar sample using low-molecular-weight **P1** (20:80) (see Figure S20 in Supporting Information). The **P1** sample showed similar PCBM segregation with a minimum domain size of ca. 35 nm, estimated from FFT.

The existence of nanoscale segregation of the donor and acceptor materials is key as exciton diffusion lengths are on the order of 10 nm. The coarsening of the phase segregation with increasing PCBM concentration might be expected to lead to decreased photocurrent density and diminished device performance; however, the opposite is observed to be true. The optimum device active layer composition of 80 wt % PCBM reflects the importance of light absorption and exciton formation, which occurs predominantly on PCBM. Employing a PTV derivative with increased light absorption or photoluminescence would likely shift the optimum PCBM composition closer to the PCBM solubility limit.

CONCLUSIONS

A series of well-defined C16-PTVs were prepared using ADMET polymerization and integrated in BHJ OPVs for a systematic molecular weight investigation. By varying the monomer *Z*:*E* ratio, using a more active catalyst (**G3**), and optimizing polymerization conditions, a broad range of molecular weights (6−30 kg/mol) was accessed. PCE increased with chain length, reaching a maximum efficiency of 0.80% with **P7**, which was predominantly the result of an enhanced J_{sc}. This observation was corroborated by FET results, which showed a molecular weight dependent increase in hole mobility brought on by enhanced polymer aggregation. A DSC-based temperature−composition morphology map was also constructed giving a PCBM solubility limit of ca. 28%. We consider this phase behavior to be paramount in assigning the long-term stability of C16-PTV:PCBM films.

ADMET has proven useful in the controlled synthesis of PTVs and has made fundamental molecular weight and phase behavior studies possible. We believe that studies of this nature will contribute to the basic understanding of conjugated polymer behavior and will lead to the development of improved devices and efficiencies. Additional systematic studies of conjugated polymers prepared by ADMET are currently underway.

ASSOCIATED CONTENT

Supporting Information

Synthesis of monomers and polymers, NMR spectra, TGA curves, WAXS patterns, UV−vis spectra, DSC thermograms, external quatum efficiency (EQE) data, and AFM analyses. This material is available free of charge via the Internet at http://pubs.acs.org.

AUTHOR INFORMATION

Corresponding Author

*E-mail: hillmyer@umn.edu (M.A.H.), frisbie@umn.edu (C.D.F.).

Notes

The authors declare no competing financial interest.

ACKNOWLEDGMENTS

The authors thank Richa Pandey for help with EQE measurements and acknowledge the University of Minnesota Initiative for Renewable Energy and the Environment for funding. Partial support for instrumentation was provided by the MRSEC program of the NSF under DMR-0819885.

REFERENCES

(1) Günes, S.; Neugebauer, H.; Sariciftci, N. S. *Chem. Rev.* **2007**, *107*, 1324−1338.
(2) Thompson, B. C.; Fréchet, J. M. J. *Angew. Chem., Int. Ed.* **2008**, *47*, 58−77.
(3) Heeger, A. J. *Chem. Soc. Rev.* **2010**, *39*, 2354−2371.
(4) Service, R. F. *Science* **2011**, *332*, 293.
(5) Shaheen, S. E.; Brabec, C. J.; Sariciftci, N. S. *Appl. Phys. Lett.* **2001**, *78*, 841−843.
(6) Chen, H. Y.; Hou, J.; Zhang, S.; Liang, Y.; Yang, G.; Yang, Y.; Yu, L.; Wu, Y.; Li, G. *Nat. Photonics* **2009**, *3*, 649−653.
(7) Liang, Y.; Xu, Z.; Xia, J.; Tsai, S.-T. T.; Wu, Y.; Li, G.; Ray, C.; Yu, L. *Adv. Mater.* **2010**, *22*, E135−E138.
(8) Price, S. C.; Stuart, A. C.; Yang, L.; Zhou, H.; You, W. *J. Am. Chem. Soc.* **2011**, *133*, 4625−4631.

(9) Zhou, H.; Yang, L.; Stuart, A. C.; Price, S. C.; Liu, S.; You, W. *Angew. Chem., Int. Ed.* **2011**, *50*, 2995−2998.
(10) Chu, T.-Y.; Lu, J.; Beaupré, I, S.; Zhang, Y.; Pouliot, J.-R.; Wakim, S.; Zhou, J.; Leclerc, M.; Li, Z.; Ding, J.; Tao, Y. *J. Am. Chem. Soc.* **2011**, *133*, 4250−4253.
(11) Veldman, D.; Meskers, S. C. J.; Janssen, R. A. J. *Adv. Funct. Mater.* **2009**, *19*, 1939−1948.
(12) Zen, A.; Pflaum, J.; Hirschmann, S.; Zhuang, W.; Jaiser, F.; Asawapirom, U.; Rabe, J. P.; Scherf, U.; Neher, D. *Adv. Funct. Mater.* **2004**, *14*, 757−764.
(13) Schilinsky, P.; Asawapirom, U.; Scherf, U.; Biele, M.; Brabec, C. J. *Chem. Mater.* **2005**, *17*, 2175−2180.
(14) Kline, R. J.; McGehee, M. D.; Kadnikova, E. N.; Liu, J.; Fréchet, J. M. J.; Toney, M. F. *Macromolecules* **2005**, *38*, 3312−3319.
(15) Hiorns, R. C.; de Bettignies, R.; Leroy, J.; Bailly, S.; Firon, M.; Sentein, C.; Khoukh, A.; Preud'homme, H.; Dagron-Lartigau, C. *Adv. Funct. Mater.* **2006**, *16*, 2263−2273.
(16) Chang, J. F.; Clark, J.; Zhao, N.; Sirringhaus, H.; Breiby, D. W.; Andreasen, J. W.; Nielsen, M. M.; Giles, M.; Heeney, M.; McCulloch, I. *Phys. Rev. B* **2006**, *74*, 115318.
(17) Müller, C.; Wang, E.; Andersson, L. M.; Tvingstedt, K.; Zhou, Y.; Andersson, M. R.; Inganäs, O. *Adv. Funct. Mater.* **2010**, *20*, 2124−2131.
(18) Coffin, R. C.; Peet, J.; Rogers, J.; Bazan, G. C. *Nat. Chem.* **2009**, *1*, 657−661.
(19) Huang, J.-H.; Chen, F.-C.; Chen, C.-L.; Huang, A. T.; Hsiao, Y.-S.; Teng, C.-M.; Yen, F.-W.; Chen, P.; Chu, C.-W. *Org. Electron.* **2011**, *12*, 1755−1762.
(20) Baughman, T. W.; Wagener, K. B. *Adv. Polym. Sci.* **2005**, *176*, 1−42.
(21) Tao, D.; Wagener, K. B. *Macromolecules* **1994**, *27*, 1281−1283.
(22) Fox, H. H.; Schrock, R. R.; O'Dell, R. *Organometallics* **1994**, *13*, 635−639.
(23) Miao, Y. J.; Bazan, G. C. *Macromolecules* **1997**, *30*, 7414−7418.
(24) Tsuie, B.; Wagener, K. B. *Polym. Prepr.* **1999**, *40*, 709.
(25) Nomura, K.; Morimoto, H.; Imanishi, Y.; Ramhani, Z.; Geerts, Y. *J. Polym. Sci., Polym. Chem.* **2001**, *39*, 2463−2470.
(26) Delgado, P. A.; Liu, D. Y.; Kean, Z.; Wagener, K. B. *Macromolecules* **2011**, *44*, 9529−9532.
(27) Smith, A. P.; Smith, R. R.; Taylor, B. E.; Durstock, M. F. *Chem. Mater.* **2004**, *16*, 4687−4692.
(28) Huong Nguyen, L.; Guenes, S.; Neugebauer, H.; Serdar Sariciftci, N.; Banishoeib, F.; Henckens, A.; Cleij, T.; Lutsen, L.; Vanderzande, D. *Sol. Energy Mater. Sol. Cells* **2006**, *90*, 2815−2828.
(29) Girotto, C.; Cheyns, D.; Aernouts, T.; Banishoeib, F.; Lutsen, L.; Cleij, T. J.; Vanderzande, D.; Genoe, J.; Poortmans, J.; Heremans, P. *Org. Electron.* **2008**, *9*, 740−746.
(30) Kim, J. Y.; Qin, Y.; Stevens, D. M.; Ugurlu, O.; Kalihari, V.; Hillmyer, M. A.; Frisbie, C. D. *J. Phys. Chem. C* **2009**, *113*, 10790−10797.
(31) Kossmehl, V. G.; Härtel, M.; Manecke, G. *Makromol. Chem.* **1970**, *131*, 15−54.
(32) Yamada, S.; Tokito, S.; Tsutsui, T.; Saito, S. *J. Chem. Soc., Chem. Commun.* **1987**, 1448−1449.
(33) Jen, K.-Y.; Maxfield, M.; Shacklette, L. W.; Elsenbaumer, R. L. *J. Chem. Soc., Chem. Commun.* **1987**, 309−311.
(34) Banishoeib, F.; Henckens, A.; Fourier, S.; Vanhooyland, G.; Breselge, M.; Manca, J.; Cleij, T. J.; Lutsen, L.; Vanderzande, D.; Nguyen, L. H.; Neugebauer, H.; Sariciftci, N. S. *Thin Solid Films* **2008**, *516*, 3978−3988.
(35) Cornelissen, J.; Peeters, E.; Janssen, R. A. J.; Meijer, E. W. *Acta Polym.* **1998**, *49*, 471−476.
(36) Lim, J.; Suzuki, M.; Saegusa, T. *Polym. Bull.* **1993**, *31*, 651−658.
(37) Loewe, R. S.; McCullough, R. D. *Chem. Mater.* **2000**, *12*, 3214−3221.
(38) Zhou, E.; Yang, Y.; Huo, L.; Zou, Y.; Yang, C.; Li, Y. *Macromolecules* **2007**, *40*, 1831−1837.
(39) Huo, L.; Chen, T. L.; Zhou, Y.; Hou, J.; Chen, H. Y.; Yang, Y.; Li, Y. *Macromolecules* **2009**, *42*, 4377−4380.
(40) Qin, Y.; Hillmyer, M. A. *Macromolecules* **2009**, *42*, 6429−6432.
(41) Love, J. A.; Morgan, J. P.; Trnka, T. M.; Grubbs, R. H. *Angew. Chem., Int. Ed.* **2002**, *41*, 4035−4037.
(42) Wagener, K. B.; Boncella, J. M.; Nel, J. G. *Macromolecules* **1991**, *24*, 2649−2657.
(43) Lehman, S. E.; Wagener, K. B. *Macromolecules* **2002**, *35*, 48−53.
(44) Zhang, C.; Sun, J.; Li, R.; Sun, S.-S.; Lafalce, E.; Jiang, X. *Macromolecules* **2011**, *44*, 6389−6396.
(45) Liu, J.; Loewe, R. S.; McCullough, R. D. *Macromolecules* **1999**, *32*, 5777−5785.
(46) Holdcroft, S. *J. Polym. Sci., Polym. Phys.* **1991**, *29*, 1585−1588.
(47) Biagini, S. C. G.; Davies, R. G.; Gibson, V. C.; Giles, M. R.; Marshall, E. L.; North, M. *Polymer* **2001**, *42*, 6669−6671.
(48) Chang, J.-F.; Clark, J.; Zhao, N.; Sirringhaus, H.; Breiby, D. W.; Andreasen, J. W.; Nielsen, M. M.; Giles, M.; Heeney, M.; McCulloch, I. *Phys. Rev. B* **2006**, *74*, 115318.
(49) Clark, J.; Silva, C.; Friend, R. H.; Spano, F. C. *Phys. Rev. Lett.* **2007**, *98*, 206406.
(50) Inganas, O.; Salaneck, W. R.; Osterholm, J. E.; Laakso, J. *Synth. Met.* **1988**, *22*, 395−406.
(51) Salaneck, W. R.; Inganäs, O.; Themans, B.; Nilsson, J. O.; Sjögren, B.; Österholm, J. E.; Brédas, J. L.; Svensson, S. *J. Chem. Phys.* **1988**, *89*, 4613−4619.
(52) Métivaud, V.; Lefèvre, A.; Ventolà, L.; Négrier, P.; Moreno, E.; Calvet, T.; Mondieig, D.; Cuevas-Diarte, M. A. *Chem. Mater.* **2005**, *17*, 3302−3310.
(53) Park, K. C.; Levon, K. *Macromolecules* **1997**, *30*, 3175−3183.
(54) Hamilton, R.; Bailey, C.; Duffy, W.; Heeney, M.; Shkunov, M.; Sparrowe, D.; Tierney, S.; McCulloch, I.; Kline, R. J.; DeLongchamp, D. M.; Chabinyc, M. *Proc. SPIE* **2006**, *6336*, 633611.
(55) Kline, R. J.; McGehee, M. D.; Kadnikova, E. N.; Liu, J.; Fréchet, J. M. J. *Adv. Mater.* **2003**, *15*, 1519−1522.
(56) Goh, C.; Kline, R. J.; McGehee, M. D.; Kadnikova, E. N.; Fréchet, J. M. J. *Appl. Phys. Lett.* **2005**, *86*, 122110.
(57) Diliën, H.; Palmaerts, A.; Lenes, M.; de Boer, B.; Blom, P.; Cleij, T. J.; Lutsen, L.; Vanderzande, D. *Macromolecules* **2010**, *43*, 10231−10240.
(58) Kim, Y.; Cook, S.; Choulis, S. A.; Nelson, J.; Durrant, J. R.; Bradley, D. D. C. *Chem. Mater.* **2004**, *16*, 4812−4818.
(59) Kim, Y.; Cook, S.; Tuladhar, S. M.; Choulis, S. A.; Nelson, J.; Durrant, J. R.; Bradley, D. D. C.; Giles, M.; McCulloch, I.; Ha, C.-S.; Ree, M. *Nat. Mater.* **2006**, *5*, 197−203.
(60) Kim, J. Y.; Frisbie, C. D. *J. Phys. Chem. C* **2008**, *112*, 17726−17736.
(61) Müller, C.; Ferenczi, T. A. M.; Campoy-Quiles, M.; Frost, J. M.; Bradley, D. D. C.; Smith, P.; Stingelin-Stutzmann, N.; Nelson, J. *Adv. Mater.* **2008**, *20*, 3510−3515.
(62) Zhao, J.; Swinnen, A.; Van Assche, G.; Manca, J.; Vanderzande, D.; Mele, B. V. *J. Phys. Chem. B* **2009**, *113*, 1587−1591.
(63) Hopkinson, P. E.; Staniec, P. A.; Pearson, A. J.; Dunbar, A. D. F.; Wang, T.; Ryan, A. J.; Jones, R. A. L.; Lidzey, D. G.; Donald, A. M. *Macromolecules* **2011**, *44*, 2908−2917.
(64) Miller, N. C.; Gysel, R.; Miller, C. E.; Verploegen, E.; Beiley, Z.; Heeney, M.; McCulloch, I.; Bao, Z.; Toney, M. F.; McGehee, M. D. *J. Polym. Sci., Polym. Phys.* **2011**, *49*, 499−503.
(65) Müller, C.; Bergqvist, J.; Vandewal, K.; Tvingstedt, K.; Anselmo, A. S.; Magnusson, R.; Alonso, M. I.; Moons, E.; Arwin, H.; Campoy-Quiles, M.; Inganäs, O. *J. Mater. Chem.* **2011**, *21*, 10676−10684.
(66) Zhao, J.; Bertho, S.; Vandenbergh, J.; Van Assche, G.; Manca, J.; Vanderzande, D.; Yin, X.; Shi, J.; Cleij, T.; Lutsen, L.; Van Mele, B. *Phys. Chem. Chem. Phys.* **2011**, *13*, 12285−12292.
(67) Kim, J. Y.; Qin, Y.; Stevens, D. M.; Kalihari, V.; Hillmyer, M. A.; Frisbie, C. D. *J. Phys. Chem. C* **2009**, *113*, 21928−21936.
(68) Ma, W.; Yang, C.; Heeger, A. J. *Adv. Mater.* **2007**, *19*, 1387−1390.

Macromolecules

Article

pubs.acs.org/Macromolecules

Reversible Addition–Fragmentation Chain Transfer Polymerization of Vinyl Chloride

Carlos M. R. Abreu,[†] Patrícia V. Mendonça,[†] Arménio C. Serra,[‡] Jorge F. J. Coelho,*[,†] Anatoliy V. Popov,[§] Ganna Gryn'ova,[∥] Michelle L. Coote,*[,∥] and Tamaz Guliashvili*[,⊥]

[†]Department of Chemical Engineering, University of Coimbra, Polo II, Pinhal de Marrocos, 3030-790 Coimbra, Portugal

[‡]Chemistry Department, University of Coimbra, 3004-535 Coimbra, Portugal

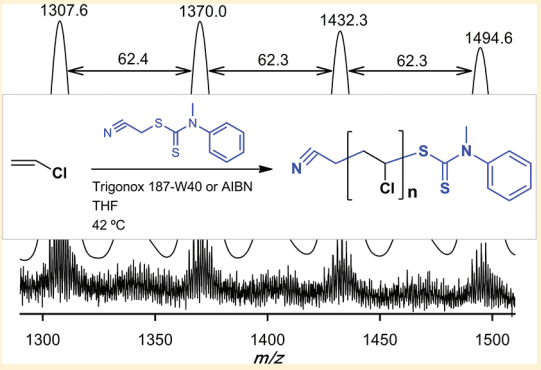
[§]Department of Radiology, University of Pennsylvania, Philadelphia, Pennsylvania 19104, United States

[∥]ARC Centre of Excellence for Free-Radical Chemistry and Biotechnology, Research School of Chemistry, Australian National University, Canberra ACT 0200, Australia

[⊥]GE Power and Water; Water & Process Technologies, 4636 Somerton Road, Trevose, Pennsylvania 19053, United States

Supporting Information

ABSTRACT: Controlled/"living" radical polymerization (CLRP) of vinyl chloride (VC) via the reversible addition–fragmentation chain transfer (RAFT) process is reported for the first time. The cyanomethyl methyl(phenyl)carbamodithioate (CMPCD) was found to be an efficient RAFT agent enabling the CLRP polymerization of VC monomer under certain experimental conditions. Two different radical initiators, having very distinct half-life times at room temperature, were employed in this study. The kinetic studies of RAFT polymerization of VC show a linear increase of the molecular weight with the monomer conversion and the lowest polydispersity (PDI) ever reported for poly(vinyl chloride) (PVC) synthesized with CLRP method (PDI ∼ 1.4). The resulting PVC was fully characterized using the matrix-assisted laser desorption ionization time-of-flight mass spectrometry (MALDI-TOF-MS), ^{1}H nuclear magnetic resonance spectroscopy (^{1}H NMR), and gel permeation chromatography (GPC) techniques. The ^{1}H NMR and MALDI-TOF-MS analysis of PVC prepared via RAFT polymerization method have shown the absence of structural defects and the presence of chain-end functional groups. The "livingness" of the PVC was also confirmed by a successful reinitiation experiment. The suitability of the RAFT agent was also confirmed via high-level *ab initio* molecular orbital calculations.



INTRODUCTION

Controlled/"living" radical polymerization (CLRP) methods provide unprecedented tools for the synthesis of polymers with controlled structures, architectures, chain-end fidelity, and narrow molecular weight distributions. The most widely used CLRP methods are transition metal catalyzed living radical polymerization, which is often called atom transfer radical polymerization (ATRP),[1] nitroxide mediated polymerization (NMP),[2] and reversible addition–fragmentation chain transfer (RAFT) polymerization.[3,4] The development of the next generation of CLRP methods for control of nonactivated vinyl monomers (such as vinyl acetate, *N*-vinylpyrrolidone, vinyl chloride, etc.) remains an important challenge. CLRP of vinyl chloride (VC) is of particular interest because poly(vinyl chloride) (PVC) is one of the most widely consumed polymers worldwide. Conventional free radical polymerization (FRP) of VC is the only available industrial process to produce the polymer in large scale. PVC made via conventional FRP process lacks the thermal stability due to the presence of structural defects (allyl and tertiary chloride groups), which are the result of different unavoidable side reactions.[5−9]

To date, the most successful CLRP of VC has been achieved by single electron transfer living radical polymerizations (SET-LRP)[10] or single electron transfer degenerative chain transfer living radical polymerizations (SET-DTLRP).[7,11−20] Since the development of these CLRP strategies for VC polymerization, several studies involving the homopolymerization, copolymerization, functionalization, and scaling-up have been published, and this topic summarized in a recent review paper by Rosen and Percec.[21] Despite these advances, it remains desirable to adapt other CLRP techniques to VC so as to broaden the scope of compatible monomers for block copolymer synthesis. To this end, in the present work we investigate the RAFT polymerization of VC in the presence of cyanomethyl methyl(phenyl)carbamodithioate (CMPCD),

Received: January 9, 2012
Revised: February 13, 2012
Published: February 23, 2012

 © 2012 American Chemical Society

using 2,2′-azobis(isobutyronitrile) (AIBN) or a very fast peroxide initiator (Trigonox 187-W40) (see Figure 1 for structures).

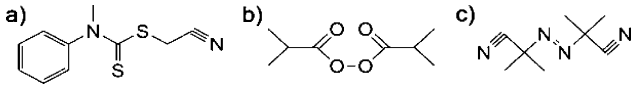


Figure 1. Structures of (a) cyanomethyl methyl(phenyl)-carbamodithioate (CMPCD), (b) Trigonox 187-W40 (diisobutyryl peroxide or DIBPO), and (c) 2,2′-azobis(isobutyronitrile) (AIBN).

EXPERIMENTAL SECTION

Materials. VC (99%) was kindly supplied by CIRES Lda, Portugal. CMPCD (Sigma-Aldrich, 98%) and Trigonox 187-W40 (40% water and methanol emulsion of diisobutyryl peroxide (DIBPO), AkzoNobel), deuterated tetrahydrofuran (d_8-THF) (Euriso-top, 99.5%), 2-(4-hydroxyphenylazo)benzoic acid (HABA) (Sigma-Aldrich, 99.5%), α-cyano-4-hydroxycinnamic acid (CHCA) (Sigma-Aldrich, 99.5%), and methanol (Labsolve, 99,5%) were used as received. AIBN (Fluka, 98%) was recrystallized three times from ethanol before use. THF (Panreac, HPLC grade) was filtered (0.2 μm filter) under reduced pressure before use. Cyclohexanone (Sigma-Aldrich, 99.8%) and dichloromethane (Fluka, 99.9%) were dried before use.

Techniques. The ^{1}H NMR spectra of reaction mixture samples were recorded with a Varian VNMRS 600 MHz spectrometer, with a warm 3 mm PFG triple resonance indirect detection probe, in THF-d_8 with tetramethylsilane (TMS) as an internal standard.

The chromatographic parameters of the samples were determined using high performance gel permeation chromatography HPSEC; Viscotek (Viscotek TDAmax) with a differential viscometer (DV); right-angle laser-light scattering (RALLS, Viscotek); low-angle laser-light scattering (LALLS, Viscotek) and refractive index (RI) detectors. The column set consisted of a PL 10 mm guard column (50 × 7.5 mm^2) followed by one Viscotek T200 column (6 μm), one MIXED-E PLgel column (3 μm), and one MIXED-C PLgel column (5 μm). HPLC dual piston pump was set with a flow rate of 1 mL/min. The eluent (THF) was previously filtered through a 0.2 μm filter. The system was also equipped with an online degasser. The tests were done at 30 °C using an Elder CH-150 heater. Before the injection (100 μL), the samples were filtered through a polytetrafluoroethylene (PTFE) membrane with 0.2 μm pore. The system was calibrated with narrow polystyrene (PS) standards. The dn/dc was determined as 0.105 for PVC. Molecular weight (M_n^{GPC}) and polydispersity (PDI) of synthesized polymers were determined by Universal Calibration (the viscosity was measured directly by the viscometer detector) using OmniSEC software version 4.6.1.354.

For the MALDI-TOF-MS analysis, the PVC samples were dissolved in THF at a concentration of 10 mg/mL. HABA and CHCA (0.05 M in THF) were used as matrix. The dried-droplet sample preparation technique was used to obtain 1:1 ratio (sample/matrix); an aliquot of 1 μL of each sample was directly spotted on the MTP AnchorChip TM 600/384 TF MALDI target, Bruker Daltonik (Bremen Germany), and before the sample dry, 1 μL of matrix solution in THF was added and allowed to dry at room temperature, to allow matrix crystallization. External mass calibration was performed with a peptide calibration standard (PSCII) for the range 700−3000 (9 mass calibration points); 0.5 μL of the calibration solution and matrix previously mixed in an Eppendorf tube (1:2, v/v) were applied directly on the target and allowed to dry at room temperature. Mass spectra were recorded using an Autoflex III smartbeam1MALDI-TOF-MS mass spectrometer Bruker Daltonik (Bremen, Germany) operating in the linear and reflectron positive ion mode. Ions were formed upon irradiation by a smartbeam1 laser using a frequency of 200 Hz. Each mass spectrum was produced by averaging 2500 laser shots collected across the whole sample spot surface by screening in the range m/z 400−8000. The laser irradiance was set to 35−40% (relative scale 0−100) arbitrary units according to the corresponding threshold required for the applied matrix systems. The theoretical isotope distribution was obtained using the Isotope Distribution Calculator software.[22]

Procedures. The VC RAFT polymerization kinetic experiments were carried out in a 50 mL glass high-pressure tube equipped with a magnetic stir bar. In the kinetic studies each point represents a single experiment.

Typical Procedure for the RAFT Polymerization of VC in THF at 42 °C with [VC]$_0$/[CMPCD]$_0$/[Trigonox]$_0$ = 250/1/0.2. A 50 mL Ace Glass 8645#15 pressure tube, equipped with bushing and plunger valve, was charged with a mixture of CMPCD (64.8 mg, 0.291 mmol), Trigonox 187 W40 (25.4 mg), and THF (5.0 mL) (previously bubbled with nitrogen for about 5 min). The precondensed VC (5 mL, 73 mmol) was added to the tube. The exact amount of VC was determined gravimetrically. The tube was closed and degassed through the plunger valve by applying reduced pressure and filling the tube with N_2 about 20 times, submerged in liquid nitrogen. The valve was closed, and the tube reactor was placed in a water bath at 42 ± 0.5 °C with stirring (700 rpm). After 24 h, the reaction was stopped by plunging the tube into ice water. The tube was slowly opened, the excess VC was distilled, and the mixture was precipitated into 250 mL of methanol. The polymer was separated by filtration and dried in a vacuum oven until constant weight to produce 2.514 g (49.7%) of PVC, M_n^{GPC} = 6044 g/mol, M_w/M_n = 1.43.

Chain Extension Experiment. The experiment was performed in a similar way to the typical polymerization, but using 46.8 mg of PVC-CTA (CTA: chain transfer agent) previously dissolved in THF (M_n^{GPC} = 3100 g/mol, M_w/M_n = 1.44) as macro-CTA, 3.3 mg of Trigonox 187 W40, a total 10 mL of THF (previously bubbled with nitrogen for about 5 min), and 5.0 mL (73 mmol) of precondensed VC were also charged into the reactor. The reaction proceeded for 72 h, and 2.19 g (42.6%) PVC was obtained. M_n^{GPC} = 10 700 g/mol, M_w/M_n = 1.42.

Computational Procedures. To assist in the selection of a suitable RAFT agent, standard *ab initio* molecular orbital theory and density functional theory calculations were carried out using Gaussian 09[23] and Molpro 2009.1[24] Calculations were performed at a high level of theory that was based on our previous assessment studies for RAFT reactions[25] and recently shown to reproduce experimental equilibrium constants to within chemical accuracy.[26,27] For all species, either full systematic conformational searches (at a resolution of 120°) or, for more complex systems, energy-directed tree searches[28] were carried out to ensure global, and not merely local minima were located. These were performed at the B3LYP/6-31G(d) level of theory in a THF solution at 25 °C to mimic experimental conditions. The PCM[29] solvent model was used in conjunction with UAKS model of spheres radii, and an electrostatic scaling factor was set equal to the recommended value of 1.2.[30] Geometries of the solution-phase lowest energy conformers of all species were then relaxed in the gas phase at the B3LYP/6-31G(d) level, and frequencies were also calculated at the same level and scaled by recommended scale factors.[31] Accurate gas-phase electronic energies were calculated using a three-layer ONIOM approach described previously.[32,33] The core layer was treated using the W1 procedure,[34] the G3(MP2)-RAD[35] method was applied to describe the effects of the primary substituents, and the full system was calculated using R(O)MP2/6-311+G(3df,2p) method. Gas-phase entropies and thermal corrections at 42 °C were calculated using standard textbook formulas[36] for the statistical thermodynamics of an ideal gas under the harmonic oscillator approximation in conjunction with the optimized geometries and scaled frequencies. Free energies of solvation for all species were calculated at the UAKS-PCM/B3LYP/6-31G(d) level of theory at 25 °C and corrected for the phase change correction term RT(ln V). Equilibrium constants were determined according to the equation

$$K(T) = (c^0)^{\Delta n} \exp\left(\frac{-\Delta G}{RT}\right)$$

where c^0 is the standard concentration unit equal to 1 mol L^{-1} in solution.

dx.doi.org/10.1021/ma300064j | Macromolecules 2012, 45, 2200−2208

Scheme 1. Equilibrium Constants (Bold; L mol^{-1}) and Corresponding Gibbs Free Energies (Italics; kJ mol^{-1}) of Addition (*a* and *c*) and Chain Transfer (*b*) Reactions in THF at 42 °C, Calculated Using Three-Layer ONIOM Approximation for Electronic Energies and UAKS-PCM/B3LYP/6-31G(d) Method for Solvation Free Energies

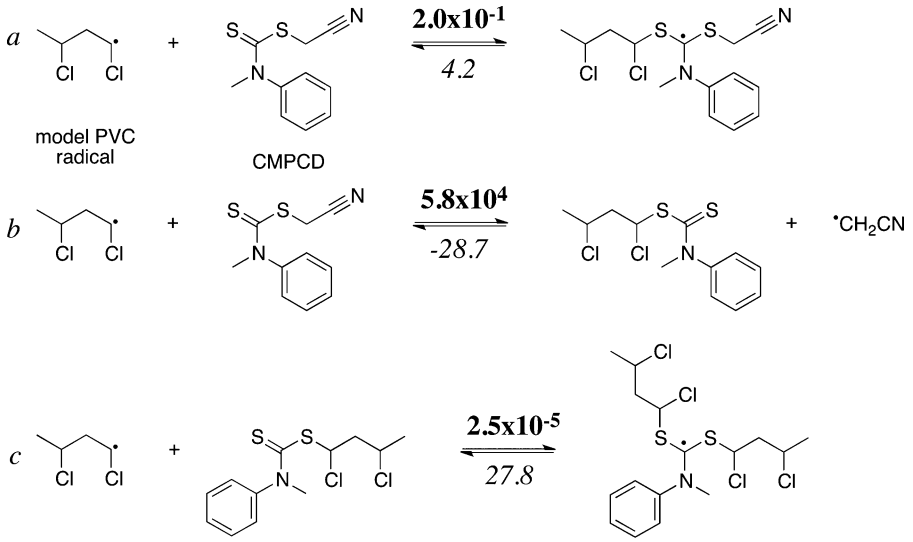


Table 1. RAFT Polymerizations of VC with CMPCD as a RAFT Agent under Different Conditions

entry	$[VC]_0/[CMPCD]_0/[Trigonox]_0$	$[VC]_0/[solvent]$ (v/v)	time (h)	T (°C)	conv (%)	M_n^{th} (g/mol)	M_n^{GPC} (g/mol)	M_w/M_n
1	250/1/0.2	1/1 (dichloromethane)	24	42	0			
2	250/1/0.2	1/1 (cyclohexanone)	24	42	36	6000	3500	1.88
	$[VC]_0/[CMPCD]_0/[Trigonox]_0$	$[VC]_0/[THF]$ (v/v)						
3	250/1/0.2	1/1	24	42	50	8500	6000	1.43
4	250/1/0.2	1/1	24	30	34	7000	4200	1.68
5	250/1/0.2	1/1	24	60	30	6000	3400	1.76
6	250/1/0.1	1/1	24	42	42	9000	5800	1.68
7	250/1/0.5	1/1	24	42	49	9900	6000	1.55
8	100/1/0.2	1/1	24	42	43	3100	2400	1.69
9	500/1/0.2	1/1	24	42	39	14600	7400	1.50
10	250/1/0.2	1/1	48	42	54	9400	7300	1.43
11	250/1/0.2	1/3	48	42	86	15200	4400	1.78
12	250/1/0.2	1/5	48	42	91	18700	3200	1.84
	$[VC]_0/[CMPCD]_0/[AIBN]_0$							
13	250/1/0.2	1/1	24	42	38	7100	4200	1.70
14	250/1/0.1	1/1	24	42	36	6800	3700	1.67
15	250/1/0.5	1/1	24	42	44	8200	4500	1.76

RESULTS AND DISCUSSION

Computational Results. VC belongs to the so-called nonactivated (or less activated) vinyl monomer class, which is characterized by having propagating radicals with relatively low radical stabilities. For instance, based on its calculated radical stabilization energy of 27.0 kJ mol^{-1} at the G3(MP2)-RAD level of theory, a unimeric VC propagating radical is only slightly more stabilized than the corresponding vinyl acetate derived unimeric propagating radical (24.4 kJ mol^{-1}) and considerably less than corresponding values for such activated monomers as methyl acrylate (41.3 kJ mol^{-1}), methyl methacrylate (54.9 kJ mol^{-1}), or styrene (68.0 kJ mol^{-1}).[37] Less activated monomers pose two key problems when selecting an appropriate RAFT agent. First, the relatively low stabilities of their propagating radicals render them poor leaving groups from standard dithioester-type RAFT agents, leading to significant inhibition or rate retardation effects. Second, many of the typical leaving groups in initial RAFT agents do not readily reinitiate polymerization of unactivated monomers.[4]

To address the first problem, one typically uses RAFT agents such as xanthates or dithiocarbamates in which the "Z-group" of the RAFT agent is a lone pair donor that can undergo resonance with the thiocarbonyl group. This resonance stabilizes the RAFT agent relative to the RAFT-adduct radical, helping to promote fragmentation. In the present work we have opted for a dithiocarbamate, cyanomethyl methyl(phenyl)carbamodithioate (CMPCD, see Figure 1 and the Supporting Information for the model thermodynamic measures), which has already found success in the control of other unactivated monomers.[4] Moreover, the $^{\bullet}CH_2CN$ leaving group of this RAFT agent is known to be an effective initiating species for VC (e.g., Fischer and Radom report a rate coefficient of 1.2×10^4 L mol^{-1} s^{-1} at 25 °C),[38] thereby simultaneously addressing the second problem. At the same time, based on previously published model calculations, this leaving group would be expected to undergo preferential fragmentation from intermediate radical.[37,39]

To confirm that this RAFT agent would be suitable, we calculated the equilibrium constant for the addition of a dimeric

dx.doi.org/10.1021/ma300064j | Macromolecules 2012, 45, 2200−2208

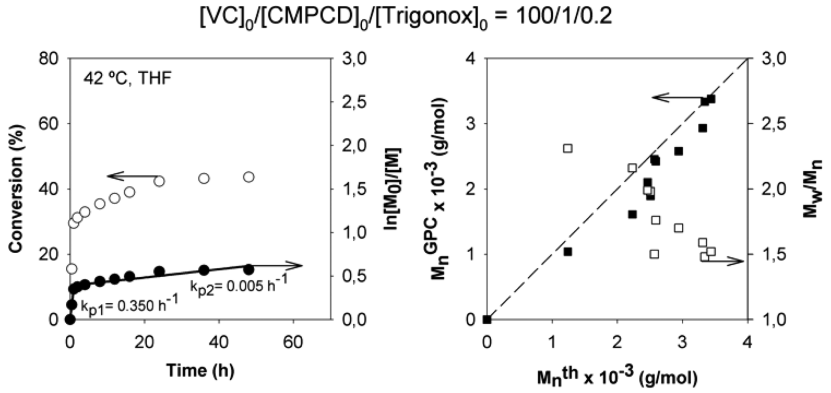


Figure 2. Kinetic plots for RAFT polymerization of VC under the following conditions: $[VC]_0/[CMPCD]_0/[Trigonox]_0$ = 100/1/0.2 at 42 °C in THF ($[VC]_0/[THF]$ (v/v) = 1/1).

VC propagating radical to CMPCD (reaction *a* in Scheme 1) in THF solution at 42 °C and also to the corresponding "polyRAFT" agent where the CH_2CN leaving group is replaced by the VC dimer radical (reaction *c* in Scheme 1). In both cases, the equilibrium constants (2.0×10^{-1} and 2.5×10^{-5} L mol^{-1}, respectively) are much less than the values of 10^6 L mol^{-1} or more typically associated with rate retardation.[40,41] We also calculated the equilibrium constant of the chain transfer reaction in the pre-equilibrium (reaction *b* in Scheme 1) to confirm that fragmentation of the $^{\bullet}CH_2CN$ leaving group is strongly favored in the pre-equilibrium, as is required for efficient chain transfer. Hence, based on these results, CMPCD is expected to be a suitable RAFT agent for control of VC polymerization.

Experimental Results. Having selected CMPCD as our RAFT agent, we then tested it experimentally. Two different initiators—AIBN (with $t_{1/2}$ = 1 h at 82 °C)[42] and Trigonox 187-W40 (with $t_{1/2}$ = 1 h at 39 °C)[42]—were used as a free radical source during the polymerization (Figure 1). Since PVC is not soluble in its monomer, the RAFT polymerization was conducted in the presence of different solvents that dissolve both VC and PVC (THF, cyclohexanone, and dichloromethane). Results of the VC RAFT polymerization under different conditions, summarized in Table 1, suggest that the combination of Trigonox 187-W40 and THF is the most successful in providing fast, yet well-controlled RAFT polymerization of VC. No polymerization occurs in dichloromethane, while a polymer with high PDI is formed in cyclohexanone (entries 1 and 2, Table 1).

In order to find optimal conditions for a successful RAFT polymerization of VC, mediated by CMPCD as a chain transfer agent in THF solution, we have evaluated the effect of temperature and VC/THF and VC/CMPCD ratios on the polymerization process (Table 1). Reactions at different temperatures (entries 3–5, Table 1) were conducted under the following conditions: $[VC]_0/[CMPCD]_0/[Trigonox]_0$ = 250/1/0.2 and $[VC]_0/[THF]$ (v/v) = 1/1. Previous studies of SET-DTLRP of VC had shown that 42–43 °C is the maximum temperature of polymerization yielding PVC with minimized structural defects and well-defined chain-end functionalities.[7,15] Under the conditions of the present study, the optimum temperature of RAFT polymerization of VC was found to be equal to 42 °C (50% monomer conversion in 24 h). Only a limited monomer conversion was observed at 30 and 60 °C (34% and 30%, respectively); moreover, the obtained PVC exhibited a broad molecular weight distribution indicating possible loss of control over the polymerization. At lower temperatures radical initiation is expected to be significantly slower, while at higher temperatures the chain transfer to VC competes with a chain transfer via RAFT mechanism.

The molar ratio [initiator]/[CTA] also has an important role in the control of the PVC molecular weight during the RAFT polymerization of VC. Results of VC RAFT polymerization at 42 °C with different [initiator]/[CTA] ratios given in Table 1 (entries 3, 6, and 7) indicate that the lowest PDI could be achieved when [initiator]/[CTA] is equal to 0.2/1.

The entries 3, 8, and 9 in Table 1 correspond to the results of RAFT polymerizations conducted at 42 °C with different $[monomer]_0/[CTA]_0$ ratios and constant [initiator]/[CTA] ratio (equal to 0.2). As expected for CLRP systems, the molecular weight of the polymers increases with the $[monomer]_0/[CTA]_0$ value. Entries 10–12 in Table 1 reflect the effect of the $[VC]_0/[THF]$ ratio on the RAFT polymerization of VC. Obtained results show that the conversion increases with the increase in the amount of solvent used. At the same time, however, control over the polymerization diminishes, since the obtained molecular weights of PVC decrease (rather than increase as expected) and the PDI values increase. Side reactions involving chain transfer from the growing macroradicals to the solvent are assumed to be responsible for this.

Finally, performance of Trigonox 187-W40 and AIBN initiators for RAFT polymerization of VC (entries 3, 6, 7, 13, 14, and 15 in Table 1) was evaluated. According to our results, Trigonox 187-W40 provides slightly higher monomer conversion and better control (lower PDI values and M_n^{th} are closer to M_n^{GPC} in case of Trigonox). These results may be explained by the fact that cyanoisopropyl radicals (formed by AIBN thermal decomposition) add slower to the VC monomers and RAFT agents when compared to the isopropyl radicals resulting from Trigonox. Also, addition of cyanoisopropyl radicals to RAFT agent is a reversible process. On the other hand, isopropyl radical (formed from $(CH_3)_2CH-C(O)-O-O-C(O)-CH(CH_3)_2$) should add much faster to both RAFT agent and VC monomer. Addition of isopropyl radical to RAFT agent is irreversible. Thus, in case of Trigonox any induction period should be eliminated, polymerization is expected to be faster (higher M_n at given monomer conversion) and the initiation efficiency is higher.

Kinetic Experiments. Figures 2–4 show typical kinetic experiments for the RAFT polymerization of VC in solution. Remarkably, in all cases the $\ln([M]_0/[M])$ exhibits two linear

dx.doi.org/10.1021/ma300064j | Macromolecules 2012, 45, 2200–2208

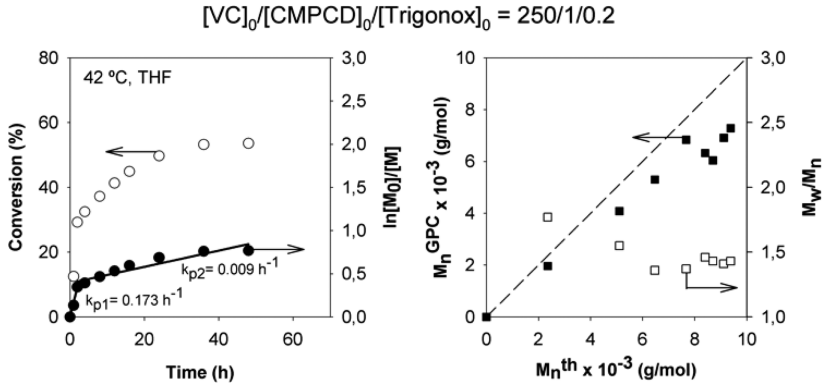


Figure 3. Kinetic plots for RAFT polymerization of VC under the following conditions: $[VC]_0/[CMPCD]_0/[Trigonox]_0$ = 250/1/0.2 at 42 °C in THF ($[VC]_0/[THF]$ (v/v) = 1/1).

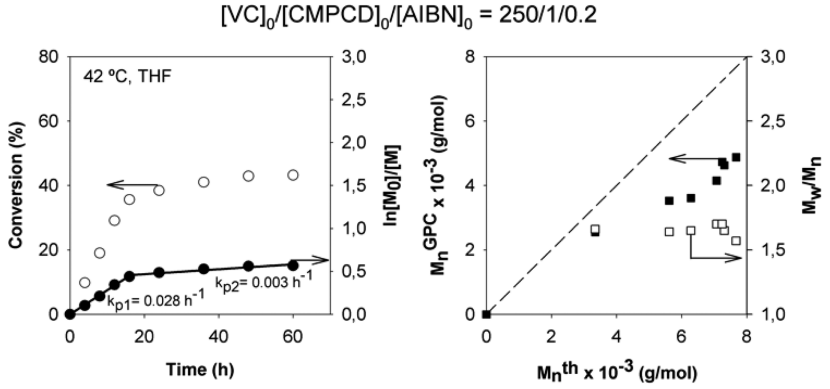


Figure 4. Kinetic plots for RAFT polymerization of VC under the following conditions: $[VC]_0/[CMPCD]_0/[AIBN]_0$ = 250/1/0.2 at 42 °C in THF ($[VC]_0/[THF]$ (v/v) = 1/1).

dependencies on the polymerization time. Similar behavior was observed during SET-DTLRP of VC in water/THF mixtures.[11,12,43] The linear dependencies of $\ln([M]_0/[M])$ vs time indicate constant concentration of growing radicals throughout the polymerization. The presence of two different linear regions, a phenomenon known as hybrid behavior, is most likely caused by the differences in the initiation and reinitiation rates (by the leaving $^{\bullet}CH_2CN$ radical in the pre-equilibrium). In all experiments M_n^{GPC} agrees with the theoretical molecular weight (M_n^{th}), and PDI is decreasing with the monomer conversion.

PVC Structure Determination. The chemical structure of the PVC synthesized by RAFT polymerization was determined with MALDI-TOF-MS and ^1H NMR techniques. In MALDI-TOF-MS experiments, two types of matrices, HABA and CHCA (Figure S1, Supporting Information), were tested, but only the former gave a clearly resolved spectrum (Figures 5–7). The MALDI-TOF-MS of RAFT-PVC in the linear mode with m/z ranging from 700 to 4000 is shown in Figure 5. Enlargement of the 1300–1500 range in the linear and reflectron modes is shown in Figure 6. Importantly, two series of main peaks (for linear mode) are separated by an interval corresponding to a VC repeating unit (62.5 mass units). The highest main series is attributed to a polymer chain R-PVC-Z′ (species 5, Scheme 2) where R-Z′ is the RAFT agent: R = $-CH_2-CN$ and Z′ = $-S-C(S)-N(Me)Ph$ (1307.6 = 40.02 + 17 × 62.5 + 182.2 + 23, where 40.02, 62.5, 182.2, and 23 correspond to the molecular weight of R, VC, Z′, and Na^+, respectively). This particular structure was confirmed by comparing the results with a theoretical distribution shown in

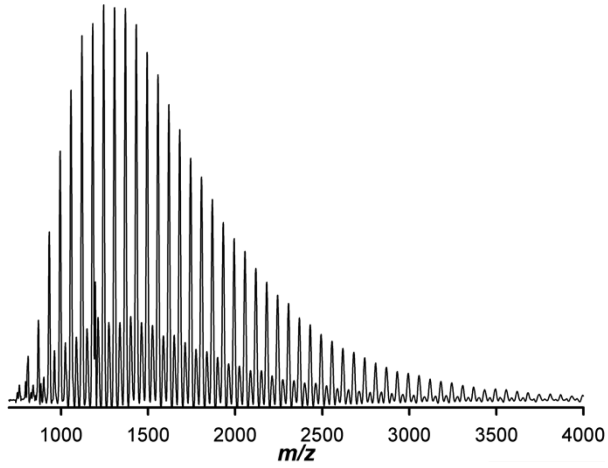


Figure 5. MALDI-TOF-MS in the linear mode of RAFT-PVC (M_n^{GPC} = 3300 g/mol, M_w/M_n = 1.48) mediated by CMPCD.

Figure 7. The enlarged spectrum (reflectron mode) from m/z 1300 to 1320 (DP = 17) shows that the isotope distribution of the polymer chain match the isotope distribution calculated for R-$(PVC)_{17}$-Z′ + Na^+ using Isotope Distribution Calculator software[22] (from m/z 925 to 945 or DP = 11; see Figure S2 in the Supporting Information). Therefore, obtained RAFT-PVC has a well-defined structure (i.e., without any detectable structural defects). The presence of possible structural defects would cause a deviation of m/z values and a different pattern of the isotope distribution. The series of less intensive peaks

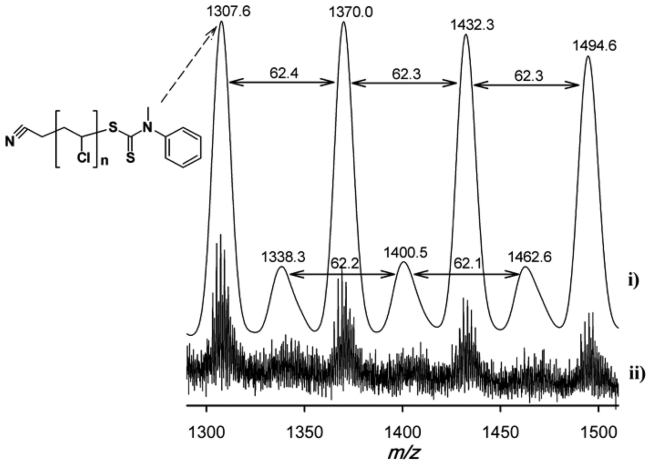


Figure 6. Enlargement of the MALDI-TOF-MS from m/z 1300 to 1500 of RAFT-PVC (M_n^{GPC} = 3300 g/mol, M_w/M_n = 1.48) mediated by CMPCD in the (i) linear and (ii) reflectron mode.

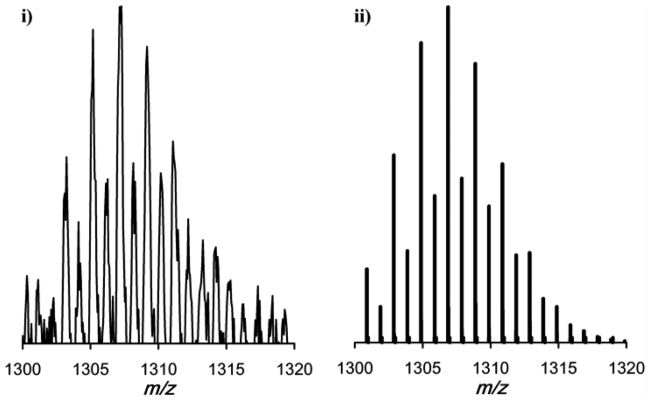
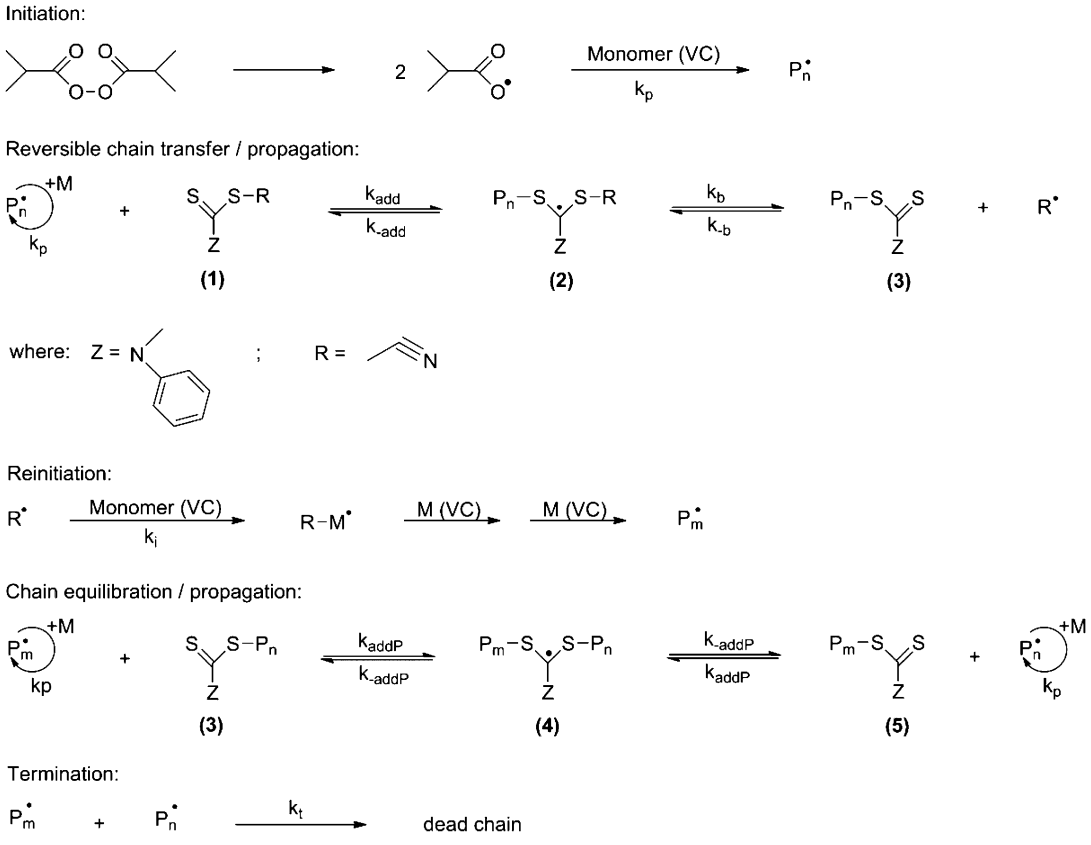


Figure 7. (i) Enlargement of the MALDI-TOF-MS in the reflectron mode of Figure 6 from m/z 1300 to 1320 and (ii) theoretical isotope distribution of the m/z 1300−1320 region (DP = 17, $C_{44}H_{61}Cl_{17}N_2S_2Na$) using Isotope Distribution Calculator software.

(Figure 6i) cannot be ascribed to any chain-end structures expected from the RAFT polymerization. The presence of these peaks is probably due to the occurrence of the fragmentation of dithiocarbamate moieties during ionization in the MALDI-TOF-MS analysis, as reported by other authors.[44−47]

The ^{1}H NMR spectrum of the PVC sample used in MALDI-TOF-MS analysis is shown in Figure 8. This spectrum confirms the main structure suggested based on the results of the MALDI-TOF-MS analysis. ^{1}H NMR spectra of the initiator (top) and the RAFT agent (in the middle) are also given in Figure 8. The spectrum of the RAFT-PVC reveals the resonances of the repeat unit CH_2−CHCl: **f** (1.9−2.7 ppm) and **g** (4.2−4.7 ppm), respectively. The terminal −CH_2−CHCl−S− (**h** and **g′**) group resonates at 2.65 and ∼4.7 ppm, respectively. The spectrum of the RAFT-PVC also reveals the resonances of the RAFT agent (**e**, **d**). Phenyl protons **e** resonate at 7.2−7.4 ppm and N-Me protons **d** signal at 3.75 ppm. The signal of NC−CH_2 group **c** is probably hidden in the resonance of the main chain methylene group **f** at 1.9−2.7 ppm. The initiator fragments (containing protons **a** and **b**) reveal no noticeable signals. Additionally, there is no significant amount

Scheme 2. Mechanism of the RAFT Polymerization of VC Initiated by Trigonox 187-W40 Using CMPCD as Chain Transfer Agent



dx.doi.org/10.1021/ma300064j | Macromolecules 2012, 45, 2200−2208

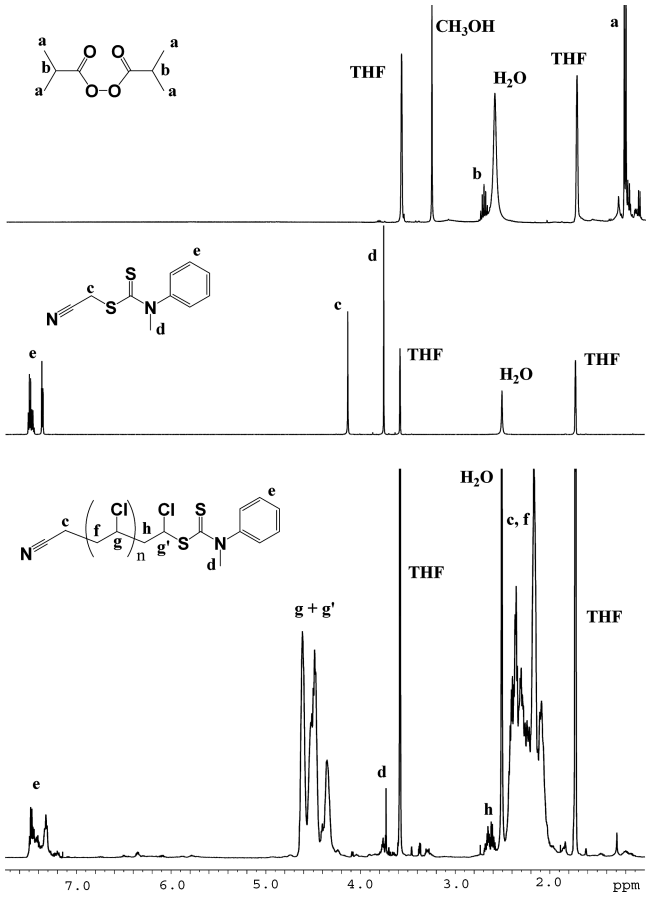


Figure 8. ^{1}H NMR spectra of Trigonox 187-W40 initiator (top), CMPCD RAFT agent (middle), and RAFT-PVC obtained (M_n^{GPC} = 3300 g/mol, M_w/M_n = 1.48) in d_8-THF.

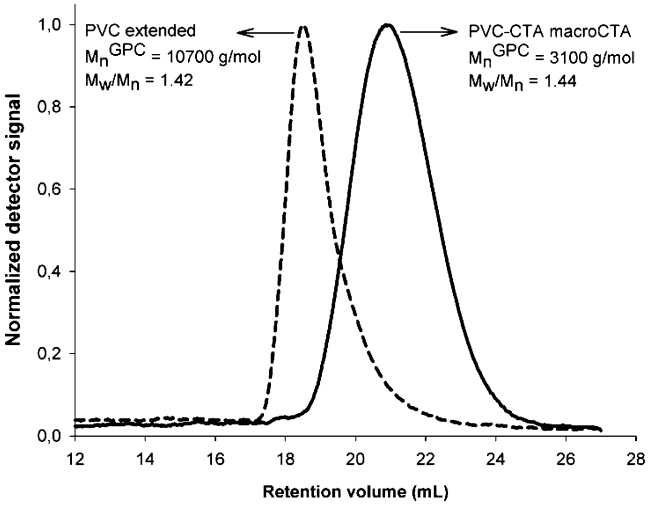


Figure 9. Normalized GPC traces of PVC-CTA samples before (on the right) and after chain extension experiment (on the left).

of vinyl protons (resonances at 5.8 and 5.9 ppm are usual for free radical PVC[7]), consistent with the vanishingly small concentrations of structural defects observed in PVC species obtained via SET-DTLRP process.[7,15]

Chain Extension Experiment. To prove the "living" nature of the VC RAFT polymerization, a reinitiation experiment was performed. As shown in Figure 9, a complete shift of the GPC trace of the PVC sample during the chain extension experiment was observed. Molecular weight of the starting PVC (M_n^{GPC} = 3100 g/mol, M_w/M_n = 1.44) has shifted toward higher molecular weight (M_n^{GPC} = 10 700 g/mol, M_w/M_n = 1.42), which proves the "living" character of the PVC obtained via RAFT polymerization mediated by a CMPCD agent.

CONCLUSIONS

To conclude, for the first time PVC with well-defined structure was successfully synthesized via RAFT polymerization using the RAFT agent cyanomethyl methyl(phenyl)-carbamodithioate (CMPCD). Careful choice of reaction conditions (initiator type and concentration, solvent type and concentration, temperature) is required to achieve low polydispersities. The structural analysis performed via ^{1}H NMR and MALDI-TOF-MS experiments revealed that PVC chains had well preserved functional groups and no structural defects. The "living" nature of the PVC synthesized via RAFT polymerization method was confirmed by a successful chain extension experiment. *Ab initio* MO calculations confirmed the suitability of CMPCD as a good RAFT agent for VC polymerization.

ASSOCIATED CONTENT

Supporting Information

Details of the ONIOM layers, optimized geometries in the form of GAUSSIAN archive entries, corresponding total energies, thermal corrections, zero-point vibrational energies, entropies, free energies and free energies of solvation, calculated thermodynamic and kinetic parameters of investigated reactions in gas and solution phases; MALDI-TOF-MS in the linear mode (using α-cyano-4-hydroxycinnamic acid (CHCA) as matrix) of RAFT-PVC; enlargement of the MALDI-TOF-MS in the reflectron mode and theoretical isotope distribution of the m/z 925−945 region (DP = 11, $C_{32}H_{43}Cl_{11}N_2S_2Na$). This material is available free of charge via the Internet at http://pubs.acs.org.

AUTHOR INFORMATION

Corresponding Author

*E-mail: jcoelho@eq.uc.pt (J.F.J.C.); mcoote@rsc.anu.edu.au (M.L.C.); tamaz.guliashvili@ge.com (T.G.).

Notes

The authors declare no competing financial interest.

ACKNOWLEDGMENTS

The authors gratefully acknowledge CIRES Lda for the collaboration and support over the past years. The MALDI-TOF-MS data were obtained by Dr. Manuel Marcos García, Dra. Beatriz Paz Pino, and Dra. Paula Álvarez Chaver at Unidad de Espectrometria de Masas do Servicio de Determinación Estructural, Proteómica y Genómica, Centro de Apoyo Científico y Tecnológico a la Investigación (CACTI, University of Vigo, Spain). The ^{1}H NMR data were obtained from Rede Nacional de RMN in the University of Coimbra, Portugal. The Varian VNMRS 600 MHz spectrometer is part of the National NMR Network and was purchased in the framework of the National Program for Scientific Re-equipment (Contract REDE/1517/RMN/2005, with funds from POCI 2010 (FEDER) and Fundação para a Ciência e Tecnologia (FCT)). Carlos M. R. Abreu

acknowledges FCT-MCTES for funding (PTDC/EQU-EPR/098662/2008). Patrícia V. Mendonça acknowledges FCT-MCTES for her PhD scholarship (SFRH/BD/69152/2010). Tamaz Guliashvili gratefully acknowledges GE Water and Process Technologies for support. M.L.C. gratefully acknowledges support from the Australian Research Council under their Centres of excellence program, receipt of an ARC Future Fellowship, and generous allocations of supercomputer time on the National Facility of the Australian National Computational Infrastructure.

REFERENCES

(1) Wang, J.-S.; Matyjaszewski, K. *J. Am. Chem. Soc.* **1995**, *117*, 5614−5615.
(2) Georges, M. K.; Veregin, R. P. N.; Kazmaier, P. M.; Hamer, G. K. *Macromolecules* **1993**, *26*, 2987−2988.
(3) Chiefari, J.; Chong, Y. K.; Ercole, F.; Krstina, J.; Jeffery, J.; Le, T. P. T.; Mayadunne, R. T. A.; Meijs, G. F.; Moad, C. L.; Moad, G.; Rizzardo, E.; Thang, S. H. *Macromolecules* **1998**, *31*, 5559−5562.
(4) Moad, G.; Rizzardo, E.; Thang, S. H. *Acc. Chem. Res.* **2008**, *41*, 1133−1142.
(5) Starnes, W. H. Jr.; Zaikov, V. G.; Chung, H. T.; Wojciechowski, B. J.; Tran, H. V.; Saylor, K.; Benedikt, G. M. *Macromolecules* **1998**, *31*, 1508−1517.
(6) Starnes, W. H. *Prog. Polym. Sci.* **2002**, *27*, 2133−2170.
(7) Percec, V.; Popov, A. V.; Ramirez-Castillo, E.; Coelho, J. F. J.; Hinojosa-Falcon, L. A. *J. Polym. Sci., Part A: Polym. Chem.* **2004**, *42*, 6267−6282.
(8) Starnes, W. H. Jr.; Ge, X. *Macromolecules* **2004**, *37*, 352−359.
(9) Starnes, W. H. Jr. *J. Polym. Sci., Part A: Polym. Chem.* **2005**, *43*, 2451−2467.
(10) Percec, V.; Guliashvili, T.; Ladislaw, J. S.; Wistrand, A.; Stjerndahl, A.; Sienkowska, M. J.; Monteiro, M. J.; Sahoo, S. *J. Am. Chem. Soc.* **2006**, *128*, 14156−14165.
(11) Percec, V.; Popov, A. V.; Ramirez-Castillo, E.; Monteiro, M.; Barboiu, B.; Weichold, O.; Asandei, A. D.; Mitchell, C. M. *J. Am. Chem. Soc.* **2002**, *124*, 4940−4941.
(12) Percec, V.; Popov, A. V.; Ramirez-Castillo, E.; Weichold, O. *J. Polym. Sci., Part A: Polym. Chem.* **2003**, *41*, 3283−3299.
(13) Percec, V.; Guliashvili, T.; Popov, A. V. *J. Polym. Sci., Part A: Polym. Chem.* **2005**, *43*, 1948−1954.
(14) Percec, V.; Popov, A. V.; Ramirez-Castillo, E.; Coelho, J. F. J.; Hinojosa-Falcon, L. A. *J. Polym. Sci., Part A: Polym. Chem.* **2005**, *43*, 779−788.
(15) Percec, V.; Ramirez-Castillo, E.; Popov, A. V.; Hinojosa-Falcon, L. A.; Guliashvili, T. *J. Polym. Sci., Part A: Polym. Chem.* **2005**, *43*, 2178−2184.
(16) Coelho, J. F. J.; Carreira, M.; Goncalves, P. M. O. F.; Popov, A. V.; Gil, M. H. *J. Vinyl Addit. Technol.* **2006**, *12*, 156−165.
(17) Coelho, J. F. J.; Mendonca, P. V.; Popov, A. V.; Percec, V.; Goncalves, P. M. O. F.; Gil, M. H. *J. Polym. Sci., Part A: Polym. Chem.* **2009**, *47*, 7021−7031.
(18) Coelho, J. F. J.; Fonseca, A. C.; Gois, J. R.; Goncalves, P. M. O. F.; Popov, A. V.; Gil, M. H. *Chem. Eng. J.* **2011**, *169*, 399−413.
(19) Coelho, J. F. J.; Fonseca, A. C.; Goncalves, P. M. F. O.; Popov, A. V.; Gil, M. H. *Polymer* **2011**, *52*, 2998−3010.
(20) Coelho, J. F. J.; Fonseca, A. C.; Gonçalves, P. M. O. F.; Popov, A. V.; Gil, M. H. *Chem. Eng. Sci.* **2012**, *69*, 122−128.
(21) Rosen, B. M.; Percec, V. *Chem. Rev.* **2009**, *109*, 5069−5119.
(22) IDCalc - Isotope Distribution Calculator, written by Michael J. MacCoss, Department of Genome Sciences, University of Washington: http://proteome.gs.washington.edu/software/IDCalc/ (accessed Feb 10, 2012).
(23) Frisch, M. J.; Trucks, G. W.; Schlegel, H. B.; Scuseria, G. E.; Robb, M. A.; Cheeseman, J. R.; Scalmani, G.; Barone, V.; Mennucci, B.; Petersson, G. A.; Nakatsuji, H.; Caricato, M.; Li, X.; Hratchian, H. P.; Izmaylov, A. F.; Bloino, J.; Zheng, G.; Sonnenberg, J. L.; Hada, M.; Ehara, M.; Toyota, K.; Fukuda, R.; Hasegawa, J.; Ishida, M.; Nakajima, T.; Honda, Y.; Kitao, O.; Nakai, H.; Vreven, T.; Montgomery Jr., J. A.; Peralta, J. E.; Ogliaro, F.; Bearpark, M.; Heyd, J. J.; Brothers, E.; Kudin, K. N.; Staroverov, V. N.; Kobayashi, R.; Normand, J.; Raghavachari, K.; Rendell, A.; Burant, J. C.; Iyengar, S. S.; Tomasi, J.; Cossi, M.; Rega, N.; Millam, N. J.; Klene, M.; Knox, J. E.; Cross, J. B.; Bakken, V.; Adamo, C.; Jaramillo, J.; Gomperts, R.; Stratmann, R. E.; Yazyev, O.; Austin, A. J.; Cammi, R.; Pomelli, C.; Ochterski, J. W.; Martin, R. L.; Morokuma, K.; Zakrzewski, V. G.; Voth, G. A.; Salvador, P.; Dannenberg, J. J.; Dapprich, S.; Daniels, A. D.; Farkas, Ö.; Foresman, J. B.; Ortiz, J. V.; Cioslowski, J.; Fox, D. J. G. *Gaussian 09*, Revision B.01 ed., Wallingford, CT, 2009.
(24) Werner, H.-J.; Knowles, P. J.; Lindh, R.; Manby, F. R.; Schütz, M.; Celani, P.; Korona, T.; Mitrushenkov, A.; Rauhut, G.; Adler, T. B.; Amos, R. D.; Bernhardsson, A.; Berning, A.; Cooper, D. L.; Deegan, M. J. O.; Dobbyn, A. J.; Eckert, F.; Goll, E.; Hampel, C.; Hetzer, G.; Hrenar, T.; Knizia, G.; Köppl, C.; Liu, Y.; Lloyd, A. W.; Mata, R. A.; May, A. J.; McNicholas, S. J.; Meyer, W.; Mura, M. E.; Nicklaß, A.; Palmieri, P.; Pflüger, K.; Pitzer, R.; Reiher, M.; Schumann, U.; Stoll, H.; Stone, A. J.; Tarroni, R.; Thorsteinsson, T.; Wang, M.; Wolf, A. *MOLPRO* **2009**.
(25) Izgorodina, E. I.; Coote, M. L. *J. Phys. Chem. A* **2006**, *110*, 2486−2492.
(26) Lin, C. Y.; Coote, M. L. *Aust. J. Chem.* **2009**, *62*, 1479−1483.
(27) Chernikova, E.; Golubev, V.; Filippov, A.; Lin, C. Y.; Coote, M. L. *Polym. Chem.* **2010**, *1*, 1437−1440.
(28) Izgorodina, E. I.; Lin, C. Y.; Coote, M. L. *Phys. Chem. Chem. Phys.* **2007**, *9*, 2507−2516.
(29) Tomasi, J.; Mennucci, B.; Cammi, R. *Chem. Rev.* **2005**, *105*, 2999−3093.
(30) Brinck, T.; Larsen, A. G.; Madsen, K. M.; Daasbjerg, K. *J. Phys. Chem. B* **2000**, *104*, 9887−9893.
(31) Merrick, J. P.; Moran, D.; Radom, L. *J. Phys. Chem. A* **2007**, *111*, 11683−11700.
(32) Izgorodina, E. I.; Brittain, D. R. B.; Hodgson, J. L.; Krenske, E. H.; Lin, C. Y.; Namazian, M.; Coote, M. L. *J. Phys. Chem. A* **2007**, *111*, 10754−10768.
(33) Lin, C. Y.; Hodgson, J. L.; Namazian, M.; Coote, M. L. *J. Phys. Chem. A* **2009**, *113*, 3690−3697.
(34) Martin, J. M. L.; de Oliveira, G. *J. Chem. Phys.* **1999**, *111*, 1843−1856.
(35) Henry, D. J.; Sullivan, M. B.; Radom, L. *J. Chem. Phys.* **2003**, *118*, 4849−4860.
(36) Steinfeld, J. I.; Francisco, J. S.; Hase, W. L. *Chemical Kinetics and Dynamics*; Prentice Hall: Englewood Cliffs, NJ, 1989.
(37) Krenske, E. H.; Izgorodina, E. I.; Coote, M. L. In *Controlled/Living Radical Polymerization: From Synthesis to Materials*; Matyjaszewski, K., Ed.; American Chemical Society: Washington, DC, 2006; Vol. *944*, pp 406−420.
(38) Fischer, H.; Radom, L. *Angew. Chem., Int. Ed.* **2001**, *40*, 1340−1371.
(39) Based on the data in Table 2 of ref 37, the chain transfer reaction $^{\bullet}CH_2CN + S{=}C(CH_3)S{-}CH(CH_3)Cl \rightarrow {}^{\bullet}CH(CH_3)Cl + S{=}C(CH_3)S{-}CH_2CN$ would be exothermic by 27.1 kJ mol^{-1}; it would be reasonable to assume similar qualitative results would be obtained for other RAFT-agent Z-groups.
(40) Vana, P.; Davis, T. P.; Barner-Kowollik, C. *Macromol. Theory Simul.* **2002**, *11*, 823−835.
(41) Coote, M. L.; Krenske, E. H.; Izgorodina, E. I. *Macromol. Rapid Commun.* **2006**, *27*, 473−497.
(42) Akzo Nobel: Initiators and Reactor Additives for Thermoplastics, http://www.akzonobel.com/polymer/system/images/AkzoNobel_Initiators_and_Reactor_Additives_for_Thermoplastics_Low-res_protected_July%202010_tcm96-39468.pdf (accessed Feb 10, 2012).
(43) Percec, V.; Popov, A. V.; Ramirez-Castillo, E.; Weichold, O. *J. Polym. Sci., Part A: Polym. Chem.* **2004**, *42*, 6364−6374.
(44) Beyou, E.; Chaumont, P.; Chauvin, F.; Devaux, C.; Zydowicz, N. *Macromolecules* **1998**, *31*, 6828−6835.

(45) Schilli, C.; Lanzendörfer, M. G.; Müller, A. H. E. *Macromolecules* **2002**, *35*, 6819−6827.
(46) Pound, G.; Aguesse, F.; McLeary, J. B.; Lange, R. F. M.; Klumperman, B. *Macromolecules* **2007**, *40*, 8861−8871.
(47) Yan, Y. F.; Zhang, W.; Qiu, Y. S.; Zhang, Z. B.; Zhu, J. A.; Cheng, Z. P.; Zhang, W. D.; Zhu, X. L. *J. Polym. Sci., Part A: Polym. Chem.* **2010**, *48*, 5206−5214.

Macromolecules

Article

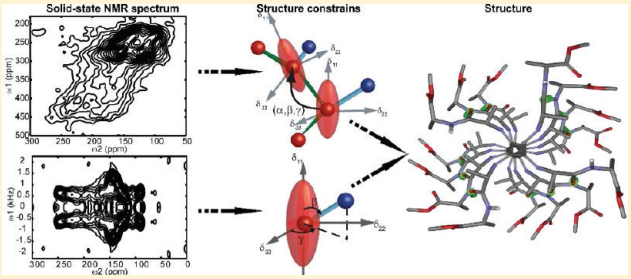
pubs.acs.org/Macromolecules

Direct Backbone Structure Determination of Polyisocyanodipeptide Using Solid-State Nuclear Magnetic Resonance

Chandrakala M. Gowda, Ernst R. H. van Eck, Arend M. van Buul, Erik Schwartz, Gijsbrecht W. P. van Pruissen, Jeroen J. L. M. Cornelissen, Alan E. Rowan, Roeland J. M. Nolte, and Arno P. M. Kentgens*

Radboud University Nijmegen, Institute for Molecules and Materials, Heyendaalseweg 135, 6525 AJ Nijmegen, The Netherlands

ABSTRACT: The success of polyisocyanides as the basic scaffold for functional materials has been attributed to its rigid and highly stable structure. It has been demonstrated that these polymers can be stabilized by formation of inter side chain hydrogen bonds (Cornelissen et al. *Science* **2001**, *293*, 676) which in turn has resulted in development of several polyisocyanide based functional materials. Despite the success of the material, the exact structure and conformation of these polymers has been subject of discussions over many years and several structural models based on evidence from different analytical and theoretical methods have been proposed. This study determines the structure of the isocyanide dipeptide polymer using solid-state NMR spectroscopy. Two-dimensional separated-local-field and double-quantum single-quantum spectroscopic methods have been employed to obtain structural constraints for the polymer backbone. These constraints were used to build a molecular model and subsequently subjected to molecular dynamics simulations. The backbone structure of the polyisocyanide is determined to be a 15_4 helix with hydrogen bonding interactions between n and $n + 4$ side chains.



1. INTRODUCTION

Polyisocyanides (Figure 1) have been targeted as scaffolds for the design of functional materials.[1−3] This derives from the fact that these polymers possess a stable and rigid structure with the possibility of attaching a range of functional groups as side chains. For example, the perylenediimide moiety incorporated as side chain substituent to the backbone scaffold of polyisocyanides showed high exciton migration rates and charge densities.[2] This property of the functionalized polymers can be exploited for applications in photovoltaic devices, field effect transistors (FETs), etc. Alternatively, carbazole functionalized polyisocyanides grown on a silicon wafer were successfully incorporated into Light Emitting Diodes (LEDs).[3] The diverse applications and performance efficiency of these materials crucially depend upon the conformation of the polymer that is formed. The backbone conformation of polyisocyanides has been a subject of discussion for several decades and there have been several experimental and theoretical efforts to determine the structure and conformation of polyisocyanides.[4−9] As early as 1968, Millich et al. built Leybold molecular models of poly-(α-phenylethyl isocyanide) and proposed a tightly coiled helical structure for the polymer.[4] In addition, X-ray diffraction data indicated one repeat unit per 1Å of the polymer chain length.[4] The study nevertheless, made assumptions regarding the packing of the polymer molecules to interpret the X-ray diffraction results. The proposed helical conformation for the polymer was further supported by optical activity studies of poly(α-phenylethyl isocyanide).[10] In order to verify the propositions regarding the helical conformations of the polymers, Nolte et al. exploited the chirality of the helices to separate the racemic mixture of poly(*tert*-butyl isocyanide) into left and right handed enantiomers by column chromatography using a chiral support.[5] Later the same authors used circular dichroism

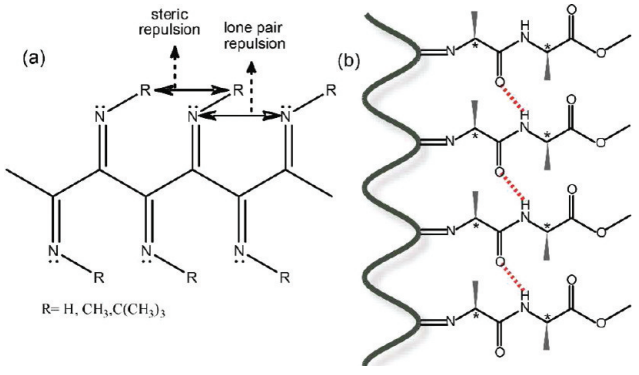


Figure 1. (a) General polyisocyanide skeleton backbone showing different interactions in the planar conformation (figure adapted from ref 13). (b) Sketch of the polymer L-isocyanoalanyl-D-alanine methyl ester (L,D-PIAA) with the proposed hydrogen bonding array between side chains n and $(n + 4)$. The asterisks indicate the chiral centers. (The side chains to the left, outward and into the plane of the drawing are omitted for clarity.)

Received: January 15, 2012
Revised: February 7, 2012
Published: February 29, 2012

 © 2012 American Chemical Society

(CD) spectroscopy and theoretical calculations to assign the screw sense of the polymer and in addition they proposed that the polymer had a 4_1 helical conformation.[11] On the other hand, there were also studies that raised questions regarding the rigorousness of the rigid 4_1 helical conformation for all the polyisocyanides. For example, molecular orbital calculations on the electronic structure of polyisocyanides showed qualitatively that N-lone pair repulsion near the backbone precludes a planar conformation and hence forces the backbone into a nonplanar conformation. However, the study also showed that the helical angle adopted by the polymers was influenced by the steric bulk of the substituent groups (Figure 1a).[9] Furthermore, a comparative study of the hydrodynamic properties of poly(α-phenylethyl isocyanide) and poly(β-phenylethyl isocyanide) led to the conclusion of a rigid rod like helical structure for the former polymer and a more flexible and undulating chain structure for the latter.[6] Green et al. also expressed strong skepticism with regard to the rigid helical conformations of the polyisocyanides based on ^{13}C solution state NMR and other analytical methods.[7] Clericuzio et al, based on theoretical studies, proposed that the more favorable minimum conformation of the polyisocyanides was the "non-helical syndio" conformation.[8] Recently, Onouchi et al. proposed a 15_4 helical structure for substituted phenyl isocyanide polymers using atomic force microscopy (AFM) and wide-angle X-ray diffraction measurements[12] of uniaxially oriented polymer films. It is not always possible to obtain such films, however, as some of the polymers do not form the required liquid crystalline phase.

Solid-state NMR (ssNMR) spectroscopy has become a powerful tool for the elucidation of the structure of compounds irrespective of the physical state (crystalline, glassy amorphous, gel, etc.) of the samples. ssNMR spectroscopy has ingeniously exploited the anisotropic nuclear spin interactions to obtain structural information such as torsion angles and distances.[14−18] The relative orientation of different chemical moieties can be inferred by determining the relative orientation of anisotropic nuclear interactions such as dipole−dipole, dipole−chemical shift anisotropy (CSA), or CSA−CSA interactions, associated with the chemical moieties. For example, the secondary structure of Samia cynthia ricini silk was determined by measurement of the relative orientation of the CSA tensors of the carbonyl groups in the polymer backbone.[18] Cornelissen et al. synthesized polyisocyanides with peptide side chains, i.e. poly(L-isocyanoalanyl-D-alanine methyl ester (L,D-PIAA) (Figure 1b) and poly(L-isocyanoalanyl-L-alanine methyl ester) (L,L-PIAA)) in order to stabilize the backbone of the polymer by means of hydrogen bonds.[19] The presence of strong N−H---O=C hydrogen bonding interactions between the amide moieties of the side chains was confirmed by ^{1}H NMR studies.[19,20] Molecular modeling calculations were indicative of a 4_1 helical conformation; however there is no direct experimental proof to confirm the structure.[19,21]

In this study we use advanced 2D solid-state NMR techniques to determine the backbone conformation of a dialanine derived polyisocyanide, L,D-PIAA. The polymer backbone structure can be fully determined from the relative orientation of the two neighboring ^{13}C CSA tensors given that the orientation of the ^{13}C CSA tensor is known in the molecular frame. The latter information can be obtained from the relative orientation of the CSA-dipolar interaction since the unique axis of the dipolar tensor coincides with the vector connecting the interacting spins. Slow magic angle spinning (MAS) experiments are used to obtain the principal components of the backbone carbon CSA tensor. 2D double-quantum single-quantum spectroscopy (DOQSY) was applied to obtain the relative orientation of the ^{13}C CSA tensors of two neighboring backbone carbons in L,D-PIAA.[15,16,18] A 2D-separated local field (2D-SLF) experiment is used to determine the orientation of the ^{13}C=^{15}N dipolar vector in the principal axis frame of the ^{13}C CSA tensor.[22,23] SIMPSON simulations were performed to extract the angles from the experimental DOQSY and 2D-SLF spectra.[24] The structural constraints obtained from the DOQSY and 2D-SLF data are used to build the L,D-PIAA model. The polymer model was subsequently subjected to molecular dynamics simulations in order to obtain the energy minimized structure.

2. MATERIALS AND METHODS

Samples. The unlabeled L,D-PIAA sample was used to record 1D carbon NMR spectra. For the 2D NMR experiments the L,D-PIAA sample was enriched with ^{13}C and ^{15}N at the backbone imine carbon and nitrogen to get a 10% ^{13}C=^{15}N spin pair enrichment in the polymer. To this end a L,D-IAA monomer, in which the isocyano group was ^{13}C and ^{15}N enriched, was synthesized. This monomer was subsequently copolymerized with an unlabeled L,D-IAA monomer using a feed ratio of 1:9 (^{13}C−^{15}N-L,D-IAA: L,D-IAA, respectively) to obtain the 10% ^{13}C=^{15}N spin pair enriched L,D-PIAA sample as previously discussed.[20]

NMR. *1D Experiments.* 1D ^{13}C NMR spectra were recorded using cross-polarization magic angle spinning (CPMAS) experiments on a Varian 600 MHz infinity spectrometer using a 4 mm triple resonance MAS probe. The proton 90° pulse length was 5 μs and the proton RF field for spinlock during cross-polarization (CP) was set to 50 kHz. Protons were decoupled in the direct dimension using the continuous modulation (CM) decoupling scheme[25] at an RF field strength of 76 kHz. The spinning speed was set to 4500 or 6000 Hz. The spectra are referenced using the CH_2 carbon peak of adamantane at 38.48 ppm as an external reference.

2D Experiments. All 2D experiments were recorded in static mode on a Varian 400 MHz infinity spectrometer using a 4 mm triple resonance MAS probe and 10% ^{13}C=^{15}N spin pair enriched L,D-PIAA sample.

The ^{13}C−^{15}N 2D-SLF spectrum (Figure 4a) was recorded using the pulse sequence shown in Figure 2a. As a first step, the proton (^{1}H) magnetization is transferred to nitrogen (^{15}N) using a 35 kHz spinlock RF field on ^{1}H and ^{15}N nuclei each for a duration of 2.4 ms. In the second step, the magnetization from nitrogen (^{15}N) to the carbons (^{13}C) is transferred using a 35 kHz spinlock RF field for both ^{15}N and ^{13}C for 2.5 ms. The ^{13}C=^{15}N dipolar coupling evolution was recorded in steps of 55.55 μs (t_1). A total of 21 t_1 increment points accumulating 2500 scans each were recorded in the indirect dimension. A ^{13}C spin echo of duration 2τ with τ = 1200 μs is created. The total echo time depends on the spin−spin relaxation time (T_2) of the ^{13}C nuclei. The ^{13}C chemical shift evolution during time τ is refocused using a 180° pulse on the carbons (^{13}C) at the center of the echo time 2τ. The refocusing of ^{13}C=^{15}N heteronuclear dipolar coupling is perturbed by an additional 180° pulse at time t_1 on nitrogen (^{15}N). The dipolar coupling is evolved by shifting the position of the 180° pulse on the nitrogen channel with small time increments t_1. Efficient ^{15}N decoupling in the direct dimension was achieved using the broad-band WALTZ-16 decoupling scheme employing 16.6 μs pulse length.[26] Quadrature detection in the indirect dimension is not necessary as it only consists of a symmetric dipolar coupling evolution.

The DOQSY spectrum was recorded using the pulse sequence shown in Figure 2b.[15] ^{1}H−^{13}C cross-polarization was done using 45 kHz spinlock field strength on ^{1}H and ^{13}C for a duration of 1.5 ms. The ^{1}H and ^{13}C 90° pulses were 3.2 and 3.3 μs, respectively. Protons were decoupled using an RF field strength of 70 kHz using the two pulse phase modulated (TPPM)[27] decoupling scheme during the excitation, evolution and acquisition time. The double-quantum (DQ) excitation time was optimized to select maximum signal from directly bonded ^{13}C−^{13}C spin pairs as calculated by the SIMPSON simulation

dx.doi.org/10.1021/ma300102e | Macromolecules 2012, 45, 2209−2218

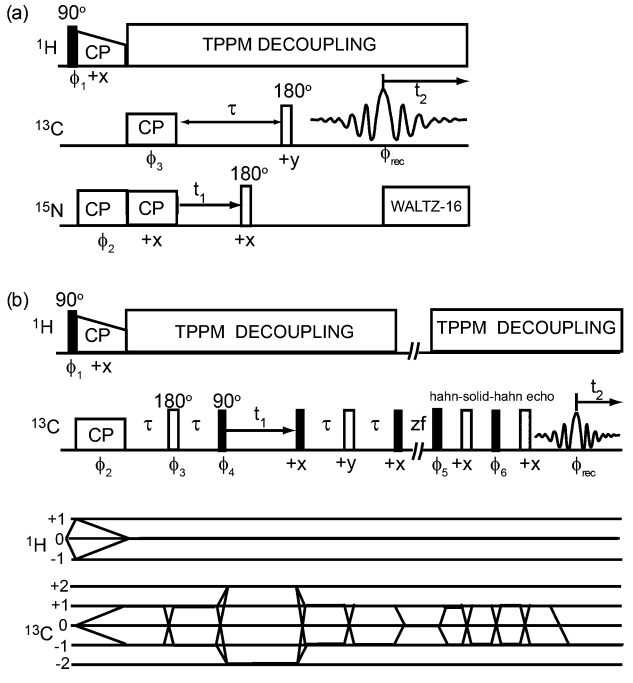


Figure 2. (a) $^{13}C-^{15}N$ 2D-SLF pulse sequence with double CP transfer steps to select ^{13}C magnetization from carbons that are directly bonded to ^{15}N nuclei. Phase cycle ϕ_1 = 1,3; ϕ_2 = 0,0,2,2; ϕ_3= {0,0,0,0,2,2,2,2}; ϕ_{rec}={3,1,1,3,1,3,3,1}; (b) DOQSY pulse sequence and the coherence transfer pathway. 2τ represents the double quantum excitation and reconversion time while t_1 is the indirect dimension evolution time. The *z*-filter (zf) time was set to 1 ms during which unwanted coherences are dephased due to the heteronuclear dipolar coupling to protons.[29] The Hahn−solid−Hahn echo is applied to avoid baseline distortions.[15] The pulse phases ϕ_2, ϕ_3, and ϕ_4 are cycled in four steps to select double quantum coherences. ϕ_1 = 1,3; ϕ_2 = 1, 1, 2, 2, 3, 3, 0, 0; ϕ_3 = {0, 0, 1, 1, 2, 2, 3, 3; 1, 1, 2, 2, 3, 3, 0, 0; 2, 2, 3, 3, 0, 0, 1, 1; 3, 3, 0, 0, 1, 1, 2, 2}; ϕ_4 = {0, 0, 1, 1, 2, 2, 3, 3}; ϕ_5 = $\{2_{32}, 3_{32}, 0_{32}, 1_{32}\}$; ϕ_6 = $\{1_{32}, 2_{32}, 3_{32}, 0_{32}; 3_{32}, 0_{32}, 1_{32}, 2_{32}\}$; ϕ_{rec} = $\{(0, 2, 2, 0, 0, 2, 2, 0, 2, 0, 0, 2, 2, 0, 0, 2)_2$; $(1, 3, 3, 1, 1, 3, 3, 1, 3, 3, 1, 1, 3, 3, 1, 1, 3)_2$; $(2, 0, 0, 2, 2, 0, 0, 2, 0, 2, 2, 0, 0, 2, 2, 0)_2$; $(3, 1, 1, 3, 3, 1, 1, 3, 1, 3, 3, 1, 1, 3, 3, 1)_2\}$.

program.[24] The double quantum excitation profile showed the maximum signal for single bond separated spin pair at 2τ = 200 μs. However, two bond separated $^{13}C-^{12}C-^{13}C$ spin pairs occur as often as directly bonded $^{13}C-^{13}C$ spin pairs potentially obscuring the spectrum. Hence a DQ excitation time of 2τ = 160 μs was chosen for DQ excitation which kept the ratios of intensities from single bond to two bond separated spin pairs to 8:1 while the DQ excitation time 2τ = 200 μs would result in a ratio of 5:1. The total DQ reconversion time was set equal to that of the DQ excitation time. Quadrature detection in the ω_1 dimension was achieved using the time proportional phase increment (TPPI) method.[28] The indirect dimension consisted of 42 t_1 increments and was acquired in a total of 6 days of time. A detailed discussion and theoretical treatment of the sequence is given in ref 29 and ref 15.

Simulation, Model Building, and Energy Minimization. ^{13}C CSA spinning sideband analyses were performed using Herzfeld and Berger analysis (HBA) software package.[30] NMR simulations were performed using the SIMPSON simulation program.[24] The simulations for extraction of the orientation angles were set up to closely mimic the experimental conditions. The 2D-SLF simulations were performed by varying the dipolar orientation angles in the principal axis frame of the ^{13}C CSA tensor (β_D^{C1N1}, γ_D^{C1N1}) over a grid of 0° to 90° in steps of 5° each. For the simulation of the DOQSY spectra, in view of reducing the computational time, initially a broad grid simulation of the spectra was run with α_{CSA}^{C1C2} and γ_{CSA}^{C1C2} varying from 0° to 360° in steps of 30° each and β_{CSA}^{C1C2} varying from 0° to 90° in steps of 20°. In the region of the probable minima obtained in the broad grid of simulations, a fine grid of simulation was further set up with α_{CSA}^{C1C2} and γ_{CSA}^{C1C2} varying in steps of 10° each and β_{CSA}^{C1C2} varying in steps of 5° in the vicinity of the minima values only. The simulated 2D-SLF and DOQSY spectra were processed identically to the experimental spectrum using the matNMR processing toolbox in Matlab.[31]

The polymer model was built in a Matlab program using the orientation angles obtained from the analysis of the DOQSY and the 2D-SLF spectrum and was subsequently energy minimized using the Accelrys Materials Studio program.[31,32]

3. RESULTS AND DISCUSSIONS

3.1. ^{13}C CSA Analysis. The 1D ^{13}C CPMAS spectrum of unlabeled L,D-PIAA is shown in Figure 3. The assignments of

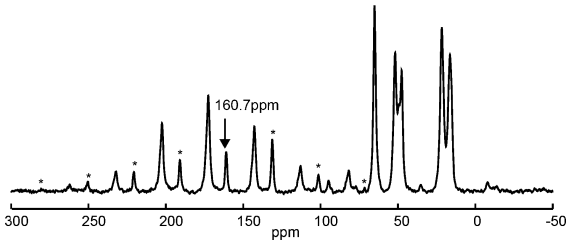


Figure 3. ^{13}C CPMAS spectrum of natural abundance L,D-PIAA. The peak at 160.7 ppm corresponds to the backbone carbon. The spinning sidebands are indicated by asterisks.

the peaks was previously discussed by Cornelissen et al.[20] The backbone carbon has an isotropic chemical shift of 160.7 ppm and exhibits large chemical shift anisotropy. At spinning speeds slower than the width of the CSA powder pattern, spinning sidebands appear on either side of the peak at the isotropic chemical shift position. The spinning sideband intensities reflect the CSA tensor information which may be extracted to a high degree of accuracy using the approach introduced by Herzfeld and Berger.[33] However, in the presence of additional anisotropic interactions such as the dipolar coupling, quadrupolar coupling etc. the spinning sideband intensities are a net effect of the CSA, dipolar coupling interaction and the residual dipolar coupling as a result of the quadrupolar coupling interaction.[34] In the natural abundant polymer sample the ^{13}C imine carbon is bonded to NMR active ^{14}N quadrupolar nuclei by means of a double bond. For a $^{13}C{=}{=}^{14}N$ group the typical dipolar coupling is of the order of 1100 Hz. At a magic-angle spinning frequency of 4500 Hz, which is ~4 times larger than the dipolar coupling interaction, the $^{13}C{=}{=}^{14}N$ heteronuclear dipolar coupling is averaged to a large extent. The cross terms between the dipolar and quadrupolar interactions at high field strengths (here 14.1 T) are generally negligible.[14] Hence in this case the CSA interaction is dominant and the principal components (δ_{11}, δ_{22}, δ_{33}) of the ^{13}C CSA tensor can be determined by the Herzfeld and Berger spinning sideband analysis.[33] Since the spinning sidebands are well separated the sideband integrals provide a highly reliable CSA tensor analysis. The principal CSA tensor components of the backbone ^{13}C were determined to be δ_{11} = 254 ppm, δ_{22} = 145 ppm, and δ_{33} = 83 ppm. The tensor values obtained at multiple spinning speeds (4500 and 6000 Hz) were reproducible to within an accuracy of ±2 ppm. The chemical shift anisotropy reflects the orientation of the molecular segments around the nucleus. Thus, the relative orientation of the molecular segments in the polymer chain is determined by measuring the relative orientation of the tensor components of the two neighboring

dx.doi.org/10.1021/ma300102e | Macromolecules 2012, 45, 2209−2218

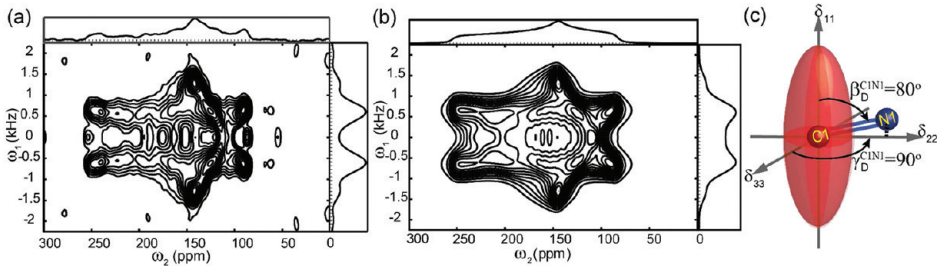


Figure 4. (a) Experimental 2D-SLF spectrum of 10% $^{13}C-^{15}N$ spin pair enriched L,D-PIAA. (b) Best fit simulation of the 2D-SLF experiment for a relative orientation of the dipolar C1−N1 vector given by the Euler angles β_D^{C1N1} =80° and γ_D^{C1N1} = 90°. (c) $^{13}C{=}^{15}N$ dipolar vector in the principal axis frame of the ^{13}C CSA tensor of the imine carbon. The labels C1 and N1 are used in the discussions below for convenience.

carbon nuclei along the polymer backbone. The exact structure determination further requires fixing the orientation of the ^{13}C CSA tensor components in the molecular frame. We use the 2D-DOQSY and 2D-SLF solid state NMR experiments to obtain this information.

3.2. Relative ^{13}C CSA and $^{13}C-^{15}N$ Dipolar Tensor Orientation. The dipolar interaction is a uniaxial tensor interaction with the unique axis oriented along the bond connecting the two interacting nuclei. Hence, measurement of the relative orientation of the ^{13}C CSA tensor to the dipolar coupling axis is valuable for structure determination as it directly correlates the anisotropic CSA interaction to the molecular frame. In NMR studies relative CSA-dipolar orientation have been determined widely using 2D-separated local field (2D-SLF) experiments.[17,22,23] Rotational echo double resonance (REDOR) sideband dephasing and rotary resonance experiment proved to be very useful for samples with multiple spin sites and for natural abundant spin systems where MAS is essential to resolve the peaks and to increase sensitivity.[14,35] However, we resorted to the 2D-SLF experiment to obtain the orientation of the $^{13}C{=}^{15}N$ dipolar vector in the principal frame of the ^{13}C CSA tensor using a 10% $^{13}C{=}^{15}N$ spin pair enriched L,D-PIAA. The two-dimensional spread of the resonance frequencies in the 2D-SLF spectrum allows a reliable spectral analysis. In addition, it does not suffer from extreme sensitivity to RF inhomogeneity as in a rotary resonance experiment.[14] A double CP is used to create ^{13}C magnetization on the backbone carbon that is directly bonded to the imino nitrogen ($^{13}C{=}^{15}N$). The magnetization is first transferred from ^{1}H to ^{15}N and subsequently transferred from ^{15}N to the directly bonded ^{13}C. The advantage of this is the complete removal of the strong nonmodulated natural abundant ^{13}C signals that would appear in the form of a central ridge of the SLF spectrum in the indirect dimension. The experimental 2D-SLF spectrum, free of such a ridge, is shown in Figure 4a. In the 2D-SLF spectrum the frequencies in the direct dimension are a function of the ^{13}C CSA tensor and the frequencies in the indirect dimension are a function of $^{13}C{=}^{15}N$ dipolar coupling. The 2D spectral features showing specific patterns of ridges are a function of the relative orientation angles of the CSA and dipolar interaction tensors.

SIMPSON simulations were performed to extract the magnitude of the $^{13}C{=}^{15}N$ dipolar coupling and the relative orientation angles of the dipolar coupling tensor in the principal axis frame of the ^{13}C CSA tensor. First, we extract the magnitude of the dipolar coupling using the sum projection of 2D-SLF spectra in the indirect dimension (ω_1) which represents the Pake doublet pattern of the $^{13}C{=}^{15}N$ dipolar coupling. 1D SIMPSON simulations with varying magnitudes of dipolar coupling were performed to generate $^{13}C{=}^{15}N$ Pake patterns. The best matching spectrum was obtained for a $^{13}C{=}^{15}N$ dipolar coupling of 1495 ± 50 Hz which corresponds to a $^{13}C{=}^{15}N$ bond length of 1.27 Å ± 0.02 Å. Second, to extract the relative CSA-dipolar orientation angles, the dipolar coupling magnitude determined above is used. In the SIMPSON spin system the principal axis frame of the ^{13}C CSA tensor is considered as the reference frame i.e. the Euler angles relating the principal axis frame, and the laboratory frame are given by $(\alpha_{CSA}^{C1}, \beta_{CSA}^{C1}, \gamma_{CSA}^{C1}) = (0, 0, 0)$. The dipolar tensor is related to this reference frame by the Euler angles $(\alpha_D^{C1N1}, \beta_D^{C1N1}, \gamma_D^{C1N1})$. The dipolar coupling is a uniaxial tensor and is invariant to rotation around the $^{13}C{=}^{15}N$ bond. The simulations thus determine two of the Euler angles that relate the unique axis of the dipolar coupling tensor in the principal axis frame of the ^{13}C CSA tensor described by β_D^{C1N1} and γ_D^{C1N1}. A plot of simulated spectra for varying β_D^{C1N1} and γ_D^{C1N1} is shown in Figure 5. It can be seen that when the β_D^{C1N1} rotation angle is zero the spectra are insensitive to a change in γ_D^{C1N1} angle. As the β_D^{C1N1} angle approaches 90° the spectral patterns become highly sensitive to variations in γ_D^{C1N1} angle. Least squares fitting of the experimental and simulated data (see experimental section for details) yields the best matching values for $(\beta_D^{C1N1}, \gamma_D^{C1N1}) = (80°, 90°)$ (Figure 4b). The simulations provide a very good match to the experimental spectrum despite the fact that the simulations were performed assuming single pulse excitation, whereas the experimental spectrum was obtained using $^{13}C{=}^{15}N$ CP. In the case of uniaxial tensors the Euler angles β_D^{C1N1} and γ_D^{C1N1} become equivalent to the polar angles (θ, ϕ) of a spherical coordinate system and hence the dipolar coupling vector can be represented as shown in Figure 4c.[36,37] However, the angles $\beta_D^{C1N1} = 80°$ and $\gamma_D^{C1N1} = 90°$ do not uniquely determine the orientation of the CN dipolar vector in the C1 CSA frame since the D2h symmetry of the dipolar coupling interaction leads to the symmetry equivalence of the angles (θ,ϕ); $(\theta,180 - \phi)$; $(\theta, 180 + \phi)$; $(\theta,-\phi)$; $(180 - \theta,\phi)$; $(180 - \theta, 180 - \phi)$; $(180 - \theta, 180 + \phi)$; $(180 - \theta,-\phi)$.[36,37] In the present case the angle $\gamma_D^{C1N1} = 90°$ restricts the symmetry related angle combinations to a total of four being (80°, 90°); (80°, 270°); (100°, 90°); (100°, 270°) that would all result in the same 2D-SLF spectrum.

4. RELATIVE ^{13}C CSA ORIENTATIONS

In the previous section, we determined the relative orientation of the dipolar tensor in the ^{13}C CSA tensor frame which partially fixes the ^{13}C CSA tensor in the molecular frame ("*partial*"—since the angle α_D^{C1N1} rotation around the CN bond is unknown). In the next step, we wish to determine the relative orientation angles between the CSA tensors of two neighboring carbons (^{13}C) in the polymer backbone. This information combined with that of the orientation of the ^{13}C CSA tensor in

dx.doi.org/10.1021/ma300102e | *Macromolecules* 2012, 45, 2209−2218

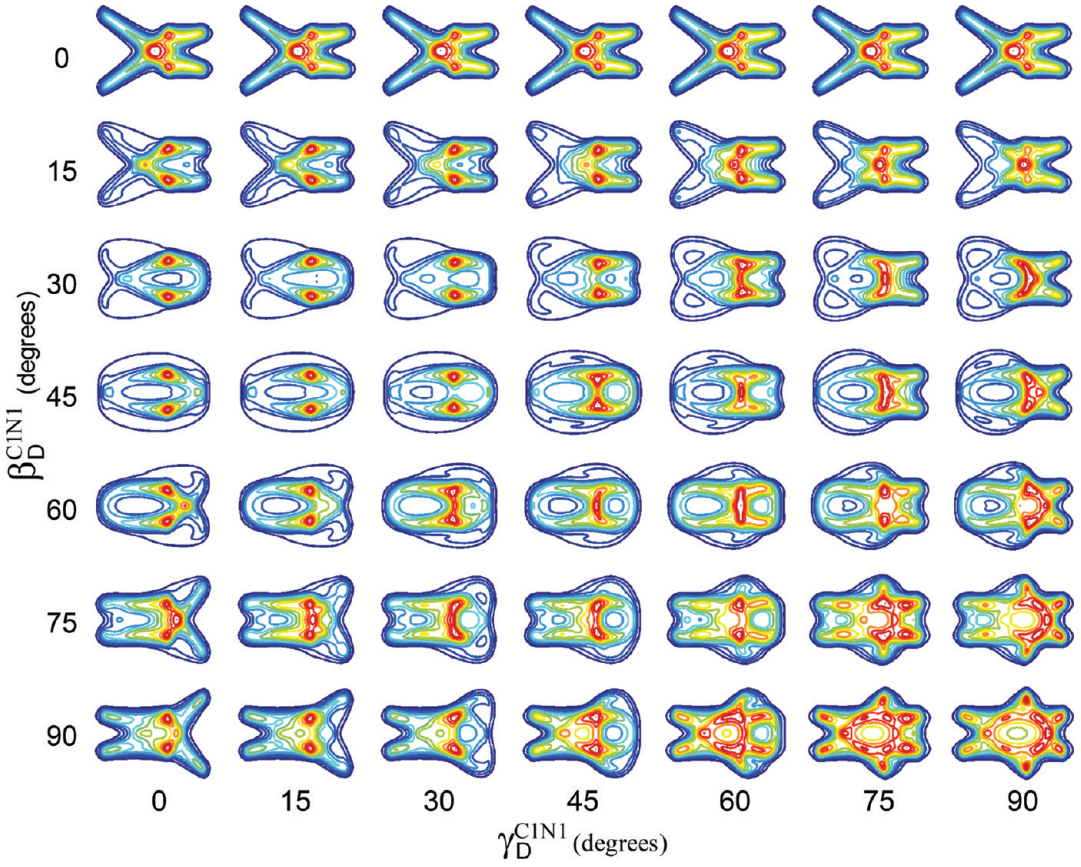


Figure 5. Series of plots of the $^{13}C-^{15}N$ 2D-SLF simulations performed with SIMPSON varying the β_D^{C1N1} and γ_D^{C1N1} angles orienting the dipolar CN vector with respect to the C1 CSA principal axis frame from 0° to 90°.

the molecular frame can be used to determine the complete backbone conformation. Several experiments have been described in the literature to extract relative orientation angles of neighboring carbon CSA tensors. For static samples, double quantum single-quantum spectroscopy (DOQSY) and its variants have been used to determine torsion angles in polymers and biopolymers such as Samia *cynthia ricini* silk.[15,16,18] Tycko et al. used the rotor synchronized 2D exchange spectroscopy under MAS to extract relative tensor orientations in peptide samples.[38] Experiments have also been designed to obtain torsion angles using dipolar interaction tensors such as the NCCN-2Q-HLF.[39] We have made use of the DOQSY pulse sequence shown in Figure 2b.[15] This sequence has the advantage that for strongly coupled spins a short DQ excitation time of the order of 160 to 240 μs can be employed to excite DQ coherences. Sequences involving a large number of pulses are not practical for strongly coupled spins, as the minimum DQ excitation time is limited by the number of pulses and pulse lengths to be used.[16] The sample used here, 10% $^{13}C{=}{=}^{15}N$ spin pair enriched L,D-PIAA contains 1% directly bonded $^{13}C-^{13}C$ spin pairs. A potential contribution to the double quantum spectra can arise from 1% two bond separated $^{13}C-^{12}C-^{13}C$ spin pairs. As described in the experimental section, the contribution from the two bond separated spin pairs was kept to a minimum by strategically restricting the DQ excitation time. The experimental DOQSY spectrum is shown in Figure 6a. The frequency in the direct dimension is determined by the ^{13}C CSA and $^{13}C-^{13}C$ dipolar coupling while the frequency in the indirect dimension is a function of the sum of the ^{13}C CSA tensors.[15] The DQ excitation efficiency is a function of $^{13}C-^{13}C$ dipolar coupling strength and hence the powder line shape of a DQ filtered carbon spectrum is a function of $^{13}C-^{13}C$ dipolar vector orientation. To obtain uniform DQ excitation over the full powder pattern, DOQSY spectra have to be recorded at varying excitation times (2τ) and added together as described in ref 15. However, in the present case we refrain from doing this and preferred to use a single DQ excitation time due to the concern of increased signal contributions from two bond separated ($^{13}C-^{12}C-^{13}C$) spin pairs in the spectrum. The effects of $^{13}C-^{13}C$ dipolar coupling on the spectrum have been taken into account in the simulations.

The relative orientations of the ^{13}C CSA tensors were extracted by the least-squares fitting of the experimental spectra with the SIMPSON simulations. All non-negligible interactions that influence the spectrum were considered in the simulations. This requires the knowledge of both the magnitude and the orientation angles of the interaction in a given reference frame. The current spin system depicted in Figure 6b consists of a $^{13}C-^{13}C$ spin pair with each carbon atom dipolar coupled to a ^{15}N atom, with the ellipsoids representing the CSA tensor of the carbons. Associated with this spin system one can identify three dominant interactions that will influence the DOQSY spectrum. First, the chemical shift anisotropy of the carbons C1 and C2. Second, the heteronuclear $^{13}C{=}{=}^{15}N$ dipolar coupling of the two carbon nitrogen spin pairs and third, the homonuclear $^{13}C-^{13}C$ dipolar coupling.

In the simulations the principal axis frame of the C1 carbon CSA tensor was fixed as the reference frame (see Figure 4c).[24,40] The magnitude and relative orientation of the $^{13}C1{=}{=}^{15}N1$ in the ^{13}C CSA reference frame is determined from the SLF data.

dx.doi.org/10.1021/ma300102e | *Macromolecules* 2012, 45, 2209−2218

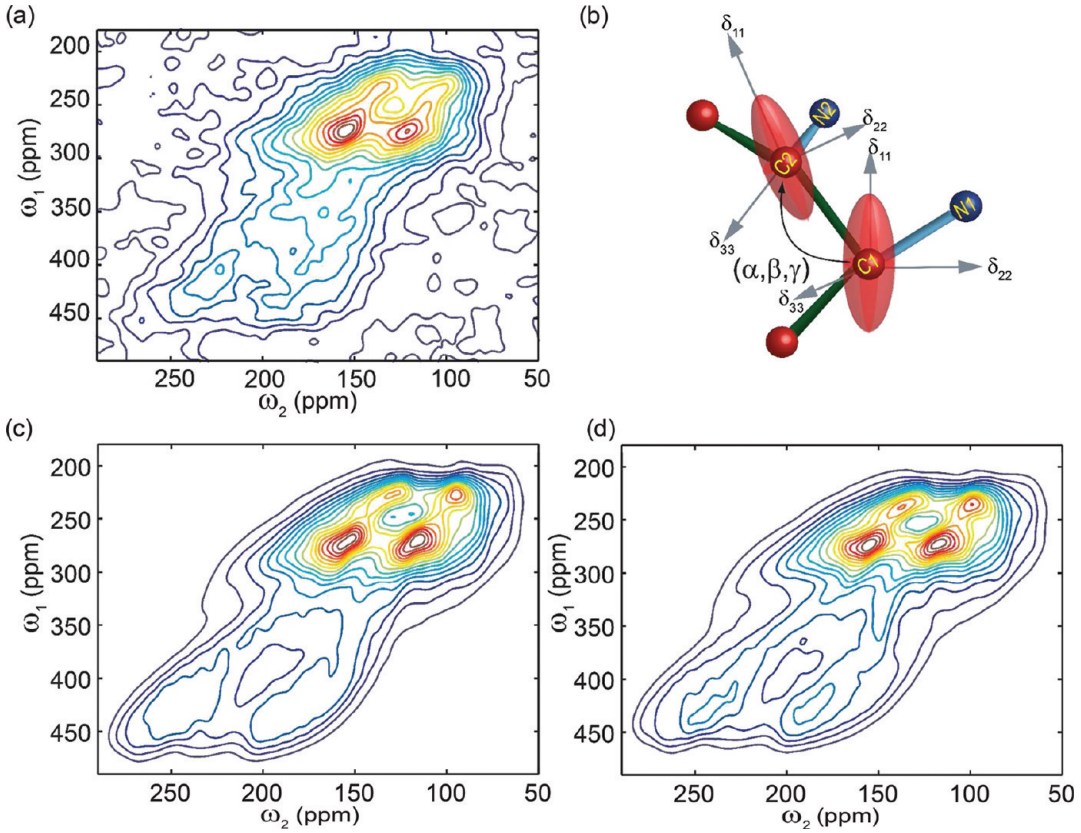


Figure 6. (a) Experimental 2D DOQSY spectrum of 10% $^{13}C{=}{}^{15}N$ spin pair labeled (L,D-PIAA) polymer using a DQ excitation and reconversion time of 160 μs. (b) Relative orientation of principal CSA tensor frames of $^{13}C{-}{}^{13}C$ carbon spin pairs along the polymer backbone. The CSA tensors are shown as ellipsoids around the respective carbons. The labels are used for convenience in discussions below. (c, d) Best matching simulations of the DOQSY spectrum indicating the Euler angles $(\alpha,\beta,\gamma)_{CSA}^{C1C2}$ of (c) (250°, 45°, 30°) and (d) (240°, 50°, 30°) respectively. This can be translated to a relative rotation of the CSA frame about a specific rotation axis (see Table 1) of 90° or 100° for parts c and d, respectively.

To simulate the effect of $^{13}C2{=}{}^{15}N2$ dipolar coupling on the DOQSY spectrum the relative orientation of $^{13}C2{=}{}^{15}N2$ dipolar tensor in the reference frame has to be determined. This is obtained by multiplying the rotation matrices $R_D^{C2N2} = R_{CSA}^{C1C2} \times R_D^{C1N1}$, where the rotation matrix R_{CSA}^{C1C2} refers to the coordinate transformation relating the C2 carbon CSA tensor to the reference frame. R_D^{C1N1} is the rotation matrix relating the C1N1 dipolar vector to the reference frame. The Euler angles from the resultant matrix R_D^{C2N2} are the Euler transformation angles orienting the C2−N2 dipolar tensor in the reference frame.[41]

The orientation of the $^{13}C1{-}{}^{13}C2$ dipolar coupling vector in the reference frame was obtained by combined consideration of the SLF result, the standard geometry of sp^2 hybridized atoms and the general orientation of δ_{33} tensor component with respect to the sp^2 plane. The backbone carbon atom of the imine (C1=N1) group is sp^2 hybridized hence all the atoms directly bonded to C1 lie in a plane with bond angles of ∼120°. Experiments and ab initio quantum mechanical calculations on several compounds with sp^2-hybridized carbon atoms indicate that the most shielded component (δ_{33}), of the sp^2 hybridized carbon is perpendicular to the sp^2 plane of the atoms.[42−45] Assuming a similar orientation of the tensors in the present case and using the orientation of the C1=N1 bond from the 2D-SLF data analysis, the arrangement of the atoms bonded to the imine carbon is as shown in Figure 7. The dipolar orientation angles $(\beta_D^{C1C2}, \gamma_D^{C1C2})$ of the $^{13}C1{-}{}^{13}C2$ dipolar vector in the principal axis frame of the C1 CSA tensor can thus be obtained.

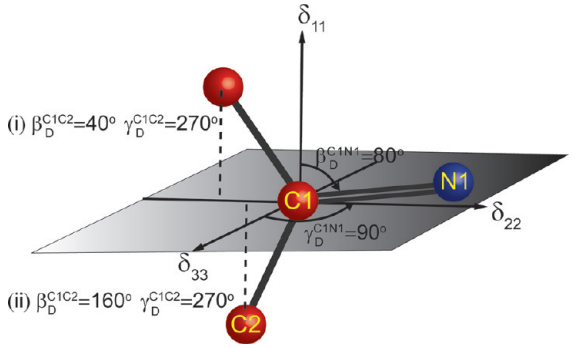


Figure 7. Angles $(\beta_D^{C1C2}, \gamma_D^{C1C2})$ and $(\beta_D^{C1N2}, \gamma_D^{C1N2})$ define the orientation of the $^{13}C{-}{}^{13}C$ dipolar vector and $^{13}C{=}{}^{15}N$ bond in the ^{13}C CSA frame of the central imine carbon. The dashed lines are the projections of the two C1C2 vectors onto the plane defined by δ_{33} and δ_{22}.

There is an equal probability of either one of the two neighboring carbon atoms being labeled. The two set of Euler angles corresponding to the two possible neighbors of C1 are $(\beta_D^{C1C2}, \gamma_D^{C1C2}) = (160°, 270°)$ and $(\beta_D^{C1C2}, \gamma_D^{C1C2}) = (40°, 270°)$. The Euler angles $(\beta_D^{C1C2}, \gamma_D^{C1C2})$ define the polar and the azimuthal angle of the $^{13}C1{-}{}^{13}C2$ vectors in the principal axis frame of C1 CSA tensor. The $^{13}C{-}{}^{13}C$ dipolar coupling has been assigned a value of 2200 Hz considering a typical $^{13}C{-}{}^{13}C$ single bond length of 1.5 Å.

Simulations were done using the angles $\beta_D^{C1C2} = 160°$, $\gamma_D^{C1C2} = 270°$ for the orientation of the $^{13}C1{-}{}^{13}C2$ dipolar tensor in the

dx.doi.org/10.1021/ma300102e | Macromolecules 2012, 45, 2209−2218

Table 1. Set of 8 Symmetry Related EULER Angle Combinations for the Relative Orientation of Principal Axis System of the CSA of Neighboring Carbons in the Polymer Backbone Yielding Equivalent DOQSY Spectra as the Minima Identified in Figure 6[a]

	α_{CSA}^{C1C2}	β_{CSA}^{C1C2}	γ_{CSA}^{C1C2}	θ	$[n_x, n_y, n_z]$	α_{CSA}^{C1C2}	β_{CSA}^{C1C2}	γ_{CSA}^{C1C2}	θ	$[n_x, n_y, n_z]$
1	240	50	30	100	[0.53, 0.14, −0.83]	110	135	210	138	[−0.75, −0.63, −0.14]
2	120	130	210	132	[−0.70, −0.70, −0.11]	250	45	30	90	[0.50, 0.18, −0.84]
3	60	130	330	132	[−0.70, 0.702, 0.11]	70	135	330	138	[−0.75, 0.63, 0.14]
4	300	50	150	100	[0.53, −0.14, 0.83]	290	45	150	90	[0.50, −0.18, 0.84]
5	300	130	210	167	[0.64, −0.64, 0.41]	70	45	30	107	[−0.16, 0.44, 0.87]
6	60	50	30	100	[−0.14, 0.53, 0.83]	290	135	210	165	[0.59, −0.71, 0.36]
7	120	50	150	100	[−0.14, −0.53, −0.83]	110	45	150	107	[−0.16, −0.44, −0.87]
8	240	130	330	167	[0.64, 0.64, −0.41]	250	135	330	165	[0.59, 0.71, −0.36]

[a]Alternatively, the Euler rotations can be mimicked by a rotation θ about a unique axis $[n_x, n_y, n_z]$ having the same overall effect. All angles are in degrees.

PAS of the ^{13}C CSA tensor of C1. Initially a broad grid simulation of the spectra was run with α_{CSA}^{C1C2} and γ_{CSA}^{C1C2} varying from 0° to 360° in steps of 30° each and β_{CSA}^{C1C2} varying from 0° to 90° in steps of 20° (the corresponding $180-\beta_{CSA}^{C1C2}$-simulations are symmetry equivalent and hence the simulations for $\beta_{CSA}^{C1C2} > 90°$ are not run). The least-squares fitting of the experimental spectrum showed minima near β_{CSA}^{C1C2} ranging from 40° to 50°. In the second step, a fine grid of simulations was set up with β_{CSA}^{C1C2} fixed at 30°, 40°, 45°, 50°, and 55° with α_{CSA}^{C1C2} and γ_{CSA}^{C1C2} in steps of 10° each near the minima values obtained in the broad grid simulations. These fine grid simulations indicated minima at β_{CSA}^{C1C2} values of 40°, 45°, and 50°. The spectra at β = 40° were examined and excluded as false minima as the simulated spectral patterns visibly did not match the experimental spectrum very well. CSA symmetry considerations theoretically yield 16 DOQSY spectra that are equivalent.[17] The presence of the $^{13}C-^{13}C$ dipolar interaction reduces the number of symmetry related angle combinations to eight, which are $[\alpha, \beta, \gamma]$, $[180 - \alpha, \beta, 180 - \gamma]$, $[180 + \alpha, \beta, \gamma]$, $[-\alpha, \beta, 180 - \gamma]$, $[-\alpha, 180 - \beta, 180 + \gamma]$, $[180 - \alpha, 180 - \beta, 180 + \gamma]$, $[180 + \alpha, 180 - \beta, -\gamma]$, $[180 + \alpha, 180 - \beta, 180 - \gamma]$. The two simulated spectra that best match the experimental spectrum are shown in Figure 6, parts c and d. The angles [250°, 45°, 30°, 90°] and [240°, 50°, 30°, 100°] corresponding to the minima are represented in the order $[\alpha, \beta, \gamma, \theta]$ where θ describes the rotation about an axis $[n_x, n_y, n_z]$ in the reference frame. This axis and rotation angle θ are obtained by an axis-angle transformation where the Euler rotations over the angles $(\alpha, \beta, \gamma)_{CSA}^{C1C2}$ are mimicked by a rotation θ about a unique axis $[n_x, n_y, n_z]$ having the same overall effect.[41] This is a convenient representation as the orientation of the ^{13}C CSA tensor of a neighboring carbon in the polymer backbone can be obtained by a rotation around the polymer chain axis over an angle depending on the pitch of the (helical) chain. Table 1 lists the symmetry related sets of Euler angles which produce spectra identical to the simulated spectra shown in Figure 6c and d together with the corresponding rotation axis $[n_x, n_y, n_z]$ and angle θ. As can be seen the symmetry related Euler angles produce rotation angles (θ) of different magnitudes such as 100°, 90°, 138°, 107°, 167° etc. The true minima were identified by building a model of the L,D-PIAA backbone using the structural constrainsts obtained from 2D-SLF and DOQSY data as is described in the next section.

5. POLYMER BACKBONE CONFORMATION

We use the relative orientation angles of the ^{13}C CSA tensors and the $^{13}C-^{15}N$ CSA-dipolar tensors as obtained from the solid state NMR data described above to model the polyisocyanide backbone chain. In the first step, using the C1═N1 dipolar orientation angles obtained from the 2D-SLF data, the C1═N1 bond of the first monomer unit (*M1*) was oriented in the C1 CSA frame with the azimuthal (γ_D^{C1N1} = 90°) and the polar (β_D^{C1N1} = 80°) angles as shown in Figure 8a. In the second step, the coordinates of the monomer *M1* were rotated using the Euler rotation matrix R_{CSA}^{C1C2}, obtained from the DOQSY analysis, to determine the coordinates of the neighboring monomer unit *M2* (Figure 8b). Successive body fixed rotations produced the coordinates for *M2* → *M3*, *M3* → *M4*.....*M*(*n*−1) → *Mn*. The rotations occur at the origin (coinciding with the position of carbon C1) hence the position coordinates of the successive carbons C1, C2, C3, ..., C*n* are fixed at the origin and the remaining atoms of the side chain change position, giving for example the position of the subsequent nitrogens N2, N3, ..., N*n*, etc. In the third step, the monomer units have to be translated away from the origin. To do this we use the earlier deduced information on the orientation of carbon C2 in the principal axis frame of the C1 carbon CSA tensor depicted in Figure 7 based on the sp^2 hybridization of the backbone carbons and the orientation of the C1═N1 bond. The monomer unit *M2* is translated in the direction of $^{13}C1-^{13}C2$ dipolar coupling, i.e., in the direction of C1---*p*, so that the translation amounts to the C−C bond length of 1.5 Å which is essentially the position of the point "*p*" (Figure 8c). The monomer units *M1* and *M2* are then translated together in the opposite direction (*p*---C1) so as to place C2 at the origin. Subsequently rotation of the point "*p*" over R_{CSA}^{C1C2} results in coordinate point "*q*", which represents the position of the backbone carbon of the monomer unit *M3* (Figure 8e). The above procedure is repeated where the monomer unit *M3* is first translated to point "*q*" and following which the entire chain consisting of *M1*, *M2*, and *M3* is moved so as to move carbon C3 of the monomer unit *M3* to the origin and so on. This ultimately produces the entire polymer chain. The same procedure was used to build models for all the eight angle combination that fitted the DOQSY spectrum. Table 2 lists the resulting bond angle $\angle C_nC_{n+1}N_{n+1}$ for the 8 models. Only four minima produce geometrically favorable bond angles $\angle C_nC_{n+1}N_{n+1}$ resulting in two isotactic helical polymer models corresponding to relative rotation angles of 100° and 90°. The geometrically favorable angle $\angle C_nC_{n+1}N_{n+1}$ also implies that in these models the helix axis $[n_x, n_y, n_z]$ and the $^{13}C═^{15}N$ bond

dx.doi.org/10.1021/ma300102e | *Macromolecules* 2012, 45, 2209−2218

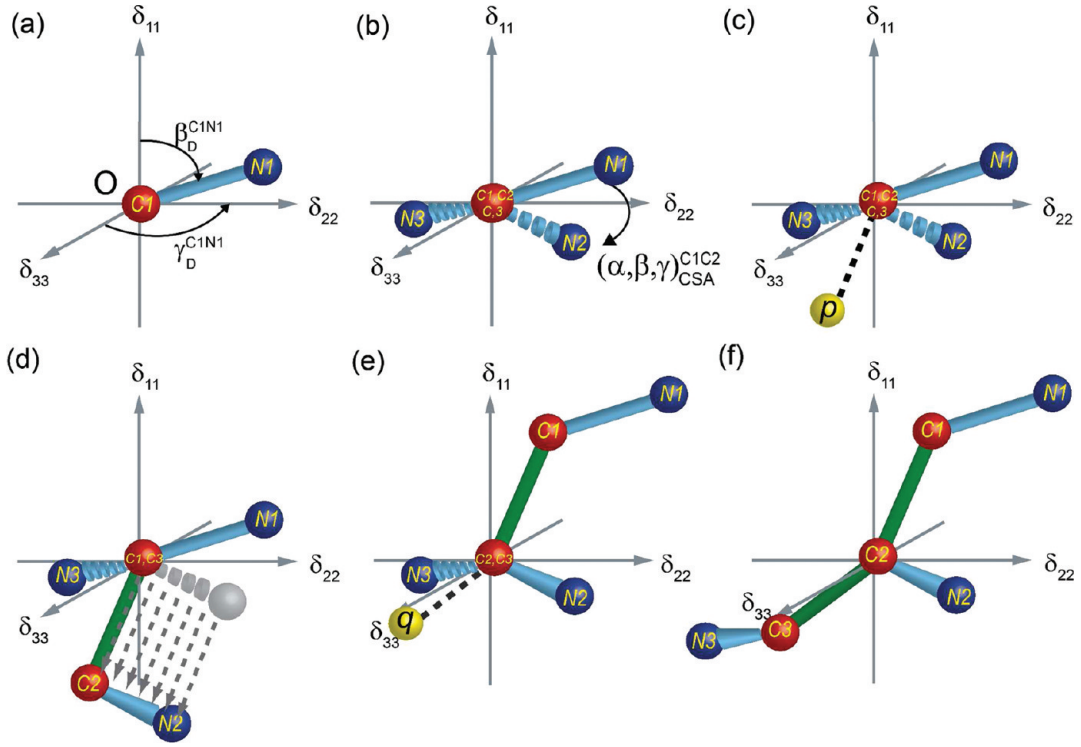


Figure 8. Illustration of polymer chain building starting from a single monomer unit using relative CSA−CSA and CSA−dipolar angles. The position '*p*' represents the carbon atom bonded to C1 and lies in the sp^2 plane defined by C1−N1-*p*.

Table 2. List of Euler Angle Combinations $(\alpha, \beta, \gamma)_{CSA}^{C1C2}$ and Relative Rotation Angle θ Obtained from Fitting the DOQSY Spectra and the Resulting Bond Angle $\angle C_nC_{n+1}N_{n+1}$ Extracted from the Polymer Model Based on These Data (See Text)[a]

	α_{CSA}^{C1C2}	β_{CSA}^{C1C2}	γ_{CSA}^{C1C2}	θ	$\angle C_nC_{n+1}N_{n+1}$	α_{CSA}^{C1C2}	β_{CSA}^{C1C2}	γ_{CSA}^{C1C2}	θ	$\angle C_nC_{n+1}N_{n+1}$
1	*240*	*50*	*30*	*100*	*123*	*250*	*45*	*30*	*90*	*118*
2	120	130	210	132	57	110	135	210	138	62
3	60	130	330	132	57	70	135	330	138	62
4	*300*	*50*	*150*	*100*	*123*	*290*	*45*	*150*	*90*	*118*
5	300	130	210	167	143	290	135	210	165	138
6	60	50	30	100	37	70	45	30	107	42
7	120	50	150	100	37	110	45	150	107	42
8	240	130	330	167	143	250	135	330	165	138

[a]The italic combinations lead to geometrically acceptable polymer models with a realistic $\angle C_nC_{n+1}N_{n+1}$ bond angle for a sp^2 hybridized atom. All angles are in degrees.

vector are perpendicular to each other. The other minima which do not form geometrically favorable $\angle C_nC_{n+1}N_{n+1}$ angles were discarded as unphysical solutions.

We started by generating polymer models with a helical angle equivalent to 90° and 100°, i.e., 4_1 and 18_5 helices respectively, that were further subjected to molecular modeling studies. Since the side chain orientations are unknown, for each of the polymer backbone models multiple structures with varying side chain orientations were built, where the side chains were arbitrarily rotated around the C═N bond in steps of 30°. This is done since in the complete polymer the side chains have less spatial freedom and hence may fall into local minima because the barrier leading to the proper energy minimum is too high to overcome in the modeling procedure. The molecular modeling studies were performed using the corrected Dreiding force field which was previously applied successfully for polyisocyanides.[2] To allow the polymer to easily rotate along the backbone and to minimize finite size effects along the polymer, a polymer with 100 repeat units without periodic boxes was used. The modeling was performed in three consecutive steps for every polymer structure. First, these structures were geometrically optimized at 0 K to correct for any remaining artifacts from the structure generation process. Subsequent molecular dynamics simulation at 293 K added enough energy to allow the polymer to explore a large conformational space and was used to determine the stability of the polymers. Finally, the resulting structure after 3 ns of molecular dynamics simulation was again geometrically optimized at 0K. The resulting structures were analyzed with respect to the backbone C−C−C−C backbone dihedral angle and the hydrogen bond parameters between the N−H and C═O groups of the side chains. Both the initial helical 4_1 and 18_5 models converged to a ~15_4 helix (~96° helical angle) with a mean C−C−C−C backbone dihedral angle of 79°. The repeat unit corresponds to 3.75 units per turn. Figure 9 shows the side view and top view of one complete rotation of the 15_4 helix. The helix angle can be compared to that of the theoretical value of ~95° obtained for poly(*tert*-butylisocyanide) (see Figure 5c in ref 9). Very recently

dx.doi.org/10.1021/ma300102e | *Macromolecules* 2012, 45, 2209−2218

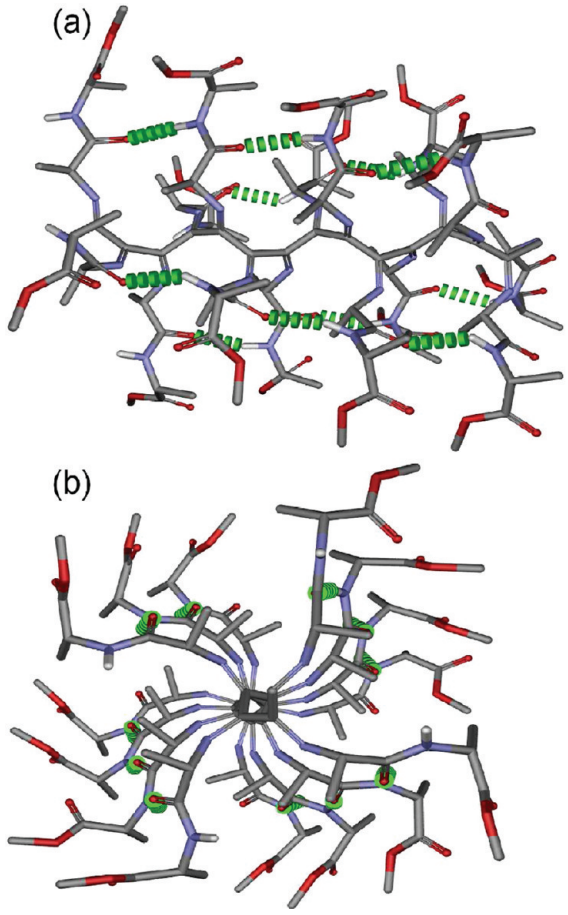


Figure 9. (a) Side view and (b) top view of one complete helical turn of the geometry-optimized L,D-PIAA polymer.

the molecular modeling calculations of the polyisocyanide with a L-alanyl perylenediimide substituent also yielded a helical structure with a rotation angle of ~96°.[2] The optimized models obtained in the present study show regular hydrogen bonds between the side chains of the polymer. Hydrogen bond distances (N----O) in the polymer models showed a mean value of ~2.5–2.7 Å and are largely unidirectional. This is in line with the earlier observed upfield shifted solid state amide proton chemical shifts of 9.2 ppm.[20] To verify the model building approach used here we also built polymer models with helix angles of 70°, 80°, 110° and 120° and the models were subjected to molecular modeling studies. However, these structures showed very irregular and weaker (large N----O distance) hydrogen bonds and also showed large variations in C–C–C–C backbone dihedral angle. In the current approach, the backbone conformation of the polymers is determined experimentally and only fine-tuning of the backbone conformation and optimization of the orientation of the side chain groups is done using modeling studies which takes less computational time. This approach is of particular value when determining the structure of functional polyisocyanides with large side chain substituents such as carbazole, perylene, or porphyrin groups since they lead to additional interactions such as the aromatic π–π interactions, steric interactions, etc. that can potentially influence the backbone conformations. For example, in a recent study of carbazole functionalized polyisocyanides we found a markedly different chemical shift (δ = 8.1 ppm) for the NH proton as compared to L,D-PIAA (δ = 9.2 ppm) indicating that the hydrogen bonding strengths might be different in the two polyisocyanide analogues, raising questions toward possible structural differences in the polymer backbone conformation.[20,46]

6. CONCLUSIONS

In this paper, we have carried out structural studies of the hydrogen bond stabilized polyisocyanodipeptide (L,D-PIAA). The presence of strong hydrogen bonds between the side chains in the L,D-PIAA, the relatively narrow ^{13}C line widths and the well-defined spectral patterns of 2D-SLF and DOQSY prove structural regularity of the dipeptide polymer. The 2D-SLF experimental analysis revealed the orientation of the backbone carbon tensor in the molecular frame, while the DOQSY experiment was used to determine the relative ^{13}C–^{13}C CSA tensor orientation of neighboring carbons. These structural restraints were used to build the polymer model of L,D-PIAA which was subsequently energy minimized. We have determined the backbone conformation of the hydrogen bond stabilized polyisocyanodipeptide (L,D-PIAA) to be a 15_4 helix. To the best of our knowledge, this is the first direct structure determination of the polyisocyanodipeptides which are a promising class of materials which are targeted as a scaffold for a host of functional materials. The question arises whether this helical structure is preserved under all circumstances when functional materials, e.g., involving bulky side chains are synthesized. The approach followed in this study is then an efficient method for the structure determination of polymers with increasing structural complexity. An example is the carbazole functionalized polyisocyanide which shows a different chemical shift for the NH proton as compared to the shift in L,D-PIAA, indicating that the hydrogen bonding strengths might be different in the two polyisocyanide analogues. A detailed ssNMR based analysis indicated that for the carbazole analogue a T-shaped arrangement of the monomer units in the crystal is driven by σ–π interactions whereas in the polymers a π–π overlap of the carbazole units in the polymer was postulated to be prevalent. This suggests an interplay between aromatic interactions and hydrogen bonding in the stabilization of the polymer backbone. A complete solid state NMR study analogous to the one described in this paper can shed more light on the precise molecular organization in these functionalized polymers. A suite of diverse NMR experiments combined with intelligent labeling strategies can help in deciphering not only the backbone conformation but explicity reveal conformation of side chains and interside chain interactions.

AUTHOR INFORMATION

Corresponding Author

*E-mail: a.kentgens@nmr.ru.nl.

Notes

The authors declare no competing financial interest.

ACKNOWLEDGMENTS

The authors thank Gerrit Janssen, Hans Janssen, and Jan van Os for their technical support. Dr. Andreas Brinkmann and Dr. Vipin Agarwal are acknowledged for very useful discussions and experimental help. We acknowledge Gerald Metselaar for his contribution to the preparation of the 10% enriched isocyanodipeptide polymer (L,D-PIAA). This research is supported by The Netherlands Organization for Scientific Research (NWO) by a NWO-TOP grant. We furthermore acknowledge

NWO for their support of the solid-state NMR facility for advanced materials research.

REFERENCES

(1) de Witte, P. A. J.; Castriciano, M.; Cornelissen, J. J. L. M.; Monsù Scolaro, L.; Nolte, R. J. M.; Rowan, A. E. *Chem.—Eur. J.* **2003**, *9* (8), 1775−1781.

(2) Schwartz, E.; Palermo, V.; Finlayson, C. E.; Huang, Y.-S.; Otten, M. B. J.; Liscio, A.; Trapani, S.; González-Valls, I.; Brocorens, P.; Cornelissen, J. J. L. M.; Peneva, K.; Müllen, K.; Spano, F. C.; Yartsev, A.; Westenhoff, S.; Friend, R. H.; Beljonne, D.; Nolte, R. J. M.; Samorì, P.; Rowan, A. E. *Chem.—Eur. J.* **2009**, *15* (11), 2536−2547.

(3) Schwartz, E.; Lim, E.; Gowda, C. M.; Liscio, A.; Fenwick, O.; Tu, G.; Palermo, V.; de Gelder, R.; Cornelissen, J. J. L. M.; Van Eck, E. R. H.; Kentgens, A. P. M.; Cacialli, F.; Nolte, R. J. M.; Samori, P.; Huck, W. T. S.; Rowan, A. E. *Chem. Mater.* **2010**, *22* (8), 2597−2607.

(4) Millich, F.; Sinclair, R. G. *J. Polym. Sci., Part C: Polym. Symp* **1968**, *22* (1), 33−43.

(5) Nolte, R. J. M.; Van Beijnen, A. J. M.; Drenth, W. *J. Am. Chem. Soc.* **1974**, *96* (18), 5932−5933.

(6) Millich, F. Rigid rods and the characterization of polyisocyanides. In *Polymerization Reactions*; Springer: Berlin/Heidelberg: 1975; Vol. *19*, pp 117−141.

(7) Green, M. M.; Gross, R. A.; Schilling, F. C.; Zero, K.; Crosby, C. *Macromolecules* **1988**, *21* (6), 1839−1846.

(8) Clericuzio, M.; Alagona, G.; Ghio, C.; Salvadori, P. *J. Am. Chem. Soc.* **1997**, *119* (5), 1059−1071.

(9) Kollmar, C.; Hoffmann, R. *J. Am. Chem. Soc.* **1990**, *112* (23), 8230−8238.

(10) Millich, F.; Baker, G. K. *Macromolecules* **1969**, *2* (2), 122−128.

(11) Van Beijnen, A. J. M.; Nolte, R. J. M.; Drenth, W.; Hezemans, A. M. F. *Tetrahedron* **1976**, *32* (16), 2017−2019.

(12) Onouchi, H.; Okoshi, K.; Kajitani, T.; Sakurai, S.-i.; Nagai, K.; Kumaki, J.; Onitsuka, K.; Yashima, E. *J. Am. Chem. Soc.* **2007**, *130* (1), 229−236.

(13) Schwartz, E.; Koepf, M.; Kitto, H. J.; Nolte, R. J. M.; Rowan, A. E. *Polym. Chem.* **2011**, *2*, 33−47.

(14) Odgaard, L.; Bak, M.; Jakobsen, H. J.; Nielsen, N. C. *J. Magn. Reson.* **2001**, *148* (2), 298−308.

(15) Schmidt-Rohr, K. *Macromolecules* **1996**, *29* (11), 3975−3981.

(16) van Beek, J. D.; Meier, B. H. *J. Magn. Reson.* **2006**, *178* (1), 106−120.

(17) Schmidt-Rohr, K.; Spiess, H. W. *Multidimensional solid-state NMR and polymers*; Academic Press: London, 1994.

(18) van Beek, J. D.; Beaulieu, L.; Schafer, H.; Demura, M.; Asakura, T.; Meier, B. H. *Nature* **2000**, *405* (6790), 1077−1079.

(19) Cornelissen, J. J. L. M.; Donners, J. J. J. M.; de Gelder, R.; Graswinckel, W. S.; Metselaar, G. A.; Rowan, A. E.; Sommerdijk, N. A. J. M.; Nolte, R. J. M. *Science* **2001**, *293* (5530), 676−680.

(20) Cornelissen, J. J. L. M.; Graswinckel, W. S.; Adams, P. J. H. M.; Nachtegaal, G. H.; Kentgens, A. P. M.; Sommerdijk, N. A. J. M.; Nolte, R. J. M. *J. Polym. Sci., Part A: Polym. Chem* **2001**, *39* (24), 4255−4264.

(21) Cornelissen, J. J. L. M.; Graswinckel, W. S.; Rowan, A. E.; Sommerdijk, N. A. J. M.; Nolte, R. J. M. *J. Polym. Sci., Part A: Polym. Chem* **2003**, *41* (11), 1725−1736.

(22) Nakai, T.; Ashida, J.; Terao, T. *J. Chem. Phys.* **1988**, *88* (10), 6049−6058.

(23) Linder, M.; Hohener, A.; Ernst, R. R. *J. Chem. Phys.* **1980**, *73* (10), 4959−4970.

(24) Bak, M.; Rasmussen, J. T.; Nielsen, N. C. *J. Magn. Reson.* **2000**, *147* (2), 296−330.

(25) De Paepe, G.; Elena, B.; Emsley, L. *J. Chem. Phys.* **2004**, *121* (7), 3165−3180.

(26) Shaka, A. J.; Keeler, J.; Freeman, R. *J. Magn. Reson.* **1983**, *53* (2), 313−340.

(27) Bennett, A. E.; Rienstra, C. M.; Auger, M.; Lakshmi, K. V.; Griffin, R. G. *J. Chem. Phys.* **1995**, *103* (16), 6951−6958.

(28) Marion, D.; Wüthrich, K. *Biochem. Biophys. Res. Commun.* **1983**, *113* (3), 967−974.

(29) Cadars, S.; Sein, J.; Duma, L.; Lesage, A.; Pham, T. N.; Baltisberger, J. H.; Brown, S. P.; Emsley, L. *J. Magn. Reson.* **2007**, *188* (1), 24−34.

(30) HBA 1.6, Eichele, K.; Wasylishen, R. E. Dalhousie University and Universität Tübingen, 2010.

(31) van Beek, J. D. *J. Magn. Reson.* **2007**, *187* (1), 19−26.

(32) *Materials Studio version 5.0.0.0*; Accelrys Software Inc.: San Diego, CA., 2009.

(33) Herzfeld, J.; Berger, A. E. *J. Chem. Phys.* **1980**, *73* (12), 6021−6030.

(34) Davies, N. A.; Harris, R. K.; Olivieri, A. C. *Mol. Phys.* **1996**, *87* (3), 669−677.

(35) Goetz, J. M.; Schaefer, J. *J. Magn. Reson.* **1997**, *129* (2), 222−223.

(36) Edén, M.; Levitt, M. H. *J. Magn. Reson.* **1998**, *132* (2), 220−239.

(37) Edén, M. *Concepts Magn. Reson. A* **2003**, *17A* (1), 117−154.

(38) Weliky, D.; Tycko, R. *J. Am. Chem. Soc.* **1996**, *118* (35), 8487−8488.

(39) Feng, X.; Eden, M.; Brinkmann, A.; Luthman, H.; Eriksson, L.; Graslund, A.; Antzutkin, O. N.; Levitt, M. H. *J. Am. Chem. Soc.* **1997**, *119* (49), 12006−12007.

(40) Note: The Euler angles in the SIMPSON spinsys relate the coordinate transformation from the principal axis frame to the laboratory frame.

(41) Altmann, S. L., *Rotations, quaternions, and double groups.* Clarendon Press ; Oxford University Press: Oxford, U.K., 1986; p 317.

(42) Orendt, A. M.; Facelli, J. C.; Beeler, A. J.; Reuter, K.; Horton, W. J.; Cutts, P.; Grant, D. M.; Michl, J. *J. Am. Chem. Soc.* **1988**, *110* (11), 3386−3392.

(43) Curtis, R. D.; Penner, G. H.; Power, W. P.; Wasylishen, R. E. *J. Phys. Chem.* **1990**, *94* (10), 4000−4006.

(44) Wasylishen, R. E.; Penner, G. H.; Power, W. P.; Curtis, R. D. *J. Am. Chem. Soc.* **1989**, *111* (16), 6082−6086.

(45) Veeman, W. S. *Prog. Nucl. Magn. Reson. Spectrosc.* **1984**, *16*, 193−235.

(46) Gowda, C. M.; Vasconcelos, F.; Schwartz, E.; van Eck, E. R. H.; Marsman, M.; Cornelissen, J. J. L. M.; Rowan, A. E.; de Wijs, G. A.; Kentgens, A. P. M. *Phys. Chem. Chem. Phys.* **2011**, *13* (28), 13082−13095.

Macromolecules

Article

pubs.acs.org/Macromolecules

Counteranion Sensitization Approach to Photoinitiated Free Radical Polymerization

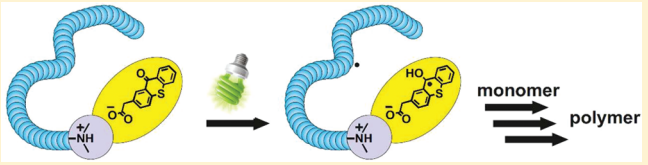
Gorkem Yilmaz,[†] Gokhan Acik,[†] and Yusuf Yagci*[,†,‡]

[†]Department of Chemistry, Istanbul Technical University, 34469, Maslak, Istanbul, Turkey

[‡]Faculty of Science, Chemistry Department, King Abdulaziz University, Jeddah, Saudi Arabia

Supporting Information

ABSTRACT: A novel polymeric type II photoinitiator, namely poly(ethylene oxide) dimethylammonium thioxanthonemethyl-carboxylate (PEO-$NH^+(Me)_2$ TX-CH_2COO^-), possessing both photochromophoric and hydrogen donating groups in the structure was synthesized and characterized. In contrast to existing type II photoinitiators, the present photoinitiator initiates free radical polymerization by counteranion excitation even in the absence of added hydrogen donors. The photoinitiator can be applied to the polymerization of monomers soluble in organic solvents or water.



INTRODUCTION

Photopolymerization forms the basis of numerous applications in coatings, inks, adhesives, optoelectronics, stereolithography, and nanotechnology.[1] Photopolymerization has several advantages compared to thermal polymerization such as low energy requirement, spatial control, and fulfillment of green chemistry demands since polymerization processes may operate without solvent. Both free radical and cationic polymerizations have been used, and the mechanisms of initiation have been studied in detail.[2] However, most of the applications are based on the free radical mode due to the less purity demand, applicability to a wide range of formulations based on (meth)acrylates, unsaturated polyesters, and acrylated polyurethanes and the availability of photoinitiators having spectral sensitivity in a broad wavelength range.[1c,3]

Despite its superior status of free radical polymerization, there has been tremendous effort to develop free radical photoinitiators with enhanced absorption characteristics, solubility, low odor, low migration, and nonyellowing properties.[1a,b,4] If the photon energy is absorbed by an added initiator, these photosensitive substances undergo homolytic bond rupture or hydrogen abstraction reactions forming radicals, which may initiate the polymerization.[2b,5] In addition, onium salts belonging iodonium,[2a,6] sulfonium,[7] ammonium,[8] alkoxypyridium,[9] and phosphonium[10] families also represent a class of free radical photoinitiators.[11] Under favorable conditions, these salts can initiate the polymerization by the photoexcitation of the cationic part.[12] The selection of a photoinitiator is undoubtedly of great importance and depends on the chemical constitution of the particular formulation used. Depending on the absorption characteristics and specific application involved, either cleavage and hydrogen abstraction types of photoinitiators or their appropriate combinations can be used.[13] In some cases, these photoinitiators are incorporated into polymer structures. In this way, the macromolecules having covalently bonded photoinitiator groups overcome the problems associated with high volatility and high migration often observed with low-molar-mass photoinitiators.[14] Previously, we reported that 1,3-dipolar azide−alkyne [3 + 2] "click chemistry"[15] and Diels−Alder [4 + 2] cycloaddition reactions[16] could be used for obtaining macrophotoinitiators containing thioxanthone photoinitiator moieties as side chains and terminal groups. The resulting polymeric photoinitiators were shown to efficiently initiate the free-radical polymerization of mono- and multifunctional monomers via the hydrogen abstraction mechanism. We now report that structurally similar polymeric photoinitiators can be prepared by counterion incorporation of the light sensitive group, namely thioxanthone (TX) into poly(ethylene oxide) (PEO) which provides a novel means of photoinitiation of free radical polymerization by counteranion sensitization.

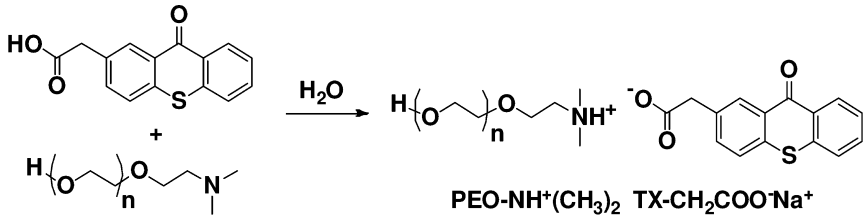
EXPERIMENTAL SECTION

Materials. Thiosalicylic acid (97%, Sigma-Aldrich), 2-phenylacetic acid (99%, Merck), and sodium hydroxide (NaOH, Carlos Erba) were used without further purification. Methyl methacrylate (MMA, ≥99%, Aldrich) and styrene (St, ≥99%, Merck) were passed through basic alumina column before use to remove the inhibitor. 2-Dimethylaminoethanol (99.5%, Aldrich), *N*-vinylpyrrolidone (NVP, 99%, Aldrich), and hydroxyethyl methacrylate (HEMA, 98%, Aldrich) were disttiled under vacuum before use. Acrylamide (AAm, 97%, Aldrich) and *N,N′*-methylenebis(acrylamide) (BAAm, 99%, Aldrich) were crystallized from methanol prior to use. Dichloromethane (CH_2Cl_2, 98%, Sigma-Aldrich) was distilled over P_2O_5 and collected in molecular sieves prior to use. Trimethylolpropane triacrylate (TMPTA, 95%, Aldrich) was passed through a short column of basic alumina prior to use. Poly(ethylene glycol) dimethyl ether (PEG, $M_n \sim 1000$, Aldrich) were

Received: July 28, 2011
Revised: February 27, 2012
Published: March 1, 2012

 © 2012 American Chemical Society dx.doi.org/10.1021/ma3000169 | *Macromolecules* 2012, 45, 2219−2224

Scheme 1. Synthesis of PEO-$NH^+(Me)_2$ TX-CH_2COO^-



used as received. All solvents were used as received without further purification.

Instrumentation. ^1H NMR measurements were recorded in $CDCl_3$ with $Si(CH_3)_4$ as internal standard, using a Bruker AC250 (250.133 MHz) instrument. FT-IR spectra were recorded on a Perkin-Elmer FT-IR Spectrum One-B spectrometer. UV spectra were recorded on a Shimadzu UV-1601 spectrometer. Molecular weights of the polymers soluble in organic solvents were determined by a gel permeation chromatography (GPC) instrument, Viscotek GPCmax Autosampler system, consisting of a pump, three ViscoGEL GPC columns (G2000HHR, G3000HHR, and G4000HHR), and a Viscotek differential refractive index (RI) detector with a THF flow rate of 1.0 mL min^{-1} at 30 °C. The RI detector was calibrated with PS standards having narrow molecular weight distribution. Data were analyzed using Viscotek OmniSEC Omni-01 software. Gel permeation chromatography (GPC) measurements with the water-soluble polymers were performed at room temperature with a setup consisting of a pump (HP 1050), a refractive index detector (HP 1047A), and three high-resolution Waters columns (AQ3.0, AQ4.0, and AQ5.0). The effective molecular weight ranges were 1000−60 000, 10 000−400 000, and 50 000−4 000 000, respectively. Water was used as eluent at a flow rate of 0.5 mL/min at room temperature. Data analyses were performed with HP Chemstation Software. Calibration with linear poly(ethylene oxide) standards (Polymer Laboratories) was used to estimate the molecular weights

Photopolymerizations. Appropriate solutions of the monomer and initiator were irradiated with a light source emitting light nominally at 350 nm with a light intensity of 3.0 mW cm^{-2} and a dental LED lamp (Bluephase, supplied by Ivoclar Vivadent Co.) with a wavelength range of 430−490 nm and maximum light performance of 1110 mW cm^{-2} ± 10%. Polymers were obtained after precipitation in convenient nonsolvents and drying under vacuum. Conversions were calculated for all samples gravimetrically.

Photocalorimetry (Photo-DSC). The photodifferential scanning calorimetry (photo-DSC) measurements were carried out by means of a modified Perkin-Elmer Diamond DSC equipped with a high-pressure mercury arc lamp (320−500 nm). A uniform UV light intensity is delivered across the DSC cell to the sample and reference pans. The intensity of the light was measured as 53 mW cm^{-2} by a UV radiometer capable of broad UV range coverage. The mass of the sample was 3 mg, and the measurements were carried out in an isothermal mode at 30 °C under a nitrogen flow of 20 mL min^{-1}. The reaction heat liberated in the polymerization was directly proportional to the number of acrylate groups reacted in the system. By integrating the area under the exothermic peak, the conversion of the acrylate groups (C) or the extent of the reaction was determined according to eq 1:

$$C = \Delta H_t / \Delta H_0^{\text{theory}} \quad (1)$$

where ΔH_t is the reaction heat evolved at time t and ΔH_0 theory is the theoretical heat for complete conversion. $\Delta H_0^{\text{theory}}$ = 86 kJ mol^{-1} for an acrylic double bond.

Synthesis of α-Dimethylamino-Functionalized Poly(ethylene oxide) (PEO-$N(CH_3)_2$). Calibrated amounts of dimethylaminoethanol (1 mL, 10 mmol), potassium naphthalene (0.46 mol L^{-1}, 14 mL) in THF, THF (total 115 mL), and EO (10 mL, 200 mmol), each in an ampule with a breakable seal, were fitted into a flask, baked under vacuum, and sealed off from the vacuum line. Dimethylamino alcohol and THF were first introduced into the cleanly dried flask and then reacted with potassium naphthalene in THF. The dark green color due to potassium naphthalene almost immediately disappeared. Then, EO, chilled by dry ice/isopropanol, was introduced to the flask and polymerized at 40 °C over 3 days. The flask was then fitted into a vacuum line with calibrated ampules containing HCl/ethanol. After evacuation, the system was sealed off, and the contents were mixed to react by breaking the breakable seals. After a subsequent time, the polymers were purified as described previously and freeze-dried from benzene.[17] The polymer yield was almost quantitative.

Synthesis of Thioxanthone−Carboxylic Acid (TX-CH_2COOH). Thiosalicylic acid (0.2 g, 1.3 mmol) was slowly added to concentrated sulfuric acid (10 mL), and the mixture was stirred for 5 min to ensure through mixing. 2-Phenylacedic acid (0.85 g, 3.9 mmol) was added slowly to the stirred mixture over a period of 30 min. After the addition, the reaction mixture was stirred at 75 °C for 2 h, and later it was left to stand at room temperature overnight. Afterward, the resulting mixture was poured carefully with stirring into a 10-fold excess of boiling water, and it was then boiled further for 5 min. The solution was cooled and filtered. The residue was recrystallized from dioxane/water mixture to give the pure blue solid. Yield: 83%. ^1H NMR (250 MHz, $CDCl_3$, 25 °C, TMS): δ = 8.59−7.50 (m, 7H, aromatic), 3.97 (s, 2H, $-CH_2-COO$).

Synthesis of PEO-NH^+ $(Me)_2$ TX-CH_2COO^-. PEO-$N(Me)_2$ (1.0 g, 1.0 mmol) was dissolved in 20 mL of water and heated to 60 °C. Next, TX-CH_2COOH (0.41 g, 1.5 mmol) was slowly added to the solution, and the reaction mixture was allowed to stir for overnight. In the following step, the reaction mixture was cooled and filtrated to remove the unreacted TX-COOH. Then, water was evaporated using a rotary evaporator. The polymer was further dissolved in THF and precipitated into diethyl ether to give pale yellow PEO-$NH(Me)_2^+$ TX-COO^- . Yield: 94%. ^1H NMR (250 MHz, $CDCl_3$, 25 °C, TMS): δ = 8.60−7.44 (m, 7H, aromatic), 3.62 (s, PEO chain), 2.86 (s, 2H, $-CH_2-COO^-$), 2.76 (s, 6H, $-N(CH_3)_2$), 2.60 (s, 2H, $-CH_2-N$).

Synthesis of Sodium Thioxanthone−Carboxylate (TX-CH_2COO^- Na^+). TX-CH_2COOH (0.5 g, 1.8 mmol) was added into 25 mL of distilled water. Aqueous solution containing NaOH (0.06 g, 1.5 mmol) was added to the suspension which was refluxed for overnight through mixing. The reaction mixture is cooled and filtrated to remove the unreacted TX-CH_2COOH. The water is evaporated to yield the yellow TX-CH2COO^-Na^+ crystals. Yield: 96%. ^1H NMR (250 MHz, D_2O, 25 °C, TMS): δ = 7.96−7.03 (m, 7H, aromatic), 3.45 (s, 2H, $-CH_2-COO^-Na^+$).

RESULTS AND DISCUSSION

For the simple acid−base salt forming reaction to be applied, the thioxanthone group must be equipped with a carboxylic acid functionality. The carboxylic group was attached to TX using 2-phenylacetic acid as the functional substrate in the synthesis of the photoinitiator. The other component of the salt forming process, α-amino functional PEO, was prepared by utilizing functional initiator approach in the ring-opening anionic polymerization of ethylene oxide (EO). Starting with dimethylethanol amine and adding potassium naphthalene to initiate the EO polymerization readily afforded the mono-amino-functional PEO. Subsequent simple acid−base reaction of the amine chain end with the thioxanthone carboxylic acid

dx.doi.org/10.1021/ma3000169 | Macromolecules 2012, 45, 2219−2224

(TX-CH_2COOH) led to the formation of the polymeric salt with ionically attached thioxanthone moieties (Scheme 1) in high yields (ca. 94%) as determined by NMR analysis.

The salt formation process was followed by ^1H NMR analysis (Figure 1). The presence of the aromatic peaks between 7.09

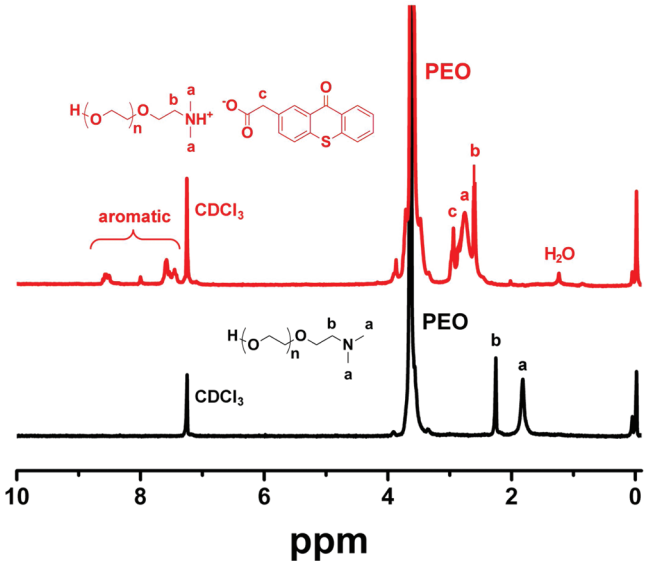


Figure 1. ^1H NMR Spectra of α-dimethylamino-functional PEO (black) and PEO-$NH^+(Me)_2$ TX-CH_2COO^- (red) in CH_2Cl_2.

and 8.60 ppm evidence the incorporation of the thioxanthone chromophore at the chain end. Moreover, after quaternization, the methyl protons of the amine functionality completely shift to lower frequencies (from 1.82 to 2.60 ppm), indicating quantitative functionalization.

The GPC, ^1H NMR, and UV analyses revealed that molecular weight and molecular weight distribution of the polymer did not significantly change during the process (Table 1).

Table 1. Molecular Weight Characteristics of the Polymers at Different Stages

polymers	$M_{n,NMR}$ (g mol^{-1})	$M_{n,UV}$ [a] (g mol^{-1})	$M_{n,GPC}$ [b] (g mol^{-1})	M_w/M_n [b]
PEO-$N(Me)_2$	1005		1025	1.07
PEO-$NH^+(Me)_2$ TX-CH_2COO^-	1150	1270	1280	1.03

[a]Estimated by using $\lambda_{max}(\varepsilon)$ = 380 (4925) L mol^{-1} cm^{-1} of TX-CH_2COOH. [b]Determined by gel permeation chromatography using polystyrene standards.

Absorption characteristics of the polymeric photoinitiator were examined by UV spectroscopy. Figure 2 shows the UV spectra of PEO-$NH^+(Me)_2$ TX-CH_2COO^- and the parent compound, TX-CH_2COOH. It can be seen that both of the compounds exhibit similar absorption characteristics in the UV–vis range (300–400 nm). Interestingly, an unexpected absorption between 470 and 630 nm is observed for TX-CH_2COOH molecule.

On the other hand, TX-$CH_2COO^-Na^+$ has a very similar absorption signature with that of PEO-$NH^+(Me)_2$ TX-CH_2COO^- (Figure 3). This observation demonstrates that the visible range absorption is clearly due to the hydrogen

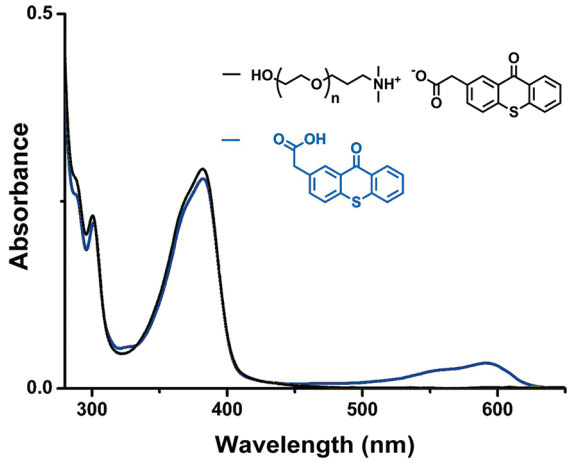


Figure 2. Comparison of the UV–vis absorption spectra of PEO-$NH^+(Me)_2$ TX-CH_2COO^- with TX-CH_2COOH in CH_2Cl_2 at equal concentrations (6.0×10^{-5} mol L^{-1}).

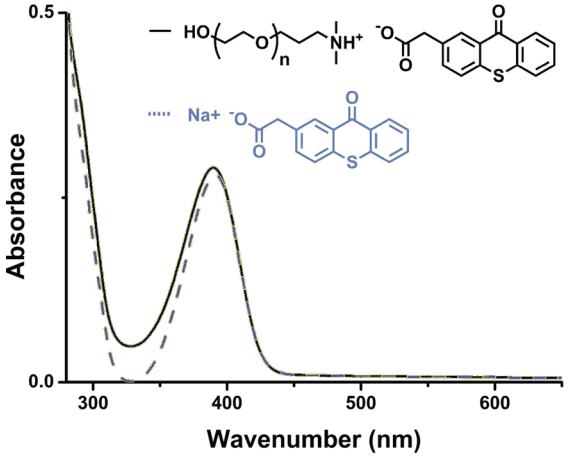


Figure 3. Comparison of the UV–vis absorption spectra of PEO-$NH^+(Me)_2$ TX-CH_2COO^- with TX-CH_2COO^- Na^+ in water at equal concentrations (6.0×10^{-5} mol L^{-1}).

bonding. The sodium derivative is not susceptible to hydrogen bonding, eliminating the possibility of visible range absorption.

To further confirm the contribution of hydrogen bonding to the absorption characteristics of TX-CH_2COOH, the visible absorption spectra in different solvents are taken (Figure 4b). As expected, increase in the dielectric constant of the solvents results in the destruction of hydrogen bonding, which eventually changes the absorption regime of the chromophore. The affect is known as solvatochromism, and images of the different solutions of TX-CH_2COOH are shown in Figure 4a.

The choice of PEO as the polymer support enables us to tailor readily the solubility properties of the photoinitiator, while providing hydrogen donating sites in the structure.[14] The one-component nature of the photoinitiator was evidenced by photobleaching experiments (Figure 5a). PEO-$NH^+(Me)_2$ TX-CH_2COO^- rapidly decomposes itself upon irradiation because it contains hydrogen donating ether groups in the structure. Interestingly, TX-CH_2COOH also undergoes similar photodecomposition (Figure 5b).[13i] Expectedly, the absorption band in the visible range also decreases by irradiation as a result of loss of hydrogen bonding by the abstraction of acidic hydrogen.

Photochemical behavior of the system in the visible range was also of interest. Thus, similar photobleaching (see

dx.doi.org/10.1021/ma3000169 | Macromolecules 2012, 45, 2219–2224

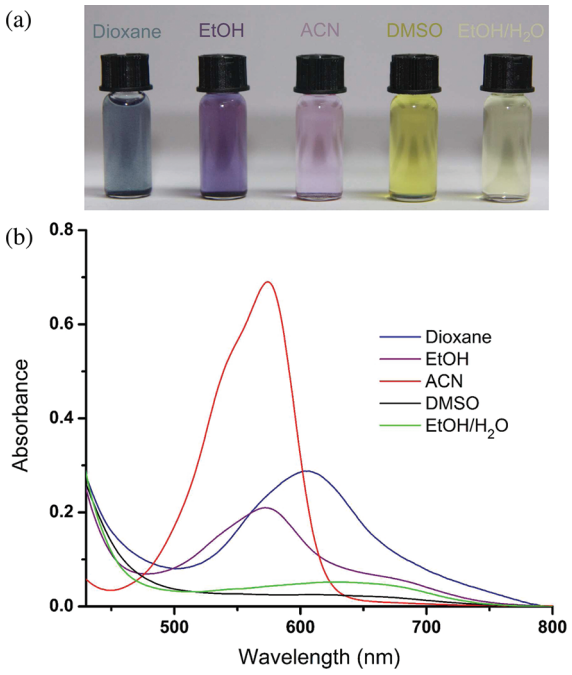


Figure 4. Images of TX-CH_2COOH solutions (a) and their respective visible absorption spectra (b) in various solvents.

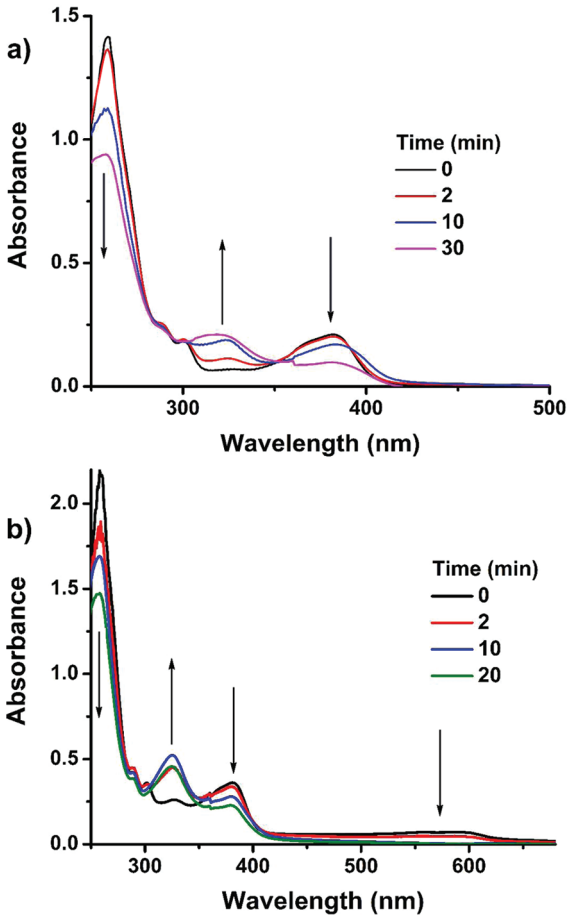


Figure 5. Photobleaching studies of PEO-$NH^+(Me)_2$ TX-CH_2COO^- (a) and TX-CH_2COOH (b) in CH_2Cl_2 with identical initial concentrations (4.0×10^{-5} mol L^{-1}) at 350 nm.

Supporting Information, SF1) have been conducted at 430–490 nm. Although at lower rate, upon irradiation PEO-$NH^+(Me)_2$ TX-CH_2COO^- efficiently undergoes a similar photochemical reaction. In this case, the salt is excited through its tail absorption in the visible range. The respective photopolymerization experiments at these wavelengths gave sufficient yields (see Table 2).

Table 2. Photoinitiated Free Radical Polymerization of Conventional Monomers[a]

monomer	initiator	λ (nm)	conv (%)[b]	M_n[c] (g mol^{-1})	PDI[c]
MMA[d]	PEO-$NH^+(Me)_2$ TX-CH_2COO^-	350	12.1	19 660	2.01
MMA[d]	PEO-$NH^+(Me)_2$ TX-CH_2COO^-	430–490	8.3	9 500	4.75
MMA[d]	CQ/PEO	350	9.9	46 980	1.49
MMA[d]	CQ/PEO	430–490	7.0	9 500	4.25
MMA[d]	TX/PEO	350	7.3	15 640	2.16
MMA[d]	TX/PEO	430–490	<1		
MMA[e]	PEO-$NH^+(Me)_2$ TX-CH_2COO^-	350	28.8	23 290	2.32
MMA[e]	PEO-$NH^+(Me)_2$ TX-CH_2COO^-	430–490	13.4	17 000	1.18
St[d]	PEO-$NH^+(Me)_2$ TX-CH_2COO^-	350			
St[d]	PEO-$NH^+(Me)_2$ TX-CH_2COO^-	430–490			

[a][Monomer]/[PEO-$NH^+(Me)_2$ TX-CH_2COO^-] = 200/1, irradiation time = 2 h. [b]Determined gravimetrically. [c]Determined by gel permeation chromatography using polystyrene standards where THF as the eluent. [d]In CH_2Cl_2. [e]In bulk.

Polymerization experiments confirm the crucial role of PEO segment (Tables 2 and 3). Thus, comparative photopolymerization studies of methyl methacrylate (MMA) using PEO-$NH^+(Me)_2$ TX-CH_2COO^- itself and combination of bare TX or camphorquinone (CQ) with PEO with the same molecular weight as initiators were performed (Table 2). The conversion of the polymerization initiated with the salt was higher than that with the combined initiating system involving TX or CQ. Furthermore, irradiations using styrene failed to produce any precipitable polymer because of quenching of excited triplet TX moiety with the monomer.[5]

Table 3. Photoinitiated Free Radical Polymerization[a] in Aqueous Media Using PEO-$NH^+(Me)_2$ TX-CH_2COO^- as Initiator at Different Irradiation Wavelengths

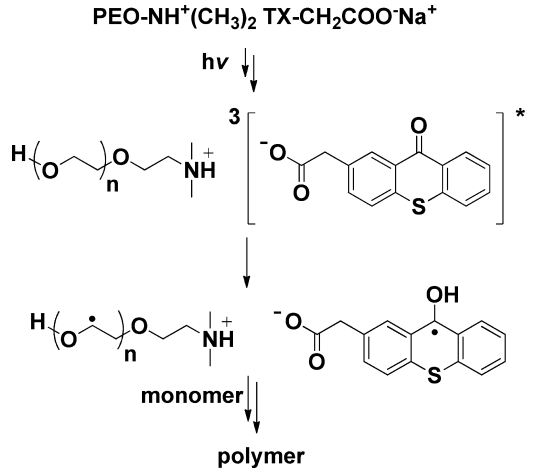
monomer	λ (nm)	conv (%)[b]	M_n[c] (g mol^{-1})	PDI[c]
AAm	350	93.4	32 790	4.80
AAm	430–490	85.7	nd[d]	nd[d]
NVP	350	26.1	nd[d]	nd[d]
NVP	430–490	14	nd[d]	nd[d]
HEMA	350	48	∞	
HEMA	430–490	27.7	∞	

[a][Monomer]/[PEO-$NH^+(Me)_2$ TX-CH_2COO^-] = 200/1, irradiation time = 2 h. [b]Determined gravimetrically. [c]Determined by gel permeation chromatography using PEO standards with water as eluent. [d]The total exclusion limit of the GPC column was exceeded.

The proposed polymerization mechanism is demonstrated in Scheme 2.

dx.doi.org/10.1021/ma3000169 | Macromolecules 2012, 45, 2219–2224

Scheme 2. Photoinitiated Free Radical Polymerization Using PEO-$NH^+(Me)_2$ TX-CH_2COO^- as Initiator



The hydrophilic nature of cationic part of the photoinitiator facilitates solubility in water and aqueous polymerizations can be performed (Table 3). Indeed, water-soluble monomers such as acrylamide (AAm), *N*-vinylpyrolidone (NVP), and hydoxyethyl methacrylate (HEMA) were efficiently polymerized by PEO-$NH^+(Me)_2$ TX-CH_2COO^- with high conversion. Notably, insoluble polymers were obtained with HEMA. This behavior may be explained by the possibility of generation of the additional initiating radicals through hydrogen abstraction reaction from the hydroxymethylene group present in the monomer since alcohols are known to be good hydrogen donors for triplet aromatic carbonyl compounds.

As a very simple demonstration of the possible value of PEO-$NH^+(Me)_2$ TX-CH_2COO^- in UV curing applications, several experiments were performed using multifunctional monomers. All the formulations tested underwent rapid cross-linking upon irradiations for few minutes (Table 4).

Table 4. Photoinduced Gelation Time and Gel Contents of Several Formulations[a] Consisting of PEO-$NH^+(Me)_2$ TX-CH_2COO^- and Multifunctional Monomers

monomers	λ (nm)	gelation time (s)	gel content[d] (%)
TMPTA[b]	350	35	97
TMPTA[b]	430−490	50	91
PEG-diacrylate[c]	350	40	92
PEG-diacrylate[c]	430−490	60	81
AAm + BAAm[c]	350	90	97
AAm + BAAm[c]	430−490	145	97

[a][Monomer]/[PEO-$NH^+(CH_3)_2$ TX-CH_2COO^-] = 200/1. [b]In CH_2Cl_2. [c]In water, [AAM]/[BisAAM] = 100/1. [d]Determined gravimetrically after the gels are washed with the reaction solvents and dried.

The efficiency of the in the photocuring of formulations containing multifunctional monomers was also studied. In Figure 6, photo-DSC exotherm referring to the polymerization of trimethylolpropane triacrylate (TMPTA) initiated by PEO-$NH^+(Me)_2$TX-CH_2 under polychromatic light is shown. In the inset, the plot of the conversion vs irradiation time derived from the same polymerization system is given. The shape of this "conversion time" kinetics curve indicates two stages: a rapid first stage followed by a slow stage. At the second stage,

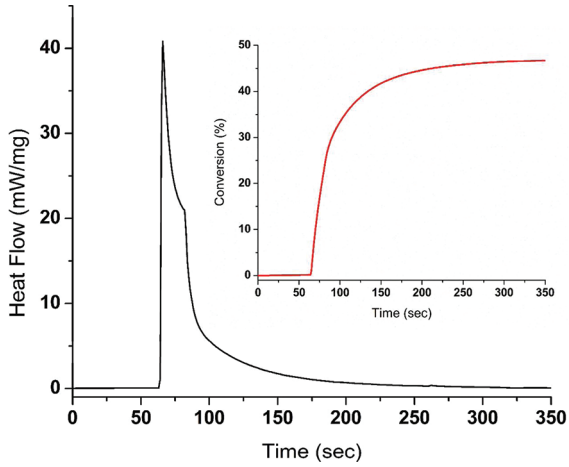


Figure 6. Photo-DSC profile for polymerization of TPTA in the presence of PEO-$NH^+(Me)_2$TX-CH_2 (27%) macrophotoinitiator, cured at 30 °C by UV light (λ = 320−500 nm) with an intensity of 180 mW/cm^2. Inset: conversion vs time curves derived from the heat flow data.

gelation and vitrification of the polymerizing trifunctional acrylate most likely render the diffusion of the components more difficult.

In summary, we established an easy and efficient method to form a polymeric type II photoinitiator possessing both chromophoric and hydrogen donating sites in the structure. This novel photoinitiator initiates the free radical polymerization by hydrogen abstraction of excited triplet TX moiety from PEO segment. To the best of our knowledge, this is the first description of a method that initiates free radical polymerization by counteranion excitation. The concept described here will further be expanded to the newly emerging polymeric materials such as polymeric ionic liquids.[18] We anticipate that photolysis of such polyelectrolytes equipped with photosensitive anions will provide possibility to regulate ionic liquid properties and design photoinitiating systems for environmental friendly UV-curing applications due its polymeric nature eliminating problems associated with volatility and migration.

■ ASSOCIATED CONTENT

Ⓢ Supporting Information

Photobleaching studies performed at visible light. This material is available free of charge via the Internet at http://pubs.acs.org.

■ AUTHOR INFORMATION

Corresponding Author

*E-mail: yusuf@itu.edu.tr, Fax +90-212-2856386, Tel +90-212-2853241.

Notes

The authors declare no competing financial interest.

■ ACKNOWLEDGMENTS

The authors thank Istanbul Technical University Research Fund for financial support.

■ REFERENCES

(1) (a) Yagci, Y.; Jockusch, S.; Turro, N. J. *Macromolecules* **2010**, *43* (15), 6245−6260. (b) Crivello, J. V.; Dietliker, K.; Bradley, G.; Limited, S. T. *Chemistry & Technology of UV & EB Formulation for*

Coatings, Inks & Paints; J. Wiley: Chichester, 1998; Vol. 3. (c) Arsu, N.; Reetz, I.; Yagci, Y.; Mishra, M. K. *Photoinitiated Radical Vinyl Polymerization*; Taylor & Francis: London, 2009; Vol. *73*, pp 141−204.
(2) (a) Crivello, J. V. *Adv. Polym. Sci.* **1984**, *62*, 1−48. (b) Yagci, Y.; Reetz, I. *Prog. Polym. Sci.* **1998**, *23* (8), 1485−1538. (c) Decker, C. *Prog. Polym. Sci.* **1996**, *21* (4), 593−650.
(3) (a) Wicks, Z. W.; Jones, F. N.; Pappas, S. P. *Organic Coatings: Science and Technology*; Wiley-Interscience: Hoboken, NJ, 2007. (b) Tasdelen, M. A.; Yagci, Y. *Aust. J. Chem.* **2011**, *64* (8), 982−991. (c) Gruber, H. F. *Prog. Polym. Sci.* **1992**, *17* (6), 953−1044.
(4) Sangermano, M.; Crivello, J. V. *ACS Symp. Ser.* **2003**, *847*, 242−252.
(5) Fouassier, J.-P. In *Photoinitiation, Photopolymerization, and Photocuring: Fundamentals and Applications*; Hanser/Gardner Publications: Munich, 1995.
(6) (a) Crivello, J. V.; Lam, J. H. W. *Macromolecules* **1977**, *10* (6), 1307−1315. (b) Dursun, C.; Degirmenci, M.; Yagci, Y.; Jockusch, S.; Turro, N. J. *Polymer* **2003**, *44* (24), 7389−7396. (c) Durmaz, Y. Y.; Moszner, N.; Yagci, Y. *Macromolecules* **2008**, *41* (18), 6714−6718. (d) Kahveci, M. U.; Tasdelen, M. A.; Yagci, Y. *Polymer* **2007**, *48* (8), 2199−2202.
(7) Crivello, J. V.; Lam, J. H. W. *J. Polym. Sci., Part A: Polym. Chem.* **1979**, *17* (4), 977−999.
(8) Ko, M.; Sato, T.; Otsu, T. *J. Polym. Sci., Part A: Polym. Chem.* **1974**, *12* (12), 2943−2951.
(9) (a) Schnabel, W. *Macromol. Rapid Commun.* **2000**, *21* (10), 628−642. (b) Yagci, Y.; Kornowski, A.; Schnabel, W. *J. Polym. Sci., Part A: Polym. Chem.* **1992**, *30* (9), 1987−1991. (c) Yagci, Y.; Endo, T. *Adv. Polym. Sci.* **1997**, *127*, 59−86.
(10) Abuabdoun, I. I.; Aaleali.. *Eur. Polym. J.* **1993**, *29* (11), 1439−1443.
(11) Yagci, Y.; Durmaz, Y. Y.; Aydogan, B. *Chem. Rec.* **2007**, *7* (2), 78−90.
(12) Kahveci, M. U.; Yilmaz, A. G.; Yagci, Y. Photoinitiated Cationic Polymerization: Reactivity and Mechanistic Aspects. In *Photochemistry and Photophysics of Polymer Materials*; John Wiley & Sons, Inc.: New York, 2010; pp 421−478.
(13) (a) Hutchiso., J.; Ledwith, A. *Polymer* **1973**, *14* (9), 405−408. (b) Jockusch, S.; Timpe, H. J.; Schnabel, W.; Turro, N. J. *J. Phys. Chem. A* **1997**, *101* (4), 440−445. (c) Neumann, M. G.; Gehlen, M. H.; Encinas, M. V.; Allen, N. S.; Corrales, T.; Peinado, C.; Catalina, F. *J. Chem. Soc., Faraday Trans.* **1997**, *93* (8), 1517−1521. (d) Encinas, M. V.; Rufs, A. M.; Corrales, T.; Catalina, F.; Peinado, C.; Schmith, K.; Neumann, M. G.; Allen, N. S. *Polymer* **2002**, *43* (14), 3909−3913. (e) Allen, N. S. *J. Photochem. Photobiol., A* **1996**, *100* (1−3), 101−107. (f) Aydin, M.; Arsu, N.; Yagci, Y. *Macromol. Rapid Commun.* **2003**, *24* (12), 718−723. (g) Cokbaglan, L.; Arsu, N.; Yagci, Y.; Jockusch, S.; Turro, N. J. *Macromolecules* **2003**, *36* (8), 2649−2653. (h) Balta, D. K.; Arsu, N.; Yagci, Y.; Jockusch, S.; Turro, N. J. *Macromolecules* **2007**, *40* (12), 4138−4141. (i) Yilmaz, G.; Aydogan, B.; Temel, G.; Arsu, N.; Moszner, N.; Yagci, Y. *Macromolecules* **2010**, *43* (10), 4520−4526. (j) Yilmaz, G.; Tuzun, A.; Yagci, Y. *J. Polym. Sci., Part A: Polym. Chem.* **2010**, *48* (22), 5120−5125. (k) Allonas, X.; Fouassier, J. P.; Angiolini, L.; Caretti, D. *Helv. Chim. Acta* **2001**, *84* (9), 2577−2588. (l) Jakubiak, J.; Allonas, X.; Fouassier, J. P.; Sionkowska, A.; Andrzejewska, E.; Linden, L. A.; Rabek, J. F. *Polymer* **2003**, *44* (18), 5219−5226. (m) Fouassier, J. P.; Allonas, X.; Burget, D. *Prog. Org. Coat.* **2003**, *47* (1), 16−36. (n) Lalevee, J.; El-Roz, M.; Allonas, X.; Fouassier, J. P. *J. Polym. Sci., Part A: Polym. Chem.* **2008**, *46* (6), 2008−2014. (o) Ullrich, G.; Herzog, D.; Liska, R.; Burtscher, P.; Moszner, N. *J. Polym. Sci., Part A: Polym. Chem.* **2004**, *42* (19), 4948−4963.
(14) (a) Corrales, T.; Catalina, F.; Peinado, C.; Allen, N. S. *J. Photochem. Photobiol., A* **2003**, *159* (2), 103−114. (b) Corrales, T.; Catalina, F.; Peinado, C.; Allen, N. S.; Rufs, A. M.; Bueno, C.; Encinas, M. V. *Polymer* **2002**, *43* (17), 4591−4597. (c) Tasdelen, M. A.; Demirel, A. L.; Yagci, Y. *Eur. Polym. J.* **2007**, *43* (10), 4423−4430.
(15) Temel, G.; Aydogan, B.; Arsu, N.; Yagci, Y. *Macromolecules* **2009**, *42* (16), 6098−6106.
(16) (a) Akat, H.; Gacal, B.; Balta, D. K.; Arsu, N.; Yagci, Y. *J. Polym. Sci., Part A: Polym. Chem.* **2010**, *48* (10), 2109−2114. (b) Gacal, B.; Akat, H.; Balta, D. K.; Arsu, N.; Yagci, Y. *Macromolecules* **2008**, *41* (7), 2401−2405.
(17) Yilmaz, F.; Cianga, I.; Ito, K.; Senyo, T.; Yagci, Y. *Macromol. Rapid Commun.* **2003**, *24* (4), 316−319.
(18) (a) Yu, S. H.; Antonietti, M.; Colfen, H.; Giersig, M. *Angew. Chem., Int. Ed.* **2002**, *41* (13), 2356−2360. (b) Antonietti, M.; Kuang, D. B.; Smarsly, B.; Yong, Z. *Angew. Chem., Int. Ed.* **2004**, *43* (38), 4988−4992. (c) Yuan, J.; Antonietti, M. *Polymer* **2011**, *52* (7), 1469−1482.

Macromolecules

Article

pubs.acs.org/Macromolecules

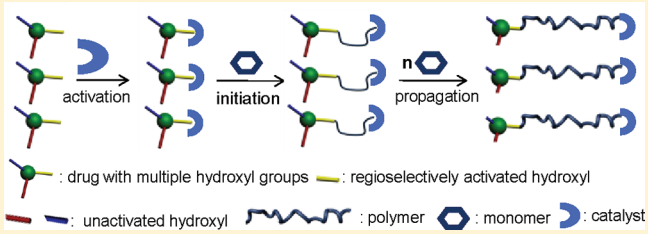
Drug-Initiated, Controlled Ring-Opening Polymerization for the Synthesis of Polymer–Drug Conjugates

Rong Tong† and Jianjun Cheng*

Department of Materials Science and Engineering, University of Illinois at Urbana–Champaign, Urbana, Illinois 61801, United States

Supporting Information

ABSTRACT: Paclitaxel, a polyol chemotherapeutic agent, was covalently conjugated through its 2′-OH to polylactide with 100% regioselectivity via controlled polymerization of lactide mediated by paclitaxel/(BDI-II)ZnN(TMS)$_2$ (BDI-II = 2-((2,6-diisopropylphenyl)amino)-4-((2,6-diisopropylphenyl)-imino)-2-pentene). The steric bulk of the substituents on the *N*-aryl groups of the BDI ligand drastically affected the regiochemistry of coordination of the metal catalysts to paclitaxel and the subsequent ring-opening polymerization of lactide. The drug-initiated, controlled polymerization of lactide was extended, again with 100% regioselectivity, to docetaxel, a chemotherapeutic agent that is even more structurally complex than paclitaxel. Regioselective incorporation of paclitaxel (or docetaxel) to other biopolymers (i.e., poly(δ-valerolactone), poly(trimethylene carbonate), and poly(ε-caprolactone)) was also achieved through drug/(BDI-II)ZnN(TMS)$_2$-mediated controlled polymerization. These drug–polylactide conjugates with precisely controlled structures are expected to be excellent building blocks for drug delivery, coating, and controlled-release applications.



INTRODUCTION

Research on the use of drug-containing polymeric nanoparticles for improved cancer treatments is an emerging field.[1] Chemotherapeutic agents incorporated in polymeric nanoparticulate delivery vehicles typically have improved water solubility,[2] prolonged retention in circulation,[3] and reduced drug resistance[4] relative to conventional chemotherapeutics. Therefore, polymeric nanomedicines are expected to have reduced toxicity and improved efficacy.[5] A handful of polymeric nanomedicines have been developed for clinical cancer treatment in the past 2–3 decades;[6] among these, polymer–drug conjugates have been one of the most intensively investigated delivery platforms.[7]

The preparation of polymer–drug conjugates with well-defined structures and compositions is extremely important for their in vivo applications, but this task can be difficult. Polymer–drug conjugates usually exhibit heterogeneous structures. Heterogeneities may result from (1) molecular weight distributions (MWDs) of the polymers (Scheme 1A), (2) lack of control of the drug conjugation site on the polymer backbone (Scheme 1B), and (3) lack of regioselectivity with regard to the conjugation site on drugs with multiple conjugation-amenable functional groups. These heterogeneities, which are not easily addressed, may present bottlenecks in the clinical translation of polymer–drug conjugates.[6d] In the past several decades, there have been numerous efforts to minimize these heterogeneities, including the development of polymers with low MWDs (e.g., dendrimer),[8] the conjugation of therapeutic agents to specific sites along the polymer backbone (e.g., the termini),[2,9] and the activation of specific functional groups on the therapeutic agents by means of protection/deprotection chemistry.[10]

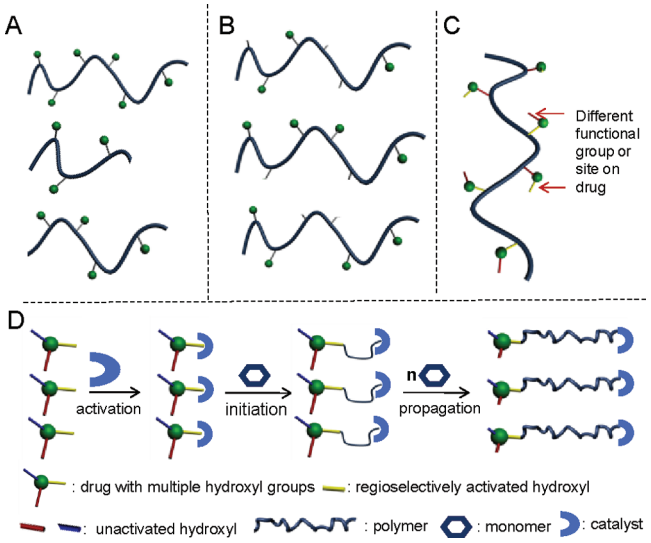
We have been interested in controlling the conjugation of drugs to polymers with reduced heterogeneity via a controlled ring-opening polymerization (ROP) strategy. In our initial attempt, we used a complex of paclitaxel (Ptxl), a mitotic inhibitor with three hydroxyl groups, and a Zn catalyst to initiate the ROP of lactide (LA), which results in efficient conjugation of Ptxl molecules to the termini of polylactide (PLA) chains.[11] In ROP studies conducted by the chemistry community, the focus is on control of the molecular weights (MWs), MWDs, and structures of the polymer products (that is, the chain propagation step),[12] whereas the focus of our studies on drug-initiated ROP has been more on the initiation step. We are particularly interested in controlling the regioselective coordination of a structurally complex drug molecule (the initiator) bearing multiple hydroxyl groups with the metal catalyst. In the Ptxl/Zn polymerization system specifically, investigation of Zn catalysts that interact with Ptxl to afford regioselective initiation and controlled polymerization is imperative. Exploring whether this chemistry is widely applicable for the synthesis of drug–polymer conjugates with various hydroxyl-containing therapeutics and with various polymer backbones is also important.

Here, we report the rationale design of metal catalysts that allow for regioselective conjugation of PLA to Ptxl via its 2′-OH

Received: November 27, 2011
Revised: February 3, 2012
Published: February 27, 2012

 © 2012 American Chemical Society dx.doi.org/10.1021/ma202581d | *Macromolecules* 2012, 45, 2225–2232

Scheme 1. (A) Polymer−Drug Conjugates with a Broad Distribution of Polymer Chain Lengths; (B) Polymer−Drug Conjugates in Which the Conjugation Site on the Polymer Backbone Is Uncontrolled; (C) Polymer−Drug Conjugates in Which a Multifunctional Therapeutic Agent Is Conjugated without Regioselectivity; (D) Drug-Initiated, Controlled Polymerization for the Synthesis of Polymer−Drug Conjugates with Low MWDs[a]



[a]The drug molecules are conjugated regioselectively to the polymer chain termini.

to afford Ptxl−PLA conjugates with precisely controlled MWs, predefined drug loading, and narrow MWDs (Scheme 1D). We found that this chemistry could be extended to the ROP of cyclic esters and carbonates to prepare a large variety of drug−polyester and drug−polycarbonate conjugates. Docetaxel−PLA conjugates were also prepared with remarkably controlled MWs and low MWDs. These materials are expected to be excellent building blocks for the design of systems for drug delivery, coating, and controlled release applications.

RESULTS AND DISCUSSION

(BDI-EE)Zn/Ptxl-Mediated LA Polymerization. Metal oxides (M-ORs) are well-known initiators for living ROP of cyclic esters such as LA (Figure 1).[12c] By judicious design, labile M-ORs prepared in situ by mixing a hydroxyl-containing compound with an active metal complex[12a] can initiate the controlled living ROP of LA, resulting in quantitative incorporation of the initiating alcohol group at the PLA terminals with nearly 100% monomer conversion.[12c] The use of various hydroxyl-containing cholesterol derivatives coordinated with an Al(III) or a Sn(II) complex as co-initiators for cyclic ester polymerization has been reported previously.[13] Because Ptxl has hydroxyl groups, we attempted to use it to initiate the ROP of LA in the presence of (BDI-X)ZnN(TMS)$_2$ (BDI = 2-((2,6-dialkylphenyl)amino)-4-((2,6-dialkylphenyl)imino)-2-pentene, Table 1),[11] a class of catalysts developed by Coates and co-workers for controlled ROP of LA. (BDI-EE)ZnN(TMS)$_2$ (Table 1) was synthesized and mixed with Ptxl, instantly resulting in (BDI-EE)Zn/Ptxl; this active complex subsequently initiated LA polymerization at a LA/Ptxl/(BDI-EE)ZnN(TMS)$_2$ ratio of 200:1:1.01. Ptxl was quantitatively conjugated to PLA to afford Ptxl-LA$_n$ (in this paper, PLA is denoted as LA$_n$, where n = M/I) as indicated by HPLC and ^{1}H NMR analysis (entry 1, Table 2). The drug loadings could be

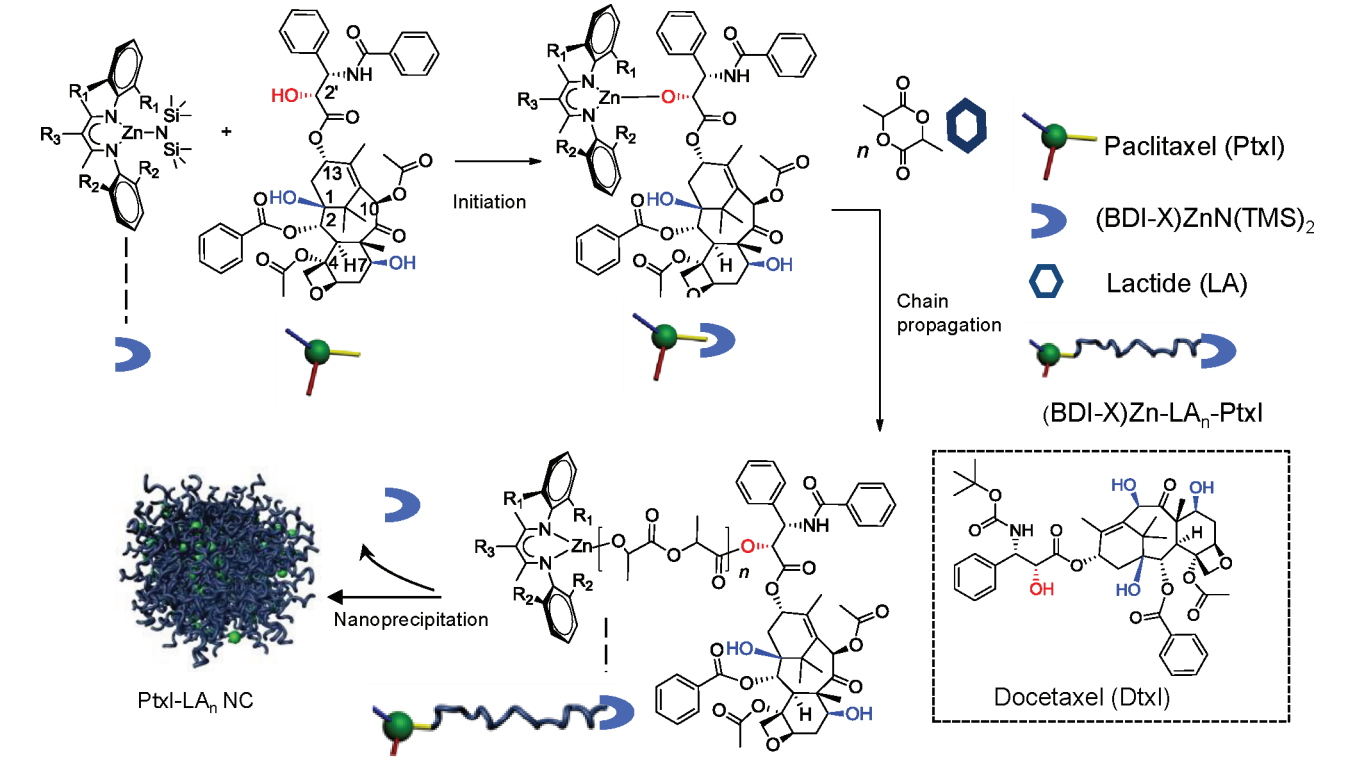
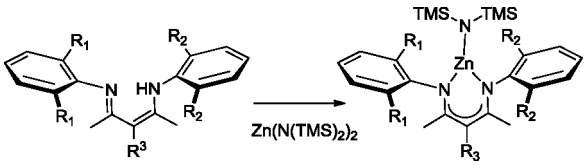


Figure 1. Preparation of PEGylated Ptxl−PLA nanoconjugates (NCs) via Ptxl-initiated LA polymerization in the presence of (BDI-X)ZnN(TMS)$_2$ (X = II, EE, EI, IICN; see Table 1), followed by nanoprecipitation and noncovalent surface modification[11,19] with poly(lactide-*co*-glycolide)-methoxy poly(ethylene glycol) (PLGA-mPEG) or poly(lactide)-methoxy poly(ethylene glycol) (PLA-mPEG).

dx.doi.org/10.1021/ma202581d | *Macromolecules* 2012, 45, 2225−2232

Table 1. Synthesis of (BDI-X)ZnN(TMS)$_2$[a]



BDI-X	R_1	R_2	R_3
BDI-II	^{i}Pr	^{i}Pr	H
BDI-EE	Et	Et	H
BDI-EI	Et	^{i}Pr	H
BDI-IICN	^{i}Pr	^{i}Pr	CN

[a]Abbreviations: ^{i}Pr, isopropyl; Et, ethyl.

precisely controlled by adjusting the LA/Ptxl ratio. The M_n value was 30.2 × 10^3 g/mol, which is in excellent agreement with the expected value (29.7 × 10^3 g/mol). However, the MWD was fairly broad (M_w/M_n = 1.30).

Use of Reductive Reaction To Determine Regioselectivity of Ptxl-LA$_5$ Formation. Ptxl has three hydroxyl groups, at the C-2′, C-1, and C-7 positions (Figure 1). All three can potentially initiate LA polymerization, resulting in Ptxl-PLA conjugates with one to three PLA chains attached to Ptxl. The tertiary 1-OH is least accessible and is typically inactive,[14] but both the 2′-OH and 7-OH are active, with the 2′-OH being sterically more accessible.[15] We next evaluated the regioselectivity of polymerization initiation in the presence of (BDI-EE)ZnN(TMS)$_2$.

Tetrabutylammonium borohydride (Bu_4NBH_4) has been used for selectively and quantitatively reducing the C13-ester bond of Ptxl to afford baccatin III (BAC) and (1*S*,2*R*)-*N*-1-(1-phenyl-2,3-dihydroxypropyl)benzamide (PDB; Figure 2A).[16] We attempted to use this reductive reaction to disassemble Ptxl-LA$_5$ obtained from (BDI-EE)ZnN(TMS)$_2$/Ptxl-mediated polymerization and then determine whether PLA was attached only to the 2′-OH or to both the 2′-OH and 7-OH (Figure 2B). If the initiation occurred regioselectively at the 2′-OH, no BAC-PLA should have been observed. However, analysis of the fragments obtained from the reductive cleavage of the C13-ester bond of Ptxl-LA$_5$ clearly showed the presence of both PDB−PLA and BAC−PLA, indicating that the (BDI-EE)ZnN(TMS)$_2$/Ptxl-mediated polymerization exhibited poor regioselectivity (Figure 2C), which may explain the relatively broad MWD of the Ptxl-LA$_{200}$ synthesized with (BDI-EE)ZnN(TMS)$_2$/Ptxl (entry 1, Table 2).

The substituents on the *N*-aryl groups (R_1 and R_2) and at the *β*-position (R_3) of the BDI ligand drastically affect its ability to control the ROP of LA.[12a,17] By varying the steric bulk of the *N*-aryl substituents and the electronic properties of R_3, we studied the effects of the BDI substituents on the initiation regioselectivity and the LA polymerization mediated by

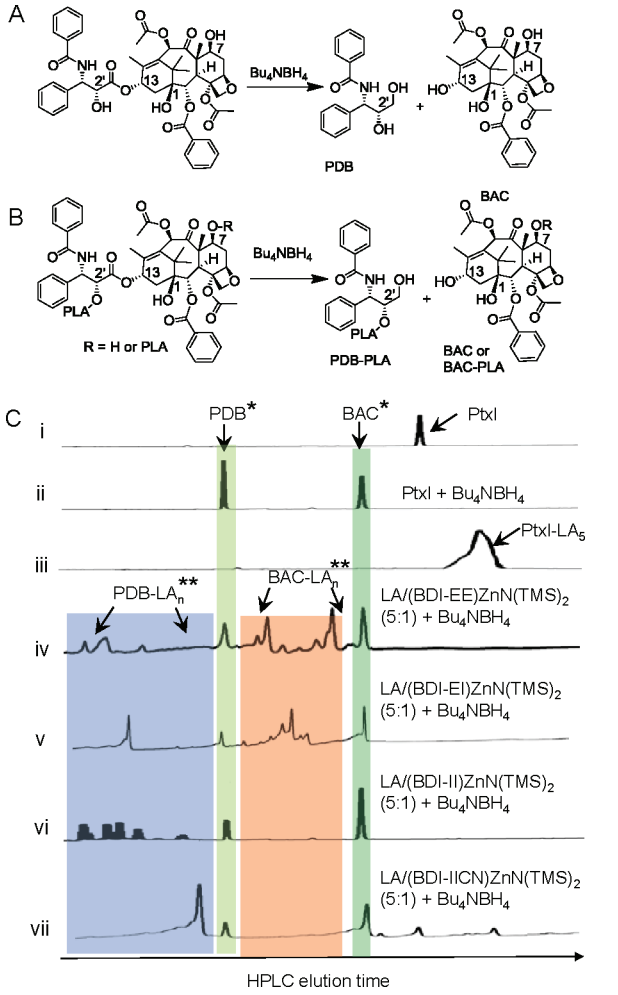


Figure 2. (A) Bu_4NBH_4-induced site-specific degradation of Ptxl to form PDB and BAC. (B) Reductive degradation of C13-ester of Ptxl-PLA. (C) HPLC traces for (i) Ptxl, (ii) Ptxl treated with Bu_4NBH_4, (iii) Ptxl-LA$_5$, and (iv−vii) Ptxl-LA$_5$ prepared using (BDI-X)ZnN(TMS)$_2$ (X = EE, EI, II, and IICN; see Table 1) and subsequent treatment with Bu_4NBH_4. *The PDB and partial BAC detected in (iv−vii) were produced from free Ptxl not completely consumed during the polymerization at low [LA]/[Ptxl] (i.e., ≤5). Separation of Ptxl was not attempted. Comparison of the patterns of BAC and PDB in (vi) and (ii) clearly indicates that the BAC in (vi) was produced partially by degradation of unreacted Ptxl and partially by reduction of Ptxl-PLA with the PLA being attached to the 2′-OH of Ptxl. **Peaks were verified by mass spectrometry.

Table 2. Effect of Ligand Substituents on LA ROP Mediated by Ptxl/(BDI-X)ZnN(TMS)$_2$[a]

entry	ligand (BDI-X)	[LA]/[Ptxl]	LA conv (%)	incorp eff (%)	M_{exp} (×10^3 g/mol)	M_n (×10^3 g/mol)	MWD (M_w/M_n)
1	BDI-EE	200	>99	>99	29.7	30.2	1.30
2	BDI-EI	200	>99	>99	29.7	31.4	1.17
3	BDI-II	200	>99	>99	29.7	28.1	1.02
4	BDI-IICN	200	>99	>99	29.7	27.4	1.04
5	BDI-II	50	>99	>99	8.1	7.8	1.04
6	BDI-II	100	>99	>99	15.3	12.7	1.03

[a]All reactions were performed with [Ptxl]/[(BDI-X)ZnN(TMS)$_2$] = 1:1.01 in anhydrous THF with $[LA]_0$ = 0.69 M at room temperature for 12 h. Abbreviations: LA, lactide; Ptxl, paclitaxel; conv, conversion; incorp eff, incorporation efficiency; M_{exp}: expected MW; MWD, molecular weight distribution. LA conversion was measured by monitoring the disappearance of the LA peak (1772 cm^{-1}) in the FT-IR spectrum. Incorporation efficiency was determined by reversed-phase HPLC analysis of unincorporated Ptxl. M_n and MWD were measured by GPC.

dx.doi.org/10.1021/ma202581d | *Macromolecules* 2012, 45, 2225−2232

(BDI-X)Zn(TMS)$_2$/Ptxl (Table 1).[18] When one of the ethyl groups in BDI-EE was replaced with the more bulky isopropyl (^{i}Pr) group (BDI-EI), the polymerization reaction afforded Ptxl-LA$_{200}$ with a much narrower MWD (M_w/M_n = 1.17, LA/Ptxl/(BDI-EI)ZnN(TMS)$_2$ = 200:1:1.01, entry 2, Table 2). When both the ethyl groups were replaced with ^{i}Pr groups, remarkably well controlled polymerization was observed: Ptxl-LA$_{200}$ was obtained with the expected MW (M_n = 28.1 × 10^3 g/mol) and an extremely narrow MWD (M_w/M_n = 1.02, entry 3).

Interestingly, the regioselectivities obtained with these catalysts followed a similar trend as the polymerization results. Analysis of the fragments of the reductive cleavage of Ptxl-LA$_5$ prepared from (BDI-EI)ZnN(TMS)$_2$/Ptxl showed reduced amounts of BAC-PLA relative to the amount observed with (BDI-EE)ZnN(TMS)$_2$/Ptxl. When Ptxl-LA$_5$ prepared from (BDI-II)ZnN(TMS)$_2$/Ptxl was treated with Bu_4NBH_4 and analyzed similarly, no BAC-PLA peaks were identified, indicating that (BDI-II)ZnN(TMS)$_2$/Ptxl-mediated polymerization was highly regioselective (Figure 2). The steric bulk of the substituents at the 2- and 6-positions of the *N*-aryl group clearly had a strong effect on the regioselectivity and controlled polymerization. The bulky ^{i}Pr groups on the BDI ligand may have hindered metal complexation with the 7-OH of Ptxl, thereby minimizing undesired chain initiation and propagation via this hydroxyl group. To determine whether R_3 also affected initiation regioselectivity and polymerization, we prepared BDI-IICN, an analogue of BDI-II with an additional CN group on R_3. (BDI-IICN)ZnN(TMS)$_2$ behaved similarly to (BDI-II)ZnN(TMS)$_2$ (entry 4).

Controlled polymerizations of PLA were observed when (BDI-II)ZnN(TMS)$_2$/Ptxl was used at various [LA]/[Ptxl] ratios (50:1−300:1; Figure 3A): the obtained MWs were in excellent agreement with the expected MWs (Table S1); the MWDs were in a range of 1.02−1.09. Monomodal gel permeation chromatography (GPC) curves were observed in all cases (Figure 3B).

Regioselectivity of Ptxl/Anhydride Reaction. We next investigated whether the regioselectivity observed at the initiation step for the formation of Ptxl-LA$_n$ could be achieved with other substrates besides LA. Previous studies showed that (BDI-II)-ZnO^{i}Pr (or other Zn-alkoxides) can mediate controlled ROP of LA via a coordination−insertion mechanism (Scheme 2A). In addition, the same catalyst can also mediate ROP of anhydrides and epoxides by a similar mechanism.[20] These results suggested that succinic anhydride (SA) could be used as a model monomer and that ROP reactions mediated by (BDI-X)ZnN(TMS)$_2$/Ptxl could terminate after the initiation step (*O*-acylation, Scheme 2B). Such reactions would afford not a polymer but the small molecule Ptxl-succinic acid (Ptxl-SA), whose structure could be easily and precisely determined by routine characterization methods.

To perform the acylation, we prepared various (BDI-X)ZnN-(TMS)$_2$/Ptxl complexes in situ and mixed them with SA for 4 h at 40 °C at a Ptxl/SA ratio of 1:1.1 (Table 3). The reaction mixtures were quenched and analyzed by HPLC. The structures of the acylation products were determined by NMR after separation by TLC or HPLC (^{1}H NMR shown in Figure 4). The chemical shift of the C2′-H of Ptxl-2′-SA was shifted downfield relative to that of Ptxl (from 4.78 to 5.53 ppm), whereas the chemical shifts of C7-H were nearly the same (δ = 4.40 ppm, Figure 4). For Ptxl-2′,7-diSA, both C2′-H and C7-H were shifted downfield relative to the corresponding protons of Ptxl (δ (C2′-H) from 4.78 to 5.53 ppm; δ(C7-H) from 4.40 to 5.64 ppm). By measuring the yields of Ptxl-2′-SA and Ptxl-2′,7-diSA (Table 3), we found that the 2′-OH regioselectivity obtained with the various catalysts followed exactly

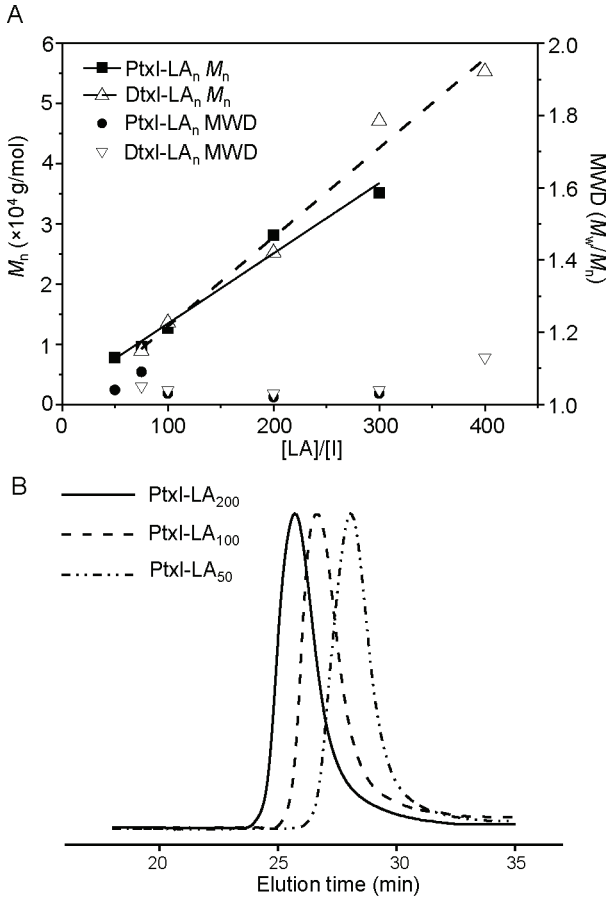
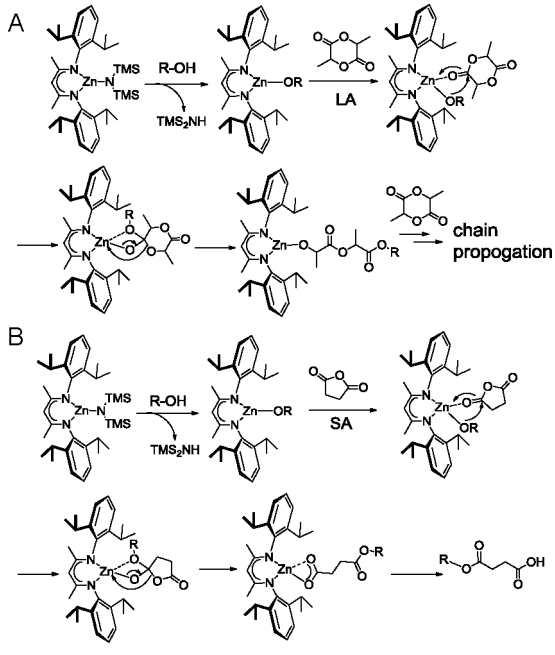


Figure 3. (A) Plots of M_n and MWD versus [LA]/[I] (I = Ptxl or Dtxl) for LA polymerization initiated by Ptxl/(BDI-II)ZnN(TMS)$_2$ and Dtxl/(BDI-II)ZnN(TMS)$_2$. (B) Overlay of GPC chromatograms for Ptxl-LA$_{200}$, Ptxl-LA$_{100}$, and Ptxl-LA$_{50}$ obtained by (BDI-II)ZnN-(TMS)$_2$-mediated polymerization.

Scheme 2. (BDI-II)ZnN(TMS)$_2$-Mediated Ring-Opening of (A) LA and (B) SA via a Coordination−Insertion Mechanism



dx.doi.org/10.1021/ma202581d | *Macromolecules* 2012, 45, 2225−2232

Table 3. Ring-Opening Reactions of SA Mediated by Ptxl (or Dtxl)/(BDI-X)ZnN(TMS)$_2$[a]

entry	initiator (R)	catalyst ligand (BDI-X)	yield of R-2′-SA (%)	yield of R-2′,7-diSA and other R-SA (%)	total yield of R-SA (%)	regioselectivity for 2′-OH (%)
1	Ptxl	BDI-EE	29.6	55.4	85	34.8
2	Ptxl	BDI-EI	45	13.4	58.4	77.1
3	Ptxl	BDI-II	39.7	0	39.7	100
4	Ptxl	BDI-IICN	53.6	0	53.6	100
5	Dtxl	BDI-II	71.5	0	71.5	100

[a]All reactions were performed with [Ptxl]/[(BDI-X)ZnN(TMS)$_2$]/[SA] = 1/1.01/1.1 in anhydrous THF with [SA]$_0$ = 0.011 M at 40 °C for 4 h. Abbreviations: SA, succinic anhydride; Ptxl, paclitaxel; Dtxl, docetaxel. Yields were determined by reversed-phase HPLC analysis. SA derivatives were confirmed by NMR and MS.

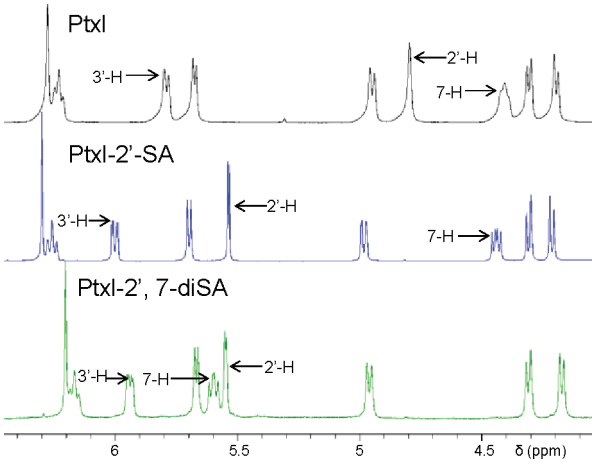
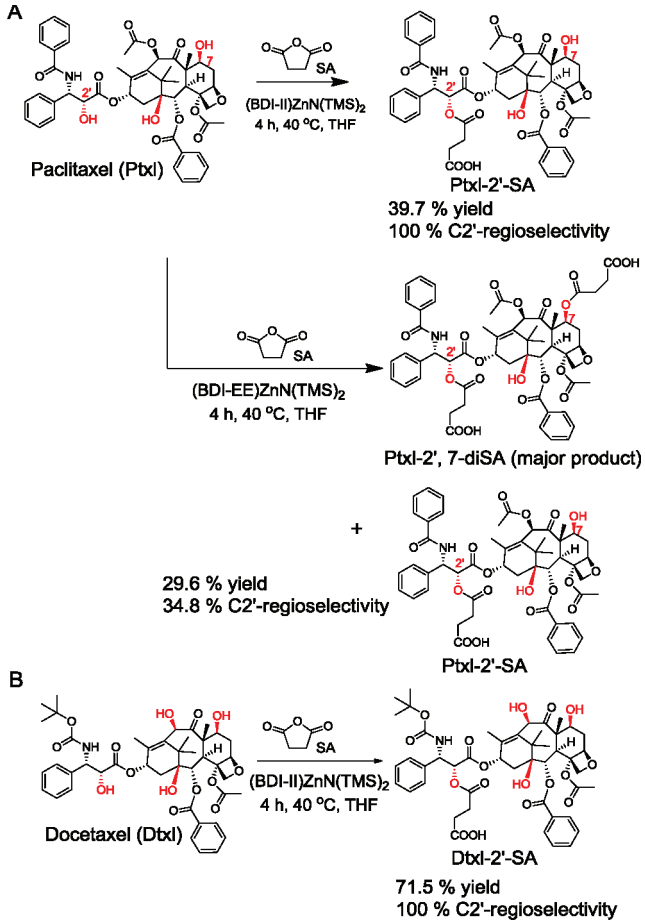


Figure 4. ^{1}H NMR spectrum of Ptxl, Ptxl-2′-SA, and Ptxl-2′,7-diSA.

Scheme 3. Regioselective Acylation of (A) Ptxl and (B) Dtxl with SA



the same trend observed for the reactions with LA, as determined by Bu_4NBH_4-mediated reductive cleavage (Figure 2). That is, the regioselectivity of the Ptxl/SA reaction increased as the sizes of R_1 and R_2 increased; (BDI-II)ZnN(TMS)$_2$ showed the best regioselectivity and (BDI-EE)ZnN(TMS)$_2$ the worst (Scheme 3A).

Specifically, the (BDI-EE)ZnN(TMS)$_2$/Ptxl-mediated ring-opening acylation with SA showed poor regioselectivity (34.8%, entry 1, Table 3). Only 29.6% of the Ptxl was converted to Ptxl-2′-SA), whereas 55.4% was converted to Ptxl-2′,7-diSA, the undesired byproduct. In contrast, with (BDI-EI)ZnN(TMS)$_2$/Ptxl, the regioselectivity of the acylation was 77.1% (entry 2). When Ptxl/(BDI-II)ZnN(TMS)$_2$ was used, the regioselectivity of the reaction was 100%: Ptxl-2′-SA was the only acylation product (entry 3). Although the reactions of Ptxl with SA and LA showed similar regioselectivity trends, the overall reactivity of (BDI-X)ZnN(TMS)$_2$ was inversely correlated with the sizes of R_1 and R_2, as indicated by the overall yields of the Ptxl/SA reactions (entries 1−3). Changing R_3 from −H (BDI-II) to the electron-withdrawing −CN group (BDI-IICN) did not change the regioselectivity of the Ptxl/SA reaction. However, additional of the CN group enhanced the reactivity of the resulting catalyst ((BDI-IICN)ZnN(TMS)$_2$), leading to a higher yield of Ptxl-2′-SA (entry 4).

Regioselective (BDI-II)ZnN(TMS)$_2$/Docetaxel-Initiated Ring-Opening of LA and SA. After demonstrating the regioselectivity of the Ptxl ring-opening reactions with LA and SA in the presence of (BDI-II)ZnN(TMS)$_2$, we determined whether this catalyst could be used for regioselective ROP of LA and for ring-opening acylation of SA with a more structurally complex therapeutic agent. We chose docetaxel (Dtxl), which is an important clinical therapeutic for the treatment of prostate cancer and which has four hydroxyl groups, at C-2′, C-1, C-7, and C-10 (Figure 1). When complexed with (BDI-II)ZnN(TMS)$_2$, Dtxl reacted with SA to yield Dtxl-2′-SA with 100% regioselectivity and 71.5% yield (entry 5, Table 3; Scheme 3B). In addition, (BDI-II)ZnN(TMS)$_2$/Dtxl showed excellent control for the ROP of LA, affording Dtxl-PLA with predictable MWs and very narrow MWDs (Figure 3A and Supporting Information Table S2).

Ptxl-Initiated Controlled Polymerization of δ-Valerolactone, Trimethylene Carbonate, and ε-Caprolactone. Poly(δ-valerolactone) (PVL), poly(trimethylene carbonate) (PTMC), and poly(ε-caprolactone) (PCL) have been extensively used as alternatives to PLA in suturing, drug delivery, and tissue engineering applications. We next studied whether the Ptxl (or Dtxl)/(BDI-II)ZnN(TMS)2-mediated controlled ROP of LA could be extended to the synthesis of Ptxl-PCL, Ptxl-PVL, and Ptxl-PTMC conjugates from the corresponding monomers. Ptxl/(BDI-II)ZnN(TMS)$_2$ showed excellent control over the polymerization of δ-valerolactone (VL), trimethylene carbonate (TMC), and ε-caprolactone (CL) (Table 4; for comprehensive polymerization results, see Supporting Information Table S3). All the polymerization reactions gave drug−polymer conjugates with the expected MWs and narrow MWDs (M_w/M_n < 1.2); Ptxl (or Dtxl) was quantitatively conjugated to the termini of the polymers via ester bonds. The

dx.doi.org/10.1021/ma202581d | Macromolecules 2012, 45, 2225−2232

Table 4. Ptxl (or Dtxl)/(BDI-II)ZnN(TMS)$_2$-Mediated ROP of VL, TMC, and CL[a]

entry	initiator (R)	monomer	[M]/[R]	time (h)	temp (°C)	conv (%)	incorp eff (%)	M_n/M_{exp} (× 10^3 g/mol)	MWD (M_w/M_n)
1	Ptxl	VL	100	12	rt	>99	>99	15.1/10.8	1.17
2	Ptxl	VL	200	12	rt	>99	>99	23.1/20.8	1.18
3	Ptxl	VL	300	12	rt	>99	>99	31.2/30.8	1.18
4	Ptxl	CL	200	10	rt	>99	>99	20.3/23.7	1.07
5	Dtxl	CL	100	10	rt	>99	>99	11.2/12.2	1.05
6	Ptxl	TMC	100	6	50	>99	>99	14.7/11.1	1.10

[a]All reactions were performed in anhydrous THF with $[monomer]_0$ = 0.69 M. Abbreviations: conv = conversion; Dtxl = docetaxel; incorp eff = incorporation efficiency; M_{exp}, expected MW; MWD = molecular weight distribution; Ptxl = paclitaxel; rt = room temperature. Monomer conversion was measured by FT-IR. Incorporation efficiency was determined by reversed-phase HPLC analysis of unreacted Ptxl (or Dtxl). M_n and MWD were determined by GPC.

polymerizations of VL and CL proceeded at room temperature, and the monomer conversions were quantitative (entries 1−5, Table 4). However, the polymerization of TMC required a slightly elevated reaction temperature; quantitative TMC conversation took place in 6 h at 50 °C (entry 6).

CONCLUSION

When complexed with hydroxyl-containing therapeutics, Zn catalysts mediated the polymerization of LA and afforded PLA chains with drugs incorporated at the chain termini through ester linkages.[6a,11,21] Our previous work showed that the resulting drug−polymer conjugates could be nanoprecipitated to formulate nanoparticles with high drug loadings, nearly quantitative loading efficiencies, controlled release profiles without burst release effects, and narrow particle size distributions.[11,19] We systemically investigated the effects of BDI ligand substituents on the initiation and chain propagation during LA polymerization. The steric bulk of the *N*-aryl substituents of the BDI ligand drastically affected the regioselectivity of the coordination of the metal catalysts with the drugs. (BDI-II)ZnN(TMS)$_2$, which bears bulky ^{i}Pr groups at the 2- and 6-positions of the *N*-aryl rings, formed coordination complexes with Ptxl only via the 2′-OH of Ptxl and yielded Ptxl-2′-PLA and Ptxl-2′-SA with 100% regioselectivity. This strategy for the controlled polymerization of LA (and acylation with SA) was extended to Dtxl, which has a more complex structure, with 100% regioselectivity. We also demonstrated that the scope of the Ptxl (or Dtxl)/(BDI-II)ZnN(TMS)$_2$-mediated controlled polymerization could be expanded to three other biopolymers, poly(δ-valerolactone, poly(trimethylene carbonate), and poly(ε-caprolactone). Importantly, the heterogeneity of the resulting polyester−drug conjugates was substantially reduced by means of this unprecedented controlled chemistry. Particularly noteworthy is that the extension of the reaction to various monomers may have benefits for drug delivery: drugs could be entrapped within separate populations of particles with different release kinetics because different polyesters degrade at different rates.[22]

EXPERIMENTAL SECTION

Materials and Methods. *General.* BDI ligands and the corresponding metal catalysts (BDI-X)ZnN(TMS)$_2$ were prepared by following the published procedure[12a] and were stored at −30 °C in a glovebox. All anhydrous solvents were purified through alumina columns and kept anhydrous over molecular sieves. Paclitaxel (Ptxl) and docetaxel (Dtxl) were purchased from LC Laboratories (Woburn, MA) and used as received. All other chemicals were purchased from Sigma-Aldrich (St. Louis, MO) and used as received unless otherwise noted. The molecular weights of polymer−drug conjugates were determined by gel permeation chromatography (GPC) on a system equipped with an isocratic pump (Model 1100, Agilent Technology, Santa Clara, CA), a DAWN HELEOS 18-angle laser light scattering detector (MALLS), and an Optilab rEX refractive index detector (Wyatt Technology, Santa Barbara, CA). The wavelength of the HELEOS detector was set at 658 nm. Size-exclusion columns used for the separation of PLA or drug−PLA conjugates were connected in series to the GPC system (Phenogel columns 100, 500, 10^3, and 10^4 Å, 5 μm, 300 × 7.8 mm, Phenomenex, Torrance, CA). THF (HPLC grade) was used as the mobile phase for PLA. DMF containing 0.1 M LiBr at 60 °C was used as the mobile phase for PVL, PCL, and PTMC. Low-resolution electrospray ionization mass spectrometry (LR-ESI-MS) experiments were conducted on a Waters Quattro II mass spectrometer. HPLC analysis was performed on a System Gold system (Beckman Coulter, Fullerton, CA) equipped with a 126P solvent module, a System Gold 128 UV detector, and an analytical pentafluorophenyl column (Curosil-PFP or Luna C18(2), both 250 × 4.6 mm, 5 μ, Phenomenex, Torrance, CA). The UV wavelengths for Ptxl and Dtxl were set at 227 nm; the mobile phase was acetonitrile/water containing 0.1 wt % trifluoroacetic acid. NMR analyses were conducted on a Varian U500, VXR500, or UI500NB (500 MHz).

Monomer. DL-Lactide (LA) was purchased from TCI America (Portland, OR). It was recrystallized three times from toluene and stored in a glovebox. ε-Caprolactone (CL) was purchased from Sigma-Aldrich, dried over CaH_2 for 48 h, and fractionally distilled under reduced pressure. δ-Valerolactone (VL) was purchased from Sigma-Aldrich, dried over CaH_2 overnight, and fractionally distilled under reduced pressure. The whole process was repeated. Trimethyl carbonate (TMC) was synthesized according to published procedures.[23] The monomer was recrystallized from ether twice, dried, and stored in a glovebox. All monomers were stored in the freezer of a glovebox at −30 °C before use.

Ptxl-Mediated Ring-Opening Polymerization of LA in the Presence of a Zn Catalyst. In a glovebox, Ptxl (8.5 mg, 0.01 mmol) was dissolved in anhydrous THF (2 mL). (BDI-II)ZnN(TMS)$_2$[12a] (6.4 mg, 0.01 mmol) was added and allowed to react with Ptxl for 15−20 min. LA (144.0 mg, 1.0 mmol) in THF (1 mL) was added dropwise to the mixture of Ptxl and (BDI-II)ZnN(TMS)$_2$ with vigorous stirring. The polymerization was monitored using FT-IR by following the lactone band at 1772 cm^{-1} or using ^{1}H NMR by checking the methine (−C*H*−) peak of LA around 5.2−5.0 ppm. After the polymerization was complete, an aliquot of the polymerization solution was analyzed using HPLC to quantify the unreacted Ptxl to determine the efficiency of Ptxl incorporation into Ptxl-LA$_{100}$. One drop of water was added to the polymerization solution to hydrolyze the Zn-Ptxl oxide. The resulting Ptxl-LA$_{100}$ was precipitated from ethyl ether (10 mL), and the precipitate was washed with ether and toluene to remove the BDI ligand, dried under vacuum, and characterized by GPC. Complete removal of BDI from Ptxl-PLA was verified by TLC.

Reductive Degradation of Ptxl-PLA Using Bu_4NBH_4. The reductive degradation of Ptxl at C-13 was achieved by following the literature reported procedure.[16] Ptxl (5 mg, 5.8 mmol) in anhydrous dichloromethane (1 mL) was allowed to react with Bu_4NBH_4 (2.5 mg, 10 mmol) for 1.5 h in a glovebox. Acetic acid (∼100 μL) was added to the reaction mixture to terminate the reaction. The reaction solution was stirred for 20 min, and then the solvent was completely removed. The residual solid was redissolved in acetonitrile. An aliquot of the solution was analyzed on an HPLC equipped with a Curosil RP

column (250 × 4.6 mm, 5 μm; Phenomenex, Torrance, CA). The desired fractions were collected and analyzed by LR-ESI-MS. The Ptxl-PLA conjugate was reductively degraded and analyzed similarly.

Reaction of Ptxl with SA in the Presence of a Zn Catalyst. In a glovebox, Ptxl (8.5 mg, 0.01 mmol) was dissolved in anhydrous THF (400 μL). (BDI-II)ZnN(TMS)$_2$ (6.5 mg, 0.01 mmol) was added and allowed to react with Ptxl for 15−20 min. SA (1.1 mg, 0.011 mmol) in THF (600 μL) was added dropwise to the mixture of Ptxl and (BDI-II)ZnN(TMS)$_2$ with vigorous stirring ([SA] = 0.011 M). The reaction vial was tightly sealed and heated at 40 °C outside the glovebox. The reaction was allowed to proceed for 4 h and quenched with 1 mL of ice-cold methanol. The resulting solution was immediately analyzed by HPLC.

Pure Ptxl-2′-SA (or Dtxl-2′-SA) for NMR analysis was obtained by preparative TLC on a silica gel matrix (UV254, 1500 μm thickness, Sigma-Aldrich). Silica gel containing the desired compounds was scraped from the glass plate and extracted with methanol (2 × 30 mL). The resulting solution was evaporated under vacuum for NMR analysis.

Ptxl-2′-SA. ^{1}H NMR (500 MHz, $CDCl_3$): δ 8.13 (d, J = 7.28 Hz, 2H), 7.77 (d, J = 7.36 Hz, 2H), 7.61−7.36 (m, 15H), 7.26−7.24 (m, 6H), 7.03 (d, J = 9.16 Hz, 1H), 6.25 (s, 1H), 6.22 (d, J = 8.9 Hz, 1H), 5.97, 5.95 (dd, J = 2.84 Hz, 2.76 Hz, 1H), 5.67 (d, J = 7.08 Hz, 1H), 5.56 (d, 1H), 5.47 (d, J = 2.96 Hz, 1H), 4.96 (d, J = 9.36 Hz, 1H), 4.85−4.79 (m, 3H), 4.65 (d, J = 11.9 Hz, 1H), 4.41 (s, 1H), 4.31 −4.27 (m, 2H), 4.19 (d, J = 8.44 Hz, 1H), 3.99 (t, J = 9.20 Hz, 1H), 3.81−3.73 (m,3H), 3.64 (t, J = 9.20 Hz, 1H), 3.31 (s, 3H), 2.72−2.51 (m, 4H), 2.42 (s, 3H), 2.40−2.30 (m, 1H), 2.21 (s, 3H), 1.89 (s, 3H), 1.66 (s, 6H), 1.64 (s, 3H), 1.23 (s, 3H), 1.20 (s, 3H), 1.11 (s, 3H). ^{13}C NMR (125 MHz, $CDCl_3$): δ 203.8, 171.5, 171.2, 171.1, 169.8, 167.9, 167.3, 167.0, 142.6, 138.4,137.2, 136.9, 133.7, 133.6, 132.8, 132.0, 130.2, 129.2, 129.1, 129.0, 128.7, 128.5, 128.3, 127.7, 127.6, 127.2, 126.6, 126.0, 101.4, 97.5, 84.4, 82.1, 81.0, 79.0, 76.4, 75.6, 75.1, 74.3, 73.1,72.1, 71.9, 58.5, 52.8, 49.1, 45.6, 43.2,35.6, 33.9, 29.7, 29.0, 28.9, 26.8, 25.6, 24.9, 22.7, 22.1, 20.8, 14.8, 9.6. ESI-MS (low resolution, positive mode): calculated for $C_{52}H_{57}NO_{16}$, m/z 954.3 $[M + H]^+$; found 954.8 $[M + H]^+$.

Ptxl-2′-7-diSA. ^{1}H NMR (500 MHz, $CDCl_3$): δ 8.13 (d, 2H), 7.77 (d, 2H), 7.61−7.36 (m, 15H), 7.26−7.24 (m, 6H), 6.21(s, 1H), 6.16 (s, 1H), 6.09 (d, 1H), 5.95 (dd, 1H), 5.86 (dd, 1H), 5.64 (m, 1H), 5.58 (d, 1H), 4.91 (d, 1H), 4.85−4.79 (m, 3H), 4.65 (d, J = 11.9 Hz, 1H), 4.41 (s, 1H), 4.31 −4.27 (m, 2H), 4.17 (d, 1H), 3.99 (t, 1H), 3.86 (m, 3H), 3.64 (t, J = 9.20 Hz, 1H), 3.31 (s, 3H), 2.8−2.5 (m, 8H), 2.39 (s, 3H), 2.40−2.30 (m, 1H), 2.13 (s, 3H), 1.88 (s, 3H), 1.79 (s, 6H), 1.64 (s, 3H), 1.19 (s, 3H), 1.15 (s, 3H), 1.09 (s, 3H). ^{13}C NMR (125 MHz, $CDCl_3$): δ 203.8, 171.6, 169.8, 169.1, 168.3, 167.5, 166.8, 162.7, 141.2, 138.0, 136.8, 133.7, 133.5, 132.4, 132.0, 130.2, 129.1, 129.0, 128.7, 128.5, 128.2, 127.2, 126.7, 127.2, 126.6, 103.6, 100.2, 99.3, 83.9, 80.8, 78.5, 76.4, 75.8, 75.3, 74.4, 74.1, 71.7, 71.9, 65.8, 55.9, 53.1, 46.9, 43.2, 36.6, 35.2, 33.1, 31.5, 29.0, 28.8, 27.3, 26.4, 24.7, 22.6, 21.1, 20.7, 15.2, 14.5, 10.8. ESI-MS (low resolution, positive mode): calculated for $C_{55}H_{59}NO_{20}$, m/z 1054.4 $[M + H]^+$; found 1054.8 $[M + H]^+$.

Dtxl-2′-SA. ^{1}H NMR (500 MHz, $CDCl_3$): δ = 8.10 (d, 2H), 7.66 (t, 1H), 7.54 (t, 2H), 7.40 (m, 2H), 7.37 (m, 3H), 6.20 (s, 1H), 5.71 (d, 1H), 5.50 (s, 1H), 5.26 (s, 1H), 4.40−4.20 (m, 3H), 3.94 (s, 1H), 2.85 (m, 1H), 2.6 (m, 4H), 2.45−2.35 (m, 2H), 1.98 (s, 3H), 1.87 (t, 1H), 1.79 (s, 3H), 1.54 (s, 3H), 1.38 (s, 9H), 1.29 (s, 3H), 1.25 (s, 3H). ESI-MS (low resolution, positive mode): calculated for $C_{47}H_{57}NO_{17}$, m/z 907.4 $[M + H]^+$; found 907.4 $[M + H]^+$.

Synthesis of Ptxl-VL$_n$ (or Ptxl-CL$_n$) Polymer. In a glovebox, Ptxl (8.6 mg, 0.010 mmol) and (BDI-II)ZnN(TMS)$_2$ (6.5 mg, 0.01 mmol) were dissolved in 300 μL of THF. The mixture was stirred for 20 min. δ-Valerolactone (VL, 92.6 μL, 100 mg, 1.0 mmol) in THF (0.5 mL) was added to the mixture of Ptxl and (BDI-II)ZnN(TMS)$_2$. The polymerization was monitored by FT-IR; the 1739 cm^{-1} peak of the lactone bond in VL shifted to 1728 cm^{-1} for the ester bond in poly(δ-valerolactone) (PVL). The reaction solution was quenched with 1 mL of ice-cold methanol. The conversion of VL was determined by ^{1}H NMR. The polymer was precipitated with ethyl ether (10 mL), and the precipitate was washed with ether and toluene to remove BDI ligand, dried under vacuum, and characterized by GPC. Complete removal of BDI from Ptxl-PVL was verified by TLC. Similar procedures were used for Ptxl-PCL synthesis. The ^{1}H NMR spectra of Ptxl-VL$_{100}$ and Ptxl-CL$_{100}$ are shown in Figures S4 and S5.

Synthesis of Ptxl-TMC$_n$ Polymer. In a glovebox, Ptxl (8.6 mg, 0.010 mmol) and (BDI-II)ZnN(TMS)$_2$ (6.6 mg, 0.011 mmol) were mixed in 300 μL of THF. The mixture stirred was stirred for 20 min. TMC (102 mg, 1.0 mmol) in toluene (300 μL) was added into the mixture. The reaction vessel was tightly sealed and heated at 50 °C for 5 h out of the box. The reaction solution was quenched with 5 mL of ice-cold methanol. The conversion of TMC was determined by ^{1}H NMR. The polymer was precipitated with ethyl ether (10 mL), and the precipitate was washed with ether and toluene to remove the BDI ligand, dried under vacuum, and characterized by GPC. The ^{1}H NMR spectrum of Ptxl-TMC$_{100}$ is shown in Figure S6.

■ ASSOCIATED CONTENT

Ⓢ Supporting Information

Polymerization data; characterization of polymer−drug conjugates. This material is available free of charge via the Internet at http://pubs.acs.org.

■ AUTHOR INFORMATION

Corresponding Author

*E-mail: jianjunc@illinois.edu.

Present Address

†Department of Chemical Engineering, Massachusetts Institute of Technology, 77 Massachusetts Avenue, Cambridge, MA 02139; Laboratory for Biomaterials and Drug Delivery, Department of Anesthesiology, Division of Critical Care Medicine, Children's Hospital Boston, Harvard Medical School, 300 Longwood Avenue, Boston, MA 02115.

Notes

The authors declare no competing financial interest.

■ ACKNOWLEDGMENTS

J.C. acknowledges support from the NSF (DMR-0748834), the NIH (NIH Director's New Innovator Award 1DP2OD007246-01), and the Midwest Cancer Nanotechnology Training Center, University of Illinois at Urbana−Champaign (UIUC). R.T. acknowledges a student fellowship (2007−2010) from the Siteman Center for Cancer Nanotechnology Excellence (SCCNE, Washington University)−Center for Nanoscale Science and Technology (CNST, UIUC).

■ REFERENCES

(1) Some recent reviews about nanomedicine: (a) Alexis, F.; Rhee, J. W.; Richie, J. P.; Radovic-Moreno, A. F.; Langer, R.; Farokhzad, O. C. *Urol. Oncol: Semin. Orig. Invest.* **2008**, *26*, 74. (b) Peer, D.; Karp, J. M.; Hong, S.; FaroKhzad, O. C.; Margalit, R.; Langer, R. *Nature Nanotechnol.* **2007**, *2*, 751. (c) Farokhzad, O. C.; Langer, R. *Adv. Drug Delivery Rev.* **2006**, *58*, 1456. (d) Pun, S. H.; Tack, F.; Bellocq, N. C.; Cheng, J. J.; Grubbs, B. H.; Jensen, G. S.; Davis, M. E.; Brewster, M.; Janicot, M.; Janssens, B.; Floren, W.; Bakker, A. *Cancer Biol. Ther.* **2004**, *3*, 641. (e) Pack, D. W.; Hoffman, A. S.; Pun, S.; Stayton, P. S. *Nat. Rev. Drug Discovery* **2005**, *4*, 581. (f) Zhang, L.; Gu, F. X.; Chan, J. M.; Wang, A. Z.; Langer, R. S.; Farokhzad, O. C. *Clin. Pharmacol. Ther.* **2008**, *83*, 761.

(2) (a) Cheng, J. J.; Khin, K. T.; Jensen, G. S.; Liu, A. J.; Davis, M. E. *Bioconjugate Chem.* **2003**, *14*, 1007. (b) Cheng, J.; Khin, K. T.; Davis, M. E. *Mol. Pharmaceutics* **2004**, *1*, 183.

(3) Schluep, T.; Cheng, J.; Khin, K. T.; Davis, M. E. *Cancer Chemother. Pharmacol.* **2006**, *57*, 654.

(4) (a) Schluep, T.; Hwang, J.; Cheng, J.; Heidel, J. D.; Bartlett, D. W.; Hollister, B.; Davis, M. E. *Clin. Cancer Res.* **2006**, *12*, 1606. (b) Duncan, R. *Nat. Rev. Cancer* **2006**, *6*, 688. (c) Bagalkot, V.; Farokhzad, O. C.; Langer, R.; Jon, S. *Angew. Chem., Int. Ed.* **2006**, *45*, 8149.

(5) Ferrari, M. *Nat. Rev. Cancer* **2005**, *5*, 161.
(6) Examples: (a) Chan, J. M.; Zhang, L. F.; Tong, R.; Ghosh, D.; Gao, W. W.; Liao, G.; Yuet, K. P.; Gray, D.; Rhee, J. W.; Cheng, J. J.; Golomb, G.; Libby, P.; Langer, R.; Farokhzad, O. C. *Proc. Natl. Acad. Sci. U. S. A.* **2010**, *107*, 2213. (b) Farokhzad, O. C.; Cheng, J. J.; Teply, B. A.; Sherifi, I.; Jon, S.; Kantoff, P. W.; Richie, J. P.; Langer, R. *Proc. Natl. Acad. Sci. U. S. A.* **2006**, *103*, 6315. (c) Tong, R.; Christian, D. A.; Tang, L.; Cabral, H.; Baker, J. R.; Kataoka, K.; Discher, D. E.; Cheng, J. J. *MRS Bull.* **2009**, *34*, 422. (d) Tong, R.; Cheng, J. J. *Polym. Rev.* **2007**, *47*, 345. (e) Almutairi, A.; Rossin, R.; Shokeen, M.; Hagooly, A.; Ananth, A.; Capoccia, B.; Guillaudeu, S.; Abendschein, D.; Anderson, C. J.; Welch, M. J.; Frechet, J. M. J. *Proc. Natl. Acad. Sci. U. S. A.* **2009**, *106*, 685. (f) Kwon, Y. J.; James, E.; Shastri, N.; Frechet, J. M. J. *Proc. Natl. Acad. Sci. U. S. A.* **2005**, *102*, 18264. (g) Murthy, N.; Xu, M. C.; Schuck, S.; Kunisawa, J.; Shastri, N.; Frechet, J. M. J. *Proc. Natl. Acad. Sci. U. S. A.* **2003**, *100*, 4995. (h) Davis, M. E. *Mol. Pharmaceutics* **2009**, *6*, 659. (i) Davis, M. E. *Adv. Drug Delivery Rev.* **2009**, *61*, 1189. (j) Davis, M. E.; Zuckerman, J. E.; Choi, C. H. J.; Seligson, D.; Tolcher, A.; Alabi, C. A.; Yen, Y.; Heidel, J. D.; Ribas, A. *Nature* **2010**, *464*, 1067.
(7) Some recent reviews about polymer−drug conjugates: (a) Wagner, V.; Dullaart, A.; Bock, A. K.; Zweck, A. *Nat. Biotechnol.* **2006**, *24*, 1211. (b) Li, C.; Wallace, S. *Adv. Drug Delivery Rev.* **2008**, *60*, 886. (c) Li, C. *Adv. Drug Delivery Rev.* **2002**, *54*, 695. (d) Nori, A.; Kopeček, J. *Adv. Drug Delivery Rev.* **2005**, *57*, 609. (e) Duncan, R. *Curr. Opin. Biotechnol.* **2011**, *22*, 492. (f) Joralemon, M. J.; McRae, S.; Emrick, T. *Chem. Commun.* **2010**, *46*, 1377. (g) Duncan, R.; Vicent, M. J. *Adv. Drug Delivery Rev.* **2010**, *62*, 272. (h) Khandare, J.; Minko, T. *Prog. Polym. Sci.* **2006**, *31*, 359. (i) Greco, F.; Vicent, M. J. *Adv. Drug Delivery Rev.* **2009**, *61*, 1203.
(8) Examples: (a) Lee, C. C.; MacKay, J. A.; Frechet, J. M. J.; Szoka, F. C. *Nat. Biotechnol.* **2005**, *23*, 1517. (b) Srinivasachari, S.; Fichter, K. M.; Reineke, T. M. *J. Am. Chem. Soc.* **2008**, *130*, 4618. (c) Lu, H.; Cheng, J. *J. Am. Chem. Soc.* **2008**, *130*, 12562. (d) Lu, H.; Cheng, J. J. *J. Am. Chem. Soc.* **2007**, *129*, 14114. (e) Cheng, J. J.; Deming, T. J. *J. Am. Chem. Soc.* **2001**, *123*, 9457. (f) Medina, S. H.; El-Sayed, M. E. H. *Chem. Rev.* **2009**, *109*, 3141. (g) Gillies, E. R.; Frechet, J. M. J. *J. Am. Chem. Soc.* **2002**, *124*, 14137. (h) Lee, C. C.; Gillies, E. R.; Fox, M. E.; Guillaudeu, S. J.; Frechet, J. M. J.; Dy, E. E.; Szoka, F. C. *Proc. Natl. Acad. Sci. U. S. A.* **2006**, *103*, 16649. (i) Liu, G.; Jia, L. *J. Am. Chem. Soc.* **2004**, *126*, 14716.
(9) Examples: (a) Zhang, X. F.; Li, Y. X.; Chen, X. S.; Wang, X. H.; Xu, X. Y.; Liang, Q. Z.; Hu, J. L.; Jing, X. B. *Biomaterials* **2005**, *26*, 2121. (b) Shen, Y. Q.; Jin, E. L.; Zhang, B.; Murphy, C. J.; Sui, M. H.; Zhao, J.; Wang, J. Q.; Tang, J. B.; Fan, M. H.; Van Kirk, E.; Murdoch, W. J. *J. Am. Chem. Soc.* **2010**, *132*, 4259. (c) Kim, S. C.; Kim, D. W.; Shim, Y. H.; Bang, J. S.; Oh, H. S.; Kim, S. W.; Seo, M. H. *J. Controlled Release* **2001**, *72*, 191. (d) Benny, O.; Fainaru, O.; Adini, A.; Cassiola, F.; Bazinet, L.; Adini, I.; Pravda, E.; Nahmias, Y.; Koirala, S.; Corfas, G.; D'Amato, R. J.; Folkman, J. *Nat. Biotechnol.* **2008**, *26*, 799. (e) Lee, S. H.; Zhang, Z. P.; Feng, S. S. *Biomaterials* **2007**, *28*, 2041. (f) Zhang, Z. P.; Feng, S. S. *Biomaterials* **2006**, *27*, 262.
(10) Examples: (a) Sengupta, S.; Eavarone, D.; Capila, I.; Zhao, G. L.; Watson, N.; Kiziltepe, T.; Sasisekharan, R. *Nature* **2005**, *436*, 568. (b) Yoo, H. S.; Lee, K. H.; Oh, J. E.; Park, T. G. *J. Controlled Release* **2000**, *68*, 419.
(11) Tong, R.; Cheng, J. *J. Angew. Chem., Int. Ed.* **2008**, *47*, 4830.
(12) (a) Chamberlain, B. M.; Cheng, M.; Moore, D. R.; Ovitt, T. M.; Lobkovsky, E. B.; Coates, G. W. *J. Am. Chem. Soc.* **2001**, *123*, 3229. (b) du Boullay, O. T.; Marchal, E.; Martin-Vaca, B.; Cossio, F. P.; Bourissou, D. *J. Am. Chem. Soc.* **2006**, *128*, 16442. (c) Dechy-Cabaret, O.; Martin-Vaca, B.; Bourissou, D. *Chem. Rev.* **2004**, *104*, 6147.
(13) Kricheldorf, H. R.; Kreisersaunders, I. *Polymer* **1994**, *35*, 4175.
(14) Mastropaolo, D.; Camerman, A.; Luo, Y. G.; Brayer, G. D.; Camerman, N. *Proc. Natl. Acad. Sci. U. S. A.* **1995**, *92*, 6920.
(15) Mathew, A. E.; Mejillano, M. R.; Nath, J. P.; Himes, R. H.; Stella, V. J. *J. Med. Chem.* **1992**, *35*, 145.
(16) Magri, N. F.; Kingston, D. G. I.; Jitrangsri, C.; Piccariello, T. J. *Org. Chem.* **1986**, *51*, 3239.
(17) Moore, D. R.; Cheng, M.; Lobkovsky, E. B.; Coates, G. W. *Angew. Chem., Int. Ed.* **2002**, *41*, 2599.
(18) (a) Moore, D. R.; Cheng, M.; Lobkovsky, E. B.; Coates, G. W. *J. Am. Chem. Soc.* **2003**, *125*, 11911. (b) Cheng, M.; Moore, D. R.; Reczek, J. J.; Chamberlain, B. M.; Lobkovsky, E. B.; Coates, G. W. *J. Am. Chem. Soc.* **2001**, *123*, 8738.
(19) Tong, R.; Yala, L.; Fan, T. M.; Cheng, J. *Biomaterials* **2010**, *31*, 3043.
(20) (a) Jeske, R. C.; DiCiccio, A. M.; Coates, G. W. *J. Am. Chem. Soc.* **2007**, *129*, 11330. (b) Jeske, R. C.; Rowley, J. M.; Coates, G. W. *Angew. Chem., Int. Ed.* **2008**, *47*, 6041.
(21) (a) Tong, R.; Cheng, J. *J. Bioconjugate Chem.* **2010**, *21*, 111. (b) Tong, R.; Yala, L. D.; Fan, T. M.; Cheng, J. *J. Biomaterials* **2010**, *31*, 3043. (c) Tong, R.; Cheng, J. J. *J. Am. Chem. Soc.* **2009**, *131*, 4744.
(22) (a) Grayson, A. C. R.; Choi, I. S.; Tyler, B. M.; Wang, P. P.; Brem, H.; Cima, M. J.; Langer, R. *Nature Mater.* **2003**, *2*, 767. (b) Grayson, A. C. R.; Voskerician, G.; Lynn, A.; Anderson, J. M.; Cima, M. J.; Langer, R. *J. Biomater. Sci., Polym. Ed.* **2004**, *15*, 1281.
(23) Helou, M.; Miserque, O.; Brusson, J. M.; Carpentier, J. F.; Guillaume, S. M. *Chem.—Eur. J.* **2008**, *14*, 8772.

Macromolecules

Article

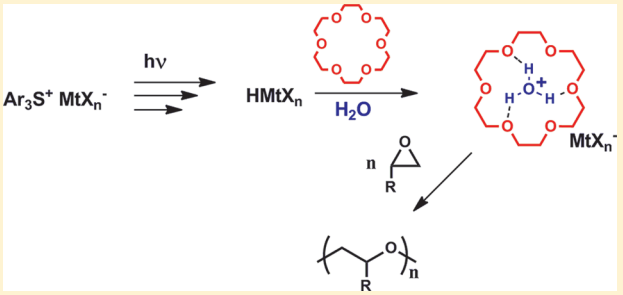
pubs.acs.org/Macromolecules

Involvement of Supramolecular Complexes in the Capture and Release of Protonic Acids During the Cationic Ring-Opening Polymerization of Epoxides

C. Y. Ryu, M. J. Spencer, and J. V. Crivello*

Department of Chemistry and Chemical Biology, Rensselaer Polytechnic Institute, 110 Eighth Street, Troy, New York 12180, United States

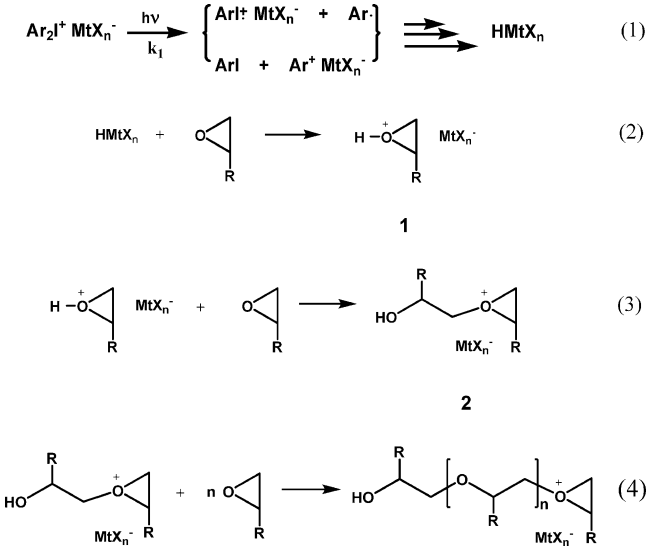
ABSTRACT: The kinetics of the cationic ring-opening polymerizations of epoxide monomers were controlled through the use of supramolecular proton complexes. α,ω-Diglycidyl oligoethylene oxides bearing multiple ethyleneoxy spacer groups form metastable supramolecular proton complexes with strong Brønsted acids generated either by the photolysis of onium salts or by their redox reactions with reducing agents. Trapping of the Brønsted acids by *in situ* complex formation results in a delay of the onset of cationic ring-opening. However, once polymerization begins, the epoxide groups of the monomer are very rapidly consumed resulting in characteristically highly exothermic autoaccelerated polymerization reactions. Crown ethers can also form supramolecular complexes with hydronium ions derived from the reaction of protonic acids with water and these complexes can be used to modify the kinetic behavior of the cationic ring-opening thermal and photopolymerizations of a variety of epoxide monomers. The ring size of a crown ether has a strong influence on the stability of the supramolecular complex formed, and this was shown to have a major impact on the kinetics of the cationic ring-opening polymerizations.



INTRODUCTION

In a series of publications from this laboratory, we have described the results of our investigations into the mechanisms of the cationic ring-opening polymerizations of epoxide[1−3] and oxetane[4,5] monomers initiated by photogenerated Brønsted acids derived from the UV irradiation of diaryliodonium and triarylsulfonium salts. When the cationic ring-opening photopolymerizations of a variety of different epoxide monomers were carried out under homogeneous conditions at room temperature, four different characteristic types of kinetic behavior were observed and were subsequently related to the respective structures of the monomers.[3] The polymerizations of cycloaliphatic epoxides with highly strained oxirane rings, such as cyclohexene oxide and cyclopentene oxide, exhibit high rates of reaction with little or no induction periods. Aryl glycidyl ethers undergo rather slow polymerizations with rather short induction periods. In contrast, the cationic photopolymerizations of alkyl glycidyl ethers are typically preceded by rather long induction periods that are followed by rapid, exothermic, autoaccelerated polymerizations. A number of other epoxides, such as tri- and tetra-substituted oxiranes, while reactive, undergo inefficient photopolymerization due to rearrangements and other side reactions. A unified explanation was offered for the apparent wide range of kinetic behaviors of the cationic photopolymerizations of the above-mentioned epoxide monomers based on the generalized ring-opening mechanism depicted in Scheme 1.

Scheme 1. Mechanism of the Cationic Ring-Opening Photopolymerization of Epoxide Monomers



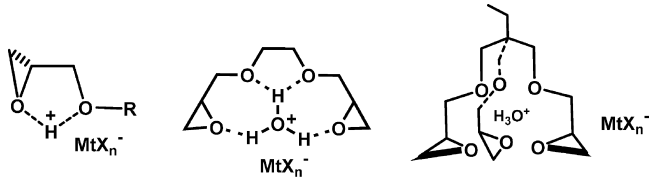
The photolysis of an onium salt, as depicted in Scheme 1 for diaryliodonium salts, (eq 1) generates a strong Brønsted acid

Received: December 2, 2011
Revised: February 3, 2012
Published: February 22, 2012

ACS Publications © 2012 American Chemical Society

($HMtX_n$) by a complex process, in which both heterolysis and homolysis of the diaryliodonium salt photoinitiator takes place. For efficient cationic ring-opening polymerization, the diaryliodonium salt photoinitiator is selected such that the anion, MtX_n^-, is of low nucleophilic character such as PF_6^-, AsF_6^-, or SbF_6^-. The resulting Brønsted acid, $HMtX_n$, generated protonates the epoxide monomer (eq 2) to give the secondary oxiranium ion, **1**. A tertiary oxiranium ion, **2**, is formed by the S_N2 attack of monomer on **1** (eq 3). Once **2** is formed, polymer growth takes place by the repetitive addition of monomers to the tertiary oxiranium chain end (eq 4).

The overall rate of a cationic epoxide ring-opening photopolymerization is determined by the slowest step in Scheme 1. Under conditions of high intensity UV irradiation and using diaryliodonium salts with high quantum yields for Brønsted acid production ($\Phi = 0.7-0.9$[6,7]), the rate controlling step in Scheme 1 has been shown to be eq 3. Ultimately, the reactivity of the secondary oxiranium ion intermediate **1** governs the rate at which the entire polymerization process proceeds. Consequently, those structural factors that increase the stability of **1** and decrease its reactivity tend to slow the polymerization and vice versa. Cycloaliphatic epoxides that possess no additional stabilizing features produce secondary oxiranium ions that are highly strained and unstable and this explains the correspondingly high rates of polymerization observed with these monomers. Aryl glycidyl ethers and terminal epoxy alkanes undergo protonation to yield less strained secondary oxiranium ions that are correspondingly less reactive and, therefore, these monomers display intermediate reactivity. Of more interest are the aforementioned alkyl glycidyl ethers that exhibit long induction periods followed by very rapid, autoaccelerated photopolymerization profiles. We[3] have attributed the prominent induction period as due to the formation of stabilized secondary oxiranium ion intermediates such as **3** in which a proton is coordinated by both the ether and epoxide oxygen atoms in the monomer to form supramolecular complexes. The basicities of the oxygen atoms of open chain ethers and epoxides are similar.[8] While coordination as shown in structure **3** is depicted for the sake of simplicity as involving a proton, it is recognized that other species, such as water if present, may also be involved in coordination sphere. In such cases, coordination by the epoxide can be viewed as involving a hydronium ion, H_3O^+, $H_5O_2^+$, or similar species. Since most epoxide monomers are hygroscopic and the experiments described herein were not carried out under rigorously dry vacuum line conditions, the presence of water can be assumed in all cases. In addition, complexation of the Brønsted acid may involve the glycidyl ether groups of more than one monomer. As photolysis proceeds, the photogenerated Brønsted acids immediately form the corresponding supramolecular complexes, **3**, and their concentration begins to builds up in the reaction mixture. At some point, the concentration of **3** reaches a sufficiently high value that even a slight increase in temperature results in its destabilization with the consequent spontaneous rapid thermally autoaccelerated polymerization of the monomer. The more heat generated from the exothermic ring-opening polymerization, the faster the protonic acid is released from the destabilized supramolecular



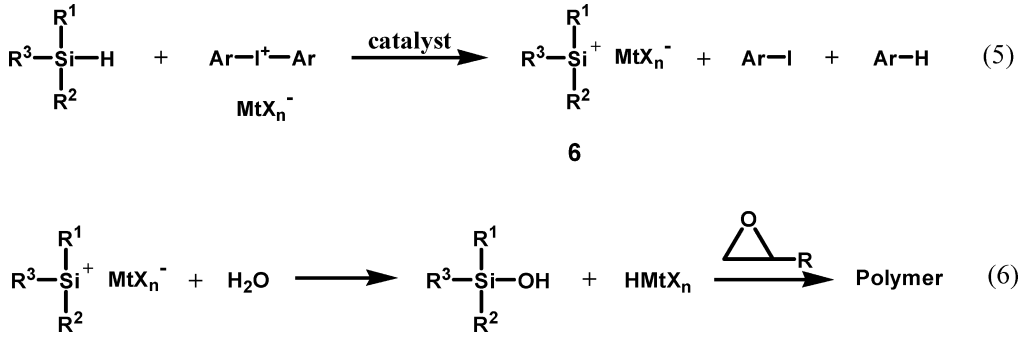
3 **4** **5**

complex and this escalates the rate of the polymerization with a consequent sharp rise in the sample temperature.

Extension of the concept of the involvement of supramolecular complexes in the "capture and release" of Brønsted acids led to the proposal that increasing the coordinating ability of the monomer ligands from bidentate to tetradentate should result in the formation of complexes with enhanced stability. Indeed, it was observed that 1,2-ethanediol diglycidyl ether as shown in **4**, which can optimally undergo tetradentate coordination with a hydronium ion and trimethylolpropane triglycidyl ether that is capable of forming a cage-like complex as shown in **5** by hexadentate coordination, give supramolecular complexes that are considerably more stable than **3**. This enhanced stability is reflected in the observed lengthening of the induction periods during the photoinitiated cationic polymerization of these latter two monomers.

The effectiveness of hydrogen bonding is greatly influenced by temperature. For example, the solution phase behavior of the lower critical solution temperature (LCST) has been experimentally[9,10] and theoretically[11] studied for poly(ethylene oxide) in aqueous solution in terms of weakened hydrogen bonding at elevated temperatures. As expected, temperature has a similar marked effect on the stability of the hydrogen bonded supramolecular complexes which, controls the overall rates of the photoinitiated cationic ring-opening polymerizations of epoxides and oxetanes. In the case of alkyl glycidyl ether monomers, raising the temperature at which a photoinitiated cationic polymerization is carried out results in an appreciable

Scheme 2. Proposed Mechanism for the Redox Initiated Cationic Polymerization of Epoxides

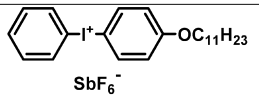
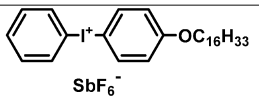
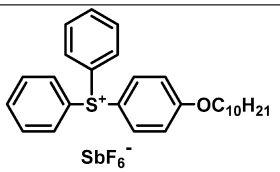
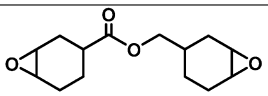
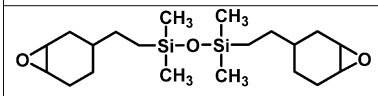


(5)

(6)

dx.doi.org/10.1021/ma202618r | Macromolecules 2012, 45, 2233–2241

Table 1. Materials Used in this Investigation

Structure	Name	Abbreviation
	(4-*n*-undecyloxyphenyl)-phenyliodonium hexafluoroantimonate	IOC-11 SbF_6
	(4-*n*-hexadecyloxyphenyl)-phenyliodonium hexafluoroantimonate	IOC-16 SbF_6
	S(4-*n*-decyloxyphenyl)-S,S-diphenylsulfonium hexafluoridoantimonate	SOC-10 SbF_6
	cyclohexene oxide	CHO
	3,4-epoxycyclohexylmethyl 3',4'-epoxycyclohexanecarboxylate	ERL
	1,3-bis(2(3,4-epoxycyclohexyl)ethyl)1,1,3,3-tetramethyldisiloxane	PC-100

decrease in the induction period. On the other hand, when the photopolymerizations of 1,2-epoxyalkanes are carried out at −10 to 0 °C, they display prolonged induction periods that are similar to those observed for the cationic photopolymerizations of alkyl glycidyl ethers conducted at room temperature. It was also interesting to note that, under the same temperature conditions, the polymerization of cyclohexene oxide was not appreciably slowed. This may be attributed to the high of reactivity of both the monomer and the instability of the corresponding secondary oxonium ion intermediate produced by protonation.

Recently,[12−15] a series of onium salt-based redox couples whereby strong Brønsted acids can be rapidly generated at and below room temperature has been developed by our group. For example, the platinum or palladium catalyzed reductions of a diaryliodonium or a triarylsulfonium salt with a silane bearing a Si−H group releases Brønsted acids such as $HMtX_n$ that function as powerful initiators for both cationic ring-opening and vinyl addition polymerizations. As shown in Scheme 2, the proposed mechanism of the initiation process involves the formation of a highly reactive silicenium cation intermediate, **6** (eq 5). This intermediate undergoes further reaction with traces of water or other protonic agents (eq 6) present in the monomer to generate the Brønsted acid, $HMtX_n$, which subsequently initiates cationic polymerization in a manner as previously depicted in Scheme 1. The different characteristic kinetic behaviors of the various types of epoxy compounds described above for photopolymerizations was also observed when redox cationic initiation was applied to these same monomers.

In this article, we describe the results of our efforts to design and use supramolecular complexes analogous to **3**−**5** to control the rates of cationic ring-opening epoxide polymerizations using both photo- and redox initiation.

EXPERIMENTAL SECTION

Materials. Cyclohexene oxide was obtained from the Aldrich Chemical Co. and was dried and distilled from CaH_2. All glycidyl ether monomers were kindly provided as samples by CVC Specialty Chemicals, Inc., Maple Shade, NJ. 1,2-Epoxydecane was provided as a gift from the Viking Chemical Co. Blooming Prairie, MN. 3,4-Epoxycyclohexylmethyl 3′,4′-epoxycyclohexane carboxylate (ERL-4221E) was obtained from the Union Carbide Corp. (now Dow Chemical Co.). 1,3-Bis(2(3,4-epoxycyclohexyl)ethyl)-1,1,3,3-tetramethyldisiloxane was prepared by platinum catalyzed hydrosilylation of 4-vinylcyclohexene oxide with 1,1,3,3,-tetramethyldisiloxane according to a previously described method.[16] Organosilanes, 1,1,3,3-tetramethyldisiloxane, triethylsilane, and the Lamoreaux (2.0−2.5% Pt in octanol) catalyst were purchased from Gelest, Inc., Morrisville, PA. Cl_2(COD)-Pd(II) was purchased from Strem Chemicals, Inc., Newburyport, MA and used as a 2.0% solution in nitromethane. Hexafluoroantimonic acid (98%) was purchased from Acros Organics, Geel, Belgium. All other monomers, reagents, chemicals and crown ethers, tetraethylene glycol dimethyl ether and poly(ethylene glycol) dimethyl ether were used as purchased from the Aldrich Chemical Co., Milwaukee, WI.

The onium salts, (4-*n*-undecyloxyphenyl)phenyliodonium hexafluoroantimonate (IOC-11 SbF_6), (4-*n*-hexadecyloxyphenyl)-phenyliodonium hexafluoroantimonate (IOC-16 SbF_6), (4-*n*-octyloxyphenyl)phenyliodonium hexafluoroantimonate (IOC-8 SbF_6),[17] and *S*-(4-*n*-decyloxyphenyl)-*S*,*S*-diphenylsulfonium hexafluoroantimonate (SOC-10 SbF_6),[18] were synthesized and purified by previously described methods.

Shown in Table 1 are the structures, names, and abbreviations of the photoinitiators and monomers used during the course of this investigation.

Synthesis of the Hydronium Hexafluoroantimonate-18-crown-6 Complex. To 0.590 g (2.23 mmol) 18-crown-6 there were added 0.688 g (2.0 mmol) hexafluoroantimonic acid hexahydrate and 5 mL distilled water. An immediate precipitate of a white crystalline product was formed. The mixture was stirred and allowed to stand for 1.5 h. Then the product was vacuum filtered and washed with cold distilled water. Because of the solubility of the complex in water, there were considerable losses. After drying in vacuo, there were obtained 0.342 g

dx.doi.org/10.1021/ma202618r | *Macromolecules* 2012, 45, 2233−2241

of the desired complex with a melting point of 185 °C. Extensive discoloration and decomposition took place at 199 °C.

Anal. Calcd for $C_{12}H_{27}F_6O_7Sb$: C, 27.77; H, 5.24. Found: C, 28.02; H, 5.43.

Addition of the hydronium hexafluoroantimonate-18-crown-6 complex to cyclohexene oxide results in spontaneous exothermic polymerization. Analogous results were obtained with *n*-butyl vinyl ether

Synthesis of the Hydronium Hexafluoroantimonate-15-crown-5 Complex. In a similar manner, the addition of 0.4906 g (2.23 mmol) 15-crown-5 to 0.688 g (2.0 mmol) hexafluoridoantimonic acid hexahydrate resulted in the immediate formation of a white precipitate. The reaction was exothermic. There was added 0.5 mL of distilled water, and this resulted in the partial dissolution of the product. The remaining product was vacuum filtered. There were obtained 0.311 g (33%) complex as a white crystalline powder. The complex is insoluble in chloroform and an additional 0.09 g of product were recovered on standing from the filtrate. There were obtained 0.401 g (42% yield) of the complex having a melting point of 98−100 °C.

Anal. Calcd for $C_{10}H_{23}F_6O_6Sb$: C, 25.3; H, 4.88. Found: C, 24.24; H, 5.16.

The hydronium hexafluoroantimonate-15-crown-5 complex was soluble in nitromethane. Addition of this solution to 4-vinylcyclohexene-1,2 dioxide resulted in immediate exothermic polymerization.

Optical Pyrometry (OP). General descriptions[19−21] of the apparatus construction, sample and analytical techniques used in the optical pyrometric analysis for photo- and redox initiated polymerization reactions were given in previous publications from this laboratory. The basic optical pyrometry (OP) apparatus was modified slightly to adapt it for the study of the thermally induced cationic polymerizations of bulk monomers. The progress of an exothermic polymerization was remotely monitored by following the sample temperature using an infrared camera (optical pyrometer). The sensitivity of the OP technique is largely determined by the infrared camera that is used. In these experiments, an Omega Corp. Model OS 552-V1-6 infrared camera with a sensitivity of +0.5 °C over the range of −18 to +538 °C was employed. Reactions that produce a sample temperature change of at least 1 °C/min can be monitored with this instrument.

Polymerizations were carried out in standard Fischer Scientific aluminum weighing dishes. These containers were very regular both in size and in weight (1.0−1.1 g). To the weighing dish was added 1.0 g of the liquid monomer followed by a predetermined amount of the diaryliodonium or triarylsulfonium salt initiator followed by the addition by means of a syringe of a solution of the metal-containing catalyst. The commercially available platinum-containing Lamoreaux catalyst was purchased as a 2.0%. platinum solution in n-octanol. Also employed as a catalyst was a 2.0% solution of $Cl_2(COD)Pd^{II}$ in nitromethane. An acetone washed and dried 22 mm long #1 steel paper clip was added to serve as a stirrer. The monomer−onium salt mixture was stirred until the onium salt had completely dissolved. Assuming a density of approximately 1 g/mL, the thickness of the liquid layer in the weighing dish was 0.33 mm. The container was positioned on the sample stage of the OP apparatus with focal point of the infrared camera located at the surface of the monomer film. This was achieved with the aid of a laser sighting device. After an equilibration period of 20 s, a predetermined amount of the designated silane was added using a syringe while the monomer−catalyst−onium salt solution was rapidly stirred. All polymerizations were carried out at an initial temperature of 23−25 °C. The samples were slowly heated at a rate of 7 °C/min by means of a heater positioned directly below the sample. A baseline heating curve was established by the monitoring the temperature of a prepolymerized sample of monomer using the infrared camera. During kinetic runs, the temperature of the sample was monitored by OP at a rate of one measurement per second.

RESULTS AND DISCUSSION

A long-term objective of this investigation was to develop epoxide monomer-initiator systems that would both possess long shelf lives, while retaining the desirable ability to undergo rapid polymerization at low temperatures. The approach we have pursued in this work was to employ cationic photo- and redox initiator systems that generate strong Brønsted acids *in situ* in the presence of monomers and other agents that can reversibly sequester those acids as supramolecular proton complexes such as **3** and **4** rendering them inactive or poorly reactive for the initiation of polymerization at room temperature. It was expected that such supermolecular complexes could be easily dissociated at relatively low temperatures to trigger cationic polymerization.

During this investigation, we have relied upon optical pyrometry to characterize both the photo- and redox initiated cationic ring-opening polymerizations of epoxide monomers. Optical pyrometry (OP) is a convenient, highly reliable technique that was originally developed in this laboratory for remotely monitoring the rapid kinetics of free radical and cationic photopolymerization reactions.[19−21] The technique is based on the principle that bulk addition polymerizations are highly exothermic events that result in a readily measurable elevation in the temperature of the sample. Using an infrared camera (i.e., an optical pyrometer), the course of the evolution of the temperature of a monomer sample is remotely measured as a function of the time. The OP technique is especially well suited for the study of the photoinduced polymerizations of multifunctional monomers that undergo cross-linking reactions. It has been shown[19] that the initial portion of the temperature versus time curve of an optical pyrometry trace is proportional to the corresponding conversion versus time curves as determined by either real-time infrared spectroscopy (RTIR) or by differential scanning photocalorimetry (DSP). As described in detail in the Experimental Section of this article, the original OP apparatus that was designed for the study of photopolymerizations was modified to equip it with the capability to study redox cationic polymerizations conducted under controlled conditions.[13,14]

Our initial experiments were focused on α,ω-diglycidyl ethers of oligoethylene oxides such as diethylene glycol diglycidyl ether and triethylene glycol diglycidyl ether. It was proposed that such monomers, respectively, would form crown ether-like complexes **7** and **8** by penta- and hexadentate proton coordination. As previously indicated, structures **7** and **8** are both simplified and idealized. Traces of water are nearly always present in such hydrophilic monomers and, in addition, one or more moles of water may also be involved in the coordination sphere. Figure 1 depicts a study of the thermal profile obtained by optical pyrometry of the photopolymerization of triethylene glycol diglycidyl ether carried out using (4-*n*-hexadecyloxyphenyl)phenyliodonium hexafluoroantimonate (IOC-16 SbF_6) under relatively high intensity (1580 mJ/cm^2 min) UV irradiation conditions. Unless otherwise noted, continuous UV irradiation was applied throughout the entire course of this as well as in other studies shown in the present article. Polymerization was preceded by a very long (200 s) induction period during which the temperature rises slowly from 25 to 50 °C over the course of 200 s. After this induction period, a very abrupt and highly exothermic polymerization occurs with the temperature spontaneously rising to 220 °C over the course of approximately 3−5 s. During this thermally

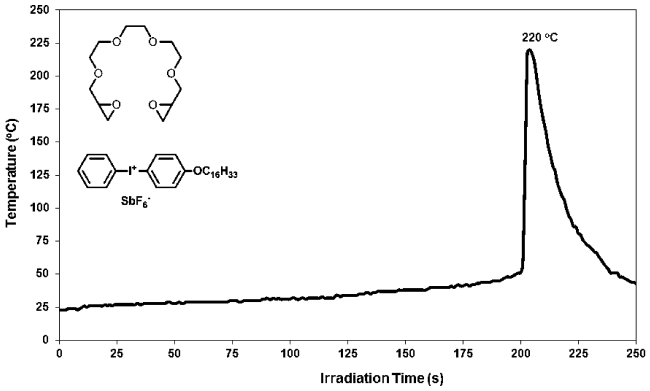
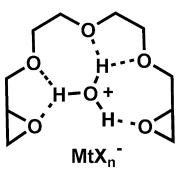
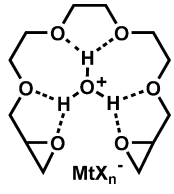


Figure 1. Photopolymerization of triethylene glycol diglycidyl ether with 2.0 mol % (4-*n*-hexadecyloxyphenyl)phenyliodonium hexafluoroantimonate (IOC-16 SbF_6) at a UV light intensity of 1580 mJ/cm^2 min.

induced autoaccelerated cationic polymerization, there is very rapid consumption of the epoxide functional groups and the final conversions are always nearly quantitative. This has been verified by real-time IR studies and is indicated in the OP curves by the very sharp peaks that are obtained. When the UV irradiation of the thin film sample was discontinued prior to the onset of the highly exothermic portion of the polymerization, there appeared to be no change in the appearance of the monomer. However, heating a film of the irradiated monomer briefly at temperatures ranging from 50 to 70 °C resulted in the rapid, exothermic polymerization of the sample. When the hot tip of a soldering iron was brought into contact with the liquid monomer film, we also observed that the polymerization quickly took place as a front that proceeded from that point outward and extending to all portions of the irradiated film. This exothermic frontal cross-linking of the epoxy monomer suggests that there would be a temperature threshold (50−70 °C), where the cationic polymerization propagates autocatalytically.



7



8

Figure 2 depicts the redox initiated cationic ring-opening polymerization of a 2.0 g sample of dipropylene glycol diglycidyl ether carried out using 1.0 wt % (4-*n*-undecyloxyphenyl)phenyliodonium hexafluoroantimonate (IOC-11 SbF_6), and 50 μL triethylsilane in the presence of 30 ppm of Cl_2(COD)Pd(II) as a catalyst. The redox reaction rapidly generates $HSbF_6$ at room temperature. However, polymerization takes place only very slowly on standing over the course of 1−2 h. This appears due to the capture of the redox generated acid by the monomer with the formation of a supramolecular hydronium ion complex analogous to **7**. As Figure 2 shows, slowly heating this mixture at a programmed rate of 7 °C/min results in polymerization of the monomer that begins slowly as heating progresses and then sharply accelerates at approximately 70 °C with the temperature rising to a maximum of 184 °C.

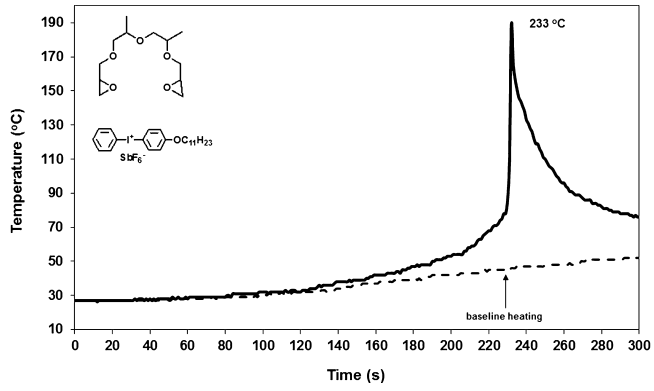


Figure 2. Redox cationic polymerization of a 2.0 g sample of dipropylene glycol diglycidyl ether using 1.0 wt % (4-*n*-undecyloxyphenyl)phenyliodonium hexafluoroantimonate (IOC-11 SbF_6), and 50 μL of triethylsilane in the presence of 30 ppm of Cl_2(COD)Pd^{II}.

On the basis of the above experiments, it was concluded that even very powerful Brønsted acids, such as $HSbF_6$, can be sequestered in the presence of α,ω-diglycidyl ethers of oligoethylene oxides that can form planar cyclic or three-dimensional supramolecular proton complexes. With this information in hand, it was decided to investigate the possibility of employing crown ethers as additives to modify the reactivity of epoxide monomers. The complexation of protonic acids by crown ethers has considerable literature precedent. Izatt et al.[22] showed that stable crystalline complexes between the hydronium ion and *cis-syn-cis*-cyclohexano-18-crown-6 can be prepared. Further work by Weber et al.,[23] Chevenert et al.,[24,25] Junk and Atwood,[26] McKenna and Eyring,[27] and Koltoff and Chantooni[28] have also reported the formation, isolation and spectroscopic identification of similar complexes. Leis et al.[29] have described the complexation of hydronium ions at the surfaces of hydrogen dodecyl sulfate micelles. We were especially interested to determine whether such crown ether complexes would preferentially form in the presence of epoxide monomers and how this would influence the character of the subsequent cationic ring-opening polymerization. The results of a study of the photopolymerization of cyclohexene oxide carried out in the presence and absence of various amounts of 18-crown-6 are shown in Figure 3. In this experiment, we have

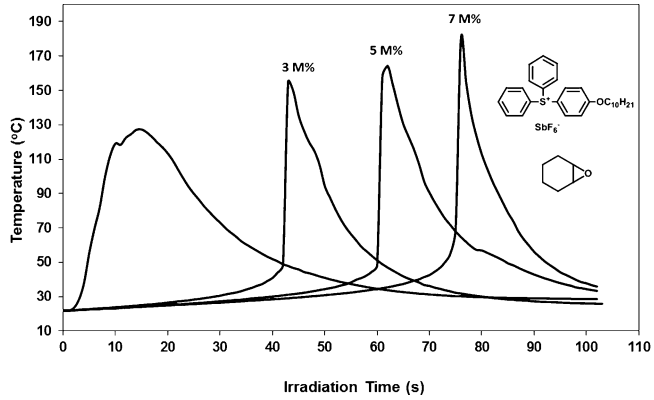
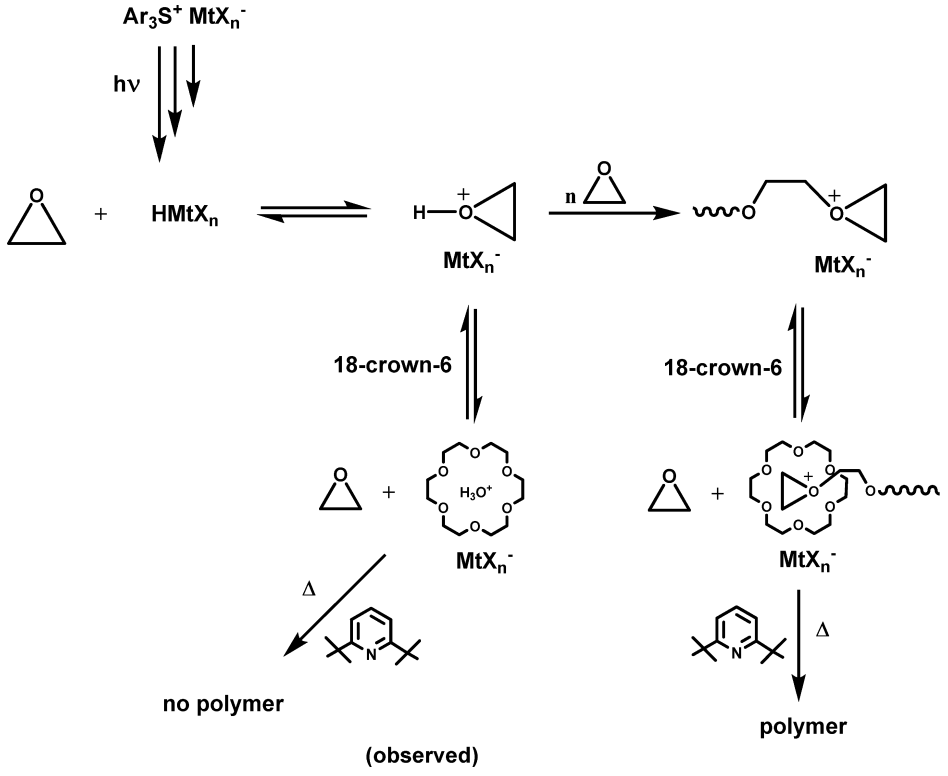


Figure 3. Photopolymerization of cyclohexene oxide with 0.5 mol % of SOC-10 SbF_6 in the presence and absence of 3.0, 5.0, and 7.0 mol % 18-crown-6 (light intensity 2350 mJ/cm^2 min).

dx.doi.org/10.1021/ma202618r | *Macromolecules* 2012, 45, 2233−2241

Scheme 3. Test for Complexation of Secondary versus Tertiary Oxiranium Ions by 18-Crown-6



employed *S*-(4-*n*-decyloxyphenyl)-*S*,*S*-diphenylsulfonium hexafluoridoantimonate (SOC-10 SbF_6) as the photoinitiator. We have found that diaryliodonium salts undergo complexation with 18-crown-6 and further work in this area will be reported in a separate communication. Under similar conditions, it is important to note that triarylsulfonium salts do not complex with crown ethers. Previously,[30] we have commented on the lower reactivity of triarylsulfonium salts compared to their diaryliodonium salt counterparts as cationic photoinitiators. Under the standardized irradiation conditions of this experiment,[3] the photoinitiated cationic polymerization of cyclohexene oxide monomer proceeds rapidly and exothermically with a short (2−3 s) induction period that is mainly due to a delay in the response of the OP instrumentation and to the sample configuration. When 3 mol % of 18-crown-6 is added and the experiment repeated, photopolymerization is delayed and proceeds eventually after approximately a 40 s induction period. This suggests that although the crown ether is present in a small concentration, it is highly effective in sequestering the very strong Brønsted acid, $HSbF_6$ before the onset of the exothermic autocatalytic cationic polymerization. Our postulate of the supramolecular arrested acid catalyst is also supported by the dependence of the induction period on the crown ether concentration. A further increase in the concentration of 18-crown-6 on the photopolymerization of cyclohexene oxide to 5 and then 7 mol % based on the monomer results in a progressive lengthening of the induction period. It is noteworthy, that the peaks in the OP temperature profiles of the modified photopolymerizations of the cyclohexene oxide sharpen appreciably with an increase in the amount of crown ether added. We interpret this behavior as due to the buildup of the concentration of crown ether sequestered protonic acid in the reaction mixture as photolysis proceeds. As the thermally induced polymerization begins, the release of heat generated as a result of the ring-opening polymerization of the monomer triggers the autoacceleration of the cationic polymerization. When more reactive cationic centers are created and arrested by supramolecular complexation, triggering the release of the accumulated acid gives rise to a more rapid polymerization with a consequent sharper rise in the sample temperature.

The possibility that the crown ether may also complex with the reactive tertiary oxiranium chain ends was considered. Additional experiments were carried out with the objective of verifiying or discounting this postulate. A 1.26 g (0.5 mmol) sample of 3,4-epoxycyclohexylmethyl 3′,4′-epoxycyclohexanecarboxylate was combined with 2.5×10^{-4} mol of SOC-10 SbF_6 and 7.5×10^{-4} mol of 18-crown-6. The liquid sample was irradiated for 45 s with UV light with an intensity of 3000 mJ/cm^2 min. To the irradiated liquid sample there was added 1.0×10^{-4} mol 2,6-di-*tert*-butylpyridine. Subsequently, the mixture was heated to 80 °C over the course of 6 min. Under these conditions, no polymerization was observed to take place. 2,6-Di-*tert*-butylpyridine is a "proton trap" that due to the steric hindrance about the nitrogen atom allows it to neutralize protons. However, it is not capable of trapping larger ions such as oxonium ions. These results tend to support our postulate that crown ethers bind initiating species such as protons or hydronium ions but not tertiary oxiranium ions that constitute the propagating chain ends present in epoxide ring-opening polymerizations. Scheme 3 shows the overall plan of this experiment.

It is well-known that linear poly(ethylene oxides) can complex metal cations.[31] It was of interest to determine whether these same linear polyethers can also effectively undergo proton complexation with Brønsted acids. In Figure 4 are compared the cationic photopolymerizations of cyclohexene oxide carried out in the presence and absence of 5 mol % of two methyl ether terminated poly(ethylene oxides); tetra-

dx.doi.org/10.1021/ma202618r | *Macromolecules* 2012, 45, 2233−2241

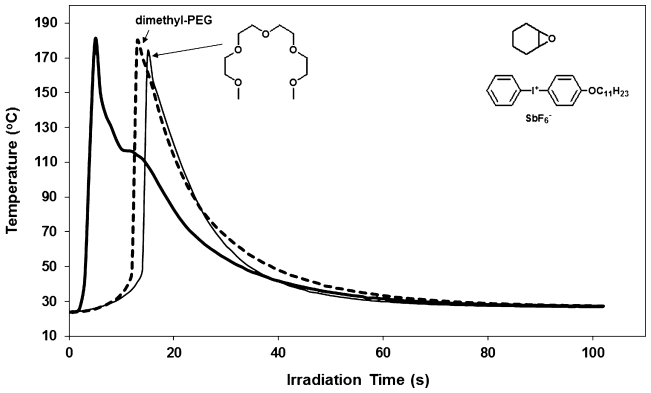
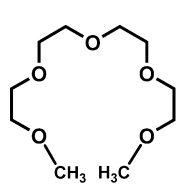
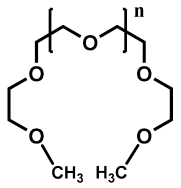


Figure 4. Comparison of the cationic photopolymerizations of cyclohexene oxide using 0.5 mol % IOC-11 SbF_6 carried out in the presence and absence of 5.0 mol % tetraethylene glycol dimethyl ether and 1000 g/mol poly(ethylene oxide) dimethyl ether (light intensity 1050 mJ/cm^2 min).

methylene glycol dimethyl ether, **9**, and poly(ethylene glycol) dimethyl ether (M_n = 1000 g/mol), **10**. Such compounds are generally referred to as "podands". While not as effective complexing agents as 18-crown-6, both podands display the ability to significantly delay the onset of the cationic photopolymerization of cyclohexene oxide. This observation is consistent with our postulate that such polymers can also form supramolecular complexes with protonic acids.



9



10

It was of interest to explore whether this effect could be extended to include other related monomers such as 3,4-epoxycyclohexylmethyl 3′,4′-epoxycyclohexanecarboxylate. Accordingly, the photopolymerization of this monomer containing 1.0 mol % IOC-11 SbF_6 was carried out in the presence and absence of 3.0 mol % tetraethylene glycol dimethyl ether. This study is shown in Figure 5. While the effect of this linear ether

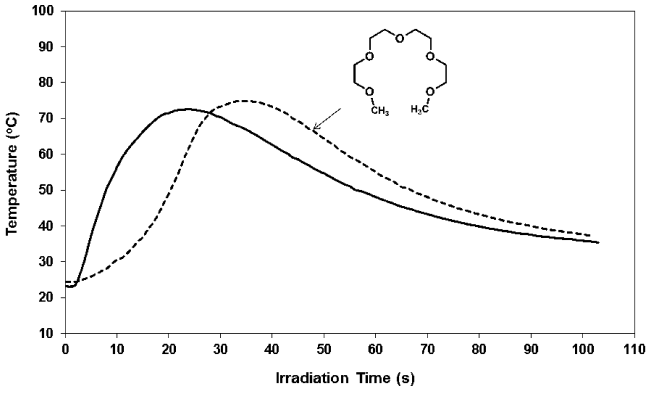


Figure 5. Study of the photopolymerization of 3,4-epoxycyclohexylmethyl 3′,4′-epoxycyclohexanecarboxylate with 1.0 mol % IOC-11 SbF_6 conducted in the presence and absence of 3 mol % tetraethylene glycol dimethyl ether (light intensity 2700 mJ/cm^2 min).

in delaying the onset of the cationic photopolymerization is clearly evident, it is very less pronounced than for this less reactive monomer.

The metal cation complexing ability of crown ethers has been shown to depend on the size of the rings and their associated number of coordination sites.[23,32,33] Crown ethers with large ring sizes preferentially coordinate with larger metal cations, while those with smaller diameter rings form complexes that accommodate metal cations with smaller ionic radii. It was proposed that similar effects should also be observed for the formation of crown ether complexes with hydronium ions derived from Brønsted acids as well. In Figure 6 is shown a

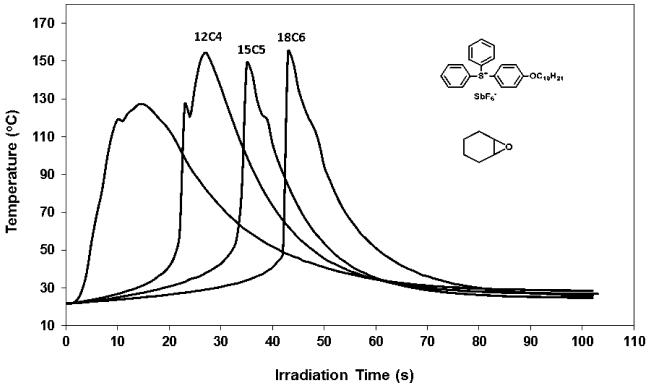


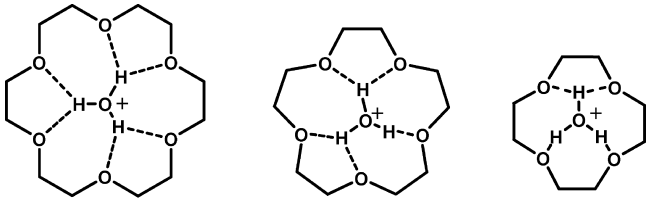
Figure 6. Effect of the crown ether ring size on the photopolymerization of cyclohexene oxide with 0.5 mol % SOC-10 SbF_6. (3 mol % crown ether, light intensity 2350 mJ/cm^2 min).

comparison of the effects of the addition of 3 mol % of a series of crown ethers with different ring sizes on the photopolymerization of cyclohexene oxide in the presence of 0.5 mol % of SOC-10 SbF_6. Included in this study for comparative purposes is an OP trace for the photopolymerization conducted in the absence of a crown ether. As noted previously, the photoinitiated polymerization of the epoxide monomer takes place rapidly in the absence of a crown ether.

When crown ethers are added, in all cases, the onset of the photopolymerizations is delayed for appreciable periods of time. However, the length of the induction period is directly related to the size of the crown ether and increases in the order: 18-crown-6 > 15-crown-5 > 12-crown-4. This was interpreted to be indicative of the poorer coordinating ability of both 12-crown-4 and 15-crown-5 for $H_3O^+SbF_6^-$ as compared to 18-crown-6. The respective sizes of the cavities of the three crown ethers have been reported to be as follows: 12-crown-4, 120−150 pm; 15-crown-5, 170−220 pm; 18-crown-6, 260−320 pm.[34] Fornili et al.[35] calculated the size of the hydronium ion to be 248 pm which is midway between the radii of the Na (190 pm) and potassium (266 pm) cations. These two metal cations are respectively preferentially complexed by 15-crown-5 and 18-crown-6. Lastly, the gas-phase binding energies between the hydronium ion and 18-crown-6 and 15-crown-5 were calculated by Sharma and Kebarle[36] and found to be −88.5 kcal/mol and −76.9 kcal/mol, respectively. These values are higher than the binding constants for 18-crown-6 with the alkali metal cations Na^+ or K^+ (−56 kcal/mol and −72 kcal/mol, respectively) and were attributed by Bühl and Wipff[37] to the formation of the formation of the multiply hydrogen bonded highly symmetrical complexes, **11** and **12**. It is expected that the magnitudes of the above binding energies will be somewhat different in monomer

dx.doi.org/10.1021/ma202618r | Macromolecules 2012, 45, 2233−2241

solutions of varying polarity and complexing ability. As molecular modeling shows, the small cavity of 12-crown-4 does not allow the hydronium ion to form a planar complex. Rather, the hydronium ion is perched above the plane of the crown ether ring forming a weaker complex, **13**. It is also worthwhile to note that as one proceeds through the series **11** to **13**, the number of coordination sites of the crown ether with the hydronium ion decreases resulting in weaker, more easily thermally dissociable complexes.



11 **12** **13**

$MtX_n^- = ClO_4^-, PF_6^-, SbF_6^-$, etc.

Further evidence for the formation of the above crown ether-hydronium ion supramolecular complexes was sought. The 1:1 hydronium hexafluoroantimonate-18-crown-6 supramolecular complex (**11**, $MtX_n^- = SbF_6^-$)was prepared for the first time in this laboratory as a colorless crystalline solid (mp 185 °C dec) by combining hexafluoroantimonic acid hexahydrate with 18-crown-6 in a manner similar to that described by Izatt et al.[22] The desired complex precipitated from the reaction mixture and was recovered by filtration. The analogous crystalline (mp 98−100 °C) $H_3O^+SbF_6^-$-15-crown-5 complex was also prepared in a similar manner. Attempts to prepare and isolate the analogous $H_3O^+SbF_6^-$-12-crown-4 complex resulted in a low melting, amorphous waxy solid. The addition of $H_3O^+SbF_6^-$-18-crown-6 complex to cyclohexene oxide resulted in slow exothermic polymerization at room temperature. Under the same conditions, the polymerization of the diepoxide monomer, 3,4-epoxycyclohexylmethyl 3′,4′-epoxycyclohexane carboxylate, did not take place. However, gelation was noted when the monomer-complex mixture was gently warmed. Research on the preparation, characterization and use of this and other crown ether-strong Brønsted acid supramolecular complexes in cationic ring-opening and vinyl polymerizations is currently in progress and will be reported in a forthcoming publications.

The ability of crown ethers to modify the character of the cationic polymerizations of epoxide monomers is a general phenomenon that can be applied to epoxide monomers other than cyclohexene oxide. For example, Figure 7 depicts the results of a study of the photopolymerization of 3,4-epoxycyclohexylmethyl 3′,4′-epoxycyclohexanecarboxylate, conducted in the presence and absence of 18-crown-6. Duplicate kinetic runs are shown in this figure for each case. It is interesting that based on the thermal OP profiles that were obtained; the nature of the polymerization was markedly altered in the presence of the crown ether. When no crown ether is present, the polymerization proceeds rather sluggishly under continuous UV irradiation, although without a substantial induction period and a sharp rise in sample temperature. The maximum temperature attained by the sample was only 55 °C. We have commented on the sluggish cationic ring-opening polymerization behavior of this monomer previously.[38] When 18-crown-6 is added to the monomer-

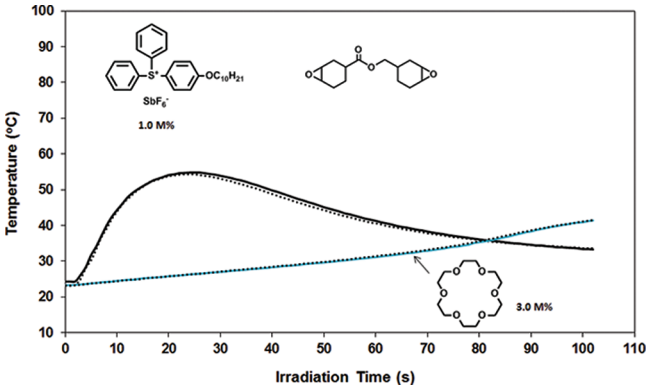


Figure 7. Study of the photopolymerization of 3,4-epoxycyclohexylmethyl 3′,4′-epoxycyclohexanecarboxylate with 0.5 mol % SOC-10 SbF_6 conducted in the presence and absence of 3 mol % 18-crown-6 (light intensity 2700 mJ/cm^2 min).

photoinitiator mixture, polymerization proceeds slowly and only after a long induction period.

1,3-Bis(2(3,4-epoxycyclohexyl)ethyl)-1,1,3,3-tetramethyldisiloxane (Figure 8) is a difunctional biscycloaliphatic epoxide that

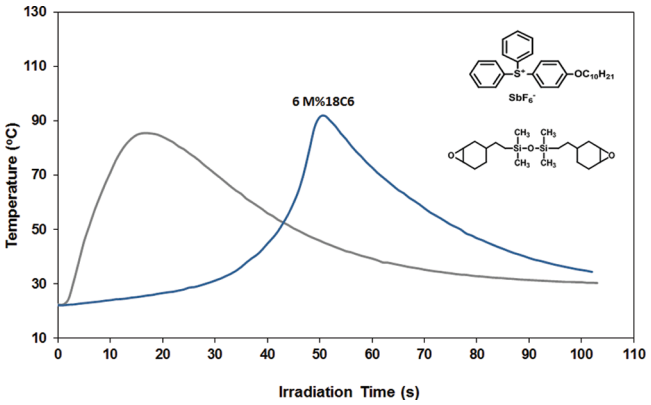
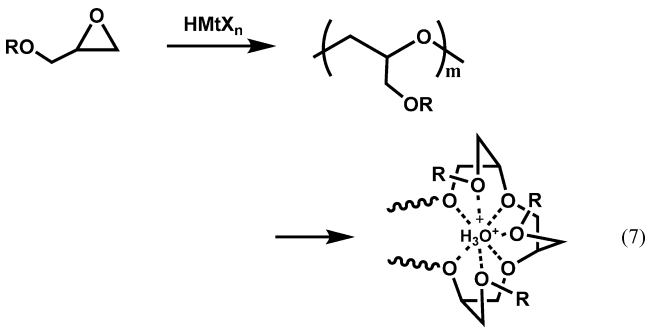


Figure 8. Study of the photopolymerization of 1,3-bis(2(3,4-epoxycyclohexyl)ethyl)-1,1,3,3-tetramethyldisiloxane with 0.5 mol % SOC-10 SbF_6 conducted in the presence and absence of 6 mol % 18-crown-6 (light intensity 2350 mJ/cm^2 min).

is considerably more reactive than 3,4-epoxycyclohexylmethyl 3′,4′-epoxycyclohexanecarboxylate (Figure 7) due to the fact that it possesses no nucleophilic centers other than the highly strained epoxide oxygen atoms. As shown in Figure 8, when the photopolymerization of this former monomer is carried out using 1.0 mol % SOC-10 SbF_6, polymerization ensues rapidly and exothermically without a substantial induction period. In contrast, when the photopolymerization is conducted in the presence of 3 mol % 18-crown-6, initially polymerization proceeds slowly. This induction period culminates in a rapid, exothermic autoaccelerated polymerization. The sharp rise in the temperature of the sample is consistent with the arrest and accumulation of the supramolecular complex and the final thermally induced release of acid which initiates the cationic polymerization.

As a final consideration, it is worthwhile to note that the photo- and redox induced cationic ring-opening polymerizations of α,ω-diglycidyl oligoethylene oxides yields three-dimensional networks that are similar to cryptates.[39] These cryptates are capabable of binding many cationic species

including; metal cations, protons, hydronium ions and reactive oxiranium chain ends. Equation 7 depicts the proposed



(7)

supramolecular intramolecular coordination of hydronium ions by a polymer produced from a monofunctional glycidyl ether. Because of the multiplicity of oxygen atoms that can serve as coordination sites, the corresponding polymerization of α,ω-diglycidyl oligoethylene oxides would be expected be even more effective as supramolecular complexing agents. In support of this concept, Dimonie and Teodorescu[40] have reported that beads of α,ω-diglycidyl oligoethylene oxides cross-linked using triethylenetetramine exhibit phase transfer catalytic activity in typical S_N2 reactions.

CONCLUSIONS

α,ω-Diglycidyl ether monomers in which the two epoxide groups are separated by multiple ethyleneoxy or propyleneoxy units possess the ability to form *in situ* supramolecular complexes with hydronium ions derived from strong protonic acids. Because of the stability of these complexes, the cationic ring-opening polymerization of the epoxide groups is suppressed. The suppression is manifested as an induction period. However, since such supramolecular complexes possess a low threshold for dissociation, once polymerization begins, it proceeds rapidly as a highly exothermic process. Similarly, crown ethers form supramolecular complexes with hydronium ions derived from Brønsted acids and we have demonstrated in this article that when these complexes are added to epoxide monomers rapid cationic polymerization ensues. Further, the addition of crown ethers to highly reactive epoxide monomers significantly modifies their reaction profiles in both thermally and photochemically initiated cationic ring-opening polymerizations.

AUTHOR INFORMATION

Notes

The authors declare no competing financial interest.

REFERENCES

(1) Crivello, J. V.; Bulut, U. *J. Polym. Sci., Part A: Polym. Chem.* **2006**, *44*, 6750−6764.
(2) Crivello, J. V. *J. Polym. Sci., Part A: Polym. Chem.* **2006**, *44*, 3036−3052.
(3) Crivello, J. V. In *Basics and Applications of Photopolymerization Reactions*; Fouassier, J. P., Allonas, X., Eds.; Research Signpost: Triverandum, India, 2010, Vol. 2, Chapter 27, pp 101−117.
(4) Crivello, J. V.; Falk, B.; Zonca, M. R. Jr. *J. Polym. Sci., Part A: Polym. Chem.* **2004**, *42*, 1630−1646.
(5) Crivello, J. V.; Bulut, U. *J. Polym. Sci., Part A: Polym. Chem.* **2005**, *43*, 3205−3220.
(6) Pappas, S. P.; Gatechair, L. R. *Proc. Soc. Photogr. Sci. Eng.* **1982**, 46−49.
(7) Baumann, H.; Timpe, H.-J.; Böttcher, H. *Z. Chim.* **1983**, *23* (11), 394−402.
(8) Penczek, S.; Kubisa, P.; Matyjaszewski, K. *Adv. Polym. Sci.*: Springer-Verlag: Berlin, 1980, *37*, p6.
(9) Bae, Y. c.; Lambert, S. M.; Soane, D. S.; Prausnitz, J. M. *Macromolecules* **1991**, *24*, 4403−4407.
(10) Saeki, S.; Kuwarhara, N.; Nakata, M.; Kaneko, M. *Polymer* **1976**, *17*, 685−689.
(11) Dormindontova, E. E. *Macromolecules* **2002**, *35*, 987−1001.
(12) Crivello, J. V. *J. Polym. Sci., Part A: Polym. Chem.* **2011**, *49*, 2147−2154.
(13) Crivello, J. V. *J. Polym. Sci., Part A: Polym. Chem.* **2009**, *47*, 1825−1835.
(14) Crivello, J. V. *Silicon* **2009**, *1*, 111−124.
(15) Crivello, J. V.; Molleo, M. *Macromolecules* **2009**, *42*, 3982−3991.
(16) Crivello, J. V.; Lee, J. L. *Radiation Curing of Polymeric Materials*; ACS Symposium Series 417; Hoyle, C. E.; Kinstle, J. F., Eds.; American Chemical Society: Washington, DC, 1989; pp 398−411.
(17) Crivello, J. V.; Lee, J. L. *J. Polym. Sci., Part A: Polym. Chem.* **1989**, *27*, 3951−3968.
(18) Akhtar, S. R.; Crivello, J. V.; Lee, J. L.; Schmitt, M. L. *Chem. Mater.* **1990**, *2* (6), 732−737.
(19) Falk, B.; Vallinas, S. M.; Crivello, J. V. *J. Polym. Sci., Part A: Polym. Chem.* **2003**, *41* (4), 579−596.
(20) Crivello, J. V.; Falk, B.; Vallinas, S. M. *Polym. Mater. Sci. Eng. Prepr.* **2003**, *88*, 209−210.
(21) Crivello, J. V.; Falk, B.; Jang, M.; Zonca, M. R.; Vallinas, S. M. *RadTech Rep.* **2004**, *May/June*, 36−43.
(22) Izatt, R. M.; Haymore, B. L.; Cristensen, J. J. *J. Chem. Soc. Chem. Commun.* **1972**, *23*, 1308−1309.
(23) Weber, E.; Toner, J. L.; Goldberg, I.; Vögtle, F.; Laidler, D. A.; Stoddart, J. F.; Bartsch, R. A.; Liotta, C. L. *Crown Ether and Analogs*; John Wiley: New York, 1989; pp 420−425.
(24) Chenevert, R.; Rodrigue, A.; Chamberland, D.; Oullet, J.; Savagie, R. *J. Mol. Struct.* **1985**, *131*, 187−200.
(25) Chenevert, R.; Chamberland, D.; Simard, M.; Brisse, F. *Can. J. Chem.* **1989**, *67*, 32−36.
(26) Junk, P. C.; Atwood, J. L. *J. Chem. Sci., Dalton Trans.* **1997**, 4393−4400.
(27) McKenna, W. P.; Eyring, E. M. *Appl. Spectrosc.* **1986**, *40*, 16−20.
(28) Kolthoff, I. M.; Chantooni, M. K. Jr. *Can. J. Chem.* **1992**, *70*, 177−185.
(29) Agra, C.; Amado, S.; Leis, J. R.; Rios, A. *J. Phys. Chem. B* **1977**, *101*, 7780−7785.
(30) Crivello, J. V. *Comprehensive Polymer Science: Ring-Opening Polymerizations*; Penczek, S., Ed.; Springer Verlag: Berlin, in press.
(31) Tuemmler, B.; Maass, G.; Weber, E.; Wehner, W.; Voegtle, F. *J. Am. Chem. Soc.* **1977**, *99*, 4683−4690.
(32) *Crown Ethers and Analogous Compounds*; Studies in Organic Chemistry 45; Hiraoka, M., Ed., Elsevier Science: Amsterdam. 1992.
(33) Gokel, G. W. *Crown Ethers and Cryptands*; Monographs in Supramolecular Chemistry 3; Royal Society of Chemistry: Cambridge, U.K., 1991.
(34) Vögtle, F. *Supramolecular Chemistry*; Wiley: New York, 1991; p 38.
(35) Fornili, S. L.; Migliore, M.; Palazzo, M. A. *Chem. Phys. Lett.* **1986**, *125*, 419−424.
(36) Sharma, R. B.; Kebarle, P. . *J. Am. Chem. Soc.* **1984**, *106*, 3913−3916.
(37) Bühl, M.; Wipff, G. *J. Am. Chem. Soc.* **2002**, *124*, 4473−4480.
(38) Crivello, J. V.; Varlemann, U. *J. Polym. Sci., Polym. Chem. Ed.* **1995**, *33*, 2463−2472.
(39) Bulut, U.; Crivello, J. V. *Macromolecules* **2005**, *38*, 3584−3595.
(40) Dimonie, M.; Teodorescu, M. *Angew. Makromol. Chem.* **1993**, *209*, 55−61.

Macromolecules

Article

pubs.acs.org/Macromolecules

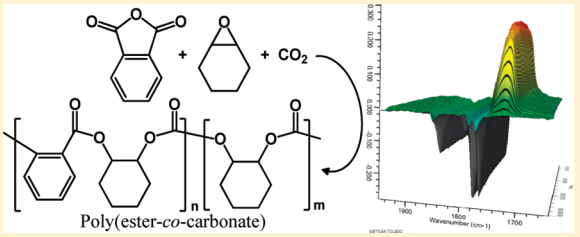
Kinetic Studies of the Alternating Copolymerization of Cyclic Acid Anhydrides and Epoxides, and the Terpolymerization of Cyclic Acid Anhydrides, Epoxides, and CO_2 Catalyzed by (salen)$Cr^{III}Cl$

Donald J. Darensbourg,* Ross R. Poland, and Christina Escobedo

Department of Chemistry, Texas A&M University, College Station, Texas 77843, United States

Supporting Information

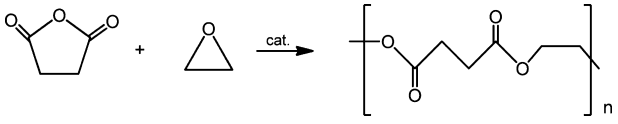
ABSTRACT: Copolymerization of a series of cyclic acid anhydrides with several epoxides using (salen)CrCl/onium salt catalysts has afforded polyesters with high molecular weights and narrow molecular weight distributions. The (salen)CrCl catalyst in the presence of the onium salts with formula PPNX (X = Cl^-, N_3^-) for the copolymerization of the anhydrides, maleic (MA), succinic (SA), phthalic (PA), cyclohexene (CHE), and cyclohexane (CHA) with the epoxides, cyclohexene oxide (CHO), propylene oxide (PO), and styrene oxide (SO) resulted in completely alternating enchainment of monomers to provide pure polyesters. Temperature dependent studies of the ring-opening copolymerization of phthalic anhydride and cyclohexene oxide monomers in toluene solution have yielded activation parameters of $\Delta H^{\ddagger}$ = 67.5 kJ mol^{-1} and $\Delta S^{\ddagger}$ = −95.3 J mol^{-1}, where the rate limiting step was ring-opening of the epoxide by the enchained anhydride. For the cyclic acid anhydride (CHA), the relative order of reactivity with epoxides decreased PO > CHO ≥ SO, and for the epoxide (CHO) the relative rate of copolymerization was CHA > PA > CHE. The (salen)CrCl/$PPNN_3$ catalyst system was also shown to effectively terpolymerize CHO/phthalic anhydride/CO_2 to afford diblock copolymers, thereby producing in a one pot synthesis poly(ester-*co*-carbonate). T_g values of the synthesized polyesters displayed a temperature range over 130 °C, from +95 °C to −39 °C.



INTRODUCTION

It has become increasingly more apparent that there is a need to develop the synthesis of new polymeric materials which incorporate renewable resources.[1] In this regard, the synthesis of polyesters by way of ring-opening polymerization of cyclic anhydrides and epoxides offers the possibility of providing a wide variety of polyesters, including some from replenishable reserves. For example, copolymers from succinic anhydride and ethylene oxide or limonene oxide constitute polymeric materials from such sources (Scheme 1).[2,3] Furthermore,

Scheme 1



many of these aliphatic polyesters exhibit a wide range of mechanical and thermal properties in addition to being biodegradable.

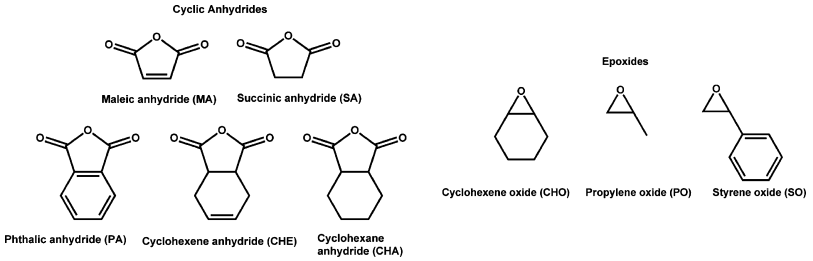
Several early publications have reported upon catalytic systems utilizing a range of metal initiators which are able to accomplish these copolymerization reactions.[4] However, these processes generally display low catalytic activities and provide copolymers of relatively low molecular weights.[5−8] More recently, Coates and co-workers have employed (BDI)ZnOAc (BDI = β-diiminate) complexes as active catalysts for the ring-opening polymerization of epoxides and cyclic anhydrides.[9] In this manner, these researchers were able to synthesize new aliphatic polyesters in a highly alternating copolymerization of epoxides and cyclic anhydrides which afforded high molecular weight copolymers with narrow molecular weight distributions.

Because (salen)CrCl complexes in the presence of onium salts, like (BDI)ZnOAc complexes, have been very effective at coupling CO_2 and epoxides, it is anticipated that these complexes will be productive catalysts for the copolymerization of epoxides and cyclic anhydrides.[10−13] Indeed, while this work was in progress, DiCiccio and Coates presented results on the ring-opening polymerization of maleic anhydrides with epoxides catalyzed by (salen)$CoO_2CC_6F_5$ or (salen)CrCl.[14] Additional reports containing extensive MALDI−ToF−MS studies of the ring-opening co- and terpolymerization of cyclohexene oxide and a series of cyclic acid anhydrides and CO_2 catalyzed by chromium(III) porphyrinate and salen complexes have been published by Duchateau and co-workers.[15] Herein, we report kinetic studies of the copolymerization of a variety of epoxides and cyclic anhydrides catalyzed by this single-site chromium(III) catalyst. In addition *in situ* infrared monitoring of the terpolymerization of phthalic

Received: December 5, 2011
Revised: February 10, 2012
Published: February 22, 2012

 © 2012 American Chemical Society dx.doi.org/10.1021/ma2026385 | *Macromolecules* 2012, 45, 2242−2248

Scheme 2



anhydride, cyclohexene oxide, and CO_2 to provide a diblock copolymer of polyester and polycarbonate, i.e., poly(ester-*co*-carbonate) is examined.

EXPERIMENTAL SECTION

Reagents and Methods. Unless otherwise specified, all syntheses and manipulations were carried out on a double-manifold Schlenk vacuum line under an atmosphere of argon or in an argon filled glovebox. Propylene oxide, cyclohexene oxide, and styrene oxide were purchased from VWR and either distilled from CaH_2 or used as received. Phthalic anhydride, succinic anhydride, cyclohexane anhydride, cyclohexene anhydride, and maleic anhydride were purchased from VWR and used as received. Oxetane (Alfa Aesar) was freshly distilled from CaH_2 and stored in the freezer of the glovebox. (Salen)$Cr^{III}Cl$ was purchased from Strem. PPNCl was purchased from Aldrich and recrystallized from diethyl ether and acetonitrile. $PPNN_3$ was synthesized by mixing molar equivalents of NaN_3, followed by recrystallization from diethyl ether and acetonitrile. *n*-Bu_4NCl was purchased from VWR and recrystallized before use. *n*-Bu_4NX, where X = Br^-, N_3^-, or I^- was synthesized from *n*-Bu_4NCl and the appropriate salt, followed by recrystallization.

Measurements. All ^1H and ^{13}C NMR spectra were performed in $CDCl_3$. ^1H NMR spectra were recorded at 295 K using an Inova Varian spectrometer at 500 MHz, and ^{13}C NMR spectra were recorded at 295 K at 125 MHz. Chemical shifts are given in ppm relative to TMS and coupling constants (*J*) in hertz. High-pressure reaction kinetic measurements were performed using an ASI ReactIR 1000 reaction analyses system with stainless steel Parr autoclave modified with a permanently mounted ATR crystal (SiComp) at the bottom of the reactor (purchased from Mettler Toledo). *In situ* infrared experiments were performed using a ReactIR ic10 with a SiComp ATR crystal. T_g values were measured using a Mettler Toledo polymer DSC equipped with a liquid nitrogen cooling system and 50 mL/min purge of nitrogen gas. Samples (~10 mg) were weighed into 40 μL aluminum pans and subjected to two heating cycles, first cycle was at 10 °C/min from −100 to +200 °C, second was at 5 °C/min over the same range of temperatures. Molecular weight determination was performed using a Viscotek GPC instrument with a low angle light scattering (LALS), right angle light scattering (RALS), and refractive index (RI) detectors with THF as eluent.

Representative ReactIR Monitored Copolymerization. A jacketed reaction vessel was charged with 64 mg (1 equiv) of (salen)$Cr^{III}Cl$, 57 mg $PPNN_3$ (1 equiv), and 3 g of phthalic anhydride (200 equiv) followed by purging with argon. Then 23 mL of toluene was added to the flask, at which point the flask was heated to 80 °C and allowed to equilibrate for 15 min. Once it became apparent that all the phthalic anhydride had dissolved, 2 mL of cyclohexene oxide (200 equiv) was injected into the flask, at which point the FTIR monitoring was started. Reactions were allowed to proceed until 100% conversion was achieved.

Representative Copolymerization. A vial was charged with a stirring bar, 2 g of phthalic anhydride (533 equiv), 16 mg of (salen)$Cr^{III}Cl$ (1 equiv), and 7.5 mg of *n*-Bu_4NCl (1 equiv). The vial was purged for several minute with argon, then 10 mL of toluene and 1 mL of cyclohexene oxide (400 equiv) were injected into the vial. The vial was inserted into an oil bath heated to 80 °C and allowed to react overnight. Excess anhydride and catalyst were removed by dissolution in 1.0 M HCl in methanol.

RESULTS AND DISCUSSION

The various epoxide and cyclic anhydride monomers examined in these studies are listed in Scheme 2. Initially we investigated the copolymerization of phthalic anhydride (PA) and cyclohexene oxide (CHO) employing the (salen)CrCl catalyst (Figure 1) in the presence of several onium salts to optimize

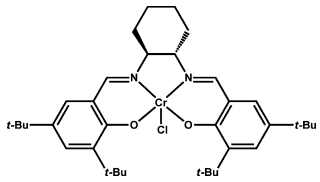


Figure 1. *N,N′*-Bis(3,5-di-*tert*-butylsalicylidine)-1,2-cyclohexane diaminochromium(III) chloride.

the catalytic activity. As illustrated in the infrared traces of polymer formation in Figure 2, the chromium(III) catalyst alone was ineffective and the onium salt alone was less effective than a combination of the two species. This is to be contrasted with the previous literature report where (salen)CrCl did not require a cocatalyst for the copolymerization of maleic anhydride and propylene oxide.[14] On the other hand, in the Duchateau studies a DMAP (4-*N,N*-dimethylamino-pyridine) cocatalyst was necessary in the presence of (Salophen)CrCl to impart catalytic activity.[15] In both instances employed in this study the polyesters afforded exhibited narrow molecular weight distributions, with PDIs ranging from 1.07 to 1.13. Utilizing the two monomers (PA and CHO) in the accompaniment of (salen)CrCl and various anions derived from PPN^+ and *n*-Bu_4N^+ salts we endeavored to determine the optimal anionic initiator.

The rates of copolymerization initiated by the anions of several PPN^+ (bis(triphenylphosphine)iminium) salts in the presence of (salen)CrCl did not vary significantly with the anion or its concentration. For example, the second-order rate constants employing one equivalent of Cl^-, N_3^-, and DNP^- (dinitrophenoxide) spanned the range $1.44-1.76 \times 10^{-2}$ M^{-1} s^{-1} at 80 °C and were not altered upon carrying out the process using two equivalents of onium salts. The use of *n*-Bu_4NX (X = Br or I) salts resulted in a modest decrease in the reaction rate. The lack of copolymerization rate on [onium salt] in the presence of the (salen)CrCl catalyst indicates that the process proceeds solely via a coordination insertion mechanism in these instances. Further confirmation of this mechanistic pathway is seen in the terpolymerization of PA/CHO/CO_2, where the coupling of CHO and CO_2 only occurs with the aid of the (salen)CrCl complex (*vide infra*).

dx.doi.org/10.1021/ma2026385 | *Macromolecules* 2012, 45, 2242−2248

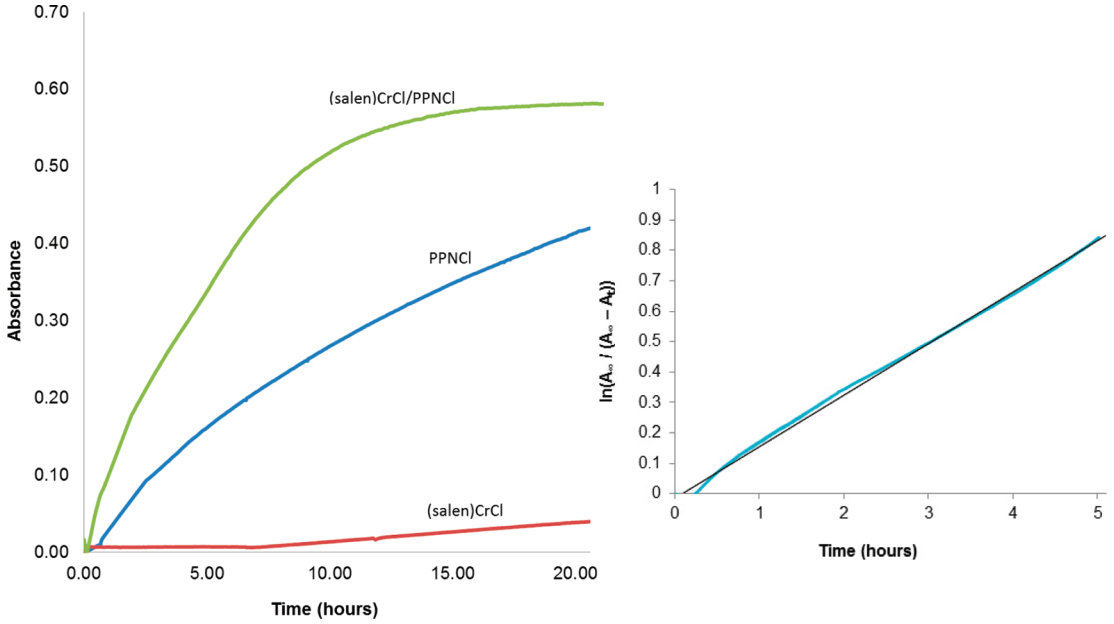


Figure 2. Growth of polyester peak at 1738 cm^{-1} as monitored by *in situ* ATR-FTIR spectroscopy for various combinations of catalyst and cocatalyst: (green line) [Cr]:[Cl]:[PA]:[CHO] = 1:1:200:200, (red line) [Cr]:[Cl]:[PA]:[CHO] = 1:0:200:200, and (blue line) [Cr]:[Cl]:[PA]:[CHO] = 0:1:200:200. Cr = (salen)CrCl, Cl = PPNCl, PA = phthalic anhydride, and CHO = cyclohexene oxide. Inset shows the linear plot of $\ln(A_\infty/A_\infty - A_t)$ vs time, where A_∞ and A_t are the absorbances of the band at 1738 cm^{-1} at t_∞ = infinity and t = time, respectively.

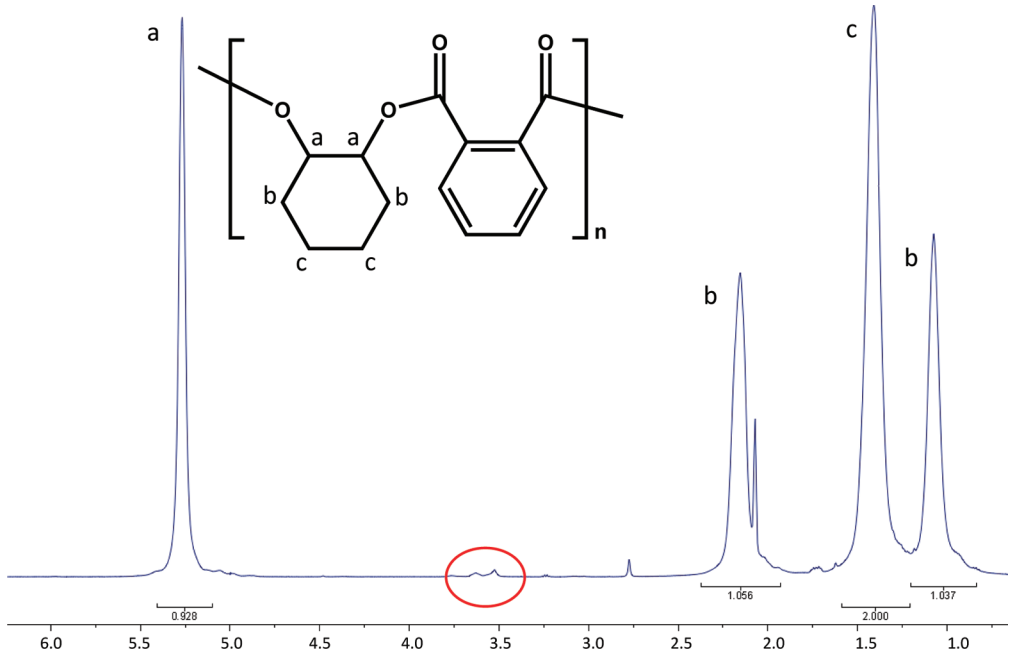
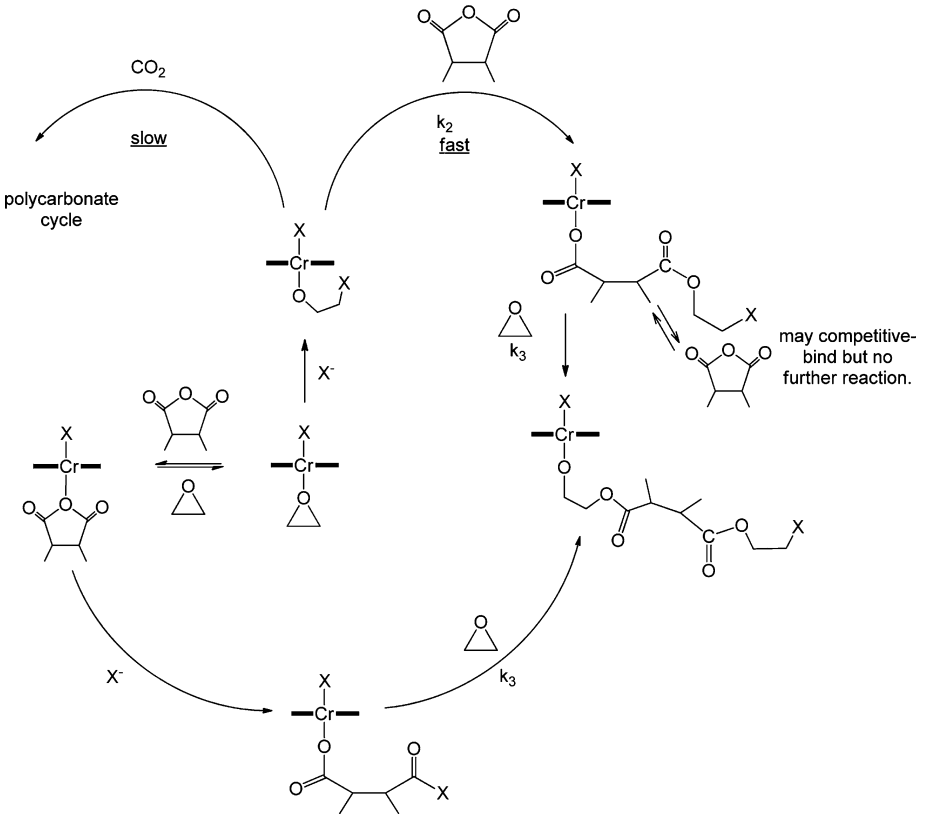


Figure 3. ^{1}H NMR spectrum of PA/CHO. PA phenyl appears at 7.65 ppm. Encircled region represents where ether linkages should appear, hence copolymer is >99% completely alternating.

Since the common PPN^+ salts of chloride and azide provide similar rates of initiation of polymerization, we have chosen to use the azide anion in our comprehensive studies because of its strong ν_{N_3} absorption band in the infrared. For these investigations we have synthesized a series of polyesters employing the combination of anhydride and epoxide monomers listed in Scheme 2. The appropriate monomers were dissolved in toluene and heated at 80 °C in the presence of (salen)CrCl and 1 equiv of $PPNN_3$. The resultant polyesters were characterized by infrared spectroscopy, ^{1}H NMR spectroscopy, differential scanning calorimetry (DSC), and selected samples were subjected to molecular weight analysis by gel permeation chromatography. Infrared analysis of the purified polyester confirmed the location of the ν_{CO} stretching frequency at 1738 cm^{-1} for all of the polyesters described herein. The $\nu_{C=O}$ vibration is significantly different from that of the cyclic anhydrides, located at approximately 1770 cm^{-1}, which allows for the monitoring of polyester formation *via in situ* ATR-FTIR analysis. The ^{1}H NMR spectra of the polyesters displayed chemical shifts in the 4−6 ppm range indicative of hydrogens bound to the carbons α to the ester group, both from the anhydride and epoxide units (Figure 3). ^{1}H NMR

dx.doi.org/10.1021/ma2026385 | *Macromolecules* 2012, 45, 2242−2248

Scheme 3



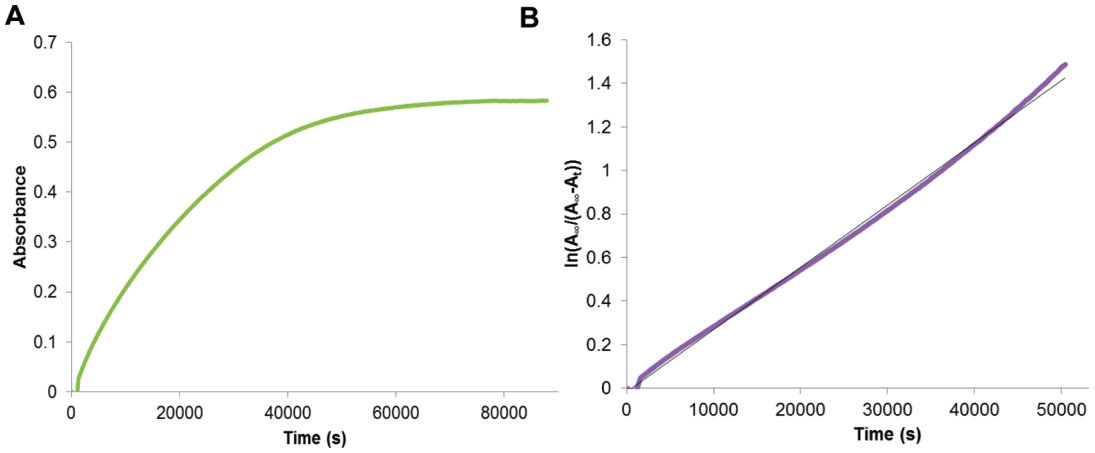


Figure 4. Copolymerization of equimolar quantities of cyclohexene oxide and phthalic anhydride in the presence of 4.05 mM (salen)CrCl and one equivalent of $PPNN_3$ in 2.5 mL of toluene at 80 °C. (A) Absorbance of the growth of the 1738 cm^{-1} band of the polyester vs time. (B) Plot of $\ln(A_\infty/[A_\infty - A_t])$ vs time.

spectra of all other polyester synthesized in this report may be found in the Supporting Information. Furthermore, analysis of the ^1H NMR spectra revealed that the copolymerization of epoxide and anhydride takes place in an almost exclusive (>99%) alternating fashion.

Kinetic Studies. The suggested reaction pathways for the formation of alternating copolymers from epoxides and anhydrides are summarized in Scheme 3. As indicated, the rate of epoxide and CO_2 coupling to provide polycarbonates is slow relative to polyester formation (*vide infra*). This latter observation provides a one-step production of diblock copolymers of polyesters and polycarbonates as previously demonstrated by Coates and co-workers employing β-diiminate zinc catalysts,[9] and Duchateau and co-workers employing (salophen)CrCl/DMAP as catalyst.[15] The rate of the alkoxide anion reacting with an anhydride monomer (k_2) is generally much faster than a carboxylate anion ring-opening an epoxide (k_3), hence the latter process is rate-determining. At constant initiator concentration, the copolymerization is first-order with respect to the epoxide monomer (Figure 4) and to the initiator at equimolar ratios of monomers. An increase in the cyclic anhydride concentration by 50% lead to only a slight change in reaction rate.[16] In the absence of the (salen)CrCl catalyst, a slower copolymerization pathway similar to that described in Scheme 3 presumably takes place initiated by ring-opening of the epoxide by the free anion from the onium salt followed by

dx.doi.org/10.1021/ma2026385 | *Macromolecules* 2012, 45, 2242–2248

successive alternating ring-opening of anhydride and epoxide. Such a reaction scheme is included in the Supporting Information.

The copolymerization reactions of equimolar quantities of phthalic anhydride and cyclohexene oxide at a constant catalyst concentration were monitored by *in situ* infrared spectroscopy over a temperature range of 40 °C. Table 1 lists the rate constants obtained from the linear plots in Figure 5 as a

Table 1. Temperature Dependent Rate Constants for the Copolymerization of PA and CHO.[a]

temperature (°C)	$k_3 \times 10^3$ M^{-1} s^{-1}	M_n (PDI)[b]
70.0	4.42	13 000 (1.12)
80.0	7.06	–
90.0	17.8	18 000 (1.13)
100.0	29.6	17 000 (1.12)

[a]Reaction conditions: (salen)CrCl/$PPNN_3$/PA/CHO = 1:1:200:200, where the [(salen)CrCl] = 4.05×10^{-3} M in toluene solution. [b]Determined by GPC in tetrahydrofuran using monodisperse polystyrene standards.

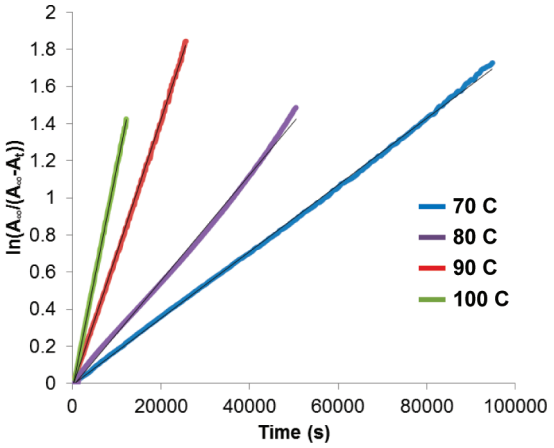


Figure 5. First-order plots for the copolymerization of PA and CHO as a function of temperature.

function of temperature, with an Eyring plot of these data shown in Figure 6. The $\Delta H^{\ddagger}$ and $\Delta S^{\ddagger}$ values derived from Figure 6 for the copolymerization of PA and CHO were determined to be 67.5 and −95.3 J/mol, respectively, with $\Delta G^{\ddagger}$ being 101 kJ/mol at 80 °C.

Consistent with earlier studies, the terpolymerization of cyclohexene oxide, phthalic anhydride, and CO_2 catalyzed by (salen)CrCl and $PPNN_3$ afforded a one-pot synthesis of a diblock copolymer of polyester and polycarbonate (Figure 7).[15] As noted in Scheme 3 this observation requires that the route governed by k_2 and k_3 to be much faster that the pathway proceeding via CO_2 insertion and subsequent polycarbonate formation. This has been interpreted as resulting from a slower rate of CO_2 insertion vs cyclic anhydride insertion into the metal alkoxide intermediate.[17] Alternatively, since CO_2 insertion into metal-alkoxides is highly reversible and generally thought to be nonrate-limiting, this behavior may be the result of a much slower ring-opening step of the metal−carbonate intermediate with the epoxide monomer, a process driven by k_4 in Scheme 4. Differential scanning calorimetry analysis of the

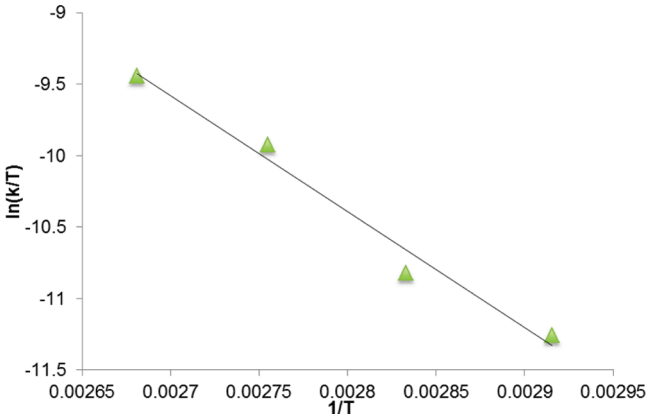


Figure 6. Eyring plot of the PA and CHO copolymerization reaction, with R^2 = 0.980.

resulting polymer revealed it to be a well-defined copolymer with two distinct T_g values (48 °C for PA/CHO and 115 °C PCHC).

The reaction rates for the copolymerization of cyclohexene oxide with various cyclic anhydrides observed under similar reaction conditions provided relative reactivities of CHA > PA > CHE. Additionally, employing the CHA monomer while varying the epoxide under identical reaction conditions afforded a reactivity trend of PO > CHO ≥ SO (Figure 8). The percent conversions were determined by integration of monomer ^{1}H NMR peaks vs polymer peaks. A representative series of ^{1}H NMR spectra for the CHA/PO copolymerization process is included in the Supporting Information. However, the four-membered cyclic ether, oxetane, was essentially unreactive under these reaction conditions.

Thermal Properties of Copolymers. The glass transition temperatures of the various polyesters synthesized from the monomers listed in Scheme 2 utilizing a (salen)CrCl/$PPNN_3$ catalyst system in toluene at 80 °C were determined by differential scanning calorimetry (DSC) analysis. These data, along with the corresponding molecular weight data for selected copolymers obtained from GPC measurements, are summarized in Table 2. As anticipated, the steric bulk of the pendant groups and rigidity of the monomeric structure have a direct effect on the T_g of the resultant polyester. That is, in general the T_g values increased with epoxides in the order CHO > SO > PO, and increased with cyclic anhydrides in the order CHE > PA ≥ CHA > MA > SA. Specifically, the glass transition temperature found for the polyesters formed from propylene oxide and CHE, PA, MA, and SA were +36, +41, −23, and −39 °C, respectively. Similarly, the copolymer provided by the alternative coupling of SA with CHO or SO displayed corresponding T_g values of 34 and 4.4 °C.

The range of T_g values achievable from the alternating ring-opening copolymerization of the studied epoxides and cyclic anhydrides is over 130 °C, with a high T_g of +95 °C for the copolymer from CHE and CHO and a low T_g of −39 °C for that produced from SA and PO. Furthermore, it has been shown that only a small percentage of cross-linking can drastically increase the T_g of resultant polyesters. In this regard, we have observed two vastly different T_g parameters (−23 and +28 °C) for maleic anhydride/propylene oxide copolymer samples obtained from very similar synthetic procedures. We speculate here that this is due to a spontaneous photo-dimerization reaction. Consistent with the suggestions is the

dx.doi.org/10.1021/ma2026385 | *Macromolecules* 2012, 45, 2242−2248

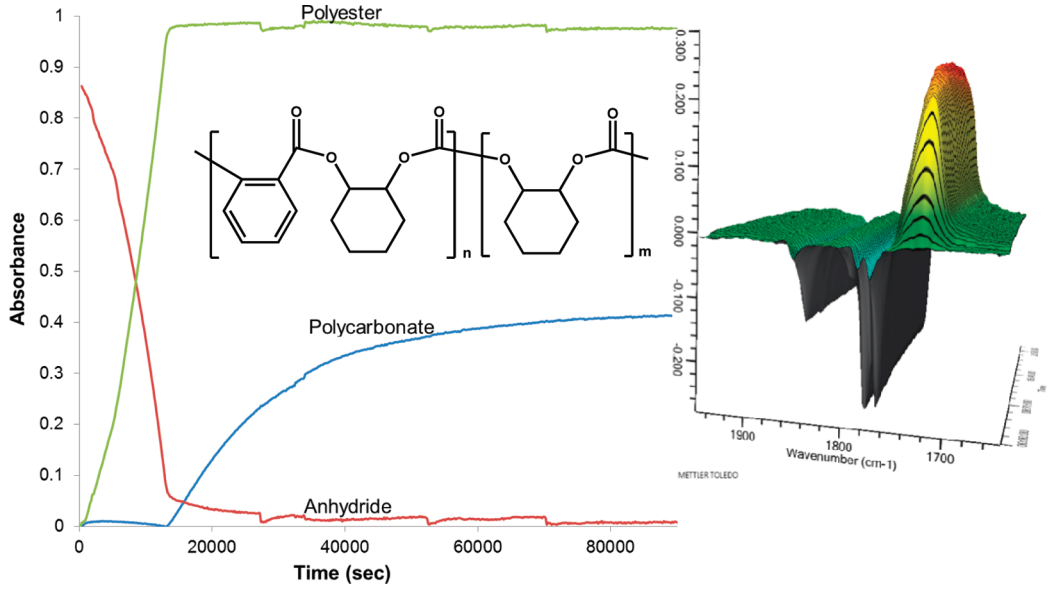
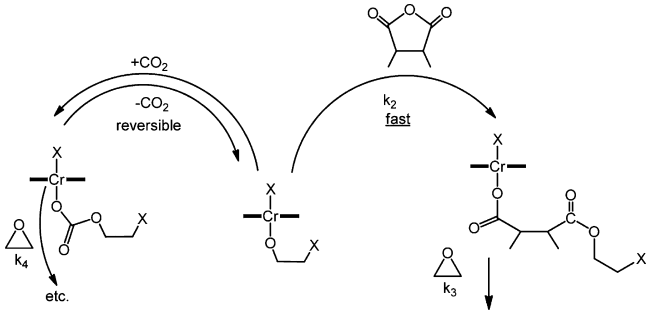


Figure 7. *In situ* FTIR analysis of block copolymerization process. Reaction conditions used were (salen)CrCl/PPNCl/PA/CHO = 1:1:200:600 under 500 psi CO_2, 80 °C with 19 mL toluene (solvent, volume totaling 25 mL). Deconvolution was performed by ReactIR ic10 software. Green line = polyester growth (1738 cm^{-1}), red line = anhydride consumption (1770 cm^{-1}), and blue line = polycarbonate growth (1750 cm^{-1}). The three-dimensional surface of the reaction is shown in the inset on the right.

Scheme 4



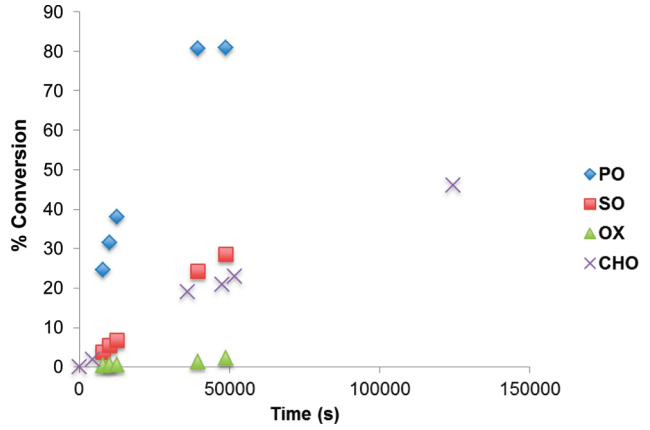


Figure 8. Comparison of epoxides: polymer growth vs time. Reactions were performed in sealed NMR tubes using 2.0 mL of toluene-d_8 as solvent. Then 200 equiv of the appropriate epoxide was added to tube, which was then dissolved in a stock solution of 1.8 mL of toluene-d_8, 300 mg of CHA (200 equiv), 6.3 mg of (salen)CrCl (1 equiv), and 5.7 mg of $PPNN_3$ (1 equiv). The tubes were then heated to 80 °C and allowed to react until 100% conversion was achieved.

observation that copolymers from MA and epoxides have the broadest polydispersity indices (~2.3) of all polyester synthesized in this report. That is, the other polyester synthesized displayed narrow polydispersity indices (<1.30) with M_w values of about 10 000 or greater.

Table 2. GPC and DSC Data for Selected Polyesters

polyester (cyclic anhydride/epoxide)	M_n ($\times 10^{-3}$)	M_w ($\times 10^{-3}$)	PDI	T_g (°C)[c]
CHE/CHO	10	14	1.34	95
CHA/CHO	9.2	9.7	1.06	85
CHE/SO	5.7	6.5	1.14	53
MA/CHO	8.5	20	2.3	53
PA/SO	19	24	1.27	46
PA/CHO[a]	18	20	1.13	48
PA/CHO[b]	14	15	1.07	–

[a]Sample was synthesized using both $PPNN_3$ and (salen)CrCl. [b]Sample was synthesized using only PPNCl as initiator. [c]T_g values represent the midpoint temperature during the second heating cycle.

CONCLUSIONS

Herein, we have reported kinetic studies of the alternating ring-opening copolymerization of various epoxides with cyclic acid anhydrides to afford polyesters of high molecular weights and narrow molecular weight distributions using a (salen)CrCl catalyst in the presence of onium salts. The activation parameters for the process involving phthalic anhydride/cyclohexene oxide monomers in toluene solution were determined to be $\Delta H^{\ddagger}$ = 67.5 kJ mol^{-1} and $\Delta S^{\ddagger}$ = −95.3 J mol^{-1}, where the rate-determining step was ring-opening of the epoxide by the enchained anhydride. For a given cyclic anhydride, cyclohexane anhydride, the relative rate of coupling with epoxide decreased in the order PO > CHO ≥ SO, whereas, for cyclohexene oxide the relative reactivity order with anhydrides was CHA > PA > CHE. This catalytic system was also shown to terpolymerize epoxide/cyclic anhydride/CO_2 to afford diblock copolymers with very little tapering, thereby providing a one-step synthesis of poly(ester-*co*-carbonate). In the polyester product resulting from the ring-opening polymer-

dx.doi.org/10.1021/ma2026385 | *Macromolecules* 2012, 45, 2242−2248

ization of maleic anhydride and propylene oxide two vastly different T_gs were observed at −23 and +28 °C. We have proposed the higher T_g value to be the result of some degree of cross-linking by photoinduced dimerization. Further efforts are being directed at providing a more definitive assessment of this possibility.

■ ASSOCIATED CONTENT

Supporting Information

Reaction scheme for cyclic anhydride/epoxide copolymerization initiated by onium salts alone, ^{1}H NMR spectra of all polyesters, and ^{1}H NMR monitoring of the copolymerization of cyclohexane anhydride and propylene oxide. This material is available free of charge via the Internet at http://pubs.acs.org.

■ AUTHOR INFORMATION

Notes

The authors declare no competing financial interest.

■ ACKNOWLEDGMENTS

We are grateful to the National Science Foundation (CHE 0543133 and CHE 1057743) and the Robert A.Welch Foundation (A-0923) for financial support for this work.

■ REFERENCES

(1) Williams, C. K.; Hillmyer, M. A. *Polym. Rev.* **2008**, *48*, 1.
(2) Lenz, R. W.; Marchessault, R. H. *Biomacromolecules* **2005**, *6*, 1−8.
(3) Chen, X.; Zhang, Y.; Shen, Z. *Chin. J. Polym. Sci.* **1997**, *15*, 262−272.
(4) Fischer, R. F. *J. Polym. Sci.* **1960**, *44*, 155−172.
(5) Lukaszczyk, J.; Jaszcz, K. *React. Funct. Polym.* **2000**, *43*, 25−32.
(6) Aida, T.; Inoue, S. *J. Am. Chem. Soc.* **1985**, *107*, 1358.
(7) Aida, T.; Sanuki, K.; Inoue, S. *Macromolecules* **1985**, *18*, 1049.
(8) Maeda, Y.; Nakayama, A.; Kawasaki, N.; Hayashi, K.; Aiba, S.; Yamamoto, N. *Polymer* **1997**, *38*, 4719.
(9) Jeske, R. C.; DiCiccio, A. M.; Coates, G. W. *J. Am. Chem. Soc.* **2007**, *129*, 11330.
(10) Coates, G. W.; Moore, D. R. *Angew. Chem., Int. Ed.* **2004**, *43*, 6618.
(11) Darensbourg, D. J.; Mackiewicz, R. M.; Phelps, A. L.; Billodeaux, D. R. *Acc. Chem. Res.* **2004**, *37*, 836.
(12) Darensbourg, D. J. *Chem. Rev.* **2007**, *107*, 2388.
(13) Kember, M. R.; Buchard, A.; Williams, C. K. *Chem. Commun.* **2011**, 141.
(14) DiCiccio, A. M.; Coates, G. W. *J. Am. Chem. Soc.* **2011**, *133*, 10724.
(15) (a) Huijser, S.; HosseiniNejad, E.; Sablong, R.; de Jong, C.; Koning, C. E.; Duchateau, R. *Macromolecules* **2011**, *44*, 1132−1139. (b) Huijser, S. Ph.D. Thesis, Eindhoven University of Technology: 2009; ISBN 978-90-386-1801-2.
(16) For an early review of kinetic studies of anionic copolymerization of cyclic ethers with cyclic anhydrides see: Luston, J.; Vass, F. *Adv. Polym. Sci.* **1984**, *56*, 92−133.
(17) Jeske, R. C.; Rowley, J. M.; Coates, G. W. *Angew. Chem., Int. Ed.* **2008**, *47*, 6041−6044.

Macromolecules

Article

pubs.acs.org/Macromolecules

Cyclic Guanidines as Efficient Organocatalysts for the Synthesis of Polyurethanes

Jérome Alsarraf,[†,‡] Yacine Ait Ammar,[†,‡,§] Frédéric Robert,[†,‡] Eric Cloutet,[§,⊥] Henri Cramail,*[,§,⊥] and Yannick Landais*[,†,‡]

[†]Univ. Bordeaux, ISM, UMR 5255, 33400 Talence, France

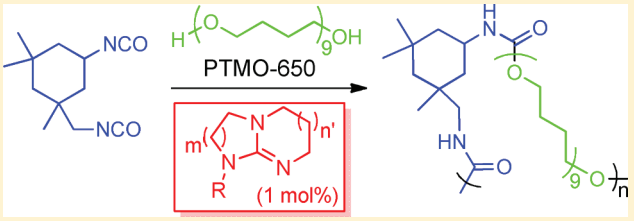
[‡]CNRS, ISM, UMR 5255, 33400 Talence, France

[§]Univ. Bordeaux, LCPO, UMR 5629, 33600 Pessac, France

[⊥]CNRS, LCPO, UMR 5629, 33600 Pessac, France

Supporting Information

ABSTRACT: A systematic survey of basic/nucleophilic organocatalysts for the polyaddition in bulk of polyols, PEG-600, and PTMO-650, to isophorone diisocyanate (IPDI) has been performed. Guanidines were shown to be very efficient catalysts for the urethane linkage formation. Bicyclic penta-alkylated guanidines such as MTBD led to polyurethane molecular weight and dispersity that are in the range of those observed with tin-based catalysts such as DBTDL. Tetra-alkylated guanidine such as TBD was shown to be a weaker catalyst as compared to pentaalkylated guanidines, as a result of its high reactivity toward isocyanate, resulting in the formation of a less nucleophilic urea. Although the mechanism has not yet been firmly established, these experiments suggest that a nucleophilic-catalysis mechanism, involving the attack of one of the nitrogen of the guanidine onto the unsaturated system of the isocyanate, should not be totally ruled out with such strong Brönsted base catalysts.



INTRODUCTION

Polyurethanes constitute an important class of polymeric materials, estimated around 5 wt % of the current world polymer production[1] with numerous technical applications (foams, coatings, biomaterials, fibers, etc.). Polyurethanes are usually prepared, based on the original discovery of Bayer[2] by the most straightforward route involving the addition of polyols to polyisocyanates in the presence of a catalyst. Organometallic reagents or tertiary amines are commonly employed to mediate this polyaddition. Dibutyltin dilaurate (DBTDL) is the most active catalyst currently in use,[3] but environmental concerns should lead, in not too distant a future, to a ban of such toxic organometallic reagents.[4] The presence of heavy metals in the resulting polymer also has detrimental effects on the aging of the final material. Recent efforts in polymer synthesis have thus focused on the design of organocatalysts that could advantageously replace metal-based catalysts.[5] Small organic molecules, including carbenes, thioureas, and guanidines (TBD) were thus shown to drive various polymerizations, enabling good selectivities, relatively high rates[6] and excellent functional group tolerance. Polyurethane synthesis is well-known to be catalyzed by tertiary amines, such as 1,4-diazabicyclo[2.2.2]octane (DABCO), 2,2′-bis-(dimethylaminoethyl ether) (BDMAEE) or amidines such as 1,8-diazabicyclo[5.4.0]undec-7-ene (DBU).[7] However, none of these organocatalysts have permitted yet reaching the reaction rates attained with tin reagents. The search for more efficient catalysts that would also display delayed catalytic activity allowing the premixing of the monomers is thus continuing and has concentrated a lot of efforts recently.[8] In the course of our investigations on the synthesis of biosourced polyurethanes,[9] we studied the catalytic activities of several nitrogen-based organocatalysts. Among the various small organic activators that were tested, cyclic guanidines were shown to exhibit attractive catalytic activities, rivaling with the commonly used dibutyltin dilaurate (DBTDL). We provide here a preliminary account of these studies, including the selection of the best catalysts using polymerization in bulk and a comparison with closely related amidines DBU and DBN.

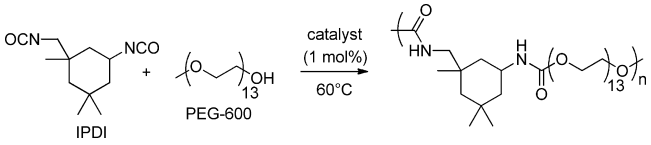
RESULTS AND DISCUSSION

Screening of Organocatalysts in Polyurethane Synthesis Using IPDI and PEG-600 (or PTMO-650) as Precursors. The synthesis of PU from equimolar amounts of commercially available isophorone diisocyanate (IPDI) and dried poly(ethylene glycol) 600 (PEG-600) (Scheme 1) was first studied using a panel of structurally and functionally different basic/nucleophic organocatalysts **2**−**8** (1 mol %) (Scheme 2). DABCO and DBU, standard catalysts for PU synthesis, were thus studied, as well as amino-pyridine and guanidines, including acyclic guanidines **7a**,**b** and guanidine dimer **8** (obtained by coupling TBD **2a** with 1,4-bis-

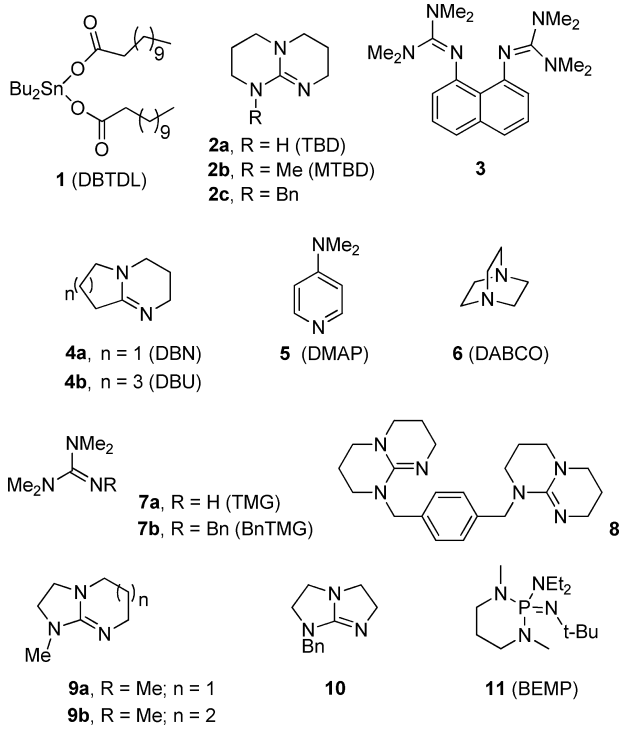
Received: December 6, 2011
Revised: January 22, 2012
Published: February 21, 2012

 © 2012 American Chemical Society

Scheme 1. Organocatalyzed Synthesis of Polyurethane (PU) from IPDI and PEG-600



Scheme 2. Structure of Organocatalysts 2−11



(bromomethyl)benzene) (Supporting Information). Dibutyltin dilaurate **1** was used as a reference. IPDI and PEG-600 were investigated as to perform the reaction in bulk at 60 °C, the low viscosity of the polymer formed allowing aliquots sampling and monitoring of the reaction using FT-IR. Reaction progress was estimated by measuring the disappearance of the NCO and OH stretching vibrations at 2252 and 3464 cm^{-1}, respectively, and the formation of the intense urethane C═O bond at 1715 cm^{-1} as a function of time. Quantification was carried out, relying on the unchanged absorption of CH_2 bonds at 2867 cm^{-1}. From these preliminary experiments, summarized in Figure 1, most catalysts were found to be active in the polyaddition of PEG-600 with IPDI, leading to PUs with complete conversion after 1 h, all catalysts leading to 50% conversion after less than 45 min. Amidines and guanidines clearly emerged as superior catalysts. Strikingly, strongly basic and nucleophilic guanidine MTBD **2b** and amidine DBU **4b** were both found to be more active than DBTDL, leading to complete conversion after only 15 min. They exhibit remarkable catalytic activities as compared to other less basic, hence nucleophilic heterocycles including substituted DMAP **5** and DABCO **6**, which required almost 5 h to reach completion. In contrast, guanidine **2a** (TBD) which was recently reported to be an excellent catalyst for polyester synthesis, acting through an original dual activation,[10] and for polyurethane synthesis[11] displayed poor activity as compared to *N*-alkylated guanidine **2b**. This behavior contrasts with the observations of Waymouth and Hedrick during catalyzed ring-opening polymerization of lactides and lactones, where **2a** was reported to be more efficient than **2b**.[12] Acylic guanidines **7a**,**b** were slightly less reactive.[13] It is worth noticing that the presence of a free imino group in **7a** had no effect on the rate of the reaction (*vide infra*). Finally, the dimer **8** showed the same reactivity than MTBD when used in only 0.5 mol %. PU characteristics, with respect to molecular weight and molecular weight distribution obtained from SEC analysis are given in Table 1. These data of PU samples quenched with methanol after 18 h clearly demonstrate the efficiency of the organocatalysts in comparison to DBTDL **1** (entries 2−3). In all cases, PUs with reasonable high molecular weights could be obtained, in particular when mechanical stirring was used to overcome the viscosity increase (entries 3, 6, 7, 9). PUs were carefully analyzed through FT-IR spectroscopy (see Supporting Information). Whatever the catalyst used, all PUs exhibit similar molecular IR spectra without detectable isocyanurate, allophanate or urea bands that prove the high selectivity of the tested organocatalysts. It is finally worth adding that treatment of polyurethanes with **2b** in the presence of EtOH was tested and led to no noticeable changes in the ^1H NMR spectrum, demonstrating that guanidine **2b** does not catalyze the transurethanization reaction.

The scope of applications of the catalyzed PU synthesis was then further extended to the polymerization of IPDI and poly(tetramethylene oxide) (PTMO-650) restricting our study to the most efficient amidine and guanidine catalysts (1 mol %) (Scheme 3). As above, equimolar amounts of IPDI and PTMO-650 were reacted in bulk at 60 °C in the presence of various organocatalysts. Time course of the reaction, summarized in Figure 2, confirm the general trend observed in the previous polymerization experiment. While the activity of the tin catalyst **1** does not seem to be affected by traces of water present in commercial PTMO-650 (entry 1, Table 2), such was not the case with guanidines. Overlapping FT-IR spectra of PU prepared using tin catalyst **1** and MTBD **2b** showed no significant difference, except a small enlargement of the band at 1716 cm^{-1} due to the presence of traces of urea (see Supporting Information). This could be considerably reduced through purification by azeotropic distillation (toluene) of PTMO-650 before use. As indicated by experiments in entry 4 (vs entry 3), PU of higher molecular weights were repeatedly obtained upon catalysis with **2b**, when water was removed from the diol prior to the reaction. Use of a slight excess of IPDI also provided higher molecular weight (entry 5), proving that some NCO function is generally lost through secondary reactions, in particular reaction with water traces (leading to urea). MTBD **2b** was found to be as active as DBTDL, leading to a complete conversion after 1 h. Interestingly, **2b** and its dimeric analogue **8** displayed much higher reactivity than the unsubstituted TBD **2a** (entry 3 and 10 vs 2), in contrast with precedent in the literature.[10,11] The analogous DBN **4a** (entry 8) showed a surprising behavior with a very fast initial polymerization rate, leading to more than 50% of the conversion of NCO functions after 1 min and then a complete loss of activity, suggesting that inhibition of the catalyst occurs very rapidly (*vide infra*). The superbasic "proton sponge" but poorly nucleophilic naphthylbisguanidine (TMGN) **3**,[14] surprisingly led to a poor catalytic activity. Considering the high efficiency of the cyclic penta-alkyl guanidine catalysts **2a**−**c** in the PU synthesis, new bicyclic guanidines, having different ring sizes, were prepared[12b,15] (Supporting Information) and tested in the con-

dx.doi.org/10.1021/ma2026258 | *Macromolecules* 2012, 45, 2249−2256

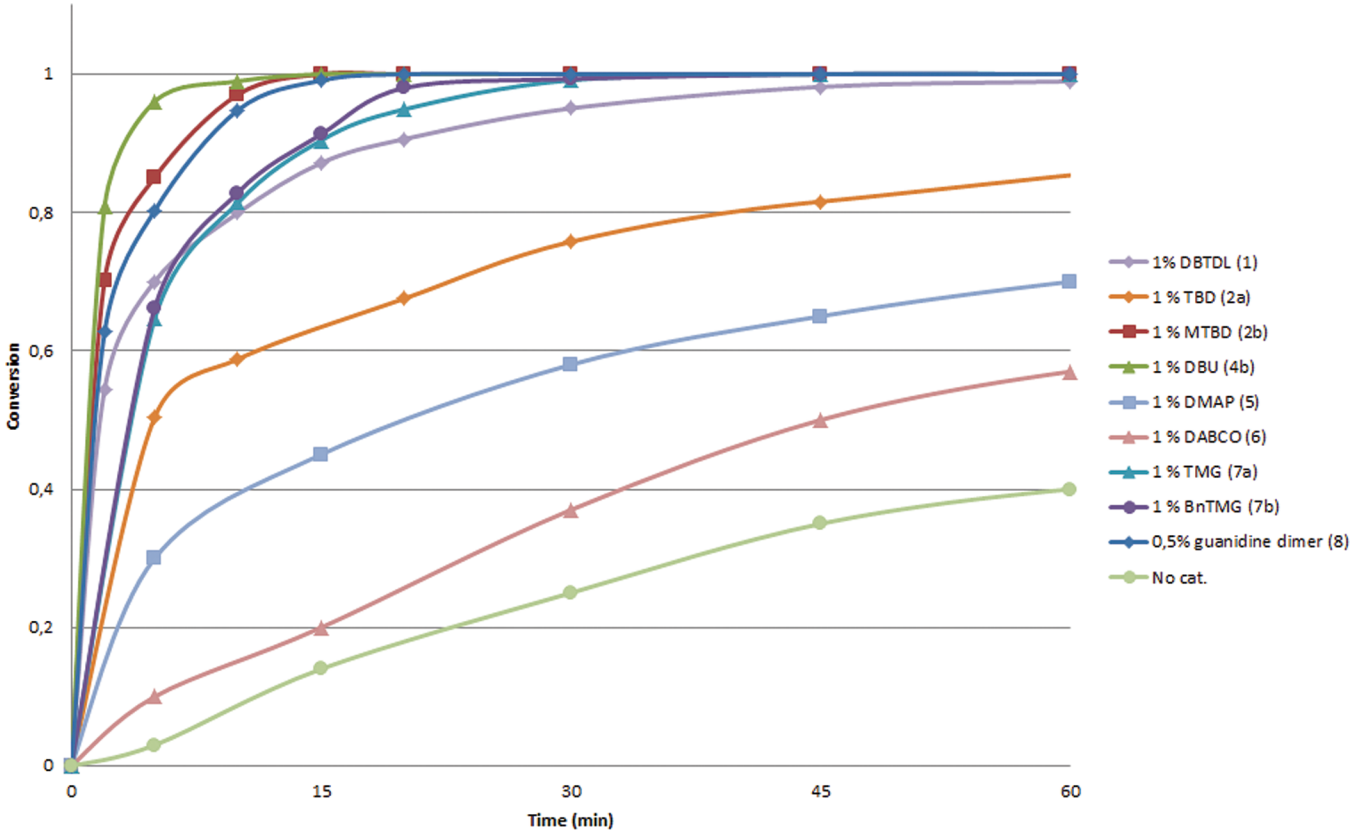


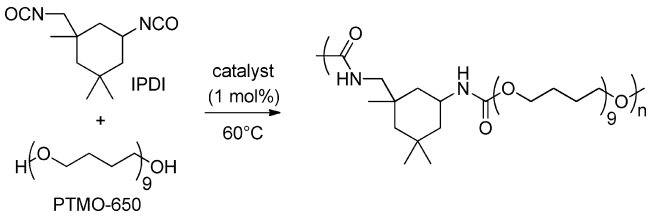
Figure 1. Screening of various organocatalysts in the synthesis of PU from IPDI and PEG-600.

Table 1. Synthesis of Polyurethanes from Bulk Polyaddition of IPDI and PEG-600 (Stoichiometric Ratio) in the Presence of Organocatalysts 2−8 at 60°C

entry	catalyst[a]	M_w (g mol^{-1})[b,c]	M_n (g mol^{-1})[b,c]	$D = M_w/M_n$[c]
1	no catalyst	35 000	25 000	1.40
2	DBTDL **1**	48 100	33 400	1.44
3[d]	DBTDL **1**	54 000	34 600	1.56
4	**2a**	28 900	21 700	1.33
5	**2b**	33 700	24 800	1.36
6[d]	**2b**	48 000	33 100	1.45
7[d]	**4b**	74 000	39 800	1.89
8	**7a**	29 800	22 400	1.33
9[d]	**7a**	43 000	30 100	1.43
10	**7b**	29 300	22 000	1.33
11	**8**[e]	31 250	23 300	1.34

[a]1 mol % of catalyst was used. [b]Aliquots of PU were taken after quenching the reaction mixture with MeOH (after 18 h of stirring). [c]Estimated through SEC analysis onto PU samples quenched as above; DMF as eluent with PS standards. [d]Performed using a mechanical stirrer. [e]0.5 mol % of dimeric catalyst **8** was used.

Scheme 3. Organocatalyzed Synthesis of Polyurethane (PU) from IPDI and PTMO-650



densation between IPDI and PTMO-650. The size of the ring of the different guanidines was found to have an effect on the polymerization rate. Guanidine **10** thus led to a lower activity than the larger analogues **9a** and **9b** (entry 11−13), with incomplete conversion of NCO moieties even after 3 h, indicating that an amidyl functional group (N−CH═N) embedded in a 6- or 7-membered ring is required to get efficient catalysis. As above, dimeric **8** at 0.5 mol % showed the same reactivity than **2b**. Highly basic phosphazene **11**[15] led to reasonable catalytic activity, albeit lower than that observed with guanidines (entry 14). Finally, the reaction afforded the PU with complete conversion after 6 h at 60 °C using only 0.05 mol % of MTBD **2b**, demonstrating the high efficiency of such guanidines (entry 15). As already discussed with PEG-600 as diol monomer, Table 2 below indicates that polymerization in the presence of guanidines provide PUs having satisfying molecular weights. These studies demonstrate unambiguously that substituted guanidines exhibit unprecedented catalytic activities in polymerization of diols and di-isocyanates, whatever the nature of the monomer with catalyst loading as low as 0.05 mol %.

Preliminary Mechanistical Investigations. Two mechanisms have been proposed to rationalize the course of the base/nucleophile-catalyzed addition of alcohols onto isocyanates, which are still subject to controversy. The first kinetic studies by Baker et al.[16] suggested that a nucleophilic catalysis was involved, with the addition of the catalyst onto the N═C═O functional group as a preliminary step (nucleophilic catalysis mechanism). More recent studies[17] showed that this mechanism is not general and that activation of the alcohol by the basic catalyst (general base catalysis mechanism) more appropriately describes the addition of an alcohol onto an

dx.doi.org/10.1021/ma2026258 | *Macromolecules* 2012, 45, 2249−2256

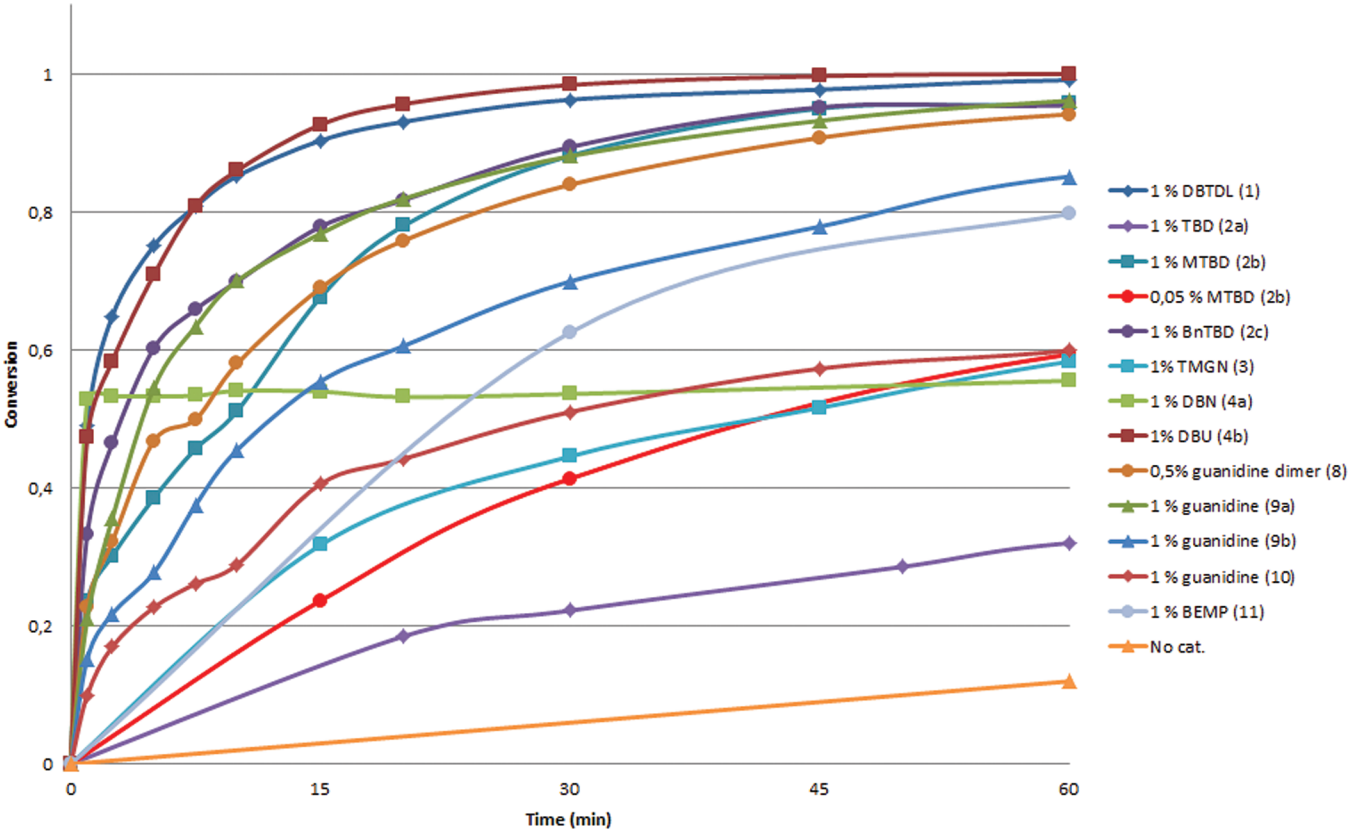


Figure 2. Screening of various organocatalysts in the synthesis of PU from IPDI and PTMO-650.

Table 2. Polyaddition of IPDI and PTMO-650 using organocatalysts 2a–c, 4a,b, 8–10

entry	catalyst[a]	convn (%)[b]	M_w (g mol^{-1})[c,d]	M_n (g mol^{-1})[c,d]	$D = M_w/M_n$[d]
1[e]	DBTDL **1**	>98	93 000	67 900	1.37
2[e]	**2a**	82	21 000	14 200	1.48
3[e]	**2b**	>98	36 000	26 700	1.35
4[f]	**2b**	>98	50 200	32 600	1.54
5[g]	**2b**	>98	85 000	58 600	1.45
6[e]	**2c**	>98	42 700	29 400	1.45
7[e]	**3**	>98	28 250	18 800	1.50
8[e]	**4a**	86	-	-	-
9[e]	**4b**	>98	31 500	20 700	1.52
10[e]	**8**[h]	>98	32 300	21 500	1.50
11[e]	**9a**	>98	41 600	27 500	1.51
12[e]	**9b**	>98	50 400	32 500	1.55
13[e]	**10**	>98	33 800	21 900	1.54
14[e]	**11**	>98	29 600	19 500	1.52
15[e]	**2b**[i]	>98	55 000	34 800	1.58

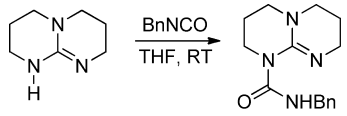
[a]1 mol % of catalyst was used. [b]Estimated by measuring, using FT-IR, the disappearance of the isocyanate N=C = O band. [c]Aliquots of PU were taken after quenching the reaction mixture with MeOH (after 18 h of stirring). [d]Estimated through SEC analysis; DMF as eluent with PS standards. [e]The PTMO-650 used was not dried before polymerization. [f]The PTMO-650 used was carefully dried through azeotropic distillation in toluene before polymerization. [g]1.1 equiv of IPDI was used for 1 equiv of commercial PTMO-650. [h]0.5 mol % of **8** was used. [i]0.05 mol % of **2b** was used.

isocyanate.[18] Several refinements on the latter mechanism (complete proton transfer or concerted single step proton transfer followed by nucleophilic attack) have also been proposed. Finally, dual activation of the alcohol and the isocyanate may also be invoked. Recent reports on this latter mode of action have been reported, for instance in ROP of lactides.[10,19] In order to get better insights into the mechanism of the guanidine-catalyzed addition of alcohols onto isocyanates, a series of experiments with guanidine **2a–b** was thus performed using 2,3-dimethoxyphenethyl alcohol and benzyl isocyanate (BnNCO) as model compounds in solution (Supporting Information). For instance, ^{1}H NMR of an equimolar mixture of this alcohol model and **2b** revealed proton chemical shifts for the alcohol hydrogen, which indicates that hydrogen bonded complex MTBD-2,3-dimethoxyphenethyl alcohol might be involved at some stage (Supporting Information).[10,20] However, activation through general base catalysis should also imply that the reaction rate increases with the basicity of the catalyst.[21] As shown above, catalytic activities of organocatalysts follow the order: DABCO **6** < DMAP **5** (17.95) < TBD **2a** (26.03) < TMGN **3** (25.4) < BEMP **11** (27,5) < TMG **7a** (23.3) ~ BnTMG **7b** < MTBD **2b** (25.43) ~ DBU **4b** (24.33), which does not fit with the corresponding pK_a's (in CH_3CN).[21,22] It is thus worthy of note that bis-guanidine **3** (TMGN) and phosphazene **11** led to poor activity despite their strong basicity (Figure 2). The difference in catalytic activity between TMGN **3** and MTBD **2b**, which exhibit similar pK_a's (25.4 and 25.43 respectively) during polymerization of IPDI and PTMO-650 (Figure 2), is also striking, suggesting that other mechanism(s) than general base catalysis may operate.[10] Additional experiments led us speculate that a nucleophilic mechanism should not be completely ruled out (*vide infra*). For instance, the low nucleophilicity of **3**, due to steric hindrance around the nitrogen centers would explain its low catalytic activity, supporting such a mechanism. Figures

dx.doi.org/10.1021/ma2026258 | *Macromolecules* 2012, 45, 2249–2256

1 and 2 also show that TBD **2a**, which is more basic than MTBD **2b** and TMG **7a**, is comparatively a weaker catalyst. This was ascribed to the ability of **2a** to react with isocyanates. We thus observed that reaction of a 1:1 mixture of **2a** and BnNCO, led to the rapid formation of the corresponding urea **12** (Scheme 4).[23] Interestingly, the latter was shown to catalyze

Scheme 4. Reaction of TBD 2a with Benzylisocyanate

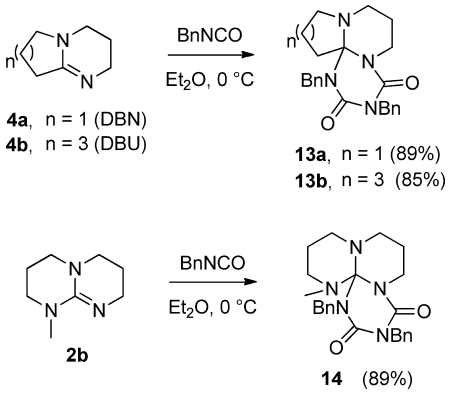


2a **12** (89%)

the formation of polyurethanes from IPDI and PTMO-650 at 60 °C (Figure 3), with the same efficiency than TBD **2a** alone, suggesting that the formation of PU is probably catalyzed by an urea such as **12** and not by **2a**.[11,13] This also indicates that guanidines are likely to react with isocyanates in the presence of alcohols in the medium (*vide infra*). The reduced catalytic activity of **2a** as compared to the alkylated analogue **2b**, would be due to the presence of the electron-withdrawing C(=O)NHR moiety, as in **12**, which likely decreases the electron density on the guanidine framework, reducing both the basicity and the nucleophilicity of **2a**. The high reactivity of TBD toward electrophiles (including CO_2)[24] also implies that impurities in the medium might reduce its catalytic activity. Repeating the polymerization using freshly sublimated TBD **2a** however led to similar results than those obtained with unpurified commercial TBD (Figure 3).

Finally, reasoning that amidines **4a,b** might catalyze the above reaction through a mechanism similar to that of guanidines, the reactivity of **4a,b** toward isocyanates was studied, treating both amidines with BnNCO. Pleasingly, this led to the formation, in good yields, of tricyclic compounds **13a,b** incorporating two molecules of BnNCO (Scheme 5).[25] Similarly, guanidine **2b** provided under the same conditions, compound **14** in high yield.[26] Interestingly, when **13a**, **13b**, and **14** were left in THF under reflux in the presence of a primary

Scheme 5. Reactions of 2b and 4a,b with BnNCO



4a, n = 1 (DBN)
4b, n = 3 (DBU)

13a, n = 1 (89%)
13b, n = 3 (85%)

2b

14 (89%)

alcohol such as 3,4-dimethoxyphenethyl alcohol used previously, they exhibited contrasting behavior. While **13a** and **13b** were stable under these conditions, **14** returned guanidine **2b** along with the corresponding carbamate (Supporting Information). The rapid deactivation of **4a** during reaction of IPDI and PTMO-650 (Figure 2) might thus be explained by the irreversible formation in the medium of an adduct between **4a** and IPDI, similar to **13a**. The difference in reactivity between DBN **4a** and DBU **4b** (Figure 2) is striking and may be rationalized invoking a much higher reactivity of **4a** toward isocyanates as compared to **4b**. Although calorimetric experiments have not been performed, we noticed that addition of BnNCO onto **4a** was much more exothermic than that with **4b**. As the formation of **13a** is not reversible, no free amidine **4a** remains in the medium during polymerization, thus explaining its *in situ* deactivation after less than 1 min. This also shows that the free amidine is the real catalyst in this case, in contrast to TBD **2a** where the urea adduct, **12**, catalyzes the reaction. This difference in reactivity between closely related bicyclic amidines points out again the importance of the ring size in these bicyclic organocatalysts. The difference in stability between adducts **12** and **14** issued from guanidines and **13a,b** generated from amidines is also of interest and suggests that cyclic *N*-alkylguanidines such as **2b** should be superior and selective

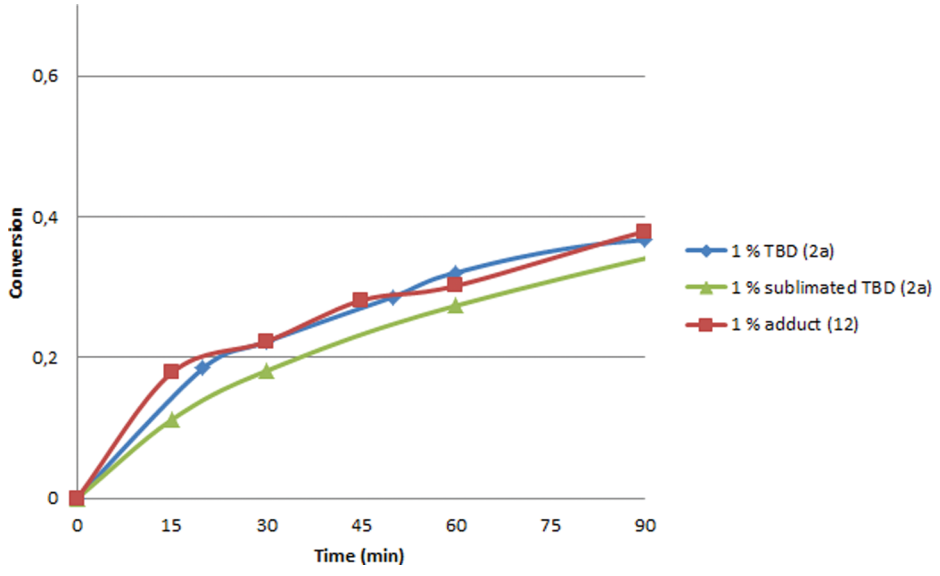


Figure 3. Organocatalyzed polymerization of IPDI and PTMO-650 in the presence of **2a** and urea **12**.

dx.doi.org/10.1021/ma2026258 | *Macromolecules* 2012, 45, 2249–2256

catalysts, whatever the reactivity of isocyanates, as their adducts form reversibly, thus allowing the catalysis, which is not the case with amidine adducts such as **13a,b**.

In order to obtain further mechanistical insights, we finally varied the order of addition of the reagents and catalysts (**2b**) and compare these new conditions (conditions B and C, Figure 4) with those used previously (conditions A, Figure 1 and 2).

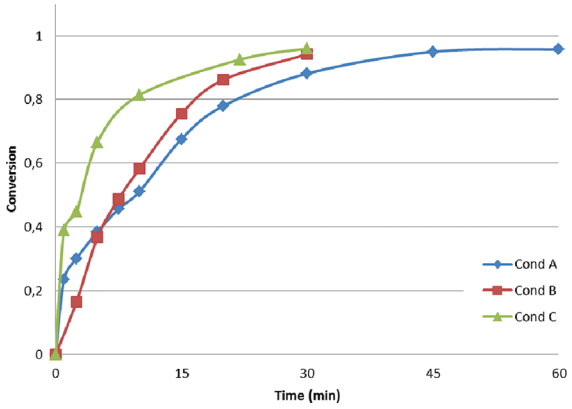


Figure 4. Organocatalyzed polymerization of IPDI and PTMO-650 varying the order of addition. Condition A: IPDI and PTMO-650 are premixed at 20 °C, then MTBD **2b** is added, and the reaction mixture is heated to 60 °C. Condition B: catalyst **2b** is premixed with IPDI at 20 °C before the addition of PTMO-650. The reaction mixture is then heated to 60 °C. Condition C: catalyst **2b** is premixed with PTMO-650 at 20 °C before the addition of IPDI. The reaction mixture is then heated to 60 °C.

For instance, when guanidine **2b** was premixed with IPDI before the addition of the alcohol (condition B), one observes a rather slow initiation period, that may be attributed to the *in situ* formation of an adduct such as **14**, which decomposition would be necessary to restore the catalytic activity. In turn, when **2b** was premixed with the alcohol (PTMO, conditions C), the reaction was found to be slightly faster as compared to conditions A and also led to PU with higher molecular weight (Table 3). This may be explained by an H-bonding activation

Table 3. Organocatalyzed Polymerization of IPDI and PTMO-650 Varying the Order of Addition

conditions	convn (%)[a]	M_w (g mol^{-1})[b,c]	M_n (g mol^{-1})[b,c]	$D = M_w/M_n$[c]
conditions A	>98	36 000	26 700	1.35
conditions B	>98	28 700	18 400	1.56
conditions C	>98	61 300	38 800	1.58

[a]Estimated by measuring, using FT-IR, the disappearance of the isocyanate N=C=O band. [b]Aliquots of PU were taken after quenching the reaction mixture with MeOH (after 18 h of stirring). [c]Estimated through SEC analysis; DMF as eluent with PS standards.

of the alcohol by the guanidine (similar to the MTBD-3,4-phenethyl alcohol complex above), that would accelerate the addition of the alcohol onto the isocyanate, and in the same time, prevent the formation of an adduct such as **14** mentioned above.

In summary, we have shown that addition of diols onto diisocyanates is efficiently catalyzed by guanidines, leading to polyurethanes with high molecular weight. Cyclic guanidines are slightly more reactive than acyclic ones as in the former, the ring constrains the nitrogen into a conformation where the lone pairs are properly aligned to favor lone pairs delocalization.[27] Preliminary mechanistical investigations provide some original and unexpected features of this catalysis with the isolation of adducts issued from the nucleophilic addition of guanidines onto isocyanates. Similar behavior was observed with amidines. Although the presence of these adducts in the medium in the presence of the alcohol partner has not been firmly proved (*vide supra*), these investigations suggest that the nucleophilic catalysis mechanism should not be *a priori* ruled out with these strongly basic catalysts. This would involve an initial nucleophilic attack of the guanidine onto the isocyanate C=O functional group[28,29] (nucleophilic monomer activation), followed by the reaction of the activated zwitterionic acyl intermediate with the alcohol partner to provide the urethane linkage (Figure 5). Activation of the alcohol by a general base

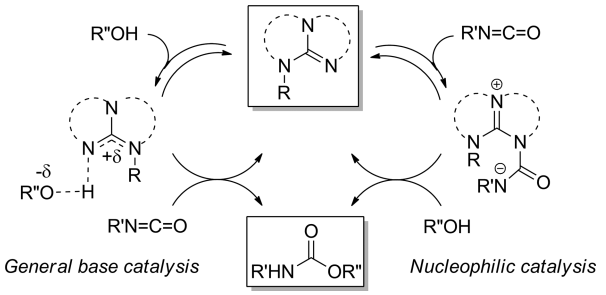


Figure 5. Catalytic cycles for the formation of the urethane linkage using guanidines as organocatalysts.

catalysis mechanism may also operate as suggested by ^{1}H NMR studies on model alcohols. It is also worth adding that the order of addition of the different partners might also influence the mechanistical outcome of the process as shown by experiments summarized in Figure 4 and Table 3. Further kinetic investigations along with theoretical studies at the DFT level will thus be needed to definitely establish the mechanism of these guanidine-catalyzed PU synthesis. Studies along these lines are now underway in our laboratory.

CONCLUSION

We have reported along these lines the efficiency of cyclic guanidines as catalysts in the polyaddition of diols onto diisocyanates. Relatively high molecular weight polyurethanes with a good control of the molecular structure are obtained without the formation of allophanates or isocyanurates moieties. A straightforward preparation of guanidines has been devised enabling an easy access to a wide range of new guanidine structures. Elaboration of new guanidines based on readily available TBD **2a** and synthesis of 5-membered ring guanidines such as **9** and **10** offers an alternative route to further extend the screening. Efforts are now focusing on kinetic studies to get insights into the mechanism of this catalyzed PU synthesis and on the design of novel and more efficient catalysts.

EXPERIMENTAL SECTION

General Information. All reactions were carried out under an argon atmosphere with dry solvents under anhydrous conditions, unless otherwise noted. Yields refer to chromatographically and spectroscopically (^{1}H and ^{13}C NMR) homogeneous materials, unless otherwise stated. Commercial reagents were used without further purification, unless otherwise stated. ^{1}H NMR and ^{13}C NMR were recorded on a Brüker AC-300 FT and (^{1}H: 300 MHz, ^{13}C: 75.46

dx.doi.org/10.1021/ma2026258 | Macromolecules 2012, 45, 2249–2256

MHz) and a Brüker ARX-400 FT (^{1}H: 400 MHz, ^{13}C: 100.6 MHz) using $CDCl_3$ as internal reference unless otherwise indicated. The chemical shifts (δ) and coupling constants (J) are expressed in ppm and Hz, respectively. The following abbreviations were used to explain the multiplicities: s = singlet, d = doublet, t = triplet, q = quartet, quint = quintet, m = multiplet, br = broad. IR spectra were recorded on a Perkin-Elmer 1710 spectrophotometer, on a Perkin-Elmer Paragon 500 FT-IR spectrophotometer or on a Perkin-Elmer Mattson Unicam 500 16PC FT-IR using a ZnSe crystal ATR accessory. High resolution mass spectra (HRMS) were recorded with a Q-TOF 2 spectrometer in the electrospray ionization (ESI) mode. Melting points were not corrected and determined by using a Büchi Totolli apparatus. Merk silica gel 60 (70−230 mesh) was used for flash chromatography. Size exclusion chromatography (SEC) analyses were performed at room temperature in DMF at 80 °C with a setup consisting of a PL-GPC 50 plus Integrated GPC from Polymer laboratories-Varian and a series of three columns PLgel 5 μm MIXED-D. The elution of the filtered samples was monitored using simultaneous UV and refractive index detections. The elution times were converted to molar mass using a calibration curve based on low dispersity (M_w/M_n) polystyrene (PS) standards.

General Procedure for the Synthesis of Polyurethanes. IPDI (0.8 mL, 3.78 mmol) was added to PTMO-650 (2.45 g, 3.78 mmol) at room temperature. A solution of catalyst (75.5 μmol, 0.02 mmol) in THF (0.5 mL) was then added and the mixture stirred at 60 °C. Aliquots were taken at various period of time and FT-IR spectra recorded to monitor the time course of the reaction (see Figure 2 and Supporting Information). After 18 h, the reaction mixture was quenched with methanol and the polymer analyzed using SEC (Table 2).

Synthesis of Urea 12. Benzylisocyanate (200 μL, 1.63 mmol) was added dropwise to a solution of TBD **2a** (227 mg, 1.63 mmol) in THF (6 mL) leading to an exothermic reaction. The homogeneous reaction mixture was stirred 1 h at room temperature (*ca.* 17 °C). The solvent was then removed under vacuum affording a viscous oil. A small amount of ether was then added to precipitate traces of unreacted **2a**. The solid was removed by filtration and the filtrate was concentrated under vacuum to afford the expected product **12** as a pale yellow oil (397 mg, 89%). IR (neat): υ = 2932, 2852, 1664, 1543, 698 cm^{-1}. ^{1}H NMR (C_6D_6, 300 MHz): δ = 12.2 (br s, 1H), 7.44−7.37 (m, 2H), 7.19−7.09 (m, 2H), 7.07−6.99 (m, 1H),4.68 (d, J = 5.6 Hz, 2H), 3.83−3.75 (m, 2H), 3.19 (t, J = 5.7 Hz, 2H), 2.42 (t, J = 6.2 Hz, 2H), 2.23 (t, J = 6.5 Hz, 2H), 1.29 (qt, J = 6.4 Hz, 2H), 1.25−1.15 ppm (m, 2H). ^{13}C NMR (C_6D_6, 75 MHz): δ = 157.0, 149.8, 141.2, 127.9, 126.8, 49.0, 48.4, 44.7, 43.2, 40.1, 22.8, 22.2 ppm. HRMS (ESI): m/z calcd for $C_{15}H_{21}N_4O$ $[M + H]^+$, 273.1715; found, 273.1712.

General Procedure for the Synthesis of Adducts 13a,b, 14. Benzylisocyanate (1.9 mmol) was added dropwise to a solution of amidine (or guanidine) (1 mmol) in Et_2O (1 mL) at 0 °C. The homogeneous reaction mixture was then stirred 5 min at 0 °C. After recrystallization of the crude mixture at −40 °C, the crystals were filtered and washed with a small amount of ether affording the expected compound as colorless solid.

MTBD-2 BnNCO Adduct (14). Mp = 96−97 °C (THF/pentane). IR (neat): υ = 2925, 1683, 1645, 1470, 1377, 751, 700 cm^{-1}. ^{1}H NMR (C_6D_6, 300 MHz): δ = 7.79−7.73 (m, 2H), 7.56−7.50 (m, 2H), 7.25−7.01 (m, 6H), 5.31 (dd, J = 11.7 Hz, J = 13.7 Hz, 2H), 5.06 (d, J = 14.1 Hz, 1H), 4.63−4.52 (m, 1H), 4.35 (d, J = 14.1 Hz, 1H), 2.55−2.42 (m, 2H), 2.30−2.08 (m, 4H), 1.79 (s, 3H), 1.72−1.47 (m, 2H), 1.25−1.08 ppm (m, 3H). ^{13}C NMR (C_6D_6, 75 MHz): δ = 153.7, 151.4, 140.5, 139.1, 130.0, 129.4, 128.5, 127.5, 126.9, 97.3, 47.8, 46.8, 45.7, 45.1, 42.2, 36.4, 35.7, 23.3, 20.5 ppm. HRMS (ESI): m/z calcd for $C_{24}H_{30}N_5O_2$ $[M + H]^+$, 420.23995; found, 420.2396.

■ ASSOCIATED CONTENT

Supporting Information

General experimental procedures and information, synthesis and spectroscopic data for guanidines **9a,b**, **10**, time course experiments, and the corresponding FT-IR and ^{1}H NMR data. This material is available free of charge via the Internet at http://pubs.acs.org

■ AUTHOR INFORMATION

Corresponding Author

*(H.C.) E-mail: cramail@enscbp.fr. Fax: (+ 33) 05 40 00 84 87. (Y.L.) E-mail: y.landais@ism.u-bordeaux1.fr. Fax: (+ 33) 05 40 00 62 86.

Notes

The authors declare no competing financial interest.

■ ACKNOWLEDGMENTS

We thank the French "Agence Nationale de la Recherche" (ANR-09-CP2D-15), and the French Ministry of Research and Technology for financial support.

■ REFERENCES

(1) (a) Oertel, G. *Polyurethane Handbook*; Hanser Publishers: Munich, Germany, 1985. (b) Wirpska, Z. *Poly(urethane)s: Chemistry, Technology, and Application*: Ellis Horwood: London, 1993. (c) Becker, R. L. Thiele, *Isocyanate reactions in Polyurethane catalysis*: CRC Press, Inc.: Boca Raton, FL, 1996; p 6940. (d) Hepburn, C. *Polyurethane Elastomers*; Springer: Berlin, 1992.

(2) (a) Bayer, O. *Angew. Chem.* **1947**, *59*, 257−272. (b) Bayer, O.; Müller, E. *Angew. Chem.* **1960**, *72*, 934−939.

(3) (a) Lipatova, T. E.; Bakalo, L. A.; Niselsky, Yu N.; Sirotinskaya, A. L. *J. Macromol. Sci.—Chem.* **1970**, *A4* (8), 1743−1758. (b) Frisch, K. C.; Rumao, L. P. *J. Macromol. Sci.—Rev. Macromol. Chem.* **1970**, *5c*, 103−149. (c) Luo, S. G.; Tan, H. M.; Zhang, J. G.; Wu, Y. J.; Pei, F. K.; Meng, X. H. *J. Appl. Polymer Sci.* **1997**, *65*, 1217−1225. (d) Majundar, K. K.; Kundu, A.; Das, I.; Roy, S. *Appl. Organomet. Chem.* **2000**, *14*, 79−85.

(4) For an overview see: (a) Toxicological Profile for Tin and Tin compounds, ATSDR (Agency for Toxic Substances and Disease Registry) , 2005. (b) Revised assessment of the risks to health and the environment associated with the use of the four organotin compounds TBT, DBT, DOT and TPT, The Scientific Committee on Health and Environmental Risks (SCHER), 2006.

(5) (a) Kamber, N. E.; Jeong, W.; Waymouth, R. M.; Pratt, R. C.; Lohmeijer, B. G. G.; Hedrick, J. L. *Chem. Rev.* **2007**, *107*, 5813−5840. (b) Raynaud, J.; Ciolino, A.; Baceiredo, A.; Destarac, M.; Bonnette, F.; Kato, T.; Gnanou, Y.; Taton, D. *Angew. Chem., Int. Ed.* **2008**, *47*, 5390−5393. (d) Raynaud, J.; Gnanou, Y.; Taton, D. *Macromolecules* **2009**, *42*, 5996−6005.

(6) For the observations of similar reaction rates between organo- and metal-based catalysts, see: McLaughlin, M.; Garcia Rubio, S.; Muthyala, R.; Antunes, O. A. C.; Tilstam, U.; Zlota, A.; Yadav, G. D.; Laird, T. *Org. Process Res. Dev.* **2006**, *10*, 853−865.

(7) Silva, A. L.; Bordado, J. C. *Catal. Rev.* **2004**, *46*, 31−51.

(8) (a) Bantu, B.; Manohar Pawar, G.; Decker, U.; Wurst, K.; Schmidt, A. M.; Buchmeiser, M. R. *Chem.—Eur. J.* **2009**, *15*, 3103−3109. (b) Bantu, B.; Manohar Pawar, G.; Wurst, K.; Decker, U.; Schmidt, A. M.; Buchmeiser, M. R. *Eur. J. Inorg. Chem.* **2009**, *15*, 1970−1976.

(9) (a) Cramail, H.; Boyer, A.; Cloutet, E.; Bakhiyi, R.; Alfos, C. WO 2011030076, FR2950051. (b) Cramail, H.; Boyer, A.; Cloutet, E.; Alfos, C. WO 2011030075, FR2950052. (c) Cramail, H.; Boyer, A.; Cloutet, E.; Alfos, C. WO 2011045536, FR2951166. (d) Palaskar, D. V.; Boyer, A.; Cloutet, E.; Alfos, C.; Cramail, H. *Biomacromolecules* **2010**, *11*, 1202−1211. (e) Boyer, A.; Cloutet, E.; Tassaing, T.; Gadenne, B.; Alfos, C.; Cramail, H. *Green Chem.* **2010**, *12*, 2205−2213. (f) Palaskar, D. V.; Boyer, A.; Cloutet, E.; Le Meins, J. F.; Gadenne, B.; Alfos, C.; Farcet, C.; Cramail, H. *J. Polym. Sci., Part A: Polym. Chem.* **2012**, DOI: 10.1002.

(10) (a) Lohmeijer, B. G. G.; Pratt, R. C.; Leibfarth, F.; Logan, J. W.; Long, D. A.; Dove, A. P.; Nederberg, F.; Choi, J.; Wade, C.; Waymouth, R. M.; Hedrick, J. L. *Macromolecules* **2006**, *39*, 8574−

8583. (b) Chuma, A.; Horn, H. W.; Swope, W. C.; Pratt, R. C.; Zhang, L.; Lohmeijer, B. G. G.; Wade, C. G.; Waymouth, R. M.; Hedrick, J. L.; Rice, J. E. *J. Am. Chem. Soc.* **2008**, *130*, 6749−6754.
(11) Tang, D.; Mulder, D.-J.; Noordover, B. A. J.; Koning, C. E. *Macromol. Rapid Commun.* **2011**, *32*, 1379−1385.
(12) (a) Zhang, L.; Pratt, R. C.; Nederberg, F.; Horn, H. W.; Rice, J. E.; Waymouth, R. M.; Wade, C. G.; Hedrick, J. L. *Macromolecules* **2010**, *43*, 1660−1664. (b) Kiesewetter, M. K.; Scholten, M. D.; Kirn, N.; Weber, R. L.; Hedrick, J. L.; Waymouth, R. M. *J. Org. Chem.* **2009**, *74*, 9490−9496.
(13) Maliverney, C.; Saint-Jalmes, L. Patent, WO 2010/043353 A1.
(14) Raab, V.; Kipke, J.; Gschwind, R. M.; Sundermyer, J. *Chem.—Eur. J.* **2002**, *8*, 1682−1693.
(15) Ishikawa, T. *Guanidines in Organic Synthesis in Guanidines, amidines, phosphazenes and related organocatalysts. Superbases for organic synthesis*, Ed. J. Wiley & Sons: Chichester, U.K., 2009 p Chapter 4, pp 93−143.
(16) Baker, J.; Holsworth, J. B. *J. Chem. Soc.* **1947**, 713−726.
(17) Schwetlick, K.; Noak, R.; Stebner, F. *J. Chem. Soc., Perkin Trans. 2* **1994**, 599−608.
(18) Similar mechanisms have been proposed for base-catalyzed alcoholysis of anhydrides, see: Chen, Y.; McDaid, P.; Deng, L. *Chem. Rev.* **2003**, *103*, 2965−2983.
(19) Bonduelle, C.; MartinVaca, B.; Cossio, F. P.; Bourissou, D. *Chem.—Eur. J.* **2008**, *14*, 5304−5312.
(20) Rappo-Abiuso, M.; Llauro, M.-F.; Chevalier, Y.; Le Perchec, P. *Phys. Chem. Chem. Phys.* **2001**, *3*, 99−106.
(21) Bacaloglu, R.; Cotarga, L.; Marcu, N.; Tolgyi, S. *J. Prakt. Chem.* **1988**, *330*, 530−540.
(22) For an exhaustive list of pK_a of amines in CH_3CN, see: Kajjurand, I.; Kütt, A.; Sooväli, L.; Rodima, T.; Mäemets, V.; Leito, I.; Koppel, I. A. *J. Org. Chem.* **2005**, *70*, 1019−1028.
(23) Deutsch, J.; Eckelt, R.; Köckritz, A.; Martin, A. *Tetrahedron* **2009**, *65*, 10365−10369.
(24) Pereira, F. S.; deAzevedo, E. R.; da Silva, E. F.; Bonagamba, T. J.; da Silva Agostini, D. L.; Magalhaes, A.; Job, A. E.; Pérez Gonzalez, E. R. *Tetrahedron* **2008**, *64*, 10097−10106.
(25) Oediger, H., Moeller, F. *Ger. Offen. DE 2640964*, 1978.
(26) Richter, R. *Tetrahedron Lett.* **1968**, *48*, 5037−5039.
(27) Coles, M. P. *Chem. Commun.* **2009**, 3659−3676.
(28) Similar activation of CO_2 by MTBD and TBD has recently been proposed, see: (a) Barbarini, A.; Maggi, R.; Mazzacani, A.; Mori, G.; Sartori, G.; Sartorio, R. *Tetrahedron Lett.* **2003**, *44*, 2931−2934. (b) Villers, C.; Dognon, J.-P.; Pollet, R.; Thuéry, P.; Ephritikhine, M. *Angew. Chem., Int. Ed.* **2010**, *49*, 3465−3468. (c) Das Neves Gomes, C.; Jacquet, O.; Villers, C.; Thuéry, P.; Ephritikhine, M.; Cantat, T. *Angew. Chem., Int. Ed.* **2012**, *51*, 187−190.
(29) Nederberg, F.; Connor, E. F.; Möller, M.; Glauser, T.; Hedrick, J. L. *Angew. Chem., Int. Ed.* **2001**, *40*, 2712−2715.

Macromolecules

Article

pubs.acs.org/Macromolecules

Elucidating the Early Steps in Photoinitiated Radical Polymerization via Femtosecond Pump−Probe Experiments and DFT Calculations

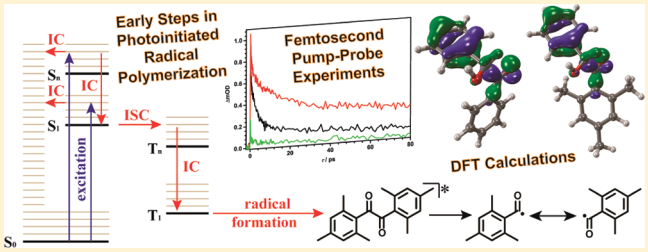
Thomas J. A. Wolf,[†,§] Dominik Voll,[‡,§] Christopher Barner-Kowollik,*[,‡] and Andreas-Neil Unterreiner*[,†]

[†]Institut für Physikalische Chemie and Center for Functional Nanostructures (CFN), Karlsruhe Institute of Technology (KIT), 76128 Karlsruhe, Germany

[‡]Preparative Macromolecular Chemistry, Institut für Technische Chemie und Polymerchemie and Center for Functional Nanostructures (CFN), Karlsruhe Institute of Technology (KIT), Engesserstr. 18, 76128 Karlsruhe, Germany

Supporting Information

ABSTRACT: The excited states and dynamics of the three triplet radical photoinitiators benzoin (2-hydroxy-1,2-diphenylethanone, Bz), 2,4,6-trimethylbenzoin (2-hydroxy-1-mesityl-2-phenylethanone, TMB), and mesitil (1,2-bis(2,4,6-trimethylphenyl)-1,2-ethanedione, Me)—employed in our previous studies for quantifying net initiation efficiencies in pulsed laser polymerization with methacrylate monomers [Voll, D.; Junkers, T.; Barner-Kowollik, C. *Macromolecules* **2011**, *44*, 2542−2551]—are investigated via both femtosecond transient absorption (TA) spectroscopy and density functional theory (DFT) methods to elucidate the underlying mechanisms causing different initiation efficiencies when excited at 351 nm. Bz and TMB are found to have very similar properties in the calculated excited states as well as in the experimentally observed dynamics. After excitation into the first excited singlet state (S_1) Bz and TMB undergo rapid intersystem crossing (ISC). The ISC can compete with ultrafast internal conversion (IC) processes because an excited triplet state (T_n) of nearly the same energy is present in both cases. ISC is therefore the dominating depopulation channel of S_1, and subsequent α-cleavage to produce radicals takes place on the picosecond time scale. In contrast, Me is excited into the second excited singlet state (S_2). In this case no isoenergetic triplet state is available, which inhibits ISC from competing with ultrafast deactivation processes. ISC is therefore assigned to be a minor deactivation channel in Me. Employing these findings, quantitative photoinitiation efficiency relations of Bz, TMB, and Me obtained by pulsed laser polymerization can be directly correlated with the relative TA intensities found in the femtosecond experiments. The ISC efficiency is thus a critical parameter for evaluating the overall photoinitiation efficiency and demonstrates that the employment of the herein presented method represents a powerful tool for attaining a quantitative picture on the suitability of a photoinitiator.



INTRODUCTION

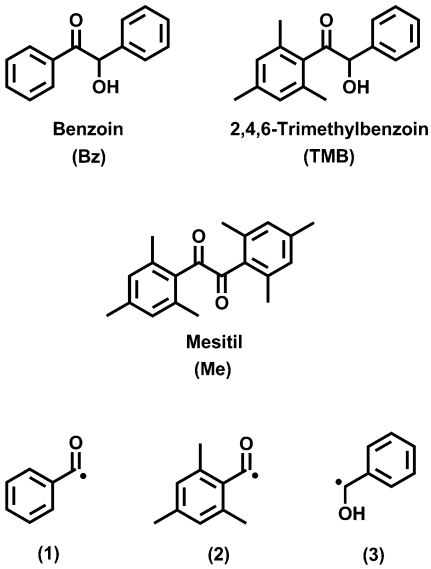
Triplet radical photoinitiators have recently been subjected to intense research activities due to their large variety of applications including dental restorative materials,[1,2] biomaterials,[3,4] fabrication of 3-dimensional objects,[5] and lithography.[6] For further details about photoinitiated polymerizations and their opportunities, the reader is referred to a recently published review by Yagci and colleagues.[7] In particular substituted thioxanthones,[8−11] Barton esters,[12,13] disulfides,[14] and photoinitiators based on silyl radical chemistry[15,16] are currently being described. Our research activities are more focused on the constitution of the resulting polymers as well as initiation efficiencies of photoinitiator-derived radicals. Recently, we published a quantitative comparison of the net initiation efficiencies of benzoyl (**1**) and mesitoyl (**2**) radicals with the monomers methyl methacrylate (MMA), ethyl methacrylate (EMA), and butyl methacrylate (BMA).[17] As photoinitiators, we employed benzoin (2-hydroxy-1,2-diphenylethanone, Bz), 2,4,6-trimethylbenzoin (2-hydroxy-1-mesityl-2-phenylethanone, TMB), and mesitil (1,2-bis(2,4,6-trimethylphenyl)-1,2-ethanedione, Me). It was found that not only the type of the radical (benzoyl (**1**) vs mesitoyl (**2**), i.e., the kinetics of addition to double bonds) is important for the initiation efficiency but also its origin (TMB vs Me for mesitoyl radicals (**2**), i.e., excited state dynamics leading to radical formation). In a further recently published study we employed six benzoin-type photoinitiators—each of them substituted with a different amount of methyl groups—in one single cocktail experiment to investigate their initiation efficiency in free radical polymerization with MMA.[18] The final result of this unique experiment was that an increasing number of methyl substituents leads to a decrease in incorporation of the respective radical fragments into the polymer.

The Bz-derived benzoyl radical (**1**) is between 2.4 and 3.0 times more likely to initiate polymerization than the TMB-derived mesitoyl fragment (**2**), depending on the monomer.

Received: December 9, 2011
Revised: February 16, 2012
Published: February 28, 2012

 © 2012 American Chemical Society

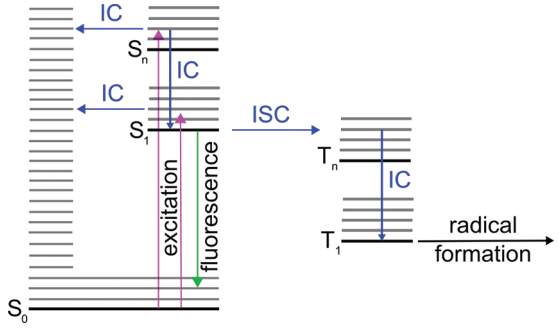
Scheme 1. Photoinitiators Employed in the Present Study (Benzoin (Bz), 2,4,6-Trimethylbenzoin (TMB), and Mesitil (Me)) as well as Their Resulting Radicals after Irradiation with UV Light at a Wavelength of 351 nm during Pulsed Laser Polymerization (PLP) Experiments (Benzoyl Radical (1), Mesitoyl Radical (2), and Benzyl Alcohol Radical (3))



Interestingly, the Bz-derived benzoyl radical (**1**) is 8.6 times more likely to initiate the bulk free radical polymerization than mesitoyl radicals (**2**) derived from Me.[19] This observation is especially surprising as Me has a considerably higher absorbance than TMB at 351 nm, the excitation wavelength of the experiments. Furthermore, it is not possible to employ Me for pulsed laser polymerization (PLP) experiments at low laser energies (≤0.5 mJ).[17] These experimental findings can only be explained by significant differences in the intrinsic excited state properties of the molecules Bz, TMB, and Me. Possible relaxation and reaction processes in the excited states of these molecules after photoexcitation are summarized in a Jabłoński-type diagram in Scheme 2.

Typically, the excitation from the ground state (S_0) leads to population of the first (S_1) or higher excited singlet states (S_n). Subsequent rapid radiationless deactivation of these excited singlet states by internal conversion (IC) into S_0 is an unwanted process, yet cannot be ruled out in most cases, especially after excitation into higher excited states. From S_n IC can take place into S_1. S_1 can be depopulated by intersystem crossing (ISC) into an excited triplet state (T_n), which is considered to be the dominant process for excited photoinitiators. Thus, IC and fluorescence into S_0 have to be weak depopulation channels of S_1. The fluorescence intensity is dependent both on the electronic transition dipole moment and on the Franck−Condon overlap. As the very low oscillator strengths of the $S_1 \leftarrow S_0$ transitions in the absorption spectra of many photoinitiators suggest,[6,8,20] the low value of the electronic dipole moment is the relevant effect in most cases. Thus, the lack of fluorescence is an intrinsic property of the electronic wave function of S_1. Furthermore, the T_n energy levels should be as close in energy as possible to the S_n states because the ISC transition probability is crucially sensitive to this energy gap.[21] Having arrived in the triplet manifold the molecule rapidly relaxes to T_1. T_1 has to be sufficiently long-lived that radical formation can compete with other depopulation processes such as phosphorescence. Bz has been subjected to several theoretical[22] and experimental[23−25] studies. It is known that after photoexcitation Bz performs rapid ISC.[23,24] The triplet state is depopulated on the picosecond time scale by α-cleavage leading to a benzoyl radical (**1**) and a benzyl alcohol radical (**3**) which both can induce polymerization reactions.[23,24] However, the exact mechanism and time scale of the ISC in Bz could so far not be investigated due to poor time resolution.[23,24] The excited state properties of TMB and Me are to the best of our knowledge hitherto investigated neither experimentally nor theoretically. The aim of the present investigation is to elucidate the mechanistic aspects leading the molecules to the T_1 state. By exploring excited state structure, applying theoretical methods and elucidating excited state dynamics by femtosecond time-resolved spectroscopy, a better understanding is to be developed, which not only explains the previous findings[17,19] in initiation disparity of Bz, TMB, and Me—observed by mass spectrometric analysis of photoinitiated polymer synthesized via PLP—yet also serves as a classification tool for the efficiency of triplet radical photoinitiators.

Scheme 2. Jabłoński-Type Diagram of the Possible Processes Following Excitation of a Photoinitiator into the First (S_1) or Higher (S_n) Excited States[a]



[a]These include internal conversion (IC) into S_1 or S_0 and intersystem crossing (ISC) into excited triplet states (T_n), followed by IC into T_1. From T_1 radical formation can be achieved.

EXPERIMENTAL SECTION

UV/vis Spectra. The UV/vis steady-state absorption spectra in methanol (Carl Roth, HPLC grade) solution were recorded with a Varian Cary 500 spectrometer in fused silica cuvettes with an optical path length of 1 mm.

Femtosecond Pump−Probe Experiments. In the femtosecond pump−probe experiments, a Clark 2210 laser system was employed with a repetition rate of 1 kHz, a central wavelength of 775 nm, a typical pulse duration of 150 fs, and an energy of 1.6 mJ/pulse. A small portion was used to pump a noncollinear optical parametric amplifier,[26] which produced tunable pulses in the visible region. These pulses were up-converted with another portion of the fundamental laser output to produce pump pulses at excitation wavelengths (λ_{pump}) between 300 and 370 nm by a sum frequency mixing process in a BBO crystal. The pulse length of the desired excitation (pump) wavelength (351 nm) was dispersion optimized by a prism compressor and weakly focused into the sample. A further portion of the laser output was employed to pump another noncollinear optical parametric amplifier, which produced probe pulses with wavelengths (λ_{probe}) tunable between 470 and 750 nm. The probe pulses were also dispersion optimized by a second prism compressor and delayed via a translation stage with respect to the pump pulses; their polarization was rotated with a wave plate to magic angle relative to the pump−pulse polarization, and the pulses were

dx.doi.org/10.1021/ma202673q | Macromolecules 2012, 45, 2257−2266

temporally and spatially overlapped with the pump pulses in the sample. The time resolution was measured by cross-correlation in the dye stilbene 3 to be below 200 fs. The pump intensity was kept below 4×10^8 W/cm^2 to ensure that only small changes in optical density (OD) occur. The repetition rate of the pump pulses was reduced by a chopper wheel to allow the recording of the change in optical density with and without pump−pulse, ΔOD. The samples were prepared as methanol solutions in 1 mm fused silica cuvettes with an OD of 0.5 at the excitation wavelength resulting in concentrations of 7.8×10^{-2} mol L^{-1} (Bz), 1.9 mol L^{-1} (TMB). and 4.9×10^{-3} mol L^{-1} (Me). All samples were excited at a central wavelength λ_{pump} = 351 nm, in agreement with earlier experiments,[17] and probed at wavelengths of λ_{probe}= 470, 500, and 600 nm. The maximum delay between pump and probe pulses was 1.6 ns.

Theoretical Methods. Quantum chemical calculations were carried out with the TURBOMOLE V-6.3 program package.[27] Ground state minimum geometries were optimized with DFT/BP86/def2-SV(P).[28−33] Ground state energies at the optimized geometries were calculated with DFT/B3LYP/aug-cc-pVDZ,[28−32,34] singlet and triplet excitations with TDDFT/B3LYP/aug-cc-pVDZ.[34−37] (For Cartesian coordinates of the optimized structures, see the Supporting Information section, Tables S3−S5.)

Photoinitiators. Benzoin (purchased from Sigma-Aldrich, 98%) was recrystallized twice in ethanol prior to use. The preparation procedures for TMB[17,38−40] and Me[19,41,42] are adapted from the literature.

RESULTS AND DISCUSSION

Absorption Spectra. The wavelength-dependent extinction coefficients of Bz, TMB, and Me in methanol solution are shown in Figure 1. Both the excitation wavelength and the probe wavelength range of the transient absorption (TA) experiment are indicated within the graph. Bz (red) exhibits a very weak absorption band centered at 320 nm and a strong absorption band at 247 nm (not shown in Figure 1, see the Supporting Information, Figures S1−S3). This band has two weak shoulders at ∼289 and 282 nm. The first absorption band of TMB is blue-shifted with respect to Bz and appears as a shoulder centered at ∼304 nm of a stronger absorption band centered at 254 nm. Thus, interestingly, the difference of the TMB spectrum compared to the Bz spectrum is a blue shift of the first absorption band and a red shift of the higher absorption band. The shoulders observed in the UV spectrum of Bz cannot be resolved in TMB. Me, in contrast, features a spectrum that is distinctively red-shifted with respect to the other two spectra. Its first very weak absorption band exhibits two maxima at 493 and 467 nm. The second strong absorption band is also structured and centered at 285 nm. The absolute extinction coefficients at the excitation wavelength of both the earlier pulsed laser polymerization (PLP)[17] and the transient absorption experiment (351 nm) differ considerably for the three photoinitiators. TMB has a low extinction coefficient (ε = 12 L mol^{-1} cm^{-1}), with Bz (ε = 64 L mol^{-1} cm^{-1}) the extinction coefficient is considerably higher, while Me displays by far the highest extinction coefficient (ε = 1075 L mol^{-1} cm^{-1}). Assuming the same excited state properties of all three species and that the excitation promotes the molecules into comparable higher states, Me would be expected to be the by far most efficient polymerization initiator as also initially assumed in our previous publication.[17] However, as the analysis of the spectra reveals, the excited state into which the molecules are promoted into is not the same. Bz and TMB are excited almost nonresonantly at the red wing of the first, very weak absorption band, while Me is excited much more likely into a higher lying excited state. It can already be concluded here that the extinction coefficient at the excitation wavelength is no suitable tool to estimate the efficiency of a photoinitiator, particularly when employing different systems as photoinitiators—Bz and TMB as benzoin-type initiators and Me as a benzil-type initiator. For the following considerations the efficiency relationships observed in the earlier PLP/ESI-MS experiments,[17,19] which are normalized to the concentration of the photoinitiators, thus have to be made independent of the excitation probability by normalizing them with the extinction coefficients at 351 nm (dividing both sides of the efficiency relation by the respective extinction coefficient). Such normalization leads to the prediction that an excited TMB molecule is between 1.8 and 2.2 times more likely to induce polymerization than an excited Bz molecule and that an excited Bz molecule is 144 times more likely to induce polymerization than an excited Me molecule. It is thus evident that especially the relation between Bz and Me regard to their relative absorptivities is drastically altered compared with a direct comparison of the extinction coefficients.

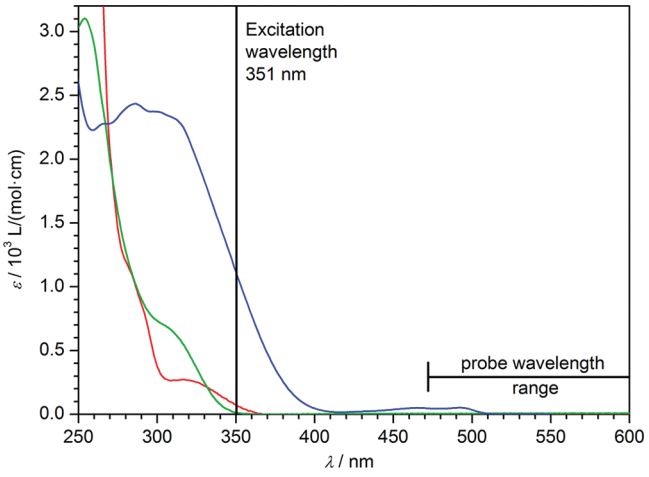


Figure 1. Wavelength-dependent absolute extinction coefficients of the three photoinitiators benzoin (Bz) (red), 2,4,6-trimethylbenzoin (TMB) (green), and mesitil (Me) (blue). The excitation wavelength of 351 nm and the probe wavelength range of the transient absorption experiment are marked. Note the different extinction coefficients of the photoinitiators at this wavelength.

Time-Resolved Spectroscopy. To obtain a deeper insight into the nature and order of the time scale of the processes included in the excited states dynamics of the three photoinitiators Bz, TMB, and Me, transient absorption (TA) traces were measured in methanol solution (for the concentration of the photoinitiators in methanol please refer to the Experimental Section). Thereby, the sample under investigation is excited by a femtosecond excitation pulse to a specific electronic state. The evolution of the excited state's population is investigated by projecting it through a femtosecond probe pulse, which has a variable time delay with respect to the excitation pulse, onto either a set of higher excited states or the ground state. In the first case, the sample is further excited into a region of the molecule's energy diagram with high density of electronic states in the vicinity but still well below the ionization threshold for absorption leading to positive TA values. The knowledge of the exact electronic state, which is populated by absorption of the probe photon, is thereby not mandatory. In fact, due to the high density of electronic states with their respective vibrational substructure

dx.doi.org/10.1021/ma202673q | Macromolecules 2012, 45, 2257−2266

and consequently overlapping bands, an assignment to particular states is problematic in most cases. In the second case, the emission of photons is stimulated by the probe pulse, leading to negative TA values. The TA traces thus represent the spectral properties of the excited states of the investigated molecule, convoluted with their time-dependent population. It has to be noted that the central wavelength of the femtosecond excitation pulse was 351 nm, as in the earlier PLP experiments followed by mass spectrometric analysis.[17,19] However, the spectral bandwidth of the femtosecond excitation pulse was considerably larger (with a full width at half-maximum of 490 cm^{-1}, assuming a Gaussian profile), caused by time−bandwidth limitations.[43] Nevertheless, the steady state absorption spectra give no hint about excited state features, which could be additionally excited by the broader pulse spectrum. On the other hand, the number of vibrational states in the electronically excited state prepared by the femtosecond pulse is substantially larger than in the earlier PLP experiments.[17,19] The same considerations apply to the probe pulses with central wavelengths of 470, 500, and 600 nm (see Figure 2). These wavelengths were chosen to be outside of the spectral regions where the samples have considerable absorption to avoid the influence of ground state bleaching on the TA traces. Me shows low absorption both at 470 and 500 nm, yet with the extinction coefficients at these wavelengths being lower by at least a factor of 22 than at the excitation wavelength, this contribution can be neglected. The TA traces of Bz, TMB, and Me in methanol solution at pump−probe delays τ from −2 to 80 ps are shown in parts a, b, and c of Figure 2, respectively, together with global fit functions of the type

$$\Delta OD(\tau) = \left(1 + \mathrm{erf}\left(\sqrt{4\ln(2)}\,\frac{\tau}{\tau_0}\right)\right)\sum_{i=1}^{3} A_i e^{-\tau/\tau_i} \quad (1)$$

representing the sum of three exponential decay functions with time constants τ_i and amplitudes A_i as parameters, convoluted with an error function with τ_0 as parameter. The latter models the onset of the TA within the temporal overlap of excitation and probe pulses. The fit parameters are listed in Tables 1 and 2 and the Supporting Information section, Tables S1 and S2. A comparison of the TA traces of Bz and TMB at a probe wavelength of 500 nm and pump−probe delays from −4 ps to 1.6 ns is shown in Figure 3a. A comparison of the TA traces of Bz, TMB, and Me at a probe wavelength of 500 nm is shown in Figure 3b.

Table 1. Time Constants (refer to Eq 1) Derived from Global Multiexponential Fits for the Three Studied Photoinitiators Benzoin (Bz), 2,4,6-Trimethylbenzoin (TMB), and Mesitil (Me)

photoinitiator	τ_1/ps	τ_2/ps	τ_3/ns
Bz	1.2 ± 0.2	14.3 ± 0.9	>1.6
TMB	0.7 ± 0.2	15.9 ± 0.4	>1.6
Me	0.2 ± 0.2	25 ± 2	>1.6

Table 2. Relative Amplitudes (Refer to Eq 1) of the Transient Absorption Probed at 500 nm Derived from Global Multiexponential Fits for the Three Studied Photoinitiators Benzoin (Bz), 2,4,6-Trimethylbenzoin (TMB), and Mesitil (Me)

photoinitiator	$A_{1,rel}$	$A_{2,rel}$	$A_{3,rel}$
Bz	0.60 ± 0.03	0.32 ± 0.02	0.07 ± 0.01
TMB	0.33 ± 0.03	0.40 ± 0.01	0.28 ± 0.01
Me	0.85 ± 0.04	0.12 ± 0.01	0.03 ± 0.01

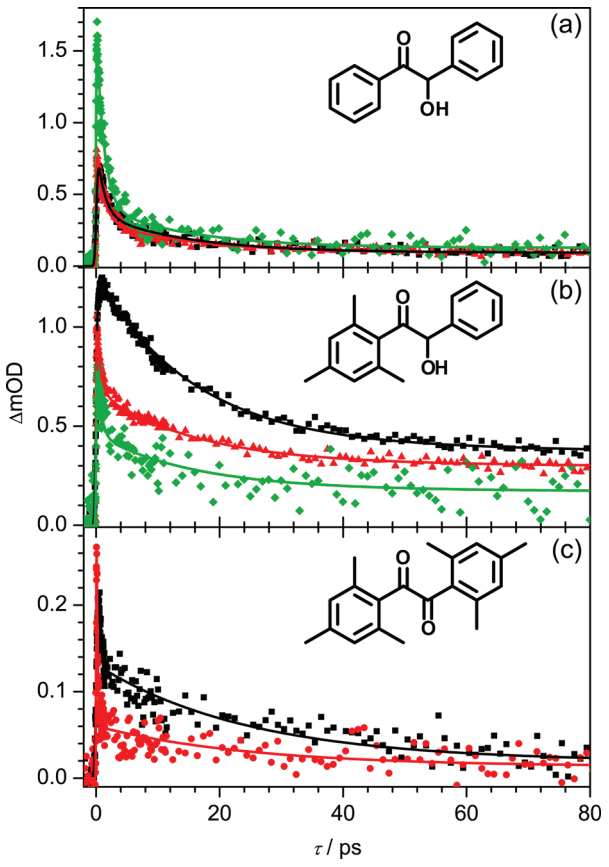


Figure 2. Transient absorption of (a) benzoin (Bz), (b) 2,4,6-trimethylbenzoin (TMB), and (c) mesitil (Me) in methanol solution pumped at 351 nm and probed at 470 nm (black), 500 nm (red), and 600 nm (green), respectively, together with fit functions (according to eq 1 and the fit parameters collated in Tables 1 and 2 as well as Tables S1 and S2 within the Supporting Information).

The TAs of all three samples have two features in common (see Figures 2 and 3): They show an initial biexponential decay on the picosecond time scale and a residual TA stable throughout the whole investigated time window (1.6 ns). In the case of Me, this residual TA is too low to be detected on the nanoseconds time scale. The two time constants for the biexponential decay found in the fits of Bz and TMB are similar (τ_1 = 1.2 ps and τ_2 = 14.3 ps for Bz vs τ_1 = 0.7 ps and τ_2 = 15.9 ps for TMB), while the fits of Me display considerably different values (τ_1 = 0.2 ps and τ_2 = 25 ps). The value of the first time constant of Me is approaching the experimental time resolution. Thus, the underlying dynamical process is most likely faster than the value suggests. The second time constant of Me is by a factor of ∼1.7 higher than in Bz and TMB. The respective third time constants of all three samples are considerably higher than the experimentally accessible time window and therefore undefined. As inspection of Figures 2 and 3 reveals the absolute initial TA values at τ = 0 are comparable in the cases of Bz and TMB. For Me the values are lower by a factor of 4 with respect to the other two samples.

dx.doi.org/10.1021/ma202673q | Macromolecules 2012, 45, 2257−2266

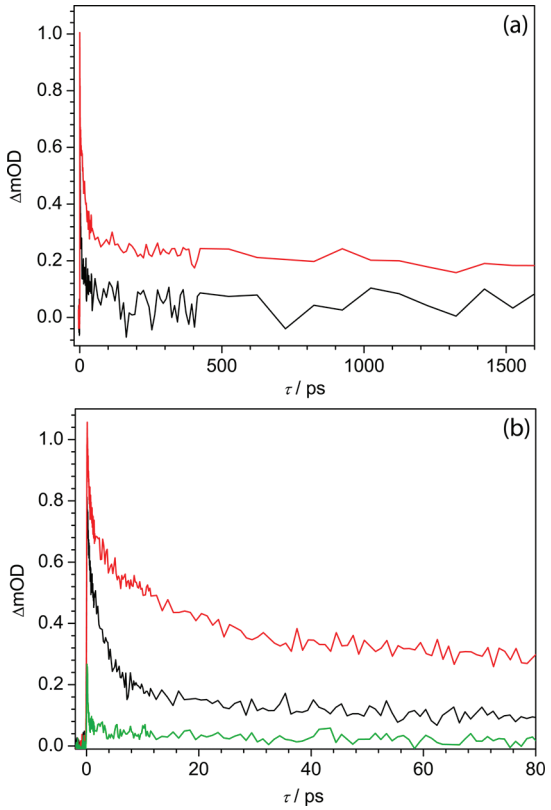


Figure 3. (a) Transient absorption of benzoin (Bz) (black) and 2,4,6-trimethylbenzoin (TMB) (red) pumped at 351 nm and probed at 500 nm and (b) transient absorption of benzoin (Bz) (black), 2,4,6-trimethylbenzoion (TMB) (red), and mesitil (Me) (green) in methanol solution pumped at 351 nm and probed at 500 nm.

The residual TA is the highest with TMB (see for example Figure 3), the values of Bz are lower by a factor of 3. Me shows a very low residual TA. A large wavelength dependence of TA can only found in TMB. For comparison, the relative amplitudes from the fits at a probe wavelength of 500 nm are collated in Table 2. For Bz the first component has the highest contribution to the TA. The second and third components have smaller contributions by factors of close to 2 and 10, respectively. In TMB all three components nearly equally contribute to the TA. In Me the first component has the by far highest contribution. The second component is lower by a factor of 7 and the third by a factor of 30.

Results from DFT Calculations. To obtain insights into the electronic structure properties of the three experimentally investigated photoinitiators, minimum energy geometries were optimized with DFT/BP86/def2-SV(P).[28−33] In good agreement with the literature,[22] two low energy minimum geometries of Bz could be found: one with an intramolecular hydrogen bond between the carbonyl group and the OH group (geometry 1) and one geometry without this hydrogen bond (geometry 2). These two minimum geometries are shown in Figures 4a and 4b, respectively. Corresponding geometries could also be found for TMB. They are depicted in Figures 4c and 4d. At the minimum geometries, single-point calculations with DFT/B3LYP/aug-cc-pVDZ[28−32,34] were performed. The resulting energies are depicted in Table 3.

The energy differences between the two geometries are 21.8 kJ mol^{-1} for Bz and 24.7 kJ mol^{-1} for TMB and can predominantly be attributed to the intramolecular hydrogen bond. Their values are in the range of typical energies of intermolecular hydrogen bonds between methanol molecules.[44] Thus, geometry 2 is very likely to compensate its disfavor in energy by developing intermolecular hydrogen bonds with solvent molecules. Additionally, clear experimental evidence was reported in ref 24 for geometry 2 of Bz being the most stable and active structure for α-cleavage from the triplet state in methanol solution. We therefore assign geometry 2 to be the active geometry in both Bz and TMB. As can be seen in Figure 4a−d, the common feature of all Bz and TMB geometries is the hydroxyl-substituted sp^3-carbon effectively isolating the two phenyl and benzoyl (mesitoyl) π-systems from each other, resulting in overall nonplanar geometries. In agreement with crystal structures and calculations of Me and its analogue without methyl substituents at the aromatic rings, benzil,[45−47] two low energy geometries could also be found for Me (geometry 1 and geometry 2). They are depicted in Figure 4 e and f. The energies of the two geometries are listed in Table 3. Geometry 1 is calculated to be 4.7 kJ mol^{-1} lower in energy

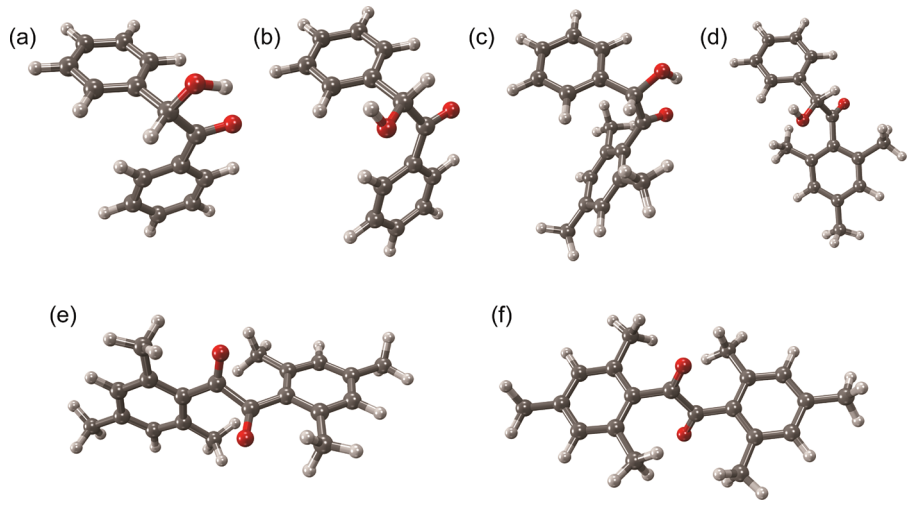


Figure 4. Optimized geometries of benzoin (Bz) with an intramolecular hydrogen bond (a) and without a hydrogen bond (b), 2,4,6-trimethylbenzoin (TMB) with an intramolecular hydrogen bond (c) and without a hydrogen bond (d) and mesitil (Me) with aromatic ring planes perpendicular (e) and parallel (f) to each other. Optimization: DFT/BP86/def2-SV(P).[28−33]

dx.doi.org/10.1021/ma202673q | *Macromolecules* 2012, 45, 2257−2266

Table 3. Energies at Optimized Geometries of the Three Investigated Photoinitiator Molecules Benzoin (Bz), 2,4,6-Trimethylbenzoin (TMB), and Mesitil (Me) Obtained via DFT/B3LYP/aug-cc-pVDZ[28−32,34]

	Bz		TMB		Me	
	geometry 1	geometry 2	geometry 1	geometry 2	geometry 1	geometry 2
energy [hartree]	−690.8328	−690.8230	−808.6958	−808.6864	−925.3540	−925.3513
energy + zero point correction [hartree]	−690.6104	−690.6024	−808.3939	−808.3845	−924.9923	−924.9905
ΔE [kJ/mol]		21.8		24.7		4.7

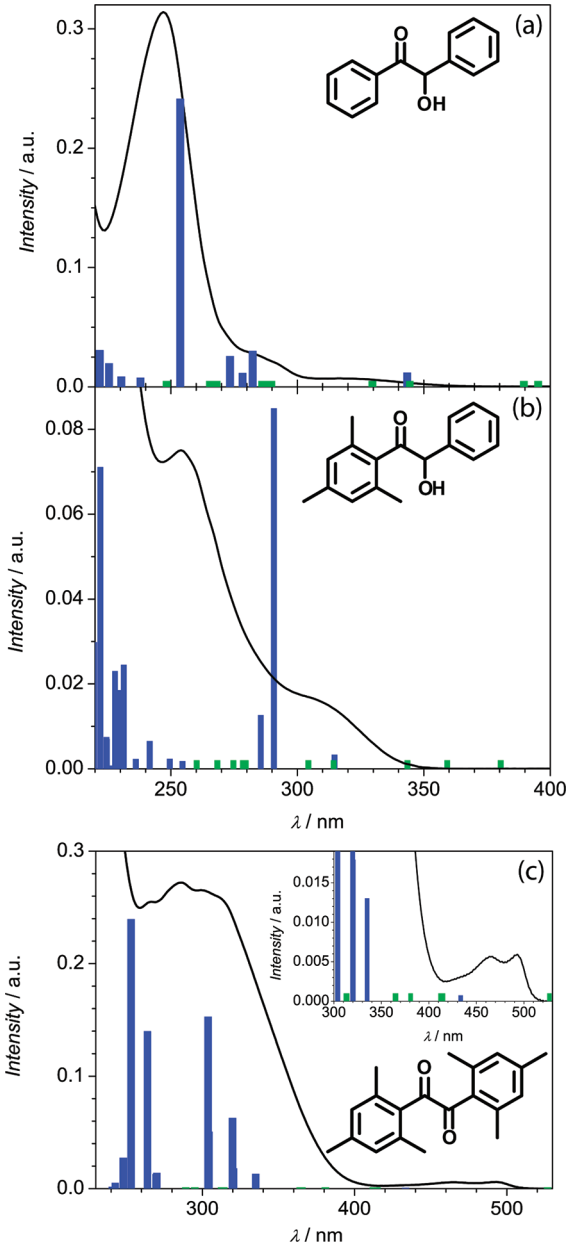


Figure 5. Experimental absorption spectrum of benzoin (Bz) (a), 2,4,6-trimethylbenzoin (TMB) (b), and mesitil (Me) (c) in methanol solution (black) and calculated singlet (blue) and triplet (green) excitations, calculated at the TDDFT/B3LYP/aug-cc-pVDZ level of theory.[34−37] The inset in (c) represents a more detailed plot of the region between 300 and 530 nm.

than geometry 2, which cannot be attributed to a solvent-dependent stabilization effect as the intramolecular hydrogen bond in Bz and TMB. Therefore, geometry 1 is assigned to be the active geometry for the further considerations. In Me an isolating sp^3-carbon between the two mesitoyl π-systems is missing. However, because of steric effects induced by the methyl groups, the two mesityl ring planes are perpendicular in geometry 1. From that one can assume a considerable disturbance of the resonance between the two rings. For the active geometries singlet and triplet excitations are calculated at the TDDFT/B3LYP/aug-cc-pVDZ[34−37] level of theory. A comparison between experimental and calculated spectra is shown in Figure 5. Selected transition energies are summarized in Table 4.

Table 4. Energies of Selected Excited Singlet and Triplet States Relative to the Singlet Ground State of Benzoin (Bz), 2,4,6-Trimethylbenzoin (TMB), and Mesitil (Me), Respectively, Calculated at the TDDFT/B3LYP/aug-cc-pVDZ Level of Theory[34−37]

photoinitiator	singlet state	E_{rel} [eV]	triplet state	E_{rel} [eV]
Bz	S_1	3.59	T_1	3.13
	S_2	4.37	T_2	3.17
	S_3	4.43	T_3	3.58
	S_4	4.51	T_4	3.74
TMB	S_1	3.93	T_1	3.27
	S_2	4.25	T_2	3.46
	S_3	4.33	T_3	3.62
	S_4	4.85	T_4	3.96
Me	S_1	2.85	T_1	2.36
	S_2	3.68	T_2	3.01
	S_3	3.84	T_3	3.02
	S_4	3.85	T_4	3.28
	S_5	4.04	T_5	3.41
	S_6	4.05	T_6	3.43
	S_7	4.55	T_7	3.98

The agreement between experimental spectrum and calculations is very reasonable, if one takes into account that no solvent effect is included in the calculations. It can be clearly seen that irradiation of the sample at 351 nm leads exclusively to excitation of the first singlet transition of Bz and TMB as well as the second singlet transition of Me (the calculated first singlet transition of TMB is—in agreement with the experimental spectrum—centered at a shorter wavelength with respect to the excitation wavelength of 351 nm). By molecular orbital (MO) analysis this transition can be assigned to an excitation from the highest occupied MO (HOMO) to the lowest unoccupied MO (LUMO) in the case of Bz. These MOs are visualized in Figures 6a and 6b, respectively.

It can be seen that the HOMO has both the character of a π-MO on the side of the phenyl π-system and the character of a lone pair at the carbonyl oxygen. The LUMO has mainly the character of a π-MO in the benzoyl part of the molecule. The LUMO ← HOMO transition can therefore be described as a charge-transfer excitation into an $n\pi^*$ state. Such states are known to easily undergo intersystem crossing into $\pi\pi^*$ states,

dx.doi.org/10.1021/ma202673q | Macromolecules 2012, 45, 2257−2266

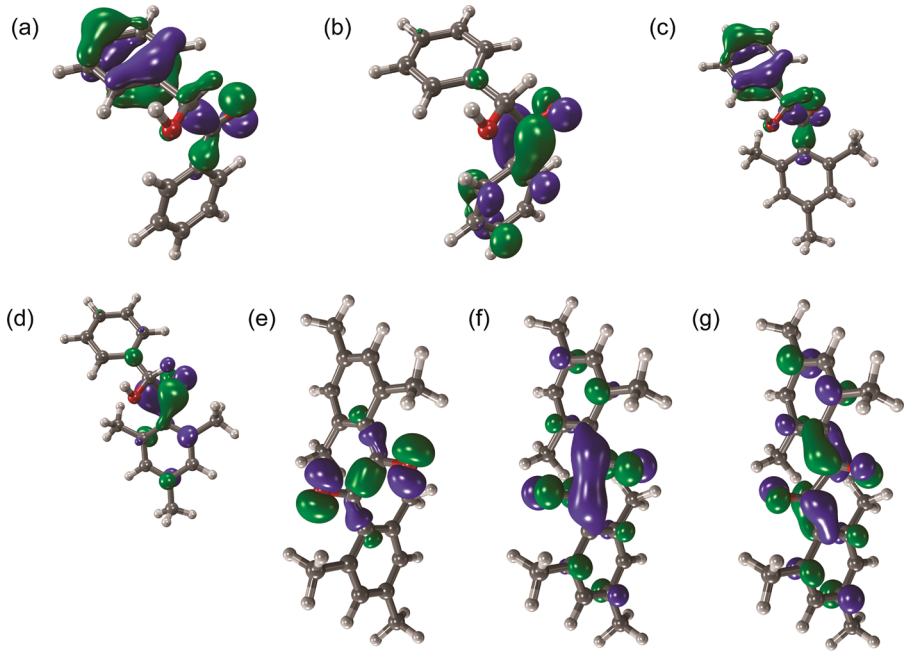


Figure 6. Visualization of the HOMO (a) and LUMO (b) of benzoin (Bz), of the HOMO-2 (c) and LUMO (d) of 2,4,6-trimethylbenzoin (TMB), and of the HOMO (e), LUMO (f), and LUMO+1 (g) of mesitil (Me), calculated at the DFT/B3LYP/aug-cc-pVDZ level of theory.[28−31,34]

as predicted by the well-known El-Sayed selection rule.[48] In the case of TMB, the first singlet transition is governed by a LUMO ← HOMO-2 excitation. The corresponding MOs can be seen in Figures 6c and 6d, respectively. They match quite precisely the ones of Bz. The first singlet transition of Me is governed by a LUMO ← HOMO excitation. A visualization of the involved molecular orbitals is depicted in Figures 6e and 6f. The striking observation is that despite the considerations discussed above based on the rectangular position of the two phenyl rings relative to each other, the two Me π-systems are far from being isolated from each other. The HOMO is predominantly of oxygen lone-pair character and the LUMO of carbonyl-π^* character. Thus, again it is an nπ^* transition, but in contrast to Bz and TMB not a charge-transfer transition. The second singlet transition which was actually excited in the experiments is a LUMO+1 ← HOMO transition (see Figures 6e and 6g). The LUMO+1 has also strong π^*-character, but is of different symmetry compared to the LUMO, which accounts for the stronger absorption probability of the second singlet transition.

Reviewing the presented experimental and theoretical results, Bz and TMB seem to behave relatively similar. Transient absorption experiments show relaxation in a comparable manner on near-identical time scales. Theoretical calculations relate the excitation wavelength employed in the experiments to corresponding transitions into the first excited singlet state. Thus, in the following, the two systems are discussed together. Considering Scheme 2, the first question to address is whether the overall process from photoexcitation to depopulation of T_1 by α-cleavage can be observed within the time window of 1.6 ns investigated by our experiments. Earlier studies of Bz[23,24] found values of 830 and 20 ps for the triplet lifetime, whereas only the second value was derived by time-resolved experiments.[24] An ISC time constant could only be estimated due to 20 ps time resolution.[24] Other studies of similar systems also found time constants for the α-cleavage reaction in the order of picoseconds.[49−51] This suggests that the depopulation of T_1 by α-cleavage should be observable in our TA traces. Thus, the residual transient absorption observed in Bz and TMB samples and associated with the time constant τ_3 can be attributed to absorption of the reaction products of α-cleavage. Hence, the process connected with the time constant τ_2 has to be assigned to the depopulation of T_1. The observed values of 14.3 and 15.9 ps for Bz and TMB, respectively, reveal a surprisingly fast α-cleavage reaction, yet are in good agreement with earlier findings.[24] Furthermore, the process associated with the time constant τ_1 is at least in part attributable to ISC. Although even sub-100 fs ISC has been reported for aromatic systems,[52] such values could be connected to special substituent features which are not present in Bz and TMB. Typical intersystem crossing time constants are on the time scale of several picoseconds to microseconds.[53] ISC time constants of 2−3 ps have already been observed in similar photoinitiators undergoing α-cleavage,[54] but the values of 0.7 and 1.2 ps observed here seem to be surprisingly fast. They can only be explained by the assumption of convolution of an additional ultrafast IC deactivation channel competing with ISC in depopulation of S_1. The observed time constant is in this case related to the ISC and IC time constant by $\tau_1 = (\tau_{IC}\tau_{ISC})/(\tau_{IC} + \tau_{ISC})$ and can therefore be only regarded as a lower limit for τ_{ISC}. Nevertheless, ISC has to take place within a few picoseconds in both Bz and TMB. The most probable reason for this behavior is apparent when comparing the calculated energies of S_1 and T_3 (T_4) in Bz (TMB) as collated in Table 4. As pointed out earlier, ISC efficiency is crucially dependent on the singlet−triplet energy gap.[21] According to the calculations in both Bz (0.01 eV) and TMB (0.03 eV) this energy gap is negligible. A very efficient and therewith fast ISC can thus be suggested. Its time scale is even competitive to IC processes.

Analysis of the TA of Me reveals the same number of components as for Bz and TMB, but the values of the associated time constants and particularly their relative amplitudes differ by a substantial amount. The excited states dynamics of benzil—the same system as Me, but without methyl substituents at the aromatic rings—were studied

dx.doi.org/10.1021/ma202673q | Macromolecules 2012, 45, 2257−2266

earlier.[55] In this system the dynamics take place on comparable time scales and were assigned to conformational rearrangements on the S_1 potential energy surface. Taking our experimental results into account, the assignment to configurational rearrangements seems questionable, because substitution at the carbon rings of benzil—as it is the case in Me—should hinder such rearrangements. However, a substantial shift in time constants between benzil and Me cannot be observed. Furthermore, an additional channel into triplet states leading to photoinitiation, as evidenced for benzil[56] was not discussed. Thus, the question is if the observed differences in photoinitiation efficiency[17] can be explained by employing the same reaction model as it was utilized for Bz and TMB. In this case, the process connected with τ_1 would be assigned to depopulation of the excited S_2, τ_2 would be assigned to α-cleavage and the residual absorption with a decay time τ_3 to the produced radicals. The value of τ_1 is substantially lower than in Bz and TMB and within the experimental time resolution. Applying the same considerations as before, the value would point to a convolution of the ISC with an ultrafast IC channel. In opposite to Bz and TMB this IC channel is the by far dominating channel in Me. The assignment is also supported by the relative amplitude ratios of Me. There are several reasons for the prevalence of IC processes. First, the molecule is excited to a higher singlet state (S_2), where the density of states and therewith the probability for IC is strongly increased. At least one ultrafast depopulation channel leading to S_1 is predicted by Kasha's rule.[57] Additionally, as already observed, the MOs involved in the transition are much more delocalized over the whole system increasing the probability of conical intersections between singlet states, which allows for very efficient IC. Moreover, as can be seen from Table 4, Me does not provide excited triplet states with an energy gap to either S_2 or S_1, which is nearly as low as in the case of Bz and TMB. Thus, whether ISC starts from S_2 or S_1 in Me cannot be discerned. The α-cleavage reaction takes place with a time constant τ_2 of 25 ps, which is substantially slower than in TMB (15.9 ps). This finding can be explained again by the different structure of the mesitoyl radical (**2**) producing molecules TMB and Me. The residual TA of Me then partly consists of the same absorbing species like TMB.

The earlier observations of different photoinitiation efficiency[17,19] are thus in the framework of the mechanism proposed here ascribed mainly to a competition between IC and ISC processes in the photoinitiator molecules, while the efficiency of ISC can be estimated sufficiently by TDDFT calculations. The process of radical formation, i.e., the triplet lifetime and kinetics of radical addition to double bonds, seems to play a much less important role. It has to be stressed that the crucial condition, which causes the high efficiency of Bz and TMB, is the excitation of S_1, which shows low oscillator strength to S_0, only minor IC deactivation channels and a quasi-isoenergetic triplet state. It is very likely that excitation into S_n states of both Bz and TMB leads to a breakdown of the ISC efficiency for the same reasons mentioned in the case of Me. In the following considerations an attempt has been made to also quantitatively describe the earlier observed efficiency ratios obtained from the hyphenated PLP/ESI-MS experiments.[17,19] As pointed out during the examination of the steady state spectra of Bz, TMB, and Me, the relation of initiation efficiency between excited Bz and excited TMB is 1:1.8 to 1:2.2 and between excited Bz and excited Me 144:1. As the presented results clearly reveal, the properties of Bz and TMB are very similar. The efficiency ratio between the excited Bz and TMB photoinitiators is therefore predominantly assigned to different initiation efficiencies of the benzoyl radicals (**1**) and mesitoyl radicals (**2**), formed from the photoinitiators in their triplet state. Because Bz and TMB only differ by the radicals they produce (benzoyl (**1**) vs mesitoyl (**2**)), an efficiency relation between TMB and Me can be achieved by multiplying the ratio retrieved for excited Bz and Me (144:1) with the relation between excited Bz and TMB, i.e., approximately a factor of 0.5. The relation between excited TMB and Me is therefore 72:1. This relation is now only dependent on the excited state properties of the respective photoinitiators and not on the nature of the radicals and their reaction kinetics. Assuming comparable TA values of the initially excited state and the produced radicals of TMB and Me, this relation should be revealed by ISC quantum yields, estimated from the relative amplitudes A_1 and A_3 of the fit functions collected in Table 2, which originate from the fits of the TA probed at 500 nm. It is thereby assumed that the quantum yield of radical formation from molecules in their triplet state is $\Phi_R = 1$. As mentioned above, there are differences in TA depending on the probe wavelength. These differences can be ascribed to features in the excited state absorption spectra. However, in the cases of TMB and Me these probe wavelength dependent differences are small compared to the differences between TA of TMB and Me. Because of the difference in initial TA values by a factor of 4, a convolution of the initial relaxation process of Me with the time resolution of the experiment is assumed. This is justified by the value of the time constant as discussed above. Therefore, A_1 of Me is multiplied by a factor of 4. The considerations result in A_3 having a relative value of 85% with respect to A_1 in the case of TMB, resulting in a quantum yield $\Phi_{ISC} = 0.85$. The same considerations result in quantum yields of $\Phi_{ISC} = 0.01$ for Me and $\Phi_{ISC} = 0.12$ for Bz. This leads to an approximated relation of TMB being more efficient than Me by a factor of 82 or Bz being more efficient than Me by a factor of 164. The values are in reasonably good agreement with the factor of 72 (144), derived from the steady state spectra presented herein as well as the normalized extinction coefficients discussed in the context of our PLP/ESI-MS experiments.[17,19] It should be mentioned that due to the low TA intensities observed for Me, the neglect of any radical addition kinetics to monomers and the convolution of ISC dynamics with both the experimental time resolution and additional IC channels, the considerations made above only allow for an estimation of quantum yields and efficiency ratios with relatively large error bars (at least a factor of 2). The same holds for estimated quantum yields where additional uncertainties due to the lack of reproducible pump–probe overlaps in the experiments have to be taken into account.

■ CONCLUSIONS

In summary, it can be stated that the crucial steps for efficient photoinduced polymerization initiation take place in the investigated photoinitiator molecules Bz, TMB, and Me within the first tens of picoseconds after excitation. The absence of dominating ultrafast radiationless deactivation channels is thereby a critical property of a molecule suitable for triplet photoinitiation. The efficiency of photoinitiation is predominantly governed by the efficiency of ISC. Care should be taken with the choice of the state to be excited, e.g., primarily the excitation wavelength, as the initiation efficiency is likely to significantly decrease if the molecule is excited into unsuitable

states. Importantly, the irradiation at the highest absorption band does not correlate with the most efficient excitation and thus initiation pathway.

TA experiments with the concomitant electronic structure theory calculation prove to be a highly useful tool not only for the clarification of the underlying mechanism but in particular for attaining a quantitative picture on the suitability of a particular photoinitiating system. The performance of the studied systems can be estimated by combining femtosecond transient absorption spectroscopy with DFT calculations via a comparison of the derived efficiency relation between Bz and Me of 164:1 with a value of 144:1 obtained by PLP/ESI-MS experiments.[17,19] Thereby, determinations of excited singlet and triplet energies at the respective ground state minimum geometry by TDDFT, which are computationally inexpensive, prove to give sufficient information about excited state structure for estimation of ISC efficiencies preventing computationally intensive excited state surface scans. Because of large differences in extinction coefficients (64 L mol^{-1} cm^{-1} (Bz) vs 12 L mol^{-1} cm^{-1} (TMB) vs 1075 L mol^{-1} cm^{-1} (Me)) and TA intensities at the detection limit in the case of Me, the comparison of the three photoinitiators Bz, TMB, and Me presented here can be regarded as a test case for the capability of the employed combined experimental and theoretical approach.

■ ASSOCIATED CONTENT

Supporting Information

UV/vis spectra of Bz, TMB, and Me in methanol solution (200−400 or 200−530 nm), relative amplitudes of the transient absorption probed at 470 and 600 nm, derived from global multiexponential fits, and structural data of Bz, TMB, and Me, obtained by DFT calculations. This material is available free of charge via the Internet at http://pubs.acs.org.

■ AUTHOR INFORMATION

Corresponding Author

*Tel (+49) 721 608-45642; Fax (+49) 721 608-45740; e-mail christopher.barner-kowollik@kit.edu (C.B.-K.). Tel (+49) 721 608-47807; Fax (+49) 721 608-46524; e-mail andreas.unterreiner@kit.edu (A.-N.U.).

Author Contributions

§These authors equally contributed to the current work.

Notes

The authors declare no competing financial interest.

■ ACKNOWLEDGMENTS

A.-N.U. and T.J.A.W. acknowledge financial support provided by the German Research Council (DFG) and the State of Baden-Württemberg through the Center for Functional Nanostructures within subproject C 3.02 as well as by the Fonds der Chemischen Industrie. C.B.-K. acknowledges financial support for the current project from the German Research Council (DFG) as well as from the Karlsruhe Institute of Technology (KIT) in the context of the Excellence Initiative for leading German universities and the Ministry for Science and Arts of the state of Baden-Württemberg.

■ REFERENCES

(1) Ge, J.; Trujillo, M.; Stansbury, J. W. *J. Dent. Mater.* **2005**.
(2) Anseth, K. S.; Newman, S. M.; Bowman, C. N. *Adv. Polym. Sci.* **1995**, *122*, 177−217.
(3) Fisher, J. P.; Dean, D.; Engel, P. S.; Mikos, A. G. *Annu. Rev. Mater. Res.* **2001**, *31*, 171−181.
(4) Anseth, K. S.; Metters, A. T.; Bryant, S. J.; Martens, P. J.; Elisseeff, J. H.; Bowman, C. N. *J. Controlled Release* **2002**, *78*, 199−209.
(5) Sun, H. B.; Kawata, S. *Adv. Polym. Sci.* **2004**, *170*, 169−273.
(6) Wolf, T. J. A.; Fischer, J.; Wegener, M.; Unterreiner, A.-N. *Opt. Lett.* **2011**, *36*, 3188−3190.
(7) Yagci, Y.; Jockusch, S.; Turro, N. J. *Macromolecules* **2010**, *43*, 6245−6260.
(8) Yilmaz, G.; Tuzun, A.; Yagci, Y. *J. Polym. Sci., Part A: Polym. Chem.* **2010**, *48*, 5120−5125.
(9) Balta, D. K.; Cetiner, N.; Temel, G.; Turgut, Z.; Arsu, N. *J. Photochem. Photobiol., A* **2008**, *199*, 316−321.
(10) Balta, D. K.; Temel, G.; Aydin, M.; Arsu, N. *Eur. Polym. J.* **2010**, *46*, 1374−1379.
(11) Yilmaz, G.; Aydogan, B.; Temel, G.; Arsu, N.; Moszner, N.; Yagci, Y. *Macromolecules* **2010**, *43*, 4520−4526.
(12) Saraiva, M. F.; Couri, M. R. C.; Le Hyaric, M.; de Almeida, M. V. *Tetrahedron* **2009**, *65*, 3563−3572.
(13) Dietlin, C.; Allonas, X.; Morlet-Savary, F.; Fouassier, J. P.; Visconti, M.; Norcini, G.; Romagnano, S. *J. Appl. Polym. Sci.* **2008**, *109*, 825−833.
(14) Lalevée, J.; Morlet-Savary, F.; Roz, M. E.; Allonas, X.; Fouassier, J. P. *Macromol. Chem. Phys.* **2009**, *210*, 311−319.
(15) Lalevee, J.; Blanchard, N.; Tehfe, M. A.; Fries, C.; Morlet-Savary, F.; Gigmes, D.; Fouassier, J. P. *Polym. Chem.* **2011**, *2*, 1077−1084.
(16) Lalevee, J.; E. I. Roz, M.; Tehfe, M. A.; Alaaeddine, M.; Allonas, X.; Fouassier, J. P. *J. Photopolym. Sci. Technol.* **2009**, *22*, 587−590.
(17) Voll, D.; Junkers, T.; Barner-Kowollik, C. *Macromolecules* **2011**, *44*, 2542−2551.
(18) Voll, D.; Hufendiek, A.; Junkers, T.; Barner-Kowollik, C. *Macromol. Rapid Commun.* **2012**, *33*, 47−53.
(19) Günzler, F.; Wong, E. H. H.; Koo, S. P. S.; Junkers, T.; Barner-Kowollik, C. *Macromolecules* **2009**, *42*, 1488−1493.
(20) Jankowiak, A.; Kaszynski, P. *J. Org. Chem.* **2009**, *74*, 7441−7448.
(21) Englman, R.; Jortner, J. *Mol. Phys.* **1970**, *18*, 145−164.
(22) Pawelka, Z.; Kryachko, E. S.; Zeegers-Huyskens, T. *Chem. Phys.* **2003**, *287*, 143−153.
(23) Lewis, F. D.; Lauterbach, R. T.; Heine, H. G.; Hartmann, W.; Rudolph, H. *J. Am. Chem. Soc.* **1975**, *97*, 1519−1525.
(24) Lipson, M.; Turro, N. J. *J. Photochem. Photobiol., A* **1996**, *99*, 93−96.
(25) Shrestha, N. K.; Yagi, E. J.; Takatori, Y.; Kawai, A.; Kajii, Y.; Shibuya, K.; Obi, K. *J. Photochem. Photobiol., A* **1998**, *116*, 179−185.
(26) Riedle, E.; Beutter, M.; Lochbrunner, S.; Piel, J.; Schenkl, S.; Spörlein, S.; Zinth, W. *Appl. Phys. B: Laser Opt.* **2000**, *71*, 457−465.
(27) Ahlrichs, R.; Bär, M.; Häser, M.; Horn, H.; Kölmel, C. *Chem. Phys. Lett.* **1989**, *162*, 165−169.
(28) Treutler, O.; Ahlrichs, R. *J. Chem. Phys.* **1995**, *102*, 346−354.
(29) Eichkorn, K.; Treutler, O.; Öhm, H.; Häser, M.; Ahlrichs, R. *Chem. Phys. Lett.* **1995**, *240*, 283−290.
(30) Eichkorn, K.; Treutler, O.; Öhm, H.; Häser, M.; Ahlrichs, R. *Chem. Phys. Lett.* **1995**, *242*, 652−660.
(31) Eichkorn, K.; Weigend, F.; Treutler, O.; Ahlrichs, R. *Theor. Chim. Acc.* **1997**, *97*, 119−124.
(32) Weigend, F. *Phys. Chem. Chem. Phys.* **2006**, *8*, 1057−1065.
(33) Schafer, A.; Horn, H.; Ahlrichs, R. *J. Chem. Phys.* **1992**, *97*, 2571−2577.
(34) Kendall, R. A.; Dunning, J. T. H.; Harrison, R. J. *J. Chem. Phys.* **1992**, *96*, 6796−6806.
(35) Furche, F.; Rappoport, D. In *Computational Photochemistry*; Olivucci, M., Ed.; Elsevier: Amsterdam, 2005; Vol. *16*.
(36) Bauernschmitt, R.; Ahlrichs, R. *Chem. Phys. Lett.* **1996**, *256*, 454−464.
(37) Bauernschmitt, R.; Ahlrichs, R. *J. Chem. Phys.* **1996**, *104*, 9047−9052.
(38) Gray, A. R.; Fuson, R. C. *J. Am. Chem. Soc.* **1934**, *56*, 739−741.

(39) Fuson, R. C.; Weinstock, H. H.; Ullyot, G. E. *J. Am. Chem. Soc.* **1935**, *57*, 1803−1804.
(40) Weinstock, H. H.; Fuson, R. C. *J. Am. Chem. Soc.* **1936**, *58*, 1986−1988.
(41) Nudelman, N.; Schulz, H. *J. Chem. Res., Synop.* **1999**, 422−423.
(42) Rathman, T. L.; Woltermann, C. J. *Pharma Chem.* **2003**, *2*, 6−8.
(43) Kryukov, P. G. *Quantum Electron.* **2001**, *31*, 95.
(44) Fileti, E. E.; Canuto, S. *Int. J. Quantum Chem.* **2005**, *104*, 808−815.
(45) Biswas, S. C.; Sen, R. K. *Chem. Phys. Lett.* **1983**, *94*, 415−416.
(46) Brown, C. J.; Sadanaga, R. *Acta Crystallogr.* **1965**, *18*, 158−164.
(47) Das, K. K.; Majumdar, D. *J. Mol. Struct.: THEOCHEM* **1993**, *288*, 55−61.
(48) El-Sayed, M. A. *J. Chem. Phys.* **1963**, *38*, 2834−2838.
(49) Seidl, B.; Liska, R.; Grabner, G. *J. Photochem. Photobiol., A* **2006**, *180*, 109−117.
(50) Jockusch, S.; Koptyug, I. V.; McGarry, P. F.; Sluggett, G. W.; Turro, N. J.; Watkins, D. M. *J. Am. Chem. Soc.* **1997**, *119*, 11495−11501.
(51) Jockusch, S.; Landis, M. S.; Freiermuth, B.; Turro, N. J. *Macromolecules* **2001**, *34*, 1619−1626.
(52) Morales-Cueto, R.; Esquivelzeta-Rabell, M.; Saucedo-Zugazagoitia, J.; Peon, J. *J. Phys. Chem. A* **2007**, *111*, 552−557.
(53) Turro, N. J.; Ramamurthy, V.; Scaiano, J. C. *Modern Molecular Photochemistry of Organic Molecules*; University Science Books: Sausalito, 2010.
(54) Ma, C.; Du, Y.; Kwok, W. M.; Phillips, D. L. *Chem.—Eur. J.* **2007**, *13*, 2290−2305.
(55) Singh, A. K.; Palit, D. K.; Mittal, J. P. *Chem. Phys. Lett.* **2002**, *360*, 443−452.
(56) Lemee, V.; Burget, D.; Jacques, P.; Fouassier, J. P. *J. Polym. Sci., Part A: Polym. Chem.* **2000**, *38*, 1785−1794.
(57) Kasha, M. *Faraday Discuss.* **1950**, *9*, 14−19.

Macromolecules

Article

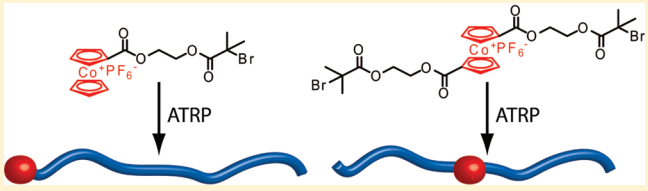
pubs.acs.org/Macromolecules

Preparation of Cobaltocenium-Labeled Polymers by Atom Transfer Radical Polymerization

Lixia Ren, Jiuyang Zhang, Christopher G. Hardy, Deon Doxie, Barbara Fleming, and Chuanbing Tang*

Department of Chemistry and Biochemistry and USC Nanocenter, University of South Carolina, 631 Sumter Street, Columbia, South Carolina 29208, United States

ABSTRACT: Cobaltocenium-labeled polymers were prepared by atom transfer radical polymerization (ATRP) using cobaltocenium-containing α-haloesters as initiators. The locations of the cobaltocenium moiety in the polymer chains (either at the end or in the middle) were dictated by the chemical structures of initiators. Kinetic studies showed that polymerizations of styrene, tert-butyl acrylate, and methyl methacrylate monomers followed a controlled/living manner, except that polymerization of methyl methacrylate with the aid of cobaltocenium monoinitiator displayed significant termination. All resultant polymers were redox-active and exhibited characteristic UV−vis absorption from the cobaltocenium moiety.



INTRODUCTION

Labeled polymers are a class of important functional materials[1,2] which have found applications in molecular imaging,[3−6] (bio)sensing,[5,7−9] targeting,[10−14] electrode-decorating,[15−18] etc. Based on their specific applications, labeled polymers are designed to be optically active,[3,5,19−23] redox-active,[8,15,17,18,24−28] or radioactive.[29−31] By labeling the polymer chain with detectable probes, the study of polymer behavior in solution, especially single polymer chains, would be more accurate. For example, molecular weight of a chromophore-labeled polymer can be precisely determined by analyzing the chromophore probe using UV−vis spectroscopy.[23] Among diverse probes, redox-active probes have attracted special attention due to their high sensitivity, rapid response, and easy detection via appropriate analytical tools,[24] which can make them "visible" in solution. Metallocenes, which are widely used as sensors and catalysts,[8,32,33] are often used as redox probes due to their reversible electrochemical oxidation and reduction as well as their notable environmental stability.[27,34] Metallocenes have been used to label natural biopolymers including DNA,[35,36] proteins,[25] and drugs,[26] and synthetic polymers such as poly(ethylene oxide)[37] and polyamides.[27] Assembly of ferrocene-labeled streptavidin on biotinylated electrodes results in a reproducible unidirectional current flow in the presence of electron donors in solution.[15] Ferrocene-labeled polymers can be mapped via electrochemical atomic force microscopy.[18] A ferrocene-labeled poly(ethylene glycol) was used to study the chain dynamics of a poly(ethylene glycol) matrix via quantitative electrochemical diffusion measurements.[21,37,38] Recently, Zhu et al. prepared ferrocene-containing transfer agents for reversible addition−fragmentation transfer polymerization.[39]

Cobaltocenium, an 18-electron cationic metallocene, has been used as a redox probe due to its one-electron reversible reduction (to cobaltocene) and high sensitivity (detection limit up to 10^{-8} M solution).[16] In addition, cobaltocenium has extremely high structure integrity stability toward oxidation (the half-wave potential ($E_{1/2}$) of the Co(III)/Co(IV) couple falling at ca. 2.7 V vs ferrocene).[16,26] These properties make cobaltocenium a desirable candidate as a redox-active probe for use in polymeric materials. In addition, cobaltocenium has characteristic optical absorption in the UV region. We have recently developed a class of side-chain cobaltocenium-containing polymers through both postpolymerization modification and direct polymerization.[40−44] A few other groups have developed cobaltocenium-containing dendrimers and main-chain cobaltocenium-containing polymers.[45−49] However, cobaltocenium-labeled polymers have not been reported in the literature.

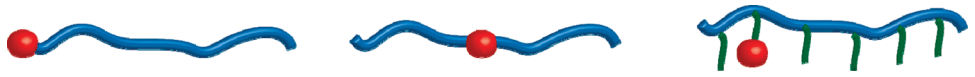
There are three major pathways to prepare labeled polymers:[5] (1) Postpolymerization modification by labeling probes through covalent attachment[27] or supramolecular interactions.[50] However, this strategy requires highly efficient postpolymerization modification reactions. Additionally, the number of probe units is rather difficult to control. (2) Direct polymerization using a probe-labeled functional monomer as a comonomer.[51] However, the accurate position of probes is difficult to measure. (3) With the development of controlled and living polymerization,[52−56] probes can be also integrated into initiators,[13,57] transfer agents,[39] or mediating agents,[3,58] which can be used to prepare polymers with precise information about location and number of probes. These probes can be located at the end of or in the middle of polymer chain, or placed at the side chain or the backbone of polymers, as shown in Scheme 1.

Herein, we report the preparation of novel cobaltocenium-labeled polymers by atom transfer radical polymerization (ATRP), one of the most widely used controlled radical

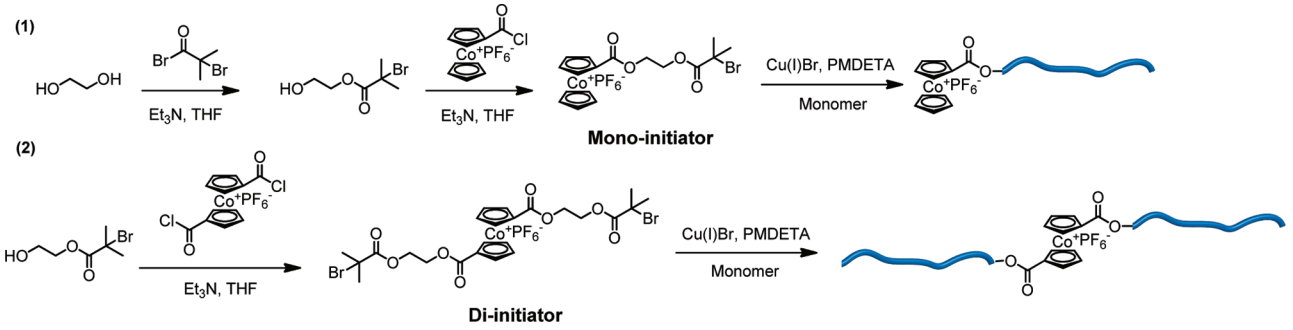
Received: December 16, 2011
Revised: February 7, 2012
Published: February 16, 2012

 © 2012 American Chemical Society dx.doi.org/10.1021/ma202725c | *Macromolecules* 2012, 45, 2267−2275

Scheme 1. Labeled Polymers with a Probe at Diverse Locations of Polymer Chains



Scheme 2. Synthesis of Cobaltocenium-Containing α-Haloesters and Their Use as Initiators To Prepare Cobaltocenium-Labeled Polymers by ATRP



polymerizations to prepare functional materials.[54,55,59−61] Specifically, we designed two cobaltocenium-based α-haloesters, monosubstituted and 1,1′-disubstituted bromoisobutyrate cobaltoceniumcarboxylate, which were used as ATRP initiators. With the aid of these initiators, polymers from three different classes of monomers (acrylate, methacrylate, and styrene) with cobaltocenium as the optically active redox-active probe were prepared. As shown in Scheme 2, all polymers have one cobaltocenium probe per chain with a predetermined location, either at the chain end or in the middle of chain. Kinetic studies using both initiators were conducted. The optical and redox properties of resultant cobaltocenium-containing polymers were studied by UV−vis spectroscopy and cyclic voltammetry, respectively.

EXPERIMENTAL SECTION

Materials. Ethylene glycol (anhydrous, Aldrich), 2-bromoisobutyryl bromide (Aldrich), Cu(I)Br (99.999%, Aldrich), *N*,*N*,*N*′,*N*″,*N*″-pentamethyldiethylenetriamine (PMDETA, Aldrich), sodium hexafluorophosphate ($NaPF_6$, 99%, Alfa Aesar), and tetra-*n*-butylammonium hexafluorophosphate ($TBAPF_6$, 98%, Acros) were used as received. Triethylamine (Et_3N, 99%, Aldrich) and tetrahydrofuran (THF, Alfa Aesar) were distilled before use. Cobaltocenium monoacyl chloride and diacyl chloride were synthesized according to our early reports.[40,41] Styrene (St, Aldrich), *tert*-butyl acrylate (tBA, Aldrich), and methyl methacrylate (MMA, Aldrich) were freshly distilled before use. All other chemicals were obtained from commercial sources and used as received unless otherwise mentioned.

Characterization. ^{1}H NMR (400 MHz) and ^{13}C NMR (100 MHz) spectra were recorded on a Varian Mercury 400 spectrometer with tetramethylsilane (TMS) as an internal reference. Gel permeation chromatography (GPC) was performed in dimethylformamide (DMF, containing 0.1% LiBr) at a flow rate of 0.8 mL/min at 50 °C on a Varian system equipped with a ProStar 210 pump and a Varian 356-LC RI detector and three 5 μm phenogel columns (Phenomenex Co.) with narrow dispersed polystyrene as standards. High-resolution mass spectrometry (MS) was conducted on a Waters Micromass quadropole time-of-flight mass spectrometer, using electrospray ionization in a positive ion mode. UV−vis spectra were recorded on a Shimadzu UV 2450 spectrophotometer. Cyclic voltammetry (CV) characterization was carried on a BAS CV-50W voltametric analyzer. The samples were dissolved in 0.1 M $TBAPF_6$ solution in DMF at a concentration of 0.5 mM. The samples were then purged with nitrogen gas for 10 min before running CV. The samples were scanned at a rate of 100 mV/s at different potential ranges vs Ag/AgCl electrode.

Synthesis of 2-Hydroxyethyl 2-Bromoisobutyrate (HEBiB). HEBiB was synthesized following reported procedures.[62−64] Ethylene glycol (40.0 mL, 7.2 × 10^{-1} mol) and triethylamine (6.0 mL, 4.3 × 10^{-2} mol) were added into a dry flask followed by adding 2-bromoisobutyryl bromide (5.4 mL, 4.3 × 10^{-2} mol) dropwise over 1 h at 0 °C. The reaction mixture was kept at 60 °C overnight, followed by adding water (300 mL) and extracting with dichloromethane (3 × 200 mL). The organic layer was collected and dried over anhydrous magnesium sulfate. The product was purified by passing through a silica column with dichloromethane as eluent. Yield: 85%. ^{1}H NMR ($CDCl_3$) δ: 3.84 (t, 2H, $HOCH_2CH_2$); 4.30 (t, 2H, $HOCH_2CH_2$); 1.92 (s, 6H, CH_3). ^{13}C NMR ($CDCl_3$) δ: 171.7 ($Br(CH_3)_2CCO$); 66.8 ($HOCH_2CH_2$); 60.1 ($HOCH_2CH_2$); 50.9 ($Br(CH_3)_2C$); 32.8 (CH_3).

Synthesis of Cobaltocenium Di-initiator. Freshly prepared cobaltocenium 1,1′-diacyl chloride (0.56 g, 1.2 × 10^{-3} mol) and HEBiB (1.50 g, 7.2 × 10^{-3} mol) were added into a dry round-bottom flask with 100 mL of dry THF. Triethylamine (1.0 mL, 7.4 × 10^{-3} mol) was added slowly. The reaction mixture was stirred at room temperature for 5 days. Afterward, solvents were evaporated and the crude product was dissolved in dichloromethane followed by sequential extraction with aqueous $NaPF_6$ solution and water. The organic layer was dried over anhydrous magnesium sulfate and precipitated from diethyl ether to give the product. Yield: 90%. ^{1}H NMR ($CDCl_3$) δ: 6.25 (broad, 4H, Cp); 6.15 (broad, 4H, Cp); 4.56 (dt, 8H, OCH_2CH_2O); 1.92 (s, 12H, CH_3). ^{13}C NMR ($CDCl_3$) δ: 171.5 ($Br(CH_3)_2CCO$); 162.5 (CpCO); 85−89 (carbon from Cp ring); 64.2 and 65.0 (OCH_2CH_2O); 56.2 ($Br(CH_3)_2CCO$); 30.2 (CH_3). MS: theoretical m/z 569.94; found m/z 569.85.

Synthesis of Cobaltocenium Monoinitiator. The preparation was similar to the synthesis of cobaltocenium di-initiator. Cobaltocenium monoacyl chloride (0.48 g, 1.2 × 10^{-3} mol) and HEBiB (0.75 g, 3.6 × 10^{-3} mol) were mixed in a THF (100 mL) solution, followed by adding triethylamine (0.5 mL, 3.7 × 10^{-3} mol) slowly. The reaction mixture was stirred at room temperature for 5 days. The product was purified using the same procedure as the synthesis of cobaltocenium di-initiator. Yield: 90%. ^{1}H NMR ($CDCl_3$) δ: 6.20 (broad, 2H, Cp); 5.95 (broad, 2H, Cp); 5.82 (broad, Cp, 5H); 4.61 (d, broad, 4H, OCH_2CH_2O); 1.91 (s, 6H, CH_3). ^{13}C NMR ($CDCl_3$) δ: 171.7 ($Br(CH_3)_2CCO$); 163.6 (CpCO); 85−89 (carbon from Cp ring); 62.9 and 65.0 (OCH_2CH_2O); 55.7 ($Br(CH_3)_2CCO$); 30.2 (CH_3). MS: theoretical m/z 424.98; found m/z 424.89.

Polymerization Procedure. The polymerization of all three monomers was very similar. A typical procedure was as follows. Cu(I)Br (2 equiv) and cobaltocenium monoinitiator (1 equiv) or cobaltocenium di-initiator (1 equiv of bromide) were charged into a Schlenk flask and degassed under nitrogen. Degassed monomer (400 equiv) and PMDETA (2 equiv) were then transferred into the Schlenk flask under the protection of nitrogen. The polymerization was

conducted at 90 °C for St or tBA, while the polymerization of MMA was conducted at room temperature. Samples were taken out at predetermined intervals to monitor the reaction conversion before stopping the reaction. The final polymers were obtained by precipitation in methanol.

(1) Polymer PMMA-*Cc*-PMMA: ^{1}H NMR ($CDCl_3$, δ): 3.35−3.75 (broad, OCH_3), 2.15−2.40 (broad, CH_2−C(CH_3)), 1.20−1.95 (broad, CH_2−C(CH_3)). GPC M_n: 120 100 g/mol; PDI: 1.20.

(2) Polymer PtBA-*Cc*-PtBA: ^{1}H NMR ($CDCl_3$, δ): 2.00−2.35 (broad, CH_2−CH), 1.65−1.80 (broad, CH_2−CH), 1.00−1.65 (broad, −C(CH_3)$_3$). GPC M_n: 22 500 g/mol; PDI: 1.45.

(3) Polymer PSt-*Cc*-PSt: ^{1}H NMR ($CDCl_3$, δ): 6.00−7.2 (broad, aromatic), 0.80−2.00 (broad, CH_2−CH). GPC M_n: 123 000 g/mol; PDI: 1.20.

(4) Polymer *Cc*-PMMA: ^{1}H NMR ($CDCl_3$, δ): 3.35−3.75 (broad, OCH_3), 2.15−2.40 (broad, CH_2−C(CH_3)), 1.20−1.95 (broad, CH_2−C(CH_3)).

(5) Polymer *Cc*-PtBA: ^{1}H NMR ($CDCl_3$, δ): 2.00−2.35 (broad, CH_2−CH), 1.65−1.80 (broad, CH_2−CH), 1.00−1.65 (broad, −C(CH_3)$_3$). GPC M_n: 135 000 g/mol; PDI: 1.18.

(6) Polymer *Cc*-PSt: ^{1}H NMR ($CDCl_3$, δ): 6.00−7.2 (broad, aromatic), 0.80−2.00 (broad, CH_2−CH). GPC M_n: 134 200 g/mol; PDI: 1.35.

Kinetic Study of Monomers Initiated by Cobaltocenium Di-initiator and Monoinitiator. All kinetic studies were conducted similarly as aforementioned. Here, the St polymerization is described as an example. Cobaltocenium di-initiator (4.1 mg, 5.0×10^{-6} mol) and Cu(I)Br (2.8 mg, 2.0×10^{-5} mol) were charged into a Schlenk flask and purged with nitrogen for 30 min. Degassed St (0.9 mL, 9.0×10^{-3} mol) and PMDETA (5 μL, 2.0×10^{-5} mol) were transferred into the Schlenk flask. The flask was placed in an oil bath set at 90 °C. Samples were taken at different intervals under the protection of nitrogen. The conversion of the monomers was calculated by ^{1}H NMR analyses. The kinetic studies of all three monomers initiated by cobaltocenium monoinitiator were also conducted similarly to those using the cobaltocenium di-initiator. It should be noted that the kinetic studies of MMA monomers were conducted at room temperature.

RESULTS AND DISCUSSION

Synthesis of Cobaltocenium-Ended and Cobaltocenium-Centered Polymers by ATRP. As shown in Scheme 2, cobaltocenium-containing ATRP initiators were synthesized via esterification reactions between cobaltocenium acyl chloride and 2-hydroxyethyl 2-bromoisobutyrate (HEBiB), in the presence of triethylamine. The use of 1,1′-diacyl chloride and monoacyl chloride produced cobaltocenium di-initiator and monoinitiator respectively, with yields at ∼90%. Both initiators were characterized by proton and carbon NMR. As shown in Figure 1A, the ^{1}H NMR spectrum of the di-initiator showed peaks at 5.97−6.33, 4.37−4.73, and 1.75−2.10 ppm, corresponding to characteristic Cp protons, ethylene protons, and methyl protons, respectively. The integration ratios of each group were in great agreement with theoretical ones. ^{13}C NMR agreed very well with the ^{1}H NMR result, and each signal was clearly assigned (Figure 1B). The identity of di-initiator was further confirmed by high-resolution MS, which showed a mass/charge (m/z) ratio of 569.85, consistent with the theoretical m/z of 569.94. Compared to the di-initiator, monoinitiator showed slight shift to the lower field for both the Cp protons (5.75−6.25 ppm) and the ethylene protons (4.50−4.70 ppm), as shown in Figure 2A. Three distinct peaks were observed for the Cp protons. The ^{13}C NMR spectrum showed similar chemical shifts for all characteristic protons to those of the di-initiator (Figure 2B). High-resolution MS showed that the m/z ratio was 424.89, in a good agreement with the theoretical ratio of 424.98. Therefore, both

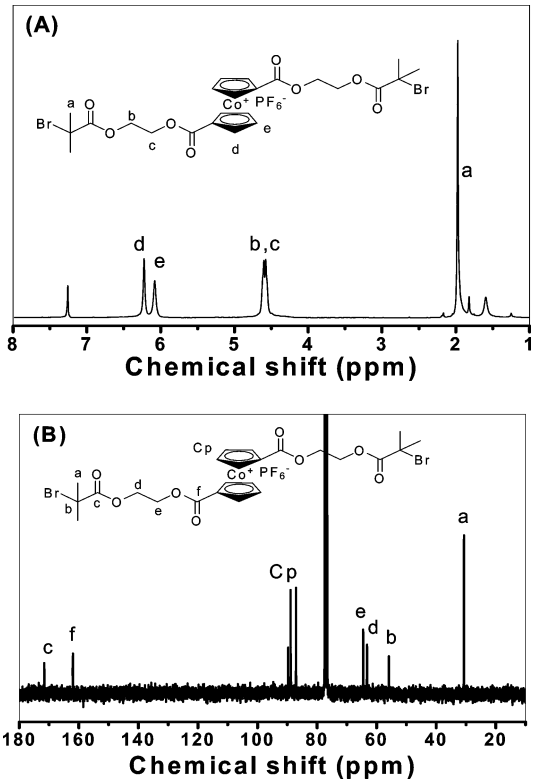


Figure 1. (A) ^{1}H NMR and (B) ^{13}C NMR spectra of cobaltocenium di-initiator in $CDCl_3$.

cobaltocenium-containing ATRP initiators were successfully synthesized by simple esterification reactions with high yields.

We first conducted polymerization of tBA in solution. However, the polymerization was very slow, as only 30% conversion was reached after 24 h. Hence, bulk polymerization was carried out for all monomers initiated by cobaltocenium-containing initiators reported in this paper. Both tBA and St polymerizations were carried out at 90 °C, while MMA polymerization was employed at room temperature. Bulk polymerizations of monomers including tBA, St, and MMA were first carried out with the aid of cobaltocenium-containing di-initiator. The catalyst system consisted of copper(I) bromide and PMDETA. The molar ratio of catalyst to initiator was 4:1 (2:1 for copper bromide to the bromide in the initiator). As reactions continued, all reaction mixtures clearly turned more viscous. Figure 3A shows the ^{1}H NMR spectrum of PMMA polymers initiated by the di-initiator. The vinyl protons (5.0−6.0 ppm) from the monomers disappeared completely, while broad peaks from 1.0 to 2.5 ppm appeared, corresponding to protons from the PMMA backbone. More importantly, for a polymer with relatively lower molecular weight, two peaks were clearly observed at lower field from 6.05 to 6.23 ppm, which originated from Cp protons of the cobaltocenium moiety from the initiator in the middle of polymer chain. Similarly, PtBA and PSt prepared by ATRP with the cobaltocenium di-initiator showed their respective signals in the NMR spectra (Figure 3B,C). Figure 4 shows the GPC traces of the polymers, PtBA-*Cc*-PtBA, PSt-*Cc*-PSt, and PMMA-*Cc*-PMMA, synthesized using the cobaltocenium di-initiator. In all cases, symmetric monomodal peaks were observed. The polydispersity indexes (PDI) of PSt-*Cc*-PSt and PMMA-*Cc*-PMMA were ∼1.20 while the PtBA-*Cc*-PtBA had a higher PDI of 1.45.

dx.doi.org/10.1021/ma202725c | *Macromolecules* 2012, 45, 2267−2275

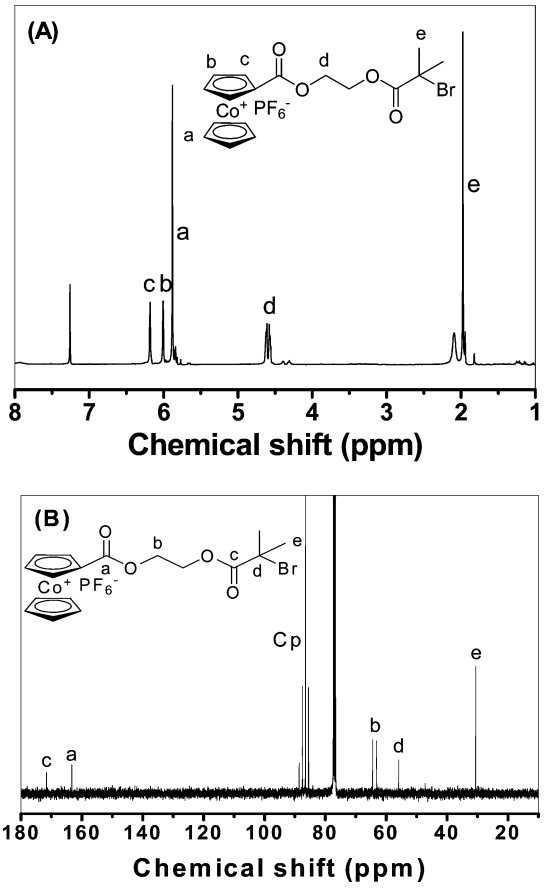


Figure 2. (A) ^{1}H NMR and (B) ^{13}C NMR spectra of cobaltocenium monoinitiator in $CDCl_3$.

In order to verify whether the polymerization was living and controlled, kinetic studies of all monomer polymerization were carried out. The conversion was determined from in situ ^{1}H NMR analysis by comparing the integration areas between the monomers and polymers in the reaction system. Figure 5A shows the semilogarithmic plots of $\ln([M_0]/[M])$ vs reaction time for polymerization of monomers initiated by the cobaltocenium di-initiator. These plots exhibited linear kinetics, indicating that all polymerizations followed a controlled and living manner. While the rates of polymerization of St and tBA were very close, the polymerization of MMA was much faster. The conversion of MMA reached 50% within 2.5 h, while it took 10 h for St to reach a comparable conversion. The evolution of molecular weight vs conversion was also monitored in the polymerizations of tBA, St, and MMA. Clearly the molecular weight increased linearly with the conversion, another signature of controlled and living polymerizations (Figure 5B).

The cobaltocenium monoinitiator was then used to conduct ATRP of tBA, St, and MMA under similar conditions. Figure 6 shows the ^{1}H NMR spectra of *Cc*-PtBA, *Cc*-PSt, and *Cc*-PMMA polymers, which showed similar characteristic peaks to those observed from polymers prepared by the cobaltocenium di-initiator. A representative ^{1}H NMR spectrum of *Cc*-PtBA with relatively lower molecular weight clearly showed typical signals in the range of 5.85−6.45 ppm, corresponding to the Cp protons from the ended cobaltocenium moiety. Figure 7 shows the GPC traces of the polymers synthesized using the cobaltocenium monoinitiator. *Cc*-PtBA had a symmetric trace

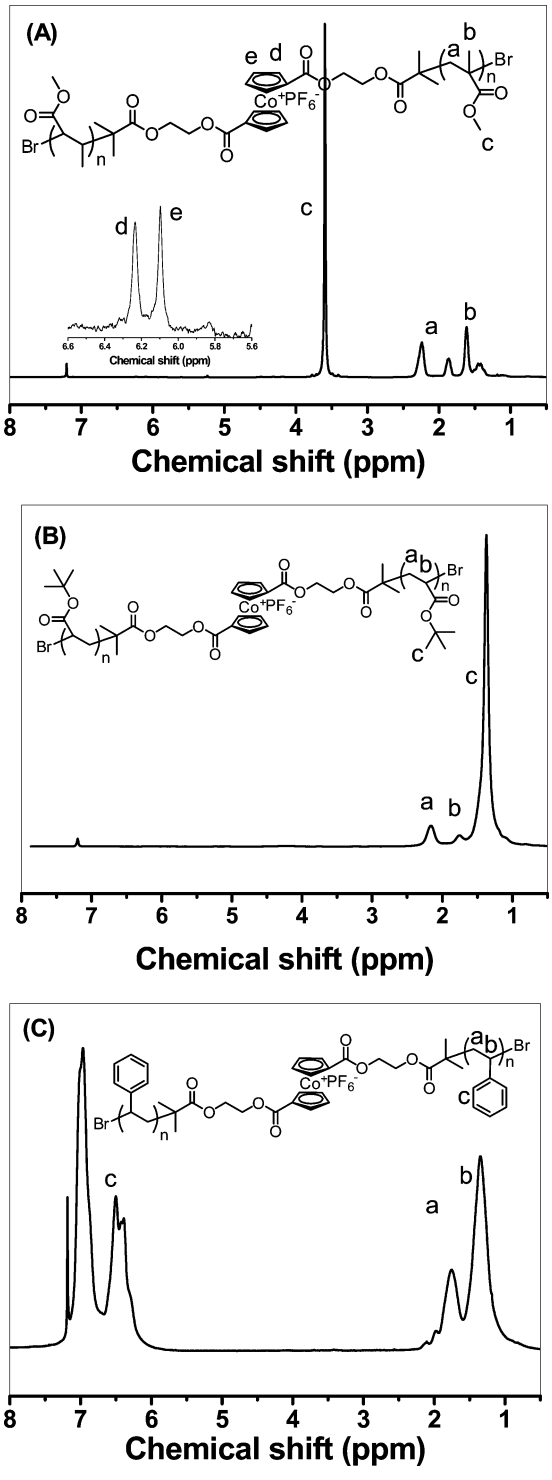


Figure 3. ^{1}H NMR spectra of (A) PMMA, (B) PtBA, and (C) PSt prepared by ATRP with the use of cobaltocenium di-initiator in $CDCl_3$.

with the PDI as low as 1.18. Although *Cc*-PSt had a PDI of 1.35, a shoulder appeared at the higher molecular weight end, suggesting that some bimolecular termination may occur. The *Cc*-PMMA polymer exhibited an asymmetrical trace with a rough baseline, indicating the polymerization was not controlled.

Kinetic studies were conducted using the cobaltocenium monoinitiator and the same procedures as those with the

dx.doi.org/10.1021/ma202725c | *Macromolecules* 2012, 45, 2267−2275

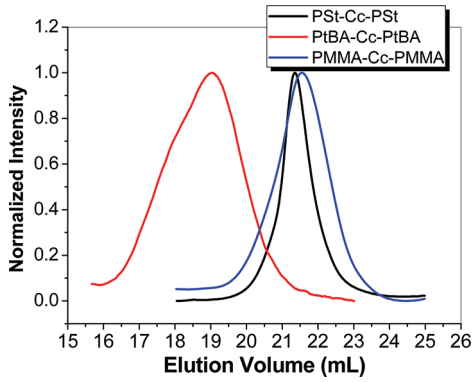


Figure 4. GPC traces of PtBA-*Cc*-PtBA, PSt-*Cc*-PSt, and PMMA-*Cc*-PMMA prepared by ATRP with the use of cobaltocenium di-initiator.

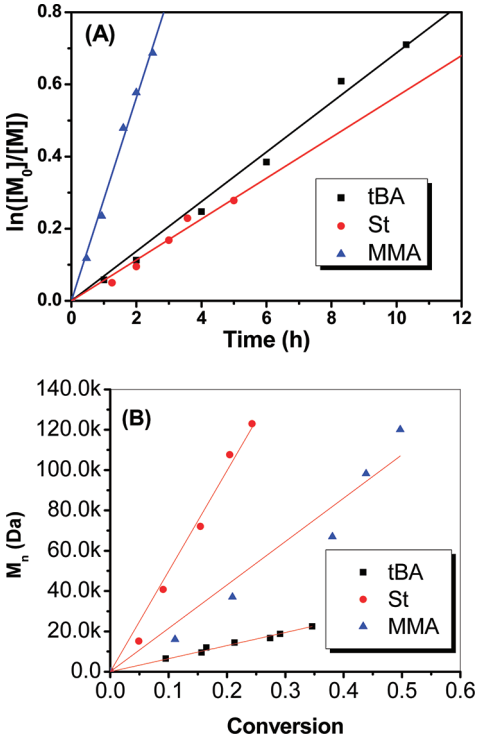


Figure 5. (A) Semilogarithmic plots and (B) number-average molecular weight vs conversion for bulk polymerizations of tBA, St, and MMA initiated by the cobaltocenium di-initiator.

cobaltocenium di-initiator. As shown in Figure 8, bulk polymerizations of both St and tBA exhibited linear kinetics, while the molecular weight had a linear relationship with conversion. All these results indicated the polymerizations of tBA and St were controlled and living. In addition, the rates of polymerization for tBA and St were also comparable. However, the kinetic plot of polymerization of MMA showed a distinct curvature, a signature of significant termination. Nevertheless, at conversions below 50% the polymerization of MMA was still much faster than that of St and tBA. Repeated experiments showed similar kinetics. This is in sharp contrast with the living characteristics of MMA initiated by the cobaltocenium di-initiator. Given that both initiators have similar functionalities, this behavior was quite peculiar. It is not very clear at this stage what could induce the significant termination reactions.

Ion-Exchange Effect on the Polymerization. In our early study,[41,43] we have demonstrated that the counterions of

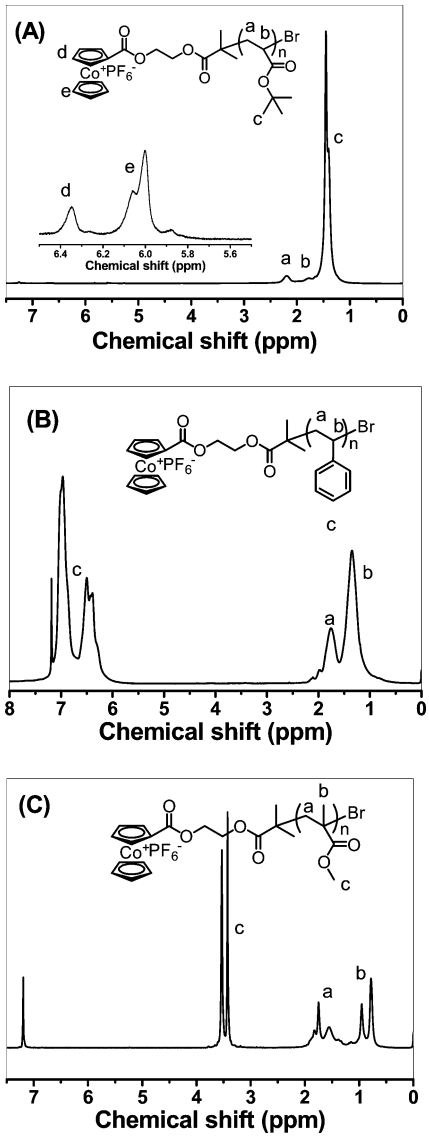


Figure 6. ^{1}H NMR spectra of (A) PtBA, (B) PSt, and (C) PMMA prepared by ATRP with the use of the cobaltocenium monoinitiator.

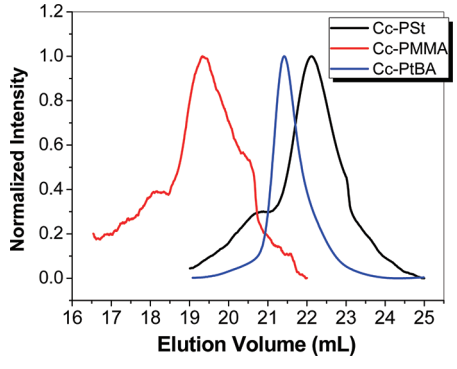


Figure 7. GPC traces of *Cc*-PtBA, *Cc*-PSt, and *Cc*-PMMA prepared by ATRP with the use of the cobaltocenium monoinitiator.

cobaltocenium can undergo exchange with other anions. With the use of chloride-based anionic exchange resin, hexafluorophosphate ions can be readily exchanged to chloride ions. This early work indicated that a similar ion exchange between hexafluorophosphate ions in the cobaltocenium initiators and

dx.doi.org/10.1021/ma202725c | *Macromolecules* 2012, 45, 2267–2275

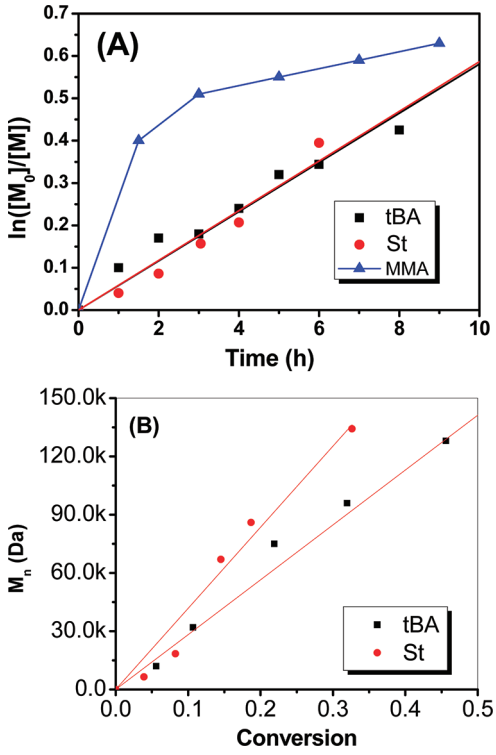


Figure 8. (A) Semilogarithmic plots of bulk polymerization of tBA, St, and MMA initiated by cobaltocenium monoinitiator. (B) number-average molecular weight vs conversion for bulk polymerizations of tBA and St initiated by cobaltocenium monoinitiator (due to the nonliving behavior of MMA polymerization, M_n vs conversion was not monitored).

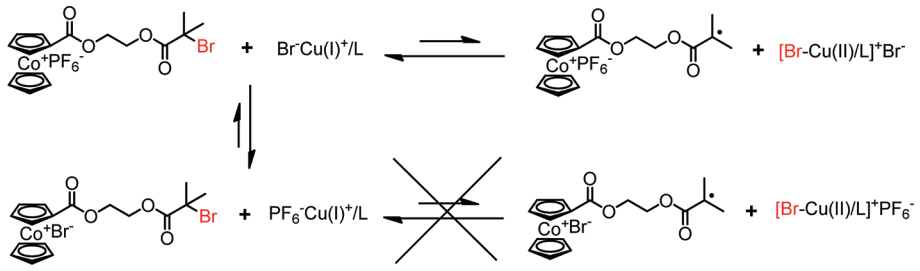
bromide ions in the copper catalysts should occur. Such exchange could induce significant undesirable effects on the activation and deactivation equilibrium of the ATRP process. This hypothesis was confirmed with the following experiments, in which the 1:1 molar ratio of the bromide in the initiators and copper(I) bromide led to the formation of uncontrolled polymers with very low molecular weight. As shown in Scheme 3, the exchange between hexafluorophosphate ions and copper(I) bromide would significantly alter the activation and deactivation equilibrium, as copper hexafluorophosphate is a very poor catalyst. Therefore, all the reaction systems were intentionally designed with the 1:2 molar ratio of the bromide in the initiators and copper(I) bromide. The 1 equiv of excess of copper(I) bromide would be used as a "buffer reagent" to digest the hexafluorophosphate ions and therefore minimize the ion-exchange effect on the control of polymerization. Another possible strategy is to prepare cobaltocenium initiators with halide as the counterions. However, our preliminary study indicated that these initiators were somehow not stable, ultimately leading to the decomposition of the cobaltocenium moiety. More investigations on this matter are currently in progress.

The ion-exchange process was further confirmed with ATRP experiments on cobaltocenium-containing monomers. We have failed to polymerize any cobaltocenium hexafluorophosphate-containing vinyl monomers by ATRP. Most likely, the reaction system was involved with the ion-exchange process between cobaltocenium hexafluorophosphate in the vinyl monomers and catalyst copper(I) bromide, as shown in Scheme 4. Since the molar ratio of monomer to catalyst is usually very high (i.e., 100:1), even a small fraction of monomers (i.e., 1%) participating the ion exchange would cause all catalysts to lose activity.

Optical and Redox Properties. Using the cobaltocenium-containing ATRP initiators, single cobaltocenium-labeled polymers PtBA, PSt, and PMMA were obtained. The presence of cobaltocenium was quantitatively verified from ^{1}H NMR analysis discussed above. In our early report,[41] we have shown that side-chain cobaltocenium-containing polymers exhibited characteristic UV−vis absorption from their cobaltocenium units. Therefore, UV−vis spectroscopy was first used to monitor the cobaltocenium moiety in these labeled polymers prepared by ATRP. Figure 9 showed the representative UV−vis absorption spectra of cobaltocenium-containing initiators and their polymers. Both cobaltocenium mono- and di-initiators exhibited two characteristic absorptions at 229 and 276 nm, which were assigned to $\pi-\pi^*$ or $n-\pi^*$ transitions of cobaltocenium, very similar to transitions in ferrocene studied by Scott and Becker.[65] A weak absorption at 410 nm corresponded to the d−d* transition of cobaltocenium. All cobaltocenium-labeled polymers showed a typical absorption at ca. 230 nm, similar to the initiators. In addition, these polymers also showed an absorption peak in the range of 260−300 nm. The peak at ~400 nm was much weaker in most cobaltocenium-labeled polymers. The change of peak intensity and the variation of peak positions were most likely related with the change of surroundings of cobaltocenium, as these polymer chains have different diffusion dynamics. In contrast, no distinct UV−vis absorptions were observed from polymers synthesized via ATRP without the cobaltocenium moiety, further confirming the presence of cobaltocenium group in the polymers.

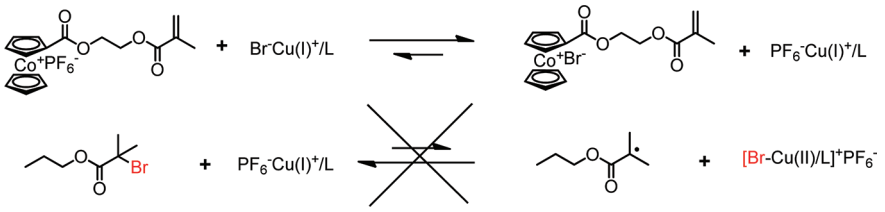
Redox properties of cobaltocenium initiators and cobaltocenium-labeled polymers were investigated with the aid of cyclic voltammetry.[40,41] As shown in Figure 10, the redox process of cobaltocenium mono- and di-initiators was not reversible. The oxidation peak current was much higher than the reduction peak current. The irreversibility was likely due to solubility

Scheme 3. Possible Side Effects of Ion-Exchange between Initiators and Catalysts



dx.doi.org/10.1021/ma202725c | Macromolecules 2012, 45, 2267−2275

Scheme 4. Possible Side Effects of Ion-Exchange between Monomers and Catalysts



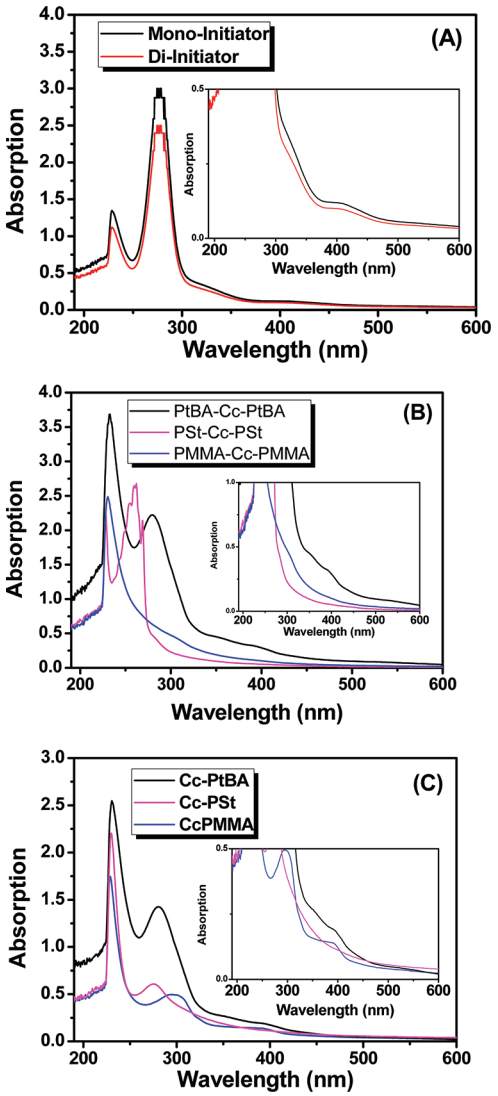


Figure 9. UV−vis absorption spectra of (A) cobaltocenium monoinitiator and di-initiator, (B) polymers prepared by di-initiator, and (C) polymers prepared by monoinitiator (solvent: dichloromethane).

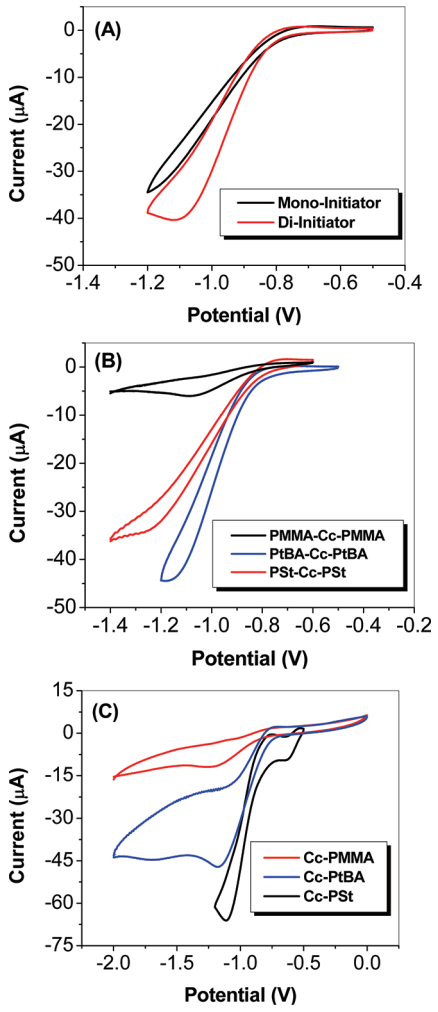


Figure 10. Cyclic voltammetry curves of (A) cobaltocenium monoinitiator and cobaltocenium di-initiator, (B) polymers prepared by di-initiator, and (C) polymers prepared by monoinitiator.

change of cobaltocenium mono- and di-initiators under redox process. Although cobaltocenium mono- and di-initiators are soluble in DMF, the reduced cobaltocenium-labeled polymers (cobaltocene-containing mono- and di-initiators) might have different solubility in DMF. The styrene-based polymers (*Cc*-PSt and PS-*Cc*-PSt) had the similar redox process to the initiators, while the acrylate polymers showed different redox behaviors between end- and centered cobaltocenium-labeled polymers. Both PMMA polymers (*Cc*-PMMA and PMMA-*Cc*-PMMA) exhibited a much more reversible redox process. Nevertheless, all polymers exhibited redox-active properties.

CONCLUSIONS

In conclusion, we synthesized cobaltocenium-containing mono- and dihaloesters, which were used as initiators to prepare cobaltocenium-labeled polymers by atom transfer radical polymerization. Three different classes of monomers including styrene, acrylate, and methacrylate were polymerized by ATRP. Because of the potential ion exchange between copper catalysts and counterions of cobaltocenium moiety, excess copper catalysts (compared to initiators) were used. Most polymerization systems exhibited a living and control kinetics, while polymerization of MMA by the monoinitiator showed significant termination. Both cobaltocenium-ended and centered-polymers showed characteristic UV−vis absorption of cobaltocenium. All polymers exhibited redox-active behaviors,

dx.doi.org/10.1021/ma202725c | *Macromolecules* 2012, 45, 2267−2275

indicating the retention of cobaltocenium moiety although the redox process was not reversible. These optically active and redox-active cobaltocenium-labeled polymers may find applications in the field such as sensing, imaging, etc.

AUTHOR INFORMATION

Corresponding Author

*E-mail: tang4@mailbox.sc.edu.

Notes

The authors declare no competing financial interest.

ACKNOWLEDGMENTS

We acknowledge the University of South Carolina for financial support.

REFERENCES

(1) Bellan, L. M.; Wu, D.; Langer, R. S. *WIRES Nanomed. Nanobi.* **2011**, *3*, 229−246.
(2) Bonanni, B.; Andolfi, L.; Bizzarri, A. R.; Cannistraro, S. *J. Phys. Chem. B* **2007**, *111*, 5062−5075.
(3) Bowden, N. B.; Willets, K. A.; Moerner, W. E.; Waymouth, R. M. *Macromolecules* **2002**, *35*, 8122−8125.
(4) Haley, J. C.; Liu, Y.; Winnik, M. A.; Demmer, D.; Haslett, T.; Lau, W. *Rev. Sci. Instrum.* **2007**, *78*, 084101−084101−084105.
(5) Beija, M.; Charreyre, M.-T.; Martinho, J. M. G. *Prog. Polym. Sci.* **2010**, *36*, 568−602.
(6) Malpei, F.; Andreoni, V.; Daffonchio, D.; Rozzi, A. *Biores. Technol.* **1998**, *63*, 49−56.
(7) Isaad, J.; Salaun, F. *Sens. Actuator, B* **2011**, *157*, 26−33.
(8) Chen, Y.-f.; Banerjee, I. A.; Yu, L.; Djalali, R.; Matsui, H. *Langmuir* **2004**, *20*, 8409−8413.
(9) Li, F.; Westphal, A. H.; Marcelis, A. T. M.; Sudholter, E. J. R.; Cohen Stuart, M. A.; Leermakers, F. A. M. *Soft Matter* **2011**, *7*, 1214−1218.
(10) Kim, J.; Nam, H. Y.; Kim, T. I.; Kim, P. H.; Ryu, J.; Yun, C. O.; Kim, S. W. *Biomaterials* **2011**, *32*, 5158−5166.
(11) De Koker, S.; De Cock, L. J.; Rivera-Gil, P.; Parak, W. J.; Auzéy Velty, R.; Vervaet, C.; Remon, J. P.; Grooten, J.; De Geest, B. G. *Adv. Drug Delivery Rev.* **2011**, *63*, 748−761.
(12) Cortez, C.; Tomaskovic-Crook, E.; Johnston, A. P. R.; Radt, B.; Cody, S. H.; Scott, A. M.; Nice, E. C.; Heath, J. K.; Caruso, F. *Adv. Mater.* **2006**, *18*, 1998−2003.
(13) Bathfield, M.; D'Agosto, F.; Spitz, R.; Charreyre, M.-T.; Delair, T. *J. Am. Chem. Soc.* **2006**, *128*, 2546−2547.
(14) Callahan, J.; Kopecek, J. *Biomacromolecules* **2006**, *7*, 2347−2356.
(15) Azzaroni, O.; Mir, M.; Alvarez, M.; Tiefenauer, L.; Knoll, W. *Langmuir* **2008**, *24*, 2878−2883.
(16) Degrand, C.; Limoges, B.; Gautier, A.; Blankespoor, R. L. *Appl. Organomet. Chem.* **1993**, *7*, 233−241.
(17) Yang, X.-Q.; Guo, L.-H. *Anal. Chim. Acta* **2009**, *632*, 15−20.
(18) Anne, A.; Cambril, E.; Chovin, A.; Demaille, C. *Anal. Chem.* **2010**, *82*, 6353−6362.
(19) Chen, M.; Ghiggino, K. P.; Mau, A. W. H.; Rizzardo, E.; Thang, S. H.; Wilson, G. J. *Chem. Commun.* **2002**, 2276−2277.
(20) Pietsch, C.; Vollrath, A.; Hoogenboom, R.; Schubert, U. S. *Sensors* **2010**, *10*, 7979−7990.
(21) Duhamel, J. *Acc. Chem. Res.* **2006**, *39*, 953−960.
(22) Hu, J. M.; Li, C. H.; Cui, Y.; Liu, S. Y. *Macromol. Rapid Commun.* **2011**, *32*, 610−615.
(23) Tillman, E. S.; Roof, A. C.; Palmer, S. M.; Zarko, B. A.; Goodman, C. C.; Roland, A. M. *J. Chem. Educ.* **2006**, *83*, 1215−null.
(24) Bier, F. F.; Ehrentreich-Forster, E.; Dolling, R.; Eremenko, A. V.; Scheller, F. W. *Anal. Chim. Acta* **1997**, *344*, 119−124.
(25) Hromadov, M.; Salmain, M.; Sokolov, R.; Pospsil, L.; Jaouen, G. *J. Organomet. Chem.* **2003**, *668*, 17−24.
(26) Limoges, B.; Degrand, C.; Brossier, P. *J. Electroanal. Chem.* **1996**, *402*, 175−187.
(27) Meirim, M. G.; Neuse, E. W.; Caldwell, G. *J. Inorg. Organomet. Polym.* **1998**, *8*, 225−236.
(28) Nakadan, N.; Imabayashi, S.-i.; Watanabe, M. *Langmuir* **2004**, *20*, 8786−8791.
(29) Sun, G.; Xu, J.; Hagooly, A.; Rossin, R.; Li, Z.; Moore, D. A.; Hawker, C. J.; Welch, M. J.; Wooley, K. L. *Adv. Mater.* **2007**, *19*, 3157−3162.
(30) Fukukawa, K.-i.; Rossin, R.; Hagooly, A.; Pressly, E. D.; Hunt, J. N.; Messmore, B. W.; Wooley, K. L.; Welch, M. J.; Hawker, C. J. *Biomacromolecules* **2008**, *9*, 1329−1339.
(31) Welch, M. J.; Hawker, C. J.; Wooley, K. L. *J. Nucl. Med.* **2009**, *50*, 1743−1746.
(32) Wollenberger, U. *Biotechnol. Genet. Eng. Rev.* **1996**, *13*, 237−266.
(33) Kawahara, N.; Saito, J.; Matsuo, S.; Kaneko, H.; Matsugi, T.; Kashiwa, N. In *New Frontiers in Polymer Synthesis*; Springer-Verlag: Berlin, 2008; Vol. *217*, pp 79−119.
(34) Nishihara, H.; Murata, M. *J. Inorg. Organomet. Polym. Mater.* **2005**, *15*, 147−156.
(35) Ricci, F.; Lai, R. Y.; Plaxco, K. W. *Chem. Commun.* **2007**, 3768−3770.
(36) Wlassoff, W. A.; King, G. C. *Nucleic Acids Res.* **2002**, *30*, e58.
(37) Haas, O.; Velazquez, C. S.; Porat, Z. e.; Murray, R. W. *J. Phys. Chem.* **1995**, *99*, 15279−15284.
(38) Teertstra, S. J.; Lin, W. Y.; Gauthier, M.; Ingratta, M.; Duhamel, J. *Polymer* **2009**, *50*, 5456−5466.
(39) Zhou, N.; Zhang, Z.; Zhu, J.; Cheng, Z.; Zhu, X. *Macromolecules* **2009**, *42*, 3898−3905.
(40) Ren, L.; Hardy, C. G.; Tang, C. *J. Am. Chem. Soc.* **2010**, *132*, 8874−8875.
(41) Ren, L.; Hardy, C. G.; Tang, S.; Doxie, D. B.; Hamidi, N.; Tang, C. *Macromolecules* **2010**, *43*, 9304−9310.
(42) Ren, L.; Zhang, J.; Bai, X.; Hardy, C. G.; Shimizu, K. D.; Tang, C. *Chem. Sci.* **2012**, *3*, 580−583.
(43) Ren, L.; Zhang, J.; Hardy, C. G.; Tang, C. *Macromol. Rapid Commun.* **2012**, DOI: 10.1002/marc.201100732.
(44) Hardy, C. G.; Ren, L.; Zhang, J.; Tang, C. *Isr. J. Chem.* **2012**, DOI: 10.1002/ijch.201100110.
(45) Astruc, D.; Ornelas, C.; Ruiz, J. *Acc. Chem. Res.* **2008**, *41*, 841−856.
(46) Casado, C. M.; Gonzalez, B.; Cuadrado, I.; Alonso, B.; Moran, M.; Losada, J. *Angew. Chem., Int. Ed.* **2000**, *39*, 2135−2138.
(47) Cuadrado, I.; Casado, C. M.; Lobete, F.; Alonso, B.; Gonzalez, B.; Losada, J.; Amador, U. *Organometallics* **1999**, *18*, 4960−6969.
(48) Mayer, U. F. J.; Gilroy, J. B.; O'Hare, D.; Manners, I. *J. Am. Chem. Soc.* **2009**, *131*, 10382−10383.
(49) Gilroy, J. B.; Patra, S. K.; Mitchels, J. M.; Winnik, M. A.; Manners, I. *Angew. Chem., Int. Ed.* **2011**, *50*, 5851−5855.
(50) Horikoshi, R.; Mochida, T. *Eur. J. Inorg. Chem.* **2010**, *2010*, 5355−5371.
(51) Winnik, F. M.; Ottaviani, M. F.; Bossman, S. H.; Pan, W.; Garcia-Garibay, M.; Turro, N. J. *J. Phys. Chem.* **1993**, *97*, 12998−13005.
(52) Hawker, C. J.; Bosman, A. W.; Harth, E. *Chem. Rev.* **2001**, *101*, 3661−3688.
(53) Kamigaito, M.; Ando, T.; Sawamoto, M. *Chem. Rev.* **2001**, *101*, 3689−3745.
(54) Matyjaszewski, K., Ed. *Controlled/Living Radical Polymerization. From Synthesis to Materials*; American Chemical Society: Washington, DC, 2006; Vol. *944*.
(55) Matyjaszewski, K.; Xia, J. *Chem. Rev.* **2001**, *101*, 2921−2990.
(56) Moad, G.; Rizzardo, E.; Thang, S. H. *Aust. J. Chem.* **2005**, *58*, 379−410.
(57) High, L. R. H.; Holder, S. J.; Penfold, H. V. *Macromolecules* **2007**, *40*, 7157−7165.
(58) Turro, N. J.; Lem, G.; Zavarine, I. S. *Macromolecules* **2000**, *33*, 9782−9785.
(59) Hardy, C. G.; Ren, L.; Tamboue, T. C.; Tang, C. *J. Polym. Sci., Part A: Polym. Chem.* **2010**, *49*, 1409−1420.

(60) Zheng, Y.; Yao, K.; Lee, J.; Chandler, D.; Wang, J.-F.; Wang, C.-P.; Chu, F.-X.; Tang, C. *Macromolecules* **2010**, *43*, 5922−5924.
(61) Dufour, B.; Tang, C.; Koynov, K.; Zhang, Y.; Pakula, T.; Matyjaszewski, K. *Macromolecules* **2008**, *41*, 2451−2458.
(62) Xia, J.; Gaynor, S. G.; Matyjaszewski, K. *Macromolecules* **1998**, *31*, 5958−5959.
(63) Wilbon, P. A.; Zheng, Y.; Yao, K.; Tang, C. *Macromolecules* **2010**, *43*, 8747−8754.
(64) Yao, K.; Wang, J.; Zhang, W.; Lee, J. S.; Wang, C.; Chu, F.; He, X.; Tang, C. *Biomacromolecules* **2011**, *12*, 2171−2177.
(65) Scott, D. R.; Becker, R. S. *J. Chem. Phys.* **1961**, *35*, 516−531.

Macromolecules

Article

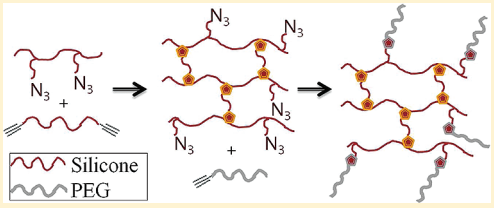
pubs.acs.org/Macromolecules

Generic, Metal-Free Cross-Linking and Modification of Silicone Elastomers Using Click Ligation

Talena Rambarran, Ferdinand Gonzaga, and Michael A. Brook*

Department of Chemistry and Chemical Biology, McMaster University, 1280 Main Street West, Hamilton, Ontario, Canada L8S 4M1

ABSTRACT: Silicone elastomers are widely used in a variety of biomaterials applications. Their high hydrophobicity can, in some cases, compromise their utility. There exist few convenient, efficient and metal-free processes to introduce hydrophilic groups onto the elastomer surface. We describe the utilization of the metal-free click reaction between azido- and alkynyl-modified silicones to both cross-link and functionalize silicone elastomers. Initial cross-linking at, optionally, reduced or elevated temperatures depending on the alkyne used, results in elastomers whose moduli and tackiness can be controlled by manipulation of cross-link density through use of different chain length constituents: the systematic capping of azides on the azide-rich partner provides a level of control of both cross-linking and residual functionality after cross-linking. The residual azides or alkynes resulting from nonstoichiometric mixing of the starting materials can be used for sequential functionalization of the elastomer as shown through the improved wettability that results from the grafting of alkyne-functional PEG to azide-rich silicone elastomers: contact angles decrease from ~105° for the pure silicone elastomers to 85° for the azide-rich silicone elastomer, and to as low as 41° for the PEG-modified product. It is possible to modify the entire elastomer body or only the surface by judicious choice of the solvent used for the hydrophilic modification.



INTRODUCTION

Considerable advances have been made in understanding the factors that are associated with compatibility of biomedical devices in certain biological environments. These can include surface modulus,[1] roughness, hydrophilicity, and the presence of target biomolecules,[2] among others. Silicone elastomers are widely used in a variety of biomedical applications where their electrical stability, gas permeability, flexibility and biocompatibility in various sites in the body are particularly beneficial.[3,4] However, even in the applications where they are widely used (e.g., silicone hydrogel contact lenses) their high hydrophobicity can result in significant lipid and protein adsorption onto the surface,[3,5,6] which can be problematic. In more challenging environments, such as catheters in contact with blood, the situation is much worse: extensive biofouling occurs. In spite of an exemplary record of safety, concern has also been raised in some instances about the metallic catalysts—typically tin- or platinum-based—that are used to cross-link silicone elastomers used as biomaterials.

The ideal silicone elastomer for a given biomaterials application cannot currently be predicted. Advances toward materials that have better surface characteristics are hindered by the traditional paradigm for biomaterials synthesis, which involves "one-off" preparation and characterization of materials and surfaces. Some examples of generic surfaces, which can be readily and systematically modified by a related series of compounds, have been reported. For example, monofunctional poly(ethylene glycol) (PEG) can be tethered to silicone surfaces.[7,8] After functional group conversion of the terminal alcohol into an activated ester, the surface can react readily with a wide variety of (bio)functional amines, including proteins. However, such protocols are not sufficiently explicit to be useful in developing surface character/biological response relationships—it is not possible to control which amine on the protein will react. Thus, there remains a need to develop versatile generic methods to modify the surfaces of silicone elastomers.

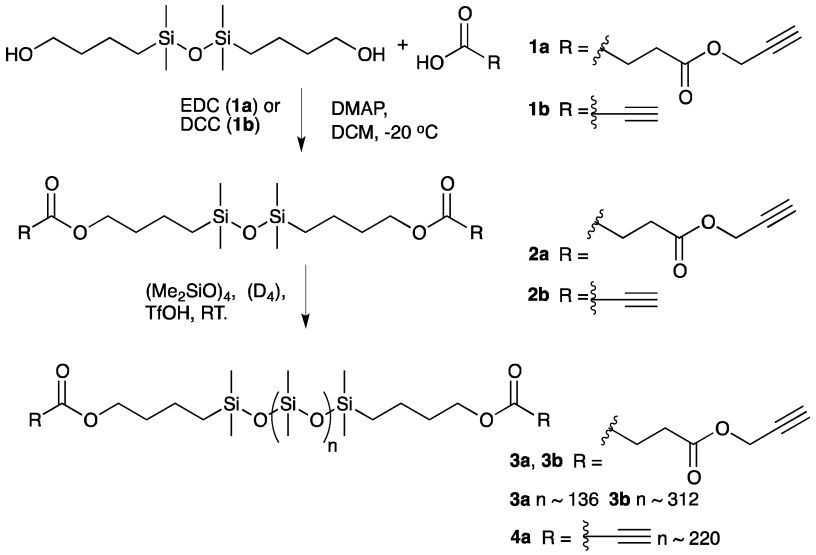
The utility of copper-catalyzed azide−alkyne 1,3-dipolar cycloaddition (CuAAC) has been shown in a wide variety of applications, including the functionalization of polymeric materials.[9] Selective labeling of biomolecules such as proteins,[10−13] polysaccharides,[14,15] and nucleic acids,[16] with either azides or alkynes has been demonstrated. We reasoned that if complementary silicone elastomers could be prepared, which possessed controlled concentrations of azide and alkynes internally within the elastomer body and at the external interface, it would be possible to perform high-throughput synthesis of modified silicone elastomers, which could then be assessed for biocompatibility in various biological tests: specific biomolecules and/or groups that deliver different properties like charge, nonionic hydrophiles (e.g., PEG[7,8]) and other materials could be systematically added to the silicone.

As noted above, it is preferable to avoid the use of heavy metals in materials destined for human contact. The necessity of a copper(I) catalyst[17] for the azide/alkyne click reaction would therefore be disadvantageous. Recently, it has been shown that the Huisgen 1,3-dipolar cycloaddition of azides to alkynes ("click" chemistry) can be used to thermally functionalize[18] or cross-link silicones,[19] without the use of a catalyst, at low temperatures and without generating any byproduct. Here,

Received: December 23, 2011
Revised: February 13, 2012
Published: February 27, 2012

 © 2012 American Chemical Society dx.doi.org/10.1021/ma202785x | *Macromolecules* 2012, 45, 2276−2285

Scheme 1. Synthesis of Alkyne-Terminated Polysiloxanes



we extend the straightforward methodology to prepare functional silicone elastomers that optionally contain an excess of alkynes, or azides that can be secondarily functionalized using another click reaction. Subsequent click chemistry using these reactive groups permits further chemical modification of the silicone rubbers. The process is illustrated by the internal and external grafting of various hydrophilic polymers (PEG of different molecular weights), leading to a substantial reduction in the hydrophobic character of "click" cross-linked elastomers. This simple, versatile and efficient methodology allows cross-linking and functionalization of silicone elastomers with great control over many experimental parameters, including temperature of cure, stoichiometry, cross-link density, and composition, extending the range of potential applications of siloxane elastomers.

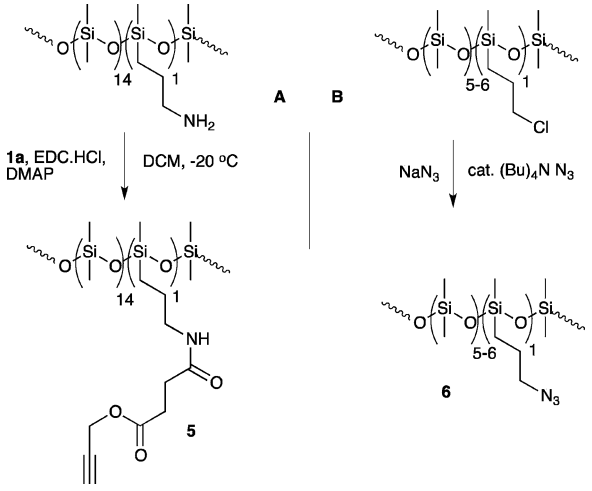
RESULTS AND DISCUSSION

Synthesis of Functional Polymers to Optimizing Cross-Link Density. The preparation of functional silicone elastomers that can participate in the Huisgen 1,3-dipolar cycloaddition first required the synthesis of alkyne- and azido-functionalized silicone precursors, respectively. A variety of alkyne- and azide-modified building blocks were synthesized to permit control over the cure process and also over the final mechanical properties of the elastomers via manipulation of both the cross-link density and the residual functionality.

Several alkyne-terminated polysiloxanes, which varied in the nature of their molecular weights and the alkyne terminal group (both activated or nonactivated), were prepared as reaction partners for the azidoalkylsilicone. First, nonactivated (propargyl) or activated (propiolate) alkyne-terminated disiloxanes were prepared, as shown in Scheme 1. The esterification of acids **1a**[60] or **1b** with 1,3-bis(hydroxybutyl)tetramethyl disiloxane, catalyzed by EDC, yielded the alkyne-terminated disiloxanes **2a** and **2b**, respectively. With these compounds as end groups, acid-catalyzed equilibration of **2a** and **2b** with various amounts of D_4 ($(Me_2SiO)_4$) was used to grow the PDMS chains, giving the propargyl-terminated polysiloxane **3a** (81% yield; MW 10 600 g·mol^{-1}), **3b** (77% yield; MW 23 700 g·mol^{-1}), and propiolate-terminated **4a** (85% yield; MW 16 500 g·mol^{-1}), respectively. Molecular weights were determined by ^{1}H NMR using end group analysis. The method was validated by gel permeation chromatography (GPC) for compound **3b**, which gave an M_n of 17 000 g·mol^{-1}, in good agreement with values determined by ^{1}H NMR (less than 3% error).

Alternatively, a polysiloxane with multiple pendant alkyne groups was prepared using an EDC coupling reaction between a commercially available (aminopropyl)methylsiloxane–dimethylsiloxane copolymer (MW 3000–6000 g·mol^{-1}; 6–7 mol % (aminopropyl)methyl-siloxane unit, trimethylsiloxy-terminated) and nonactivated **1a** (Scheme 2A). The resultant polymer **5** was obtained in an 84% yield.

Scheme 2. (A) Synthesis of Poly(alkyne)siloxane 5 and (B) Synthesis of Poly(azidopropyl)siloxane 6

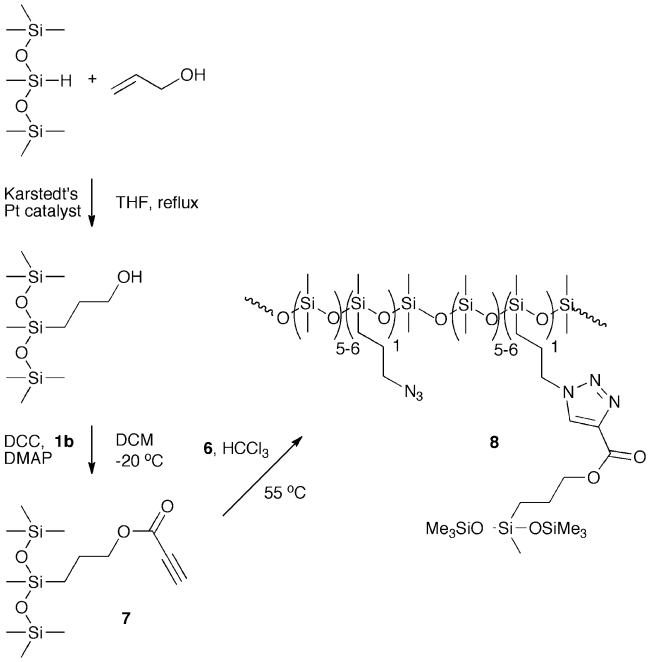


A multifunctional poly(dimethylsiloxane)-*co*-(methyl-(azidopropyl)siloxane) was prepared from a commercially available poly(dimethylsiloxane)-*co*-((chloropropyl)-methylsiloxane) (MW: 7500–10000 g·mol^{-1}; 14–16 mol % chloropropyl units, trimethylsiloxy-terminated) using azide anions in refluxing THF, with tetra-*n*-butylammonium azide as a phase transfer catalyst (Scheme 2B). The resulting polysiloxane **6** with multiple azido functionalities was obtained

dx.doi.org/10.1021/ma202785x | Macromolecules 2012, 45, 2276–2285

in an almost quantitative yield; an average molecular weight of 537.8 g·mol^{-1} per repeat unit was calculated from proton NMR. The number of active azido groups, which correlates to the cross-link density, could be controlled by 'capping' a selected fraction with a monoalkyne-terminated trisiloxane **7** as shown in Scheme 3, yielding polymer **8**, in which about 50% of

Scheme 3. Synthesis of Monoalkyne-Trisiloxane 7 and Its Click Reaction with Polymer 6 To Yield Poly(azidopropyl)siloxane 8



the available azides have been converted to the a trisiloxane-substituted triazole ring.

Elastomer Synthesis. The thermal "click" reaction between alkyne- and azido-modified polysiloxanes led to cross-linked elastomeric networks with stable aromatic triazole rings connecting the precursors (Figure 1 step A). A total of

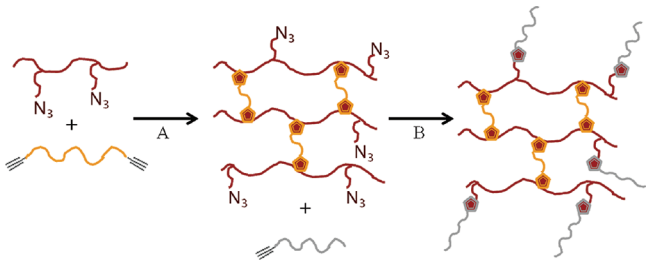


Figure 1. Schematic representation showing: (A) cross-linking; (B) grafting alkynyl PEG to the residual azide groups.

four different types of reactive elastomers were created using experimental methodologies that differed only in temperature: three of them contained excess azido functional groups (series **I**, **II**, and **III**) and one containing excess alkyne-functionality (series **IV**). Three series of elastomers: **I**, **II** and **III** containing excess azide functionality were created by cross-linking **6** with dialkyne-terminated polysiloxanes **3a**, **3b**, and **4a**, respectively. Series **IV** resulted from the reaction of 5 with **8**.

The onset temperature for a thermal, metal-free "click" reaction depends on the electronic properties of the alkyne being used.[20] The presence of electron-withdrawing groups adjacent to the alkyne lowers the energy level of the LUMO. The alkyne activation manifests itself in cycloaddition reactions that occur at lower temperatures than nonactivated alkynes: we,[18,19] and others,[21−23] have shown that esters of propiolic acid or acetylene dicarboxylic acid can "click" at or near room temperature within a few hours, and without the need of any catalyst. Recently, we applied this metal-free, activated alkyne to azide cycloaddition to prepare elastomeric silicones.[19] When combined with ring strain effects (first discovered by Wittig),[24] the reaction is even more facilitated (strain-promoted alkyne−azide cycloaddition or SPAAC) and is increasingly being applied in covalent modifications of living systems,[25] in vivo imaging,[26] lipid[27] and peptide[28] labeling, hydrogel cross-linking,[29] and polymer[30,31] or dendrimer[32] functionalization.

The choice of nonactivated alkynes **3a**, **3b** (of different molecular weights) or activated alkyne **4a** allowed control over both the temperature and time of the curing process and the mechanical properties of the resulting rubbers by changing the cross-link density. The cross-linking of **6** with **3a** to give Series **I** was performed at 90 °C for 48 h using a 2-, 4-, 6-, 8- or 10-fold excess of the azido functionality, respectively, to leave various quantities of residual reactive groups in the resultant elastomers. Small amounts of toluene or $CHCl_3$ were used to homogenize the pre-elastomer mixture. In general, cross-linking resulted in transparent, colorless monolithic elastomers. However, the entire series **I** of elastomers obtained were mechanically fragile. For example, when attempting to remove them from their curing vessel, the elastomers cracked or fragmented completely. Low tear resistance and resistance to crack propagation is a common feature of unfilled silicones (those not reinforced with a mineral filler, typically silica[33]). To reduce the cross-link density, an analogous series of elastomers, series **II**, was created using the higher molecular weight propargyl-terminated PDMS **3b** and **6** while maintaining the same molar quantities of reactive groups. The resulting monolithic rubbers **IIA-IIE** were mechanically more robust but sticky elastomers, completely unlike the previous crack-prone series, **IA-IE**. As expected, the hardness of elastomers in series **II** tracked with cross-link density (Table 1). Rubbers prepared with a 2-fold excess of azide were firm with a Shore OO hardness of 56 (corresponding approximately to a Shore A hardness of 10), the elastomer containing a 10-fold excess of azido groups was extremely soft with a Shore OO hardness of only 18, and elastomers prepared at other alkyne/azide ratios fell between these two extremes: the larger the difference in stoichiometry between azide- and alkyne reactive groups, the more reactive groups that were left over, and the lower cross-link density in the obtained material.

Another series of azido-rich elastomers, series **III**, was created by cross-linking the activated alkyne polymer **4a** with **6** using a 2-, 4-, 6-, 8-, and 10-fold molar excess of azido groups, respectively. As before, toluene and/or chloroform were initially added to homogenize the mixture of polymers prior to cross-linking, which was completed at 60 °C in only 12 h, or in less than 8 h at 70 °C. The resultant elastomer series **III** exhibited improved properties over the previous two series **I** and **II**: the rubbers were flexible yet firm and neither sticky nor gummy (Table 1). This series was comparable, in terms of mechanical properties, to lightly cross-linked conventional silicone elastomers obtained via platinum-catalyzed addition

dx.doi.org/10.1021/ma202785x | Macromolecules 2012, 45, 2276−2285

Table 1. Summary of the Various Elastomeric Materials Prepared

entry	alkyne	azide	ratio (RC≡C R′:N_3)	cure conditions	outcome	Shore OO hardness
IA	**3a**	**6**	1:2	5 mL of toluene, 90 °C, 48 h	readily cracked	51 ± 2
IB			1:4		systematically varies between **IA** and **IE**	48 ± 2
IC			1:6			43 ± 4
ID			1:8			37 ± 3
IE			1:10		soft/gummy	28 ± 2
IIA	**3b**	**6**	1:2	5 mL of toluene, 90 °C, 48 h	very flexible	54 ± 2
IIB			1:4		systematically varies between **IIA** and **IIE**	49 ± 2
IIC			1:6			41 ± 2
IID			1:8			23 ± 2
IIE			1:10		soft, sticky, gummy	18 ± 1
IIIA	**4a**	**6**	1:2	3 mL of toluene, 60 °C, 12 h or 3 mL toluene 70 °C, 8 h	firm	68 ± 3
IIIB			1:4		systematically varies between **IIIA** and **IIIE**	57 ± 4
IIIC			1:6			47 ± 3
IIID			1:8			35 ± 4
IIIE			1:10		softer	22 ± 3
IVA	**5**	**8**	4:1	1 mL of toluene, 90 °C, 12 h	more firm	56 ± 1
IVB			6:1		systematically varies between **IVA** and **IVE**	45 ± 2
IVC			8:1			35 ± 1
IVD			10:1			18 ± 6
IVE			12:1		more flexible, soft	7 ± 3

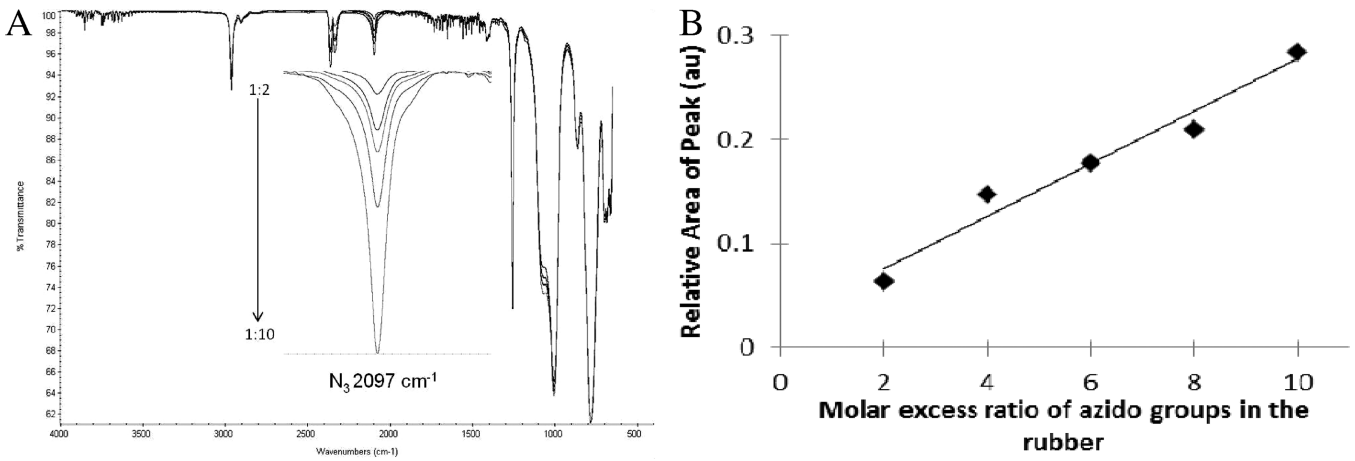


Figure 2. (A) FT-IR of series **III** showing an increase of residual azides in the product elastomers. (B) Relative area under the azide peak.

cure: the Shore A hardness value for **IIIA** was 12 (**IIA** had a Shore A value of 9). In series **III**, the distance between cross-links (~16 000 g·mol^{-1}) provided by the dipropiolate-terminated alkyne **4a** was optimal with respect to mechanical and surface properties when compared to the lower MW propargyl-terminated polysiloxanes **3a** (10 600 g·mol^{-1}; mechanically weak products resulted) and higher MW **3b** (23 700 g·mol^{-1}, soft/sticky materials resulted).

To ensure that the integrity of the residual functional groups was preserved during the curing process, excess azido series **I**, **II** and **III** were analyzed using ATR-IR: the asymmetric azide stretch presents an intense band at 2097 cm^{-1}. Taking series **III** as an example, it was observed qualitatively that the signal corresponding to the azide stretch was larger with increasing azide concentration in the formulations, correlating across the series with the amount of excess of the incorporated azido groups theoretically present (Figure 2A). Additionally, setting the $SiMe_2$ signal at 1260 cm^{-1} in the silicone elastomers as an internal standard (as its signal remains constant throughout the series of elastomers[34]), the ratio of relative areas between the standard $SiMe_2$ band and the azide band versus the calculated stoichiometry were plotted for every formulation. A linear correlation was observed, indicating that as the formulation moves away from a stoichiometric ratio of alkyne/azide, more and more azide moieties are retained in the final elastomer (Figure 2B). This confirms that the curing process did not degrade the excess azido reactive groups.

To show the versatility of this synthetic approach, a series of elastomers, series **IV**, containing excess alkyne (rather than azide) functionality was also prepared. First, **6** was reacted with a propiolate-containing trisiloxane, **7**, at 55 °C for 20 h to consume ~50% of the azido groups (Scheme 3), giving polysiloxanes **8** in quantitative yields (MW ~ 1408 g·mol^{-1} per repeat unit). This prefunctionalization reduced the number of possible cross-link units in the resulting elastomer. Polymers **5** and **8** were mixed in offset ratios to give a 4-, 6-, 8-, 10-, and 12-fold molar excess, respectively, of alkyne functional groups and cross-linked at 90 °C. After a few hours, elastomeric gels had already formed and transparent, faint yellow monolithic elastomers, **IVA-IVE**, were obtained after 12 h. Although

dx.doi.org/10.1021/ma202785x | *Macromolecules* 2012, 45, 2276–2285

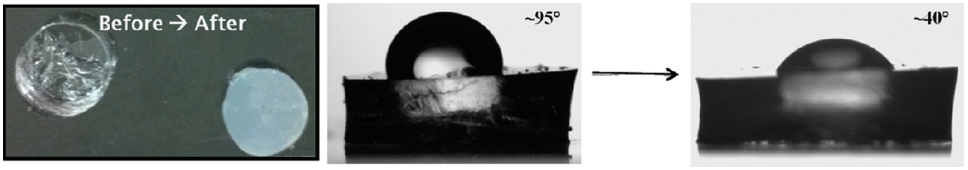


Figure 3. Compound **IIID** and **IIID-PEG9b**. Left photograph: Right: Sessile drop contact angles after at t = 0 and ~30 min, 40° (Rubber **IIID**).

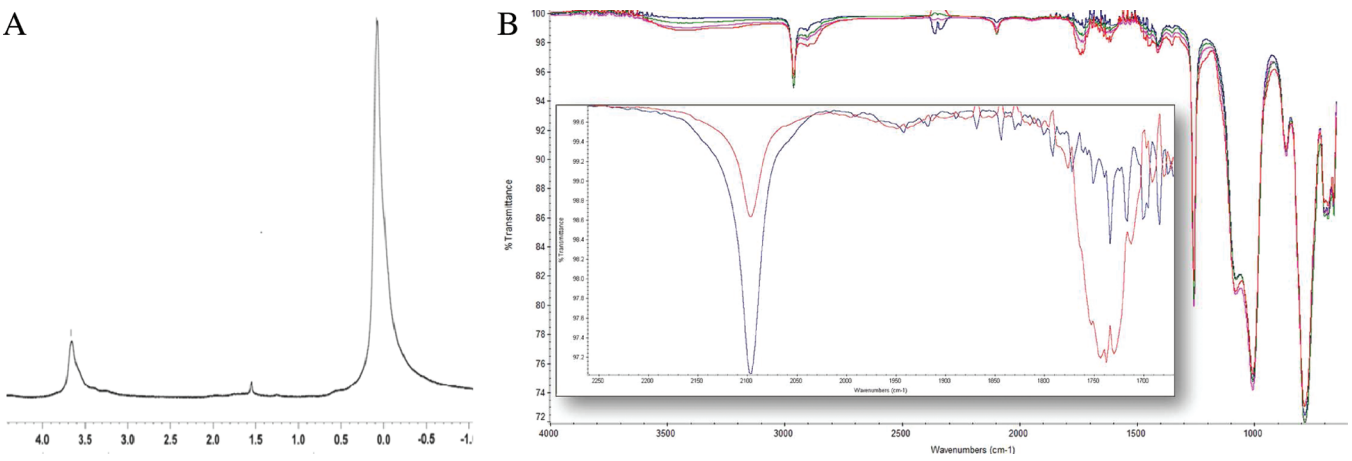


Figure 4. (A) NMR of **IIIE** after modification with **9a** showing the introduction of PEG at 3.66 ppm. (B) IR of the **III-9a** series, Inset spectrum: Expanded IR spectra of **IIIE** (blue) and **IIIE-9a** (red), showing the disappeance of 2079 cm^{-1} azide signal and appearance of the 1737 cm^{-1} carbonyl signal.

these elastomers were created using a nonactivated alkyne functionality, similar to **3a** and **3b**, the gelation process occurred in a much shorter time, due to the fact that both precursors are multifunctional and thus present higher densities of reactive groups, leading to enhanced cycloaddition rates. The samples were cooled to room temperature after 12 h, at which time the resultant elastomers (**IVA-IVE**) were flexible, firm and strong (although it was possible to measure Shore OO hardness, some of the elastomers cracked when attempting to measure Shore A hardness, Table 1), and easy to work with: they could be removed from the curing vessel without tearing, surface modification or adhesion to the glass (by contrast, elastomers prepared with **3a** and **3b** were either extremely soft or had barely gelled at this time point). Moreover, as both precursors **5** and **8** were multifunctional, the improved curing process permitted the preparation of elastomers containing an even higher molar excess of reactive groups (ratio 1:12, azide:alkyne) than the elastomers derived from difunctional polymers **3a**, **3b**, or **4a**, without being detrimental to the final mechanical properties of the elastomers.

It is instructive to compare the mechanical properties of the four different series of elastomers (Table 1). The trends of Shore OO hardness within a given series and between series are very similar, as are the absolute values. However, the importance of network structures on elastomer mechanical properties was evident from the differences in the ability to simply manipulate the materials. Here, the pure network structure manifests itself. Series **III** and **IV** have appropriate cross-link densities, to give mechanically robust materials. They also exhibit fewer dangling chains, when compared to the series **II**, resulting in much less tacky materials. For practical application, these materials would normally be reinforced by silica fillers to improve the intrinsically poor tear resistance exhibited by silicones, as is exemplified by the behavior of series **I**.

Functionalization of Elastomers using Poly(ethylene glycol) (PEG). Chemical modification of the elastomer series **III** was performed using monopropiolate-terminated poly(ethylene glycol)s (PEG) **9a** and **9b** (MW = 750 and 2000 g mol^{-1}) (Figure 1, step B). PEG, a highly hydrophilic polymer, was chosen to demonstrate the efficiency with which the hydrophobic silicone elastomer can be synthetically modified: wettability of the resulting polymers can be easily monitored by contact angle measurements. Two strategies were used. In the first, the elastomer was modified either with PEG in water or neat: in neither case does the silicone effectively swell,[35,36] such that only modification of the surface would occur. In the second process the entire elastomer body was modified by reacting an excess of PEG and the elastomers in refluxing chloroform for 24 h. During this process, the disks swelled to several times their original volume. The functionalized elastomers of series **III** were purified by Soxhlet extraction to remove any ungrafted PEG and were dried at 50 °C for 1 day, during which time the rubbers shrunk back to their original size.

Upon visual inspection of the elastomers, it was in some cases immediately apparent that modification had occurred: some elastomers were transformed from transparent and colorless to slightly opaque or whitish after the modification (Figure 3). To characterize the materials and obtain an estimation of the amount of grafted PEG, an NMR of a rubber **IIIE** modified with **9a** was obtained by swelling the material in deuterated chloroform. The resulting ^{1}H NMR (Figure 4A) displayed two broad signals, one at 0.08 ppm corresponding to the methyl protons of the polysiloxane chains $-((CH_3)_2SiO)-$ and a signal at 3.66 ppm corresponding to the $-CH_2-$ repeating unit of the PEG chains, confirming successful functionalization. By comparing the relative integration of these two signals, it was estimated that about 20% of the azido groups had undergone the click reaction. In addition to a

dx.doi.org/10.1021/ma202785x | *Macromolecules* 2012, 45, 2276–2285

noticeable reduction in the azido signal at 2097 cm^{-1} in the IR, there was the emergence of a small signal at 1737 cm^{-1} corresponding to the carbonyl group of the grafted PEG-monopropiolate ester (Figure 4B).

Hydrophobic surfaces, such as pristine PDMS rubbers, have a high contact angle (normally >100°):[37] the water droplet beads up because of differences in energy between the water and the silicone as a result of hydrophobic interactions. Even relatively subtle changes, such as the addition of azide groups, can increase wettability. For example, elastomer **IIID** saw a decrease in contact angle from 103° to a plateau value of 83° over 30 min. This slightly lower contact angle value, when compared to nonfunctionalized PDMS, may be attributed to the presence of numerous azido groups. We note that contact angles are also affected by surface roughness.[38,39] The pre-elastomers are fluids and flow to give very low roughness surfaces.

Much more hydrophilic silicone surfaces can be generated by modification with PEG.[5,7,8,40−45] Static contact angle measurements in air at two time points were made in triplicate of the Series **III** elastomers that had been modified with **9b** PEG swollen in chloroform (Table 2). Samples that initially contained a larger quantity of azido groups were found, after modification by PEG, to have lower initial and final contact angles than those with fewer azides. For example, the initial contact angle of **IIIA-PEG9b** was 98° while for **IIID-PEG9b** it was 80° and final values (after 30 min) were 87° and 55°, respectively. These changes can be attributed to two different phenomena. First, and obviously, an increasing concentration of water-soluble PEG will reduce the water contact angle. Second, elastomers in a given Series initially containing a larger excess of azido groups have lower cross-link densities. A more flexible network allows for better diffusion of PEG into the swelled elastomers during grafting and, thus, a higher grafting density of hydrophilic chains. In addition, after grafting, the same flexible network will permit the grafted PEG chains to have higher mobility, and thus a better ability to reorganize to the surface, allowing the water droplet to more rapidly wet out.[34,46]

Table 2. Advancing Contact Angles of Series III Elastomers Modified with 9a or 9b

elastomer series III + 9b	ratio alkyne:azide	initial (deg)	60 s (deg)	30 min (deg)
IIIA-PEG9b	1:2	98 ± 6	n/a	87 ± 6
IIIB-PEG9b	1:4	87 ± 5	81 ± 9	69 ± 8
IIIC-PEG9b	1:6	86 ± 3	73 ± 9	61 ± 7
IIID-PEG9b	1:8	80 ± 3	66 ± 8	55 ± 6
IIIE-PEG9b	1:10	74 ± 1	62 ± 1	55 ± 1
After Soaking in Water, Rinsing in Acetone and Drying under N_2				
rubber	ratio	final (deg)		
IIIB-PEG9b	1:4	57 ± 3		
IIIB-PEG9a	1:4	46 ± 5		
IIID-PEG9b	1:8	51 ± 2		
IIID-PEG9a	1:8	41 ± 6		
IIID no PEG	1:8	85 ± 3		
Surface Functionalization: Absence of Swelling Solvents				
rubber	ratio	final (deg)		
IIIC-PEG9a (60 °C in water)	1:6	61 ± 5		
IIIC-PEG9a (60 °C neat)	1:6	70 ± 1		
IIIC-PEG9a (21 °C in water)	1:6	68 ± 4		

To allow comparisons of changes in wettability between elastomers bearing different length PEG chains, contact angle measurements were performed for the elastomers **IIIB** and **IIID** modified with **9a** or **9b**, respectively. The elastomers were soaked for an hour in water, rinsed with acetone and dried under a nitrogen flow prior to measurement. It was observed that the contact angle values (Table 2) were lower when the elastomers were first soaked in water, which has also been observed by Murthy et al.;[47] for example, the contact angle of **IIIB-PEG9b** dried in air reached a value of 69° whereas the same sample presoaked for an hour in water reached a value of 57°. Shorter PEG chains allowed the modified rubbers to reach lower contact angle values: **IIIB-PEG9a** reached a lower contact angle (46°) than **IIIB-PEG9b** (57°). The lower contact angle can be rationalized by steric considerations; shorter PEG chains should be more easily grafted and the corresponding material may contain a higher density of hydrophilic PEG chains. Shorter hydrophilic chains should also have a higher mobility within the silicone to rearrange to the surface as has been previously observed.[5,7,8] Furthermore, as previously observed by Fortuniak et al.,[39] water sorption onto the surface of siloxane elastomers can change the surface roughness additionally impacting the contact angle.

Elastomers modified by PEG in poor solvents (water and neat: at 60 °C and at room temperature) for silicone similarly showed improved wettabilities (Table 2). The increase in wettability, over the series studied, unsurprisingly showed a correlation between available residual azide concentration in the elastomer and wettability of the PEG-modified elastomers. It is thus possible to "dial in", within limits, the desired degree of surface/bulk functionalization simply by manipulating the nature of the pre-elastomer starting materials. More importantly, the ability to perform the metal-free click process in both hydrophobic and hydrophilic solvents extends the utility of the reaction for the surface modification of silicone elastomers.

The manipulation of surfaces of silicone-based elastomers is nontrivial. Strategies to increase surface hydrophilicity include the addition of a new polymer layer, for example, by plasma polymerization,[48] by surface oxidation, again typically using a plasma or other high energy techniques[49−57] or by the introduction of functional groups that can be used to tether hydrophiles including biomolecules.[5,7,8] With the former process, hydrophilization can be quite efficient, but it is challenging to control the introduction of specific quantities of hydrophiles in specific orientations; subsequently tethering additional (bio)molecules adds its own challenges. Plasma oxidation renders silicone elastomers hydrophilic for short periods of time. However, the process of surface reversion, in which highly mobile chains are able to migrate to the air interface, is extremely efficient and soon returns the surface to a hydrophobic state.[52] In our experience, it is difficult to reproducibly trap the silanols formed during oxidation at the interface.

It is possible to graft hydrophiles, such as PEG, on the surface using combinations of organic transformations that may (e.g., platinum-catalyzed hydrosilylation),[7,8] or may not (e.g., Michael addition[58,59]) require the use of metal catalysts. The advantages of the surface grafting approach is that, under ideal conditions, the graft density, graft thickness and types of (bio)molecules that modify the surface can be controlled. Often, however, conditions are not ideal. For example, the use of Michael group acceptors is problematic with protein

grafting—any of the available free amine groups could intervene.

The use of azide/alkyne click reactions[9,60] offers significant benefits for the controlled modification of silicone elastomers. As demonstrated above, without the need for catalysts—metal-based or not—and in a reaction that produces no byproduct, it is possible to efficiently control both silicone elastomer formation and surface functionalization. The properties of the initially formed silicone elastomer are controlled by simply varying the ratio of simple and readily available azide-/alkyne-containing building blocks. Thus, network morphology, cross-link density, and the concentration of residual functional groups in the elastomer are all readily manipulated. In addition, the temperature used to initiate the reaction can be controlled. While low temperature processes would normally be perceived to be of highest utility, the use of higher temperature processes allows much more working time after mixing of the functionalized prepolymers.

The ability to specifically label (bio)molecules with azides or alkynes has previously been demonstrated.[10−16] Alkyne- or azide-rich silicone elastomer surfaces should make excellent targets as a biomaterials support, as it is possible to modify the functional elastomers throughout using good solvents for silicone (alkanes, aromatics, halocarbons, 2-propanol) or preferentially at the external interface using poorer solvent (water, methanol). The latter route is particularly useful for polar biomolecules as it should be possible to avoid the use of protection/deprotection strategies and directly couple suitably modified biomolecules to the silicone surface in water. The development of click functional silicone elastomers as high-throughput biomaterials' supports will form the basis of future reports.

■ CONCLUSIONS

Simple, efficient metal-free click reactions can be used both to cross-link azide-and alkyne-modified silicones, and to facilitate their subsequent chemical modification with hydrophilic species. Silicone elastomers were prepared by reacting compounds selected from a series of di- and multialkyne functionalized polysiloxanes of varying reactivities with one of several poly(azide)-containing siloxanes. After curing, and depending on the ratios of the starting materials, alkyne- or azide-rich elastomers resulted. The process allows extensive control over the quantity and nature of the excess reactive groups incorporated into the elastomers, as well as the conditions under which the elastomers are cured, such as the temperature and time required to cross-link the precursors. Further chemical modification of the elastomers was demonstrated by the click ligation of alkyne-modified PEGs of various chain lengths either at the interface, or throughout the entire body of the elastomer. After PEG modification, the wettability of the elastomers was considerably increased. The ability to use metal-free "click" reaction both for cross-linking and surface modification in two simple, sequential reactions should be applicable to high-throughput preparation of potential biomaterials surfaces.

■ EXPERIMENTAL SECTION

Materials and Methods. (Chloropropyl)methylsiloxane-dimethylsiloxane copolymer (14−16 mol % (chloropropyl)methylsiloxanes, MW 7500−10000 g·mol^{-1}, trimethylsiloxy-terminated), (aminopropyl)methylsiloxane-dimethylsiloxane copolymer (6−7 mol % (aminopropyl)methyl-siloxanes, MW 3000−6000 g·mol^{-1}, trimethylsiloxy-terminated), octamethylcyclotetrasiloxane (D_4), and 1,3-bis(hydroxybutyl)tetramethyldisiloxane were obtained from Gelest. Propiolic acid (95%), propargyl alcohol (99%), succinic anhydride (99%), *N*-(3-(dimethylamino)propyl)-*N*′-ethyl-carbodiimide hydrochloride (EDC·HCl, commercial grade), sodium azide and dimethylaminopyridine (DMAP, 99%) were obtained from Sigma-Aldrich. Tetra-*n*-butylammonium azide was obtained from TCI. All materials were used as received. Compound **1a**, the monopropargyl ester of butanedioic acid was prepared according to a published procedure.[61] 1,3-Bis(propiolatobutyl)tetramethyldisiloxane (**2b**) was synthesized following the procedure by Gonzaga et al.[19]

IR analyses were made with a Bio-Rad infrared spectrometer (FTS-40). ^{1}H NMR were recorded at room temperature on a Bruker AC-200 spectrometer (at 200 MHz for ^{1}H and 50 MHz for ^{13}C) or a Bruker AV 600 spectrometer (at 600 MHz for ^{1}H and 150 MHz for ^{13}C) using deuterated solvents ($CDCl_3$). Contact angle measurements were performed using a Kruss DSA Contact Angle Apparatus using 18.1 mΩ·cm (Milli-Q) water. GPC analysis was performed on a Viscoteck GPCmax VE-2001 chromatograph using toluene as the eluent.

Alkyne Synthesis. *Synthesis of Propargyl-Terminated Disiloxane **2a**.* Compound **1a** (1.05 g, 6.7 mmol) and bis(4-hydroxybutyl)tetramethyldisiloxane (0.89 g, 3.2 mmol) were solubilized in dry dichloromethane (DCM, 30 mL) in a 50 mL round-bottomed flask. The mixture was cooled at −20 °C in a dry ice/acetone bath and then a catalytic amount of DMAP (0.10 g, 0.8 mmol) was added. EDC·HCl (1.29 g, 6.7 mmol) was slowly added and the reaction was allowed to stir under a positive pressure of nitrogen for 24 h. Cooling at −20 °C was maintained for 8 h, then the mixture was allowed to return to room temperature. The DCM was evaporated and the mixture was dissolved in diethyl ether (30 mL). The organic phase was washed with 2 × 20 mL of 0.08 M aqueous HCl followed by 2 × 25 mL 5% $NaHCO_3$ solution. The organic phase was dried over $MgSO_4$ and gravity filtered. Diethyl ether (40 mL) and activated charcoal (1 g) were added and the mixture was allowed to stir for 12 h. The suspension was filtered and the volatiles removed in vacuo to yield 2.10 g (76% yield) of pure propargyl-terminated disiloxane, **2a**.

^{1}H NMR ($CDCl_3$, 600 MHz, δ): 0.01 (s, 12H, $SiCH_3$); 0.49 (t, 4H, J = 8.2 Hz, $SiCH_2CH_2CH_2CH_2$); 1.37 (m, 4H, $SiCH_2CH_2CH_2CH_2$); 1.62 (m, 4H, $SiCH_2CH_2CH_2CH_2$); 2.46 (s, 2H, $C{\equiv}CH$); 2.63 (m, 8H, $O{=}CCH_2CH_2C{=}O$); 4.06 (t, 4H, J = 6.0 Hz, $SiCH_2CH_2CH_2CH_2$); 4.67 (s, 4H, $CH_2C{\equiv}CH$). ^{13}C NMR ($CDCl_3$, 150.9 MHz, δ): 0.2 ($SiCH_3$); 17.7 ($SiCH_2CH_2CH_2CH_2$); 19.5 ($SiCH_2CH_2CH_2CH_2$); 28.8 ($SiCH_2CH_2CH_2CH_2$); 31.8 ($CH{\equiv}CCH_2OO{=}CCH_2CH_2C{=}O$); 52.0 ($CH_2C{\equiv}CH$); 64.4 ($SiCH_2CH_2CH_2CH_2$); 74.9 ($C{\equiv}CH$); 77.4 ($C{\equiv}CH$); 171.9, 171.3 ($O{=}CCH_2CH_2C{=}O$). MS (ES-positive mode): m/z [M + NH_4^+] calculated = 572.2711; [M + NH_4^+] found = 572.2739.

*Synthesis of Propargyl-Terminated Polysiloxanes **3a** and **3b**.* Octamethylcyclotetrasiloxane (D_4, 8.10 g, 27.3 mmol) and **2a** (0.55 g, 1.0 mmol) were placed in a 50 mL round-bottomed flask fit with a septum and purged with nitrogen. The mixture was agitated with a magnetic stirrer followed by the addition of triflic acid (200 μL, 2.3 mmol). The mixture was stirred for 1 d at room temperature, after which time magnesium oxide (1.00 g) was added followed by dry hexanes (25 mL). The slurry was stirred for 1 h. An additional 25 mL of hexanes was added, and then the mixture was filtered through a short pad of Celite on a fritted funnel, vacuum was applied to speed up the filtration. Volatiles were removed in vacuo to yield 8.10 g of crude product, which was purified by kugelrohr distillation (2 h at 140 °C). The polymer was redissolved in diethyl ether (100 mL), 1.00 g of activated carbon was added, and the slurry was stirred for 20 h, at which time the suspension was filtered though a short pad of Celite on a fritted funnel, vacuum was applied to speed up the filtration. Volatiles including excess D_4 were removed *in vacuo* (<0.1 mm) at 140 °C to yield 6.90 g of a transparent colorless oil, **3a**. ^{1}H NMR spectroscopy indicated that the resulting polysiloxane chain was comprised of ∼136 dimethylsiloxane units (relative integration of the 8H (OC═

dx.doi.org/10.1021/ma202785x | *Macromolecules* 2012, 45, 2276−2285

$CH_2CH_2C{=}O$ protons at 2.66 ppm) and 4H ($O{=}COCH_2CH_2CH_2CH_2Si$ protons at 4.09 ppm) versus 818 for dimethylsiloxane ($SiCH_3$ at 0.07 ppm)), which corresponds to an average molecular weight of ~10 600 g·mol^{-1} (yield: 81%). The same procedure using a larger amount of octamethylcyclotetrasiloxane (D_4, 18.08 g, 61 mmol) and **2a** (0.60 g, 1.1 mmol) yielded 14.14 g of a polysiloxane chain **3b** constituted of 313 dimethylsiloxane units, which correspond to an average molecular weight of 23 700 g·mol^{-1} (yield: 77%).

^{1}H NMR ($CDCl_3$, 200 MHz, δ): 0.01 (s, 818H for **3a** and 1875H for **3b**, $SiCH_3$); 0.49 (t, 4H, J = 8.2 Hz, $SiCH_2CH_2CH_2CH_2$); 1.37 (m, 4H, $SiCH_2CH_2CH_2CH_2$); 1.62 (m, 4H, $SiCH_2CH_2CH_2CH_2$); 2.46 (s, 2H, $C{\equiv}CH$); 2.63 (s, 8H, $O{=}CCH_2CH_2C{=}O$); 4.06 (t, 4H, J = 6.0 Hz, $SiCH_2CH_2CH_2CH_2$); 4.67 (s, 4H, $CH_2C{\equiv}CH$).

*Synthesis of Propiolate-Terminated Polysiloxane **4a**.* 1,3-Bis-(propiolatobutyl)tetramethyldisiloxane (**2b**) was synthesized following the procedure by Gonzaga et al. [19] The same equilibration methodology as outlined in the above procedure (synthesis of **3a** and **4a**) was followed, but using **2b** (0.78 g, 2.0 mmol) as the end group, with D_4 (34.09 g, 115.0 mmol) and triflic acid (200 μL, 2.3 mmol), yielding 29.77 g of propiolate-terminated polysiloxane, **4a**. The polysiloxane chain was constituted of 220 dimethylsiloxane units, corresponding to an average molecular weight of 16,500 g·mol^{-1} (yield: 85%) determined by ^{1}H NMR and confirmed by GPC (M_n= 17 000 g·mol^{-1}; PDI = 1.6). ^{1}H NMR ($CDCl_3$, 200 MHz, δ): 0.07 (s, 1320H, $SiCH_3$); 0.56 (t, 4H, J = 8.3 Hz, $SiCH_2CH_2CH_2CH_2$); 1.37 (m, 4H, $SiCH_2CH_2CH_2CH_2$); 1.68 (m, 4H, $SiCH_2CH_2CH_2CH_2$); 2.86 (s, 2H, $C{\equiv}CH$); 4.20 (t, 4H, J = 6.5 Hz, $SiCH_2CH_2CH_2CH_2$).

*Synthesis of Poly(alkyne)-Functionalized Polymer **5**.* In a 100 mL round-bottomed flask, (aminopropyl)methylsiloxane-dimethylsiloxane copolymer (6−7 mol % (aminopropyl)methylsiloxane, 11.30 g, 10.1 mmol) and **1a** (1.89 g, 12.1 mmol) were dissolved in dry DCM (50 mL). The mixture was cooled at −20 °C in a dry ice/acetone bath, and a catalytic amount of DMAP (0.02 g, 0.2 mmol) was added. EDC·HCl (2.33 g, 12.1 mmol) and additional DCM (15 mL) were slowly added. The reaction was covered, purged with nitrogen and allowed to stir under a positive pressure of nitrogen for 48 h. The mixture was then washed with 2 × 50 mL of 0.1 M HCl (it took several hours for the mixture to phase separate) followed by 2 × 25 mL of distilled water. The organic phase was dried over $MgSO_4$, gravity filtered and the volatiles removed in vacuo to yield 10.60 g (84% yield) of the title compound as a faint yellow oil.

^{1}H NMR ($CDCl_3$, 600 MHz, δ): 0.07 (s, 84H, $SiCH_3$); 0.50 (m, 2H, $SiCH_2CH_2CH_2N$); 1.53 (m, 2H, $SiCH_2CH_2CH_2N$); 2.47 (m, 3H, $O{=}CCH_2CH_2C{=}ON$ and $C{\equiv}CH$); 2.72 (m, 2H, $O{=}CCH_2CH_2C{=}ON$); 3.22 (m, 2H, $SiCH_2CH_2CH_2N$); 4.68 (s, 2H, $CH_2C{\equiv}CH$). ^{13}C NMR ($CDCl_3$; 150 MHz): δ = −0.33, 1.25, 1.99, 14.12, 23.40, 31.10, 42.57, 52.33, 75.14, 171.02, 172.40.

*Synthesis of Propiolate Functional Trisiloxane **7**.* In a round-bottomed flask were successively introduced allyl alcohol (4.36 g, 75.0 mmol), bis(trimethylsiloxy)methylsilane (5.56 g, 25.0 mmol), and dry toluene (25 mL). Karstedt's platinum hydrosilylation catalyst (platinum divinyltetramethyldisiloxane complex, solution in xylenes: 0.05 mL) was added, and the mixture was stirred at 50 °C in a dry atmosphere (connected to a Drierite tube) for 16 h. The volatiles were then removed *in vacuo*, and the light brown oily residue was directly esterified as follow: propiolic acid (3.50 g, 50.0 mmol) in dry dichloromethane (40 mL) was added, and the solution was cooled at −20 °C using a dry ice/acetone bath. A catalytic amount of DMAP (0.10 g, 0.8 mmol) was added, followed by small portions addition of DCC (6.19 g. 30.0 mmol). Cooling at −20 °C was maintained for 8 h. The mixture was then allowed to return to room temperature (overnight). The DCM was evaporated *in vacuo*, and the residue redissolved in dry diethyl ether. The insoluble dicyclohexyl urea was removed by filtration. The filtrate was concentrated *in vacuo* and the resulting oil was chromatographed over silica gel eluting using 1% ethyl acetate in hexanes to afford 6.54 g (79% for the 2 steps) of the title compound as a colorless oil.

^{1}H NMR ($CDCl_3$; 200 MHz, δ): 0.02 (s, 3H, $SiCH_3$); 0.08 (s, 18H, $Si(CH_3)_3$); 0.47 (m, 2H, $SiCH_2CH_2CH_2O$); 1.69 (m, 2H, $SiCH_2CH_2CH_2O$); 2.87 (s, 1H, $C{\equiv}CH$); 4.14 (t, 2H, J = 7.0 Hz, $SiCH_2CH_2CH_2O$). ^{13}C NMR ($CDCl_3$; 150 MHz, δ): −0.2 ($SiCH_3$); 2.0 ($Si(CH_3)_3$); 13.5 ($SiCH_2CH_2CH_2O$); 22.4 ($SiCH_2CH_2CH_2O$); 68.8 ($SiCH_2CH_2CH_2O$); 74.5 ($C{\equiv}CH$); 75.0 ($C{\equiv}CH$); 153.0 ($C{=}O$). HRMS (EI): m/z [M^+] calculated = 332.1295, found = 332.1279.

*Synthesis of Propiolate-Terminated PEOs **9a** (750 MW) and **9b** (2000 MW).* Propiolate-terminated monomethoxy poly(ethylene oxide) **9a**: in a round-bottomed flask containing monomethoxypoly-(ethylene-oxide) (av. mol. wt: 750) (15.0 g, 20.0 mmol), was successively added propiolic acid (4.2 g, 60.0 mmol), toluene (90 mL) and a catalytic amount of *p*-toluenesulfonic acid (0.5 g, 2.6 mmol). The flask was equipped with a Dean−Stark apparatus, and heated to reflux with azeotropic removal of water. Completion of the reaction was monitored by ^{1}H NMR, by comparison of the 3 protons of terminal methoxy with the appearance of the methylenic ester protons at 4.34 ppm (ca. 20 h). The solution was then cooled to room temperature, and washed three times with 50 mL of an aqueous potassium carbonate solution. The organic phase was then dried over magnesium sulfate and concentrated *in vacuo*, and the crude product was directly loaded onto a chromatography column packed with silica gel. Elution started with pure dichloromethane, then increasing amounts of methanol were added to the eluent (up to 5%, v:v). The fractions containing the propiolate ester were combined, evaporated under reduced pressure to afford pure monopropiolate-terminated monomethoxy poly(ethylene oxide), (12.1 g, 77% yield).

^{1}H NMR ($CDCl_3$, 600 MHz, δ): 4.34 (t, 2H, $-COOCH_2-$, J = 6.0 Hz), 3.74 to 3.55 (m, ~ 60H, $-OCH_2CH_2O-$), 3.37 (s, 3H, OCH_3), 2.89 (s, broad, 1H, $HCCCOO$). ^{13}C NMR ($CDCl_3$, 125 MHz, δ): 152.68, 75.67, 74.56, 71.94, 70.57, 68.57, 65.24, 59.03. HRMS (ES positive mode): m/z [$M + NH_4^+$] calculated = 806.4749, found = 806.4768.

Monopropiolate-terminated monomethoxy poly(ethylene oxide) **9b**: in a round-bottomed flask containing monomethoxy poly(ethylene oxide) (av. mol. wt: 2000) (20.0 g, 10 mmol), was successively added propiolic acid (2.8 g, 40 mmol), toluene (70 mL), and a catalytic amount of *p*-toluenesulfonic acid (0.75 g, 3.9 mmol). The flask was equipped with a Dean−Stark apparatus, and heated with azeotropic removal of water. Completion of the reaction was monitored by ^{1}H NMR, by comparison of the three protons of terminal methoxy with to the appearance of the methylenic ester protons at 4.27 ppm. Once the reaction was complete, the mixture was then concentrated in vacuo, and the crude product was dissolved in a minimal amount of dichloromethane. The mixture was then added dropwise to a beaker containing ice-cold diethyl ether (150 mL). Once complete, the mixture was allowed to stir for a further 20 min to ensure complete precipitation. The precipitate was then collected using a fritted funnel and dried under reduced pressure. The white powder was redissolved in DCM, and the precipitation procedure (drop by drop addition into ice-cold diethyl ether) was repeated. The precipitate was collected in a fritted funnel, dried under reduced pressure in a desiccator to afford the title compound (16.8 g; 82%) as a white powder.

^{1}H NMR ($CDCl_3$, 500 MHz, δ): 4.27 (t, 2H, $-COOCH_2-$, J = 5.0 Hz), 3.47 to 3.68 (m, ~ 233H, $-OCH_2CH_2O-$), 3.31 (s, 3H, $-OCH_3$), 3.01 ppm (s, 1H, $HCCCOO$). ^{13}C NMR ($CDCl_3$, 125 MHz, δ): 152.59, 75.62, 74.48, 71.88, 70.60, 68.50, 65.14, 58.97 ppm. HRMS (ES positive mode): m/z [$M + H$]$^+$ calculated = 2065.2008, found = 2065.1916.

Azide Synthesis. *Synthesis of Poly(azidopropylmethyl)-co-(dimethylsiloxane) **6**.* The preparation of **6** is an improvement of the previously published method by Gonzaga et al.[19] (Chloropropylmethyl)siloxane-dimethylsiloxane copolymer (14−16 mol % (chloropropyl)methylsiloxane, by ^{1}H NMR ($(Me_2SiO)_{5.5}(Cl(CH_2)_3MeSiO)_1)_n$; 543.45 g/mol repeat unit) 20.00 g, 36.8 mmol of chloropropyl groups), NaN_3 (3.62 g, 55.7 mmol) and $(n\text{-butyl})_4NN_3$, (0.50 g, 1.8 mmol) were dissolved in dry THF (60 mL). The mixture was refluxed with stirring for 24 h. At this stage, the reaction was found to be almost complete by ^{1}H NMR spectroscopy. Additional $(n\text{-butyl})_4NN_3$ (0.30 g, 1.00 mmol) was therefore added, and the mixture was refluxed an additional 24 h. THF was removed *in*

vacuo. The mixture was redissolved in diethyl ether (60 mL) and filtered though neutral alumina. Volatiles were removed in vacuo to yield 19.43 g (96% yield) of the title compound. Characterization by ^{1}H and ^{13}C NMR was in agreement with previously reported values.[19] In subsequent elastomer synthesis, ^{1}H NMR spectroscopy was to calculate the molecular weight of an average repeat unit using the ratio of azide (using the CH_2 adjacent to N_3 at 3.26 ppm as a diagnostic) to alkyne groups.

^{1}H NMR ($CDCl_3$, 200 MHz, δ): 0.07 (s, 35H, $SiCH_3$); 0.56 (m, 2H, $SiCH_2CH_2CH_2N_3$); 1.62 (m, 2H, $SiCH_2CH_2CH_2N_3$); 3.24 (t, J = 6.9 Hz, 2H, $SiCH_2CH_2CH_2N_3$).

Synthesis of Polymer ***8****: Poly(azido)siloxane with a Reduced (by 50%) Amount of Azido Groups.* Compound **6** (3.00 g, 5.6 mmol), **7** (0.93 g, 2.80 mmol), and chloroform (1 mL) were added to a vial and stirred for 20 h at 55 °C, at which time volatiles were removed to give the title compound in quantitative yield. The resulting polymer was characterized by ^{1}H NMR, which confirmed that about half of the initial azide functional groups had reacted to form triazole rings with trisiloxane blocking groups.

^{1}H NMR ($CDCl_3$; 600 MHz, δ): 0.07 (s, 101H, $SiCH_3$); 0.3 (m, 6H, $SiCH_2$); 1.63 (m, 2H, $SiCH_2CH_2CH_2N_3$); 1.79 (m, 2H, $SiCH_2CH_2CH_2$–triazole); 1.95 (m, 2H, $SiCH_2CH_2CH_2O$); 3.21 (t, 2H, J = 6.9 Hz, $SiCH_2CH_2CH_2N_3$); 4.30 (m, 2H, O=$COCH_2CH_2CH_2Si$); 4.37 (m, 2H, CH_2–triazole); 8.03, 8.08 (s, 1H, C=C*H*).

Elastomer Synthesis. Four distinct series of elastomers were prepared (**I**, **II**, **III**, and **IV**), as summarized in Table 1. These different series differ in the precursors used: alkynes **3a**, **3b**, **4a**, and **5**; azides **6** and **8**. Different alkyne to azide ratios were used in each series, generating elastomers with various amounts of residual reactive azide or alkyne groups. According to the alkyne used, the cross-linking process could be performed at different temperatures, as stated in Table 1. Finally, the Shore OO hardness (durometer) of the elastomers were determined.

The general procedure is illustrated by the synthesis of a reactive elastomer containing an excess of azide that was formed by a cross-linking reaction between **3b** and **6** with an alkyne to azide ratio of 1:2 respectively (**IIa**). Polymer **6** (0.38 g, 0.7 mmol of azido functional units) was placed in a small glass Petri dish followed by dialkyne **3b** (4.16 g, 0.35 mmol of alkyne), and toluene (5 mL). After vigorous mixing, a homogeneous and transparent mixture resulted. The dish was then covered and placed in an oven at 90 °C for 48 h. The initially formed solution turned into a monolithic elastomer during this time. The same procedure was followed using molar ratios of alkyne:azide functional groups (**3b**:**6**) of 1:4, 1:6, 1:8 and 1:10, respectively, to give **IIB**, **IIC**, **IID**, and **IIE** (Table 1).

The above procedure was repeated using **6** and dialkyne **3a** to give more rigid elastomers **IA-IE** compared to series **II**. An analogous series was made using **4a** with **6** and toluene (3 mL); cross-linking at 60 °C occurred after 12 h to yield colorless and transparent monolithic elastomers **IIIA-IIIE**. Slightly higher temperatures (70 °C) led to more rapid curing (8 h). Finally, a series of elastomers **IVA-IVE** using a molar excess of alkyne functional groups were made on a smaller scale; cross-linking of **5** and **8** on a 1 g scale in 10 mL beakers using toluene (600 μL) to homogenize the mixture was performed with molar ratios of azide:alkyne (**8**:**5**) of: 1:4, 1:6, 1:8, 1:10, and 1:12, respectively. The mixtures were cured at 90 °C for 12 h to form monolithic elastomers that were transparent and slightly yellow, **IVA**, **IVB**, **IVC**, **IVD**, and **IVE** respectively.

All elastomers were removed from their respective vessels, cut into smaller cylindrical disks, and characterized by IR then stored in the dark in plastic Petri dishes until further use.

Table 1 summarizes the precursors used, stoichiometry ratios, curing conditions, and outcome of the different cross-linking processes we performed.

PEG-Functionalized Silicones. Elastomers of Series **IIIA-IIIE** were functionalized using with **9a** and **9b**, respectively. The general procedure is outlined for the elastomer **IIIA** using **9b**. Four elastomer disks (total mass of 0.23 g) were placed into a 50 mL round-bottomed flask fit with a condenser under a positive pressure of nitrogen. The weight ratio of **6** used in the formation of each elastomer was determined to ensure that an excess of PEG was used during the functionalization process; elastomer **IIIA** contained 13% **6** by mass (0.03 g, 0.06 mmol). Chloroform (20 mL) and excess **9b** (0.11 g, 0.05 mmol) were added to the flask and the elastomers were refluxed with stirring for 24 h. The rubbers swelled to several times their original volume. Purification was carried out by Soxhlet extraction using DCM for 24 h. The elastomers were dried in a glass Petri dish at 50 °C for several days yielding slightly opaque, whitish elastomers that had shrunk back to their original size. This procedure was repeated using **IIIB**–**IIIE** with **9b** as well as with **IIIA**–**IIIE** modified with **9b** using a 3× molar excess. The resultant modified elastomers were characterized using IR and contact angle measurements; **IIID-9b** was characterized by ^{1}H NMR (Figure 4A).

Elastomers **IIIC** were also functionalized with **9a** via 3 different methods in poor solvents for silicones. **IIIC** (1 disk) and **9a** (300 mg) were placed in a vial with 0.5 mL of distilled water and stir bar. The rubber-PEG mixture was stirred at 60 °C for 72 h then purified by a Soxhlet extraction with methanol for 24 h. The rubber was then placed in a glass Petri dish to air-dry at room temperature for 30 min. This process was also repeated with fresh **IIIC** elastomers at room temperature as well as in neat **9a** at 60 °C. After extraction and air drying the rubbers were characterized by static contact angle measurements (Table 2).

AUTHOR INFORMATION

Corresponding Author

*E-mail: mabrook@mcmaster.ca. Telephone: +1 905 525 9140 x 23483. Fax: +1 905 522 2509..

Notes

The authors declare no competing financial interest.

ACKNOWLEDGMENTS

We acknowledge with gratitude the financial support of the Natural Sciences and Engineering Research Council of Canada (NSERC). T.R. also thanks NSERC for the award of a Julie Payette Scholarship.

REFERENCES

(1) Colley, H. E.; Mishra, G.; Scutt, A. M.; McArthur, S. L. *Plasma Proc. Polym.* **2009**, *6*, 831–839.

(2) Yuan, L.; Yu, Q.; Li, D.; Chen, H. *Macromol. Biosci.* **2011**, *11*, 1031–1040.

(3) Brook, M. A. *Silicon in Organic, Organometallic, and Polymer Chemistry*: John Wiley & Sons, Inc.: New York, NY, 2000.

(4) Himstedt, A. L.; Gettings, R. L. *Silicones for pharmaceutical and biomedical applications*; Technomic: Lancaster, PA, 1998.

(5) Chen, H.; Brook, M. A.; Sheardown, H. *Biomaterials* **2004**, *25*, 2273–2282.

(6) Rana, D.; Matsuura, T. *Chem. Rev.* **2010**, *110*, 2448–2471.

(7) Chen, H.; Brook, M. A.; Sheardown, H. D.; Chen, Y.; Klenkler, B. *Bioconjugate Chem.* **2006**, *17*, 21–28.

(8) Alauzun, J. G.; Fortuna, J. N.; Sheardown, H.; Gonzaga, F.; Brook, M. A. *J. Mater. Chem.* **2009**, *19*, 5033–5038.

(9) Canalle, L. A.; van Berkel, S. S.; de Haan, L. T.; van Hest, J. C. T. *Adv. Funct. Mater.* **2009**, *19*, 3464–3470.

(10) Li, Y.; Santos, C. M.; Kumar, A.; Zhao, M. R.; Lopez, A. I.; Qin, G. T.; McDermott, A. M.; Cai, C. Z. *Chem.—Eur. J.* **2011**, *17*, 2656–2656.

(11) Shamsi, F.; Coster, H.; Jolliffe, K. A. *Surf. Sci.* **2011**, *605*, 1763–1770.

(12) Larregola, M.; Lequin, O.; Karoyan, P.; Guianvarc'h, D.; Lavielle, S. *J. Peptide Sci.* **2011**, *17*, 632–643.

(13) Ran, Q.; Peng, R.; Liang, C.; Ye, S. G.; Xian, Y.; Zhang, W. J.; Jin, L. T. *Anal. Chim. Acta* **2011**, *697*, 27–31.

(14) Tian, X.; Pai, J.; Baek, K. H.; Ko, S. K.; Shin, I. *Chem. Asian J.* **2011**, *6*, 2106–2112.

(15) Russo, L.; Landi, E.; Tampieri, A.; Natalello, A.; Doglia, S. M.; Gabrielli, L.; Cipolla, L.; Nicotra, F. *Carbohydr. Res.* **2011**, *34*, 1564−1568.
(16) Patel, K. G.; Swartz, J. R. *Bioconj. Chem.* **2011**, *22*, 376−387.
(17) Kolb, H. C.; Finn, M. G.; Sharpless, K. B. *Angew. Chem., Int. Ed.* **2001**, *40*, 2004−2021.
(18) Gonzaga, F.; Yu, G.; Brook, M. A. *Chem. Commun.* **2009**, 1730−1732.
(19) Gonzaga, F.; Yu, G.; Brook, M. A. *Macromolecules* **2009**, *42*, 9220−9224.
(20) Sustmann, R. *Pure Appl. Chem.* **1974**, *40*, 569−593.
(21) Li, Z.; Seo, T. S.; Ju, J. *Tetrahedron Lett.* **2004**, *45*, 3143−3146.
(22) van Berkel, S. S.; Dirks, A. J.; Meeuwissen, S. A.; Pingen, D. L. L.; Boerman, O. C.; Laverman, P.; van Delft, F. L. J.; Cornelissen, J. L. M. J.; Rutjes, F. P. J .T. *ChemBioChem* **2008**, *11*, 1805−1815.
(23) van Berkel, S. S.; Dirks, A. J.; Debets, M. F.; van Delft, F. L.; Cornelissen, J. J. M. L.; Nolte, R. J. M.; Rutjes, F. P. J. T. *ChemBioChem* **2007**, *8*, 1504−1508.
(24) Wittig, G.; Krebs, A. *Chem. Ber.-Recl.* **1961**, *94*, 3260−3275.
(25) Agard, N. J.; Prescher, J. A.; Bertozzi, C. R. *J. Am. Chem. Soc.* **2004**, *126*, 15046−15047.
(26) Laughlin, S. T.; Baskin, J. M.; Amacher, S. L.; Bertozzi, C. R. *Science* **2008**, *320*, 664−667.
(27) Neef, A. B.; Schultz, C. *Angew. Chem., Int. Ed.* **2009**, *48*, 1498−1500.
(28) Kele, P.; Mezo, G.; Achatz, D.; Wolfbeis, O. S. *Angew. Chem., Int. Ed.* **2009**, *48*, 344−347.
(29) Meredith, C.; Patrick, K. *Polym. Int.* **2009**, *58*, 1190−1195.
(30) Lallana, E.; Fernandez-Megia, E.; Riguera, R. *J. Am. Chem. Soc.* **2009**, *131*, 5748−5750.
(31) Canalle, L. A.; van Berkel, S. S.; de Haan, L. T.; van Hest, J. C. M. *Adv. Funct. Mater.* **2009**, *19*, 3464−3470.
(32) Ornelas, C.; Broichhagen, J.; Weck, M. *J. Am. Chem. Soc.* **2010**, *132*, 3923−3931.
(33) Noll, W. J. *Chemistry and Technology of Silicones*; Academic Press: New York, 1968.
(34) Guo, D.; Han, H.; Wang, J.; Xiao, S.; Dai, Z. *Colloids Surf. A: Physicochem. Eng. Aspects* **2007**, *308*, 129−135.
(35) Brook, M. A.; Zhao, S.; Liu, L.; Chen, Y. *Can. J. Chem.* **2012**, *90*, 153−160.
(36) Brook, M. A.; Liu, L.; Zhao, S.; Mammo, Z. N. in *Synthesis and Properties of Silicones and Silicone-Modified Materials*, Clarson, S. J., Fitzgerald, J. J., Owen, M. J., Smith, S. D., Van Dyke, M. E., Eds.; American Chemical Society: Washington DC, 2010; pp 147−155.
(37) Roucoules, V.; Ponche, A.; Geissler, A.; Siffer, F.; Vidal, L.; Ollivier, S.; Vallat, M. F.; Marie, P.; Voegel, J. C.; Schaaf, P.; Hemmerle, J. *Langmuir* **2007**, *23*, 13136−13145.
(38) Müller, B.; Riedel, M.; Michel, R.; De Paul, S. M.; Hofer, R.; Heger, D.; Grutzmacher, D. *J. Vacuum Sci. Tech. B* **2001**, *19*, 1715−1720.
(39) Fortuniak, W.; Mizerska, U.; Chojnowski, J.; Basinska, T.; Slomkowski, S.; Chehimi, M. M.; Konopacka, A.; Turecka, K.; Werel, W. *J. Inorg. Organomet. Polym.* **2011**, *21*, 576−589.
(40) de Gennes, P. G. *Rev. Mod. Phys.* **1985**, *57*, 827−863.
(41) Kingshott, P.; Griesser, H. J. *Curr. Opin. Solid State Mater. Sci.* **1999**, *4*, 403−412.
(42) Morra, M. *J. Biomater. Sci. Polymer Edn.* **2000**, *11*, 547−569.
(43) Unsworth, L. D.; Sheardown, H.; Brash, J. L. *Langmuir* **2005**, *21*, 1036−1041.
(44) Bailon, P.; Won, C. Y. *Expert Opin. Drug Deliv.* **2009**, *6*, 1−16.
(45) Ryan, S. M.; Mantovani, G.; Wang, X. X.; Haddleton, D. M.; Brayden, D. J. *Expert Opin. Drug Deliv.* **2008**, *5*, 371−383.
(46) Murthy, R.; Cox, C. D.; Hahn, M.; Grunlan, M. *Biomacromolecules* **2007**, *8*, 3244−3525.
(47) Murthy, R.; Bailey, B.; Valentin-Rodriguez, C.; Ivanisevic, A.; Grunlan, M. *J. Polym. Sci.* **2010**, *48*, 4108−4119.
(48) Siow, K. A.; Britcher, L.; Kumar, S.; Griesser, H. J. *Plasma Proc. Polym.* **2006**, *3*, 392.
(49) Hollahan, J. R.; Carison, G. L. *J. Appl. Polym. Sci.* **1970**, *14*, 2499−2508.
(50) Efimenko, K.; Wallace, W. E.; Genzer, J. *J. Colloid Interface Sci.* **2002**, *254*, 306−315.
(51) Hillborg, H.; Gedde, U. W. *Polymer* **1998**, *39*, 1991−1998.
(52) Morra, M.; Occhiello, E.; Marola, R.; Garbassi, F.; Humphrey, P.; Johnson, D. *J. Colloid Interface Sci.* **1990**, *137*, 11−24.
(53) Chaudhury, M. K.; Whitesides, G. M. *Langmuir* **1991**, *7*, 1013−1025.
(54) Chaudhury, M. K.; Whitesides, G. M. *Science* **1992**, *255*, 1230−1232.
(55) Genzer, J.; Efimenko, K. *Science* **2000**, *290*, 2130−2133.
(56) Hu, S.; Ren, X.; Bachman, M.; Sims, C. E.; Li, G. P.; Allbritton, N. *Anal. Chem.* **2002**, *74*, 4117−4123.
(57) Wang, B.; Chen, L.; Abdulali-Kanji, Z.; Horton, J. H.; Oleschuk, R. D. *Langmuir* **2003**, *19*, 9792−9798.
(58) Heggli, M.; Tirelli, N.; Zisch, A.; Hubbell, J. A. *Bioconjugate Chem.* **2003**, *14*, 967−973.
(59) Nilsson, K.; Mellin, L.; Nederberg, F.; Bowden, T. *Macromolecules* **2007**, *40*, 901−908.
(60) Li, G. L.; Wan, D.; Neoh, K. G.; Kang, E. T. *Macromolecules* **2010**, *43*, 10275−10282.
(61) Antoni, P.; Hed, Y.; Nordberg, A.; Nystum, D.; von Holst, H.; Hult, A.; Malkoch, M. *Angew. Chem., Int. Ed.* **2009**, *48*, 2126−2130.

Macromolecules

Article

pubs.acs.org/Macromolecules

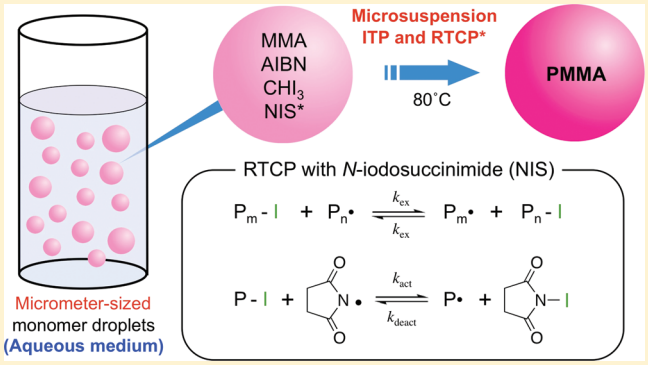
Iodine Transfer Polymerization (ITP with CHI_3) and Reversible Chain Transfer Catalyzed Polymerization (RTCP with Nitrogen Catalyst) of Methyl Methacrylate in Aqueous Microsuspension Systems: Comparison with Bulk System

Yukiya Kitayama,[†] Mika Yorizane,[†] Hideto Minami,[†] and Masayoshi Okubo*[,†,‡]

[†]Department of Chemical Science and Engineering, Graduate School of Engineering, Rokko, Nada, Kobe University, Kobe 657-8501, Japan

[‡]Smart Spheres Workshop Co. Ltd., Koyo-cho Naka 2-1-214-122, Higashi-Nada, Kobe 658-0032, Japan

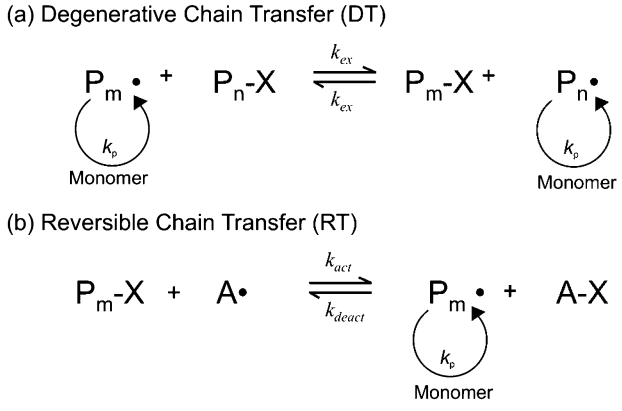
ABSTRACT: Iodine transfer polymerization (ITP) with CHI_3 as transfer agent and reversible chain transfer catalyzed polymerization (RTCP) with *N*-iodosuccinimide (NIS) as catalyst of methyl methacrylate (MMA) were successfully applied to aqueous microsuspension systems (respectively, microsuspension ITP and microsuspension RTCP). Both microsuspension ITP and RTCP proceeded smoothly without induction period and with a controlled/living manner. Polydispersity index (PDI, M_w/M_n) of the microsuspension RTCP was smaller than that of the microsuspension ITP, and it was larger than RTCP in a bulk system (bulk RTCP). The difference seems to be based on that NIS would partly react with water dissolved in the MMA phase, and formed succinimide, which is a low controllable catalyst in comparison with NIS. With decreasing particle (monomer droplet) size, the polymerization rate increased, and a reasonable control was maintained throughout the polymerization based on the segregation effect.



INTRODUCTION

Controlled/living radical polymerization (CLRP) leads to the preparation of well-defined vinyl polymers having predetermined molecular weight, narrow molecular weight distribution, and various complex architectures.[1−9] One of the most frequently employed CLRP techniques is iodine transfer polymerization (ITP) (Scheme 1a).[10−19] ITP is based on degenerative chain transfer (DT) process between dormant chains and propagating radicals, in which the iodide compounds such as cyanopropyl iodide and CHI_3 were used as a control agent. ITP has attracted much attention as a simple and robust method which dose not use metal. Moreover, ITP is well-known as a only technique for the synthesis of the well-defined polymers based on the particular monomers such as fluoromonomers and phosphonic monomers.[11,12,19,20] Therefore, the various kinds of techniques developed from the ITP system have been proposed until now. Lacroix-Desmazes and co-workers advanced the ITP technique to reverse iodine transfer polymerization (RITP), in which the iodide compounds were formed *in situ* from thermal initiator and iodine (I_2).[21,22] RITP is an important technique because the iodide compounds, which demand a lot of attention to storage, need not to be prepared before the polymerization. Until now, the various kinds of polymers were successfully synthesized by RITP including methacrylates, in which the polydispersity index

Scheme 1. Reversible Chain Transfer Catalyzed Polymerization (RTCP) (NIS = *N*-Iodosuccinimide)



Received: January 12, 2012
Revised: February 17, 2012
Published: February 28, 2012

 © 2012 American Chemical Society

was >1.46 because of the low frequency of iodine compounds by the exchange constant.[21,23,24] Percec and co-workers discovered that vinyl chloride could be polymerixed with CHI_3 as a control agent via single electron transfer and DT mechanisms with copper(0) or $Na_2S_2O_4$ as catalyst (SET-DTLRP).[25,26] The SET-DTLRP enabled to synthesize various vinyl polymers with higher molecular weight in short polymerization time.[27,28]

Montairo and co-workers simulated the evolution of PDI with conversion in reversible addition−fragmentation chain transfer (RAFT) polymerization,[29,30] which is based on the DT mechanism as well as the ITP system, using a numerical simulation.[15,31] The simulation indicates that the ratio of the chain transfer constant to propagation rate constant (C_{ex}) is very important for obtaining a low PDI value. When C_{ex} value is 5.0, the PDI value is small (1.3). However, when the C_{ex} value is decreased to 1.0, the PDI value is maintained at a constant value (2.0). The trend was also clarified by the experimental work.[12,32] C_{ex} value in the ITP system is normally below 5.0; therefore, the obtaining PDI value normally was approximately >1.5.

Recently, Goto and co-workers developed a new CLRP named reversible chain transfer catalyzed polymerization (RTCP) (Scheme 1).[33,34] This technique is controlled by adding very small amount of catalyst (A-I) such as germanium (Ge)[35,36] or nitrogen (N)[33,37] compound, e.g., *N*-iodosuccinimide (NIS) to a ITP system. A-I works as deactivator of $P^{\bullet}$, *in situ* producing $A^{\bullet}$. $A^{\bullet}$ works as activator of P−I, producing $P^{\bullet}$ and A-I. Because this cycle (Scheme 1b) occurs frequently, the controllability of polydispersity is improved dramatically (∼1.2). Attractive features of RTCP include low cost, environmentally friendliness, and simplicity.

In order for CLRP to be useful for industrial applications, it must be developed from homogeneous systems to heterogeneous systems, and significant progress in this area has been made in recent years.[38−44] Several CLRP techniques, which are nitroxide-mediated radical polymerization (NMP),[38,45,46] atom transfer radical polymerization (ATRP),[47−49] RAFT polymerization,[29,50,51] and organotellurium-mediated radical polymerization (TERP),[52−56] were successfully applied to the aqueous dispersed systems.

ITP was also successfully applied to the aqueous dispersed systems. Charleux and co-workers carried out ITP with $C_6F_{13}I$ as a control agent in the miniemulsion systems (miniemulsion ITP) and successfully synthesized polystyrene (PS) and PS-*b*-poly(*n*-butyl acrylate).[18] Lacroix-Desmazes and co-workers synthesized triblock copolymers by the miniemulsion ITP using an end-iodefunctionalized dimethylsiloxane macrotransfer agent.[57] Moreover, they successfully applied RITP to the miniemulsion systems, in which well-defined PS was synthesized.[58] The Lacroix-Desmazes group is also a pioneer for the RITP in the emulsion polymerization system (emulsion RITP) using water-soluble and nonhazardous NaI as a precursor to the control agent.[32,59,60]

In our previous work, it was reported that ITP in a microsuspension system (microsuspension ITP) of methyl methacrylate (MMA) with 2-cyanopropyl iodide (CP-I) was not carried out with a control/living manner. On the other hand, microsuspension RTCP with NIS was successfully conducted with a good control/living manner for the first time;[61] however, the molecular weight distribution was broader than RTCP in a bulk system (bulk RTCP). The reason for the difference was unclear.

In this article, the reason for the difference between bulk and microsuspension RTCPs with NIS of MMA will be clarified, in which the chain transfer agent was replaced from CP-I to CHI_3 because CHI_3 is a commercially available and inexpensive. The additional important point is a stability of CHI_3 during storage. Moreover, the improving technique for the PDI control will be suggested.

EXPERIMENTAL PART

Materials. MMA (Tokyo Kasei Kogyo Co. Ltd., Tokyo, Japan, >99.8%) was purified by distillation under reduced pressure in a nitrogen atmosphere. Water used in all experiments was obtained using an Elix UV (Millipore, Japan) purification system and had a resistivity of 18.2 MΩ·cm. Reagent grade 2,2′-azobis(isobutyronitrile) (AIBN) (Nacalai Tesque, Kyoto, Japan) was purified by recrystallization. Iodoform (CHI_3), *n*-hexadecane (Nacalai Tesque), *N*-iodosuccinimide (NIS) (Aldrich Chem Co. Ltd., 95%), *n*-tetradecyltrimethylammonium bromide (TTAB) (Tokyo Kasei Kogyo), sodium dodecyl sulfate (SDS) (Wako Chemical Industries, Ltd., Japan), and poly(vinyl alcohol) (PVA) (Nippon Synthetic Chemical Ind. Co., Ltd., Japan; Gohsenol GH-17: degree of polymerization, 1700; degree of saponification, 88%) were used as received.

ITP in Microsuspension System (Microsuspension ITP). A monomer solution (MMA 10 g, 100 mmol; AIBN 20 mg, 0.13 mmol; CHI_3 0.39 g, 1.0 mmol) was mixed with an aqueous (90 g) solution of TTAB (0.45 g) and stirred vigorously at 5000 rpm using a homogenizer (NISSEI ABM-2) for 2 min. The monomer emulsion was transferred to glass ampules and degassed using several vacuum/N_2 cycles, and then the ampules were sealed off under vacuum. Microsuspension ITP of MMA was carried out at 80 °C with shaking of the ampules horizontally at 80 cycles min^{-1} (3 cm strokes). All of these processes were performed under a safe light because iodo compounds are light-sensitive.

RTCP in Microsuspension System (Microsuspension RTCP). Microsuspension RTCP of MMA was carried out in the same way as the microsuspension ITP, except for containing NIS (3.0 mg, 13 μmol) in the monomer phase.

Conversion Measurement. Conversion was determined by gas chromatography (GC-18A, Shimadzu Co., Kyoto, Japan) employing helium as carrier gas, *N*,*N*-dimethylformamide as solvent, and *p*-xylene as internal standard.

Molecular Weight Measurement. Number-average molecular weight (M_n), weight-average molecular weight (M_w), and molecular weight distribution (MWD) were measured by gel permeation chromatography (GPC) with two S/divinylbenzene gel columns (TOSOH Corp., TSKgel GMH_{HR}-H, 7.8 mm i.d. × 30 cm; bead size = 5 μm) using tetrahydrofuran (THF) as eluent at 40 °C at a flow rate of 1.0 mL/min employing refractive index (RI) (TOSOH RI-8020/21) and ultraviolet (UV) detectors (TOSOH UV-8II). The columns were calibrated with six standard PS samples (1.05×10^3−5.48×10^6, M_w/M_n = 1.01−1.15). Theoretical molecular weight ($M_{n,th}$) was obtained using $M_{n,th} = \alpha M_M[M]_0/[R\text{-}I]_0$, where α is the fractional conversion of monomer, M_M is the molecular weight of monomer, and $[M]_0$ and $[R\text{-}I]_0$ are the initial concentrations of monomer and transfer agent (alkyl iodide), respectively. It was reported that CHI_3 works as a bifunctional chain transfer agent;[25] however, the $M_{n,th}$ is not dependent on mono- or bifunctional.

Particle Size Measurement. The number-average diameter (D_n) and coefficient of variation (C_v) of the particles were measured the diameters of more than 200 particles using transmission electron microscopy (TEM) (JEM-1230, JEOL Ltd., Tokyo, Japan) using image analysis software (WinROOF, Mitani Co. Ltd., Fukui, Japan) for a Macintosh computer.

Partitioning of NIS to Aqueous Phase. A MMA/NIS/water mixture, where NIS was used a larger amount (90 mg), which dissolves in an aqueous phase (i.e., the solubility of NIS in water is >1.0 mg/g-water), to facilitate the detection of absorbance, consisting of the same composition as the polymerization recipe except for NIS was stirred at 80 °C for 1 h in Schlenk flask protected with an aluminum film. In this

dx.doi.org/10.1021/ma3000829 | *Macromolecules* 2012, 45, 2286−2291

experiment, NIS was initially dissolved in MMA. The absorbance of NIS in water was determined by UV−vis (Shimazdu UV-2500). The concentration of NIS in the aqueous phase was calculated from the difference in absorbencies (at 463 nm) before and after partitioning.

RESULTS AND DISCUSSION

Select of Proper Emulsifier. In this article, we tried to use CHI_3 as transfer agent, which is a commercially available, for microsuspension ITP and RTCP of MMA. Matyjaszewski and co-workers have already reported that bulk ITP of styrene using CHI_3 was successfully controlled.[14] To our knowledge, ITP and RTCP using CHI_3 as a transfer agent in aqueous dispersed systems has not been reported.

First of all, in order to choose an appropriate emulsifier for microsuspension RTCP of MMA with NIS as catalyst, the preliminary polymerizations with various kinds of emulsifiers (SDS, TTAB, and PVA) were carried out. Coagulation occurred in the microsuspension RTCP systems with SDS. Using PVA as a surfactant, the emulsion has a small amount of coagulation. On the other hand, the microsuspension RTCP system with TTAB proceeded without coagulation. Therefore, TTAB was chosen as an appropriate emulsifier in the microsuspension RTCP of MMA with NIS. The reason is unclear in this work. We will clarify the reason in a following paper.

Microsuspension ITP and RTCP of MMA. Figure 1 shows conversion−time plots and first-order plots of microsuspension

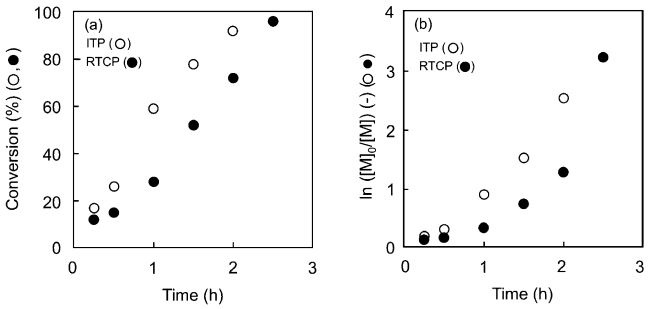


Figure 1. Conversion vs time plots (a) and first-order plots (b) for iodine transfer polymerization (ITP) (open circles) with CHI_3 and reversible chain transfer catalyzed polymerization (RTCP) (closed circles) with *N*-iodosuccinimide (NIS) of methyl methacrylate (MMA) in microsuspension systems with 2,2′-azobis(isobutyronitrile) (AIBN) at 80 °C. $[CHI_3]_0/[AIBN]_0/[NIS]_0$ molar ratios for ITP and RTCP were respectively 80/10/0 and 80/10/1.

ITP with CHI_3 as transfer agent (closed circles) and microsuspension RTCP with NIS as catalyst (open circles) of MMA in aqueous dispersed systems. Both polymerizations smoothly proceeded without an induction period and almost finished within a couple of hours. Size distributions of obtained particles were almost the same as those of original droplets, which were measured with an optical microscope. The rate of the microsuspension RTCP was somewhat slower than that of the microsuspension ITP. This must be based on that the nitrogen compound radical ($A^\bullet$), which was generated from the reaction between NIS and radical species (reversible chain transfer reaction) in the RTCP system, could not add with MMA, leading to the retardation of the polymerization relative to the ITP system, in which NIS did not exist. However, $A^\bullet$ derived from the NIS terminates with propagating radical species during the polymerization, leading to gradual decreasing the NIS concentration. As a result, the reaction between NIS and radical species, which leads to a retardation of the polymerization, gradually decreased. This would be the reason why the polymerization did not follow the first-order kinetics in the microsuspension RTCP (Figure 1b).

Figure 2 shows MWD, M_n and M_w/M_n at different conversions of the microsuspension ITP (a, b) and RTCP (c, d). In the microsuspension ITP, the M_n increased linearly with conversion, and the values were always higher than corresponding $M_{n,th}$ and the M_w/M_n values were relatively high (∼1.84). These results suggest that CHI_3 worked as transfer agent in an aqueous dispersed system, but the control was not enough like bulk ITP in comparison with the other CLRP because of the low chain transfer rate constant of poly(MMA) (PMMA) radical to CHI_3 relative to propagation rate constant.

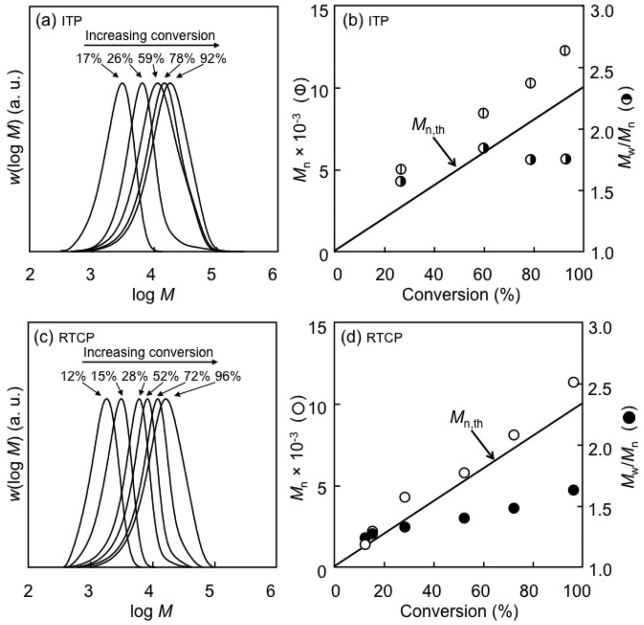


Figure 2. Molecular weight distribution (with RI detector) at different conversions (a, c) and number-average molecular weight (M_n) (open circles) and polydispersity index (M_w/M_n) (closed circles) vs conversion plots (b, d) for the microsuspension ITP (a, b) and microsuspension RTCP (c, d) of MMA at 80 °C. $[CHI_3]_0/[AIBN]_0/[NIS]_0$ for ITP and RTCP were respectively 80/10/0 and 80/10/1 (molar ratios).

In the microsuspension RTCP, the M_n increased linearly with conversion and the values agreed with the corresponding $M_{n,th}$ values. The M_w/M_n values were lower (1.3−1.6) than those in the microsuspension ITP. These results indicate that NIS works effectively as catalyst in the microsuspension RTCP.

Comparison between Bulk and Microsuspension RTCP Systems. Figure 3 shows conversion−time plots of bulk and microsuspension RTCPs of MMA with NIS and CHI_3. Both polymerizations proceeded smoothly, but the polymerization rate of the microsuspension RTCP was slightly lower than that of the bulk RTCP conducted under the same conditions except for without TTAB aqueous solution as medium.

Figure 4 shows M_n and M_w/M_n at different conversions of the bulk and microsuspension RTCPs of MMA with NIS as catalyst. The M_w/M_n of the microsuspension RTCP was ∼1.48

dx.doi.org/10.1021/ma3000829 | Macromolecules 2012, 45, 2286−2291

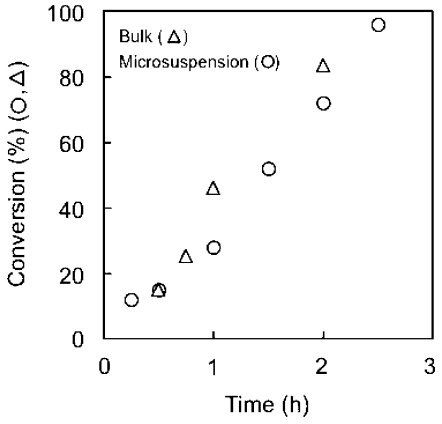


Figure 3. Conversion vs time plots for the bulk (triangles) and microsuspension (circles) RTCPs of MMA at 80 °C. $[CHI_3]_0/[AIBN]_0/[NIS]_0$ = 80/10/1 (molar ratio).

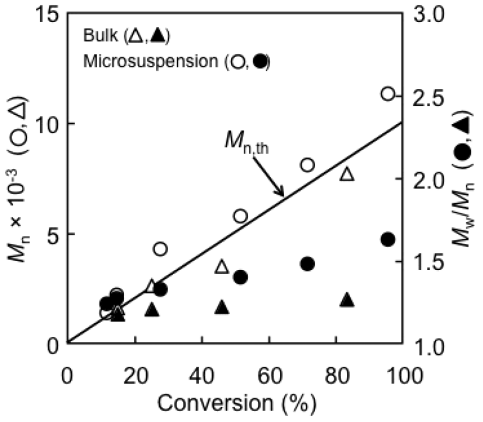


Figure 4. M_n (open circles) and M_w/M_n (closed circles) vs conversion plots for the bulk (triangles) and microsuspension (circles) RTCPs of MMA at 80 °C. $[CHI_3]_0/[AIBN]_0/[NIS]_0$ = 80/10/1 (molar ratio).

at 73% conversion. This value was higher than that of the bulk RTCP ($M_w/M_n \sim 1.27$ at 83% conversion). Such a difference in the MWD controls between the bulk and microsuspension RTCPs to be based on following aspects: (i) partitioning of the catalyst between monomer and aqueous phases; (ii) denaturation of the catalyst resulting from reaction with water. Because the amount of NIS partitioned to the aqueous phase was less than 3% of the total, the partitioning of NIS to the aqueous phase would be negligible.

In order to confirm whether of NIS reacts with water, powder NIS, of which color is yellow, was dispersed in water and heated at 80 °C. The color of the original NIS aqueous solution was orange. During the heat treatment a red-tinged vapor, which should be I_2, was generated, and the dried powder was white. It would be possible that NIS was hydrolyzed in water, resulting in succinimide.

Figure 5 shows FT-IR spectra of (a) original NIS, (b) succinimide, and (c) NIS after treatment in water. The spectrum of the treated NIS did not fit in that of the original NIS (the peak of 3000−3200 cm^{-1} can be assigned to the NH group), but succinimide.

To compare PDI controls between RTCPs with NIS and succinimide, bulk RTCPs with (i) NIS, (ii) succinimide, and (iii) NIS that had dispersed in water for 3 h at 80 °C, followed by a drying at room temperature, were carried out. Figure 6a shows M_n and M_w/M_n at different conversions of the bulk

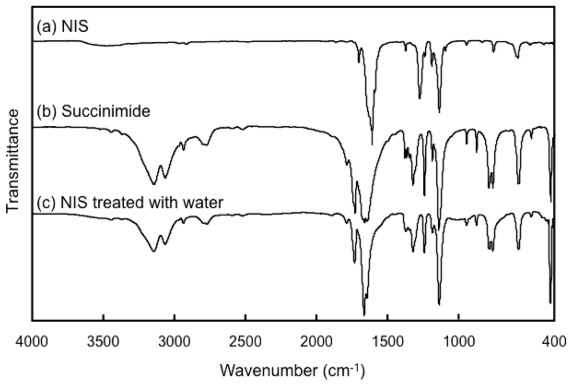


Figure 5. FT-IR spectra of (a) NIS, (b) succinimide, and (c) NIS reacted with water previously.

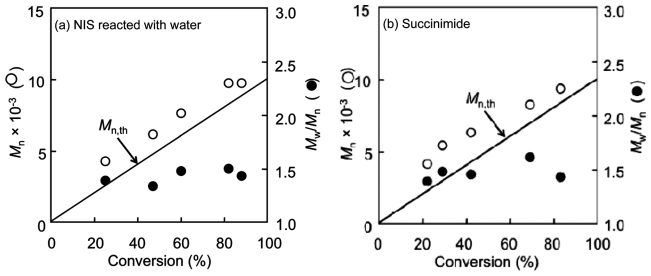


Figure 6. M_n (open circles) and M_w/M_n (closed circles) vs conversion plots for bulk RTCPs of MMA at 80 °C. Catalyst: (a) treated NIS in water for 3 h at 80 °C; (b) succinimide. $[CHI_3]_0/[AIBN]_0/[NIS]_0$ = 80/10/1 (molar ratio).

RTCP with the NIS. M_w/M_n values were larger than those of the bulk RTCP with NIS, but similar to those in the bulk RTCP with succinimide and in the microsuspension RTCP with NIS (Figure 4). These results indicate that NIS in the microeuspension RTCP with NIS reacted with water, resulting in succinimide.

Improving PDI Control in Microsuspension RTCP with NIS. In order to improve PDI control by suppressing hydrolysis of NIS in the microsuspension RTCP, the polymerization time should be shortened. In CLRP in aqueous dispersed systems based on the DT mechanism, the particle size was an important parameter for the polymerization rate.[62,63] Radicals located in separated particles do not react each other (segregation effect).[39] When the particle size is small (<100 nm), the segregation effect works efficiently and the polymerization rate should be higher, resulting in the suppression the hydrolysis of NIS in a certain conversion, which leads to a good PDI control. Moreover, shortening of the polymerization decreases the amount of generated radicals from the initiator, which also leads the good PDI control.

In order to confirm the particle size effect, various sizes of MMA droplets were prepared by varying conditions of emulsification with *n*-hexadecane as hydrophobe, which is well-known to suppress the Ostwald ripening,[64] using a homogenizer: (1) at 2000 rpm for 2 min followed by 3500 rpm for an additional 4 min, (2) at 2000 rpm for 4 min followed by 8000 rpm for 10 min; (3) at 2000 rpm for 4 min followed by ultrasonication for 12 min at 0 °C.

Figure 7 shows conversion−time plots of microsuspension RTCP with NIS for various sizes of MMA droplets, in which the sizes were expressed as final particle sizes (D_n). All polymerizations smoothly proceeded without induction period

dx.doi.org/10.1021/ma3000829 | *Macromolecules* 2012, 45, 2286−2291

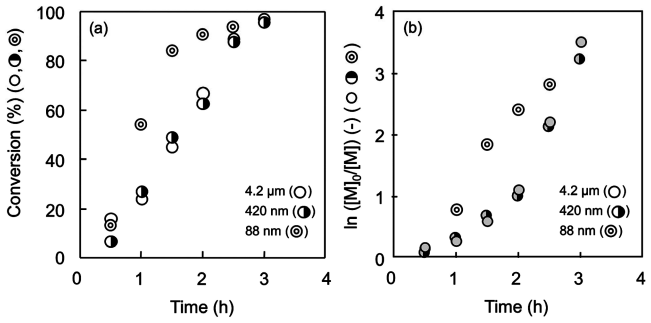


Figure 7. Conversion vs time plots (a) and first-order plots (b) for microsuspension RTCP of MMA with various droplet sizes (final polymer particle size (D_n): ○, 4.2 μm; ◑, 410 nm; ◎, 88 nm) with AIBN, NIS, and CHI_3 at 80 °C. $[CHI_3]_0/[AIBN]_0/[NIS]_0 = 80/10/1$.

and reached 90% in 3 h. In a case of the smallest D_n of 88 nm, the polymerization rate was the highest in comparison with the other systems (D_n = 410 nm, 4.2 μm). As expected, the segregation effect was responsible for higher polymerization rate.[39]

Figure 8 shows M_n and M_w/M_n of PMMA obtained at different conversions of the microsuspension RTCP with NIS for the various droplet sizes. The M_n increased linearly with

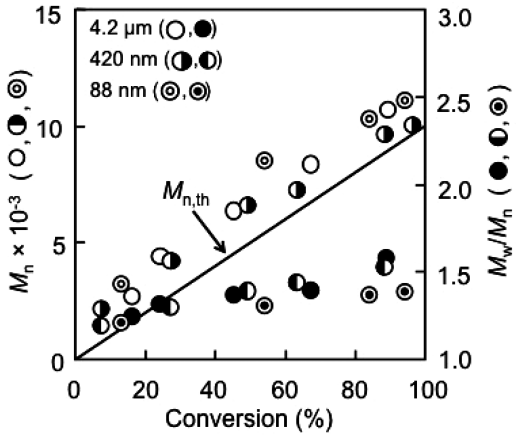


Figure 8. M_n (open circles) and M_w/M_n (closed circles) vs conversion plots for microsuspension RTCP of MMA with various droplet sizes (final polymer particle size (D_n): ○, ●: 4.2 μm; ◑, ◐: 410 nm, ◎, ⊙: 88 nm) with AIBN, NIS and CHI_3 at 80 °C. $[CHI_3]_0/[AIBN]_0/[NIS]_0 = 80/10/1$.

increasing conversion, and the values agreed corresponding with $M_{n,th}$ values, and the M_w/M_n values were relatively low, which indicates that a reasonable control was maintained throughout the polymerization in all systems. If the control agent was adsorbed at the monomer/water interface, the PDI control must become worth with decreasing the particle size. However, in reverse the PDI control became better with decreasing particle size; that is, in the case of D_n = 88 nm, M_w/M_n values were lower than the other two systems of 410 nm and 4.2 μm. These results indicate that most control agents were not adsorbed at the monomer/water interface.

Next, in order to confirm the hydrolysis of NIS with water, which dissolved in the monomer phase, we carried out a bulk RTCP with NIS of MMA with water layer at the bottom, where the monomer phase was previously contacted with the water layer for 1 h. MMA is relatively hydrophilic monomer and well-known to dissolve a certain amount of water.[62] In order to measure the water solubility in MMA, we measured the solubility of water in MMA at rt and 80 °C. At rt, 1.3 g of water was dissolved in 100 g of MMA (1.3 g/100 g MMA). With increasing the temperature, the solubility of water in MMA was also increased. At 80 °C, 4.0 g of water was dissolved in 100 g of MMA (4.0 g/100 g MMA).

The result for PDI control was very similar to the microsuspension RTCP and larger than bulk RTCP without water. This indicates that the NIS was hydrolyzed with water, which is dissolved in the monomer phase. In the smallest particle size the polymerization time was shortest because of the segregation effect of radical species. The short polymerization time should suppress the hydrolysis of NIS, resulting in the best PDI control.

CONCLUSIONS

ITP with CHI_3 and RTCP with NIS of MMA at 80 °C were successfully applied to aqueous microsuspension systems. As well as a bulk system, PDI control was better in microsuspension RTCP than microsuspension ITP. NIS used as catalyst in microsuspension RTCP. It was suggested that NIS would partly react with water dissolved in monomer phase and form succinimide, which is a catalyst having low control ability for molecular weight distribution in comparison with NIS. In the smallest droplet system (D_n = 88 nm) the microsuspension RTCP indicated the highest polymerization rate and the best control manner.

AUTHOR INFORMATION

Corresponding Author

*E-mail: okubo@kobe-u.ac.jp.

Notes

The authors declare no competing financial interest.

ACKNOWLEDGMENTS

This work was partially supported by Grant-in-Aid for Scientific Research (A) (Grant 21245050) from the Japan Society for the Promotion of Science (JSPS) and by Research Fellowship of JSPS for Young Scientists (given to Y.K.).

REFERENCES

(1) Gao, H.; Matyjaszewski, K. *Prog. Polym. Sci.* **2009**, *34*, 317−350.
(2) Georges, M. K.; Veregin, R. P. N; Kazmaier, P. M.; Hamer, G. K. *Macromolecules* **1993**, *26*, 2987−2988.
(3) Hawker, C. J.; Bosman, A. W.; Harth, E. *Chem. Rev.* **2001**, *101*, 3661−3688.
(4) Chiefari, J.; Chong, Y. K.; Ercole, F.; Krstina, J.; Jeffery, J.; Le, T. P. T; Mayadunne, R. T. A.; Meijs, G. F.; Moad, C. L.; Moad, G.; Rizzardo, E.; Thang, S. H. *Macromolecules* **1998**, *31*, 5559−5562.
(5) Moad, G.; Chong, Y. K.; Postma, A.; Rizzardo, E.; Thang, S. H. *Polymer* **2005**, *46*, 8458−8468.
(6) Moad, G.; Rizzardo, E.; Thang, S. H. *Aust. J. Chem.* **2006**, *59*, 669−692.
(7) Goto, A.; Kwak, Y.; Fukuda, T.; Yamago, S.; Iida, K.; Nakajima, M.; Yoshida, J. *J. Am. Chem. Soc.* **2003**, *125*, 8720−8721.
(8) Yamago, S.; Iida, K.; Yoshoda, J. *J. Am. Chem. Soc.* **2002**, *124*, 13666−13667.
(9) Valade, D.; Boyer, C.; Ameduri, B.; Boutevin, B. *Macromolecules* **2006**, *39* (25), 8639−8651.
(10) Tatemoto, M.; Tomoda, M.; Ueta, Y. U.S. Patent 81895, 1981.
(11) Boyer, C.; Valade, D.; Sauguet, L.; Ameduri, B.; Boutevin, B. *Macromolecules* **2005**, *38* (25), 10353−10362.

(12) Boyer, C.; Valade, D.; Lacroix-Desmazes, P.; Ameduri, B.; Boutevin, B. *J. Polym. Sci., Part A: Polym. Chem.* **2006**, *44* (19), 5763−5777.
(13) Matyjaszewski, K.; Gaynor, S.; Wang, J. S. *Macromolecules* **1995**, *28*, 2093−2095.
(14) Gaynor, S. G.; Wang, J. S.; Matyjaszewski, K. *Macromolecules* **1995**, *28*, 8051−8056.
(15) David, G.; Boyer, C.; Tonnar, J.; Ameduri, J.; Lacroix-Desmazes, P.; Boutevin, B. *Chem. Rev.* **2006**, *106* (9), 3936−3962.
(16) Lacroix-Desmazes, P.; Severac, R.; Boutevin, B. *Macromolecules* **2005**, *38* (15), 6299−6309.
(17) Imran-ul-haq, M.; Tiersch, B.; Beuermann, S. *Macromolecules* **2008**, *41* (20), 7453−7462.
(18) Lansalot, M.; Farcet, C.; Charleux, B.; Vairon, J.-P.; Pirri, R. *Macromolecules* **1999**, *32* (22), 7354−7360.
(19) David, G.; El Asri, Z.; Rich, S.; Castignolles, P.; Guillaneouf, Y.; Lacroix-Desmazes, P.; Boutevin, B. *Macromol. Chem. Phys.* **2009**, *210* (8), 631−639.
(20) David, G.; Boyer, C.; Tayouo, R.; Seabrook, S.; Ameduri, B.; Boutevin, B.; Woodward, G.; Destarac, M. *Macromol. Chem. Phys.* **2008**, *209* (1), 75−83.
(21) Boyer, C.; Lacroix-Desmazes, P.; Robin, J. J.; Boutevin, B. *Macromolecules* **2006**, *39* (12), 4044−4053.
(22) Lacroix-Desmazes, P.; Severac, R.; Boutevin, B. *Macromolecules* **2005**, *38* (15), 6299−6309.
(23) Patra, B. N.; Rayeroux, D.; Lacroix-Desmazes, P. *React. Funct. Polym.* **2010**, *70*, 408−413.
(24) Rayeroux, D.; Patra, B. N.; Lacroix-Desmazes, P. *Polym. Prepr.* **2011**, *52* (2), 716.
(25) Percec, V.; Popov, A. V.; Ramirez-Castillo, E.; Coelho, J. F. J. *J. Polym. Sci., Part A: Polym. Chem.* **2005**, *43*, 773−778.
(26) Monteiro, M. J.; Guliashvili, T.; Percec, V. *J. Polym. Sci., Part A: Polym. Chem.* **2006**, *45*, 1835−1847.
(27) Percec, V.; Guliashvili, T.; Ladislaw, J. S.; Wistrand, A.; Stjerndahl, A.; Sienkowska, M. J.; Monteiro, M. J.; Sahoo, S. *J. Am. Chem. Soc.* **2006**, *128*, 14156−14165.
(28) Percec, V.; Guillaneouf, Y.; Popov, A. V.; Ramirez-Castillo, E.; Hinojosa-Falcon, L. A. *J. Polym. Sci., Part A: Polym. Chem.* **2005**, *43* (8), 1660−1669.
(29) Boyer, C.; Stenzei, M. H.; Davis, T. P. *J. Polym. Sci., Part A: Polym. Chem.* **2011**, *49* (3), 551−595.
(30) Boyer, C.; Bulmus, V.; Davis, T. P.; Ladmiral, V.; Liu, J. Q.; Perrier, S. *Chem. Rev.* **2009**, *109* (11), 5402−5436.
(31) Monteiro, M. J. *J. Polym. Sci., Part A: Polym. Chem* **2005**, *43* (15), 3189−3204.
(32) Lacroix-Desmazes, P.; Boutevin, B. *Macromol. Symp.* **2007**, *248* (1), 150−157.
(33) Goto, A.; Tsujii, Y.; Fukuda, T. *Polymer* **2008**, *49*, 5177−5185.
(34) Goto, A.; Hirai, N.; Tsujii, Y.; Fukuda, T. *Macromol. Symp.* **2008**, *261*, 18−22.
(35) Goto, A.; Zushi, H.; Hirai, N.; Wakada, T.; Kwak, Y.; Fukuda, T. *Macromol. Symp.* **2006**, *248*, 126−131.
(36) Goto, A.; Zushi, H.; Hirai, N.; Wakada, T.; Tsujii, Y.; Fukuda, T. *J. Am. Chem. Soc.* **2007**, *129*, 13347−13354.
(37) Goto, A.; Hirai, N.; Wakada, T.; Nagasawa, K.; Tsujii, Y.; Fukuda, T. *Macromolecules* **2008**, *41*, 6261−6264.
(38) Charleux, B. Nitroxide-mediated polymerization in miniemulsion: A direct way from bulk to aqueous dispersed systems. In *Advances in Controlled/Living Radical Polymerization*; Matyjaszewski, K., Ed.; ACS Symposium Series 854; American Chemical Society: Washington, DC, 2003; pp 438−451.
(39) Zetterlund, P. B.; Kagawa, Y.; Okubo, M. *Chem. Rev.* **2008**, *108*, 3747−3794.
(40) Cunningham, M. F. *Prog. Polym. Sci.* **2008**, *33* (4), 365−398.
(41) Lansalot, M.; Farcet, C.; Charleux, B.; Vairon, J. P.; Pirri, R.; Tordo, P. Nitroxide-mediated controlled free-radical emulsion and miniemulsion polymerizations of styrene. In *Controlled/Living Radical Polymerization: Progress in ATRP, NMP and RAFT*; Matyjaszewski, K., Ed.; ACS Symposium Series 768; American Chemical Society: Washington, DC, 2000; pp 138−151.
(42) Cunningham, M. F. *Prog. Polym. Sci.* **2002**, *27*, 1039−1067.
(43) Pham, B. T. T.; Nguyen, D.; Ferguson, C. J.; Hawkett, B. S.; Serelis, A. K.; Such, C. H. *Macromolecules* **2003**, *36*, 8907−8909.
(44) Tonnar, J.; Lacroix-Desmazes, P.; Boutevin, B. *ACS Symp. Ser.* **2006**, *944*, 604−619.
(45) Nakamura, T.; Zetterlund, P. B.; Okubo, M. *Macromol. Rapid Commun.* **2006**, *27*, 2014−2018.
(46) Zetterlund, P. B.; Okubo, M. *Macromolecules* **2006**, *39*, 8959−8967.
(47) Kagawa, Y.; Minami, H.; Okubo, M.; Zhou, H. *Polymer* **2005**, *46* (4), 1045−1049.
(48) Kagawa, Y.; Zetterlund, P. B.; Minami, H.; Okubo, M. *Macromolecules* **2007**, *40* (9), 3062−3069.
(49) Kitayama, Y.; Yorizane, M.; Kagawa, Y.; Minami, H.; Zetterlund, P. B.; Okubo, M. *Polymer* **2009**, *50*, 3182−3187.
(50) Manguian, M.; Save, M.; Charleux, B. *Macromol. Rapid Commun.* **2006**, *27*, 399−404.
(51) Rieger, J.; Stoffelbach, F.; Bui, C.; Alaimo, D.; Jerome, C.; Charleux, B. *Macromolecules* **2008**, *41*, 4065−4068.
(52) Sugihara, Y.; Kagawa, Y.; Yamago, S.; Okubo, M. *Macromolecules* **2007**, *40*, 9208−9211.
(53) Okubo, M.; Sugihara, Y.; Kitayama, Y.; Kagawa, Y.; Minami, H. *Macromolecules* **2009**, *42*, 1979−1984.
(54) Kitayama, Y.; Chaiyasat, A.; Okubo, M. *Macromol. Symp.* **2010**, *288*, 25−32.
(55) Kitayama, Y.; Chaiyasat, A.; Minami, H.; Okubo, M. *Macromolecules* **2010**, *43* (18), 7465−7471.
(56) Moribe, H.; Kitayama, Y.; Suzuki, T.; Okubo, M. *Macromolecules* **2011**, *44* (2), 263−268.
(57) Pouget, E.; Tonnar, J.; Eloy, C.; Lacroix-Desmazes, P.; Boutevin, B. *Macromolecules* **2006**, *39* (18), 6009−6016.
(58) Tonnar, J.; Lacroix-Desmazes, P.; Boutevin, B. *Macromolecules* **2007**, *40*, 186−190.
(59) Tonnar, J.; Lacroix-Desmazes, P. *Soft Matter* **2008**, *4* (6), 1255−1260.
(60) Tonnar, J.; Lacroix-Desmazes, P. *Angew. Chem., Int. Ed.* **2008**, *47* (7), 1294−1297.
(61) Yorizane, M.; Nagasuga, T.; Kitayama, Y.; Tanaka, A.; Minami, H.; Goto, A.; Fukuda, T.; Okubo, M. *Macromolecules* **2010**, *43*, 8703−8705.
(62) Gilbert, R. G. *Emulsion Polymerization*; Academic Press: London, 1995.
(63) Nakamura, T.; Zetterlund, P. B.; Okubo, M. *Macromol. Rapid Commun.* **2006**, *27* (23), 2014−2018.
(64) Blythe, P. J.; Morrison, B. R.; Mathauer, K. A.; Sudol, E. D.; El-Aasser, M. S. *Langmuir* **2000**, *16*, 898−904.

Macromolecules

Article

pubs.acs.org/Macromolecules

New Class of Biodegradable Polymers Formed from Reactions of an Inorganic Functional Group

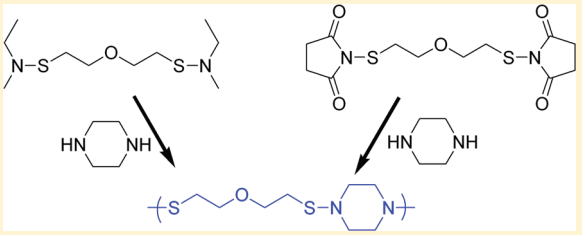
Jun Yoo,[†] Denison J. Kuruvilla,[‡] Sheetal R. D'Mello,[‡] Aliasger K. Salem,[‡] and Ned B. Bowden*,[†]

[†]Department of Chemistry, University of Iowa, Iowa City, Iowa 52242, United States

[‡]College of Pharmacy, University of Iowa, Iowa City, Iowa 52242, United States

Supporting Information

ABSTRACT: Although numerous small molecules have been synthesized with sulfenamide bonds (R_2N-SR), this is the first report of the synthesis of polysulfenamides. These polymers are readily synthesized at room temperature using secondary diamines and dithiosuccinimides. The dithiosuccinimides were readily synthesized in one step by the reaction of dithiols such as $HS(CH_2)_6SH$ with *N*-chlorosuccinimide. The resulting dithiosuccinimides were either recrystallized or readily purified by chromatography on silica gel and required no special handling. The conversions of polymerization ranged from 95 to 98%, and the molecular weights of the polymer reached as high as 6300 g mol^{-1}. The sulfenamide bond was very stable in organic solvents, and no degradation was observed under atmospheric conditions in C_6D_6 for 30 days. In contrast, the sulfenamide bond readily decomposed in less than 12 h in D_2O. Polysulfenamides were fabricated into micrometer-sized particles loaded with dye and endocytosed into JAWSII immature dendritic and HEK293 cells. Polysulfenamides represent a new class of polymers that are readily synthesized, stable in aprotic solvents, and readily degrade in water.



INTRODUCTION

Biodegradable polymers have shown wide utility in a variety of biomedical applications ranging from sutures, scaffolds for the growth of cells, and polymeric depots that provided sustained release of therapeutic agents.[1−6] Optimal use of these materials requires their molecular and macromolecular properties be tailored to the specific application for which the material is to be used.[3,7−9] For instance, polymeric particles loaded with drugs that are targeted to the endosomal compartments of cells should ideally be stable at physiological pH in the bloodstream but readily break down at a lower pH to release its drug cargo in the endosome where the pH is approximately 5−6.[10−13] Biodegradable polymers are attractive in drug delivery applications because polymeric particles injected *in vivo* can accumulate in several organs including the liver, spleen, lungs, and heart and often result in toxic side effects if they do not break apart into smaller, easily excretable side products.[14,15] The degradation of these polymers is also the mechanism by which controlled release of drugs and other therapeutics is achieved. Most synthetic polymers in biomedical research are polyesters, polyamides, polyanhydrides, or some combination of these three functional groups. These polymers degrade to short polymers or small molecules at reasonable times without the use of enzymes.[16−18] Thus, these polymers may be excreted from the body before toxic side effects occur.

Integrating new functional groups into polymer chemistry allows the fabrication of polymers with new properties and the ability to tailor new materials.[19,20] Specifically, the introduction of a new functional group to synthesize biopolymers has the potential to open up new applications in this field and will allow more complex, potentially "smart" drug delivery vehicles to be synthesized. It is very challenging to design a polymer with a new functional group along its backbone that renders it stable at physiological pH but also allows it to be degraded at reasonable time scales in the body. Recent work has shown the promise of using biodegradable polymers linked with acetals or disulfides in medical applications that provide alternatives to functional groups based on carbonyls.[21−24] In this paper, we report the first synthesis of polymers with the sulfenamide functional group within the backbone of macromolecules, how these polymers degrade under different conditions, and how they can be fabricated into micrometer-sized particles loaded with fluorescent dye that are internalized into cells. Polysulfenamides are a new class of polymers that we believe will have real applications in medicine.

Sulfenamides are an understudied functional group with the general formula of RS-NR′R″ that are used as protecting groups for amines (typically as $(Ph_3C)S-NR_2$),[25] vulcanizing agents in the rubber industry,[26−28] in the activation of C−H bonds,[29] as ligands on metals to promote O atom transfer,[30,31] as intermediates in the synthesis of sulfonamides,[32] as oxidants for alcohols,[33,34] and as ligands in the synthesis of inorganic coordination compounds.[35−40] In a recent article we reported on the synthesis of the first polydiaminosulfides based on the

Received: January 24, 2012
Revised: February 6, 2012
Published: February 21, 2012

 © 2012 American Chemical Society

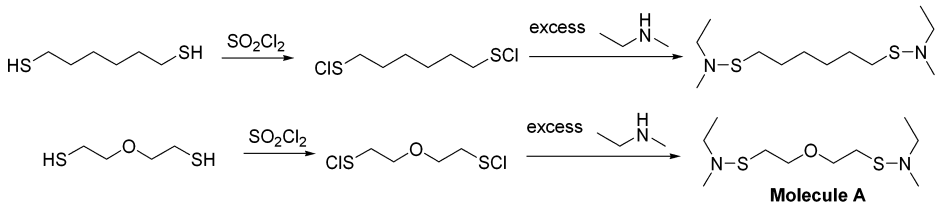


Figure 1. Two different disulfenamides were synthesized in one pot from dithiols.

diaminosulfide functional group ($R_2N-S-NR_2$).[41] The diaminosulfide functional group differs from the sulfenamide functional group in its structure, reactivity, and reaction products. A loose analogy to explain the differences between diaminosulfides and sulfenamides is to compare this pair to esters and anhydrides. Structurally, an anhydride is an ester with an extra carbonyl. Similarly, a diaminosulfide is a sulfenamide with an extra amine. Much as the structural differences between an ester and anhydride lead to different reactivities and products of reaction, the structural differences between a sulfenamide and diaminosulfide lead to different reactivities and products of reaction. A diaminosulfide should not be confused for a sulfenamide any more than an ester is confused for an anhydride.

Some of the general properties of sulfenamides made them attractive functional groups to pursue for the synthesis of polymers. Prior work by others with small molecules containing sulfenamide bonds demonstrated that they were readily synthesized and possessed reasonable stabilities.[35,42−44] Molecules with sulfenamide bonds degraded into radicals at elevated temperatures which led to their applications as vulcanizing agents in the rubber industry.[26−28] On the basis of their properties as protecting groups for amines, it was known that sulfenamides were stable under neutral and basic conditions but could be cleaved under acidic conditions.[35] Furthermore, sulfenamides have been synthesized in high yields from activated thiols and amines at room temperature.

These properties were desirable for the development of new biodegradable polymers. We sought a functional group that was stable in organic solvents, would rapidly break down in acidic water, and would possess higher stability in water at neutral pH than at acidic pH. Additionally, prior reports of the synthesis of sulfenamides in high yields were promising because the development of a step growth polymerization requires that the yield of the reaction to form the polymer be high and typically exceed 95%.[45]

In this article we report the first synthesis of polysulfenamides. No prior examples of polymers containing this functional group have been reported so their synthesis was developed by us for the first time. Additionally, we report the stability of this functional group to different conditions and how they can be applied as new drug delivery vehicles.

RESULTS AND DISCUSSION

Synthesis of Polysulfenamides from Disulfenamides. Because polysulfenamides were unknown prior to our work, the first step in this project was to develop their synthesis. In one approach two different dithiols were activated with sulfuryl chloride to yield intermediates with S−Cl bonds (Figure 1).[35] If left overnight exposed to air, these molecules formed disulfides. To prevent the formation of disulfides, these molecules were reacted with an excess of *N*-ethylmethylamine immediately after their formation. When molecule A was purified by chromatography on silica gel, the isolated yield was only 6%. When this molecule was purified by chromatography on basic alumina oxide, the isolated yield was 76%. This result was consistent with prior reports that described the decomposition of sulfenamides on acidic silica gel.[32,46] All subsequent purifications of sulfenamides were completed by vacuum distillation or by chromatography on basic alumina oxide.

Simple bimolecular reactions were studied to measure the kinetics of the transamination reaction shown in Figure 2 to determine the best conditions for polymerizations. Molecule B was synthesized and reacted with *N*-benzylmethylamine in C_6D_6, DMSO-d_6, and CD_3OD at different temperatures. This reaction was very slow in C_6D_6 with no conversion after 24 h at room temperature and only 11% conversion after 24 h at 60 °C. When DMSO-d_6 was used as the solvent, the reaction was faster and the conversion reached 7% after 24 h at room temperature and 32% after 24 h at 50 °C. The reaction proceeded rapidly in CD_3OD and reached a conversion of 40% after 3 h, and at longer periods of time it reached an equilibrium mixture of 50% of each sulfenamide. The rate constant for the reaction in CD_3OD was 5.1×10^{-4} M^{-1} s^{-1}. This reaction was most rapid in a polar, protic solvent which suggests a charged transition state that is stabilized by hydrogen bonding. It is believed that the reaction proceeded through an S_N2 reaction mechanism when *N*-benzylmethylamine attacked the sulfur of the sulfenamide. It was possible that the hydrogen bond donating ability of CD_3OD lowered the energy requirement for *N*-ethylmethylamine to leave.

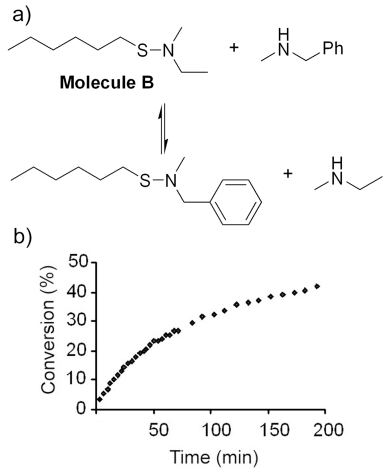


Figure 2. Kinetics of the transamination reaction in (a) was studied by ^1H NMR spectroscopy in CD_3OD as shown in (b). The conversion in (b) refers to the conversion of molecule B to the indicated product. The NMR tube was sealed to prevent the release of *N*-ethylmethylamine.

When the polymerization of a disulfenamide with a diamine was attempted, the results were not promising (Figure 3).

dx.doi.org/10.1021/ma300190b | *Macromolecules* 2012, 45, 2292−2300

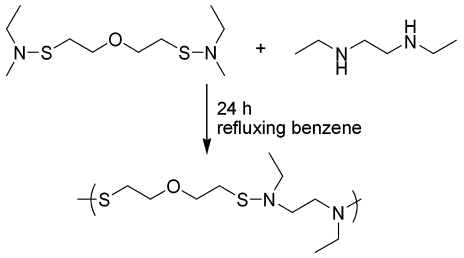


Figure 3. Polymerization of a disulfenamide with a secondary diamine in benzene yielded a low molecular weight polymer.

Although the kinetics of reaction were rapid in methanol, the resulting polymer was insoluble in methanol which made this solvent a poor choice to conduct polymerizations. Polymerizations at high concentrations of monomers in solvent mixtures of (1/1 v/v) $CD_3OD/CDCl_3$ or (1.2/1 v/v) $CD_3OD/DMSO\text{-}d_6$ at 40 °C yielded oligomers even after 3 days. A polymerization was attempted in refluxing benzene for 24 h with the reaction vented to allow *N*-ethylmethylamine (boiling point of 36−37 °C) to boil off resulted in a low yield of a modest molecular weight polymer (M_w = 2840 g mol^{-1}). This method of polymerization was hindered by lack of solubility of the polymer in methanol and the slow kinetics for polymerization in aprotic solvents.

Synthesis of Polysulfenamides from Dithiosuccinimides. To increase the rate of transamination and to allow the use of aprotic solvents in a polymerization, dithiols were activated with *N*-chlorosuccinimide (Figure 4). This reaction

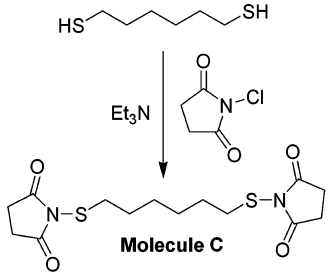


Figure 4. Dithiosuccinimides were readily synthesized from *N*-chlorosuccinimide and triethylamine.

went to high yields at room temperature, and the dithiosuccinimides were stable to chromatography on silica gel. Furthermore, molecule C was readily purified by crystallization. The dithiosuccinimides were stable at room temperature under ambient atmosphere, and they required no special handling.

The reaction of a thiosuccinimide (molecule D in Figure 5) with *N*-benzylmethylamine was much faster in aprotic solvents than the same reaction between molecule B and *N*-benzylmethylamine. In CD_2Cl_2 at room temperature the reaction between molecule D and *N*-benzylmethylamine had a rate constant of 8.2 × 10^{-4} M^{-1} s^{-1} and reached 35% conversion after 4 h. This transamination reaction was ~2 times faster than the reaction between molecule B and *N*-benzylmethylamine in CD_3OD. The difference in solvent was critically important because methylene chloride and chloroform were excellent solvents for both monomers and polymers in contrast to CD_3OD where the polymer precipitated. In addition, the reaction of a thiosuccinimide with *N*-benzylmethylamine went to >97% conversion at room temperature. The

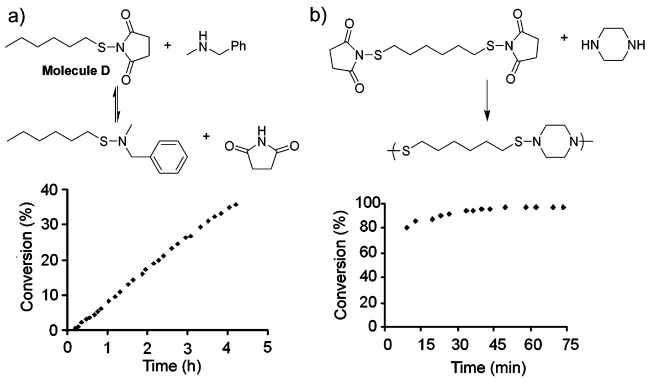
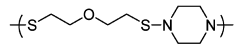
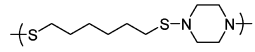
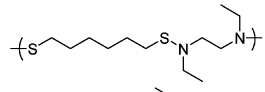
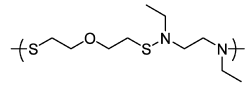
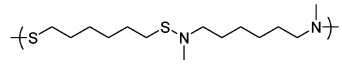


Figure 5. (a) Reaction of a thiosuccinimide with a secondary amine in CD_2Cl_2 is shown. The yield of the reaction was >97% after extended reaction times. (b) Kinetics of a typical polymerization to demonstrate that the polymerizations were rapid and went to quantitative conversions at reasonable concentrations. The starting materials in (b) were 3 times more concentrated than the starting materials in (a).

test polymerization shown in Figure 5b went to >95% conversion within 50 min in $CDCl_3$ at room temperature. This polymerization method was used in all subsequent polymerizations.

A series of polymers were synthesized from dithiosuccinimides and secondary diamines (Table 1). The polymerizations

Table 1. Synthesis of Polysulfenamides from Dithiosuccinimides

Entry	Composition	M_w (g mol^{-1})[a]	Conversion (%)[b]	PDI
1		3,700	97	1.42
2[c]		6,300	98	1.22
3[c]		3,700	97	1.06
4		2,300	95	1.60
5[c]		2,900	96	1.13

[a]The absolute M_w and PDI were measured with multiangle laser light scattering and refractive index detectors unless otherwise noted. [b]The conversion was calculated based on the molecular weight of the polymer and monomers according to the equation Xn = 1/(1 − *P*). [c]The M_w and PDI were measured versus polystyrene standards using a calibration curve.

were completed in methylene chloride or chloroform at room temperature for 24 h. The polymers had molecular weights up to 6300 g mol^{-1}, degrees of polymerization that ranged from 95% to 98%, and they were isolated in >80% yields by precipitation in methanol. Secondary diamines were chosen for this work because the synthesis of polymers using primary diamines (such as $NH_2CH_2CH_2NH_2$) resulted in cross-linked, insoluble polymers. The cross-links were possibly due to the reaction of an amine with 2 equiv of a thiosuccinimide to yield cross-links of the form $RN(SR')_2$.

These polymers were well characterized by size exclusion chromatography (SEC). Entries 1 and 4 of Table 1 had strong

dx.doi.org/10.1021/ma300190b | *Macromolecules* 2012, 45, 2292−2300

peaks in both the multiangle laser light scattering detector and the refractive index detector so absolute molecular weights were calculated. For entries 2, 3, and 5 the light scattering signal was too weak so the molecular weights were found by calibration with polystyrene standards. In all examples the polymers were analyzed by ^{1}H NMR spectroscopy to study the end groups. The peaks corresponding to the end groups integrated to very low values which supported the SEC data for the molecular weights and high conversions. An example of a SEC micrograph is shown in Figure 6.

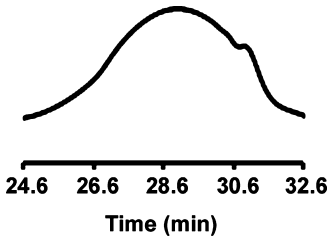


Figure 6. SEC micrograph of the polymer from entry 1 in Table 1.

Degradation of Sulfenamides in Aprotic and Protic Solvents. Little data were available on the stabilities of sulfenamides in various solvents that could be used to anticipate the stabilities of polysulfenamides. To address this limitation, a sulfenamide was synthesized and its stability was studied in

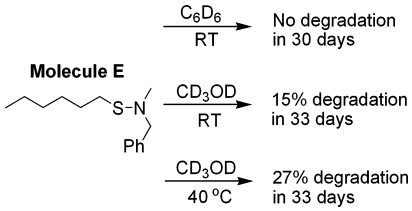


Figure 7. Stability of molecule E was studied under three different conditions.

NMR tubes in CD_3OD and C_6D_6 (Figure 7). After 30 days, the ^{1}H NMR spectrum of the sulfenamide in C_6D_6 was unchanged which demonstrated its stability in aprotic solvents. This molecule slowly degraded in CD_3OD; after 33 days 15% of it degraded at room temperature and only 27% degraded when heated to 40 °C for the same period of time. These conditions indicated that sulfenamides possessed reasonable stabilities under neutral conditions in organic solvents. It should be noted that the polysulfenamides were synthesized in organic solvents under ambient conditions without any special handling.

The kinetics and products of degradation of molecule E were studied under acidic conditions. First, molecule E was added to CD_3OD with 5 equiv of benzoic acid. In contrast to the degradation of molecule E without benzoic acid (33 days to reach 15% degradation), the degradation of molecule E in the presence of benzoic acid reached 51% degradation within 4 min. When molecule E was exposed to 2 mol equiv of *p*-toluenesulfonic acid ($pK_a < -2$) or trifluoroacetic acid ($pK_a = 0.3$) in CD_3OD, it degraded to >90% within 4 min. Clearly, the decomposition of sulfenamides was catalyzed by acid as observed by others in prior work.[32,46]

The products of degradation of molecule E were studied under acidic conditions in D_2O to understand how polysulfenamides would break down under these conditions. Molecule E was added to D_2O with 7 mol equiv of acetic acid. Because molecule E was insoluble in D_2O, the reaction mixture was vigorously stirred. After 41 h the organics were extracted and initially studied by ^{1}H NMR spectroscopy prior to isolation by column chromatography. The ^{1}H NMR spectrum of the extract before chromatography indicated that ~75% of the product was the thiosulfinate (molecule F in Figure 8a) with the remainder mostly composed of molecules G and H. The initial reaction of molecule E with water yielded a sulfenic acid, but sulfenic acids are transient intermediates that very rapidly condense as shown in Figure 8b.[40,47−49] On the basis of literature precedent, molecule F decomposed via multiple pathways to yield molecule G, molecule H, and a sulfinic acid (molecule I).[48,50−52] Thiosulfinate esters such as molecule F are known oxidation states for cysteine residues and found in nature products such as allicin (a component of garlic; Figure 8c). As such, thiosulfinates are already present in the body and are known to decompose at reasonable rates—the half-life of the decomposition of allicin at pH = 7.5 at 37 °C is ~2 days.[8,50]

To further study the degradation of sulfenamides in D_2O, a water-soluble sulfenamide was synthesized (Figure 9). The

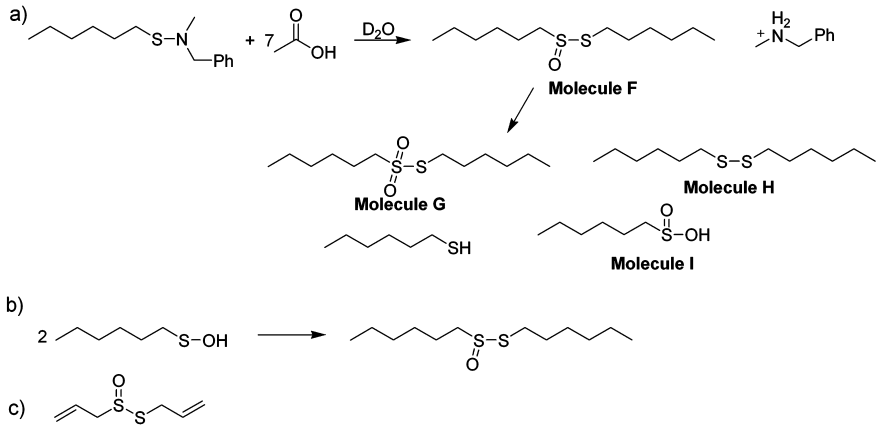


Figure 8. (a) The first degradation product of the decomposition of a sulfenamide in D_2O was molecule F. This molecule further decomposed to yield molecules G and H. Molecules F, G, and H were observed by ^{1}H NMR spectroscopy. Molecule I and hexanethiol were not observed but were predicted by literature precedent. (b) Sulfenic acids were the first product of degradation of molecule E but they were known to rapidly react to yield thiosulfinates as shown. (c) The structure of allicin.

dx.doi.org/10.1021/ma300190b | *Macromolecules* 2012, 45, 2292−2300

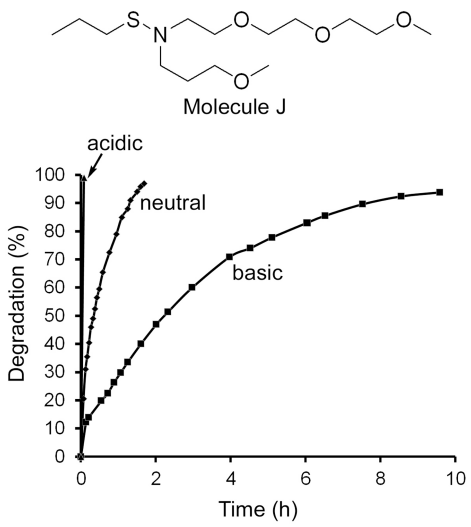


Figure 9. Kinetics of decomposition of a sulfenamide was studied by ^{1}H NMR spectroscopy in D_2O with either 9 mol equiv of NaOH, 8 mol equiv of acetic acid, or no added acid or base.

decomposition of this molecule was studied in D_2O with 8 mol equiv of acetic acid, 9 mol equiv of KOH, or under neutral conditions without the addition of acid or base. The rates of decomposition were found under neutral ($k = 4.7 \times 10^{-4}$ s^{-1}) and basic conditions ($k = 8.0 \times 10^{-5}$ s^{-1}), but the decomposition was too rapid under acidic conditions to measure a rate constant. Because the sulfenamide completely decomposed within 4 min after addition to D_2O with acetic acid, only a lower limit for its rate of decomposition was found (1.6×10^{-2} s^{-1}). It is important to note that these rate constants are several orders of magnitude higher than the neutral and acidic degradation of esters.[53] Because of the rapid decomposition, we were unable to determine a value for the pK_a of a protonated sulfenamide.

Fabrication and Degradation of Microparticles of Polysulfenamides. Microparticles were fabricated from the polymer in entry 2 in Table 1 to study whether these polymers could form the basis of drug delivery vehicles. The microparticles were prepared using an oil-in-water single emulsion solvent evaporation methodology. In this approach, the polymer was dissolved in chloroform and then emulsified in surfactant containing water phase. The emulsion was stirred overnight until the chloroform evaporated. Drugs and fluorescent molecules such as rhodamine can be incorporated into the microparticles by mixing them in the polymer/chloroform mixture prior to emulsification. The average size of the microparticle was 2.6 μm with a PDI of 0.62. They were spherical in shape, had a smooth surface, and had a negative charge of −41 mV in PBS buffer at pH = 7.4 (Figure 10). The reason for the negative charge was understood in terms of prior experiments that demonstrated that sulfenamides slowly degraded to yield sulfinic acids that deprotonated and led to a negatively charged surface.

Microparticle degradation was studied at both physiological pH (7.4) and acidic pH (4.0) to learn whether these particles would decompose over time. Figure 10 shows the percentage weight loss of the samples at different points in time. After 1 week, a weight loss of 24% was observed for microparticles in acetate buffer as compared to a weight loss of 13% for particles in PBS. On day 35, the weight loss in acidic buffer was ∼33% as compared to ∼17% at physiological pH. Weight loss was significantly higher for particles in acetate buffer as compared to particles in PBS, indicating faster degradation of the microparticles in acidic environments. SEM images of the acidic pH-degraded particles revealed a rough morphology of the polymer surface that was consistent with polymer degradation (Figure 10c). The differences in the rates of degradation of microparticles at pH 7.4 and 4.0 were expected based on the rapid degradation of molecule J under acidic conditions in D_2O and its slower degradation in neutral D_2O.

The overall rate of degradation of a microparticle depends on many factors other than the rate of degradation of the functional group along the backbone. For instance, microparticles fabricated from polycaprolactone lose less than 1% of their weight after 26 weeks in aqueous buffer,[54] but microparticles fabricated from poly(lactic-*co*-glycolic acid) with 50% lactic acid and 50% glycolic acid lose approximately half of their weight in 2 weeks in aqueous buffer.[55] This difference in rates of degradation of two similar polyesters is due to factors such as differences in crystallinity, molecular weight, molecular weight distribution, porosity, and hydrophobicity of the polymers.[56] Thus, although the degradation of the sulfenamide bond is rapid in water, microparticles fabricated from polysulfenamides will exhibit a wide range of degradation profiles based on the monomers used in their synthesis.

The uptake of these microparticles was studied in JAWSII and human embryonic kidney (HEK293) cells using confocal microscopy. JAWSII cells are immature dendritic cells derived from mouse bone marrow and are commonly targeted by

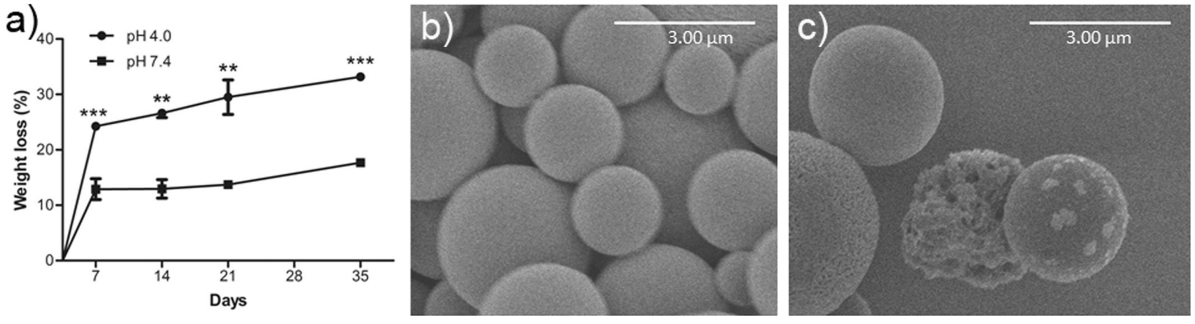


Figure 10. Microparticles with the structure of entry 2 in Table 1 were studied for their degradation and surface reactions. (a) Time-dependent weight loss of the polymer incubated at acidic pH (4.0) and physiological pH (7.4). Data represent the percentage weight loss as mean of three samples. (b) Scanning electron microscopy (SEM) image of microparticles as prepared. (c) SEM image of microparticles after incubation in acetate buffer (pH 4.0) for 14 days. Microparticles at various stages of degradation can be observed.

dx.doi.org/10.1021/ma300190b | *Macromolecules* 2012, 45, 2292−2300

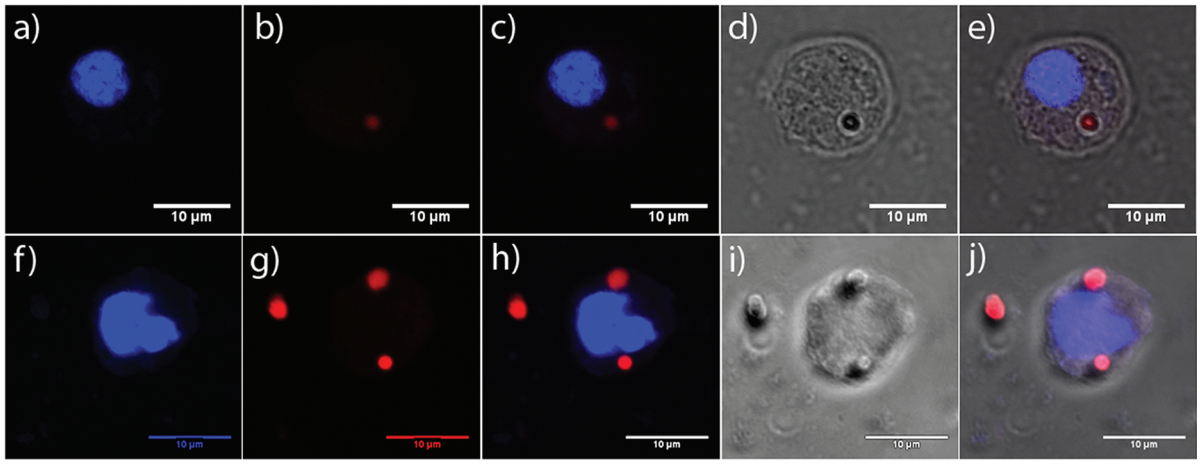


Figure 11. Uptake of microparticles fabricated from entry 2 in Table 1 and loaded with rhodamine and studied using confocal microscopy. (a–e) The cells are JAWSII immature dendritic cells, and in (f–j) they are HEK293 cells. The nucleus of the cell was stained with DAPI to appear blue and the rhodamine appeared red. In (d) and (i) the transmitted light images indicate the periphery of the cells and the location of the microparticles. In (e) and (j) merged images clearly outline the periphery of the cell, the location of the nucleus, and the microparticles to clearly demonstrate that the microparticles were found on the interior of the cells. The images were taken at different sections to ensure that the microparticles were in the same focal plane as the planes taken through the cells. The microparticle in the far left of images (g–j) was not found in a cell and was used to show a free microparticle.

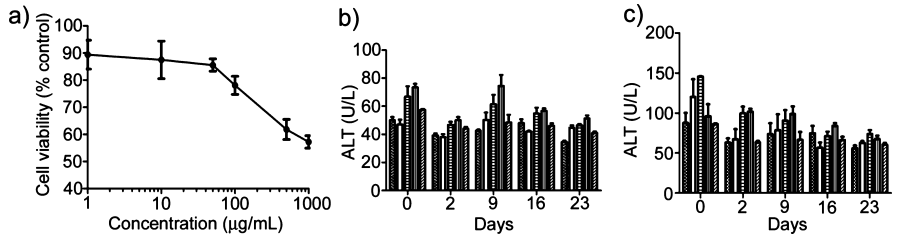


Figure 12. (a) Cytotoxicity of polysulfenamide microparticles fabricated from entry 2 in Table 1 toward HEK293 cells. Cell viability was determined by MTS assay and the expressed as percentage of control without microparticles. (b, c) These graphs show the *in vivo* ALT and AST levels in BALB/c mice following i.p. injection of microparticles. There are five sets of data for each day in the graphs in (b) and (c). The data for each day are presented in order of mice injected with PBS buffer, 10 mg of PLGA microparticles, 5 mg of polysulfenamide microparticles, 10 mg of polysulfenamide microparticles, and 15 mg of polysulfenamide microparticles.

particle based vaccines for generation of therapeutic immune responses. HEK293 cells are one of the most common cell lines used to evaluate novel gene therapies. Microparticles were loaded with rhodamine B during fabrication and were then exposed to the JAWSII and HEK293 cells. The microparticles were found to be located near the cytoplasm of the cell, indicating the phagocytosis of the microparticles by cells (Figure 11; see also the Supporting Information for an additional image). The uptake of microparticles by both cell lines suggests that this system has potential in immunological applications, especially in vaccine delivery and potential for gene therapy applications.

Toxicity of Polysulfenamide Microparticles. The *in vitro* toxicity of these microparticles was evaluated with HEK293 cells. In initial work, these cells were incubated with the microparticles at a range of concentrations of 1–1000 μg per mL of growth medium for 4 h. The cell viability was measured by standard techniques of measuring the metabolic activity of cells in a control without microparticles and the metabolic activity of cells that were exposed to the microparticles. The ratio of these concentrations was plotted as the "cell viability" in the *y*-axis of Figure 12a. No toxicity was observed at even the highest concentrations after 4 h, so a longer incubation time of 24 h was studied and shown in Figure 12a. At the expected working concentrations of microparticles minimal toxicity was observed. Interestingly, at the highest concentration of 1 mg of microparticles per mL of solution where the wells containing HEK293 cells were beginning to become saturated with microparticles, the cell viability was still 57%. This suggests that polysulfenamides have low toxicity and are therefore suitable for drug, gene, and vaccine delivery applications.

The *in vivo* toxicity of the polysulfenamide microparticles were evaluated in BALB/c mice. Microparticles were administered via intraperitoneal (i.p.) injection because this route of administration is commonly utilized for evaluating microparticle based vaccines which are an intended application for this novel polymer and because the i.p. route allows particles to enter the systemic circulation allowing for a better gauge of systemic toxicity than subcutaneous or intramuscular injection. The mice were divided into five groups and were injected with either 5, 10, or 15 mg of polysulfenamide microparticles from entry 2 in Table 1; 10 mg of microparticles of poly(D,L-lactide-*co*-glycolide) as a control group; or a sterile PBS buffer solution. The mass of particles injected in these experiments was significantly higher than the typical therapeutic mass of microparticles injected for vaccine based application. The mice were followed for 23 days, and blood was drawn at 0, 2, 9, 16, and 23 days to test for the levels of liver enzymes. Specifically, alanine aminotranferease (ALT) and aspartate aminotransferase (AST) are liver enzymes (transaminases) that

dx.doi.org/10.1021/ma300190b | *Macromolecules* 2012, 45, 2292–2300

can be detected systemically as a result of hepatocellular damage (liver inflammation, necrosis, cellular degeneration, and increased membrane permeability) and are approved FDA assays for determination of preclinical toxicity in new chemical entities.

The *in vivo* study showed that the polysulfenamide microparticles did not result in any significant increase in the serum ALT and AST levels over the study period, relative to either day 0 or poly(D,L-lactide-*co*-glycolide) microparticles, indicating lack of any liver damage (Figure 12b,c). In addition, mice were monitored daily and remained in good health as determined by the body condition scoring technique. The vertebrae and dorsal pelvis were not prominent but palpable with slight pressure, indicating a state of good health in the mice. No adverse injection site reactions such as infection, redness, or wounding were observed. Furthermore, no mice died as a result of injections of polysulfenamide microparticles over the entire study period. In summary, the *in vivo* and *in vitro* studies showed little or no adverse effects from the polysulfenamides. Although these results are promising for an initial demonstration of toxicity, the toxicity of polysulfenamides will require a more thorough investigation in future studies to fully probe any toxicity resulting from the polymers or their degradation products (such as the sulfenic acids).

CONCLUSIONS

We report the first synthesis and characterization of polysulfenamides. These polymers are unique because they integrate a new functional group into polymer chemistry that has found some applications in small molecule chemistry. Two methods to synthesize polysulfenamides were reported, and both polymerization reactions went to high conversions (up to 98%). It is notable that the synthesis of polysulfenamides from dithiosuccinimides proceeded at room temperature in methylene chloride; these reaction conditions are mild and suggest that more complex monomers can be used. Although the molecular weights of the polysulfenamides reported here did not reach 10 000 g mol^{-1}, higher molecular weights are possible if the conversions of polymerization are increased or if higher molecular weight monomers are used. These polymers were stable in aprotic solvents and only slowly degraded in protic, organic solvents.

Polysulfenamides present new opportunities in macromolecules because they possess a functional group that was previously unknown in polymer chemistry. In this article we describe how polysulfenamides possess many of the right characteristics for applications in the delivery of pharmaceuticals. For instance, they were stable in organic solvents but degraded in water and degraded more rapidly in acidic water. Microparticles were fabricated from a polysulfenamide, and these microparticles were readily internalized by two different cell lines. Other applications of polysulfenamides are envisioned that take advantage of the thermal lability of sulfenamide bonds, oxidation of the sulfurs, or their rapid degradation under acidic medium. Because many new opportunities for macromolecules arise when a new functional group is integrated into polymer science, we anticipate new applications for polysulfenamides.

EXPERIMENTAL PROCEDURES

Materials. Phosphate buffer saline (PBS) is a product of Sigma-Aldrich (St. Louis, MO). Dulbecco's Modified Eagle's Medium (DMEM) was obtained from Gibco BRL (Grand Island, NY). LysoTracker Green was obtained from Invitrogen (Eugene, OR). Paraformaldehyde (16% solution, EM grade) was obtained from electron microscopy services (Hatfield, PA), and Vectashield mounting medium for fluorescence with DAPI was a product of Vector laboratories (Burlingame, CA). 1-Hexanethiol, 1,6-hexanedithiol, 2-mercaptoethyl ether, *N*-benzylmethylamine, *N*-ethylmethylamine, *N,N′*-dimethyl-1,6-hexanediamine, *N*-chlorosuccinimide, triethylamine, ethylenediamine, benzoic acid, *p*-toluenesulfonic acid, acetic acid, and sulfuryl chloride were purchased from Aldrich or Acros Organics at their highest purity and used as received. HPLC grade chloroform purchased from Acros Organics was used as the GPC solvent after filtering it through a glass frit. All other solvents were reagent grade and purchased from Acros Organics. Piperazine (99%) was purchased from Aldrich. It was purified by sublimation under vacuum at 130 °C. *N,N′*-Diethylethylenediamine (95%) was purchased from Aldrich and distilled under vacuum at 30 °C. Genduran silica gel 60 (230−400 mesh) and basic alumina Brockman activity I (60−325 mesh) were purchased from Fisher Scientific and used for column chromatography.

Characterization of Small Molecules and Polysulfenamides. ^{1}H and ^{13}C NMR spectra were recorded on a Bruker DPX 300 at 300 and 75 MHz, respectively. $CDCl_3$ was used as NMR solvent with tetramethylsilane (TMS) as an internal standard. SEC was performed using chloroform as the mobile phase (1.00 mL min^{-1}) at 40 °C. A Waters 515 HPLC pump and two Waters columns (Styragel HR4 and HR5E) were used in series. A DAWN EOS 18 angle laser light scattering detector from Wyatt Corp. to measure light scattering and a Wyatt Optilab DSP to measure changes in refractive index were used to measure absolute molecular weights of polymers. Polystyrene standards (1260, 3790, 13 000, and 30 300 g mol^{-1}) were used to generate a calibration curve to measure relative molecular weights of some polysulfenamides as indicated in Table 1.

Hexanesulfenyl Chloride. Alkylsulfenyl chlorides were prepared according to a literature procedure.[57] Since they quickly returned to thiols after being exposed to air, alkylsulfenyl chlorides were used *in situ* for the preparation of sulfenamides. Sulfuryl chloride (6.28 g, 0.047 mol) was added dropwise to a solution of hexanethiol (5 g, 0.042 mol) in CH_2Cl_2 (30 mL) at 0 °C under nitrogen and stirred for 2 h 45 min. ^{1}H NMR ($CDCl_3$): δ 0.90 (t, 3H, J = 6.8 Hz), 1.39 (m, 6H), 1.78 (m, 2H), 3.11 (t, 2H, J = 7.1 Hz). ^{13}C NMR ($CDCl_3$): δ 14.03, 22.52, 27.83, 28.02, 31.31, 41.52.

2,2′-Oxydiethanesulfenyl Dichloride. 2-Mercaptoethyl ether (3 g, 0.22 mol) was reacted with a solution of sulfuryl chloride (6.15 g, 0.046 mol) in CH_2Cl_2 (30 mL) following the previous procedure. ^{1}H NMR ($CDCl_3$): δ 3.33 (t, 4H, J = 6.3 Hz), 3.88 (t, 4H, J = 6.2 Hz). ^{13}C NMR ($CDCl_3$): δ 40.92, 68.10.

***N*-Ethylmethylhexanesulfenamide (Molecule B).** A solution of hexanesulfenyl chloride (6.45 g, 0.042 mol) in CH_2Cl_2 (30 mL) was slowly added to a solution of *N*-ethylmethylamine (7.50 g, 0.13 mol) in CH_2Cl_2 (50 mL) at 0 °C under nitrogen and stirred for 7 h. The reaction was diluted with anhydrous Et_2O (130 mL) and washed with saturated NaCl solution in water (3 × 50 mL). The organic phase was dried over anhydrous magnesium sulfate and evaporated to give a brown oil. The product was isolated by vacuum distillation at 30 °C to yield a colorless oil (3.93 g, 53% yield). ^{1}H NMR ($CDCl_3$): δ 0.89 (t, 3H, J = 6.8 Hz), 1.14 (t, 3H, J = 7.2 Hz), 1.35 (m, 6H), 1.54 (m, 2H), 2.65 (t, 2H, J = 7.2 Hz), 2.75 (s, 3H), 2.82 (q, 2H, J = 7.1 Hz). ^{13}C NMR ($CDCl_3$): δ 13.79, 14.09, 22.58, 28.27, 28.89, 31.59, 31.86, 46.82, 53.93. HRMS calcd for $C_9H_{21}NS$: 175.1395. Found: 175.1392.

***N,N′*-Ethylmethylbis(2-mercaptoethyl)disulfenamide (Molecule A).** A solution of 2,2′-oxidiethanesulfenyl dichloride (4.49 g, 0.022 mol) in CH_2Cl_2 (30 mL) was reacted with a solution of *N*-ethylmethylamine (7.70 g, 0.13 mol) in CH_2Cl_2 (50 mL) following the previous procedure. The extract was filtered through basic alumina to yield a colorless oil (3.29 g, 60% yield). ^{1}H NMR ($CDCl_3$): δ 1.13 (t, 6H, J = 7.1 Hz), 2.74 (s, 6H), 2.82 (m, 8H), 3.67 (t, 4H, J = 7.1 Hz). ^{13}C NMR ($CDCl_3$): δ 13.70, 32.68, 46.89, 54.13, 70.01. HRMS calcd for $C_{10}H_{24}N_2OS_2$: 252.1321. Found: 252.1324.

***N*-(Hexanethio)succinimide (Molecule D).**[58] Hexanethiol (3 g, 25.37 mmol) was added dropwise to a solution of *N*-chlorosuccinimide (3.36 g, 26.64 mmol) in CH_2Cl_2 (70 mL) at 0 °C under nitrogen

and stirred for 20 min. The solution changed to a yellow-green color and immediately became cloudy. A solution of triethylamine (2.82 g, 27.91 mmol) in CH_2Cl_2 (10 mL) was added dropwise to the reaction. After the mixture was stirred for 2.5 h, it was washed with a saturated NaCl solution in water (4 × 30 mL). The organic layer was dried over anhydrous magnesium sulfate and evaporated to give a colorless oil. The product was isolated by column chromatography using silica gel and 20% ethyl acetate in hexanes to yield a colorless oil (4.73 g, 87% yield). ^{1}H NMR ($CDCl_3$): δ 0.88 (t, 3H, J = 6.6 Hz), 1.28 (m, 4H), 1.40 (m, 2H), 1.54 (m, 2H), 2.85 (m, 6H). ^{13}C NMR ($CDCl_3$): δ 13.99, 22.45, 27.90, 28.11, 28.61, 31.28, 37.62, 177.23. HRMS calcd for $C_{10}H_{17}NO_2S$: 215.0980. Found: 215.0979.

(2,2′-Oxydiethenthio)disuccinimide. 2-Mercaptoethyl ether (10 g, 0.072 mol) was reacted with a solution of *N*-chlorosuccinimide (20.28 g, 0.15 mol) in CH_2Cl_2 (300 mL) and a solution of triethylamine (16.10 g, 0.16 mol) in CH_2Cl_2 (55 mL) following the previous procedure. The mixture was purified by column chromatography using 95% ethyl acetate in hexanes to yield a white solid (11.42 g, 48% yield). ^{1}H NMR ($CDCl_3$): δ 2.78 (s, 8H), 2.95 (t, 4H, J = 5.9 Hz), 3.68 (t, 4H, J = 5.9 Hz). ^{13}C NMR ($CDCl_3$): δ 28.68, 36.93, 70.90, 177.29. HRMS calcd for $C_{12}H_{16}N_2O_5S_2$ + Na^+: 355.0398. Found: 355.0387.

***N,N′*-(Hexanethio)disuccinimide (Molecule C).** 1,6-Hexanedithiol (7 g, 0.047 mol) was reacted with a solution of *N*-chlorosuccinimide (13.06 g, 0.098 mol) in CH_2Cl_2 (230 mL) and a solution of triethylamine (10.37 g, 0.102 mol) in CH_2Cl_2 (35 mL) following the previous procedure to give a brown solid. The solid was recrystallized from methanol (350 mL) 3 times to yield a white solid (9.90 g, 62% yield). ^{1}H NMR ($CDCl_3$): δ 1.47 (m, 8H), 2.83 (m, 12H). ^{13}C NMR ($CDCl_3$): δ 27.62, 27.65, 28.62, 37.48, 177.26. HRMS calcd for $C_{14}H_{20}N_2O_4S_2$ + Na^+: 367.0762. Found: 367.0757.

***N*-Benzylmethylhexanesulfenamide.** *N*-Benzylmethylamine (1.11 g, 9.19 mmol) was added to a solution of molecule B (1.94 g, 9.01 mmol) in CH_2Cl_2 (2.5 mL) and stirred at room temperature for 19 h. The reaction was diluted with anhydrous Et_2O (30 mL) and washed with water (4 × 20 mL). The organic phase was dried over anhydrous magnesium sulfate and evaporated to give a yellowish oil (1.7 g, 81% yield). ^{1}H NMR ($CDCl_3$): δ 0.89 (t, 3H, J = 6.8 Hz), 1.34 (m, 6H), 1.56 (m 2H), 2.69 (m 5H), 4.01 (s, 2H), 7.28 (m, 5H). ^{13}C NMR ($CDCl_3$): δ 14.07, 22.56, 28.26, 28.80, 31.56, 32.88, 45.97, 65.47, 127.25, 128.23, 128.68, 138.90. HRMS calcd for $C_{14}H_{23}NS$: 237.1551. Found: 237.1541.

Polymer from Entry 1 in Table 1. Piperazine (0.176 g, 2.05 mmol) was added to a stirred solution of (2,2′-oxidiethenthio)-disuccinimide (0.71 g, 2.05 mmol) in $CHCl_3$ (3.5 mL) and reacted at room temperature for 24 h. The polymer was precipitated into methanol (35 mL) and washed with methanol 3 times. The polymer was dried under vacuum to yield a white powder. ^{1}H NMR ($CDCl_3$): δ 2.86 (t, 4H, J = 6.8 Hz), 2.97 (s, 8H), 3.65 (t, 4H, J = 6.9 Hz). ^{13}C NMR ($CDCl_3$): δ 32.92, 57.28, 70.10.

Polymer from Entry 2 in Table 1. *N,N′*-(Hexanethio)-disuccinimide (3 g, 8.71 mmol) in $CHCl_3$ (19 mL) was reacted with piperazine (0.75 g, 8.71 mmol) following the previous procedure to yield a white powder. ^{1}H NMR ($CDCl_3$): δ 1.40 (m, 4H), 1.56 (m, 4H), 2.69 (t, 4H, J = 7.5 Hz), 2.99 (s, 8H). ^{13}C NMR ($CDCl_3$): δ 28.62, 28.82, 32.17, 57.30.

Polymer from Entry 3 in Table 1. *N,N′*-(Hexanethio)-disuccinimide (1 g, 2.90 mmol) in $CHCl_3$ (5 mL) was reacted with *N,N′*-diethylethylenediamine (0.34 g, 2.90 mmol) following the previous procedure. The polymer was precipitated into methanol (10 mL). The polymer was redissolved in a minimal amount of $CHCl_3$ and precipitated into methanol (2 mL) to yield a yellowish oil after drying under vacuum. ^{1}H NMR ($CDCl_3$): δ 1.14 (t, 6H, J = 7.1 Hz), 1.40 (m, 4H), 1.54 (m, 4H), 2.60 (t, 4H, J = 7.4 Hz), 2.90 (q, 4H, J = 7.1 Hz), 3.05 (s, 4H). ^{13}C NMR ($CDCl_3$): δ13.99, 27.92, 28.91, 34.27, 53.23, 56.52.

Polymer from Entry 4 in Table 1. (2,2′-Oxydiethenthio)-disuccinimide (0.625 g, 1.77 mmol) in CH_2Cl_2 (1.5 mL) was reacted with *N,N′*-diethylethylenediamine (0.21 g, 1.77 mmol) following the previous procedure. After evaporating the solvent, the polymer was precipitated into methanol (10 mL) and washed with methanol (15 mL). The polymer was dried under vacuum to yield a yellowish oil. ^{1}H NMR ($CDCl_3$): δ 1.14 (t, 6H, J = 6.9 Hz), 2.77 (t, 4H, J = 7.1 Hz), 2.90 (q, 4H, J = 7.0 Hz), 3.04 (s, 4H), 3.65 (t, 4H, J = 7.2 Hz). ^{13}C NMR ($CDCl_3$): δ 14.27, 35.14, 53.66, 56.79, 69.98.

Polymer from Entry 5 in Table 1. *N,N′*-(Hexanethio)-disuccinimide (1 g, 2.90 mmol) in $CHCl_3$ (6 mL) was reacted with *N,N′*-dimethyl-1,6-hexanediamine (0.42 g, 2.90 mmol) following the previous procedure. The polymer was precipitated into methanol (10 mL). The polymer was redissolved in a minimal amount of $CHCl_3$ and precipitated into methanol (7 mL) to yield a yellowish oil after drying under vacuum. ^{1}H NMR ($CDCl_3$): δ 1.31 (m, 4H), 1.41 (m, 4H), 1.55 (m, 8H), 2.64 (t, 4H, J = 7.4), 2.76 (m, 10H). ^{13}C NMR ($CDCl_3$): δ 26.87, 28.18, 28.40, 28.89, 31.68, 47.12, 59.87.

Polymer from a Disulfenamide (Figure 3). *N,N′*-Ethylmethylbis(2-mercaptoethyl)disulfenamide (1.34 g, 5.32 mmol) was reacted with *N,N′*-diethylethylenediamine (0.62 g, 5.32 mmol) in refluxing benzene (5 mL) for 24 h. After evaporating the solvent, the polymer was precipitated into methanol (2 × 15 mL). The polymer was dried under vacuum to yield a yellowish oil (0.12 g). ^{1}H NMR ($CDCl_3$): δ 1.14 (t, 6H, J = 6.9 Hz), 2.77 (t, 4H, J = 7.1 Hz), 2.90 (q, 4H, J = 7.0 Hz), 3.04 (s, 4H), 3.65 (t, 4H, J = 7.2 Hz). ^{13}C NMR ($CDCl_3$): δ 14.27, 35.14, 53.66, 56.79, 69.98.

Preparation of Microparticles. Blank microparticles were prepared by oil-in-water (o/w) single emulsion, solvent evaporation technique. Briefly, 300 mg of polymer was dissolved in 3.5 mL of chloroform in a heated water bath (55 °C). This organic phase was then emulsified with 35 mL of 1% (w/v) Mowiol at 13 500 rpm for 1 min using an IKA Ultra-Turrax T25 basic homogenizer (IKA, Wilmington, NC). The mixture was stirred overnight to evaporate the organic phase. The microparticles were then washed three times with deionized water (5000 rpm for 10 min) and lyophilized (Labconco FreeZone 4.5, Kansas City, MO). Microparticles were stored at −20 °C until use.

Surface Morphology. Microparticle morphology was assessed by scanning electron microscopy (SEM, Hitachi S-4000). Air-dried microparticles were placed on silicon wafers mounted on SEM specimen stubs. The stubs were coated with ∼5 nm of gold by ion beam evaporation followed by imaging using SEM operated at 3 kV accelerating voltage.

Particle Size and Zeta Potential. Microparticle size and zeta potential was measured using the Zetasizer Nano ZS (Malvern, Southborough, MA). The microparticles were suspended in deionized water at a concentration of 1 mg mL^{-1}. The zeta potential was measured using folded capillary cell in automatic mode, and the size was measured using a disposable sizing cuvette (DTS0012). The size was measured at 25 °C at a 173° scattering angle.

***In Vitro* Analysis of Microparticle Degradation.** For *in vitro* analysis, ∼85 mg of the microparticles was suspended in either phosphate buffer saline (PBS, pH 7.4) or acetate buffer (pH 4). The samples were agitated at 37 °C, 150 rpm in a horizontal shaker (C24 incubator shaker, New Brunswick Scientific, Edison, NJ). At specific time points, the samples were centrifuged for 10 min at 7000 rpm. The pellet was washed three times with deionized water and lyophilized. The dry weight of the pellet was recorded, and percentage weight loss was calculated for each sample. In addition, the samples were also analyzed by scanning electron microscopy to observe change in surface morphology of microparticles.

Particle Uptake. Uptake of rhodamine labeled microparticles was studied in JAWSII cells and HEK293 cells. Chambers were initially coated with 300 μL of poly(L-lysine) (0.1% w/v) overnight. Following coating, ∼1 × 10^4 cells were seeded per well and incubated overnight at 37 °C in a humidified 5% CO_2-containing atmosphere. Rhodamine-labeled particles were added to the media at a concentration of 50 μg per well. The particles were incubated with the cells for ∼18 h. Cells were washed three times with sterile PBS and fixed with 4% paraformaldehyde. The nucleus was stained with DAPI. Vectashield mounting medium was added onto slide and sealed with coverslip. The samples were imaged using LSM710 confocal microscope (Carl Zeiss MicroImaging).

■ ASSOCIATED CONTENT

Supporting Information

Synthesis of the water-soluble sulfenamide in Figure 9, kinetic experiments, and degradation of sulfenamides. This material is available free of charge via the Internet at http://pubs.acs.org.

■ AUTHOR INFORMATION

Corresponding Author

*E-mail ned-bowden@uiowa.edu, Tel (319) 335-1198.

Notes

The authors declare no competing financial interest.

■ ACKNOWLEDGMENTS

N.B.B. gratefully thanks the NSF for generous funding (CHE-0848162). A.K.S. gratefully acknowledges support from the American Cancer Society (RSG-09-015-01-CDD), the National Cancer Institute at the National Institutes of Health (1R21CA13345-01/1R21CA128414-01A2/UI Mayo Clinic Lymphoma SPORE), and the Pharmaceutical Research and Manufacturers(PhRMA) Foundation. A.K.S. thanks the Core Microscopy Research Facility for use of imaging equipment.

■ REFERENCES

(1) Nguyen, D. N.; Green, J. J.; Chan, J. M.; Langer, R.; Anderson, D. G. *Adv. Mater.* **2009**, *21*, 847.
(2) Twaites, B.; de las Heras Alarcon, C.; Alexander, C. *J. Mater. Chem.* **2005**, *15*, 441.
(3) Green, J. J.; Langer, R.; Anderson, D. G. *Acc. Chem. Res.* **2008**, *41*, 749.
(4) Cao, J.; Langer, R. *Nano Lett.* **2010**, *10*, 3223.
(5) Jabbari, E.; Lu, L.; Yaszemski, M. J. *Synthesis and Characterization of Injectable and Biodegradable Composites for Orthopedic Applications*; 2006; Vol. *2*.
(6) Peter, S. J.; Miller, M. J.; Yasko, A. W.; Yaszemski, M. J.; Mikos, A. G. *J. Biomed. Mater. Res.* **1998**, *43*, 422.
(7) Anderson, D. G.; Nurdick, J. A.; Langer, R. *Science* **2004**, *305*, 1923.
(8) Ciuffarin, E.; Gambarotta, S.; Isola, M.; Senatore, L. *J. Chem. Soc., Perkin Trans. 2* **1978**, 554.
(9) Saito, G.; Swanson, J. A.; Lee, K.-D. *Adv. Drug Delivery Rev.* **2003**, *55*, 199.
(10) Mohanad, M.; Dixon, A. S.; Lim, C. S. *Ther. Delivery* **2010**, *1*, 169.
(11) Meng, H. X. M.; Xia, T.; Zhao, Y.-L.; Tamaoi, F.; Stoddart, J. F.; Zink, J. I.; Nel, A. E. *J. Am. Chem. Soc.* **2010**, *132*, 12690.
(12) Arima, H.; Motoyama, K. *Sensors* **2009**, *9*, 6346.
(13) Oh, K. T.; Yin, H.; Lee, E. S.; Bae, Y. H. *J. Mater. Chem.* **2007**, *17*, 3987.
(14) Kroeze, R. J.; Helder, M. N.; Govaert, L. E.; Smit, T. H. *Materials* **2009**, *2*, 833.
(15) Kohane, D. S.; Langer, R. *Chem. Sci.* **2010**, *1*, 441.
(16) Williams, C. K. *Chem. Soc. Rev.* **2007**, *36*, 1573.
(17) Vert, M. *J. Mater. Sci.: Mater. Med.* **2009**, *20*, 437.
(18) Kwon, G. S.; Furgeson, D. Y. *Biomed. Polym.* **2007**, 83.
(19) Leibfarth, F. A.; Kang, M.; Ham, M.; Kim, J.; Campos, L. M.; Gupta, N.; Moon, B.; Hawker, C. J. *Nature Chem.* **2010**, *2*, 207.
(20) Leibfarth, F. A.; Schneider, Y.; Lynd, N. A.; Schultz, A.; Moon, B.; Kramer, E. J.; Bazan, G. C.; Hawker, C. J. *J. Am. Chem. Soc.* **2010**, *132*, 14706.
(21) Zhongfan, J.; Jingquan, L.; Cyrille, B.; Davis, T. P.; Boulmus, V. *Biomacromolecules* **2009**, *10*, 3253.
(22) Breunig, M.; Lungwitz, U.; Liebl, R.; Goepferich, A. *Proc. Natl. Acad. Sci. U. S. A.* **2007**, *104*, 14454.
(23) Cohen, J. A.; Beaudetter, T. T.; Cohen, J. L.; Broaders, K. E.; Bachelder, E. M.; Frechet, J. M. J. *Adv. Mater.* **2010**, *22*, 3593.
(24) Broaders, K. E.; Cohen, J. A.; Beaudetter, T. T.; Bachelder, E. M.; Frechet, J. M. J. *Proc. Natl. Acad. Sci. U. S. A.* **2009**, *106*, 5497.
(25) Greene, T. W.; Wuts, P. G. M. *Protective Groups in Organic Synthesis*; John Wiley & Sons, Inc.: New York, 1991.
(26) Zhao, F.; Bi, W.; Zhao, S. *J. Macromol. Sci., Part B: Phys.* **2011**, *50*, 1460.
(27) Wang, Z.; Zhao, H.; Zhao, J.; Wang, X. *J. Appl. Polym. Sci.* **2010**, *117*, 2523.
(28) Guo, R.; Talma, A. G.; Datta, R. N.; Dierkes, W. K.; Noordermeer, J. W. M. *Eur. Polym. J.* **2008**, *44*, 3890.
(29) Man, W.-L.; Lam, W. W. Y.; Kwong, H.-K.; Peng, S.-M.; Wong, W.-T.; Lau, T.-C. *Inorg. Chem.* **2010**, *49*, 73.
(30) Huynh, M. H. V.; White, P. S.; Meyer, T. J. *Angew. Chem., Int. Ed.* **2000**, *39*, 4101.
(31) Huynh, M. H. V.; Morris, D. E.; White, P. S.; Meyer, T. J. *Angew. Chem., Int. Ed.* **2002**, *41*, 2330.
(32) Lopez, M.; Drilland, N.; Bornaghi, L. F.; Poulsen, S.-A. *J. Org. Chem.* **2009**, *74*, 2811.
(33) Mukaiyama, T.; Matsuo, J.-I.; Iida, D.; Kitagawa. *Chem. Lett.* **2001**, *30*, 846.
(34) Matsumoto, Y.; Kawana, A.; Hiroyuki, Y.; Mukaiyama, T. *Chem. Lett.* **2003**, *32*, 182.
(35) Koval, I. V. *Russ. Chem. Rev.* **1996**, *65*, 421.
(36) Matsuo, J.-I.; Kawana, A.; Yamanaka, H.; Mukaiyama, T. *Chem. Lett.* **2003**, *32*, 182.
(37) Guarino, V. R.; Karunaratne, V.; Stella, V. J. *Bioorg. Med. Chem. Lett.* **2007**, *17*, 4910.
(38) Knapp, S.; Darout, E.; Amorelli, B. *J. Org. Chem.* **2006**, *71*, 1380.
(39) Craine, L.; Raban, M. *Chem. Rev.* **1989**, *89*, 689.
(40) Capozzi, G.; Modena, G.; Pasquato, L. *The Chemistry of Sulphenic Acids and Their Derivatives*; John Wiley & Sons: New York, 1990.
(41) Yoo, J.; D'Mello, S. R.; Graf, T.; Salem, A. K.; Bowden, N. B. *Macromolecules* **2012**, *45*, 688.
(42) Stasevych, M. V.; Plotnikov, M. Y.; Platonov, M. O.; Sabat, S. I.; Musyanovych, R. Y.; Novikov, V. P. *Heteroat. Chem.* **2005**, *16*, 587.
(43) Bao, M.; Shimizu, M. *Tetrahedron* **2003**, *59*, 9655.
(44) Wanner, M. J.; Hauwert, P.; Schoemaker, H. E.; Gelder, R. d.; Maarseveen, J. H. v.; Hiemstra, H. *Eur. J. Org. Chem.* **2008**, *2008*, 180.
(45) Odian, G. G. *Principles of Polymerization*; Wiley: New York, 1991.
(46) Owen, D. J.; Davis, C. B.; Hartnell, R. D.; Madge, P. D.; Thomson, R. J.; Chong, A. K. J.; Coppel, R. L.; von Itzstein, M. *Bioorg. Med. Chem. Lett.* **2007**, *17*, 2274.
(47) Kice, J. L. *Adv. Phys. Org. Chem.* **1980**, *17*, 65.
(48) Nagy, P.; Ashby, M. T. *Chem. Res. Toxicol.* **2007**, *20*, 1364.
(49) Shelton, J. R.; Davis, K. E. *J. Am. Chem. Soc.* **1967**, *89*, 718.
(50) Freeman, F.; Kodera, Y. *J. Agric. Food Chem.* **1995**, *43*, 2332.
(51) Nagy, P.; Ashby, M. T. *Chem. Res. Toxicol.* **2005**, *18*, 919.
(52) Kice, J. L.; Rogers, T. E. *J. Am. Chem. Soc.* **1974**, *96*, 8009.
(53) Wolfenden, R. Y., Y. *J. Am. Chem. Soc.* **2011**, *133*, 13821.
(54) Tarvainen, T.; Karjalainen, T.; Malin, M.; Perakorpi, K.; Tuominen, J.; Seppala, J.; Jarvinen, K. *Eur. J. Pharm. Sci.* **2002**, *16*, 323.
(55) Yeo, Y.; Park, K. *Arch. Pharm. Res.* **2004**, *27*, 1.
(56) Anderson, J. A.; Shive, M. S. *Adv. Drug Delivery Rev.* **1997**, *28*, 5.
(57) Branchaud, B. P. *J. Org. Chem.* **1983**, *48*, 3531.
(58) Henke, A.; Srogl, J. *J. Org. Chem.* **2008**, *73*, 7783.

Macromolecules

Article

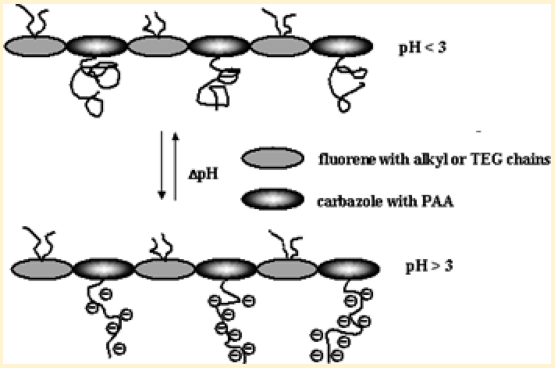
pubs.acs.org/Macromolecules

Highly Charged Conjugated Polymers with Polyphenylene Backbones and Poly(acrylic acid) Side Chains

Nicole Rugen-Penkalla, Markus Klapper, and Klaus Müllen*

Max Planck Institute for Polymer Research, Ackermannweg 10, D-55128 Mainz, Germany

ABSTRACT: A synthetic strategy to prepare various amphiphilic, conjugated graft copolymers by means of the grafting onto technique via click coupling reaction is described. In particular, amphiphilic, conjugated polyelectrolyte brush copolymers based on 2,7-linked carbazole−fluorene copolymers as main chains and pH-sensitive, highly charged poly(acrylic acid) side chains (PAA) are presented. The main chain is obtained by a Suzuki polycondensation of dibromo- and diboronic ester of fluorene and carbazole monomers, resulting in conjugated polyphenylene-type copolymers with both alternating and statistical carbazole−fluorene structures. In order to vary the amphiphilicity of the graft copolymers, 9,9-disubstituted fluorene derivatives with different polarities, induced by branched alkyl as well as by methoxytetra(ethylene glycol) (TEG) groups, were used. To graft the side chains on the conjugated backbone, the carbazole units are, first, N-functionalized by pentynyl groups. These units are reacted in a click reaction with an azide end-functionalized poly(*tert*-butyl acrylate) which has previously been obtained by atom transfer radical polymerization (ATRP). After cleavage of the *tert*-butyl groups, the neutral comb-type copolymers were converted into a conjugated polyelectrolyte brush copolymer carrying poly(acrylic acid) side chains. The described synthetic strategy facilitates to adjust the polarity and the grafting density of the graft copolymers and might be applied to other functional side chains.



INTRODUCTION

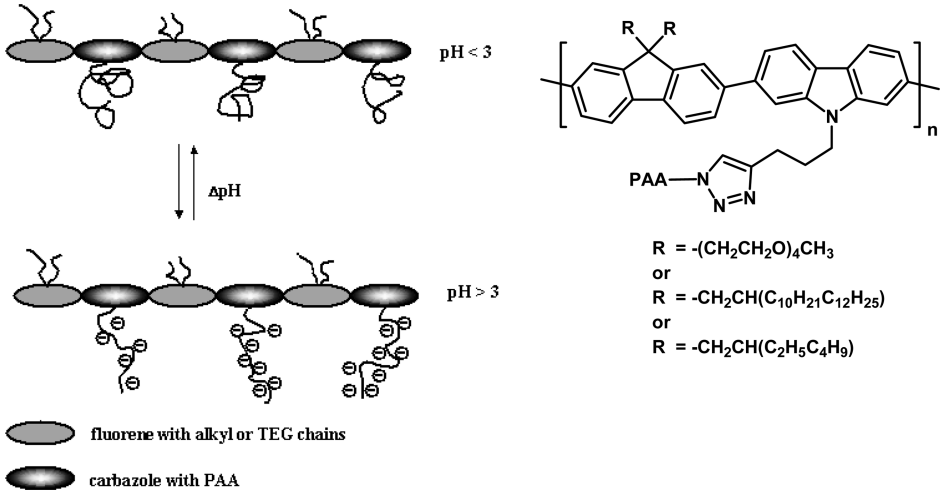
Conjugated polymers have received significant attention due to their application in electronic devices and optoelectronics.[1−3] Unfortunately, unsubstituted conjugated polymers suffer from low solubility, which limits the processability.[4] Therefore, various side chains were attached to the backbone to allow a controlled synthesis of soluble conjugated polymers with high molecular weight.[5] In most cases, these polymers were unpolar and the side chains very short compared with the conjugated backbone.[6] The number of conjugated polymers with either longer or charged side chains is quite limited. First reports of poly(*p*-phenylene)s (PPP) with sulfonic acids or quarternized amines came up in the 1990s.[7,8] Later on, polyfluorene copolymers with charged side chains were described, too.[9−11] However, the charge density per repeating unit of these polymers was quite low, since only the end groups of the substituents were charged.

The synthesis of amphiphilic cylindrical polymer brushes with conjugated backbones is of major interest for both experimental and theoretical chemists because of the expectation that their unique structure may cause unusual optical and electronic properties.[4] For example, in contrast to brush polymers with flexible backbones, the incorporation of a rigid main chain reduces the number of possible conformations, since extended wormlike structures are only formed. The latter are caused by the rod-type backbone and not strongly affected by steric repulsion between grafted side chains. In case of attaching polyelectrolytes to a conjugated backbone amphiphilic, conjugated polyelectrolyte brush polymers were created.[12] These polymers demonstrated in solution conformational changes by a polyelectrolyte effect or by altering pH.[12] Previous surveys of Bazan et al. and Bunz et al. on *p*-phenylene-based copolymers with a maximum of 2−4 carboxylic groups per repeating unit showed different absorption and fluorescence behavior depending on pH.[13,14] Bunz et al. observed an influence of the concentration of charged groups on electrostatic forces, which dominated aggregation as well as excimer formation and therefore optoelectronic properties. They reported a protonation of the carboxylic groups at low pH values, resulting in an uncharged polymer species and a decreased interchain electrostatic repulsion.[13−15] Accordingly, $\pi-\pi$ stacking was preferred and aggregates formed. Furthermore, Bunz et al. anticipated a maximally twisted backbone at a pH value higher than 3 to minimize electrostatic repulsion of the negatively charged substituents. Therefore, interchain interactions were decreased, and a blue-shifted absorption in neutral solutions occurred.[14] The same results were found for the fluorescence measurements. An increasing degree of uncharged groups led to quenching of emission at lower pH.[13,14] This effect was attributed to emission from an "excimer-like" state arising from an increased interchain $\pi-\pi$

Received: October 4, 2011
Revised: February 1, 2012
Published: February 28, 2012

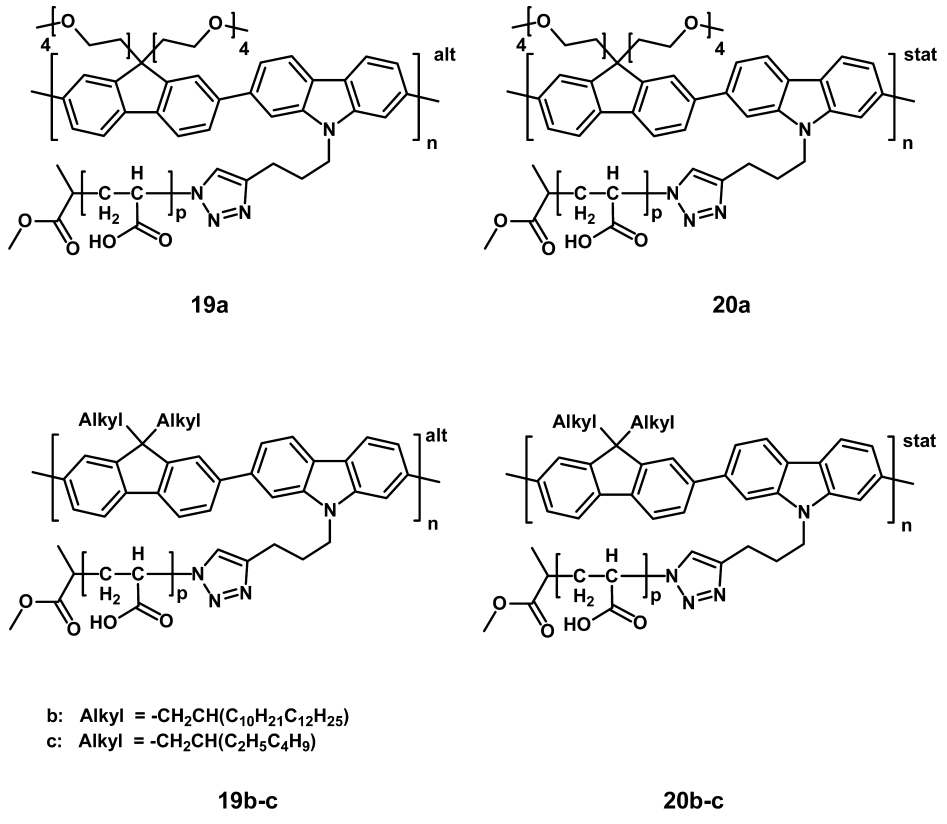
 © 2012 American Chemical Society dx.doi.org/10.1021/ma202209u | *Macromolecules* 2012, 45, 2301−2311

Scheme 1. Schematic Illustration of Comb-Type Polyelectrolytes with a Conjugated Backbone of Alternating Fluorene and Carbazole Units[a]



[a]At low pH values PAA (poly(acrylic acid)) is protonated, while at higher pH values deprotonation takes place leading to increased electrostatic repulsion.

Scheme 2. Polyelectrolyte Brush Copolymers Based on Alternating or Statistical Carbazole−Fluorene Backbones with Poly(acrylic acid) Side Chains as Well as TEG or Alkyl Chains

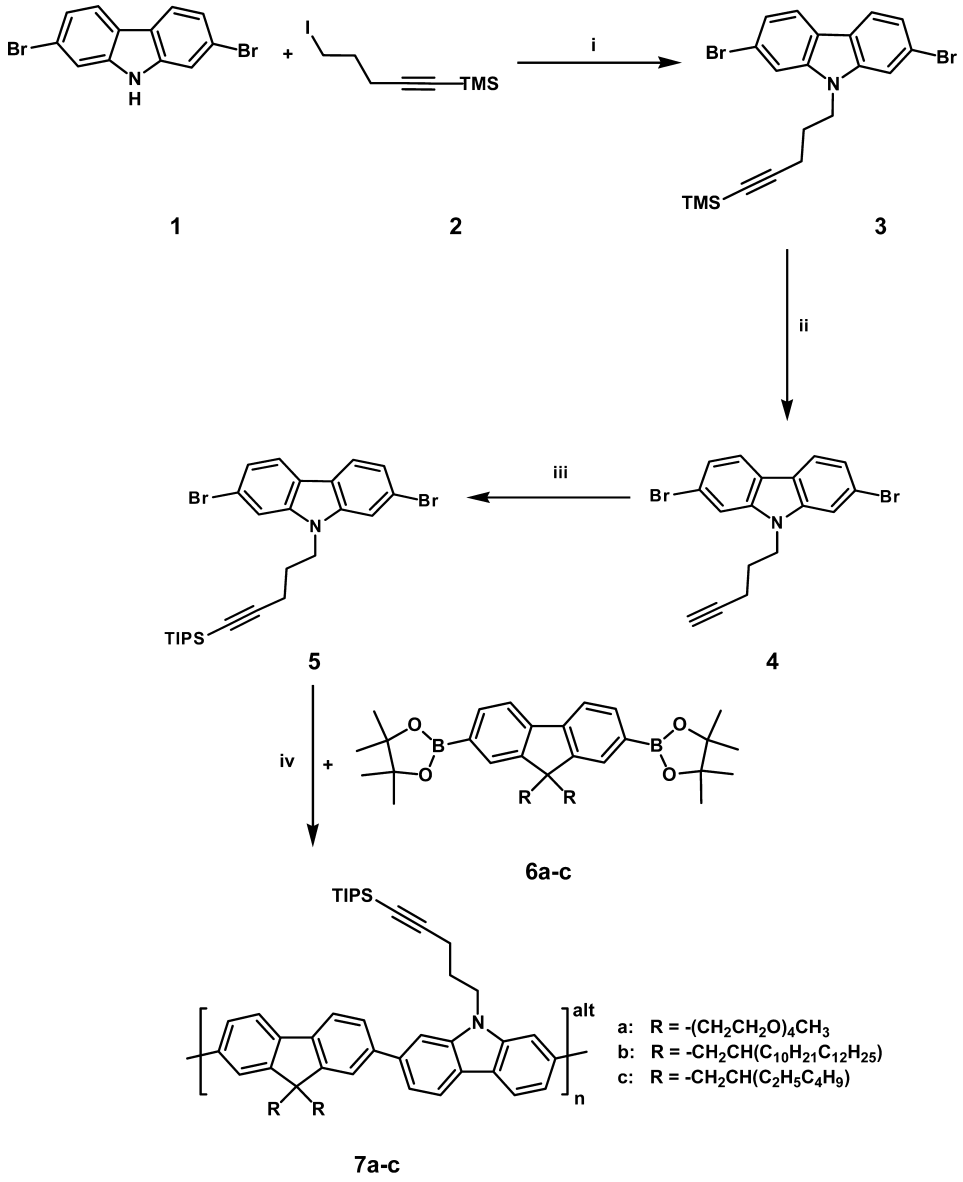


stacking resulting in aggregates.[15] Furthermore, a control of adsorption at interfaces and of self-assembly was possible.[12,16]

Brush polymers can be typically obtained by means of grafting onto, grafting from, and macromonomer methods.[17] For example, we reported the synthesis of pH-responsive conjugated polyelectrolyte brush polymers via the macromonomer technique.[18] These copolymers were polymerized via Suzuki reaction of 2,7-dibromocarbazole macromonomers with monodisperse poly(L-lysine) (PLL) side chains and diboronate ester carbazoles with branched alkyl chains to give an alternating substitution pattern. However, it was difficult to achieve high polymerization degrees due to the low concentration as well as the steric hindrance of polymerizable groups caused by the side chains.[19,18] As a result, the synthesized polymers have only starlike structures. To achieve cylindrical structures and to simplify the synthesis of the pH-responsive side chains, a different synthetic strategy was required. First, instead of the PLL homopeptide, poly(acrylic

dx.doi.org/10.1021/ma202209u | Macromolecules 2012, 45, 2301−2311

Scheme 3. Synthesis of Alternating Carbazole−Fluorene Copolymers with TIPS Alkynyl Groups 7a−c[a]



[a]Reagents and conditions: (i) NaH (60% w/w dispersion in mineral oil), anhydrous DMF, argon, rt, 1 day, 73%; (ii) KOH aqueous (10%), MeOH, THF, rt, 1 day, 88%; (iii) (a) anhydrous THF, −75 °C, LDA, argon, 1 h, (b) anhydrous THF, anhydrous DMSO, TIPS-Cl, 1 day, 51%, (iv) toluene, $Pd(PPh_3)_4$, Et_4NOH (35 wt %), argon, 90 °C, 3 h; (7**a**) 63%, (7**b**) 68%, (7**c**) 89%.

acid) (PAA), which can be switched between charged and uncharged structures when going from a neutral to an acidic solution, was used as polyelectrolyte side chains.[20] Even though no direct ATRP of PAA is possible, due to a deactivation of the catalyst by the acid groups, *tert*-butyl acrylate (*t*-BA) can be used as precursor.[21] The conversion of the obtained P(*t*-BA) into PAA takes place in a second step by removing the *tert*-butyl protecting groups via acid hydrolysis.[47] Second, we chose a grafting onto method via click cycloaddition between azide end-functional side chains and alkynyl groups at the conjugated backbone.[22−24] This approach allowed a separate synthesis of main and side chain which has the advantage of the determination of molecular weight as well as polydispersity of both polymers prior to the synthesis of the conjugated polyelectrolyte brush polymers.

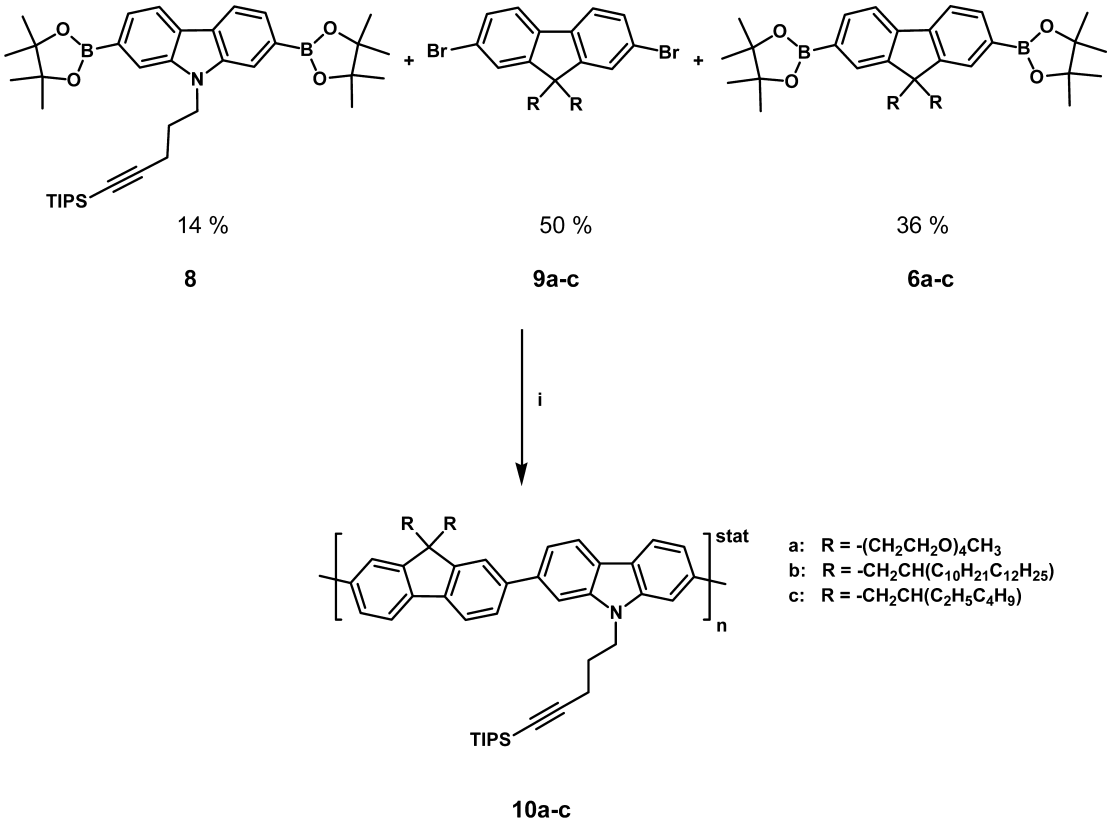
Instead of polycarbazoles, carbazole−fluorene copolymers (Scheme 1) were synthesized which guarantee a sufficient solubility of the conjugated backbone before grafting.[1] The latter show an increased solubility due to a higher amount of solubilizing substituents caused by 9,9-disubstituted fluorene units.[1]

RESULTS AND DISCUSSION

Polymer Synthesis. The synthesis of conjugated polymers with polyelectrolyte side chains (**19a−c** and **20a−c**, Scheme 2) was investigated via the grafting onto technique. It had to be considered that the grafting density is limited due to kinetic and thermodynamic reasons.[19] Consequently, with increasing grafting density further coupling reactions become entropically unfavorable. Additionally, the steric hindrance increases as well, resulting in a decreased diffusion of the end-functional side chains to the coupling groups along the backbone. To reduce these limits and to obtain a high conversion of the click cycloaddition, the potential grafting positions along the

dx.doi.org/10.1021/ma202209u | *Macromolecules* 2012, 45, 2301−2311

Scheme 4. Statistical Copolymerization of Fluorene and Carbazole Units[a]



[a]Reagents and conditions: (i) toluene, $Pd(PPh_3)_4$, Et_4NOH (35 wt %), argon, 90 °C, 3 h; (**10a**) 56%, (**10b**) 65%, (**10c**) 59%.

polymeric backbone were diluted. Therefore, alternating and statistical carbazole–fluorene copolymers **7a–c** and **10a–c** bearing reactive alkynyl groups only at the carbazole units were formed. These polymers were obtained via Suzuki polycondensation of 2,7-dibromo- (**5**, **9a-c**) and 2,7-diboronic ester (**6a–c**, **8**) monomers (Schemes 3 and 4). The introduction of fluorene units should enhance the solubility in common solvents compared to polycarbazoles due to the difunctionalization in the 9-position. Furthermore, the introduction of substituents with various steric requirements (branched alkyl chains) and polarities (methoxytetra(ethylene glycol) (TEG)) allowed a variation of the amphiphilicity. To obtain the polyelectrolyte brush polymers **19a–c** and **20a–c** (Scheme 2) by means of a click reaction, a carbazole repeating unit with a pendant alkyne group was required.

Hence, the carbazole derivative **3** was synthesized by attaching (5-iodopent-1-inyl)trimethylsilane (**2**) to 2,7-dibromocarbazole (**1**) (Scheme 3). Since TMS would be cleaved under the basic Suzuki condition, a TIPS group with sufficient stability was introduced. Therefore, the removal of the TMS-protecting group was carried out with potassium hydroxide in methanol. Finally, compound **4** was converted into the TIPS-protected derivative **5** via reaction with TIPS chloride. The quantitative cleavage of the TMS group and the quantitative introduction of the TIPS group were verified by ^{1}H NMR spectroscopy.

Control over pendent alkynyl density along the backbone was achieved by using dibromo- as well as diboronic ester fluorene and carbazole units in different ratios during Suzuki reactions, resulting in both alternating (Scheme 3) and statistical copolymers (Scheme 4).

An equimolar ratio of 2,7-dibromocarbazole with a TIPS-protected alkynyl group **5** and a 2,7-diboronic ester of a fluorene derivative **6a–c**, which were synthesized according to the literature,[25–27] led to alternating backbones via Suzuki reaction (Scheme 3). The reactions were stopped after 3 h since with increasing reaction time precipitation of insoluble high molecular weight copolymers occurred.

By using 50 mol % of the dibromo derivatives **9a–c**, 36 mol % of the diboronic esters of the alkylated fluorene derivative **6a–c** and 14 mol % of the alkynyl substituted carbazole **8** statistical carbazole–fluorene copolymers **10a–c** with a ratio of 1:6 (carbazole:fluorene) were achieved (Scheme 4). These backbones were synthesized for two reasons. First, it should be investigated if the arrangement of charged and uncharged segments along the polyelectrolyte brush polymers influences the aggregation behavior. Second, fluorene units, which bear two solubilizing groups, were copolymerized as it is known that such units improve the solubility.[1]

The fractions of carbazole repeating units in the copolymers **10a–c** were determined by measuring the nitrogen amount via elemental analyses. The calculated values were in good agreement with the concentration of **8** in the reaction mixture (Table 1). ^{1}H NMR spectroscopic characterization confirms the structures of **6a–c** and **10a–c**. The amount of TIPS-protected alkynyl groups after the polycondensation was calculated from the relative signal intensities of signals at 1.10 ppm (TIPS group) and at 7.64–8.25 ppm (aromatic protons in the polymer backbone). Since the relative signal intensities corresponded to the expected 21 protons of the silyl group and 12 aromatic protons for the alternating copolymer **6a–c**, no loss of protecting groups had taken place. The molecular

dx.doi.org/10.1021/ma202209u | *Macromolecules* 2012, 45, 2301–2311

Table 1. GPC Data (Determined against PS Standard in THF) and Calculated Values of Both Alternating (7a–c) and Statistical (10a–c) Conjugated Backbones with TIPS Protecting Groups

backbone	M_n [g/mol]	M_w [g/mol]	M_n/M_w	DP	yield [%]	conv	amount of Cz [%]
7a	18 100	64 800	3.6	39	94	0.97	45
7b	15 100	39 100	2.6	24	68	0.96	43
7c	18 600	38 100	2.1	42	89	0.98	44
10a	41 400	152 000	3.7	76	56	0.99	13
10b	15 200	28 200	1.9	18	65	0.94	14
10c	20 000	47 100	2.4	52	59	0.98	11

weights and polydispersities of the backbones **7a–c** and **10a–c** were analyzed by GPC (THF, polystyrene standard (PS)) (Table 1).

As it turned out, the yields of the Suzuki polycondensations were found to be lower than the ones expected by the Carothers equation for these M_n values. These deviations were attributed to fractionation of low molecular weight oligomers, which were still soluble during the precipitation of the polymers.[28]

Before attaching side chains via click reaction, cleavage of the protecting group was carried out in the presence of tetrabutylammonium fluoride (TBAF) yielding alternating **11a–c** statistical **12a–c** (Scheme 5).

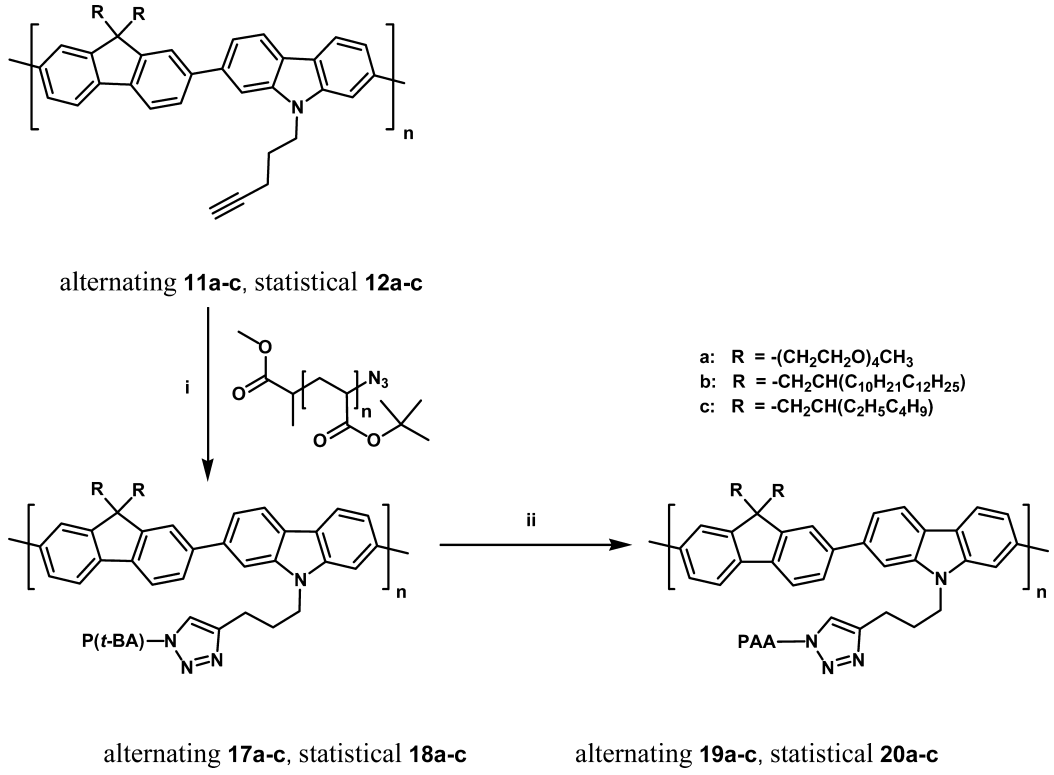
The quantitative conversion was confirmed by the disappearance of the signal at 1.10 ppm (TIPS group) in the ^{1}H NMR spectra and the appearance of an acetylene C–H band at 3240 cm^{-1} (lit.: 3257 cm^{-1})[29] in the FT-IR spectra.

The synthesis of the side chains was achieved by polymerization of *tert*-butyl acrylate (**14**) under ATRP conditions using methyl-2-bromopropionate (MBP) (**13**) as initiator and CuBr/$CuBr_2$/PMDETA as catalyst system at 60 °C.[30] The use of this controlled polymerization method has the advantage to obtain bromo-terminated polymers with low polydispersities, which can be easily converted into the corresponding azide functionalized molecules.

To receive comb-type polymers, the side chains should be short in comparison to the backbone. Therefore, P(*t*-BA) (**15**) with a number-average molecular weight of 5300 g/mol and a molecular weight distribution of 1.23 (measured by GPC, (PS standard; THF)) was prepared (95% conversion). To ensure the transformation into the azide derivative **16**, the amount of halogen end-functional P(*t*-BA) chains (**15**) was determined. For this reason, the polymer was analyzed by ^{1}H NMR spectrosopy. The NMR spectrum showed a signal at 3.63 ppm attributed to the methyl ester protons from the MBP, a signal at 1.41 ppm due to the *tert*-butyl ester resonance, and a signal from 4.01 to 4.17 ppm due to the methine proton neighboring the bromo end group. The relative signal intensities of methyl ester protons compared to the methine protons gave a ratio of approximately 3:1. Hence, a high fraction of polymer **15** was terminated by a halogen atom after the polymerization.

To obtain the required azide functionality, **15** was treated with sodium azide for 3 days at room temperature. Complete conversion of the nucleophilic substitution was verified by means of ^{1}H NMR and FT-IR spectroscopy. The multiplet corresponding to the methine proton shifted from ~4.09 ppm

Scheme 5. Grafting onto of Azide-Terminated P(*t*-BA) Side Chains (16) via Click Reaction and Cleavage of *tert*-Butyl Protecting Groups To Obtain Polyelectrolyte Brush Copolymers 19a–c and 20a–c[a]



[a]Reagents and conditions: (i) CuBr, PMDETA, anhydrous toluene, argon, rt, 5 days, quantitative; (ii) TFA, DCM, rt, 1 day, 99%.

dx.doi.org/10.1021/ma202209u | *Macromolecules* 2012, 45, 2301–2311

(bromo species **15**) to ~3.75 ppm in the azide derivative **16**, indicating a quantitative conversion

Additionally, the FT-IR spectrum (Figure 1) of the azide end-functional P(*t*-BA) (**16**) showed the carbonyl band at 1722

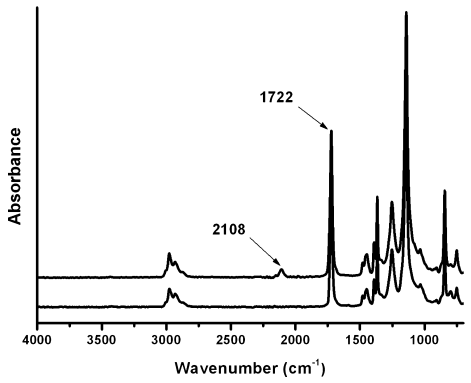


Figure 1. FT-IR spectra of P(*t*-BA)Br (**15**, lower line) and P(*t*-BA)N_3 (**16**, upper line).

cm^{-1} (lit.: 1726 cm^{-1})[31] and the azide band at 2108 cm^{-1} (lit.: 2100 cm^{-1}).[32,33] Consequently, the replacement of the bromo end group was confirmed.

The attachment of azide-terminated P(*t*-BA) side chains (**16**) was achieved via "Sharpless-type-click" reaction under Cu(I) catalysis and in the presence of PMDETA (Scheme 5).[34,35] Under these conditions, the cycloaddition is regioselective and highly efficient since copper can bind to the alkyne.[24] Finn et al. showed that such a type of reaction can be accelerated by using appropriate ligands like 4,4′-di(5-nonyl-2,2′-bipyridine) (dNbipy) and PMDETA.[36,37] Thus, this reaction is an excellent candidate to functionalize polymeric materials.

A proof of the quantitative 1,3-dipolar cycloaddition via ^{1}H NMR spectroscopy was not possible. Although a signal at 1.4 ppm demonstrated the appearance of *tert*-butyl groups, the proton of the 1,2,3-triazole group in the range of 7.5−8.0 ppm was not distinguishable from the aromatic backbone protons. Also, due to the low concentration of alkynyl groups, the absence of a signal at 2.1 ppm could not be considered as a strong evidence for a quantitative click reaction. The success of the grafting process was confirmed by FT-IR spectroscopy. The spectra, for example, of brush copolymer **17a** (Figure 2) showed the carbonyl signal at 1715 cm^{-1} of the *tert*-butyl

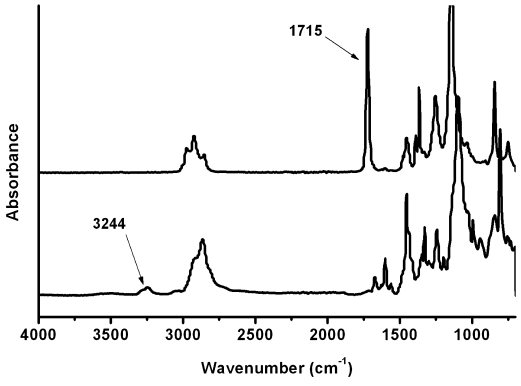


Figure 2. FT-IR spectra of backbone **11a** (lower line) and graft copolymer **17a** (upper line).

groups and the disappearance of the very specific alkynyl band at 3244 cm^{-1}.

A further indication of the successful grafting process was the increase of the molecular weights for all copolymers **17a−c** and **18a−c** (Table 2) in comparison with the backbones **7a−c** and **10a−c** (Table 1).

Table 2. GPC Data (Determined against PS Standard in THF) of Both Alternating (17a−c) and Statistical (18a−c) Conjugated Backbones with P(*t*-BA) Side Chains

backbone	M_n [g/mol]	M_w [g/mol]	M_n/M_w	no. of Cz units	no. of grafted P(*t*-BA) chains	conv of alkyne groups [%]
17a	103 000	316 000	3.0	18	16	89
17b	48 000	133 000	2.8	10	6	60
17c	66 000	649 000	10	18	9	50
18a	74 000	229 000	3.1	10	6	60
18b	15 300	35 000	2.3	3	0	0
18c	41 000	70 000	1.7	6	4	67

However, an exact quantification of the degree of functionalization was rather difficult. From literature it is known that typically for graft copolymers the real molecular weights are underestimated as comb-type structures have a more compact structure than the used polymeric standards. Thus, the herein calculated values can only be considered as a rough estimation. Therefore, the number of alkynyl groups at the main chains of **7a−c** and **10a−c** (Table 2) was determinated based on the degrees of polymerization (GPC) and on the amount of carbazole units (elemental analyses) (Table 1). The differences between the molecular weights of the backbones **7a−c** and **10a−c** and the comb-type polymers **17a−c** and **18a−c** were calculated as these values correspond to the contribution of the P(*t*-BA) chains to the overall molecular weights in the comb-type polymer. By dividing these values with the molecular weight of the P(*t*-BA) chains, the average number of grafts per brush polymer was calculated (Table 2). As expected, the increase of molecular weight after click reaction was too low for a quantitative grafting, resulting in degrees of conversion of 50−89% (Table 2). In case of brush polymer **18b**, no attachment of polymeric side chains could be confirmed by GPC measurements, since no increase of the molecular weight was detected. One possible reason is the very low number of alkynyl groups along the backbone **10b**, since even a quantitative conversion would cause no high increase of molecular weight. In contrast to these results, Bunz et al. detected degrees of postfunctionalization >95% by ^{1}H NMR spectroscopy after functionalization of poly(*p*-phenylene−ethynylene)s by means of 1,3-dipolar cycloaddition.[38] Reasons for the higher conversion might be the use of shorter and monodisperse substituents, e.g., dodecyl or 3,4-dibenzyloxybenzyl groups, and the possibility to confirm the conversion by integration of the signal of the formed triazole at 7.5−8.0 ppm in ^{1}H NMR spectra. In contrast to GPC measurements, the latter are not affected by a comb-type or linear structure of the analyzed polymer and therefore provide precise results.

To achieve the desired polyelectrolyte structures **19a−c** and **20a−c**, the precursor polymers **17a−c** and **18a−c** were treated with trifluoroacetic acid (Scheme 5). The cleavage of protecting groups was proved by ^{1}H NMR spectroscopy. Comparison of the integrals of the signals of the methyl ester protons from the MBP moiety and the protecting groups allowed the calculation

dx.doi.org/10.1021/ma202209u | *Macromolecules* 2012, 45, 2301−2311

of the conversion. After deprotection the ratio of these methyl ester protons shifted from 3:~148 ($-COOCH_3$:$-COOC-(CH_3)_3$) in the neutral copolymers **17a−c** and **18a−c** to 3:2 for the polyelectrolytes **19a−c** and **20a−c**. Therefore, more than 98% of the protecting groups were removed, indicating an almost quantitative reaction.

Additionally, the appearance of a broad signal from 3680−2200 cm^{-1} in the FT-IR-spectra of the graft copolymers **19a−c** and **20a−c** confirmed the formation of carbonic acid groups (Figure 3).

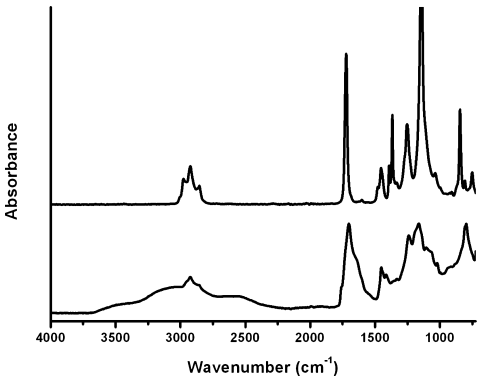


Figure 3. FT-IR spectra of the comb-type polymer with P(*t*-BA) side chains **17a** (upper line) and after hydrolysis to PAA **19a** (lower line).

In conclusion, various comb-type polyelectrolytes with carbazole−fluorene backbones and PAA side chains were polymerized by means of the grafting onto technique via click chemistry. The amphiphilicity of the graft polymers was varied by using polar and unpolar substituents at the 9-position of the fluorene units and different ratios of charged and uncharged segments. The utilization of carbazole−fluorene copolymers as well as a grafting onto technique instead of a macromonomer technique to polymerize polycarbazole graft polymers with poly(L-lysine) side chains[18] led to higher degrees of polymerization. This result was attributed to a decreased steric hindrance by using low molecular weight monomers during polymerization of the conjugated backbones via Suzuki reaction.

As conjugated polyelectrolyte brush polymers have already shown pH-dependent conformational changes along the backbone resulting in different optical properties,[13,14] a similar behavior from the here described comb-type polymers with highly charged side chains can be expected. For this reason, investigations on the pH sensitivity were performed on brush polymer **19a** in a DMF/water mixture (1:1).

pH-dependent UV−vis and PL spectra of **19a** are shown in Figure 4, and the absorption and emission maxima are reported in Table 3. To achieve a comparable concentration for all

Table 3. Absorption and Emission Maxima of Compound 19a at Different pH Values in a DMF/Water Mixture (1:1)

pH value	λ_{max}^{abs} [nm]	λ_{max}^{em} [nm]
0.5	406	435
2	405	434
5	402	427
7	400	425

absorption and photoluminescence measurements, a stock solution of polymer **19a** in DMF (c = 1.0 × 10^{-6} M) was prepared. Exactly 5 mL of this solution was pipetted into a 10 mL volumetric flask and filled up with an aqueous solution with the desired pH.

Polymer **19a** showed a strong absorption band in the range of 400−406 nm, which arose from the π, π^* transition. The band shape was very similar to those of uncharged polycarbazole, polyfluorene, and carbazole−fluorene copolymer derivatives.[39]

By increasing the acidity of the solution, a red shift (6 nm) of the absorption maximum of **19a** occurred. A similar bathochromic shift in absorption when going from a neutral to an acidic solution has been observed for conjugated anionic polyelectrolytes with 2−4 carboxylic acid groups on every second repeating unit.[13,14] Thus, it is assumed, that in case of polyelectrolyte **19a** the same processes as described by Bazan et al. and Bunz et al. took place. The protonation of the carboxylic groups led to a decreasing electrostatic interchain repulsion and resulted in $\pi-\pi$ stacking. However, the detected changes during pH-dependent UV−vis measurements were influenced by the structure of the conjugated backbone. While the absorption maximum of poly(*p*-phenylene−ethynylene)s with carboxylic acid functionalities shifted from 425 to 455 nm (30 nm) by varying the pH from 7 to 3,[14] the absorption maximum of poly(*p*-phenylene−fluorene) derivatives shifted from 370 to 382 nm (12 nm) by changing the pH from 7 to 1.[13] In comparison to these results, the UV−vis properties of **19a**

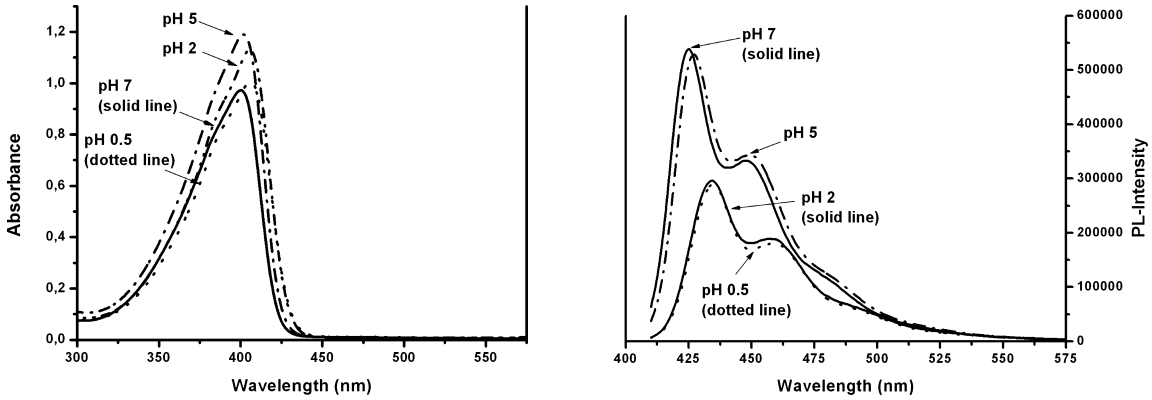


Figure 4. Absorption and photoluminescence spectra (λ_{exc} = 403 nm) of compound **19a** (c = 0.5 × 10^{-6} M) as a function of pH in a DMF/water mixture (1:1).

dx.doi.org/10.1021/ma202209u | *Macromolecules* 2012, 45, 2301−2311

shifted only slightly (6 nm). Furthermore, our previously reported polyelectrolyte brush polymer based on a polycarbazole backbone and poly(L-lysine) side chains did not show any changes of the absorption maxima at different pH-values ranging from 0 to 14.[18] Thus, the conformation of the polycarbazole backbone was not strongly affected by switching the PLL chains from random coil to helix. These results show that with a loss of conformational freedom of the main chain, caused by the bridged phenylene units in the fluorene and carbazole units, the influence of pH-responsive side chains on the absorption properties decreases too.[40] However, because of the increase of the number of charged units per side chain from 20 in the PLL homopeptides to ~40 in the PAA side chains, pH-dependent UV−vis properties were obtained.

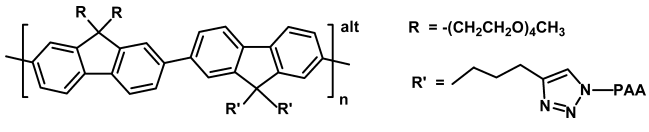
In accordance with the absorption behavior of **19a** the fluorescence was pH-dependent, too. At low pH the emission intensity was decreased and red-shifted in comparison to a neutral solution. The bathochromic shift was attributed to a protonation of the carboxylic groups resulting in uncharged polymers, a decreased interchain electrostatic repulsion, and a planarization of the main chain.[13,14] Thus, $\pi-\pi$ stacking was preferred and aggregation took place. In contrast to the pH-independent conformation of the polycarbazole backbone in the polyelectrolyte brush polymer with poly(L-lysine) side chains, both UV−vis and fluorescence characteristics of **19a** showed conformation changes.

CONCLUSION

A versatile synthetic strategy to prepare comb-type polyelectrolytes with conjugated backbones and sufficient degrees of polymerization is presented. By employing a grafting onto technique via click chemistry, a series of conjugated, highly charged brush copolymers based on 2,7-linked fluorene and carbazole units with poly(acrylic acid) side chains were prepared. In dependence upon the ratio of dibromo- and diboronic ester fluorene and carbazole monomers, Suzuki polycondensation led to alternating or statistical copolymers. Furthermore, the amphiphilicity of the graft polymers was varied by using polar TEG and unpolar alkyl groups at the 9-position of the fluorene units as well as by changing the substitution pattern.

It is expected that the solubility of the conjugated brush copolymers can be adjusted by using a polyfluorene backbone with an alternating substitution pattern of PAA and TEG side chains due to two polyelectrolyte side chains at one conjugated repeating unit.

Scheme 6. Polyelectrolyte Brush Copolymer with a Polyfluorene Backbone and Alternating PAA and TEG Side Chains



Furthermore, polyfluorene graft polymers with a high number of carboxylate groups on each conjugated monomer might be useful as cylindrical, wirelike templates for conductive and/or magnetic inorganic/organic nanoparticles by coordinating metal ions. In comparison with aliphatic templates the use of polyfluorenes might allow a broader range of applications because of the high thermal stability of conjugated polymers.

EXPERIMENTAL PART

Analysis. ^{1}H and ^{13}C nuclear magnetic resonance (NMR) spectra were recorded on a Bruker DPX 250, AMX 500, or Avance 700 with use of the solvent signal as an internal standard. Melting points were determined on a Büchi hot stage apparatus and are not corrected. Mass spectra were obtained on a VG Instruments ZAB2-SE-FPD by using field desorption (FD). Elemental analyses were carried out on a Foss Heraeus Vario EL. Gel permeation chromatography (GPC) was performed with PSS columns (500, 10^5, and 10^6 Å pore widths) with THF as a solvent or with PSS-SDV columns (500, 10^5, and 10^6 A pore widths) and DMF as solvent (concentration of the polymer 0.1 g/L). Both columns were connected to an UV−vis/refractive index (RI) detector. The calibration was based on polystyrene standards with narrow molecular weight distribution. Infrared (IR) data were obtained on a Nicolet FT-IR 730 using the attenuated total reflection (ATR) under a nitrogen atmosphere. UV−vis absorption spectra were measured using a Perkin-Elmer Lambda 900 spectrophotometer. The fluorescence emission spectra were recorded on a SPEX Fluorolog 2 type F 212 spectrofluorometer (Xe, 450 W).

Materials. 2,7-Dibromofluorene was purchased from Aldrich and used as received. 2,7-Dibromocarbazole (**1**),[41] (5-iodopent-1-ynyl)-trimethylsilane (**2**),[42] 2,7-bis(4,4,5,5-tetramethyl-1,3,2-dioxaborolan-2-yl)-9,9-bis(1-{2-[2-(2-methoxyethoxy)ethoxy]ethoxy}ethyl)fluorene (**6a**),[25] 2,7-bis(4,4,5,5-tetramethyl-1,3,2-dioxaborolan-2-yl)-9,9-bis(2-decyltetradecyl)fluorene (**6b**),[26] 2,7-bis(4,4,5,5-tetramethyl-1,3,2-dioxaborolan-2-yl)-9,9-bis(2-ethylhexyl)fluorene (**6c**),[26] 2,7-bis(4,4,5,5-tetramethyl-1,3,2-dioxaborolan-2-yl)-*N*-(5-triisopropylsilyl-pent-4-inyl)carbazole (**8**),[43] 2,7-dibromo-9,9-bis(1-{2-[2-(2-methoxyethoxy)-ethoxy]ethoxy}ethyl)fluorene (**9a**),[25] 2,7-dibromo-9,9-bis(2-decyltetradecyl)fluorene (**9b**),[27] and 2,7-dibromo-9,9-bis(2-ethylhexyl)fluorene (**9c**)[41] were synthesized according to the literature. *tert*-Butyl acrylate (**14**) (*t*-BA, 99%, Acros) was stirred over CaH_2 and distilled in high vacuum. CuBr (95%, Aldrich) was refluxed in acetic acid for 1 h. After filtration, it was washed with ethanol and diethyl ether and then dried. *N,N,N′,N″,N″*-Pentamethyldiethylenetriamine (PMDETA, 99%, Aldrich), methyl 2-bromopropionate (**13**) (99%, Aldrich), $CuBr_2$ (99+%, Acros), triisopropylsilyl chloride (97%, Aldrich), (5-chloro-1-pentynyl)trimethylsilane (97%, Aldrich), and sodium azide (99%, Aldrich) were used without further purification.

Synthesis of 2,7-Dibromo-*N*-(5-trimethylsilyl-4-pentinyl)-carbazole (3). To a solution of 2,7-dibromocarbazole (**1**) (4.1 g, 12.5 mmol) in anhydrous DMF (50 mL), NaH (450 mg, 60% w/w dispersion in mineral oil, 18.8 mmol) was added under an argon atmosphere. After 30 min, (5-iodopent-1-ynyl)trimethylsilane (5.0 g, 18.8 mmol) was added, and the solution was stirred overnight under argon. The reaction was quenched with water and extracted with DCM. The organic phase was dried ($MgSO_4$), and the solvent was removed under reduced pressure. The product was purified by column chromatography (hexane/DCM 4/1) to give 2,7-dibromo-*N*-(5-trimethylsilanylpent-4-ynyl)carbazole (**3**) as a colorless solid. Yield: 4.2 g (73%); mp: 82 °C. ^{1}H NMR (250 MHz, $CDCl_3$): δ [ppm] = 7.87 (d, J = 8.3 Hz, 2 H, Cz), 7.62 (d, J = 1.5 Hz, 2 H, Cz), 7.33 (dd, J = 1.5 Hz, J = 8.3 Hz, 2 H, Cz), 4.36 (t, J = 6.7 Hz, 2 H, (Cz−CH_2−)), 2.24 (t, J = 6.4 Hz, 2 H, (−CH_2−C≡C−TMS)), 2.08−1.98 (m, 2 H, (−CH_2−CH_2−CH_2−)), 0.24 (s, 9 H, (−C≡C−Si(CH_3)$_3$)). ^{13}C NMR (63 MHz, $CDCl_3$): δ [ppm] = 141.44, 122.75, 121.46, 119.82, 112.05, 105.45, 86.61, 41.64, 27.50, 17.41, 0.18. FD-MS: m/z = 463.6 [M^+] (calcd: 463.28). Anal. Calcd for $C_{20}H_{21}Br_2NSi$: 51.85% C, 4.57% H, 3.02% N. Found: 51.76% C, 4.41% H, 3.04% N.

Deprotection of the TMS Protecting Group (4). Compound **3** (4.0 g, 8.71 mmol) was dissolved in THF (100 mL) and treated with MeOH (50 mL) and KOH (10% in water, 6 mL). The solution was stirred at room temperature overnight. The solvent was removed under reduced pressure, and the product was purified by column chromatography (hexane/DCM 1/4) to give 2,7-dibromo-*N*-(pent-4-ynyl)carbazole (**4**) as a colorless solid. Yield: 3.0 g (88%); mp: 85 °C. ^{1}H NMR (250 MHz, CD_2Cl_2): δ [ppm] = 7.87 (d, J = 8.3 Hz, 2 H, Cz), 7.61 (d, J = 1.4 Hz, 2 H, Cz), 7.33 (dd, J = 1.5 Hz, J = 8.3 Hz, 2

dx.doi.org/10.1021/ma202209u | Macromolecules 2012, 45, 2301−2311

H, Cz), 4.36 (t, J = 6.8 Hz, 2 H, (Cz−CH_2−)), 2.37−1.85 (m, 5 H, (−CH_2−CH_2−C≡CH)). ^{13}C NMR (63 MHz, CD_2Cl_2): δ [ppm] = 141.77, 122.96, 121.85, 121.67, 120.00, 112.51, 83.37, 69.96, 42.12, 27.74, 16.31. FD-MS: m/z = 391.8 [M^+] (calcd: 391.10). Anal. Calcd for $C_{17}H_{13}Br_2N$: 52.21% C, 3.35% H, 3.58% N. Found: 52.22% C, 3.44% H, 3.39% N.

Synthesis of 2,7-Dibromo-*N*-(5-triisopropylsilylpent-4-inyl)-carbazole (5).[44] A solution of compound **4** (4.8 g, 12.2 mmol) and anhydrous THF (40 mL) was cooled to −75 °C under an argon atmosphere. Subsequently, lithium diisopropylamide (7.3 mL, 14.7 mmol) was added dropwise, and the solution was stirred for 1 h. In a second step, a mixture of triisopropyl chloride (5.2 mL, 24.4 mmol), anhydrous THF (30 mL), and anhydrous DMSO (9.5 mL) was added. This solution was stirred overnight while the temperature was allowed to rise to room temperature. After the addition of 2 N hydrochloric acid (500 mL), the water fraction was extracted with CH_2Cl_2. The combined organic fractions were dried ($MgSO_4$) and filtered. Finally, the solvent was removed under reduced pressure, and the crude product was purified by column chromatography (5% EtOAc in hexane) to give compound **5** as a colorless solid (3.4 g, 51%). Yield: 3.40 g (51%); mp: 82 °C. ^{1}H NMR (250 MHz, $CDCl_3$): δ [ppm] = 7.87 (d, J = 8.3 Hz, 2 H, Cz), 7.58 (d, J = 1.5 Hz, 2 H, Cz), 7.33 (dd, J = 1.6 Hz, J = 8.3 Hz, 2 H, Cz), 4.37 (t, J = 7.1 Hz, 2 H, (Cz−CH_2−)), 2.35 (t, J = 6.5 Hz, 2 H, (Cz−CH$_2$−CH$_2$−CH_2−)), 2.13−1.89 (m, 2 H, (Cz−CH$_2$−CH_2−CH$_2$−)), 1.12 (s, 21 H, TIPS). ^{13}C NMR (63 MHz, $CDCl_3$): δ [ppm] = 141.38, 122.77, 121.46, 121.32, 119.84, 111.89, 106.91, 82.29, 41.99, 27.88, 18.77, 17.66, 11.34. FD-MS: m/z = 547.8 [M^+] (calcd: 547.44). Anal. Calcd for $C_{26}H_{33}Br_2NSi$: 57.04% C, 6.08% H, 2.56% N. Found: 57.32% C, 6.23% H, 2.35% N.

Synthesis of the Conjugated Backbones via Suzuki Polycondensation (Table 1). *Alternating Carbazole−Fluorene Copolymers **7a−c**.* A mixture (ratio 1:1) of a dibromide and a diboronic ester monomer (one fluorene and one carbazole unit) was dissolved in toluene (c = 0.18 mol/L). After the addition of aqueous Et_4NOH (35 wt %, 3.5 mL, 6.5 equiv) the reaction mixture was degassed four times by applying the freeze-and-thaw technique. Finally, $Pd^0(PPh_3)_4$ (5 mol %) was added under an argon atmosphere, and the reaction mixture was stirred at 90 °C for 3 h. After cooling to room temperature the solution was diluted with CH_2Cl_2. The organic fraction was washed with water until the filtrate had a neutral pH value, dried ($MgSO_4$), and filtrated. Finally, the solvent was evaporated in order to obtain a concentrated solution, which was added dropwise either in *n*-hexane (**7a**) or in methanol (**7b,c**). The precipitate was filtered off, dissolved in THF, and reprecipitated to remove impurities. The yellow polymer was dried under reduced pressure.

*Statistical Carbazole−Fluorene Copolymers **10a−c**.* A procedure identical to the one described above was utilized. However, the fluorene amount was higher than 50%. Therefore, three different conjugated monomers instead of two were used. While only one carbazole derivative (14% of either dibromide or diboronic acid) was selected, both types of fluorene units were applied. Nevertheless, the ratio of the two coupling groups was 1:1.

^{1}H NMR (**7a**) (500 MHz, CD_2Cl_2) δ [ppm] = 8.25−7.64 (m, 12 H, (Cz + Fl)), 4.67 (s, 2 H, (Cz−CH$_2$−)), 3.46−2.28 (m, 42 H, ((−CH$_2$−), (−CH$_3$))), 1.11 (s, 21 H, TIPS). Anal. Calcd for $C_{57}H_{77}O_8NSi$: 73.46% C, 8.27% H, 1.50% N. Found (**7a**): 70.93% C, 7.26% H, 1.35% N. Found (**10a**): 66.21% C, 8.30% H, 0.34% N. ^{1}H NMR (**7b**) (500 MHz, CD_2Cl_2) δ [ppm] = 8.41−7.28 (m, 12 H, (Cz + Fl)), 4.61 (s, 2 H, (Cz−CH_2−)), 2.51−2.24 (m, 8 H, alkyl), 1.36−0.70 (m, 117 H, (alkyl, TIPS)). Anal. Calcd for $C_{87}H_{137}NSi$: 85.36% C, 11.20% H, 1.14% N. Found (**7b**): 84.53% C, 11.26% H, 0.99% N. Found (**10b**): 86.14% C, 14.01% H, 0.25% N. ^{1}H NMR (**7c**) (250 MHz, CD_2Cl_2) δ [ppm] = 8.24−7.18 (m, 12 H, (Cz + Fl)), 4.61 (s, 2 H, (Cz−CH_2−)), 2.49−2.22 (m, 8 H, (−CH$_2$−) + (Cz−CH$_2$−CH_2−CH_2−)), 1.36−0.65 (m, 51 H, (alkyl, TIPS)). Anal. Calcd for $C_{55}H_{73}NSi$: 85.16% C, 9.41% H, 1.80% N. Found (**7c**): 84.23% C, 8.87% H, 1.58% N. Found (**10c**): 85.33% C, 10.81% H, 0.41% N.

Cleavage of the TIPS Protecting Group (11a−c, 12a−c).[45] Copolymer **7a−c** or **10a−c** (100 mg) was dissolved in THF (25 mL). After the addition of tetrabutylammonium fluoride (1.2 equiv per TIPS group, 1 M THF solution), the reaction mixture was stirred for 3 h at room temperature. Subsequently, the solvent was removed under reduced pressure and the residue was dissolved in CH_2Cl_2. The organic fraction was washed with water, dried (Na_2SO_4), and filtered. Finally, the solvent was evaporated in order to obtain a concentrated solution, which was added dropwise into *n*-hexane (**11a** and **12a**) or methanol (**11b−c** and **12b−c**). The crude product was dissolved in THF and reprecipitated to remove impurities. The precipitate was filtered off and dried in a vacuum to give copolymer **11a−c** and **12a−c**. ^{1}H NMR (**11a**) (500 MHz, CD_2Cl_2): δ [ppm] = 8.25−7.64 (m, 12 H, (Cz + Fl)), 4.72 (bs, 2 H, (Cz−CH$_2$−)), 3.46−2.28 (m, 42 H (−CH$_2$−), (−CH$_3$)). ^{1}H NMR (**11b**) (500 MHz, CD_2Cl_2): δ [ppm] = 8.21−7.49 (m, 12 H, (Cz + Fl)), 4.64 (bs, 2 H, (Cz−CH_2−)), 2.34−2.16 (m, 5 H, (Cz−CH$_2$−CH_2−CH_2−C≡CH)), 0.93−0.61 (m, 34, (−CH$_2$−) + (−CH$_3$)). ^{1}H NMR (**11c**) (500 MHz, CD_2Cl_2): δ [ppm] = 8.66−7.19 (m, 12 H, (Cz + Fl)), 4.64 (s, 2 H, (Cz−CH_2−)), 2.35−2.09 (m, 5 H, (Cz−CH$_2$−CH_2−CH_2−C≡CH)), 1.26−0.82 (m, 98 H, (−CH$_2$−), (−CH$_3$)).

Preparation of Bromine End-Functional Poly(*tert*-butyl acrylate) by Atom Transfer Radical Polymerization (15).[30] CuBr (117 mg, 0.81 mmol) and $CuBr_2$ (9 mg, 0.04 mmol) were added to a flask, which was sealed with a septum, degassed, and backfilled with argon three times. Deoxygenated acetone (3 mL) and *t*-BA (12 mL, 82 mmol) were added with a syringe. After PMDETA (180 μL, 0.86 mmol) was added, the solution was stirred until it became clear, and the color turned into light green due to the formation of the copper complex. Finally, methyl 2-bromopropionate (183 μL, 1.64 mmol) was added, and the flask was placed in an oil bath thermostated at 60 °C. After stirring for 320 min the solution was cooled to room temperature. The mixture was filtered through a funnel containing Al_2O_3 to obtain a colorless solution as result of the copper complex extraction. The polymer was precipitated into a methanol/water (1/1) mixture and freeze-dried to give colorless poly(*tert*-butyl acrylate). Yield: 10.0 g (95%); M_n = 5300 g/mol; M_n/M_w = 1.23. ^{1}H NMR (250 MHz, $CDCl_3$) δ [ppm] = 4.17−4.01 (m, (−CH$_2$−CH(COO(*t*-butyl)−Br))), 3.63 (s, −(COOCH$_3$)), 2.21 (bs, (−CH−)), 1.80 (bs, (−CH$_2$−)), 1.41 (bs, (−C(CH$_3$)$_3$)), 1.11 (bs, (−CH−(COOCH$_3$)−CH_3)).

Azidation of the Bromo End Group of Poly(*tert*-butyl acrylate) (16).[46] P(*t*-BA)-Br (**15**) (M_n = 5300 g/mol, 10.00 g, 2.2 mmol) was solved in a mixture of DMF (155 mL) and water (6 mL) and treated with NaN_3 (325 mg, 5.0 mmol). The solution was stirred at room temperature for 3 days. Then, the solution was diluted with dichloromethane and washed with water. The organic layer was dried over $MgSO_4$, filtered, and concentrated. Finally, the polymer **16** was precipitated into a methanol/water (1/1) mixture and freeze-dried. Yield: 9.85 g (98%) M_n = 6100 g/mol, M_n/M_w = 1.14. ^{1}H NMR (250 MHz, $CDCl_3$) δ [ppm] = 3.78−3.71 (m, (−CH$_2$−CH(COO(*t*-butyl)−N$_3$))), 3.63 (s, −(COOCH$_3$)), 2.20 (bs, (−CH−)), 1.80 (bs, (−CH$_2$−)), 1.41 (bs, (−C(CH$_3$)$_3$)), 1.15 (bs, (−CH−(COOCH$_3$)−CH_3)). Anal. Calcd for $C_{340}H_{583}N_3O_{98}$: 67.52% C, 8.63% H, 0.62% N. Found: 64.76% C, 9.26% H, 0.66% N.

Click Reaction of Azide End-Functional P(*t*-BA) Chains and an Alkyne Containing Conjugated Backbone (17a−

c, 18a–c).[34] An alkyne containing conjugated backbone (1.0 equiv), P(*t*-BA)-N_3 (**16**) (1.2 equiv), CuBr (0.5 equiv), and PMDETA (0.5 equiv) were dissolved in anhydrous toluene under an argon atmosphere. The flask was sealed with a septum, and the solution was stirred for 5 days at room temperature. The mixture was diluted with THF, filtered through a funnel with Al_2O_3 to extract the copper complex, and concentrated. Finally, the polymers **17a** and **18a** were precipitated into hexane whereas **17b–c** and **18b–c** were precipitated into methanol. The crude products were dissolved in THF and reprecipitated to remove impurities. The precipitation was filtered off and dried under reduced pressure to give the graft polymers **17a–c** and **18a–c**.

Table 4. Optical Properties, Yields, and GPC Data of the Comb-Type Polymers with P(*t*-BA) Side Chains 17a–c and 18a–c

graft polymer	*m* (backbone) [mg]	M_n [g/mol]	M_n/M_w	*m* (graft polymer) [mg]	λ_{max}^{abs} [nm]	λ_{max}^{em} [nm]
17a	300	103 000	3.0	560	395	424
17b	100	48 000	2.8	108	395	422
17c	80	66 000	10	113	393	420
18a	200	74 000	3.1	221	394	421
18b	100	15 300	2.3	78	379	417
18c	100	41 000	1.7	15	387	419

Deprotection of the *tert*-Butyl Protecting Group (19a–c, 20a–c).[47] Quantitative deprotection of *tert*-butyl groups was achieved by hydrolysis with 10-fold excess of trifluoroacitic acid in DCM at room temperature for 24 h. During the hydrolysis, precipitation of the resulting PAA copolymers **19a–c** and **20a–c** took place. Finally, DCM and trifluoroacetic acid were removed via rotating evaporation and the polymer was dried in a vacuum.

Table 5. Yields of the Conjugated Polyelectrolytes 19a–c and 20a–c

polyelectolyte	*m* (precursor) [mg]	*m* (polyelectrolyte) [mg]
19a	100	93
19b	95	93
19c	65	29
20a	185	100
20b	37	36
20c	15	10

AUTHOR INFORMATION

Notes

The authors declare no competing financial interest.

REFERENCES

(1) Leclerc, M. *J. Polym. Sci., Part A: Polym. Chem.* **2001**, *39*, 2867–2873.
(2) Mitschke, U.; Bauerle, P. *J. Mater. Chem.* **2000**, *10*, 1471–1507.
(3) Grimsdale, A. C.; Müllen, K. *Macromol. Rapid Commun.* **2007**, *28*, 1676–1702.
(4) Cianga, I.; Yagci, Y. *Prog. Polym. Sci.* **2004**, *29*, 387–399.
(5) Schlüter, A. D. *J. Polym. Sci., Part A: Polym. Chem.* **2001**, *39*, 1533–1556.
(6) Ranger, M.; Leclerc, M. *Chem. Commun.* **1997**, 1597–1598.
(7) Wallow, T. J.; Novak, B. M. *J. Am. Chem. Soc.* **1991**, *113*, 7411–7412.
(8) Kim, S.; Jachino, J.; Robinson, E.; Schanze, K. S.; Reynolds, J. R.; Baur, J.; Rubner, M. F. *Macromolecules* **1998**, *31*, 964–974.
(9) Liu, B.; Bazan, G. C. *J. Am. Chem. Soc.* **2006**, *128*, 1188–1196.
(10) Huang, F.; Hou, L.; Wu, H.; Wang, X.; Shen, H.; Cao, W.; Yang, W.; Cao, Y. *J. Am. Chem. Soc.* **2004**, *126*, 9845–9853.
(11) Liu, B.; Yu, W.-L.; Lai, Y.-H.; Huang, W. *Macromolecules* **2002**, *35*, 4975–4982.
(12) Pinto, M. R.; Schanze, K. S. *Synthesis* **2002**, *9*, 1293–1309.
(13) Wang, F.; Bazan, G. C. *J. Am. Chem. Soc.* **2006**, *128*, 15786–15792.
(14) Kim, I.-B.; Philips, R.; Bunz, U. H. F. *Macromolecules* **2007**, *40*, 5290–5293.
(15) Pinto, M. R.; Kristal, B. M.; Schanze, K. S. *Langmuir* **2003**, *19*, 6523–6533.
(16) McLean, S. C.; Gee, M. L. *Macromolecules* **2007**, *40*, 4644–4653.
(17) Rempp, P.; Franta, E. *Adv. Polym. Sci.* **1984**, *58*, 1–53.
(18) Fruth, A.; Klapper, M.; Müllen, K. *Macromolecules* **2010**, *43*, 467–472.
(19) Zhang, M.; Müller, A. H. E. *J. Polym. Sci., Part A: Polym. Chem.* **2005**, *43*, 3461–3481.
(20) André, X.; Zhang, M.; Müller, A. H. E. *Macromol. Rapid Commun.* **2005**, *26*, 558–563.
(21) Matyjaszewski, K.; Xia, J. *Chem. Rev.* **2001**, *101*, 2921–2990.
(22) Lutz, J.-F. *Angew. Chem.* **2007**, *119*, 1036–1043.
(23) Kolb, H. C.; Finn, M. G.; Sharpless, K. B. *Angew. Chem., Int. Ed.* **2001**, *40*, 2004–2021.
(24) Rostovtsev, V. V.; Grenn, L. G.; Fokin, V. V.; Sharpless, K. B. *Angew. Chem., Int. Ed.* **2002**, *41*, 2596–2599.
(25) Sax, S.; Rugen-Penkalla, N.; Neuhold, A.; Schuh, S.; Zojer, E.; List, E. J. W.; Müllen, K. *Adv. Mater.* **2010**, *22*, 2087–2091.
(26) Thiem, H.; Jandke, M.; Hanft, D.; Strohriegel, P. *Macromol. Chem. Phys.* **2006**, *207*, 370–381.
(27) Dierschke, F. Dissertation, Universität Mainz, 2005.
(28) Hassan, J.; Sévignon, M.; Gozzi, C.; Schulz, E.; Lemaire, M. *Chem. Rev.* **2002**, *102*, 1359–1470.
(29) Qin, A.; Jim, C. K. W.; Lu, W.; Lam, J. W. Y.; Häussler, M.; Dong, Y.; Sung, H. H. Y.; Williams, I. D.; Wong, G. K. L.; Tang, B. Z. *Macromolecules* **2007**, *40*, 2308–2317.
(30) Davis, K. A.; Matyjaszewski, K. *Macromolecules* **2000**, *33*, 4039–4047.
(31) Parrish, B.; Breitenkamp, R. B.; Emrick, T. *J. Am. Chem. Soc.* **2005**, *127*, 7404–7410.
(32) Kluger, C.; Binder, W. H. *J. Polym. Sci., Part A: Polym. Chem.* **2007**, *45*, 485–499.
(33) Agut, W.; Taton, D.; Lecommandoux, S. *Macromolecules* **2007**, *40*, 5653–5661.
(34) Vogt, A. P.; Sumerlin, B. S. *Macromolecules* **2006**, *39*, 5286–5292.
(35) Huisgen, R. In *1,3-Dipolar Cycloaddtion Chemistry*; Padwa, A., Ed.; Wiley: New York, 1984; p 1.
(36) Chan, T. R.; Hilgraf, R.; Sharpless, K. B.; Fokin, V. V. *Org. Lett.* **2004**, *6*, 2853–2855.
(37) Lewis, W. G.; Magallon, F. G.; Fokin, V. V.; Finn, M. G. *J. Am. Chem. Soc.* **2004**, *126*, 9152–9153.
(38) Englert, B. C.; Bakbak, S.; Bunz, U. H. F. *Macromolecules* **2005**, *38*, 5868–5877.
(39) Morin, J.-M.; Beaupré, S.; Leclerc, M.; Lévesque, I.; D'Iorio, M. *Appl. Phys. Lett.* **2002**, *80*, 341–343.
(40) Kim, B.; Chen, L.; Gong, J.; Osada, Y. *Macromolecules* **1999**, *32*, 3964–3969.
(41) Dierschke, F.; Grimsdale, A. C.; Müllen, K. *Synthesis* **2003**, *16*, 2470–2472.
(42) Miller, J. A.; Nunn, M. J. *J. Chem. Soc., Perkin Trans. 1* **1976**, 416–420.
(43) Fruth, A. Dissertation, Universität Mainz, 2009.

(44) Brandsma, L. In *Preparative Acetylenic Chemistry*, 2nd ed.; Elsevier: Amsterdam, 1992; pp 26 and 122.
(45) Bauer, R. E.; Clark, C. G.; Müllen, K. *New J. Chem.* **2007**, *31*, 1275−1282.
(46) Golas, P. L.; Tsarevsky, N. V.; Sumerlin, B. S.; Matyjaszewski, K. *Macromolecules* **2006**, *39*, 6451−6457.
(47) Zhang, M.; Breitner, T.; Mori, H.; Müller, A. H. E. *Polymer* **2003**, *44*, 1449−1458.

Macromolecules

Article

pubs.acs.org/Macromolecules

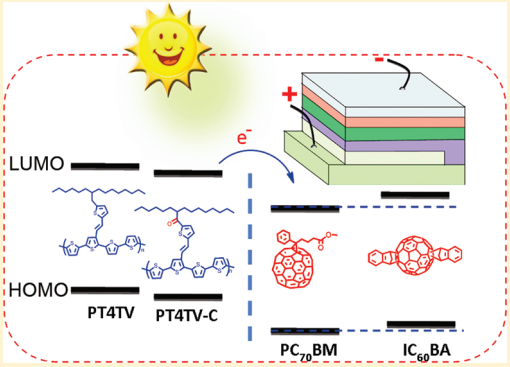
Side Chain Engineering of Polythiophene Derivatives with a Thienylene−Vinylene Conjugated Side Chain for Application in Polymer Solar Cells

Zhi−Guo Zhang, Siyuan Zhang, Jie Min, Chaohua Cui, Hua Geng, Zhigang Shuai, and Yongfang Li*

Beijing National Laboratory for Molecular Sciences, CAS Key Laboratory of Organic Solids, Institute of Chemistry, Chinese Academy of Sciences, Beijing 100190, China

Supporting Information

ABSTRACT: Two new conjugated side-chain isolated polythiophene derivatives, **PT4TV** and **PT4TV-C**, were designed and synthesized by copolymerization of thiophene unit with thienylene−vinylene (TV) conjugated side chain and unsubstituted terthiophene unit. The difference of the two polymers is an additional carbonyl group on the conjugated TV side chain in **PT4TV-C**. Compared to previous reported conjugated side chain polythiophenes (CSC-PTs) with concentrated side chains, **PT4TV** and **PT4TV−C** showed red-shifted and enhanced $\pi-\pi^*$ transition absorption of the polymer backbone along with the shoulder peak and steep absorption edge, indicating ordered polymer main chains and well-packed side chains. **PT4TV** possessed an absorption edge of 663 nm and a HOMO energy level at −5.21 eV. The introducing of electron deficient carbonyl group in **PT4TV−C** led to 17 nm red-shifted absorption and a down-shifted HOMO energy level at −5.26 eV, but aroused the issue of poorer planarity of the polymer backbone. The more ordered structure in **PT4TV** translated into better hole mobility and better photovoltaic properties. The polymer solar cell based on **PT4TV** as donor and indene−C_{60} bisadduct as acceptor displayed a power conversion efficiency of 3.05% with a high open circuit voltage of 0.93 V, under the illumination of AM1.5G, 100 mW/cm^2. The results indicate that the side chain isolated CSC-PTs could be promising high performance photovoltaic polymers.



1. INTRODUCTION

Bulk heterojunction (BHJ) polymer solar cells (PSCs) based on *p*-type conjugated polymers[1] as donor and *n*-type fullerene derivatives[2] as acceptor have been intensively studied in recent years for the generation of affordable, clean, and renewable energy. Advantages of the BHJ PSCs include low-cost fabrication of large-area devices, lightweight, mechanical flexibility, and easy tunability of chemical properties of the photovoltaic materials.

Polythiophene derivatives (PTs) are among the most extensively investigated conjugated polymers due to their high charge carrier mobility, strong absorption in visible region and synthetic accessibility.[3−6] Soluble poly(3-alkylthiophene)s, especially regioregular poly(3-hexylthiophene) (P3HT), are the most important semiconducting polymers for the applications in polymer solar cells (PSCs). However, the power conversion efficiency (PCE) of the PSCs based on P3HT as donor and PCBM as acceptor is limited at 4−5%,[7] because of its relatively large band gap and its high HOMO (the highest occupied molecular orbital) energy level, which result in limited light absorption and a low open circuit voltage (V_{oc}) of the PSCs.

For broadening the absorption of the PTs, the polythiophene derivatives with conjugated side chain (CSC-PTs) were designed and synthesized in our group.[8−10] The CSC-PTs possess higher hole mobility thanks to the 2-D conjugation structure, and broad absorption deriving from both the main chains and conjugated side chains, thus this family of CSC-PTs demonstrated good device performances in PSCs and organic field−effect transistors (OFETs). However, due to asymmetric nature and high concentration of the substituents employed, the as-synthesized polymers showed poorer regioregularity in terms of the direction of the concentrated alkyl chains and/or conjugated side chains projecting from the thiophene main chains. The regiorandom structure can cause a nonplanar orientation of the thiophene backbone, which is detrimental for the close packing of polymer chains in the solid state, as clearly evidenced for the featureless absorption along with the low absorption intensity of $\pi-\pi^*$ absorption.[8−10] To overcome this problem, we recently proposed a "side-chain-isolation" concept for the PTs and synthesized a CSC-PT of **PT5TPA** with styryl−triphenylamine (TPA) side chain and unsubstituted tetrathienyl spacer. **PT5TPA** showed improved planarity of the polymer backbone with red-shifted and enhanced absorption.[11] Considering the diverse molecular engineering approaches under this side chain isolated polythiophenes, such as changing the nature of side chain and spacer as well as introducing the

Received: December 6, 2011
Revised: February 17, 2012
Published: February 29, 2012

ACS Publications © 2012 American Chemical Society

dx.doi.org/10.1021/ma2026463 | *Macromolecules* 2012, 45, 2312−2320

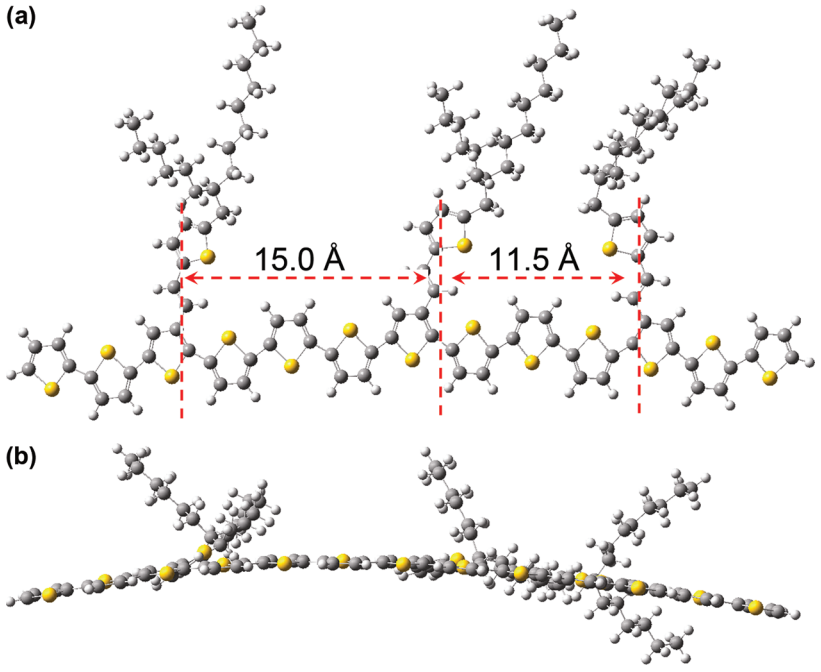
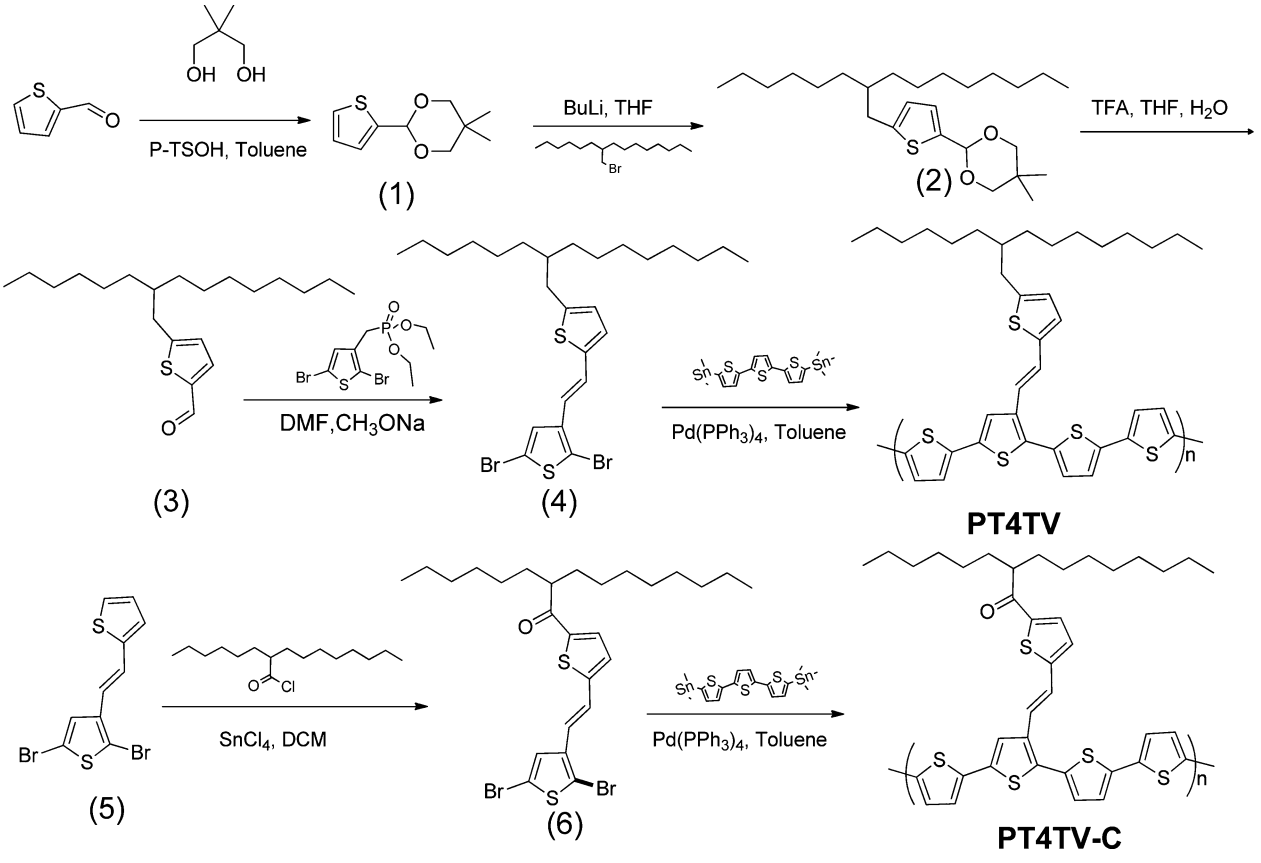


Figure 1. Optimized geometry of PT4TV: (a) top view and (b) side view.

Scheme 1. Synthetic Routs of PT4TV and PT4TV-C

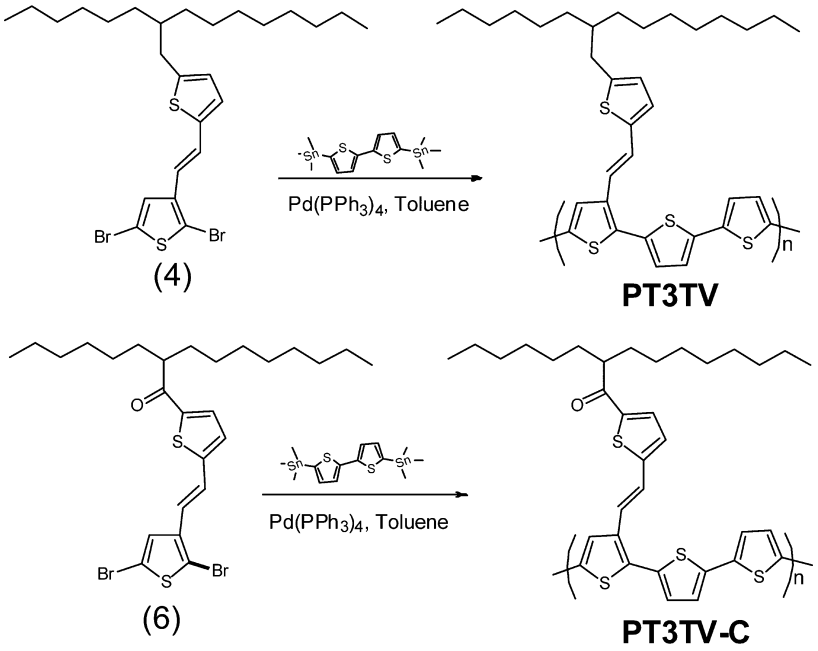


donor–acceptor (D–A) concept, CSC-PTs could open a new way for developing high performance polymer semiconductors.

Here, we designed and synthesized two new conjugated side chain isolated PTs **PT4TV** with conjugated thienylene vinylene (TV) side chain and **PT4TV-C** with the TV side chain attaching the electron-withdrawing carbonyl group. In these polymer systems, the synthesis methodology and the structure optimization were further explored. The two polymers show red-shifted and enhanced absorption of polymer backbone. The PSC based on **PT4TV** as donor and indene–C_{60} bisadduct (ICBA) as acceptor exhibited a power conversion efficiency of 3.05% with a high open circuit voltage of 0.93 V, under the

dx.doi.org/10.1021/ma2026463 | *Macromolecules* 2012, 45, 2312–2320

Scheme 2. Synthetic Routs of Reference Polymers of PT3TV and PT3TV-C



illumination of AM1.5G, 100 mW/cm^2. These results demonstrated a promising future for such types of polymers.

2. RESULTS AND DISCUSSION

Polymer Design and Side Chain Engineering. The molecular conformations of **PT4TV** and its polymer analogue of **PT3TV** (for comparison) were investigated by molecular mechanics simulation with COMPASS force field within the materials studio package.[12] As shown in Figure 1, in the proposed molecular structure of the conjugated side-chain-isolated **PT4TV**, the side−chains oriented in the tail-to-tail directions in the extended polymer conformation are spaced approximately 11.5 Å apart while those side chains orientated in the head-to-tail fashions are 15.0 Å apart. For the polymer analogue with bithienyl spacer (**PT3TV**), the optimized geometry is shown in Figure S1 in the Supporting Information. This shortening in the thiophene spacer brought a tail-to-tail side chains orientation distance of 9.5 Å and aroused clear twisting of the backbone, due to steric hindrance of the large side chains with each other. Thus, this side chain isolation approach combines the asymmetric thiophene units with conjugated side chains and the unsubstituted trithienyl spacers to minimize the steric interactions between the neighboring side chains, hence preserving backbone planarity.

Compared to our recently developed side chain isolated PT5TPA,[11] the replacing of the twisted propeller TPA side chain with planar thiophene side chain is aimed at promoting the planarity of the whole backbone and thus denser packing of the polymer chains in the solid. Another benefit of replacing TPA with the thiophene unit is brought by the shorter side chain width of thiophene (2.6 Å) unit relative to that of bulky TPA (7.1 Å). Consequently, the side chain isolated spacer can be shortened from four thiophene units (in PT5TPA)[11] to three units (in **PT4TV** and **PT4TV-C**). In synthesis methodology, this change in thiophene spacer can overcome the tedious synthetic approach used in developing PT5TPA for easy realization of the side chain isolation concept.

In addition, appending electron-deficient group at the terminal of the conjugated side chain can lower the HOMO energy level and narrow the band gap of the side-chain-conjugated polymers.[13,14] Therefore, we designed and synthesized **PT4TV-C** with an additional electron-withdrawing carbonyl group attaching to the TV conjugated side chain. Thus, the as-presented synthesis strategy allows direct comparison of polymers with the same polymer backbone and conjugated side chains but different functional groups on the side chain for elucidating their structure−property relationships.

Polymer Synthesis and Characterization. Chemical structures and synthetic routes of **PT4TV** and **PT4TV-C** are depicted in Scheme 1. Initially, thiophen-2-carbaldehyde was protected by reacting with 2,2-dimethyl-1,3-propandiol under acidic conditions, yielding the acetal **1**. The alkylation of acetal **1** was performed by lithiation with *n*-butyllithium followed by quenching with alkyl bromide, giving acetal derivative **2**. The acetal derivative **2** was converted into its corresponding aldehyde **3** by dedioxanylation with trifluoroacetic acid (TFA). Coupling reaction of carbaldehyde **3** with phosphonate precursor under Horner−Emmons−Wittig reaction led to the dibrominated monomer.[15] The conformation of the vinylic bonds of monomer **4** have unequivocally been designated as E on the basis of J_{HH} vinylic coupling constant (ca. 16 Hz). In contract to Monomer **4**, acylated thiophene monomer **6** is more easily accessible via the Friedel−Crafts acylation of compound **5** with 2-hexyldecanoyl chloride and $SnCl_4$. The two polymers, **PT4TV** and **PT4TV-C** were successfully synthesized by Stille coupling reaction[16] of the distannyl trithiophene and dibromo compounds (**4** or **6**). The two polymers have good solubility in chlorinated solvents, such as dichlomathane, chloroform and dichlorobenzene, which is important for their application in PSCs. The chemical structures of **PT4TV** and **PT4TV-C** were confirmed by ^{1}H NMR spectra and Fourier transform infrared (FT-IR) absorption spectroscopy. In the ^{1}H NMR spectra (see Figure S2 in the Supporting Information), the ratios of integrated peak areas of olefinic to aliphatic

dx.doi.org/10.1021/ma2026463 | Macromolecules 2012, 45, 2312−2320

protons are consistent with the proposed structures. And the appearance of carbonyl group in **PT4TV-C** is clearly supported by characteristic C=O stretching vibrations at 1648 cm^{-1} in the FT-IR spectra (see Figure S3 in the Supporting Information). For the reference polymers with bithienyl spacer (**PT3TV** and **PT3TV−C**), the synthetic routs are depicted in Scheme 2 and the details of synthesis were provided in the Supporting Information.

Thermal Stability. Thermal stability of the polymers was investigated with thermogravimetric analysis (TGA), as shown in Figure S4 in the Supporting Information. The TGA analysis reveals that the onset temperatures with 5% weight loss (T_d) of **PT4TV** and **PT4TV-C** are 394 and 374 °C, respectively (see Table 1). This indicates that the polymers are stable enough for the applications in optoelectronic devices.

Table 1. Thermal, Optical and Electrochemical Properties of the Polymers

polymers	T_d[a] (°C)	λ_{max}[b] (nm)	λ_{edg}[c] (nm)	E_g^{opt} (eV)	HOMO (eV)	LUMO (eV)	E_g^{ec}[d] (eV)
P3HT	–	550	650	1.91	−4.90	−2.80	2.10
PT4TV	394	372, 557	663	1.87	−5.21	−3.15	2.06
PT4TV-C	374	378, 561	680	1.82	−5.26	−3.35	1.91

[a]5% weight loss temperature measured by TGA under N_2. [b]Film absorption maximum. [c]Film absorption edge. [d]Estimated using the equations $E_g^{ec} = E_{LUMO}^{ec} - E_{HOMO}^{ec}$

Optical Properties. Figure 2 shows the absorption spectra of **PT4TV and PT4TV-C** solution in chloroform and film on quartz plate, along with the absorption spectra of reference polymers of **PT3TV** and **PT3TV-C** with concentrated side chains for comparison. The molar extinction coefficients per repeating unit of **PT4TV** at peak wavelength is 3.43 × 10^4 M^{-1} cm^{-1}, higher than that of **PT4TV-C** (3.20 × 10^4 M^{-1} cm^{-1}). The solution and film absorptions of **PT4TV** and **PT4TV-C** display similar broad absorption band with two distinct absorption peaks and steep absorption edges. The weak absorption peaks around 400 nm originate from the absorption of the conjugated side chain, while the maximum absorptions of **PT4TV** and **PT4TV-C** at 580 nm correspond to the $\pi-\pi^*$ transition of the polymer backbone. Thus, both the main chain and side chain contribute to the broad nature of the absorption spectra of the polymers, which is a common feature for the PTs with conjugated side chains.[8,9] Because of an enlarged π-system, the film absorption of **PT4TV** is red-shifted by ca. 10 nm than that of **P3HT**, while for that of **PT4TV-C**, more pronounced red-shift by ca. 20 nm was recorded largely brought by additional charge transfer effect between polymer main chain and pendant carbonyl group. Thus, the absorption edges of the polymer film reached 663 nm for **PT4TV** and 680 nm for **PT4TV-C**, corresponding to respective optical band gap of 1.87 and 1.82 eV (see Table 1). Owing to improved planarity of the polymer main chain and denser packing of side chains, the absorption spectra of the two polymers are red-shifted relative to that (658 nm) of their polymer analogue of **PT5TPA** with propeller TPA side chain.[11] Furthermore, shoulder peak at ca. 620 nm, especially for **PT4TV**, appears in the absorption spectra of the polymer solutions and films, indicative of aggregated polymer chains in both states. As shown in Figure 2a, when the polymer solution was heated to 80 °C, the absorption peaks blue shift, and the shoulder peak at ca. 600 nm weakened, reflecting partial disaggregation of the polymer backbone at high temperature. For the control polymers (**PT3TV** and **PT3TV-C**), both solution and film absorptions demonstrated blue-shifted and featureless absorptions with decreased absorption intensity of $\pi-\pi^*$ transition due to the nonplanarity conformation. These results further highlighted the importance of the side chain isolation approach in developing two-dimensional conjugated polymers.

Electrochemical Properties. The highest occupied molecular orbital (HOMO) and the lowest unoccupied molecular orbital (LUMO) energy levels of the conjugated polymers are important parameters in determining the V_{oc} and excitons dissociation efficiency in PSCs, and they can be measured from the onset oxidation potential (φ_{ox}) and onset reduction potential (φ_{red}) of cyclic voltammograms of the polymers according to the following equations:[17] $E_{HOMO} = -e(\varphi_{ox} + 4.71)$ (eV) and $E_{LUMO} = -e(\varphi_{red} + 4.71)$, where the unit of potential is V vs. Ag/Ag^+.

Figure 3 shows the cyclic voltammograms of the two copolymers. The onset reduction potential (φ_{red}) and onset oxidation potential (φ_{ox}) of **PT4TV** are −1.55 and +0.50 V vs Ag/Ag^+, respectively, corresponding to LUMO and HOMO energy levels of −3.16 and −5.21 eV, respectively. After introducing the electron deficient carbonyl group in **PT4TV-C**, its LUMO energy level is decreased to −3.35 eV and its HOMO energy level is down-shifted to −5.26 eV, leading to a reduced electrochemical bandgap (E_g^{ec}) of 1.91 eV for **PT4TV-C**. The electronic energy levels and electrochemical bandgaps of the two polymers along with that of P3HT were also listed in

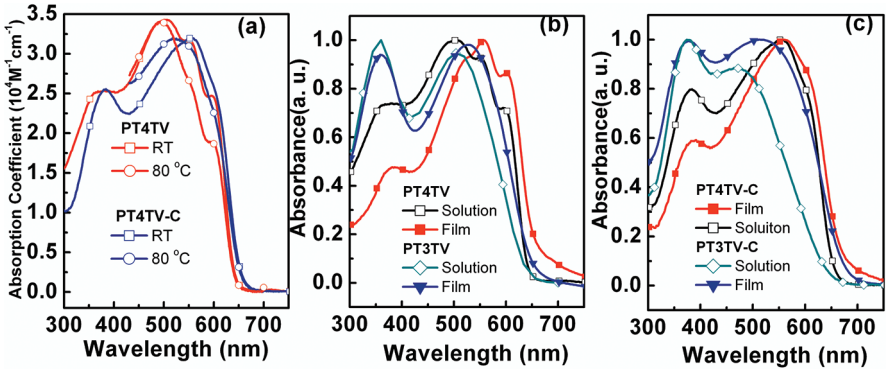


Figure 2. (a) Solution absorption spectra of **PT4TV** and **PT4TV-C** at room temperature and at 80 °C; (b) Solution and film absorption spectra of **PT4TV** and **PT3TV**; (c) Solution and film absorption spectra of **PT4TV-C** and **PT3TV-C**.

dx.doi.org/10.1021/ma2026463 | *Macromolecules* 2012, 45, 2312−2320

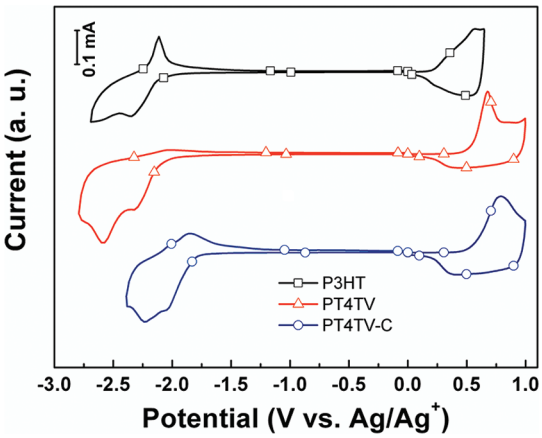


Figure 3. Cyclic voltammograms of **PT4TV** and **PT4TV-C** films on a Pt electrode measured in 0.1 mol L^{-1} Bu_4NPF_6 acetonitrile solutions at a scan rate of 100 mV s^{-1}.

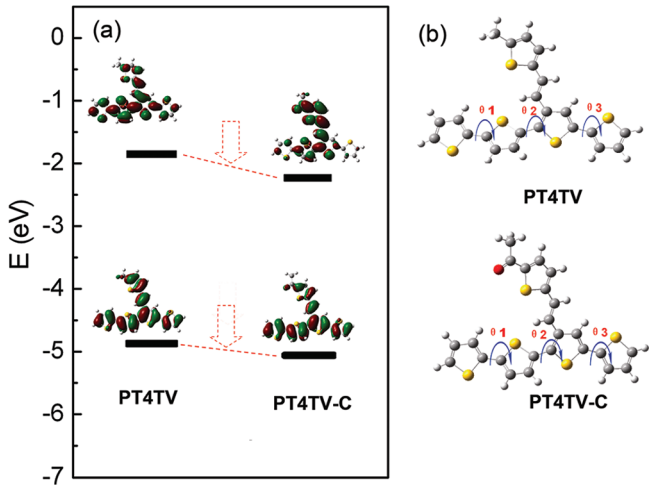


Figure 4. (a) HOMO and LUMO energy levels (eV) and the frontier molecular orbitals obtained from DFT calculations on **PT4TV** and **PT4TV-C** with a chain length n = 1 at B3LYP/6-31G* level of theory along with (b) optimized geometry.

Table 1 for clear comparison. For both polymers, the lower HOMO energy level relative to P3HT can provide better air stability in ambient conditions and higher open circuit voltage (V_{oc}) of the PSCs because the V_{oc} is usually proportional to the difference between the LUMO level of the acceptor and the HOMO level of the donor.[6]

X-ray Diffraction and Hole Mobility. As shown in Figure S5 in the Supporting Information, X-ray diffraction patterns of the pristine polymer films exhibit (100) diffraction peaks at 2θ = 3.42° and 3.20°, respectively, corresponding to an interchain d-spacing of 25.82 Å for **PT4TV** and 27.60 Å for **PT4TV-C**. These values are larger than that of P3HT (16.4 Å)[7a] due to the bulky side chain incorporated. However, the (010) diffraction peaks are not observed for the two polymers.

Hole mobility of the two polymers was measured by space charge limit current (SCLC) method, as shown in Figure S6 in Supporting Information. **PT4TV** demonstrated a hole mobility of 4.08×10^{-3} cm^2 V^{-1} s^{-1}, which is four times higher than that (9.5×10^{-4} cm^2 V^{-1} s^{-1}) of **PT4TV-C**. Notably, the hole mobility of **PT4TV** is also higher than that of our previously developed side chain isolated PT5TPA,[11] and the improved planarity of **PT4TV** can account for this phenomenon.

Theoretical Calculations. To provide further insight into the fundamentals of molecular architecture, molecular simulation was carried out for **PT4TV** and **PT4TV-C**, with a chain length of n = 1 at the DFT B3LYP/6-31G(d) level with the Gaussian 03 program package.[18] The bulky alkyl chain was replaced with methyl group in the calculation to avoid excessive computation demand, since they do not significantly affect the equilibrium geometry and thus the electronic properties. All C=C bonds outside the aromatic rings were set to be in trans configuration.

As depicted in Figure 4a, for **PT4TV**, there is a significant overlap between the HOMO and LUMO. However, for **PT4T-C**, the electron density distributions at LUMO become slightly localized near the electron-withdrawing carbonyl groups, and the well-separated distribution of HOMO and LUMO energy levels indicate that a transition between them can be considered to be a charge-transfer transition.[13] As a result, both the HOMO and LUMO energy level as well as the bandgap are decreased.

The optimized geometries are shown in Figure 4b, and relevant dihedral angles are listed in Table 2. Notably, the appearance of ICT interaction in **PT4TV-C** also aroused

Table 2. Calculated Dihedral Angles of Polymers

	dihedral angle (deg)			
polymers	$\theta 1$	$\theta 2$	$\theta 3$	θ^a
PT4TV	16.84	35.08	19.35	71.27
PT4TV-C	19.44	34.83	19.16	73.43

[a]The dihedral angle of the entire unit, $\theta = \theta 1 + \theta 2 + \theta 3$.

increased dihedral angles along the backbone, which is detrimental for the planarity of the backbone and close packing of polymer chains in the solid state. Similar phenomena were also observed in conjugated polymers with pendant acceptors.[13,14] And the calculated results can partly explain the better hole mobility of **PT4TV** relative to that of **PT4TV-C**.

In addition, it can be seen from Figure 4 and Table 1 that although discrepancies exist between the calculation and experimental results, the trends of variation in the HOMO and LUMO energy levels, as well as the energy gaps, are consistent.

Photovoltaic Properties. The photovoltaic properties of **PT4TV and PT4TV−C** (Table 3) were studied by fabricating the bulk heterojunction PSCs with the device configuration of ITO/PEDOT: PSS/polymer: acceptors/Ca/Al. Here, two different fullerene derivatives $PC_{70}BM$ and $IC_{60}BA$ were used as acceptor in the PSCs. The molecular structures and the electronic energy level diagrams of the donor and acceptor materials were displayed in Figure 5. Figure 6 shows the $J-V$ curves of the PSCs based on **PT4TV** or **PT4TV-C** as donor and $PC_{70}BM$ or $IC_{60}BA$ as acceptor under the illumination of AM 1.5, 100 mW·cm^{-2}.

With the widely used $PC_{70}BM$ as acceptor, the PSC based on PT4TV showed a moderate PCE of 2.80% along with a V_{oc} of 0.67 V and a FF of 51.1%. The FF value is significantly improved in comparison with the PTs with concentrated side chains. For example, FF values of the PSCs based on the concentrated side chain CSC-PTs, PT-1,[8a] and PT-2[8d] (their molecular structures are shown in Scheme 1 in Supporting Information) were only 43% and 38% respectively. The higher FF of the **PT4TV**-based PSCs could be related to the closely packing of the polymer main chains in this side-chain-isolated PTs and its higher hole mobility. The appending of carbonyl

dx.doi.org/10.1021/ma2026463 | Macromolecules 2012, 45, 2312−2320

Table 3. Photovoltaic Parameters of PSCs Based on Fullerene Acceptor of $PC_{70}BM$, $IC_{60}BA$

polymers	acceptors	ratio[a]	V_{oc} (V)	J_{sc} (mAcm^{-2})	FF (%)	PCE (%)	thickness (nm)
PT4TV	$PC_{70}BM$	1:1	0.67	7.59	55.1	2.80	78
	$IC_{60}BA$	1:0.8	0.93	5.83	56.2	3.05	75
PT4TV-C	$PC_{70}BM$	1:1	0.74	4.48	36.4	1.21	70
	$IC_{60}BA$	1:1	1.01	3.78	36.8	1.41	75

[a]Polymer/fullerene weight ratio.

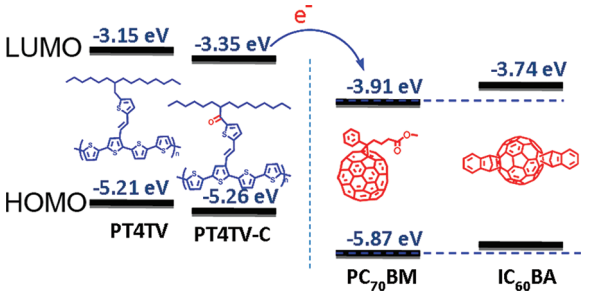


Figure 5. Energy level diagrams for polymer donor of PT4TV and PT4TV−C along with acceptors of $PC_{70}BM$ and $IC_{60}BA$.

group in **PT4TV-C** produced a higher V_{oc} of 0.74 V, 0.07 V higher than that of the **PT4TV**-based device due to its lower lying HOMO energy level. But due to a lower hole mobility, the PSC based on **PT4TV-C** showed a lower J_{sc} of 4.48 mAcm^{-2} and a lower FF of 36.4%, which result in an overall lower efficiency of 1.21%.

To further improve the efficiency, it is important to use fullerene acceptors with higher LUMO energy to increase V_{oc}. Along this line, an indene−C_{60} bisadduct (ICBA)[2] developed in our group with a higher LUMO energy level of −3.74 eV was incorporated in further device optimization. As a result, a higher V_{oc} of 0.93 V for **PT4TV** and 1.01 V for **PT4TV-C** were obtained. Although $IC_{60}BA$−based devices generate smaller J_{sc} values than those of $PC_{70}BM$ devices, presumably as a result of lower molar extinction coefficients of $IC_{60}BA$ relative to that of $PC_{70}BM$, improved PCE of 3.05% for **PT4TV** and 1.41% for **PT4TV-C** was still achieved because the increased V_{oc} partially compensates the decreased J_{sc} value. The J_{sc} values of the PSCs were confirmed by the IPCE results as shown in Figures 6, parts b and d.

Morphology. The morphologies of the blend films were investigated by atomic force microscopy (AFM). As shown in Figure S7 in Supporting Information, the blend films demonstrated different phase separation state with root-mean-square (rms) roughness of 2.16 nm for **PT4TV**/$PC_{70}BM$ composite film, 9.62 nm for **PT4TV**/$IC_{60}BA$ composite film, 1.39 nm for **PT4TV-C**/$PC_{70}BM$ composite film and 1.36 nm for **PT4TV-C**/$IC_{60}BA$ composite film, indicating different miscibility between the copolymers and fullerene derivatives. The large domain size for **PT4TV**/$IC_{60}BA$ composite film suggested that even better device performance can be expected by further device engineering, such as thermal annealing, solvent annealing, and additives to promote proper phase separation.

3. CONCLUSION

Two new conjugated side chain isolated PTs with thienylene−vinylene (TV) conjugated side chain and unsubstituted trithienyl spacer, **PT4TV** and **PT4TV-C**, were designed and

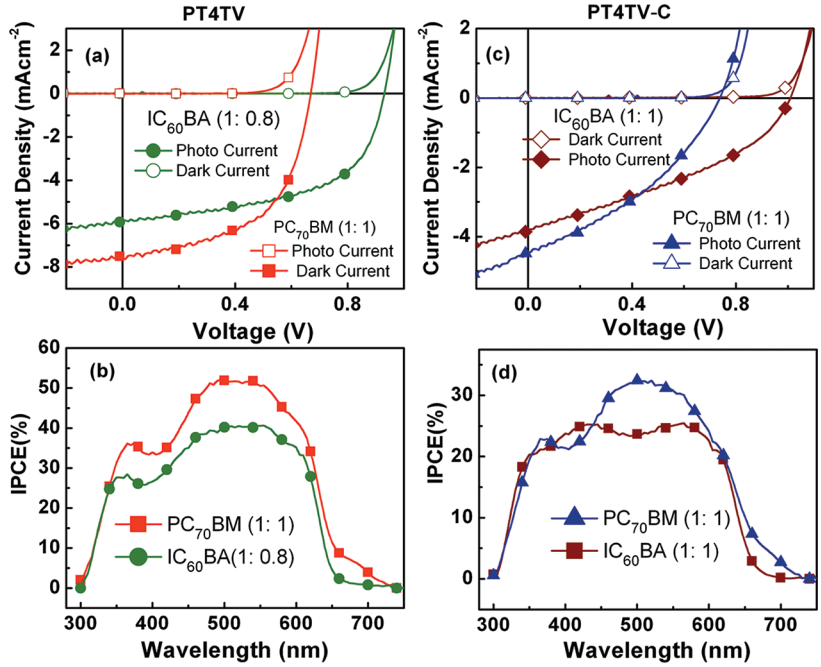


Figure 6. Current density−voltage curves of PSCs based on composite films of (a) **PT4TV**−fullerenes and (c) **PT4TV-C**−fullerenes under the illumination of AM 1.5, 100 mW·cm^{-2}. Incident-photon-to-converted-current efficiency (IPCE) spectra of the corresponding devices: (b) **PT4TV**−fullerenes and (d) **PT4TV-C**−fullerenes.

dx.doi.org/10.1021/ma2026463 | *Macromolecules* 2012, 45, 2312−2320

synthesized. In comparison with PT4TV, PT4TV-C possesses an additional electron-withdrawing group attaching to the TV side chain. **PT4TV** showed lower HOMO energy levels at −5.21 eV, higher hole mobility of 4.08×10^{-3} cm^2 V^{-1} s^{-1}, and red-shifted and enhanced absorption with steep absorption edge at 663 nm. **PT4TV-C** possessed further down-shifted HOMO level at −5.26 eV and red-shifted absorption band with absorption edge at 680 nm due to the electron-withdrawing carbonyl group on its side chain, but lower hole mobility due to the poorer planarity of the polymer. The PSC based on **PT4TV** as donor and $IC_{60}BA$ as acceptor displayed a power conversion efficiency of 3.05% with a high V_{oc} of 0.93 V, under the illumination of AM1.5G, 100 mW/cm^2.

4. EXPERIMENTAL SECTION

4.1. Instrumentation. ^{1}H NMR spectra and ^{13}C NMR spectra were measured on a Bruker DMX−400 spectrometer with *d*-chloroform as the solvent and trimethylsilane as the internal reference. UV−visible absorption spectra were measured on a Hitachi U-3010 UV−vis spectrophotometer. Mass spectra were recorded on a Shimadzu spectrometer. Elemental analyses were carried out on a flash EA 1112 elemental analyzer. Thermogravimetric analysis (TGA) was conducted on a Perkin−Elmer TGA−7 thermogravimetric analyzer at a heating rate of 20 °C/min and under a nitrogen flow rate of 100 mL/min. Molecular weight of the polymer was measured by Gel permeation chromatography (GPC), using polystyrene as standard and THF as the eluent. The electrochemical cyclic voltammetry was performed on a Zahner IM6e Electrochemical Workstation, in an acetonitrile solution of 0.1 mol/L tributylammonium hexafluorophosphate (*n*-Bu_4NPF_6) at a potential scan rate of 100 mV/s with an Ag/Ag^+ reference electrode and a platinum wire counter electrode. Polymer film was formed by drop-casting 1.0 mL of polymer solutions in THF (analytical reagent, 1 mg/mL) onto the glassy carbon working electrode, and then dried in the air. The film morphology was measured using an atomic force microscope (AFM, SPA-400) using the tapping mode.

4.2. Photovoltaic Device Fabrication and Characterization. The PSCs were fabricated with a configuration of ITO/PEDOT:PSS (40 nm)/active layer (ca. 70−80 nm)/ Ca(20 nm)/Al(80 nm). A thin layer of PEDOT:PSS (poly(3,4-ethylenedioxythiophene): poly(styrenesulfonate)) was spin-cast on precleaned ITO-coated glass from a PEDOT:PSS aqueous solution (Baytron P VP AI 4083 from H. C. Starck) at 2000 rpm and dried subsequently at 150 °C for 30 min in air, then the device was transferred to a glovebox, where the active layer of the blend of the polymer and fullerene derivatives was spin-coated onto the PEDOT:PSS layer. Finally, a Ca/Al metal top electrode was deposited in vacuum onto the active layer at a pressure of ca. 5×10^{-5} Pa. The active area of the device was ca. 4 mm^2.

The thickness of the active layer was determined by an Ambios Tech. XP-2 profilometer. The current density−voltage (J−V) characteristics were measured on a computer−controlled Keithley 236 Source−Measure Unit. A xenon lamp coupled with AM 1.5 solar spectrum filter was used as the light source, and the optical power at the sample was 100 mW/cm^2. The hole mobility was calculated by fitting the dark J-V curves for the hole-only devices to SCLC model at low voltages, in which the current density is given by $J = 9\varepsilon_0\varepsilon_r\mu V^2/8L^3\exp[0.891\gamma(V/L)^{0.5}]$, where $\varepsilon_0\varepsilon_r$ represents the permittivity of the material, μ is the mobility, γ is the field activation factor, and L the thickness of the active layer. The applied bias voltage is corrected for the built-in potential so that $V = V_{applied} - V_{bi}$. Thin-film X-ray diffraction (XRD) was recorded on a Bruker D8 Discover thin-film diffractometer with Cu Kα radiation (λ = 1.540 56 Å) operated at 40 keV and 40 mA.

4.3. Materials. Diethyl (2,5-dibromothiophen-3-yl) methylphosphonate,[8] 5,5″-Bis(trimethylstannyl)-2,2′:5′,2″-terthiophene[19] were prepared according to the method reported in literatures. Tris(triphenylphosphine)palladium, *N*-bromosuccinimide, and benzoyl peroxide were purchased from Sigma-Aldrich Chemical Co. P3HT with regioregularity of 90%-94% was purchased from Rieke Metals Inc.

4.4. Synthesis of the Polymers. The synthetic routes of the polymers are shown in Scheme 1. The detailed synthetic processes of the monomers and polymers are described in the following.

*5,5-Dimethyl-2-(thiophen-2-yl)-1,3-dioxane (**1**).* To 200 mL of a three-necked flask attached with a Dean−Stark trap condenser were added thiophen-2-carbaldehyde (22.4 g, 200 mmol), 2,3-dimethylbutane-2,3-diol (31.2 g, 300 mmol), *p*-TsOH (1.92 g, 10 mmol), and toluene (120 mL) under N_2.The mixture was refluxed by stirring overnight and was neutralized with saturated $NaHCO_3$ aqueous solution. The organic layer was extracted with ether, dried over anhydrous Na_2SO_4, and evaporated to dryness. The residue was purified by Al_2O_3 column chromatography to afford the title compound (**1**) (18 g, 50.0%). GC−MS: m/z = 180. ^{1}H NMR (400 MHz, $CDCl_3$, δ, ppm): 7.30 (d, J = 4.8 Hz, 1H), 7.05−7.04 (m, 5H, ArH), 6.99 (d, J = 4 Hz, 2H, ArH), 7.14 (d, J = 3.4 Hz, 1H), 7.00−6.98 (m, 1H), 5.65 (s, 1H), 3.76 (d, J = 11.5 Hz, 2H), 3.64 (d, J = 10.9 Hz, 2H), 1.29 (t, J = 6.4 Hz, 3H), 0.80 (t, J = 6.4 Hz, 3H). Anal. Calcd for $C_{10}H_{14}O_2S$: C, 60.57; H, 7.12; S, 16.17. Found: C, 60.49; H, 7.02; S: 16.25.

*2-(5-(2-Hexyldecyl)thiophen-2-yl)-5,5-dimethyl-1,3-dioxane (**2**).* Compound **1** (10.8 g, 60 mmol) was dissolved in 300 mL of dry THF in a three−neck flask. The flask was filled with nitrogen and cooled to −78 °C. A solution of *n*-butyllithium in *n*-hexane (2 mol L^{-1}, 15 mL) was added dropwise to the flask using a glass injector through a septum cap. The solution was stirred at −78 °C for 1 h. Then, 1-bromo-2-hexyldecane (18.3 g, 60 mmol) was dissolved in 50 mL of dry THF and added to the solution. The solution was stirred at RT overnight, then 300 mL of saturated NH_4Cl aq. was added to the solution and the product was extracted with ethyl acetate. The ethyl acetate solution was dried with Na_2SO_4, and the solvent was evaporated. The product was purified by column chromatography on silica−gel to yield a slightly yellow oil of 21.1 g (yield: 83.3%). GC−MS: m/z = 422. ^{1}H NMR (400 MHz, $CDCl_3$, δ, ppm): 6.90 (d, J = 3.2 Hz, 1H), 6.60 (d, J = 3.2 Hz, 1H), 5.55 (s, 1H), 3.74 (d, J = 11.5 Hz, 2H), 3.48 (d, J = 10.9 Hz, 2H), 2.68 (d, J = 6 Hz, 2H), 1.58 (s, 1H), 1.26−1.23 (m, 24H), 1.00−0.80 (m, 12H). Anal. Calcd for $C_{26}H_{46}O_2S$: C, 73.88; H, 10.97; S, 7.59. Found: C, 74.01; H, 11.05; S: 7.45.

*5-(2-Hexyldecyl)thiophene-2-carbaldehyde (**3**).* THF (30 mL) and water (30 mL) were added to a flask containing acetal **2** (18.9 g, 45 mmol) and TFA (10 mL). The resulting reaction mixture was refluxed for overnight, quenched with saturated aqueous sodium bicarbonate, and extracted with dichloromethane. The combined organic phases were washed with aqueous sodium bicarbonate, dried over anhydrous Na_2SO_4, and evaporated in vacuo. The pure product **3** was obtained by silica gel chromatography using a mixture of methylene chloride and *n*-hexane (1:10) as an eluent to yield an oil of 13.44 g(yield 95%). GC−MS: m/z = 336. ^{1}H NMR (400 MHz, $CDCl_3$, δ, ppm): 9.80 (s, 1H), 7.58 (d, J = 3.6 Hz, 1H), 6.85 (d, J = 3.6 Hz, 1H), 2.68 (d, J = 6 Hz, 2H), 1.58 (s, 1H), 1.26−1.23 (m, 24H), 0.80 (m, 6H). Anal. Calcd for $C_{21}H_{36}OS$: C, 74.94; H, 10.78; S, 9.53. Found: C, 74.85; H, 10.89; S: 9.68.

*(E)-2,5-Dibromo-3-(2-(5-(2-hexyldecyl)thiophen-2-yl)vinyl)-thiophene. (**4**).* Under an ice−water bath, diethyl (2,5-dibromothiophen-3-yl) methylphosphonate (1.38 g, 5 mmol) and aldehyde **3** (2.01 g, 6 mmol) were dissolved in 30 mL of DMF, and then CH_3ONa (0.6 g, 11 mmol) in 10 mL of DMF was added dropwise to the solution. After reaction for 2 h at room temperature, 300 mL of saturated NH_4Cl(aq) was added to the solution and the product was extracted with ethyl acetate. The ethyl acetate solution was dried with Na_2SO_4, and the solvent was evaporated. The product was purified by column chromatography on silica gel to yield a yellow oil of 1.77 g (yield: 60.0%). ^{1}H NMR (400 MHz, $CDCl_3$, δ, ppm): 7.13 (s, 1H), 6.95 (d, J = 15 Hz, 1H), 6.87 (d, J = 3.5 Hz, 1H), 6.70 (d, J = 15 Hz, 1H), 6.40 (d, J = 3.5 Hz, 1H), 7.47 (m, 4H), 2.72 (d, J = 6.7 Hz, 1H), 1.65 (s, 1H), 1.28−1.27 (br, 24H), 0.80 (t, J = 6.4 Hz, 6H). ^{13}C NMR (150 MHz, $CDCl_3$, δ, ppm): 146.250; 140.776; 140.077; 128.233; 128.049; 127.4101; 126.890; 125.999; 125.887; 119.774; 119.714; 119.205;

dx.doi.org/10.1021/ma2026463 | *Macromolecules* 2012, 45, 2312−2320

112.806; 110.158; 78.305; 78.093; 77.881; 61.401; 41.033; 35.929; 34.267; 34.253; 32.982; 32.946; 31.014; 30.685; 30.399; 27.647; 27.631; 23.748; 22.055; 15.258; 15.159. Anal. Calcd for $C_{26}H_{38}Br_2S_2$: C, 54.35; H, 6.67; S, 11.16. Found: C, 54.51; H, 6.71; S: 11.24.

*(E)-1-(5-(2-(2,5-Dibromothiophen−3-yl)vinyl)thiophen-2-yl)-2-hexyldecan-1-one (**6**).* $SnCl_4$ (0.336 g, 9 mmol) was added to a mixture of 2-((*E*)-2-(2,5-dibromothiophen-3-yl)vinyl)thiophene (compound **5**, 3.1 g, 6 mmol) and 2-hexyldecanoyl chloride (2.2 g, 8 mmol) in 50 mL of methylene chloride at 0 °C. After stirring at 0 °C for about 1 h, water was added, and the reaction mixture was diluted with methylene chloride. The mixture was washed successively with water and a saturated aqueous solution of $NaHCO_3$ and then dried over $MgSO_4$. Upon the removal of solvent, the dark-black residue was subjected to column chromatography on silica gel with ethyl acetate/hexane (v/v, 1:10) as the eluent, followed by recrystallization from acetate to offer a yellow solid (2.34 g, 50.0% yield). ^{1}H NMR (400 MHz, $CDCl_3$, δ, ppm): 7.59 (s, J = 3.6 Hz 1H), 7.17 (s, 1H), 7.10 (d, J = 3.6 Hz, 1H), 6.98 (s, 2H), 6.40 (d, J = 3.5 Hz, 1H), 3.15 (s, 1H), 1.76 (s, 1H), 1.58 (s, 2H), 1.28−1.27 (br, 20H), 0.80 (t, J = 6.4 Hz, 6H). ^{13}C NMR (150 MHz, $CDCl_3$, δ, ppm): 198.338; 150.638; 144.997; 139.210; 133.093; 128.239; 128.186; 124.595; 123.755; 113.380; 112.846; 49.300; 34.066; 32.859; 32.678; 30.830; 30.492; 30.427; 30.269; 28.749; 28.715; 23.668; 23.615; 15.123; 150.78. Anal. Calcd for $C_{26}H_{36}Br_2OS_2$: C, 53.06; H, 6.17; S, 10.90. Found: C, 53.12; H, 6.23; S: 10.83.

PT4TV. Under the protection of argon atmosphere, 0.5 mmol of 5,5″-bis(trimethylstannyl)-2,2′:5′,2″-terthiophene (0.287 g) was put into a two-neck flask. Then 12 mL of degassed toluene and 0.5 mmol of Monomer **4** (0.287 g) were added to the mixture. The solution was flushed with argon for 10 min, and then 25 mg of $Pd(PPh_3)_4$ was added. After another flushing with argon for 20 min, the reactant was heated to reflux for 24 h. Then the reactant was cooled to room temperature and the polymer was precipitated by adding 200 mL of methanol, filtered through a Soxhlet thimble, and then subjected to Soxhlet extraction with methanol, hexane, and chloroform. The polymer was recovered as solid from the chloroform fraction by rotary evaporation. The solid was dried under vacuum for 12 h to get **PT4TV**. The yield of the polymerization reaction was about 60%. GPC: M_n = 7.57 kg·mol^{-1}, M_w/M_n = 3.4. ^{1}H NMR (400 MHz, $CDCl_3$, δ, ppm): 7.40−7.27 (br, 4H), 7.27−7.17 (br, 7H), 2.70 (br, 1H), 1.66 (br, 1H), 1.28−1.27 (br, 24H), 0.80 (m, 6H).

PT4TV−C. The synthesis is the same as that for **PTTVC**, except that monomer **4** is replaced by monomer **6**. GPC: M_n = 23.66 kg·mol^{-1}, M_w/M_n = 3.5. ^{1}H NMR (400 MHz, $CDCl_3$, δ, ppm): 7.70−7.27 (br, 5H), 7.26−7.10 (br, 6H), 3.18 (s, 1H), 1.80 (s, 1H), 1.62 (s, 2H), 1.29−1.24 (br, 20H), 0.80 (br, 6H).

■ ASSOCIATED CONTENT

Supporting Information

Synthesis details of **PT3TV** and **PT3TV-C**, figures showing ^{1}H NMR spectra, FT-IR spectra, TGA plots, X-ray diffraction patterns, hole mobility measurement, AFM topography images of **PT4TV** and **PT4TV-C**, and optimized geometry of **PT3TV**, a scheme showing chemical structures of two polythiophene derivatives (PT-1 and PT-2) with concentrated conjugated side chains. This material is available free of charge via the Internet at http://pubs.acs.org.

■ AUTHOR INFORMATION

Corresponding Author

*E-mail: liyf@iccas.ac.cn.

Notes

The authors declare no competing financial interest.

■ ACKNOWLEDGMENTS

This work was supported by NSFC (Nos. 51103064, 50933003, and 21021091), The Ministry of Science and Technology of China and Chinese Academy of Sciences.

■ REFERENCES

(1) (a) Li, Y. F. *Acc. Chem. Res.* **2012**, DOI: 10.1021/ar2002446. (b) Chen, J.; Cao, Y. *Acc. Chem. Res.* **2009**, *42*, 1709. (c) Cheng, Y.-J.; Yang, S.-H.; Hsu, C.-S. *Chem. Rev.* **2009**, *109*, 5868.

(2) (a) He, Y. J.; Li, Y. F. *Phys. Chem. Chem. Phys.* **2011**, *13*, 1970. (b) He, Y. J.; Chen, H.-Y.; Hou, J. H.; Li, Y. F. *J. Am. Chem. Soc.* **2010**, *132*, 1377. (c) Zhao, G. J.; He, Y. J.; Li, Y. F. *Adv. Mater.* **2010**, *22*, 4355−4358. (d) He, Y. J.; Zhao, G. J.; Peng, B.; Li, Y. F. *Adv. Funct. Mater.* **2010**, *20*, 3383−3389.

(3) (a) Yu, G.; Gao, J.; Hummelen, J. C.; Wudl, F.; Heeger, A. J. *Science* **1995**, *270*, 1789. (b) Thompson, B. C.; Fréchet, J. M. J. *Angew. Chem., Int. Ed.* **2008**, *47*, 58.

(4) (a) Nagarjuna, G.; Yurt, S.; Jadhav, K. G.; Venkataraman, D. *Macromolecules* **2010**, *43*, 8045. (b) Grenier, C. R. G.; George, S. J.; Joncheray, T. J.; Meijer, E. W.; Reynolds, J. R. *J. Am. Chem. Soc.* **2007**, *129*, 10694. (c) Perepichka, I. F.; Perepichka, D. F.; Meng, H.; Wudl, F. *Adv. Mater.* **2005**, *17*, 2281. (d) Li, Y. F.; Zou, Y. P. *Adv. Mater.* **2008**, *20*, 2952.

(5) (a) Sugiyasu, K.; Song, C.; Swager, T. M. *Macromolecules* **2006**, *39*, 5598. (b) Wu, P.-T.; Xin, H.; Kim, F. S.; Ren, G.; Jenekhe, S. A. *Macromolecules* **2009**, *42*, 8817. (c) Miyanishi, S.; Tajima, K.; Hashimoto, K. *Macromolecules* **2009**, *42*, 1610. (d) Li, H.; Sundararaman, A.; Pakkirisamy, T.; Venkatasubbaiah, K.; Schödel, F.; Jäkle, , F. *Macromolecules* **2010**, *44*, 95. (e) Rieger, R.; Beckmann, D.; Pisula, W.; Kastler, M.; Müllen, K. *Macromolecules* **2010**, *43*, 6264. Liu, P.; Wu, Y.; Pan, H.; Ong, B. S.; Zhu, S. *Macromolecules* **2010**, *43*, 6368. (f) Ong, B. S.; Wu, Y.; Liu, P.; Gardner, S. *J. Am. Chem. Soc.* **2004**, *126*, 3378. (g) Ong, B. S.; Wu, Y.; Li, Y.; Liu, P.; Pan, H. *Chem.−Eur. J.* **2008**, *14*, 4766.

(6) (a) Liang, Y.; Xiao, S.; Feng, D.; Yu, L. *J. Phys. Chem. C* **2008**, *112*, 7866. (b) Thompson, B. C.; Kim, B. J.; Kavulak, D. F.; Sivula, K.; Mauldin, C.; Fréchet, J. M. J. *Macromolecules* **2007**, *40*, 7425. (c) Hou, J. H.; Chen, T. L.; Zhang, S. Q.; Huo, L. J.; Sista, S.; Yang, Y. *Macromolecules* **2009**, *42*, 9217.

(7) (a) Ma, W.; Yang, C.; Gong, X.; Lee, K.; Heeger, A. J. *Adv. Funct. Mater.* **2005**, *15*, 1617. (b) Li, G.; Shrotriya, V.; Huang, J.; Yao, Y.; Moriarty, T.; Emery, K.; Yang, Y. *Nat. Mater.* **2005**, *4*, 864.

(8) (a) Hou, J. H.; Tan, Z. A.; Yan, Y.; He, Y. J.; Yang, C. H.; Li, Y. F. *J. Am. Chem. Soc.* **2006**, *128*, 4911. (b) Hou, J. H.; Yang, C. H.; He, C.; Li, Y. F. *Chem. Commun.* **2006**, 871−873. (c) Hou, J. H.; Huo, L. J.; He, C.; Yang, C. H.; Li, Y. F. *Macromolecules* **2006**, *39*, 594−603. (d) Zhou, E. J.; Tan, Z. A.; Huo, L. J.; He, Y. J.; Yang, C. H.; Li, Y. F. *J. Phys. Chem. B.* **2006**, *110*, 26062−26067.

(9) (a) Zou, Y. P.; Sang, G. Y.; Wu, W.; Liu, Y. Q.; Li, Y. F. *Synth. Met.* **2009**, *159*, 182. (b) Wang, Y.; Zhou, E. J.; Liu, Y. Q.; Xi, H.; Ye, S.; Wu, W.; Guo, Y.; Di, C.-A.; Sun, Y. M.; Yu, G.; Li, Y. F. *Chem. Mater.* **2007**, *19*, 3361. (c) Zou, Y. P.; Wu, W.; Sang, G. Y.; Yang, Y.; Liu, Y. Q.; Li, Y. F. *Macromolecules* **2007**, *40*, 7231−7237.

(10) (a) Wagner, K.; Crowe, L. L.; Wagner, P.; Gambhir, S.; Partridge, A. C.; Earles, J. C.; Clarke, T. M.; Gordon, K. C.; Officer, D. L. *Macromolecules* **2010**, *43*, 3817. (b) Wang, H.-J.; Chan, L.-H.; Chen, C.-P.; Lin, S.-L.; Lee, R.-H.; Jeng, R.-J. *Polymer* **2011**, *52*, 326. (c) Saini, G.; Jacob, J. *Polym. Int.* **2011**, *60*, 1010. (d) Park, J. W.; Lee, D. H.; Chung, D. S.; Kang, D.-M.; Kim, Y.-H.; Park, C. E.; Kwon, S.-K. *Macromolecules* **2010**, *43*, 2118. (e) Wagner, K.; Crowe, L. L.; Wagner, P.; Gambhir, S.; Partridge, A. C.; Earles, J. C.; Clarke, T. M.; Gordon, K. C.; Officer, D. L. *Macromolecules* **2010**, *43*, 3817. (f) Yu, C.-Y.; Ko, B.-T.; Ting, C.; Chen, C.-P. *Sol. Energy Mater. Sol. Cells* **2009**, *93*, 613.

(11) Zhang, Z.-G.; Zhang, S. Y.; Min, J.; Chui, C. H.; Zhang, J.; Li, Y. F. *Macromolecules* **2012**, *45*, 113−118.

(12) Sun, H. *J. Phys. Chem. B* **1998**, *102*, 7338.

(13) (a) Zhang, Z.-G.; Zhang, K.-L.; Liu, G.; Zhu, C.-X.; Neoh, K.-G.; Kang, E.-T. *Macromolecules* **2009**, *42*, 3104. (b) Zhang, Z.-G.; Liu, Y.-

L.; Yang, Y.; Hou, K.; Peng, B.; Zhao, G. J.; Zhang, M. J.; Guo, X.; Kang, E.-T.; Li, Y. F. *Macromolecules* **2010**, *43*, 9376. (c) Zhang, Z.-G.; Fan, H. J.; Min, J.; Zhang, S.; Zhang, J.; Zhang, M. J.; Guo, X.; Zhan, X. W.; Li, Y. F. *Polym. Chem.* **2011**, *2*, 1678. (d) Zhang, Z.-G.; Yang, Y.; Zhang, S. Y.; Min, J.; Zhang, J.; Zhang, M. J.; Guo, X.; Li, Y. F. *Synth. Met.* **2011**, *161*, 1383.

(14) (a) Huang, F.; Chen, K.-S.; Yip, H.-L.; Hau, S. K.; Acton, O.; Zhang, Y.; Luo, J.; Jen, A. K. Y. *J. Am. Chem. Soc.* **2009**, *131*, 13886−13887. (b) Duan, C.; Cai, W.; Huang, F.; Zhang, J.; Wang, M.; Yang, T.; Zhong, C.; Gong, X.; Cao, Y. *Macromolecules* **2010**, *43*, 5262−5262. (c) Hsu, S.-L.; Chen, C.-M.; Wei, K.-H. *J. Polym. Sci., Part A: Polym. Chem.* **2010**, *48*, 5126−5134. (d) Cheng, Y.-J.; Hung, L.-C.; Cao, F.-Y.; Kao, W.-S.; Chang, C.-Y.; Hsu, C.-S. *J. Polym. Sci., Part A: Polym. Chem.* **2011**, *49*, 1791−1801. (e) Sahu, D.; Padhy, H.; Patra, D.; Huang, J.-H.; Chu, C.-W.; Lin, H.-C. *J. Polym. Sci., Part A: Polym. Chem.* **2010**, *48*, 5812−5823.

(15) Wadsworth, W. S.; Emmons, W. D. *J. Am. Chem. Soc.* **1961**, *83*, 1733.

(16) Carsten, B.; He, F.; Son, H. J.; Xu, T.; Yu, L. *Chem. Rev.* **2011**, *111*, 1493.

(17) Sun, Q. J.; Wang, H. Q.; Yang, C. H.; Li, Y. F. *J. Mater. Chem.* **2003**, *13*, 800.

(18) Gaussian 03, R. E.; Frisch, M. J.; Trucks, G. W.; Schlegel, H. B.; Scuseria, G. E.; Robb, M. A.; Cheeseman, J. R.; Montgomery, J. A.; Vreven, J., T.; Kudin, K. N.; Burant, J. C.; Millam, J. M.; Iyengar, S. S.; Tomasi, J.; Barone, V.; Mennucci, B.; Cossi, M.; Scalmani, G.; Rega, N.; Petersson, G. A.; Nakatsuji, H.; Hada, M.; Ehara, M.; Toyota, K.; Fukuda, R.; Hasegawa, J.; Ishida, M.; Nakajima, T.; Honda, Y.; Kitao, O.; Nakai, H.; Klene, M.; Li, X.; Knox, J. E.; Hratchian, H. P.; Cross, J. B.; Bakken, V.; Adamo, C.; Jaramillo, J.; Gomperts, R.; Stratmann, R. E.; Yazyev, O.; Austin, A. J.; Cammi, R.; Pomelli, C.; Ochterski, J. W.; Ayala, P. Y.; Morokuma, K.; Voth, G. A.; Salvador, P.; Dannenberg, J. J.; G., Z. V.; Dapprich, S.; Daniels, A. D.; Strain, M. C.; Farkas, O.; Malick, D. K.; Rabuck, A. D.; Raghavachari, K.; Foresman, J. B.; Ortiz, J. V.; Cui, Q.; Baboul, A. G.; Clifford, S.; Cioslowski, J.; Stefanov, B. B.; Liu, G.; Liashenko, A.; Piskorz, P.; Komaromi, I.; Martin, R. L.; Fox, D. J.; Keith, T.; Al-Laham, M. A.; Peng, C. Y.; Nanayakkara, A.; Challacombe, M.; Gill, P. M. W.; Johnson, B.; Chen, W.; Wong, M. W.; Gonzalez, C.; Pople, J. A. Gaussian, Inc.: Wallingford CT, 2004.

(19) Asawapirom, U.; Güntner, R.; Forster, M.; Farrell, T.; Scherf, U. *Synthesis 2002* **2002**, 1136.

Macromolecules

Article

pubs.acs.org/Macromolecules

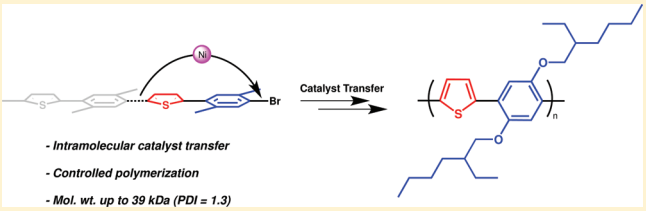
Controlled Chain-Growth Kumada Catalyst Transfer Polycondensation of a Conjugated Alternating Copolymer

Robert J. Ono, Songsu Kang, and Christopher W. Bielawski*

Department of Chemistry and Biochemistry, The University of Texas at Austin, 1 University Station A5300, Austin, Texas 78712, United States

Supporting Information

ABSTRACT: The Ni-catalyzed Kumada catalyst transfer polycondensation of a novel biaryl monomer, 2-(4-bromo-2,5-bis(2-ethylhexyloxy)phenyl)-5-chloromagnesiothiophene (**2**), afforded the respective π-conjugated alternating copolymer poly(thiophene-*alt*-*p*-phenylene) (PTPP). Under optimized conditions, the polystyrene-equivalent number-average molecular weight (M_n) of the copolymers prepared using this method were varied between 6.4 and 39 kDa by adjusting the initial monomer-to-catalyst ratios and, in all cases, the resulting materials exhibited narrow polydispersity indices (PDIs $\leq$ 1.33). Moreover, the M_n of the copolymers produced were found to increase linearly with monomer conversion. The ability of PTPP to be utilized as a macroinitiator for further copolymerization was confirmed through a series of chain extension experiments as well as block copolymerizations involving 2-bromo-5-chloromagnesio-3-hexylthiophene. MALDI-MS analysis showed that the major population of the PTPP prepared using the aforementioned method contained H/Br end groups, as would be expected for efficient catalyst transfer during the polymerization with minimal occurrence of chain termination. Collectively, these results were consistent with a controlled polymerization reaction and constituted the first such example in which a conjugated polymer with an alternating repeat unit was produced via a chain-growth process.



INTRODUCTION

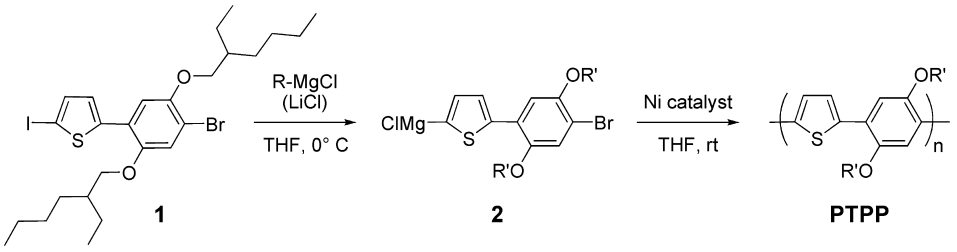
McCullough's[1] and Yokozawa's[2] seminal reports on the chain-growth polymerization of 3-hexylthiophene have enabled the corresponding polymer, P3HT, to become one of the most prevalent conjugated polymers (CPs) in the literature. Despite the synthetic versatility and impressive electronic properties of P3HT, significant research efforts are now being directed toward the synthesis of new CPs that feature properties tailored toward specific applications. For example, in the field of organic photovoltaics, a growing number of CPs have been shown to outperform P3HT when incorporated into solar cells,[3,4] generally owing to the former's broad absorption overlap with the solar spectrum and better energy matching with commonly used electron acceptors (e.g., phenyl-C61-butyric acid methyl ester; PCBM). Many of these new, high performance CPs are effectively "donor−acceptor" (D−A) polymers, designed to feature reduced optical bandgaps (and hence broader absorptions that extend into the red) by virtue of incorporating electron-donating and -withdrawing components into the polymer main chain.[5] Structurally, nearly all of these types of CPs take the form of an alternating copolymer comprised of donor and acceptor groups (e.g., -[D-A]-$_n$) and are generally synthesized by metal-catalyzed step-growth polycondensations. As such, these methods do not permit rigorous control over polymer molecular weight or polydispersity (M_w/M_n) and oftentimes afford ill-defined materials. A controlled, chain-growth synthesis of donor−acceptor CPs would not only allow for precise control over the aforementioned polymerization metrics but could also enable the preparation of more advanced macromolecular structures such as block copolymers and surface-grafted polymers. Moreover, the successful preparation of such well-defined structures could potentially facilitate greater control over the polymer morphology, which is another important parameter that governs the performance of organic electronic devices.[6,7]

We reasoned that such controlled polymerizations may be achieved by applying the Ni-catalyzed Kumada catalyst transfer polycondensation (CTP) to monomers that feature "built in" alternating repeat units. Recently, during the course of our investigations, Huck and co-workers reported a synthesis of the alternating copolymer poly(9,9′-dioctylfluorene-*alt*-benzothiadiazole) (PF8BT) using Pd-catalyzed Suzuki CTP.[8] While the chain-growth nature of the aforementioned polymerization was elegantly demonstrated, only polymers having moderate molecular weights (up to ca. 10 kDa or 19 repeat units) were isolated and efforts toward controlling the polymerization (e.g., establishing a linear relationship between polymer molecular weight and monomer conversion) appeared to be underway. We chose to continue our pursuit of Ni-catalyzed Kumada CTPs because they offer, as a complementary methodology, several potential advantages over analogous Suzuki-type polycondensations. For instance, Kumada CTPs do not require

Received: January 3, 2012
Revised: February 4, 2012
Published: February 23, 2012

ACS Publications © 2012 American Chemical Society

Scheme 1. Synthesis of PTPP[a]



[a]R = *t*-butyl or *i*-propyl. R′ = 2-ethylhexyl.

the use of specially synthesized catalysts or *ex-situ* initiation. Furthermore, despite the evidence that a chain-growth mechanism is operative in the Kumada CTP of monomers having relatively large molecular lengths (e.g., fluorenes, carbazoles, oligothiophenes, etc.), control over such polymerizations largely remains an unsolved problem, presumably due to inefficient catalyst transfer across the length of the monomer.[9−15] Here, we report the first controlled, chain-growth synthesis of a π-conjugated alternating copolymer, poly(thiophene-*alt*-*p*-phenylene) (PTPP), via the Kumada catalyst transfer polycondensation of a novel bicyclic monomer.

RESULTS AND DISCUSSION

We elected to incorporate thiophene and dialkoxybenzene into a single monomer unit because the Kumada catalyst transfer polymerizations of both thiophenes[1,2] and dialkoxybenzenes[16] have already been independently established.[17] Premonomer **1** was prepared in two steps by the Suzuki coupling of 2-thiopheneboronic acid and 1,4-dibromo-2,5-di(2-ethylhexyloxy)benzene followed by iodination with *N*-iodosuccinimide in 57% overall yield (see the Supporting Information for additional details). As summarized in Scheme 1, treatment of **1** with 1.0 equiv of ^{i}PrMgCl at 0 °C in THF resulted in the fast, quantitative conversion to **2**, as deduced by ^{1}H NMR spectroscopic analysis of the reaction mixture after quenching with HCl(aq). The reaction was complete within 20 min, and metalation occurred selectively at the α-position of the thiophene, leaving the aryl bromide intact, also evidenced by ^{1}H NMR spectroscopy of the corresponding quenched product, which revealed signals that were identical to that of 2-(4-bromo-2,5-bis(2-ethylhexyloxy)phenyl)thiophene (i.e., the precursor to **1**).

Polymerization was carried out at 23 °C by the addition of a Ni catalyst (3 mol %) to the THF solution of **2** and monitored by gel permeation chromatography (GPC) over time until the respective polymer molecular weight ceased to increase. Two Ni catalysts, Ni(dppp)Cl$_2$ and Ni(dppe)Cl$_2$ (dppp = 1,3-bis(diphenylphosphino)propane; dppe = 1,2-bis-(diphenylphosphino)ethane), were investigated for the polymerization of **2**, as they have been shown to be suitable catalysts for the homopolymerization of 2,5-dibromo-3-alkylthiophenes as well as 2,5-dibromo-1,4-dialkoxybenzenes.[2,16,18] As summarized in Table 1, both of the aforementioned catalysts afforded polymeric products. When Ni(dppe)Cl$_2$ was used as the catalyst, a relatively high number-average molecular weight (M_n) polymer was obtained; however, the resulting polymer also exhibited a broad polydispersity index (PDI) (Table 1, entry 1). In contrast, when Ni(dppp)Cl$_2$ was used, the PDI of the resultant polymer was much narrower, but only materials with relatively low M_ns were obtained (entry 2).

Table 1. Polycondensation of 2 with Various Ni Catalysts[a]

entry	catalyst	equiv of LiCl	Grignard reagent	M_n[b]	M_w/M_n[b]
1	Ni(dppe)Cl$_2$	0	^{i}PrMgCl	12 000	2.03
2	Ni(dppp)Cl$_2$	0	^{i}PrMgCl	3 700	1.32
3	Ni(dppe)Cl$_2$	1.0	^{i}PrMgCl	12 000	1.74
4[c]	Ni(dppp)Cl$_2$	1.0	^{i}PrMgCl	14 500	1.33
5	Ni(dppe)Cl$_2$	1.0	^{t}BuMgCl	15 200	2.03
6	Ni(dppp)Cl$_2$	1.0	^{t}BuMgCl	10 500	1.53

[a]Polymerizations were carried out by treating **1** with 1.0 equiv of Grignard reagent in THF ($[\mathbf{1}]_0$ = 0.1 M) for 20 min at 0 °C, followed by warming to 23 °C and addition of the Ni catalyst ($[\mathbf{1}]_0/[\mathrm{Ni}]_0$ = 33). In all cases, the expected M_n was based on a degree of polymerization of 33 and calculated to be 13 700 Da. [b]Determined by GPC based on polystyrene standards (eluent: THF). [c]Conversion of **2** to polymer: 87%; isolated yield: 71%.

It has been shown that the addition of LiCl to Kumada CTP reactions can have beneficial effects on the chain-growth polymerization characteristics of aryl-Grignard monomers. For example, Yokozawa and co-workers reported that the addition of LiCl conferred controlled, chain-growth characteristics to the polymerization of 1-bromo-4-chloromagnesio-2,5-dihexyloxybenzene to afford poly(*p*-phenylene)s with high molecular weights and narrow PDIs (e.g., 1.18).[16] We thus performed the polymerization of **2** with the aforementioned Ni catalysts in the presence of 1.0 equiv of LiCl. As shown in Table 1, the addition of LiCl had little effect on the polymerization when Ni(dppe)Cl$_2$ was used as the catalyst, as the molecular weight of PTPP remained unchanged from that which was obtained from the corresponding reaction without LiCl, although a slight decrease in polydispersity was observed (entry 3). When Ni(dppp)Cl$_2$ was used, however, the M_n of the resulting polymer increased significantly compared to that obtained from the analogous polymerization without LiCl, while the polymer's PDI remained relatively low (entry 4). After quenching the polymerization with HCl(aq), the pure homopolymer, poly(thiophene-*alt*-*p*-phenylene) (PTPP), was isolated in 71% yield by means of precipitation from methanol, followed by collection with the aid of vacuum filtration. When the polymerization was repeated in the presence of an internal standard (1,4-dihexyloxybenzene) and monitored over time by ^{1}H NMR spectroscopy, we found that the polymerization proceeded rapidly at 23 °C, consuming 87% of **2** within 15 min (Figure S1). Substituting ^{t}BuMgCl for ^{i}PrMgCl to facilitate the Grignard metathesis reaction did not lead to any significant molecular weight increase or narrowing of the polydispersity of the respective polymers (entries 5 and 6).

dx.doi.org/10.1021/ma300013e | *Macromolecules* 2012, 45, 2321−2326

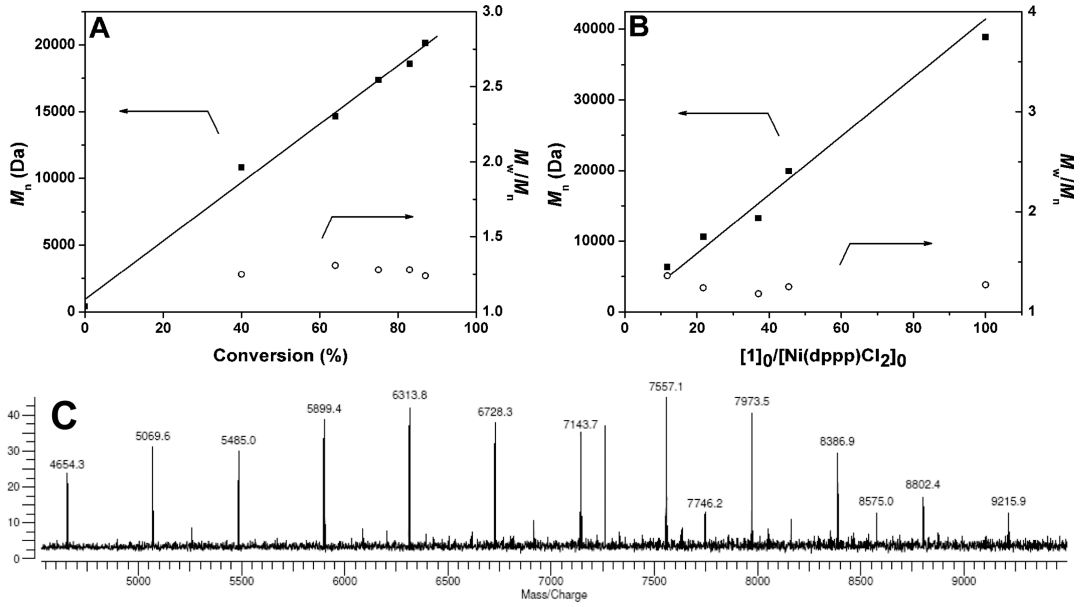
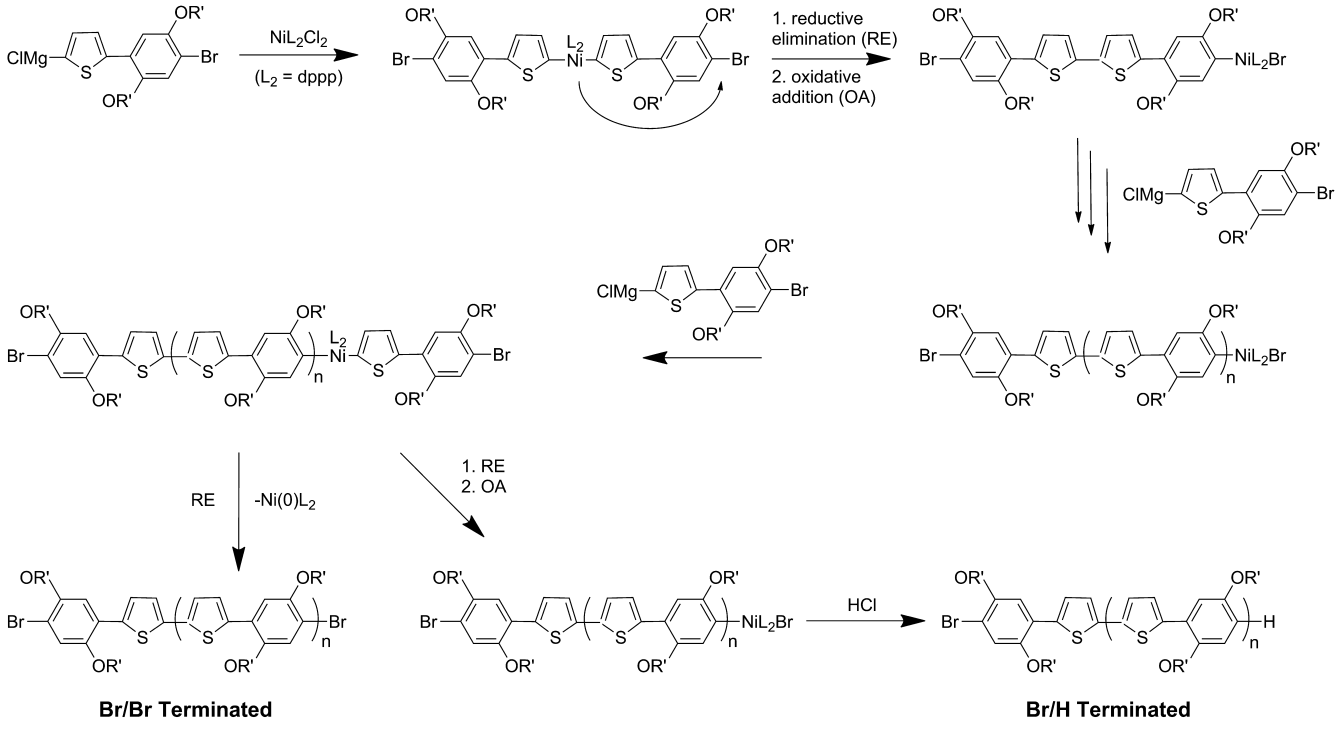


Figure 1. (A) M_n and M_w/M_n of PTPP plotted as a function of monomer conversion ($[\mathbf{1}]_0/[Ni(dppp)Cl_2]_0 = 56$); see text for further details. (B) M_n and M_w/M_n of PTPP plotted as a function of $Ni(dppp)Cl_2$ loading (conversion of **2** to polymer: 78−85%). Solid line indicates the theoretically expected M_n at a given $Ni(dppp)Cl_2$ loading. (C) MALDI mass spectrum of PTPP (M_n = 10 800 Da, M_w/M_n = 1.25, as determined by GPC). The peak at $m/z \sim 7257$ reflects electronic noise. For all polymerizations, $[\mathbf{1}]_0$ = 0.10 M.

Scheme 2. Proposed Mechanistic Pathways Leading to the Formation of H/Br end-Capped PTPP



Elegant mechanistic studies by McNeil and co-workers revealed that the role of LiCl in the controlled formation of poly(*p*-phenylene) and P3HT depends on the catalyst used. In $Ni(dppe)Cl_2$-catalyzed polymerizations, LiCl was found to have no effect on the polymerization rate, whereas in $Ni(dppp)Cl_2$-catalyzed polymerizations a rate dependence on LiCl was observed.[18,19] Our results were consistent with these observations: the addition of LiCl had a significant effect on the polymerization of **2** when $Ni(dppp)Cl_2$ was used as the catalyst, affording PTPP with a high molecular weight and low polydispersity, and little effect when $Ni(dppe)Cl_2$ was used. We therefore presume that the polymerization of **2**, as catalyzed by $Ni(dppp)Cl_2$, exhibits a rate dependence on [LiCl], which may serve to explain the rapid kinetics of polymerization observed in the presence of LiCl.

The M_n of the PTPP obtained using $Ni(dppp)Cl_2$ as the catalyst in the presence of 1.0 equiv LiCl (M_n = 14 500 Da, M_w/M_n = 1.33) was close to the theoretically expected value of

dx.doi.org/10.1021/ma300013e | *Macromolecules* 2012, 45, 2321−2326

13 700 Da, assuming both quantitative initiation and conversion of monomer to polymer. These results suggested to us that the polymerization was proceeding via a chain-growth mechanism. To probe whether the polymerization was controlled, the molecular weight of the polymer formed in the reaction was monitored as a function of monomer conversion. Briefly, a polymerization reaction was set up under the aforementioned conditions (i.e., catalyst = Ni(dppp)-Cl_2, 1.0 equiv LiCl, 23 °C in THF) at an initial monomer-to-catalyst ratio of 56 in the presence of an internal standard (1,4-dihexyloxybenzene); aliquots were then removed at regular intervals, quenched with aqueous HCl, and poured into excess methanol. After collection of the precipitated solids via filtration, the isolated polymers and filtrates were analyzed by GPC and ^{1}H NMR spectroscopy, respectively. As shown in Figure 1A, a linear dependence of the M_n versus the percent conversion of monomer over the course of the polymerization was observed. Moreover, the PDIs of the isolated polymers remained at or below 1.3 over the course of the polymerization reaction. When the polymerization of **2** was performed using varying initial catalyst loadings, the M_n increased proportionally with the initial monomer-to-catalyst ratio ($[\mathbf{1}]_0/[\text{Ni(dppp)Cl}_2]_0$) while PDIs remained relatively low (Figure 1B), indicating that the molecular weight of PTPP was successfully controlled over a wide M_n range (i.e., 6.4−39 kDa). Furthermore, the experimentally determined M_ns were in good agreement with the theoretically expected values at all of the initial catalyst loadings explored. Taken together, these results suggested to us that the polymerization followed a controlled chain-growth mechanism. It is also worth noting that PTPP, even at high molecular weights, maintained excellent solubility in THF (ca. 80 mg mL^{-1}), presumably due to the presence of the branched alkoxy side chains in every repeat unit.

End-group analysis using matrix-assisted laser desorption ionization (MALDI) mass spectrometry has been shown to provide important insight into polymerization mechanisms.[2,8,20] We therefore obtained MALDI mass spectra of a sample of PTPP (isolated after quenching the polymerization with HCl). As shown in Figure 1C, we observed a major population of signals that corresponded to H_2O adducts of H/Br end-capped PTPP, as calculated by the formula 414.3n (mass of n repeat units) + 1 (H) + 79.9 (Br) + 18 (H_2O).[21] The presence of H/Br end-capped polymers, along with a negligible population of polymers bearing Br/Br or H/H end groups, is a hallmark of efficient catalyst transfer in self-initiated catalyst transfer polycondensation reactions.[2,20] Collectively, these results suggested to us that nearly every polymer grew via catalyst transfer to the end of the polymer chain, as opposed to the catalyst freely diffusing through the reaction mixture to initiate a new polymerization or transferring to another chain. Therefore, we concluded that the polymerization proceeded through a chain-growth mechanism with minimal chain termination (Scheme 2).

To further demonstrate the controlled, chain-growth nature of the aforementioned Kumada CTPs, a series of chain extension and block copolymerization experiments were performed. First, a monomer addition experiment was conducted, wherein a fresh feed of monomer **2** was added to an unquenched, stirring solution of PTPP (PTPP-1) (initial conditions: $[\mathbf{1}]_0/[\text{Ni(dppp)Cl}_2]_0$ = 20; conversion of **2** to PTPP-1: 80%; PTPP-1 M_n = 8700 Da, M_w/M_n = 1.25). As shown in Figure 2A, the GPC trace of the polymer formed at

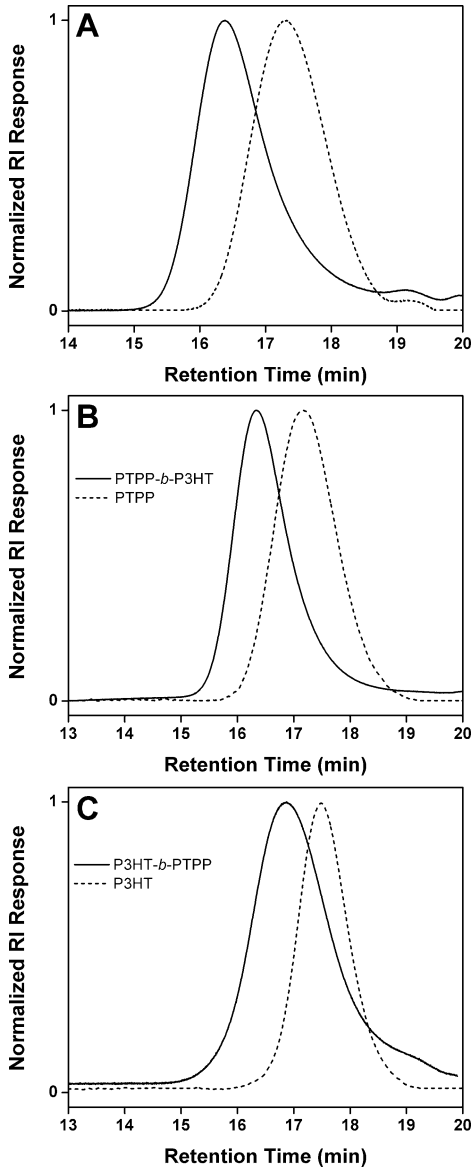
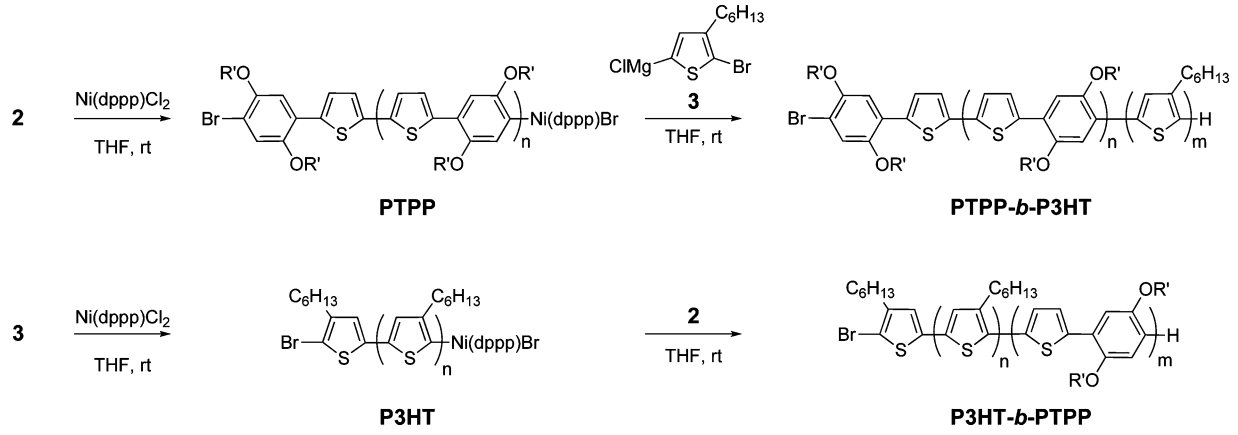


Figure 2. GPC traces of polymers obtained from chain extension polymerization experiments. (A) A monomer addition experiment: PTPP-1 (dashed line) ($[\mathbf{1}]_0/[\text{Ni(dppp)Cl}_2]_0$ = 20, conversion of **2** to polymer: 80%; PTPP-1: M_n = 8700 Da, M_w/M_n = 1.25); PTPP-1′ (solid line) ([remaining and added **1**]$_0$/$[\text{Ni(dppp)Cl}_2]_0$ = 31; conversion of **2** to polymer: 72%; PTPP-1′: M_n = 17 000 Da, M_w/M_n = 1.29). (B) A block copolymerization experiment (polymerization order: PTPP followed by P3HT). PTPP (dashed line): $[\mathbf{1}]_0/[\text{Ni(dppp)Cl}_2]_0$ = 18, conversion of **2** to polymer: 86%; polymer: M_n = 11 600 Da, M_w/M_n = 1.29. PTPP-*b*-P3HT (solid line): $[\mathbf{3}]_0/[\text{Ni(dppp)Cl}_2]_0$ = 51, conversion of **3** to polymer: 96%; polymer: M_n = 21 900 Da, M_w/M_n = 1.33. (C) A block copolymerization experiment (polymerization order: P3HT followed by PTPP). P3HT (dashed line): $[\mathbf{3}]_0/[\text{Ni(dppp)Cl}_2]_0$ = 60; conversion of **3** to polymer: 84%; polymer: M_n = 7500 Da, M_w/M_n = 1.22. P3HT-*b*-PTPP (solid line): $[\mathbf{1}]_0/[\text{Ni(dppp)Cl}_2]_0$ = 24, conversion of **2** to polymer: 67%; polymer: M_n = 9200 Da, M_w/M_n = 1.70.

the conclusion of this reaction (PTPP-1′) was clearly shifted toward higher molecular weight ([remaining and added **1**]$_0$/$[\text{Ni(dppp)Cl}_2]_0$ = 31; PTPP-1′: conversion of **2** = 72%, M_n = 17 000 Da, M_w/M_n = 1.29) with respect to PTPP-1. No discernible signal attributable to the presence of unreacted PTPP-1 was observed, suggesting to us that the added feed of **2**

dx.doi.org/10.1021/ma300013e | *Macromolecules* 2012, 45, 2321−2326

Scheme 3. Synthesis of Diblock Copolymers PTPP-*b*-P3HT and P3HT-*b*-PTPP[a]



[a]R′ = 2-ethylhexyl.

was successfully polymerized via chain extension from the terminus of PTPP-1.

We subsequently shifted our attention to the formation of diblock copolymers, choosing to incorporate P3HT as the second block because of its well-behaved polymerization behavior via Kumada CTP (Scheme 3).[9] As shown in Figure 2B, addition of 2-bromo-5-chloromagnesio-3-hexylthiophene[20] (**3**) to an unquenched solution of PTPP (M_n = 11 600 Da, M_w/M_n = 1.29) afforded a polymer with a monomodal GPC profile that was of higher molecular weight (M_n = 21 900 Da) than that obtained for its parent PTPP homopolymer. Furthermore, the PDI of the product remained low (M_w/M_n = 1.33), indicating that the unquenched PTPP in solution was active and effectively initiated the polymerization of **3**, which also proceeded in a chain-growth manner. The formation of a diblock copolymer, consistent with the expected structure (i.e., PTPP-*b*-P3HT), was further confirmed by ^{1}H NMR spectroscopy, which revealed signals attributable to both PTPP and P3HT (Figure S10).

Considering recent reports that have shown that the order of polymerization can affect the outcome of block copolymerizations involving Kumada CTPs,[13,22,23] we next attempted to synthesize the aforementioned diblock copolymer P3HT-*b*-PTPP by reversing the order of monomer addition. Thus, a THF solution of **2** ($[\mathbf{1}]_0/[Ni(dppp)Cl_2]_0$ = 24) was added to a stirring solution of unquenched P3HT (M_n = 7500 Da, M_w/M_n = 1.22). In this case, the resulting copolymer (M_n = 9200 Da, M_w/M_n = 1.70) displayed a broader molecular weight distribution than the parent P3HT homopolymer, and the conversion of **2** remained relatively low (conversion of **2** to polymer: 67%), even after prolonged reaction periods (Figure 2C). This result suggested to us that P3HT was not an efficient macroinitiator for the polymerization of PTPP, possibly due to the strong association of the Ni catalyst with P3HT.[22,24] Nevertheless, successful chain extension polymerizations of PTPP were achieved, which provided additional support that chain-growth polymerization of **2** proceeded in a controlled fashion.

The absorption and fluorescence spectra of the PTPP synthesized using the aforementioned procedures were acquired in dilute $CHCl_3$ solution and in the solid state (as thin films) (Figure S3). A slight bathochromic shift was observed in the respective absorption spectra upon concentration (λ_{max} = 467 nm → 477 nm), with a small shoulder appearing at 500 nm for the thin film. The emission spectra of PTPP in solution and as a thin film exhibited maxima at 523 and 629 nm, respectively. These results were consistent with those obtained for similar copolymers (e.g., poly(alkoxyphenylene−thienylene)s) previously reported in the literature.[15,25−28] The absorption spectra of the diblock copolymer PTPP-*b*-P3HT were also recorded in dilute $CHCl_3$ solution as well as in the solid state as a thermally annealed thin film (Figure S4). In this case, a large red shift of absorption was observed upon concentration (λ_{max} = 464 → 505 nm), likely a consequence of the $\pi-\pi$ stacking and subsequent planarization of the P3HT chains.[29,30] Moreover, vibronic structures reminiscent of P3HT homopolymer thin films were clearly visible at 560 and 605 nm. Compared to the solid state absorption of a P3HT homopolymer, however, the corresponding spectrum of PTPP-*b*-P3HT exhibited an absorption maximum at higher energies (λ_{max} = 560[31] and 505 nm for P3HT homopolymer and PTPP-*b*-P3HT, respectively). We believe that the solid state spectrum of PTPP-*b*-P3HT reflects the summed profiles of PTPP and P3HT homopolymers; thus, the blue-shifted λ_{max} of PTPP-*b*-P3HT compared to that of P3HT is a consequence of the overwhelming contribution of PTPP to the copolymer's absorption profile, rather than a morphological and/or energy transfer effect. Regardless, the absorption characteristics of PTPP-*b*-P3HT should be amenable to further fine-tuning by controlling the relative block lengths of the respective polymers, an otherwise laborious synthetic task that is effectively streamlined by the methodologies presented here, thus highlighting the potential utility of Kumada CTPs for producing conjugated alternating copolymers with tunable optical properties.

In conclusion, we have demonstrated that Kumada catalyst transfer polycondensation is a viable method for synthesizing well-defined conjugated *alt*-copolymers. We found that controlled chain-growth characteristics were conferred to the polymerization when $Ni(dppp)Cl_2$ was used as the catalyst in the presence of LiCl, a result that was consistent with efficient intramolecular catalyst transfer within the growing polymer backbone, despite the relatively large length of the repeat unit. As a benefit of this chain-growth mechanism, excellent control over copolymer molecular weight, polydispersity, and end-group composition was obtained, all of which facilitated the successful preparation of a new, well-defined block copolymer,

dx.doi.org/10.1021/ma300013e | *Macromolecules* 2012, 45, 2321−2326

PTPP-*b*-P3HT. These results unambiguously show, for the first time, that conjugated polymers with alternating repeating units can be synthesized in a controlled, chain-growth manner. Many low-bandgap and D−A conjugated polymers exhibit complex, alternating structures but are currently synthesized by means that do not permit the aforementioned degree of control over the polymerization. It is expected that the method presented herein will be amenable to attaining control over the synthesis of such D−A and other conjugated polymers and enable access to more complex macromolecular structures thereof.

■ ASSOCIATED CONTENT

Ⓢ Supporting Information

Detailed experimental procedures and additional characterization details. This material is available free of charge via the Internet at http://pubs.acs.org.

■ AUTHOR INFORMATION

Corresponding Author

*E-mail: bielawski@cm.utexas.edu.

Notes

The authors declare no competing financial interest.

■ ACKNOWLEDGMENTS

This material is based upon work supported by the National Science Foundation through the Centers for Chemical Innovation (CCI) under Grant CHE-0943957 as well as the Robert A. Welch Foundation (F-1621). We thank Dr. Karin Keller for conducting the MALDI mass spectrometry and Dr. Johanna Brazard for assistance with the fluorescence spectroscopy experiments as well as for helpful discussions.

■ REFERENCES

(1) Sheina, E. E.; Liu, J.; Iovu, M. C.; Laird, D. W.; McCullough, R. D. *Macromolecules* **2004**, *37*, 3526−3528.

(2) Miyakoshi, R.; Yokoyama, A.; Yokozawa, T. *J. Am. Chem. Soc.* **2005**, *127*, 17542−17547.

(3) Liang, Y.; Feng, D.; Wu, Y.; Tsai, S.-T.; Li, G.; Ray, C.; Yu, L. *J. Am. Chem. Soc.* **2009**, *131*, 7792−7799.

(4) Peet, J.; Kim, J. Y.; Coates, N. E.; Ma, W. L.; Moses, D.; Heeger, A. J.; Bazan, G. C. *Nature Mater.* **2007**, *6*, 497−500.

(5) Cheng, Y.-J.; Yang, S.-H.; Hsu, C.-S. *Chem. Rev.* **2009**, *109*, 5868−5923.

(6) Adachi, T.; Brazard, J.; Ono, R. J.; Hanson, B.; Traub, M. C.; Wu, Z.-Q.; Li, Z.; Bolinger, J. C.; Ganesan, V.; Bielawski, C. W.; Vanden Bout, D. A.; Barbara, P. F. *J. Phys. Chem. Lett.* **2011**, *2*, 1400−1404.

(7) Segalman, R. A.; McCulloch, B.; Kirmayer, S.; Urban, J. J. *Macromolecules* **2009**, *42*, 9205−9216.

(8) Elmalem, E.; Kiriy, A.; Huck, W. T. S. *Macromolecules* **2011**, *44*, 9057−9061.

(9) Proper spacial arrangement of neighboring aromatic rings has been shown to promote the controlled chain-growth Kumada CTP of a nonconjugated monomer, 3-(5-bromo-2-thienyl)-3-(5-iodo-2-thienyl)nonane. See: Wu, S.; Sun, Y.; Huang, L.; Wang, J.; Zhou, Y.; Geng, Y.; Wang, F. *Macromolecules* **2010**, *43*, 4438−4440.

(10) Beryozkina, T.; Senkovskyy, V.; Kaul, E.; Kiriy, A. *Macromolecules* **2008**, *41*, 7817−7823.

(11) Huang, L.; Wu, S.; Qu, Y.; Geng, Y.; Wang, F. *Macromolecules* **2008**, *41*, 8944−8947.

(12) Javier, A. E.; Varshney, S. R.; McCullough, R. D. *Macromolecules* **2010**, *43*, 3233−3237.

(13) Wu, S.; Bu, L.; Huang, L.; Yu, X.; Han, Y.; Geng, Y.; Wang, F. *Polymer* **2009**, *50*, 6245−6251.

(14) Stefan, M. C.; Javier, A. E.; Osaka, I.; McCullough, R. D. *Macromolecules* **2008**, *42*, 30−32.

(15) Wang, F.; Wilson, M. S.; Rauh, R. D.; Schottland, P.; Thompson, B. C.; Reynolds, J. R. *Macromolecules* **2000**, *33*, 2083−2091.

(16) Miyakoshi, R.; Shimono, K.; Yokoyama, A.; Yokozawa, T. *J. Am. Chem. Soc.* **2006**, *128*, 16012−16013.

(17) Our decision to use a monomer that metalates at the thiophene as opposed to the phenyl moiety was based on the work of Yokozawa and co-workers, who demonstrated that the order of polymerization was critical to the outcome of forming block copolymers containing P3HT and poly(*p*-phenylene) (PPP) segments: successive polymerization of the phenylene monomer followed by the thiophene monomer yielded a well-defined block copolymer with narrow molecular weight distribution, while reversing the order of monomer addition resulted in polymers with broad molecular weight distributions.[22] In other words, we anticipated that if metalation occurred at the thiophene unit, the propagating end of the resulting polymer (i.e., polymer−NiLBr) would feature a terminus where Ni is connected to a phenyl group, reminiscent of a Ni-terminated PPP, and ultimately result in a controlled polymerization process. In contrast, metalation at the phenyl unit would lead to polymers with termini that are reminiscent of Ni-terminated P3HT and afford ill-defined polymers.

(18) Lanni, E. L.; McNeil, A. J. *Macromolecules* **2010**, *43*, 8039−8044.

(19) Lanni, E. L.; McNeil, A. J. *J. Am. Chem. Soc.* **2009**, *131*, 16573−16579.

(20) Lohwasser, R. H.; Thelakkat, M. *Macromolecules* **2011**, *44*, 3388−3397.

(21) The signals observed at *m*/*z* 7746 and 8575 were assigned to an H/I terminated polymer as adducts of Li and dihydroxybenzoic acid (DHB, the matrix material) according to the following formula 414.3*n* (mass of *n* repeat units) + 1 (H) + 127 (I) + 7 (Li) + 154 (DHB). An H/I terminated polymer can arise from the generation of a small concentration of (2,5-bis(2-ethylhexyloxy)-4-(5-iodothiophen-2-yl) phenyl)magnesium chloride formed during the Grignard metathesis reaction, where the metalation of **1** occurs at the phenyl instead of at the thiophene moiety. This monomer can then initiate a polymerization reaction, thereby establishing an iodo group on one end of a polymer chain and, after catalyst transfer and quenching with HCl, a hydrogen group on the other.

(22) Miyakoshi, R.; Yokoyama, A.; Yokozawa, T. *Chem. Lett.* **2008**, *37*, 1022−1023.

(23) Yokoyama, A.; Kato, A.; Miyakoshi, R.; Yokozawa, T. *Macromolecules* **2008**, *41*, 7271−7273.

(24) Tkachov, R.; Senkovskyy, V.; Komber, H.; Sommer, J.-U.; Kiriy, A. *J. Am. Chem. Soc.* **2010**, *132*, 7803−7810.

(25) Bao, Z.; Chan, W.; Yu, L. *Chem. Mater.* **1993**, *5*, 2−3.

(26) Kim, Y. g.; Galand, E. M.; Thompson, B. C.; walker, J.; Fossey, S. A.; McCarley, T. D.; Abboud, K. A.; Reynolds, J. R. *J. Macromol. Sci., Part A: Pure Appl. Chem.* **2007**, *44*, 665−674.

(27) Lere-Porte, J.-P.; Moreau, J. J. E.; Serein-Spirau, F.; Torreilles, C.; Righi, A.; Sauvajol, J.-L.; Brunet, M. *J. Mater. Chem.* **2000**, *10*, 927−932.

(28) Tanese, M. C.; Farinola, G. M.; Pignataro, B.; Valli, L.; Giotta, L.; Conoci, S.; Lang, P.; Colangiuli, D.; Babudri, F.; Naso, F.; Sabbatini, L.; Zambonin, P. G.; Torsi, L. *Chem. Mater.* **2005**, *18*, 778−784.

(29) Xu, B.; Holdcroft, S. *Macromolecules* **1993**, *26*, 4457−4460.

(30) Kiriy, N.; Jähne, E.; Adler, H.-J.; Schneider, M.; Kiriy, A.; Gorodyska, G.; Minko, S.; Jehnichen, D.; Simon, P.; Fokin, A. A.; Stamm, M. *Nano Lett.* **2003**, *3*, 707−712.

(31) Liu, C.-Y.; Holman, Z. C.; Kortshagen, U. R. *Nano Lett.* **2008**, *9*, 449−452.

Macromolecules

Article

pubs.acs.org/Macromolecules

Polymer-Chain-Induced Tunable Luminescence Properties: Amphiphilic Poly(2-oxazoline)s Possessing a *N,N*-Dialkylpyrene-1-carboxamide Chromophore in the Side Chain

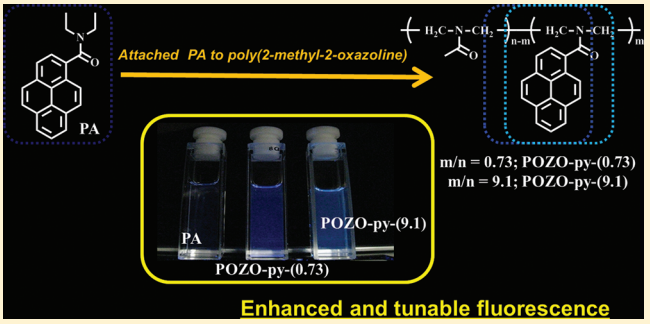
Yosuke Niko[†] and Gen-ichi Konishi*[,†,‡]

[†]Department of Organic and Polymeric Materials, Tokyo Institute of Technology, O-okayama, Tokyo 152-8552, Japan

[‡]PRESTO, Japan Science and Technology Agency (JST), Kawaguchi, Saitama 332-0012, Japan

Supporting Information

ABSTRACT: We report a polymer-chain-induced tunable luminescence system based on a newly synthesized fluorescent polymer, *N,N*-dialkylpyrene-1-carboxamide-modified poly(2-methyl-2-oxazoline) (**POZO-py**) at various ratios of pyrene induction. Photoluminescence and thermal properties of the **POZO-py** were analyzed in detail. Differential scanning calorimetry (DSC) measurements revealed that the glass-transition temperature (T_g) of **POZO-py** was above room temperature, which implies that **POZO-py** is in the glassy state at room temperature. **POZO-py-(0.73)** (i.e., pyrene content of 0.73%, M_n = 2270, T_g = 40 °C), having the lowest pyrene induction ratio, showed higher fluorescence quantum yields in several solvents, e.g., water, or in the thin film state than did *N,N*-diethylpyrene-1-carboxamide (a model compound, **PA**), because the polymer chain prevented the molecular mobilities of the pyrene moieties. In particular, **POZO-py** showed strong emission (Φ_{fl} = 0.52) in glycerin, which is a highly viscous solvent. Highly modified **POZO-py-(2.9)** (i.e., with a pyrene content of 2.9%, M_n = 2450, T_g = 48 °C) and **POZO-py-(9.1)** (M_n = 2640, T_g = 57 °C) exhibited both monomer and excimer emissions. These excimers consisted of a *static excimer* and a *dynamic excimer*. These results were not obtained for the low-molecular **PA**. Thus, **POZO** can induce improved and tunable photoluminescence properties of *N,N*-dialkylpyrene-1-carboxamide. The synthesis and photoluminescence properties of *N,N*-dialkylpyrene-1-carboxamide-modified poly(2-ethyl-2-oxazoline)-gel (**PEtOZO-py-gel**) were also determined.



INTRODUCTION

Pyrene is used widely as a chromophore because of its high fluorescence quantum yield, long fluorescence lifetime, ability to form excimers, and sensitive vibrational structure.[1] Because such characteristics are very useful in the analyses of local structures and molecular mobilities, pyrene has been utilized as a fluorescence probe in multimolecular systems.[2] Moreover, in recent years, pyrene has also been used as a fluorescence label for structural analyses and to study the electron transfer physics of polypeptides, DNA oligomers, and duplexes. Specifically, its use as a fluorescence label permitted these molecules to be examined in terms of their distances,[3] electric field effects,[4] and the conformational dependence of their electron transfer rates.[5] Similarly, in the field of polymer science, the use of pyrene, especially its excimer emission, is very popular for carrying out structural analyses. This is because when designing a new material using a polymer, it is extremely important to understand the relationship between the structure and the properties of the polymer. Pyrene is especially useful for studying water-soluble polymers.[2d] Therefore, the photophysics and structures of water-soluble polymers in water and other organic solvents have been investigated in detail.[6] Almost all pyrene chromophores that have been used in the investigation of pyrene-containing polymers were introduced into the main or side chain of the polymers through a nonconjugated alkyl spacer, π-extended spacer, or donor-group substituents such as triphenylamine or pyridine to develop analytical probes or photonic devices.[6,7] It is important to apply the properties of low-molecular pyrene derivatives to polymer materials in such studies.[8] As a result, very few investigations have been conducted on polymers modified by using pyrene derivatives that have lost the original pyrene characteristics owing to being functionalized by adding moieties such as carbonyl groups.[9] This is despite the fact that many chromophores that have been functionalized by carbonyl groups exhibit unique fluorescence phenomena in response to their external environment.[9,10] Consequently, fundamental investigations that have evaluated how polymer chains affect the properties of pyrene dyes are few and far between.

Received: January 17, 2012
Revised: February 13, 2012
Published: February 27, 2012

ACS Publications © 2012 American Chemical Society

Recently, we reported a new pyrene chromophore that possesses a tertiary *N*,*N*-dialkyl carboxamide group. The chromophore exhibits weak fluorescence in several organic solvents but shows relatively strong emissions in viscous solvents.[9] On the basis of these phenomena, we considered that the photophysical behavior of the chromophore is dominated by molecular motion that results in internal conversion.[11] Our latest endeavor has been to discover new photoluminescence properties of *N*,*N*-dialkylpyrene-1-carboxamide when it is attached to a polymer chain. More precisely, we think that it might be possible to not only exploit the properties of low-molecular pyrene derivatives but also improve them using chromophores such as *N*,*N*-dialkylpyrene-1-carboxamide. The polymer chain could efficiently suppress the molecular motion that leads to internal conversion during photophysical processes, which is similar to the behavior exhibited by glycerin.[11] In addition, it may be possible to observe polymer chain scaffold-mediated excimer emissions by controlling the pyrene content ratio.

In this paper, we report on poly(2-alkyl-2-oxazoline)s with an *N*,*N*-dialkylpyrene-1-carboxamide moiety in its side chain as a novel pyrene-containing fluorescent polymer. We also analyze the photoluminescence properties of poly(2-alkyl-2-oxazoline)s in detail to determine the influence that a polymer chain can have on a pyrene dye. Our target polymers were synthesized easily by cationic ring-opening polymerization, subsequently hydrolyzed, and then modified with carboxamide.[12,13] In addition, since poly(2-methyl-2-oxazoline) is amphiphilic,[13] we were able to study its photoluminescent behavior in various organic solvents and water. In recent years, many researchers have investigated poly(2-oxazoline)s because of its potential applications.[14] However, to the best of our knowledge, investigations on chromophore-modified poly(2-oxazoline)s have been limited to photogelation,[15] the analysis of local structures,[16] and temperature sensors using solvatochromic dyes.[17] Therefore, the photoluminescence properties of chromophore-modified poly(2-oxazoline)s and their applications have rarely been explored in detail. On the basis of what has been mentioned above, we believe that it is important to evaluate the photoluminescence properties of the tertiary *N*,*N*-dialkylpyrene-1-carboxamide chromophore in poly(2-oxazoline)s and photofunctional poly(2-oxazoline)s.

EXPERIMENTAL SECTION

Materials. Unless otherwise noted, all reagents and chemicals were used without further purification. Benzyl bromide and pyrene-1-carboxylic acid were obtained from TCI (Tokyo, Japan). Diisopropylcarbodiimide were purchased from Wako (Tokyo, Japan). 2-Methyl-2-oxazoline and poly(2-ethyl-2-oxazoline) (M_w = 50 000) were purchased from Sigma-Aldrich and 2-methyl-2-oxazoline was used after purification by distillation. Poly(methyl methacrylate) (PMMA: M_w = 100 000 atactic beads) was purchased from Polyscience, Inc. (Warrington PA). As a model compound, *N*,*N*-diethylpyrene-1-carboxamide (**PA**) was prepared along with previous report.[9] Spectrograde dichloromethane, ethanol, glycerin and special grade ethylene glycol were purchased from Nacalai Tasque (Kyoto, Japan). Distilled water was prepared from EYELA STILL ACE SA-2100A.

Instrumentals. All the ^{1}H NMR spectra were recorded on a 400 MHz JEOL LMN-EX400 instrument with tetramethylsilane (TMS) as the internal standard. FT-IR spectra were recorded on a JASCO FT-IR 469 plus spectrometer. Thermogravimetric analysis (TGA) was performed using a SII TG/DTA 6200 (SEIKO) with a heating rate of 10 °C/min under a nitrogen atmosphere. Differential scanning calorimetry (DSC) was carried out on a SII DSC 220C (SEIKO) at a heating rate of 20 °C/min and cooling rate 20 °C/min under a nitrogen atmosphere three times, respectively. All photophysical measurements performed in solutions were carried out using dilute solutions with optical density (O.D.) around 0.1 at the maximum absorption wavelength in 1 cm path length quarz cells. Thin films were spin coated from solution of PMMA and 1,2-dichloroethane on quarz plates using MIKASA SPIN COATER 1H-D7. Weight ratios of synthesized *N*,*N*-dialkylpyrene-1-carboxamide-modified poly(2-methyl-2-oxazoline) (**POZO-py**) for PMMA were less than 2%. The conditions of prepared films were with O.D. around 0.1 and their thickness were 300−400 nm. UV−vis spectra were recorded with a Beckman Coulter DU800 UV−vis Spectrophotometer. Fluorescence spectra were recorded on a JASCO FP-6500 Spectrofluorometer. Absolute Quantum Yields were measured by a Hamamatsu Photonics Quantaurus QY. Fluorescence lifetimes were measured using a Hamamatsu Photonics Quantaurus Tau. In situation where **POZO-py-(2.9)** and **POZO-py-(9.1)** were monitored at 500 nm, measurements at short-range were performed to investigate short-lived components in addition to those at long-range.

Polymerization of 2-Methyl-2-oxazoline. A mixture of 2-methyl-2-oxazoline (33.2 g, 390 mmol), benzyl bromide (2.66 g, 16 mmol) and acetonitrile (50 mL) was placed in a 200 mL two necked flask and sealed under nitrogen, which was then heated at 120 °C for 24 h. The resulting poly(*N*-acetylethylenimine) (**POZO**) was isolated by dissolving in MeOH and precipitation into diethyl ether. It was purified by fractionation with MeOH and diethyl ether and drying in vacuo. Yield was 29.8 g (90%, M_n = 2220).

Partial Hydrolysis of POZO. **POZO** was dissolved in aqueous NaOH solution (15 mL). The resulting solution was refluxed for 12 h. Water was removed under reduced pressure. Poly(ethylenimine/*N*-acetylethylenimine)random copolymer (**POZO-NH**) was extracted with dichloromethane and dried *in vacuo*. The degree of hydrolysis was determined by the ^{1}H NMR spectrum. The amounts of reagents, yields and number-average molecular weight of the obtained **POZO-NH** are summarized in Table S1 (Supporting Information).

Amidation of POZO-NH (POZO-py). A benzene suspension of **POZO-NH** and pyrene-1-carboxylic acid was freeze-dried. After argon was introduced, the mixture was dissolved in a mixture of dry 1,2-dichloroethane and distilled DMF under nitrogen atmosphere and cooled at 0 °C. To this solution was added diisopropylcarbodiimide. After the mixture was stirred overnight, the resulting urea was removed by filtration, and the filtrate was concentrated to yield a yellowish polymer, which was purified by using Sephadex LH-20 (Pharmacia, size-exclusion chromatography). Furthermore, resulting polymer was redissolved in dichloromethane and reprecipitated into diethyl ether (five times). Pyrene modified polymer **POZO-py** was obtained after vacuum-dry oven. The amounts of reagents, yields and number-average molecular weight of the obtained **POZO-py** are summarized in Table S2 (Supporting Information).

Partial hydrolysis of PEtOZO. **PEtOZO** (6.0 g) was dissolved in aqueous NaOH (1.4 mmol) solution. The refluxed for 12 h. Water was removed under reduced pressure. Poly(ethylenimine/*N*-ethanoylethylenimine) random copolymer (**PEtOZO-NH**) was extracted with dichloromethane and obtained after vacuum-dry oven. Yield was 3.1 g (67%). The degree of hydrolysis was determined by the ^{1}H NMR spectrum.

Partial amidation of PEtOZO-NH. A benzene (6 mL) suspension of a mixture of **PEtOZO-NH** (2.6 g, including 0.59 mmol amine unit) and pyrene-1-carboxylic acid (80 mg, 0.32 mmol) was freeze-dried. After argon was introduced, the mixture was dissolved in a mixture of dry 1,2-dichloroethane (6 mL) and distilled DMF (5 mL) under nitrogen atmosphere and cooled at 0 °C. To this solution was added diisopropylcarbodiimide (44 mg, 0.030 mmol). After the mixture was stirred overnight, the resulting urea was removed by filtration, and the filtrate was concentrated to yield a yellowish solid, which was purified by using Sephadex LH-20. Furthermore, resulting polymer was redissolved in dichloromethane and reprecipetated into diethyl ether (five times). Pyrene-modified polymer **POZO-NH-py** was obtained after vacuum-dry oven. Yield was 1.8 g (69%). The degrees of hydrolysis and amidation were determined by the ^{1}H NMR spectroscopy.

Scheme 1. Synthesis of POZO-py and Structure of Model Compound PA

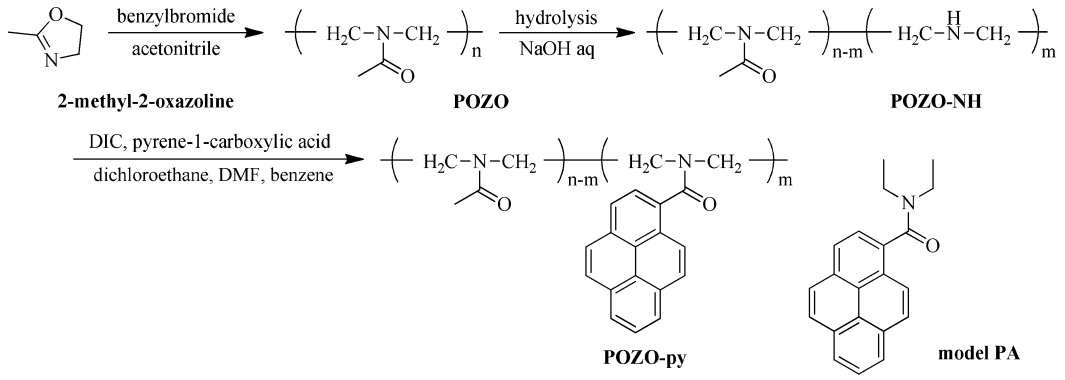


Table 1. ^{1}H NMR Analysis and Thermal Properties of POZO, POZO-NH, and POZO-py. (* Estimated by ^{1}H NMR)

entry	$n-m$	m	hydrolysis[a] m/n	amidation[a] m/n	T_g [°C]	T_{d5} [°C]	T_{d50} [°C]	M_n
POZO	26	–	–	–				2220
POZO-NH-(0.73)	28	0.22	0.0078	–				2400
POZO-py-(0.73)	26	0.19	–	0.0073	40	332	383	2270
POZO-NH-(2.9)	25	1.5	0.057	–				2230
POZO-py-(2.9)	26	0.79	–	0.029	48	330	384	2450
POZO-NH-(9.1)	24	4.6	0.16	–				2370
POZO-py-(9.1)	23	2.3	–	0.091	57	322	390	2640

[a]Estimated by ^{1}H NMR.

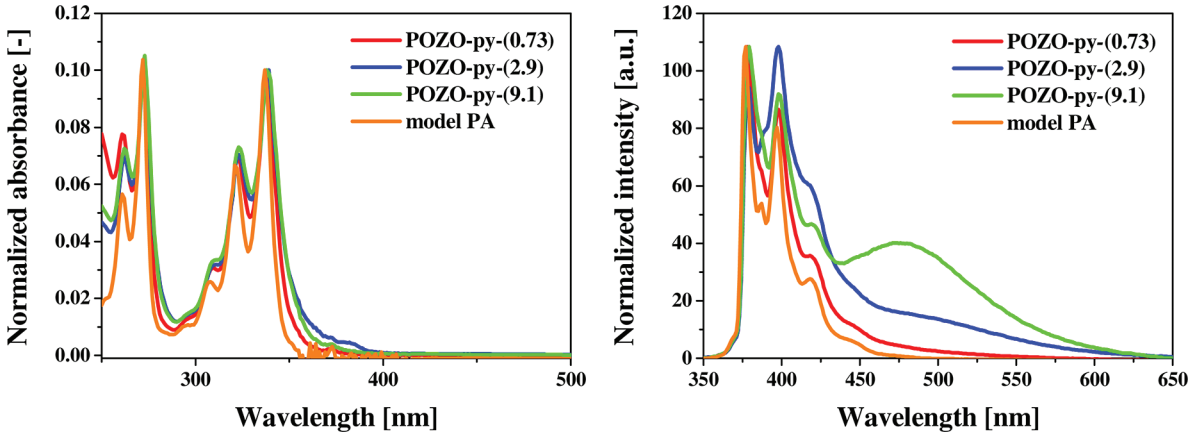


Figure 1. Normalized UV–vis absorption and fluorescence spectra of **POZO-py** and PA in ethanol solution ($\lambda_{ex} = \lambda_{abs}$, room temperature).

Cross-Linking Reaction of PEtOZO-NH-py. **PEtOZO-NH-py** (1.0 g, including 0.12 mmol amine unit), hexamethylene diisocyanate (50 mg, 0.30 mmol), DBU (84 mg, 0.50 mmol), and DMF (3 mL) were placed in a 50 mL flask and stirred at room temperature for 72 h under nitrogen atmosphere. The isolation of the gel (**PEtOZO-py-gel**) was purified by Soxhlet extraction with methanol, tetrahydrofuran, and dichloromethane. Yield was 0.86 g (85%).

RESULTS AND DISCUSSION

Synthesis and Characterization of Pyrene-Modified Poly(2-methyl-2-oxazoline) (POZO-py). **POZO-NH**, a poly(*N*-acetylethylenimine)/poly(ethylenimine) random copolymer, was synthesized through the partial hydrolysis of poly(2-methyl-2-oxazoline) (**POZO**).[15] Pyrene-modified **POZO** (**POZO-py**) was obtained subsequently by introducing pyrene-1-carboxylic acid to the resulting N–H group by using *N*,*N*-diisopropylcarbodiimide (DIC) as a condensing agent. (Scheme 1) In all samples, the number-average molecular weight (M_n), ratio of hydrolysis, and the ratio of pyrene induction were estimated by using the integral values obtained from ^{1}H NMR spectra. **POZO-py** was purified using reprecipitation and gel filtration (Sephadex LH-20). The results of these preparations are summarized in Table 1. We obtained three samples, which contained 0.73%, 2.9%, and 9.1% pyrene units, and named them **POZO-py-(0.73)**, **POZO-py-(2.9)**, and **POZO-py-(9.1)**, respectively. As shown in Table 1, purified **POZO-py** had a lower pyrene content than the ratio of hydrolysis of corresponding **POZO-NH**. From the comparison between **POZO-py** modified using large and small amounts of pyrene, we inferred that this lower ratio was the result of either the removal of low-molecular-weight components possessing pyrene moieties or the difference in the solubility of the reprecipitation solvents. Because of the disappearance of the peak derived from the hydrogen atoms on the carbon atoms adjacent to the amine sites, we concluded that the reaction between pyrene-1-carboxylic acid and **POZO-NH** proceeded completely. In addition to these **POZO-py**, we

dx.doi.org/10.1021/ma3001252 | *Macromolecules* 2012, 45, 2327–2337

prepared low-molecular *N,N*-dialkylpyrene-1-carboxamide **PA**, which has already been reported in ref 9, as a model compound.

Differential scanning calorimetry (DSC) and thermogravimetric analysis (TGA) were carried out to determine the thermal transition and degradation behavior of **POZO-py** (Table 1, Figure S3 and Figure S4 in Supporting Information). DSC measurements revealed that all **POZO-py** at various pyrene content ratios showed a glass-transition temperature (T_g) higher than room temperature and that T_g increased with increasing pyrene content. **POZO-py** tends to form dimers in the ground state with increasing pyrene content. Therefore, we expected that $\pi-\pi$ interactions were strong in **POZO-py-(9.1)**. Owing to the limited mobility of the chain around pyrene, T_g increased for **POZO-py-(9.1)**. The TGA curves of **POZO-py** revealed a single thermal decomposition temperature. Although a clear correlation between the decomposition temperature and the ratio of pyrene induction was not found, the values of T_{d5} and T_{d50} were almost the same for all the samples.

Although the molecular weights of **POZO-py** were around 2000, they exhibited the sufficiently high glass transition temperature, and film-forming properties as mentioned below. Therefore, we considered that it is enough to expect the polymer-chain effects.

Photoluminescence Properties of POZO-py in Ethanol Solution. *UV–Vis Spectra.* The UV–vis absorption spectra of **POZO-py** and the model compound **PA** in a deaerated ethanol solution were obtained. As shown in Figure 1, the UV–vis spectra of **POZO-py** were red-shifted slightly and broadened with increasing pyrene content compared to the UV–vis spectra of **PA**. On the basis of a previous report from Todesco,[18] we inferred that these changes in the spectra were the result of a strong hypochromic effect caused by the aggregation of pyrene in the ground state, often called *preassociation*. In our previous work,[9] we assigned the peak of *N,N*-dialkylpyrene-1-carboxamide derivatives at around 340 nm to the $S_0 \rightarrow S_1$ transition by means of time-dependent density functional theory (TD-DFT) calculations. In this work, we obtained similar results from the absorption spectra. It is widely known that the peak-to-valley ratio of this absorption (P_a) indicates the degree of preassociation.[2d]

In general, a decrease in the value of P_a corresponds to an increase in the degree of preassociation. In this study, we measured the UV–vis spectra under conditions in which the optical density (O.D.) of all the samples was 0.1. Therefore, it can be said that they possessed the same amount of pyrene but that the pyrene density of each sample was clearly different. As can be seen from Table 2, the value of P_a for **POZO-py** tended to decrease with increasing pyrene content. In addition, the P_a values for all the samples were less than those for **PA**. These results support the claim that **POZO-py** formed preassociations in the ground state and that the red-shifted absorption spectra were derived from the hypochromic effect caused by such associations.

Fluorescence and Excitation Spectra. The fluorescence spectra of **POZO-py** and the model compound **PA** in a deaerated ethanol solution were obtained. We noticed that within the fluorescence spectra (Figure 1), **POZO-py-(0.73)** had a spectrum similar to that of **PA**, whereas **POZO-py-(2.9)** showed a slightly broadened spectrum. In addition, a clear excimer emission was observed at around 480 nm within the spectrum for **POZO-py-(9.1)**. As previously reported, **PA** does not exhibit an excimer emission because Debye's diffusion equation indicates that the collision rate of **PA** under this condition is slower than that of radiative and nonradiative processes.[9,19] Therefore, the excimer species of **POZO-py**, which were measured under the same conditions as those for **PA**, were induced by the aggregation of hydrophobic pyrene moieties in the hydrophilic **POZO** chain matrix similar to that for aqueous pyrene-modified polymer.[2d] We continuously measured the excitation spectra of **POZO-py** and **PA** and obtained two parameters, P_M and P_E, which we calculated from observations made at 380 nm (monomer emission) and 480 nm (excimer emission), respectively. In general, the excitation spectra provided compelling evidence for the ground-state interactions of pyrene. For cases in which pyrene preassociation occurs, P_E is always less than P_M and the spectra monitored in the excimer regions are slightly red-shifted relative to those in the monomer regions. As shown in Figure 2 and Table 3, the results of the excitation spectra support the claim that preassociation of **POZO-py** occurs, which we also noted based on our analysis of the UV–vis spectra. Thus, we considered that similar spectra were obtained because the values of all of the parameters were relatively close for both **PA** and **POZO-py-(0.73)**. On the other hand, **POZO-py-(2.9)** and **POZO-py-(9.1)** were estimated to form relatively large associative ground-state pyrene dimers, resulting in broadened or excimer emissions. As is common among pyrene-labeled aqueous polymers, polymers with partially overlapping pyrene moieties in an excited state often emit a broad and structureless emission at 420 nm, which is called a *static excimer* (ref 2d, see Figure 3). In our present work, a static excimer was generated from the preassociation state. Therefore, **POZO-py-(2.9)**, which possesses more pyrene moieties than **POZO-py-(0.73)**, showed an emission that was a mixture of a monomer emission and a static excimer emission. In **POZO-py-(9.1)**, clear excimer and monomer emissions were observed at around 475 and 380 nm, respectively. This excimer emission was not due to a static excimer. Rather, it was due to a dynamic excimer, as defined by Birks.[20] This was generated by further pyrene modification and the subsequent encounter of an electronically excited pyrene with a second pyrene in its ground electronic state. Considering the shape of the emission spectra, we also inferred that **POZO-py-(2.9)** and **POZO-py-(9.1)** contained slightly dynamic and static excimers, respectively.

Fluorescence Quantum Yield. As shown in Table 2, **POZO-py-(0.73)**, which has an emission similar to that of **PA**, exhibited a higher fluorescence quantum yield (Φ_{fl} = 0.17) than **PA** (Φ_{fl} = 0.061). Slightly red-shifted **POZO-py-(2.9)** also

Table 2. Spectroscopic Properties of POZO-py and PA in Ethanol Solutions

entry	λ_{abs} [nm]	P_a[a]	λ_{em} [nm]	Φ_{fl}[b]	P_M[c]	P_E[d]
POZO-py-(0.73)	338	2.24	378, 398, 420	0.17	1.59	1.48
POZO-py-(2.9)	339	1.90	379, 398, 420	0.22	1.56	1.45
POZO-py-(9.1)	339	1.86	379, 398, 475	0.17	1.53	1.50
model PA	337	2.75	377, 387, 397, 419	0.061	1.78	1.79

[a] P_a: Peak-to-valley ratio for the $S_0 \rightarrow S_1$ transition. [b] Φ_{fl}: Measurement for calibrating the integration sphere. [c] P_M: Peak-to-valley ratio for the $S_0 \rightarrow S_1$ transition in the excitation spectrum viewed at a monomer emission (ca. 380 nm). [d] P_E: Peak-to-valley ratio for the $S_0 \rightarrow S_1$ transition in the excitation spectrum viewed at the excimer emission (ca. 480 nm).

dx.doi.org/10.1021/ma3001252 | *Macromolecules* 2012, 45, 2327–2337

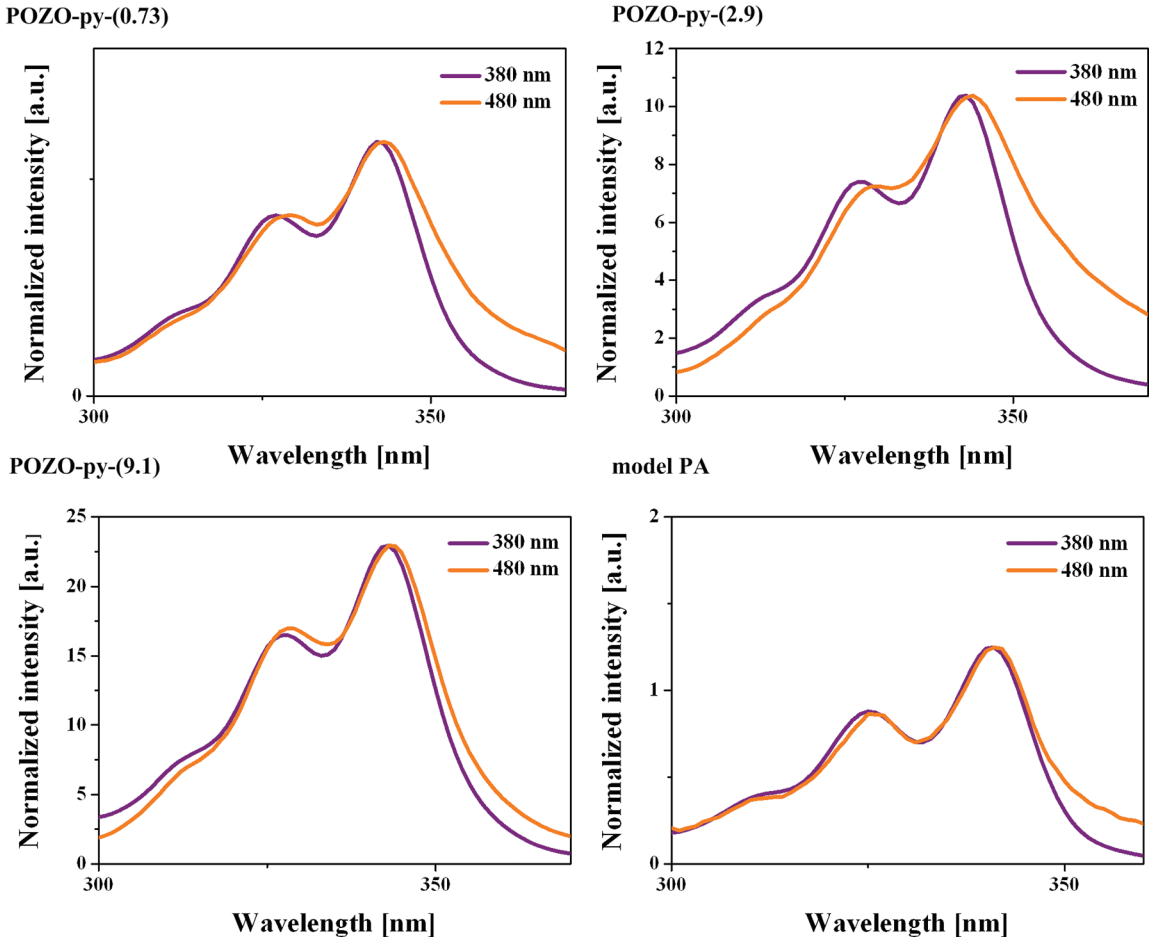
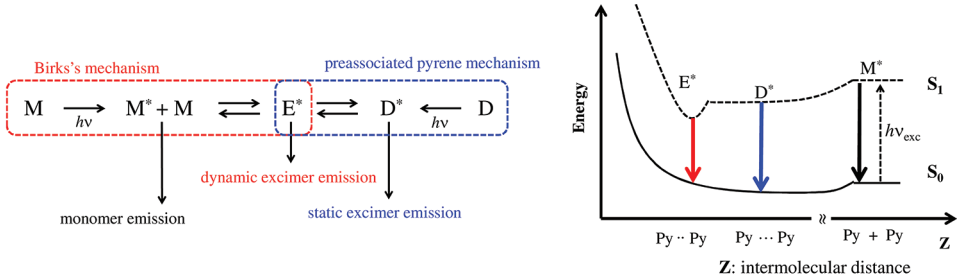


Figure 2. Excitation spectra of **POZO-py** (purple line, λ_{ex} = 380 nm; orange line, λ_{ex} = 480 nm).

Table 3. Fluorescence Lifetime Decay of POZO-py in Ethanol Solution (λ_{ex} = 340 nm, Room Temperature)

entry	τ_1	τ_2	τ_3	τ_4	A_1	A_2	A_3	A_4	χ^2
POZO-py-(0.73) (380 nm)	1.6	12.4	36.3		0.22	0.30	0.48		1.10
POZO-py-(0.73) (420 nm)	1.06	7.59	35.1		0.43	0.33	0.24		1.06
POZO-py-(2.9) (380 nm)	4.2	17.1	39		0.47	0.32	0.21		1.11
POZO-py-(2.9) (420 nm)	3.11	7.94	34		0.59	0.33	0.08		1.13
POZO-py-(2.9) (500 nm)	0.055[21]	2.42	44	0.44	−0.65	0.07	0.08	0.20	1.05
POZO-py-(9.1) (380 nm)	3.39	13.9	33.3		0.45	0.38	0.17		1.1
POZO-py-(9.1) (420 nm)	3.39	13.2	35.0		0.56	0.29	0.15		1.02
POZO-py-(9.1) (500 nm)	0.013[21]	2.7	41.2		−0.41	0.15	0.44		1.09



M and M*: Monomer pyrene in the ground state and in the first excited state, respectively.

E*: Dynamic excimer in the first excited state.

D and D*: Dimer pyrene in the ground state (pre-association) and in the first excited state, respectively.

Figure 3. Two proposed mechanisms for excimer formation (left) and schematic potential energy diagrams for pyrene excimer formation in the absence of ground-state and with pyrene ground-state association (right).[2d,20]

dx.doi.org/10.1021/ma3001252 | *Macromolecules* 2012, 45, 2327−2337

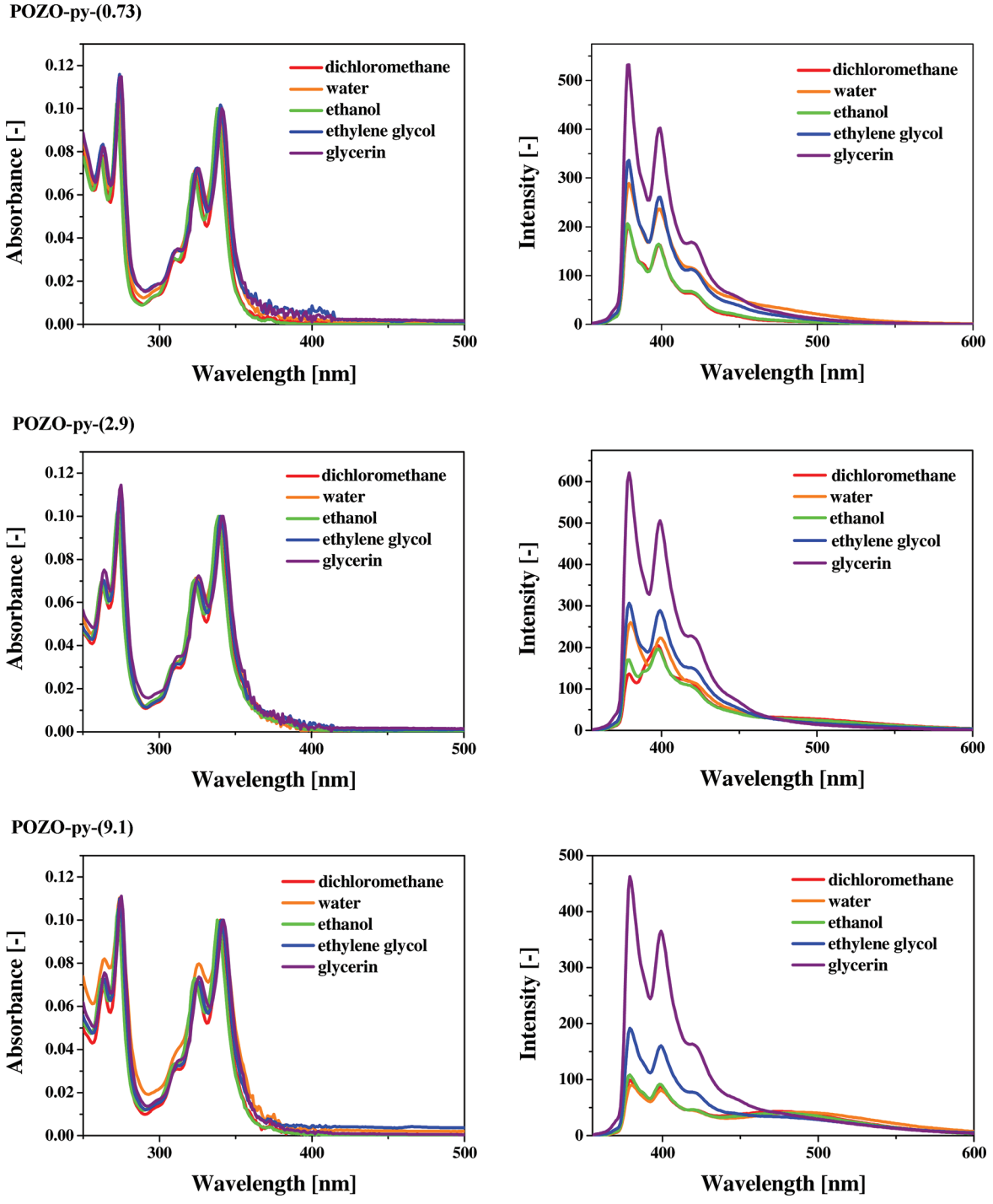


Figure 4. UV–vis absorption and fluorescence spectra of POZO-py and PA in dichloromethane, ethanol, and water solutions ($\lambda_{ex} = \lambda_{abs}$, room temperature).

showed a high quantum yield (Φ_{fl} = 0.22), similar to **POZO-py-(0.73)**. Although **POZO-py-(9.1)** had a higher quantum yield (Φ_{fl} = 0.17) than **PA**, the intensity of the monomer emission was reduced because of the large contribution made by the excimer emission. Considering that increases in the fluorescence intensity and excimer emission were not observed for **PA**-doped **POZO**. Moreover, the fluorescence properties of **PA** are almost not influenced by the polarities of solvents as mentioned our previous work.[9] It can be considered that the above-mentioned improved fluorescence was derived from the addition of *N*,*N*-dialkylpyrene-1-carboxamide to the polymer chain (Figure S5, Supporting Information). In a previous study,[9] we demonstrated that fluorescence quantum yields of tertiary *N*,*N*-dialkylpyrene-1-carboxamide derivatives were enhanced significantly with increasing viscosity of the media owing to the suppression of molecular motions, which sometimes cause the occurrence of internal conversion.[11] Therefore, the mobilities of the pyrene-1-carboxamide dyes were probably suppressed by the polymer chain, just as would occur in viscous media. The **POZO** chain has a beneficial structure whereby pyrene moieties can be directly introduced onto the side chain almost like substituents to inhibit the

dx.doi.org/10.1021/ma3001252 | *Macromolecules* 2012, 45, 2327–2337

Table 4. Spectroscopic Parameters of POZO-py in Various Solvents

entry	solvent	λ_{abs} [nm]	λ_{em} [nm]	P_a	Φ_{fl}	P_M	P_E
POZO-py-(0.73)	dichloromethane	341	378, 398, 420	2.26	0.15	1.60	1.57
	water	339	379, 398, 420	1.78	0.27	1.46	1.41
	ethanol	338	378, 398, 420	2.24	0.17	1.59	1.48
	ethylene glycol	340	379, 399, 420	1.94	0.26	1.59	1.43
	glycerin	341	379, 399, 420	2.06	0.52	1.59	1.44
POZO-py-(2.9)	dichloromethane	340	379, 397, 418	1.91	0.41	1.59	1.51
	water	340	380, 399, 421	1.60	0.25	1.43	1.28
	ethanol	339	379, 398, 420	1.90	0.21	1.56	1.45
	ethylene glycol	341	379, 399, 422	1.82	0.30	1.56	1.46
	glycerin	342	379, 399, 420	1.82	0.54	1.52	1.30
POZO-py-(9.1)	dichloromethane	340	379, 399, 474	1.90	0.21	1.60	1.50
	water	341	380, 399, 488	1.45	0.15	1.42	1.23
	ethanol	339	379, 398, 475	1.86	0.17	1.53	1.50
	ethylene glycol	341	379, 399, 422	1.76	0.21	1.54	1.34
	glycerin	342	379, 399, 420	1.71	0.41	1.52	1.30

molecular mobilities of pyrene-1-carboxamides. We think that the enhanced fluorescence emission of **POZO-py-(0.73)** resulted from the suppression of pyrene-1-carboxamide dye mobility caused by **POZO**. Additionally, the fluorescence of tertiary *N*,*N*-dialkylpyrene-1-carboxamide was enhanced without modification by changing the electronic state of the dye. Thus, a polymer-chain-induced emission was observed for **POZO-py-(0.73)**.

Fluorescence Lifetime Decay. For the fluorescence lifetime measurements, significant trends were observed as described below.

1. Roughly three components were observed for almost all of the measurements.
2. As observed in the long-wavelength region, the contribution of long-lived components decreased and that of short-lived components increased.
3. The tendencies described in point 2 became more pronounced as the pyrene content increased.
4. For the results of **POZO-py-(2.9)** and **POZO-py-(9.1)** at 500 nm, clear rising components were observed.

Although **PA** showed only a single component (τ = 30.4 ns, observed at 380 nm in ethanol solution) in a previous study,[9] in this study, almost all samples of **POZO-py** exhibited three components in ethanol solution. However, at a short wavelength (380 nm) for **POZO-py-(0.73)**, which showed behavior most similar to **PA**, the most dominant component (τ = 36.3 ns) was relatively close to that of **PA**. Therefore, it can be inferred that this component was derived from monomer emission. Given the above results, we considered that the other short-lived components, which were observed predominantly for measurements of highly pyrene modified **POZO-py** or for measurements at long wavelengths, were derived from preassociated dimers or other geometries induced by the polymer chain. As shown in Table 3, this indicates that **POZO-py-(0.73)** possesses several excited species. For the measurements of **POZO-py-(2.9)** and **POZO-py-(9.1)**, in addition to monomer and other short-lived species components, clear rising components were observed at 500 nm. These results are evidence for the formation of dynamic excimer species and support the fact that emissions obtained from **POZO-py-(2.9)** and **POZO-py-(9.1)** were a mixture of monomer, static excimer, and dynamic excimer emissions, as mentioned above.

Solvent Dependence of Luminescent Properties of POZO-py. In order to investigate the dependence of the luminescent properties of **POZO-py** on solvent viscosity or polarization, UV−vis absorption (Figure 4), fluorescence spectra, and other photophysical parameters of **POZO-py** were measured in several solvents.

For all measurements, enhancements in fluorescence quantum yields of **POZO-py** were observed with increasing solvent viscosity. Furthermore, in the most viscous medium (glycerin), the dynamic excimer emission of **POZO-py-(9.1)** at around 480 nm almost disappeared. We believed that a sandwich-shaped excimer failed to form because the glycerin medium suppressed the arrangement of excited species. With respect to **POZO-py-(9.1)**, the enhanced fluorescence quantum yields were derived not only from the suppression of internal conversion by viscous media but also from the suppression of deactivation brought about by energy transfer from high-energy excited species to low-energy excimer species. For the measurement of **POZO-py-(0.73)**, a highly enhanced monomer emission (Φ_{fl} = 0.52), which was much higher than that of **PA** (Φ_{fl} = 0.23), was observed for the glycerin solvent.[9] This highly luminescent performance was not obtained from low-molecular *N*,*N*-dialkylpyrene-1-carboxamide derivatives. Therefore, we considered that this phenomenon was caused by the interaction between the polymer matrix and the glycerin solvent. Considering that **POZO-py** consists of polarized amide units, we inferred that a strong hydrogen-bond network was formed between **POZO-py** and the glycerin medium. As a result, in addition to suppressing vibration of the pyrene moieties, the motion of the **POZO-py** chain was frozen and highly luminescent performance was achieved. In other words, the poly-2-methyl-2-oxazoline chain induced dramatic improvement in the fluorescence emission of the *N*,*N*-dialkylpyrene-1-carboxamide derivatives.

With respect to the dependence of the luminescent properties of **POZO-py** on polarization, changes in **POZO-py-(2.9)** and **POZO-py-(9.1)**, which showed relatively large pyrene aggregation in the ground state, were observed. As can be seen in Table 4, red-shifted and broadened spectra were observed in most polarized water solvents. It is known generally that an excited complex, just like an excimer, is stabilized in polar solvents, and a stabilized excited complex tends to be inactivated by energy transfer. In the nonpolar dichloromethane solvent, such deactivation was suppressed. Therefore, a relatively strong emission was observed.

dx.doi.org/10.1021/ma3001252 | *Macromolecules* 2012, 45, 2327−2337

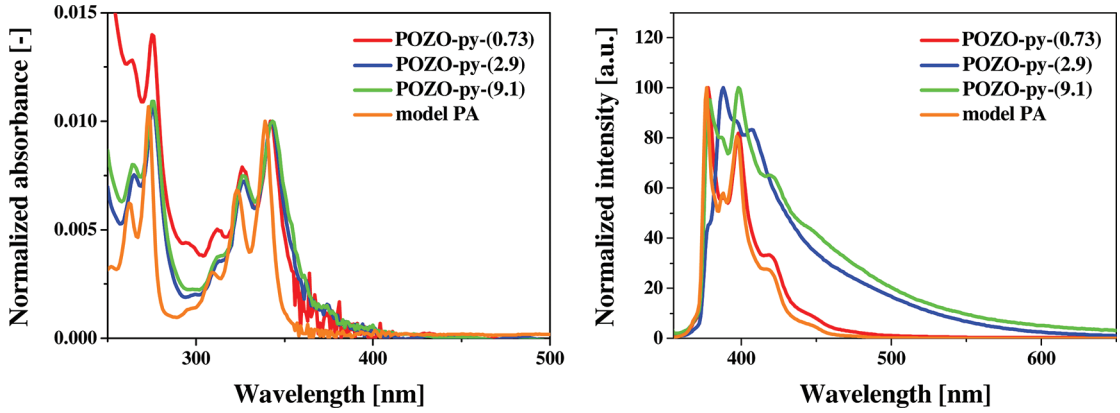


Figure 5. Normalized UV−vis and fluorescence spectra of POZO-py in the thin film state ($\lambda_{ex} = \lambda_{abs}$, room temperature).

Photoluminescent Properties of Thin-Film POZO-py. Thin films of **POZO-py** and **PA** were prepared by spin-coating of a 1,2-dichloroethane solution containing **POZO-py** or **PA** and PMMA. The films that we obtained had an O.D. of around 0.1 and a film thickness of approximately 300 to 400 nm. In order to investigate the photophysical behavior of thin-film **POZO-py**, its UV−vis and fluorescence spectra and other photophysical parameters were measured.

As shown in Figure 5 and Table 5, the UV−vis spectra of **POZO-py-(0.73)** and **PA** were red-shifted slightly and P_a was less than that for the ethanol solution. These results indicated that thin-film **POZO-py-(0.73)** and **PA** each formed a preassociation. From the excitation spectra measurements, the values of P_M and P_E also provided evidence for such aggregation. For the fluorescence spectra, both **POZO-py-(0.73)** and **PA** showed clear and strong monomer emissions. From the DSC results, we considered that the **POZO-py** films were in a glassy state at room temperature. Therefore, a stronger monomer emission was expected than for that under any other conditions, owing to the suppression of molecular motions. Although **PA** in the film state showed a slightly stronger emission than that it did in the glycerin solvent, **POZO-py-(0.73)** in the film state exhibited slightly weaker emissions than it did in the glycerin solvent. From the values of P_a, we considered that the preassociated dimer formed more tightly in the thin film than in the other solution states. Therefore, the fluorescence quantum yield of thin-film **POZO-py-(0.73)** decreased owing to the energy transfer from a monomer excited state to a low-energy dimer excited state.

Table 5. Spectroscopic Parameters of POZO-py in the Thin Film State

entry	λ_{abs} [nm]	P_a	λ_{em} [nm]	Φ_{fl}	P_M	P_E
POZO-py-(0.73)	342	1.67	378, 388, 398, 420	0.36	1.72	1.68
POZO-py-(2.9)	343	1.67	388, 396, 407	0.24	1.46	1.34
POZO-py-(9.1)	343	1.59	378, 388, 398, 420	0.11	1.48	1.22
model PA	339	2.59	377, 388, 397, 420	0.28	1.79	1.68

For the fluorescence lifetime measurements (Table 6), **POZO-py-(0.73)** showed results similar to those of **PA**. Both **POZO-py-(0.73)** and **PA** exhibited long-lived components (τ > 100 ns) and one component derived from monomeric excited species (τ = 32.2 and 30.8 ns, respectively). Furthermore, **POZO-py-(0.73)** showed short-lived excited species, and we considered that this component was derived from preassociation species, similar to what occurred in the ethanol solution.

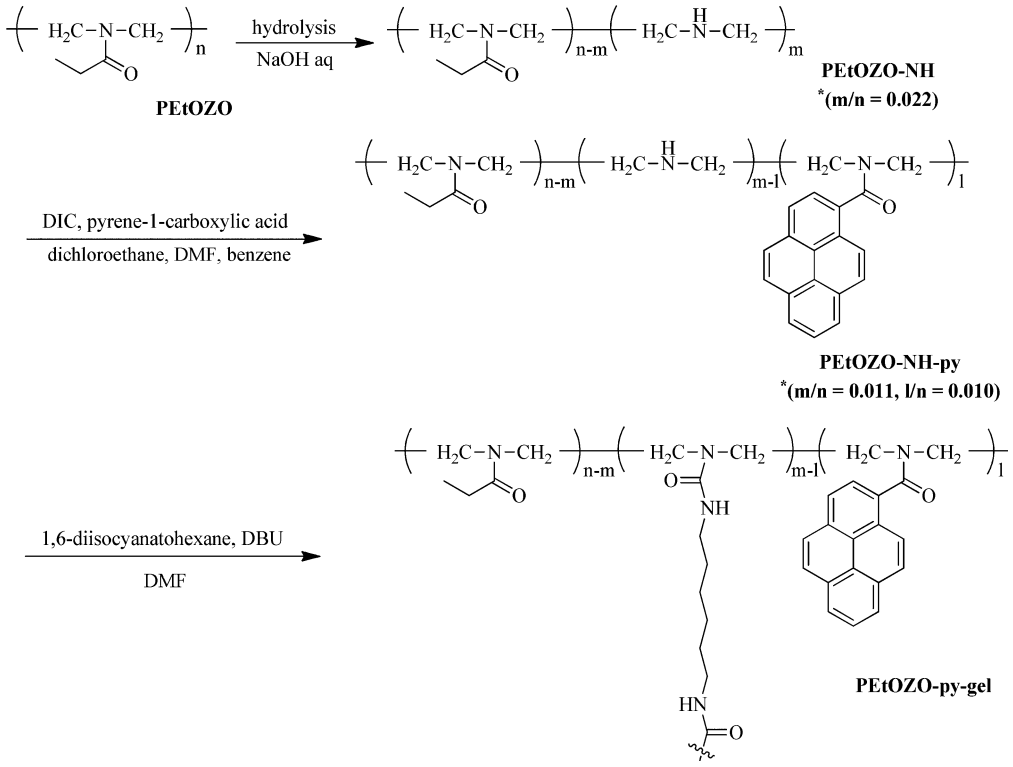
Similar to the results for the glycerin solutions, **POZO-py-(2.9)** and **POZO-py-(9.1)** did not exhibit a clear dynamic excimer, showing a broad fluorescence emission that extended to 600 nm. As reported by Sluch,[22] the molecular motion of the pyrene-forming dimer in the ground state was frozen. Therefore, it was difficult to form a parallel- or sandwich-shaped dimer in the excited state. As a result, static excimer emissions were primarily observed. The value of P_a, which was less than that in any other state without water solution, is one piece of evidence that supports this conclusion. For the fluorescence lifetime measurements, minor components, which were expected from monomer excited species, and dominant components, which were expected to be due to preassociated

Table 6. Fluorescence Lifetime Decay of POZO-py in the Film State (λ_{ex} = 340 nm, Room Temperature)

entry	τ_1	τ_2	τ_3	A_1	A_2	A_3	χ^2
POZO-py-(0.73) (380 nm)	7.09	32.2	100.9	0.27	0.41	0.32	1.07
POZO-py-(0.73) (420 nm)	10.1	43.9	106.6	0.50	0.30	0.20	1.07
POZO-py-(2.9) (380 nm)	2.32	9.93	41.5	0.54	0.44	0.02	1.38
POZO-py-(2.9) (420 nm)	3.41	9.86	41.6	0.69	0.28	0.03	1.07
POZO-py-(2.9) (500 nm)	0.4	10.8	43	−0.32	0.47	0.21	1.31
POZO-py-(9.1) (380 nm)	1.56	8.39	62	0.82	0.16	0.02	1.4
POZO-py-(9.1) (420 nm)	1.9	6.34	28	0.72	0.25	0.03	1.11
POZO-py-(9.1) (500 nm)	0.18	4.31	21.1	−0.41	0.15	0.44	1.27
model PA1 (380 nm)	30.8	127.8		0.41	0.59		1.28
model PA1 (420 nm)	28.6	129.3		0.40	0.60		1.36

dx.doi.org/10.1021/ma3001252 | *Macromolecules* 2012, 45, 2327−2337

Scheme 2. Synthesis of PEtOZO-py-gel[a])



[a]An asterisk indicates data estimated by ^{1}H NMR.

dimer excited species, were observed for both **POZO-py-(2.9)** and **POZO-py-(9.1)**. In addition, clear rising components were also observed. Thus, it can be said that these results were quite similar to those for the ethanol solution.

Pyrene-Modified Poly(2-ethyl-2-oxazoline) Gel (PEtOZO-py-gel). In order to prepare pyrene-modified poly(2-ethyl-2-oxazoline) gel (**POZO-py-gel**), we used commercially available poly(2-ethyl-2-oxazoline). We expected **POZO-py-gel** to possess a structure that can suppress the molecular motion of the pyrene dye on account of cross-linking. **PEtOZO-NH** was synthesized by the partial hydrolysis of **PEtOZO** and **PEtOZO-NH-py** was prepared subsequently by introducing pyrene-1-carboxylic acid into half of the amine sites of **PEtOZO-NH**. **PEtOZO-py-gel** was obtained by the reaction between the remaining amine sites of **PEtOZO-NH-py** and hexamethylene diisocyanate (Scheme 2).[12c]

The swelling and photoluminescent properties of the **PEtOZO-py-gel** were determined; the values of the associated parameters are listed in Table 7.

The results of the swelling behavior revealed that the degree of swelling was relatively high for good solvents of **PEtOZO-NH-py**. As shown in Figure 6, except for chloroform, the swollen and dried **PEtOZO-py-gel** exhibited similar fluorescence spectra. Given that chloroform is the best swelling solvent, we expected that the mobility of pyrene moieties would increase. Consequently, pyrene might form a dimer and show broad red-shifted emission. For all the solvents and the dried gel, the same fluorescence quantum yields were obtained. Contrary to our expectation, the improvement in the fluorescence quantum yields for the model compound was small. This small degree of improvement might be attributed to the fact that the method for measuring the fluorescence quantum yields was not very accurate. This was because of the difficulty associated with removing oxygen and controlling optical density during the measurement of gel compounds.

Table 7. Swelling and Photophysical Properties of PEtOZO-py-gel

solvent	$(W' - W)/W^a$	λ_{em} [nm]	Φ_{fl}
–	–	378, 398, 419	0.089
chloroform	3.85	379, 398, 419	0.11
ethanol	1.11	379, 399, 421	0.12
DMF	1.38	378, 397, 419	0.10
H_2O	0.4	379, 398, 419	0.11

[a]W: Weight of the dried gel. W': Weight of the swollen gel.

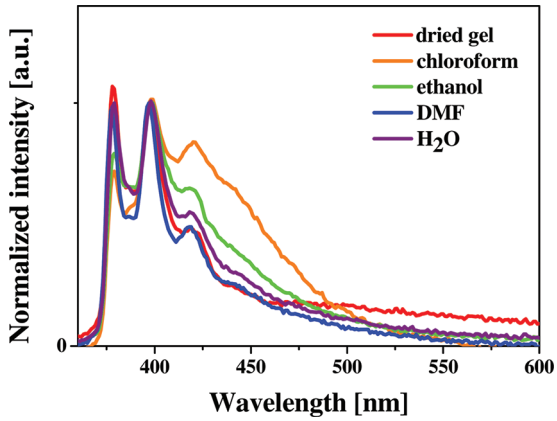


Figure 6. Fluorescence spectra of **PEtOZO-py-gel** swollen by various solvents (λ_{ex} = 350 nm, room temperature).

dx.doi.org/10.1021/ma3001252 | *Macromolecules* 2012, 45, 2327−2337

Therefore, quenching caused by a high concentration in a local area around the chromophore or triplet oxygen might have prevented the fluorescence from contribution to the extent of the expected improvement.

The swelling solvents, degree of swelling, and absorbance coefficient of *N,N*-dialkylpyrene-1-carboxamide moiety could be changed by adjusting the pyrene content, types of 2-oxazoline, types of cross-linking reagents, and their ratios. Therefore, we believe that the swelling and photoluminescence properties of **PEtOZO-py-gel** can be controlled as desired.

CONCLUSIONS

A novel fluorescent polymer, tertiary *N,N*-dialkylpyrene-1-carboxamide modified-poly(2-methyl-2-oxazoline) (**POZO-py**), was successfully prepared by the condensation of partially hydrolyzed **POZO-NH** with pyrenecarboxylic acid. The photophysical properties of **POZO-py** (in both solution and film states) for various pyrene content ratios were analyzed. The absorption and fluorescence spectra of **POZO-py-(0.73)**, which was the polymer with the lowest pyrene induction ratio, were very similar to those of the model compound **PA**. However, the fluorescence quantum yields of **POZO-py-(0.73)** were considerably higher than those of **PA** and improved with increasing viscosity of the surrounding media, especially for the most viscous solvent, glycerin (Φ_{fl} = 0.52). We believe that these enhancements in quantum yield were derived from suppression of molecular motion leading to internal conversion by introducing pyrene moieties onto the polymer chain and by interactions between polarized **POZO** units and the surrounding media. Therefore, the **POZO** chain induced a dramatic improvement in the fluorescence emission of the chromophore such that the emission was the same as that of the model compound. The photophysical behaviors of **POZO-py-(2.9)** and **POZO-py-(9.1)**, which were more strongly pyrene-modified, depended on not only the viscosity but also the polarization of the surrounding media because of the occurrence of relatively large preassociation interactions in the ground state. The static and dynamic excimer emissions of **POZO-py-(2.9)** and **POZO-py-(9.1)** could be controlled by changing the conditions under which they were synthesized. In other words, it can be said that **POZO**, or other poly(2-oxazoline), is one of beneficial substituent that can improve the photoluminescence properties of *N,N*-dialkylpyrene-1-carboxamide.

Fluorescent **POZO-py** is easy to prepare, is amphiphilic, and should have the potential to be blended with several other polymers similar to **POZO**. Furthermore, **POZO** itself has been investigated widely, so we expect that these photofunctionalized **POZO-py** polymers will have many applications. We are now investigating the compatibility of **POZO-py** with other polymers and the luminescence properties of the resulting polymer blends.

ASSOCIATED CONTENT

Supporting Information

Additional experimental section for *N,N*-dialkylpyrene-1-carboxamide modified poly(2-oxazoline)s, synthesis conditions (Tables S1 and S2), ^{1}H NMR spectra of all prepared samples without **PEtOZO-py-gel** (Figures S1 and S2), DSC and TGA spectra of **POZO-py** (Figures S3 and S4), fluorescence spectra of **PA** and **PA**-doped **POZO** (Figure S5), and fluorescence decay profiles of **POZO-py** in ethanol or thin flim state (Figure S6–S15). This material is available free of charge via the Internet at http://pubs.acs.org.

AUTHOR INFORMATION

Corresponding Author

*E-mail: konishi.g.aa@m.titech.ac.jp.

Notes

The authors declare no competing financial interest.

REFERENCES

(1) Montalti, M.; Credi, A.; Prodi, L. Gandolfi, M. T. *Handbook of photochemistry*, 3rd ed.; Taylor & Francis: New York, 2005.

(2) (a) Kalyanasundaram, K.; Thomas, J. K. *J. Am. Chem. Soc.* **1977**, *99*, 2039–2044. (b) Karpovic, D. S.; Blanchard, G. J. *Langmuir* **1996**, *12*, 5522–5524. (c) Galla, H.-J.; Hartmann, W.; Theilen, U.; Sackmann, E. *Membrane Biol.* **1979**, *48*, 215–236. (d) Winnik, F. M. *Chem. Rev.* **1993**, *93*, 587–614. (e) Saito, Y.; Shinohara, Y.; Ishioroshi, S.; Suzuki, A.; Tanaka, M.; Saito, I. *Tetrahedron Lett.* **2011**, *52*, 2359–2361. (f) Saito, Y.; Suzuki, A.; Imai, K.; Nemoto, N.; Saito, I. *Tetrahedron Lett.* **2010**, *51*, 2606–2609. (g) Fujimoto, K.; Yamada, S.; Inouye, M. *Chem. Commun.* **2009**, 7164–7166. (h) Yang, Y.; Gou, X.; Blecha, J.; Cao, H. *Tetrahedron Lett.* **2010**, *51*, 3422–3425.

(3) (a) Isied, S. S.; Ogawa, M. Y.; Wishart, J. F. *Chem. Rev.* **1992**, *92*, 381–394. (b) Sisido, M.; Hoshino, S.; Kusano, H.; Kuragaki, M.; Makino, M.; Sasaki, H.; Smith, T. A.; Ghiggino, K. P. *J. Phys. Chem B.* **2001**, *105*, 10407–10415.

(4) (a) Piotrowiak, P. *Chem. Soc. Rev.* **1999**, *28*, 143–150. (b) Fox, M. A.; Galoppini, E. *J. Am. Chem. Soc.* **1997**, *119*, 5277–5285.

(5) Manoharan, M.; Tivel, K. L.; Zhao, M.; Nafisi, K.; Netzel., T. L. *J. Phys. Chem.* **1995**, *99*, 17461–17472.

(6) (a) Winnik, F. M.; Winnik, M. A.; Tazuke, S. *J. Phys. Ckem.* **1987**, *91*, 594–597. (b) Tsujii, Y.; Itoh, T.; Fukuda, T.; Miyamoto, T.; Ito, S.; Yamamoto, M. *Langmuir.* **1992**, *8*, 936–941. (c) Turro, N. J.; Arora, K. S. *Polymer.* **1986**, *27*, 783–796. (d) Chu, D.-Y.; Thomas, J. K. *Macromolecules* **1984**, *17*, 2142–2147. (e) Stramel, R. D.; Nguyen, C.; Webber, S. E.; Rodgerd, M. A. J. *J. Phys. Chem.* **1988**, *92*, 2934–2938. (f) Ezzel1, S. A.; Hoyle, C. E.; Creed, D.; McCormick, C. L. *Macromolecules* **1992**, *25*, 1887–1895. (g) Winnik, F. M.; Tamai, N.; Yonezawa, J.; Nishimura, Y.; Yamazaki, I. *J. Phys. Chem.* **1992**, *96*, 1967–1972. (h) Wilhelm, M.; Zhao, C. L.; Wang, Y.; Xu, R.; Winnik, M. A. *Macromolecules* **1991**, *24*, 1033–1040. (i) Yekta, A.; Winnik, M. A. *Langmuir.* **1995**, *11*, 730–737. (j) Chen, W. H.; Liaw, D. J.; Wang, K. L.; Lee, K. R.; Lai, J. Y. *Polymer* **2009**, *50*, 5211–5219.

(7) (a) Yukawa, S.; Omayu, A.; Matsumoto, A. *Macromol. Chem. Phys.* **2009**, *210*, 1776–1784. (b) Okamoto, A.; Tainaka, K.; Nishiza, K.; Saito, I. *J. Am. Chem. Soc.* **2005**, *127*, 13128–13129. (c) Liaw, D. J.; Wang, K. L.; Chang, F. C. *Macromolecules* **2007**, *40*, 3568–3574. (d) Lian, W. R.; Wu, H. Y.; Wang, K. L.; Liaw, D. J.; Lee, K. R.; Lai, J. Y. *J. Polym. Sci., Part A: Polym. Chem.* **2011**, *49*, 3673–3680. (e) Lian, W. R.; Ho, C.; Huang, Y. C.; Liao, Y. A.; Wang, K. L.; Liaw, D. J.; Lee, K. R.; Lai, J. Y. *J. Polym. Sci., Part A: Polym. Chem.* **2011**, *49*, 5350–5357. (f) Lian, W. R.; Liao, Y. A.; Li, L. J.; Su, C. Y.; Liaw, D. J.; Lee, K. R.; Lai, J. Y. *Macromolecules* **2011**, *44*, 9550–9555. (g) Fujioka, T.; Taketani, S.; Nagasaki, T.; Matsumoto, A. *Bioconjugate Chem.* **2009**, *20*, 1879–1887.

(8) (a) Shimizu, H.; Fujimoto, K.; Furusyo, M.; Maeda, H.; Nanai, Y.; Mizuno, K.; Inouye, M. *J. Org. Chem.* **2007**, *72*, 1530–1533. (b) Maeda, H.; Maeda, T.; Mizuno, K.; Fujimoto, K.; Shimizu, H.; Inouye, M. *Chem.—Eur. J.* **2006**, *12*, 824–831. (c) Watanabe, Y.; Uchimura, M.; Araoka, F.; Konishi, G.; Watanabe, J.; Takezoe, H. *Appl. Phys. Express* **2009**, *2*, 102501. (d) Uchimura, M.; Watanabe, Y.; Araoka, F.; Watanabe, J.; Takezoe, H.; Konishi, G. *Adv. Mater.* **2010**, *22*, 4473–4478. (e) Sumi, K.; Konishi, G. *Molecules* **2010**, *15*, 7582–7592. (f) Yamashita, K.; Kimura, K.; Tazawa, S.; Asano, M. S.; Sugiura, K. *Chem. Lett.* **2011**, *40*, 1459–1461.

(9) Niko, Y.; Kawauchi, S.; Konishi, G. *Tetrahedron Lett.* **2011**, *52*, 4843–4847.

(10) (a) Nucci, N. V.; Zelent, B.; Vanderkooi, J. M. *J. Fluoresc.* **2007**, *18*, 41−49. (b) Tulock, J. J.; Blanchard, G. j. *J. Phys. Chem B.* **1998**, *102*, 7148−7155. (c) Kumar, C. V.; Chattopadhyay, S. K.; Das, P. K. *Photochem. Photobiol.* **1983**, *38*, 141−152. (d) Costta, S. M. B.; Macanita, A. L.; Prieto, M. J. *J. Photochem.* **1979**, *11*, 109−119. (e) Kumar, M.; Babu, J. N.; Bhalla., V.; Kumar, R. *Sens. Actuators* **2010**, *B144*, 183−191. (f) Azumaya, I.; Kagechika, H.; Fujiwara, Y.; Itoh, M.; Yamaguchi, K.; Shudo, K. *J. Am. Chem. Soc A.* **1991**, *113*, 2833−2838. (g) Lewis, F. D.; Long, T. M. *J. Phys. Chem A.* **1998**, *102*, 5327−5332. (h) Heldt., J. *J. Photochem. Photobiol. A Chem.* **1991**, *60*, 183−191.

(11) Kummer, A. D.; Kompa, C.; Niwa, H.; Hirano, T.; Kojima, S.; Michel-Beyerle, M. E. *J. Phys. Chem. B* **2002**, *106*, 7554−7559.

(12) (a) Saegusa, T.; Ikeda, H. *Macromolecules* **1973**, *6*, 808−811. (b) Kobayashi, S.; Kaku, M.; Sawada, S.; Saegusa, T. *Polym. Bull.* **1985**, *13*, 447−451. (c) Chujo, Y.; Yoshifuji, Y.; Sada, K.; Saegusa, T. *Macromolecules* **1989**, *22*, 1074−1077. (d) Chujo, Y.; Sada, K.; Matsumoto, K.; Saegusa, T. *Macromolecules* **1990**, *23*, 1234−1237.

(13) (a) Kobayashi, S. *Prog. Polym. Sci.* **1990**, *15*, 751−823. (b) Aoi, K.; Okada, M. *Prog. Polym. Sci.* **1996**, *21*, 151−208.

(14) (a) Hoogenboom, R. *Angew. Chem., Int. Ed.* **2009**, *48*, 7978−7994. (b) Bloksma, M. M.; Weber, C.; Perevyazko, I. Y.; Kuse, A.; Baumgartel, A.; Vollrath, A.; Hoogenboom, R.; Schubert, U. S. *Macromolecules* **2011**, *44*, 4057−4064. (c) Lambermont-Thijs, H. M. L.; Kranenburg, J. M.; Hoogenboom, R.; Unger, M. V.; Siesler, H. W.; Schubert, U. S. *J. Mater. Chem.* **2011**, *21*, 17331−17337. (d) Bloksma, M. M.; Schubert, U. S.; Hoogenboom, R. *Polym. Chem.* **2011**, *2*, 203−208. (e) Lambermont-Thijs, H. M. L.; Heuts, J. P. A.; Hoeppener, S.; Hoogenboom, R.; Schubert, U. S. *Polym. Chem.* **2011**, *2*, 313−322. (f) Zhao, J.; Hoogenboom, R.; Van Assche, G.; Van Mele, B. *Macromolecules* **2010**, *43*, 6953−6860. (g) Weber, C.; Becer, C. R.; Guenther, W.; Hoogenboom, R.; Schubert, U. S. *Macromolecules* **2010**, *43*, 160−167. (h) Bloksma, M. M.; Hendrix, M. M. R. M.; Schubert, U. S.; Hoogenboom, R. *Macromolecules* **2010**, *43*, 4654−4659. (i) Lambermont-Thijs, H. M. L.; Bonami, L.; Du Prez, F. E.; Hoogenboom, R. *Polym. Chem.* **2010**, *1*, 747−754. (j) Hoogenboom, R.; Thijs, H. M. L.; Wouters, D.; Hoeppener, S.; Schubert, U. S. *Macromolecules* **2008**, *41*, 1581−1583. (k) Hoogenboom, R.; Wiesbrock, F.; Leenen, M. A. M.; Thijs, H. M. L.; Huang, H. Y.; Fustin, C. A.; Guillet, P.; Gohy, J. F.; Schubert, U. S. *Macromolecules* **2007**, *40*, 2837−2843. (l) Huang, H. Y.; Hoogenboom, R.; Leenen, M. A. M.; Guillet, P.; Jonas, A. M.; Schubert, U. S.; Gohy, J. F. *J. Am. Chem. Soc.* **2006**, *128*, 3784−3788. (m) Adachi, K.; Achimuthu, A. K.; Chujo, Y. *Macromolecules* **2004**, *37*, 9793−9797. (n) Aoi, K.; Miyamoto, M.; Chujo, Y.; Saegusa, T. *Macromol. Symp.* **2002**, *183*, 53−64. (o) Naka, K.; Itoh, H.; Park, S. Y.; Chujo, Y. *Polym. Bull.* **2004**, *52*, 171−176. (p) Naka, K.; Nakamura, T.; Ohki, A.; Maeda, S. *Macromol. Chem. Phys.* **1997**, *98*, 101−116. (q) Naka, K.; Yamashita, R.; Nakamura, T.; Ohki, A.; Maeda, S.; Aoi, K.; Takasu, A.; Okada, M. *Int. J. Bio. Macromol.* **1998**, *23*, 259−262. (r) Aoi, K.; Takasu, A.; Okada, M. *Macromolecules* **1997**, *30*, 6134−6138. (s) Tsutsumiuchi, K.; Aoi, K.; Okada, M. *Macromolecules* **1997**, *30*, 4013−4017. (t) Shin, D.-M.; Ozeki, N.; Nakamoto, Y.; Konishi, G. *Macromol. Res.* **2006**, *14*, 255−256. (u) Konishi, G.; Tajima, T.; Kimura, T.; Tojo, Y.; Mizuno, K.; Nakamoto, Y. *Polym. J.* **2010**, *42*, 443−449. (w) Nemoto, T.; Konishi, G.; Tojo, Y.; An, Y. C.; Funaoka, M. *J. Appl. Polym. Sci.* **2012**, *123*, 2636−2642.

(15) Chujo, Y.; Sada, K.; Saegusa, T. *Macromolecules* **1990**, *23*, 2693−2697.

(16) Imai, Y.; Chujo, Y. *Macromolecules* **2000**, *33*, 3059−3064.

(17) Pietsch, C.; Schubert, U. S.; Hoogenboom, R. *Chem. Commun.* **2011**, *47*, 8750−8765.

(18) Todesco, R. V.; Basheer, R. A.; Kamat, P. V. *Macromolecules* **1986**, *19*, 2390−2397.

(19) We evaluated the collisional rate of model compound *N,N*-diethyllpyrene-1-carboxamide (**PA**), $k_{col,\ PA}$, by using the following parameters: (a) diffusion-controlled rate constant in ethanol: k_{diff} = 6.1×10^9 [L mol^{-1} s^{-1}] (ethanol, 25 °C) (b) concentration of **PA**: $[M_{PA}] = 3.2 \times 10^{-6}$ [mol L^{-1}] (O.D. = 0.1, calculated by using the molar absorbance coefficient of **PA**[9]). From the above parameters, $k_{col,\ py}$ was calculated to be 2.0×10^4 [s^{-1}]. On the other hand, the values of radiative and non-radiative rate constants of **PA**, obtained by using the value of fluorescence quantum yields and lifetime, were estimated to be 2.0×10^6 and 3.1×10^7 [s^{-1}], respectively.

(20) Birks, J. B. *Rep. Prog. Phys.* **1975**, *38*, 903−974.

(21) The lifetime (τ_1) values of **POZO-py-(2.9)** and **POZO-py-(9.1)** monitored at 500 nm in ethanol solutions are probably inaccurate because the resolution of the instrument we used was not enough to measure such extremely short-lived components.

(22) Sluch, M. I.; Vitukhnovsky, A. G.; Petty, M. C. *Thin Solid Films* **1996**, *284−285*, 622−626.

Macromolecules

Article

pubs.acs.org/Macromolecules

Photo-Cross-Linkable Azide-Functionalized Polythiophene for Thermally Stable Bulk Heterojunction Solar Cells

Chang-Yong Nam,*[,†,∥] Yang Qin,[†,∥,⊥] Young S. Park,[†] Htay Hlaing,[‡] Xinhui Lu,[‡] Benjamin M. Ocko,[‡] Charles T. Black, and Robert B. Grubbs*[,†,§]

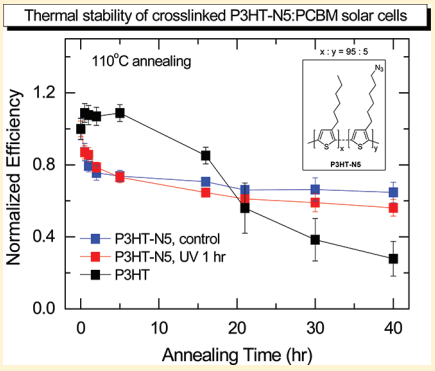
[†]Center for Functional Nanomaterials, Brookhaven National Laboratory, Upton, New York 11973, United States

[‡]Condensed Matter Physics and Materials Science Department, Brookhaven National Laboratory, Upton, New York 11973, United States

[§]Department of Chemistry, Stony Brook University, Stony Brook, New York 11794, United States

Supporting Information

ABSTRACT: We have synthesized photo-cross-linkable azide-functionalized poly(3-hexylthiophene) to explore improvements in the thermal stability of bulk heterojunction solar cells. Exposing blends of photo-cross-linkable polythiophene and [6,6]-phenyl-C_{61}-butyric acid methyl ester to ultraviolet light preferentially cross-linked the polythiophene without degrading its optical or electrical properties. X-ray scattering measurements showed that cross-linking slightly compacted the polythiophene chain lamellar stacking while increasing the polymer crystal coherence length by 20%. Optimized solar cells having cross-linked active blend layers retained 65% of their initial photovoltaic power conversion efficiency after 40 h of thermal annealing at 110 °C, while devices using un-cross-linked commercial polythiophene underwent significant phase separation and retained less than 30% of their initial efficiency after annealing.



INTRODUCTION

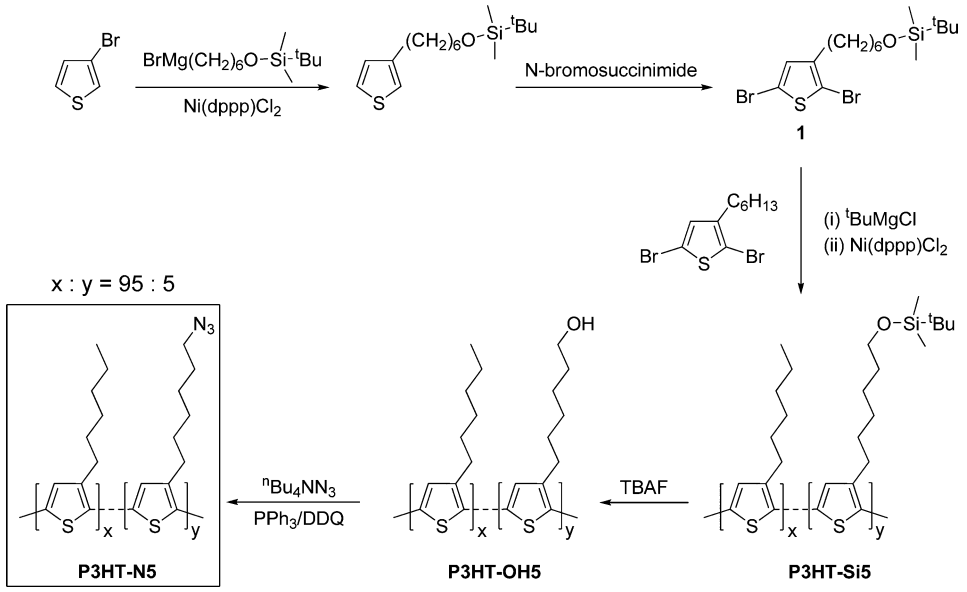
Organic solar cells based on blended conjugated polymers and fullerenes have significant potential as cost-effective alternatives to inorganic semiconductor based solar cells, with state-of-the-art device power conversion efficiencies now approaching 10%.[1,2] These devices typically utilize a bulk heterojunction (BHJ) architecture wherein active layer blends of an electron-donating polymer and a fullerene-based electron-acceptor form a nanoscale morphology with phase segregation on length scales comparable to the exciton diffusion length (5−20 nm).[3−8] This architecture decouples the device active layer thickness from the exciton diffusion length, permitting thicker blend layers for increased light absorption and resulting in improved device photovoltaic (PV) efficiency over a bilayer device structure. The extent of blend phase separation critically affects PV device performance and is generally controlled by thermal annealing[5,9−12] or exposure to solvent vapor.[4,13−16] However, the optimized active layer morphology is only metastable, and over time continued phase separation and domain coarsening can deteriorate device PV performance.[17,18] Achieving sufficient device thermal stability is a significant challenge for practical implementation of organic solar cells.

Previous efforts to improve the thermal stability of polymer:fullerene BHJ solar cells include use of phase compatibilizers,[19] cross-linked fullerenes,[20,21] cross-linked conjugated polymers,[22,23] and cross-linked polymer−fullerene complexes.[24] Polymer cross-linking has proven to be a promising approach, evidenced by recent reports of high performance in photo-cross-linkable brominated conjugated polymers.[22,23] Most approaches to cross-linking conjugated polymers rely on cross-linking the insulating side chains, since chemical reactions on the polymer backbones are believed to detrimentally affect polymer electronic properties. Such cross-linking is generally mediated either by a bimolecular reaction between specific functional groups such as pendant acrylates,[25] peripheral oxetane groups,[26,27] and diacetylene moieties[28] or by small molecule additives, including di-*tert*-butyl peroxide[29] and difunctional perfluoroaryl azides,[30] with the cross-linking reactions being activated by either heat (thermal)[26,27,29,31] or ultraviolet (UV) light.[22,23,25,30,32] However, both types of approaches can potentially disrupt polymer packing morphologies, affecting the material electronic properties, as a high loading of functional groups or small molecule additives can interfere with polymer diffusion and phase behaviors. Additionally, for some of these approaches, especially ones utilizing halogenated side chains such as bromine,[22,23] the fate of the functional group after cross-linking reaction remains ambiguous, though the high efficiencies reported for these devices suggest that the byproducts of these cross-linking reactions are not necessarily detrimental to device performance. To better understand the effect of cross-linking on polymer:fullerene BHJ solar cells, it would be desirable to develop a cross-linking

Received: January 22, 2012
Published: March 1, 2012

 © 2012 American Chemical Society dx.doi.org/10.1021/ma3001725 | *Macromolecules* 2012, 45, 2338−2347

Scheme 1. Synthesis of P3HT-N5



strategy that will minimally change the chemistry of the active layer.

In this study, we have synthesized a photo-cross-linkable azide-functionalized poly(3-hexylthiophene) analogue poly(3-hexylthiophene-*stat*-3-(6-azidohexyl)thiophene) (P3HT-N5), which can be cross-linked by UV light with minimal impact on the polymer morphological and electronic properties and without the need for small molecule additives. Building upon previous work by Murray et al.,[31] in which cross-linkable azide-functionalized undecyl polythiophenes were synthesized in order to study the effects of their thermal cross-linking on optical absorption and photoluminescence, we have developed a modified synthetic route and created photo-cross-linkable P3HT that is well-suited for organic polymer solar cell applications.

In order to understand the behavior of these devices when prepared under conditions that are compatible with the cost-effective large-scale manufacturing schemes envisioned for organic solar cells, such as roll-to-roll printing, all of the devices described in this article have been prepared without any effort being taken to exclude air. Because oxygen doping creates charge traps in the active organic layers of organic PV devices and can result in oxidation of metal contacts, the performance of PV devices prepared in the presence of oxygen is generally worse than those of high-performance polymer:fullerene BHJ solar cells, which are typically fabricated in oxygen-free environments.[4−6,33] There are several reported examples of air-processed organic BHJ solar cells,[34,35] but photo-cross-linking of active layers in air-processed organic BHJ solar cells has not previously been reported.

We have fabricated photo-cross-linkable P3HT-N5:fullerene BHJ solar cells in air and report the feasibility of photo-cross-linking in air-processed conjugated polymer:fullerene blends and the improved thermal stability of PV device performance. We also study the effects of thermal annealing on polymer structure and PV device properties to develop guidelines for optimizing device processing conditions in cross-linkable polymer:fullerene BHJ solar cells.

RESULTS AND DISCUSSION

Synthesis and Characterization of P3HT-N5. Polythiophenes with azide-functionalized side chains have previously been prepared by postpolymerization modification strategies, either through nucleophilic substitution of haloalkyl side chains with azide anions[36] or through the Mitsunobu azidation of hydroxyalkyl side chains.[31] The previously reported routes to these polymers can suffer from low yields in monomer synthesis (~30% for the monocoupling of 1,6-dibromohexane with 3-bromothiophene in the synthesis of 6-bromohexylthiophene-based polymers)[22,36] or from the requirement of multiple steps in monomer synthesis (e.g., four steps in 42% yield for the synthesis of the THP-protected hydroxyalkylthiophene monomer used by Murray et al.).[31] We have developed a modified route to these polymers involving polymerization of a *tert*-butyldimethylsilyl (TBDMS)-protected thiophene with subsequent desilylation and conversion of the resulting alcohols to azides (Scheme 1). TBDMS ether monomer **1** was prepared in an overall 46% yield in two steps through a typical Grignard coupling between 3-bromothiophene and (6-bromohexyloxy)-*tert*-butyldimethylsilane followed by dibromination of the thiophene ring with *N*-bromosuccinimide. The Grignard metathesis (GRIM) polymerization protocol developed by McCullough and co-workers[37] was then used to copolymerize a 1:19 mixture of monomer **1** and 2,5-dibromo-3-hexylthiophene to obtain regioregular random poly(3-hexylthiophene-*stat*-3-(6-(*tert*-butylmethylsilyloxy)hexyl)thiophene) (P3HT-Si5) copolymers. The monomer feed ratio was chosen to provide more than two azide groups per polymer chain which, given the high photo-cross-linking efficiency of nitrene groups,[38] would be sufficient to facilitate efficient cross-linking. Similarly, photo-cross-linking of 1:19 copolymers of 3-hexylthiophene and 3-(6-bromohexyl)thiophene copolymers has been previously reported to render copolymer films largely insoluble.[22]

P3HT-Si5 was purified by Soxhlet extraction, and proton nuclear magnetic resonance (^{1}H NMR) spectroscopy confirmed high regioregularity (>95% head−tail configuration) and showed the chain composition (5 mol % monomer **1** incorporation according to the NMR peak integration) to match the monomer feed composition. Removal of TBDMS

dx.doi.org/10.1021/ma3001725 | *Macromolecules* 2012, 45, 2338−2347

groups by tetrabutylammonium fluoride gave the hydroxyl-functionalized polymer P3HT-OH5, as monitored by ^{1}H NMR (Figure 1). The TBDMS methyl peak (0.05 ppm) in the

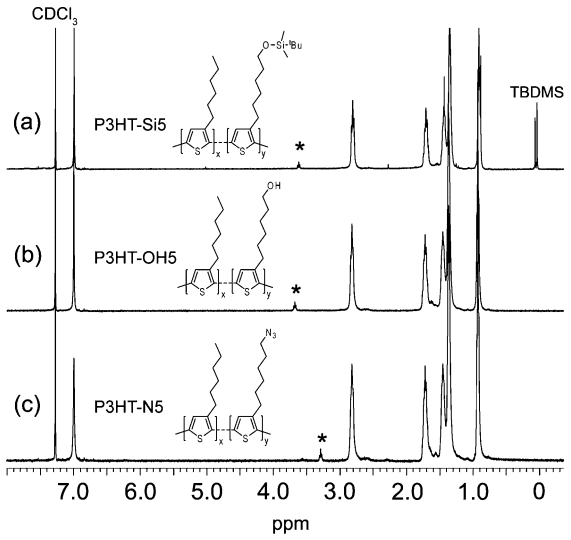


Figure 1. ^{1}H NMR spectra overlay of (a) P3HT-Si5, (b) P3HT-OH5, and (c) P3HT-N5. The star denotes methylene group next to either an oxygen atom for (a) and (b) or nitrogen atom for (c).

spectrum of P3HT-Si5 completely disappeared after the reaction, and the peak corresponding to the methylene group adjacent to the oxygen atom shifted from 3.63 ppm for P3HT-Si5 (Figure 1a, marked with a star) to 3.67 ppm for P3HT-OH5 (Figure 1b), confirming quantitative deprotection. Finally, the P3HT-OH5 hydroxyl groups were transformed to azide functional groups according to a reported procedure, which uses tetrabutylammonium azide in the presence of triphenylphosphine (PPh_3) and 2,3-dichloro-5,6-dicyano-*p*-benzoquinone (DDQ),[39] as confirmed by the shift of the signal adjacent to the functional group from 3.67 ppm in P3HT-OH5 to 3.29 ppm in P3HT-N5 (Figure 1c).[36] Gel permeation chromatography (GPC, vs polystyrene standards) indicated M_n values of 14.0 kg/mol for P3HT-OH5 (M_w/M_n = 1.5) and 14.5 kg/mol for P3HT-N5 (M_w/M_n = 1.6), implying a smooth and selective reaction without polymer degradation or cross-linking. This is the first example of the application of this highly selective reaction to the functionalization of polymer analogues and is especially useful in conjugated polymer systems since the reaction can be run in good solvents for conjugated polymers, as opposed to those reactions involving sodium azide that typically require poor solvents for conjugated polymers. While chloroform ($CHCl_3$) can be used as the solvent for the azidation reaction, for safety reasons tetrahydrofuran (THF) was substituted in our studies with no change in efficiency of the reaction.

Photo-Cross-Linking of P3HT-N5. Exposure of organic azides to UV light results in the extrusion of nitrogen and creates highly reactive nitrene functional groups, which can participate in cross-linking reactions through insertion into C−H bonds of other molecules as demonstrated in the thermally cross-linked azide-functionalized polythiophenes.[31] In our experiments, photo-cross-linking was performed by exposing P3HT-N5 films to UV light for 60 min. We find that the P3HT-N5 optical absorption remains unchanged after photo-cross-linking (Figure 2a). The vibronic feature related to

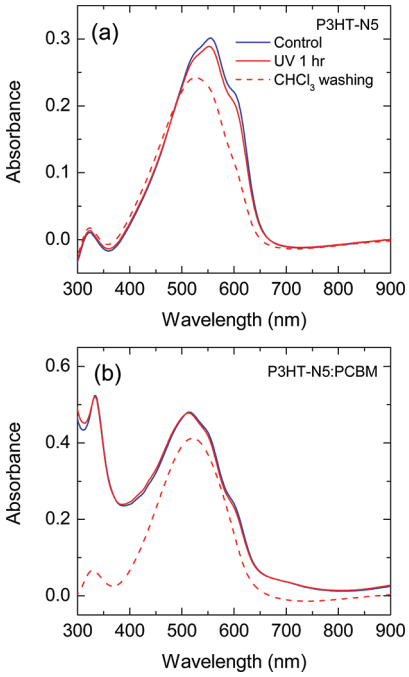


Figure 2. Optical absorption spectra of (a) P3HT-N5 and (b) P3HT-N5:PCBM blend samples before UV exposure (solid blue line), after 60 min UV exposure (solid red line), and after 60 min UV exposure and $CHCl_3$ washing (dashed red line).

polymer lamellar stacking appears as a shoulder near 600 nm, rather than as a distinct peak, indicating a lesser degree of P3HT-N5 lamellar stacking after cross-linking as we confirm by the X-ray scattering measurements discussed later. When rinsed with $CHCl_3$, the film retained ~85% of the initial integrated optical absorbance, confirming that cross-linking renders the polymer largely insoluble. A possible reason for the disappearance of P3HT-N5 vibronic features (near 680 nm) after $CHCl_3$ rinsing is reduced $\pi-\pi$ coupling between polymer backbones due to swelling or the loss of small amounts of un-cross-linked polymer. Fourier-transform infrared spectroscopy (FT-IR) analysis showed that ~95% of the azido groups were dissociated after a 60 min UV exposure (see Supporting Information), and longer UV exposure times did not further affect the retention of optical absorption in the cross-linked polymer after solvent rinsing.

Blends of P3HT-N5 and [6,6]-phenyl-C_{61}-butyric acid methyl ester (PCBM) (1:1 w/w) similarly showed a small change in optical absorption after a 60 min UV exposure (Figure 2b). In this case, however, rinsing the cross-linked blend in $CHCl_3$ rendered the optical absorption spectrum nearly identical to that of $CHCl_3$-rinsed cross-linked P3HT-N5, suggesting selective cross-linking between P3HT-N5 chains with minimal reaction between P3HT-N5 and PCBM. The low azide:PCBM ratio ($[N_3]/[PCBM]$) helps to minimize the participation of PCBM in the cross-linking reaction. The $[N_3]/[PCBM]$ ratio in a 1:1 w/w blend of PCBM and P3HT-N5 ($M_n \approx 14.5$ kg/mol; degree of polymerization 89; ~4.5 azide groups per polymer chain) should be 0.27, implying that, at most, less than 0.33 mol % of the PCBM in the blend can react with azide groups. Reactions between P3HT azide groups and PCBM are unlikely to lead to the formation of cross-links, given the low $[N_3]/[PCBM]$ ratio and the requirement that 2 azide groups react with the same PCBM molecule to form a cross-link. The blend stoichiometry in combination with the

dx.doi.org/10.1021/ma3001725 | *Macromolecules* 2012, 45, 2338−2347

absorbance data suggests that blend cross-linking occurs through intrachain reactions of P3HT-N5.

Grazing incidence wide-angle X-ray scattering (GIWAXS) measurements on pure P3HT-N5 and P3HT-N5:PCBM blend samples, before and after cross-linking, confirmed that UV cross-linking does not significantly alter the structural properties of P3HT and PCBM domains (Figure 3a–d). In both pure P3HT-N5 and P3HT-N5:PCBM blend films, cross-linking shifts the P3HT-N5 (100) lamellar stacking peak, originally located at q_z ~0.40 Å^{-1}, toward higher q_z, while simultaneously reducing its width (Figure 3e,f). The cross-linking-induced shift in the peak position correspond to a ~1–2% contraction in the lamellar spacing (distance between neighboring P3HT-N5 backbones separated by alkyl chains) from 1.68 to 1.64 nm for pure P3HT-N5 and from 1.73 to 1.70 nm for P3HT-N5:PCBM film. In addition, the lamellar domain size (coherence length), extracted from Scherrer analysis,[40] increased after cross-linking, both in pure materials and in blends. For P3HT-N5, the coherence length increased from 8.1 to 9.3 nm, and for the P3HT-N5:PCBM, the length increased from 5.3 to 6.5 nm. The UV cross-linking also appears to broaden the orientation distribution of the polymer lamellar stacking as evidenced by the more extended scattering intensity profile of the (100) peak along the radial orientation in both pure P3HT-N5 and P3HT-N5:PCBM blend films. For all P3HT-N5 samples studied here, the lamellar spacing is comparable to commercially available P3HT, yet the coherence length is somewhat smaller.[41,42] The broadened lamellar stacking orientation can induce more efficient hole transport along the out-of-plane direction,[29] coinciding with generally higher performance of cross-linked P3HT-N5:PCBM blend solar cells over un-cross-linked counterparts as we discuss later. The cross-linking process does not significantly change either the position or width of the (010) scattering peak corresponding to polymer chain $\pi-\pi$ stacking. The (010) peak position remains the same at q_{x-y} ~1.63 Å^{-1} (Figure 3g) which is equivalent to a $\pi-\pi$ stacking distance of ~0.38 nm, suggesting that cross-linking between P3HT-N5 alkyl side chains does not affect the $\pi-\pi$ coupling between polymer backbones. In general, GIWAXS data alone cannot provide explicit information regarding intermixing behaviors of polymer (P3HT-N5) and fullerene (PCBM), which is known to be important in the operation of polymer:fullerene blend devices.[43,44] Nevertheless, the observation that the P3HT-N5 domain size in the un-cross-linked P3HT-N5:PCBM film (5.3 nm) is comparable to the lower-bound values typically observed in commercial P3HT:PCBM blends (4–16 nm)[45,46] implicates minimal impact of the azide functional group on the initial intermixing behavior of the polymer:fullerene blend. Likewise, the similar P3HT-N5 domain size observed in the photo-cross-linked blend (6.5 nm) supports an insignificant change in phase separation morphology induced by the cross-linking in this system.

The hole mobility (μ) of UV-cross-linked P3HT-N5, deduced from high bias (V > 2 V) $J-V$ characteristics of ITO/PEDOT:PSS (poly(3,4-ethylenedioxythiophene):poly(styrenesulfonate))/P3HT-N5/Au devices (Supporting Information) using a space charge limited current (SCLC) model, was ~10^{-4} cm^2/(V s), comparable to previously reported values for P3HT.[47] Our measurements show that azide-mediated UV cross-linking minimally affects the polythiophene electronic properties, consistent with the structural information obtained by X-ray scattering. The $J-V$ characteristics of un-cross-linked P3HT-N5 devices were dominated by ohmic current, such that we were unable to apply the SCLC model to extract μ.[29,34] The un-cross-linked P3HT-N5 hole conductivity obtained from the ohmic current region (V < 1 V; see Supporting Information) is ~2 times higher than that measured after UV-cross-linking. We suspect that oxygen doping, originating from ambient air device processing, is likely the cause of higher ohmic current, since oxygen can act as p-type dopant in P3HT and thus increase dark carrier density.[34,48−52] If an appreciable amount of residual DDQ from the synthesis step is present, it can form charge

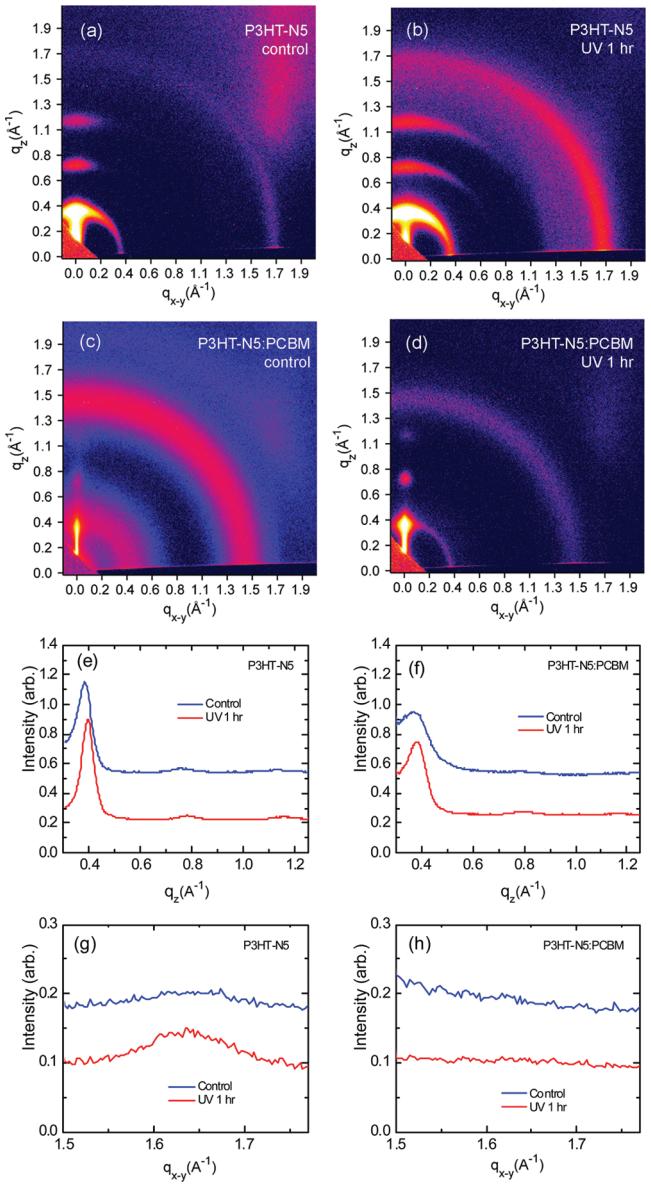


Figure 3. Two-dimensional GIWAXS intensity data (a–d) and their line plots along q_z (perpendicular to substrate plane) and q_{x-y} (in substrate plane) (e–h) for P3HT-N5 and P3HT-N5:PCBM blend films before and after 60 min UV exposure (cross-linking): (a) as-prepared P3HT-N5 without UV exposure, (b) P3HT-N5 after UV exposure, (c) as-prepared P3HT-N5:PCBM blend without UV exposure, (d) P3HT-N5:PCBM blend after UV exposure. (e, f) Scattering intensity vs q_z plots for P3HT-N5 and P3HT-N5:PCBM blend samples, respectively. (g, h) Intensity vs q_{x-y} plots for P3HT-N5 and P3HT-N5:PCBM blend samples. In the plots, solid blue and solid red lines denote as-prepared (control) and UV exposed cases, respectively.

dx.doi.org/10.1021/ma3001725 | Macromolecules 2012, 45, 2338–2347

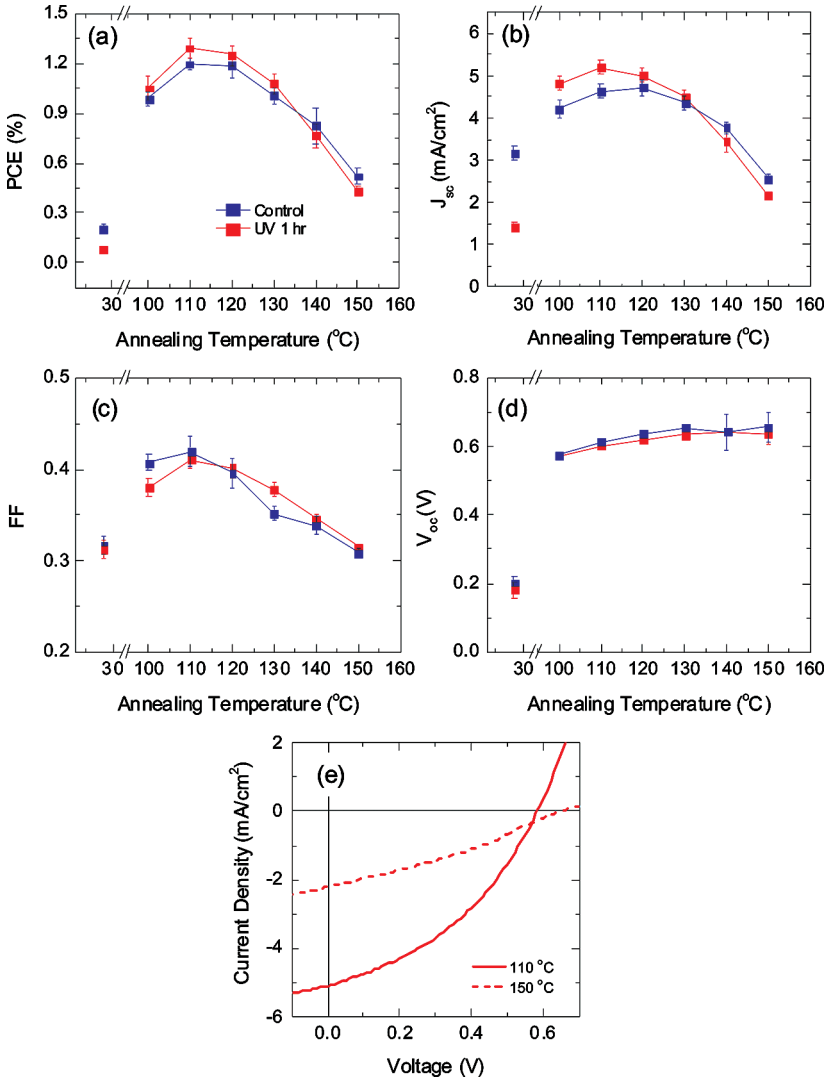


Figure 4. PV characteristics of control and 60 min UV-cross-linked P3HT-N5:PCBM blend solar cells with varying 10 min postfabrication device vacuum anneal temperatures from 100 to 150 °C, compared with nonannealed control solar cells (25 °C). Data points represent average values of 4–5 measured devices, with error bars denoting one standard deviation. (a) PCE, (b) J_{sc}, (c) FF, and (d) V_{oc}, with solid blue and solid red lines denoting as-prepared (control) and UV-exposed samples, respectively. (e) Representative J–V characteristics of UV-cross-linked P3HT-N5:PCBM blend solar cells annealed at 110 °C (solid red line) and 150 °C (dashed red line).

transfer complex with P3HT-N5, possibly increasing dark carrier density. After purification of P3HT-N5, however, there was no evidence of residual DDQ by thin layer chromatography or by FT-IR spectroscopy (DDQ: CN 2234 cm^{-1}, CO 1701 cm^{-1}; DDQ charge transfer complex: CN 2206 cm^{-1}, CO 1562 cm^{-1}).[53] Cross-linking P3HT-N5 may have reduced the carrier concentration by dedoping through the reaction of oxygen with photogenerated nitrene groups,[54−56] allowing the sample to recover its SCLC behavior.

Postfabrication Thermal Annealing Behavior of P3HT-N5:PCBM BHJ Solar Cells. With the goal of creating optimal UV-cross-linked P3HT-N5:PCBM BHJ solar cells, we first established a postfabrication thermal treatment that maximized PV power conversion efficiency (PCE) (Figure 4). We fabricated devices by sandwiching a ∼100 nm thick P3HT-N5:PCBM blend layer (1:1 P3HT-N5:PCBM weight ratio) between ITO/PEDOT:PSS and aluminum (Al) electrical contacts each with a nominal device area of 0.0314 cm^2. UV-cross-linked P3HT-N5:PCBM solar cells that had been subjected to six thermal annealing steps (10 min/step) at temperatures increased in 10 °C increments from 100 to 150 °C, achieving a maximum PCE of ∼1.2% at 110 °C (AM1.5G 1 SUN condition, red curves in Figure 4a). Increasing the postfabrication annealing temperature beyond 150 °C decreased the PCE, primarily by reducing the short-circuit current density (J_{sc}) and device fill factor (FF) (Figure 4b,c). The device open-circuit voltage (V_{oc}) did not change significantly with increasing annealing temperature after reaching ∼0.6 V at 110 °C (Figure 4d). The decrease in device J_{sc} and FF for temperatures higher than 110 °C coincided with an increased device series resistance, evidenced by the high resistance at V_{oc} after a 150 °C anneal (Figure 4e). Un-cross-linked P3HT-N5:PCBM blend devices showed a nearly identical variation in PV parameters with postfabrication annealing temperature (blue curves in Figure 4a–d). The relatively low PV performance is mainly attributed to the fabrication of the devices under ambient conditions in the presence of air and light,[34] where oxygen can reduce the efficiency of organic solar cells by photochemically reacting with the organic components[57,58] and creating localized

dx.doi.org/10.1021/ma3001725 | Macromolecules 2012, 45, 2338–2347

trapped charges in P3HT.[51] Thermogravimetric analysis (TGA) and differential scanning calorimetry (DSC) of un-cross-linked P3HT-N5 powders indicated that thermal decomposition of azide groups begins at ~110 °C (Figure 5a). When gradually heated from room temperature to 200 °C,

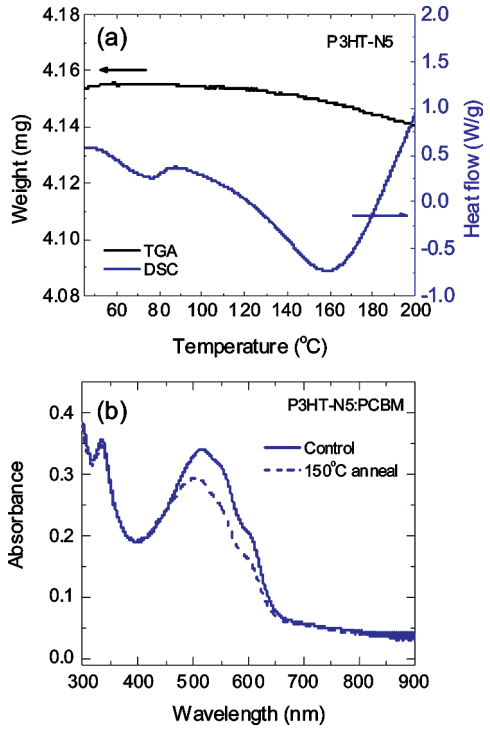


Figure 5. (a) TGA and DSC data for as-prepared P3HT-N5 powder. (b) Optical absorbance of as-prepared P3HT-N5:PCBM blend before (solid blue line) and after (dashed blue line) 10 min 150 °C vacuum anneal.

the un-cross-linked P3HT-N5 begins losing weight at ~90−100 °C (Figure 5a, solid black line), matching an exothermic reaction in the DSC profile that begins at ~100 °C and peaks at 160 °C (Figure 5a, solid blue line). We believe that this reaction corresponds to thermal activation of azide groups. Indeed, P3HT-N5:PCBM films that were not exposed to UV light became insoluble after annealing for 10 min at 150 °C in vacuum (Supporting Information).

Because thermal energy can both activate azide cross-linking and induce diffusion of polymer chains, thermal cross-linking is more likely to involve reactions with aromatic C−H bonds, which would create structural and electronic defects and reduce the polymer conjugation length. Chain diffusion could also lead to trapping of polymer chains in nonideal configurations. Measurements of the P3HT optical absorbance of un-photo-cross-linked P3HT-N5:PCBM blend films support this scenario, showing a reduced amplitude and a shift of peak absorption to shorter wavelengths after 150 °C vacuum annealing (Figure 5b). We expect this type of P3HT degradation can occur during postfabrication device annealing through thermal activation of residual azide groups, reducing PV performance of the cross-linked P3HT-N5:PCBM blend solar cells with increasing device postfabrication annealing temperature over 110 °C. Because the FT-IR analysis suggested 95% dissociation of the azide groups after a 60 min UV exposure, this implies that a very low concentration of azide groups (less than one azide group per polymer chain) is sufficient to cause degradation of device performance at elevated temperatures. In contrast, the PCBM region optical absorption showed little change after the thermal anneal (Figure 5b), again suggesting minimal participation of PCBM in cross-linking reactions.

Thermal Stability of Cross-Linked P3HT-N5:PCBM BHJ Solar Cells. Cross-linking P3HT-N5 significantly improves the thermal stability of P3HT-N5:PCBM BHJ solar cells. We subjected optimized UV-cross-linked P3HT-N5:PCBM solar cells to 110 °C (in vacuum) for as long as 40 h to measure the effect on PV characteristics and compare device performance with that of un-cross-linked P3HT-N5:PCBM and commercial P3HT (Rieke Metal):PCBM blend solar cells.

The UV-cross-linked P3HT-N5:PCBM blend solar cells retained as much as 65% of the initial PCE (~1.5%) after 40 h at 110 °C, as compared to commercial un-cross-linked P3HT:PCBM devices whose PCE decreased to 28% of their initial value (~2.2%) (Figure 6a). We note that control devices made using initially un-cross-linked P3HT-N5:PCBM blends also exhibited improved thermal stability, likely due to P3HT thermal cross-linking by azide groups activated at 110 °C. In P3HT-N5:PCBM devices (both control and UV-cross-linked), J_{sc} and V_{oc} remain largely unchanged during the entire 40 h anneal (Figure 6b,c), with the decrease in PCE primarily due to a ~20% reduction in the FF that stabilized after ~5 h at 110 °C (Figure 6d). The device FF decrease stems from an increased device serial resistance as the comparison of representative $J-V$ curves for unannealed starting samples (Figure 6e) and the 40 h annealed devices (Figure 6f) shows decreased slopes at V_{oc} after the anneal. We expect this is most likely caused by higher electrical resistance of somewhat degraded P3HT due to thermal activation of residual azide groups, rather than by the change in blend phase separation morphology.

The decreased performance of commercial un-cross-linked P3HT:PCBM devices after the 40 h 110 °C anneal was due to deteriorating J_{sc}, V_{oc}, and FF, which decreased by ~60%, ~20%, and ~25%, respectively (Figure 6b). In contrast to cross-linked P3HT-N5:PCBM samples, the un-cross-linked P3HT:PCBM devices show a less significant increase in series resistance after annealing (Figure 6e), implying that coarsening of the blend internal morphology, rather than the degradation of the polymers, is responsible for the decreasing PV performance. A comparison of optical micrographs of commercial un-cross-linked P3HT:PCBM and UV-cross-linked P3HT-N5:PCBM further confirms the improved thermal stability of the cross-linked BHJ morphology. The commercial P3HT:PCBM blend film developed significant numbers of macroscopic 3−5 μm diameter domains (Figure 7a), while the UV-cross-linked P3HT-N5:PCBM remain free of any optically visible aggregates (Figure 7b).

■ CONCLUSION

We have synthesized a reactive azide-functionalized polythiophene (P3HT-N5) that can be photo-cross-linked without addition of small molecule cross-linkers. The synthetic route we report was carried out using good solvents under mild conditions, potentially expanding the synthetic portfolio of functionalized P3HT. UV-cross-linked P3HT-N5:PCBM BHJ solar cells have improved thermal stability of PV performance compared with solar cells prepared with commercial un-cross-linked P3HT:PCBM active layers. Our device measurements are consistent with UV-cross-linking stabilizing the optimized BHJ morphology against domain coarsening by macrophase

dx.doi.org/10.1021/ma3001725 | Macromolecules 2012, 45, 2338−2347

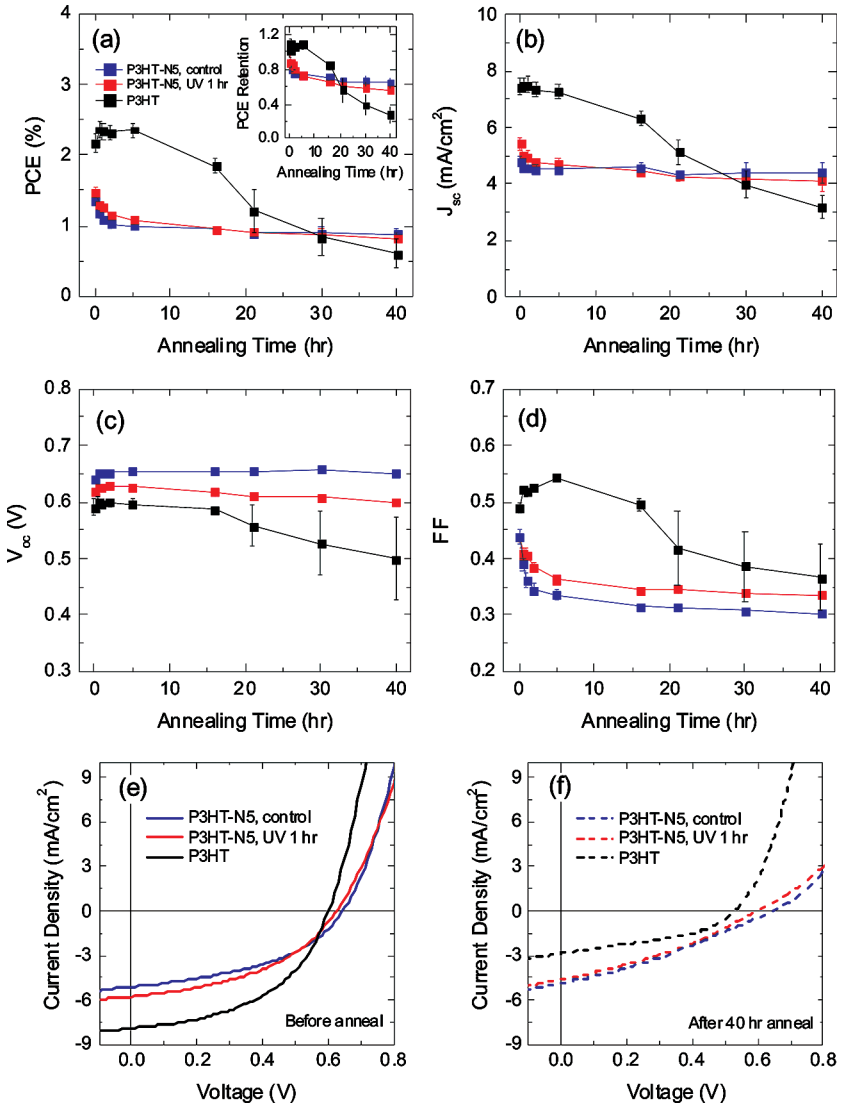


Figure 6. PV characteristics of control (solid blue line), 60 min UV-cross-linked (solid red line) P3HT-N5:PCBM blend, and commercial P3HT:PCBM blend (solid black line) solar cells with varying vacuum annealing duration at 110 °C up to 40 h. Data points represent average values of 4–5 measured devices, with error bars denoting one standard deviation. (a) PCE, (b) J_{sc}, (c) V_{oc}, and (d) FF. (e, f) Representative J–V characteristics of control (blue line), UV-cross-linked (red line) P3HT-N5:PCBM blend, and commercial P3HT:PCBM blend (black line) solar cells before and after 40 h vacuum anneal at 110 °C.

separation. By varying the postfabrication device annealing temperature, we identified influences of thermally activated azide cross-linkers on device PV characteristics, providing useful information for designing new cross-linkable conjugated polymers and their device processing. While these studies were carried out with devices that were prepared in air, which consequently show lower efficiencies than comparable devices prepared under inert atmospheres, it is clear that the analyses of P3HT-N5 photo-cross-linking behavior and the influences of cross-linking on polymer:fullerene blend structure, active layer optical properties, and device PV performance and thermal stability should be generally applicable to all P3HT-based blend solar cells, considering that the structure of the P3HT-N5:PCBM blend, as characterized by GIWAXS, is nearly identical to typical commercial P3HT:PCBM blends.

EXPERIMENTAL SECTION

Materials and General Methods. The compounds 3-bromothiophene (97%), (6-bromohexyloxy)-*tert*-butyldimethylsilane (99%), Mg (turnings, ≥99.5%), [1,3-bis(diphenylphosphino)propane]-dichloronickel(II), *N*-bromosuccinimide (99%), *tert*-butylmagnesium chloride (1.0 M in THF), tetrabutylammonium fluoride trihydrate (≥97%), triphenylphosphine (99%), 2,3-dichloro-5,6-dicyano-*p*-benzoquinone (98%), 1,2-dichlorobenzene (anhydrous, 99%), and poly(3,4-ethylenedioxythiophene)–poly(styrenesulfonate) were purchased from Aldrich and used without further purification. Tetrabutylammonium azide (95%) was purchased from TCI America and used without further purification. Aluminum (99.999%) and gold (99.99%) pellets were purchased from Kurt J. Lesker Co. Reactions and manipulations involving air-sensitive species were carried out under an atmosphere of prepurified argon using either Schlenk techniques or an inert-atmosphere glovebox (Vacuum Atmospheres Co.). THF and $CHCl_3$ were purified using a solvent purification system (Vacuum Atmospheres Co.). The 400 MHz ^{1}H NMR and 100 MHz ^{13}C NMR spectra were recorded on a Bruker AVANCE 400 MHz spectrometer and referenced internally to the solvent peaks. The mass spectra were obtained on a Thermo Electron Corp. DSQ II using electron ionization. GPC analyses were performed in $CHCl_3$ (1 mL/min) using a Viscotek GPCmax system equipped with a VE-2001 solvent/sample module, a TDA 305 triple detector array, and a UV

dx.doi.org/10.1021/ma3001725 | *Macromolecules* 2012, 45, 2338–2347

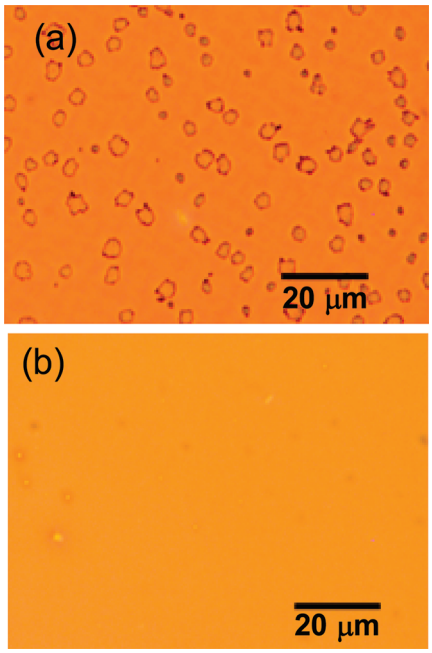


Figure 7. Optical micrographs of (a) commercial P3HT:PCBM and (b) UV-cross-linked P3HT-N5:PCBM blend films after 40 h vacuum anneal at 110 °C.

2600 detector. Two columns (Viscotek, I-MBMMW-3078), which were kept in a column heater at 35 °C, were used for separation. The columns were calibrated with polystyrene standards (Varian). Optical absorption spectra were recorded on a PerkinElmer Lambda 25 UV−vis spectrometer. FT-IR spectra were obtained using a Nicolet 6700 FT-IR spectrometer operated under attenuated total reflectance mode. A programmable spincoater from Brewer Science (Model 200) was used for thin film preparation. Film thickness was measured by a Dektak 150 surface profiler. A UV-ozone cleaning system (model T1oX/OES, UVOCS Inc.) was used for ITO substrate cleaning. A Fisher Scientific Isotemp vacuum oven (282A) was used for sample thermal annealing. The Kurt J. Lesker PVD 75 evaporation system was used for metal deposition. For thermal analyses, PerkinElmer Diamond DSC and Diamond TG/DTA were used, and the sample was heated under a nitrogen atmohsphere at rate of 5 and 10 °C/min, respectively.

Synthesis. *(6-(3-Thienyl)hexyloxy)-tert-butyldimethylsilane.* To a suspension of Mg (4.3 g, 0.18 mol) in 200 mL of THF was added slowly (6-bromohexyloxy)-*tert*-butyldimethylsilane (26.3 g, 0.089 mol) while maintaining the temperature below 60 °C. The reaction mixture was stirred at 60 °C for 2 h and then transferred at 0 °C to another Schlenk flask containing 3-bromothiophene (15.3 g, 0.094 mol) and [1,3-bis-(diphenylphosphino)propane]dichloronickel(II) (1.0 g, 1.85 mmol) in 100 mL of THF. The mixture was then warmed to room temperature and stirred overnight. After standard aqueous work-up, the product was isolated by vacuum distillation (0.3 Torr, 99−10 °C) as a colorless liquid (20.4 g, 77% yield). ^{1}H NMR (400 MHz, $CDCl_3$): δ = 7.25, 6.93 (m, 3H, aromatic H's), 3.60 (t, 2H, $-SiOCH_2-$), 2.63 (t, 2H, $ThCH_2-$), 1.64−1.35 (m, 8H, $ThCH_2(CH_2)_4CH_2OSi$), 0.90 (s, 9H, *tert*-butyl H's), 0.05 (s, 6H, $Si(CH_3)_2$). ^{13}C NMR (100 MHz, $CDCl_3$): δ = 143.38, 128.49, 125.27, 120.01, 63.46, 33.01, 30.76, 30.43, 29.32, 26.21, 25.85, 18.60, −5.04. MS (EI) calculated (m/z) for $C_{16}H_{30}OSSi$: 298.2; found: 240.9 [M − 57 (*tert*-butyl)]$^+$.

(6-(3-(2,5-Dibromothienyl)hexyloxy)-tert-butyldimethylsilane (1). (6-(3-Thienyl)hexyloxy)-*tert*-butyldimethylsilane (20.4 g, 0.068 mol) was dissolved in 250 mL of DMF and cooled to 0 °C. *N*-Bromosuccinimide (24.9 g, 0.14 mol) was added in one portion, and the mixture was slowly warmed to room temperature and stirred overnight. After standard aqueous work-up, the product was isolated by vacuum distillation (30 mTorr, 111−113 °C) as a slightly yellow liquid (18.3 g, 59% yield). ^{1}H NMR (400 MHz, $CDCl_3$): δ = 6.79 (s, 1H, Th−H4), 3.62 (t, 2H, $-SiOCH_2-$), 2.54 (t, 2H, $ThCH_2-$), 1.57−1.34 (m, 8H, $ThCH_2(CH_2)_4CH_2OSi$), 0.91 (s, 9H, *tert*-butyl H's), 0.05 (s, 6H, $Si(CH_3)_2$). ^{13}C NMR (100 MHz, $CDCl_3$): δ = 143.11, 131.16, 110.55, 108.18, 63.38, 32.93, 29.79, 29.62, 29.07, 26.21, 25.79, 18.60, −5.04. MS (EI) calculated (m/z) for $C_{16}H_{28}Br_2OSSi$: 456.0; found: 398.7 [M − 57 (*tert*-butyl)]$^+$.

P3HT-Si5. 2,5-Dibromo-3-hexylthiophene (4.95 g, 15.18 mmol) and (6-(3-(2,5-dibromothienyl)hexyloxy)-*tert*-butyldimethylsilane (0.37 g, 0.80 mmol) were dissolved in 150 mL of THF under Ar, and *tert*-butylmagnesium chloride (16.0 mL, 16.0 mmol) was added through a syringe. The mixture was refluxed for 2 h and cannula transferred to another Schlenk flask containing [1,3-bis(diphenylphosphino)-propane]dichloronickel(II) (87 mg, 0.16 mmol) cooled at 0 °C. The mixture was warmed to room temperature and stirred overnight. The red solution was concentrated under vacuum and precipitated into a large excess of methanol. After filtration, the solid was Soxhlet extracted with acetone, THF, and $CHCl_3$ for 24 h, and P3HT-Si5 was isolated by combining and concentrating the THF and $CHCl_3$ fractions followed by precipitation into methanol and dried under vacuum as a black solid (1.43 g, 52% yield). ^{1}H NMR (400 MHz, $CDCl_3$): δ = 6.99 (1H, Th−H4), 3.63 (0.1H, $-SiOCH_2-$), 2.82 (2H, $ThCH_2-$), 1.74−1.23 (8H, $ThCH_2(CH_2)_4CH_2OSi$ and $ThCH_2(CH_2)_4CH_3$), 0.93 (3.5H, $ThCH_2(CH_2)_4CH_3$ and *tert*-butyl H's), 0.05 (0.15 H, $Si(CH_3)_2$).

P3HT-OH5. P3HT-Si5 (1.43 g) was dissolved in 20 mL of THF at 65 °C, and tetrabutylammonium fluoride trihydrate (0.27 g, 0.86 mmol) was added. The mixture was stirred at 65 °C overnight and precipitated into 400 mL of methanol and dried at 60 °C under vacuum for 12 h to give P3HT-OH5 as a black solid (1.18 g, 84% yield). ^{1}H NMR (400 MHz, $CDCl_3$): δ = 6.99 (1H, Th−H4), 3.67 (0.1H, CH_2OH), 2.82 (2H, $ThCH_2-$), 1.74−1.23 (8H, $ThCH_2(CH_2)_4CH_2OH$ and $ThCH_2(CH_2)_4CH_3$), 0.93 (3H, $ThCH_2(CH_2)_4CH_3$). GPC ($CHCl_3$, 1 mL/min, RI): M_n = 14.0 kDa, M_w = 21.2 kDa, PDI = 1.51.

P3HT-N5. Triphenylphosphine (0.092 g, 0.35 mmol) and 2,3-dichloro-5,6-dicyano-*p*-benzoquinone (DDQ, 0.079 g, 0.35 mmol) were dissolved in ca. 30 mL of anhydrous THF, and tetrabutylammonium azide (0.10 g, 0.35 mmol) was added as a powder and stirred for 5 min at room temperature under argon. P3HT-OH5 (0.12 g, 0.042 mmol of −OH) was then added, and the mixture was stirred at 60 °C under Ar for 1 h. Then the solution was poured into methanol (100 mL), and a crude product was collected by filtration. The crude P3HT-N5 was further purified by dissolving the crude solid in a minimal amount of THF and precipitating the THF solution into methanol (50 mL). The resulting purified P3HT-N5 was then dried under high vacuum at 60 °C for 12 h to give a black powder (0.10 g, 83% yield).

Alternatively, the reaction can be performed in $CHCl_3$ by the following procedure, but it is not advisible due to the possible formation of explosive azidomethane derivatives. Triphenylphosphine (0.33 g, 1.26 mmol) and DDQ (0.38 g, 1.68 mmol) were dissolved in ca. 20 mL of anhydrous $CHCl_3$, and tetrabutylammonium azide (0.48 g, 1.68 mmol) was added as a powder and stirred for 5 min. P3HT-OH5 (1.18 g, 0.42 mmol −OH) in ca. 20 mL was then added, and the mixture was stirred at room temperature under Ar for 16 h. P3HT-N5 was isolated by precipitation into ca. 400 mL of methanol and dried under high vacuum at 60 °C for 12 h as a black powder (1.05 g, 89% yield). ^{1}H NMR (400 MHz, $CDCl_3$): δ = 6.99 (1H, Th−H4), 3.29 (0.1H, CH_2N_3), 2.82 (2H, $ThCH_2-$), 1.74−1.23 (8H, $ThCH_2(CH_2)_4CH_2N_3$ and $ThCH_2(CH_2)_4CH_3$), 0.93 (3H, $ThCH_2(CH_2)_4CH_3$). GPC ($CHCl_3$, 1 mL/min, RI): M_n = 14.5 kDa, M_w = 22.7 kDa, PDI = 1.57.

Photo-Cross-Linking. First, ∼100 nm thick films of P3HT-N5 or P3HT-N5:PCBM blend were prepared by spin-casting a 2 wt % solution in chlorobenzene on either glass or ITO-coated glass substrates at ∼700 rpm for 45 s in an ambient air condition. The

dx.doi.org/10.1021/ma3001725 | *Macromolecules* 2012, 45, 2338−2347

samples were then transferred into an argon-filled glovebox and sealed in a metal enclosure with a quartz optical window. The enclosure was transferred outside the glovebox, and the films were exposed for 60 min to UV light generated by a 200 W mercury lamp (Newport) which has a nominal spectral coverage ranging from ~250 over ~2400 nm as specified by the manufacturer. We use a color filter (Newport, FSR-U340) to select ~254 nm wavelength, and the light intensity irradiating on a sample was ~180 mW/cm^2 as measured by a calibrated Si detector (Newport).

Solar Cell Fabrication. All device processing described here was performed in ambient air unless indicated otherwise. P3HT-N5, P3HT (Rieke Metal), and PCBM powders (American Dye Source) were separately dissolved in chlorobenzene with 1:50 weight ratio to obtain a 2 wt % solution. P3HT-N5 (or P3HT) and PCBM solutions were mixed in a 1:1 ratio to form 2 wt % blend solutions. A PEDOT:PSS (Sigma-Aldrich) solution was spin-coated at 5000 rpm for 45 s on a 140 nm thick ITO-coated glass substrate and baked at 140 °C in air for 10 min. The 2% blend solution was then spin-cast at 700 rpm for 45 s and dried in an enclosed sample carrier for ~15−20 min to facilitate blend phase separation at room temperature. The active blend layer was then UV cross-linked by the procedure described above. Device fabrication was then completed by depositing top ~80 nm Al contacts by thermal evaporation through a shadow mask, with active device area 0.0314 cm^2. Completed devices were subjected to thermal anneal in vacuum for 10 min (~100 mTorr) at various temperatures ranging from 100 to 150 °C.

SCLC Mobility Measurement. Devices for SCLC mobility measurement were fabricated by procedures similar to those used for BHJ solar cells. First, 2 wt % P3HT-N5 solution in chlorobenzene was spin-cast at 700 rpm for 45 s on ITO-glass substrates coated with PEDOT:PSS, and ~100 nm Au was thermally evaporated and deposited on the P3HT-N5 layer (either un-cross-linked or 60 min UV cross-linked). Device $J-V$ characteristics were then obtained by Agilent 4156C precision semiconductor parameter analyzer. Mobility was calculated by fitting the forward $J-V$ data (i.e., PEODT:PSS contact is positively biased with respect to Au) to the SCLC model;[59] $J = (9/8)\varepsilon_0\varepsilon_r\mu V^2 d^{-3}$, where ε_0 is the vacuum permittivity, ε_r is the relative dielectric constant of P3HT (~3), and d is the P3HT-N5 layer thickness.

PV Characterization. A 150 W solar simulator (Oriel) equipped with an AM1.5G filter was used for solar illumination. The light intensity was calibrated for 100 mW/cm^2 (1 SUN) condition by using a KG5 color filtered Si reference solar cell (Newport) to account for spectral mismatch between Si and P3HT. $J-V$ characteristics of dark and illuminated solar cells or transport analysis devices were measured using a custom-modified probe station and an Agilent 4156C precision semiconductor parameter analyzer. For each experimental condition, we fabricated 4−5 devices and report the average PV and electrical parameters as well as their standard deviations.

GIWAXS Measurement. GIWAXS measurements were performed at the X9 undulator-based beamline at the National Synchrotron Light Source, Brookhaven National Laboratory. The incident X-ray beam (λ = 0.0886 nm) was collimated using slits and focused onto the sample position using Kirkpatrick-Biaz mirrors. This provides a 200 μm wide by 80 μm high spot at the sample position whose footprint along the sample spreads out by the inverse incident angle. The sample stage was located inside the vacuum chamber (pressure ~40 Pa) where the incident angle is computer controlled. A two-dimensional charged-coupled device (CCD) detector was positioned ~270 mm from the center of the sample stage to collect the GIWAXS images inside the same vacuum chamber. Data conversion to q-space was accomplished by calibration using silver behenate powder.

■ ASSOCIATED CONTENT

Ⓢ Supporting Information

FT-IR spectra of P3HT-N5 before and after 60 min UV exposure; FT-IR spectra (transmittance) for P3HT-Si5, P3HT-OH5, and P3HT-N5; $J-V$ characteristics of ITO/PEDOT:PSS/P3HT-N5/Au devices used for deducing hole mobility by SCLC model; low-magnification optical micrographs of 60 min UV exposed and 10 min 150 °C vacuum annealed P3HT-N5:PCBM blends compared with commercial P3HT:PCBM blend after chlorobenzene rinsing. This material is available free of charge via the Internet at http://pubs.acs.org.

■ AUTHOR INFORMATION

Corresponding Author

*E-mail: cynam@bnl.gov (C.-Y.N.), rgrubbs@bnl.gov (R.B.G.).

Present Address

[⊥]Department of Chemistry and Chemical Biology, University of New Mexico, Albuquerque, NM 87131.

Author Contributions

[‖]These authors contributed equally.

Notes

The authors declare no competing financial interest.

■ ACKNOWLEDGMENTS

This research was carried out at the Center for Functional Nanomaterials, Brookhaven National Laboratory, which is supported by the U.S. Department of Energy, Office of Basic Energy Sciences, under Contract DE-AC02-98CH10886. We thank Xiao-Liang Wang and Weiqiang Han for collecting and discussing DSC and TGA data.

■ REFERENCES

(1) Hou, J. H.; Chen, H. Y.; Zhang, S. Q.; Liang, Y. Y.; Yang, G. W.; Yang, Y.; Yu, L. P.; Wu, Y.; Li, G. *Nat. Photonics* **2009**, *3*, 649−653.

(2) Service, R. F. *Science* **2011**, *332*, 293−293.

(3) Yu, G.; Gao, J.; Hummelen, J. C.; Wudl, F.; Heeger, A. J. *Science* **1995**, *270*, 1789−1791.

(4) Li, G.; Shrotriya, V.; Huang, J. S.; Yao, Y.; Moriarty, T.; Emery, K.; Yang, Y. *Nat. Mater.* **2005**, *4*, 864−868.

(5) Ma, W. L.; Yang, C. Y.; Gong, X.; Lee, K.; Heeger, A. J. *Adv. Funct. Mater.* **2005**, *15*, 1617−1622.

(6) Liang, Y. Y.; Feng, D. Q.; Wu, Y.; Tsai, S. T.; Li, G.; Ray, C.; Yu, L. P. *J. Am. Chem. Soc.* **2009**, *131*, 7792−7799.

(7) Park, S. H.; Roy, A.; Beaupre, S.; Cho, S.; Coates, N.; Moon, J. S.; Moses, D.; Leclerc, M.; Lee, K.; Heeger, A. J. *Nat. Photonics* **2009**, *3*, 297−302.

(8) Liang, Y.; Xu, X.; Xia, J.; Tsai, S.-T.; Wu, Y.; Li, G.; Ray, C.; Yu, L. *Adv. Mater.* **2010**, *22*, E135−E138.

(9) Hoppe, H.; Sariciftci, N. S. *J. Mater. Chem.* **2006**, *16*, 45−61.

(10) Li, G.; Shrotriya, V.; Yao, Y.; Yang, Y. *J. Appl. Phys.* **2005**, *98*, 043704.

(11) Chirvase, D.; Parisi, J.; Hummelen, J. C.; Dyakonov, V. *Nanotechnology* **2004**, *15*, 1317−1323.

(12) Padinger, F.; Rittberger, R. S.; Sariciftci, N. S. *Adv. Funct. Mater.* **2003**, *13*, 85−88.

(13) Yang, Y.; Li, G.; Yao, Y.; Yang, H.; Shrotriya, V.; Yang, G. *Adv. Funct. Mater.* **2007**, *17*, 1636−1644.

(14) Xie, Z. Y.; Zhao, Y.; Qu, Y.; Geng, Y. H.; Wang, L. X. *Appl. Phys. Lett.* **2007**, *90*, 043504.

(15) Vanlaeke, P.; Vanhoyland, G.; Aernouts, T.; Cheyns, D.; Deibel, C.; Manca, J.; Heremans, P.; Poortmans, J. *Thin Solid Films* **2006**, *511*, 358−361.

(16) Mihailetchi, V. D.; Xie, H. X.; de Boer, B.; Popescu, L. M.; Hummelen, J. C.; Blom, P. W. M.; Koster, L. J. A. *Appl. Phys. Lett.* **2006**, *89*, 012107.

(17) Gunes, S.; Neugebauer, H.; Sariciftci, N. S. *Chem. Rev.* **2007**, *107*, 1324−1338.

(18) Frechet, J. M. J.; Thompson, B. C. *Angew. Chem., Int. Ed.* **2008**, *47*, 58−77.

(19) Sivula, K.; Ball, Z. T.; Watanabe, N.; Frechet, J. M. J. *Adv. Mater.* **2006**, *18*, 206−210.

(20) Drees, M.; Hoppe, H.; Winder, C.; Neugebauer, H.; Sariciftci, N. S.; Schwinger, W.; Schaffler, F.; Topf, C.; Scharber, M. C.; Zhu, Z. G.; Gaudiana, R. *J. Mater. Chem.* **2005**, *15*, 5158−5163.
(21) Zhu, Z.; Hadjikyriacou, S.; Waller, D.; Gaudiana, R. *J. Macromol. Sci., Pure Appl. Chem.* **2004**, *A41*, 1467−1487.
(22) Kim, B. J.; Miyamoto, Y.; Ma, B. W.; Frechet, J. M. J. *Adv. Funct. Mater.* **2009**, *19*, 2273−2281.
(23) Frechet, J. M. J.; Griffini, G.; Douglas, J. D.; Piliego, C.; Holcombe, T. W.; Turri, S.; Mynar, J. L. *Adv. Mater.* **2011**, *23*, 1660−1664.
(24) Holdcroft, S.; Gholamkhass, B. *Chem. Mater.* **2010**, *22*, 5371−5376.
(25) Contoret, A. E. A.; Sr, F.; O'Neill, M.; Nicholls, J. E.; Richards, G. J.; Kelly, S. M.; Hall, A. W. *Chem. Mater.* **2002**, *14*, 1477−1487.
(26) Muller, C. D.; Falcou, A.; Reckefuss, N.; Rojahn, M.; Wiederhirn, V.; Rudati, P.; Frohne, H.; Nuyken, O.; Becker, H.; Meerholz, K. *Nature* **2003**, *421*, 829−833.
(27) Charas, A.; Ferreira, Q.; Farinhas, J.; Matos, M.; Alcacer, L.; Morgado, J. *Macromolecules* **2009**, *42*, 7903−7912.
(28) Rutherford, D. R.; Stille, J. K.; Elliott, C. M.; Reichert, V. R. *Macromolecules* **1992**, *25*, 2294−2306.
(29) Gearba, I. R.; Nam, C. Y.; Pindak, R.; Black, C. T. *Appl. Phys. Lett.* **2009**, *95*, 173307.
(30) Chua, L. L.; Png, R. Q.; Chia, P. J.; Tang, J. C.; Liu, B.; Sivaramakrishnan, S.; Zhou, M.; Khong, S. H.; Chan, H. S. O.; Burroughes, J. H.; Friend, R. H.; Ho, P. K. H. *Nat. Mater.* **2010**, *9*, 152−158.
(31) Murray, K. A.; Holmes, A. B.; Moratti, S. C.; Rumbles, G. *J. Mater. Chem.* **1999**, *9*, 2109−2115.
(32) Li, Y. F.; Zou, Y. P. *Adv. Mater.* **2008**, *20*, 2952−2958.
(33) Kim, Y.; Cook, S.; Tuladhar, S. M.; Choulis, S. A.; Nelson, J.; Durrant, J. R.; Bradley, D. D. C.; Giles, M.; Mcculloch, I.; Ha, C. S.; Ree, M. *Nat. Mater.* **2006**, *5*, 197−203.
(34) Nam, C. Y.; Su, D.; Black, C. T. *Adv. Funct. Mater.* **2009**, *19*, 3552−3559.
(35) Wu, S. J.; Li, J. H.; Tai, Q. D.; Yan, F. *J. Phys. Chem. C* **2010**, *114*, 21873−21877.
(36) Zhai, L.; Pilston, R. L.; Zaiger, K. L.; Stokes, K. K.; McCullough, R. D. *Macromolecules* **2003**, *36*, 61−64.
(37) Jeffries-El, M.; McCullough, R. D. *Handbook of Conducting Polymers*, 3rd ed.; CRC Press: Boca Raton, FL, 2007.
(38) Png, R. Q.; Chia, P. J.; Tang, J. C.; Liu, B.; Sivaramakrishnan, S.; Zhou, M.; Khong, S. H.; Chan, H. S. O.; Burroughes, J. H.; Chua, L. L.; Friend, R. H.; Ho, P. K. H. *Nat. Mater.* **2010**, *9*, 152−158.
(39) Iranpoor, N.; Firouzabadi, H.; Akhlaghinia, B.; Nowrouzi, N. *Tetrahedron Lett.* **2004**, *45*, 3291−3294.
(40) Langford, J. I.; Wilson, A. J. C. *J. Appl. Crystallogr.* **1978**, *11*, 102−113.
(41) Erb, T.; Zhokhavets, U.; Gobsch, G.; Raleva, S.; Stuhn, B.; Schilinsky, P.; Waldauf, C.; Brabec, C. J. *Adv. Funct. Mater.* **2005**, *15*, 1193−1196.
(42) Zhokhavets, U.; Erb, T.; Hoppe, H.; Gobsch, G.; Sariciftci, N. S. *Thin Solid Films* **2006**, *496*, 679−682.
(43) Collins, B. A.; Gann, E.; Guignard, L.; He, X.; McNeill, C. R.; Ade, H. *J. Phys. Chem. Lett.* **2010**, *1*, 3160−3166.
(44) Chen, W.; Xu, T.; He, F.; Wang, W.; Wang, C.; Strzalka, J.; Liu, Y.; Wen, J. G.; Miller, D. J.; Chen, J. H.; Hong, K. L.; Yu, L. P.; Darling, S. B. *Nano Lett.* **2011**, *11*, 3707−3713.
(45) Chiu, M. Y.; Jeng, U. S.; Su, C. H.; Liang, K. S.; Wei, K. H. *Adv. Mater.* **2008**, *20*, 2573−2578.
(46) Shin, M.; Kim, H.; Park, J.; Nam, S.; Heo, K.; Ree, M.; Ha, C. S.; Kim, Y. *Adv. Funct. Mater.* **2010**, *20*, 748−754.
(47) Mihailetchi, V. D.; Xie, H. X.; de Boer, B.; Koster, L. J. A.; Blom, P. W. M. *Adv. Funct. Mater.* **2006**, *16*, 699−708.
(48) Abdou, M. S. A.; Orfino, F. P.; Son, Y.; Holdcroft, S. *J. Am. Chem. Soc.* **1997**, *119*, 4518−4524.
(49) Meijer, E. J.; Detcheverry, C.; Baesjou, P. J.; van Veenendaal, E.; de Leeuw, D. M.; Klapwijk, T. M. *J. Appl. Phys.* **2003**, *93*, 4831−4835.
(50) Yoshino, K.; Takahashi, H.; Muro, K.; Ohmori, Y.; Sugimoto, R. *J. Appl. Phys.* **1991**, *70*, 5035−5039.
(51) Schafferhans, J.; Baumann, A.; Deibel, C.; Dyakonov, V. *Appl. Phys. Lett.* **2008**, 93.
(52) Liao, H. H.; Yang, C. M.; Liu, C. C.; Horng, S. F.; Meng, H. F.; Shy, J. T. *J. Appl. Phys.* **2008**, *103*, 104506.
(53) Miller, J. S.; Dixon, D. A. *Science* **1987**, *235*, 871−873.
(54) Abramovitch, R. A.; Challand, S. R. *J. Chem. Soc., Chem. Commun.* **1972**, 964−966.
(55) Bendig, J.; Harder, T.; Wessig, P.; Stosser, R. *J. Am. Chem. Soc.* **1999**, *121*, 6580−6588.
(56) Hadad, C. M.; Liu, J.; Platz, M. S. *Org. Lett.* **2005**, *7*, 549−552.
(57) Krebs, F. C.; Spanggaard, H. *Chem. Mater.* **2005**, *17*, 5235−5237.
(58) Krebs, F. C.; Norrman, K. *Prog. Photovoltaics* **2007**, *15*, 697−712.
(59) Lampert, M. A.; Mark, P. *Current Injection in Solids*; Academic Press: New York, 1970.

Macromolecules

Article

pubs.acs.org/Macromolecules

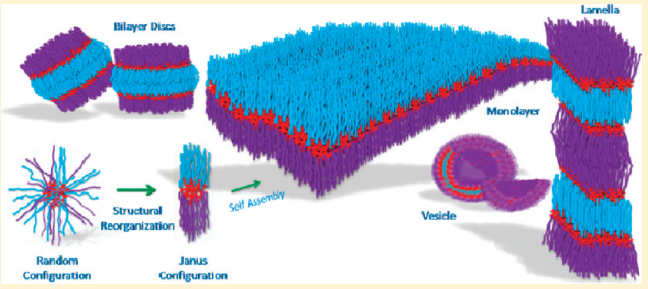
Janus Hybramers: Self-Adapting Amphiphilic Hyperbranched Polymers

Ashok Zachariah Samuel and S. Ramakrishnan*

Department of Inorganic and Physical Chemistry, Indian Institute of Science, Bangalore 560012, India

Supporting Information

ABSTRACT: Janus structures have attracted a great deal of interest because of their fascinating properties and potential for applications. In this study, we demonstrate that hyperbranched polymers, bearing randomly placed docosyl (C22 alkyl segment) and PEG segments on their periphery, can readily reconfigure so as to segregate the alkyl and PEG segments, thereby generating Janus-type structures that we have termed *Janus hybramers*. DSC studies clearly reveal an endothermic transition that corresponds to the melting of the docosyl domains, while Langmuir isotherms demonstrate that these polymers form stable monolayers that appear to undergo a slight densification beyond a critical surface pressure; this suggested possible crystallization of the docosyl segments at the air−water interface. AFM studies of the transferred monolayers reveal various interesting aggregate morphologies at different surface pressures suggestive of island formation at the air−water interface; at the same time they also provided an estimate of the monolayer thickness. These Janus HBPs also form vesicles as evident from TEM and AFM studies; the AFM height of the deposited vesicles, as expected, was roughly 4 times that of the monolayer. SAXS studies revealed the formation of lamellar structures; the interlamellar spacing was largest when the relative mole fractions of docosyl and PEG segments were similar, but the spacing decreased when the mole fraction of either of these peripheral segments is substantially smaller; this suggested the possible presence of interdigitation within the domains of the minor component.



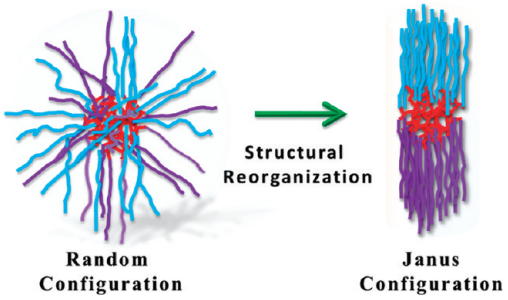
INTRODUCTION

Self-assembly of molecular systems has received a great deal of attention not only because of its fundamental importance in understanding cellular evolution[1] but also because understanding biological systems helps design nanoscale "smart materials" that mimic biological functions.[2] From this perspective, well-defined molecular architectures based on simple amphiphiles,[3] block copolymers,[4] dendrimers,[5] linear−dendritic blocks, hyperbranched polymers,[6] and other dendronized structures[7] have been extensively studied. Janus architectures have recently drawn a lot of attention because of the fascinating range of structural variability.[8] Müller and co-workers have pioneered the efforts to prepare polymeric Janus nanoparticles by exploiting the rich range of phase-separated morphologies formed by ABC type triblock copolymers; they have used selective cross-linking within the central B-block to generate a variety of Janus nanoparticles, ranging from spheres, cylinders to disks.[9−14] While all of these approaches generate Janus nanoparticles using an aggregate of polymer chains, the synthesis of readily tunable Janus molecular analogues has remained a difficult synthetic challenge. Janus dendrimers, which carry hydrophilic and hydrophobic units on either sides of their molecular periphery, is one exception that has been known for over a decade now.[15−19] However, there are only limited reports that describe their self-assembly properties. Recently, Percec and co-workers have carried out exhaustive studies to examine the self-assembly of a variety of lower generation Janus dendrimeric structures.[8] While dendrimers possess elegant structural symmetry, there is growing evidence that several functional properties may not require such rigorous structural perfection. Yan and co-workers, for instance, have demonstrated the self-assembly of polydisperse core−shell type hyperbranched polymers (HBPs) into tubes, micelles, and vesicles;[20] this proves undeniably that the monodisperse and structurally perfect molecular architectures are not essential criteria for generating self-assembled nanostructures. Several examples of core−shell domain separation in suitably designed hyperbranched polymers also provide evidence for conformational adaptability of the flexible hyperbranched backbone and their tolerance to high defect levels.[21−24] Additionally, studies by Tsukruk and co-workers have clearly shown that amphiphilic core−shell type HBPs reconfigure to jellyfish-like structures.[25,26] An interesting example of solvent-dependent self-adapting dendrimers was described by Aathimanikandan et al., wherein they showed that lower generation dendrimers carrying hydrophobic and hydrophilic segments on each repeat unit can conformationally readapt to enable solublity in both nonpolar and polar solvents.[27] In this context, it would be

Received: October 4, 2011
Revised: February 10, 2012
Published: February 27, 2012

ACS Publications © 2012 American Chemical Society

interesting to pose the question: *Can hyperbranched polymers, wherein peripheral end groups are randomly functionalized by hydrophobic and hydrophilic segments, conformationally readapt to form Janus structures, as depicted below?* Very recently, Chute et al. have suggested, based on a computational study, that reorganization to Janus-type structures is unlikely in the extreme case of dendrimers that bear hydrophobic and hydrophilic segments on each of their terminal units.[28] In an effort to address this question experimentally, we describe studies on hyperbranched (HB) polyesters, whose peripheral propargyl groups have been randomly clicked with both hydrophobic and hydrophilic segments. The parent polymer was synthesized using our recently developed single-step synthesis for the generation of peripherally clickable hyperbranched polyesters.[29] On the basis of their behavior in solution, at the air−water interface, small-angle X-ray scattering (SAXS), and differential scanning calorimetric (DSC) studies, we provide concrete evidence to demonstrate that hyperbranched polymers carrying randomly clicked hydrophobic and hydrophilic segments do indeed readapt to exhibit Janus-type behavior.

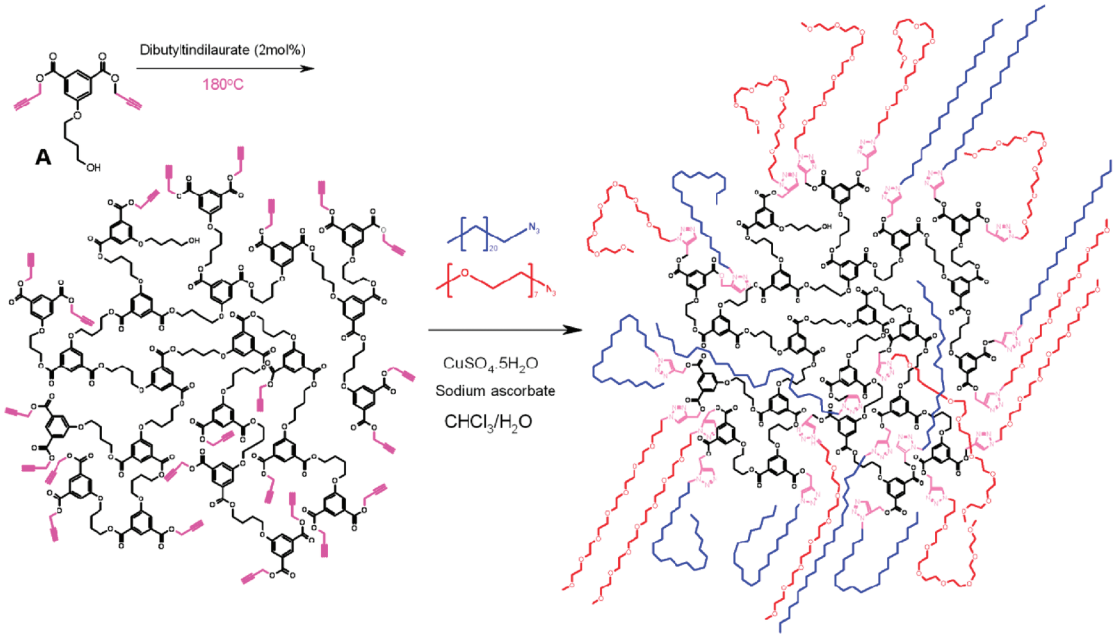


RESULTS AND DISCUSSION

The parent peripherally clickable hyperbranched polyester was prepared from monomer **A** via a melt transesterification process, as depicted in Scheme 1; the monomer was prepared readily from 5-hydroxyisophthalic acid.[29] The polymer exhibited a very broad molecular weight distribution—M_w = 84 000 and M_n 5600—which is often seen in the case of hyperbranched polymers prepared via the self-condensation of AB_2 type monomers. The degree of branching (DB) of the polyester could not be readily estimated; however, based on an earlier report by Feast et al.,[30] on a similar HB polyester we believe the value would be around 60%. This single-step process provides an attractive route to access useful molecular scaffolds on to which a variety of units could be clicked using the versatile copper-catalyzed quantitative azide−yne reaction.[31] In order to prepare amphiphilic systems, the clickable polyester scaffold was treated with two different azides, namely docosyl azide (a linear C-22 alkyl azide) and PEG-350 monomethyl ether azide. Polymers containing three different compositions of these hydrophobic and hydrophilic segments were thus prepared; these have been labeled as DOCOPEG-*xy*, where *x* and *y* represent the mole percentage of docosyl azide and PEG azide, respectively, used during the click reaction. In principle, two approaches could be taken to prepare these amphiphilic hyperbanched structures: one where the docosyl azide and the PEG azide are clicked sequentially and the second where both of the azides are taken in the required mole ratio and clicked simultaneously. We chose the latter approach as we expected this to produce a more randomly clicked structure (with a homogeneous distribution of PEG and docosyl groups on the periphery).

The proton NMR spectra of the parent clickable polyester (HBP-PE) carrying propargyl ester groups at the periphery, along with one that was clicked with docosyl azide and PEG azide in the mole ratio 70:30 (DOCOPEG-7030), are shown in Figure 1; the peaks are assigned as shown in the figure. It is evident that the click reaction has gone to completion, as no peaks due to residual propargyl groups (at ∼2.55 and 4.95 ppm) are seen in the spectrum of the clicked polymer. The peaks due to the terminal methyl protons of the docosyl and PEG units, at

Scheme 1. Synthesis of Clickable Hyperbranched Polyesters and Their Derivatization To Generate Amphiphilic DOCOPEG-*xy* Systems



dx.doi.org/10.1021/ma2022277 | *Macromolecules* 2012, 45, 2348−2358

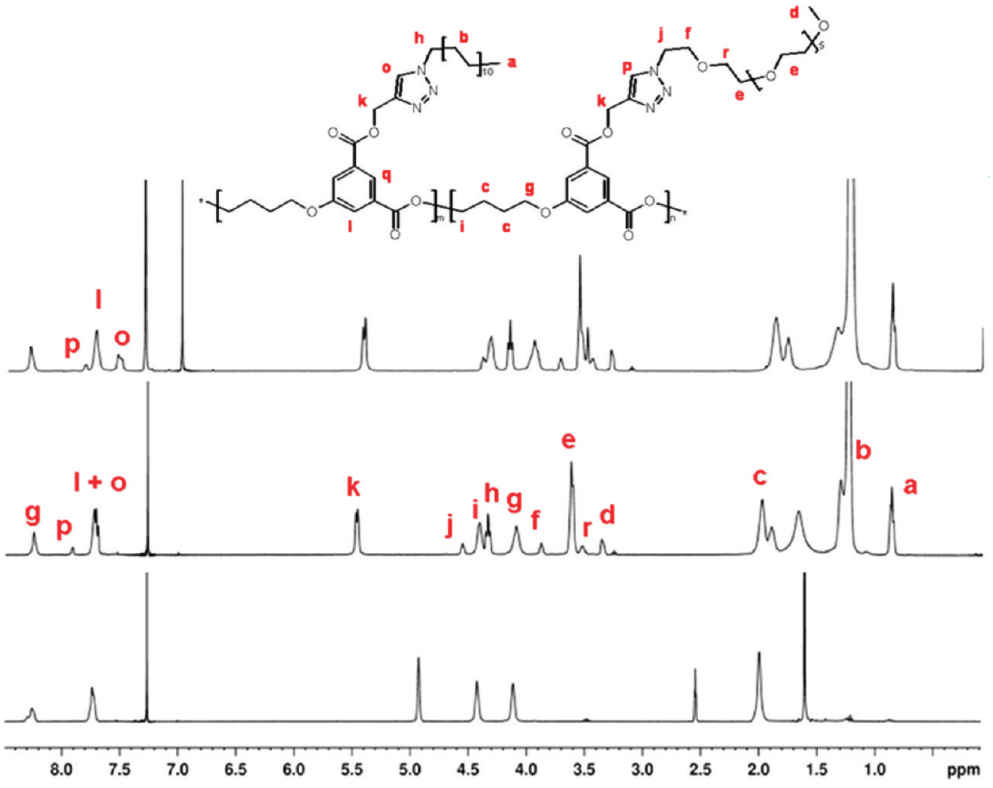


Figure 1. ^{1}H NMR spectra of parent HBP-PE (bottom), DOCOPEG-7030 in $CDCl_3$ (middle), and in $CDCl_3$ + C_6D_6 (top); use of a solvent mixture helped resolve the peaks l and o, the ratio of which was used as an internal consistency check of the percentage incorporation of docosyl azide and PEG (350) azide. Complete disappearance of propargyl peaks, at 4.9 and 2.6 ppm, demonstrates the efficacy of click reaction.

Table 1

	percentage incorporation from NMR		percentage feed					
name	docosanol	PEG	docosanol	PEG	mol wt (M_w) (g/mol)	PDI	enthalpy of melting (J/g)[a]	mp (°C)
parent HBP					84 000	15		
DOCOPEG-3070	34	66	30	70	35 400	2.5	120[c]	50[d]
DOCOPEG-5050	56	44	50	50	39 900	2.9	146	57
DOCOPEG-7030	81	19	70	30	145 600	8.8[b]	147	61

[a]Enthalpy values were taken from the heating curves and were normalized with respect to the wt % of docosyl segments in the HBP. [b]Possibly due to aggregation. [c]Estimated during the cooling curve, as the melting endotherm was very broad. [d]The endotherm was very broad and hence this value is not very accurate (see Figure S15).

around 0.9 and 3.4 ppm (peaks a and d), respectively, are well-resolved, and therefore, their intensities were directly employed to estimate the extent of their incorporation in the HBP. Furthermore, recording the spectrum in the presence of C_6D_6 permitted the resolution of peaks due to the triazole ring proton that belongs to docosyl and PEG units (peaks marked p and o);[32] the intensities of these protons could also be used to estimate the relative composition of the two units in the final clicked polymer. The composition obtained from both these methods match well and thus helps reconfirm the peak assignments. Similarly, the composition of the other two HB polyesters, clicked with different mole ratios of the docosyl and PEG units, namely 50/50 and 30/70, were also estimated based on their NMR spectra (Figure S1). The composition of the HBPs varies in reasonable accordance with the feed composition as evident from Table 1, although the incorporation of the docosyl unit is consistently slightly higher in all cases. The molecular weights of the parent HBP and the amphiphilic derivatives were estimated by GPC (Figure S2), and the values obtained have been listed in Table 1; the parent polymer as stated earlier had a very broad molecular weight distribution; however, upon derivatization the polydispersity index (PDI) decreased substantially in two cases, while in DOCOPEG-7030 a very broad distribution was seen. The reduction in PDI in two cases could either reflect the inherent insensitivity of the hydrodynamic volumes of such peripherally functionalized HBPs to molecular weight variations and/or could be due to fractionation that could have occurred during the purification of the postfunctionalized polymers. In the case of DOCOPEG-7030, although a similar procedure of isolation was used, the PDI continues to be high; this may be due to some aggregation, even though at this time we have no direct evidence for such aggregation.

Thermal Studies. One of the reasons for choosing the docosyl unit was to exploit the strong tendency of these long-chain alkyl segments to crystallize, which in turn would provide an added motivation for intrachain self-segregation. The simplest way to study phase separation is to examine the DSC curves of the

dx.doi.org/10.1021/ma2022277 | *Macromolecules* 2012, 45, 2348−2358

peripherally functionalized HBPs. In Figure 2, both the heating and cooling DSC curves of the three samples are presented; it is

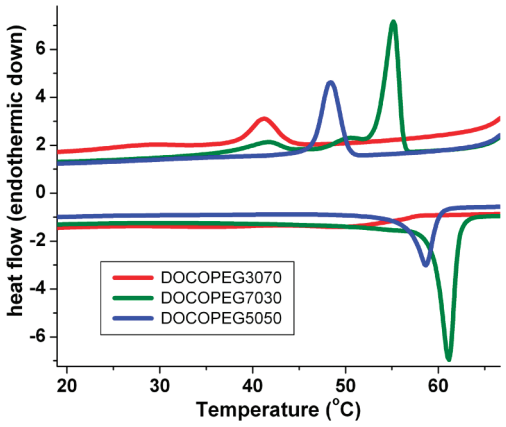


Figure 2. DSC curves (heating and cooling) of the DOCOPEG-*xy* polymers, showing clear melting and crystallization peaks. The melting transition of DOCOPEG-3070 appears as a very broad peak, while the crystallization exotherm during the cooling is sharper.

evident that the two samples having the higher mole fraction of docosyl units exhibit a clear melting peak during the heating scan, while DOCOPEG-3070 exhibits a very broad peak during the heating scan, although the crystallization exotherm during the cooling scan is sharper. The presence of this clear endothermic peak is ascribed to the melting of the docosyl segment,[33] and it provides the first evidence for the ability of the hyperbranched core to reorganize and permit segregation of the randomly placed peripheral PEG and docosyl segments. The DSC curves also reveal some other interesting trends: (a) both T_m and T_c and their associated enthalpies are seen to vary with the composition, and (b) the extent of supercooling is seen to change with composition. In order to compare the melting enthalpies, they should be normalized with respect to the docosyl content in the polymer; the normalized enthalpy values thus obtained for the three HBPs are listed in Table 1. Since the peak has been ascribed to the melting of the crystalline domains formed by the docosyl segments, one would expect the melting temperature and the normalized enthalpies to remain invariant with composition; however, as evident from Table 1, the T_m decreases with the docosyl composition. The ΔH_m values, however, are nearly the same for DOCOPEG-7030 and -5050 but substantially smaller for DOCOPEG-3070. This suggests that the phase separation in the former two samples is fairly complete, while this may not be the case when the PEG content is very high, thereby causing the melting peak to broaden out considerably, and this also causes the enthalpy value to decrease. The DSC thermograms of the hyperbranched polymers containing only docosyl or PEG units were also recorded; DOCO-100 exhibited a clear melting peak (normalized ΔH_m was ~136 mJ/mg; see Figure S-13), while the PEGylated HBP was completely amorphous (Figure S-14). The slightly lower value of normalized melting enthalpy of DOCO-100 probably reflects the larger mismatch in solubility parameters in the DOCOPEG-*xy* polymers, leading to more effective phase separation. It may be relevant to recall that the enthalpy of melting of a long-chain hydrocarbon of a similar size has been reported to be around 157 mJ/mg,[34] which is clearly in the vicinity of those seen for the higher docosyl-containing samples.

Studies at the Air–Water Interface. It is well-known that amphiphilic molecules and block copolymers demonstrate a strong tendency to orient themselves at the air–water interface with the polar segments solvated in water;[35,36] the spreading behavior of such systems is typically evaluated by measuring the surface pressure–area isotherms (π–A diagram) using a Langmuir trough. Langmuir isotherms have been effectively used in the past to clearly demonstrate the conformational adaptability of core–shell type PAMAM dendrimers[37] and hyperbranched polyesters[38] wherein the polar core was shown to flatten out and spread at the water surface pushing the long-chain alkylene peripheral groups upward. In the case of our randomly functionalized hyperbranched DOCOPEGs, the π–A isotherms will serve to probe the ability of randomly amphiphilic structures to reconfigure to Janus-type ones.

The π–A isotherms of the three different HBPs are shown in Figure 3; two distinctive features of DOCOPEG-7030 are the

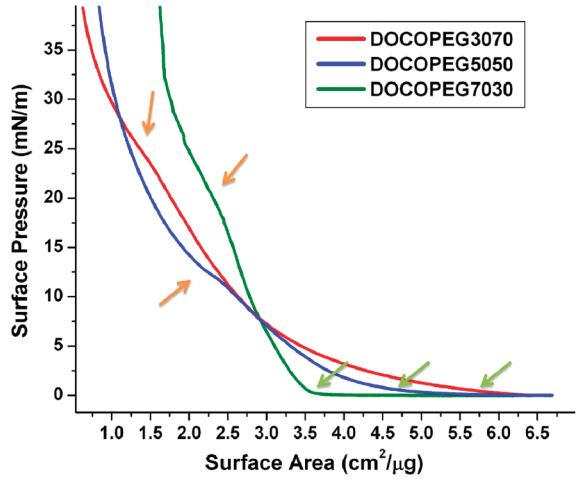


Figure 3. Langmuir isotherms for DOCOPEG-7030 (green), DOCOPEG-5050 (blue), and DOCOPEG-3070 (red); the green arrows indicate the points at which the surface pressure begins to increase, while the orange arrows mark the break in the curve, indicating a slight densification. The surface area has been normalized with respect to the weight of the polymer sample added to the interface.

sharpness in the rise of the surface pressure during compression and the area at which this rise begins. Another important aspect is the break in the slope of the curve during the compression (indicated by the orange arrow); this inflection occurs at different surface pressures for the different HBPs. These observations, taken together with the earlier DSC data, suggest that the inflection in the π–A isotherms could reflect a pseudocrystallization associated with the docosyl chains, which would lead to a densification of the alkylene segments at the air–water interface and cause a reduction in surface pressure; under experimental conditions where the area is being continuously reduced, this would be reflected as a change in slope. Earlier studies using simple surfactants,[39,40] as well as amphiphilic polymers,[41] have also exhibited a similar change in the slope. In the case of simple surfactants one often observes a plateau while in the case of the polymers it appears as a break in the slope; this has been ascribed to a fluid–gel phase transition of the long-chain alkyl segments. As the composition of the HBPs is varied, the volume fraction occupied by the docosyl segment decreases and therefore the surface area at which the inflection occurs also decreases, as seen in the figure. The structural ramification of the inflection is also revealed by

dx.doi.org/10.1021/ma2022277 | *Macromolecules* 2012, 45, 2348–2358

examining the hysteresis in the $\pi-A$ isotherms; the break in the curve is not seen during the decompression segment (Figure S3). This suggests the presence of residual densely packed islands during the decompression, which disintegrates very slowly only at much lower surface pressures. The presence of such islands is also revealed in the interesting aggregate structures that are seen in the AFM images of monolayers transferred onto silicon substrates, as will be discussed later. One other difference in behavior of DOCOPEG-7030 is that there is a continuous change in the isotherm with the cycling, although in the other two samples the isotherms are perfectly reproducible (Figure S4). We presently do not completely understand the origin of this difference; the possibility of sample dissolution was, however, discounted by control experiments using a prewashed sample. Furthermore, of the three samples, DOCOPEG-7030 has the lowest solubility in water which further weakens this possible explanation.

Further evidence for the pseudocrystallization of the docosyl segments comes from quasi-static studies; here, at different points of the isotherm, the compression was stopped and the surface pressure was monitored as a function of time. A drop in surface pressure at constant area is a clear indication of densification. The results of such experiments are shown in Figure S5; the sawtoothed curve represents the drop in surface pressure seen at different points along the quasi-static isotherms. In order to obtain a relative estimate of the extent of this pressure drop, the quasi-static experiments were carried out at a single point (after the inflection point) during the compression (Figure 4); the

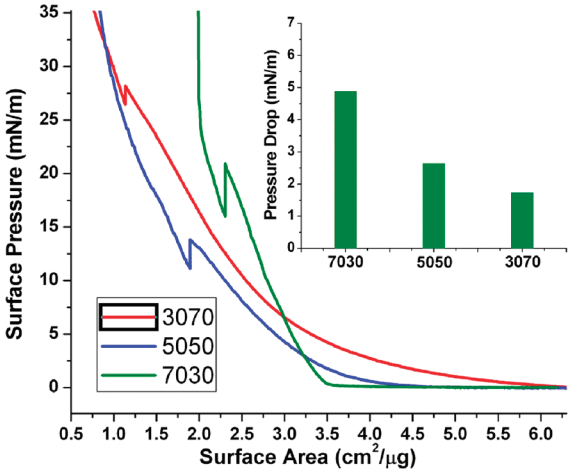


Figure 4. Langmuir isotherms of the three HBPs during a two-step quasi-static compression. The pressure drop (inset) is largest for DOCOPEG-7030, which has the highest docosyl content. The surface area has been normalized with respect to the weight of the polymer sample added to the interface.

duration for which the pressure drop was monitored was fixed (~10 min) to ensure that maximum drop had been attained (see Figures S6 and S7). The magnitude of this pressure drop would be proportional to the extent of densification; the inset in Figure 4 clearly reveals that this drop is highest in the case of DOCOPEG-7030, as expected, and it decreased with decrease in docosyl content. These experiments again clearly demonstrate these randomly amphiphilic HBPs do reconfigure at the air−water interface to generate Janus structure.

Atomic Force Microscopic Studies. In order to visualize the state of molecular aggregation during the compression at the air−water interface, the monolayer was transferred onto a hydrophilic (piranha-treated) silicon wafer; in each case this was done at two different surface pressures—one at a high value just before the collapse of monolayer and the other at a point immediately following the inflection in the isotherm. The AFM images of the three samples at the two different surface pressures are shown in Figure 5. At the higher surface pressure, the samples with higher PEG content (3070 and 5050) appear to form fairly uniform films; the average film thickness was estimated to be around ~3 nm, as measured by the depth of the holes in the film. On the other hand, DOCOPEG-7030 exhibited incomplete coverage, and the average film thickness was slightly lower at ~2.5 nm. Interestingly, at lower surface pressures, the two higher PEG samples exhibit uniform elongated bundles (height ~2.0−2.5 nm; single bundle width ~44 nm); this suggests that some type of clustering to form islands may be occurring on the air−water interface due to the interaction between the docosyl segments, and these islands get transferred (see Figure S8 for a schematic depiction of this process) onto the substrate during the formation of the LB films. Similar observations of dendritic aggregate structures at the air−water interface were earlier made in the case of simple surfactants; direct fluorescence microscopic observations of dye-stained samples revealed that such structures are already formed at the air−water interface.[42] Such structures were, however, not seen in the case of DOCOPEG-7030; this observation evades a simple explanation. It is also interesting to note that the lengths of elongated bundles are significantly smaller in DOCOPEG-3070, while the heights in both cases are similar and correspond roughly to the monolayer thickness.

Model for Interfacial Behavior of Amphiphilic HBPs. From the above observations it is clear that randomly clicked HBPs, bearing varying amounts of the hydrophilic (PEG) and hydrophobic (docosyl) segments at their molecular periphery, can exhibit Janus-type behavior by conformational reorganization of the hyperbranched polymer backbone. This leads to the typical amphiphilic behavior at the air−water interface, as evident from the Langmuir isotherms. However, to further understand the subtle nuances of the $\pi-A$ isotherms, one needs to take into account the relative volume fractions of the hydrophobic and hydrophilic segments; a simplistic model representation of the HBPs with three different compositions is shown in Scheme 2. Depending on the relative volume fractions of the docosyl, PEG, and the HB polymer backbone, several possible scenarios can arise during the compression at the air−water interface (Scheme 2): (a) the volume and projected surface area of the solvated PEG chains in the aqueous subphase is larger than that of the docosyl segments, (b) these are roughly of similar magnitude, and (c) the docosyl segments occupy larger volume that the PEG units. Thus, during the compression the first contact between individual macromolecules could occur either in the subphase between the PEG chains or above the interface between the docosyl units. In DOCOPEG-7030, it appears that the contact occurs above the air−water interface; a rapid rise in surface pressure is noted as the area is reduced. Beyond a certain surface pressure the docosyl chains appear to go into an ordered 2D lattice that leads to a more efficient packing, and hence a densification occurs; this causes a slight change in the slope during the compression and is also the reason for the considerable drop in surface pressure upon prolonged holding at a constant area, as seen in the quasi-static measurement. On the other hand, in both the other polymers, namely DOCOPEG-5050 and

dx.doi.org/10.1021/ma2022277 | Macromolecules 2012, 45, 2348−2358

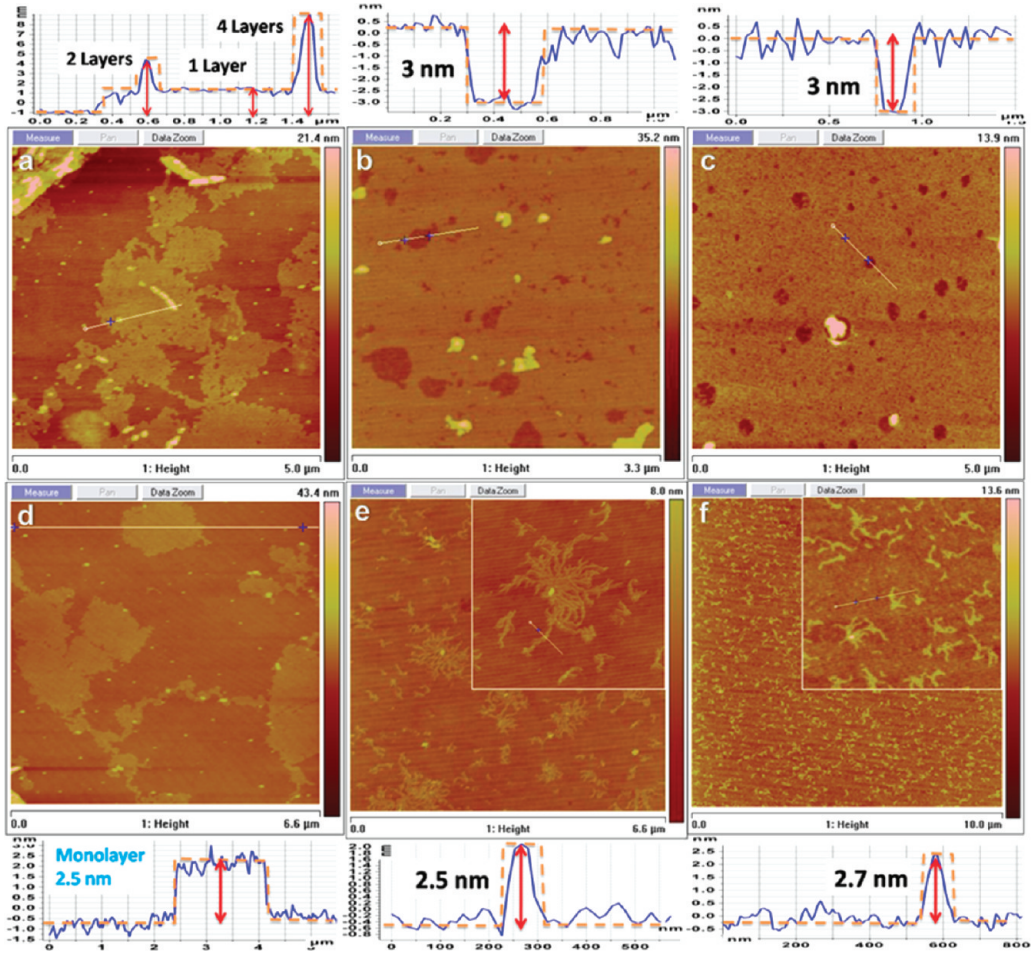
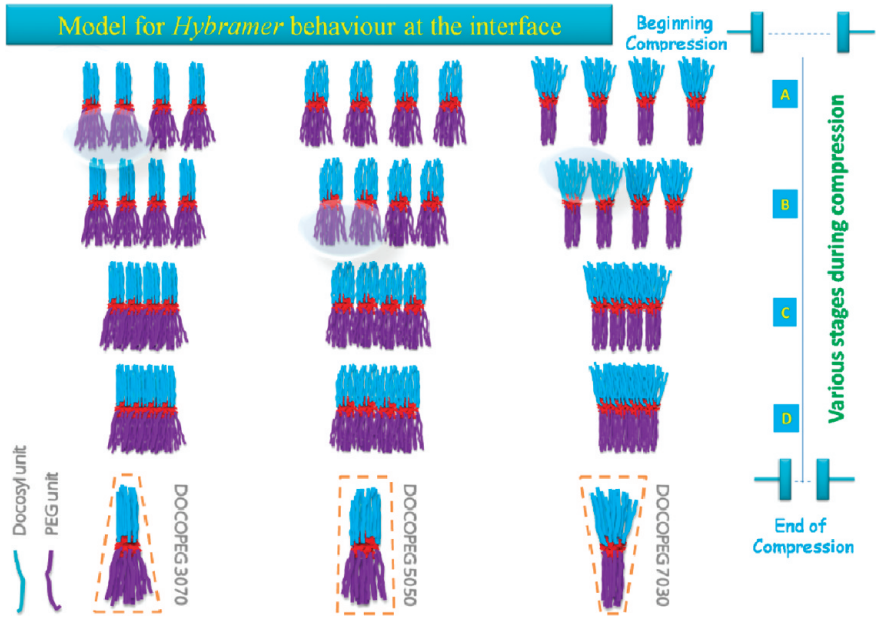


Figure 5. AFM images of monolayers transferred onto hydrophilic silicon wafer: images a, b, and c are a monolayer of DOCOPEG-7030, -5050, and -3070, respectively, transferred at a surface pressures of ~35 mN/m, while images d, e, and f represent those transferred at a surface pressure slightly above the respective inflection points for each sample.

Scheme 2. A Pictorial Representation of Possible Events during the Compression of the Amphiphilic Janus HBPs at the Air–Water Interface[a]



[a]The points of first contact between the chains for the polymers are highlighted.

dx.doi.org/10.1021/ma2022277 | *Macromolecules* 2012, 45, 2348–2358

DOCOPEG-3070, one notices that the change in surface pressure during compression is much more gradual and occurs at much larger surface areas. This is interpreted as being due to the fact that the first contact between molecules may be occurring in the aqueous subphase between the solvated PEG chains; the significantly higher conformational flexibility (*softer*) of these PEG chains leads to the significantly slower rise in the surface pressure at the early stages. Beyond a certain compression, the docosyl chains come in contact, and a similar densification due to pseudocrystallization causes the kink in the isotherm; the point at which this happens is evidently dependent on the relative volume fraction of the docosyl segments. Thus, the area at which this kink occurs would be roughly proportional to the relative volume fraction of the docosyl segments, as seen in the isotherms. A schematic depiction of these events at the air−water interface is presented in Scheme 2; further detailed calculations of the relative volumes of the hydrophobic and hydrophilic (solvated) segments would be required to strengthen this hypothesis.

SAXS Studies of Bulk Samples. DSC studies of the three HBPs clearly revealed that the docosyl segments self-segregate and crystallize independently. In order to gain a better understanding of the bulk morphology of these HBPs, we carried out small-angle X-ray scattering (SAXS) measurements. Prior to studying the amphiphilic systems, we examined the HBP that contains only docosyl chains at their periphery, as this would also help address the question of conformational adaptability of the hyperbranched core to permit the peripheral alkyl segments to segregate and organize in a crystalline lattice. Similar studies on peripherally alkylated PPI dendrimers were reported earlier by Meijer and co-workers;[43] they had suggested the formation of lamellar morphology wherein the dendrimers adopt a jellyfish-like conformation. The SAXS data of completely alkylated polymer (DOCO100) are shown in Figure 6. A typical lamellar pattern is evident, suggesting a

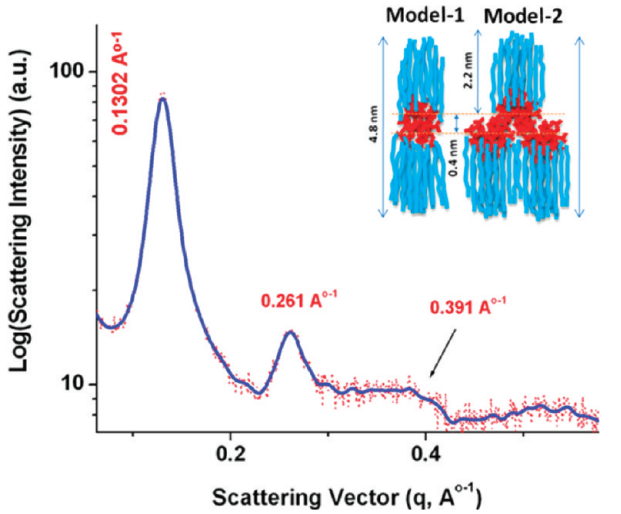


Figure 6. SAXS pattern observed for DOCO-100; the peak positions were in the ratio 1:2:3, confirming the lamellar morphology. A pictorial depiction of the two possible models is shown in the inset; the SAXS data do not permit the discrimination between these two possibilities.

lamellar thickness of 4.8 nm; based on the model by Meijer, this spacing could be explained by two possible molecular arrangements, as shown in the figure. The spacing obtained here matches reasonably well with those seen in alkylated poly(propyleneimine) dendrimer carrying 16 terminal alkyl units.[43] On the basis of an all-trans conformation of the docosyl unit, which would give a length of about 2.2 nm, a rough estimate of the expected lamellar thickness can be readily made; two of the docosyl segments within a lamella would roughly account for about 4.4 nm implying that the HBP backbone roughly adds only about 0.4 nm, suggesting a fairly compact and flattened conformation.

The SAXS patterns of the three amphiphilic HBPs clearly revealed their strong tendency to form lamellar morphologies; DOCOPEG-7030 and DOCOPEG-5050 exhibited a higher degree of ordering. The SAXS profiles of three polymers are shown in Figure 7; in all cases the polymers were melted and

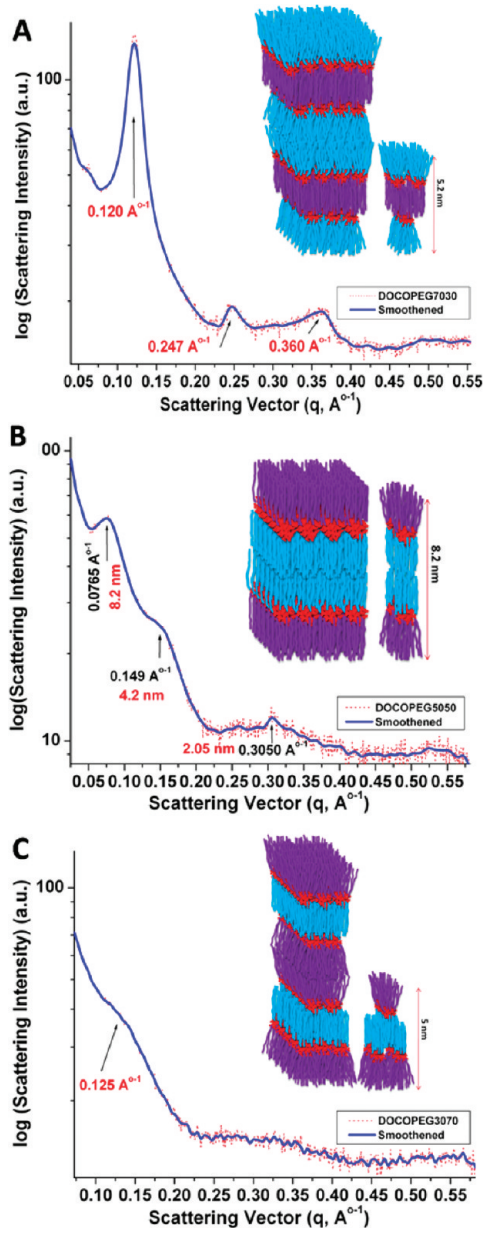


Figure 7. SAXS pattern observed in the case of DOCOPEG-7030 (A), DOCOPEG-5050 (B), and DOCOPEG-3070 (C). The peak positions are in the ratio 1:2:3, confirming the lamellar morphology.

short fibers were pulled and used for the experiments (the waxy samples readily permitted pulling short fibers from the melt by simply using a capilliary). In the two samples with higher docosyl content, several higher order scattering peaks are

dx.doi.org/10.1021/ma2022277 | *Macromolecules* 2012, 45, 2348−2358

clearly visible; this suggests the formation of highly ordered structures. Interestingly, the treatment of the samples with hot water lead to a substantial improvement in the sharpness of the scattering peaks, suggesting a solvent-induced annealing process; however, in this case the solvent probably improves the phase separation by diffusing into the PEG domains, leading to a more effective compaction of the paraffinic domains (Figure S9). While the fibers permitted easy handling of the samples, this could also induce some alignment; in order to check this we carried out the SAXS measurement of a solid sample of DOCOPEG-5050 (Figure S10), precipitated out of methanol. The pristine untreated sample also exhibited peaks at nearly identical positions, suggesting the formation of lamellar morphology even in as-precipitated samples; this confirmed the strong tendency for intrachain phase separation in these HBPs that is facilitated by the readaptation of the polymer backbone to permit the self-segregation of the docosyl and PEG chains.

The *d*-spacing retrieved from the SAXS data of the three HBPs reveal some very interesting insights into the possible molecular ordering in these systems; the lamellar spacing is about 8.2 nm in the case of DOCOPEG-5050, while it is only 5.2 and 5.0 nm in the case of DOCOPEG-7030 and DOCOPEG-3070, respectively. This suggests that when the relative volumes of the docosyl and PEG segments are comparable, as in DOCOPEG-5050, there is little interdigitation and the spacing reflects the dimension of the self-segregated HBP. While in the other cases wherein the relative volume fractions of either docosyl or PEG segments are significantly smaller, there is considerable interdigitation to achieve complete volume filling which causes the lamellar spacing to reduce considerably; a schematic depiction of this ordering is presented in Figure 7 (inset). In DOCOPEG-3070, the phase separation is less pronounced possibly because the added motivation for phase separation, which is the strong tendency for the docosyl segments to crystallize, is less pronounced in this case; this contention is also supported by the DSC data.

In a final experiment, SAXS studies were carried out as a function of sample temperature in the case of DOCOPEG-5050; the SAXS patterns of the sample below and above the melting point of the docosyl segments are shown in Figure 8.

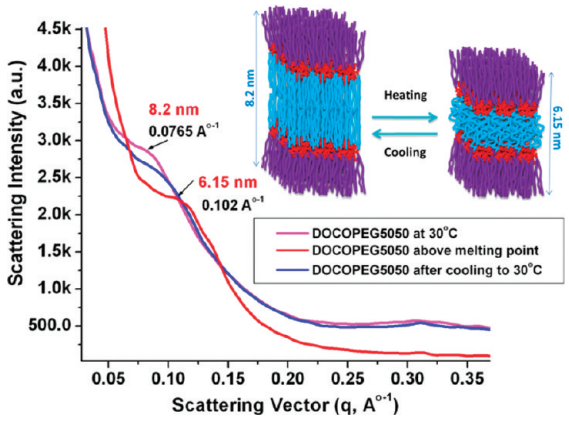


Figure 8. SAXS data of DOCOPEG-5050 sample reprecipitated from methanol. Effect of thermal cycling causes reversible melting and recrystallization of docosanol domains and which is reflected in the SAXS peak shift. The data after melting (red line) are *y*-scaled for clarity.

It is evident that there is a shift of the peak to higher *q* values at a temperature above the melting point of the docosyl segments; this is a clear indication of melting and consequent shrinking of the hydrocarbon domains causing the lamellar spacing to reduce to 6.15 nm. Interestingly, upon cooling the SAXS pattern reverts back to nearly its original form, indicating that recrystallization of the docosyl segments leads to near complete recovery of the original lamellar structure.

Self-Assembly of *Janus HBPs* in Solution. Just as traditional amphiphiles, these Janus HBPs may also form aggregates in solution under suitable conditions. In order to probe this, a chloroform solution of DOCOPEG-7030 was added into methanol, which is a selective solvent for PEG segments alone; this lead to a light-blue scattering solution indicating aggregate formation. AFM images of the aggregates revealed the existence of uniform flat disklike aggregates of height ~5 nm, which roughly corresponds to a bilayer (recall that the monolayer thickness was around 2.5 nm); the proposed structure of these disklike aggregates is shown in Figure 9, wherein the PEG units sandwich the central domains formed by the docosyl segments, thereby minimizing their exposure to the polar medium. In the case of DOCOPEG-5050, the aggregates do not form immediately; however, a light blue scattering solution is formed only upon prolonged aging (~2 weeks) (Figure S11). In the case of DOCOPEG-3070, however, no aggregates are formed evidently due to its higher solubility in a polar solvent, like methanol. The formation of these aggregates is clearly driven by the desire to minimize contact between the hydrophobic docosyl segments and the polar medium and is further stabilized by the tendency for the docosyl segments to crystallize. Apart from generating aggregates, we also attempted to prepare vesicles using the standard hydration protocol;[44] it was observed that DOCOPEG-3070 formed exclusively vesicles of fairly uniform size (Figure 10), while in the case of DOCOPEG-5050 both vesicles and disklike aggregates are seen. As evident from the AFM and TEM images, the height of the vesicles (deflated upon deposition) roughly corresponded to twice the bilayer thickness, as expected; similarly, a rough estimate of vesicle wall thickness from the TEM was found to be ~5 nm (Figure S12), which also agrees with bilayer thickness estimated from SAXS studies. DOCOPEG-7030 did not form vesicles; attempts to do so simply resulted in the formation of a macroscopic precipitate. On the basis of simple geometric arguments put forward by Israelachvili,[45] the relative volumes of the hydrophobic and hydrophilic segments would govern the nature of the aggregates formed; for vesicles the projected areas of these segments must be roughly equal. Hence, on the basis of our observations, it appears that DOCOPEG-3070 best meets this criteria followed by DOCOPEG-5050. Evidently, the interdigitation of the docosyl segment and the curvature of the vesicle membrane together appear to most favor the formation of vesicles in the case of DOCOPEG-3070.

One feature common to all the amphiphilic HBPs examined in this study is their highly polydisperse nature; it may, therefore, be pertinent to reflect on the possible influence of such broad molecular weight distribution on the properties that have been examined. Considering the structural adaptability of the relatively small hyperbranched backbone (typical DP ~ 20), it may be reasonable to view the Janus structure as a cluster of nonionic surfactants stitched together at the center by the HBP backbone. The polydispersity of the sample would primarily affect its DP value, and consequently it will amount to varying the number of surfactants bundled together to form the Janus structure. It may, therefore, be expected that most of the properties that have been presented in this study, namely melting

dx.doi.org/10.1021/ma2022277 | *Macromolecules* 2012, 45, 2348–2358

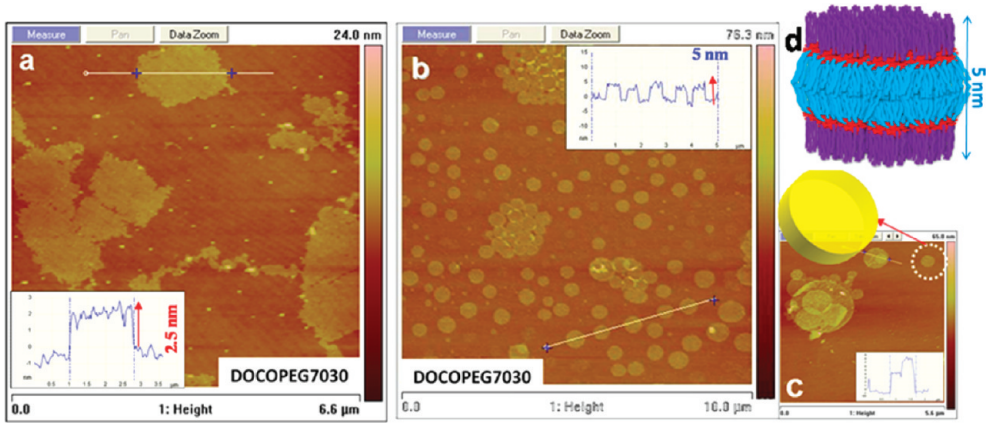


Figure 9. (a) AFM image of the monolayer from LB studies (DOCOPEG-7030); (b) self-assembled bilayer disk obtained from methanol (DOCOPEG); (c) multilayered deposition of the disks formed in methanol; and (d) proposed model structure of the bilayer.

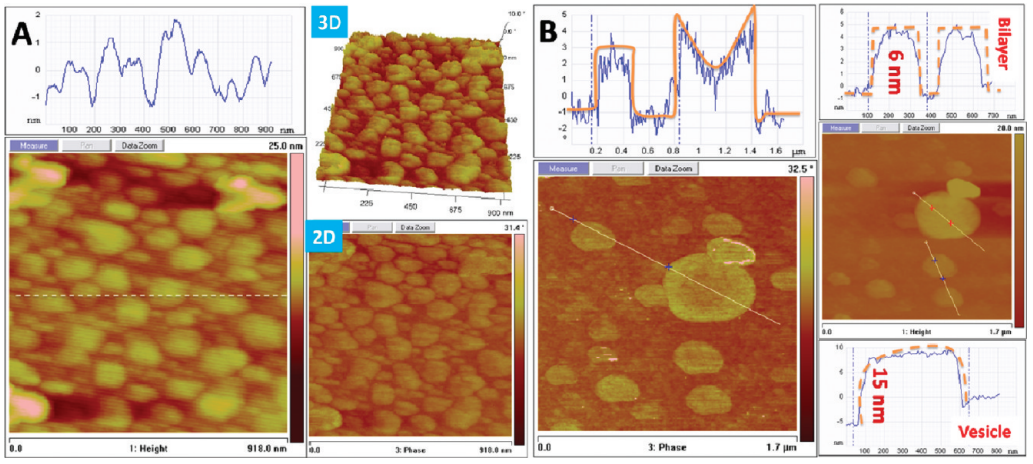


Figure 10. AFM images of vesicles obtained from (A) DOCOPEG-3070 and (B) DOCOPEG-5050. DOCOPEG-3070 forms exclusively vesicles while DOCOPEG-5050 forms vesicles (curved line profile) and bilayer disks (flat line profile). Since the center of vesicle is relatively flexible than the edges, line profile of the phase image shows a dip at the center of the vesicle, while the bilayer disks shows a flat line profile. (More TEM and AFM images are available in the Supporting Information, Figures S11 and S12.)

enthalpies, lamellar spacing, etc., are not likely to be affected by the polydispersity of the samples. Although this structural analogy may be strictly applicable only to DOCOPEG-5050, arguments along similar directions would suggest that the polydisperse nature of all these amphiphilic HBPs will have minimal effect on the properties examined.

In conclusion, we have shown that peripherally clickable hyperbranched polyesters can be readily functionalized using the azide−yne click reaction to generate a range of amphiphilic systems, wherein the relative mole fractions of the long-chain hydrocarbon segment (C22-docosyl) and PEG (PEG300-monomethyl ether) can be varied. Although the click reaction of the peripheral propargyl groups would lead to a random placement of the docosyl and PEG units, *we have demonstrated unequivocally that the hyperbranched polymer backbone reconfigures to permit the self-segregation of the docosyl and PEG segments to form Janus-type structures.* DSC studies clearly revealed a transition corresponding to the melting of the crystalline domains formed by the docosyl segments, the enthalpy of which varied in proportion to the docosyl content. Langmuir isotherms of these amphiphilic HBPs showed several interesting features that again confirmed the ability for these systems to reconfigure into Janus-type structures; importantly, we see evidence for densification due to pseudocrystallization of the docosyl segments above a threshold surface pressure; the extent of densification was again proportional to the volume fraction of the docosyl units. The nature of the aggregates formed upon precipitation of a dilute solution of the polymers into methanol was also examined. AFM studies clearly revealed the formation of disklike aggregates whose heights suggested the formation of bilayers containing docosyl segments in the center with PEG segments on either side; these segments, in a sense, encapsulate the hydrophobic domains from the polar solvent. DOCOPEG-3070 formed fairly uniform vesicles under standard hydration protocol, which was confirmed both by AFM and TEM studies. Finally, SAXS investigations clearly reveal the formation of lamellar morphology, providing further evidence for the self-segregation of the docosyl and PEG units. Interestingly, the lamellar spacing also suggests that molecular organization depends strongly on the relative volume fractions of the docosyl and PEG segments; a high level of interdigitation appears to occur when the volume fraction of either of these segments are small, causing a shrinkage in the lamellar spacing, but when their volumes are roughly similar, the spacing is significantly larger. *In summary, these investigations clearly demonstrate for the first time that structural perfection in placement of the hydrophilic and hydrophobic entities, such as those present in Janus Dendrimers, is not essential for eliciting*

dx.doi.org/10.1021/ma2022277 | *Macromolecules* 2012, 45, 2348−2358

Janus-type properties. The conformational flexibility of the hyperbranched polymers permits reconfiguration of the polymer backbone to generate Janus-type structures; if there is adequate thermodynamic motivation, which in the present systems are immiscibility of the docosyl and PEG segments and the strong tendency for the docosyl segments to crystallize, then the self-segregated structures formed could be further stabilized. These self-adapting Janus-type hyperbranched structures, which we have termed *Janus hybramers*, could serve as useful scaffolds for further derivatization and thereby permit strategic placement of a variety of function-performing entities with a controllable periodicity.

EXPERIMENTAL SECTION

Materials and Methods. All the solvents used for synthesis were purified prior to use following standard procedures. 5-Hydroxyisophthalic acid, 1,2-dibromoethylene, magnesium turnings, propargyl alcohol, dicyclohexylcarbodiimide (DCC), (*N*,*N*-dimethylamino)-pyridine (DMAP), PEG-350, monomethyl ether, docosonol, tosyl chloride, and sodium azide were purchased from Aldrich Chemical Co. The ^{1}H NMR spectra were recorded using a Bruker AV 400 MHz spectrometer in suitable deuterated solvents using tetramethylsilane (TMS) as internal reference. GPC measurements were carried out using Viscotek triple detector analyzer (TDA) model 300 system, which has a refractive index (RI), a differential viscometer (DV), and light scattering (LS) detectors connected in series. The separation was achieved using a series of two PL gel mixed bed columns (300 × 7.5 mm) operated at 30 °C using THF as the eluent. Molecular weights were determined using a universal calibration curve based on the data from the RI and DV detectors using narrow polystyrene standards. The thermal analysis was performed using a Mettler Toledo DSC instrument at a heating rate of 10 °C/min under a dry N_2 atmosphere. Typically, 2−3 mg of the sample was first heated to a temperature above its melting (to ensure that the sample flows and makes the contact with the pan) and then cooled; two subsequent heating and cooling runs were conducted to ensure reproducibility. Since the melting transitions primarily reflect the melting of the docosyl segments, the enthalpies associated with these transitions were normalized with respect to the weight percent of docosyl segments in the sample, which in turn was estimated from the copolymer composition using NMR.

Click Reaction. The parent hyperbranched polyester was synthesized following the procedure reported earlier.[29] 100 mg (0.36 mmol of peripheral propargyl units) of the parent HB polyester was dissolved in THF and purged with dry N_2 gas. 64.13 mg of docosyl azide (0.18 mmol) and the PEG azide 68.4 mg (0.18 mmol) were added into it. $CuSO_4 \cdot 5H_2O$ (4.66 mg, 0.018 mmol) and sodium ascorbate (7.17 mg, 0.0364 mmol) were separately dissolved in a small amount of water and added into the reaction mixture. After degassing, the mixture was stirred at 50 °C for 3 days. Later, the reaction mixture was concentrated and precipitated into methanol to get white polymer product (DOCOPEG-5050). Similarly, by varying the composition of docosyl azide and PEG-azide, DOCOPEG-7030 and DOCOPEG-3070 were also prepared. DOCOPEG-3070 was reprecipitated in petroleum ether. The yields of the polymers DOCOPEG-7030, DOCOPEG-5050, and DOCOPEG-3070 were 88, 80, and 75%, respectively. Although it was possible to retrieve the dissolved fraction by concentrating the solvent layer, it was not used for further study.

Langmuir−Blodgett (LB) and AFM Measurements. LB studies of DOCOPEG-*xy* were performed using NIMA 1232D1D2 Langmuir−Blodgett trough. Polymer solutions (0.5 mg/mL) were prepared in $CHCl_3$ (HPLC grade), 150 μL of which was spread on the trough. It was found that 150 μL at 0.5 mg/mL of the polymer sample was optimum for generating good monolayer; at higher concentrations aggregation at the interface was seen to occur. Compression experiments were performed at a rate of 50 cm^2/min, and the isocycles were recorded at a rate of 300 cm^2/min. The plots are normalized with respect to the weight of polymer sample delivered on to the air−water interface. The rate of compression for quasi-static compression experiment was 100 cm^2/min. Compressed monolayer was transferred onto a solid substrate at a rate of 1 mm/min. Piranha-treated silicon wafer was used as solid substrate. Quasi-static compression experiments were performed at steps of 20 cm^2 (compression) for DOCOPEG-5050 and at 10 cm^2 for other two samples. The waiting time was 3 min for each step in the quasi-static experiments during the multistep QSC experiment (Figure S5). In order to measure the total pressure drop, the monolayer was compressed to an area which corresponds to largest pressure drop point during the multistep QSC curve for each sample. For example, DOCOPEG-5050 was compressed to an area 140 cm^2; this area corresponds to the point of largest pressure drop (0.96 mN/m) in the multistep QSC curve. Waiting time for the single step compression static event was 560 s for DOCOPEG-7030 and 5050, but a 600 s wait time was used for DOCOPEG-3070. A control water isotherm was recorded, and no significant surface pressure was noticed until the barrier is fully closed; such a flat baseline was ensured before beginning the experiment. AFM measurements were performed using MultiMode SPM (Digital Instruments, Santa Barbara, CA) equipped with NanoScope IV A controller. FESP (Veeco) tips of force constant 1−5 N/m and resonance frequency of 75 kHz were used for imaging the sample; measurements were conducted in the tapping mode. Images were analyzed using the software provided with the instrument.

Small-Angle X-ray Scattering (SAXS). SAXS experiments were performed in Hecus S3Micro system with X-ray point-focusing optics (from Xenocs, Grenoble) equipped with PSD using wavelength 1.542 Å. Three different SAXS experiments were performed. Measurements were performed by filling the sample into a small capillary. SAXS pattern of polymer samples (solid) were recorded without any thermal treatment as well as after melting and recrystallization. The scattering data were also recorded for the melt. Aligning of polymer sample was performed in the following way: the samples were taken in a small glass vial and dipped in a water bath maintained above the melting point of the polymer. A glass needle was plunged into the melt and pulled out slowly to draw small fibers of the polymer; as the fiber cooled it solidified. These fibers were then placed on the surface of water (Millipore) maintained at 40−50 °C for about 10−20 min. The fibers were then dried and filled into capillary tubes for recording the SAXS. The scattering was accumulated for 2−3 h for each sample. Completely alkylated derivative of the hybramer (DOCO-100) was similarly aligned and directly used without treatment with water.

Preparation of Vesicle and Disklike Micelles. Vesicles were prepared following standard procedures.[44] 1 mL of the DOCOPEG-*xy* solution in chloroform (1 mg/mL) was taken in a curved bottom vial, and solvent was evaporated slowly under nitrogen purge. The thin film formed at the bottom was dried under vacuum for 2 h. 3−5 mL of distilled water was added and kept overnight at 4 °C for hydration. Then the sample was sonicated for 10 min at 80 °C and immediately cooled down by dipping into ice-cold water. After 5 min, the sample was vortexed for 10 min; the heating−cooling−sonication cycle was repeated several times until a clear solution resulted. 50−100 μL of the sample solution was cast onto a clean piranha-treated silicon wafer, and AFM images were recorded. Flat disklike aggregates were prepared by adding 100 μL of the DOCOPEG-*xy* solution in chloroform (0.5 mg/mL) into methanol (10 mL) with stirring; stirring was continued for an additional 15 min, after which 50−100 μL of the sample solution was cast onto a clean piranha-treated silicon wafer.

ASSOCIATED CONTENT

Supporting Information

Detailed experimental procedures, NMR spectra, GPC curves, Langmuir isotherm cycles, SAXS data, AFM images, and TEM images. This material is available free of charge via the Internet at http://pubs.acs.org.

AUTHOR INFORMATION

Corresponding Author

*E-mail: raman@ipc.iisc.ernet.in.

Notes

The authors declare no competing financial interest.

■ ACKNOWLEDGMENTS

We thank V. A. Raghunathan from Raman Research Institute for the SAXS measurements and S. Sampath for the monolayer studies; many valuable discussions with both of them are gratefully acknowledged. We also thank S. Umapathy for his valuable suggestions and discussions. S.R. thanks the Department of Atomic Energy for the ORI-Award for the period 2006−2011, and A.Z.S. thanks CSIR for a fellowship.

■ REFERENCES

(1) Cohen, J. *Science* **1995**, *267*, 1265−1266.
(2) Haluska, C. K.; Riske, K. A.; Artzner, V. M.; Lehn, J. M.; Lipowsky, R.; Dimova, R. *Proc. Natl. Acad. Sci. U. S. A.* **2006**, *103*, 15841−15846.
(3) Shimizu, T.; Masuda, M.; Minamikawa, H. *Chem. Rev.* **2005**, *105*, 1401−1443.
(4) Kim, H. C.; Park, S. M.; Hinsberg, W. D. *Chem. Rev.* **2010**, *110*, 146−177.
(5) Zeng, F.; Zimmerman, S. C. *Chem. Rev.* **1997**, *97*, 1681−1712.
(6) Zhou, Y.; Yan, D. *Chem. Commun.* **2009**, 1172−1188.
(7) Rosen, B. M.; Wilson, C. J.; Wilson, D. A.; Peterca, M.; Imam, M. R.; Percec, V. *Chem. Rev.* **2009**, *109*, 6275−6540.
(8) Percec, V.; Wilson, D. A.; Leowanawat, P.; Wilson, C. J.; Hughes, A. D.; Kaucher, M. S.; Hammer, D. A.; Levine, D. H.; Kim, A. J.; Bates, F. S.; Davis, K. P.; Lodge, T. P.; Klein, M. L.; DeVane, R. H.; Aqad, E.; Rosen, B. M.; Argintaru, A. O.; Sienkowska, M. J.; Rissanen, K.; Nummelin, S.; Ropponen, J. *Science* **2010**, *328*, 1009−1014.
(9) Erhardt, R.; Bo1ker, A.; Zettl, H.; Kaya, H.; Pyckhout-Hintzen, W.; Krausch, G.; Abetz, V.; Muller, A. H. E. *Macromolecules* **2001**, *34*, 1069−1075.
(10) Xu, H.; Erhardt, R.; Abetz, V.; Muller, A. H. E.; Goedel, W. A. *Langmuir* **2001**, *17*, 6787−6793.
(11) Erhardt, R.; Zhang, M.; Boker, A.; Zettl, H.; Abetz, C.; Frederik, P.; Krausch, G.; Abetz, V.; Muller, A. H. E. *J. Am. Chem. Soc.* **2003**, *125*, 3260−3267.
(12) Walther, A.; Andre, X.; Drechsler, M.; Abetz, V.; Muller, A. H. E. *J. Am. Chem. Soc.* **2007**, *129*, 6187−6198.
(13) Walther, A.; Hoffmann, M.; Muller, A. H. E. *Angew. Chem., Int. Ed.* **2008**, *47*, 711−714.
(14) Walther, A.; Matussek, K.; Muller, A. H. E. *ACS Nano* **2008**, *2*, 1167−1178.
(15) Nierengarten, J. F.; Eckert, J. F.; Rio, Y.; Carreon, M. P.; Gallani, J. L.; Guillon, D. *J. Am. Chem. Soc.* **2001**, *123*, 9743−9748.
(16) Hawker, C. J.; Wooley, K. L.; Frechet, J. M. J. *J. Chem. Soc., Perkin Trans. 1* **1993**, *12*, 1287−1297.
(17) Meyers, S. R.; Juhn, F. S.; Griset, A. P.; Luman, N. R.; Grinstaff, M. W. *J. Am. Chem. Soc.* **2008**, *130*, 14444−14445.
(18) Antoni, P.; Hed, Y.; Nordberg, A.; Nystrom, D.; Holst, H. V.; Hult, A.; Malkoch, M. *Angew. Chem., Int. Ed.* **2009**, *48*, 2126−2130.
(19) Feng, X.; Taton, D.; Ibarboure, E.; Chaikof, E. L.; Gnanou, Y. *J. Am. Chem. Soc.* **2008**, *130*, 11662−11676.
(20) Yan, D.; Zhou, Y.; Hou, J. *Science* **2004**, *303*, 65−67. Zhou, Y.; Yan, D. *Chem. Commun.* **2009**, *10*, 1172−1188.
(21) Sunder, A.; Krämer, M.; Hanselmann, R.; Mülhaupt, R.; Frey, H. *Angew. Chem., Int. Ed.* **1999**, *38*, 3552−3555.
(22) Sunder, A.; Hanselmann, R.; Frey, H.; Mülhaupt, R. *Macromolecules* **1999**, *32*, 4240−4246.
(23) Saha, A.; Ramakrishnan, S. *J. Polym. Sci., Part A: Polym. Chem.* **2009**, *47*, 80−91.
(24) Saha, A.; Ramakrishnan, S. *Macromolecules* **2008**, *41*, 5658−5664.
(25) Ornatska, M.; Peleshanko, S.; Genson, K. L.; Rybak, B.; Bergman, K. N.; Tsukruk, V. V. *J. Am. Chem. Soc.* **2004**, *126*, 9675−9684.
(26) Ornatska, M.; Bergman, K. N.; Goodman, M.; Peleshanko, S.; Shevchenko, V. V.; Tsukruk, V. V. *Polymer* **2006**, *47*, 8137−8146.
(27) Aathimanikandan, S. V.; Savariar, E. N.; Thayumanavan, S. *J. Am. Chem. Soc.* **2005**, *127*, 14922−14929.
(28) Chute, J. A.; Hawker, C. J.; Rasmussen, K. Ø.; Welch, P. M. *Macromolecules* **2011**, *44*, 1046−1052.
(29) Ramkumar, S. G.; Rose, K. A. A.; Ramakrishnan, S. *J. Polym. Sci., Part A: Polym. Chem.* **2010**, *48*, 3200−3208.
(30) Feast, W. J.; Stainton, N. M. *J. Mater. Chem.* **1995**, *5*, 405−411.
(31) Rostovtsev, V. V.; Green, L. G.; Fokin, V. V.; Sharpless, K. B. *Angew. Chem., Int. Ed.* **2002**, *41*, 2596−2599.
(32) The effect of an aromatic solvent, like C_6D_6, on the spectral resolution in hyperbranched polymers was discussed earlier; see: Behera, G. C.; Ramakrishnan, S. *J. Polym. Sci., Part A: Polym. Chem.* **2007**, *45*, 1474−1480.
(33) Sunder, A.; Bauer, T.; Mülhaupt, R.; Frey, H. *Macromolecules* **2000**, *33*, 1330−1337.
(34) Dirand, M.; Bouroukba, M.; Briard, A. J.; Chevallier, V.; Petitjean, D.; Corriou, J. P. *J. Chem. Thermodyn.* **2002**, *34*, 1255−1277.
(35) Peleshanko, S.; Gunawidjaja, R.; Jeong, J.; Shevchenko, V. V.; Tsukruk, V. V. *Langmuir* **2004**, *20*, 9423−9427.
(36) Busse, K.; Peetla, C.; Kressler, J. *Langmuir* **2007**, *23*, 6975−6982.
(37) Sweet, Y. S.; Hedstrand, D. M.; Spinder, R.; Tomalia, D. A. *J. Mater. Chem.* **1997**, *7*, 1199−1205.
(38) Ornatska, M.; Bergman, K. N.; Rybak, B.; Peleshanko, S.; Tsukruk, V. V. *Angew. Chem., Int. Ed.* **2004**, *43*, 5246−5249.
(39) Miller, A.; Mohwald, H. *J. Chem. Phys.* **1987**, *86*, 4258−4265.
(40) Hossain, M. M.; Iimura, K.; Yoshida, M.; Kato, T. *J. Colloid Interface Sci.* **2011**, *353*, 220−224.
(41) Kasai, W.; Kuga, S.; Magoshi, J.; Kondo, T. *Langmuir* **2005**, *21*, 2323−2329.
(42) Hussain, S. A.; Chakraborty, S.; Bhattacharjee, D. *Indian J. Phys.* **2010**, *84*, 729−733.
(43) Schenning, A. P. H. J.; Roman, C. E.; Weener, J. W.; Baars, M. W. P. L.; Gaast, S. J. V.; Meijer, E. W. *J. Am. Chem. Soc.* **1998**, *120*, 8199−8208.
(44) Bangham, A. D. *Annu. Rev. Biochem.* **1972**, *41*, 753−776.
(45) Israelachvili, J. N.; Mitchell, D. J.; Ninham, B. W. *J. Chem. Soc., Faraday Trans. 2* **1976**, *72*, 1525−1568.

Macromolecules

Article

pubs.acs.org/Macromolecules

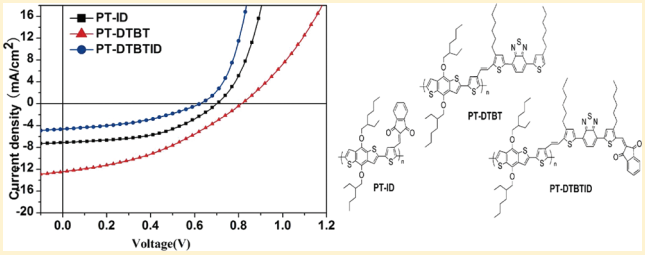
Synthesis and Photovoltaic Properties of Copolymers Based on Benzo[1,2-*b*:4,5-*b*′]dithiophene and Thiophene with Different Conjugated Side Groups

Zhaojie Gu,[†] Peng Tang,[†] Bin Zhao,[†] Hao Luo,[‡] Xia Guo,[‡] Huajie Chen,[‡] Gui Yu,[‡] Xinping Liu,[†] Ping Shen,[†] and Songting Tan*[,†]

[†]College of Chemistry, Key Laboratory of Polymeric Materials & Application Technology, and Key Laboratory of Advanced Functional Polymeric Materials of the College of Hunan Province, Xiangtan University, Xiangtan 411105, P. R. China

[‡]Beijing National Laboratory for Molecular Science, Institute of Chemistry, Chinese Academy of Sciences, Beijing 100190, P. R. China

ABSTRACT: Three novel copolymers (**PT-ID**, **PT-DTBT**, and **PT-DTBTID**) of benzo[1,2-*b*:4,5-*b*′]dithiophene and thiophene with different conjugated side groups (1,3-indanedione (**ID**), 4,7-dithien-5-yl-2,1,3-benzodiathiazole (**DTBT**), and **DTBT-ID**) were synthesized and developed for polymer solar cell applications. The effects of the different conjugated side groups on the thermal, photophysical, electrochemical and photovoltaic properties of these copolymers were investigated. As the length of the conjugated side groups increased, the absorption of the UV−vis region in solution was red-shifted. By changing the different side groups, the energy levels and band gaps of the resulted copolymers were effectively tuned. The three copolymers exhibit deep HOMO energy level and relatively high open-circuit voltage (V_{oc}). Bulk heterojunction solar cells with these copolymers as electron donors and (6,6)-phenyl-C_{61}-butyric acid methyl ester ($PC_{61}BM$) as an electron acceptor exhibit power conversion efficiencies of 2.48%, 4.18% and 1.16% for **PT-ID**, **PT-DTBT**, and **PT-DTBTID**, respectively.



INTRODUCTION

Polymer solar cells (PSCs) have attracted considerable attention in recent years due to their potential for low cost, lightweight, and good compatibility with the roll-to-roll process for making flexible large area devices.[1−3] So far, the most successful polymer solar cells are bulk heterojunction (BHJ) devices,[4−7] which use a phase separated blend of organic electron donor and acceptor components, where the conjugated polymer is often used as the donor and the fullerene derivative is used as the acceptor.[8] It has been realized that an ideal polymer donor in PSCs should exhibit broad absorption with high absorption coefficient in the visible region, high hole mobility, suitable energy level matching with the fullerene acceptor, and appropriate compatibility with the fullerene acceptor to form nanoscale bicontinuous interpenetrating network.[9] Optimizing the properties of the polymer donor will offer higher short-circuit current density (J_{sc}), open-circuit voltage (V_{oc}), fill-factor (FF), and power conversion efficiency (PCE) of the PSCs.

One feasible approach toward broadening the absorption spectrum and tuning the energy levels is to design alternating donor−acceptor (D−A) copolymers, in which the hybridization of the highest occupied molecular orbital (HOMO) located on the donor moiety with the lowest unoccupied molecular orbital (LUMO) located on the acceptor moiety provides a means of narrowing the band gap and tuning the HOMO and LUMO energy levels of the conjugated polymers.[10,11] Among these main chain D−A copolymers, it has been demonstrated that benzo(1,2-*b*:4,5-*b*′)dithiophene (BDT) is the most potential and effective electron-rich donor unit.[12] In the past two years, a series of new D−A low band gap polymers based on BDT have been reported. For example, the solar cells based on a BDT copolymer PBDTTT have achieved a series of high PCE values in the range of 5−7%.[9,13] Although main chain D−A copolymers have been witnessed great success for achieving high performance PSCs, they may suffer from lower hole mobility due to the influence of the acceptor units on the polymer main chain.[14]

A new family of polymers with conjugated side groups or side chains has been developed by several research groups, including ours.[8,15,16] This type of polymers features high hole mobility benefiting from the overlapping of the conjugated side chain interactions with the conjugated main chains, and broad absorption spectra deriving from both the main chains and the conjugated side chains, thus demonstrated prominent device performances in PSCs.[15] Here, we designed and synthesized three copolymers **PT-ID**, **PT-DTBT**, **PT-DTBTID** (as shown in Figure 1) based on BDT and thiophene with different

Received: December 8, 2011
Revised: February 20, 2012
Published: March 1, 2012

 © 2012 American Chemical Society dx.doi.org/10.1021/ma202399n | *Macromolecules* 2012, 45, 2359−2366

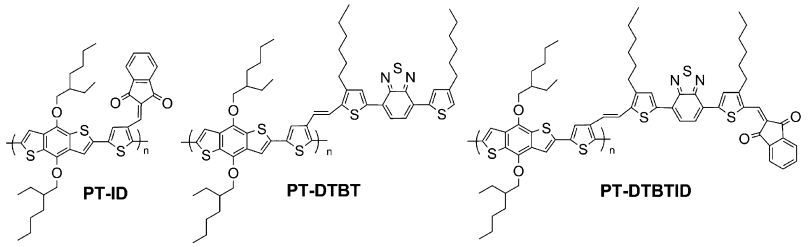
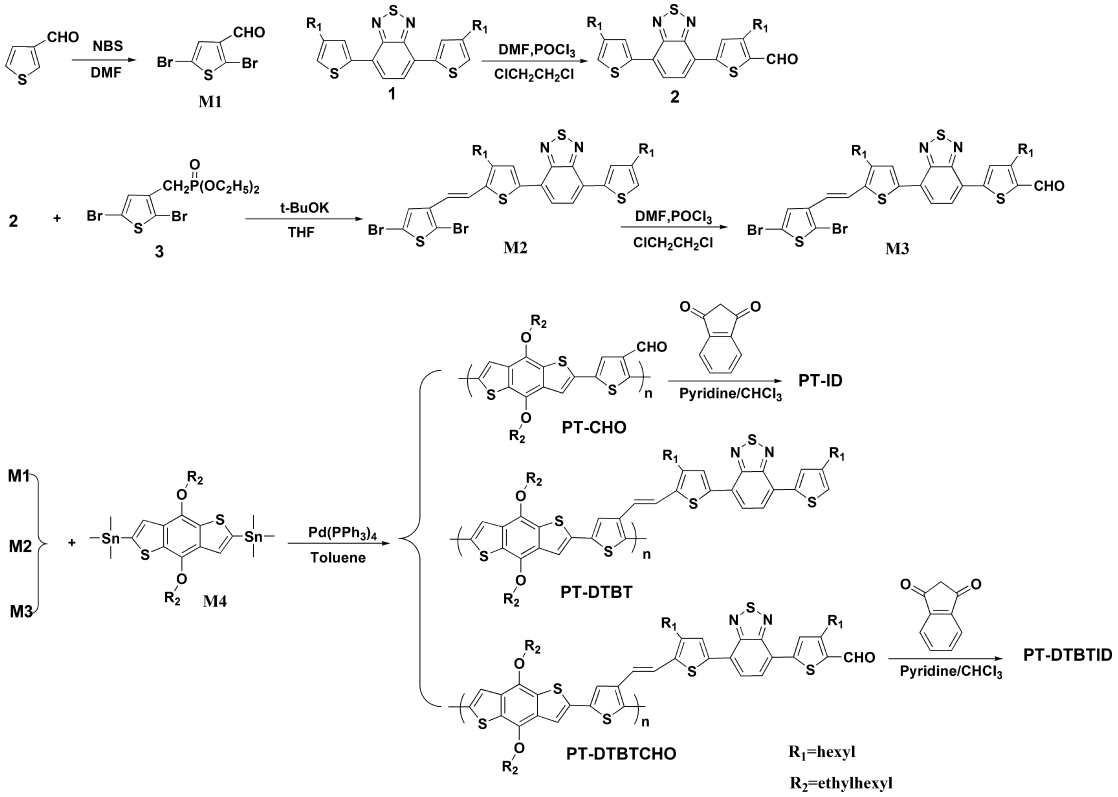


Figure 1. Molecular structures of **PT-ID**, **PT-DTBT**, and **PT-DTBTID**.

Scheme 1. Synthetic Routes of the Monomers and the Corresponding Copolymers



conjugated side groups. In order to broaden the absorption spectra of the π-conjugated polymers, 1,3-indanedione (ID) and 4,7-dithien-5-yl-2,1,3-benzodiathiazole (DTBT) as electron-deficient units are to be introduced into side chains of **PT-ID** and **PT-DTBT**, respectively. Furthermore, a long side chain (DTBT-ID) composed of DTBT and ID is introduced to form the polymer **PT-DTBTID**. These conjugated side groups attached to the main chains via vinylene groups. The vinylene linkage serves to enhance coplanarity of the polymer backbone and extend the π-conjugation by further eliminating torsional strains between the main chain and electron-deficient side groups, leading to a lower optical band gap and tunable frontier molecular orbital energy levels. The effects of the conjugated side groups on the thermal, photophysical, electrochemical, and photovoltaic properties of the copolymers were investigated in detail.

RESULTS AND DISCUSSION

Synthesis and Chemical Characterization. Synthetic routes of the monomers and copolymers are shown in Scheme 1. The crucial monomer **M4** was synthesized by the reported method.[17] The monomer **M1** was obtained by bromination of thiophene-3-carbaldehyde with NBS under argon atmosphere. The important intermediate, monomer **M2**, was synthesized from compounds **2** and **3** in a moderate yield (65%) according to the Wittig–Horner reaction, and purified using a silica gel column with an ether/dichloromethane (1/1, v:v) eluent. The aldehyde-functionalized monomer **M3** was prepared by Vilsmeier–Haack formylation of **M2** under a mild condition.[18] The precursor polymers PT-CHO and PT-DTBTCHO were synthesized by the Stille coupling reaction. Two target copolymers, **PT-ID** and **PT-DTBTID**, were obtained by the Knoevenagel condensation between the aldehyde-functionalized precursor polymers (PT-CHO and PT-DTBTCHO) and 1,3-indanedione in yields of 49% and 46%, respectively. The other target copolymer **PT-DTBT** was directly synthesized by the Stille coupling reaction between the monomer **M2** and **M4**. The chemical structures of the copolymers were verified by ^{1}H NMR and elemental analysis. The complete disappearance of the aldehyde proton signals at 10.19 for PT-CHO and 10.10 ppm[10,19] for PT-DTBTCHO, and the appearance of olefinic proton signals at 8.75 for **PT-ID** and 8.72 ppm for **PT-DTBTID** confirm the efficient conversion reaction of the aldehyde and the successful

dx.doi.org/10.1021/ma202399n | *Macromolecules* 2012, 45, 2359–2366

preparation of target copolymers. **PT-ID**, **PT-DTBT**, and **PT-DTBTID** exhibit good solubility in common organic solvents such as $CHCl_3$, THF, CH_2Cl_2 and chlorobenzene at room temperature. Table 1 summarized the polymerization results

Table 1. Molecular Weights and Thermal Properties of Copolymers

copolymers	yield (%)	M_n (kg mol^{-1})[a]	PDI	T_g (°C)[b]	T_d (°C)[c]
PT-ID	49	12.1	2.2	160	321
PT-DTBT	78	20.2	2.6	155	368
PT-DTBTID	46	12.5	1.8	165	301

[a]Determined by GPC in THF based on polystyrene standards. [b]Determined by DSC at scan rate of 20 °C/min under nitrogen. [c]Decomposition temperature, determined by TGA in nitrogen, based on 5% weight loss.

and thermal properties of the copolymers. The number-average molecular weight (M_n) of PT-CHO and PT-DTBTCHO are 11.6 and 11.4 kg mol^{-1} with polydispersity index (PDI) of 1.66 and 2.00, respectively. The M_n of the target copolymers **PT-ID** (12.1 kg mol^{-1}) and **PT-DTBTID** (12.5 kg mol^{-1}) show a slight increase than those of PT-CHO and PT-DTBTCHO due to the reaction between of 1,3-indanedione and aldehyde group.

Thermal Properties. The thermal properties of the target copolymers were obtained by thermogravimetric analysis (TGA) and differential scanning calorimetry (DSC) measurements. As shown in Figure 2 and Table 1, the TGA curves

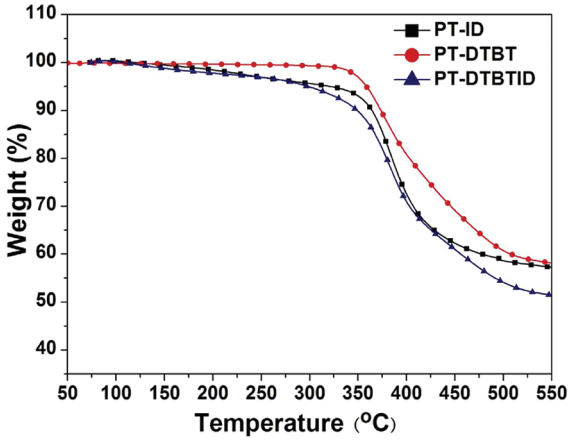


Figure 2. TGA curves of copolymers at scan rate of 20 °C/min under nitrogen atmosphere.

reveal that the degradation temperatures (T_d) of 5% weight loss of **PT-ID**, **PT-DTBT**, and **PT-DTBTID**, are 321, 368, and 301 °C, respectively. And the glass transition temperatures (T_g) are 160, 155, and 165 °C for **PT-ID**, **PT-DTBT**, and **PT-DTBTID**, respectively (Figure 3). We have also measured the DSC curves at different scan rates, and no crystallization or melting peaks are observed upon further heating beyond the T_g. The results indicate that these copolymers are amorphous. It is clear that the introduction of 1,3-indanedione group in the side chains of the conjugated polymers improves the glass transition temperature. The good thermal stability of the copolymers retards the deformation of the polymer morphology and the degradation of the active layer at elevated temperatures, which are desirable for polymers in PSCs applications.[20]

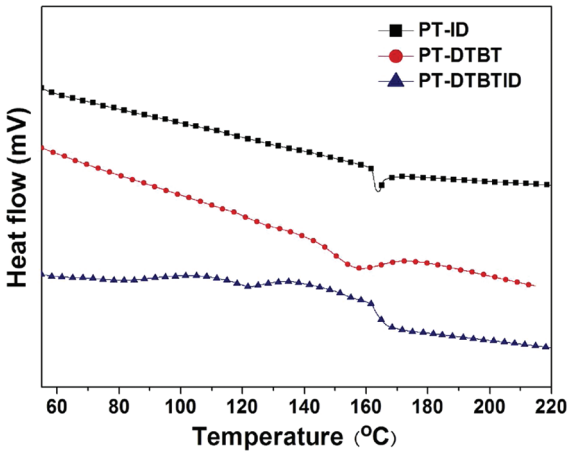


Figure 3. DSC curves of copolymers collected at a scan rate of 20 °C/min.

Photophysical Properties. The photophysical properties of the copolymers were investigated by UV−vis and fluorescence spectroscopy. The correlative data of the copolymers are summarized in Table 2. Figure 4 gives the UV−vis absorption spectra of **PT-ID**, **PT-DTBT**, and **PT-DTBTID** in diluted $CHCl_3$ solution. All copolymers show two distinct absorption bands. The first absorption bands with the absorption maxima ($\lambda_{s,max}$) at 423 nm for **PT-ID**, 390 nm for **PT-DTBT** and 387 nm for **PT-DTBTID** can be identified with a delocalized excitonic $\pi-\pi^*$ transition and the second absorption bands of them with $\lambda_{s,max}$ at 565, 504, and 526 nm, respectively, can be attributed to a localized transition between donor−acceptor charge transfer states.[21,22] **PT-DTBTID** exhibits the broader absorption which derived from the ICT interaction between the main chain and the conjugated side chains.[23] Obviously, the ICT interactions of the **PT-DTBTID** are progressively enhanced due to the increase of the electron affinity of the DTBTID group.[10] In comparison with the absorption spectra of the polymer solutions, the absorption spectra of the films are broadened and the peaks are red-shifted. This phenomenon results from the enhanced interchain interaction in the solid films, which is probably related to the increased extent of $\pi-\pi$ stacking of the backbones and increased polarizability of the film, or both.[24−26] The optical band gaps (E_g^{opt}) of **PT-ID**, **PT-DTBT** and **PT-DTBTID** are 1.75, 1.92, and 1.66 eV, respectively, calculated from the onset of the film absorptions.

The photoluminescence (PL) spectra of copolymers in the diluted $CHCl_3$ solution are shown in Figure 5. The copolymers are excited at the wavelength corresponding to the two $\lambda_{s,max}$. For example, **PT-DTBT** exhibits the same PL spectra when it is excited at 390 and 504 nm, respectively, which indicates that there is a thorough intramolecular energy transfer of the excitons from the conjugated side chains to the main chains. This phenomenon ensures that all photons absorbed by the copolymers are useful for the photovoltaic conversion.[27] In $CHCl_3$ solution, **PT-ID** exhibits a maximum emission peak ($\lambda_{f,max}$) at 663 nm. With **DTBT** and **DTBTID** as the conjugated side groups, the $\lambda_{f,max}$ of **PT-DTBT** (682 nm) and **PT-DTBTID** (705 nm) are red-shifted by 19 and 42 nm, respectively, compared with that of **PT-ID**. All the results clearly indicate that the photophysical properties of these copolymers could be tuned by changing conjugated side groups.

Electrochemical Properties. The highest occupied molecular orbital (HOMO) and lowest unoccupied molecular

dx.doi.org/10.1021/ma202399n | Macromolecules 2012, 45, 2359−2366

Table 2. Optical and Electrochemical Properties of the Three Copolymers

	solution $\lambda_{s,max}$ (nm)[a]		abs (nm)					
copolymers	abs	PL	film $\lambda_{f,max}$(nm)	film λ_{edge}(nm)	E_g^{opt} (eV)[b]	HOMO (eV)	LUMO (eV)	E_g^{ec} (eV)
PT-ID	423	663	443	707	1.75	−5.22	−3.40	1.82
PT-DTBT	504	682	517	644	1.92	−5.44	−3.44	2.00
PT-DTBTID	526	705	534	748	1.66	−5.25	−3.54	1.71

[a]Measured in chloroform solution. [b]Band gap estimated from the optical absorption band edge of the films.

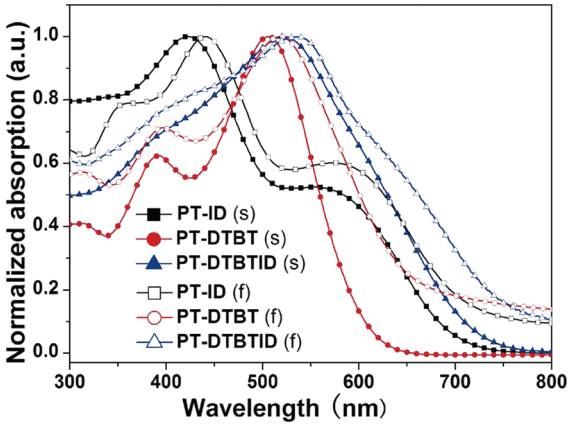


Figure 4. UV−vis absorption spectra of the copolymers in chloroform solutions and in the film states.

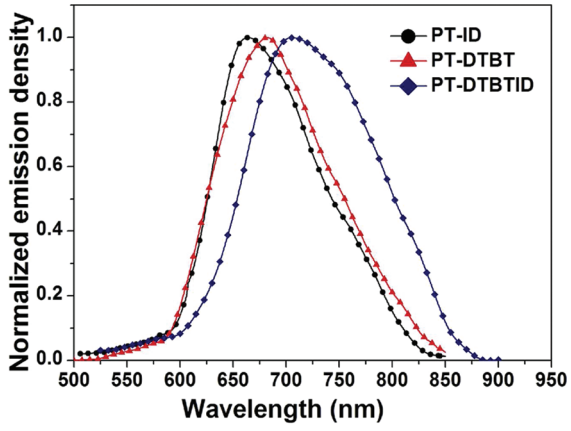


Figure 5. Photoluminescence spectra of copolymers in the $CHCl_3$ solution.

orbital (LUMO) energy levels of the conjugated polymers are important parameters in the design of optoelectronic devices, and they can be estimated from the onset oxidation and reduction potentials of cyclic voltammogram (CV).[28] Figure 6 shows the CV curves of the three copolymers and that of ferrocene for potential calibration. The redox potential of ferrocene is 0.51 V vs SCE. On the basis of 4.8 eV below vacuum for the energy level of Fc/Fc^+, the HOMO and LUMO energy levels of as well as the electrochemical energy gaps (E_g^{ec}) of copolymers were calculated according to the following equations:

$$\text{HOMO} = -e(E_{ox} + 4.29)\ (\text{eV})$$

$$\text{LUMO} = -e(E_{red} + 4.29)\ (\text{eV})$$

$$E_g^{ec} = e(E_{ox} - E_{red})\ (\text{eV})$$

The onset potentials for oxidation (E_{ox}) were observed to be 0.93, 1.15, and 0.96 V for **PT-ID**, **PT-DTBT**, and **PT-DTBTID**, respectively. On the other hand, the onset potentials for reduction (E_{red}) of them were found to be −0.89, −0.85, and −0.75 V, respectively. Accordingly, the HOMO energy levels of **PT-ID**, **PT-DTBT**, and **PT-DTBTID**, are −5.22, −5.44, zand −5.25 eV, respectively. Regarding the threshold HOMO energy level for air stable conjugated polymers being estimated to be −5.2 eV,[29,30] the deep HOMO levels of the three copolymers with acceptor groups (DTBT, ID, and DTBTID) should be beneficial to their chemical stability in ambient conditions. In addition, the deep HOMO levels of the copolymers are desirable for higher open-circuit voltage (V_{oc}) of the PSCs with copolymers as donor materials[31] because the V_{oc} is usually proportional to the difference between the HOMO energy level of the donor and the LUMO energy level of the acceptor. The HOMO energy level of **PT-DTBT** is ∼0.2 eV lower than those of **PT-ID** and **PT-DTBTID**, predicting that **PT-DTBT** would achieve the highest V_{oc} value. On the other hand, a donor polymer intended for use with a soluble fullerene acceptor (e.g., $PC_{61}BM$) should have a LUMO offset of approximately 0.3−0.4 eV relative to $PC_{61}BM$ (−4.2 eV)[32,33] for the effective charge transfer. The LUMO levels of **PT-ID**, **PT-DTBT**, and **PT-DTBTID** are −3.40, −3.44, and −3.54 eV, respectively, which imply an effective charge transfer could occur from the copolymers to $PC_{61}BM$.[34] The electrochemically estimated band gaps of the copolymers are 1.71−2.00 eV and they are different from corresponding optical band gaps (E_g^{opt}), but within the range of error (0.2−0.5 eV).[35] Furthermore, compared with **PT-ID**, the lower LUMO energy levels of polymers **PT-DTBT** and **PT-DTBTID** should be a result of the extension of π-electron delocalization in the polymer backbone.[36] In a word, with the increase the length of conjugated side chains, the LUMO energy levels of the three copolymers are lowered gradually.

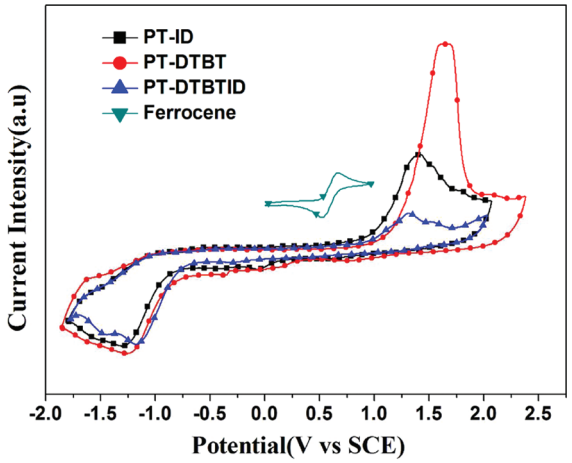


Figure 6. Cyclic voltammograms of the polymer films on platinum electrode in 0.1 mol/L Bu_4NPF_6 acetonitrile solution.

Photovoltaic Properties. In order to investigate whether the conjugated side groups of the three copolymers make a

dx.doi.org/10.1021/ma202399n | *Macromolecules* 2012, 45, 2359−2366

contribution to the photoelectric conversion in the PSCs, the bulk heterojunction PSC devices based on the blend of the copolymers and $PC_{61}BM$ have been fabricated. The structure of fabricated devices is ITO/PEDOT:PSS/polymer:$PC_{61}BM$-(1:4,w/w)/Ca/Al. Figure 7 shows the current−voltage (J−V)

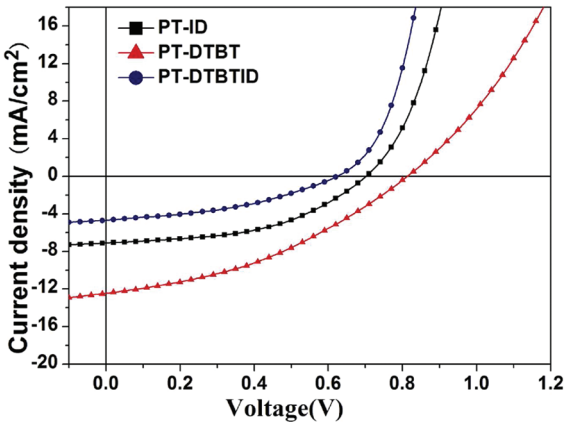


Figure 7. J−V curves of the photovoltaic cells based on **PT-ID**, **PT-DTBT**, and **PT-DTBTID** under the illumination of AM 1.5, 100 mW/cm^2.

curves of the PSCs based on the three copolymers. The photovoltaic parameters of the PSCs are summarized in Table 3. Under standard global AM 1.5 solar condition, the

Table 3. Photovoltaic Properties and Mobility of PT-ID, PT-DTBT, and PT-DTBTID

copolymers/$PC_{61}BM$ (1:4, w/w)	V_{oc} (V)	J_{sc} (mA/cm^2)	FF	PCE (%)	mobility (cm^2/V S)
PT-ID	0.71	7.19	0.49	2.48	6×10^{-5}
PT-DTBT	0.81	12.65	0.41	4.18	3.2×10^{-3}
PT-DTBTID	0.62	4.67	0.40	1.16	3×10^{-5}

photovoltaic cells based on **PT-DTBT** exhibit better photovoltaic performance (J_{sc} = 12.65 mA/cm^2, V_{oc} = 0.81 V, FF = 0.41, and PCE = 4.18%) than **PT-ID** based device (J_{sc} = 7.19 mA/cm^2, V_{oc} = 0.71 V, FF = 0.49, and PCE = 2.48%) and **PT-DTBTID** based device (J_{sc} = 4.67 mA/cm^2, V_{oc} = 0.62 V, FF = 0.40, and PCE = 1.16%). In comparison with **PT-ID**, the better overlap of the absorption spectrum of **PT-DTBT** with the solar spectrum can account for the increase in J_{sc} as revealed by incident-photon-to-current efficiency (IPCE) spectra (Figure 8). On the other hand, the PCE based on **PT-DTBTID** is considerably lower than those of **PT-ID** and **PT-DTBT**, despite the fact that the absorption spectrum of **PT-DTBTID** better match the solar spectrum in comparison with the other two. That is because the electron deficient nature of the DTBTID group provides a wider photo responsive range (Figure 8), but it can also act as a trapping site, inhibiting electron transfer from the main chain to the acceptor and as a result to produce low IPCE values and poor photovoltaic performance for **PT-DTBTID**.[37] In addition, the bulky side chain (DTBTID) of the **PT-DTBTID** leads to a significant decrease in J_{sc}, consequently, a decrease in the PCE of the solar cell. **PT-DTBT** with DTBT as the side chains shows the highest PCE due to the highest J_{sc} and V_{oc}. Therefore, the side group DTBT seems to be better than ID, and ID seems to be better than DTBTID.

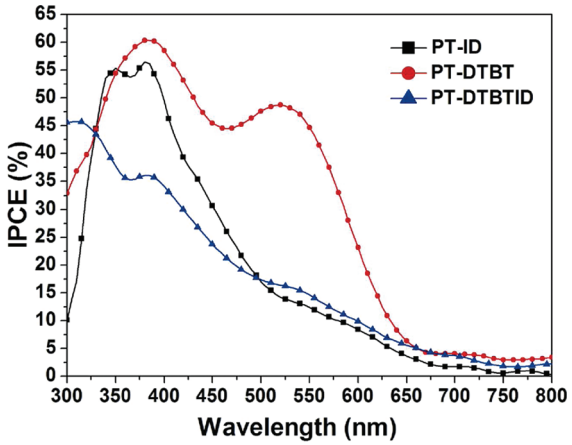


Figure 8. IPCE of the polymer solar cells based on **PT-ID**, **PT-DTBT**, and **PT-DTBTID**.

To further understand the cause of variation in solar cell performance, the hole mobility of these copolymers was measured using the OTFT technique under the same conditions. The mobility values of the copolymers are listed in Table 3. **PT-DTBT** with the DTBT side chain demonstrated a relatively high hole mobility of 3.2×10^{-3} cm^2 V^{-1} s^{-1} which is two order higher than those of **PT-ID** (6×10^{-5} cm^2 V^{-1} s^{-1}) and **PT-DTBTID** (3×10^{-5} cm^2 V^{-1} s^{-1}) (Table 3). Furthermore, the hole mobility of **PT-ID** is double of **PT-DTBTID**. Therefore, the high hole mobility of the **PT-DTBT** further clearly explain why the photovoltaic properties of the **PT-DTBT** are better than those of **PT-ID** and **PT-DTBTID**.

CONCLUSION

In summary, three novel alternating copolymers based on benzo 1,2-b:4,5-b′ dithiophen and thiophene with different conjugated side groups have been successfully synthesized and characterized. The three copolymers show good solubility and film-forming ability. Through manipulating the length of the acceptor groups attached at the conjugated side chains of the copolymers, the photophysical and electrochemical properties of the copolymers are effectively tuned. The best power conversion efficiency of the PSCs based on **PT-DTBT**/$PC_{61}BM$ (1:4, w/w) reached to 4.18% under the illumination of AM1.5, 100 mW cm^{-2}. The broad absorption spectrum, deep HOMO level and the noticeably high hole mobility of **PT-DTBT** contribute to the outstanding J_{sc}, V_{oc} as well as the high device efficiency.

EXPERIMENTAL SECTION

Materials and Characterization. All the chemicals were purchased from Alfa Aesar or Shanghai Medical Company (China). THF and toluene were refluxed over sodium and benzophenone, then distilled prior to use. DMF was dried and distilled under reduced pressure. All other commercially available materials were used as received unless noted otherwise. Column chromatography was carried out on silica gel (merck, 200−300 mesh)

^{1}H NMR and ^{13}C NMR spectra were measured with Bruker AVANCE 400 spectrometer. FT-IR spectra were obtained on Perkin-Elmer Spectra One. UV−vis spectra and photoluminescence (PL) spectra of the copolymers were measured on Perkin-Elmer Lamada 25 spectrometer and Perkin-Elmer LS-50 luminescence spectrometer, respectively. Molecular mass was determined by matrix assisted laser desorption-ionization time-of-flight mass spectrometry (MALDI−TOF MS) using a Bruker Aupoflex-III mass spectrometer. The elemental analysis of all monomers and copolymers were performed with

dx.doi.org/10.1021/ma202399n | Macromolecules 2012, 45, 2359−2366

an Elementar Vario EL III element analyzer for C, H, and S determination. Thermogravimetric analyses (TGA) were performed under nitrogen at a heating rate of 20 °C/min with Netzsch TG 209 analyzer, and differential scanning calorimetric measurement (DSC) was recorded with TA DSCQ10 instrument at a heating rate of 20 °C/min. The average molecular weight and polydispersity index (PDI) of the copolymers were determined using Waters 1515 gel permeation chromatography (GPC) analysis with THF as eluent and polystyrene as standard. Cyclic voltammetry (CV) was conducted on an electrochemistry workstation (CHI660A, Chenhua Shanghai) with the polymer film on Pt plate as the working electrode, Pt slice as the counter electrode, and saturated calomel electrode (SCE) as a reference electrode in a 0.1 M tetra-*n*-butylammonium hexafluorophosphate acetonitrile solution at a scan rate of 50 mV/s.

Fabrication and Characterization of Polymer Solar Cells. The photovoltaic cells were constructed in the traditional sandwich structure through several steps. The ITO coated glass substrates were cleaned by successive ultrasonic treatment in acetone and isopropyl alcohol, then treated with a nitrogen−oxygen plasma oven for 5 min. Poly(3,4-ethylene dioxythiophene)−poly(styrenesulfonate) (PEDOT:PSS, from Bayer AG) was spin-coated from an aqueous solution on a cleaned indium tin oxide (ITO) glass substrate giving a thickness of about 40 nm as measured by Ambios Technology XP-2 surface profilometer, then it was dried at 150 °C for 15 min. Subsequently, the photoactive layer was prepared by spin-coating the dichlorobenzene solution of polymer:$PC_{60}BM$ (1:4, w/w) with the polymer concentration of 6 mg/mL on the top of the PEDOT:PSS layer and the thickness of the active layers of ca. 80 nm, and then annealed at 150 °C for 5 min in a nitrogen-filled glovebox. Finally, the substrates were transferred into an evaporator and pumped down to 5×10^{-4} Pa. to deposit 10 nm of Ca and 100 nm of aluminum cathodes, producing an active area of 4 mm^2 for each cell. Current density−voltage (J−V) characteristics were measured by a Keithley 2602 Source Meter under 100 mW cm^{-2} irradiation using a 500W Xe lamp equipped with a global AM 1.5 filter for solar spectrum simulation, and the incident light intensity was calibrated using a standard Si solar cell. The measurement of monochromatic incident photon-to-current conversion efficiency (IPCE) was performed using a Zolix DCS300PA Data acquisition system.

OTFTs Device Fabrication. OTFTs fabricated on OTS-modified SiO_2/Si substrates. OTFT devices were fabricated in a top-contact configuration. Before the deposition of organic semiconductors, octyltrichlorosilane (OTS) treatment was performed on the gate dielectrics which were placed in a vacuum oven with OTS at a temperature of 120 °C to form an OTS self-assembled monolayer. Then the polymer thin films were spin-coated on the OTS modified SiO_2/Si substrates from the chloroform solutions, followed by Au deposition through a shadow mask to define the source and drain electrodes. The OTFTs characteristics of the devices were determined at room temperature in air by using a Keithley 4200 SCS. The mobility of the devices was calculated in the saturation regime. The equation is listed as follows:

$$I_{DS} = (W/2L)C_i\mu(V_{GS} - V_{th})^2$$

Here W/L is the channel width/length, C_i is the insulator capacitance per unit area, and V_{GS} and V_{th} are the gate voltage and threshold voltage, respectively.

Synthesis of the Monomers and Copolymers. The synthetic routes of the monomers and copolymers are shown in Scheme 1. 4,7-Bis(4-hexylthiophen-2-yl)benzo[1,2,5]thiadiazole (**1**),[38] (2,5-dibromothiophen-3-ylmethyl) phosphonic acid diethyl ester (**3**),[39] and 2,6-bis(trimethyltin)-4,8-bis(2-ethylhexyloxy)benzo[1,2-*b*:4,5-*b*′]-dithiophene (**M4**),[17] were synthesized according to already published procedures. The detailed synthetic procedures of other compounds are as follows.

2,5-Dibromothiophene-3-carbaldehyde (M1). *N*-Bromosuccinimide (NBS) (5.337 g, 30 mmol) was dissolved in 35 mL of anhydrous DMF. The mixture was added dropwise to a mixture of thiophene-3-carbaldehyde (1.68 g, 15 mmol) in anhydrous DMF (15 mL) in the dark. The resulting solution was stirred at room temperature under argon overnight. Then, the organic material was extracted with dichloromethane and washed with water. After the solvent was removed, the crude product was purified on silica gel chromatography using a petroleum ether/dichloromethane mixture (3:1 by volume) as eluent. A light yellow solid was obtained. Yield: 2.82 g (70%). ^{1}H NMR (400 MHz, $CDCl_3$, δ/ppm): 9.82 (s, 1H), 7.36 (s, 1H). ^{13}C NMR (100 MHz, $CDCl_3$, δ/ppm): 183.04, 139.37, 128.70, 124.03, 113.34.

3-Hexyl-5-(7-(4-hexylthiophen-2-yl)benzo[1,2,5]thiadiazol-4-yl)thiophene-2-carbaldehyde (2). The compound **2** was synthesized by the Vilsmeier reaction. To the mixture of compound **1** (2.4 g, 5.1 mmol) in dichloroethane (25 mL) and anhydrous DMF (0.4 mL, 5.1 mmol) was added dropwise under nitrogen atmosphere, then $POCl_3$ (0.48 mL, 5.1 mmol) was added slowly. The mixture was stirred at 85 °C for 12 h. Then the mixture was cooled to room temperature, 30 mL of water was added to quench the reaction. The mixture was extracted with CH_2Cl_2. After the solvent was removed, the crude product was purified on silica gel chromatography using a petroleum ether/dichloromethane mixture (1:1 by volume) as eluent. An orange solid was obtained. Yield: 1.78 g (70%). ^{1}H NMR (400 MHz, $CDCl_3$, δ/ppm): 10.12 (s, 1H), 8.08 (s, 1H), 8.06 (s, 1H), 7.99 (d, 1H, J = 7.64 Hz), 7.89 (d, 1H, J = 7.60 Hz), 7.11 (s, 1H), 3.06 (t, 2H, J = 7.66 Hz), 2.72 (t, 2H, J = 7.62 Hz), 1.72−1.83 (m, 4H), 1.44−1.36 (m, 12H), 0.96 (m, 6H).

(E)-4-(5-(2-(2,5-dibromothiophen-3-yl)vinyl)-4-hexylthiophen-2-yl)-7-(4-hexylthiophen-2-yl)benzo[1,2,5]thiadiazole (M2). Compound **2** (0.497 g, 1 mmol) and **3** (0.39 g, 1 mmol) were dissolved in THF (20 mL) and the solution was stirred at room temperature for 30 min under nitrogen atmosphere. Then potassium tertbutoxide (0.13 g, 1.15 mmol) was dissolved in THF (20 mL) and added dropwise to the solution. The reaction mixture was stirred for 5 h at room temperature, and then heated to 50 °C for 12 h. After cooling to room temperature, the reaction mixture was extracted with dichloromethane and washed with dilute aqueous HCl solution. The organic phase was dried over anhydrous $MgSO_4$, and then the solvent was removed by rotary evaporation. The crude product was purified on silica gel chromatography using a petroleum ether/dichloromethane mixture (1:1 by volume) as eluent. A red solid was obtained. Yield: 0.48 g (65%). FT-IR (KBr, cm^{-1}): 938 (*trans*-vinylene). ^{1}H NMR (400 MHz, $CDCl_3$, δ/ppm): 8.01 (s, 1H), 7.98 (s, 1H), 7.86 (d, 2H, J = 1.44 Hz), 7.22 (s, 1H), 7.12 (d, 1H, J = 15.96 Hz), 7.07 (s, 1H), 6.90 (d, 1H, J = 15.96 Hz), 2.70 (m, 4H), 1.72−1.71 (m, 4H), 1.42−1.36 (m, 12H), 0.93−0.92 (m, 6H). ^{13}C NMR (100 MHz, $CDCl_3$, δ/ppm): 152.63, 143.39, 143.37, 139.03, 137.39, 136.92, 130.55, 129.15, 127.31, 126.32, 125.47, 122.57, 121.69, 119.50, 111.91, 109.72, 31.68, 30.64, 29.01, 22.59, 14.02. Anal. Calcd for $C_{32}H_{34}Br_2N_2S_4$: C, 52.31; H, 4.66; N, 3.81; S, 17.46. Found: C, 53.26; H, 5.19; N, 3.80; S, 17.31. MALDI−TOF MS ($C_{32}H_{34}Br_2N_2S_4$), m/z: calcd, 734.000; found, 733.905.

(*E*)-5-(7-(5-(2-(2,5-Dibromothiophen-3-yl)vinyl)-4-hexylthiophen-2-yl)benzo[1,2,5]thiadiazol-4-yl)-3-hexylthiophene-2-carbaldehyde (M3). By following a similar method, as for compound **2**, monomer **M3** was synthesized from anhydrous DMF (0.80 mL, 10.2 mmol), $POCl_3$ (0.94 mL, 10.0 mmol) and monomer **M2** (0.743 g, 1 mmol). The crude product was purified on silica gel chromatography using a petroleum ether/dichloromethane mixture (3:1 by volume) as eluent. A black red solid was obtained. Yield: 0.32 g (40%). FT-IR (KBr, cm^{-1}): 1657 ($\nu_{C=O}$), 929 (*trans*-vinylene). ^{1}H NMR (400 MHz, $CDCl_3$, δ/ppm): 10.12 (s, 1H), 8.09 (s, 1H), 8.04 (s, 1H), 7.99 (d, 1H, J = 7.60 Hz), 7.90 (d, 1H, J = 7.56 Hz), 7.23 (s, 1H), 7.11 (d, 1H, J = 15.88 Hz), 6.91 (d, 1H, J = 15.76 Hz), 3.06 (t, 2H, J = 7. 48 Hz), 2.76 (t, 2H, J = 7.42 Hz), 1.81−1.69 (m, 4H), 1.56−1.27 (m, 12H), 0.930−0.927 (m, 6H). ^{13}C NMR (100 MHz, $CDCl_3$, δ/ppm): 181.98, 153.27, 147.38, 143.48, 139.05, 138.00, 137.52, 136.81, 131.41, 130.57, 127.26, 124.98, 122.35, 119.99, 112.03, 31.47, 28.96, 22.55, 14.00. Anal. Calcd for $C_{33}H_{34}Br_2N_2OS_4$ C, 51.92; H, 4.46; N, 3.67; S, 16.78. Found: C, 52.42; H, 4.72; N, 3.44; S, 15.74. MALDI−TOF MS ($C_{33}H_{34}Br_2N_2OS_4$) m/z: calcd, 762.700; found 761.951.

2,6-Bis(trimethyltin)-4,8-bis(2-ethylhexyloxy)benzo[1,2-b:4,5-b′]dithiophene (M4). **M4** were synthesized according to already published procedures[17] with a yield of 75%. ^{1}H NMR (400 MHz, $CDCl_3$, δ/ppm): 7.55 (s, 2 H), 4.23−4.22 (d, 4 H, J = 4.52 Hz), 1.85−1.71 (m, 2 H), 1.65−1.29 (m, 16 H), 1.08−0.98 (m, 12 H), 0.48 (s, 18 H). ^{13}C NMR (100 MHz, $CDCl_3$, δ/ppm): 143.3, 140.3, 133.8, 132.9, 128.0, 75.66, 40.72, 30.58, 29.26, 23.95, 23.14, 14.12, 11.32. MALDI−TOF MS (m/z): calcd, 772.160; found, 772.130.

Synthesis of the Precursor Polymer PT-CHO. **M1** (67.25 mg, 0.25 mmol) and **M4** (193 mg, 0.25 mmol) were dissolved in 20 mL of toluene, and the solution was flushed with argon for 15 min; then, 30 mg of $Pd(PPh_3)_4$ was added into the solution. The mixture was again flushed with argon for 30 min. The polymerization was carried out at 110 °C for 3 days. Finally, the reaction mixture was cooled to room temperature and slowly added to methanol (120 mL). The precipitate was collected by filtration from methanol and further purified by Soxhlet extraction with methanol, hexane, and chloroform in sequence. The chloroform fraction was evaporated by rotary evaporation. The final product was obtained as a green solid and dried under vacuum for 24 h. Yield: 152 mg (60%). ^{1}H NMR (400 MHz, $CDCl_3$, δ/ppm): 10.19 (br, 1H), 7.41−7.35 (br, 3H), 4.08 (br, 4H), 1.82−1.57 (br, 18H), 1.23−0.96 (br, 12H). Anal. Calcd for $(C_{31}H_{38}O_3S_3)_n$: C, 67.10; H, 6.91; N, 0; S, 17.33. Found: C, 66.07; H, 6.92; N, 0.084; S, 17.22.

Synthesis of the Copolymer PT-ID. The compound was synthesized according to procedures similar to reported in the literature.[40] A mixture of PT-CHO (0.120 g, 0.21 mmol of basic units) and 1,3-indanedione (0.306 g, 2.1 mmol) in 10 mL of chloroform was stirred for 0.5 h, then 0.5 mL pyridine was added. The mixture solution was stirred for 24 h at room temperature, after which the resulting mixture was poured into methanol and the precipitate was filtered. The precipitate was purified by Soxhlet extraction with methanol, hexane and chloroform in sequence. The chloroform fraction was evaporated by rotary evaporation. The final product was obtained as a black solid and dried under vacuum for 24 h. Yield: 72 mg (49%). ^{1}H NMR (400 MHz, $CDCl_3$, δ/ppm): 8.75 (br, 1H), 7.98−7.97 (d, 2H), 7.84−7.82 (d, 2H), 7.76−7.12 (br, 3H), 4.37−4.04 (br, 4H), 1.81−1.01 (br, 30H). Anal. Calcd for $(C_{40}H_{42}O_4S_3)_n$: C, 70.28; H, 6.15; N, 0.00; S, 14.05. Found: C, 66.56; H, 6.12; N, 0.09; S, 12.84.

Synthesis of the Copolymer PT-DTBT. By following the similar method used for PT-CHO, **PT-DTBT** was synthesized with monomer **M2** (0.193 g, 0.25 mmol) and **M4** (0.1835 g, 0.25 mmol). The final product was obtained as a green solid. Yield: 0.2 g (78%). ^{1}H NMR (400 MHz, $CDCl_3$, δ/ppm): 8.08−7.12 (br, 10H), 4.26−4.23 (br, 4H), 2.67−2.63 (br, 4H), 1.37−0.94 (br, 52H). Anal. Calcd for $(C_{58}H_{70}N_2O_2S_6)_n$: C, 68.32; H, 6.92; N, 2.75; S, 18.87. Found: C, 67.73; H, 7.79; N, 2.63; S, 19.08.

Synthesis of the Precursor PT-DTBTCHO. By following the similar method as for PT-CHO, PT-DTBTCHO was synthesized with **M3** (0.229 g, 0.30 mmol) and **M4** (0.231 g, 0.30 mmol)). The final product was obtained as a green solid. Yield: 0.32 g (70%). ^{1}H NMR (400 MHz, $CDCl_3$, δ/ppm): 10.10−10.06 (br, 1H), 8.11−7.01 (br, 9H), 4.25 (br, 4H), 2.98−2.26 (br, 4H), 1.70−0.92 (br, 52H). Anal. Calcd for $(C_{59}H_{70}N_2O_3S_6)_n$: C, 67.64; H, 6.75; N, 2.67; S, 18.36. Found: C, 67.08; H, 7.28; N, 2.69; S, 18.29.

Synthesis of the Polymer PT-DTBTID. By following the similar method as for **PT-ID**, **PT-DTBTID** was synthesized with PT-DTBTCHO (0.12 g, 0.117 mmol of basic units) and 1,3-indanedione (0.178 g, 1.17 mmol)). The final product was obtained as a black purple solid. Yield: 62 mg (46%). ^{1}H NMR (400 MHz, $CDCl_3$, δ/ppm): 8.72 (s, 1H), 8.06−7.27 (br, 13H), 4.35−4.21 (br, 4H), 2.97−2.44 (br, 4H), 2.17−2.13 (m, 2H), 1.68−1.01 (br, 50H). Anal. Calcd for $(C_{68}H_{74}N_2O_4S_6)_n$: C, 69.46; H, 6.36; N, 2.38; S, 16.36. Found: C, 67.28; H, 7.07; N, 2.28; S, 15.36.

AUTHOR INFORMATION

Corresponding Author

*E-mail: tanst2008@163.com.

Notes

The authors declare no competing financial interest.

ACKNOWLEDGMENTS

This work was supported by the National Nature Science Foundation of China (Nos. 50973092, 51003089, 21004050, 51173154), National Basic Research Program of China (No. 2011CBA00701), and Specialized Research Fund for the Doctoral Program of Higher Education of China (Nos. 20094301120005 and 20104301110003).

REFERENCES

(1) Yu, G.; Gao, J.; Hummelen, J. C.; Wudl, F.; Heeger, A. J. *Science* **1995**, *270*, 1789.
(2) Li, Y. F.; Zou, Y. P. *Adv. Mater.* **2008**, *20*, 2952.
(3) Chen, J.; Cao, Y. *Acc. Chem. Res.* **2009**, *42*, 1709.
(4) Liang, Y.; Wu, Y.; Feng, D.; Tsai, S. T.; Son, H. J.; Li, G.; Yu, L. *J. Am. Chem. Soc.* **2008**, *131*, 56.
(5) Kim, J. Y.; Lee, K.; Coates, N. E.; Moses, D. T.; Nguyen, Q.; Dante, M.; Heeger, A. J. *Science* **2007**, *317*, 222.
(6) Chu, T.; Lu, J.; Beaupr, S.; Zhang, Y.; Pouliot, J. R.; Wakim, S.; Zhou, J.; Leclerc, M.; Li, Z.; Ding, J.; Tao, Y. *J. Am. Chem. Soc.* **2011**, *133*, 4250.
(7) Peet, J.; Kim, J. Y.; Coates, N. E.; Ma, W. L.; Moses, D.; Heeger, A. J.; Bazan, G. C. *Nat. Mater.* **2007**, *6*, 497.
(8) Huang, F.; Chen, K. S.; Yip, H. L.; Hau, S. K.; Acton, O.; Zhang, Y.; Luo, J. D.; Jen., A. K. Y. *J. Am. Chem. Soc.* **2009**, *131*, 13886.
(9) Liang, Y.; Feng, D.; Wu, Y.; Tsai, S. T.; Li, G.; Ray, C.; Yu, L. *J. Am. Chem. Soc.* **2009**, *131*, 7792.
(10) Zhang, Z. G.; Zhang, K. L.; Liu, G.; Zhu, C. X.; Neoh, K. G.; Kang, E. T. *Macromolecules* **2009**, *42*, 3104.
(11) Wettach, H.; Pasker, F.; Hoger, S. *Macromolecules* **2008**, *41*, 3104.
(12) Liang, Y.; Yu, L. *Acc. Chem. Res.* **2011**, *43*, 1277.
(13) Chen, H. Y.; Hou, J. H.; Zhang, S. Q.; Liang, Y. Y.; Yang, G. W.; Yang, Y.; Yu, L. P.; Wu, Y.; Li, G. *Nat. Photonics* **2009**, *3*, 649.
(14) Zhang, Z. G.; Liu, Y. L.; Yang, Y.; Hou, K. Y.; Peng, B.; Zhao, G. J.; Zhang, M. J.; Guo, X.; Kang, E. T.; Li, Y. F. *Macromolecules* **2010**, *43*, 9376.
(15) Hou, J.; Tan, Z.; Yan, Y.; He, Y.; Yang, C.; Li, Y. *J. Am. Chem. Soc.* **2006**, *128*, 4911.
(16) Shen, P.; Sang, G. Y.; Lu, J. J.; Zhao, B.; Wan, M. X.; Zou, Y. P.; Li, Y. F.; Tan, S. T. *Macromolecules* **2008**, *41*, 5716.
(17) Nie, Y. J.; Zhao, B.; Tang, P.; Jiang, P.; Tian, Z. F.; Shen, P.; Tan, S. T. *J. Polym Sci. A Polym. Chem.* **2011**, *49*, 3604.
(18) Shen, P.; Liu, Y. J.; Huang, X. W.; Zhao, B.; Xiang, N.; Fei, J. J.; Liu, L. M.; Wang, X. Y.; Huang, H.; Tan, S. T. *Dyes Pigments* **2009**, *83*, 187.
(19) Zhang, W.; Fang, Z.; Su, M. J.; Saeys, M.; Liu, B. *Macromol. Rapid Commun.* **2009**, *30*, 1533.
(20) Li, J. Y.; Liu, D.; Li, Y. Q.; Lee, C. S.; Kwong, H. L.; Lee, S. T. *Chem. Mater.* **2005**, *17*, 1208.
(21) Gadisa, A.; Mammo, W.; Andersson, L. M.; Admassie, S.; Zhang, F.; Andersson, M. R.; Inganas, O. *Adv. Funct. Mater.* **2007**, *17*, 3836.
(22) Leriche, P.; Frere, P.; Cravino, A.; Aleveque, O.; Roncali, J. *J. Org. Chem.* **2007**, *72*, 8332.
(23) Jin, J. K.; Choi, J. K.; Kim, B. J.; Kang, H. B.; Yoon, S. C.; You, H.; Jung, H. T. *Macromolecules* **2011**, *44*, 502.
(24) Shang, Y. L.; Wen, Y. Q.; Li, S. L.; Du, S. X.; He, X. B.; Cai, L.; Li, Y. F.; Yang, L. M.; Gao, H. J.; Song, Y. *J. Am. Chem. Soc.* **2007**, *129*, 11674.
(25) Surin, M.; Sonar, P.; Grimsdale, A. C.; Mullen, K.; De Feyter, S.; Habuchi, S.; Sarzi, S.; Braeken, E.; Heyen, A. V.; Van der Auweraer, M.; De Schryver, F. C.; Cavallini, M.; Moulin, J. F.; Biscarini, F.; Femoni, C.; Roberto, L.; Leclere, P. *J. Mater. Chem.* **2007**, *17*, 728.
(26) Price, S. C.; Stuart, A. C.; You, W. *Macromolecules* **2010**, *43*, 10.
(27) Shen, P.; Ding, T. P.; Huang, H.; Zhao, B.; Tan, S. T. *Synth. Met.* **2010**, *160*, 1291.

(28) Li, Y.; Cao, Y.; Gao, J.; Wang, D.; Yu, G.; Heeger, A. J. *Synth. Met.* **1999**, *99*, 243.
(29) Thompson, B. C.; Kim, Y. G.; Reynolds, J. R. *Macromolecules* **2005**, *38*, 5359.
(30) Leeuw, D. M. D.; Simenon, M. M. J.; Brown, A. R.; Einerhand, R. E. F. *Synth. Met.* **1997**, *87*, 53.
(31) Sariciftci, N. S.; Smilowitz, L.; Heeger, A. J.; Wudl, F. *Science* **1992**, *258*, 1474.
(32) Bredas, J. L.; Beljonne, D.; Coropceanu, V.; Cornil, J. *Chem. Rev.* **2004**, *104*, 4971−5004.
(33) Scharber, M. C.; Mühlbacher, D.; Koppe, M.; Denk, P.; Waldauf, C.; Heeger, A. J.; Brabec, C. J. *Adv. Mater.* **2006**, *18*, 789−794.
(34) Kraabel, B.; McBranch, D.; Sariciftci, N. S.; Moses, D.; Heeger, A. J. *J. Phys. Rev. B.* **1994**, *50*, 18543.
(35) Chen, W. C.; Liu, C. L.; Yen, C. T.; Tasi, F. C.; Tonzola, C. J.; Olson, N.; Jenekhe, S. A. *Macromolecules* **2004**, *37*, 5959.
(36) Karastairis, P.; Mikroyannidis, J. A.; Spiliopoulos, I. K. *J. Polym. Sci. A: Polym. Chem.* **2008**, *46*, 2367.
(37) Zhang, Z. G.; Fan, H. J.; Min, J.; Zhang, S. Y.; Zhang, J.; Zhang, M. J.; Guo, X.; Zhan, X. W.; Li, Y. F. *Polym. Chem.* **2011**, *2*, 1678.
(38) Zhang, S.; Guo, Y.; Fan, H.; Liu, Y.; Chen, H.; Yang, G.; Zhan, X.; Liu, Y.; Li, Y.; Yang, Y. *J. Polym. Sci., Part A: Polym. Chem.* **2009**, *47*, 5498.
(39) Hou, J.; Huo, L.; He, C.; Yang, C.; Li, Y. *Macromolecules* **2006**, *39*, 594.
(40) Wagner, K.; Crowe, L. L.; Wagner, P.; Gambhir, S.; Partridge, A. C.; Earles, J. C.; Clarke, T. M.; Gordon, K. C.; Officer, D. L. *Macromolecules* **2010**, *43*, 3817.

Macromolecules

Article

pubs.acs.org/Macromolecules

Introduction of Perylene Units for Enhanced Interchain Interaction in Conjugated Polymers for Organic Photovoltaic Devices

Ji-Hoon Kim,[†] Hee Un Kim,[†] Dongbo Mi,[†] Sung-Ho Jin,[‡] Won Suk Shin,[∥] Sung Cheol Yoon,[∥] In-Nam Kang,[§] and Do-Hoon Hwang*[,†]

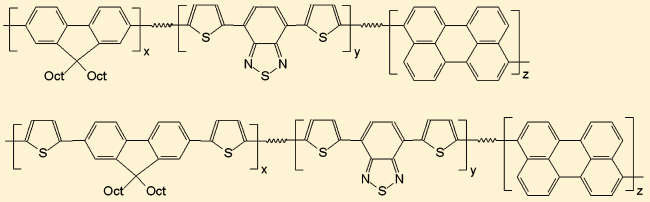
[†]Department of Chemistry, and Chemistry Institute for Functional Materials, Pusan National University, Busan 609-735, Korea

[‡]Department of Chemistry Education and Interdisciplinary Program of Advanced Information and Display Materials, Pusan National University, Busan 609-735, Korea

[∥]Korea Research Institute of Chemical Technology, 100 Jang-dong, Yuseong-gu, Daejeon 305-343, Korea

[§]Department of Chemistry, The Catholic University of Korea, Bucheon 420-743, Korea

ABSTRACT: A series of semiconducting copolymers, poly-[2,7-(9,9′-dioctylfluorene)-*alt*-5,5′-(4′,7′-di-2-thienyl-2′,1′,3′-benzothiadiazole)] (PFDTBT), poly[2,2′-(9,9-dioctyl-9*H*-fluorene-2,7-diyl)dithiophene-*alt*-5,5′-(4′,7′-di-2-thienyl-2′,1′,3′-benzothiadiazole)] (PFD2TBT), and their *ter*-polymers containing perylene units were synthesized using Suzuki coupling polymerization. The perylene units were introduced to improve the charge-transport ability by enhancing the $\pi-\pi$ interaction between polymer chains. The resulting polymers were characterized by ^{1}H NMR, elemental analysis, DSC, and TGA. The synthesized polymers were soluble in common organic solvents, and formed smooth and uniform spin-coated thin films. All of the polymers studied were found to exhibit good thermal stability, losing less than 5% of their weight upon heating to approximately 350 °C. Perylene- containing polymers showed higher field-effect mobilities than the corresponding PFDTBT or PFD2TBT polymers because of the enhanced $\pi-\pi$ interaction between polymer chains upon the introduction of perylene units. Bulk heterojunction solar cells were fabricated with configuration of ITO/PEDOT:PSS/polymer:$PC_{71}BM$/TiO_x/Al. The devices using the perylene-containing polymers showed higher short-circuit currents, and fill factors than the corresponding PFDTBT or PFD2TBT devices. One of the fabricated devices using a perylene-containing copolymer showed a maximum power conversion efficiency of 3.16%, with a short circuit current density of 9.61 mA/cm^2, open circuit voltage of 0.81 V, and fill factor of 41%.



1. INTRODUCTION

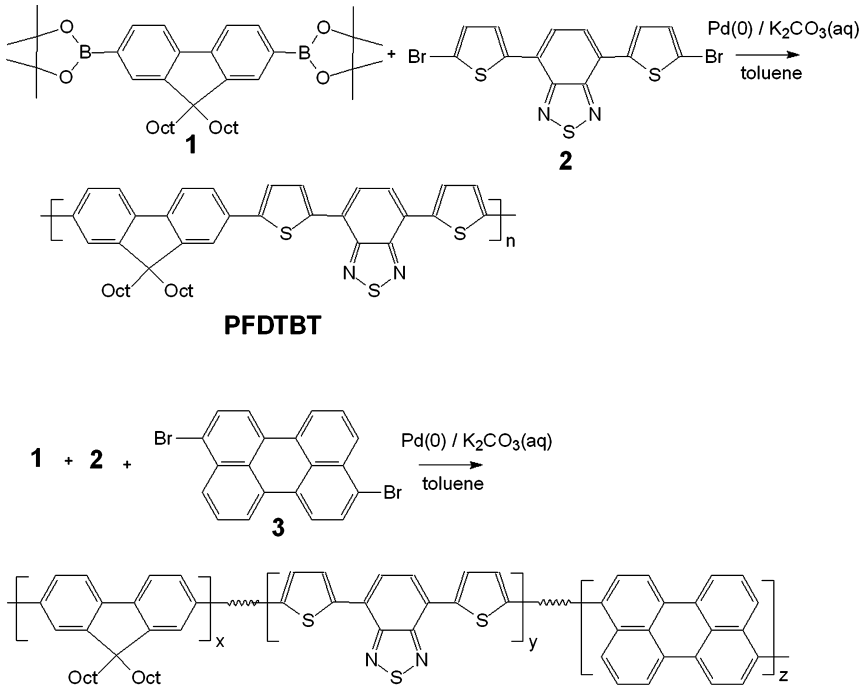
Extensive research has been carried out during the past decade on bulk heterojunction solar cells that utilize organic semiconducting materials.[1] The main advantages of organic photovoltaic devices (OPVs) are their lightweight, flexible nature, and their cost-effective manufacture by various printing technologies. The photoconversion process in OPVs is accomplished by efficient light absorption by conjugated polymers and accepting materials, charge separation at the interface of the donor polymer and the accepting materials, and subsequent charge collection at the electrodes. Matching the absorption of the conjugated polymer to the solar spectrum determines the ultimate performance of the solar cell. Among the variety of conjugated polymers that have been studied, poly(*p*-phenylenevinylene) (PPV),[2] poly(alkylfluorene) (PF), and polythiophene (PT)[3] derivatives are typical p-type electron donor materials.

However, the performance of photovoltaic cells with these polymers is limited by their relatively large band gap energies, which are not yet optimized with respect to the solar spectrum. Therefore, the design and synthesis of new low-band gap polymers become very important to better harvest the solar spectrum, especially in the red and near-infrared ranges, which can lead to possible enhancements in the photocurrents of OPVs.[4] The most widely used approach for obtaining low-band gap structures is to utilize internal charge transfer (ICT) from an electron-donating to an electron-accepting moiety.[5−7] Some interesting structures using the ICT approach have been reported. For example, Brabec et al. reported a low-band gap polymer, poly[2,6-(4,4-bis(2-ethylhexyl)-4*H*-cyclopenta[2,1-*b*;3,4-*b*′]-dithiophene)-*alt*-4,7-(2,1,3-benzothiadiazole)] (PCPDTBT), which showed absorption in the range 380−900 nm in the AM 1.5 G spectrum, good hole mobility (0.01−0.1 cm^2 V^{-1} s^{-1}) and a high power conversion efficiency (PCE) of 3.2% with $PC_{71}BM$ as the electron acceptor.[8,9] A 9,9-dialkylfluorene unit has previously been used as a building block for constructing donor−acceptor-type conjugated polymers in OPVs such as poly[2,7-(9,9′-dialkylfluorene)-*alt*-5,5′-(4′,7′-di-2-thienyl-2′,1′,3′-benzothiadiazole)] (PFDTBT). PFDTBT showed a maximum PCE of 2.2%, and PFDTBT derivatives containing branched alkyl chains (BisDMO-PFDTBT) showed higher PCEs.[10,11]

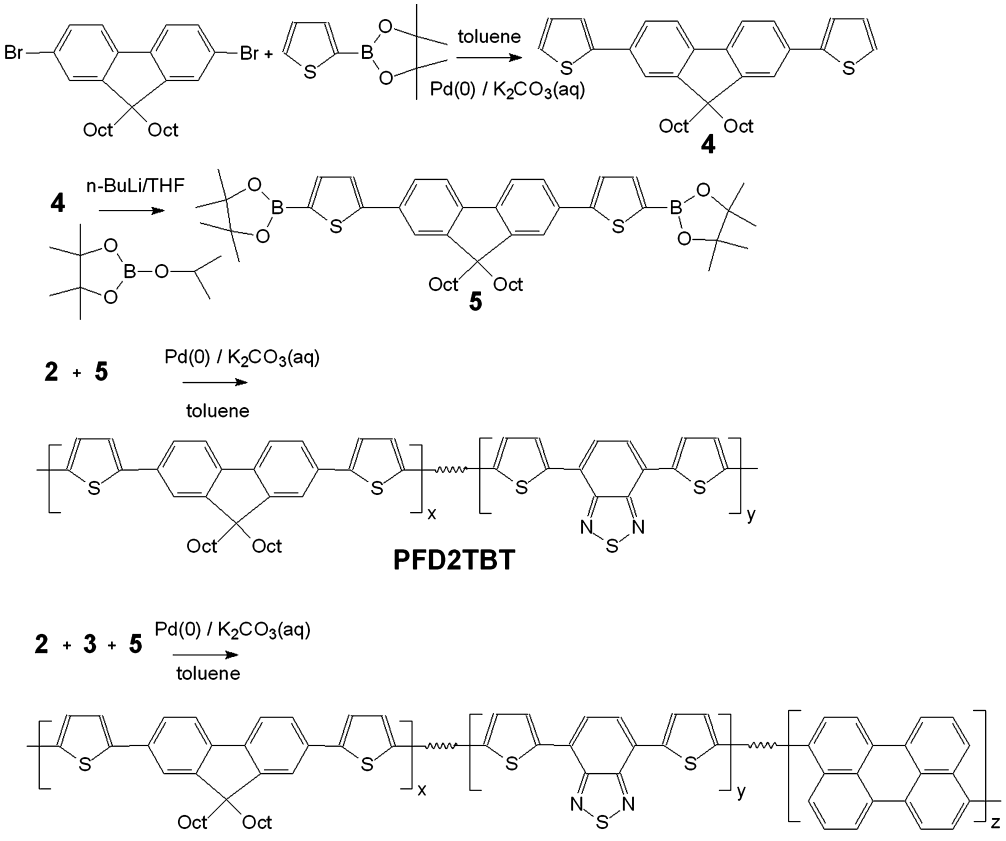
Received: December 15, 2011
Revised: February 18, 2012
Published: February 24, 2012

ACS Publications © 2012 American Chemical Society

Scheme 1. Synthetic Routes of PFDTBT and the Perylene Terpolymers



Scheme 2. Synthetic Routes of PFD2TBT and the Perylene Terpolymers



Some molecules and polymers that have flat structures such as fluorene,[12−16] anthracene,[17] and pyrene[18,19] have been reported to form excimers or aggregates by strong interchain $\pi-\pi$ interactions. Excimer formation could affect the emission properties of molecules or polymers, therefore, the excimer or exciplex formation has been used as a fluorescence probe for molecular recognition.[19] In organic photovoltaic devices, $\pi-\pi$ interactions between low-band gap donor polymers are important for charge transportation. Enhanced $\pi-\pi$ interactions in p-type donor polymers could improve their charge-transport ability, and thus increase short-circuit currents in solar cells.

dx.doi.org/10.1021/ma202712r | Macromolecules 2012, 45, 2367−2376

In this study we report on a new approach to improve PCE of OPVs by enhancing the interchain $\pi-\pi$ interaction. To do this we introduced flat perylene units into the conjugated polymers. We synthesized poly[2,7-(9,9′-dioctylfluorene)-*alt*-5,5′-(4′,7′-di-2-thienyl-2′,1′,3′-benzothiadiazole)] (PFDTBT), poly[2,2′-(9,9-dioctylfluorene-2,7-diyl)dithiophene-*alt*-5,5′-(4′,7′-di-2-thienyl-2′,1′,3′-benzothiadiazole)] (PFD2TBT), and their *ter*-polymers with perylene units. Optical, electrical and photovoltaic properties of the polymers were investigated. Synthetic routes and polymer structures are shown in Schemes 1 and 2.

2. EXPERIMENT

2.1. Materials. Fluorene, HBr, 2,1,3-benzothiadiazole, *n*-octyl bromide, bromine, perylene, diethyl ether, *N*-bromosuccinimide, tripropyl(thiophen-2-yl)stannane, CCl_4, 2-isopropoxy-4,4,5,5-tetramethyl-1,3,2-dioxaborolane, tetrakis(triphenylphosphine)palladium were all purchased from Aldrich. [6,6]-Phenyl C_{71}-butyric acid methyl ester ($PC_{71}BM$) was purchased from Nano-C. All chemicals were used without further purification.

2.2. Measurements. ^{1}H and ^{13}C NMR spectra were recorded using a Bruker AM-400 spectrometer and absorption spectra were measured using a JASCO JP/V-570 spectrometer. The molecular weights of the polymers were determined by gel permeation chromatography (GPC) analysis relative to a polystyrene standard using a Waters high-pressure GPC assembly model M590. Thermal analyses were carried out on a Mettler Toledo TGA/SDTA 851^e, DSC 822 ^{e} analyzer under a N_2 atmosphere with a heating and cooling rate of 10 °C/min. Cyclic voltammetry (CV) measurements were performed on an AUTOLAB/PGSTAT12 at room temperature with a three-electrode cell in a solution of $TBABF_4$ (0.10 M) in acetonitrile and with a scan rate of 50 mV/s. Polymer films were prepared by dipping platinum working electrodes into the polymer solutions and then drying in air. A platinum wire was used as a counter electrode and a Ag/Ag^+ electrode was used as a reference electrode.

2.3. Fabrication of Organic Thin-Film Transistor Devices. Organic thin-film transistor (OTFT) were fabricated using a bottom-contact geometry device (channel length L = 12 μm, and width, W = 120 μm). The source and drain contacts consisted of gold (100 nm), and the dielectric was silicon oxide (SiO_2) with a thickness of 300 nm. The SiO_2 surface was cleaned, dried, and pretreated with a solution of 10.0 mM octyltrichlorosilane (OTS-8) in toluene at room temperature for 2 h under a N_2 atmosphere to produce nonpolar and smooth surfaces onto which the polymers could be spin-coated. The polymers were dissolved to a concentration of 0.5 wt % in chlorobenzene. Films of the organic semiconductors were spin-coated at 1000 rpm for 50 s to a thickness of 60 nm. All device fabrication procedures and measurements were carried out in air at room temperature.

2.4. Fabrication of Photovoltaic Devices. Composite solutions (1:5 wt % ratio) of polymers and $PC_{71}BM$ were prepared using 1,2-dichlorobenzene as a solvent. The concentration was adequately controlled in the range 1.0−2.0 wt %. For the measurement of the optical absorption spectra of PCBM, the solutions were spun on precleaned UV-grade silica substrates. The polymer photovoltaic devices were fabricated with a typical sandwich structure of ITO/PEDOT:PSS/active layer/LiF or TiO_x/Al. The ITO coated glass substrates were cleaned through a routine cleaning procedure, including sonication in detergent followed by distilled water, acetone, and 2-propanol. A 45 nm thick layer of PEDOT:PSS (Baytron P) was spin-coated onto a cleaned ITO substrate after exposing the ITO surface to ozone for 10 min. The PEDOT:PSS layer was then baked on a hot plate at 140 °C for 10 min. The active layer was spin-coated from the predissolved composite solution after filtering through a 0.45 μm (PTFE) syringe filter. The device structure was completed by depositing 0.7 nm of LiF and a 100 nm Al cathode (to act as the top electrode) onto the polymer active layer under vacuum (3×10^{-6} Torr) in a thermal evaporator. Current density−voltage ($J-V$) characteristics of all polymer photovoltaic cells were measured under the illumination of simulated solar light with 100 mW/cm^2 (AM 1.5 G) by an Oriel 1000 W solar simulator. Electric data were recorded using a Keithley 236 source-measure unit, with all characterizations carried out in an ambient environment. The illumination intensity was calibrated by a standard Si photodiode detector (PV Measurements . Inc.) which had been calibrated at the NREL. The incident photon-to-current conversion efficiency (IPCE) was measured as a function of the wavelength in the range 360−800 nm by using a halogen lamp as the light source, where the calibration was performed using a silicon reference photodiode. Measurements were carried out after masking the fabricated device except the active cell area. All the characterization steps were carried out under ambient air conditions.

2.5. Synthesis of Monomers and Polymers. 2,7-Dibromo-9,9-dioctyl-9*H*-fluorene and 2,2′-(9,9-dioctyl-9*H*-fluorene-2,7-diyl)bis-(4,4,5,5-tetramethyl-1,3,2-dioxaborolane) were synthesized according to a previous report.[20]

Dibromo-9,9-dioctyl-9H-fluorene. ^{1}H NMR ($CDCl_3$, ppm): δ 7.52 (d, 1H). 7.50 (s, 1H), 7.44−7.47 (m, 3H), 7.43 (d, 1H), 1.99−1.95 (m, 4H), 1.31−1.29 (m, 24H), 0.98 (t, 6H). ^{13}C NMR ($CDCl_3$, ppm): δ 151.1, 141.8, 134.1, 130.5, 127.4, 125.1, 50.8, 44.3, 33.1, 30.2, 29.9, 29.1, 22.4, 14.8.

*2,2′-(9,9-Dioctyl-9H-fluorene-2,7-diyl)bis(4,4,5,5-tetramethyl-1,3,2-dioxaborolane) (**1**).* ^{1}H NMR ($CDCl_3$, ppm): δ 7.77 (d, 2H), 7.72 (d, 2H), 7.69 (s, 2H), 1.99−1.95 (m, 4H), 1.37 (s, 24H), 1.09−1.21 (m, 20H), 0.78 (t, 6H), 0.53 (m, 4H).^{13}C NMR ($CDCl_3$, ppm): δ 150.71, 144.14, 133.87, 130.90, 129.16, 119.58, 83.93, 55.40, 40.30, 32.00, 30.15, 29.41, 29.36, 25.16, 23.83, 22.80, 14.27. Anal. Calcd for $C_{41}H_{64}B_2O_4$:C, 76.64; H, 10.04; B, 3.36; O, 9.96. Found: C, 76.61; H, 10.01; B, 3.32; O, 9.89.

Synthesis of 4,7-Dibromobenzo[c][1,2,5]thiadiazole. A solution of bromine (35.21 g, 22.32 mmol) in 100 mL of HBr (48%) was slowly added dropwise to a solution of 10 g (73.44 mmol) of benzothiadiazole. After refluxing for 6 h, an orange solid precipitated was formed. The mixture was allowed to cool to room temperature, and a saturated solution of $NaHSO_3$ was then added to neutralize the residual Br_2. The mixture was filtered and exhaustively washed with water. The solid was then washed once with cold diethyl ether and purified by flash chromatography to give 20.51 g (95%) of compound **3**. ^{1}H NMR ($CDCl_3$, ppm): δ 7.73 (s, 2H). ^{13}C NMR ($CDCl_3$, ppm): δ 152.6, 132.1. 113.6.

Synthesis of 4,7-Di-2′-thienyl-2,1,3-benzothiadiazole. Tripropyl-(thiophen-2-yl)stannane (1.5 g, 11.7 mmol) was added to a stirred solution of 4,7-dibromo-2,1,3-benzothiadiazole (1.32 g, 4.5 mmol), and bis(triphenylphosphine)palladium(II) dichloride (95 mg, 0.09 mmol) in THF (50 mL). The mixture was refluxed overnight. The resulting mixture was extracted with ethyl acetate and brine. The organic layer was separated, dried with anhydrous $MgSO_4$ and the resulting solution was then concentrated by evaporation. A red solid (product yield 85%) was obtained by recrystallizing the crude product in methanol. ^{1}H NMR ($CDCl_3$, ppm): δ 7.84 (s, 2H), 7.43 (d, 2H), 7.21 (t, 2H), 6.61 (d, 2H) ^{13}C NMR ($CDCl_3$, ppm): δ 155.1, 142.8, 135.2, 129.1, 128.0, 127.9, 127.1.

*Synthesis of 4,7-Di-2′-(5′-bromo)-thienyl-2,1,3-benzothiadiazole (**2**).* *N*-Bromosuccinimide (2.05 g, 11.5 mmol) was added to a stirred solution of 4,7-di-2′-thienyl-2,1,3-benzothiadiazole (1.44 g, 4.8 mmol) in acetic acid (25 mL) in darkness. The mixture was stirred at room temperature for 36 h, and 2 M HCl was added to this mixture. The product was extracted with chloroform and the organic phase was successively washed with 10% sodium bisulfate, 2 M HCl and water before being dried over $MgSO_4$. The solvent was removed to afford a dark-red crystalline product (1.30 g, 59%) after recrystallization from chloroform. ^{1}H NMR ($CDCl_3$, ppm): δ 7.80 (dd, 4H), 7.13 (d, 2H) ^{13}C NMR ($CDCl_3$, ppm): δ 154.2, 140.8, 131.1, 129.6, 129.1, 128.0, 111.6. Anal. Calcd for $C_{14}H_6Br_2N_2S_3$: C, 36.70; H, 1.32; Br, 34.88; N, 6.11;S, 20.99. Found: C, 36.68; H, 1.28; Br, 34.78; N, 6.08; S, 20.88.

*Synthesis of 3,9-Dibromoperylene (**3**).* Bromine (8.81 g, 7.92 mmol) was added in darkness to a stirred solution of perylene (5 g, 19.81 mmol) in carbon tetrachloride (200 mL). The mixture was stirred at 110 °C for 12 h and 2 M HCl was added to the mixture. The product was extracted with chloroform and the organic phase was

successively washed with 10% sodium bisulfate, 2 M HCl and water before being dried over $MgSO_4$. The solvent was removed to afford dark-red crystals (2.81 g, 63%) that were recrystallized from hot hexane. ^{1}H NMR ($CDCl_3$, ppm): δ 8.21 (dd, 2H), 7.83 (dd, 2H), 7.80(dd, 2H), 7.40−7.37(m, 4H) ^{13}C NMR ($CDCl_3$, ppm): δ 118.0, 121.3, 124.1, 125.9, 126.9, 127.1, 128.2, 128.9, 130.1, 135.8. Anal. Calcd for $C_{20}H_{10}Br_2$: C, 58.55; H, 2.42; Br, 38.94. Found: C, 58.30; H, 2.30; Br, 38.66.

Synthesis of 2,2′-(9,9-Dioctyl-9H-fluorene-2,7-diyl)dithiophene (4). Compound **1** (7.3 g, 13.31 mmol),5-(4,4,5,5-tetramethyl-1,3,2-dioxaborolan-2-yl)thiophen-2-ylium (6.23 g, 29.28 mmol) and 50 mL of toluene were placed in two neck flasks under a N_2 atmosphere. Then 32 mL of a 2 M K_2CO_3 solution was injected, and $Pd(PPh_3)_4$ (0.46 g, 0.39 mmol) and Aliquat 336 (0.53 g, 1.33 mmol) were added to the solution. The solution was refluxed at 90 °C for 2 days. The reaction mixture was them cooled to room temperature. The reaction mixture was extracted with methylene chloride and brine and the solvent was evaporated. The mixture was purified by column chromatography using hexane to give a liquid product yield was of 75%. ^{1}H NMR ($CDCl_3$, ppm): δ 7.65 (d, 2H), 7.60 (d, 2H), 7.55 (s, 2H), 7.37 (d, 2H), 7.28 (d, 2H), 7.09 (t, 2H), 2.01 (t, 4H), 1.20 (m, 20H), 0.77 (t, 6H), 0.67 (m, 4H). ^{13}C NMR ($CDCl_3$, ppm): δ 149.1, 141.0, 140.7, 133.5, 131.2, 129.0, 128.8, 128.2, 127.3, 125.1, 53.8, 44.1, 32.1, 30.0, 29.5, 29.3, 24.3, 22.5, 13.9.

Synthesis of 2,2′-(5,5′-(9,9-Dioctyl-9H-fluorene-2,7-diyl)bis-(thiophene-5,2-diyl))bis(4,4,5,5-tetramethyl-1,3,2-dioxaborolane) (5). A *n*-BuLi solution in hexanes (11.26 mL, 2.0 M) was added at −70 °C to a solution of compound **4** (5 g, 9.01 mmol) in dry THF (150 mL). The mixture was stirred for 30 min at −70 °C, and 2-(4,4,5,5-tetramethyl-1,3,2-dioxaborolan-2-yloxy)propan-1-ylium (5.52 mL, 27.03 mmol) was then added at −70 °C. This mixture was allowed to reach room temperature overnight. The resulting mixture was extracted with methylene chloride and brine and then dried with anhydrous $MgSO_4$. After filtering, the solvent was evaporated, to provide a product yield of 56%. ^{1}H NMR ($CDCl_3$, ppm): δ 7.43−7.63 (m, 10H), 1.96 (t, 4H), 1.35 (s, 24H), 1.20 (m, 20H), 0.77 (t, 6H), 0.67 (m, 4H). ^{13}C NMR ($CDCl_3$, ppm): δ 152.14, 151.93, 140.68, 138.30, 133.24, 128.20, 125.19, 124.42, 120.73, 120.31, 84.30, 55.37, 40.52, 31.89, 30.11, 29.34, 29.28, 24.92, 23.87, 22.71, 14.20. Anal. Calcd for $C_{49}H_{68}B_2O_4S_2$: C,72.94; H,8.50; B,2.68; O,7.93;S,7.95. Found: C,72.89; H,8.42; B,2.55; O,7.89; S,7.81.

General Polymerization Procedure. Three copolymers were synthesized by Suzuki coupling polymerization.[21,22] The 2,2′-(9,9-dioctyl-9*H*-fluorene-2,7-diyl)bis(4,4,5,5-tetramethyl-1,3,2-dioxaborolane), 2,2′-(5,5′-(9,9-dioctyl-9*H*-fluorene-2,7-diyl)bis(thiophene-5,2-diyl))bis(4,4,5,5-tetramethyl-1,3,2-dioxaborolane), and 4,7-di-2′-(5′-bromo)-thienyl-2,1,3-benzothiadiazole, 3,9-dibromoperylene monomers were synthesized according to previous reports. The reaction mixture of 2 M K_2CO_3 (8 mL), tetrakis(triphenylphosphine)palladium (0.06 g), and Aliquat 336 (0.07 g) in 15 mL of anhydrous toluene was stirred at 90 °C for 3 days. Following this an excess amount of 1-bromobenzene and phenylboronic acid (the end-capper) was dissolved in 1 mL of anhydrous toluene and stirred continuously for 12 h. The reaction mixture was cooled to approximately 50 °C and 200 mL of methanol was added slowly with vigorous stirring of the reaction mixture. The polymer fibers were collected by filtration and reprecipitation from methanol and acetone. The polymers were then purified further by washing for 2 days in a Soxhlet apparatus, with acetone used to remove oligomers and catalyst residues. Column chromatography with a chloroform solution was then performed on the polymer. The reprecipitation procedure in chloroform/methanol was then repeated several times. The resulting polymers were soluble in common organic solvents.

Poly[2,7-(9,9′-dioctylfluorene)-alt-5,5′-(4′,7′-di-2-thienyl-2′,1′,3′-benzothiadiazole)] (PFDTBT). 2,2′-(9,9-Dioctyl-9*H*-fluorene-2,7-diyl)-bis(4,4,5,5-tetramethyl-1,3,2-dioxaborolane) (0.5 g, 0.78 mmol) was mixed with 4,7-di-2′-(5′-bromo)thienyl-2,1,3-benzothiadiazole (0.40 g, 0.87 mmol, 1.1 equiv), tetrakis(triphenylphosphine)palladium (3.0 mg, 2.6 μmol), and toluene (10 mL) for this polymerization. ^{1}H NMR ($CDCl_3$, ppm): δ 8.12−7.44 (12H), 1.96 (4H), 1.35−0.67 (30H). Found: C, 70.98; H, 6.17; N, 4.86; S, 20.16.

Poly[2,7-(9,9′-dioctylfluorene)-co-5,5′-(4′,7′-di-2-thienyl-2′,1′,3′-benzothiadiazole)-co-3″,9″-perylene] (PFDTBT_5Per). 2,2′-(9,9-Dioctyl-9*H*-fluorene-2,7-diyl)bis(4,4,5,5-tetramethyl-1,3,2-dioxaborolane) (0.5 g, 0.78 mmol) was mixed with 4,7-di-2′-(5′-bromo)thienyl-2,1,3-benzothiadiazole (0.32 g, 0.691 mmol, 0.9 equiv), 3,6-dibromoperylene(0.032 g, 0.078 mmol, 0.1 equiv), tetrakis-(triphenylphosphine)palladium (3.0 mg, 2.6 μmol), and toluene (10 mL) for this polymerization. ^{1}H NMR ($CDCl_3$, ppm): δ 8.22−7.44 (∼22H), 1.96 (4H), 1.35−0.67 (∼30H). Found: C, 75.47; H, 6.78; N, 3.41; S, 14.99.

Poly[2,7-(9,9′-dioctylfluorene)-co-5,5′-(4′,7′-di-2-thienyl-2′,1′,3′-benzothiadiazole)-co-3″,9″-perylene] (PFDTBT_10Per). 2,2′-(9,9-Dioctyl-9*H*-fluorene-2,7-diyl)bis(4,4,5,5-tetramethyl-1,3,2-dioxaborolane) (0.5 g, 0.78 mmol) was mixed with 4,7-di-2′-(5′-bromo)thienyl-2,1,3-benzothiadiazole (0.28 g, 0.62 mmol, 0.8 equiv), 3,6-dibromoperylene(0.06 g, 0.14 mmol, 0.2 equiv), tetrakis-(triphenylphosphine)palladium (3.0 mg, 2.6 μmol) and toluene (10 mL) for this polymerization. ^{1}H NMR ($CDCl_3$, ppm): δ 8.22−7.44 (∼22H), 1.96 (4H), 1.35−0.67 (∼30H). Found: C, 76.29; H, 6.38; N, 3.78; S, 16.19.

Poly[2,7-(9,9′-dioctylfluorene)-co-5,5′-(4′,7′-di-2-thienyl-2′,1′,3′-benzothiadiazole)-co-3″,9″-perylene] (PFDTBT_20Per). 2,2′-(9,9-Dioctyl-9*H*-fluorene-2,7-diyl)bis(4,4,5,5-tetramethyl-1,3,2-dioxaborolane) (0.5 g, 0.78 mmol) was mixed with 4,7-di-2′-(5′-bromo)thienyl-2,1,3-benzothiadiazole (0.24 g, 0.35 mmol, 0.6 equiv), 3,6-dibromoperylene(0.09 g, 0.31 mmol, 0.4 equiv), tetrakis-(triphenylphosphine)palladium (3.0 mg, 2.6 μmol), and toluene (10 mL) for this polymerization. ^{1}H NMR ($CDCl_3$, ppm): δ 8.22−7.44 (∼22H), 1.96 (4H), 1.35−0.67 (∼30H). Found: C, 77.28; H, 5.98; N, 3.31; S, 13.65.

Poly[2,2′-(9,9-dioctylfluorene-2,7-diyl)dithiophene-alt-5,5′-(4′,7′-di-2-thienyl-2′,1′,3′-benzothiadiazole)] (PFD2TBT). 2,2′-(5,5′-(9,9-Dioctyl-9*H*-fluorene-2,7-diyl)bis(thiophene-5,2-diyl))bis(4,4,5,5-tetramethyl-1,3,2-dioxaborolane) (0.5 g, 0.61 mmol) was mixed with 4,7-di-2′-(5′-bromo)thienyl-2,1,3-benzothiadiazole (0.34 g, 0.74 mmol, 1.2 equiv) tetrakis(triphenylphosphine)palladium (3.0 mg, 2.6 μmol), and toluene (10 mL) for this polymerization. ^{1}H NMR ($CDCl_3$, ppm): δ 8.18−7.44 (∼16H), 1.96 (4H), 1.35−0.67 (∼30H). Found: C, 66.82; H, 5.08; N, 3.30; S, 22.76.

Poly(2,2′-(9,9-dioctyl-9H-fluorene-2,7-diyl)dithiophene-co-5,5′-(4′,7′-di-2-thienyl-2′,1′,3′-benzothiadiazole)-co-3″,9″-(perylene)) (PFD2TBT_5Per). 2,2′-(5,5′-(9,9-Dioctyl-9*H*-fluorene-2,7-diyl)bis-(thiophene-5,2-diyl))bis(4,4,5,5-tetramethyl-1,3,2-dioxaborolane) (0.5 g, 0.61 mmol) was mixed with 4,7-di-2′-(5′-bromo)thienyl-2,1,3-benzothiadiazole (0.25 g, 0.54 mmol, 0.9 equiv), 3,6-dibromoperylene (0.025 g, 0.06 mmol, 0.1 equiv), tetrakis(triphenylphosphine) palladium (3.0 mg, 2.6 μmol), and toluene (10 mL) for this polymerization. ^{1}H NMR ($CDCl_3$, ppm): δ 8.21−7.44 (∼26H), 1.96 (4H), 1.35−0.67 (∼30H). Found: C, 68.65; H, 5.46; N, 3.01; S, 23.12.

Poly[2,2′-(9,9-dioctylfluorene-2,7-diyl)dithiophene-co-5,5′-(4′,7′-di-2-thienyl-2′,1′,3′-benzothiadiazole)-co-3″,9″-perylene] (PFD2TBT_10Per). 2,2′-(5,5′-(9,9-Dioctyl-9*H*-fluorene-2,7-diyl)bis-(thiophene-5,2-diyl))bis(4,4,5,5-tetramethyl-1,3,2-dioxaborolane) (0.5 g, 0.61 mmol) was mixed with 4,7-di-2′-(5′-bromo)-thienyl-2,1,3-benzothiadiazole (0.22 g, 0.49 mmol, 0.8 equiv), 3,6-dibromoperylene (0.05 g, 0.12 mmol, 0.2 equiv), tetrakis(triphenylphosphine)palladium (3.0 mg, 2.6 μmol), and toluene (10 mL) for this polymerization. ^{1}H NMR ($CDCl_3$, ppm): δ 8.21−7.44 (∼26H), 1.96 (4H), 1.35−0.67 (∼30H). Found: C, 73.40; H, 5.94; N, 2.41; S, 20.91.

3. RESULTS AND DISCUSSION

3.1. Synthesis and Characterization of Polymers. The synthesis of the polymers was carried out using palladium-catalyzed Suzuki coupling reactions between dibromoaryl and diborolanylaryl monomers (Schemes 1 and 2). The synthesized polymers were soluble in common organic solvents such as chloroform, chlorobenzene, and toluene, and the polymer

solutions formed uniform thin films after spin-coating. The number-average molecular weights (M_n) of the synthesized polymers were determined by GPC using polystyrene as a standard. PFDTBT showed a relatively low molecular weight but other synthesized polymers including PFD2TBT gave number-average molecular weights higher than 10 000 g/mol with polydispersity index (PDI = M_w/M_n) ranging from 1.86 to 3.49. The actual compositions of the polymers were determined by elemental analysis using the sulfur contents as the standard. The actual compositions of the copolymers were not the same as the feed ratios but we found that the differences were not significant.

3.2. Thermal Properties. The thermal properties of the polymers were investigated by using thermo-gravimetric analysis (TGA) and a differential scanning calorimeter (DSC). PFDTBT-based polymers showed better thermal stability than PFD2TBT-based polymers. Moreover, PFDTBT-based polymers exhibited good thermal stability, losing less than 5% of their weight upon heating to temperatures greater than 400 °C. The thermally induced phase-transition behavior of the polymers was investigated by using a DSC under a N_2 atmosphere. The glass transition temperatures (T_g) of the polymers were in the range 105−161 °C and were found to be dependent on the polymer structure. PFD2TBT-based polymers showed higher glass transition temperatures than PFDTBT-based polymers, and as the perylene contents in the copolymers increased, the polymer gave a higher glass transition temperature. No synthesized polymer showed any crystalline temperature (T_c), except PFDTBT_20Per. The value of T_c for PFDTBT_20Per was 191 °C. TGA thermograms of the polymers and DSC curve of PFDTBT_20Per are shown in Figure 1. Molecular weights and thermal properties of the synthesized polymers are summarized in Table 1.

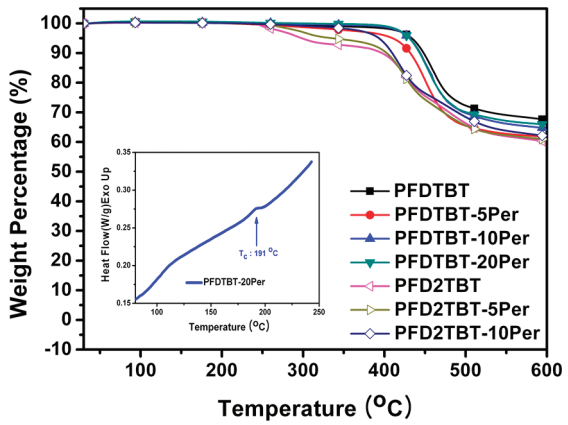


Figure 1. TGA thermograms of polymers and DSC curve of PFDTBT_20Per.

3.3. Optical Properties. The UV−visible absorption spectra of the synthesized polymers were recorded in both chloroform solution and as a solid thin film. PFDTBT and the *ter*-polymer solutions exhibited two distinct absorption bands, where the first absorption peak is at around 387 nm, corresponding to the $\pi-\pi^*$ transition of the conjugated polymer backbone,[23,24] and the second absorption band in the longer wavelength region at around 530 nm, can be attributed to the strong internal charge-transfer (ICT) interaction between donating and accepting groups in the main chain.[21] Peak and edge positions were almost equivalent for PFDTBT, PFDTBT_5Per and PFDTBT_10Per, but the maximum absorption peak for PFDTBT_20Per moved to a shorter wavelength region. This might be due to a decrease in the internal charge- transfer (ICT) interaction cause by a decreased content of electron-withdrawing DTBT monomer in the copolymer. PFD2TBT and the *ter*-polymer solutions also exhibited two absorption bands at around 410 and 520 nm. The absorption maxima and edges of the polymer solutions showed little dependence upon perylene contents. The UV−visible absorption spectra of the synthesized polymers in a chloroform solution are shown in Figure 2.

The polymer thin films showed a similar absorption trend; however, the films showed increasingly larger redshifts in absorption than those for the solution as shown in Figure 3. A strong interchain interaction between polymer chains in the solid state would result in the red-shifting of the absorption peak and the onset. Optical band-gaps of the polymers were obtained from the absorption onsets of the polymer films. The measured optical band gaps of the copolymers were in the range 1.95−1.82 eV.

3.4. Electrochemical Properties. Electrochemical cyclic voltammetry (CV) was employed to investigate the redox behavior of the polymers and to determine their HOMO and LUMO energy levels.[25] CV was performed under an Ar atmosphere in a solution of $TBABF_4$ (0.10 M) in acetonitrile at a scan rate of 50 mV/s and room temperature. A platinum plate was used as a working electrode. A platinum wire was used as the counter electrode, and a $Ag/AgNO_3$ electrode was used as the reference electrode. The HOMO energy level was determined by using oxidation onsets (E_{ox}) of the polymer films.[26] The LUMO energy levels of the polymers were determined by combining the HOMO energy levels obtained from CV and the optical bandgap energies obtained from the edges of absorption.[26] To obtain the oxidation potentials of the polymer films, the reference electrode was calibrated using a ferrocene/ferrocenium (Fc/Fc^+) salt couple, whose redox potential is assumed to have an absolute energy level of −4.80 eV in a vacuum.[26] The potential of this external standard determined under the same conditions was 0.4 eV. As a result, the HOMO energy values were calculated using the equation $E_{HOMO} = -(E_{ox}^{onset} + 4.4)$ eV, where E_{ox}^{onset} is the onset oxidation potential vs Ag/Ag^+.

The HOMO energy levels of PFDTBT, PFD2TBT, and the *ter*-polymers were determined to lie in the range from −5.58 to −5.41 eV. Optical band gap energies show little change with by changing perylene unit ratios, but the HOMO energy levels of the polymers were moved slightly toward higher positions with the introduction of perylene units, as illustrated in Figure 4. This arises from the result of a decrease in the contents of high electron affinity DTBT units as the number of perylene units in the polymers increased.[27] The UV−visible absorption spectra, optical band-gaps, and HOMO/LUMO energy levels of the polymers are summarized in Table 2.

3.5. TFT Characteristics of the Polymer Thin Films. To measure the field effect mobility of the charge carriers, OTFT were fabricated on a silicon wafer using a bottom contact geometry (channel length L = 12 μm, and width, W = 120 μm) under nitrogen. The TFT devices of the polymers exhibited typical *p*-channel transistor characteristics. Figure 5 shows the transfer curves of the devices fabricated using the polymers as the active layer. The field-effect mobility was calculated in the saturation regime using the following equation: $I_{ds} = (W/$

dx.doi.org/10.1021/ma202712r | Macromolecules 2012, 45, 2367−2376

Table 1. Average Molecular Weights and Thermal Properties of the Synthesized Polymers

polymer	polymer yield (%)	M_n[a] (g/mol)	M_w[a] (g/mol)	PDI[a]	T_d[b] (°C)	T_g[c] (°C)	ratio (perylene mol %) feed ratio	ratio (perylene mol %) actual ratio[d]
PFDTBT	72	4500	7900	1.8	434	105	–	–
PFDTBT_5Per	78	14 000	50 000	3.5	408	110	5.0	2.8
PFDTBT_10Per	69	12 000	32 000	2.7	430	124	10.0	11.4
PFDTBT_20Per	58	11 000	33 000	3.0	431	128	20.0	17.3
PFD2TBT	71	16 000	36 000	2.3	300	154	–	–
PFD2TBT_5Per	73	12 000	39 000	3.3	332	158	5.0	6.1
PFD2TBT_10Per	65	11 000	30 000	2.7	392	161	10.0	13.3

[a]M_n, M_w, and PDI of the polymers were determined by gel permeation chromatography using polystyrene standards in $CHCl_3$. [b]Temperature at 5% weight loss by a heating rate of 10 °C/min under nitrogen. [c]Determined by DSC at a heating rate of 10 °C/min under nitrogen. [d]Calculated by elemental analysis through the amount of sulfur contained in copolymers as a standard.

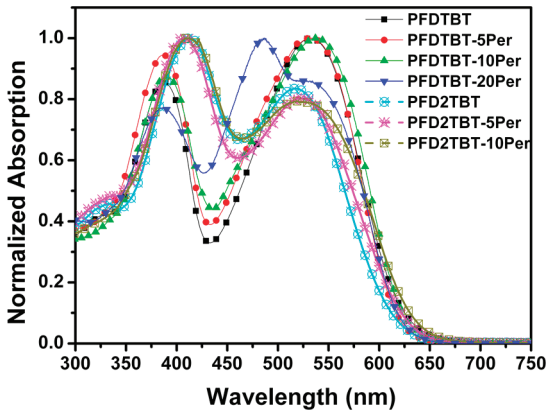


Figure 2. UV−visible absorption spectra of the polymers in chloroform solution.

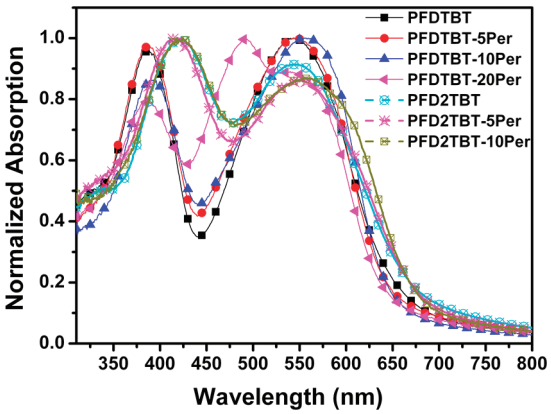


Figure 3. UV−visible absorption spectra of the polymer thin films.

$2L)\mu C_i(V_{gs} - V_{th})^2$, where I_{ds} is the drain-source current in the saturated region, W and L are the channel width and length, respectively, μ is the field-effect mobility, C_i is the capacitance per unit area of the insulating layer, and V_{gs} and V_{th} are the gate and threshold voltages, respectively.[28,29] Interestingly, the field-effect mobility increased with an increase in the number of perylene units in the corresponding parent polymers. The field-effect mobility for PFDTBT, PFDTBT-5Per, PFDTBT-10Per, and PFDTBT-20Per was determined to be 1.0×10^{-4}, 1.2×10^{-4}, 5.3×10^{-4}, and 1.2×10^{-3} $cm^2/(V\ s)$, respectively. Similarly, the measured field-effect mobility of PFD2TBT, PFD2TBT-5Per, and PFD2TBT-10Per was 2.7×10^{-6}, 1.1×10^{-5}, and 2.1×10^{-5} $cm^2/(V\ s)$, respectively. This result suggests that the introduction of the flat perylene structure to PFDTBT and PFD2TBT plays an important role in increasing the carrier mobility, possibly due to the enhanced interchain $\pi-\pi$ interaction. The characteristics of the TFTs using the polymers as the active layers are summarized in Table 3.

3.6. Photovoltaic Properties. Photovoltaic devices were fabricated using PFDTBT, PFD2TBT and the *ter*-polymers as p-type electron donors and by using [6,6]-phenyl C_{71}-butyric acid methyl ester ($PC_{71}BM$) as an n-type acceptor. Two different types of photovoltaic devices were fabricated and characterized, with the device structures of ITO/PEDOT:PSS/polymer:$PC_{71}BM$/LiF/Al and ITO/PEDOT:PSS/polymer:$PC_{71}BM$/TiO_x/Al shown in Figure 6. The solution-processable titanium suboxide (TiO_x) layer was employed as an optical spacer[30,31] and as a hole blocker[27] between the bulk heterojunction(BHJ) layer and the top metal electrode.

Figure 7 shows the current−voltage ($J-V$) characteristics of the ITO/PEDOT:PSS/polymer:$PC_{71}BM$/LiF/Al devices. It can be observed that the open circuit voltages of cells fabricated using PFDTBT and its *ter*-polymers range from 0.70 to 0.77 V. The device fabricated using PFDTBT showed higher open circuit voltages than those of perylene-containing copolymers. This coincides with the relative HOMO energy levels of the polymers. As the perylene content in the copolymers increased, the amount of DTBT contents decreased, and so the HOMO of the polymers moved to higher energy levels. PFDTBT has the deepest HOMO energy level, thus it showed the highest open circuit voltage (0.77 V). It is also noteworthy that, the short circuit current of the devices increased with an increase in the number of perylene units in the polymer, except for the case of PFDTBT_20Per. Even though PFDTBT_20Per showed the highest hole mobility among the PFDTBT-based copolymers, it is UV−visible absorption spectrum showed greater blue-shifting than PFDTBT, as shown in Figures 2 and 3, and it showed the widest band gap energy among all of the polymers considered herein. This may be why the short circuit current of the device fabricated using PFDTBT_20Per is lower than that of PFDTBT, despite it higher mobility. The device fabricated using PFDTBT-10Per showed the best photovoltaic performance among the PFDTBT-based polymers (V_{oc} = 0.74 V, J_{sc} = 7.19 mA/cm^2, PCE = 2.16%). For the photovoltaic devices fabricated using PFD2TBT-based polymers, the short-circuit currents of the devices also increased as the perylene content in the copolymers increased; however, the PCEs of the devices using PFD2TBT-based polymers were lower than those of PFDTBT-based polymers because of lower open-circuit voltages and short-circuit currents. The device fabricated using PFD2TBT_10Per showed the highest PCE (1.51%) among the PFD2TBT-based polymers. The characteristics of the ITO/

dx.doi.org/10.1021/ma202712r | *Macromolecules* 2012, 45, 2367−2376

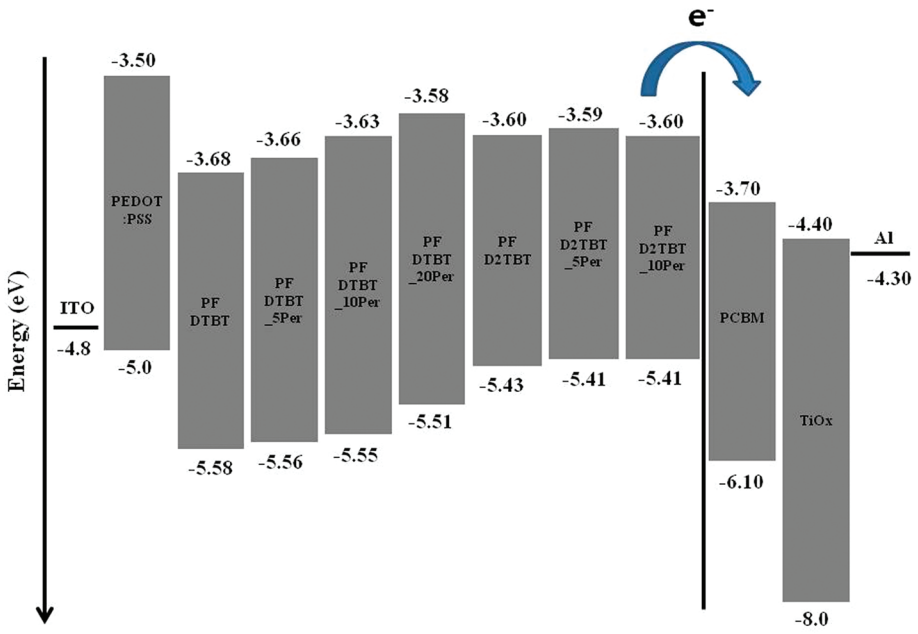


Figure 4. Band diagram for $PC_{71}BM$ and the synthesized polymers.

Table 2. Optical and Electrochemical Properties of the Synthesized Polymers

	$\lambda_{max,\ abs}$ (nm)		λ_{onset} (nm)			
polymers	solution[a]	film[b]	film[b]	optical E_g^{opt} (eV)[c]	HOMO (eV)	LUMO (eV)
PFDTBT	387, 531	387, 543	652	1.90	−5.58	−3.68
PFDTBT_5Per	385, 534	387, 545	650	1.90	−5.56	−3.66
PFDTBT_10Per	387, 537	390, 558	645	1.92	−5.55	−3.63
PFDTBT_20Per	387, 487	385, 522	642	1.93	−5.51	−3.58
PFD2TBT	412, 518	422, 547	675	1.83	−5.43	−3.60
PFD2TBT_5Per	406, 524	416, 550	679	1.82	−5.41	−3.59
PFD2TBT_10Per	409, 527	420, 560	682	1.81	−5.41	−3.60

[a] 1×10^{-5} M in anhydrous chloroform. [b] Polymer film on a quartz plate by spin-casting from a solution in chloroform at 1500 rpm for 30 s. [c] Calculated from the absorption band edge of the copolymer films.

PEDOT:PSS/polymer:$PC_{71}BM$/LiF/Al devices are summarized in Table 4.

Figure 8 shows that the $J-V$ characteristics of ITO/PEDOT:PSS/polymer:$PC_{71}BM$/TiO_x/Al devices provide a similar trend to those of ITO/PEDOT:PSS/polymer:$PC_{71}BM$/LiF/Al devices but their PCEs increased mainly due to increased short circuit currents. The increase in the short circuit current originates from the introduction of the thin titanium suboxide (TiO_x) layer (ca. ∼10 nm). The titanium suboxide layer could block holes to the aluminum electrode, thus it could increase the short circuit current of the photovoltaic device. The device fabricated using PFDTBT-10Per showed the highest PCE of 3.16% with an open circuit voltage of 0.81 V, a short circuit current of 9.61 mA/cm^2 and the highest fill factor (0.41) among the fabricated devices. The characteristics of the ITO/PEDOT:PSS/polymer:$PC_{71}BM$/TiO_x/Al devices are summarized in Table 5.

Figure 9 shows the incident photon-to-current conversion efficiency (IPCE) spectra of the ITO/PEDOT:PSS/PFDTBT-10Per + $PC_{71}BM$/LiF and TiO_x/Al devices. The absorption onset corresponding to the photon-to-current conversion efficiency was about 750 nm for these devices, and the absorption onset values corresponding to the maximum conversion efficiency values were 427 and 560 nm.

The morphologies of the polymers and $PC_{71}BM$ blend films were observed by tapping-mode atomic force microscopy (AFM). Figure 10 shows the AFM images of the polymer:$PC_{71}BM$ (1:5 wt %) films, which were taken after removal of the Al electrode and after device fabrication. The Al electrode was removed by dipping the devices for 1 min in a mixed acid solution containing of 16 mL of concentrated phosphoric acid, 1 mL of concentrated hydrochloric acid, 1 mL of acetic acid, and 2 mL of D_2O. The blend films showed almost equivalently measured smooth surfaces (according to their root-mean-square (rms) roughness) with small degrees of phase separation. The rms roughness of the active layers were 0.49 nm for PFDTBT, 0.44 nm for PFDTBT-10Per, 0.51 nm for PFD2TBT, and 0.50 nm for PFD2TBT-10Per, respectively. This result suggests that the morphologies of all the active films are very similar, so that such a property will not affect the J_{sc} of the photovoltaic devices. Therefore, the improvement of PCE and J_{sc} in the fabricated photovoltaic devices is derived from the enhanced $\pi-\pi$ interaction between polymers that results from the introduction of perylene units.

4. CONCLUSIONS

We introduced perylene units into PFDTBT and PFD2TBT to enhance the interchain $\pi-\pi$ interaction. The optical and electrochemical properties of the synthesized copolymers

dx.doi.org/10.1021/ma202712r | Macromolecules 2012, 45, 2367−2376

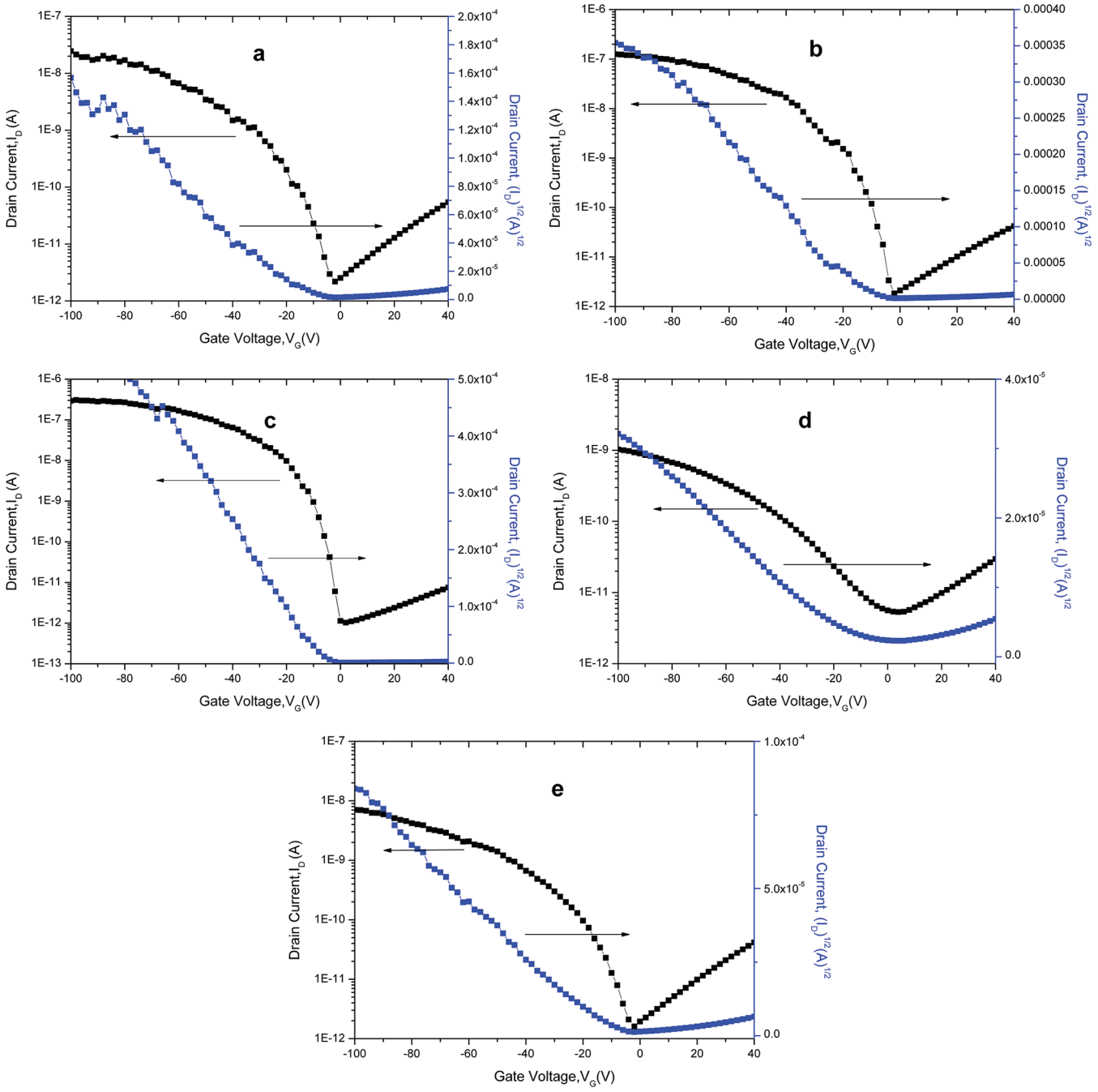


Figure 5. Transfer characteristics of OTFTs fabricated using the copolymers as the active layer at a constant source-drain voltage of −80 V. (a) PFDTBT, (b) PFDTBT-10Per, (c) PFDTBT-20Per, (d) PFD2TBT, and (e) PFD2TBT-10Per.

Table 3. Summary of the characteristics of OTFTs fabricated using the polymers as the active layers

polymer	Mobility ($cm^2/(V\ s)$)	I_{on}/I_{off}
PFDTBT	1.0×10^{-4}	1×10^4
PFDTBT-5Per	1.2×10^{-4}	1×10^4
PFDTBT-10Per	5.3×10^{-4}	1×10^5
PFDTBT-20Per	1.2×10^{-3}	2×10^5
PFD2TBT	2.7×10^{-6}	6×10^2
PFD2TBT-5Per	1.1×10^{-5}	1×10^3
PFDTBT-10Per	2.1×10^{-5}	5×10^3

showed were slight modification upon perylene addition. Interestingly, the field-effect mobility of the TFTs, using the

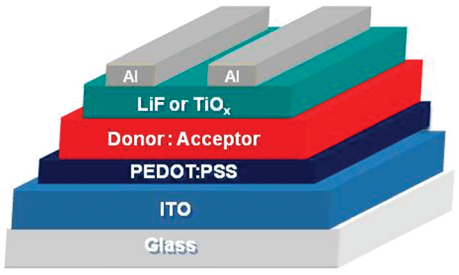


Figure 6. Structure of photovoltaic devices fabricated using the polymers.

dx.doi.org/10.1021/ma202712r | *Macromolecules* 2012, 45, 2367−2376

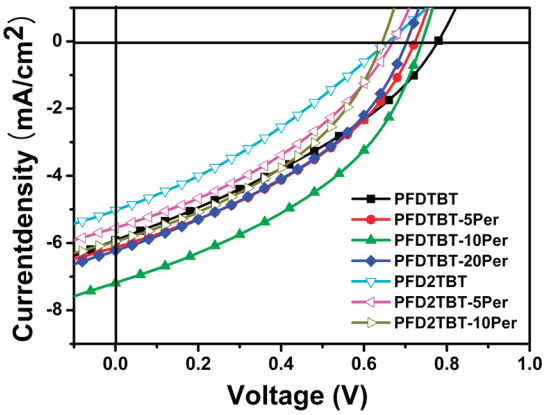


Figure 7. $J-V$ characteristics of the photovoltaic devices with ITO/PEDOT:PSS/polymer+$PC_{71}BM$ (1:5)/LiF/Al configuration.

Table 4. Summary of the Characteristics of Photovoltaic Devices with ITO/PEDOT:PSS/Polymer + $PC_{71}BM$ (1:5)/LiF/Al Configuration

polymer	V_{oc} (V)	J_{sc} (mA/cm^2)	FF (%)	PCE (%)
PFDTBT	0.77	5.92	0.34	1.56
PFDTBT_5Per	0.72	6.13	0.38	1.69
PFDTBT_10Per	0.74	7.19	0.40	2.16
PFDTBT_20Per	0.70	6.23	0.38	1.67
PFD2TBT	0.65	5.02	0.31	1.03
PFD2TBT_5Per	0.67	5.54	0.36	1.35
PFD2TBT_10Per	0.64	5.95	0.39	1.51

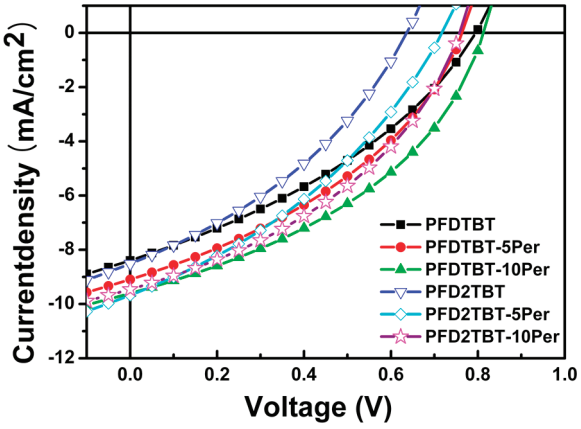


Figure 8. $J-V$ characteristics of the photovoltaic devices with ITO/PEDOT:PSS/polymer + $PC_{71}BM$(1:5)/TiOx/Al configuration.

Table 5. Summary of the Characteristics of Photovoltaic Devices with ITO/PEDOT:PSS/Polymer + $PC_{71}BM$(1:5)/TiO_x/Al Configuration

polymer	V_{oc} (V)	J_{sc} (mA/cm^2)	FF (%)	PCE (%)
PFDTBT	0.79	8.40	0.35	2.35
PFDTBT_5Per	0.76	9.09	0.38	2.64
PFDTBT_10Per	0.81	9.61	0.41	3.16
PFD2TBT	0.64	8.52	0.35	1.92
PFD2TBT_5Per	0.72	9.46	0.36	2.46
PFD2TBT_10Per	0.76	9.68	0.38	2.82

polymers as the active layer increased with an increasing perylene content in the copolymers. The short circuit currents of the photovoltaic devices fabricated using the polymers as an electron donor, also increased as the perylene content in the copolymers increased, which is consistent with the field-effect mobility results of the polymers. We conclude that the introduction of perylene to the conjugated polymer chain enhances the $\pi-\pi$ interaction between polymer chains and improves its charge-transport ability, leading to increases short circuit currents in the photovoltaic devices.

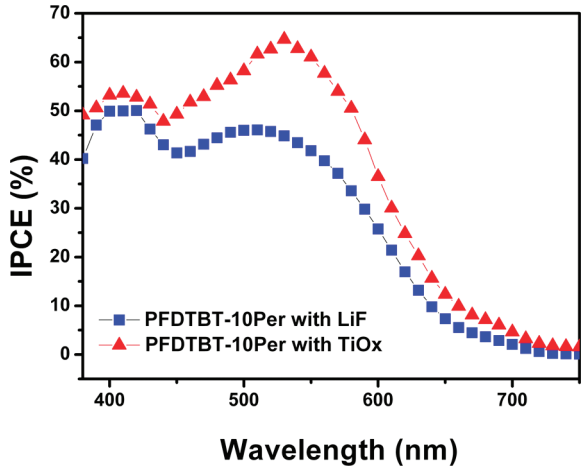


Figure 9. Incident photon-to-current efficiency (IPCE) spectra of the two different structured devices using PFDTBT-10Per.

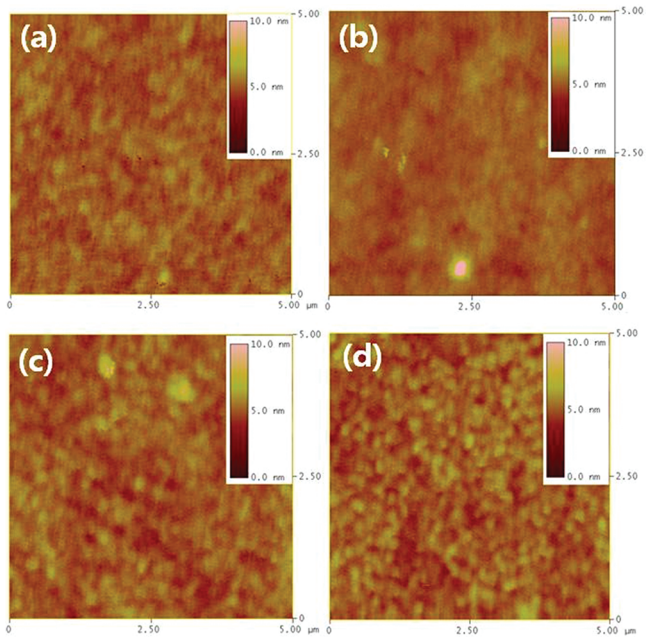


Figure 10. AFM topography images (5 × 5 μm) of active composite films of (a) PFDTBT:$PC_{71}BM$(1:5), (b) PFDTBT-10Per:$PC_{71}BM$-(1:5), (c) PFD2TBT:$PC_{71}BM$(1:5), and (d) PFD2TBT-10Per:$PC_{71}BM$(1:5).

AUTHOR INFORMATION

Corresponding Author

*E-mail: dohoonhwang@pusan.ac.kr.

Notes

The authors declare no competing financial interest.

■ ACKNOWLEDGMENTS

This research was financially supported by the Ministry of Knowledge Economy (MKE) under the New & Renewable Energy Program through a KETEP grant (No. 20103020010050 and No. 2011T100200034), and by the National Science Foundation (NRF) grant funded by the Korean government (MEST) (No. 2011-0011122) through GCRC-SOP (Grant 2011-0030668).

■ REFERENCES

(1) Sariciftci, N. S.; Braun, D.; Zhang, C.; Srdanov, V. I.; Heeger, A. J.; Stucky, G.; Wudl, F. *Appl. Phys. Lett.* **1993**, *62*, 585.
(2) Greenham, N. C.; Moratti, S. C.; Bradley, D. D. C.; Friend, R. H.; Holmes, A. B. *Nature* **1993**, *365*, 628.
(3) Dang, T. T. M.; Park, S −J.; Park, J.−W.; Chung, D.−S.; Park, C. E.; Kim, Y.−H.; Kwon, S.−K. *J. Polym. Sci., Part A: Polym. Chem.* **2007**, *45*, 5277.
(4) Peng, Q.; Liu, X.; Su, D.; Fu, G.; Xu, J.; Dai, L. *Adv. Mater.* **2011**, *23*, 4554.
(5) Zhang, M.; Fan, H.; Guo, X.; He, Y.; Zhang, Z.−G.; Min, J.; Zhang, J.; Zhao, G.; Zhan, X.; Li, Y. *Macromolecules* **2010**, *43*, 8714.
(6) Huo, L.; Guo, X.; Zhang, S.; Li, Y.; Hou., J. *Macromolecules* **2011**, *44*, 4035.
(7) Li, H.; Tam, T. L.; Lam, Y. M.; Mhaisalkar, S. G.; Grimsdale, A. C. *Org. Lett.* **2011**, *13*, 46.
(8) Mühlbacher, D.; Scharber, M.; Morana, M.; Zhu, Z.; Waller, D.; Gaudiana, R.; Brabec, C. *Adv. Mater.* **2006**, *18*, 2884.
(9) Zhu, Z.; Waller, D.; Gaudiana, R.; Morana, M.; Mühlbacher, D.; Scharber, M.; Brabec, C. *Macromolecules* **2007**, *40*, 1981.
(10) Svensson, M.; Zhang, F.; Veenstra, S. C.; Verhees, W. J. H.; Hummelen, J. C.; Kroon, J. M.; Inganas, O.; Andersson, M. R. *Adv. Mater.* **2003**, *15*, 988.
(11) Chen, M,-H.; Hou, J.; Hong, Z.; Yang, G.; Sista, S.; Chen, L,-M.; Yang, Y. *Adv. Mater.* **2009**, *21*, 4238.
(12) Zeng, W. L.; Yu, S. J.; Chua, W. H. *Macromolecules* **2002**, *35*, 6907.
(13) Yu, W.-L.; Pei, J.; Huang, W.; Heeger, A. J. *Adv. Mater.* **2000**, *12*, 828.
(14) Lee, J.-H.; Hwang, D.-H. *Chem. Commun.* **2003**, *22*, 2836.
(15) Grimsdale, A. C. *Curr. Org. Chem.* **2010**, *14*, 2196.
(16) Ferenczi, T. A. M.; Sims, M.; Bradley, D. D. C. *J. Phys.: Condens. Matter.* **2008**, *20*, 045220.
(17) Landis, C. A.; Parkin, S. R.; Anthony, J. E. *Jpn. J. Appl. Phys.* **2005**, *44*, 3921.
(18) Pandey, M. D.; Mishra, A. K.; Chandrasekhar, V.; Verma, S. *Inorg. Chem.* **2010**, *49*, 2020.
(19) Seo, Y. J.; Lee, I. J.; Yi, J. W.; Kim, B. H. *Chem. Commun.* **2007**, 2817.
(20) Park, M,-J.; Lee, J.; Jung, I.-H.; Park, J,-H.; Hwang, D.-H.; Shim, H,-K. *Marcromolecules* **2008**, *41*, 9643.
(21) Ranger, M.; Rondeau, D.; Leclerc, M. *Marcromolecules* **1997**, *30*, 7686.
(22) Miyaura, N.; Suzuki, A. *Chem. Rev.* **1995**, *95*, 2457.
(23) Ranger, M.; Leclerc, M. *Macromolecules* **1999**, *32*, 3306.
(24) Huang, F.; Chen, K.-S.; Yip, H.-L.; Hau, S. K.; Acton, O.; Zhang, Y.; Luo, J.; Jen, A. K. Y. *J. Am. Chem. Soc.* **2009**, *131*, 13886.
(25) Zhang, Z.-G.; Zhang, K.-L.; Liu, G.; Zhu, C.-X.; Neoh, K.-G.; Kang, E.−T. *Macromolecules* **2009**, *42*, 3104.
(26) Leriche, P.; Frere, P.; Cravino, A.; Aleveque, O.; Roncali, J. *J. Org. Chem.* **2007**, *72*, 8332.
(27) Li, Y.; Xu, B.; Li, H.; Cheng, W.; Xue, L.; Chen, F.; Lu, H.; Tian, W. *J. Phys. Chem. C.* **2011**, *115*, 2386.
(28) Shaw, J. M.; Seidler, P. F. *IBM J. Res. Dev.* **2001**, *45*, 3.
(29) Dimitrakopoulos, C. D.; Mascaro, D. J. *IBM J. Res. Dev.* **2001**, *45*, 11.
(30) Kim, J. Y.; Kim, S. H.; Lee, H.-H.; Lee, K.; Ma, W.; Gong, X. *Adv. Mater.* **2006**, *18*, 572.
(31) Park, S. H.; Roy, A.; Beaupre, S.; Cho, S.; Coates, N.; Moon, J. S.; Moses, D.; Leclerc, M.; Lee, K.; Heeger, A. J. *Nat. Photonics* **2009**, *3*, 297.

Macromolecules

Article

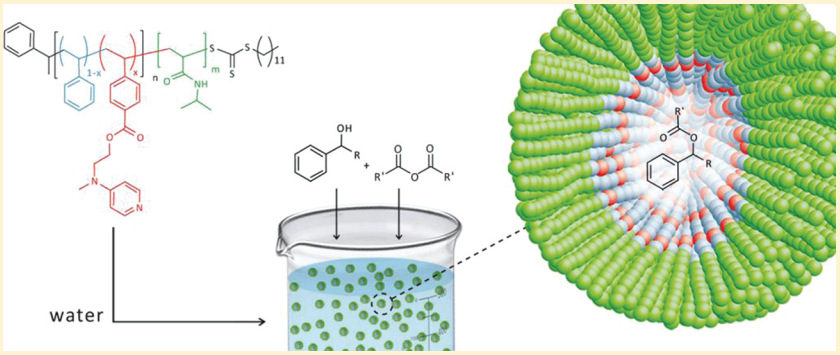
pubs.acs.org/Macromolecules

Functionalized Organocatalytic Nanoreactors: Hydrophobic Pockets for Acylation Reactions in Water

Pepa Cotanda, Annhelen Lu, Joseph P. Patterson, Nikos Petzetakis, and Rachel K. O'Reilly*

Department of Chemistry, University of Warwick, Gibbet Hill Road, Coventry CV4 7AL, United Kingdom

Supporting Information



ABSTRACT: The effect of covalently attaching 4-(dimethylamino)pyridine (DMAP) functionality to the hydrophobic core of a polymeric micelle in water has been investigated in the context of acylation reactions employing non-water-soluble substrates. For this purpose a novel temperature-responsive polymeric micelle has been synthesized using reversible addition−fragmentation chain transfer (RAFT) polymerization techniques. The reactivity of the tethered organocatalyst within the nanostructure was found to be extremely high, improving in some cases the acylation rates up to 100 times compared to those for unsupported DMAP in organic solvents. Moreover, the catalytic nanoreactors have been demonstrated to be capable of reuse up to 6 times while maintaining high activity.

INTRODUCTION

The use of water as a solvent for organic reactions has increased in the past decade, as it is the most abundant and cheapest liquid on earth, it is safe, and it has shown unique properties such as improving rate and selectivity in some organic reactions.[1−4] However, the use of water for synthetic organic chemistry is restricted because most organic compounds are nonpolar and hence insoluble in water. Based on previous results from Breslow and Rideout,[1] in 2005 the group of Sharpless reported the "on water" protocol where organic substrates were added to water and stirred vigorously forming small droplets of reactants, and the products were easily isolated by phase separation or filtration.[2] This protocol showed an unexpected increase in rates for several organic reactions using hydrophobic reactants in aqueous solutions compared to those in organic solvents or neat conditions.

Nevertheless, the environmental and economic assessment of an aqueous reaction is shown to involve a complex set of parameters.[5] Catalysts are often the most expensive component in organic reactions and are usually very toxic; hence, there is great interest in the immobilization of catalysts for simplification of product work-up, separation, isolation, and facile recovery. In nature, enzymes make use of a compartmentalized hydrophobic cavity within the structure, protected by a hydrophilic shell. The isolated hydrophobic pocket allows for efficient, selective catalysis. Inspired by enzymes, several groups have designed a wide range of artificial catalysts based on star polymers or dendrimers, where the catalytic active cores are isolated from the outer environment.[6−14]

Indeed, the development of new systems to create organic microenvironments in aqueous media using surfactants has been widely investigated.[15,16] These amphiphiles form spherical aggregates with hydrophilic surfaces and hydrophobic cores; the hydrophobic reactants are concentrated within the core, resulting in the observed acceleration in reaction rate and introducing selective effects. Kobayashi et al. carried out dehydration reactions in water using dodecylbenzenesulfonic acid as a surfactant-type catalyst.[17,18] In this system, the catalyst enhanced the reaction rate and the hydrophobic interior of the droplets facilitated the exclusion of the water, obtaining esters in high yields for highly hydrophobic substrates.

DMAP is a useful nucleophilic catalyst which can be used in a variety of reactions such as esterifications with anhydrides, the Baylis−Hillman reaction, hydrosilylations, tritylation, the Steglich rearrangement, Staudinger synthesis of β-lactams, and many more.[19−21] Although it is not remarkably expensive, this organocatalyst exhibits high dermal toxicity; hence, its incorporation to a solid support to avoid dissemination in the

Received: December 20, 2011
Revised: February 20, 2012
Published: February 29, 2012

 © 2012 American Chemical Society dx.doi.org/10.1021/ma2027462 | *Macromolecules* 2012, 45, 2377−2384

environment is an important target. DMAP containing polymers have been a subject of interest in the past decades;[22,23] linear polymers, dendrimers, multiarm star copolymers, polymeric capsules, polymer brushes, and cross-linked polymers containing DMAP functionality have been synthesized and used in supported catalysis.[12,24−27]

In 2006, McQuade et al. published the first example of catalysis using encapsulated linear polymer−catalyst conjugates. The copolymerization of a DMAP-modified monomer with styrene and encapsulation by interfacial polymerization gave a DMAP-functionalized microcapsule that showed higher activity for DMAP-catalyzed acylation than when supported on cross-linked polystyrene.[25]

In 2005, Fréchet et al. demonstrated that DMAP modified monomers can be copolymerized, assembled and encapsulated for applications in homogeneous catalysis.[12] In this work the authors reported a one-pot reaction cascade performed with two different star polymers (unimolecular micelles), each containing a different catalytic group confined in its core. The same year, the group reported how the nanoenvironment and polymer architecture play an important role in acylation reactions catalyzed by DMAP-containing dendrimers.[24] By comparing two DMAP dendritic polymers with different polarities within the core domain, they proved the "concentrator effect" whereby catalytic reactions benefit from the gradient polarity core−shell. Their system behaves like a free energy driven catalytic pump that favors the migration of the polar substrate from the nonpolar medium (hexane) to the more polar core containing DMAP. Recent work by Meijer and co-workers reported a compartmentalized catalyst synthesized by supramolecular folding of a single polymer chain that catalyzes carbonyl reductions in water; the authors described this system as an enzyme mimic.[28] Inspired by this work, it would be desirable to synthesize a system that combines the use of water for the reaction of hydrophobic organic substrates using a hydrophobic environment to improve the reaction rates with the advantages of the facile synthesis of amphiphilic diblock copolymer supported catalysts.

A strategy that has successfully been employed is the synthesis of functionalized monomers, which can be incorporated selectively into the hydrophobic domain of a polymeric micelle via copolymerization techniques.[26,29−32] The covalent attachment of the catalytic motifs within the hydrophobic core block (protected by the hydrophilic corona) allows for the selective reaction of hydrophobic reagents in an overall aqueous environment. The main advantage of these polymeric self-assembled systems over surfactant-based micelles is their stability and the facile recovery of the catalyst by precipitation or ultrafiltration methods.[33]

New advancements in controlled radical polymerization techniques (CRP) such as RAFT have enabled the facile synthesis of many different polymer architectures with fine control over their molecular weight, polydispersity, and chain-end functionality.[34] The application of RAFT to the synthesis of functionalized amphiphilic homo- and block copolymers which contain hydrophobic and hydrophilic groups is particularly important for their self-assembly in water.[35] Moreover, the incorporation of stimuli-responsive blocks and/or functional groups is essential for their use in so-called "smart" applications.[36] Following this strategy, Liu and co-workers used RAFT to synthesize stimuli-responsive block copolymers, poly(*N*-isopropylacrylamide)-*b*-poly(*N*-vinylimidazole) (PNIPAM-*b*-PVim), which self-assembled above the LCST of NIPAM (~32 °C) into micelles with the hydrophobic NIPAM core and the catalytic imidazole block forming the corona.[31] They found that in the presence of the catalytic micelles the rate of esterolysis increased up to 7 times, and they suggested that this was due to the hydrophobic affinity of the reactants for the hydrophobic NIPAM core brought the reactants in close proximity to the catalytic shell and increased their local concentration.

In order to explore how the incorporation of the catalyst into the hydrophobic core of a polymeric micelle will affect its catalytic activity, Zhao et al. used atom transfer radical polymerization (CRP technique) to synthesize a diblock copolymer containing DMAP functionality tethered within the temperature-responsive block which formed the hydrophobic core of the micelle upon heating.[26] They envisioned that if the partition coefficient of the substrate between micelles and water is sufficiently high, the substrates could be concentrated in the core of the micelle, resulting in an enhanced reaction rate. However, on the contrary to their hypothesis, the DMAP-containing polymer did not accelerate the rate of the reaction upon self-assembly. They related this observation to a mass transport limitation of their starting materials from the water to the core of the micelles.

The unique hydrophobic environment created in the core of a polymeric micelle can be tuned by selecting the degree of hydrophobicity of the core block.[37] Weck and co-workers, based on previous work by Weberskrich, designed an optimal system for the hydrolytic kinetic resolution of epoxides in water.[30,32] In this work, the high local concentration of catalyst in the hydrophobic core of the micelle together with the small amount of water that can penetrate during catalysis has been proven to be crucial to achieve higher activity and better enantioselectivity than that obtained under homogeneous conditions in organic media. In addition, the system exhibited outstanding recycling properties.

The overall objective of our work is to synthesize new polymer supported catalytic micelles with stimuli-responsive properties, where DMAP is selectively supported in the hydrophobic core. These micelles will act as nanoreactors to carry out catalysis of hydrophobic organic molecules in aqueous media and hopefully accelerate the reaction rates by the "concentrator effect" reported by Fréchet and co-workers.[24] The temperature-responsive PNIPAM shell is envisioned to facilitate the recovery of the catalyst without the need of organic solvents.[38]

RESULTS AND DISCUSSION

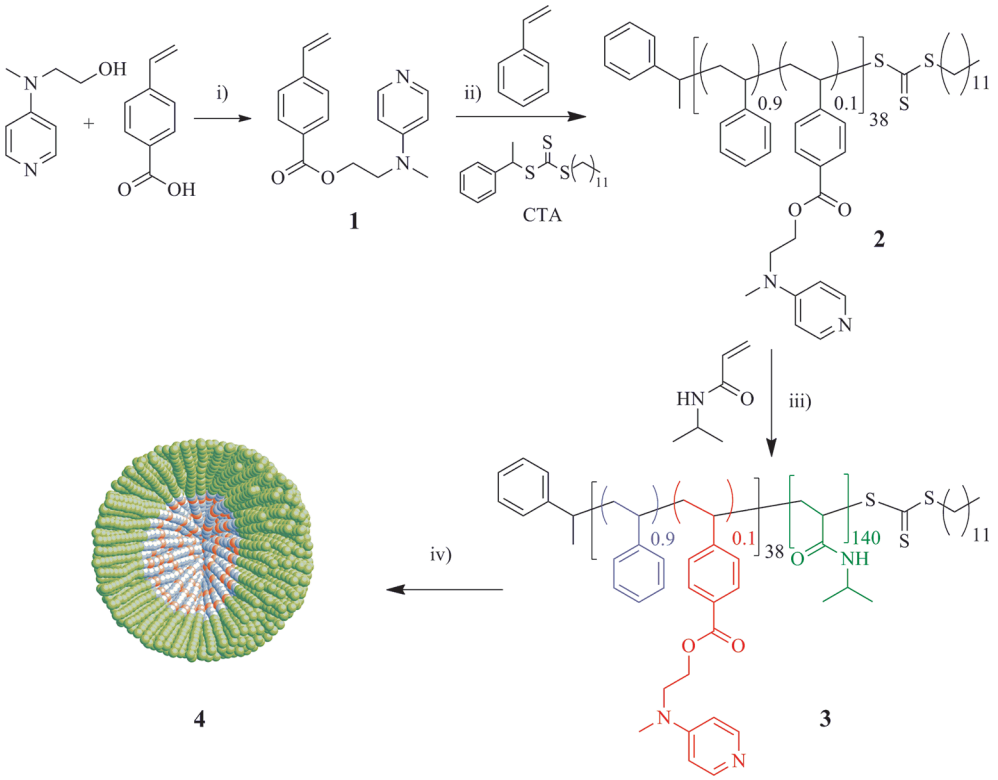
Synthesis of DMAP Containing Micelles 4. Styrene-based polymers chain extended with a water-soluble block are known to form kinetically frozen micelles in water.[39,40] We hypothesize that the confinement of the catalytic moiety in a completely hydrophobic glassy core will create a water-free environment and mimic nonpolar hydrophobic conditions for efficient catalysis reactions.

In order to obtain stable micelles with the catalytic functionality locked into the hydrophobic core, a styrenic monomer **1** containing DMAP was synthesized from commercially available 4-vinylbenzoic acid and 4-(*N*-methyl-*N*-(2-hydroxyethyl)amino)pyridine at room temperature by established procedures using Steglich esterification route (Scheme 1).[41,42] The product was isolated as a white powder in 60% yield and characterized by ^{1}H and ^{13}C NMR spectroscopy, high-resolution mass spectroscopy (HR-MS), and IR spectroscopy (Supporting Information).

The DMAP containing monomer, **1**, was copolymerized with styrene by RAFT using dodecyl 1-phenylethyltrithiocarbonate,

dx.doi.org/10.1021/ma2027462 | *Macromolecules* 2012, 45, 2377−2384

Scheme 1. Synthesis of Micelles, 4, That Contain DMAP Functionality Covalently Attached in the Hydrophobic Core[a]



[a]Reactants and conditions: (i) CH_2Cl_2, EDCI, RT; (ii) DMF, 110 °C; (iii) AIBN, THF, 65 °C; (iv) solvent switch from acetone to water at 5 °C.

as trithiocarbonates are known to be good chain transfer agents (CTA) for the polymerization of styrene and styrenic monomers.[43,44] RAFT is one of the most versatile CRP techniques due to its tolerance to functionality and its ability to polymerize a wide range of monomers in a controlled manner in both aqueous and organic media.[34,45−49] A kinetic study of the copolymerization using **1** was carried out in order to gain further polymerization data regarding the degree of living behavior and rate of polymerization with an intended 5% incorporation of **1**, with a view of obtaining an overall target DP of ca. 50. Samples were taken from the polymerization ampule at different times and analyzed by SEC (THF eluent) and ^{1}H NMR spectroscopy in $CDCl_3$ (Table S1). As shown in Figure S3, the kinetic plot is linear, which indicates a controlled polymerization process is occurring with a constant radical concentration. Given the higher rate of polymerization for **1** than St (k_p(styrene) = 0.0262 min^{-1} and k_p(**1**) = 0.0573 min^{-1}), there is a higher than predicted incorporation of the functional monomer at low monomer conversion. Hence, the polymers have a gradient type structure, and the resultant polymers contain significantly more than the expected 5% incorporation of monomer **1**.

A copolymer DMAP-*co*-St, **2**, with an overall degree of polymerization of 38, containing 10% of monomer **1** was obtained with good polymerization control (M_n(NMR) = 5.1 kDa, M_w/M_n = 1.11). The degree of incorporation of functional monomer **1** was determined by examination of the ^{1}H NMR spectrum of the resultant polymer via the comparison of the signals attributable to monomer **1** (ca. 4.4 and 8.2 ppm) and the signals for the backbone at ca. 1.5 ppm with those for the CTA at 0.85 ppm (see Figure S1). These calculations assume complete end-group fidelity; this was supported by the good overlap of the UV signal at 309 nm (characteristic wavelength for the trithiocarbonate end group) with the RI response for the same sample using both detectors in the SEC (see Figure S2).

PNIPAM has been widely studied mainly because of the sharpness of its phase transition, the closeness of its LCST about 32 °C, to physiological temperature, and the easiness to vary its LCST by copolymerization, addition of salts or surfactants to the polymer solution.[50−58] Applications of this switchable behavior include the dissolution of amphiphilic block copolymer to form micelles in an aqueous media and its reversible switching upon heating above its LCST to a double hydrophobic block copolymer which will collapse and precipitate for facile recovery.

For the preparation of the targeted DMAP containing micelles, the macro-CTA **2** was chain extended with NIPAM to form a diblock copolymer with a permanently hydrophobic styrenic−DMAP block and a temperature responsive block, which is hydrophilic at room temperature (**3**, M_n(NMR) = 20.5 kDa, M_w/M_n = 1.42). The degree of polymerization of NIPAM and its molecular weight were determined using the ^{1}H NMR spectrum of the resultant polymer by comparing the signals attributable to monomer **1** in polymer **2** (ca. 4.4 and 8.2 ppm) and the signals for the NIPAM proton at ca. 4.0 ppm (Figure 1). Because of the length of the hydrophilic NIPAM block (degree of polymerization = 140), the hydrophobic chain end of the RAFT CTA was not expected to play an important role in the self-assembly of the polymer. The validity of this assumption was evident from the characterization data showing spherical micelles, which is the morphology predicted based on the packing parameter for the given block lengths.[59]

The amphiphilic block copolymer was dissolved in a minimum amount of acetone (at 100 mg/mL), which is a good solvent for both blocks. Cold water was added dropwise, with stirring, to the

dx.doi.org/10.1021/ma2027462 | Macromolecules 2012, 45, 2377−2384

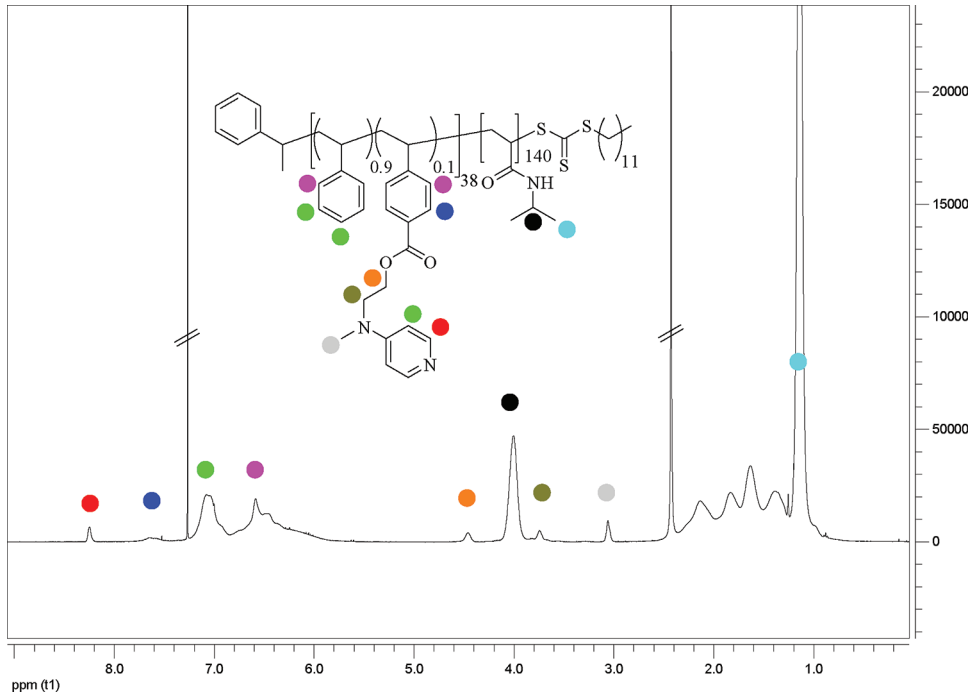


Figure 1. ^{1}H NMR spectrum of diblock copolymer **3** in $CDCl_3$.

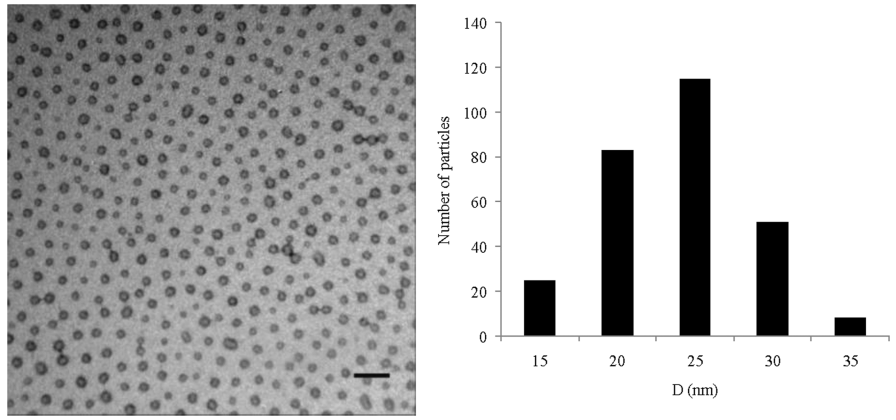


Figure 2. Representative TEM micrograph of catalyst **4** stained with uranyl acetate (1% solution) and histogram. Scale bar 100 nm.

polymer solution using a peristaltic pump (rate = 15 mL/h) to form spherical micelles **4** following evaporation of the acetone under reduced pressure at low temperature. This yielded DMAP-functionalized micelles, **4**, at a micellar concentration of ca. 6.8 mg/mL. The resulting spherical micelles were found to be ca. 25 nm in diameter, determined by both TEM (Figure 2, D_{av} = 23.8 nm) and DLS analysis (D_h = 31.2 nm, PD = 0.234, Figure S5).

The LCST of micelles **4** was measured spectrophotometrically by determining the turbidity of the solution at various temperatures (Figure 3). It has been previously reported that temperature responsive polymers exhibit lower phase separation temperatures when self-assembled into micelles.[60] Our DMAP containing micelles presented an LCST of 27 °C, which is 5 °C lower than that reported for PNIPAM homopolymer. The broad hysteresis observed in the cooling process, first observed by Wu et al.,[61] indicates that the solution must be cooled below 32 °C to re-form the micelles.

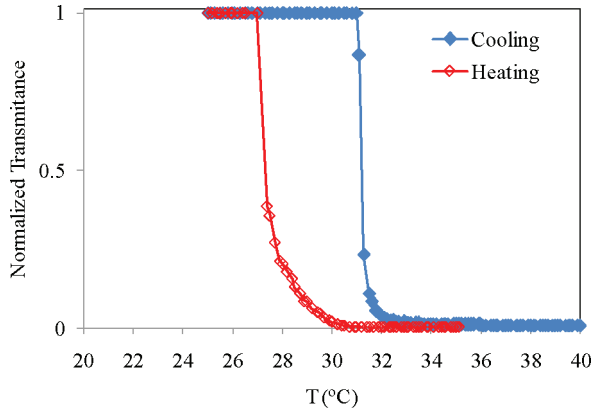


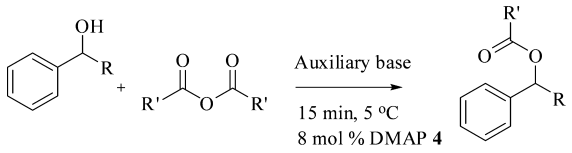
Figure 3. Normalized transmittance versus temperature plot for **4** at 1 mg/mL in water.

Acylation Reactions. In order to probe the effects of encapsulating a catalyst in a hydrophobic environment in an overall aqueous media, the well-established DMAP catalyzed acylation reaction of an alcohol was investigated as a model system. DMAP-containing micelles in water were tested as

dx.doi.org/10.1021/ma2027462 | *Macromolecules* 2012, 45, 2377−2384

catalytic nanoreactors for different substrates, as indicated in Table 1. Similar conditions to those reported by Fréchet were targeted.[24] However, anhydrides partially hydrolyze to their corresponding acids in aqueous solutions; hence, an excess of anhydride was employed (3 equiv vs 1.5 equiv) due to the aqueous environment of our system. All catalytic reactions were carried out with stirring at 5 °C to ensure polyNIPAM was completely dissolved. Aliquots were taken from the reaction mixture at different times and the conversion was determined by HPLC analysis. All reactions were performed in triplicate. In these reactions 8 mol % of DMAP was employed, taking into account that each polymer chain contain an average of 4 units of the catalytic active DMAP.

Table 1. Data Showing Conversions after 15 min for Acylation Reactions in the Micelles, 4[a]



entry	R	R′	% conv (15 min)	% conv (24 h)
1	CH_3	CH_3	26	32
2	CH_2CH_3	CH_3	28	29
3	CH_3	$CH_2CH_2CH_3$	47	53
4[b]	CH_3	$CH_2CH_2CH_3$	65	66
5[b]	CH_2CH_3	$CH_2CH_2CH_3$	94	98

[a]All reactions contained 8 mol % DMAP, [OH] = 0.02 M, 1.5 equiv of auxiliary base (TEA), 1 equiv of alcohol, and 3 equiv of anhydride. Conversions determined by HPLC measurements with mesitylene as the internal standard. [b]*N,N*-Diisopropylethylamine (DIPEA) was used as auxiliary base instead of TEA.

In the first approach (entry 1, Table 1) the acylation reaction was carried out using 1 equiv of 1-phenylethanol (0.02 M) with 3 equiv of anhydride and 1.5 equiv of TEA in the aqueous micelle solution **4** (at 8 mol % DMAP loading). When using acetic anhydride as the substrate, the reaction reached 26% conversion in 15 min and then appeared to stop. The drastic decrease in the reaction rate after achieving ~25% conversion may be attributed to a mass transport limitation as predicted by Zhao and co-workers.[26] If the hydrophobicity of the reactants is the driving force of the reaction, when the product is more hydrophobic than the substrates, the nanoreactor will eventually become saturated, preventing the starting materials in the water from moving into the reactive hydrophobic core and hence stopping the reaction. This hypothesis was investigated by adding a new batch of starting materials (alcohol, anhydride, and auxiliary base) to the micellar solution after reaching this point. As expected, only 25% of this additional batch was acylated, and the reaction stopped when the ratio of reactants−products reached the equilibrium between the hydrophobic core of the reactor and the water. The addition of fresh starting materials was repeated four times, and the results observed were reproducible; the acylation reached equilibrium, and in all cases only 25% conversion was observed 15 min after each addition (see Figure S8).

The addition of a fifth batch ([OH] = 0.10 M) resulted in the partial precipitation of the polymer. This observation gave us an indication about the concentration limits of our micellar system. While the lower limit ([OH] = 0.02 M) is determined by the detection limit of the method of analysis (HPLC), the higher limit appears to be dependent on the amount of hydrophobic materials that the nanoreactor can house inside the hydrophobic core domain.

Effect of Substrates on the Equilibrium Position. In order to overcome the above-mentioned mass transport limitation and achieve higher acylation conversion, further experiments were carried out using different alcohol and anhydride substrates (entries 2−5, Table 1). We expect that the use of more hydrophobic starting materials will favor the diffusion of reactants to the core and hence increase the conversions before equilibrium is reached. In all cases the acylation reaction of different substrates in the aqueous solution containing DMAP micelles **4** reached the equilibrium position after 15 min. Initially, a less water-soluble alcohol (R = ethyl versus methyl) was targeted, but unfortunately, the hydrophobicity of the alcohol did not show any significant contribution to the reaction rate at this point (entry 2, Table 1).

Studies by Steglich et al. based on kinetic measurements of the DMAP-catalyzed acetylation of alcohols concluded that the rate-determining step of esterification reactions of this type is the reaction of the *N*-acylpyridinium carboxylate with the alcohol.[62] Neither DMAP nor the auxiliary base enters the kinetic equation. Hence, in our micellar system the use of a more hydrophobic anhydride seems to be key, as suggested by the reaction mechanism (Figure 4).

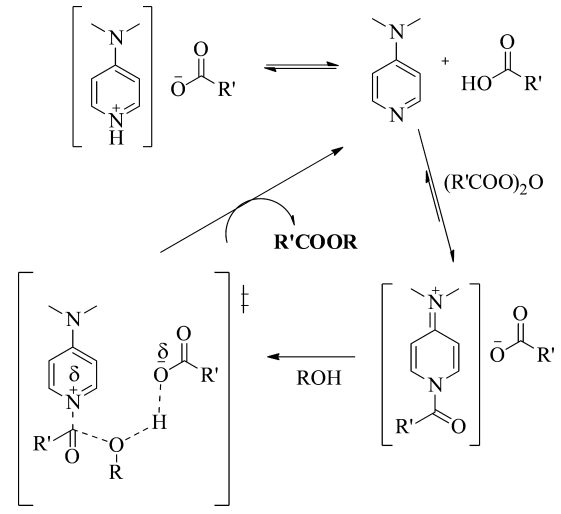


Figure 4. Proposed mechanism for the DMAP-catalyzed acylation.[62,63]

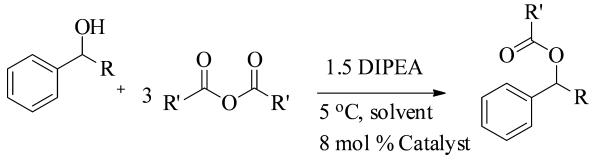
When using the more hydrophobic butyric anhydride in exactly the same conditions as previously discussed (entry 3, Table 1), the conversion of the esterification reaction increased, obtaining an acceptable 47% after 15 min. This promising result was slightly improved by introducing a more hydrophobic auxiliary amine, *N,N*-diisopropylethylamine (DIPEA), which increased the conversion to 65% (entry 4, Table 1). However, when a more hydrophobic alcohol, anhydride, and auxiliary amine were used, the acylation reaction was completed within 15 min (entry 5, Table 1). This is not unexpected that the use of longer alkyl chains on the starting materials afforded higher conversions due to improved partitioning and concentration within the catalytically active micellar core. On the other hand, when the reactions were carried out in THF using unsupported DMAP as a catalyst, the use of more hydrophobic substrates did not significantly affect the reaction rates (see Figure S7 and

dx.doi.org/10.1021/ma2027462 | *Macromolecules* 2012, 45, 2377−2384

Table S2). These results emphasize the importance of the hydrophobicity of the substrates in our micellar system.

Comparison with Organic Solvents and Bulk. To obtain further data about how the environment created inside the micelle affects the rates of reaction, the acylation of 1-phenylpropanol with butyric anhydride was carried out in different solvents and in neat conditions using unsupported DMAP as a catalyst. The reaction proceeded very fast in less polar solvents (hexane) and solvent-free conditions compared to more polar solvents such as THF or water (entries 1–4, Table 2).

Table 2. Data Showing Reaction Conversion Determined by HPLC after 15 min and 24 h for the Acylation Reactions in Different Solvent Conditions[a]



			% conversion	
entry	catalyst	solvent	15 min	24 h
1	DMAP[b]	water	2	8
2	DMAP[b]	THF	13	87
3	DMAP[b]	hexane	85	86
4	DMAP[b]	bulk	58	96
5	DMAP[b]	**6**[c]	0	3
6	**3**	**4**[c]	94	98
7	**3**	THF	2	60

[a]All reactions were carried out with 8 mol % DMAP, [OH] = 0.02 M, 1.5 equiv of auxiliary base, 1 equiv of alcohol, and 3 equiv of anhydride. Conversions were determined by HPLC measurements, with mesitylene as the internal standard. R = CH_2CH_3, R′ = $CH_2CH_2CH_3$. [b]Unsupported DMAP was used as a catalyst. [c]Micelle in water.

This behavior has previously been reported by Ishihara and co-workers for the acylation reactions of a range of alcohols under different conditions.[63] The use of less polar solvents aids the regeneration of the DMAP catalyst which results in higher reactivities, while polar solvents cause the formation of ammonium salts and leads to a decrease in reactivity.

For this reason it is not surprising that the acylation in water only achieved 8% conversion when nonsupported DMAP was used (entry 1, Table 2). It is noteworthy that, although the reactions in bulk and in the micellar system (entries 4 and 6) yielded the same conversion at the equilibrium position, the reaction in the aqueous micelles is 8 times faster than that in hexane, which can be attributed to the "concentrator effect" observed by Fréchet and co-workers.[24]

On the other hand, the higher conversion for the DMAP-containing micelle system 4 compared to the acylation in bulk (entries 4 and 6, Table 2) agree with the polarity effects observed by Ishihara et al.[63] The substrates themselves are a more polar solvent than hexane, resulting in a deceleration of the acetylation under solvent-free conditions. These reactions confirm that the micelles create a more favorable environment for the acylation to occur in pure water similar to that created in organic solvent or neat conditions. We were also interested in whether simple addition of DMAP to a unfuctionalized micellar system would allow for similar activities. Hence, we next explored the requirement of encapsulating the catalyst in the hydrophobic environment of a micelle. For this purpose a

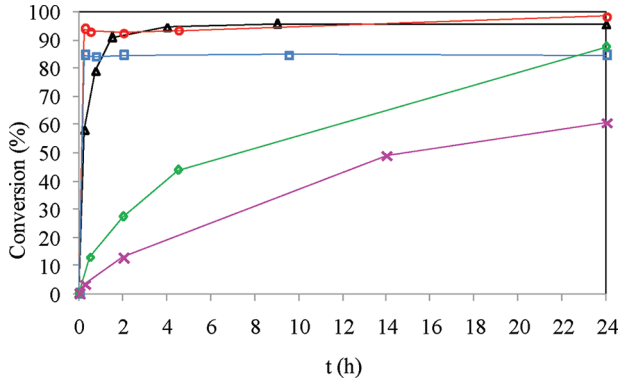


Figure 5. Conversions vs reaction times for DMAP-catalyzed acylation reactions in Table 2: entry 2 (◇), entry 3 (□), entry 4 (△), entry 6 (○), and entry 7 (×); R = CH_2CH_3, R′ = $CH_2CH_2CH_3$.

new block copolymer PSt_{38}-*b*-$PNIPAM_{140}$ (**5**, M_n (NMR) = 19.2 kDa, M_w/M_n (GPC) = 1.29, which contained no DMAP functionality) was synthesized and self-assembled into micelles **6**, via the procedure described for the DMAP nanoreactors. DLS and TEM studies show that the unfunctionalized micelles **6** were of similar size to the DMAP containing micelles **4** (D_{av} = 23.1 nm, D_h = 35.4 nm, Figures S4 and S6). DMAP small molecule (8 mol % loading) was added to micellar solution **6** and stirred for 1 h before addition of the alcohol, anhydride, and DIPEA. The aliquots taken from the reaction after 24 h showed that the acylation does not occur in water if the DMAP functionality is not covalently attached within the hydrophobic environment. We attribute this important observation to two different factors: unlike the starting materials, DMAP is water-soluble, and given the small amount added to the solution (1.3 mg in 8 mL of water), it is unlikely that the organic substrates find any DMAP in the hydrophobic core. Second, it is likely that the DMAP catalyst is poisoned by protonation from the acid created by the excess of anhydride hydrolyzed in the aqueous media.

The rate of acylation using polymer-supported DMAP **3** in THF is lower and less efficient than the nonsupported DMAP (entries 2 and 7, Table 2). THF is a good solvent for both blocks of the amphiphilic polymer; hence, self-assembly into micelles does not occur, and the acylation will proceed as a conventional "polymer supported" catalyzed reaction, where unlike the nonsupported catalyst, the DMAP functionality is more sterically hindered. These results demonstrate the advantages of tethering the catalyst into a polymeric nanoreactor rather than just a simple polymer support. The high local concentration of catalyst leads to enhanced activity similar to that for organic solvents or neat conditions, and the hydrophobic core creates a hydrophobic nonpolar environment preventing DMAP protonation.

Catalyst Loading. To further investigate the potential of our DMAP-containing micelles, the amount of catalyst was reduced to 0.8 and 0.08 mol %. When the most efficient esterification reaction (entry 5, Table 1) was repeated, lowering the catalyst 10 times only resulted in a 10% drop in conversion, and similarly the equilibrium point was reached in 15 min. However, lowering the catalyst 100 times lead to a significant decrease in conversion, achieving ca. 50% of the acylation product at the equilibrium position after 6 h (Figure 6).

To provide a direct comparison the acylation was explored under the same conditions with DMAP small molecule in THF and hexane (Figure 6). The reduction of the catalyst content in

dx.doi.org/10.1021/ma2027462 | *Macromolecules* 2012, 45, 2377–2384

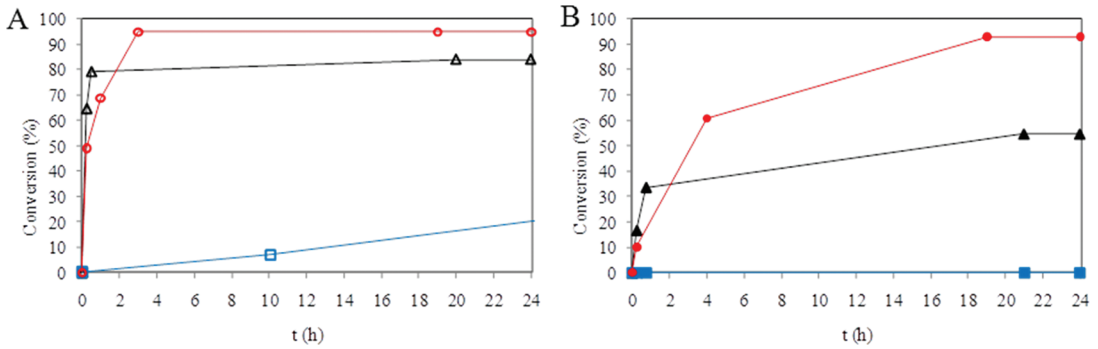


Figure 6. Acylation reactions using 0.8% (A) and 0.08% (B) DMAP catalyst in the micelles (triangle) compared to the small molecule reaction in THF (square) or hexane (circle) for conditions shown in Table 2.

the THF homogeneous system induced a drastic decrease in reaction rates compared to those from the DMAP-containing micelles. By reducing the nonsupported catalyst to 0.8 mol % (Figure 6A), the conversion decreased more than 50%, and furthermore, no reaction was observed after 24 h when the amount of catalyst was reduced to 0.08% (Figure 6B). When homogeneous catalysis was carried out in hexane, the reaction rates decreased compared to those for the same conditions using 8% catalyst; however, both reactions (0.8 and 0.08% catalyst) achieved more than 95% conversion.

In our experiments with lower catalyst loading the micelle solution **4** was diluted to the desired concentration; however, given the kinetically frozen nature of our micelles we hypothesize that this essentially resulted in a reduction in the total number of micelles in the solution and hence less "catalytic pumps" to catalyze the reaction. For this reason we believe that the equilibrium of the substrates between water and the micelles is reached faster, leading to lower conversions compared to those for hexane. We postulate that the synthesis of a new polymer containing lower DMAP loadings but retaining the same block lengths as **3** will allow us to reduce the amounts of catalyst but maintaining the same number of "hydrophobic pockets" and hence potentially reaching higher conversions. This work is currently ongoing.

Recycling Experiments. One of the main advantages of tethering the catalyst to a polymeric support over the widely studied catalysis using surfactants is the facile recovery of the polymer for recycling. In our recycling experiments 0.8 mol % DMAP-supported catalysts from a diluted solution of **4** was employed to catalyze the acylation reaction of 1-phenylpropanol with 3 equiv of butyric anhydride and 1.5 equiv of DIPEA as auxiliary base. The reactants together with a known amount of mesitylene were added to the micelles solution at 5 °C, and after 1 h a sample was taken and analyzed by HPLC to calculate the conversion. The product was extracted with diethyl ether and the same aqueous solution was reused in a new reaction. The catalyst was reused with little or no change in reaction rate or conversion for five times (80%, 74%, 83%, 70%, and 79% after 1 h). However, after this point it was noted that the reaction mixture became brown due to the excess of water-soluble auxiliary base in solution, which is not removed by organic extraction.

Hence, a new recycling route was investigated using the stimulus-responsive property of our system. After extraction of the synthesized product with diethyl ether, the aqueous phase containing the micellar catalyst was heated to a temperature above 50 °C. At this temperature, the polymer exists as a fine powder and was collected by centrifugation. The recovered catalyst was reused in another reaction cycle using the same amount of reactants and water to keep the concentration of reactants the same as in a fresh cycle, achieving 85% conversion after 1 h reaction. The product was extracted with diethyl ether after the six recycling cycles, and the aqueous solution was freeze-dried in order to analyze the solid residue by ^{1}H NMR spectroscopy; integration of the DMAP peak at ca. 4.4 ppm confirms that the DMAP functionality is present and still attached to the polymer backbone following recycling.

The polymer can be purified to be used in a different reaction by heating the micellar solution above the LCST of the micelles. The precipitated polymer can then be recovered by filtration and washed with ethyl acetate in order to remove all organics. A ^{1}H NMR spectrum of the clean polymer after reaction can be found in the Supporting Information (Figure S9).

■ CONCLUSIONS

A new temperature-responsive amphiphilic block copolymer containing DMAP functionality incorporated within the hydrophobic block has been successfully synthesized by RAFT and self-assembled into micelles by dissolution in water at low temperatures. The catalytic activity of these DMAP nanoreactors in the acylation of hydrophobic substrates in aqueous media was determined and compared to that of unsupported DMAP in organic solvents. The data indicate that the high local concentration of catalyst and the hydrophobic environment created in the core of the nanoreactors are crucial to achieving high acylation reactivities. The reaction rates in the aqueous micellar system are comparable and in some instances greater than those for homogeneous reactions in organic media. Moreover, the polymeric catalyst could be reused in six consecutive cycles without loss of activity, and the stimulus-responsive property could be utilized to assist in the recovery of the active polymer. The applicability of the system has been shown to be very dependent on mass transport limitations of reagents, products, and regenerative species, and a deep mechanistic understanding of the reaction catalyzed is necessary. Studies on how the hydrophobicity/stability of the hydrophobic core could be tuned to improve reaction conditions are ongoing. These new synthetic methodologies will provide the basis for further development of a range of polymeric stimuli-responsive supported catalysts for utilization in organic synthesis.

dx.doi.org/10.1021/ma2027462 | *Macromolecules* 2012, 45, 2377−2384

■ ASSOCIATED CONTENT

Supporting Information

Further synthetic procedures and characterization data for the monomer, CTA, acylation products, copolymer and nanostructures. This material is available free of charge via the Internet at http://pubs.acs.org.

■ AUTHOR INFORMATION

Notes

The authors declare no competing financial interest.

■ ACKNOWLEDGMENTS

The EPSRC, AWE, and the Royal Society are thanked for financial support. Guillermo Frank Cotanda is thanked for micelle images. The GPC equipment used in this research was obtained through Birmingham Science City: Innovative Uses for Advanced Materials in the Modern World (West Midlands Centre for Advanced Materials Project 2), with support from Advantage West Midlands (AWM) and part funded by the European Regional Development Fund (ERDF).

■ REFERENCES

(1) Rideout, D. C.; Breslow, R. *J. Am. Chem. Soc.* **1980**, *102*, 7816.
(2) Narayan, S.; Muldoon, J.; Finn, M. G.; Fokin, V. V.; Kolb, H. C.; Sharpless, K. B. *Angew. Chem., Int. Ed.* **2005**, *44*, 3275.
(3) Gruttadauria, M.; Giacalone, F.; Noto, R. *Adv. Synth. Catal.* **2009**, *351*, 33.
(4) Scroggins, S. T.; Chi, Y.; Fréchet, J. M. J. *Angew. Chem., Int. Ed.* **2010**, *49*, 2393.
(5) Blackmond, D. G.; Armstrong, A.; Coombe, V.; Wells, A. *Angew. Chem., Int. Ed.* **2007**, *46*, 3798.
(6) Bosman, A. W.; Vestberg, R.; Heumann, A.; Fréchet, J. M. J.; Hawker, C. J. *J. Am. Chem. Soc.* **2002**, *125*, 715.
(7) Terashima, T.; Kamigaito, M.; Baek, K.-Y.; Ando, T.; Sawamoto, M. *J. Am. Chem. Soc.* **2003**, *125*, 5288.
(8) Terashima, T.; Ouchi, M.; Ando, T.; Sawamoto, M. *J. Polym. Sci., Part A: Polym. Chem.* **2010**, *48*, 373.
(9) Chi, Y. G.; Scroggins, S. T.; Frechet, J. M. J. *J. Am. Chem. Soc.* **2008**, *130*, 6322.
(10) Grayson, S. M.; Fréchet, J. M. J. *Chem. Rev.* **2001**, *101*, 3819.
(11) Helms, B.; Fréchet, J. M. J. *Adv. Synth. Catal.* **2006**, *348*, 1125.
(12) Helms, B.; Guillaudeu, S. J.; Xie, Y.; McMurdo, M.; Hawker, C. J.; Frechet, J. M. J. *Angew. Chem., Int. Ed.* **2005**, *44*, 6384.
(13) Helms, B.; Meijer, E. W. *Science* **2006**, *313*, 929.
(14) Yu, J.; RajanBabu, T. V.; Parquette, J. R. *J. Am. Chem. Soc.* **2008**, *130*, 7845.
(15) Dwars, T.; Paetzold, E.; Oehme, G. *Angew. Chem., Int. Ed.* **2005**, *44*, 7174.
(16) Wang, Y.; Xu, H.; Ma, N.; Wang, Z.; Zhang, X.; Liu, J.; Shen, J. *Langmuir* **2006**, *22*, 5552.
(17) Manabe, K.; Sun, X.-M.; Kobayashi, S. *J. Am. Chem. Soc.* **2001**, *123*, 10101.
(18) Manabe, K.; Iimura, S.; Sun, X.-M.; Kobayashi, S. *J. Am. Chem. Soc.* **2002**, *124*, 11971.
(19) Spivey, A. C.; Arseniyadis, S. *Angew. Chem., Int. Ed.* **2004**, *43*, 5436.
(20) Höfle, G.; Steglich, W.; Vorbrüggen, H. *Angew. Chem., Int. Ed.* **1978**, *17*, 569.
(21) Steglich, W.; Höfle, G. *Angew. Chem., Int. Ed.* **1969**, *8*, 981.
(22) Benaglia, M.; Puglisi, A.; Cozzi, F. *Chem. Rev.* **2003**, *103*, 3401.
(23) Vaidya, R. A.; Mathias, L. J. *J. Am. Chem. Soc.* **1986**, *108*, 5514.
(24) Helms, B.; Liang, C. O.; Hawker, C. J.; Fréchet, J. M. J. *Macromolecules* **2005**, *38*, 5411.
(25) Price, K. E.; Mason, B. P.; Bogdan, A. R.; Broadwater, S. J.; Steinbacher, J. L.; McQuade, D. T. *J. Am. Chem. Soc.* **2006**, *128*, 10376.
(26) O'Lenick, T. G.; Jiang, X.; Zhao, B. *Polymer* **2009**, *50*, 4363.
(27) Jiang, X.; Wang, B.; Li, C. Y.; Zhao, B. *J. Polym. Sci., Part A: Polym. Chem.* **2009**, *47*, 2853.
(28) Terashima, T.; Mes, T.; De Greef, T. F. A.; Gillissen, M. A. J.; Besenius, P.; Palmans, A. R. A.; Meijer, E. W. *J. Am. Chem. Soc.* **2011**, *133*, 4742.
(29) Ievins, A. D.; Wang, X. F.; Moughton, A. O.; Skey, J.; O'Reilly, R. K. *Macromolecules* **2008**, *41*, 2998.
(30) Rossbach, B. M.; Leopold, K.; Weberskirch, R. *Angew. Chem., Int. Ed.* **2006**, *45*, 1309.
(31) Ge, Z. S.; Xie, D.; Chen, D. Y.; Jiang, X. Z.; Zhang, Y. F.; Liu, H. W.; Liu, S. Y. *Macromolecules* **2007**, *40*, 3538.
(32) Liu, Y.; Wang, Y.; Wang, Y.; Lu, J.; Piñón, V.; Weck, M. *J. Am. Chem. Soc.* **2011**, *133*, 14260.
(33) O'Reilly, R. K. *Philos. Trans. R. Soc., A* **2007**, *365*, 2863.
(34) Moad, G.; Rizzardo, E.; Thang, S. H. *Polymer* **2008**, *49*, 1079.
(35) McCormick, C. L.; Sumerlin, B. S.; Lokitz, B. S.; Stempka, J. E. *Soft Matter* **2008**, *4*, 1760.
(36) Vriezema, D. M.; Aragones, M. C.; Elemans, J.; Cornelissen, J.; Rowan, A. E.; Nolte, R. J. M. *Chem. Rev.* **2005**, *105*, 1445.
(37) Lejeune, E.; Drechsler, M.; Jestin, J.; Müller, A. H. E.; Chassenieux, C.; Colombani, O. *Macromolecules* **2010**, *43*, 2667.
(38) Bergbreiter, D. E.; Case, B. L.; Liu, Y. S.; Caraway, J. W. *Macromolecules* **1998**, *31*, 6053.
(39) Zhang, L.; Eisenberg, A. *Polym. Adv. Technol.* **1998**, *9*, 677.
(40) Zhang, L.; Eisenberg, A. *Macromolecules* **1999**, *32*, 2239.
(41) Deratani, A.; Darling, G. D.; Frechet, J. M. J. *Polymer* **1987**, *28*, 825.
(42) Neises, B.; Steglich, W. *Angew. Chem., Int. Ed.* **1978**, *17*, 522.
(43) Benaglia, M.; Chiefari, J.; Chong, Y. K.; Moad, G.; Rizzardo, E.; Thang, S. H. *J. Am. Chem. Soc.* **2009**, *131*, 6914.
(44) Skey, J.; O'Reilly, R. K. *Chem. Commun.* **2008**, 4183.
(45) Chiefari, J.; Chong, Y. K.; Ercole, F.; Krstina, J.; Jeffery, J.; Le, T. P. T; Mayadunne, R. T. A.; Meijs, G. F.; Moad, C. L.; Moad, G.; Rizzardo, E.; Thang, S. H. *Macromolecules* **1998**, *31*, 5559.
(46) Lowe, A. B.; McCormick, C. L. *Prog. Polym. Sci.* **2007**, *32*, 283.
(47) Moad, G.; Rizzardo, E.; Thang, S. H. *Aust. J. Chem.* **2005**, *58*, 379.
(48) Moad, G.; Rizzardo, E.; Thang, S. H. *Aust. J. Chem.* **2006**, *59*, 669.
(49) Perrier, S.; Takolpuckdee, P. *J. Polym. Sci., Part A: Polym. Chem.* **2005**, *43*, 5347.
(50) Schild, H. G. *Prog. Polym. Sci.* **1992**, *17*, 163.
(51) Liu, B.; Perrier, S. *J. Polym. Sci., Part A: Polym. Chem.* **2005**, *43*, 3643.
(52) Eeckman, F.; Moes, A. J.; Amighi, K. *Int. J. Pharm.* **2004**, *273*, 109.
(53) Schilli, C. M.; Zhang, M. F.; Rizzardo, E.; Thang, S. H.; Chong, Y. K.; Edwards, K.; Karlsson, G.; Muller, A. H. E. *Macromolecules* **2004**, *37*, 7861.
(54) Arotcarena, M.; Heise, B.; Ishaya, S.; Laschewsky, A. *J. Am. Chem. Soc.* **2002**, *124*, 3787.
(55) Virtanen, J.; Arotcarena, M.; Heise, B.; Ishaya, S.; Laschewsky, A.; Tenhu, H. *Langmuir* **2002**, *18*, 5360.
(56) Nuopponen, M.; Ojala, J.; Tenhu, H. *Polymer* **2004**, *45*, 3643.
(57) Hong, C. Y.; You, Y. Z.; Pan, C. Y. *J. Polym. Sci., Part A: Polym. Chem.* **2004**, *42*, 4873.
(58) Hales, M.; Barner-Kowollik, C.; Davis, T. P.; Stenzel, M. H. *Langmuir* **2004**, *20*, 10809.
(59) Israelachvili, J. N.; Mitchell, D. J.; Ninham, B. W. *J. Chem. Soc., Faraday Trans. 2* **1976**, *72*, 1525.
(60) Ieong, N. S.; Redhead, M.; Bosquillon, C.; Alexander, C.; Kelland, M.; O'Reilly, R. K. *Macromolecules* **2011**, *44*, 886.
(61) Wang, X.; Qiu, X.; Wu, C. *Macromolecules* **1998**, *31*, 2972.
(62) Xu, S.; Held, I.; Kempf, B.; Mayr, H.; Steglich, W.; Zipse, H. *Chem.—Eur. J.* **2005**, *11*, 4751.
(63) Sakakura, A.; Kawajiri, K.; Ohkubo, T.; Kosugi, Y.; Ishihara, K. *J. Am. Chem. Soc.* **2007**, *129*, 14775.

Macromolecules

Article

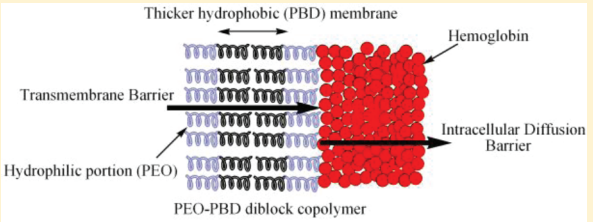
pubs.acs.org/Macromolecules

Reactivity of Polymersome Encapsulated Hemoglobin with Physiologically Important Gaseous Ligands: Oxygen, Carbon Monoxide, and Nitric Oxide

Shahid Rameez, Uddyalok Banerjee, Jorge Fontes, Alexander Roth, and Andre F. Palmer*

William G. Lowrie Department of Chemical and Biomolecular Engineering, The Ohio State University, 425 Koffolt Laboratories, 140 West 19th Avenue, Columbus, Ohio 43210, United States

ABSTRACT: Two distinct preparations of amphiphilic diblock copolymer vesicles (i.e., polymersomes), composed of (poly(ethylene oxide)−poly(butadiene)) (PEO−PBD), with molecular weights of 1.8 and 10.4 kDa, offering different hydrophobic membrane thicknesses, were used to encapsulate the oxygen (O_2) storage and transport protein hemoglobin (Hb) for possible application as a red blood cell (RBC) substitute. Key biophysical properties as well as the kinetics of polymersome encapsulated Hb (PEH) interaction with physiologically important gaseous ligands (O_2, carbon monoxide, and nitric oxide) were measured as a function of the hydrophobic membrane thickness of the PEH particle. Taken together, the results of this work show that PEHs exhibit biophysical properties and retarded ligand binding/release kinetics (compared to cell-free Hb), which are similar to the behavior of RBCs. Therefore, PEHs have the potential to serve as safe and efficacious RBC substitutes for use in transfusion medicine.



Cross-section of a Polymersome Encapsulated Hemoglobin

INTRODUCTION

The results of previous work on acellular hemoglobin (Hb)-based oxygen (O_2) carrier (HBOC) solutions, as red blood cell (RBC) substitutes for use in transfusion medicine, highlighted serious side effects such as vasoconstriction (i.e., reduction in blood vessel diameter) and the development of systemic hypertension (i.e., high blood pressure).[1−3] These side effects are hypothesized to occur via scavenging of the gaseous signaling molecules nitric oxide (NO) and carbon monoxide (CO).[1,4,5] In addition, the oversupply of O_2 to surrounding tissues can trigger an autoregulatory-induced vasoconstrictive response in order to regulate the tissue O_2 supply.[6] Therefore, it is apparent that the interaction of Hb with these gaseous ligands governs the overall toxicity of HBOCs *in vivo*.

Polymer vesicles (i.e., polymersomes) consisting of amphiphilic diblock copolymers containing poly(ethylene oxide) (PEO), the structural equivalent of poly(ethylene glycol) (PEG),[7] as the hydrophilic block have been previously used to encapsulate Hb.[8] The use of amphiphilic diblock copolymers is advantageous for vesicle formation, since these molecules can be synthesized with molecular weights (MWs) that are larger than natural lipids, which in turn facilitates control of the hydrophobic membrane thickness and size of the PEG corona.[7,9] These physical attributes in turn play a large role in regulating polymersome mechanical stability and circulatory lifetime in the blood. For example, the hydrophobic membrane thickness can be easily engineered from 3 to 40 nm through appropriate design of the diblock copolymer.[10,11] It is hypothesized that employing polymersomes to encapsulate Hb, i.e., polymersome encapsulated Hb (PEH), will enable regulation of the binding/release kinetics of the encapsulated Hb with O_2, CO, and NO by controlling gaseous ligand diffusion across the bilayer which will present a physical diffusion barrier that can potentially negate or mitigate the overall toxicity of this type of HBOC *in vivo*.

In this work, two biocompatible and nonbiodegradable PEO−poly(butadiene) (PEO−PBD) diblock copolymers were used to formulate PEHs for analysis. The two polymers varied greatly in their MWs, spanning 1.8−10.4 kDa, hence yielding polymersomes with distinctly different hydrophobic membrane thicknesses. As a first step toward testing this hypothesis, key biophysical properties of the PEH dispersions, such as particle size distribution, methemoglobin (metHb) level, O_2−PEH equilibria, O_2 affinity, cooperativity coefficient, and gaseous ligand binding/release kinetics, were evaluated as a function of the membrane thickness of the PEH particle. These experiments were geared toward exploring the ability of the PEH bilayer thickness to regulate gaseous ligand binding/release kinetics.

MATERIALS AND METHODS

Two biocompatible diblock copolymers composed of PBD−PEO were used in this study. Diblock copolymers were purchased from Polymer Source Inc. (Dorval QC, Canada). The physical properties of the two diblock copolymers are summarized in Table 1. For convenience, diblock copolymers will be referred to as PBD 1200 and PBD 6500,

Received: January 3, 2012
Revised: February 15, 2012
Published: February 24, 2012

 © 2012 American Chemical Society dx.doi.org/10.1021/ma202739f | *Macromolecules* 2012, 45, 2385−2389

Table 1. Number-Averaged MW (M_n), Polydispersity Index (M_w/M_n), PEG Block MW, Hydrophilic Mass Faction ($f_{hydrophilic}$), and Hydrophobic Membrane Thickness (d) of the Biocompatible and Nonbiodegradable PBD−PEO Copolymers Used in This Study[a]

diblock copolymer	M_n (Da)	M_w/M_n	PEG block MW (Da)	$f_{hydrophilic}$	d (nm)
PBD(1200)-*b*-PEO(600)	1800	1.17	600	0.33	4−5
PBD(6500)-*b*-PEO(3900)	10400	1.10	3900	0.38	12−13

[a]The magnitude of d was extrapolated from a mathematical correlation between d and the copolymer MW as reported in the literature.[24]

where the numeric coefficients denote the MW of the PBD block in daltons (Da).

The purification of human Hb from human RBCs, measurement of vesicle size distribution, O_2−PEH equilibria, O_2 affinity, cooperativity coefficient, and Hb and metHb concentration in vesicle dispersions have been previously described in the literature.[12]

PEH Preparation. 1−2 g of diblock polymer was completely dissolved in 30−40 mL of chloroform. The organic solvent was then removed to form a dry film using a rotary evaporator. The film was further dried under vacuum for 48 h and then hydrated with 20−40 mL of carbonyl Hb (HbCO) ([Hb] > 300 mg/mL) suspended in phosphate-buffered saline (PBS) (0.1 M, pH 7.4) inside a round-bottom flask. The polymer/Hb solution was then incubated in a water bath sonicator for 30 min followed by thoroughly mixing the contents of the flask at room temperature for 15 min. This step was repeated 2−3 times.

Unencapsulated Hb was removed from the PEH solution at room temperature via diafiltration using a 500 kDa HF cartridge (Spectrum Laboratories, Rancho Dominguez, CA), using PBS as the diafiltration buffer. To ensure complete removal of free Hb from the PEH solution, the process was repeated 7−8 times using a 1:10 v/v (sonicated PEH:PBS) ratio until no free Hb was observed in the filtrate. The filtrate was assayed for the presence of Hb using UV−vis spectroscopy and the Winterbourn equation.[13] Finally, the PEH solution was concentrated using a 500 kDa HF cartridge. Strict aseptic conditions were maintained throughout the preparation of PEHs. Prior to all experiments, all tubing, filters, and glassware used for the preparation of PEHs were immersed in 1 M NaOH solution overnight and rinsed with deionized water. The diafiltration and concentration of PEHs were performed inside a laminar flow hood.

Rapid Kinetic Measurements of PEH Dispersions. All rapid kinetic measurements of gaseous ligand binding/release were performed using an Applied Photophysics SF-17 microvolume stopped-flow spectrophotometer (Applied Photophysics Ltd., Surrey, United Kingdom). The measurements were performed on PEH dispersions converted into the HbO_2 form, prior to all experiments, using the protocols described by Rameez et al.[12]

RESULTS AND DISCUSSION

Biophysical Characterization. Figure 1 shows the O_2−PEH equilibrium curve of a representative PEH dispersion (PBD 1200) prepared in this study compared to a control of human Hb. The O_2 affinity (P_{50}) and cooperativity coefficient (n) of both PEH dispersions were regressed from the O_2−PEH equilibrium data fit to the Hill equation[8] and found to be similar to that of unencapsulated human Hb (Table 2). The sigmoidal shape of the O_2−PEH equilibrium curve qualitatively shows that the cooperative binding of O_2 to Hb was not compromised by encapsulation inside the aqueous core of the vesicle. It was further observed that the P_{50} and n of the PEH dispersions did not vary much upon increasing the MW of the hydrophobic block of the diblock copolymer. Thus, it seems

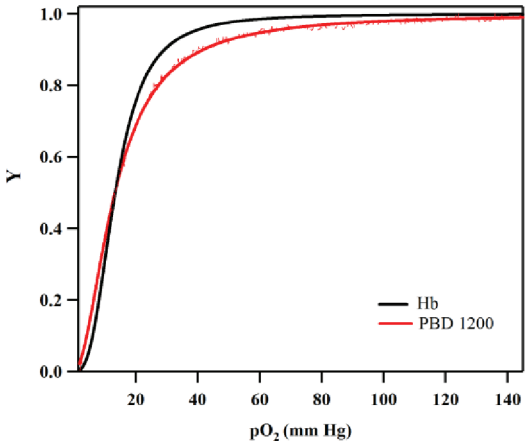


Figure 1. O_2−PEH equilibrium curves of human Hb and polymersomes encapsulating human Hb (PBD 1200). Here, Y represents the fraction of Hb saturated with O_2, and pO_2 represents the partial pressure of O_2.

that increasing the MW of the hydrophobic block, which in turn increases the membrane thickness, does not have any effect on O_2 binding equilibria. In addition, the metHb level (% of Hb in which the Fe atom in the heme ring is in the 3^+ valence state instead of the 2^+ valence state) of PEH dispersions prepared in this study was less than 1% compared to ∼0.5% for purified human Hb. This shows that the metHb level did not increase significantly during the preparation of PEH dispersions.

The concentration of Hb in the PEH dispersions was ∼1.0 g/dL. This forms the basis for one of the potential problems with PEH dispersions formulated in this study—the low Hb concentration in solution. This is mainly due to the fact that the PEO chains comprising the hydrophilic block of the diblock copolymer are also present in the inner leaflet of the PEH membrane. This reduces the aqueous core volume available for encapsulation of Hb, which results in the low Hb concentration in solution. To negate this potential problem, PEH dispersions with asymmetric membranes will be designed[14] in the future. PEH particles composed of an asymmetric membrane will facilitate the self-assembly of an outer leaflet composed of an amphiphilic copolymer with long PEG chains, while the inner leaflet will be composed of an amphiphilic copolymer with short PEG chains. The asymmetric nature of the membrane should permit higher encapsulation of Hb within the aqueous core of the vesicle.

Rapid Kinetic Measurements of PEH Dispersions. The ligand binding/release kinetics of Hb with various ligands, especially physiologically relevant ligands (O_2, CO, and NO), are just as important as equilibrium studies in providing information about the ability of these materials to store and transport gases *in vivo*.[15]

Reactions with O_2. Figure 2A shows a representative time course for deoxygenation of oxygenated PBD 1200 encapsulating human Hb. The values for the O_2 dissociation rate constant (k_{off,O_2}) are shown in Table 2. The value of k_{off,O_2} for PEH dispersions was 3.5−10-fold lower than that of acellular Hb (Table 2). A similar level of retardation in O_2 offloading has been observed in RBCs and PEG-conjugated liposome encapsulated Hbs (LEHs) as compared to acellular Hb (Table 2). This suggests that encapsulation of Hb inside the aqueous core of a polymersome can play a critical role in

dx.doi.org/10.1021/ma202739f | *Macromolecules* 2012, 45, 2385−2389

Table 2. Biophysical Properties of Various Cellular HBOCs (RBCs, PEG-LEHs, and PEHs)

type of Hb	size (diam)	P_{50} (mmHg)	n	k_{off,O_2} (s^{-1})	$k_{on,CO}$ (10^6 M^{-1} s^{-1})	$k_{ox,NO}$ (10^6 M^{-1} s^{-1})	refs
				Cell-Free Hb			
human	5.5 nm	13.34	2.8	42.22	0.225	42	*a*
				RBCs			
human and rat	8 μm	25.10	2.80	4.4	0.065	0.05	21, 25, 26
human	8 μm	20.00	2.18	16.67	0.130	0.03	
				PEG-LEHs			
human	279 nm	25−31	2.10	32.00	0.210	8.80	27, 28
human	176 nm	22.87	2.11	21.57	0.212	4.00	12
				PEHs			
human PBD 1200	380 nm	13.20	1.91	14.24	0.211	2.87	*a*
human PBD 6500	417 nm	12.13	1.95	4.16	0.206	2.20	*a*

[a]Represents results from this study.

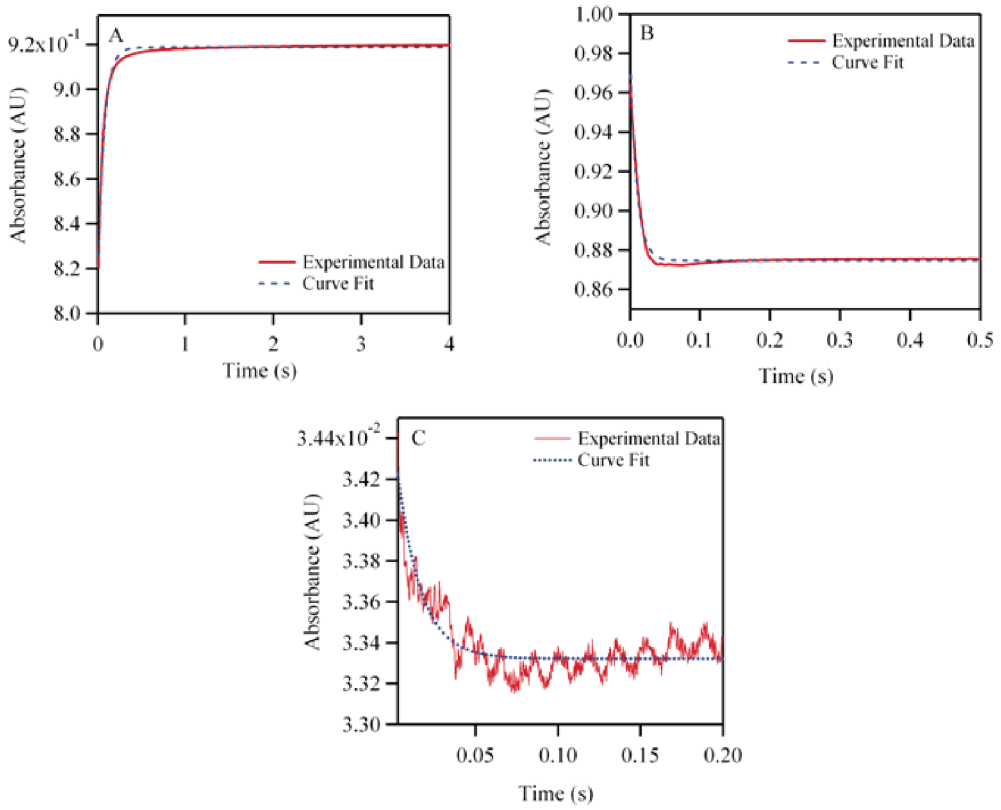


Figure 2. Kinetic time courses for PEH (PBD 1200). (A) Deoxygenation of oxygenated PEH in the presence of 1.5 mg/mL of sodium dithionite. (B) CO (464 μM) association with deoxygenated PEH. (C) NO (25 μM)-induced oxidation with oxygenated PEH. The experimental data show an average of 7−10 kinetic traces. Deoxygenation and CO association reactions were monitored at 437.5 nm and 25 °C, while NO-induced oxidation reactions were monitored at 420 nm and 25 °C. PEH solutions were made in oxygenated PBS (pH 7.4) for NO-induced oxidation and deoxygenation experiments. In the case of CO association experiments, PEH and CO solutions were made in PBS (pH 7.4) in the presence of 1.5 mg/mL of sodium dithionite.

regulating the delivery of O_2 as observed with RBCs. The values for O_2 offloading were retarded to a greater extent when the membrane thickness of PEH particles was increased (PBD 1200 has a membrane thickness of 3−4 nm compared to PBD 6500, which has a membrane thickness of 12−13 nm). Hence, increasing the PEH membrane thickness increases the membrane resistance to O_2 diffusion, thus retarding O_2 offloading from the encapsulated Hb.

Reactions with CO. Figure 2B shows a representative time course for the association reaction between CO and deoxygenated PBD 1200 encapsulating human Hb. Figure 3A shows the dependence of the observed rates on CO concentration for both PBD 1200 and PBD 6500. The values of the CO association rate constants ($k_{on,CO}$) are shown in Table 2. The $k_{on,CO}$ values for Hb and PEH dispersions were almost similar. Thus, encapsulation of Hb inside polymersomes did not affect the CO binding kinetics. A similar trend was observed for the encapsulation of Hb inside liposomes.[12,16] This can be attributed to the fact that the magnitude of the CO association rate constant is much smaller than those of O_2 and NO.[17]

Reactions with NO. Figure 2C shows a representative time course for the NO dioxygenation reaction with oxygenated PBD 1200 encapsulating human Hb. Figure 3B shows the

dx.doi.org/10.1021/ma202739f | *Macromolecules* 2012, 45, 2385−2389

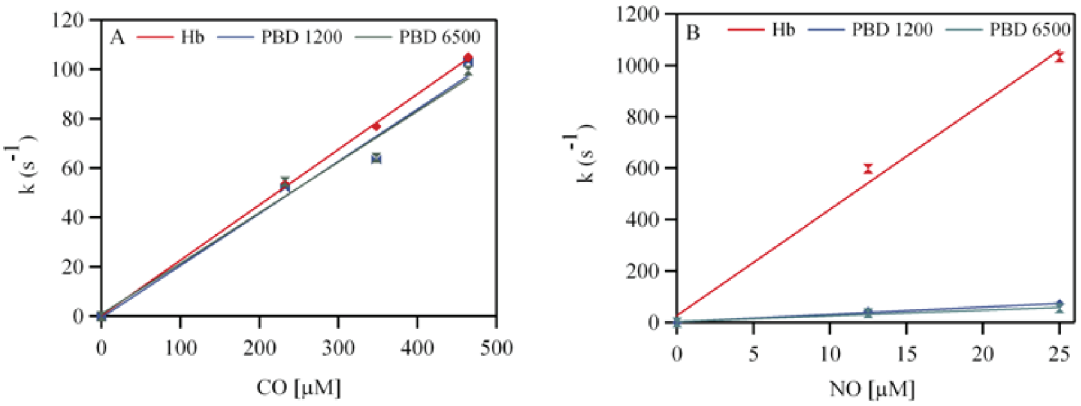


Figure 3. Dependence of the observed rates on (A) CO concentration (0−464 μM) with 15 μM of human Hb and (B) NO concentrations (0−25 μM) with 0.5 μM of human Hb.

dependence of the observed rates of NO dioxygenation on NO concentration for both PEHs (PBD 1200 and PBD 6500). The values for the NO dioxygenation rate constants ($k_{ox/NO}$) are shown in Table 2.

The magnitude of $k_{ox/NO}$ was significantly retarded for PEHs compared to cell-free Hb (Table 2). The $k_{ox/NO}$ for PEHs was 6.5−19-fold lower than that of cell-free human Hb. Moreover, the reduction in $k_{ox/NO}$ was 1.5−4-fold less than PEG-conjugated LEHs reported in the literature (Table 2). However, $k_{ox/NO}$ for PEHs is still higher than that of RBCs. This is expected given the smaller size of PEHs as compared to RBCs, which provides a smaller intracellular diffusion barrier to NO dioxygenation. Thus, increasing the membrane thickness of the vesicle did not have as pronounced a retardation effect on the magnitude of the NO dioxygenation rate constant as was observed for the O_2 offloading rate constant. Thus, the major source of retardation in the magnitude of the NO dioxygenation rate constant is due to the encapsulation of concentrated Hb inside the vesicle core, which provides for a high intracellular diffusion barrier for NO to bind Hb. This effect becomes more pronounced once the size of the particle is increased as observed in the case of RBCs (Table 2). However, the $k_{ox/NO}$ values for PEHs in this study are comparable to a recombinant Hb with low NO dioxygenation activity (2.20−2.87 μM^{-1} s^{-1} compared to 2 μM^{-1} s^{-1}) which elicited no vasoactivity when transfused *in vivo*.[18] This in turn suggests the development of little to no vasoactivity of these PEHs if administered *in vivo*.

It has been shown that the intracellular diffusion barrier, which is due to the RBC size and high intracellular Hb concentration, facilitates a reduction in the magnitude of the NO binding rate constant.[16] In addition, various other transport mechanisms have been proposed to explain the retardation of NO binding to RBCs. Some studies have demonstrated that the diffusion barrier against NO transport from the endothelium to the RBC column in the center of the blood vessel is due to the presence of an RBC-free plasma layer adjacent to the blood vessel wall.[19,20] Other work has shown that the presence of an extracellular diffusion barrier due to the undisturbed layer around the RBC retards NO scavenging.[21,22] Therefore, regardless of the exact mechanism for retardation of NO binding, all these studies suggest that encapsulation of Hb in a membrane-coated particle similar to that of a RBC plays a critical role in regulating NO transport to encapsulated Hb.

CONCLUSIONS

The results of this work show that PEHs yield low metHb levels, appropriate O_2 binding equilibria, and retarded ligand binding/release kinetics (compared to cell-free Hb), which is similar to the behavior of RBCs. In addition, engineering the hydrophobic membrane thickness of this class of particle regulates O_2 offloading from the encapsulated Hb. The moderate O_2 release rates exhibited by PEHs can be beneficial for their potential use as a HBOC in transfusion medicine, since the oversupply of O_2 can trigger autoregulatory-induced vasoconstriction.[23] Similarly, encapsulation of Hb inside polymer vesicles also retards NO binding to Hb, similar to encapsulation of Hb in other cellular HBOCs. Hence, through appropriate selection of amphiphilic diblock copolymers for subsequent formulation of PEHs, it is possible to regulate gaseous ligand binding/release kinetics which can potentially mitigate the side effects observed with previous generations of acellular HBOCs.

AUTHOR INFORMATION

Corresponding Author

*E-mail: palmer.351@osu.edu.

Notes

The authors declare no competing financial interest.

ACKNOWLEDGMENTS

This work was supported by National Institutes of Health Grants R01HL078840 and R01DK070862 to A.F.P. We also acknowledge Dr. Christopher M. Hadad, Department of Chemistry, The Ohio State University, Columbus, OH, for his willingness to let us use the UV−vis stopped-flow spectrophotometer in his laboratory.

REFERENCES

(1) Sakai, H.; Hara, H.; Yuasa, M.; Tsai, A. G.; Takeoka, S.; Tsuchida, E.; Intaglietta, M. *Am. J. Physiol. Heart. Circ. Physiol.* **2000**, *279*, H908−H915.

(2) Tsai, A. G.; Cabrales, P.; Manjula, B. N.; Acharya, S. A.; Winslow, R. M.; Intaglietta, M. *Blood* **2006**, *108*, 3603−3610.

(3) Alayash, A. I. *Nat. Rev. Drug Discovery* **2004**, *3*, 152−159.

(4) Rohlfs, R. J.; Bruner, E.; Chiu, A.; Gonzales, A.; Gonzales, M. L.; Magde, D.; Magde, M. D.; Vandegriff, K. D.; Winslow, R. M. *J. Biol. Chem.* **1998**, *273*, 12128−12134.

(5) Goda, N.; Suzuki, K.; Naito, M.; Takeoka, S.; Tsuchida, E.; Ishimura, Y.; Tamatani, T.; Suematsu, M. *J. Clin. Invest.* **1998**, *101*, 604−612.

(6) Harder, D. R.; Narayanan, J.; Birks, E. K.; Liard, J. F.; Imig, J. D.; Lombard, J. H.; Lange, A. R.; Roman, R. *J. Circ. Res.* **1996**, *79*, 54−61.
(7) Lee, J. C.; Bermudez, H.; Discher, B. M.; Sheehan, M. A.; Won, Y. Y.; Bates, F. S.; Discher, D. E. *Biotechnol. Bioeng.* **2001**, *73*, 135−145.
(8) Rameez, S.; Alosta, H.; Palmer, A. F. *Bioconjugate Chem.* **2008**, *19*, 1025−1032.
(9) Ahmed, F.; Pakunlu, R. I.; Srinivas, G.; Brannan, A.; Bates, F.; Klein, M. L.; Minko, T.; Discher, D. E. *Mol. Pharmaceutics* **2006**, *3*, 340−350.
(10) Photos, P. J.; Bacakova, L.; Discher, B.; Bates, F. S.; Discher, D. E. *J. Controlled Release* **2003**, *90*, 323−334.
(11) Bermudez, H.; Brannan, A. K.; Hammer, D. A.; Bates, F. S.; Discher, D. E. *Macromolecules* **2002**, *35*, 8203−8208.
(12) Rameez, S.; Palmer, A. F. *Langmuir* **2011**, *27*, 8829−8840.
(13) Greenwald, A. R., Ed. *CRC Handbook of Methods for Oxygen Radical Research*; CRC Press: Boca Raton, FL, 1985; pp 137−141.
(14) Stoenescu, R.; Meier, W. *Chem. Commun.* **2002**, *24*, 3016−3017.
(15) Antonini, E.; Brunori, M. *Hemoglobin and Myoglobin in their Reactions with Ligands*; North-Holland: Amsterdam, 1971.
(16) Sakai, H.; Sato, A.; Masuda, K.; Takeoka, S.; Tsuchida, E. *J. Biochem.* **2008**, *283*, 1508−1517.
(17) Olson, J. S.; Foley, E. W.; Maillett, D. H.; Paster, E. V. *Methods Mol. Med.* **2003**, 65−91.
(18) Doherty, D. H.; Doyle, M. P.; Curry, S. R.; Vali, R. J.; Fattor, T. J.; Olson, J. S.; Lemon, D. D. *Nat. Biotechnol.* **1998**, *16*, 672−676.
(19) Butler, A. R.; Megson, I. L.; Wright, P. G. *Biochim. Biophys. Acta, Gen. Subj.* **1998**, *1425*, 168−176.
(20) Liao, J. C.; Hein, W. T.; Vaughn, M. W.; Huang, K. T.; Kuo, L. *Proc. Natl. Acad. Sci. U. S. A.* **1999**, *96*, 8757−8761.
(21) Liu, X.; Miller, M. J. S.; Joshi, M. S.; Sadowska-Krowicka, H.; Clark, D. A.; Lancaster, J. R. *J. Biochem.* **1998**, *273*, 18709−18713.
(22) Liu, X.; Samouilov, A.; Lancaster, J. R.; Zweier, J. L. *J. Biochem.* **2002**, *277*, 26194−26199.
(23) Harder, D. R.; Narayanan, J.; Birks, E. K.; Liard, J. F.; Imig, J. D.; Lombard, J. H.; Lange, A. R.; Roman, R. J. *Circ. Res.* **1996**, *79*, 54−61.
(24) Srinivas, G.; Discher, D. E.; Klein, M. L. *Nat. Mater.* **2004**, *3*, 638−644.
(25) Vandegriff, K. D.; Olson, J. S. *J. Biochem.* **1984**, *259*, 12609−12618.
(26) Palmer, A. F.; Sun, G.; Harris, D. R. *Biotechnol. Prog.* **2009**, *25*, 189−199.
(27) Sakai, H.; Okuda, N.; Sato, A.; Yamaue, T.; Takeoka, S.; Tsuchida, E. *Am. J. Physiol. Heart. Circ. Physiol.* **2010**, *298*, H956−H965.
(28) Sakai, H.; Sato, A.; Sobolewski, P.; Takeoka, S.; Frangos, J. A.; Kobayashi, K.; Intaglietta, M.; Tsuchida, E. *Biochim. Biophys. Acta, Proteins Proteomics* **2008**, *1784*, 1441−1447.

Macromolecules

Article

pubs.acs.org/Macromolecules

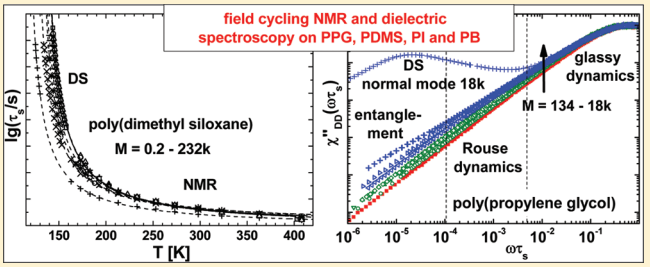
Glassy, Rouse, and Entanglement Dynamics As Revealed by Field Cycling ^{1}H NMR Relaxometry

M. Hofmann,[†] A. Herrmann,[†] A. Abou Elfadl,[†] D. Kruk,[‡] M. Wohlfahrt,[†] and E. A. Rössler*,[†]

[†]Experimentalphysik II, Universität Bayreuth, D-95440 Bayreuth, Germany

[‡]University of Warmia & Mazury Olsztyn, Faculty of Mathematics & Computer Science, Sloneczna 54, PL-10710 Olsztyn, Poland

ABSTRACT: Poly(propylene glycol), poly(isoprene), and poly(dimethlyl siloxane) (PDMS) of different molecular masses M are investigated by field-cycling ^{1}H NMR relaxometry to monitor the crossover from segmental dynamics, to Rouse and entanglement dynamics. The spin−lattice relaxation dispersions $T_1(\omega)$ obtained at different temperatures (160 K − 400 K) are converted to the susceptibility representation $\chi''_{DD}(\omega) = \omega/T_1(\omega)$. Applying frequency−temperature superposition, the data are merged to provide master curves $\chi''_{DD}(\omega\tau_s)$ with $\tau_s = \tau_s(T)$ being the segmental correlation times. Combining them with those from dielectric spectroscopy about 12 decades in time are covered. A similar M dependence of $\chi''_{DD}(\omega\tau_s)$ is observed for all polymers ($t \gg \tau_s$) and comparison with dielectric normal mode spectra is carried out. In the case of PDMS showing particularities at $t \approx \tau_s$ we attempt to separate intra- and intermolecular relaxation contributions. Transformation into time domain yields the dipolar correlation function $C_{DD}(t/\tau_s)$ which covers up to six decades in amplitude and eight decades in time. Whereas glassy dynamics is observed at shortest times, the correlation function closely follows $C_{DD}(t) \propto t^{-1}$ at intermediate times as predicted by the Rouse theory. For longer times and high M entanglement sets in yielding $C_{DD}(t) \propto t^{-\varepsilon}$ with ε (<1) being M-dependent. As for the previously studied poly(butadiene), a highly protracted transition to full reptation is observed.



1. INTRODUCTION

Since the pioneering work of Kimmich and co-workers,[1,2] field-cycling (FC) NMR relaxometry has been established as a powerful tool to probe polymer specific dynamics, i.e., dynamics on time scales longer than the segmental ("local") correlation time at $t \gg \tau_s$. The FC technique measures the spin−lattice relaxation time $T_1(\omega)$ as a function of frequency by switching cyclically the external magnetic field between a variable relaxation field and a fixed detection field. Typically a frequency range of 10 kHz to 20 MHz (for ^{1}H) is covered. T_1 dispersion curves of polymer melts show characteristic power-law regimes which have been discussed in the frame of the Rouse model in the case of nonentangled polymers ($M < M_e$), and the tube-reptation model or the renormalized Rouse model for entangled polymers ($M > M_e$) where M_e is the entanglement molecular mass.[1−3]

In a series of papers, we have recently reinvestigated the dynamics of linear polymers, in particular poly(butadiene) (PB), by employing FC ^{1}H NMR.[4−8] By turning to a susceptibility representation of the dispersion data and by applying frequency−temperature superposition (FTS), as often done in rheological experiments, one obtains master curves which monitor the dynamics over more than six decades in amplitude and eight decades in frequency, encompassing the segmental (or glassy,[59] $t \leq \tau_s$) dynamics as well as the collective polymer dynamics ($t \gg \tau_s$).

The master curves can be transformed into time domain; thereby the correlation function of the dipolarly coupled spin pairs of the polymer segments is obtained and can be checked against theory. In the case of entangled polymers, in addition to the segmental or glassy dynamics (regime 0) the free Rouse regime (I) and a regime (II) reflecting entanglement effects have been covered. These results have been combined by Chávez and Saalwächter with their data from double quantum (DQ) ^{1}H NMR which extend almost perfectly the FC ^{1}H NMR data up to even longer times.[9,10] In the light of these results, the NMR relaxation at times longer than the entanglement time τ_e in melts of linear polymers can be attributed to a highly protracted transition from Rouse dynamics to fully established tube-reptation. For example, the power-law exponent ε observed in regime II has turned out to be M-dependent decreasing continuously from $\varepsilon \approx 0.85$ for $Z = M/M_e \cong 1$ and reaching $\varepsilon \cong 0.29$ only above $Z > 100$ (see also Figure 9). The latter exponent is close to the value $\varepsilon = 0.25$ predicted by the Doi−Edwards tube-reptation model for regime II. In a subsequent DQ ^{1}H NMR work,[10] a similar protracted transition has been observed for poly(dimethylsiloxane) (PDMS) and poly(isoprene) (PI). In accordance with rheological[13,14] and dielectric experiments,[15] we have claimed that the crossover to full reptation occurs only above another characteristic molecular mass $M_r \gg M_e$.

In order to allow for a generalization of the results compiled so far for PB, further FC ^{1}H NMR studies are still lacking. Thus, for the present contribution, we have investigated a series

Received: October 24, 2011
Revised: January 27, 2012
Published: February 27, 2012

 © 2012 American Chemical Society

of poly(propylene glycol) (PPG), PI, and PDMS of molecular masses (M in g·mol^{-1}) ranging from the low-M limit up to $M \gg M_e$. Consequently, the crossover from pure glassy dynamics (very short chains) to Rouse and finally to entanglement dynamics (very long chains) is monitored for these polymer systems, and it is compared to the earlier results of PB.[5,6] Selected high-M results for PI and PDMS have already been published.[8]

PPG as well as PI belong to the group of type A polymers (Stockmayer classification[16]) showing a normal mode relaxation in the dielectric spectrum in addition to the segmental relaxation, the first reflecting fluctuations of the end-to-end vector of the polymer chain, i.e., polymer specific and M-dependent dynamics.[15] Thus, concerning polymer dynamics, a direct comparison of dielectric spectroscopy (DS) and FC ^{1}H NMR spectra measured from the same samples becomes possible. Recently, dielectric spectra of PPG have also been studied by Gainaru et al.[17,18] Our DS results on PI have been published by Abou Efadl et al.[15,19] The present study further shows that a generic NMR relaxation pattern for the different polymers is observed when M is increased systematically, and FC ^{1}H NMR allows determining the segmental correlation time $\tau_s(T)$, the molecular mass of the Rouse unit M_R, M_e, and, most important, the characteristic power-law regimes of the dipolar correlation function which are compared to those of regime I and II of the tube-reptation model.[1,3,20]

2. THEORETICAL BACKGROUND AND RELAXATION DISPERSION DATA TREATMENT

In the case of ^{1}H nuclei the spin−lattice relaxation time T_1 is determined by fluctuations of magnetic dipole−dipole interactions among proton spins which are of intra- as well as intermolecular origin.[1,2,21] Because of the dipolar interaction being short ranged, it is usually assumed that intramolecular fluctuations mediated by reorientational dynamics (via the rank-two reorientational correlation function $C^{(2)}(t)$) dominate the ^{1}H relaxation. However, direct comparison between ^{1}H and ^{2}H NMR relaxation as well as results of isotope dilution experiments clearly demonstrate that intermolecular relaxation is of importance.[22−24] The fluctuations of the intermolecular interactions are governed predominantly by translational motion. In polymer melts intermolecular relaxation shows up in particular at low frequencies. As demonstrated by Kehr et al.[22] the mean square displacement of a polymer segment can be determined by extracting the spectral density from the intermolecular relaxation contribution. Because of the intermolecular contribution to the (total) relaxation rate T_1^{-1}, we shall use the symbol $C_{DD}(t)$ for the dipolar correlation function probed in ^{1}H NMR in order to distinguish it from the purely reorientational correlation function $C^{(2)}(t)$.

In order to apply FTS and to allow comparisons with other techniques we rewrite the Bloembergen, Purcell, Pound expression[25] for the relaxation rate T_1^{-1} to the susceptibility representation[4−8]

$$\omega/T_1(\omega) = K[\chi''(\omega) + 2\chi''(2\omega)] \equiv 3K\chi''_{DD}(\omega) \qquad (1)$$

with the angular frequency given by $\omega = \gamma B$. K denotes the NMR coupling constant, γ is the gyromagnetic ratio, and $\chi''(\omega) = \omega J(\omega)$, the dissipative part of the complex susceptibility. The spectral density $J(\omega)$ is given as the Fourier transform of the correlation function. Even though $\chi''_{DD}(\omega)$ is a weighted sum of two susceptibility terms it is barely distinguishable from the individual susceptibilities for a broad relaxation dispersion discussed on logarithmic scale. The factor 3 keeps the integral over the susceptibility $\chi''_{DD}(\omega)$ normalized to $\pi/2$.

By varying temperature over a large interval glassy dynamics as well as polymer specific dynamics show up in the frequency window of the FC ^{1}H NMR technique. Glassy dynamics dominate the relaxation at low temperatures while polymer specific dynamics prevail at high temperatures. By applying FTS one is able to construct master curves $\chi''_{DD}(\omega\tau_s(T))$. For that purpose those susceptibility curves exhibiting a relaxation maximum are fitted on the high-frequency side to a Cole−Davidson (CD) function,[26] i.e., at $\omega\tau_s \geq 1$ for which no contributions from polymer dynamics are expected and only glassy dynamics are present.[27] This provides values of the correlation time τ_s. Plotting these susceptibility spectra as a function of $\omega\tau_s$ the other spectra are shifted along the frequency to obtain best overlap among each other. The temperature dependent shift factors yield the time constant $\tau_s(T)$ of the segmental motion, which can be identified with that of the structural relaxation (α-process) being characteristic of glassy dynamics occurring at short times, explicitly for $\tau_s \cong \tau_\alpha$. For simple liquids and oligomers with $M < M_R$, there is no spectral contribution at $\omega\tau_s < 1$ in excess to the "simple liquid limit" $\chi''_{DD}(\omega\tau_s) \propto \omega^1$, and their susceptibility master curves solely represent glassy dynamics ("glassy spectrum"). For polymers with $M > M_R$, additional intensity on the low-frequency side of the main relaxation ("α-peak") reflects collective, polymer specific dynamics. The master curves $\chi''_{DD}(\omega\tau_s)$ present "isofrictional spectra"[27] and allow comparing the results for different M.

3. EXPERIMENTAL SECTION

We have investigated samples of poly(propylene glycol) (PPG), poly(isoprene) (PI), and poly(dimethlyl siloxane) (PDMS) of different molecular mass $M = M_w$ (cf. Table 1) reflected by the sample name code.

PPG, PI, and PDMS were obtained from Polymer Standards Service PSS, Mainz (Germany), except PPG-18k which has been provided by the Böhmer group from TU Dortmund. Inspecting several sources for high-M PPG, we were not yet able to obtain PPG with $M > 18200$ g·mol^{-1}.

The dispersion of the spin−lattice relaxation time T_1 was measured by a STELAR relaxometer FFC 2000, which allows measurements in the temperature range 150−420 K and in ^{1}H Larmor frequency range of 10 kHz $\leq \nu \leq$ 20 MHz. The accuracy of the temperature measurements is typically better than ±0.3 K, while the stability is better than ±1 K. We observed single exponential relaxation over at least 1 order of magnitude in magnetization.

The dielectric spectra were measured using an Alpha-A spectrometer from Novocontrol as described in ref 15.

4. RESULTS

From Relaxation Dispersion Data to Susceptibility Master Curves. In Figure 1a,b, we show exemplarily the relaxation dispersion $T_1(\nu)$ together with the corresponding susceptibility representation $\chi''_{DD} \propto \omega/T_1(\omega)$ of the data for PPG-134 and in Figure 1c,d for PPG-18k as measured by FC ^{1}H NMR in the temperature range of 210 to 400 K. The data correspond to the second-lowest and to the highest molecular mass, respectively, in the series of the investigated PPG samples (*cf.* Table 1) and allow distinguishing the impact of the chain length. We have chosen PPG-134 as the low-M reference system which presumably does not yet show any polymer specific relaxation phenomena. Its susceptibility spectra at 253K, 258K and 263K are well fitted by a CD function typical of pure

dx.doi.org/10.1021/ma202371p | Macromolecules 2012, 45, 2390−2401

Table 1. Investigated Samples: Their Molecular Mass M_w (Mass Average), M_n (Number Average) and Polydispersity M_w/M_n[a]

sample PPG	M_w [g/mol]	M_w/M_n	sample PDMS	M_w [g/mol]	M_w/M_n	sample PI	M_w [g/mol]	M_w/M_n
PG	76	1.0	PDMS-162	162	1.0	PI-652	652	1.1
PPG-134	134	1.0	PDMS-311	311	1.1	PI-790	790	1.12
PPG-192	192	1.0	PDMS-860	860	1.41	PI-1.0k	1040	1.09
PPG-455	455	1.06	PDMS-1.6k	1600	1.37	PI-1.4k	1370	1.09
PPG-790	790	1.03	PDMS-2.5k	2490	1.4	PI-1.9k	1920	1.07
PPG-1k	1000	1.03	PDMS-3.6k	3620	1.23	PI-2.4k	2390	1.05
PPG-3k	3080	1.03	PDMS-5.9k	5940	1.15	PI-4.5k	4470	1.04
PPG-5k	5300	1.06	PDMS-11k	11 000	1.05	PI-10k	9910	1.02
PPG-18k	18 200	1.02	PDMS-22k	21 600	1.04	PI-14k	13 500	1.02
			PDMS-41k	41 400	1.03	PI-15k	14 900	1.02
			PDMS-128k	128 000	1.13	PI-21k	21 200	1.03
			PDMS-232k	232 000	1.06	PI 47k	47 300	1.01
						PI-110k	110 000	1.01
						PI-157k	157 000	1.01

[a]Regarding the data of PB we refer to ref 5.

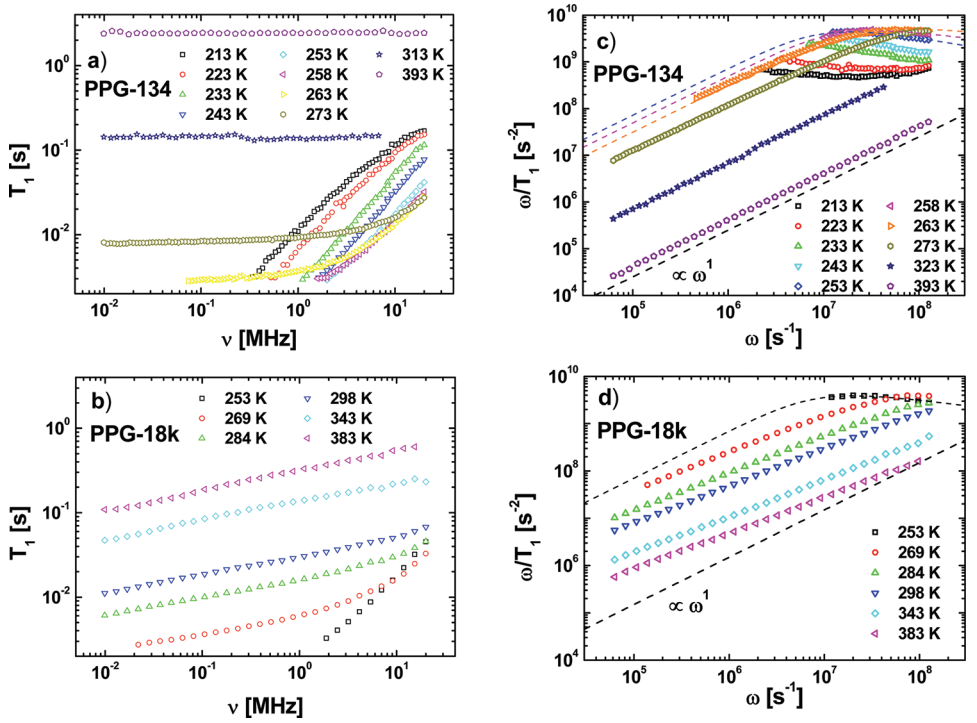


Figure 1. Dispersion of the ^{1}H spin−lattice relaxation time T_1 for (a) di(propylene glycol) PPG-134 and (b) high M PPG-18k. (c and d) Corresponding susceptibility representations of the dispersion data $\chi''_{DD} = \omega/T_1(\omega)$. Low temperature curves featuring a relaxation maximum have been fitted to a CD function (colored dashed lines). The simple liquid limit $\chi''_{DD} \propto \omega^1$ is indicated in (c) and (d) (black dashed lines).

glassy dynamics and thus providing the "simple liquid limit" $\chi''_{DD} \propto \omega^1$ at $\omega\tau_s \ll 1$ (*cf.* Figure 1c).

The PPG-134 dispersion curves (Figure 1a) feature no dispersion at all when measured at the highest temperatures of 313 K and 393 K, i.e., the susceptibility (Figure 1b) shows a Debye behavior, $\chi''_{DD} \propto \omega^1$. At low temperatures a maximum in $\chi''_{DD}(\omega)$ is observed which shifts towards low frequencies upon cooling and is attributed to the segmental dynamics reaching the condition $\omega\tau_s \cong 1$. All this is typical of the relaxation behavior of a simple liquid.[5] At the lowest temperatures even a minimum is found in $\chi''_{DD}(\omega)$ which is attributed to some secondary relaxation process and has also been observed in dielectric experiments.[18,28]

For the high-M case PPG-18k, the high temperature relaxation data already show expressed dispersion. In the susceptibility representation the spectrum at high temperatures ($\omega\tau_s \ll 1$) rises flatter than a Debye behavior. It can be described by a power-law $\chi''_{DD} \propto \nu^\alpha$ with $\alpha \leq 1$, and the exponent shows a tendency to become somewhat smaller at lower frequencies. Such a dispersion behavior is typical of polymer dynamics which determine the relaxation at $\omega\tau_s \ll 1$.[4−8] Again, at low temperatures relaxation maxima are observed in $\chi''_{DD}(\omega)$ when the segmental dynamics determines the relaxation. The maxima are fitted to a CD function for $\omega\tau_s \geq 1$ (cf. Figure 1c,d) which yields the segmental correlation time τ_s.

This fitting to a CD function has been applied to all the samples of PPG, PI, and PDMS (*cf.* Table 1), and in the next step of the data analysis, we have assumed, in accordance to our previous works[4−8] and to most rheological studies[27,29] that FTS applies. Consequently, master curves χ''_{DD} ($\omega\tau_s$) have been

dx.doi.org/10.1021/ma202371p | *Macromolecules* 2012, 45, 2390−2401

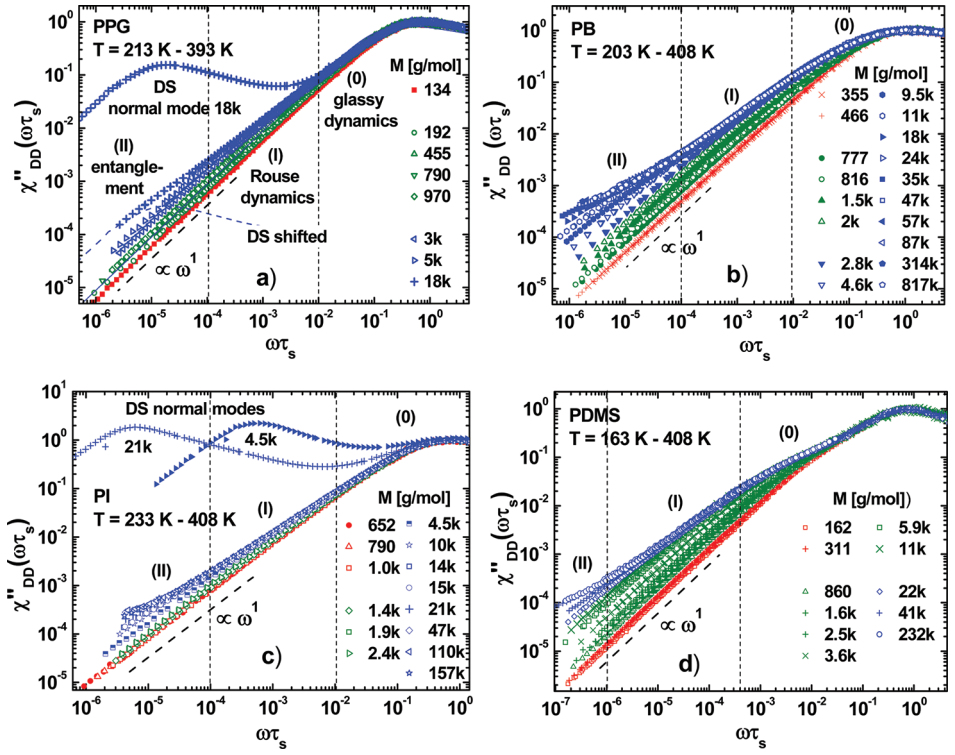


Figure 2. Scaled susceptibility master curves of PPG, PB, PI, and PDMS including dielectric normal modes for PPG-18k and PI-21k and PI-4.5k. Red symbols: curves only showing "glassy dynamics", $M < M_R$ (simple liquid limit). Green symbols: curves showing solely Rouse dynamics, $M_R < M < M_e$. Blue symbols: Polymers affected by entanglement, $M > M_e$. In part a, the normal mode spectrum is shifted on top of the NMR spectrum (blue dashed line) demonstrating good agreement at lowest frequencies where the terminal relaxation sets in.

constructed (cf. theoretical background), which are compared to those of PB previously measured[4−8] (see Figure 2, some new data for PB has been added). The master curves have further been scaled in amplitude that they agree for each polymer series in the range of the relaxation peak ($\omega\tau_s \geq 1$). Thereby slight changes in the amplitude of the relaxation maximum (about 30% for PPG, 25% for PI and 20% for PDMS) are removed. Those are attributed to some changes of the NMR coupling constant K with M possibly reflecting changes in density (*cf.* below). Thereby we have assumed implicitly that the segmental relaxation does not change with M, a fact which has been proven in a DS study of PDMS by Hintermeyer et al.[30]

Dependence of the Susceptibility on Molecular Mass. The master curves for each series (Figure 2) overlap perfectly around their main relaxation peak $\omega\tau_s \cong 1$, indicating that the segmental dynamics is indeed M-independent for all investigated systems. In the case of PPG the secondary process observed at $\omega\tau_s \gg 1$(actually not following FTS) is not shown here and will not be discussed further. With increasing M, on the low-frequency flank at $\omega\tau_s < 1$, the curves begin to deviate increasingly strong from the Debye behavior, $\chi''_{DD} \propto \omega^1$, expected for pure glassy dynamics and observed for the low-M reference systems. This low-frequency excess intensity is characteristic for polymer specific relaxations, notably Rouse and entanglement dynamics, the latter only occurring at high $M > M_e$. The samples of intermediate M (tagged in green in Figure 2) show an excess contribution which grows systematically with M. The susceptibility curves for high M (tagged in blue) show an even more enhanced relaxation contribution in $\chi''_{DD}(\omega\tau_s)$ at lower frequencies while their amplitudes saturate at intermediate frequencies, i.e., the curves display an inflection point, that is a bimodal character, which is typical of entanglement dynamics.[4,6] This sketched relaxation behavior is virtually observed for all polymers in Figure 2.

Accordingly, three dispersion regimes (indicated by 0, I, II in Figure 2) can be distinguished which are best recognized when the susceptibility spectra for high $M > M_e$ are considered.[9,10] The segmental dynamics at $\omega\tau_s \cong 1$, governed by the glassy dynamics, and the crossover to polymer dynamics at $\omega\tau_s < 1$ define regime 0 in Figure 2a−d. In the intermediate frequency region (regime I), the relaxation contributions grow with M until they saturate around $2M_e \cong M_c$ (cf. Table 2)

Table 2. Estimated Values for M_R (Molecular Mass of the Rouse Unit) and used M_e (Entanglement Molecular Mass, from Literature As Indicated) (*cf.* Figure 4)

system	M_R [g·mol^{-1}] (from Figure 4)	M_e [g·mol^{-1}] (from lit.)	ref for M_e
PPG	150	3500	40
PB	500	1800	41
PI	1000	5400	41
PDMS	600	12 200	41

demonstrating that the development of further Rouse modes is impeded for entangled polymers. At the highest M and lowest frequencies another dispersion behavior shows up which defines regime II governed by entanglement dynamics. Here, like in regime I the susceptibility is describable by a power-law with an exponent, however, significantly smaller than that in regime I.

For polymer chains being not too long the susceptibilities at lowest frequencies bend over to a $\chi''_{DD}(\omega) \propto \omega$ behavior which indicates that in these cases the terminal relaxation is reached.

dx.doi.org/10.1021/ma202371p | *Macromolecules* 2012, 45, 2390−2401

For PB this is observed for $M \leq 18$k. At higher M all PB samples show the same relaxation behavior which demonstrates that in the accessible frequency range no changes with M occur any longer. In this case, the terminal relaxation region is not covered by the FC frequency window. For PPG, the terminal relaxation is covered for all samples. For PI and PDMS, the terminal relaxation is only reached for the nonentangled samples ($M < M_e$).

Compared to PDMS, PPG and particularly to PB the susceptibility master curves of PI exhibit a much weaker contribution of polymer dynamics but qualitatively a similar dependence on M in the range $\omega\tau_s \ll 1$. The master curves of PDMS show some atypical behavior as already reported in ref 8. There appears a kind of shoulder in the regime $\omega\tau_s \leq 1$ that is a significant excess intensity with respect to the CD susceptibility of the low-M limits PB-466, PPG-134, or PI-652. This spectral feature is already present in the simple liquid limit and appears for all PDMS samples leading to a common relaxation behavior at $3 \times 10^{-2} \leq \omega\tau_s \leq 1$, i.e., in a frequency range for which M-depending spectral contributions from polymer dynamics are already found for the other polymers. Actually, M-dependent contributions only set in at $\omega\tau_s < 3 \times 10^{-2}$. In other words, the segmental or local dynamics in PDMS show an M-independent low-frequency particularity not observed in the other polymers. Here one may argue that this additional relaxation is similar to what one sometimes finds in low-molecular liquids where it is attributed to translational dynamics mediated by the intermolecular ^{1}H relaxation.[31,32] However, translational dynamics in polymers is not expected to be M-independent. Moreover, suppressing the intermolecular relaxation by diluting PDMS with deuterated PDMS, this effect is essentially not disappearing, signaling its intramolecular origin (this is demonstrated in Appendix A).

Poly(dimethylsiloxane) is among the most flexible polymers with nearly no conformational barrier[33] and which, according to neutron scattering (NS) experiments[34] shows Rouse modes up to high momentum transfers and thus no signs of anomalous segmental dynamics are found. Thus, at present we are not able to provide an explanation for the low-frequency process. That polymer dynamics sets in only at $\omega\tau_s \leq 3 \times 10^{-1}$ indicates that $\tau_0 \gg \tau_s$, i.e., the shortest Rouse time τ_0 is no longer identical with the segmental correlation time τ_s the latter controlling the main relaxation peak in Figure 2d. This is confirmed by dielectric spectroscopy[15] which yields correlation times agreeing well with those from FC ^{1}H NMR (*cf.* Appendix B, Figure 11). Therefore, the main relaxation of PDMS cannot be attributed to methyl group rotation, an issue reserved to NMR, as one could also speculate. Another feature appears special in the case of PDMS. Although the polymer specific contributions are rather weak with respect to the segmental dynamics (*cf.* Figure 4), the change of the polymer contribution with M until the Rouse dynamics reaches its saturation when entanglement effects set in is quite large. We will come back to this in the context of discussing Figure 6.

As PPG and PI carry a component of the monomeric dipole moment directed along the polymer chain (type A polymers), in addition to the segmental dynamics the fluctuation of the end-to-end vector is also probed via the normal mode relaxation appearing as an additional relaxation peak at frequencies $\omega\tau_s \ll 1$. We included some dielectric spectra of PPG-18k, PI-4.5k, and PI-21k (for PI, see also ref 15) in Figure 2, parts a and c, and scaled them to match in the frequency range of the segmental relaxation (regime 0). As the normal mode peak is dominated by the slowest polymer mode, just as the contribution to the NMR susceptibility at lowest frequencies, both manifest themselves in the similar frequency range. This is demonstrated by shifting the normal mode peak of PPG-18k on top of the NMR spectrum (dashed line in Figure 2a). At lowest frequencies both spectra follow a Debye behavior signaling the terminal relaxation to set in at similar time scales. A common quantitative description of both relaxation spectra is not an easy task as in the case of the NMR data the needed decomposition in contributions of segmental and polymer dynamics is not straightforward. We note that in the frequency range of the segmental dynamics DS and FC NMR susceptibility agree well, in particular, for PPG.

Change of the NMR Coupling Constant with *M*. In Figure 2, the susceptibilities have been scaled to coincide in the regime $\omega\tau_s \geq 1$ for which the contribution from glassy dynamics determines the relaxation. The scaling factor reflects the magnitude of the NMR coupling constant K (*cf.* Equation 1), and it turned out that it depends on M in a systematic way. In order to quantify this effect we integrated the susceptibility curve for each M. According to[21]

$$\int_0^\infty T_1^{-1}(\omega)\, d\omega = \frac{3\pi}{2}K \qquad (2)$$

this yields an effective coupling constant K which reflects the internuclear distances.[60] In Figure 3 K/K_∞ is plotted as a function of M where K_∞ denotes the limit at the highest M. For all polymers a systematic trend is observed, however, an increase as well as a decrease with M is found. The coupling constant contains intramolecular and intermolecular contributions, but only the intermolecular part is expected to alter when the density of the polymer melt changes with M. In order to compare the coupling constant K with the density we included in Figure 3 density data ρ/ρ_∞ for PPG[35,36] and PDMS.[37] Indeed, the overall trend with M found for ρ is reflected by K. Interestingly, PPG becomes less dense at high M probably due to association effects of the hydroxyl groups. Thus, we conclude that a full analysis of the relaxation curves even allows estimating the trend of the density with M. Here a note is worthwhile. We have chosen to compare K with the density and not, as often done, with the square of the density, although taking the latter would provide an even better agreement. We motivate our approach that in the polymer melt the

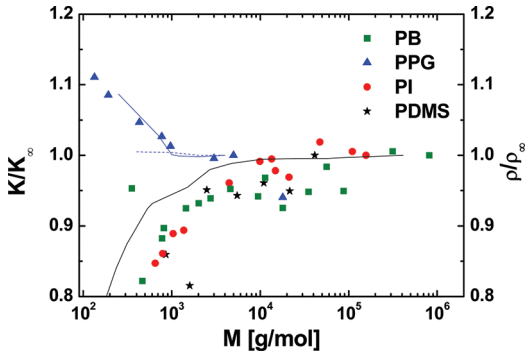


Figure 3. Effective coupling constant K/K_∞ vs. molecular mass M for PB (with $K_\infty = 2.54 \times 10^9$ Hz^2), PI ($K_\infty = 1.89 \times 10^9$ Hz^2) and PDMS ($K_\infty = 7.78 \times 10^9$ Hz^2) featuring an increase in K/K_∞ with M. For PPG ($K_\infty = 11.21 \times 10^9$ Hz^2) instead a decrease is observed. The lines reflect the density of PPG[35,36] and PDMS[37] as provided from literature.

dx.doi.org/10.1021/ma202371p | *Macromolecules* 2012, 45, 2390–2401

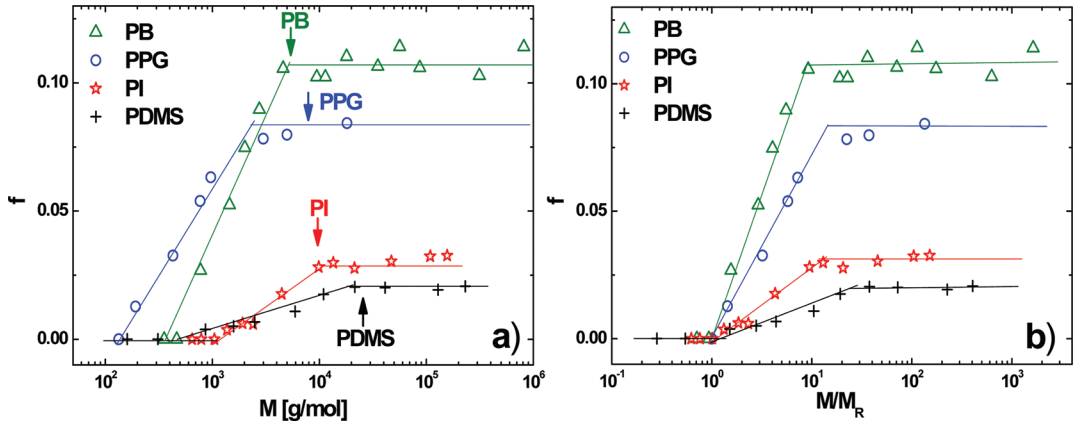


Figure 4. Relative strength of polymer dynamics f for PPG, PI, PDMS and PB as a function of M (a) and of M/M_R (b). The lines are guides-for-the-eye. The arrows indicate the crossover molecular masses $M_c \approx 2M_e$ from literature (*cf.* Table 2) around which the f values saturate in all the systems.

intermolecular relaxation rate is proportional to N/d^3, with N denoting the spin density and d the distance of closest approach.[21]

Polymer Relaxation Strength. Assuming statistical independence between glassy and polymer dynamics one can decompose the correlation function as a product[1,4−6]

$$C_{DD}(t) = C_{DD}^{\text{glassy}}(t)C_{DD}^{\text{polymer}}(t) \tag{3}$$

where $C_{DD}^{\text{glassy}}(t)$ denotes the correlation loss due to glassy dynamics and $C_{DD}^{\text{polymer}}(t)$ that due to polymer dynamics (Rouse and entanglement dynamics). Introducing the relative magnitude of polymer dynamics f, i.e., the fraction of correlation loss not relaxed by glassy dynamics (through $\phi_{DD}^{\text{glassy}}(t)$) allows us to rewrite this expression:

$$C_{DD}(t) = [(1-f)\phi_{DD}^{\text{glassy}}(t) + f]C_{DD}^{\text{polymer}}(t) \tag{4}$$

The polymer relaxation strength f can be identified with the squared order parameter of polymer dynamics[6,39] $S^2 = f$, a measure for the spatial restriction of segmental motion due to chain connectivity and confinement (entanglement) effects. The product of both correlation functions occurring in eq 4 transforms itself as a convolution of the glassy $\chi''_{\text{glassy}}(\omega)$ and the polymer susceptibility spectrum $\chi''_{\text{polymer}}(\omega)$. Under the assumption of time scale separation,[2] one can replace the convolution by the sum of the two individual susceptibilities:

$$\chi''_{DD}(\omega) \cong (1-f)\chi''_{\text{glassy}}(\omega) + f\chi''_{\text{polymer}}(\omega) \tag{5}$$

Thereof f is given by

$$f = \frac{\int_{-\infty}^{\infty} \mathrm{d}[\ln(\omega)]\chi''_{\text{polymer}}(\omega)}{\int_{-\infty}^{\infty} \mathrm{d}[\ln(\omega)]\chi''_{DD}(\omega)} \tag{6}$$

The polymer spectrum is obtained by subtraction of the spectrum of the low-M reference system from the overall susceptibility master curves. We note that the decomposition (eq 5) may be challenged on the basis that the relaxation processes in polymer melts are indeed not completely statistically independent and that the time scale separation actually does not hold for glassy and Rouse dynamics. We take f as a mere measure of characterizing the M dependence of the relaxation spectrum of the different polymers. Furthermore, given this approach any low-frequency excess contribution with respect to that of the low-M reference system will lead to some nonzero value of f. Whether it is indeed already a polymer specific contribution or has to be attributed to some relaxation process of a not yet polymeric oligomer has to be discussed for each polymer.

In Figure 4a, we show the results for f as a function of M. For very low $M < M_R$, PB, PI, and PDMS feature per definition a vanishing strength parameter f as it is expected for simple liquids. PPG provides an exception here since the relaxation strength rises quickly as even for the trimer system PPG-192 a nonvanishing f value is observed. Finally, at high M saturation is found at a level which is different for the four polymers considered here. For example PI and PDMS show quite small polymer relaxation strength when compared to PPG and to the system with the highest order parameter, PB. As previously discussed, f is not expected to be universal, instead it depends on structural details of the internuclear vectors in the monomer.[8] We associate the saturation of $f(M)$ with the onset of entanglement which leads to saturation of the amplitude in regime I (*cf.* Figure 2). The further emergence of relaxation contributions at lower frequencies, which constitutes dispersion regime II, does not significantly increase the relaxation strength due to its occurrence at very low amplitudes. It appears that saturation of f occurs rather at M_c than at M_e (*cf.* Table 2 and arrows in Figure 4a). Introducing the molecular mass M_R of the Rouse unit, i.e, the mass at which the first Rouse mode becomes active, and plotting f as a function of M/M_R a similar behavior of f is observed at $M > M_R$ (*cf.* Table 2). Yet, saturation is found at different M/M_R values indicating that M_R and M_c are not correlated.

Spectral Densities. Dividing the susceptibility master curve data $\chi''_{DD}(\omega\tau_s)$ (Figure 2) by the reduced frequency $\omega\tau_s$ one gets master curves of the spectral densities which are displayed in Figure 5a−d for the present samples. Here, all curves have been first extrapolated to highest frequencies $\omega\tau_s \gg 1$ by a CD function and then normalized in the sense that $\int_0^\infty J_{DD}(x)\,\mathrm{d}x = \pi/2$ with $x = \omega\tau_s$ is fulfilled. Of course, this representation of the data is nothing else than the originally measured relaxation rate, however, in form of a master curve. As we will demonstrate this representation of the relaxation data allows further insights; in particular, the prediction of the Rouse theory can be tested.

As in Figure 2, the coloring marks the low-M limit (red), nonentangled (green) and entangled polymer chains (blue). At high frequencies, the curves essentially overlap due to an M-independent spectral shape of the segmental relaxation (regime 0).

dx.doi.org/10.1021/ma202371p | *Macromolecules* 2012, 45, 2390−2401

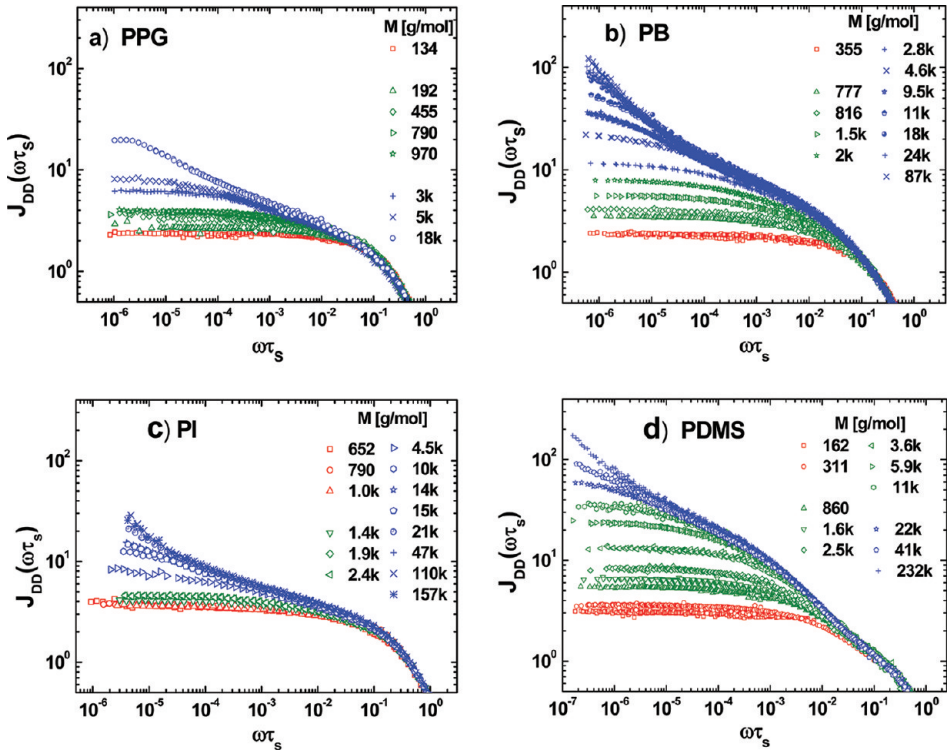


Figure 5. Normalized master curves of the spectral density for PPG (a), PB (b), PI (c), and PDMS (d) as a function of reduced frequency $\omega\tau_s$ obtained from Figure 2.

At intermediate values of $\omega\tau_s$ the curves for different M drift apart with respect to the corresponding low-M system caused by the successive emergence of Rouse modes (regime I). The amplitudes saturate in the Rouse regime at $M \cong M_c$ due to entanglement effects which lead to a further enhancement only at even lower reduced frequencies (regime II). At the lowest accessible frequencies, the curves of nonentangled systems, in some cases also of entangled polymers, saturate and form a plateau $J_{DD}(\omega \to 0) = const.$ corresponding to the Debye-behavior in the susceptibility $\chi''_{DD}(\omega\tau_s) \propto \omega$ signaling that the terminal relaxation is reached.

In the previous work on PB,[6] we analyzed the spectral density $J_{DD}(\omega)$ at the lowest frequencies, i.e., in the limit $\omega\tau_R \ll 1$ where a plateau is observed in Figure 5. Here, τ_R denotes the Rouse time, which is the correlation time of the longest Rouse mode. This plateau value gives access to the mean correlation time of the polymer dynamics, and in the case of Rouse dynamics a logarithmic N dependence is expected for large $N = M/M_R$. Explicitly[6]

$$J_{DD}^{\text{Rouse}}(0) = \left(\frac{\pi\tau_0}{2}\right) \ln N \tag{7}$$

The time τ_0 specifies the shortest Rouse time. Thus, quite a weak N (or M) dependence is expected for the Rouse dynamics, and deviations at high M will indicate entanglement effects. In Figure 6 $J_{DD}(0)$ is plotted as a function of M as obtained from Figure 5. Again, three regimes can be identified. The low-M systems presumably represent solely the M-independent glassy dynamics (all red curves in Figure 2 and 5). Above M_R, $J_{DD}(0)$ slowly increases due the emergence of Rouse modes. Here, indeed, an approximately logarithmic increase with M is observed. Beyond some M which is different for each polymer series, the values for $J_{DD}(0)$ begin to deviate

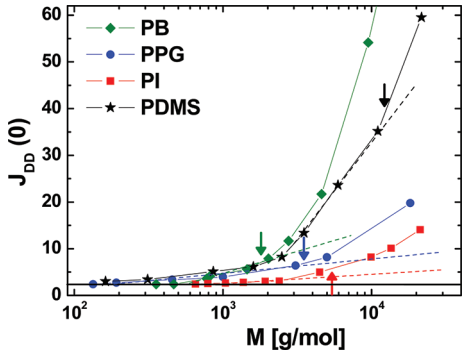


Figure 6. The spectral density at zero frequency $J_{DD}(0)$ as a function of M for all polymers with the simple liquid limit represented by the black solid line (from Figure 5). The arrows indicate the literature value for M_e (cf. Table 2) above which a stronger increase of $J_{DD}(0)$ is observed. The dashed lines mark the Rouse regime.

from the behavior predicted by the Rouse theory showing a sharp rise. This we take as a hint that entanglement effects become relevant which lead to a further retardation of the relaxation. In Figure 6 we included the M_e values reported in the literature (*cf.* Table 2) pictured by arrows. The strong increase of $J_{DD}(0)$ beyond the Rouse prediction sets essentially in when M_e is surpassed.

PDMS appears again as an exception for which a strong increase $J_{DD}(0)$ is observed in Figure 6 well before $M_e \cong 10^4$ is reached. Inspecting the susceptibility curves (Figure 2) as well as the correlation function $C_{DD}(t)$ (*cf.* Appendix D) no bimodal character (as in the case of PB) is recognized for $M < 11$k. Thus, the strong increase of $J_{DD}(0)$ below $M = 11$k originates from Rouse dynamics, and we note that M_e in PDMS is significantly larger as compared to the other polymers investigated here (*cf.* also Table 2). Extrapolation according

dx.doi.org/10.1021/ma202371p | *Macromolecules* 2012, 45, 2390−2401

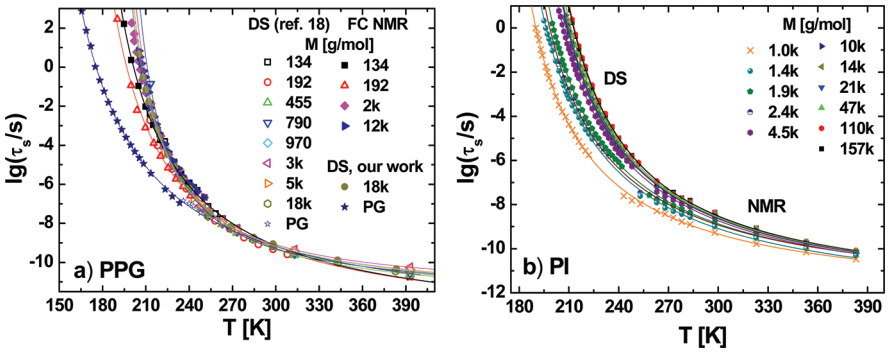


Figure 7. (a) Segmental correlation times $\tau_s(T)$ as a function of T for PPG and propylene glycol (PG) of different molecular mass M as obtained from the FC ^{1}H NMR master curves compared to the results from dielectric spectroscopy.[18] (b) Same plot for PI samples (cf. ref 15). The combined data sets have been fitted by a Vogel–Fulcher–Tammann (VFT) function (solid lines).

to eq 7 the highest $J(0)$ values down to zero yields $M \cong 2000$ which is rather large, and at this M value significant low-frequency excess intensity is still found in Figure 5. In other words, the extrapolation probably overestimates the Rouse unit M_R. Correspondingly, one recognizes a first, however weak, increase of $J(0)$ (with respect to the low-M reference, $M = 311$) already well below $M \cong 2000$. Here, one might speculate whether this initially weak increase reflects a sub-Rouse relaxation phenomena and full Rouse modes emerge only at $M \geq 2.5$k. This could also explain the increase of $J_{DD}(0)$ at very low-M in the case of PPG. As mentioned before PDMS is a highly flexible molecule with a quite short Kuhn length and M_R, respectively. Sokolov et al.[42] suggest $m_r \approx 560$ as the molecular mass of the "random step" (a term equivalent to the Rouse unit M_R) for PDMS which is only somewhat larger than the Kuhn element whereas in polystyrene $m_r \approx 5000$ is found being much larger than the Kuhn mass. As in the case of the NS study,[34] polymer specific dynamics are expected to set in at comparatively low M in the case of PDMS. In conclusion, it is not easy to define a clear-cut identification of first Rouse modes, and we refrain to use the data in Figure 6 for determining any Rouse unit M_R. Only in the case of PB and PI no excess dynamics is found up to $M \cong 500$ and $M \cong 1000$, respectively, and a clear-cut distinction between polymer specific and local dynamics appears possible.

Another question is what fixes the strength of the increase $J(0)$ with M which is much stronger for PDMS as compared to the other polymers investigated (cf. Figure 6). Inspecting eq 7 the slopes of the straight lines in Figure 6 characterizing the Rouse regime depend on the shortest Rouse time τ_0 which in the case of PDMS is much longer than τ_s, and this we think is responsible for the much stronger increase of $J(0)$ with M in the case of PDMS.

Here, a remark is worthwhile. Previously, eq 7 has been tested for FC ^{1}H NMR spectra of PB,[6] and for this purpose the "glassy spectrum" measured for the low-M reference system has been subtracted from the total susceptibility spectra whereby "polymer spectra" have been obtained. However, this procedure can be challenged because (i) actually no time scale separation holds between Rouse and glassy dynamics, and (ii) one can argue that the lowest Rouse mode has to be identified with that of glassy dynamics. Therefore, we have analyzed the total spectral densities or susceptibility spectra, respectively.

Segmental Time Constants. By constructing the master curves the segmental time constants $\tau_s(T)$ are obtained. The results for the series of PPG and PI samples are shown exemplarily in Figure 7, parts a and b, respectively and compared to findings from dielectric measurements from our group in the case of PI[15] and by those of Gainaru et al. for PPG.[18] The data for PDMS and PB are shown in the Appendix B (Figure 11), the latter have already been published before.[6] Both NMR and DS cover complementary time windows. The PPG results indicate that $\tau_s(T)$ and therefore the segmental motion is only weakly M-dependent except for propylene glycol which shows a significantly lower glass transition temperature T_g. This contradicts the result of ref 28, where large shifts of $\tau_s(T)$ with M have been reported. In the latter case, however, the hydroxyl end groups of the PPG chains were capped by methyl groups. Also in the case of PDMS (Figure 11b), good agreement is observed among the NMR and dielectric data and the time constants change with M. We take the overall agreement among the results as confirmation for the validity of FTS in all investigated samples.

In Figure 7, the time constants $\tau_s(T)$ are plotted as a function of T instead of T^{-1} as often done. For PI (as well as for PDMS, *cf.* Appendix B, Figure 11b) it is recognized that the curves for the various M values show quite similar behavior close to T_g. Thus, the quantity $F = -\mathrm{d}[\lg(\tau_\alpha)]/\mathrm{d}T|_{T=T_g}$ appears to be constant for a series of the same polymer.[15,19] Often the temperature dependence of $\tau_s(T)$ is specified by the fragility or the so-called steepness parameter $m = \mathrm{d}[\lg(\tau_\alpha)]/\mathrm{d}(T_g/T)|_{T_g} \equiv FT_g$. Given that F is M-independent the fragility m is proportional to T_g as reported by several authors.[43] The segmental correlation time close to T_g may be expressed by an M-independent function $\tau_\alpha = f(T - T_r)$ with T_r being some reference temperature, e.g., T_g.[15,19] We note that F becomes M-dependent for low M, i.e., when the system is still in the simple liquid limit (*cf.* ref 19 and Figure 7). Here, one may speculate whether fragility m is an appropriate quantity to be discussed for polymers at least. For comparison, in Figure 12 (cf. Appendix C) the time constants are plotted as a function of T^{-1}, and actually, in the latter representation the "steepness" of $\ln \tau(1/T)$ close to T_g is changing with M.

Dipolar Correlation Functions. The master curves of the spectral density in Figure 5 can be Fourier transformed into the time domain to access the dipolar correlation function $C_{DD}(t)$. Figure 8 depicts the results for PPG (a) and PB (b), which turned out to be the two most representative systems in the time domain concerning our measurements. The correlation functions for PI and PDMS can be found in the Appendix D (Figure 13). The correlation function of PPG is monitored up to six decades in amplitude and more than seven decades in (reduced) time. In going from the low-M system PPG-134 to high-M PPG-18k, the correlation decay becomes increasingly stretched. At $M \geq 3$k, the correlation displays a bimodal

dx.doi.org/10.1021/ma202371p | *Macromolecules* 2012, 45, 2390–2401

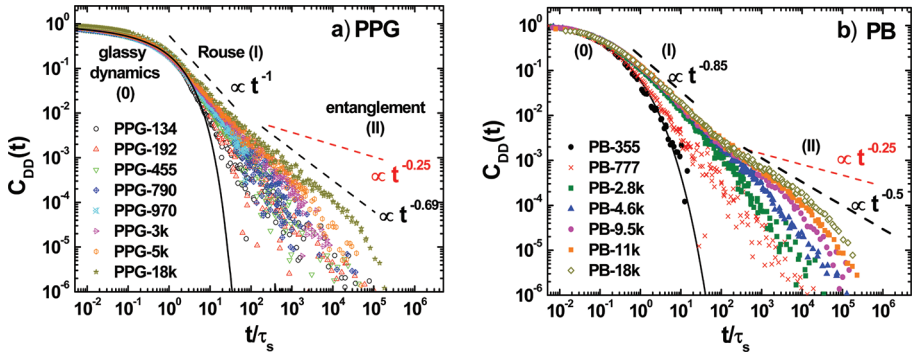


Figure 8. Dipolar correlation functions $C_{DD}(t)$ vs. reduced time t/τ_s for different molecular masses (M) of (a) PPG and (b) PB. The three relaxation regimes are marked. The low-M reference systems PPG-134 and PB-466 are fitted to a CD function (solid line). Dashed lines: power-law behavior in regime I and II, respectively; red dotted line: prediction by the tube-reptation model (regime II).

character with a well-defined second "step" at long times in particular in the case of PPG-18k. This virtually exponential cutoff at longest times reflects the terminal relaxation corresponding to the low-frequency plateau in the spectral density. Clearly, polymer effects lead to a retardation of the segmental correlation decay, as full relaxation of a segment is only possible in the course of the slow chain dynamics, *viz.* Rouse modes and reptation.

At $t/\tau_s < 2$ and down to $C_{DD}(t) \cong 0.1$ all correlation functions of PPG agree essentially. The short time behavior is M-independent while determined solely by glassy dynamics (regime 0), a fact which has already been found in the frequency domain (*cf.* Figures 2, 5, and 6). Beginning with PPG-790, all samples of higher M show a relaxation behavior close to $C_{DD}(t) \propto t^{-1}$ at intermediate times which suits the prediction of the Rouse theory. Hence, it is identified as Doi–Edwards regime I. In PPG-3k, -5k and -18k, another dynamic regime appears beyond the Rouse regime whose exponent ε systematically decreases with increasing M, leading to the interpretation that the segmental motion becomes further retarded at longest times when the chains become entangled. Finally an exponent of $\varepsilon = 0.69$ is reached in PPG-18k. We tentatively attribute this regime to Doi–Edwards regime II although the theoretical prediction of $C_{DD}(t) \propto t^{-0.25}$ is not (yet, see below) reached. The evolution of $C_{DD}(t)$ with M is very similar to that of PB (*cf.* Figure 8b where $C_{DD}(t) \propto t^{-0.85}$ is found in regime I and $C_{DD}(t) \propto t^{-0.5}$ in regime II.

As in the case of PB (as well as for PI and PDMS, *cf.* Appendix D, Figure 13) it appears that the transition to fully established reptation is only observed at much higher M, i.e., the transition from Rouse to reptation behavior is highly protracted (*cf.* refs 9, 10, and 22). As confirmed by DQ ^{1}H NMR it is only observed at $Z = M/M_e > 100$ while the highest molecular masses investigated in this work, PPG-18k, only accounts for $Z \approx 6$, PI 22k for $Z \approx 4$ and PB 18k for $Z \approx 9$. Figure 9 summarizes the exponents ε of $C_{DD}(t)$ at longest times, i.e., that of the Rouse regime (I) for $M < M_e$ and that of regime II for $M > M_e$ as a function of Z. Included are the data from DQ ^{1}H NMR which probe $C_{DD}(t)$ at even longer times and larger M values.[10] A virtually universal behavior is observed showing the protracted transition from Rouse to fully established reptation.

5. DISCUSSION AND CONCLUSIONS

Poly(propylene glycol), poly(isoprene), and poly(dimethlyl siloxane) of different molecular masses have been investigated by FC ^{1}H NMR in order to monitor the crossover from simple liquid behavior determined solely by glassy dynamics further to

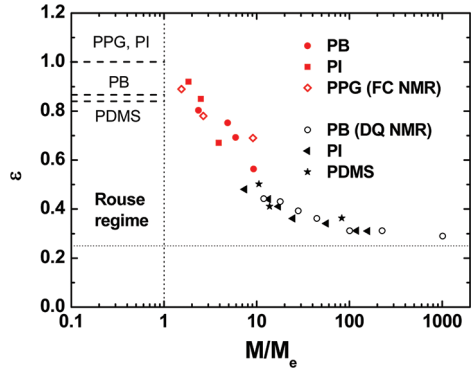


Figure 9. Power-law exponents for PPG, PB, PI and PDMS as a function of $Z = M/M_e$ from FC ^{1}H NMR (from this work and ref 6) and DQ ^{1}H NMR (from ref 10). The vertical dashed line at $\varepsilon = 0.25$ corresponds to the prediction of the tube-reptation model for regime II.

nonentangled polymers exhibiting Rouse dynamics and finally to entangled polymers most often described by the tube-reptation model. Exploiting FTS susceptibility master curves have been constructed from which the dipolar correlation function $C_{DD}(t)$ is obtained via Fourier transformation. It covers 6 decades in amplitude and about 8 decades in time indeed probing glassy dynamics at short times, Rouse at intermediate and entanglement dynamics at longest times in the case of $M \geq M_R$ and $M \geq M_e$ respectively.

FC NMR relaxometry results on PB, PI, and PDMS have also been reported by the Kimmich[1] and the Stapf group[44,45] and very similar experimental results have been obtained as in the present study. However, varying systematically molecular mass including the low-M limit, and most important constructing master curves allows us to achieve futher-reaching conclusions .[4−8]

The dynamics of PI,[46−50] PB,[48,49,51−54] and PDMS[55] has also been studied by conventional NMR relaxation experiments covering a few frequencies and focusing essentially on segmental ("local") dynamics reflecting, e. g., conformational changes of the chain as well as bond librations. Collective dynamics in terms of Rouse modes leading to a two-step reorientational correlation function have been discussed in connection with MD simulations on a semiquantitative level.[47,50−52] Yet, details of the reorientational correlation function in the Rouse regime as well as in the entanglement regime are not reliably extracted from such NMR experiments relying on probing just a few Larmor frequencies.

dx.doi.org/10.1021/ma202371p | *Macromolecules* 2012, 45, 2390−2401

In all polymers investigated, quite similar evolution of $C_{DD}(t/\tau_s)$ (or $\chi''_{DD}(\omega\tau_s)$) with M is observed, which also resembles what has been previously reported for poly(butadiene).[7] For example, while increasing M the Rouse regime is identified at $M_R \leq M \leq M_e$ with a correlation loss following closely t^{-1} as predicted by theory. At $M \geq M_e$ the dynamics in regime I (Rouse regime) saturates and a second power-law regime (II) is observed at longer times. The corresponding exponent ε is found to be M-dependent, decreasing with M until values of $\varepsilon \approx 0.5-0.7$ are reached. This is still far away from the expectation of the tube-reptation model which predicts $\varepsilon = 0.25$. However, comparing our FC ^{1}H NMR results with recent findings from DQ ^{1}H NMR[10] which extend the time-window to even longer times one can conclude that ε decreases further when higher M values are investigated. The exponent then decreases indeed down to 0.29. Whether the presence of further relaxation processes has to be assumed at highest M to understand the (slight) deviation from the tube-reptation model is matter of current debate.[10] The frequency window of FC ^{1}H NMR as given by the STELAR spectrometer is not large enough to cover sufficiently low frequencies to fully probe this highly protracted crossover reflected in $\varepsilon(M)$. Yet, by combining the two NMR techniques the full microscopic dynamics are revealed. Very recently, the results of FC ^{1}H NMR covering extremely low frequencies by applying earth and stray field compensation have essentially reached the dynamic window of DQ ^{1}H NMR and indeed confirm in the case of PB the slow decrease of ε down to a value close to $\varepsilon = 0.25$ at highest M.[56]

We have to recall that the dipolar correlation function $C_{DD}(t)$ contains both contributions from intra- as well as intermolecular fluctuations while the prediction of the tube-reptation model concerns only the reorientational segment dynamics reflected in the intramolecular relaxation contribution governed by $C^{(2)}(t)$. Up to now no full separation has been achieved which becomes possible when isotope dilution is applied (see, however, Figure 10 in the Appendix). In a first attempt Kehr et al.[22] have demonstrated that the intermolecular contribution becomes most relevant at low frequencies as translational motion occurs at longest times. Chavez and Saalwächter[9] tried to assess this problem by DQ ^{1}H NMR and concluded that suppressing intermolecular interactions leads to a change of the order parameter but the exponents of the correlation function are conserved. This is also what is found in PDMS (cf. Figure 10). Clearly, further experiments are needed to resolve this issue.

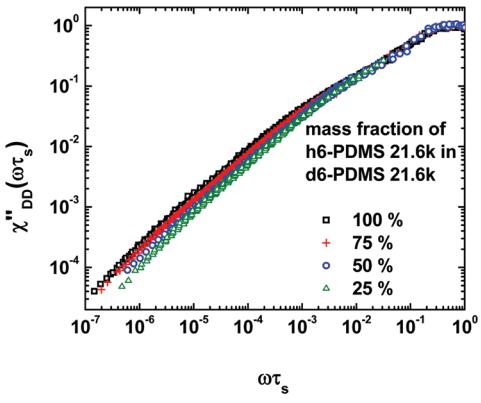


Figure 10. Scaled susceptibility master curves for different mass fractions of PDMS-h_6 diluted by PDMS-d_6 with similar $M > M_e$.

Regarding the protracted transition to full reptation as reflected in $\varepsilon(M)$ it is not yet clear whether it may be caused by probing the dynamics of the entire polymer chains including the dynamics of the chain ends. As demonstrated, for instance, by molecular dynamics simulations the chain ends exhibit an enhanced mobility which may obscure the reptation dynamics.[57] Thus, partly deuterated chains with a protonated inner part have to be investigated as it has been done, e.g., in the case of neutron scattering.[58]

By exploiting FTS not only a significant extension of the covered frequency range is achieved but also the segmental correlation times are provided which well complement those collected by dielectric spectroscopy as demonstrated. FC ^{1}H NMR provides correlation times in the range 10^{-11} s to 10^{-7} s, i.e., usually at relative high temperatures, which are not easily obtained in non-polar systems by other techniques. Furthermore, analyzing the susceptibility curves in terms of the polymer relaxation strength f or the spectral density $J_{DD}(0)$ FC ^{1}H NMR is able to give an estimate of the Rouse unit M_R as well as of the entanglement mass M_e which virtually agrees with those from other techniques. All in all, we think FC NMR will become a powerful tool of investigating various polymer systems in terms of their "molecular rheology".[10]

APPENDIX

A. Intramolecular Origin of the Anomaly in the PDMS Spectrum

In order to assess the origin of excess contribution occurring in the frequency range $3 \times 10^{-2} < \omega\tau_s < 1$, we performed an isotope dilution study. By successively diluting (protonated) PDMS with deuterated PDMS the intermolecular relaxation is suppressed. As one can see in Figure 10 in the mentioned frequency range no change is observed. This justifies our conclusion that in PDMS an additional intramolecular relaxation is present for all M. At lower frequencies, in the regime of the Rouse dynamics, systematic decrease is observed upon dilution although the apparent exponents are conserved.

B. Segmental Time Constants of PDMS and PB

For the sake of completeness we show the segmental correlation times of PDMS and PB as obtained by constructing the NMR master curves (*cf.* Fig. 2) in Figure 11 as a function of T. They are compared to those reported by dielectric spectroscopy.[6,30] Again, both data sets complement each other. In the case of PDMS with its atypical susceptibility spectrum the agreement among the two techniques clearly demonstrates that the main relaxation ($\omega\tau_s \approx 1$) has to be attributed to segmental dynamics and not, for instance, to methyl group rotation. As in the case of PPG and PI the data can be interpolated by a Vogel–Fulcher–Tammann equation. The data which are displayed as a function of T show again that the behavior close to T_g is rather similar for all M values except for the low-M limit in the case of PB ($M = 355$). Thus, the quantity F (*cf.* above) is constant for a series of the same polymer.

C. Segmental Time Constants in an Arrhenius plot

For comparison, the segmental time constants of the systems investigated are plotted in Figure 12 as a function of T^{-1} instead of T as done in Figures 7 and 11. The "steepness" of ln $\tau(1/T)$ close to T_g is changing with M in contrast when plotting the data as a function of T.

D. Dipolar Correlation Function of PI and PDMS

Figure 13 depicts the correlation function $C_{DD}(t)$ of PI and PDMS as obtained via Fourier transformation of the susceptibility master

dx.doi.org/10.1021/ma202371p | *Macromolecules* 2012, 45, 2390–2401

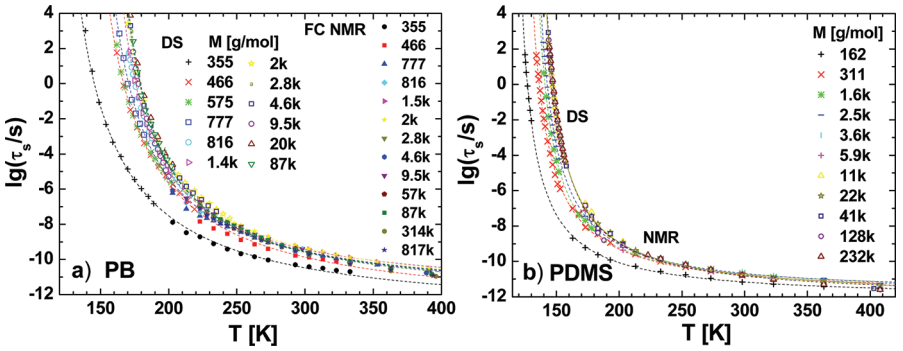


Figure 11. Segmental correlation times of PB (a) and PDMS (b) vs. temperature. Dashed lines: fit to the VFT equation.

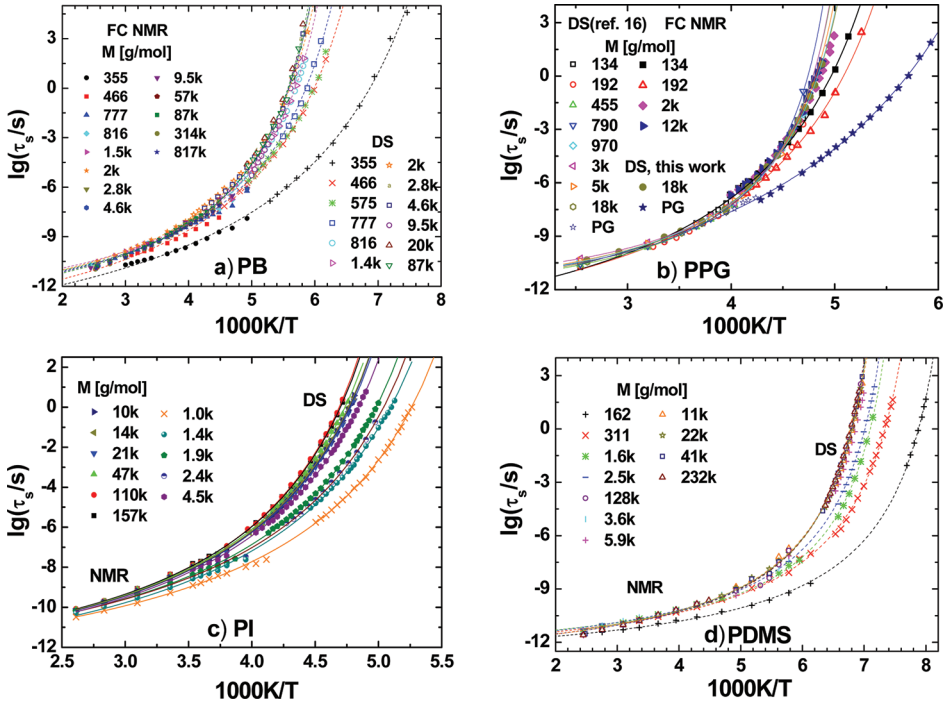


Figure 12. Arrhenius representations of the segmental correlation times of PB (a), PPG (b), PI (c), and PDMS (d). Dashed lines: fit to the VFT equation.

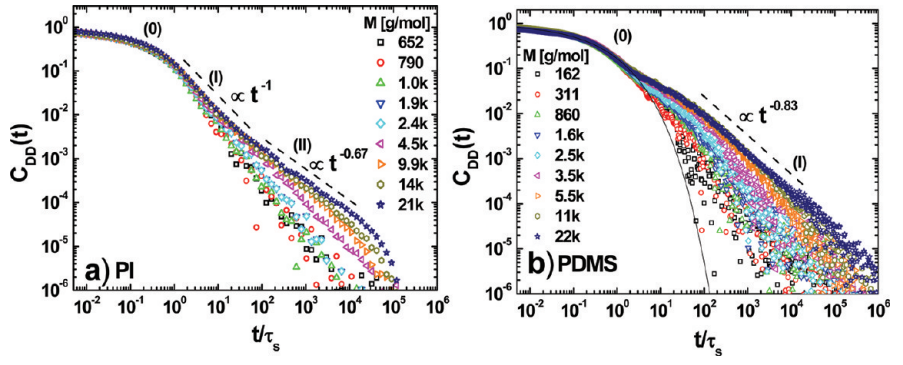


Figure 13. Dipolar correlation function $C_{DD}(t)$ of PI (a) and PDMS (b) as obtained by Fourier transforming the susceptibility master curves in Figure 2. The power-law decays in the different relaxation regimes are indicated; for PDMS only regime I (Rouse) is probed; the solid lines represent a Kohlrausch stretched-exponential decay for the low-M limit.

curves (cf. Figure 2). The corresponding power-law regimes are indicated. In the case of PI in addition to the regime 0 (glassy dynamics) the Rouse regime (I) with a power-law exponent $\varepsilon = 1$, as well as the entanglement regime II with an exponent $\varepsilon = 0.67$ for $M = 21k$ are recognized. In accordance with our discussion conducted above the correlation functions of PDMS do not reach the entanglement regime and the dynamics is determined solely by Rouse modes. The additional step-like correlation loss observed at short times and not found for the other polymers reflects an additional process. Correspondingly, the polymer specific

dx.doi.org/10.1021/ma202371p | Macromolecules 2012, 45, 2390−2401

relaxation sets in only at significant longer times making it difficult to measure the crossover to regime II.

AUTHOR INFORMATION

Notes

The authors declare no competing financial interest.

ACKNOWLEDGMENTS

Financial support by the Deutsche Forschungsgemeinschaft (DFG) through the projects SFB 481, RO 907/13, RO 907/16 (SPP 1369) and FU 308/14 is highly appreciated. We are also thankful for the PPG 18k sample obtained from R. Böhmer, Dortmund.

REFERENCES

(1) Kimmich, R.; Fatkullin, N. *Adv. Polym. Sci.* **2004**, *170*, 1.
(2) Kimmich, R.; Anoardo, E. *Prog. Nucl. Magn. Reson* **2004**, *44*, 257.
(3) Doi, M.; Edwards, S. F. *The Theory of Polymer Dynamics*; Oxford Sci. Publication: London, 1986.
(4) Kariyo, S.; Gainaru, C.; Schick, H.; Novikov, V. N.; Rössler, E. A. *Phys. Rev. Lett.* **2006**, *97*, 207803. Erratum: Kariyo, S.; Herrmann, A.; Gainaru, C.; Schick, H.; Brodin, A.; Novikov, V. N.; Rössler, E. A. *Phys. Rev. Lett.* **2008**, *100*, 109901.
(5) Kariyo, S.; Brodin, A.; Gainaru, C.; Herrmann, A.; Schick, H.; Novikov, V. N.; Rössler, E. A. *Macromolecules* **2008**, *41*, 5313.
(6) Kariyo, S.; Brodin, A.; Gainaru, C.; Herrmann, A.; Hintermeyer, J.; Schick, H.; Novikov, V. N.; Rössler, E. A. *Macromolecules* **2008**, *41*, 5322.
(7) Herrmann, A.; Novikov, V. N.; Rössler, E. A. *Macromolecules* **2009**, *42*, 2063.
(8) Herrmann, A.; Kariyo, S.; Abou Elfadl, A.; Meier, R.; Gmeiner, J.; Novikov, V. N.; Rössler, E. A. *Macromolecules* **2009**, *42*, 5236.
(9) Chavez, F. V.; Saalwächter, K. *Phys. Rev. Lett.* **2010**, *104*, 198305.
(10) Chavez, F. V.; Saalwächter, K. *Macromolecules* **2011**, *44*, 1549.
(11) Lunkenheimer, P.; Schneider, U.; Brand, R.; Loidl, A. *Contemp. Phys.* **2000**, *41*, 15.
(12) Götze, W. *Complex Dynamics of Glass-Forming Liquids: A Mode-Coupling Theory*: Oxford Univ. Pr.: Oxford, U.K., 2009.
(13) Vega, J. F.; Rastogi, S.; Peters, G. W. M.; Meijer, H. E. H. *J. Rheol.* **2004**, *48*, 663.
(14) Abdel-Goad, M.; Pyckhout-Hintzen, W.; Kahle, S.; Allgaier, J.; Richter, D.; Fetters, L. J. *Macromolecules* **2004**, *37*, 8135.
(15) Abou Elfadl, A.; Kahlau, R.; Herrmann, A.; Novikov, V. N.; Rössler, E. A. *Macromolecules* **2010**, *43*, 3340.
(16) Stockmayer, W. H. *Pure Appl. Chem.* **1967**, *15*, 539.
(17) Gainaru, C.; Böhmer, R. *Macromolecules* **2009**, *42*, 7616.
(18) Gainaru, C.; Hiller, W.; Böhmer, R. *Macromolecules* **2010**, *43*, 1907.
(19) Abou Elfadl, A.; Herrmann, A.; Hintermeyer, J.; Petzold, N.; Novikov, V. N.; Rössler, E. A. *Macromolecules* **2009**, *42*, 6816.
(20) Ball, R. C.; Callaghan, P. T.; Samulski, E. T. *J. Chem. Phys.* **1997**, *106*, 7352.
(21) Abragam, A. *The Principles of Nuclear Magnetism*: Clarendon Press: Oxford, U.K., 1961.
(22) Kehr, M.; Fatkullin, N.; Kimmich, R. *J. Chem. Phys.* **2007**, *126*, 094903.
(23) Kruk, D.; Herrmann, A.; Rössler, E. A. *Prog. NMR Spectrosc.* **2011**, DOI: 10.1016/j.pnmrs.2011.08.001.
(24) Kruk, D.; Meier, R.; Rössler, E. A. *J. Phys. Chem. B* **2011**, 951.
(25) Bloembergen, N.; Purcell, E. M.; Pound, R. V. *Phys. Rev.* **1948**, *73* (7), 679.
(26) Böttcher, C. J. F.; Bordewijk, P. *Theory of electric polarization*; Elsevier: Amsterdam, 1973; Vol. *2*.
(27) Rubinstein, M.; Colby, R. H. *Polymer Physics*: Oxford University Press: Oxford, U.K., 2003.
(28) Mattsson, J.; Bergmann, R.; Jacobsson, P.; Börjesson, L. *Phys. Rev. Lett.* **2005**, *94*, 165701.
(29) Strobl, G. *Condensed Matter Physics*: Springer Verlag: Berlin and Heidelberg, Germany, 2004.
(30) Hintermeyer, J.; Herrmann, A.; Kahlau, R.; Goiceanu, C.; Rössler, E. A. *Macromolecules* **2008**, *41*, 9335.
(31) Kruk, D.; Meier, R.; Rössler, E. A. *J. Phys. Chem. B* **2010**, *115*, 951.
(32) Meier, R.; Kruk, D.; Gmeiner, J.; Rössler, E. A. *J. Chem. Phys.* **2011**, in press.
(33) Smith, J. S.; Bedrov, D.; Smith, G. D.; Kober, E. M. *Macromolecules* **2005**, *38*, 8101.
(34) Arbe, A.; Monkenbusch, M.; Stellbrink, J.; Richter, D.; Farago, B.; Almdal, K.; Faust, R. *Macromolecules* **2001**, *34*, 1281.
(35) Indication on the web-presence of Dow Chemical (manufacturer), Midland MI, USA.
(36) Dee, G. T.; Ougizawa, T.; Walsh, D. J. *Polymer* **1992**, *33*, 3463.
(37) Kataoka, T.; Ueda, S. *Polym. Lett.* **1966**, 317.
(38) Hofmann, M.; Herrmann, A.; Ok, S.; Franz, C.; Kruk, D.; Saalwächter, K.; Steinhart, M.; Rössler, E. A. *Macromolecules* **2011**, *44*, 4017.
(39) Dollase, T.; Graf, R.; Heuer, A.; Spiess, H. W. *Macromolecules* **2001**, 298.
(40) Smith, B. A.; Samulski, E. T.; Yu, L.; Winnik, M. A. *Macromolecules* **1985**, *18*, 1901.
(41) Fetters, L. J.; Johse, D. J.; Richter, D.; Witten, T. A.; Zirkel, A. *Macromolecules* **1994**, *27*, 4639.
(42) Ding, Y.; Kisliuk, A.; Sokolov, A. P. *Macromolecules* **2004**, *37*, 161.
(43) Ding, Y.; Novikov, V. N.; Sokolov, A. P.; Cailliaux, A.; Dalle-Ferrier, C.; Alba-Simionesco, C. *Macromolecules* **2004**, *37*, 9264.
(44) Stapf, S.; Kariyo, S. *Acta Phys. Pol., A* **2005**, *108* (2), 247.
(45) Kariyo, S.; Stapf, S. *Macromol. Chem. Phys.* **2005**, *206* (13), 1300.
(46) Chernov, V. M.; Krasnopol'skii, G. S. *J. Exp. Theor. Phys.* **2007**, *2*, 302.
(47) Faller, R.; Müller-Plathe, F.; Doxastakis, M.; Theodorou, D. *Macromolecules* **2001**, *34*, 1436.
(48) Sen, T. Z.; Bahar, I.; Erman, B.; Lauprêtre, F.; Monniere, L. *Macromolecules* **1999**, *32*, 3017.
(49) Dejean de la Batie, R.; Lautprêtre, F.; Monnerie, L. *Macromolecules* **1989**, *22*, 122.
(50) Doxastakis, M.; Theodorou, D. N.; Fytas, G.; Kremer, F.; Faller, R.; Müller-Plathe, F.; Hadjichristidis, N. *J. Chem. Phys.* **2003**, *119* (13), 6883.
(51) Smith, G. D.; Borodin, O.; Bedrov, D.; Paul, W.; Qiu, X. H.; Ediger, M. D. *Macromolecules* **2001**, *34*, 5192.
(52) Smith, G. D.; Paul, W.; Monkenbusch, M.; Willner, L.; Richter, D.; Qiu, X. H.; Ediger, M. D. *Macromolecules* **1999**, *32*, 8857.
(53) Cohen Addad, J. P.; Guillermo, A. *Macromolecules* **2003**, *36*, 1609.
(54) Baysal, C.; Erman, B.; Bahar, I.; Lauprêtre, F.; Monnerie, L. *Macromolecules* **1997**, *30*, 2058.
(55) Litvinov, V. M.; Spiess, H. W. *Makromol. Chem* **1991**, *192*, 3005.
(56) Herrmann, A.; Kresse, B.; Kruk, D.; Fujara, F.; Rössler, E. A. *Macromolecules* **2012**, *45*, 1408.
(57) Kremer, K.; Grest, G. S.; Carmesin, I. *Phys. Rev. Lett.* **1988**, *61*, 566.
(58) Zamponi, M.; Monkenbusch, M.; Willner, L.; Wischnewski, A.; Farago, B.; Richter, D. *Europhys. Lett.* **2005**, *72*, 1039.
(59) To avoid confusion, we stress that regarding simple liquids, the term "glassy dynamics" is well established for the cooperative dynamics occurring above the glass transition temperature T_g;[11,12] it must not be mixed with the dynamics below T_g. In the present contribution the term is used synonymously with the term segmental or local dynamics.
(60) In our previous publication by Hofmann et al.[38] there appeared erroneously a factor of $^5/_2$ instead of $^3/_2$ in eq 3.

Macromolecules

Article

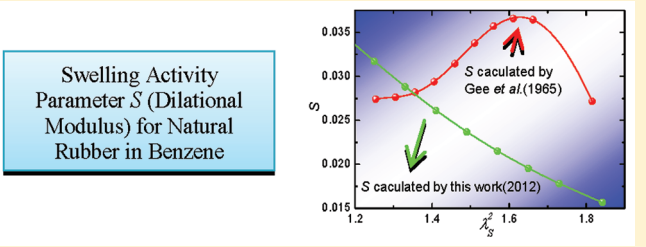
pubs.acs.org/Macromolecules

Swelling Behavior of Cross-Linked Rubber: Explanation of the Elusive Peak in the Swelling Activity Parameter (Dilational Modulus)

Ben Xu, Xiaojun Di, and Gregory B. McKenna*

Department of Chemical Engineering, Texas Tech University, Lubbock, Texas 79409-3121, United States

ABSTRACT: There is a considerable body of work in the literature that addresses the swelling of cross-linked rubber in the framework of the Frenkel–Flory–Rehner (FFR) hypothesis that the swelling is controlled by the balance of the thermodynamics of mixing and the elasticity of the network, i.e., the mixing and elastic contributions to the free energy are additive. One outcome that contradicts the FFR hypothesis of the experimental aspects of the work is that the swelling activity parameter (or dilational modulus) $S = \lambda \ln(a_c/a_u)$ frequently shows a peak when plotted as a function of the swelling stretch λ_s^2. a_c and a_u are the chemical potentials of cross-linked and un-cross-linked rubber at fixed polymer volume fraction. The focus of the present work is the behavior of S, which has remained elusive of explanation, and that we propose is an artifact of the data treatment used in the determination of the value of S as a function of λ_s^2. This is because the data treatment generally has required curve smoothing of (generally) sparse experimental data for swelling of the rubber as a function of the chemical activity and, then, taking the logarithm of the ratio of a_c/a_u at fixed volume of polymer in the system. We find that the peak in S disappears when using a model based smoothing method instead of the empirical or polynomial methods of smoothing the individual volume fraction vs chemical activity curves for the cross-linked and un-cross-linked rubbers. We propose that the "peak" in S is due to the experimental variability in sparse data and is emphasized in the common methods of data smoothing. We show that addition of less than 1% random error to the model data can lead to the peak in S. Importantly, this work shows that the Frenkel–Flory–Rehner theory is consistent with the swelling data and the elusive peak in S is actually an artifact of normal data smoothing procedures.



1. INTRODUCTION

The present story began in 1965, when Gee, Herbert, and Roberts[1] observed that for natural rubber in benzene, the swelling activity parameter S, first defined in the context of the Frenkel[2]–Flory–Rehner[3] (FFR) hypothesis and also referred to as the "dilational modulus",[4] went through a maximum as swelling stretch λ_s^2 increased in isopiestic vapor sorption experiments as shown in Figure 1a. This phenomenon cannot be explained by the FFR hypothesis, which provides the fundamental underpinning of swelling behavior and an explanation continues to be elusive. The existence of the peak is very important to our understanding of the thermodynamics of networks, i.e., is the FFR hypothesis correct or not? Furthermore, this ambiguous behavior of S would also suggest that the presence of solvent possibly affects the entropy of mixing and/or elasticity of the network. For example, Eichinger and co-workers[4−11] conducted a series of experiments on styrene–butadiene rubber (SBR) and poly(dimethylsiloxane) (PDMS) rubber swollen in different solvents and tried to use their model to "capture" the "peak" in S. However, the model used does not correctly describe the behavior of S, with especially large deviations observed in the low λ_s^2 region. The data also seemed to show somewhat erratic results in the appearance of the "peak" in S with a consequence of no particular trend in S with, e.g., solvent quality. Gottlieb and Gaylord examined the ability of nine different rubber elasticity models (elastic free energy form differed) to describe the unexplained "peak" in S.[12] They found that only four of the models can even qualitatively agree with the data for S obtained by Eichinger et al.[5−7,11] and Roberts et al.[1] One of these four models cannot describe the experimental data quantitatively while the other three can give quantitative agreement with the "peak", only if the fitting parameters used in the rubber elasticity models have unphysical values. Gottlieb and Gaylord speculated that this was because none of these molecular theories were developed enough or that there could be something wrong in the FFR hypothesis. Gottlieb and co-workers[13] also proposed a less complicated model in which it was assumed that S depended on the solvent quality. This also did not succeed in describing reported behaviors. Deloche and Samulski[14] proposed a model that considered the segment–segment (and segment-solvent) orientational/relationships, which come from the stretching of chains in the swollen network, with the aim of interpreting the appearance of a solvent-dependent maximum in S but still could not find the rule of the "peak". McKenna and Crissman[15] systematically studied the connection between the "peak" with cross-linking density and temperature in a polyisoprene cross-linked by

Received: December 7, 2011
Revised: January 25, 2012
Published: February 17, 2012

 © 2012 American Chemical Society

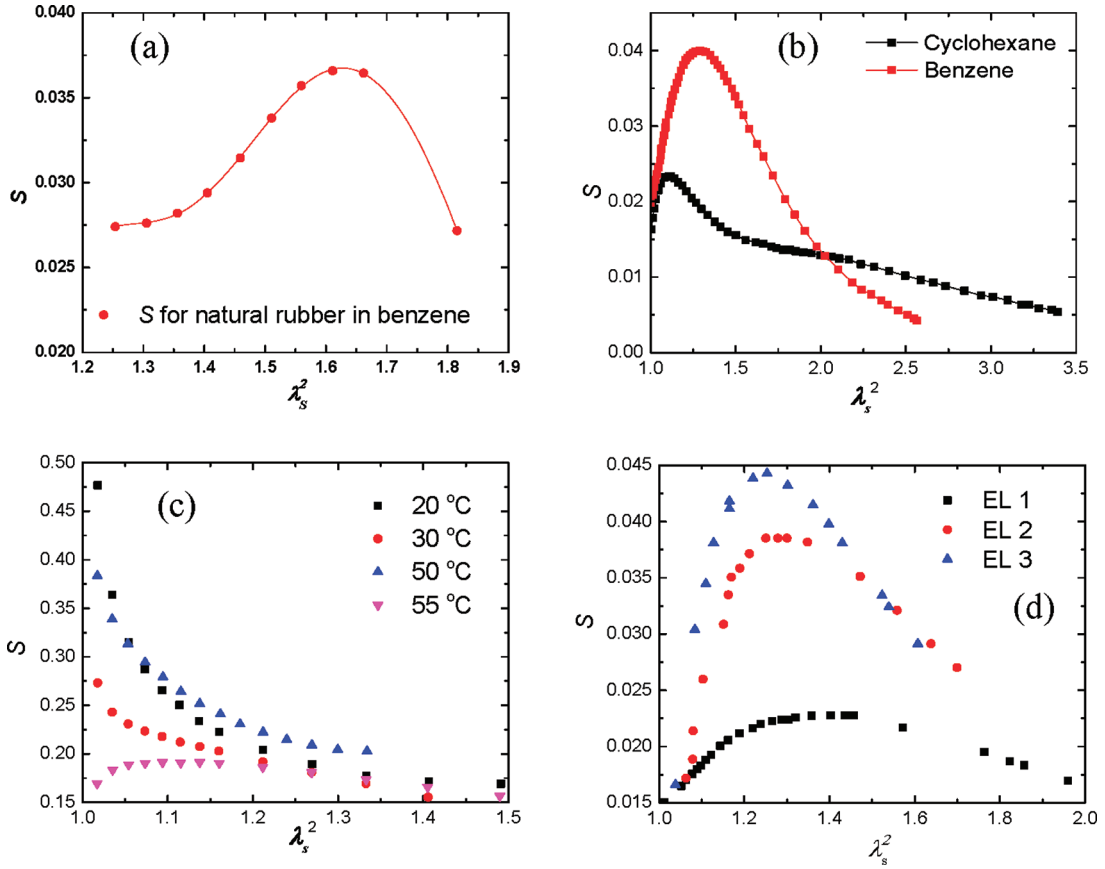


Figure 1. (a) *S* for cross-linked natural rubber swollen in benzene vapor at 25 °C obtained by Gee et al.[1] (b). *S* for PDMS in benzene and cyclohexane vapors at 30 °C[7] (c) *S* for 15 phr dicumyl peroxide cross-linked polyisoprene in benzene vapor at 20 °C, 30 °C, 50 and 55 °C.[15] (d) *S* for different cross-linking density PDMS in cyclohexane at 30 °C.[5]

different amounts of dicumyl peroxide. They found the appearance of the "peak" varies dramatically with temperature or cross-linking density and they speculated that it may be due to some unspecified special solvent−polymer interaction. Nandi and Winter[16] proposed that this ambiguous behavior in *S* may be due to a specific solvent effect because the work had only considered relatively few solvents. They also pointed out that Russ et al.[17] studied the swelling of a network in a polymeric solvent and no peak was observed, indicating that the FFR hypothesis is valid in the macromolecular solvent. Indeed, *S* might show a different dependence in the polymeric solvent, but the statement that the ambiguous *S* behavior is solvent dependent cannot be concluded from Russ et al.'s paper.[17]

In sum, many researchers have been interested in the origins of the peak in *S*, but a full explanation of *S* has remained elusive.[1,4−18] The lack of explanation for the "peak" in *S* has also resulted in questions related to the validity of the FFR hypothesis that the elastic and mixing parts of the Helmholtz free energy in swollen rubber networks are separable and additive.[4−11,15,19]

In the present paper, we show for the first time that the appearance of the peak in *S* is rooted in artifacts that arise from the smoothing procedures used for relatively sparse experimental data for volume fraction of polymer as a function of chemical potential. Previously, polynomial smoothing or "empirical smoothing[1]" methods were used to smooth the curves of isopiestic vapor sorption data and the *S* was calculated from the smoothed data.[1,4−11,15] Here we discuss and compare the results of *S* obtained by different smoothing methods to show that the "peak" in *S* may occur simply because the experimental uncertainty is magnified by the smoothing method. The data we analyze in this paper come from isopiestic vapor sorption experiments[15] (to determine *S*) and torsional experiments (to determine the elastic contribution to the Helmholtz free energy) from the literature.[20]

2. METHODOLOGY

2.1. The Origin of the *S* Problem. The FFR hypothesis states that the mixing and the elastic contributions to the free energy are additive and equal in swelling equilibrium, which is usually written in terms of the chemical potential difference between the rubber-solvent system and the pure solvent as[3,21−23]

$$(\mu_1 - \mu_1^0)_{mix} = -(\mu_1 - \mu_1^0)_{el} \quad (1)$$

It is generally accepted that the mixing term in the Flory[24]−Huggins[25] expression is

$$(\mu_1 - \mu_1^0)_{mix} = RT[\ln(1 - \nu_2) + \nu_2 + \chi\nu_2^2] \quad (2)$$

where ν_2 is the volume fraction of the rubber, χ is the Flory[24]−Huggins[25] interaction parameter. The elastic contribution to the chemical potential can be expressed in terms of the Valanis−Landel[26] function:

$$(\mu_1 - \mu_1^0)_{el} = V_1 w'(\lambda)/RT\lambda^2 \quad (3)$$

The FFR hypothesis can explain most of the problems in swelling when handled properly[27−31]with the exception of the

dx.doi.org/10.1021/ma202631u | *Macromolecules* 2012, 45, 2402−2410

swelling activity parameter S.[15] S, representing a difference in free energy between the cross-linked and the un-cross-linked systems, is defined in the context of the FFR hypothesis as[15]

$$S = \lambda \ln(a_c/a_u) \tag{4}$$

$$\lambda = {\nu_2}^{-1/3} \tag{5}$$

$$\ln(a_u) = [\ln(1 - \nu_2) + \nu_2 + \chi_u {\nu_2}^2] \tag{6}$$

$$\ln(a_c) = [\ln(1 - \nu_2) + \nu_2 + \chi_c {\nu_2}^2] + V_1 w'(\lambda)/RT\lambda^2 \tag{7}$$

where a is the solvent activity. In this paper, a is defined as $a = P/P_0$ where P = pressure and P_0 = saturation vapor pressure. The subscripts u and c refer to the un-cross-linked and the cross-linked rubbers, respectively. V_1 is the molar volume of the solvent, R is the gas constant, w is the elastic contribution to the Helmholtz free energy and interpreted in the continuum sense of a Valanis–Landel model or hyperelastic materials.[26] w' is the derivative of w with respect to the stretch λ, and w is the strain energy density function of the elastic network.

The data plots of ν_2 vs a_c and a_u are generally obtained from isobaric vapor sorption experiments as shown in Figure 2. As

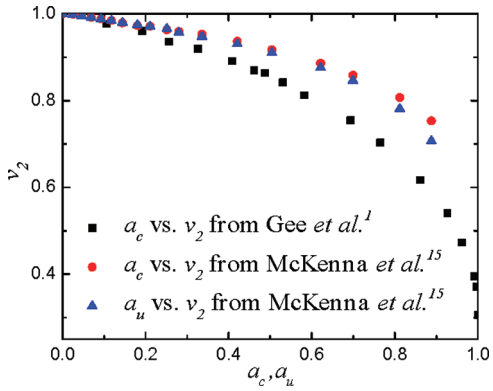


Figure 2. Isopiestic vapor sorption experimental data[1,15] illustrating that the density of points is sparse.

seen in Figure 2 and detailed subsequently, the data are relatively sparse. For the past half century, polynomial smoothing or "empirical smoothing[1]" methods were used to smooth this sparse data of ν_2 vs a or P to obtain values of a_c and a_u at the corresponding fixed ν_2 and substitute into eq 4 to calculate S.[1,4−10,14] Previous researchers have performed much work to explore the rule of S. There, strange "peaks" in S vs λ_s^2 curves, as illustrated Figure 1, have been reported to depend on solvent[7] (Figure 1b), temperature[15](Figure 1c), cross-linking density[8] (Figure 1d), and have been interpreted to contradict the FFR hypothesis. Some mathematical models and modified theories were developed to capture the "peaks" but none of them give satisfying results. As described in the Introduction, because no general rules have been concluded from the existence of the peak in S, some researchers have speculated that there might be some unknown special interaction between the solvent and the rubber.[15] However, no one has previously questioned the validity of the data smoothing procedures used to treat the swelling data and to calculate the value of S at the different values of polymer network volume fractions.

We hypothesize that this sparse experimental data causes the smoothing methods used for interpolation of the data to magnify the experimental uncertainties and, consequently, produce the ambiguous peaks in S. In order to test this assumption, we used the FFR model in analytical form, added random error to the model data to construct simulated experimental data, and then two different polynomial fitting methods were used to smooth the data. From these results we find that even a small amount of random error (<1%) can induce a peak in S. Furthermore, because error added to the smoothed data differ for each run of the computer program, the peak in S shows a different shape for each run even for the same percent of random error. We also produced simulated experimental data with different data densities or sparseness and show that this also influences the peak in S even though the underlying model is smooth and does not give a peak.

2.2.1. Methods. *Polynomial Smoothing.* For the past half century, polynomial smoothing or "empirical smoothing[1]" methods have been used to smooth the data of a or P vs ν_2 to calculate S.[1,4−11,15] For the purpose of comparison, in this paper, we used third-order and fourth-order polynomials to smooth the data plots of a vs ν_2 for both cross-linked and un-cross-linked rubbers. The obtained a_c and a_u as functions of ν_2 were then used to calculate S from eq 4.

2.2.2. FFR smoothing. We generated the FFR smoothing method from the definition of S and the Flory–Huggins equation.

$$\chi_c = \nu_2 \chi_{c0} + \chi_{c1} \tag{8}$$

$$\chi_u = \nu_2 \chi_{u0} + \chi_{u1} \tag{9}$$

$$\ln(a_u) = [\ln(1 - \nu_2) + \nu_2 + \chi_{u0} {\nu_2}^3 + \chi_{u1} {\nu_2}^2] \tag{10}$$

$$\ln(a_c) = [\ln(1 - \nu_2) + \nu_2 + \chi_{c0} {\nu_2}^3 + \chi_{c1} {\nu_2}^2] + V_1 w'(\lambda)/RT\lambda^2 \tag{11}$$

In the FFR model, we substitute eqs 8 and 9 into eqs 6 and 7 to make χ_c and χ_u polymer volume fraction ν_2 dependent as shown in eqs 10 and 11. Subsequently eqs 10 and 11 were used to smooth the data of a vs ν_2 with χ_{c0}, χ_{c1}, χ_{u0} and χ_{u1} being fitting parameters. The elasticity contribution in eq 11 was calculated from torsional data using the constrained chain model[32−38] as detailed in section 3.1.

Table 1. Equations and Fitting Parameters Used for the Three Smoothing Methods

method	equations relating ac and au vs ν_2	physical meaning	fitting parameters	elasticity
1	3rd-order polynomial	no	ν_2, a_c, a_u	no
2	4th-order polynomial	no	ν_2, a_c, a_u	no
3	FFR smoothing function, eqs 8−11	yes	χ_{c0}, χ_{c1}, χ_{u1}, χ_{u1}	yes

3. RESULTS AND DISCUSSION

Although results for S have been reported on many occasions,[1,4−11,15] few works show the original data. Rather they only report the smoothed curves. Also most researchers did not consider the contribution of the elasticity to S except for the works of McKenna and his co-workers.[15,20,27−30,34] In the present paper, we have primarily reanalyzed the isopiestic

dx.doi.org/10.1021/ma202631u | *Macromolecules* 2012, 45, 2402−2410

vapor sorption experiments conducted by McKenna and Crissman[15] and used the torsional data obtained by McKenna et al.[20] to determine the elastic contribution to the Helmholtz free energy.

3.1. Calculation of the Elasticity Contribution. According to the definition of S in the context of the FFR hypothesis, not only the mixing free energy contributes to S but also the elastic free energy. In this paper, the contribution of the elasticity $V_1w'(\lambda)/RT\lambda^2$ was calculated from the torsional measurements on dicumyl peroxide cross-linked polyisoprene conducted by McKenna et al.[20] The samples were designated by the amount of dicumyl peroxide from one part peroxide per hundred parts rubber (phr) to 15 phr. We calculated $V_1w'(\lambda)/RT\lambda^2$ from $w'(\lambda) - ((w'(1))/(\lambda))$ from the constrained chain model[32−38] fit to the data of $w'(\lambda) - ((w'(1))/(\lambda))$ vs λ. The constrained chain model has been shown to give a reasonable fit to the network elasticity by Han et al.[36] The stain energy function derivative is expressed in terms of the derivative of elastic free energy[20,27−30,36] through the Valanis−Landel function:[26]

$$\frac{\partial \Delta F_{el}}{\partial \lambda} = w'(\lambda) - \frac{w'(1)}{\lambda} \tag{12}$$

The elastic free energy is given by[32,33,36]

$$\Delta F_{el} = \Delta F_{el}^{c} + \Delta F_{el}^{ph} \tag{13}$$

where ΔF_{el}^{ph} is the elastic free energy of deformation by the phantom model, which is given by

$$\frac{\Delta F_{el}^{ph}}{kT} = \left(\frac{\xi}{2V_0}\right)(\lambda_1^2 + \lambda_2^2 + \lambda_3^2 - 3) \tag{14}$$

ΔF_{el}^{c} is the contribution arising from entanglement constraints relative to those in the phantom network, which can be written[34−38]

$$\Delta F_{el}^{c} = \frac{1}{2}\xi kT \sum_i \left\{\lambda_i^2 - 1 + \left(\frac{\nu_{el}}{\xi}\right)[B_i + D_i - \ln(1 + B_i) - \ln(1 + D_i)]\right\} \tag{15}$$

where

$$h(\lambda_i) = \kappa_G\left[1 + \frac{(\lambda_i^2 - 1)\left(1 - \frac{2}{f}\right)^{2/3}}{3}\right] \tag{16}$$

$$B_i = \frac{h(\lambda_i)\kappa_G\left[1 - \left(1 - \frac{2}{f}\right)^{2/3}\right](\lambda_i^2 - 1)}{[\lambda_i^2 + h(\lambda_i)]^2} \tag{17}$$

$$D_i = \frac{\lambda_i^2 B_i}{h(\lambda_i)} \tag{18}$$

$$\dot{B}_i = \frac{\partial B_i}{\partial \lambda} \tag{19}$$

$$\dot{B}_i = B_i\left\{\frac{1}{\lambda_i^2 - 1} - \frac{2}{\lambda_i^2 + h(\lambda_i)}\right\} + \frac{\kappa_G[\lambda_i^2 + h(\lambda_i)]\left(1 - \frac{2}{f}\right)^{2/3}}{h(\lambda_i)[\lambda_i^2 + h(\lambda_i)]} \tag{20}$$

$$\dot{D}_i = \frac{\partial D_i}{\partial \lambda} \tag{21}$$

$$\dot{D}_i = B_i\left[h(\lambda_i)^{-1} - \frac{\lambda_i^2\kappa_G\left(1 - \frac{2}{f}\right)^{2/3}}{h(\lambda_i)^2}\right] + \frac{\lambda_i^2\dot{B}_i}{h(\lambda_i)} \tag{22}$$

where f is the functionality of the network junctions, ξ is the cycle rank of the network, k is the Boltzmann constant and T is the absolute temperature.ξ,κ_G and ν_{el} are the fitting parameters. The constrained chain model[32−38] fit to the torsional measurement data for the 10 phr cross-linked rubber (data from McKenna et al.[20]) is shown in Figure 3. We extrapolate

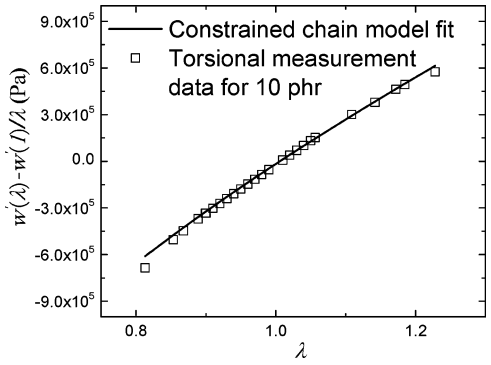


Figure 3. Constrained chain model[32−38] fit to the torsional measurement data for the 10 phr cross-linked rubber (data from McKenna et al.[20]).

the value of $w'(\lambda) - ((w'(1))/(\lambda))$ in the range of λ = 1−1.24 from the constrained chain model[32−38] fit to calculate $V_1w'(\lambda)/RT\lambda^2$.

Figure 4 shows the results of $V_1w'(\lambda)/RT\lambda^2$vs λ for the 1 phr, the 5 phr, and the 15 phr cross-linked rubber, from which it can be concluded that the higher the cross-linking density, the stronger the dependence of $V_1w'(\lambda)/RT\lambda^2$on λ, similar to the dependence of $w'(\lambda) - ((w'(1))/(\lambda))$ on λ.[27−30]

3.2.1. Results of *S*. *Smoothing of the Experimental Data of ν_2, vs a.* The volume fractions ν_2 of an un-cross-linked natural rubber and the 15 phr cross-linked rubber vs a at 55 °C in benzene vapor are shown in Figure 5 along with curves from third-order polynomial smoothing, fourth-order polynomial smoothing and FFR model smoothing. As seen from eq 4, in order to calculate S, the values of a_c and a_u at the same ν_2 must be known. Yet, in the experimental data, only a_c and a_u at different ν_2 are generally obtained. Therefore, the experimental data for ν_2 vs a_c and a_u were smoothed to get obtain fitting parameters that were used to calculate the values of a_c and a_u at the same values of ν_2. These were then substituted into eq 4 to calculate S. Prior researchers[1,4−11,15] used polynomial or "empirical smoothing" methods to smooth the isopiestic

dx.doi.org/10.1021/ma202631u | Macromolecules 2012, 45, 2402−2410

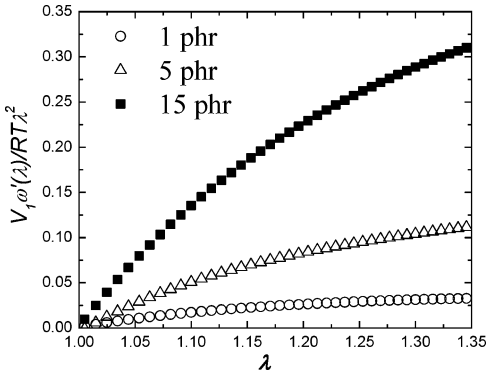


Figure 4. $V_1w'(\lambda)/RT\lambda^2$ vs λ for the 1 phr, the 5 phr, and the 15 phr cross-linked rubber. (Calculated from the data obtained by McKenna et al.[20]).

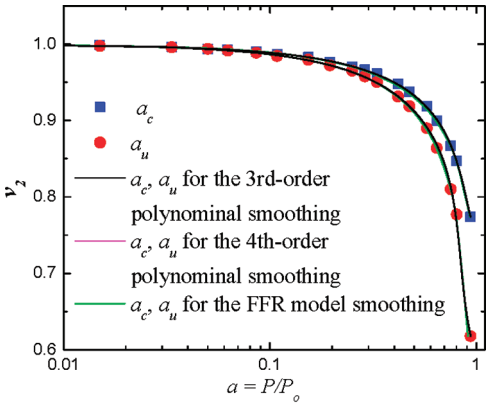


Figure 5. a vs v_2 for the 15 phr cross-linked rubber in benzene vapor at 55 °C along with the third-order polynomial smoothing, the fourth-order polynomial smoothing and the FFR model smoothing. (Data come from McKenna and Crissman.[15])

vapor sorption experimental data. As shown in Figure 5, the experimental data is relatively sparse, and the polynomial smoothing, is more likely to have slight "wiggles" that, consequently, magnify the experimental uncertainties when calculating S. It cannot be told which method is better from Figure 5, which is another reason why previous researchers did not question the validity of the polynomial smoothing procedure. However, the values of S calculated from the different smoothing methods show dramatic differences as shown in Figure 6 and discussed next.

3.2.2. Comparison of S Obtained by Different Smoothing Procedures. Figure 6 presents S vs λ_s^2 calculated by different smoothing methods for the 10 phr cross-linked rubber at 50 °C in the benzene vapor. The "peak" appears in the results obtained using the polynomial smoothing. The shape and the position of the peaks vary for the results produced by the third-order and fourth-order polynomial smoothing to the isopiestic data, indicating that the polynomial seems to introduce the peak. The S vs λ_s^2 results obtained by the FFR model smoothing, as expected, do not show any peak and their shapes are consistent with the FFR hypothesis.

For Eichinger's PDMS results,[5,7] S is 10 times smaller than the value of S in polyisoprene reported by McKenna and Crissman.[15] This is because the elastic contribution to S of PDMS is only one-quarter that of the polyisoprene and this leads to smaller differences in the vapor sorption of cross-linked and un-cross-linked PDMS and therefore smaller values of S.

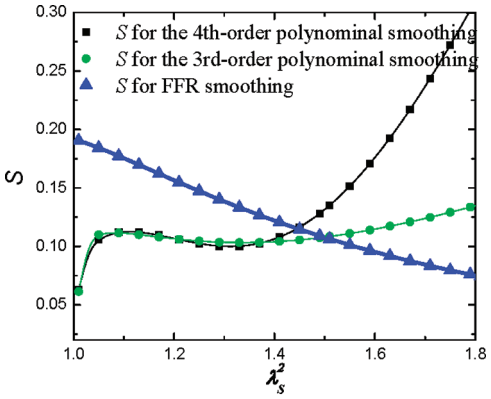


Figure 6. Comparison of S for the 10 phr cross-linked rubber at 50 °C in benzene vapor obtained by different smoothing methods: third-order polynomial smoothing, fourth-order polynomial smoothing and FFR model smoothing. (Data from McKenna and Crissman.[15])

We also recalculated the "classic peak" of Gee et al.[1] As shown in Figure 7, in the results obtained by the FFR

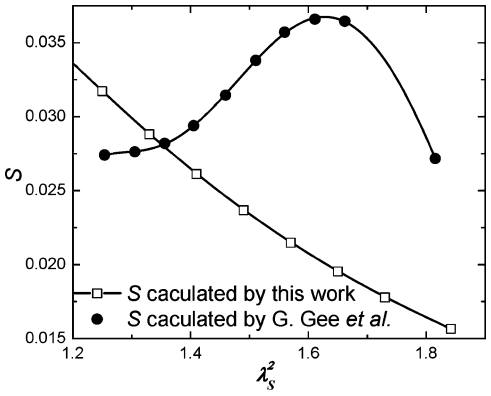


Figure 7. Comparison of S obtained by different methods. (Data from Gee et al.[1])

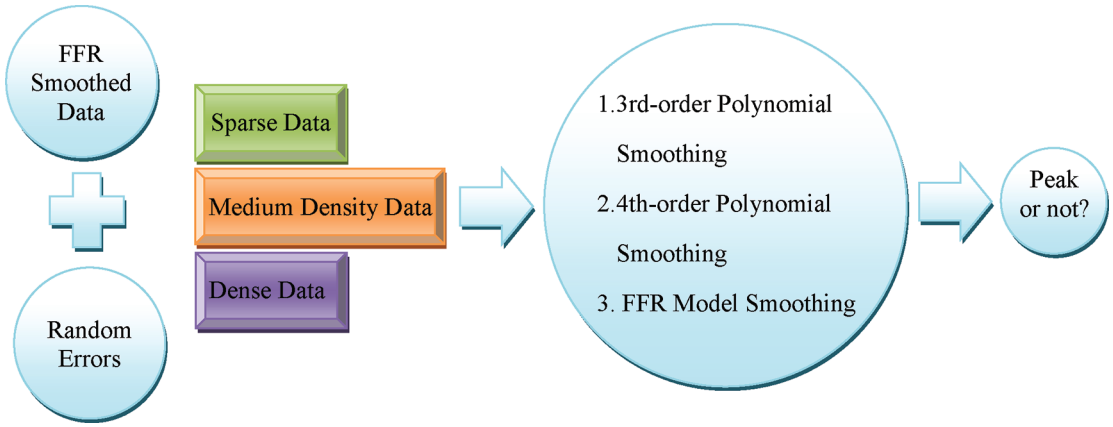
smoothing, the peak disappears and the behavior of S is, then, consistent with the FFR hypothesis. After dealing with the isopiestic vapor sorption data for different rubbers in different environments (the 1 phr, the 5 phr, the 10 phr, and the 15 phr cross-linked rubber in benzene at 10−55 °C,[15]) we found that the "peak" only appears in the S vs λ_s^2 plots obtained when using polynomial smoothing or from "empirical smoothing[1]". Since the peak is not inherent to the FFR hypothesis, this leads to a question: Is the "peak" researchers have been trying to understand simply an artifact of the data smoothing procedure and, consequently, does not lead to a need to replace the FFR hypothesis?

4. HOW TO PRODUCE THE "PEAK" IN S

In order to further explore the nature of the "peak" in S and to make comparisons with different smoothing methods, we carried out a study using model data. We used the FFR model, which does not inherently show a peak, as a model function to which noise was added. n points in v_2 with the same range as the experimental data shown previously were selected and the corresponding activities from the above analytical functions (eqs 4−7) were calculated as shown schematically in Scheme 1. The model values chosen were those we obtained by smoothing the data using the FFR model above. The elasticity

dx.doi.org/10.1021/ma202631u | *Macromolecules* 2012, 45, 2402−2410

Scheme 1. Schematic of Procedure To Test Whether Peak in *S* Is Caused by the Polynomial Data Smoothing



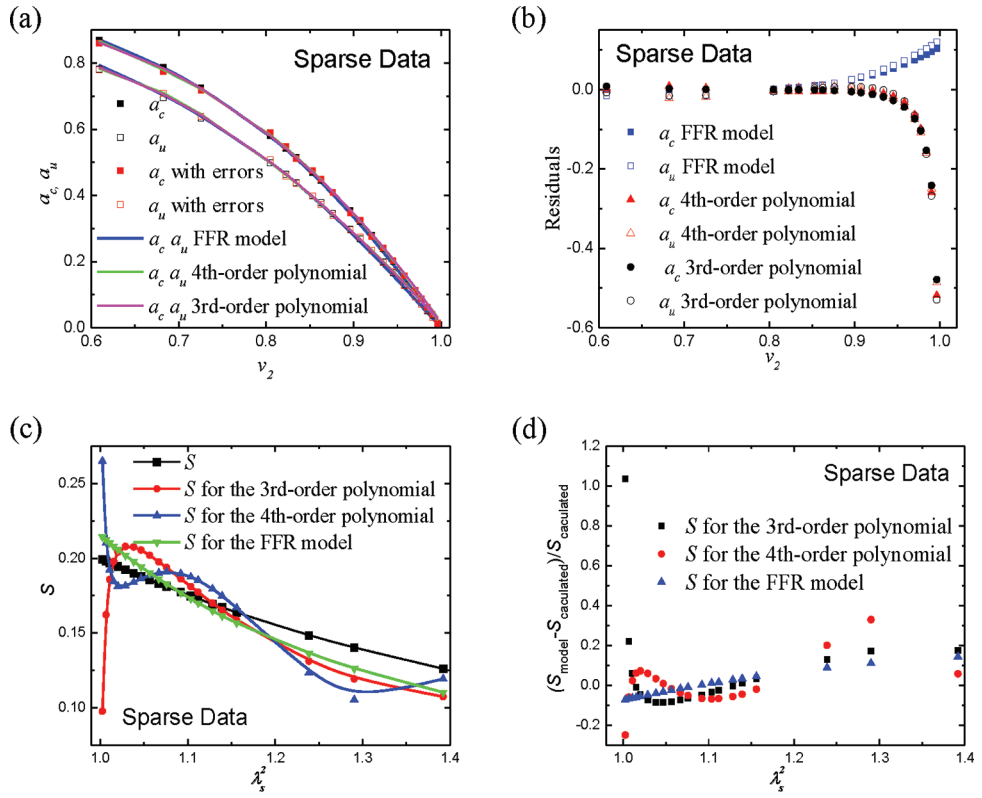


Figure 8. One example of the results of the sparse data (20 points) obtained by the Matlab[39] program (with error limits of 2%). The FFR model, third-order polynomial and fourth-order polynomial to the sparse simulated experiment data: (a) a vs v_2; (b) residuals $((a - a_{fit})/(a_{fit}))$ vs v_2; (c) S for the third-order polynomial, fourth-order polynomial, and the FFR model along with the sparse "simulated" experimental data; (d) $(s_{model} - s_{calculated})/(s_{calculated})$.

contribution was calculated from the fit of the constrained chain model[32−38] to the torsional experiments. The model data are designated as $(v_{21}, a_{u1_model}, a_{c1_model})$, $(v_{22}, a_{u2_model}, a_{c2_model})$, $(-\cdots\cdots-)$ $(v_{2n}, a_{un_model}, a_{cn_model})$. A Matlab[39] program was written and added noise $N(v_2)$ to the FFR function model data using the following expressions

$$N(v_2) = 1 + 2 \times (\text{rand} - 0.5) \times P \tag{23}$$

$$a_{c\cdot simulated} = a_{c\cdot model} \times N(v_2) \tag{24}$$

$$a_{u\cdot simulated} = a_{u\cdot model} \times N(v_2) \tag{25}$$

where P is the percent of the random error limits and rand is a random number range from 0−1 picked up by the Matlab[39] program. The random error added to the model data are different for each run of the program but do not exceed the random error limit P. Subsequently, different smoothing methods were used to smooth the simulated experimental data $((v_{21}, a_{u1_simulate}, a_{c1_simulate}), (v_{22}, a_{u2_simulate}, a_{c2_simulate}), \ldots, (v_{2n}, a_{un_simulate}, a_{cn_simulate}))$ to calculate S in order to test how big the error needs to be to induce the "peak" in S.

As mentioned previously, the sparse data also triggers the polynomial to magnify the experimental uncertainties. Here we have compared the results obtained using the polynomial for the simulated data having different data densities: 1. set the

dx.doi.org/10.1021/ma202631u | *Macromolecules* 2012, 45, 2402−2410

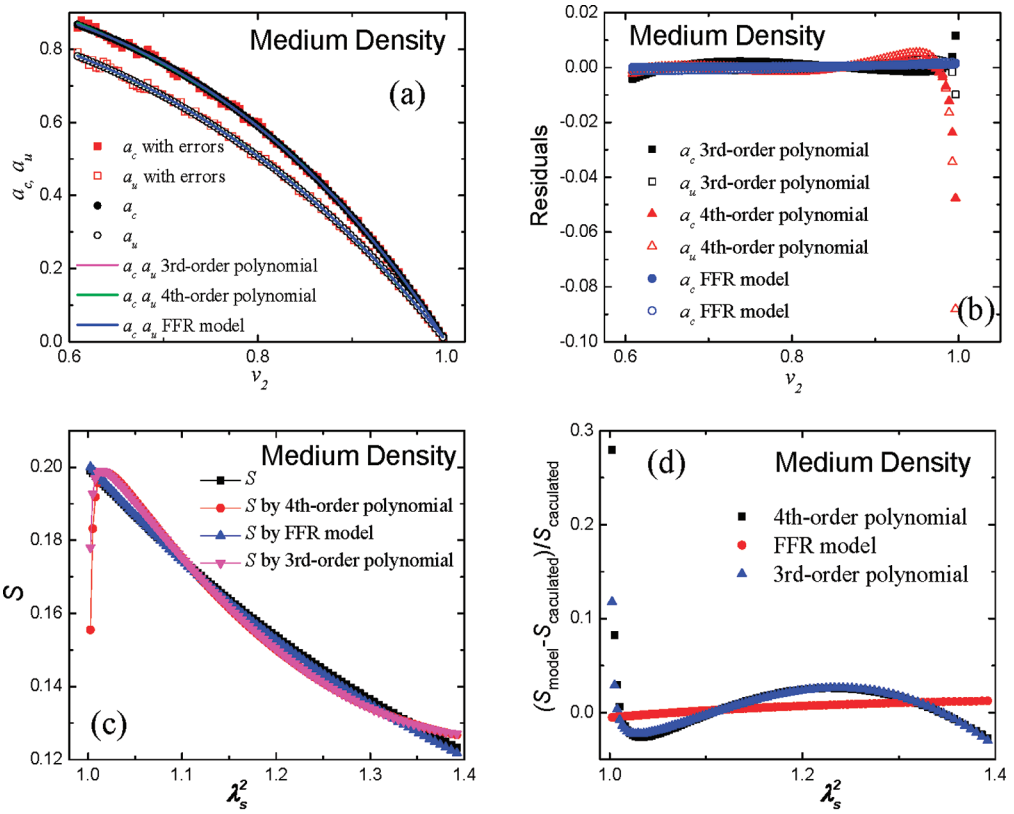


Figure 9. One example of the results of the medium density data (100 points) obtained by the Matlab[39] program (with error limits of 2%). The FFR model, the third-order polynomial, and the fourth-order polynomial to the medium density simulated experiment data: (a) a vs ν_2; (b) residuals $((a - a_{fit})/(a_{fit}))$ vs ν_2; (c) S for the third-order polynomial, fourth-order polynomial, and the FFR model along with the medium density "simulated" experimental data; (d) $(s_{model} - s_{calculated})/(s_{calculated})$

number of the model data n to be the number of the experimental data to make sparse data. 2. Generate 5× the number of the experimental data to make medium-density simulation data. 3. Generate 50× experimental data to make dense simulation data.

Here we present the results obtained by the third-order and the fourth-order polynomial methods. We also used the FFR model to smooth the sparse, medium densities, and dense simulated experimental data generated for the value of a_c and a_u vs ν_2 for polyisoprene and the 10 phr cross-linked rubber at 50 °C. The errors are random so different results will be found for each run and we only show typical representative results.

A set of typical simulated results (with error limits of 2%) are displayed in Figure 8 (sparse data) and Figure 9 (medium density data) and Figure 10 (dense data). Looking first at the sparse data of Figure 8, it cannot be told which method is better from Figure 8a, which may be the reason why the validity of the polynomial smoothing has not been generally questioned. However, as shown in Figure 8b, the residuals of the FFR smoothing are much smaller than the third and fourth-order polynomial smoothing, indicating the FFR model describes the experimental data better. As displayed in Figure 8b, large residuals from the polynomial are observed at ν_2 close to 1, which is also the range where the peak often appears. Figure 8c compares the "real value" of S (calculated from the simulated experimental data directly) and the S obtained for the FFR model smoothing and the polynomial smoothing. Peaks at small λ_s^2 (large ν_2) are observed in the results from the third-order and fourth-order polynomial smoothing, which strongly suggests that the appearance of the mysterious peak in S is rooted in the way in which the experimental uncertainty is emphasized by the polynomial or empirical data smoothing methods. Figure 8d shows the error between the model calculated data (error free) S and the third-order, the fourth-order polynomial and the FFR smoothing procedures. It can be seen that the FFR smoothing gives results that do not have the artifacts that seem to be introduced by the polynomial methods. More importantly, the results displayed in Figure 8–10 are from a single run of the model plus error. Because the errors added in the original data are random (the only constraint here is the error limits), the figures look different for each run (set of random errors).

However, some general points can be concluded from the sparse-data simulation. (1) When the added error limit is smaller than 0.2%, the differences between the results obtained by the polynomial and the FFR model are small and no peaks are observed. The bigger the added error limit, the bigger the difference between the results obtained by the polynomial and the FFR smoothing procedures. When the added error is larger than 0.5%, the "peak" produced by the polynomial method becomes notable. (2) When the added error limit is larger than 1%, the shape of the S from the polynomial smoothing shows dramatic differences for each run and the "peak" becomes prominent, because errors added are random and the polynomial is more likely to exaggerate the introduced uncertainties. The "peaks" produced by our program are similar to those reported in the literature. (3) The S obtained by the FFR model does not produce a "peak" and is consistent with the FFR hypothesis if we accept that $\chi_c > \chi_u$. From Figure 9, parts b and d, we can see that the FFR model can always fit

dx.doi.org/10.1021/ma202631u | Macromolecules 2012, 45, 2402–2410

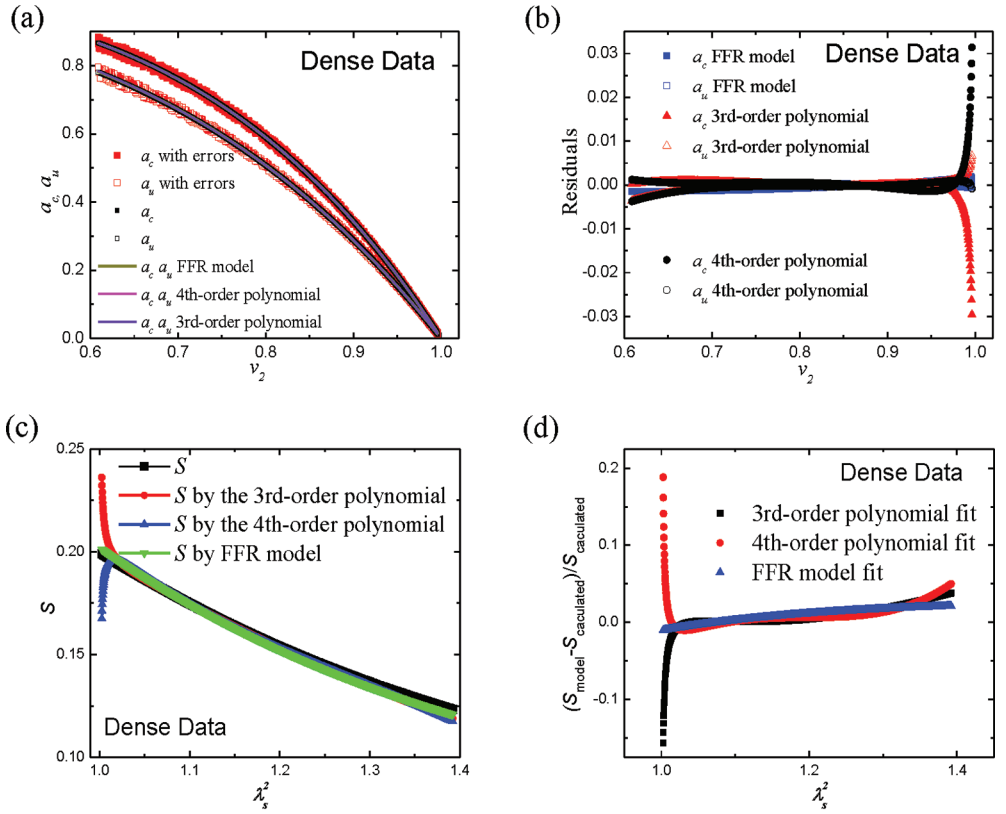


Figure 10. One example of the results of dense data (1000points) obtained by the Matlab[39] program (with error limits of 2%) The FFR model, the third-order polynomial, and the fourth-order polynomial to the dense simulated experiment data: (a) a vs v_2; (b) $(a_{c\ by\ polynomil\ fit})/(a_c)$, $(a_{u\ by\ polynomil\ fit})/(a_u)$, $(a_{c\ by\ the\ FFRmodel\ fit})/(a_c)$, $(a_{u\ by\ the\ FFRmodel\ fit})/(a_u)$); (c) S for the third-order polynomial, fourth-order polynomial and the FFR model along with the dense "simulated" experimental data; (d). $(s_{model} - s_{calculated})/(s_{calculated})$.

the simulated experimental data better than the polynomial. There are some differences for each run of the results obtained by the FFR smoothing method when the added error is larger than 1% but the results maintain a similar shape and trend which distinguish it from the polynomial smoothing.

If we compare the results from Figures 8−10, several conclusions can be made: (1) The denser the data, the less ambiguous is S and smaller errors are introduced by the polynomial smoothing. In the dense simulated results treated by polynomial smoothing, there can still be some bump in S in the region of v_2 near 1, which is because the value of mass uptake is very small and the result is more sensitive in this region. (2) The sparse data collection generally used in the isopiestic vapor sorption experiments is another cause of the ambiguous peak in S produced by the polynomial smoothing.

From the analysis above, it can be concluded that the ambiguous "peak" in S is simply a misconception engendered by experimental uncertainties magnified by the data smoothing methods, e.g. polynomial smoothing or "empirical smoothing[1]".

5. CONCLUSIONS

By comparing the results of swelling activity parameter S obtained by different data smoothing methods, we have shown that the "peak" in S that has puzzled the polymer physics community for a half century, is an artifact rooted in experimental uncertainty of sparse data that is magnified by conventional smoothing methods (polynomial smoothing and "empirical smoothing"). To test this hypothesis, we added random error to a model of the thermodynamics of swelling to create simulated experimental data and compared the values of S obtained by different smoothing methods to the simulated experimental data. It results that the polynomial smoothing of data, with as little as 0.5% random error added, causes the appearance of peaks in S which confirms the hypothesis and shows that the S is a monotonic function of swelling and the apparent peaks that have been reported in S are artifacts of the data treatment and not evidence of the breakdown of the Frenkel-Flory−Rehner theory of network swelling.

AUTHOR INFORMATION

Corresponding Author

*E-mail: greg.mckenna@ttu.edu..

Notes

The authors declare no competing financial interest.

ACKNOWLEDGMENTS

The authors are grateful to the Office of Naval Research (ONR) under Project Nos. N00014−06−1−0922, N00014−11−1−0424 and the John R.Bradford endowment at Texas Tech University for partial supportof this work.

REFERENCES

(1) Gee, G.; Herbert, J. B. M.; Roberts, R. C. *Polymer* **1965**, *6*, 541.
(2) Frenkel, J. *Acta. Phys. USSR* **1938**, *9*, 235; *Rubber Chem. Technol.* **1940**, *13*, 264.
(3) Flory, P. J.; Rehner, J. J. Jr. *J. Chem. Phys.* **1943**, *11*, 521.
(4) Neuburger, N. A.; Eichinger, B. E. *Macromolecules* **1988**, *21*, 3060.
(5) Brotzman, R. W.; Eichinger, B. E. *Macromolecules* **1983**, *16*, 1131.
(6) Brotzman, R. W.; Eichinger, B. E. *Macromolecules* **1981**, *14*, 1445.
(7) Brotzman, R. W.; Eichinger, B. E. *Macromolecules* **1982**, *15*, 531.

(8) Zhao, Y. Q.; Eichinger, B. E. *Macromolecules* **1992**, *25*, 6988.
(9) Zhao, Y. Q.; Eichinger, B. E. *Macromolecules* **1992**, *25*, 6996.
(10) Yen, L. Y.; Eichinger, B. E. *J. Polym. Sci., Part B: Polym. Phys.* **1978**, *16*, 117.
(11) Yen, L. Y.; Eichinger, B. E. *J. Polym. Sci., Part B: Polym. Phys.* **1978**, *16*, 121.
(12) Gottlieb, M.; Gaylord, R. J. *Macromolecules* **1984**, *17*, 2024.
(13) Pekarski, P.; Rabin, Y.; Gottlieb, M. *J. Phys. II Fr.* **1994**, *4*, 1677.
(14) Deloche, B.; Samulski, E. T. *Macromolecules* **1988**, *21*, 3107.
(15) McKenna, G. B.; Crissman, J. M. *J. Polym. Sci., Part B: Polym. Phys.* **1997**, *35*, 817.
(16) Nandi, S.; Winter, H. H. *Macromolecules* **2005**, *38*, 4447.
(17) Russ, T.; Brenn, R.; Geoghegan, M. *Macromolecules* **2003**, *36*, 127.
(18) Horta, A.; Pastoriza, M. A. *Eur. Polym. J.* **2005**, *41*, 2793.
(19) Geoghegan, M. *Adv. Solid State Phys.* **2006**, *45*, 29.
(20) McKenna, G. B.; Flynn, K. M.; Chen, Y. H. *Macromolecules* **1989**, *22*, 4507.
(21) Treloar, L. R. G. *The Physics of Rubber Elasticity*, 3rd ed.; Clarendon Press: Oxford, U.K., 1975.
(22) Queslel, J. P. ; Mark, J. E. In *Comprehensive Polymer Science, 2, Polymer Properties*; Booth, C., Price, C., Eds.; Pergamon: Oxford, U.K., 1989, 271.
(23) Flory, P. J. *Priciples of Polymer Chemisry*; Cornell University Press: Ithaca, NY, 1953.
(24) Flory, P. J. *J. Chem. Phys.* **1941**, *9*, 660.
(25) Huggins, M. L. *J. Chem. Phys.* **1941**, *9*, 440.
(26) Valanis, K. C.; Landel, R. F. *J. Appl. Phys.* **1967**, *38*, 2997.
(27) McKenna, G. B.; Flynn, K. M.; Chen, Y. H. *Polym. Commun.* **1988**, *29*, 272.
(28) McKenna, G. B.; Flynn, K. M.; Chen, Y. H. *Polymer* **1990**, *31*, 1937.
(29) McKenna, G. B.; Hinkley, J. A. *Polymer* **1986**, *27*, 1368.
(30) McKenna, G. B.; Flynn, K. M.; Chen, Y. H. in *Molecular Basis of Polymer Networks*; Baumgartner, A., Picot, C.E., Eds.; Springer-Verlag: Berlin, 1989, 127.
(31) McKenna, G. B.; Horkay, F. *Polymer* **1994**, *35*, 5737.
(32) James, H. M.; Guth, E. *J. Chem. Phys.* **1943**, *11*, 455.
(33) James, H. M.; Guth, E. *J. Chem. Phys.* **1947**, *15*, 669.
(34) Flory, P. J. *J. Chem. Phys.* **1977**, *66*, 5720.
(35) Flory, P. J.; Erman, B. *Macromolecules* **1982**, *15*, 800.
(36) Han, W. H.; Horkay, F.; McKenna, G. B. *Math. Mech. Solids* **1999**, *4*, 139.
(37) Erman, B.; Monnerie, L. *Macromolecules* **1989**, *22*, 3342.
(38) Erman, B.; Monnerie, L. *Macromolecules* **1992**, *25*, 4465.
(39) Matlab by Mathworks, Inc. version R2011b (7.13.0.564)

Macromolecules

Article

pubs.acs.org/Macromolecules

Phenyltrimethylammonium Functionalized Polysulfone Anion Exchange Membranes†

Nanwen Li,[‡] Qiang Zhang,[⊥] Chenyi Wang,[‡,#] Young Moo Lee,*[,‡,§] and Michael D. Guiver*[,‡,∥]

[‡]WCU Department of Energy Engineering, College of Engineering, Hanyang University, Seoul 133-791, Republic of Korea

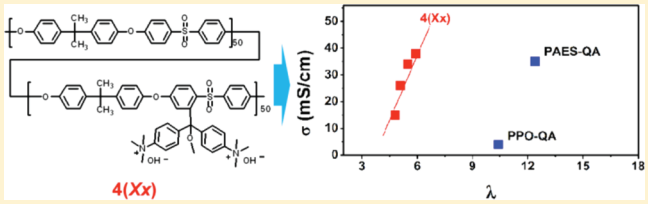
[§]School of Chemical Engineering, College of Engineering, Hanyang University, Seoul 133-791, Republic of Korea

[∥]Institute for Chemical Process and Environmental Technology, National Research Council, Ottawa, Ont. K1A 0R6, Canada

[⊥]Key Laboratory of Polymer Ecomaterials, Changchun Institute of Applied Chemistry, Chinese Academy of Sciences, Changchun 130022, China

[#]School of Materials Science and Engineering, Changzhou University, Changzhou, 213164, China

ABSTRACT: Anion exchange membrane (AEM) materials were prepared from commercial polysulfone (PSf) by functionalization with tertiary amines via lithiation chemistry. By optimizing the reaction conditions, a degree of substitution (DS) of 0.81 could be achieved without evident polymer decomposition or cross-linking. The PSf containing pendent bis(phenyldimethylamine) substituents were then quaternized with CH_3I and ion exchange reaction to provide bis(phenyltrimethylammonium) (PTMA) polymer with hydroxide-conductive properties. Flexible and tough membranes with various ion exchange capacities (IEC)s could be prepared by casting the polymers from DMAc solutions. The ionomeric membranes showed considerably lower water uptake (less than 20%), and thus dimensional swelling in water, compared with many reported AEMs. The hydroxide conductivities of the membranes were above 10 mS/cm at room temperature. The unusually low water uptake and good hydroxide conductivity may be attributed to the "side-chain-type" structures of pendent functional groups, which facilitate ion transport. Although the PTMA substituents on the AEM were found to have insufficient long-term stability for alkaline fuel cell application, the investigation gives some insight and directions for polymeric designs by postfunctionalization.



INTRODUCTION

Aromatic poly(arylene ether sulfone)s, which include bisphenol A polysulfone (PSf), are important engineering thermoplastics because they have excellent chemical and thermal stability and mechanical strength and have been widely employed as membrane materials.[1,2] The introduction of functional groups into PSf extends the range of potential applications of these high-performance materials with specific function and wider scope. The introduction of functionality into PSf has been accomplished by copolymerization with functionalized comonomers or by postfunctionalization of commercially available polymers. Examples of the functionalization chemistry include sulfonation,[3] bromination,[4] chloromethylation,[5] amidoalkylation,[6] and lithiation.[7−9] Functionalized PSfs have been actively investigated as membrane materials for gas[1,2,10,11] and liquid separation[12] and for fuel cells (FCs).[13−16] For example, sulfonated polysulfones, which have been synthesized by copolymerization with a sulfonated comonomer or by postsulfonation,[13,16] have been widely studied for proton exchange membranes (PEMs) for acidic fuel cells to provide alternatives to established Nafion that has dominated the field.[17,18] However, the requirement for Nafion and platinum precious metal-based electrocatalysts are creating cost barriers for the widespread commercialization and adoption of acidic PEMFCs.[13]

Recently, anion (hydroxide, OH^-) exchange membranes (AEMs) have been attracting growing interest, by switching from an acidic medium to a basic one in alkaline fuel cells.[19−23] A major advantage of alkaline fuel cells, relative to acidic fuel cells, is their enhanced reaction kinetics for both oxygen reduction and fuel oxidation, permitting the use of much less costly, non-noble-metal catalysts (e.g., Ni).[19,24−27] Additionally, in the case of direct methanol fuel cells (DMFC), the direction of hydroxide ion conduction opposes that of methanol crossover, thereby mitigating or possibly eliminating this process.[22,23] Some functionalized polymers have been developed as AEMs for alkaline fuel cells.[28−31] These hydroxide-conductive functional groups were obtained by introducing quaternized ammonium (QA),[32,33] guandinium,[34−36] or phosphonium groups[37] using chloromethylation on aromatic rings or bromination on the methyl groups of the polymers, followed by the Menshutkin reaction with tertiary amine, pentamethylguanidine, or tertiary phosphine. Some AEMs have exhibited good hydroxide conductivity. For example, Hibbs et al.[28] reported an AEM based on poly(phenylene), which exhibits good mechanical properties and excellent conductivity

Received: December 10, 2011
Revised: February 20, 2012
Published: February 28, 2012

†NRCC No. 53058.

 © 2012 American Chemical Society dx.doi.org/10.1021/ma202681z | Macromolecules 2012, 45, 2411−2419

(50 mS/cm at 30 °C, IEC = 1.57 mequiv/g, water uptake (WU) = 122%). Zhang et al.[38] prepared an AEM using a partially fluorinated poly(arylene ether sulfone) system that shows remarkable conductivities in excess of 60 mS/cm at 20 °C (IEC = 2.62 mequiv/g, WU = 86%). A variety of additional AEMs based upon modification of pre-existing polymers have also been described in recent literature, which display a wide range of conductivities.[22,23] More recently, multiblock PSf with QA groups have been synthesized, which showed enhanced hydroxide conductivity of 144 mS/cm at 80 °C (IEC = 1.93 mequiv/g, WU = 112%).[39,40] However, the high hydroxide conductivity in these materials could be only achieved through high ionic content, leading to excessive water uptake and dimensional swelling in water, and thus loss of mechanical properties. Therefore, while many of these polymeric materials demonstrate promise and progress for AEMs and establish the feasibility for alkaline membrane electrode assemblies, conductivity improvements and water swelling controls are still necessary to reach performance approaching current acid-based PEMFC.

In the pursuit of hydrocarbon-based aromatic PEMs with improved properties, we and others have shown that one promising approach to enhance PEM properties and performance is to position the sulfonic acid groups on side chains grafted onto the polymer main chain.[41] If the polymer structure contains flexible pendent side chains linking the polymer main chain and the sulfonic acid groups, nanophase separation between hydrophilic and hydrophobic domains may be improved, thus enhancing proton conductivity and mitigating water swelling.[42−45] While there have been few reports on AEMs based on aromatic polymers with pendent quaternary ammonium (QA) groups, the strategy of utilizing a "side-chain-type" structure is also expected to be useful in AEMs. Therefore, the objective of this research is to produce AEMs containing pendent QA groups via a simple postfunctionalization of commercial PSf and to evaluate their properties.

In our work on polysulfone modification by lithiation,[7−11,46] we and others have demonstrated that this synthetic method is an effective approach to postfunctionalized PSf with a wide variety of functional groups. Reaction of various electrophilic aryl and alkyl carbonyl compounds with PSf-Li yields the corresponding carbinol substituents,[9−11] including those containing arylamines.[46−48] Herein, we report the preparation of bis(phenyldimethylamine) functionalized PSf by facile reaction of lithiated polysulfone with Michler's ketone and subsequent conversion to bis-(phenyltrimethylammonium) (PTMA) polymer with hydroxide-conductive properties by treatment with CH_3I and ion exchange reaction. The properties of the resulting membranes, such as the stability, mechanical strength, water uptake behavior, methanol permeability, and hydroxide conductivity, are investigated.

EXPERIMENTAL SECTION

Materials. Bisphenol A polysulfone (PSf) was purchased from Solvay and dried at 110 °C for at least 24 h before using. *n*-Butyllithium (2.5 M in hexane), iodomethane, bis[4-(dimethylamino)-phenyl]methanone (Michler's ketone), dimethylacetamide (DMAc), and K_2CO_3 were obtained from Sigma-Aldrich and were used as received. Anhydrous reagent grade tetrahydrofuran (THF) was freshly distilled over lithium aluminum hydride under a constant argon purge with mechanical stirring. A dry ice/ethanol bath was used for cooling reaction mixtures. For the control polymers and experiments, quaternized poly(arylene ether sulfone) (PAES-QA)[39] and poly(phenylene oxide) (PPO-QA)[20] were prepared according to previous reports.

Preparation of Bis(phenyldimethylamine)-Modified PSf 2. A typical synthetic procedure for Michler's ketone-modified PSf, illustrated by the preparation of **2** copolymers (target degree of substitution (DS) of 1.0), is shown in Scheme 1 and described as follows: A solution of PSf (8.80 g, 20 mmol) in THF (2 wt %) was cooled to −76 °C, and 1.2 mol equiv of *n*-butyllithium (9.6 mL, 24 mmol) was injected dropwise by drop funnel over a period of 15 min, during which time changes in the color and viscosity of the homogeneous reaction solution were observed. Following addition, the resulting solution of lithiated PSf (PSf−Li) was stirred for 15 min. Precooled solution of Michler's ketone (10.7 g, 40 mmol) in THF was poured promptly into the rapidly stirred PSf−Li solution, which immediately developed a deep blue color. Within 2 min, a highly viscous gel formed that gradually changed into a pearl blue heterogeneous mixture. The viscosity decreased rapidly while the reaction was gradually warmed to −10 °C over a period of 1.5 h. Then the polymer was recovered by precipitation from an ice/ethanol mixture and then washed and dried. The light blue polymeric product (**2**(*X*81), 10.5 g, yield 77%) had a DS of 0.62, determined by NMR.

Synthesis of PSf Containing Pendant Bis(phenyltrimethylammonium iodide) 3. The following represents a typical procedure for the synthesis of **3**(*X*81) containing pendent bis(phenyltrimethylammonium iodide). **2**(*X*81) (1.0 g, 1.4 mmol) was dissolved in DMAc (15 mL), and then K_2CO_3 (0.15 g, 1.2 mmol) and iodomethane (1 g, 6.8 mmol) were added. The reaction mixture was stirred at 30 °C for 24 h in the dark and then poured into distilled water. The precipitate was filtered off, washed with ethanol and distilled water thoroughly, and dried in vacuum oven for 24 h at 100 °C to give product with 97% of yield. ^{1}H NMR was used to confirm the synthesis of **3**(*X*81), and the degree of conversion of the tertiary amine group was close to 100%.

Membrane Fabrication and Anion Exchange. Cyan-colored membranes were cast from DMAc solutions (5 wt %) of **3**(*X*81) in a custom-built flat glass dish. The membranes were initially dried at 80 °C for 12 h and then vacuum-dried at 100 °C for 24 h. Purple-colored **4** membranes were obtained by treating **3** membranes in 1 M NaOH at room temperature for 24 h; they were washed thoroughly and immersed in deionized water for 48 h to remove residual NaOH. The resulting membranes were characterized immediately.

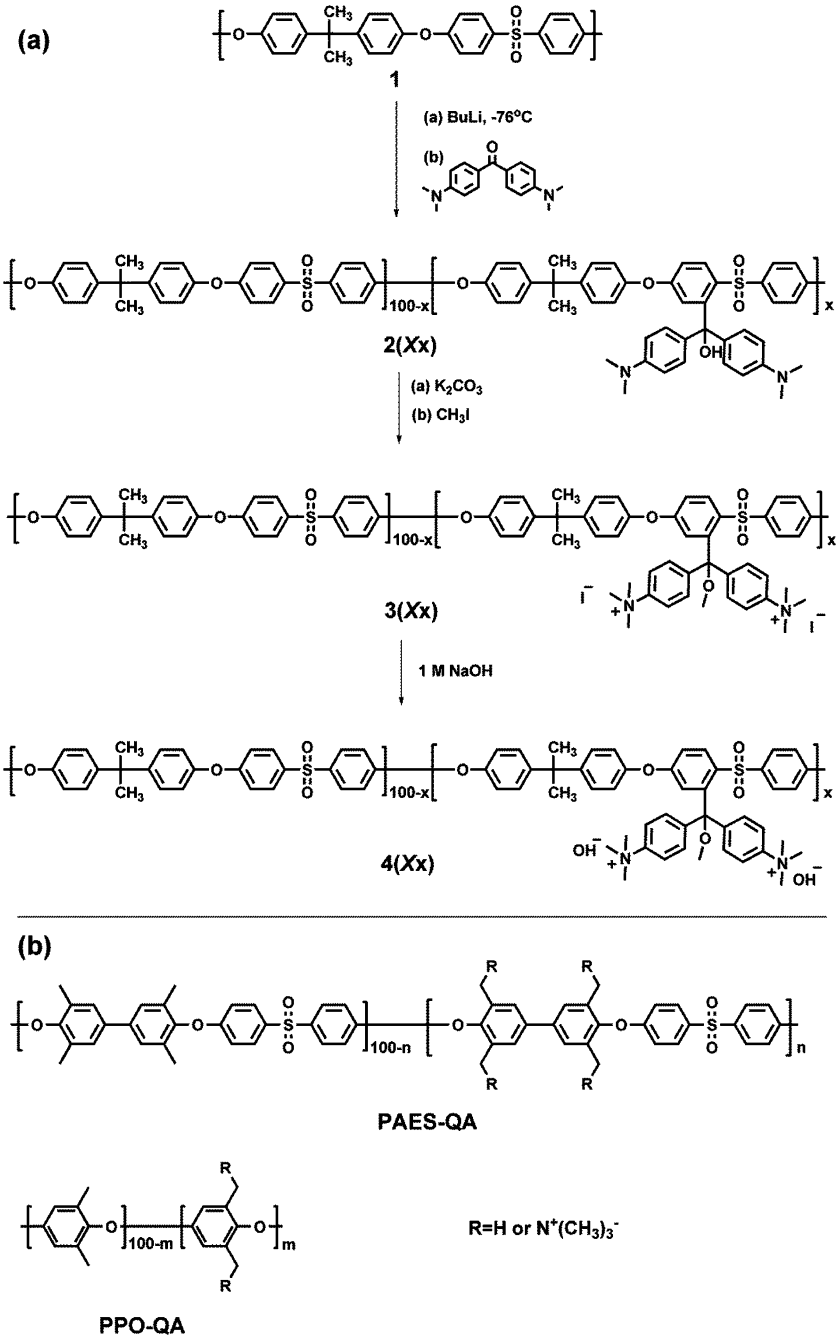
Characterization and Measurements. ^{1}H NMR spectra were measured at 300 MHz on a Bruker AV300 spectrometer. The reduced viscosities were determined with an Ubbelohde capillary viscometer at 30 °C on 0.5 g dL^{-1} concentrations of polymer in DMAc. Thermogravimetric analysis (TGA) was performed in a nitrogen atmosphere with a Perkin-Elmer TGA-2 thermogravimetric analyzer at a heating rate of 10 °C min^{-1}. Tensile measurements were carried out with an Instron-1211 mechanical testing instrument at a speed of 1 mm min^{-1} at atmosphere conditions (20 °C, 50% relative humidity). To experimentally determine ion exchange capacities (IEC), the **4** membranes in the OH^- form were immersed in 100 mL of 0.1 M HCl standard for 48 h and then titrated with a standardized NaOH solution using phenolphthalein as an indicator.

The density of the membranes was measured by a buoyancy method. Water uptake was measured after drying the membrane in hydroxide form at 60 °C under vacuum for 24 h. The dried membrane was immersed in water and periodically weighed on an analytical balance until a constant weight was obtained, giving the weight-based (IEC_w) water uptake. The volume-based IEC (IEC_v) was obtained by multiplying the membrane density by the IEC values which were estimated from the copolymer structure. This calculation resulted in IEC_v (dry) based on the dry membrane density. The IEC_v (wet) (mequiv/cm^3) was then calculated based on membrane water uptake, using the equation

$$IEC_v(\text{wet}) = \frac{IEC_w}{\frac{1}{\rho_{polymer}} + \frac{WU\ (\text{wt}\ \%)}{100 \times \rho_{water}}} \quad (1)$$

dx.doi.org/10.1021/ma202681z | Macromolecules 2012, 45, 2411−2419

Scheme 1. (a) Synthesis of Bis(phenyltrimethylammonium) (PTMA) Functionalized Copolymers 4 by Lithiation Chemistry; (b) Chemical Structures of PAES-QA and PPO-QA for the Control Experiments



where IEC_w is the gravimetric IEC (mequiv/g) and ρ (g/cm^3) is the density.

Hydroxide conductivity (σ, S cm^{-1}) of each membrane sample (size: 1 cm × 4 cm) was obtained using $\sigma = d/L_sW_sR$ (d is the distance between reference electrodes, and L_s and W_s are the thickness and width of the membrane, respectively). The resistance value (R) was measured over the frequency range from 100 mHz to 100 kHz by four-point probe alternating current (ac) impedance spectroscopy using an electrode system connected with an impedance/gain-phase analyzer (Solartron 1260) and an electrochemical interface (Solartron 1287, Farnborough Hampshire, ONR, UK). The membranes were sandwiched between two pairs of gold-plate electrodes. The conductivity measurements under fully hydrated conditions in the longitudinal direction were carried out with the cell immersed in liquid water.

The methanol permeability was determined by using a cell consisting of two half-cells separated by the membrane, which was fixed between two rubber rings. Methanol (2 M) was placed on one side of the diffusion cell, and water was placed on the other side. Magnetic stirrers were used on each compartment to ensure uniformity. The concentration of the methanol was measured by using a Shimadzu GC-1020A series gas chromatograph. Peak areas were converted into methanol concentration with a calibration curve. The methanol permeability was calculated by the equation

$$C_B(t) = \frac{A}{V_B}\frac{DK}{L}C_A(t - t_0) \quad (2)$$

where C_A and C_B are the methanol concentration of feed side and permeated through the membrane, respectively. A, L, and V_B are the effective area, the thickness of membrane, and the volume of

dx.doi.org/10.1021/ma202681z | Macromolecules 2012, 45, 2411−2419

permeated compartment, respectively. *DK* is defined as the methanol permeability, and t_0 is the time lag.

RESULTS AND DISCUSSION

Synthesis of PSf with Pendent PTMA Groups by Lithiation Chemistry. Lithiation is a versatile method allowing the attachment of a wide variety of functional groups onto polysulfones.[1,7−11] In the present study, a series of bis(phenyldimethylamine)-containing PSfs were prepared by the addition of Michler's ketone to PSf-Li, as outlined in Scheme 1. The Michler's ketone-modified polymers **2** having various DS were obtained as light blue powders and were soluble in most organic solvents such as chloroform, dichloromethane, dimethylformamide (DMF), DMAc, and *N*-methylpyrrolidone (NMP), but not in methanol or isopropanol. The chemical structures and DS were confirmed by ^{1}H NMR. As shown in Figure 1, a new singlet corresponding to the

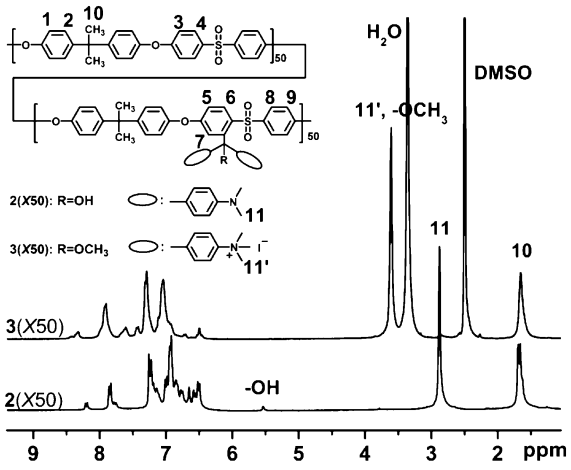


Figure 1. ^{1}H NMR spectra of 2(*X*50) in $CDCl_3$ and 3(*X*50) in DMSO-d_6 in the iodide form.

dimethylamine protons of the Michler's ketone residue was observed at 2.88 ppm. The aromatic proton signals from the Michler's ketone residue appeared at 6−7 ppm (Figure 1). The DS (Table 1) was estimated from the ratio of signal integrations of the dimethylamine protons to the 6H isopropylidene protons in the PSf chain at 1.62 ppm. Although the reaction of PSf-Li with many electrophiles has been shown to be near quantitative,[47,48] the Michler's ketone electrophile showed lower reactivity, which resulted in a less-substituted polymer; the highest DS of 0.81 was obtained by reaction of Michler's ketone with dilithiated PSf. A likely reason for the lower than expected DS is steric hindrance of the electrophilic around the sulfone linkage because the electrophilic carbon center is not easily accessible.[46] Another reason could be side reactions. However, viscosity measurements confirmed that the PSf lithiation derivatization process did not result in any significant changes in molecular weight (Table 1), which has been observed in previous studies.[47,48]

The copolymers **2** were converted to quaternized polysulfones by reaction with iodomethane. The mole ratio of iodomethane to phenyldimethyl amine groups was 2:1 to ensure complete quaternization of the tertiary amine units into the bis(phenyltrimethylammonium) (PTMA) substituents and −OH into $-OCH_3$ groups. There was no evidence of polymer chain degradation occurring under these conditions, as indicated by viscosity measurements (Table 1) and the mechanical properties of the resulting polymer membranes. The quaternized polymers **3** were isolated, which were readily soluble in common polar aprotic solvents (DMF, DMAc, and NMP), resulting in transparent solutions. Transparent and flexible cyan-colored **3** membranes were cast from DMAc solutions in the iodide form. Figure 1 shows the ^{1}H NMR spectrum of 3(*X*50) in iodide form. Comparison of 3(*X*50) with the parent copolymer 2(*X*50) revealed that the signals assigned to the nonquaternized methyl groups of bis(phenyldimethylamine) (H11) disappeared in 3(*X*50), while the polymer main-chain isopropylidene methyl protons (H10) remained after the quaternized reaction. A new signal assigned to the methyl groups in bis(phenyltrimethylammonium) (H11′) appeared at 3.47 ppm in 3(*X*50). Moreover, the disappearance of −OH protons at 5.5 ppm in 2(*X*50) indicates the complete conversion of −OH to $-OCH_3$ (3.47 ppm) which overlap with H11′. Thus, the theoretical IEC values of **3** membranes were readily calculated by comparing the integration ratios of the isolated signals H10 and H11′ and $-OCH_3$, as shown in Table 1.

The purple-colored anion exchange membranes **4** in the hydroxide form were obtained by treating **3** membranes in 1 M NaOH at room temperature for 24 h. An observed color change is common to many commercially available AEMs, such as the Tokuyama AMX and AMI membranes, which change color from light yellow to black after less than an hour of exposure to 1 M NaOH. The color change in the PSf-PTMA membranes is presumably due to the decomposition of PTMA under alkaline conditions during the hydroxide conversion step.[19] The chemical structures before and after the hydroxide conversion were analyzed by ^{1}H NMR, as shown in Figure 2. After conversion in 1 M NaOH for 24 h, the aromatic proton signals between 6.4 and 8.4 ppm showed minor changes when compared with those of pristine sample in the iodide form. However, the integration of methyl protons (H11′) in PTMA decreased, and the signal corresponding to H11 in phenyldimethyl amine reappeared. Thus, the IEC values estimated for **4** from the signal integration ratio were much lower than those of **3** membranes from ^{1}H NMR, which correlated well with the titrated values. The IEC values determined by titration were

Table 1. IEC Values and Viscosities of the Polymers

	2			3		4	
polymers	η^a	target DS	exptl DS	η^b	IEC_w (mequiv/g) (NMR)	IEC_w (mequiv/g) (NMR)	IEC_w (mequiv/g) (titration)
*X*35	0.58	0.5	0.35	0.88	1.24	0.98	1.01
*X*50	0.57	0.8	0.50	0.92	1.62	1.30	1.32
*X*62	0.60	1.0	0.62	1.05	1.88	1.43	1.46
*X*81	0.52	2.0	0.81	0.98	2.21	1.69	1.74

[a]Measured in $CHCl_3$ with 0.5 g/dL at 25 °C. The viscosity of PSf is 0.56 dL/g under the same test conditions. [b]Measured in NMP with 0.5 g/dL at 25 °C.

dx.doi.org/10.1021/ma202681z | *Macromolecules* 2012, 45, 2411−2419

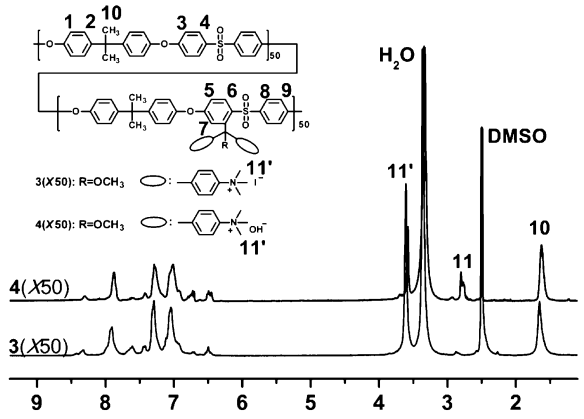


Figure 2. ^{1}H NMR spectral analysis of 3(*X*50) and 4(*X*50) membrane (hydroxide conversion, exposed to 1 M NaOH for 24 h) in DMSO-d_6.

between 73% and 83% of the theoretical IEC values of **3** membranes, suggesting some degree of instability of **4** membranes when exposed to alkaline conditions. Further investigations concerning stability will be discussed in the following section.

Water Uptake and Dimensional Swelling of 4 Membranes. Water uptake (WU) and dimensional swelling (20 and 60 °C) of the **4** membranes were measured in water and plotted as a function of IEC_w in Figure 3. Water uptake of the **4** membranes, which was in the range of 8.7−18.4% at 20 °C, increased linearly with increasing IEC_w. A comparison of **4** and typical AEMs based on PAES-QA and PPO-QA revealed that the **4** membranes absorbed much less water, as shown in Figure 3a. For a better comparison among the different IEC membranes, the number of absorbed water molecules per phenyltrimethylammonium (PTMA) group (designated as λ) was calculated (Figure 3b). Fewer water molecules per PTMA group for **4** membranes were observed even at high IEC_w levels (**4**(*X*81), IEC_w = 1.74 mequiv/g, λ = 5.9). These values were much lower than that of main-chain-type AEMs composed of aromatic polymers bearing quaternary ammonium groups (e.g., λ > 10) and Nafion (Table 2). The lower water uptake and λ values of the **4** membranes are considered to be related to the side-chain-type polymer structure with pendent PTMA groups which could contribute to suppression of excessive water uptake and swelling.

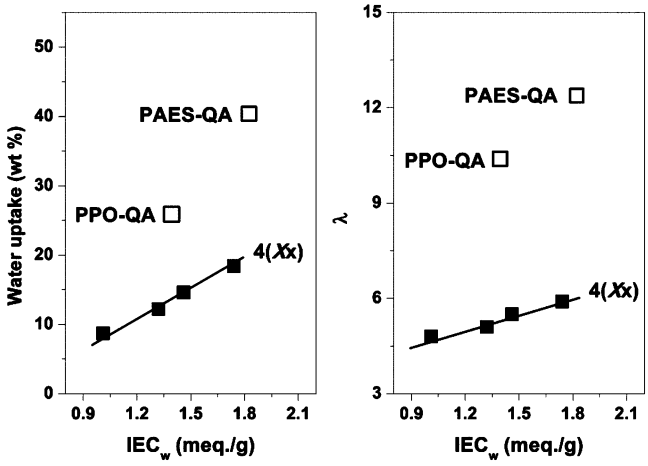


Figure 3. (a) Water uptake and (b) λ values of **4** membranes, PAES-QA and PPO-QA membranes at 20 °C in water as a function of IEC_w.

Lower water uptake of **4** membranes leads to lower dimensional swelling in water (Δl), as shown in Table 2. The in-plane water swelling ratio (Δl) at 20 °C was less than 5%. These unusually small values were much lower than that of PAES-QA and PPO-QA AEMs. Unlike main-chain-type random copolymer AEMs, in which higher temperature induced excessive water uptake and dimensional swelling, the temperature had less of an influence on the **4** membranes (Table 2). Using the **4**(*X*81) membrane (IEC_w = 1.74 mequiv./g) as an example, the water uptake of 22.4% and swelling ratio of 5% at 60 °C was not excessively higher than the corresponding values at 20 °C (18.4% water uptake and 4% swelling ratio), especially when compared with other copolymer systems at this temperature difference.[29,31]

In addition, the volumetric IEC value of water absorbed membranes (IEC_v (wet)), calculated from density and water uptake measurements,[49] reflects the concentration of ions within the polymer matrix under hydrated conditions without distinguishing between those hydroxides that are mostly associated with the PTMA groups and those that are fully dissociated. It is of interest to note how this IEC_v (wet) value itself is affected by changes in base and water uptake and whether ion concentration remains constant or whether it varies. As shown in Table 2, the density decreases slightly with increasing DS, due to the lower density of PTMA groups. The IEC_v (wet) of **4** membranes at 20 °C increased from 1.14 to 1.68 mequiv/cm^3, corresponding to IEC_w values increasing from 1.01 to 1.74 mequiv/g. All the values were only slightly lower than those of the corresponding IEC_v (dry) values because of the lower water uptake of **4** membranes, indicating their much lower dimensional swelling in water.

Hydroxide Conductivity and Methanol Permeability of 4 Membranes. For fuel cell operation using anion exchange membrane materials, there is a requirement for the hydroxide conductivity to be above 10^{-2} S/cm and for water uptake to be less than 30%.[34] The hydroxide conductivity of the **4** membranes was measured in water and compared with that of PAES-QA and PPO-QA AEMs. The conductivity values reported in Table 2 are expressed in Figure 4a as a function

Table 2. Various IEC, Water Uptake, Swelling Ratio and Hydroxide Conductivities of 4 Membranes

			IEC_v (mequiv/cm^3)		WU (wt %)			Δl (%)		σ (mS/cm)
ionomers	d (g/cm^3)	IEC_w (mequiv/g)	dry	wet	20 °C	λ	60 °C	20 °C	60 °C	20 °C
4(*X*35)	1.26	1.01	1.27	1.14	8.7	4.8	9.4	3	3	15
4(*X*50)	1.22	1.32	1.61	1.40	12.2	5.1	12.9	3	3	26
4(*X*62)	1.20	1.46	1.75	1.49	14.6	5.5	15.8	3	4	33
4(*X*81)	1.19	1.74	2.05	1.68	18.4	5.9	20.8	4	5	38
PAES-QA	1.20	1.82	2.18	1.47	40.5	12.3	52.1	13	18	35
PPO-QA	1.05	1.39	1.46	1.15	25.9	10.4	28.3	7	10	4
Nafion	1.98	0.90	1.78	1.29	19.0	11.7	15.3	12	15	90

dx.doi.org/10.1021/ma202681z | *Macromolecules* 2012, 45, 2411−2419

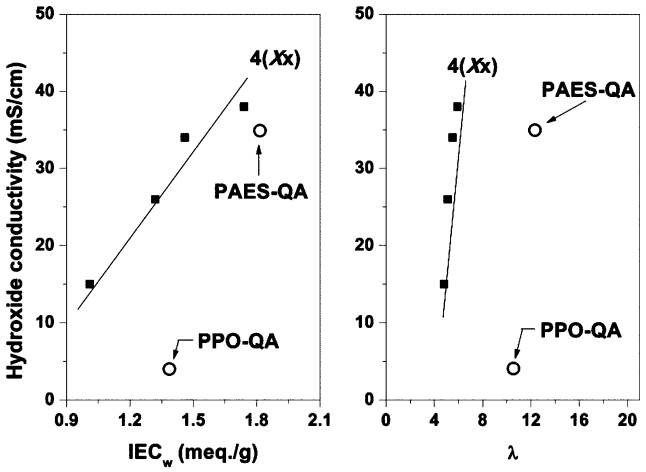


Figure 4. Conductivity of **4**, PAES-QA, and PPO-QA membranes at 20 °C as a function of (a) IEC_w and (b) λ value.

of the IEC_w. Similar to the water uptake, the hydroxide conductivity of **4** membranes increased with increasing IEC values. These values were above 10^{-2} S/cm at room temperature (20 °C) which was comparable to PAES-QA and much higher than PPO-QA. Because of the side-chain PTMA groups for OH^- transport, it is believed that the **4** membranes are able to utilize water molecules more efficiently for ion transport. The 4(*X*81) membrane achieved the highest hydroxide conductivity of 3.8×10^{-2} S/cm at 20 °C.

An important finding of the present work is that the **4** membranes showed much lower water uptake but comparable conductivity compared with those of main-chain-type AEMs PAES-QA and PPO-QA. As shown in Figure 4b, the **4** membranes located on the line on the left portion of the graph have higher hydroxide conductivity but lower water absorption (λ) values. These results suggest that the present polymer design concept of a side-chain-type structure is effective for the AEMs in mitigating dimensional swelling and improving hydroxide conductivity, as already demonstrated for acid-based PEMs. Furthermore, the hydroxide conductivities of the **4** membranes showed an approximate Arrhenius-type temperature dependence, as shown in Figure 5. The 4(*X*81) membrane (IEC = 1.74 mequiv/g) showed the highest conductivity of 5.8×10^{-2} S/cm at 80 °C.

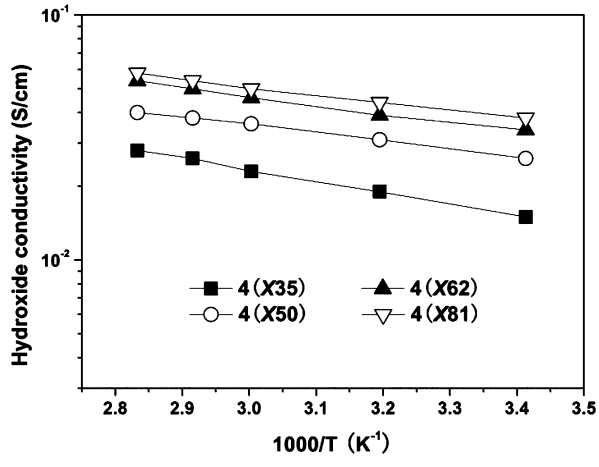


Figure 5. Hydroxide ion conductivity of **4** membranes in water as a function of temperature.

However, all alkali-based **4** membranes show much lower ion conductivity compared to that of the acid-based Nafion 112 (9.0×10^{-2} S/cm at 20 °C). The conductivity of ions is a function of both the ion mobility and the concentration of charge carriers. The **4** membranes displayed comparable or higher bulk concentrations of potential charge carriers in each case, e.g. IEC_v(wet), but lower ion conductivity. The major difference in conductivity between Nafion 112 and **4** membranes can be rationalized by considering the mobility or dissociation of the sulfonic acid and quaternary ammonium functional groups (H^+ = 4.76 and OH^- = 2.69 relative to K^+ in infinitely dilute solution at 298 K).[51,52] The sulfonic acid in Nafion is a super acid, while quaternary ammonium substituents are weak bases with pK_b values of about 4.[33] The dissociation of weakly basic quaternary ammonium groups presents a considerable theoretical barrier for efficient hydroxide conduction AEMs.

Polymer electrolyte membranes intended for direct methanol fuel cells (DMFC) must possess both sufficiently high ion conductivities and be effective barriers for methanol crossover from the anode to the cathode compartment. Methanol permeability through polymer electrolyte membranes often follows a similar relationship to ion conductivity; that is, ion conductivity has a strong trade-off in its relationship with methanol permeability. Nafion has good proton conductivity due to strongly interconnected ionic domains structure and high proton mobility, but its high methanol permeability is a shortcoming in its application in DMFC. The **4** membranes exhibited comparatively lower methanol permeability to Nafion, as shown in Figure 6. The permeability values for

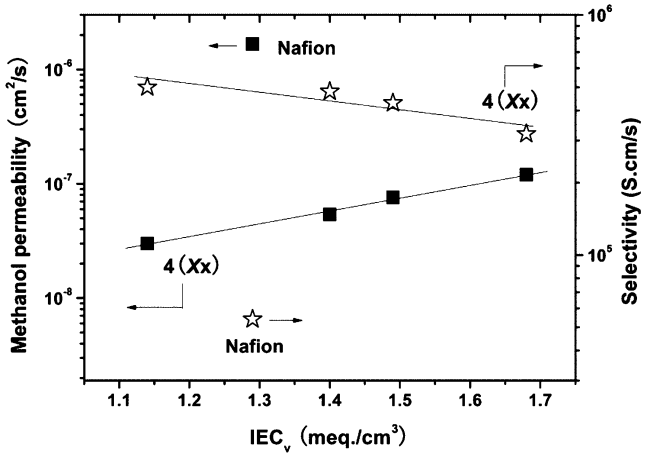


Figure 6. Performance trade-off plot of the IEC_v values vs the methanol permeability (■) and selectivity (☆).

2 M methanol at room temperature were in the range of 3×10^{-8} to 1.2×10^{-7} cm^2/s, which were almost 2 orders of magnitude lower than that of Nafion (1.67×10^{-6} cm^2/s). Although the **4** membranes have lower ion conductivities than Nafion, the conductivities are sufficiently high to achieve much better selectivity, which is the ratio of ion conductivity to methanol permeability (Figure 6).

Thermal and Alkaline Stabilities and Mechanical Properties. The TGA curves of **4** membranes are shown in Figure 7. A two-step degradation profile was observed for all membranes in their hydroxide form. There was no weight loss up to 150 °C because all the samples were preheated at 120 °C

dx.doi.org/10.1021/ma202681z | *Macromolecules* 2012, 45, 2411–2419

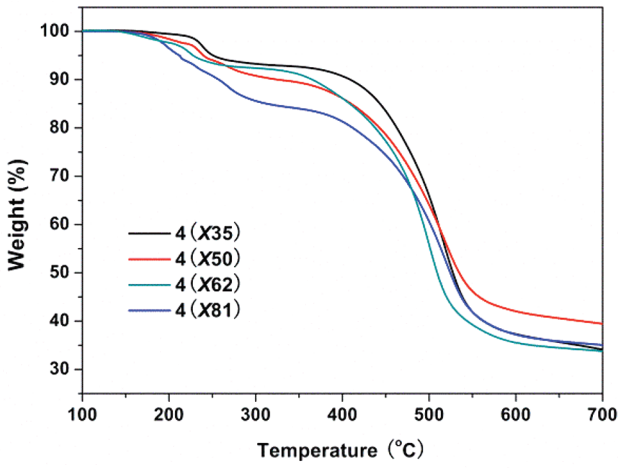


Figure 7. TGA curves for copolymer **4** membranes from measurements run at 10 °C/min in N_2.

for 20 min to remove absorbed water. As shown in Figure 7, the first weight loss occurred at about 180 °C, which is associated with the degradation of the quaternary ammonium groups. Furthermore, the membranes with lower IEC values displayed better thermal stability than those with higher IEC values. For example, the 5% decomposition temperature of **4**(*X*35) is about 220 °C, which is much higher than that of the **4**(*X*81) membrane (ca. 170 °C). The second weight loss at around 400−500 °C is related to the degradation of the polymer chain. The decomposition temperature of the polymer backbone was similar to that of the parent polymer,[7] suggesting that the decomposition of the quaternary ammonium groups did not trigger degradation of the polymer backbone, which was observed in some aromatic AEMs.[50]

As mentioned above, the degradation of PTMA functionalized **4** membranes occurs under high pH conditions probably via (i) Hoffmann elimination and (ii) direct nucleophilic substitution.[19,22,23] To further evaluate the stability and degradation mechanism of the **4** membranes, **4**(*X*50) membrane with IEC of 1.32 mequiv/g was treated with 4 M NaOH aqueous for different exposure times. The membranes maintained their toughness, flexibility, and appearance after stability tests as long as 800 h, suggesting no decomposition of PSf main chain. The chemical structures before and after the tests were analyzed by use of ^{1}H NMR spectroscopy (Figure 8). The signals for the methyl protons in the PTMA substituents in the tested membranes become smaller, while the integrations of methyl and aromatic protons (6.4−6.8 ppm) in phenyldimethylamine increase with increasing the time. Since there are no other signals assignable to methyl or methylene protons observed in Figure 8, which are assumed to appear if a Hoffmann elimination degradation mechanism were to occur, the major degradation mode of **4** membranes under these stability testing conditions is most likely to be direct nucleophilic substitution, that is, the elimination of methanol to revert to the phenyldimethyl amine substituent. After an initial period of transient behavior for 80 h, the IEC and conductivity showed a constant but slow decline, as shown in Figure 9. The IEC value after the test of 800 h was estimated to be 0.46 mequiv/g, which was ~35% of the initial IEC value of 1.32 mequiv/g, suggesting the **4** membranes have insufficient long-term stability for anion exchange membrane fuel cell application. The long-term instability of PTMA groups in the **4**

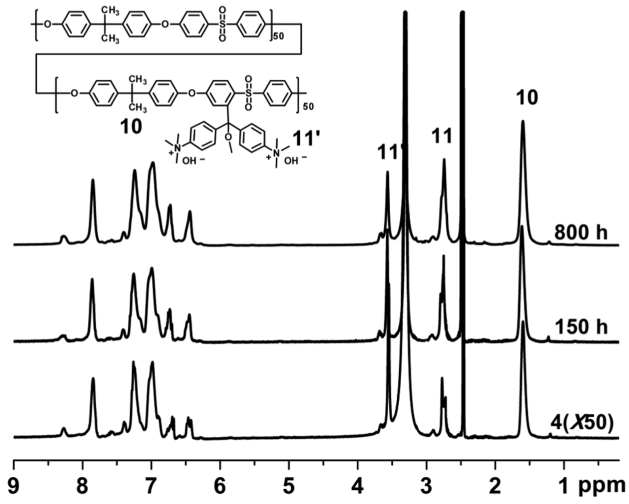


Figure 8. ^{1}H NMR spectra of 4(*X*50) in DMSO-d_6 (IEC = 1.30 mequiv/g) after stability tests in 4 M NaOH at room temperature for 150 and 800 h.

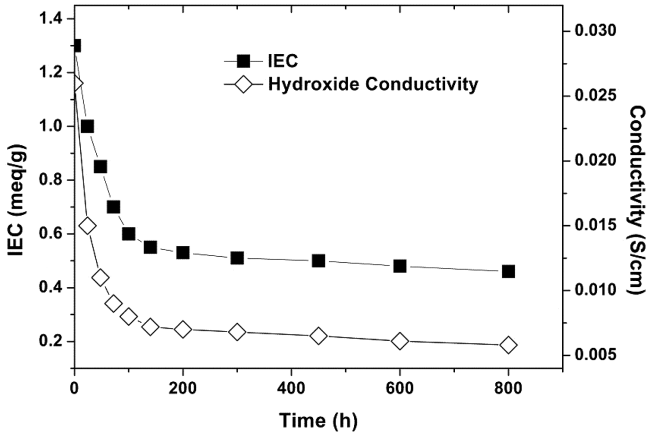


Figure 9. Decline in IEC values and hydroxide ion conductivity with time for the 4(*X*50) membrane (IEC = 1.30 mequiv/g) in 4 M NaOH at room temperature.

membranes is probably attributable to the low electron cloud density of the nitrogen atom, brought about by the electron-withdrawing phenyl, which could be attacked readily by hydroxide ion.[35,53−56]

The mechanical properties for the **4** membranes are shown in Table 3. The membranes displayed values of tensile stress at maximum load of 60.2−67.3 MPa, Young's moduli of 1.58−1.72 GPa, and values of elongation at break of 9.0−13.2%. These results indicate that the **4** membranes were tough and

Table 3. Mechanical Properties of the 4 Membranes at 20 °C and 50% RH

sample	IEC (mequiv/g)	tensile strength (MPa)	Young's modulus (GPa)	elongation at break (%)
4(*X*35)	1.01	65.8	1.72	12.6
4(*X*50)	1.32	63.6	1.62	10.3
4(*X*62)	1.46	67.3	1.67	13.2
4(*X*81)	1.74	60.2	1.58	9.0

dx.doi.org/10.1021/ma202681z | *Macromolecules* 2012, 45, 2411−2419

ductile, without any decomposition occurring during their preparation by lithiation chemistry.

CONCLUSIONS

In summary, we have demonstrated a new synthetic method for the incorporation of side-chain quaternary ammonium (QA) functional groups into a commercially available polymer using lithiation chemistry, without evident polymer decomposition and cross-linking. The resulting PTMA functionalized polymers exhibited unusually low water uptake and methanol permeability but high hydroxide conductivity. The **4**(*X*81) membrane with IEC of 1.74 mequiv/g showed the highest hydroxide conductivity (58 mS/cm) at 80 °C. Long-term stability tests over 800 h indicate that the PTMA groups do not have sufficient stability under alkaline conditions, for the probable reason that the lower electron cloud density of nitrogen atoms allows attack more readily by hydroxide ion. However, from a polymer design perspective, the results suggest that side-chain quaternary ammonium functional substituents can enhance hydroxide conductivity and mitigate water swelling in AEMs. The introduction of other kinds of tertiary amine-containing compounds such as guanidine, which could be introduced into PSf by the same lithiation approach, could help to improve the stability of quaternary ammonium groups.

AUTHOR INFORMATION

Corresponding Author

*E-mail: ymlee@hanyang.ac.kr (Y.M.L.); Michael.Guiver@nrc-cnrc.gc.ca (M.D.G.).

Notes

The authors declare no competing financial interest.

ACKNOWLEDGMENTS

Funding for the project by the WCU program, National Research Foundation (NRF) of the Korean Ministry of Science and Technology (No. R31-2008-000-10092-0), is gratefully acknowledged.

REFERENCES

(1) Guiver, M. D.; Robertson, G. P.; Yoshikawa, M.; Tam, C. M. In *Membrane Formation and Modification*; ACS Symposium Series No. 744; Pinnau, I., Freeman, B., Eds.; American Chemical Society: Washington, DC, 1999; Chapter 10, pp 137−161.
(2) Guiver, M. D.; Robertson, G. P.; Rowe, S.; Foley, S.; Kang, Y. S.; Park, H. C.; Won, J.; Thi, H. N. L. *J. Polym. Sci., Part A: Polym. Chem.* **2001**, *39*, 2103−2124.
(3) Iojoiu, C.; Maréchal, M.; Chabert, F.; Sanchez, J. Y. *Fuel Cells* **2005**, *5*, 344−354.
(4) Guiver, M. D.; Kutowy, O.; ApSimon, J. W. *Polymer* **1989**, *30*, 1137−1142.
(5) Warshawsky, A.; Kahana, N.; Deshe, A.; Gottlieb, H. E.; Arad-Yellin, R. *J. Polym. Sci., Part A: Polym. Chem.* **1990**, *28*, 2885−2905.
(6) Kahana, N.; Arad-Yellin, R.; Deshe, A.; Warshawsky, A. *J. Polym. Sci., Part A: Polym. Chem.* **1990**, *28*, 3303−3315.
(7) Guiver, M. D.; ApSimon, J. W.; Kutowy, O. *J. Polym. Sci., Polym. Lett. Ed.* **1988**, *26*, 123−127.
(8) Kerres, J.; Cui, W.; Reichle, S. *J. Polym. Sci., Part A: Polym. Chem.* **1996**, *34*, 2421−2438.
(9) Brownstein, S. K.; Guiver, M. D. *Macromolecules* **1992**, *25*, 5181−5185.
(10) Dai, Y.; Guiver, M. D.; Robertson, G. P.; Kang, Y. S. *Macromolecules* **2005**, *38*, 9670−9678.
(11) Dai, Y.; Guiver, M. D.; Robertson, G. P.; Kang, Y. S.; Lee, K. J. *Macromolecules* **2003**, *36*, 6807−6816.
(12) Park, H. B.; Freeman, B. D.; Zhang, Z.; Sankir, M.; McGrath, J. E. *Angew. Chem., Int. Ed.* **2008**, *47*, 6019−6024.
(13) Hickner, M. A.; Ghassemi, H.; Kim, Y. S.; Einsla, B. R.; McGrath, J. E. *Chem. Rev.* **2004**, *104*, 4587−4612.
(14) Harrison, W. L.; Hickner, M. A.; Kim, Y. S.; McGrath, J. E. *Fuel Cells* **2005**, *5*, 201−212.
(15) Jannasch, P. *Fuel Cells* **2005**, *5*, 248−260.
(16) Park, C. H.; Lee, C. H.; Guiver, M. D.; Lee, Y. M. *Prog. Polym. Sci.* **2011**, *36*, 1443−1498.
(17) Diat, O.; Gebel, G. *Nat. Mater.* **2008**, *7*, 13−14.
(18) Curtin, D. E.; Lousenberg, R. D.; Henry, T. J.; Tangeman, P. C.; Tisack, M. E. *J. Power Sources* **2004**, *131*, 41−48.
(19) Vorcoe, J. R.; Slade, R. C. T. *Fuel Cells* **2005**, *5*, 187−200.
(20) Xu, T. *J. Membr. Sci.* **2005**, *263*, 1−29.
(21) Hickner, M. A. *Mater. Today* **2010**, *13*, 34−41.
(22) Merle, G.; Wessling, M.; Nijmeijer, K. *J. Membr. Sci.* **2011**, *377*, 1−35.
(23) Couture, G.; Alaaeddine, A.; Boschet, F.; Ameduri, B. *Prog. Polym. Sci.* **2011**, *36*, 1521−1557.
(24) McLean, G. F.; Niet, T.; Prince-Richard, S.; Djilali, N. *Int. J. Hydrogen Energy* **2002**, *27*, 507−526.
(25) Spendelow, J. S.; Wieckowski, A. *Phys. Chem. Chem. Phys.* **2007**, *9*, 2654−2675.
(26) Dillon, R.; Srinivasan, S.; Arico, A. S.; Antonucci, V. *J. Power Sources* **2004**, *127*, 112−126.
(27) Fang, J.; Shen, P. K. *J. Membr. Sci.* **2006**, *285*, 317−322.
(28) Hibbs, M. R.; Fujimoto, C. H.; Cornelius, C. J. *Macromolecules* **2009**, *42*, 8316−8321.
(29) Varcoe, J. R.; Slade, R. T. C.; Yee, E. L. H.; Poynton, S. D.; Driscoll, D. J.; Apperley, D. C. *Chem. Mater.* **2007**, *19*, 2686−2693.
(30) Herman, H.; Slade, R. T. C.; Varcoe, J. R. *J. Membr. Sci.* **2003**, *218*, 147−163.
(31) Danks, T. N.; Slade, R. T. C.; Varcoe, J. R. *J. Mater. Chem.* **2003**, *13*, 712−721.
(32) Yan, J.; Hibbs, M. R. *Macromolecules* **2010**, *43*, 2349−2356.
(33) Hibbs, M. R.; Hickner, M. A.; Alam, T. M.; McIntyre, S. K.; Fujimoto, C. H.; Cornelius, C. J. *Chem. Mater.* **2008**, *20*, 2566−2573.
(34) Wang, J.; Li, S.; Zhang, S. *Macromolecules* **2010**, *43*, 3890−3896.
(35) Kim, D. S.; Labouriau, A.; Guiver, M. D.; Kim, Y. S. *Chem. Mater.* **2011**, *23*, 3795−3797.
(36) Zhang, Q.; Li, S.; Zhang, S. *Chem. Commun.* **2010**, *46*, 7495−7497.
(37) Gu, S.; Cai., R.; Luo, T.; Chen, Z.; Sun, M.; Liu, Y.; He, G.; Yan, Y. *Angew. Chem., Int. Ed.* **2009**, *48*, 6499−6502.
(38) Wang, J. H.; Zhao, Z.; Gong, F. X.; Li, S. H.; Zhang, S. B. *Macromolecules* **2009**, *42*, 8711−8717.
(39) Zhao, Z.; Wang, J.; Li, S.; Zhang, S. *J. Power Sources* **2011**, *196*, 4445−4450.
(40) Tanaka, M.; Fukasawa, K.; Nishino, E.; Yamaguchi, S.; Yamada, K.; Tanaka, H.; Bae, B.; Miyatake, K.; Watanabe, M. *J. Am. Chem. Soc.* **2011**, *133*, 10646−10654.
(41) Liu, B.; Robertson, G. P.; Kim, D. S.; Sun, X.; Jiang, Z.; Guiver, M. D. *Polymer* **2010**, *51*, 403−413.
(42) Lafitte, B.; Puchner, M.; Jannasch, P. *Macromol. Rapid Commun.* **2005**, *26*, 1464−1469.
(43) Lafitte, B.; Jannasch, P. *Adv. Funct. Mater.* **2007**, *17*, 2823−2834.
(44) Kim, D. S.; Robertson, G. P.; Kim, Y. S.; Guiver, M. D. *Macromolecules* **2009**, *42*, 957−963.
(45) Li, N.; Shin, D. W.; Hwang, D. S.; Lee, Y. M.; Guiver, M. D. *Macromolecules* **2010**, *43*, 9810−9820.
(46) Kerres, J.; Ullrich, A.; Hein, M. *J. Polym. Sci., Part A: Polym. Chem.* **2001**, *39*, 2874−2888.
(47) Guiver, M. D.; Robertson, G. P.; Foley, S. *Macromolecules* **1995**, *28*, 7612−7621.
(48) Robertson, G. P.; Guiver, M. D.; Bilodeau, F. O.; Yoshikawa, M. *J. Polym. Sci., Part A: Polym. Chem.* **2003**, *41*, 1316−1329.
(49) Kim, Y. S.; Einsla, B.; Sankir, M.; Harrison, W.; Pivovar, B. S. *Polymer* **2006**, *47*, 4026−4035.

(50) Tanaka, M.; Koike, M.; Miyatake, K.; Watanabe, M. *Polym. Chem.* **2011**, *2*, 99−106.
(51) Dean, J. A. *Lange's Handbook of Chemistry*, 15th ed.; McGraw-Hill: New York, 1999.
(52) Vanysek, P. Ionic conductivity and diffusion at infinite dilution. In *CRC Handbook of Chemistry and Physics*, 83rd ed.; Lide, D. R., Ed.; CRC Press: Boca Raton, FL, 2002.
(53) Fenton, G. W.; Ingold, C. K. *J. Chem. Soc.* **1929**, 2342−2357.
(54) Zanger, M.; Vanderwerf, C. A.; McEwen, W. E. *J. Am. Chem. Soc.* **1959**, *81*, 3806−3807.
(55) Einsla, B. R.; Chempath, S.; Pratt, L.; Boncella, J.; Rau, J.; Macomber, C.; Pivovar, B. *Electrochem. Soc. Trans.* **2007**, *11*, 1173−1180.
(56) Chempath, S.; Einsla, B. R.; Pratt, L. R.; Macomber, C. S.; Boncella, J. M.; Rau, J. A.; Pivovar, B. S. *J. Phys. Chem. C* **2008**, *112*, 3179−3182.

Macromolecules

Article

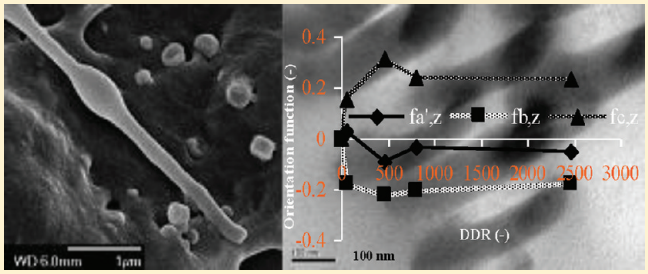
pubs.acs.org/Macromolecules

Exploiting POSS–Sorbitol Interactions: Issues of Reinforcement of Isotactic Polypropylene Spun Fibers

Sayantan Roy, Byoung J. Lee, Zahi M. Kakish, and Sadhan C. Jana*

Department of Polymer Engineering, The University of Akron, Akron, Ohio 44325-0301, United States

ABSTRACT: This study investigates the issues involving reinforcement of isotactic polypropylene (iPP) spun fibers by molecular adducts originating from the synergistic interactions of polyhedral oligomeric silsesquioxane (POSS) containing silanol functionalities (silanol–POSS) and di(benzylidene)-sorbitol (DBS). The molecular adducts of silanol–POSS and DBS were low viscosity liquids at fiber spinning temperature, turned into cylindrical domains during fiber spinning, and remained as nanoparticles in the fibers. The fibers were analyzed by differential scanning calorimetry, wide-angle X-ray diffraction , scanning electron microscopy, and transmission electron microscopy. It was observed that iPP compounds with 2–5 wt % silanol–POSS and 1 wt % DBS could be spun into fibers with close to 40% reduction in diameter compared to unfilled iPP. These fibers offered 60–80% increase in tensile modulus, 50–60% increase in tensile strength, and 100% increase in yield strength compared to unfilled iPP. The silanol–POSS particles were found to be of cylindrical shape with approximately 100 nm in diameter and 200–300 nm in length. The improvements in mechanical properties were correlated with iPP crystallinity and orientation factor.



INTRODUCTION

Polyhedral oligomeric silsesquioxanes (POSS) are a class of hybrid organic–inorganic filler materials receiving considerable attention in recent years.[1−18] These represent several elements of novelty, e.g., molecular diameter between 1 and 3 nm, low density, high thermal stability, and an array of side-chain functionalities,[19−21] the latter to account for compatibility with various host polymers. The POSS molecular size qualifies POSS-based polymer composites as true nanocomposites provided nanoscale dispersion is achieved.

Despite such optimistic outlook, very few studies reported consistent improvements in properties of polymer compounds with nonreactive POSS. Nonreactive POSS molecules do not covalently bond to host polymers. Polymer compounds of nonreactive POSS are commonly prepared by melt-blending and the degree of POSS dispersion depends upon the nature of the side groups of POSS and its compatibility with the host polymer.[2,11,22] Inferior properties result if incompatible POSS molecules are used.[7,23,24] On the other hand, a compatible POSS disperses molecularly in the polymer,[2,10,25] although desired improvements in mechanical properties are not obtained often due to plasticization of the polymer chains by the POSS side groups.[16,23] This poses a trade-off between the extent of dispersion desired and the scope of mechanical properties improvement in POSS–polymer compounds. One approach to circumvent this issue is to produce a dispersion of POSS such that POSS molecules form particle aggregates of 50–100 nm in diameter. The nanoparticles can influence polymer crystallization, affect chain orientation in processing flows, and consequently offer mechanical reinforcement. This approach was followed in current work by considering a silanol containing POSS (silanol–POSS) that was not compatible with the host polymer isotactic polypropylene (iPP) but could easily form self-assembled particle aggregates due to strong POSS–POSS noncovalent interactions. In addition, a sorbitol-type molecule, often used as a nucleating agent for iPP, was used to promote dispersion of POSS in iPP. Prior work showed the usefulness of low molecular weight dispersion aids in promoting dispersion of inorganic nanoparticles in host polymers.[26] The results of fiber spinning experiments and spun fiber properties were compared with those of a compatible POSS–iPP compound with and without the use of sorbitol dispersion aid.

It was recognized at the outset that the polar nature of silanol–POSS would deter its dispersion in the melt of nonpolar iPP. To circumvent this, up to 1 wt % of sorbitol-type molecule was added in the compounds. The sorbitol molecule was soluble in iPP at melt processing temperature and is a known nucleating agent of iPP. It was hypothesized that stronger hydrogen bonding interactions between sorbitol and silanol–POSS would promote dispersion of silanol–POSS in iPP melt and that the fibrillar networks of sorbitol formed upon cooling would serve as templates for assembly of silanol–POSS molecules into nanoparticle aggregates.[27−31]

Our previous publication[31] established that the sorbitol molecules promoted dispersion of silanol–POSS in molten iPP by forming several complex molecular adducts through hydrogen bonding and $\pi-\pi$ interactions. The complex

Received: December 23, 2011
Revised: February 12, 2012
Published: February 23, 2012

ACS Publications © 2012 American Chemical Society

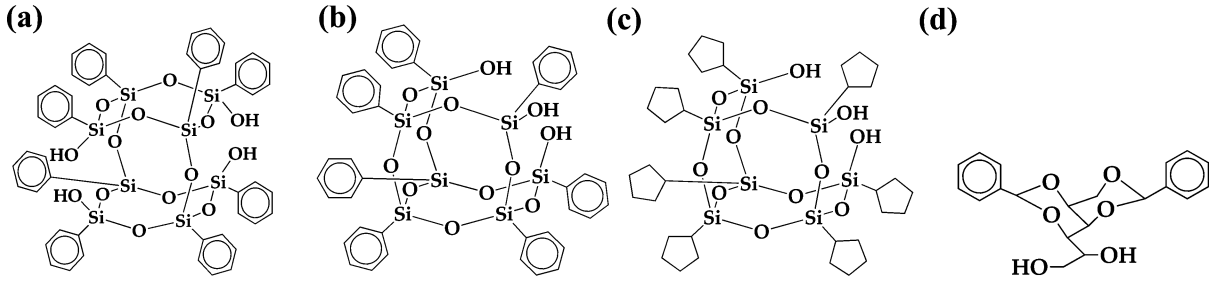


Figure 1. Chemical structure of (a) tetra-POSS, (b) tri-POSS, (c) cyclo-POSS, and (d) DBS.

formation was more abundant for silanol−POSS with higher number of silanol groups per molecule. The molecular adducts were amorphous solids at room temperature and turned into liquids above the crystalline melting temperature of iPP with almost 3 orders of magnitude lower viscosity than iPP melt. The same set of silanol−POSS molecules were melt blended with iPP for the development of melt-spun fibers, the results of which are presented in this paper.

This paper investigated several issues. First, we compared the silanol−POSS particle morphology in spun fibers with those of melt-mixed materials and correlated such morphology with the viscosity of POSS-sorbitol molecular adducts and of iPP. The silanol−POSS-sorbitol interactions "engineered" the POSS−POSS self-assembly into formation of particles with diameter of less than 200 nm in comparison to particles of diameter a few micrometer when sorbitol was not used. Second, we evaluated the tensile properties of injection-molded specimens to determine the extent of mechanical reinforcement derived from POSS particles alone. This would highlight if the mechanical reinforcement seen in spun fibers were at all contributed by the POSS nanoparticles. Third, we evaluated the specific roles of polymer chain orientation and polymer crystallinity on spun fiber tensile properties. The effects of assembled POSS particle size and morphology on crystallization behavior were evaluated in line with the findings in literature.[6,8,11,15,18,32−35]

EXPERIMENTAL SECTION

Materials. Isotactic polypropylene, grade P4G2Z-159, was obtained in the form of pellets from Flint Hill Resources (Wichita, Kansas) with MFI 1.95 g/10 min (ASTM D1238), density 0.90 g/cm^3 (ASTM D1505), and crystalline melting temperature (T_m) 165 °C. The supplier provided the following information on molecular weight of iPP from gel permeation chromatography−number-average molecular weight (M_n) ~69 600 and weight-average molecular weight (M_w) of 314 700. This grade of iPP did not contain any nucleating agent as per the information obtained from the supplier. Three grades of silanol−POSS were obtained from Hybrid Plastics (Hattiesburg, MS). Tetra-silanol phenyl−POSS (tetra-POSS, SO 1460) was available in the form of a white powder, with molecular weight 1069.5 g/mol and T_m of 260 °C. Trisilanol phenyl−POSS (tri-POSS, SO 1458) was a white powder with molecular weight of 930.07 g/mol and T_m of 230 °C. Trisilanol cyclopentyl−POSS (cyclo-POSS; SO 1430) was obtained as a white powder with molecular weight of 874.7 g/mol and T_m of 250 °C. Figure 1a−c presents the chemical structures of the silanol−POSS molecules. Note that both tri-POSS and cyclo-POSS have three silanol groups, but they differ in the nature of the side groups, e.g., phenyl in the case of tri-POSS and cyclopentyl in the case of cyclo-POSS.

The sorbitol molecule chosen for this study was di(benzylidene)-sorbitol (DBS; Millad 3905; M_w = 358.4 g/mol and T_m = 225 °C), a commonly used clarifying agent of iPP. Each molecule of DBS has two free −OH groups and two phenyl groups. The structure of DBS is shown in Figure 1d. DBS was obtained from Milliken Chemicals (Spartanburg, SC) in the form of white powder.

Polymer Compound Preparation. A series of iPP/DBS/POSS compounds were produced in an internal mixer, Brabender Plasticorder. Before mixing, all ingredients were dried for 24 h at 80 °C in vacuum. First, PP was allowed to melt in the mixer at 200 °C and then dry-blended powder mixture of DBS and POSS were added in the mixing chamber. The ingredients were mixed for 5 min at 200 °C at an angular speed of 80 rpm. The resultant compound was cooled down to room temperature and ground into small pellets for further experiments and analysis.

Rheological Properties. An advanced rheometric expansion system (ARES) from TA Instruments (New Castle, DE), operated with parallel plates, was used to measure the oscillatory rheological properties of DBS−POSS liquid complex and of iPP/DBS/POSS compounds. The limits of linear viscoelasticity and gelation of DBS in iPP was investigated and interpreted in our earlier publication.[29] The values of complex viscosity ($|\eta^*|$) of various DBS/silanol−POSS blends were recorded in the range 100−200 °C. It was reported earlier that DBS and silanol−POSS formed low viscosity molecular adducts.[30] For this purpose, a 36 mm diameter cup shaped parallel plate was custom-made to hold the low viscosity liquid complex. The upper plate diameter was 25 mm. The DBS−POSS powder specimens were hand mixed before loading in the cup. The mixture was heated at 220 °C for 5 min to turn it into a liquid during which POSS-silanol−POSS complex was formed. Rheological data were taken during cooling of the material from 200 to 100 °C at a rate of 10 °C/min at a constant angular frequency of 10 rad/s. In addition, a frequency sweep experiment was conducted at 180 °C with a varying angular frequency of 100 to 1 rad/s. The strain of the oscillatory shear flow was fixed at 15% for the above experiments.

The oscillatory shear viscosity of iPP and its compounds were determined using disk-shaped specimens of 25 mm diameter and 2 mm thickness. The strain of oscillatory shear flow was fixed at 2%. The sample specimen were kept at 220 °C for 5 min before subjecting to frequency sweep at 200 °C to identify the complex viscosity at a range of 100 to 10 rad/s. As established earlier, the strain and frequency used in these rheological measurements produced linear viscoelastic response.[29]

Preparation of Fibers from iPP and Its Compounds. Melt-spun monofilament fibers were prepared using a capillary extrusion rheometer (MELVERN Instruments, ROSAND RH7) and a home-made take-up device. Molten polymers were spun as a monofilament through a capillary die of length (L) to diameter (D) ratio of 32:2 and a D of 2 mm. The filaments were allowed to cool down naturally during spinning in ambient air at a temperature of 25 °C.

The fiber samples were prepared by varying the plunger speed between 0.3 and 2 mm/min and a take-up velocity of 0.04−0.6 m/s at a melt temperature of 200 °C. The apparent shear rate in the capillary die varied between 1.0 s^{-1} for plunger speed of 0.3 mm/min, to 7.5 s^{-1} for plunger speed of 2 mm/min. In a majority of the data reported in this paper, the plunger speed was 0.3 mm/min. The value of draw down ratio (DDR) was determined as in eq 1 from the velocity of fiber

dx.doi.org/10.1021/ma202783p | Macromolecules 2012, 45, 2420−2433

take-up (V_{fiber}) and the velocity of the polymer melt (V_{melt}) exiting the die:

$$\text{DDR} = V_{fiber}/V_{melt} = (D_{die}/D_{fiber})^2 \quad (1)$$

In eq 1, D_{die} and D_{fiber} are the diameter of the capillary die and the corresponding fiber, respectively. The diameter of the fibers of iPP and its compounds were measured by digital electronic micrometer with a precision of measurement to 4 μm. For each polymer compound, the diameter of at least 10 fiber specimens was measured and an average diameter was computed.

Thermal Analysis. Thermal properties such as melting temperature (T_m), crystallization temperature (T_c), and the respective enthalpies were determined under nitrogen gas atmosphere using a DSC 2920 calorimeter from TA Instruments (New Castle, DE). The melt-mixed compounds and their corresponding fibers were heated at a rate of 10 °C/min from 30 up to 200 °C. In the case of melt-mixed compounds, the melt was kept at 200 °C for 5 min to melt all the crystals before the recrystallization scans began with cooling of the materials from 200 to 30 °C at a rate of 10 °C/min. The value of crystallinity of the materials was determined from the amounts of heat released during crystallization scans. Note that such crystallinity referred to crystallinity under quiescent conditions. The heat of fusion (ΔH_m) for fiber samples was determined from the area under the melting peak and was used to characterize the orientation-induced crystallinity of the samples.

The percentage of crystallinity of the fibers was determined from eq 2 by comparing the enthalpy of fusion of polymer to the enthalpy of fusion of 100% crystalline iPP (ΔH_0 = 177 J/g).[36]

$$\text{crystallinity (\%)} = \Delta H_m/\Delta H_0 \times 100\% \quad (2)$$

Equation 2 was also used to obtain crystallinity of the melt-mixed materials, whereby ΔH_m was calculated from the area under the crystallization peak of iPP and its compounds. In each case, at least three measurements were taken and the average values were calculated.

Wide Angle X-ray Diffraction (WAXD). WAXD patterns of fibers of iPP and its compounds revealed the orientation of the polymer chains spun at various DDR. A Bruker wide-angle X-ray instrument with sealed tube X-ray generator was used for this purpose. The generator was operated at 40 kV and 40 mA with a beam monochromatized to Cu Kα radiation of wavelength (λ) of 1.54 Angstroms. Two-dimensional WAXD film patterns were obtained from 2θ equatorial scan of the uniaxially oriented fiber samples where θ is the diffraction angle in deg. The diffraction patterns were analyzed by the Bruker General Area Detector Diffraction System (GADDS) software.

The fiber samples were mounted around a hollow metal frame. For this purpose, fibers were aligned parallel to each other before mounting. The total diameter of the fiber bundle in each measurement was kept constant to guarantee uniform intensity. This allowed comparison of diameter and orientation function of fibers with change of compound formulation and at different values of draw ratio. The cylindrical frame with aligned fiber samples were placed in the apparatus such that the fibers were orientated vertically to the X-ray beam. A typical X-ray exposure time was 5 min for all samples.

Assuming rotational symmetry, Herman–Stein orientation factors of the crystalline regions with respect to the fiber axis can be determined from eqs 3a–3cas follows:[37−41]

$$f_{a,z} = \frac{3\overline{\cos^2 \chi_{a,z}} - 1}{2} \quad (3a)$$

$$f_{b,z} = \frac{3\overline{\cos^2 \chi_{b,z}} - 1}{2} \quad (3b)$$

$$f_{c,z} = \frac{3\overline{\cos^2 \chi_{c,z}} - 1}{2} \quad (3c)$$

In eq 3, $f_{a,z}$, $f_{b,z}$, and $f_{c,z}$ are Herman's orientation factors for a, b, and c crystallographic axes respectively, and $\overline{\cos^2 \chi_{a,z}}$, $\overline{\cos^2 \chi_{b,z}}$, and $\overline{\cos^2 \chi_{c,z}}$ are the mean square cosine of orientation angle of crystallographic axis with respect to the reference direction. If the three axes are orthogonal,

$$f_{a,z} + f_{b,z} + f_{c,z} = 0 \quad (4)$$

Equation 4 implies that two of the three orientation factors are sufficient to specify the orientation function. Average values of $\overline{\cos^2 \chi}$ were obtained from the measurement of intensity distribution $I(\chi,\phi)$ of poles of appropriate planes by WAXD, where ϕ is the angle between a given crystal axis and the fiber axis, which serves as the reference direction (azimuthal angle).

The iPP crystals are monoclinic and the molecular chains are parallel to c-axis, with the result that $\langle \cos^2 \chi_{c,z} \rangle$ is a direct measure of the molecular orientation relative to some reference direction Z in the specimen. However, the a-axis in monoclinic iPP is not perpendicular to the c-axis, but makes an angle of 99.3°. It was found convenient to assign an a′-axis that is perpendicular to both the crystallographic b- and c-axes, and the orientation factor along a'-axis can be determined from eq 4 and the values of f_b and f_c.[40] Note that a' is not a true crystallographic axis for monoclinic crystals.

The (110) and (040) planes give the strongest diffraction intensity. Wilchinsky[42,43] developed a procedure for determination of $\overline{\cos^2 \chi_{i,z}}$, from diffracting planes, where $i = a, b, c$. Therefore, $\overline{\cos^2 \chi_{b,z}}$ can be directly obtained from the intensity distribution function $I(\chi,\phi)$ of (040) planes. Since we have axial symmetry in the fibers, the function reduces to $I(\chi)$, and eqs 5 and 6 describe how the values of $\overline{\cos^2 \chi_{b,z}}$ can be derived from the values of $I(\chi)$.

$$\overline{\cos^2 \chi_{b,z}} = \overline{\cos^2 \chi_{040,z}} = \frac{\sum_{\chi=0}^{90} I(\chi)_{040} \sin \chi \cos^2 \chi}{\sum_{\chi=0}^{90} I(\chi)_{040} \sin \chi} \quad (5)$$

$$\overline{\cos^2 \chi_{110,z}} = \frac{\sum_{\chi=0}^{90} I(\chi)_{110} \sin \chi \cos^2 \chi}{\sum_{\chi=0}^{90} I(\chi)_{110} \sin \chi} \quad (6)$$

Applying Wilchinsky's equations presented above for iPP, the following relationship was obtained for the average cosine squared of the angle between the fiber axis and the c-axis.[40,44]

$$\left\langle \cos^2 \chi_{c,z} \right\rangle = 1 - 1.099 \left\langle \cos^2 \chi_{110,z} \right\rangle - 0.901 \left\langle \cos^2 \chi_{040,z} \right\rangle \quad (7)$$

The values of f_a', f_b, and f_c for each sample were obtained from eqs 3a, 3c, and 4.

Polarized Optical Microscopy. The formation of spherulites of iPP/DBS/POSS compounds was examined by polarized optical microscopy (POM). A Leitz Laborlux 12 Pol S (Oberkochen, Germany) optical microscope was used in cross-polarized mode. Images were acquired with a Diagnostic Instruments Inc. 11.2 Color Mosaic digital camera (Sterling Heights, MI). Polymer films of thickness around 100 μm were prepared by compressing the molten specimens between two glass slides on a hot stage at 200 °C. The sample specimen were heated to 220–240 °C to melt the residual crystals and cooled down to the measurement temperature at a cooling rate of 10 °C/min.

Scanning Electron Microscopy. The morphology was examined using high resolution scanning electron microscope (SEM), JEOL JSM5310. The operating voltage of SEM was 10 kV. The melt mixed composite samples and their corresponding fibers were fractured at room temperature after soaking in liquid nitrogen. The surface of the samples was sputter-coated for 1.5 min by a layer of silver using

Sputter Coater, Model ISI 5400 under argon gas atmosphere before taking images.

Transmission Electron Microscopy. The morphology of assembled structures of DBS and POSS in the melt-mixed materials and in the fibers was examined by transmission electron microscopy (TEM). For this purpose, a TACNAI-12 TEM, by FEI was used at 120 kV. Sample specimens for TEM were prepared by cryo-microtoming. To aid microtoming, a collection of fibers specimen was embedded into the epoxy curatives and cured. Fiber specimens vertical to the flow direction were cut using a Microstar Microtome with a diamond knife and the sections were mounted on 300-mesh copper grids and sections with thickness under 200 nm were obtained.

Tensile Properties. Instron tensile tester (Model 5567) was used to measure the tensile properties of the spun fibers at room temperature with a crosshead speed of 50 mm/min as per ASTM D3822 method. A 5 N load cell was used in conjunction with single fiber specimens. Fiber samples were fixed to preformed paper of gauge length 26 mm and the paper was attached to the grip of the tensile tester. For each specimen, at least 10 fibers were tested, and the average properties were calculated. The values of stress at break, yield strength, Young's modulus, and elongation at break were determined from the experimental data.

RESULTS AND DISCUSSION

It was established in our earlier publication[31] that DBS/tri-POSS and DBS/tetra-POSS mixtures turned into transparent low viscosity liquid after heating the mixtures at 200 °C for 5 min. The characteristics of the liquid complex and how the DBS−POSS molecular adducts influenced DBS fibril formation in the compounds of iPP containing both DBS and POSS were first examined in this paper.

Effect of POSS on DBS Nucleation. It is known[27,30,45] that nanofibrillar networks are formed due to sorbitol crystallization in the polymer melt. These fibrils in turn act as heterogeneous nucleation sites for iPP crystallization that leads to formation of smaller size spherulites. The nucleation efficiency of iPP can be increased by using higher concentration of DBS; typically DBS is used at less than 1 wt %. Also, the size of spherulites is reduced significantly at higher concentration of DBS.[27,28] The introduction of silanol−POSS in iPP/DBS system was expected to reduce the DBS nucleating efficiency, as the presence of POSS subdued DBS fibrillation as reported in earlier publications.[30,31]

The spherulite size of iPP/DBS/tetra-POSS (1/2 wt %) system was examined by optical microscope and the images were taken between two cross polarizer equipped with a hot-stage (Figure 2c−f). In this context, it should be noted that tetra-POSS formed a complex with DBS which turned into a low viscosity liquid at 200 °C.[31] The liquid caused a reduction of the complex viscosity of the compound, e.g. at 220 °C the complex viscosity of iPP was 2738 Pa s and that of iPP-DBS/tetra-POSS (1/2 wt %) compound was 1792 Pa s at 2% strain and a frequency of 10 rad/s.

The compound was homogeneous at 220 °C as no birefringent crystals were identified (Figure 2c). The optical images revealed the absence of DBS nanofibrils (Figure 2d) upon cooling of the melt at the rate of 10 °C/min contrary to what was observed for iPP/DBS system.[27−30] This was attributed to the formation of the liquid complex between silanol−POSS and DBS which prevented organization of DBS into fibrillar networks.[31] Nevertheless, iPP nucleation started at several sites at 150 °C (Figure 2d) and the spherulitic growth continued. The crystallization ceased after the melt was cooled from 150 to 120 °C (see Figure 2e-f).

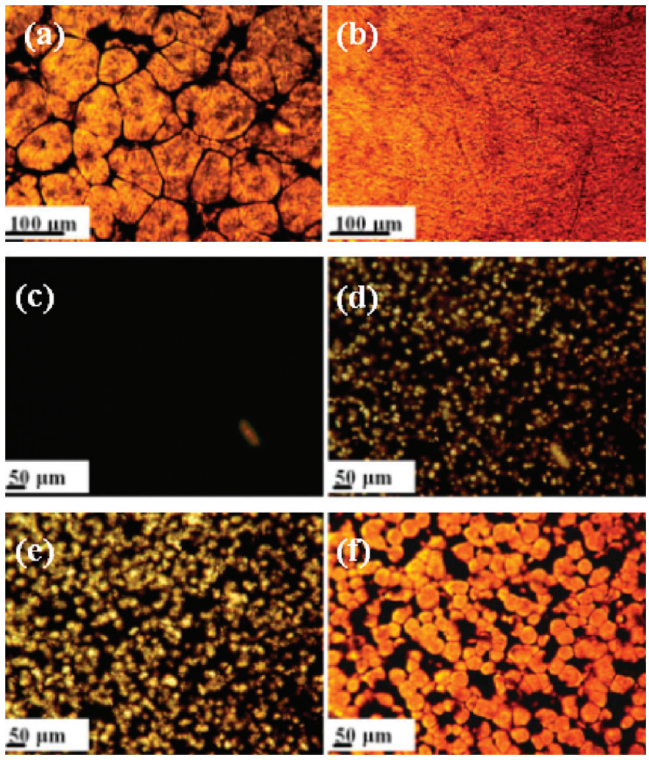


Figure 2. Optical micrographs of spherulites of (a) iPP, and (b) iPP-DBS 1 wt %; cross-polarized images taken at their corresponding crystallization temperature upon cooling the melt at the rate of 10 °C/min to 120 °C, and 140 °C respectively from 220 °C. (c−f) iPP-DBS/tetra-POSS; cross-polarized images taken at (c) 220 °C, (d) 150 °C, (e) 140 °C, and (f) 120 °C.

The size of spherulites in iPP-DBS/tetra-POSS compounds was found to remain in between the size observed for iPP and iPP/DBS system as seen in Figure 2, parts a and b, respectively. Thus, it can be inferred that although DBS no longer formed nanofibrillar structures in the presence of silanol−POSS, it still could act as sites of a few heterogeneous nucleated iPP crystals as observed in Figure 2d. A reduction of the crystallization temperature by approximately 20 °C in iPP-DBS-tetra-POSS compound was observed in comparison to iPP/DBS system, i.e., crystallization was slow in the presence of tetra-POSS.[27−30,46] It was also observed that the extent of crystallinity was reduced. These will be further analyzed from the inspection of DSC data of quiescent melt-mixed materials.

Rheological Properties of DBS/POSS Complex and iPP/DBS/POSS Compounds. The complex viscosity of the DBS/tetra-POSS and DBS/tri-POSS mixtures was obtained as a function of temperature. For this purpose, the intimate mixtures of tri-POSS/DBS and tetra-POSS/DBS at optimum ratio, e.g. 2/1 w/w and 5/1 w/w respectively as identified to be the optimum combinations for DBS/POSS complex formation,[31] were heated at 220 °C for 5 min to obtain a homogeneous liquid. The complex viscosity was noted as the materials were cooled down at a rate of 10 °C/min. Figure 3 shows how the complex viscosity varied with temperature upon cooling. The first set of data was taken at 200 °C. It is seen that the DBS/POSS complex was a low viscosity liquid with less than 10 Pa s of viscosity at 180 °C (Figure 3). The mixture of DBS/tri-POSS with 1/5 w/w showed relatively higher viscosity, e.g., 1.4 Pa s at 200 °C compared to 0.14 Pa s for 1/2 w/w of DBS/tri-POSS, and 0.32 Pa s for 1/2 w/w of DBS/tetra-POSS

dx.doi.org/10.1021/ma202783p | Macromolecules 2012, 45, 2420−2433

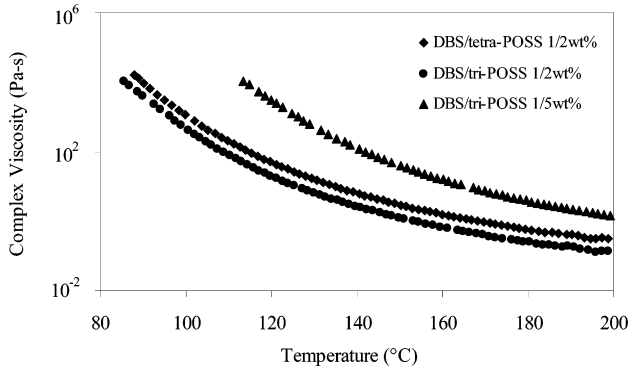


Figure 3. Complex viscosity, $|\eta^*|$, of DBS/POSS mixtures recorded at 15% strain and at 10 rad/s frequency.

mixture. This can be attributed to the presence of higher proportions of high molecular weight POSS in the mixture.

The higher viscosity in the case of DBS/tetra-POSS (1/2 w/w) compared to DBS/tri-POSS (1/2 w/w) can be attributed to more abundant higher molecular weight adducts, already reported in our earlier publication.[31] Also, one can see that the POSS/DBS complex remained as low viscosity liquids up to ~120 °C, the crystallization temperature of iPP. This will be of significance later in the analysis of morphology of POSS particles in spun fibers.

The POSS/DBS liquid mixtures were subjected to frequency sweep experiment at 180 °C to determine if the complex would exhibit Newtonian behavior. The results of such experiments are presented in Figure 4. It is seen that the viscosity remained

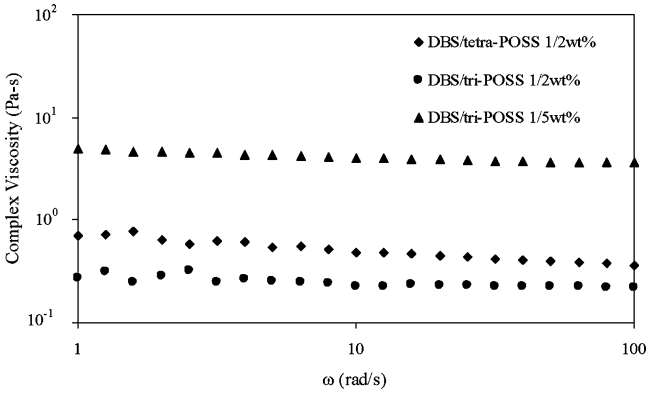


Figure 4. Complex viscosity, $|\eta^*|$, of DBS/POSS mixture recorded at 180 °C with 15% strain.

insensitive to frequency, indicating that the liquids were Newtonian. It is also seen that tri-POSS/DBS complex had lower viscosity than that of tetra-POSS/DBS mixture for the same POSS content. This can be attributed to higher order molecular complexes formed.[31]

The iPP/DBS/silanol−POSS compounds containing the same weight ratio of DBS to silanol−POSS as in Figure 4 were produced by melt mixing and their viscosity was measured. It is seen from Figure 5 that the viscosity of the compounds were almost a factor of 8 lower than the viscosity of iPP and iPP/DBS compounds at the same temperature. Similar observations were recently reported for mixtures of a fully condensed hydrophobic POSS with polyisoprene and polydimethylsiloxane and viscosity reduction was attributed to polymer−POSS solubility.[47] In our work, the greatest reduction was observed in

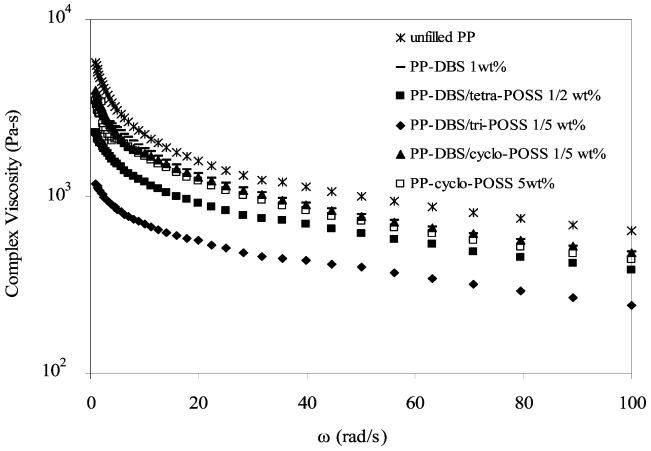


Figure 5. Complex viscosity, $|\eta^*|$, of iPP/DBS/POSS melt mixed compounds at 200 °C. The strain was 2%.

the compound of 5 wt % tri-POSS. However, the viscosity reduction in the case of iPP/DBS/cyclo-POSS compound was not much compared to the iPP/DBS compound. A liquid complex was not formed in DBS/cyclo-POSS mixture at 200 °C. In addition, despite compatibility between iPP and cyclo-POSS, the viscosity reduction in compound containing 5 wt % cyclo-POSS was not as great as those with iPP/DBS/tri-POSS and iPP/DBS/tetra-POSS compounds. For example, at ω = 40 rad/s, the values of $|\eta^*|$ were respectively 1135 Pa s for unfilled PP, 830 Pa.s for iPP/5 wt % cyclo-POSS, and 432 Pa s for iPP/DBS/tri-POSS (1/5 wt %). The data presented in Figure 5 also confirmed the shear-thinning behavior of iPP/DBS/POSS compounds.

Crystallinity of iPP Compounds. The thermal properties of the compounds crystallized under quiescent conditions were examined by DSC and the percent crystallinity was calculated (Figure 6). The iPP/DBS compound showed higher

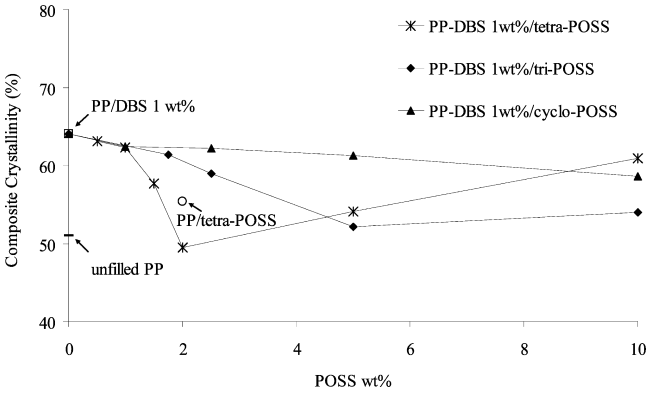


Figure 6. Trend of crystallinity with POSS content in iPP compounds containing 1 wt % DBS. The lines are used to guide the eye.

crystallinity than iPP due to increased nucleation efficiency in the presence of DBS fibrils. In the presence of silanol−POSS, the nucleation efficiency of DBS was reduced. In corroboration with the rheology data reported earlier,[31] the optimum combinations, i.e., 2 wt % tetra-POSS or 5 wt % tri-POSS in conjunction with 1 wt % DBS in iPP produced the lowest crystallinity. In these cases, the nucleating function of DBS was "arrested" due to participation of DBS in DBS/silanol−POSS complex formation.

dx.doi.org/10.1021/ma202783p | Macromolecules 2012, 45, 2420−2433

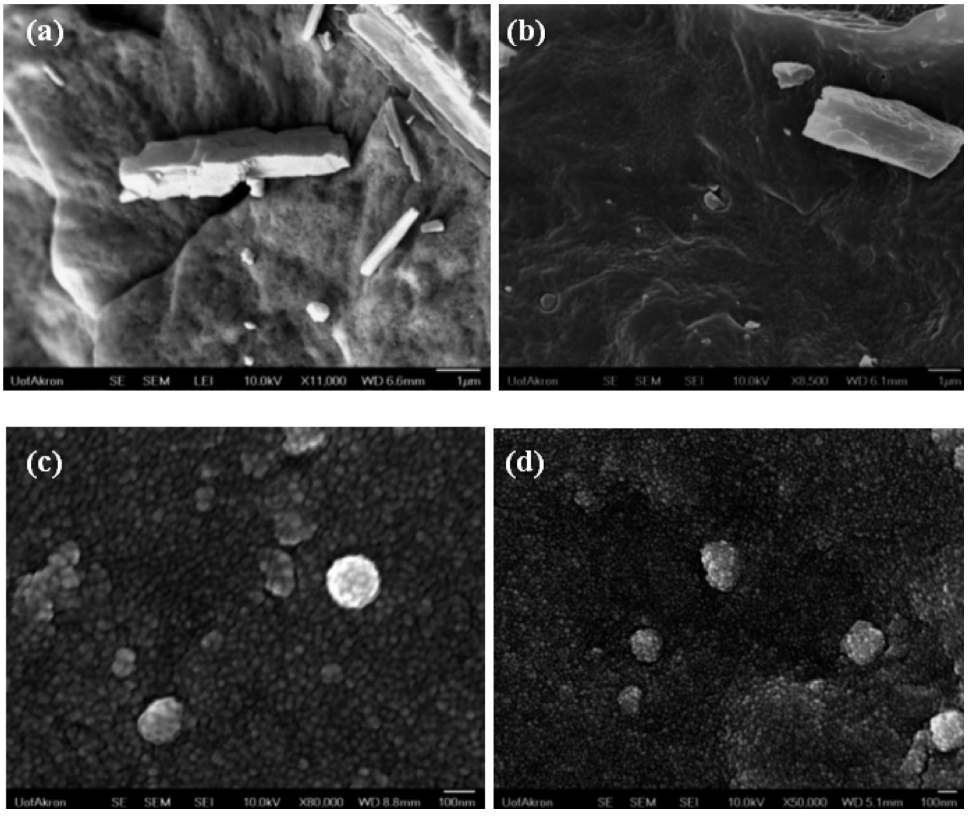


Figure 7. SEM images of POSS particles in melt-mixed iPP compounds (a–c) and spun fibers (d). Key: (a) melt mixed, tetra-POSS; (b) melt mixed, tri-POSS; (c) melt mixed, cyclo-POSS; (d) spun fiber at DDR 2500 of iPP/cyclo-POSS (5 wt %) compound.

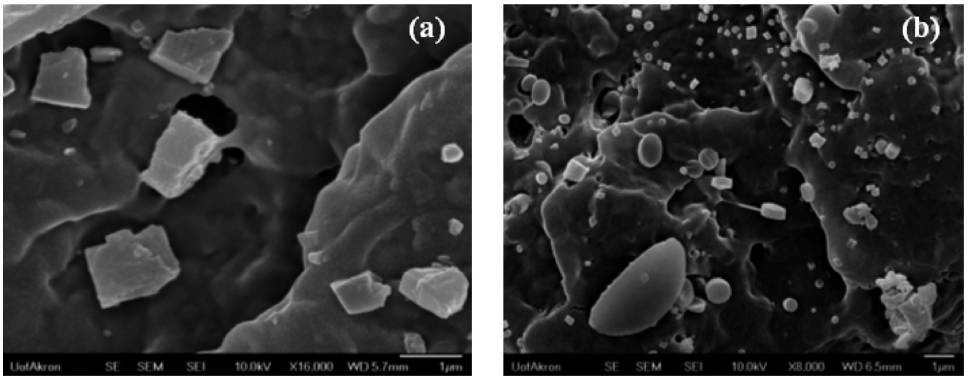


Figure 8. SEM images of POSS particles in iPP/POSS spun fiber at their maximum DDR: (a) iPP/tetra-POSS (2 wt %) compound spun fiber at DDR 1700; (b) iPP/tri-POSS (5 wt %) compound spun fiber at DDR 506.

It is noted in Figure 6 that at silanol–POSS content lower than the optimum, some DBS molecules did not participate in complex formation and gave rise to nucleation of iPP crystals, leading to higher crystallinity than at the optimum concentration but lower than the compound with no POSS. In the case of compounds of tetra-POSS, the crystallinity increased with the increase of POSS content beyond the optimum value. This can be attributed possibly to the marginal nucleation ability of tetra-POSS molecules and the formation of separate tetra-POSS domains. For example, crystallinity of iPP/2 wt % tetra-POSS compound was found 8% higher than unfilled iPP in line with earlier studies on nucleating abilities of POSS molecules.[34]

As reported earlier,[31] cyclo-POSS had insufficient interactions with DBS, which is also reflected in very small changes in crystallinity with increasing POSS content. It should be noted that DBS/tetra-POS did not form any liquid complex at 1:5 w/w ratio of DBS and tetra-POSS. Thus, the additional tetra-POSS molecules may have self-organized themselves instead of with DBS beyond a loading of 1:2 w/w ratio of DBS and tetra-POSS respectively.

Morphology of Assembled Particles of POSS in iPP Melt-Mixed Compounds and Spun Fibers. We evaluated the quality of dispersion of silanol–POSS in iPP and consequently evaluated how the synergistic interactions of DBS and silanol–POSS aided POSS particle morphology development in melt-mixed compounds and spun fibers. First, the morphology of silanol–POSS particles in iPP compounds prepared in batch mixer by melt-mixing method was examined by SEM. As seen in Figure 7, parts a and b, respectively, tetra-

dx.doi.org/10.1021/ma202783p | *Macromolecules* 2012, 45, 2420–2433

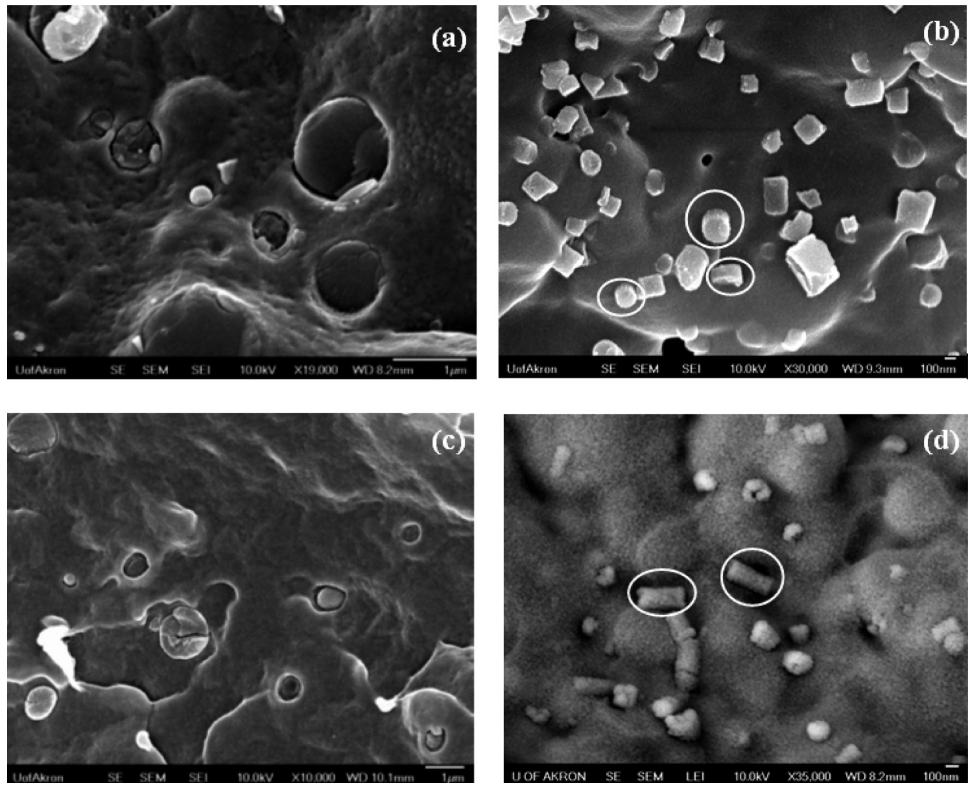


Figure 9. Morphology of iPP compounds taken by high-resolution SEM for (a) melt mixed DBS/tri-POSS (1/5 w/w), (b) spun fiber of DBS/tri-POSS (1/5 w/w) at DDR 800, (c) melt mixed DBS/tetra-POSS (1/2 w/w), and (d) spun fiber of DBS/tetra-POSS (1/2 w/w) at DDR 3673.

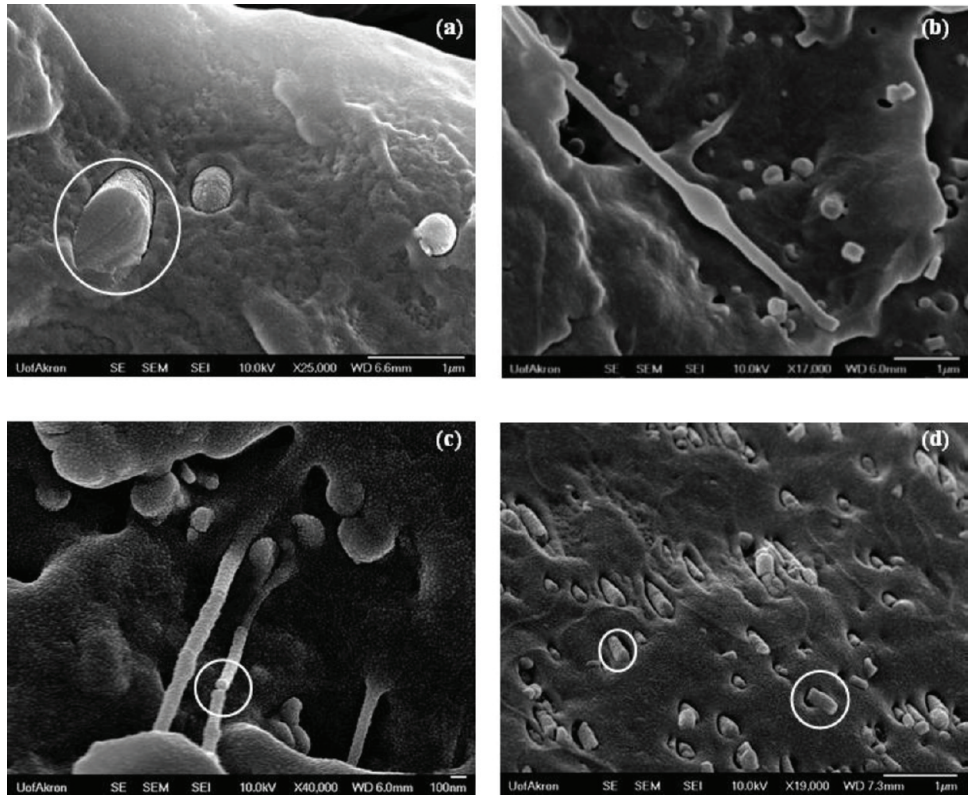


Figure 10. Morphology evolution of POSS particles in iPP/DBS/tri-POSS compounds taken by high resolution SEM (a) spun fiber at DDR 11, (b, c) spun fiber at DDR 460, and (d) spun fiber at DDR 2500.

POSS and tri-POSS formed micrometer size aggregates due to incompatibility with iPP. On the other hand, cyclo-POSS dispersed well in iPP and formed uniform spherical particles of 100 nm in diameter (Figure 7c). The amounts of tetra-POSS

dx.doi.org/10.1021/ma202783p | *Macromolecules* 2012, 45, 2420−2433

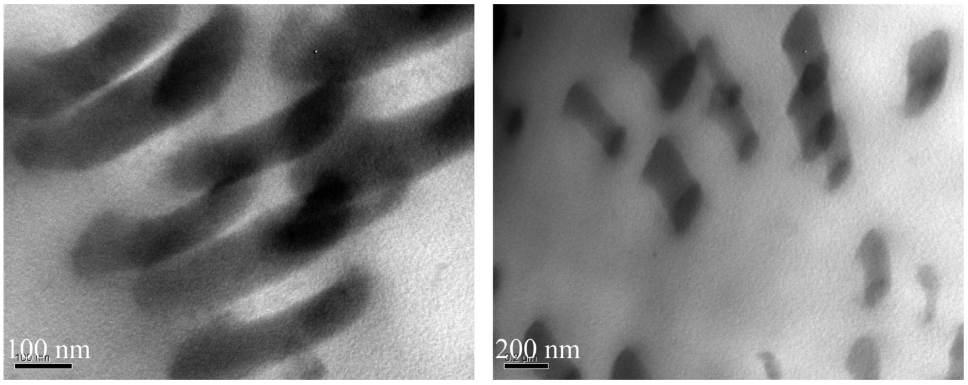


Figure 11. Two representative TEM images of POSS nanoparticles in iPP/DBS/tri-POSS spun fiber at DDR 1700.

and tri-POSS were kept at respectively 2 and 5 wt % in view of the optimum quantities needed for molecular complex formation with DBS as reported earlier.[31] The amount of cyclo-POSS was kept at 5 wt %, which was found to offer similar performance in spun fiber properties.

The morphology of POSS particles in melt spun fibers of iPP/POSS compounds were also inspected by SEM. As seen in Figure 7d, cyclo-POSS retained its spherical particles of 100 nm size even in fibers drawn to a DDR of 2500. The dispersed particles did not deform during fiber spinning operation as they remained as solid aggregates.

The compounds with small amounts (2 wt %) of tetra-POSS could be drawn at high DDR. However, the POSS particle aggregates on the fractured fiber surface showed random size distribution from 200 nm to 1.5 μm as seen in Figure 8a. Similar observations were made in the case of tri-POSS as in Figure 8b. The particles on the fractured surfaces of the fibers showed random distribution of size from 200 nm to 4 μm.

The presence of DBS changed the morphology of POSS particles in melt-mixed compounds of iPP/DBS/tri-POSS and iPP/DBS/tetra-POSS as seen in Figure 9, parts a and c—the particles were of spherical shape with the size ranging from 250 nm to 1.5 μm. On the other hand, in spun fibers, at a high DDR value, the domains of POSS particles were found to be cylindrical with close to 100 nm in diameter and 200−350 nm in length (see Figure 9, parts b and d). This became clearly apparent in the case of tetra-POSS compounds, as in Figure 9d at its maximum DDR of 3673.

A comparison of the images presented in Figure 9−11 raised a number of questions. First, what led to the formation of cylindrical particles in spun fibers of compounds of iPP, DBS, and tri-POSS or tetra-POSS, when melt-mixed compounds exhibited spherical particles? Second, what caused size reduction of the particles in spun fibers of these compounds? We resorted to low viscosity of silanol−POSS/DBS complex reported in Figure 3 for deriving possible interpretation of the particle morphology.

The complex formed between DBS and silanol−POSS were low viscosity liquids at 200 °C, the temperature of the fiber spinning die. It is conceivable that these liquids formed droplets in iPP and stretched into cylindrical shapes in uniaxial extensional flow during fiber spinning. Recall in this case that the apparent shear rate in the capillary die was approximately 1 s^{-1}. The SEM images of the fractured surface are presented in Figure 10. A reflection into Figure 10a indicates that the tri-POSS/DBS domains deformed into cylindrical shape with typical diameter of 500 nm even at DDR of 11. This poses another relevant question about the possibility of liquid droplet formation by silanol−POSS/DBS molecular adduct, while a reduction of shear viscosity presented in Figure 5 alludes to some degree of solubility of either DBS or silanol−POSS or their complex in iPP melt.

It was expected that the liquid complex of DBS and phenyl substituted silanol−POSS would have some degree of solubility in iPP melt. The rationales for such expectation are presented as follows. First, nuclear magnetic resonance (NMR) data showed that DBS did not form covalent bonds with silanol−POSS.[31] Second, the melt-mixed compounds of iPP/DBS/tri-POSS and iPP/DBS/tetra-POSS showed homogeneous states at 220 °C (Figure 2c). In addition, a slope of 2.0 was observed in log−log plots of storage modulus (G') vs loss modulus (G'') at temperatures at or above 180 °C.[30] These indicate solubility of tri-POSS/DBS and tetra-POSS/DBS complex in iPP. Third, greater reduction of shear viscosity in Figure 5 for iPP/DBS/tri-POSS and iPP/DBS/tetra-POSS compounds compared to iPP/DBS compound could only be explained if the assumption of solubility of DBS/POSS complex in iPP is invoked. Therefore, any free DBS molecules and its complex with tri-POSS and tetra-POSS would remain soluble in iPP melt, thus causing a reduction of viscosity. We now turn our attention to the existence of cylindrical and spherical droplet-type morphology of POSS seen in Figure 9a,c and Figure 10a. We make another assumption here that as the temperature of the melt-mixed compounds was lowered, the DBS/POSS complex lost solubility in iPP and phase separated into liquid droplets. This, however, could not be verified in the current study using optical means due to interference by polymer crystallization. The assumption of phase separation and droplet formation by DBS/POSS complex during cooling of the melt compounds invoked above only aids the flow of arguments in the rest of the paper and does not alter the results presented.

The extent of stretching of liquid droplets of DBS/POSS complex as a function of DDR was evaluated. An increase in DDR to 460 led to extensive elongation of DBS/POSS complex liquid (Figure 10, parts b and c). A liquid cylinder is seen frozen in Figure 10b while undergoing capillary instability and shows a length of at least 7 μm and diameter of approximately 200 nm. Some other frozen cylinders did not show capillary instability, e.g., the two cylinders in Figure 10c with diameter approximately 100 nm. It should be noted here that the T_g of the complex liquid was ∼130 °C,[31] which is above the crystallization temperature of iPP, ∼120 °C. Thus, the liquid continued to deform during fiber spinning until the temperature of the fiber reached the onset of glass transition of the

dx.doi.org/10.1021/ma202783p | *Macromolecules* 2012, 45, 2420−2433

POSS/DBS complex, at which time the complex solidified and took the final shape of the particles.

At a DDR of 2500, the fractured surface of the fibers did not reveal the presence of long cylindrical particles of DBS/POSS complex. Instead, only short cylinders of diameter 100 nm are seen. These short cylinders on the fractured surface may have been generated during the fracture of fiber specimen or were inherently present in the fibers. The sharp edges of circular surfaces of some of the cylinders in Figure 9b,d and in Figure 10c,d shown in circles may indicate that some of these particles possibly underwent brittle fracture during the cold fracture of the fibers before taking SEM images. However, a set of TEM images taken of fiber specimens microtomed at an angle with the fiber axis and presented in Figure 11 show the presence of short cylinders of diameter close to 100 nm and length of 200–300 nm, thus corroborating that these particles were created either by capillary breakup or by fracture during fiber spinning.

On the basis of the experimental characterization, a simplistic model can now be developed to describe how the POSS/DBS complex droplets deformed in iPP compounds during fiber spinning (Figure 12). The POSS/DBS liquid complex

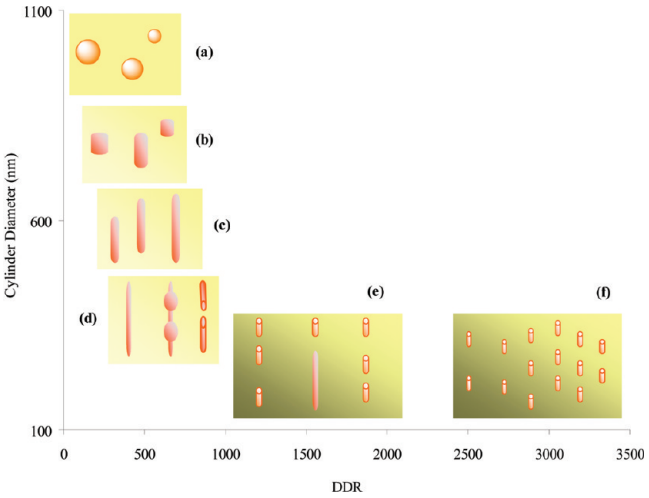


Figure 12. Schematic of morphology evolution of DBS/POSS liquid complex into nanoparticles with increasing DDR from part a to part f of iPP compound fibers (not drawn to scale).

deformed into short cylinders at low DDR and froze to take a final shape as the fiber temperature went below the glass transition temperature of the complex (Figure 12b), e.g., 130 °C for 1/2 w/w mixture of DBS/tetra-POSS. Note that iPP crystallization occurred at about 120 °C. At higher DDR, the POSS/DBS complex deformed into longer cylinders of much smaller diameter (Figure 12, parts c and d). Some of these cylinders experienced capillary instability (Figure 12d) and gave birth to droplets of much smaller diameter (Figure 12, parts e and f). Some other long stretched cylinders retained their shape and size (Figure 12e) due to freezing of the fibers, crystallization of iPP, or due to cooling of the POSS/DBS complex to below its glass transition temperature.

Characterization of Spun Fibers. The investigation began with several questions. First, why the fibers containing POSS/DBS together could be spun to much higher DDR compared to iPP/DBS or iPP/POSS systems. Second, if the tensile properties of fibers would have any relationship with POSS content or the tensile properties would be entirely governed by the iPP chains oriented at higher values of DDR. Third, if crystallinity of iPP was at all influenced by the POSS/DBS complex. Fourth, if the solid particles of POSS/DBS complex had any influence on tensile modulus, tensile strength, or yield strength. Fifth, if cyclo-POSS would be more suitable for iPP spun fibers than compounds with tri-POSS/DBS or tetra-POSS/DBS. Note that cyclo-POSS dispersed to nanoscale in melt-mixed compounds of iPP (Figure 7c), but remained as crystalline, spherical domains in spun fibers and did not cause much reduction of polymer compound viscosity.

The maximum DDR at which the stable spun fiber was produced from the composites are presented in Table 1. The

Table 1. Maximum DDR and Minimum Diameter of Spun Fibers[a]

component	DBS/POSS wt %	maximum DDR	diameter (μm)
iPP	–	840	69 ± 4
iPP-DBS	1/0	1322	55 ± 4
iPP-DBS/tetra-POSS	1/2	3673	33 ± 2
iPP-tetra-POSS	0/2	1700	49 ± 4
iPP-DBS/tri-POSS	1/5	2500	40 ± 2
iPP-tri-POSS	0/5	505	89 ± 2
iPP-DBS/cyclo-POSS	1/5	1322	55 ± 3
iPP-cyclo-POSS	0/5	2500	40 ± 3

[a]The values of standard deviation of fiber diameters are also shown.

fibers could not be continuously produced beyond the maximum draw down ratio due to intermittent spinning or fiber breakage. The maximum DDR of iPP/DBS compound was found to be higher than that of iPP.[48] In the presence of DBS, iPP crystallized at ~140 °C as a result of nucleation of iPP crystals thus providing higher melt strength to the fiber.[27] The compounds of iPP with tetra-POSS and cyclo-POSS without DBS also showed higher DDR, e.g., 1700 with 2 wt % tetra-POSS. This can be attributed to the nucleation function of tetra-POSS crystals in iPP (Figure 6), thus providing higher melt strength to the fiber. A large value of DDR in case of iPP/cyclo-POSS compound will be discussed later separately.

We now turn our attention to compounds containing both DBS and silanol–POSS. The presence of 2 wt % tetra-POSS in the iPP/DBS/tetra-POSS (1/2 w/w) compound helped increase the maximum value of DDR to 3673 from 1322 (Table 1). A reflection into complex viscosity vs temperature data presented in Figure 5 yields two possible reasons for such increase in draw ratio. First, tetra-POSS/DBS complex subdued DBS fibrillation, which delayed crystallization of iPP to ~120 °C. As a result, the compound remained much more fluid (i.e., with lower viscosity, Figure 5) and could be drawn more easily. Second, the lower viscosity of the compound allowed more polymer chains to orient. For example, the values of $|\eta^*|$ of iPP, iPP/DBS (1 wt %), and iPP/DBS/tetra-POSS (1/2 w/w) as $\omega \rightarrow 0$ were 5684, 3798, and 2291 Pa s respectively (Figure 5). As a result of the greatly reduced viscosity, the iPP/DBS/tetra-POSS compounds were in effect equivalent to an iPP grade with much higher melt index. It is known that fiber spinning grades of iPP usually have a melt flow index of 10–40.[49] One may wonder about the role of tetra-POSS/DBS complex in this regard. Recall that the T_g of the amorphous DBS/tetra-POSS (1/2 w/w) complex was 130 °C. Thus, the DBS/tetra-POSS complex was in liquid form at the exit of the die, where majority of the draw occurred. Accordingly, we do not have any evidence

dx.doi.org/10.1021/ma202783p | Macromolecules 2012, 45, 2420–2433

Table 2. Tensile Properties of Spun Fibers of iPP and Its Compounds at Respective Maximum DDR

component	DBS/POSS wt %	tensile modulus (MPa)	tensile strength (MPa)	yield strength (MPa)	elongation at break (%)
iPP	-	2196 ± 309	125 ± 16	51 ± 7	694 ± 48
iPP-DBS	1/0	2794 ± 781	166 ± 33	71 ± 15	673 ± 42
p value[a]		0.02	0.002	0.001	0.02
iPP-DBS/tetra-POSS	1/2	3545 ± 384	188 ± 24	109 ± 15	552 ± 62
p value		<0.001	<0.001	<0.001	<0.001
iPP-tetra-POSS	0/2	2923 ± 567	156 ± 25	71 ± 15	548 ± 64
p value		0.001	0.001	0.001	<0.001
iPP-DBS/tri-POSS	1/5	3993 ± 476	189 ± 26	103 ± 11	606 ± 80
p value		<0.001	<0.001	<0.001	0.02
iPP-tri-POSS	0/5	2324 ± 164	105 ± 15	47 ± 8	606 ± 91
p value		0.07	0.001	0.07	0.02
iPP-DBS/cyclo-POSS	1/5	2883 ± 247	155 ± 13	71 ± 7	670 ± 59
p value		<0.001	<0.001	<0.001	0.2
iPP-cyclo-POSS	0/5	3523 ± 510	199 ± 23	105 ± 16	608 ± 69
p value		<0.001	<0.001	<0.001	0.004

[a]Statistical significance was obtained from one-sided, two-sample unequal variance *t* test performed in Microsoft Excel for each compound in comparison to iPP and indicated by their corresponding p values.

that the complex aided fiber drawing, except that it caused a large reduction of the viscosity and lowered the crystallization temperature of iPP to 120 °C.

The maximum DDR was high ~2500 for iPP/cyclo-POSS (5 wt %) compounds. This was due to compatibility of cyclo-POSS with iPP. Also these molecules acted as lubricant[47,50] due to their almost spheroidal shape (Figure 7c). Table 1 reports the minimum fiber diameter corresponding to maximum values of DDR for each material. It is seen that the smallest diameter fibers (~33 μm) were possible for the compound iPP/DBS/tetra-POSS (1/2 w/w), which is a 52% reduction compared to fibers of iPP and 40% reduction compared to fibers of iPP/DBS compounds. The fiber diameter of iPP/cyclo-POSS (5 wt %) and iPP/DBS/tri-POSS (1/5 w/w) compounds were 40 μm.

The tensile properties of the fibers spun at maximum DDR are presented in Table 2. The trend is similar to what was observed for maximum DDR. It is evident that the tensile properties reported in Table 2 are statistically different in view of the probability (*p*) values smaller than 0.05. The compounds containing 1 wt % DBS and 2 wt % of tetra-POSS or 5 wt % of tri-POSS offered 60−80% increase in tensile modulus, 50−60% increase in tensile strength, and 100% increase in yield strength compared to unfilled iPP, and 30−40% increase in tensile modulus, 15% increase in tensile strength, and 40−50% increase in yield strength compared to iPP-DBS compound. These increases are significant considering that the compounds contained only 2 wt % tetra-POSS and 5 wt % tri-POSS. Similar increase in tensile properties was also found for fibers of a compound of iPP with 5 wt % cyclo-POSS.

However, it is evident that improvements in mechanical reinforcement of fibers at lower values of DDR were not much. In this context, we also evaluated the tensile properties of injection molded bars of the compounds at the same POSS content and found almost no improvement in comparison to iPP. Tensile bars were prepared using DSM mini-injection molder at a mean shear rate of injection of approximately 1 s^{-1}. Therefore, we infer that POSS particles at up to 5 wt % did not cause an increase of any of the tensile properties of injection molded bars.

The tensile properties of fibers of various compounds spun at the same or at very close values of DDR showed insensitivity to the composition and the types of POSS used. This was expected as only small quantities (≤5 wt %) of POSS were used in such compounds. This and the data from injection molding indicate that small quantities of nanoparticles of POSS in blends with iPP did not contribute much to the improvement of mechanical properties of bulk compound materials.[51−54] Instead, the molecular chain orientation promoted by the presence of POSS particles possibly contributed toward the improvement. This will be examined using WAXD data in the following section.

Crystallinity and Orientation of iPP Spun Fiber. The crystallinity and orientation of polymer chains in melt spun fibers of iPP and compounds of iPP with DBS and with DBS/POSS drawn at different DDR were analyzed by DSC and WAXD. The crystallinity of iPP in melt-spun fibers drawn at different DDR evaluated by DSC is plotted in Figure 13, parts a and b. The iPP crystallinity showed a monotonous increase until DDR of 480 and then showed a reduction at DDR of 840. This behavior is similar to what was previously reported for high tacticity iPP.[55] The iPP/DBS compound with 1 wt % DBS showed the same trend although higher initial crystallinity was observed due to nucleation of iPP crystals initiated by DBS.

The initial crystallinity of compounds of iPP/DBS/tetra-POSS and iPP/DBS/tri-POSS is close to that of iPP. In these cases, DBS did not function as a nucleating agent as its fibrillation was subdued due to interactions with tri-POSS and tetra-POSS molecules.[30] The fiber crystallinity of these compounds first increased significantly up to a DDR ~ 450 (e.g., 72% compared to 55%). However, the crystallinity dropped at DDR ~800. Subsequently, only small increase was observed up to DDR of ~2500−3500. This unusual trend is even more pronounced for iPP/DBS/tri-POSS 1/5 w/w compound. The increase of fiber crystallinity with DDR to well above the values for nucleated compound of iPP and DBS can be attributed to polymer chain orientation. The decrease in crystallinity of fibers from DDR of 460 to DDR of 600 in the case of iPP/DBS/tri-POSS (1/5 w/w) can be explained on the basis of polymer chain orientation presented later. This behavior is identical to the data reported for low-tactic iPP drawn at different DDR.[55]

In this work, the introduction of amorphous complex of DBS and tri-POSS or DBS and tetra-POSS decreased the overall crystallinity of the high tactic iPP in the melt mixed compounds

dx.doi.org/10.1021/ma202783p | Macromolecules 2012, 45, 2420−2433

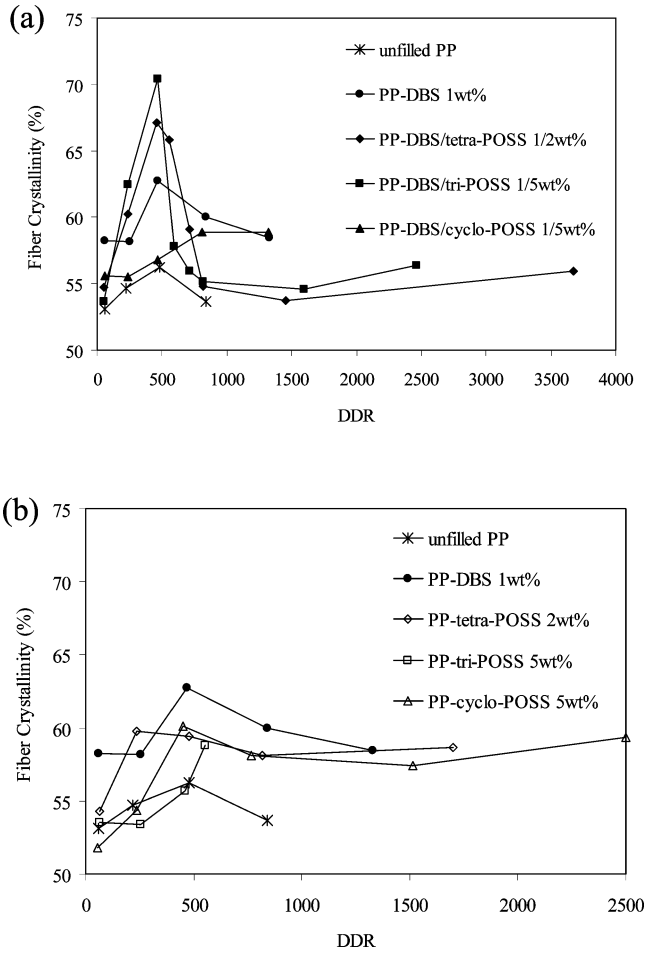


Figure 13. Crystallinity of iPP in fibers as a function of draw ratio (a) Influence of DBS and POSS mixtures. (b) Influence of POSS. The lines are used to guide the eye.

as was seen in Figure 6. Thus, the system effectively behaved in similar fashion to a lesser crystalline, low tactic iPP. In the case of iPP/DBS/cyclo-POSS compounds, the values of crystallinity gradually increased with DDR and remained constant. In this case, amorphous complex of DBS and cyclo-POSS was not formed in compound of iPP/DBS/cyclo-POSS; although some interaction was evident from the lower values of initial crystallinity. Note that both DBS and cyclo-POSS are compatible with iPP. Similar behavior was identified for iPP-cyclo-POSS compound as presented in Figure 13b.

On the other hand, crystallinity of spun fibers of compounds of incompatible tri-POSS and tetra-POSS alone followed the trend similar to iPP. However, these compounds showed higher crystallinity than iPP and lower crystallinity than iPP/DBS compound, confirming that these POSS molecules had marginal nucleation effects as reported by other researchers.[34]

The two-dimensional (2D) WAXD patterns presented in Figure 14 depict how the orientation of polymer chains developed in semicrystalline iPP fibers as a function of draw ratio. The bright arc patterns are attributed to crystalline structures of the fibers with diffraction peaks typical to α-form iPP crystals having the (110), (040), (130), and (111) equatorial planes from the inner to outer circles respectively, which gave the strongest diffraction intensity.[42,43,56−59]

At low DDR, as in Figure 14a(i), the WAXD patterns of all compounds showed weak arc image. This indicates that the

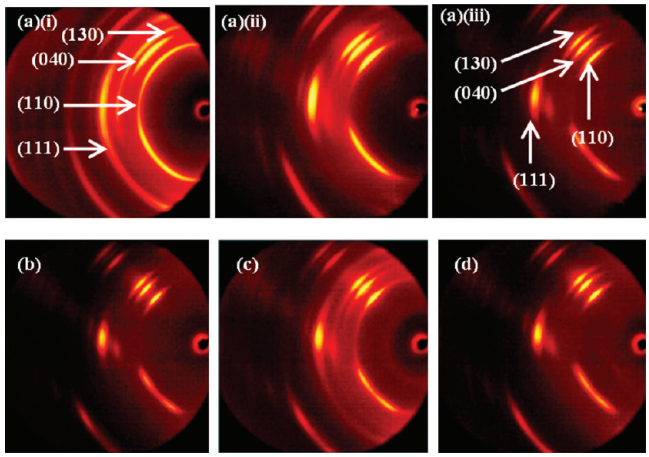


Figure 14. WAXD film pattern (fiber axis vertical) for the melt-spun fibers, (a) (i−iii) unfilled iPP-DDR 60, 480, 840; (b) iPP-DBS/tetra-POSS 1/2 wt %, DDR 3673; (c) iPP-DBS/tri-POSS 1/5 wt %, DDR 2500; (d) iPP-cyclo-POSS 5 wt %, DDR 2500.

chains were not oriented yet, thus no difference appeared in WAXD patterns from the crystal planes.[60] It is also inferred from these images that the chain structure was randomly distributed at low DDR, thus no significant peaks were observed. The azimuthal spreads of the diffraction peaks became narrower at higher values of DDR, as seen for DDR ~450 in Figure 14a(iii). The planes of the crystals became gradually localized, implying improved orientation in the crystalline region.

At low DDR, the orientation of iPP (040) reflection was much higher than (110) and (130). However, at high DDR, the reflection plane had the same orientation, implying that during fiber spinning, these planes developed differently. The orientation factor was calculated taking into account (040) and (110) planes.[56−58] Above a certain DDR, the changes in WAXD pattern was not apparent as in Figure 14, parts a(iii) and b−d; a majority of the iPP chains were already oriented and no significant change in orientation patterns was identified. A reduction of the width of bright arc with increase in DDR as seen in Figure 14c,d indicates more orientation.[42,56,57,61] Our system is, however, more complex, as the domains of DBS/tri-POSS and DBS/tetra-POSS amorphous complex were present admixed in the crystalline domains of iPP.

The orientation functions were quantitatively determined for the a', b, and c-axes of the monoclinic iPP crystals, which shows the variations of the orientation functions for each chain axis with change of DDR for fibers of iPP and its compounds. As seen in Figure 15a, for unfilled iPP, f_c increased abruptly at DDR of 60 and then gradually increased with the increase of draw-down ratio. The c-axis, i.e., the molecular chain axis becomes gradually aligned with the fiber axis with fiber drawing. Consequently, the orientation function of the c-crystallographic axis with respect to fiber axis, i.e., f_c, increases with increasing DDR. The negative value of f_b at all draw-down ratios can be attributed to the orientation of the crystallographic b-axis in the perpendicular direction of the fiber axis. It is consistent with the previous findings on the behavior of f_b and f_c with drawing of fibers.[60]

A similar behavior was observed for spun fibers of compounds of iPP-DBS/tri-POSS as seen in Figure 15b. The orientation function f_c increased up to DDR 460 similar to the increase in crystallinity in Figure 13a, decreased with further

dx.doi.org/10.1021/ma202783p | Macromolecules 2012, 45, 2420−2433

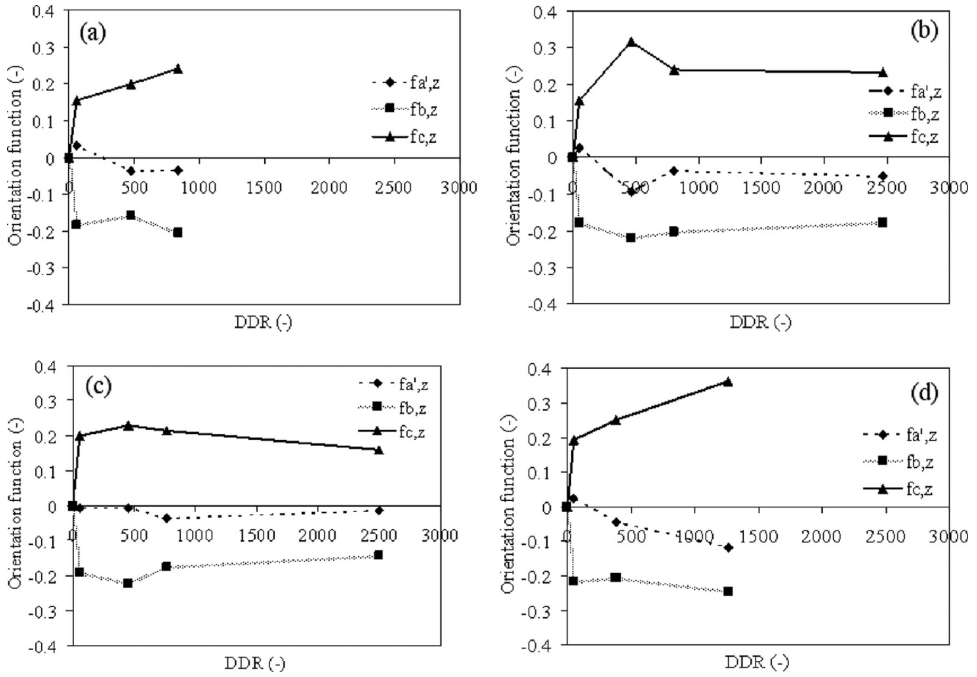


Figure 15. Orientation functions of melt-spun fibers at various DDR: (a) unfilled iPP, (b) iPP-DBS/tri-POSS 1/5 w/w, (c) iPP/cyclo-POSS 5 wt %, and (d) iPP/DBS 1 wt % compound. The lines are used to guide the eye.

increase in DDR, and then remained constant. A striking observation is that the chain axis orientation factor decreased at higher DDR, while there is an increase in the a'-axis orientation factor.

The unusual behavior in crystallinity and orientation phenomenon can now be explained by the bimodal orientation behavior of iPP where both the c- and a'-axis oriented groups can coexist. Thus, the lower viscosity and lower crystallization temperature of iPP/DBS/tri-POSS or iPP/DBS/tetra-POSS compounds possibly led to intense epitaxial lamellar branching[62] and at higher DDR generated more rigid spherulites[63] as identified from higher stiffness and strength, but lower elongation at break[64,65] of the corresponding fibers.

As seen in Figure 15b, the a'-axis oriented groups decreased at intermediate DDR and then increased again with increasing DDR. Along with monoclinic α-crystalline form, the coexistence of hexagonal β-form crystals were found prominent for such behavior.[55] The plot of crystalline planes along the 2θ axis showed the evidence of β-form crystals as presented in Figure 16. The reflection characteristics of the iPP β modification[66−68] of lower intensities can be observed at 2θ values of 16 and 21°. These are associated with the (300) and (301) planes, respectively. Additional reflections with similar intensity of iPP at 2θ = 14, 17, 18, and 22° correspond respectively to (110), (040), (130), and (111) planes of the α-form. A shift in the peak corresponding to (110) plane of the α-form was noted for all compounds containing POSS. The peak location shifted by 0.35° in 2θ scale in Figure 16. This changed the values of orientation factors reported in this paper only in the third decimal place. Similar shifts have been observed in WAXD of filled compounds of iPP.[68]

The orientation function f_c of fibers of compound iPP-DBS/tetra-POSS 1/2 w/w also increased up to DDR 461 and then decreased with further increase in DDR similar to compound iPP-DBS/tri-POSS 1/5 w/w (not shown in Figure 15). On the contrary, cyclo-POSS in iPP having uniform 100 nm circular

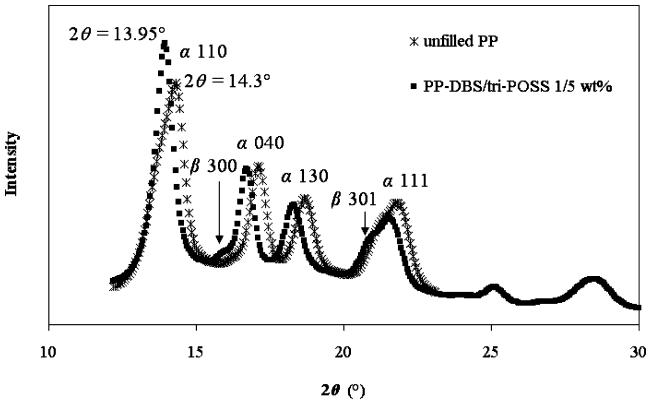


Figure 16. Intensity vs 2θ as obtained by integrating WAXD patterns of spun fibers.

domains (Figure 7, parts c and d) acted as a lubricant for iPP chains[50] and consequently, iPP/cyclo-POSS compounds could be drawn to high DDR. With increasing DDR, a gradual decrease in f_c was observed as presented in Figure 15c, which was compensated by the increase in f_a', possibly due to chain relaxation at higher DDR. DBS/tetra-POSS formed amorphous complexes similar to DBS/tri-POSS, thus these compounds behaved similarly to low tactic iPP system.[55] The iPP-DBS system as shown in Figure 15d showed a continuous increase of f_c with increasing DDR until no stable fibers were possible. This can be explained in view of formation of oriented nanofibrils of DBS during melt spinning of fibers.[69]

CONCLUSIONS

This study investigated how the molecular adducts of sorbitol and silanol−POSS influenced fiber spinning and the properties of spun fibers of compounds of iPP. The following conclusions can be made from the study. First, the sorbitol−POSS molecular adducts, being low viscosity liquids at the fiber

dx.doi.org/10.1021/ma202783p | Macromolecules 2012, 45, 2420−2433

spinning temperature, helped dramatically reduce the viscosity of their compounds with iPP. This was attributed to solubility of these adducts in iPP melt. The reduced viscosity of compounds allowed spinning of fibers to much higher draw ratio. Consequently, fibers of much smaller diameter were obtained in this study than achievable from the grade of iPP used. Second, the molecular adducts turned into cylindrical, solid nanoparticles upon cooling of the fibers. The cylindrical shape and diameter of approximately 100 nm indicated their genesis from stretching and break up from larger size precursor liquid drops found in melt-mixed compounds. Third, from comparison of tensile properties data at low draw ratio and of injection molded tensile bars we infer that the large enhancements in tensile properties observed at high draw ratio resulted mostly from polymer chain orientation and not from the presence of small quantities of POSS particles. The finer fibers and the trends of crystallinity and orientation with draw ratio were found similar to low tactic iPP and were attributed to amorphous counterpart induced by DBS/POSS combinations.

AUTHOR INFORMATION

Corresponding Author

*E-mail: janas@uakron.edu. Telephone: (330) 972-8293. Fax: (330) 972-3406.

Notes

The authors declare no competing financial interest.

ACKNOWLEDGMENTS

The authors thank National Science Foundation for providing financial support through Grant No. CMMI-0727231 and Hybrid Plastics for partnership and FHR Plastics and Milliken Chemicals for assistance with the materials. S.C.J. acknowledges Dr. David A. Schiraldi of Case Western Reserve University for introducing him to POSS and for numerous discussions on the subject. Special thanks to Dr. Rong Bai from The Department of Polymer Engineering, for her guidance in several analytical characterizations, Dr. Soumyajit Sarkar, formerly in The Department of Polymer Engineering, and Dr. Bojie Wang and Sarang P. Bhawalkar from The Department of Polymer Science, The University of Akron, for their guidance and feedback regarding morphology characterization. The author also acknowledges Dr. Ujjwal Das, from The University of Massachusetts Amherst, for his guidance in statistical analysis.

REFERENCES

(1) Phillips, S. H.; Haddad, T. S.; Tomczak, S. J. *Curr. Opin. Solid State Mater. Sci.* **2004**, *8*, 21−29.
(2) Fina, A.; Tabuani, D.; Frache, A.; Camino, G. *Polymer* **2005**, *46*, 7855−7866.
(3) Fu, B. X.; Yang, L.; Somani, R. H.; Zong, S. X.; Hsiao, B. S.; Phillips, S.; Blanski, R.; Ruth, P. *J. Polym. Sci., Part B: Polym. Phys.* **2001**, *39*, 2727−2739.
(4) Fu, B. X.; Gelfer, M. Y.; Hsiao, B. S.; Phillips, S.; Viers, B.; Blanski, R.; Ruth, P. *Polymer* **2003**, *44*, 1499−1506.
(5) Huang, J.-C.; He, C.-B.; Xiao, Y.; Mya, K. Y.; Dai, J.; Siow, Y. P. *Polymer* **2003**, *44*, 4491−4499.
(6) Jeon, H. G.; Mather, P. T.; Haddad, T. S. *Polym. Int.* **2000**, *49*, 453−457.
(7) Lee, Y.-J.; Kuo, S.-W.; Huang, W.-J.; Lee, H.-Y.; Chang, F.-C. *J. Polym. Sci., Part B: Polym. Phys.* **2004**, *42*, 1127−1136.
(8) Leu, C.-M.; Chang, Y.-T.; Wei, K.-H. *Macromolecules* **2003**, *36*, 9122−9127.
(9) Mantz, R. A.; Jones, P. F.; Chaffee, K. P.; Lichtenhan, J. D.; Gilman, J. W.; Ismail, I. M. K.; Burmeister, M. J. *Chem. Mater.* **1996**, *8*, 1250−1259.
(10) Misra, R.; Fu, B. X.; Morgan, S. E. *J. Polym. Sci., Part B: Polym. Phys.* **2007**, *45*, 2441−2455.
(11) Pracella, M.; Chionna, D.; Fina, A.; Tabuani, D.; Frache, A.; Camino, G. *Macromol. Symp.* **2006**, *234*, 59−67.
(12) Xu, H.; Kuo, S.-W.; Lee, J.-S.; Chang, F.-C. *Polymer* **2002**, *43*, 5117−5124.
(13) Yoon, K. H.; Polk, M. B.; Park, J. H.; Min, B. G.; Schiraldi, D. A. *Polym. Int.* **2005**, *54*, 47−53.
(14) Zeng, J.; Kumar, S.; Iyer, S.; Schiraldi, D. A.; Gonzalez, R. I. *High Perform. Polym.* **2005**, *17*, 403−424.
(15) Wu, J.; Haddad, T. S.; Kim, G.-M.; Mather, P. T. *Macromolecules* **2007**, *40*, 544−554.
(16) Zhao, Y.; Schiraldi, D. A. *Polymer* **2005**, *46*, 11640−11647.
(17) Zheng, L.; Farris, R. J.; Coughlin, E. B. *Macromolecules* **2001**, *34*, 8034−8039.
(18) Zheng, L.; Hong, S.; Cardoen, G.; Burgaz, E.; Gido, S. P.; Coughlin, E. B. *Macromolecules* **2004**, *37*, 8606−8611.
(19) Fasce, D. P.; Williams, R. J. J.; Mechin, F.; Pascault, J. P.; Llauro, M. F.; Petiaud, R. *Macromolecules* **1999**, *32*, 4757−4763.
(20) Sellinger, A.; Laine, R. M. *Macromolecules* **1996**, *29*, 2327−2330.
(21) Wu, J.; Mather, P. T. *Polym. Rev. (Philadelphia, PA)* **2009**, *49*, 25−63.
(22) Lin, O. H.; Mohd. Ishak, Z. A.; Akil, H. M. *Mater. Des.* **2009**, *30*, 748−751.
(23) Baldi, F.; Bignotti, F.; Fina, A.; Tabuani, D.; Ricco, T. *J. Appl. Polym. Sci.* **2007**, *105*, 935−943.
(24) Kuo, S.-W.; Lin, H.-C.; Huang, W.-J.; Huang, C.-F.; Chang, F.-C. *J. Polym. Sci., Part B: Polym. Phys.* **2005**, *44*, 673−686.
(25) Song, L.; He, Q.; Hu, Y.; Chen, H.; Liu, L. *Polym. Degrad. Stab.* **2008**, 627−639.
(26) Jana, S. C.; Jain, S. *Polymer* **2001**, *42*, 6897−6905.
(27) Lee, B.-J. Dissertation, University of Akron: 2009.
(28) Lee, B.-J.; Jana, S. C. *Annu. Tech. Conf.—Soc. Plast. Eng.* **2008**, 177−181.
(29) Lee, B.-J.; Roy, S.; Jana, S. C. *Annu. Tech. Conf.—Soc. Plast. Eng.* **2009**, 126−130.
(30) Perilla, J. E.; Lee, B.-J.; Jana, S. C. *J. Rheol.* **2010**, *54*, 761−779.
(31) Roy, S.; Scionti, V.; Jana, S. C.; Wesdemiotis, C.; Pischera, A. M.; Espe, M. P. *Macromolecules* **2011**, *44*, 8064−8079.
(32) Chen, J.-H.; Chiou, Y.-D. *J. Polym. Sci., Part B: Polym. Phys.* **2006**, *44*, 2122−2134.
(33) Chen, J.-H.; Yao, B.-X.; Su, W.-B.; Yang, Y.-B. *Polymer* **2007**, *48*, 1756−1769.
(34) Fu, B. X.; Yang, L.; Somani, R. H.; Zong, S. X.; Hsiao, B. S.; Phillips, S.; Blanski, R.; Ruth, P. *J. Polym. Sci., Part B: Polym. Phys.* **2001**, *39*, 2727−2739.
(35) Zhou, Z.; Cui, L.; Zhang, Y.; Zhang, Y.; Yin, N. *J. Polym. Sci., Part B: Polym. Phys.* **2008**, *46*, 1762−1772.
(36) Brandrup, J, I. E. *Polymer Handbook*, 3rd ed.; John Wiley and Sons: New York, 1989.
(37) Stein, R. S. *J. Polym. Sci.* **1958**, *31*, 327−334.
(38) Alexander, L. E. *X-Ray Diifraction Methods in Polymer Science*, 1st ed.; John Wiley & Sons Inc: New York, 1969.
(39) Wilchinsky, Z. W. *J. Appl. Phys.* **1960**, *31*, 1969−1972.
(40) Nadella, H. P.; Henson, H. M.; Spruiell, J. E.; White, J. L. *J. Appl. Polym. Sci.* **1977**, *21*, 3003−3022.
(41) Afshari, M.; Kotek, R.; Gupta, B. S.; Kish, M. H.; Dast, H. N. *J. Appl. Polym. Sci.* **2005**, *97*, 532−544.
(42) Wilchinsky, Z. W. *J. Appl. Phys.* **1959**, *30*, 792−803.
(43) Wilchinsky, Z. W. *Advances in X-ray Analysis*; Plenum Press: New York, 1963; Vol. 6.
(44) Arvidson, S. A.; Khan, S. A.; Gorga, R. E. *Macromolecules (Washington, DC)* **2010**, *43*, 2916−2924.
(45) Thierry, A.; Fillon, B.; Straupe, C.; Lotz, B.; Wittmann, J. C. *Prog. Colloid Polym. Sci.* **1992**, *87*, 28−31.

(46) Lee, B. J.; Roy, S.; Jana, S. C. *AIChE Annu. Meet., Conf. Proc.* **2010**, a121/121−a121/125.
(47) Nusser, K.; Schneider, G. J.; Pyckhout-Hintzen, W.; Richter, D. *Macromolecules* **2011**, *44*, 7820−7830.
(48) Cowan, M. E.; Morin, B. G. (Milliken & Company, USA). High-speed spinning procedures for manufacture of high-denier polypropylene fibers and yarns. Application: US, 2004; p 7, Spartanburg, SC.
(49) Ministry of Science & Technology, Department of Scientific & Industrial Research; Polypropylene fibre/filament yarn. Vol. 2011; http://www.dsir.gov.in/reports/techreps/tsr043.pdf (access date: 02/20/2012).
(50) Butola, B. S.; Joshi, M.; Kumar, S. *Fibers Polym.* **2010**, *11*, 1137−1145.
(51) Choi, J.; Harcup, J.; Yee, A. F.; Zhu, Q.; Laine, R. M. *J. Am. Chem. Soc.* **2001**, *123*, 11420−11430.
(52) Pan, G.; Mark, J. E.; Schaefer, D. W. *J. Polym. Sci., Part B: Polym. Phys.* **2003**, *41*, 3314−3323.
(53) Li, G. Z.; Wang, L.; Toghiani, H.; Daulton, T. L.; Koyama, K.; Pittman, C. U. Jr. *Macromolecules* **2001**, *34*, 8686−8693.
(54) Strachota, A.; Kroutilova, I.; Kovarova, J.; Matejka, L. *Macromolecules* **2004**, *37*, 9457−9464.
(55) Choi, D.; White, J. L. *Polym. Eng. Sci.* **2004**, *44*, 210−222.
(56) Ran, S.; Burger, C.; Sics, I.; Yoon, K.; Fang, D.; Kim, K.; Avila-Orta, C.; Keum, J.; Chu, B.; Hsiao, B. S.; Cookson, D.; Shultz, D.; Lee, M.; Viccaro, J.; Ohta, Y. *Colloid Polym. Sci.* **2004**, *282*, 802−809.
(57) El-Dessouky, H. M.; Mahmoudi, M. R.; Lawrence, C. A.; Lewis, E. L. V.; Voice, A. M.; Ward, I. M. *Polym. Eng. Sci.* **2010**, *50*, 200−208.
(58) Bhattacharyya, A. R.; Sreekumar, T. V.; Liu, T.; Kumar, S.; Ericson, L. M.; Hauge, R. H.; Smalley, R. E. *Polymer* **2003**, *44*, 2373−2377.
(59) Wang, Y.; Na, B.; Fu, Q.; Men, Y. *Polymer* **2004**, *45*, 207−215.
(60) Spruiell, J. E.; White, J. L. *Polym. Eng. Sci.* **1975**, *15*, 660−667.
(61) Kolb, R.; Seifert, S.; Stribeck, N.; Zachmann, H. G. *Polymer* **2000**, *41*, 1497−1505.
(62) White, J. L.; Choi, D. D. *Polyolefins: Processing, Structure Development, and Properties*; Hanser Gardner Publications: Cincinnati, OH, 2005.
(63) Tordjeman, P.; Robert, C.; Gerard, P.; Belfort-Montbéliard, U. d. t. d., Ed.; materiaux: Montbéliard, 2002; Vol. *2001*.
(64) Stern, C. Dissertation, University of Twente: Enschede, The Netherlands, 2005.
(65) Schrauwen, B. A. G.; van Breemen, L. C. A.; Spoelstra, A. B.; Govaert, L. E.; Peters, G. W. M.; Meijer, H. E. H. *Macromolecules* **2004**, *37*, 8618−8633.
(66) Romankiewicz, A.; Sterzynski, T.; Brostow, W. *Polym. Int.* **2004**, *53*, 2086−2091.
(67) Marco, C.; Gomez, M. A.; Ellis, G.; Arribas, J. M. *J. Appl. Polym. Sci.* **2002**, *86*, 531−539.
(68) Yu, Y.; White, J. L. *Polym. Eng. Sci.* **2001**, *41*, 1292−1298.
(69) Lipp, J.; Shuster, M.; Feldman, G.; Cohen, Y. *Macromolecules* **2008**, *41*, 136−140.

Macromolecules

Article

pubs.acs.org/Macromolecules

Study of the Chemical Environment inside Free Volume Holes in Halogenated Styrene Polymers Using Positron Annihilation Spectroscopy

Renwu Zhang,* Jessica Robles, and Jiwoong Kang

Department of Chemistry and Biochemistry, California State University, San Bernardino, 5500 University Parkway, San Bernardino, California 92407, United States

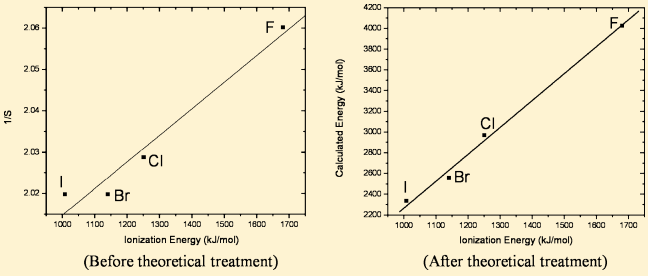
Hussein Samha

Department of Physical Science, Southern Utah University, Cedar City, Utah 84720, United States

H. M. Chen and Y. C. Jean

Department of Chemistry, University of Missouri—Kansas City, Kansas City, Missouri 64110, United States

ABSTRACT: In this paper, a systematic study is provided of the chemical environment inside free volume holes in a series of halogenated polystyrenes (*p*-position), $-[CH_2CH C_6H_5X]_n-$ (X = F, Cl, Br, I), by using positron annihilation spectroscopy. In such polymers it was determined that the chemical environment is the major effect on Doppler broadening of two 511 keV γ photons from positron−electron annihilation. Doppler broadening energy spectroscopy (DBES) and positron annihilation lifetime spectroscopy (PALS) were combined in a novel approach to study the chemical environment in a polymer system. A highly linear relationship between Doppler broadenings caused by electron kinetic energies of valence electrons and the ionization potentials of halogen elements was obtained, as well as a similar correlation with the results from *ab initio* molecular orbital (MO) calculations for monohalogenobenzenes, C_6H_5X (X = F, Cl, Br, I). The results demonstrate that the combination of DBES and PALS may provide an effective way to study the chemical environment inside free volume holes in polymers.



(Before theoretical treatment) (After theoretical treatment)

1. INTRODUCTION

Positron annihilation spectroscopy has been demonstrated to be very successful in studying the size of free volume holes at the atomic scale in polymers.[1] It is well-known that in polymeric materials, free volume is a very basic property important to many applications such as gas separation, small molecular permeation, polymer aging, filler level, blend miscibility and such.[2−5] In addition to its size, the chemical environment inside free volume holes is also an important factor in applications such as gas adsorption/absorption, hydrogen storage, polymer degradation, etc., since small molecules are trapped in free volume holes.[6−9]

There are several techniques that can be used to obtain chemical information about polymers, such as NMR, FTIR, Raman, X-ray, mass spectroscopy (MS), gas chromatography (GC), and elemental analysis techniques.[10,11] But none of these can directly detect the chemical environment of the free volume holes, which has significant effect on various applications. Fortunately positron annihilation spectroscopy can detect annihilation behavior of positron and positronium localized in those holes and provides a way to study the chemical environment in free volume holes. However, due to the technical difficulties and sample complexities, very limited work has been done so far. In this study, we demonstrate that the combination of two major positron annihilation techniques, Doppler broadening energy spectroscopy (DBES) and positron annihilation lifetime spectroscopy (PALS), provides an effective tool in the quantitative study of the chemical environment in halogenated styrene polymers.

DBES is the measurement of the average energy shift from 511 keV of two γ photons generated by the annihilation of an electron−positron pair. The technique has been extensively employed in investigating the responses of samples subjected to different physical conditions such as thermal and mechanical treatments.[12,13] Additional information related to the different chemical entities (different elements) in metal oxides

Received: January 2, 2012
Revised: February 9, 2012
Published: February 27, 2012

 © 2012 American Chemical Society dx.doi.org/10.1021/ma300007p | *Macromolecules* 2012, 45, 2434−2441

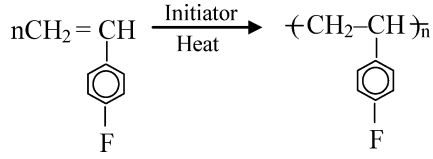
and semiconductors was also obtained from DBES spectra by utilizing two-detector coincidence.[14,15] In defect-free metals or semiconductors, the Doppler energy broadening caused by the annihilation of positrons with high momentum core electrons of atoms is relatively large. Therefore, the far high energy side of a DBES spectrum was employed to identify different elements in samples after a significant reduction of background noise by two-detector coincidence. A good correlation between the shift in high energy observed in DBES spectra and the atomic energy levels for Fe, Co, Ni, Cu, and Zn is obtained.[16] For materials with well-ordered crystal structures, a small amount of defects such as impurities and dopants may cause a variation of Doppler shifting. On the basis of this, DBES has been used to detect the impurities and doping elements in metals and semiconductors.[17,18] In polymers, it appears that the situation is more complex with amorphous polymer structures. Nevertheless, most polymers are mainly composed of carbon and hydrogen with other additives such as oxygen, halogens, sulfur, and nitrogen chemically bonded to each polymer unit. So the relative content of these chemical additives is high and therefore it is possible to apply the DBES technique to study the chemical environments in polymers.

Recently, scientists have intensively studied the chemical effects on positronium formation, but have focused less on the effects on positron/positronium annihilation in polymeric materials. Dlubek et al.[19] started an investigation of the chemical effects on positron and positronium annihilation using Doppler broadening and lifetime spectroscopy separately. Ito et al.[20] applied the positron annihilation technique to detect the early stages of polyethylene degradation, in which they concluded that the oxygen generated in the process caused a change in the energy shift of the DBES spectra. Similar work has been carried out by several other groups as well. Ito et al.[21] studied polyimides with different structures and chemical groups and suggested that the positronium formation is affected not only by the free volume hole size, but also by the electron affinity of polymers. Baranowski et al. studied chlorostyrene polymers and found that the introduction of chlorine into styrene polymers greatly reduced the intensity of positronium, and the extent of this effect depends on the position of chlorine on the benzene ring.[22] Dlubek et al.[23] compared several polymers with different chemical components and suggested that the Doppler energy broadening in DBES spectra is related to the relative content of additive elements in hydrocarbons. Kobayashi et al.[24] suggested that positrons can be trapped by polar groups in polymers. Nagai et al.[25] further demonstrated that free positrons in polyethylene/ethylene vinyl copolymer blends are likely to be trapped by acetate groups and are annihilated with oxygen elements. However, there is no systematic study of the correlations that may exist between chemical additives in polymers and Doppler broadening energy spectra. There may be two reasons for this. First, unlike in metal oxides or semiconductors with very neat crystal structures, there are many amorphous domains in polymers. This makes it difficult to normalize the chemically modified polymers (e.g., $-CH_2CCl_2-$) to the virgin samples (e.g., $-CH_2CH_2-$) as performed for metal oxides (e.g., SiO_2 to pure Si). Second, the annihilation of positron and positronium with valence electrons is proposed by some authors to be relatively large because they are trapped in free volume holes.[16] Therefore, the signal to background ratio of the high momentum component of the DBES spectra corresponding to annihilation with core electrons is very low, and hence, it presents some technical difficulties for studying the chemical environment using the same method.

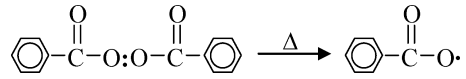
In this study, we investigated the chemical environment in polymers from a different approach. Instead of studying the chemical environment by investigating the high momentum annihilation with core electrons, we took advantage of the fact that most positrons (free or in positroniums) are annihilated with valence electrons inside free volume holes. We analyzed the low momentum component of DBES spectra. The major challenge is the Doppler energy broadening caused by *p*-Ps intrinsic annihilation disguises the chemical effects on *o*-Ps and free e^+ pick-off annihilation. By developing a simple model, we successfully excluded such interferences and extracted Doppler broadening of 511 keV γ photons solely induced by the kinetic energy of incoming annihilating electrons. As a result, we obtained an excellent correlation between such energy broadening and the ionization energies of halogen elements.

2. EXPERIMENTAL SECTION

Para-halogenated polystyrenes were chosen as a system to study on the basis of two considerations. First, styrene polymers are totally amorphous. This will eliminate the interference of polymer crystallinity on positron annihilation. Second, all substituted halogens (F−, Cl−, Br−, and I−) are from the same group in the periodic table. Thus, they all share the same electronic configuration but different energies of valence electrons. Therefore, this system is a good candidate for exploring the validation of this method in the detection of chemical environments in polymers. All samples except for poly(4-fluorostyrene) were purchased from Polytech (Maryland Height, MD). Poly(4-fluorostyrene) was not commercially available and was synthesized in our laboratory through the free radical polymerization of 4-fluorostyrene as described previously:[26]



The initiator was benzoyl peroxide (BPO) and free radicals were generated through heating:



The BPO initiator (Acros, 85%) was purified by recrystallization in chloroform and methanol (25:75 v/v) at 20 °C. The crystallized BPO was then dissolved in styrene (Aldrich, 99%) to make 0.3 mol % BPO solution. The solution was then sparged with N_2 gas in a glovebox to remove oxygen. A few drops of BPO were added to the 10 mL of liquid 4-fluorostyrene (Aldrich, 99%) inside the glovebox and the reaction cell was sealed promptly. An oil bath was used to heat the reaction system and the temperature was set to a constant 80 °C. An electronic stirrer was used to ensure the reaction remained homogeneous. After 12 h, the white product was exposed to a vacuum of 10^{-3} Torr to remove small residual molecules. According to the authors, poly(4 − fluorostyrene) with $M_n = 5.27 \times 10^4$ to 8.63×10^4 and pdi = 1.47−2.86 should be obtained.[26]

Two identical pellets of each polymer were prepared by compressing powder samples using mechanical loads. The sample size was 1 cm in diameter and 0.2 cm in thickness. A Na-22 positron source with approximate intensity of 20 μCi was sandwiched between two identical samples and the whole package was wrapped with Al foil. DBES and PALS were measured under ambient conditions (1 atm and room temperature) at the University of Missouri—Kansas City. The description of the experimental setup can be found elsewhere.[27] The *S* parameters (*S*) and lifetime data (lifetime τ_3 and intensity I_3) along with the calculated free volume hole radii are listed in Table 1.

dx.doi.org/10.1021/ma300007p | Macromolecules 2012, 45, 2434−2441

Table 1. DBES and PALS Data and the Calculated Hole Sizes for Halogenated Styrene Polymers

element	S	τ_3 (ns)	I_3 (%)	R (Å)
fluorine	0.4854 ± 0.0014	2.3417 ± 0.0155	24.7 ± 0.2	3.15 ± 0.01
chlorine	0.4929 ± 0.0014	2.0730 ± 0.0201	15.5 ± 0.2	2.92 ± 0.01
bromine	0.4951 ± 0.0014	2.0313 ± 0.0282	9.8 ± 0.2	2.88 ± 0.02
iodine	0.4951 ± 0.0014	1.9932 ± 0.0429	5.7 ± 0.2	2.85 ± 0.03

3. RESULTS AND DISCUSSIONS

3.1. DBES and PALS Measurements for Halogenated Styrene Polymers. Unlike in metals or semiconductors, when emitted into polymers a fraction of positrons form hydrogen-like atoms, positronium (Ps), by capturing ionized electrons in materials. There are two states of positronium, *ortho*-positronium (*o*-Ps), in which both the positron and electron have the same spin direction and *para*-positronium (*p*-Ps), in which the positron and electron have antispin states. Theoretically, 1/4 of Ps will be *p*-Ps and 3/4 will be *o*-Ps due to spin degeneracy. In polymers, both free positrons and Ps quickly diffuse into free volume holes and are trapped there due to the low potential inside. Eventually, both free positrons and *o*-Ps will be annihilated by electrons on the inside wall of holes via a pick-off process, but *p*-Ps will experience an intrinsic self-annihilation process. Both pick-off and intrinsic annihilation give off two γ photons with energies centered at 511 keV. The deviation of energy from 511 keV is caused by the Doppler effect and is characterized by the S parameter, which is defined as the ratio of central part (511 ± 1.59 keV) over the total counts in the DBES spectra, as shown in Figure 1.

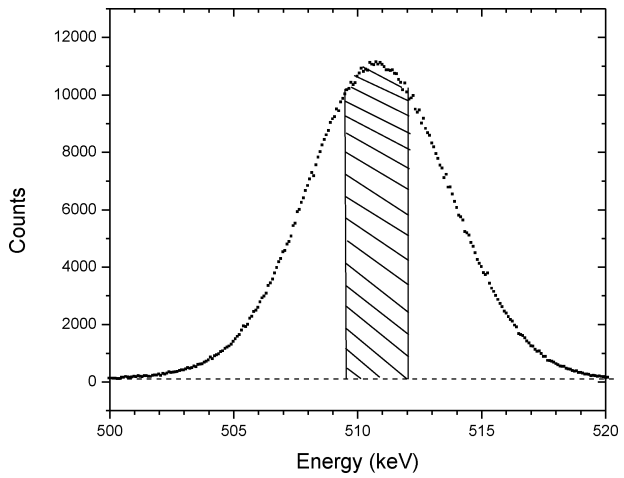


Figure 1. Typical Doppler broadening energy spectrum (DBES).

The lifetime of positrons and Ps can be measured by PALS and can be well resolved into three parts representing the lifetime of *p*-Ps, free e^+, and *o*-Ps. Even though DBES spectra cannot be resolved into three components as PALS due to the poor energy resolution of the Ge detector, the S parameter in DBES can be modeled as a sum of the same three parts as that determined in lifetime measurements (*p*-Ps, free e^+, and *o*-Ps). The *p*-Ps undergoes intrinsic annihilation and the corresponding Doppler broadening is governed by the uncertainty principle. Free e^+ and *o*-Ps will annihilate with the surrounding electrons and their Doppler broadening is caused by the large kinetic energies of electrons in atoms. Because of the very narrow energy deviation from 511 keV, most γ photons emitted from *p*-Ps intrinsic annihilation are counted as the center part in a DBES spectrum. Therefore, the amount of positronium (1/4 is *p*-Ps) formed in materials greatly affects the S parameter in the DBES technique in addition to the kinetic energies of incoming annihilating electrons from surrounding atoms.

Figure 2 shows the *S* parameter of the individual halogenated polystyrenes. It was found that the *S* parameter increased

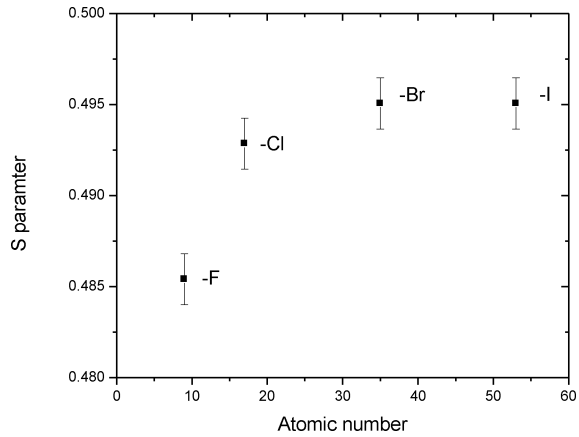


Figure 2. *S* parameter of different halogenated styrene polymers.

significantly from the fluorine- to the bromine-containing polymer. However, the *S* parameter did not increase further for the iodine-containing polymer. As discussed above, the *S* parameter is determined mainly by two factors, the kinetic energy of surrounding electrons (affecting e^+s and *o*-Ps) and the amount of positronium formed (affecting *p*-Ps). On the basis of the spur model, the mechanism of positronium formed in polymeric materials is very complex. It depends on many physical and chemical factors such as the chemical reactivity, recombination rate of ionized electrons and parent ions, spur size, diffusion length of thermolized positrons and ionized electrons, hole size and so on. This means that the chemical environment could affect the *S* parameter via the formation of positronium as well. Therefore, in order to differentiate the factors that determine the *S* parameter in those halogenated styrene polymers, the lifetime measurement was also performed in which the intensity of positronium can be resolved. Figure 3 shows the lifetime and the intensity of the selected halogenated styrene polymers.

As illustrated in Figure 3, both the lifetime and the intensity of *o*-Ps have opposite trends from that of the *S* parameter. The chemical quenching of *o*-Ps in polymers is very small based on previous studies.[24,27] Kobayashi's work shows that the lifetime of *o*-Ps has no obvious change when different ratios of ethyl vinyl acetate copolymers (E/VA) are introduced into polyethylene samples. It is demonstrated that vinyl polymers with similar structures, but different chemical components, exhibit very similar *o*-Ps lifetime; while those with similar chemical components, but different structures, display a large change in *o*-Ps lifetimes.

dx.doi.org/10.1021/ma300007p | Macromolecules 2012, 45, 2434−2441

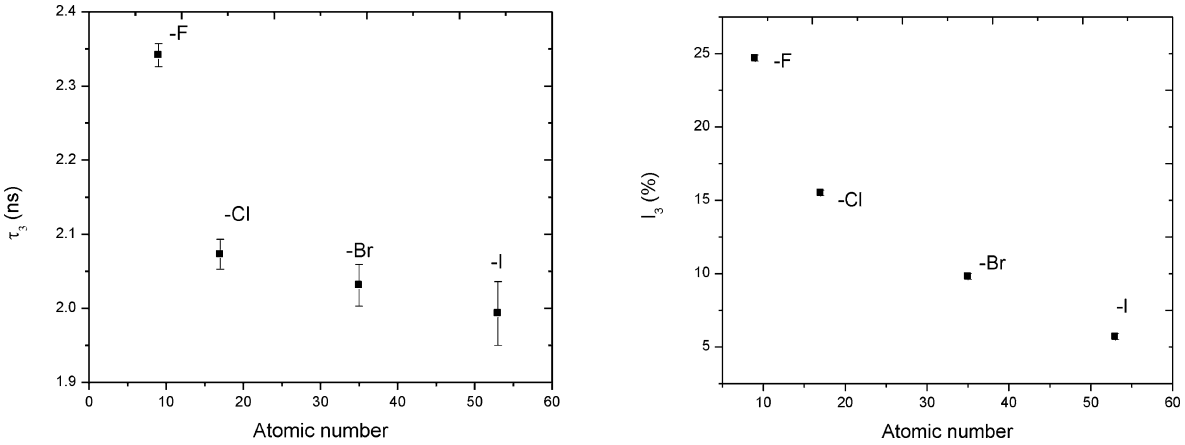


Figure 3. *o*-Ps lifetimes and intensities of halogenated styrene polymers.

This clearly demonstrates the validity of a relation between *o*-Ps lifetime and free volume hole size, as shown in eq 1

$$\tau_3 = 0.5\ \text{ns}\left(1 - \frac{r}{r + 1.656} + \frac{1}{2\pi}\sin\left(\frac{2\pi r}{r + 1.656}\right)\right)^{-1} \quad (1)$$

where τ_3 is the *o*-Ps lifetime in ns, and r is the free volume hole size in Å.

On the other hand, formation of positronium (Ps) is affected by both chemical environment and physical structure. It is expected that chemical environment such as ionization energy of molecules, competition between an ionized electron with a positron and with the parent ion, etc., affects the ability of a positron to bind with an ionized electron and hence affect the positronium formation. Since positroniums can only reside in free volume holes, the total free volume also affects the positron formation. This was verified by PALS measurements on polyethylene (PE) samples having different crystallinities. In this experiment, the relative amount of positronium formed (I_3) is significantly affected by the crystallinity (physical structure) even though the chemical environment is the same (only C and H atoms in PE molecules)[27]

The change of free volume hole size indeed has minor effect on the *S* parameter. The larger free volume hole indicates the larger uncertainty in space for *p*-Ps being trapped. According to the uncertainty principle, the larger uncertainty in the *p*-Ps localization will lead to a smaller momentum uncertainty of the *p*-Ps, and hence the Doppler energy broadening of photon energy arising from *p*-Ps intrinsic annihilation is decreased. However, due to the poor energy resolution of the Ge detector (~1.3 keV) used in Doppler broadening measurements, the energy range in defining the S parameter (±1.59 keV) is much wider than the Doppler shifting caused by the uncertainty principle in *p*-Ps intrinsic annihilation. Thus, most γ photons from *p*-Ps intrinsic annihilation will fall into the center part of DBES spectra whether *p*-Ps particles are localized in a small hole or a large hole. This is more clearly observed in one-dimensional (1D) and two-dimensional (2D) angular correlation of annihilation radiation (ACAR) with much better resolution.[28] On the other hand, since all γ photons from *p*-Ps intrinsic annihilation fall into the center part of DBES spectrum, the intensity of *p*-Ps contributes significantly to the center part of a spectrum and affects the S parameter greatly. Therefore, the S parameter positively follows the trend of the *o*-Ps intensity rather than the *o*-Ps lifetime (related to hole size), as demonstrated by several groups and illustrated in Figure 4.[21,27,29]

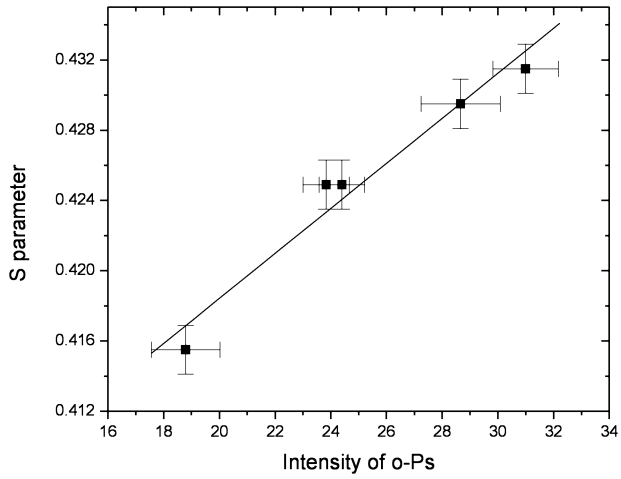


Figure 4. Correlation between the S parameter and intensity of *o*-Ps intensity in polyethylene (PE).[27]

In this experiment, however, the result is very different. As Figure 5 indicates, the *S* parameter has a negative correlation

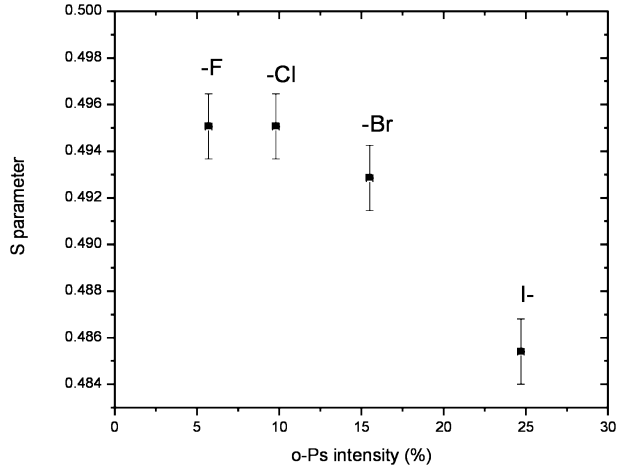


Figure 5. Correlation between the *S* parameter and *o*-Ps intensity.

with I_3 (*S* decreases as I_3 increases). Therefore, in this series of polymers, the *S* parameter appears to be mostly affected by the

dx.doi.org/10.1021/ma300007p | *Macromolecules* 2012, 45, 2434−2441

chemical environment through the kinetic energy of the incoming annihilating electrons rather than through the amount of positronium formed.

Even though the positronium formation is not a major factor, its effect on the S parameter could be significant. Data in Figure 3 seem to demonstrate that I_3 has a very large variation in proceeding from F- to I-containing polymers (decreasing from 25% to 6%). As stated above, there are two major factors in the determination of the S parameter: the amount of Ps formed and the kinetic energies of the incoming annihilating electrons. In order to extract more information on energy broadening caused by the latter factor, we need to exclude the contribution from the p-Ps intrinsic annihilation. In the following section, we develop a simple model to achieve this approach.

3.2. Theoretical Approach to Extract Doppler Broadening Induced by Halogens. It was suggested that a deconvoluted Doppler broadening energy spectrum could be expressed as the sum of three Gaussian terms[19]

$$F(E) = I_1 \times \frac{1}{\sqrt{2\pi}\sigma_1} \times e^{-(E-E_0)^2/2{\sigma_1}^2} + I_2 \times \frac{1}{\sqrt{2\pi}\sigma_2} \times e^{-(E-E_0)^2/2{\sigma_2}^2} + I_3 \times \frac{1}{\sqrt{2\pi}\sigma_3} \times e^{-(E-E_0)^2/2{\sigma_3}^2} \quad (2)$$

where I_1, I_2 and I_3 are the relative intensities of p-Ps, e^+, and o-Ps, respectively. The value of E_0 is 511 keV from 2γ annihilation, and the sum $I_1 + I_2 + I_3 = 1$. σ_1, σ_2, and σ_3 are the standard deviations of the individual distributions, which are related to the full width at half-maximum (fwhm) by the equation

$$\text{fwhm}_i = 2\sqrt{2 \ln 2}\,\sigma_i \quad (i = 1, 2, 3)$$

Convoluting the above $F(E)$ function with a resolution function generates the real DBES spectrum, as

$$D(E) = F(E) \otimes R(E) \quad (3)$$

where $D(E)$ is the DBES spectrum and $R(E)$ is the resolution function of the instrument.

The resolution function $R(E)$ of the DBES instrument is a Gaussian function as well with fwhm around 1.5 keV and standard deviation of 0.637 keV based on fwhm = $2(2 \ln 2)^{1/2}\sigma$, that is

$$R(E) = \frac{1}{\sqrt{2\pi} \times 0.637\ \text{keV}} \times e^{-(E-E_0)^2/2\times(0.637\ \text{keV})^2}$$

As a result, the DBES spectrum by eq 3 is still a Gaussian function with an increase of width, as shown in eq 4:

$$D(E) = I_1 \times \frac{1}{\sqrt{2\pi} \times \sqrt{{\sigma_1}^2 + (0.637\ \text{keV})^2}} \times e^{-(E-E_0)^2/2({\sigma_1}^2+(0.637\ \text{keV})^2)} + I_2 \times \frac{1}{\sqrt{2\pi} \times \sqrt{{\sigma_2}^2 + (0.637\ \text{keV})^2}} \times e^{-(E-E_0)^2/2({\sigma_2}^2+(0.637\ \text{keV})^2)} + I_3 \times \frac{1}{\sqrt{2\pi} \times \sqrt{{\sigma_3}^2 + (0.637\ \text{keV})^2}} \times e^{-(E-E_0)^2/2({\sigma_3}^2+(0.637\ \text{keV})^2)} \quad (4)$$

By definition, the S parameter is the ratio of the counts in the central area over the total counts in a DBES spectrum. Therefore, it can be expressed with the integral of eq 4, which is

$$S = \int_{E_0-\Delta E}^{E_0+\Delta E} D(E)\,dE \quad (5)$$

where the ΔE is selected arbitrarily. In practice, however, ΔE is chosen as the point with the highest sensitivity, for example, in our experiment, ΔE = 3.18 keV

The above integral is tedious, and it has no analytical solution. As an approximation, we replace eq 5 with a simpler one, $S \approx D_{\text{avg}}(E)\Delta E$. In our experiment, $\Delta E = 2 \times 1.59$ keV = 3.18 keV. The average value $D_{\text{avg}}(E)$ is taken around 95% of peak value $D(E_0)$ based on our measurements on a standard Si crystal. Therefore, under such condition, the peak value of DBES spectrum, $D(E_0)$, is calculated as

$$D(E_0) = s/(3.18 \times 95\%)$$

On the other hand, from eq 4, the peak value is:

$$D(E_0) = \frac{I_1}{\sqrt{2\pi} \times \sqrt{{\sigma_1}^2 + (0.637)^2}} + \frac{I_2}{\sqrt{2\pi} \times \sqrt{{\sigma_2}^2 + (0.637)^2}} + \frac{I_3}{\sqrt{2\pi} \times \sqrt{{\sigma_3}^2 + (0.637)^2}} \quad (6)$$

The physical meaning is obvious: if Doppler broadening is larger, the width of the Gaussian function σ is larger and hence the values of $D(E_0)$ and S are smaller.

By using $I_1 = I_3/3$ and $I_1 + I_2 + I_3 = 1$, we further obtain:

$$D(E_0) = \frac{S}{3.18 \times 95\%} = \frac{(I_3/3)}{\sqrt{2\pi} \times \sqrt{{\sigma_1}^2 + (0.637)^2}} + \frac{(1 - 4I_3/3)}{\sqrt{2\pi} \times \sqrt{{\sigma_2}^2 + (0.637)^2}} + \frac{I_3}{\sqrt{2\pi} \times \sqrt{{\sigma_3}^2 + (0.637)^2}} \quad (7)$$

From this equation, we can see that S is linearly dependent on the intensity of o-Ps (I_3), in the same chemical environment. It also explains the linear relationship between the S parameter and I_3 in our previous results, as shown in Figure 4.[27]

Equation 7 can be further simplified. The experimental results show that if the energy distributions of free e^+ and o-Ps are almost identical,[30,31] $\sigma_2 \approx \sigma_3$, eq 7 can be simplified to

$$D(E_0) = \frac{S}{3.18 \times 95\%} = \frac{(I_3/3)}{\sqrt{2\pi} \times \sqrt{{\sigma_1}^2 + (0.637)^2}} + \frac{(1 - I_3/3)}{\sqrt{2\pi} \times \sqrt{{\sigma_2}^2 + (0.637)^2}} \quad (8)$$

where σ_1 is the Doppler broadening caused the p-Ps intrinsic annihilation due to the uncertainty principle and σ_2 is the Doppler broadening caused by the free e^+ and o-Ps annihilation with an incoming electron.

dx.doi.org/10.1021/ma300007p | Macromolecules 2012, 45, 2434−2441

Doppler broadening energy spectroscopy measures the average lateral momentum of an $e^+ - e^-$ annihilating pair shown in Figure 6.

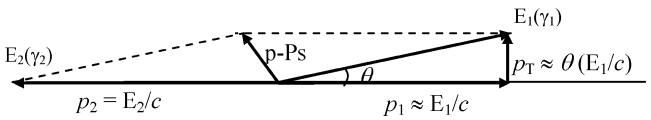


Figure 6. Momentum of e^+–e^- annihilating pair.

We propose that $\sigma_1 = \langle \Delta E \rangle = \langle |E_2 - E_1| \rangle$, where σ_1 is the width of the Gaussian function corresponding to *p*-Ps intrinsic annihilation. E_1 and E_2 are the energies of two γ photons from such annihilation. Because of the conservation of total momentum, $|E_2 - E_1| = |p_2 c - p_1 c| = p_L c$ where p_L is the lateral momentum of *p*-Ps and *c* is the speed of light. Therefore,

$$\sigma_1 = \left\langle \Delta E \right\rangle = \left\langle p_L \right\rangle c \tag{9}$$

Statistically, the average lateral momentum ($\langle p_L \rangle$) and traversal momentum ($\langle p_T \rangle$) have the same value and are related to total momentum as

$$\left\langle p_L \right\rangle = \left\langle p_T \right\rangle = \frac{\langle p \rangle}{\sqrt{2}} \tag{10}$$

Heisenberg's uncertainty principle states:

$$\Delta r \times \Delta p \sim \hbar/2 \tag{11}$$

Δr is the uncertainty of the *p*-Ps position and is the same as the diameter of the hole (2R). Δp is the same as <*p*> due to the zero value of average $\langle \mathbf{p} \rangle$. Then eq 11 is reduced to

$$2R \times \langle \mathrm{p} \rangle \sim \hbar/2 \tag{12}$$

By substituting eqs 10 and 12 into eq 9, σ_1 can be evaluated.

$$\sigma_1 = \frac{0.35}{R\ (\text{Å})}\ (\text{keV})$$

Normally, the free volume hole size in polymeric materials is about 2–3 Å. Assuming R = 2.5 Å, the Doppler broadening based on the above equations, $\sigma_1 = \langle \Delta E \rangle$ = 0.14 keV, can be calculated.

Although σ_1 (~0.14 keV) is small compared to instrumental resolution (~0.637 keV), it can still be extracted from the raw DBES spectrum, which is assumed to be the convolution of energy distribution (σ_1) from *p*-Ps intrinsic annihilation and instrumental resolution ($R(E)$). It has been demonstrated that a Doppler broadening spectrum can be resolved even though it contains a signal function with fwhm only 6% that of the resolution function.[32] Thus, by combining eq 8 and eq 12, it is possible to calculate σ_2 in the Gaussian function as shown in the Table 2.

Table 2. Calculated Energies (E) and Ionization Energies (IE) for Halogens

element	σ_2 (keV)	E (kJ/mol)	IE (kJ/mol)	E/IE
fluorine	3.27	4025	1681	2.39
chlorine	2.81	2969	1251	2.37
bromine	2.61	2558	1140	2.24
iodine	2.49	2336	1008	2.32

As discussed before, σ_2 here represents the energy broadening caused by the lateral momentum of e^+–e^- pair during the pick-off annihilation. From this value, we can calculate its total momentum, $p_{e^+-e^-}$, according to eqs 9 and 10. Since the thermolized e^+ or *o*-Ps has very little kinetic energy, the total momentum in the annihilation mostly comes from the kinetic energy of a valence electron.

Therefore, the kinetic energy of a valence electron can be calculated as

$$KE = \frac{p_{e^+-e^-}{}^2}{2m_e} \tag{13}$$

Furthermore, according to the virial theorem, the kinetic energy of an electron in an atom is the same as its total energy in magnitude, that is,

$$|\mathrm{KE}| = |E| \tag{14}$$

As a result, via eqs 9, 10, 13, and 14, the energies of annihilating electrons can be calculated as listed in Table 2.

In this series of polymers, the variation in DBES and PALS spectra is caused only by the halogen atoms and therefore the calculated energies should correspond to the halogens' annihilating electron energies. Furthermore, both e^+ and *o*-Ps are annihilated predominately by the halogens' valence electrons due to the effective trapping in free volume holes and the fully occupied outer shells.[16] As a result, the energy levels of the valence electrons in bonding halogen atoms determine the energy distributions in these DBES spectra. We may assume that the energies of the valence electrons in halogen elements have approximately the same values as those of neutral halogen atoms since only one of the seven electrons in a halogen atom is involved in the bond formation with a carbon. The calculated energy is correlated with the ionization energies of different halogens,[33] as shown in Figure 7. A very strong linear relationship is attained.

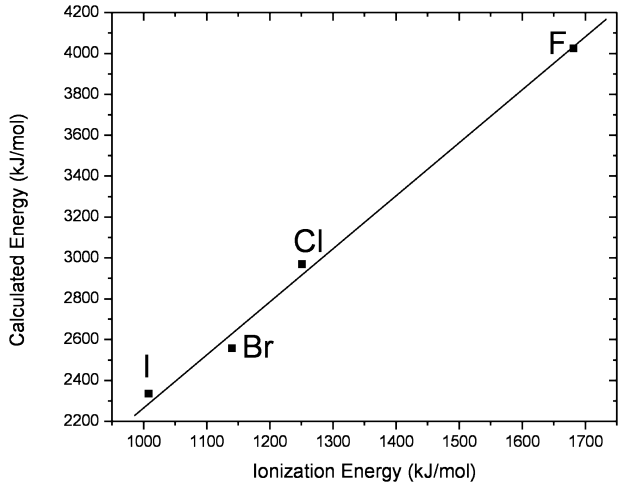


Figure 7. Correlation between calculated energy and ionization energy of halogens.

Since Doppler broadening indicates the momentum of an incoming annihilating electron, the reciprocal of the *S* parameter should be roughly correlated with the ionization energy of halogens as well, as shown in Figure 8. It is found that the data in this plot scatter more than those in Figure 7, where other factors were considered such as the uncertainty principle, positronium formation and instrumental resolution. In particular it is worth mentioning that the residuals from the linear relationship for the I- and Br-substituted polymers are much larger than

dx.doi.org/10.1021/ma300007p | *Macromolecules* 2012, 45, 2434–2441

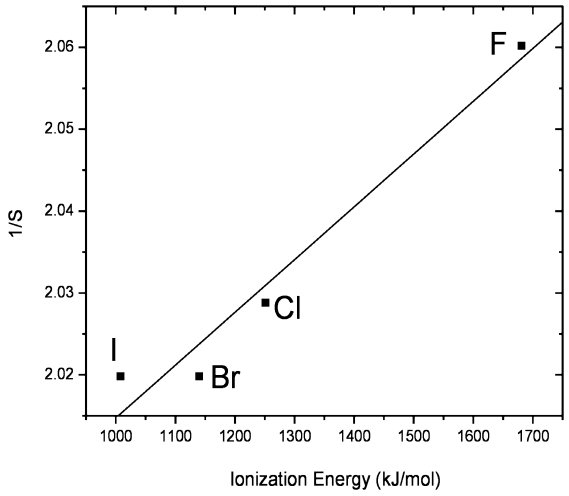


Figure 8. Correlation between *S* parameter and ionization energy of halogens.

that observed for the F- and Cl-substituted polymers. This is because their valence electron energies are lower, and so other factors become more significant. Since most other elements, such as N, O, S, have ionization energies close to those of Cl, Br, and I, the advantage of combining the two techniques of DBES and PALS to extract the annihilating electron energies from DBES spectra is obvious. In conclusion, this approach clearly demonstrates a significant improvement in data quality and content in the study of chemical environments in polymers.

3.3. Correlation with Molecular Orbital Energies. A more precise description of electronic energies in halogenated polystyrene can be obtained by using molecular orbital (MO) theory. Of course, it is practically impossible to calculate the MOs for a large polymer molecule. However, a small halogenated benzene molecule, C_6H_5X (X = F, Cl, Br, I), may be used to approximate the halogenated styrene polymers studied here. Recently, Imura et al.[34] studied the electron distribution in C_6H_5X molecules by using two-dimensional penning ionization electron spectroscopy. They described the molecular orbitals (MOs) from *ab initio* self-consistent field (SCF) calculations. In the reference, the electron density maps for each MO were shown on the surface parallel at 1.6 Å above the benzene rings. The ionization potentials (IP) obtained from Penning ionization electron spectroscopy for MOs in C_6H_5X (X = F, Cl) are listed in Table 3. From the maps, it is observed that the electron density for most MOs are very similar in terms of shape and size, except for $1a_2(\pi_2)$ where there is no electron density around the halogen atom. Therefore, as an approximation, we assume positrons have the same probabilities to annihilate with electrons having opposite spins in all of those MOs except for $1a_2(\pi_2)$. Subsequently, the energies of all MOs except for that of $1a_2(\pi_2)$ were averaged to represent the energy for the electron that annihilates the localized free positron and positronium.

The average molecular orbital energies were then correlated with the calculated energy from our experiment in Figure 9. A strong linear relationship is obtained once again. The minor scattering of data points is within expectation considering the simple model molecules (C_6H_5X, X = F, Cl, Br, I) used.

Table 3. Energies of Molecular Orbitals (MOs) in C_6H_5X (X = F, Cl).[34]

molecule	band	IP_{obsd}(eV)	orbital character
C_6H_5F	1	9.29	$3b_1(\pi_3)$
	2	9.74	$1a_1(\pi_2)$
	3	11.85	$10b_2$
	4	12.13	$2b_1(\pi_1)$
	5	12.98	$11a_1$
	6	13.90	$9b_2(n_{\|})$
	7	14.64	$8b_2$
	8	15.18	$10a_1$
	9	15.8	$1b_1(n_{\perp})$
	10	16.35	$7b_2$
	11	16.64	$9a_1$
	12	17.84	$8a_1(\sigma_{CF})$
molecule	band	IP_{obsd}(eV)	orbital character
C_6H_5Cl	1	9.05	$4b_1(\pi_3)$
	2	9.65	$1a_2(\pi_2)$
	3	11.28	$9b_2(n_{\|})$
	4	11.65	$3b_1(n_{\perp})$
	5	12.30	$15a_1$
	6	12.95	$8b_2$
	7	13.11	$12b_1(\pi_1)$
	8	14.30	$14a_1$
	9	14.63	$7b_2$
	10	15.35	$6b_2$
	11	15.64	$13a_1$
	12	17.02	$12a_1$

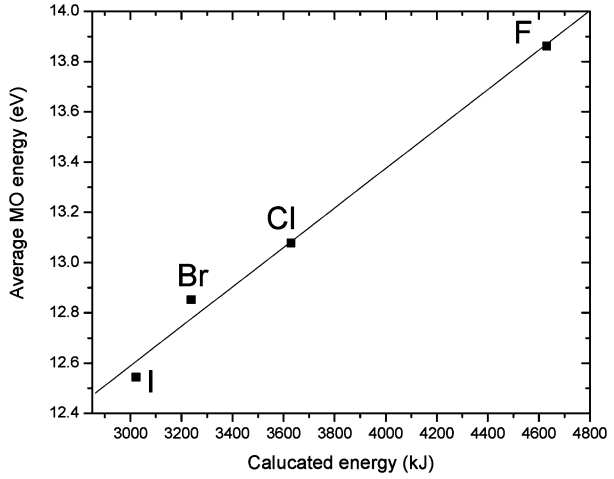


Figure 9. Correlation between average energy of MOs and the calculated energy.

4. CONCLUSIONS

In this study the chemical environment inside free volume holes of halogenated styrene polymers was investigated using positron annihilation spectroscopy. The *S* parameter is dominated by the kinetic energies of annihilating electrons, rather than the positronium formation. By combining DBES and PALS spectra, the energy of an incoming electron annihilating with positron or positronium was extracted. An excellent linear relationship between the calculated energies and the ionization potentials of halogen atoms is observed. A strong correlation of the calculated energies with the average ionization potential (IP) from electron spectroscopy for different molecular orbitals in C_6H_5X (X = F, Cl, Br, I) was also

dx.doi.org/10.1021/ma300007p | *Macromolecules* 2012, 45, 2434−2441

obtained. Furthermore, a significant improvement was demonstrated in the above correlations by combining DBES and PALS to exclude other factors such as the uncertainty principle from the chemical interaction. It is concluded that positron annihilation spectroscopy can be utilized to investigate the chemical environment in polymeric materials.

Because of the unique physical phenomenon that positron/positronium is annihilated inside free volume holes, this study provides significant information about the chemical environment inside those holes. This might be particularly important in terms of many applications related to small molecule adsorption/absorption, for example gas selectivity and H_2 storage, where the chemical environment inside free volume holes plays a critical role, rather than that in the bulk

AUTHOR INFORMATION

Corresponding Author

*E-mail: RZhang@csusb.edu. Telephone: (909) 537-5446.

Notes

The authors declare no competing financial interest.

ACKNOWLEDGMENTS

We thank Dr. Brett Stanley of the Department of Chemistry and Biochemistry at California State University, San Bernardino for his valuable discussions.

REFERENCES

(1) Jean, Y. C. *Microchemistry* **1990**, *42*, 72−102.
(2) Nagel, C.; Gunther-Schade, K.; Fritsch, D.; Strunskus, T.; Faupel, F. *Macromolecules* **2002**, *35*, 2071−2077.
(3) Merkel, T. C.; Freeman, B. D.; Spontak, R. J.; He, Z.; Pinnau, I.; Meakin, P.; Hill, A. J. *Science* **2002**, *296*, 519−522.
(4) Koros, W. J.; Coleman, M. R.; Walker, D. R. B. *Annu. Rev. Mater. Sci.* **1992**, *22*, 47−89.
(5) Hill, A. J. *ACS Symp. Ser.* **1995**, *603*, 63−80.
(6) Shiratori, S.; Inami, Y.; Kikuchi, M. *Thin Solid Films* **2001**, *393*, 243−248.
(7) McKeown, N. B.; Budd, P. M. *Chem. Soc. Rev.* **2006**, *35*, 675−683.
(8) Uhlhorn, R. J. R.; Keizer, K.; Burggraaf, A. J. *J. Membr. Sci.* **1992**, *66*, 271−287.
(9) Mavrandonakis, A.; Klontzas, E.; Tylianakis, E.; Froudakis, G. E. *J. Am. Chem. Soc.* **2009**, *131*, 13410−13414.
(10) Critchfield, F. E.; Johnson, D. P. *Anal. Chem.* **1961**, *33* (13), 1834−1836.
(11) Lawson, G. *Chemical Analysis of Polymers*; RAPRA Technology Ltd.: 1991; Vol. *4* (11).
(12) Hugenschmidt, C.; Qi, N.; Stadlbauer, M.; Schreckenbach, K. *Phys. Rev. B* **2009**, *80*, 224203.1−224203.6.
(13) Ruiz-Ripoll, M. L.; Schut, H.; Van Dijk, N. H.; Alderliesten, R. C.; Van der Zwaag, S.; Benedictus, R. *J. Phys.: Conf. Ser.* **2011**, *262*, 012052 DOI: 10.1088/1742-6596/262/1/012052.
(14) Lynn, K. G.; Goland, A. N. *Solid State Commun.* **1976**, *18*, 1549−1552.
(15) Folegati, P.; Dupasquier, A.; Ferragut, R.; Iglesias, M.; Makkonen, I.; Puska, M. J. *Physica StatusSolidi (c)* **2007**, *4* (10), 3493−3496.
(16) Myler, U.; Simpson, P. J. *Phys. Rev. B* **1997**, *56*, 14303−14309.
(17) Myler, U. R.; Goldberg, D.; Knights, A. P.; Lawther, D. W.; Simpson, P. J. *App. Phys. Lett.* **1996**, *69*, 3333−3335.
(18) Alatalo, M.; Kauppinene, H.; Saarinen, K.; Puska, M. T.; Mäkinene, J.; Hautojärvi, P.; Nieminen, R. M. *Phys. Rev. B* **1995**, *51*, 4176.
(19) Dlubek, G.; Saarinen, K.; Fretwell, H. M. *Nucl. Instrum. Methods Phys. Res. B* **1998**, *142*, 139−155.
(20) Ito, K.; Nanasawa, A.; Kobayashi, Y. *Appl. Phys. Lett.* **2003**, *82*, 654−656.
(21) Ito, Y.; Okamoto, K. I.; Tanaka, K. *J. Phys. IV* **1993**, *3*, 241.
(22) Baranowski, A.; Debowska, M.; Kerie, K.; Girulska, R. *J. Phys. IV* **1993**, *3*, 225−231.
(23) Dlubek, G.; Fretwell, H. M.; Alam, M. A. *Macromolecules* **2000**, *33*, 187−192.
(24) Kobayashi, Y.; Wang, C. L.; Hirata, K.; Zheng, W.; Zhang, C. *Phys. Rev. B* **1998**, *58*, 5384−5389.
(25) Nagai, Y.; Nonaka, T.; Hasegawa, M.; Kobayashi, Y.; Wang, C. L.; Zheng, W.; Zhang, C. *Phys. Rev. B* **1999**, *60*, 11863−11866.
(26) Pugh, C.; Tang, N. C.; Paz-Pazos, M.; Samtani, O.; Dao, H. A. *Macromolecules* **2007**, *40*, 8178−8188.
(27) Zhang, R. Ph.D. Dissertation, University of Missouri—Kansas City, Kansas City, MO, 64110, 2002.
(28) Nakanishi, H.; Wang, S. J.; Jean, Y. C. In *Positron Annihilation Studies of Fluids*; Sharma, S. C., Ed.; World Scientific: Singapore, 1988; p 159.
(29) Wu, Y. C.; Huang, C. M.; Li, Y.; Zhang, R.; Chen, H.; Mallon, P. E.; Zhang, J.; Sandreczki, T. C.; Zhu, D. M.; Jean, Y. C.; Sukuki, R.; Ohdaira, T. *J. Polym. Sci., Part B* **2001**, *39*, 2290−2301.
(30) Jain, P. C.; Eldrup, M.; Pederson, N. J.; Sherwood, J. N. *Chem. Phys.* **1986**, *106*, 303−313.
(31) Hyodo, T. Information presented during the *6th International Workshop on Positron and Positronium Chemistry*; Tsukuba, Japan, June 6−10, 1999.
(32) Dannefaer, S.; Kerr, P. D. *Nucl. Instrum. Methods* **1975**, *131*, 119−124.
(33) Weast, R. C. *CRC Handbook of Chemistry and Physics*, 56th ed.; CRC Press: Cleveland, OH, 1975.
(34) Imura, K.; Kishimoto, N.; Ohno, K. *J. Phys. Chem. A* **2001**, *105*, 4189−4199.

Macromolecules

Article

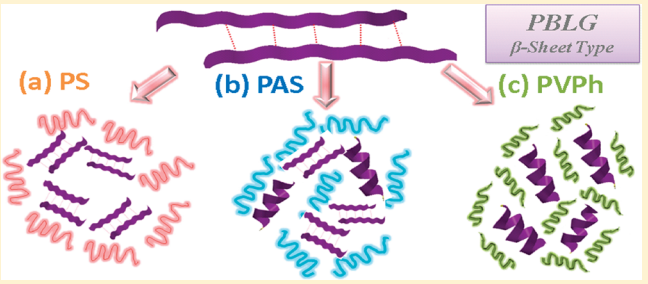
pubs.acs.org/Macromolecules

Functional Polystyrene Derivatives Influence the Miscibility and Helical Peptide Secondary Structures of Poly(γ-benzyl L-glutamate)

Shiao-Wei Kuo* and Chi-Jen Chen

Department of Materials and Optoelectronic Science, Center for Nanoscience and Nanotechnology, National Sun Yat-Sen University, Kaohsiung, Taiwan

ABSTRACT: We synthesized polystyrene (PS) and poly(acetoxystyrene) (PAS) homopolymers through atom transfer radical polymerization (of styrene and 4-acetoxystryene monomers, respectively) and then prepared poly(vinylphenol) (PVPh) through acetoxyl hydrazinolysis of PAS with hydrazine monohydrate. To investigate the influences of these three functionalized polystyrene derivatives on the helical peptide secondary structures and miscibility behavior of polypeptide homopolymers, we blended PS, PAS, and PVPh with a low-molecular-weight poly(γ-benzyl L-glutamate) (PBLG) homopolymer and analyzed these blends using differential scanning calorimetry (DSC), Fourier transform infrared (FTIR) spectroscopy, solid state nuclear magnetic resonance (NMR) spectroscopy, and wide-angle X-ray diffraction (WAXD). Variations in the intermolecular interactions (e.g., π−π, dipole−dipole, hydrogen bonding) strongly affected the miscibility behavior and secondary structures of PBLG. The weak π−π interactions between PS and PBLG resulted in only partial miscibility, with the α-helical secondary structure of PBLG remaining almost unchanged upon increasing the content of the PS homopolymer; in contrast, the stronger dipole−dipole interactions between PAS and PBLG and the hydrogen-bonding interactions between PVPh and PBLG led to complete miscibility, with the content of α-helical PBLG secondary structures increasing upon increasing the contents of both the PAS and PVPh homopolymers. Because the hydrogen-bonding interactions in the PVPh/PBLG blends were stronger than the dipole−dipole interactions in the PAS/PBLG blends, the fractions of α-helical secondary structures in the PVPh/PBLG systems were larger than those in the PAS/PBLG systems. Indeed, the contents of α-helical conformations in these three blend systems correlated strongly with the strength of their intermolecular interactions.



INTRODUCTION

The α-helical structures of polypeptides [e.g., poly(γ-benzyl L-glutamate) (PBLG)] result in the formation of rigid rod structures that can exhibit liquid crystalline ordering in concentrated solutions and cast films.[1−3] PBLG, which has been commercially available since the 1950s,[4] is often employed as a model rigid rod system in solution and in the solid state,[5−7] providing unique bulk (e.g., thermotropic liquid crystalline ordering)[8,9] and solution (thermoreversible gelation)[10−13] behavior. PBLG also forms hierarchically ordered structures containing α-helices, which can be regarded as rigid rods, stabilized through intramolecular hydrogen-bonding interactions, and β-sheets, stabilized by intermolecular interactions, as fundamental secondary motifs.[14] Conformational studies of model polypeptides are necessary if we are to mimic the biological activity of more-complex proteins because the secondary structures of peptide chains influence the formation of proteins with well-defined tertiary structures.[15]

For several decades, most of the methods for synthesizing poly(peptide-*b*-nonpeptide) (rod/coil) block copolymers, with potential applications in tissue engineering and drug delivery, have followed Nature's strategies for producing supramolecular bioactive assemblies.[16−31] These systems can exhibit significant stabilization of the α-helical secondary structures relative to those of the corresponding PBLG oligomers; for example, in the Fourier transform infrared (FTIR) spectra of poly(styrene-*b*-γ-benzyl L-glutamate) (PS-*b*-PBLG) copolymers reported by Klok et al.[16] The synthesis of diblock copolymers is, however, a difficult and time-consuming means of varying the secondary structure of a polypeptide. From practical and economical points of view, physical blending is a simpler and more effective method for modifying a polypeptide or any other useful material, with greater versatility and flexibility, than through the development of new polymers.[32−36] From a previous study,[37] we reported that the secondary structures of the polypeptides poly(γ-methyl L-glutamate) (PMLG), poly(γ-ethyl L-glutamate) (PELG), and PBLG could be altered through blending with other random-coil nonpeptide oligomers (in that case, phenolic resin), mediated by hydrogen-bonding interactions. We found that the α-helical conformation in these three blend systems correlated strongly with the rigidity of side chain groups of the polypeptides and the strength of the intermolecular hydrogen bonding with the phenolic resin.[37]

Received: January 9, 2012
Revised: February 12, 2012
Published: February 22, 2012

 © 2012 American Chemical Society dx.doi.org/10.1021/ma300061w | *Macromolecules* 2012, 45, 2442−2452

In this present study, we investigated the influence of three functionalized polystyrene derivatives (homopolymers) on the peptide secondary structure and miscibility behavior of PBLG. We synthesized polystyrene (PS) and poly(acetoxystyrene) (PAS) homopolymers through atom transfer radical polymerizations of styrene and 4-acetoxystryene, respectively, and then prepared poly(vinylphenol) (PVPh) through acetoxyl hydrazinolysis of PAS with hydrazine monohydrate. We expected weak $\pi-\pi$ interactions to exist between PS and PBLG, moderate dipole−dipole interactions between PAS and PBLG,[38−40] and strong hydrogen-bonding interactions between PVPh and PBLG, with the strength of the intermolecular interactions in the blends increasing in the order PVPh/PBLG > PAS/PBLG > PS/PBLG. Changing the functionality of the polystyrene derivative is a simple approach toward distinguishing the influence of intermolecular interactions on the miscibility behavior and secondary structure of PBLG. We have used differential scanning calorimetry (DSC), FTIR spectroscopy, solid state nuclear magnetic resonance (NMR) spectroscopy, and wide-angle X-ray diffraction (WAXD) to investigate the miscibility behavior, hydrogen-bonding interactions, and secondary structures of these three binary blends.

EXPERIMENTAL SECTION

Materials. Butylamine was purchased from Tokyo Kasei Kogyo, Japan. γ-Benzyl L-glutamate *N*-carboxyanhydride (BLG NCA) monomer was prepared according to a literature procedure[41] and stored at −30 °C. Styrene and 4-acetoxystyrene (Aldrich) were vacuum-distilled over CaH_2 and stored under N_2 at −10 °C. Copper(I) bromide (CuBr) was purified by washing sequentially with glacial AcOH (overnight), absolute EtOH, and Et_2O and then drying under vacuum. *N*,*N*-Dimethylformamide (DMF), 1-phenylethyl bromide, and *N*,*N*,*N*′,*N*′,*N*″-pentamethyldiethylenetriamine (PMDETA, 99%) were purchased from Aldrich. All solvents were distilled prior to use.

PBLG.[37] In a typical experiment, the BLG NCA monomer (2 g) was weighed in a glovebox under pure Ar, placed in a flame-dried Schlenk tube, and dissolved in anhydrous DMF (40 mL). The solution was stirred for 10 min, and then butylamine (50 μL) was added using a N_2-purged syringe. After stirring the solution for 40 h at room temperature, the polymer was recovered through precipitation in Et_2O and dried under high vacuum.

PS and PAS.[42,43] CuBr (green powder) was added to a reactor and degasser operated under vacuum, followed by dry styrene (or acetoxystyrene) and (1-bromoethyl)benzene (by syringe) as the monomer and initiator, respectively. The mixture was subjected to at least two freeze/pump/thaw cycles. The ligand PMDETA was added via syringe under Ar, and then the system was once again subjected to the freeze/pump/thaw procedure. The reactor was placed in an oil bath and heated at 110 °C for 2 h. When the reaction was complete, the mixture was diluted with THF and passed through a neutral alumina column to remove the catalyst. The polymer solution was concentrated under rotary evaporation. The polymer was precipitated with MeOH and collected by filtration. The white powder of PS (or PAS) was dried under vacuum.

PVPh.[42,43] In a typical procedure, the PAS (7.2 mmol of AS) homopolymer was dissolved in 1,4-dioxane (30 mL), and then hydrazine hydrate (3 mL) was added via syringe (volume ratio of hydrazine hydrate to 1,4-dioxane, 1:9). The reaction mixture was maintained at room temperature under an Ar atmosphere for 10 h. The solution was concentrated, washed several times with deionized H_2O, and then dried in a vacuum oven at room temperature for 72 h.

Blend Preparations. Mixtures of PS/PBLG, PAS/PBLG, and PVPh/PBLG at various blend compositions were prepared through solution casting. A DMF solution containing 5 wt % of the polymer mixture was stirred for 6−8 h, and then the solvent was evaporated slowly at 50 °C for 1 day. The film of the blend was then dried at 80 °C for 2 days to ensure total removal of residual solvent.

Characterization. ^{1}H NMR spectra were recorded at room temperature using a Bruker AM 500 (500 MHz) spectrometer, with the residual proton resonance of the deuterated solvent as the internal standard. High-resolution solid state NMR spectra were recorded at room temperature using a Bruker DSX-400 spectrometer operated at resonance frequencies of 399.53 and 100.47 MHz for ^{1}H and ^{13}C nuclei, respectively. ^{13}C cross-polarization (CP)/magic angle sample spinning (MAS) spectra were measured using a 3.9 μs 90° pulse, a 3 s pulse delay time, a 30 ms acquisition time, and 2048 scans. All NMR spectra were recorded at 300 K using broad band proton decoupling and a normal CP pulse sequence. An MAS rate of 5.4 kHz was used to avoid absorption overlapping. Differential scanning calorimetry (DSC) was performed using a TA-Q20 instrument operated at a scan rate of 10 °C/min over the temperature range from −90 to 200 °C under a N_2 atmosphere. FTIR spectra of the polymer films were recorded using a Bruker Tensor 27 FTIR spectrophotometer with the conventional KBr disk method; 32 scans were collected at a spectral resolution of 1 cm^{-1}. Because polymers containing OH groups are hygroscopic, pure N_2 gas was used to purge the spectrometer's optical box to ensure dry sample films. X-ray diffraction (XRD) data were collected on the wiggler beamline BL17A1 of the National Synchrotron Radiation Research Center (NSRRC), Taiwan. A triangular bent Si (111) single crystal was employed to obtain a monochromated beam having a wavelength (λ) of 1.330 01 Å. The XRD patterns were collected using an imaging plate (IP; Fuji BAS III; area = 20 × 40 cm^2) curved with a radius equivalent to the sample-to-detector distance (280 mm). The two-dimensional (2D) XRD patterns of the samples (typical diameter: 10 mm; thickness: 1 mm) were circularly averaged to obtain one-dimensional (1D) diffraction profiles $I(Q)$. The values of Q were calibrated using standard samples of silver behenate and Si powder (NBS 640b).

Table 1. Molecular Characteristics of PBLG, PS, PAS, and PVPh

polymer	M_n	PDI	DP	T_g (°C)
PBLG	1370	1.06	6	23
PS	6270	1.07	60	83
PAS	8910	1.12	55	122
PVPh	6600	1.12	55	170

RESULTS AND DISCUSSION

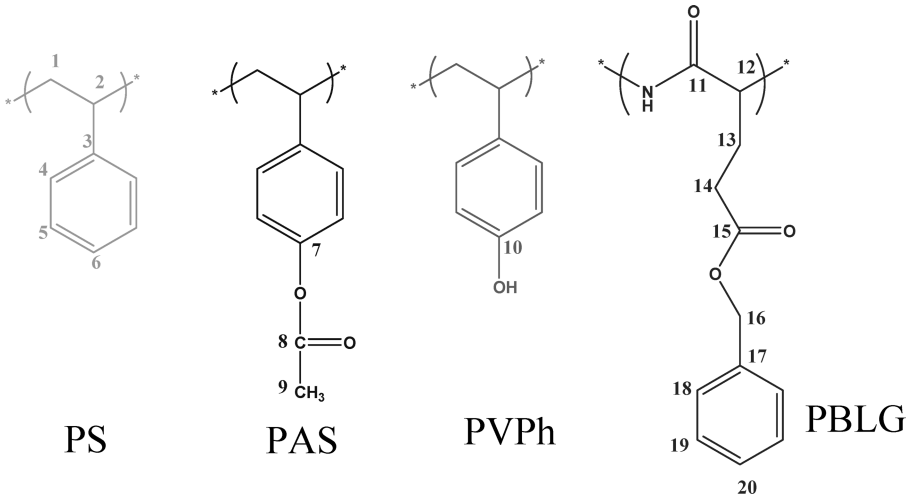
Table 1 and Scheme 1 summarize the molecular weights, thermal properties, and chemical structures of the PBLG, PS, PAS, and PVPh homopolymers prepared in this study.

FTIR Spectra of PS, PAS, and PVPh. Figure 1 presents FTIR spectra of the PS, PAS, and PVPh homopolymers at room temperature. The bands for PS appear at 3002−3100 cm^{-1}, due to C−H stretching vibrations of the aromatic rings, and 1600 cm^{-1}, due to C═C bending vibrations of the aromatic rings (Figure 1a). In the spectrum of PAS (Figure 1b),[44,45] the absorption at 1763 cm^{-1} is assigned to the C═O unit; the absorptions of the aromatic rings are similar to those in the spectrum of PS. The C═O group absorption at 1760 cm^{-1} in Figure 1b disappeared completely after deacetylation, but a broad absorbance from the OH groups of the PVPh homopolymer appeared between 3100 and 3700 cm^{-1} (Figure 1c).[46−48]

Thermal Analyses of Polymer Blends. Thermal characterization of polymer blends is a common method for

dx.doi.org/10.1021/ma300061w | Macromolecules 2012, 45, 2442−2452

Scheme 1. Chemical Structures of PS, PAS, PVPh, and PBLG



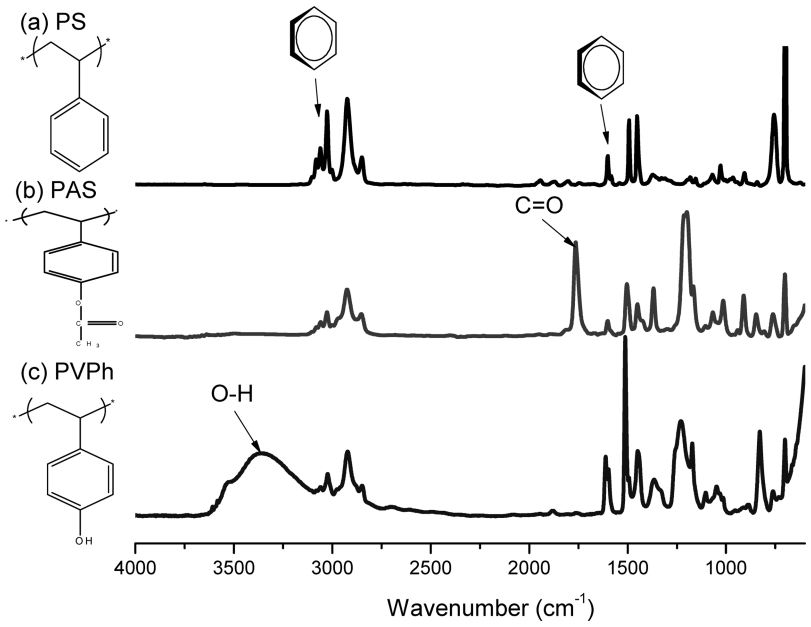


Figure 1. FTIR spectra (recorded at room temperature) of the PS, PAS, and PVPh homopolymers.

determining the miscibility of polymer blends. Some miscible blends can show a dual glass temperature with a relatively large T_g difference between two homopolymers with weak intermolecular interactions.[49,50] In this study, we found it difficult to observe the glass transition temperatures (T_g) of the polypeptides having rigid conformations and well-defined secondary structures (helices, sheets).[51] The value of T_g of pure PBLG is reported to be 23 °C;[14] in this present study, we obtained values of T_g for pure PS, PAS, and PVPh of 83, 122, and 170 °C, respectively. Because the glass transition behavior is strongly dependent on the molecular weight, the value of T_g (83 °C) for the PS (M_n = 6270 g/mol) used in this study was lower than those reported previously for high-molecular-weight PS (T_g = 100 °C).[52,53] Figure 2 presents the second heating runs in our DSC analyses of PBLG blends with PS, PAS, and PVPh at various compositions. The DSC thermograms of the PS/PBLG blend (Figure 2a) displays two values of T_g, implying that the components were phase-separated in the amorphous phase. The value of T_g of the PBLG domain remained almost unchanged upon increasing the content of the PS homopolymer; in contrast, the value of T_g of the PS domain decreased upon increasing the PBLG content (Figure 3a), indicating that the PS segment was partially miscible in the PBLG matrix as a result of $\pi-\pi$ interactions (Scheme 2a). This observation is similar to that for the microphase separation that occurs in PS-*b*-PBLG diblock copolymers.[16] All of our PAS/PBLG and PVPh/PBLG blends exhibited a single glass transition temperature over the entire range of blend compositions. The single value of T_g strongly suggested that these blends were fully miscible and possessed homogeneous amorphous phases. In addition, the values of T_g of the PAS/PBLG (Figure 3b) and PVPh/PBLG (Figure 3c) blends both decreased upon increasing their PBLG contents. As a result, we conclude that PAS and PVPh are miscible with PBLG, whereas PS is only partially miscible with PBLG. The miscibility of the PVPh/PBLG blend is inconsistent with the results reported by Painter et al.[14,32] They found that PBLG, with its flexible side chains, adopted an α-helical rigid rod conformation because of its high molecular weight (M_n = 248 000 g/mol); on the basis of FTIR spectroscopic analyses, they did not observe the presence of

dx.doi.org/10.1021/ma300061w | *Macromolecules* 2012, 45, 2442−2452

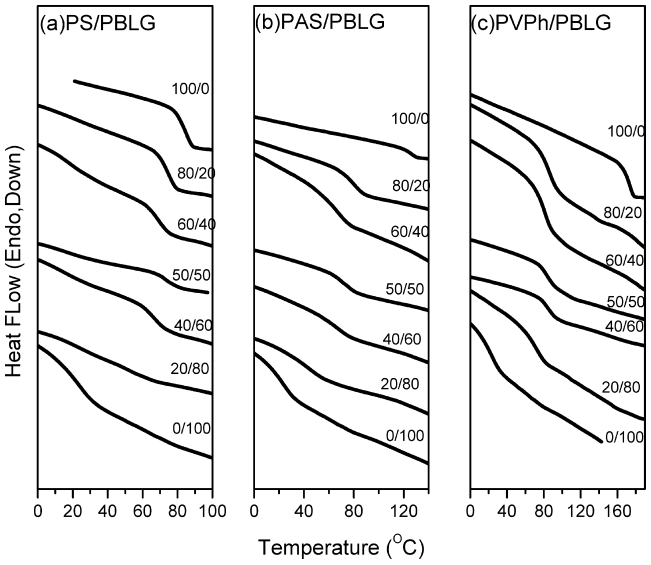


Figure 2. DSC traces (second heating run) of (a) PS/PBLG, (b) PAS/PBLG, and (c) PVPh/PBLG blends.

intermolecular hydrogen bonds between the C═O groups on the side chains of PBLG and the OH groups of PVPh, indicating that the system was immiscible and phase-separated.[32] Our conflicting observations presumably arose from the much lower molecular weight of the PBLG (1370 g/mol) used in this study, relative to that (248 000 g/mol) used previously, with the lower degree of polymerization (DP) increasing the entropic terms, which much more like solutions of PAS, and PVPh in the solvent PBLG$_6$, and, thereby, enhancing the miscibility of the polymer blend system.[54] In addition, at a low DP (e.g., <18 in this case), three secondary structures (α-helix, β-sheet, random coil) are present for PBLG; when the DP increases, however, the rigid α-helical secondary structure is favored.[14,32] As a result, the more-flexible secondary structures—β-sheet and random coil—might have a greater possibility to form intermolecular hydrogen bonds with PVPh than would the rigid α-helical conformation, contributing significantly to the enthalpic term.[54]

FTIR Spectroscopic Analyses of Polymer Blends. FTIR spectroscopy can provide information relating to the specific interactions between polymers, both qualitatively and quantitatively. The NH and OH stretching ranges in a FTIR spectrum are sensitive to the degrees of intermolecular interaction. Figure 4 displays FTIR spectra (in the range 2700−4000 cm^{-1}) of PS/PBLG, PAS/PBLG, and PVPh/PBLG blends, recorded at room temperature. For pure PBLG, we observe a sharp band at 3290 cm^{-1}, representing the NH stretching (primary amine) vibrations of the polypeptide. The characteristics of this sharp band remained unchanged upon increasing the PS, PAS, and PVPh contents, indicating that no hydrogen-bonding interactions occurred between these three homopolymers and the NH groups of PBLG. The FTIR spectrum of pure PVPh featured two distinct bands in the OH stretching region: a very broad band centered at 3350 cm^{-1}, representing the wide distribution of hydrogen-bonded OH groups, and a sharp band at 3525 cm^{-1}, representing free OH groups. The intensity of the signal for the free OH groups decreased upon increasing the PBLG content. Meanwhile, the broad signal of the hydrogen-bonded OH groups shifted to higher frequency upon increasing the PBLG content, suggesting a switch from strong intramolecular OH···OH (PVPh/PVPh) hydrogen bonds into weak intermolecular OH···O═C (PVPh/PBLG) hydrogen bonds.[55,56]

Figure 5 presents FTIR spectra recorded at room temperature to obtain information regarding the secondary structures of the PS/PBLG, PAS/PBLG, and PVPh/PBLG blends. Analyzing these spectra using the second derivative technique,[17] we observed six major peaks for pure PBLG, representing the free C═O group (1735 cm^{-1});[32] the secondary structures of the amide I groups in random coil (1692 cm^{-1}),[17] α-helical (1655 cm^{-1}),[16] and β-sheet (1626 cm^{-1})[16] conformations; and the stretching of benzene units (1610 and 1594 cm^{-1}). For our analysis, we ignored the signals for the random-coil amide I groups at 1640−1650 and 1660−1670 cm^{-1} because many bands made it difficult to calculate the

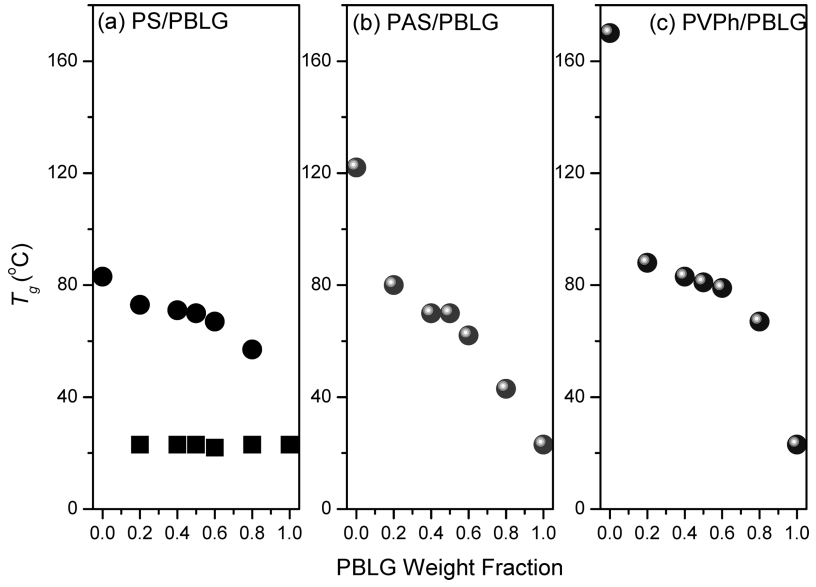
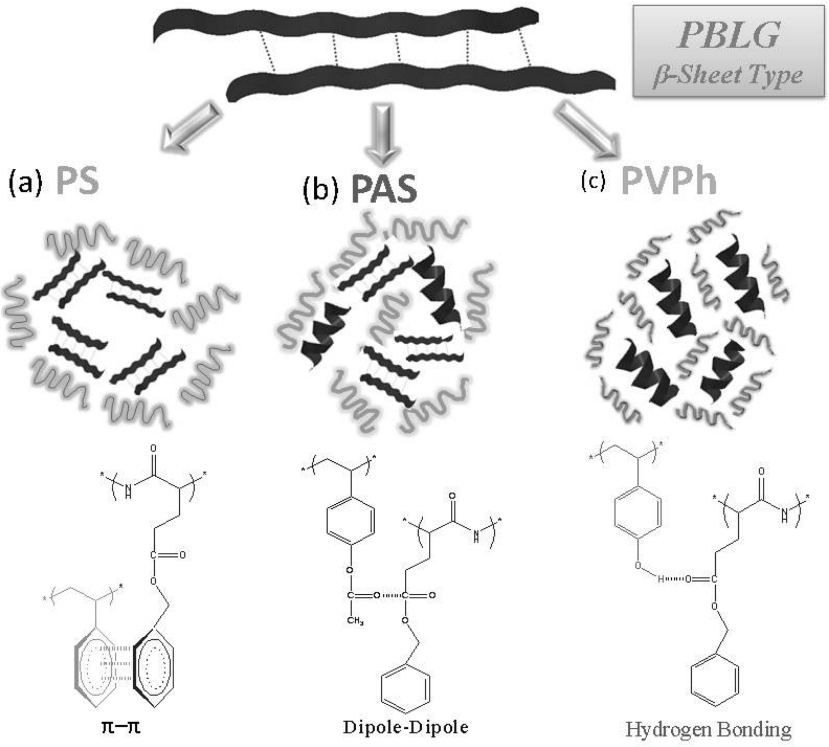


Figure 3. Glass transition temperatures plotted with respect to the PBLG weight fraction in (a) PS/PBLG, (b) PAS/PBLG, and (c) PVPh/PBLG blends.

dx.doi.org/10.1021/ma300061w | Macromolecules 2012, 45, 2442−2452

Scheme 2. Possible Morphologies, Secondary Structures, and Intermolecular Interactions of PBLG Blended with PS, PAS, and PVPh Homopolymers



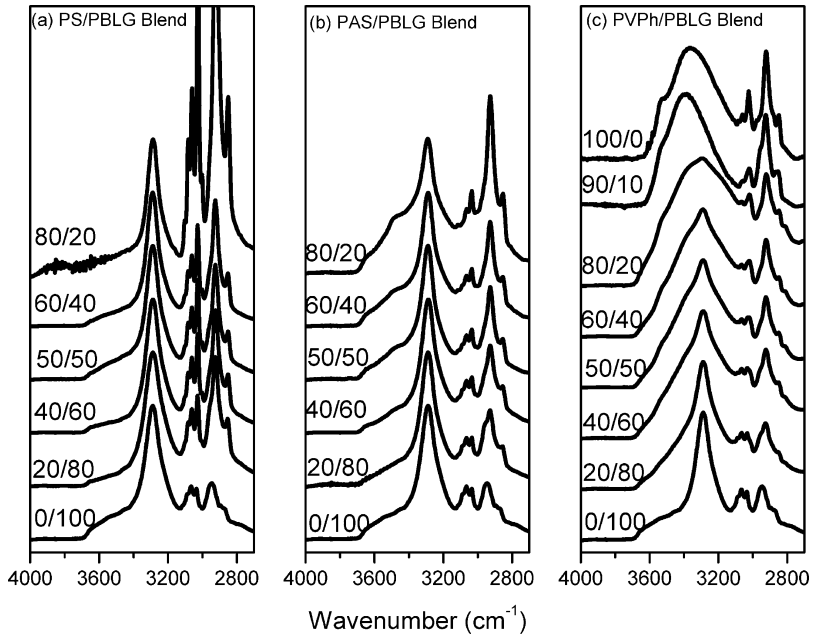


Figure 4. FTIR spectra (4000–2700 cm^{-1}, recorded at room temperature) of the (a) PS/PBLG, (b) PAS/PBLG, and (c) PVPh/PBLG blends.

quantitative area fractions of the secondary structures.[57] After blending with the PS homopolymer, the positions of these six major peaks did not change, with only the intensity of the stretching band for the benzene units at 1600 cm^{-1} increasing upon increasing the PS content. For the PAS/PBLG blends, a new signal for free C═O groups appeared at 1760 cm^{-1}, representing the PAS segment. After blending with the PVPh homopolymer, however, a new signal for hydrogen-bonded C═O units appeared at 1710 cm^{-1}, indicating that hydrogen bonding existed between the C═O groups of PBLG and the OH groups of PVPh. For deconvolution, we fitted a series of Gaussian distributions (Figure 6) to quantify the fractions of each of the peaks. Table 2 and Figures 7 and 8 summarize the curve-fitting data for the amide I groups of the β-sheet, α-helical, and random coil structures of PBLG and for the free and hydrogen-bonded C═O units in the PBLG blends with the PVPh homopolymer. Figure 7 plots the fraction of hydrogen-bonded C═O groups of PBLG with respect to the

dx.doi.org/10.1021/ma300061w | Macromolecules 2012, 45, 2442–2452

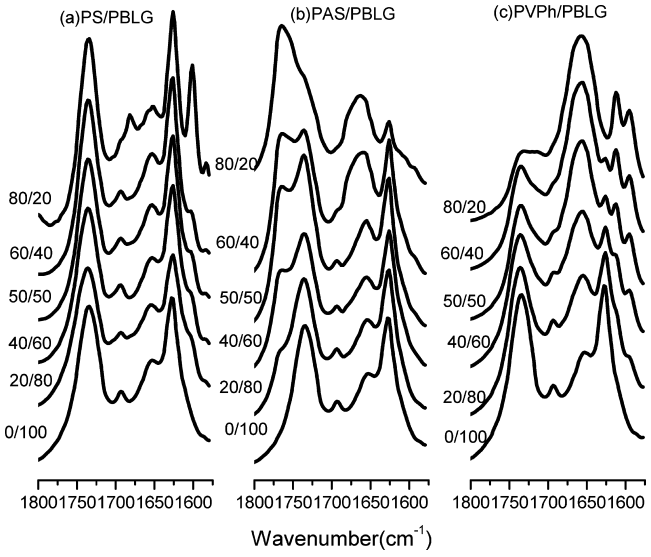


Figure 5. FTIR spectra (1800−1580 cm^{-1}, recorded at room temperature) of the (a) PS/PBLG, (b) PAS/PBLG, and (c) PVPh/PBLG blends.

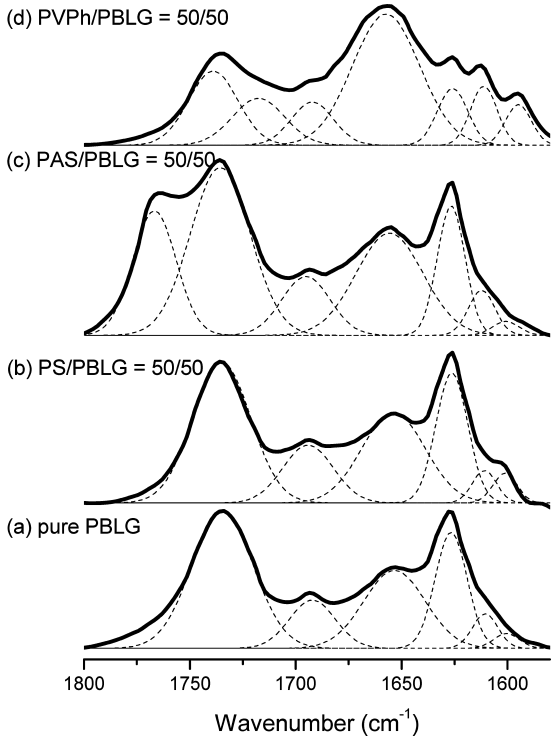


Figure 6. Curve fitting of the signals in the FTIR spectra of the (a) pure PBLG and (b) PS/PBLG = 50/50, (c) PAS/PBLG = 50/50, and (d) PVPh/PBLG = 50/50 blends.

PVPh content at room temperature; it reveals that the fraction of hydrogen-bonded C═O groups on the side chains of PBLG increased upon increasing the PVPh content. Compared with the data for PVPh/PBLG blends reported by Painter et al., the proportion of hydrogen-bonded C═O groups in our PVPh/PBLG blends was negligibly small at most compositions. In our PVPh/PBLG blends, we observed relatively higher fractions of hydrogen-bonded C═O groups of PBLG, presumably because of the molecular weight of our PBLG was much lower than that used by Painter et al. As a result, the more-flexible secondary structures (β-sheet, random coil) were more likely to form intermolecular hydrogen bonds with PVPh than were the rigid α-helical conformations. Therefore, we confirmed that the PVPh/PBLG blend was a miscible system because of the existence of intermolecular hydrogen bonds between the OH groups of PVPh and the C═O groups of PBLG. Next, we determined the corresponding inter- and self-association equilibrium constants for these systems. The self-association constants of PVPh (K_2 = 21.0; K_B = 66.8) had been determined previously.[54] We determined the interassociation constants K_A directly using a least-squares fitting procedure based on the fraction of hydrogen-bonded C═O groups observed experimentally in the PVPh/PBLG blends; using the Painter−Coleman association model, we obtained a value of K_A of 15.[54] This value of K_A for the PVPh/PBLG blends is less than that for the OH···O═C hydrogen-bonding interactions in PVPh/poly(methyl methacrylate) (PMMA) blends (K_A = 37),[54,58] but higher than that in PVPh/poly(L-lactide) blends (K_A = 10),[59] presumably because of the nature of the chemical structure of the group accepting the hydrogen bonds, as has been discussed in detail previously.[60−62]

Figure 8 summarizes the fractions of the secondary structures in the PS/PBLG, PAS/PBLG, and PVPh/PBLG blends at room temperature. It has been reported that at a low DP (<18) both the α-helix and β-sheet secondary structures of PBLG are present, but when the DP increases, the α-helical secondary structure is favored.[1] In this study, we also observed both the α-helix and β-sheet conformations for the PBLG oligomer at a DP of 6. When blended with the PS homopolymer, the fraction of α-helix conformations remained almost unchanged upon increasing the PS content—considerably different from the behavior of PS-*b*-PBLG copolymers. Thus, we observed significant stabilization of the α-helical secondary structure relative to those of the corresponding PBLG oligomers in PS-*b*-PBLG diblock copolymers because of the short-range attraction mediated by covalent bonding between the PS and PBLG segments. When blended with PAS, which can form stronger dipole−dipole interactions, the fraction of the random coil structures of PBLG decreased upon increasing the PAS content, indicating that the presence of PAS stabilized the secondary structures of PBLG. On the other hand, the fraction of α-helical conformations of PBLG increased continuously upon increasing the PAS content. It has been proposed that stacking of the side-chain benzene rings of PBLG plays a role in stabilizing its various structures.[32] Jeon et al. reported that the mobility of the side chain groups of polyglutamates also affects their the α-helical conformations.[63] Their experimental data revealed that longer flexible side chains induced weaker hydrogen bonds between the C═O groups and the amide linkages of the α-helical conformation; a corollary is that rigid benzene rings might enhance hydrogen bonding between the C═O groups and the amide linkages of the α-helical conformation. The dipole−dipole interactions between PBLG and PAS might potentially lead to the PAS coils dissolving in the PBLG domain. Upon increasing the PAS content, the interchain hydrogen bonding of the PBLG segments was initially disrupted, and then intramolecular hydrogen bonding was induced between the PBLG segments; as a result, the content of α-helical conformations increased upon increasing the PAS content. When blended with PVPh, which could form the strongest hydrogen bonds, the fraction of the α-helical conformations of PBLG increased continuously upon increasing the PVPh content—behavior that is similar to that observed

dx.doi.org/10.1021/ma300061w | *Macromolecules* 2012, 45, 2442−2452

Table 2. Curve Fitting of the FTIR Spectroscopic Data for the C═O and Amide Groups in the PS/PBLG, PAS/PBLG, and PVPh/PBLG Blends at 25 °C

	carbonyl group		amide group in PBLG					
	free C═O of PBLG		random coil		α-helix		β-sheet	
PS/PBLG	ν (cm^{-1})	A_f (%)	ν (cm^{-1})	A_f (%)	ν (cm^{-1})	A_f (%)	ν (cm^{-1})	A_f (%)
0/100	1735	100	1692	22.7	1653	45.8	1626	34.5
20/80	1735	100	1692	23.7	1654	42.3	1626	34.0
40/60	1735	100	1694	24.0	1654	40.8	1626	35.2
50/50	1735	100	1694	23.9	1654	41.6	1626	35.5
60/40	1735	100	1693	23.7	1653	41.0	1626	35.3
80/20	1734	100	1690	25.8	1652	38.0	1626	36.2

	carbonyl group				amide group in PBLG					
	PBLG C═O		PAS C═O		random coil		α-helix		β-sheet	
PAS/PBLG	ν (cm^{-1})	A_f (%)	ν (cm^{-1})	A_f (%)	ν (cm^{-1})	A_f (%)	ν (cm^{-1})	A_f (%)	ν (cm^{-1})	A_f (%)
20/80	1735	82.1	1767	17.9	1693	21.2	1654	47.6	1626	31.2
40/60	1735	65.3	1766	34.7	1694	21.1	1655	49.2	1625	29.7
50/50	1735	63.8	1766	26.2	1695	21.2	1655	51.6	1626	27.2
60/40	1735	55.4	1765	44.6	1695	13.6	1660	62.5	1625	23.9
80/20	1731	35.0	1762	65.0			1662	81.9	1625	18.1

	carbonyl group				amide group in PBLG					
	free C═O		HB C═O		random coil		α-helix		β-sheet	
PVPh/PBLG	ν (cm^{-1})	A_f (%)	ν (cm^{-1})	A_f (%)	ν (cm^{-1})	A_f (%)	ν (cm^{-1})	A_f (%)	ν (cm^{-1})	A_f (%)
20/80	1737	76.4	1712	23.6	1692	20.0	1655	55.5	1626	24.5
40/60	1737	65.8	1713	34.2	1691	17.1	1655	63.8	1626	19.1
50/50	1737	60.1	1712	39.9	1692	14.7	1657	71.6	1625	13.7
60/40	1737	49.8	1711	50.2			1658	87.9	1625	12.1
80/20	1737	44.6	1711	55.4			1658	100		

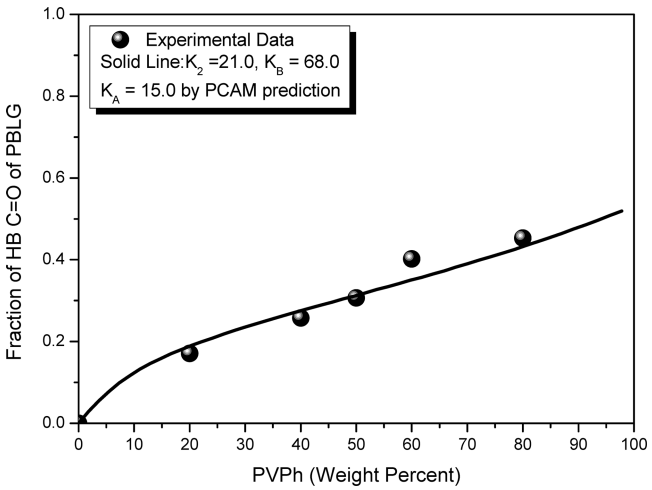


Figure 7. Fractions of hydrogen-bonded C═O groups of PBLG plotted with respect to the PVPh content, with corresponding interassociation equilibrium constants based on the Painter–Coleman association model.

upon adding PAS. Notably, however, the fraction of the α-helical conformations of PBLG in the PVPh/PBLG blend system was higher than that in the PAS/PBLG blends at the same PBLG content. Therefore, the formation of α-helical conformations for PBLG was highly dependent on the strength of the intermolecular interaction. Floudas et al. also noted that suppression of the β-sheet secondary structure of polyalanine (PALa) occurred in PBLG-*b*-PALa copolymers as a result of a thermodynamic field created by the enthalpic interactions of unlike blocks.[64] In our present study, the fraction of α-helical conformations for PBLG was related to the strength of intermolecular interaction, with both following the order PVPh/PBLG (hydrogen bonding) > PAS/PBLG (dipole–dipole) > PS/PBLG (π–π). It is well-established that the α-helical and β-sheet conformations of peptides are stabilized by intra- and intermolecular hydrogen-bonding interactions, respectively. In miscible PVPh/PBLG blends, interchain hydrogen bonding of the PBLG segments initially disrupted and then induced intrachain hydrogen bonding between the PBLG segments upon increasing the PVPh content; as a result, the content of α-helical conformations increased upon increasing the PVPh content.

Solid State NMR Spectroscopic Analyses of Polymer Blends. We also identified the secondary structures of the polypeptides on the basis of their distinctly different resonances in solid state NMR spectra. Figure 9 displays the ^{13}C CP/MAS spectra of the PS/PBLG, PAS/PBLG, and PVPh/PBLG blends at room temperature. The different ^{13}C chemical shifts of the C_α and amide C═O resonances were related to the different local conformations of the individual amino acid residues, characterized by the dihedral angles and their types of intermolecular and intramolecular hydrogen-bonding interactions.[65,66] In the case of pure PBLG, the side chains could stabilize the α-helical secondary structure; the chemical shifts of the corresponding C_α and amide C═O resonances appeared at 57.5 and 176 ppm, respectively. In the β-sheet conformation, these chemical shifts (52.7 and 172 ppm, respectively) were located upfield by approximately 4–5 ppm relative to those for the α-helical conformations.[1,67] Figure 10 provides assignments for the other peaks, as annotated in Scheme 1. From the C═O region of the spectrum of the PS/PBLG blend system, the content of α-helical conformations was almost identical to that

dx.doi.org/10.1021/ma300061w | *Macromolecules* 2012, 45, 2442–2452

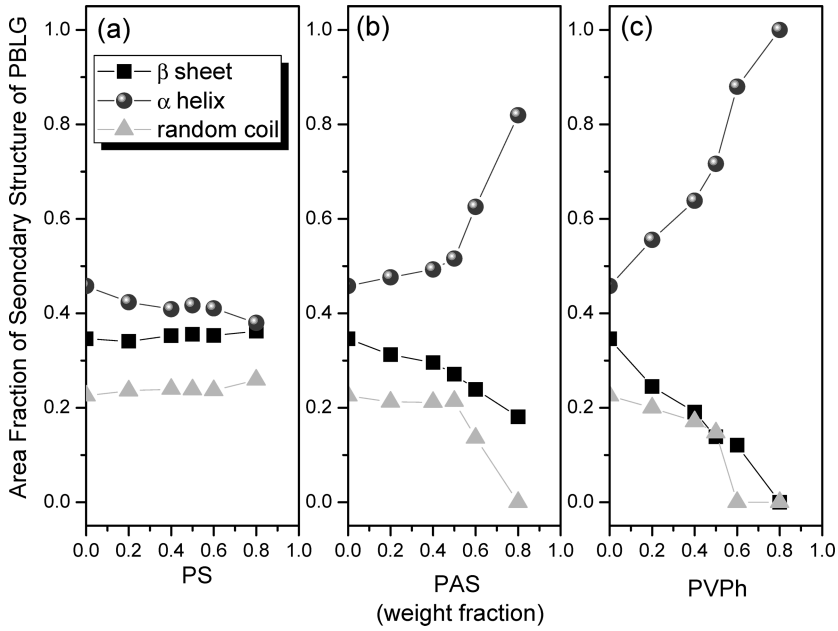


Figure 8. Secondary structures of PBLG in the (a) PS/PBLG, (b) PAS/PBLG, and (c) PVPh/PBLG blends.

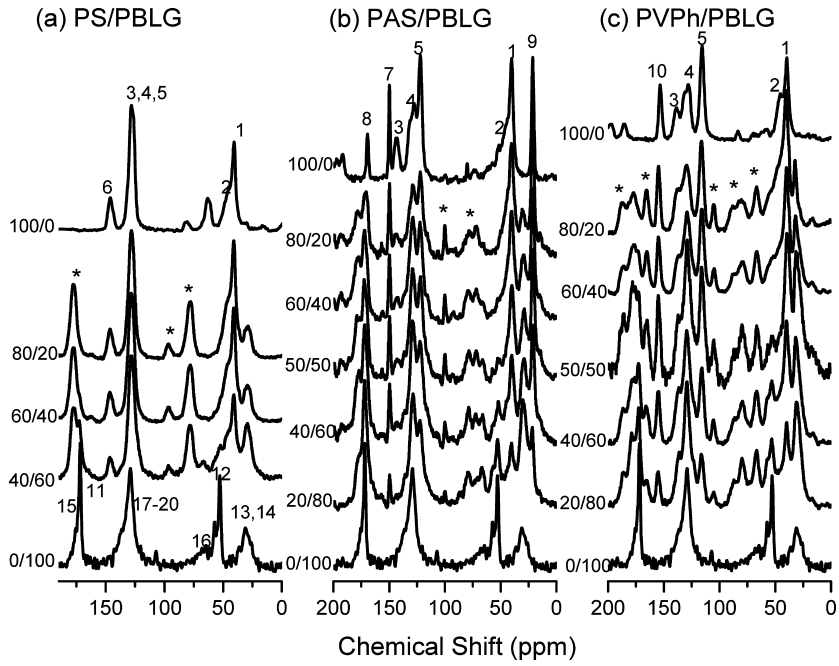


Figure 9. ^{13}C CPMAS spectra (recorded at room temperature) of the (a) PS/PBLG, (b) PAS/PBLG, and (c) PVPh/PBLG blends.

of pure PBLG; in the PAS/PBLG and PVPh/PBLG blend systems, however, the contents of α-helical conformations increased upon increasing the PAS and PVPh contents (Figure 10). In addition, the peak at 153.2 ppm represents the resonance of the phenolic carbon atom of pure PVPh (C-2, Figure 10b);[46−48] we observed a downfield shift of 2.1 ppm for this signal in the PVPh/PBLG = 20/80 blend, relative to that the pure PVPh, implying that intermolecular interassociation occurred between the OH groups of PVPh and the C═O groups of PBLG. We also observed a new peak near 173−174 ppm (downfield to the signals of both the C═O groups and β-sheet of PBLG) in the C═O region, presumably representing the hydrogen-bonded C═O groups. The contribution of a second signal related to the hydrogen-bonded C═O groups is consistent with our observations from the FTIR spectroscopic analyses. Specific interactions in polymer blends can affect the chemical environments of neighboring molecules, resulting in upfield or downfield shifts of the signals representing their resonances.[68,69]

WAXD Analyses of Polymer Blends. We used WAXD at 393 K to identify the secondary structural changes in the PS/PBGL, PAS/PBLG, and PVPh/PBLG blends (Figure 11). Here, we discuss the effects of the strength of the intermolecular interactions between the PS derivatives and PBLG on the type of secondary structure. For pure PBGL at a DP of 6, the diffraction pattern reveals the presence of β-sheet secondary structures. The first peak at a value of q of 0.38 reflects the distance (d = 1.67 nm) between the backbones in

dx.doi.org/10.1021/ma300061w | *Macromolecules* 2012, 45, 2442−2452

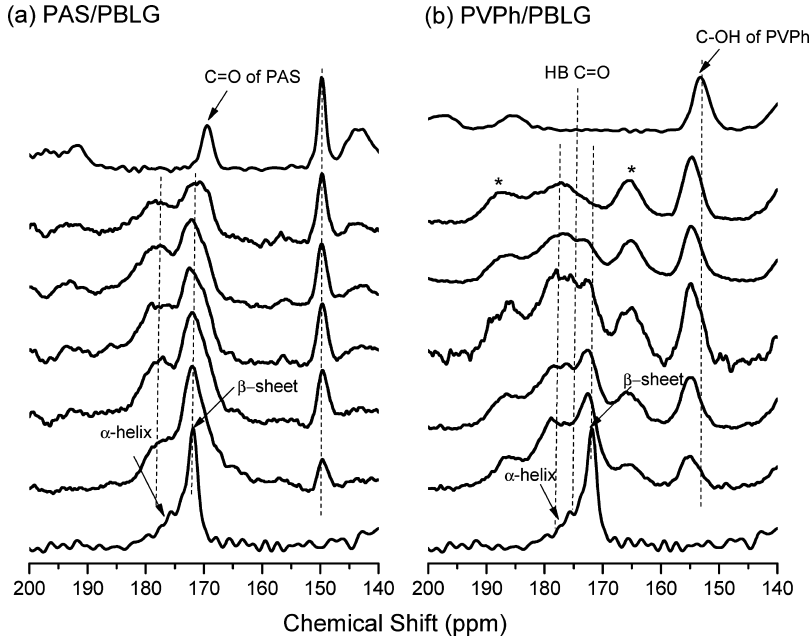


Figure 10. Scale-expanded solid state ^{13}C NMR spectra (displaying signals for the C═O groups) of the (a) PAS/PBLG and (b) PVPh/PBLG blends.

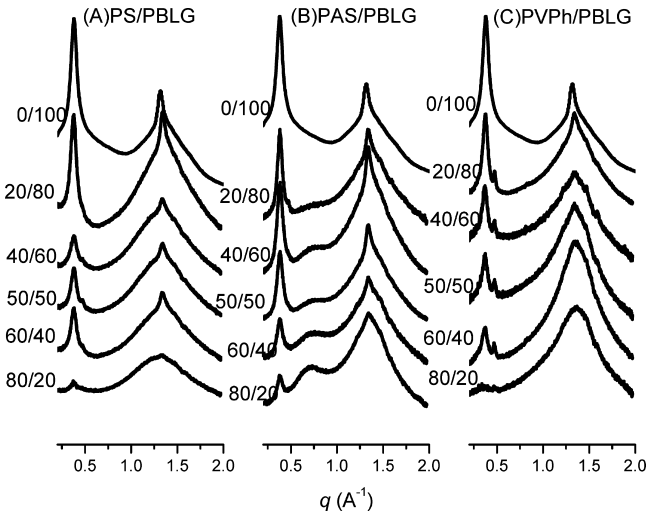


Figure 11. WAXD patterns (recorded at 393 K) of the (a) PS/PBLG, (b) PAS/PBLG, and (c) PVPh/PBLG blends.

the antiparallel β-pleated sheet structure; the reflection at a value of q of 1.34 (d = 0.468 nm) represents the intermolecular distance between adjacent peptide chains within one lamellae, and the broad amorphous region at a value of q of 1.54 originates mainly from the long amorphous side chains.[1] The X-ray patterns at values of q of 0.38 and 1.34 remained almost unchanged upon increasing the PS content, indicating that the secondary structure of PBLG was insensitive to the $\pi-\pi$ interactions occurring with PS, consistent with the conclusions drawn from our analysis of the FTIR spectra. In contrast, the X-ray patterns remained almost unchanged upon increasing the PAS content in the blends; this result differs from that determined from our FTIR spectroscopic analyses, where the α-helical conformation was stabilized, through dipole−dipole interactions, upon increasing the PAS content. We suspect that the conflicting evidence arose because we recorded the WAXD data at a higher temperature (393 K), with the fraction of α-helical conformations decreasing upon increasing the temperature. For the blends with PVPh, which could form the strongest interactions (hydrogen bonds), we observed the appearance of a diffraction peak at a value of q of 0.48, associated with α-helical secondary structures. This feature suggests the presence of that particular conformation in PBLG/PVPh blends, with 2D hexagonal packing of cylinders composed of 18/5 α-helices with a cylinder distance of 1.36 nm.[1] The structure of PBLG has been described as a nematic-like paracrystal with periodic packing of α-helices in the direction lateral to the chain axis. From FTIR spectra, solid state NMR spectra, and WAXD patterns, we obtained the following information regarding the PBLG blends with PS, PAS, and PVPh: (i) for pure PBLG, β-sheet secondary structures are favored; (ii) the α-helical secondary structure is favored for PBLG when dipole−dipole interactions exist with PAS or strong hydrogen bonds occur with PVPh; (iii) weak $\pi-\pi$ interactions with PS do not induce the α-helical secondary structure of PBLG. Thus, the formation of α-helical conformations for PBLG is strongly dependent on the strength of the intermolecular interactions with the functional groups presented on the PS derivatives. Accordingly, even if peptides adopt both α-helical and β-sheet conformations in their pure state, the incorporation of strongly hydrogen-bonding donor polymers (e.g., phenolic resin, PVPh) can induce conformational stabilization, resulting in most of the peptide segments being constrained into the α-helical secondary structures.

Scheme 2 summarizes the possible morphologies, secondary structures, and intermolecular interactions in the blends of PBLG with the PS, PAS, and PVPh homopolymers. The α-helical and β-sheet conformations are stabilized by intra- and intermolecular hydrogen-bonding interactions, respectively. Upon blending with PS, which interacts with PBLG through $\pi-\pi$ stacking, phase separation occurred such that the PS units could not dissolve in the PBLG matrix; because the intra- and intermolecular hydrogen-bonding interactions of PBLG were not disrupted by the PS coils, the secondary structures of PBLG remained almost unchanged upon increasing the PS content.

dx.doi.org/10.1021/ma300061w | Macromolecules 2012, 45, 2442−2452

Because of the stronger dipole−dipole interactions that occurred upon blending with the PAS homopolymer, the PAS coils could dissolve in the PBLG matrix, forming a miscible blend as determined through DSC analysis; thus, the intermolecular hydrogen bonding of PBLG was disrupted in the blends with PAS, favoring greater intramolecular hydrogen bonding of PBLG. That is, the partial fraction of β-sheets transformed into α-helical conformations upon increasing the PAS content. When blending PBLG with PVPh, which could form the strongest noncovalent interactions (hydrogen bonds), we observed phenomena similar to that in the PBLG/PAS system. Notably, however, because the intermolecular interactions with the PVPh coils were stronger than the dipole−dipole interactions with the PAS coils, the fractions of α-helical conformations in the PVPh/PBLG blends were higher than those in the PAS/PBLG blends at the same PBLG content. The fraction of α-helical conformations for PBLG correlated with the strength of the intermolecular interactions, with both increasing in the order PVPh/PBLG (hydrogen bonding) > PAS/PBLG (dipole−dipole) > PS/PBLG ($\pi-\pi$).

CONCLUSIONS

We used ATRP to synthesize homopolymers of three different polystyrene derivatives that we then blended with PBLG to induce changes in its secondary structures. DSC analysis revealed that the PS/PBLG blends were partially miscible, whereas the PAS/PBLG and PVPh/PBLG blends were completely miscible with an amorphous phase over the entire range of compositions. Data obtained from FTIR spectra revealed that the strength of the intermolecular interactions in the blends increased in the order PVPh/PBLG (hydrogen bonding) > PAS/PBLG (dipole−dipole) > PS/PBLG ($\pi-\pi$). FTIR and solid state NMR spectra and WAXD analyses all confirmed that the fraction of α-helical conformations in these three blend systems correlated strongly with the strength of the intermolecular interactions.

AUTHOR INFORMATION

Corresponding Author

*E-mail kuosw@faculty.nsysu.edu.tw; Tel 886-7 5254099.

Notes

The authors declare no competing financial interest.

ACKNOWLEDGMENTS

This study was supported financially by the National Science Council, Taiwan, Republic of China, under Contracts NSC 100-2221-E-110-029-MY3 and NSC100-2628-E-110-003.

REFERENCES

(1) Klok, H. A.; Lecommandoux, S. *Adv. Polym. Sci.* **2006**, *202*, 75.
(2) Yang, J. T.; Doty, P. *J. Am. Chem. Soc.* **1957**, *79*, 761.
(3) Perutz, M. F. *Nature* **1951**, *167*, 1053.
(4) Doty, P.; Bradbury, J. H.; Holtzer, A. M. *J. Am. Chem. Soc.* **1956**, *78*, 947.
(5) Flory, P. J. *Proc. R. Soc. London, Ser. A* **1956**, *234*, 73.
(6) Yang, J. T.; Doty, P. *J. Am. Chem. Soc.* **1957**, *79*, 761.
(7) Perutz, M. F. *Nature* **1951**, *167*, 1053.
(8) Tohyama, K.; Miller, W. G. *Nature* **1981**, *289*, 813.
(9) Prystupa, D. A.; Donald, A. M. *Macromolecules* **1993**, *26*, 1947.
(10) Tohyama, K.; Miller, W. G. *Nature* **1981**, *289*, 813.
(11) Prystupa, D. A.; Donald, A. M. *Macromolecules* **1993**, *26*, 1947.
(12) Kuo, S. W.; Lee, H. F.; Chang, F. C. *J. Polym. Sci., Polym. Chem.* **2008**, *46*, 3108.
(13) Kuo, S. W.; Lee, H. F.; Huang, W. J.; Jeong, K. U.; Chang, F. C. *Macromolecules* **2009**, *42*, 1619.
(14) Papadopoulous, P.; Floudas, G.; Klok, H. A.; Schnell, I.; Pakula, T. *Biomacromolecules* **2004**, *5*, 81.
(15) Klok, H. A.; Lecommandoux, S. *Adv. Mater.* **2001**, *13*, 1217.
(16) Klok, H. A.; Langenwalter, J. F.; Lecommandoux, S. *Macromolecules* **2000**, *33*, 7819.
(17) Sanchez-Ferrer, A.; Mezzenga, R. *Macromolecules* **2010**, *43*, 1093.
(18) Zhou, Q, H.; Zheng, J. K.; Shen, Z. H.; Fan, X, H.; Chen, X. F.; Zhou, Q. F. *Macromolecules* **2010**, *43*, 5367.
(19) Lee, H. F.; Sheu, H. S.; Jeng, U. S.; Huang, C. F.; Chang, F. C. *Macromolecules* **2005**, *38*, 6551.
(20) Papadopoulos, P.; Floudas, G.; Schnell, I.; Aliferis, T.; Iatrou, H.; Hadjichristidis, N. *Biomacromolecules* **2005**, *6*, 2352.
(21) Ibarboure, E.; Rodriguez-Hernandez, J. *J. Polym. Sci., Polym. Chem.* **2006**, *44*, 4668.
(22) Lecommandoux, S.; Achard, M. F.; Langenwalter, J. F.; Klok, H. A. *Macromolecules* **2001**, *34*, 9100.
(23) Crespo, J. S.; Lecommandoux, S.; Borsali, R.; Klok, H. A.; Soldi, V. *Macromolecules* **2003**, *36*, 1253.
(24) Floudas, G.; Papadopoulos, P.; Klok, H. A.; Vandermeulen, G. W. M.; Rodriguez-Hernandez, J. *Macromolecules* **2003**, *36*, 3673.
(25) Hua, C.; Dong, C. M.; Wei, Y. *Biomacromolecules* **2009**, *10*, 1140.
(26) Huang, C. J.; Chang, F. C. *Macromolecules* **2008**, *41*, 7041.
(27) Kong, X.; Jenekhe, S. A. *Macromolecules* **2004**, *37*, 8180.
(28) Kuo, S. W.; Tsai, H. T. *Polymer* **2010**, *51*, 5695.
(29) Lin, Y. C.; Kuo, S. W. *J. Polym. Sci., Part A: Polym. Chem.* **2011**, *49*, 2127.
(30) Hermes, F.; Otte, K.; Brandt, J.; Grawert, M.; Borner, H. G.; Schlaad, H. *Macromolecules* **2011**, *44*, 7489.
(31) Kotharangannagari, V. K.; Sanchez-Ferrer, A.; Ruokolainen, J.; Mezzenga, R. *Macromolecules* **2011**, *44*, 4569.
(32) Painter, P. C.; Tang, W. L.; Graf, J. F.; Thomson, B.; Colema, M. M. *Macromolecules* **1991**, *24*, 3929.
(33) Asano, A.; Kurotu, T. *J. Mol. Struct.* **1998**, *441*, 129.
(34) Murata, K.; Katoh, E.; Kuroki, S.; Ando, I. *J. Mol. Struct.* **2004**, *689*, 223.
(35) Deng, X.; Hao, J.; Yuan, M.; Xiong, C.; Zhao, S. *Polym. Int.* **2001**, *50*, 37.
(36) Aoi, K.; Nakamura, R.; Okada, M. *Macromol. Chem. Phys.* **2000**, *201*, 1059.
(37) Kuo, S. W.; Chen, C. J. *Macromolecules* **2011**, *44*, 7315.
(38) Kuo, S. W.; Huang, W. J.; Huang, C. F.; Chan, S. C.; Chang, F. C. *Macromolecules* **2004**, *37*, 4164.
(39) Sheen, Y. C.; Lu, C. H.; Huang, C. F.; Kuo, S. W.; Chang, F. C. *Polymer* **2008**, *49*, 4017.
(40) Huang, K. W.; Tsai, L. W.; Kuo, S. W. *Polymer* **2009**, *50*, 4876.
(41) Daly, W. H.; Poche, D. *Tetrahedron Lett.* **1988**, *29*, 5859.
(42) Kuo, S. W.; Huang, C. F.; Lu, C. H.; Lin, H. M.; Jeong, K. U.; Chang, F. C. *Macromol. Chem. Phys.* **2006**, *207*, 2006.
(43) Kuo, S. W.; Huang, C. F.; Tung, P. H.; Huang, W. J.; Huang, J. M.; Chang, F. C. *Polymer* **2005**, *46*, 9348.
(44) Kuo, S. W.; Chang, F. C. *Polymer* **2001**, *42*, 9843.
(45) Kuo, S. W.; Chang, F. C. *Macromol. Chem. Phys.* **2002**, *203*, 868.
(46) Kuo, S. W.; Chang, F. C. *Macromolecules* **2001**, *34*, 4089.
(47) Kuo, S. W.; Chang, F. C. *Macromolecules* **2001**, *34*, 5224.
(48) Kuo, S. W.; Tung, P. H.; Chang, F. C. *Macromolecules* **2006**, *39*, 9388.
(49) Lodge, T. P.; Wood, E. R.; Haley, J. C. *J. Polym. Sci., Part B: Polym. Phys.* **2006**, *44*, 756.
(50) Lodge, T. P.; Mcleish, T. C. B. *Macromolecules* **2000**, *33*, 5278.
(51) Papadopoulos, P.; Floudas; Schnell, I.; Klok, H. A.; Aliferis, T.; Iatrou, H.; Hadjichristidis, N. *J. Chem. Phys.* **2005**, *122*, 224906.
(52) Fox, A.; Loshaek, S. *J. Polym. Sci.* **1955**, *15*, 371.
(53) Barclay, G. G.; Hawker, C. J.; Ito, H.; Orellana, A.; Malenfant, P. R. L.; Sinta, R. F. *Macromolecules* **1998**, *31*, 1024.

(54) Coleman, M. M.; Graf, J. F.; Painter, P. C. *Specific Interactions and the Miscibility of Polymer Blends*; Technomic Publishing: Lancaster, PA, 1991.
(55) Coleman, M. M.; Painter, P. C. *Prog. Polym. Sci.* **1995**, *20*, 1.
(56) Coleman, M. M.; Painter, P. C. *Polymer Blend*; Paul, D. R., Bucknall, C. B., Eds.; Wiley: New York, 2000.
(57) Surewicz, W. K.; Mantsch, H. H. *Biochim. Biophys. Acta* **1988**, *952*, 115.
(58) Lin, C. L.; Chen, W. C.; Liao, C. S.; Su, Y. C.; Huang, C. F.; Kuo, S. W.; Chang, F. C. *Macromolecules* **2005**, *38*, 6435.
(59) Kuo, S. W. *J. Polym. Res.* **2008**, *15*, 459.
(60) He, Y.; Zhu, B.; Inoue, Y. *Prog. Polym. Sci.* **2004**, *29*, 1021.
(61) Lin, C. T.; Kuo, S. W.; Chang, F. C. *J. Phys. Chem. B* **2010**, *114*, 1603.
(62) Kuo, S. W.; Lin, C. T.; Chen, J. K.; Ko, F. H.; Chang, F. C.; Jeong, K. U. *Polymer* **2011**, *52*, 2600.
(63) Jeon, S.; Choo, J.; Sohn, D.; Lee, S. N. *Polymer* **2001**, *42*, 9915.
(64) Gitsas, A.; Floudas, G.; Mondeshki, M.; Spiess, H. W.; Aliferis, T.; Iatrou, H.; Hadjichristidis, N. *Macromolecules* **2008**, *41*, 8072.
(65) Murata, K.; Katoh, E.; Kuroki, S.; Ando, I. *J. Mol. Struct.* **2004**, *689*, 223.
(66) Kricheldorf, H. R.; Muller, D. *Macromolecules* **1983**, *16*, 615.
(67) Floudas, G.; Spiess, H. W. *Macromol. Rapid Commun.* **2009**, *30*, 278.
(68) Huang, M. W.; Kuo, S. W.; Wu, H. D.; Chang, F. C.; Fang, S. Y. *Polymer* **2002**, *43*, 2479.
(69) Hill, D. J. T.; Whittaker, A. K.; Wong, K. W. *Macromolecules* **1999**, *32*, 5285.

Macromolecules

Article

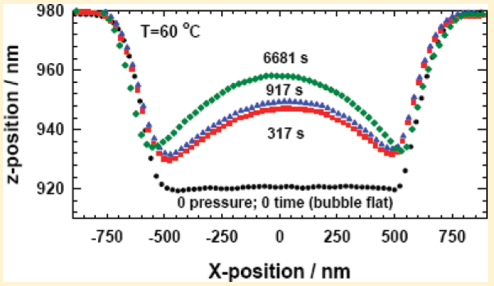
pubs.acs.org/Macromolecules

Exceptional Property Changes in Ultrathin Films of Polycarbonate: Glass Temperature, Rubbery Stiffening, and Flow

Paul A. O'Connell,[†] Jian Wang,[†] T. Adeniyi Ishola, and Gregory B. McKenna*

Department of Chemical Engineering, Whitacre College of Engineering, Texas Tech University, Lubbock, Texas 79409-3121, United States

ABSTRACT: The TTU nanobubble inflation method has been used to determine the creep compliance of ultrathin films of polycarbonate over a thickness range of 3−22 nm and a temperature range from ambient (25 °C) to 112 °C. The compliance from the segmental regime through a stiffened rubbery plateau regime was able to be measured for films of thickness from 4.2 nm and above, and the results show a greatly reduced glass temperature and stiffening of the rubbery regime relative to that of the macroscopic material. In the case of the 3 nm film, we found that even at ambient conditions the system is above the enhanced rubbery plateau and is in the terminal flow regime as evidenced by a slope of unity on a double-logarithmic representation of the compliance versus time. The biaxial viscosity of the film at this temperature is ∼2.7 × 10^{11} Pa s. We also observed flow behavior in a 9.1 nm thick film that had been heated to 75 °C, i.e., 10 °C above the reduced glass transition of the thin film. These are the first evidence of polymer flow in the equibiaxial deformation geometry in the nanobubble inflation experiments. Interpretation of the results suggests that the glass transition of the 3 nm film is ∼10 °C below room temperature, which implies a glass transition reduction of 122 °C, which is substantially greater than has been reported previously for any polymer and particularly surprising because the polymer is of relatively low molecular weight, in a regime where one might anticipate a weak dependence of T_g on film thickness. We also observe that the plateau stiffening of the polycarbonate, even to 4.2 nm thickness, falls on the extrapolation of the compliance vs thickness behavior of polystyrene and poly(vinyl acetate) observed previously. This implies a stiffening of over 3 orders of magnitude in the nominal rubbery regime. There is also a stiffening of approximately a factor of 2 in the glassy regime for these films. The results are considered in the context of prior work on ultrathin films.



INTRODUCTION

In past work,[1−7] we have successfully used the Texas Tech University (TTU) nanobubble inflation device to investigate the viscoelastic creep behavior of nanometric thickness polystyrene (PS) and poly(vinyl acetate) (PVAc) through the glass transition regime and to the rubbery plateau region. In addition, we were successful in the examination of the rubbery plateau behavior of a poly(*n*-butyl methacrylate) (PBMA) above its glass transition regime.[8] In all of those instances we found, surprisingly, that the rubbery plateau regime exhibited considerable stiffening relative to that of the macroscopic material, with the stiffening following approximately an inverse square law in film thickness for the PS and PVAc, while the stiffening was somewhat less for the PBMA exhibiting a power law closer to 0.83 in film thickness. Along with these findings, we found that the PS exhibited a dramatic reduction in the glass transition temperature, consistent with that seen in other measurements of the T_g reduction in freely standing polystyrene films, though not of the same magnitude. The measurements on PVAc films showed little to no change in the glass transition temperature. A very interesting result in all of those investigations was that we did not see in any circumstance the terminal flow of the material; i.e., the creep compliance did not increase once the rubbery plateau was achieved even when times longer than the expected reptation time for the material were reached.

In the present work, we enlarge our investigation of materials to polycarbonate ultrathin films and show two landmark results not previously achieved. First, we are able to measure the creep compliance from glassy regime to the rubbery regime for films as thin as 4.2 nm, and there, we observe extreme rubbery stiffening, very large reductions of the glass transition temperature (≈97 °C), and stiffening of the glassy compliance. Second, we have been able to make measurements on films as thin as 3 nm and evidence continued reduction of the glass temperature as film thickness decreases to this dimension. As we show, the polycarbonate at this film thickness exhibits flow at room temperature, though under conditions of deformation significantly smaller than what would be expected if one were to attain the macroscopic rubbery plateau.

The rest of the paper is organized as follows: after this introduction, we present the experimental materials and methods, we then present the results of the bubble inflation measurements, and follow this with a discussion of the results and an attempt to put them into the context of the current

Received: January 14, 2012
Revised: February 17, 2012
Published: February 27, 2012

 © 2012 American Chemical Society dx.doi.org/10.1021/ma300098h | *Macromolecules* 2012, 45, 2453−2459

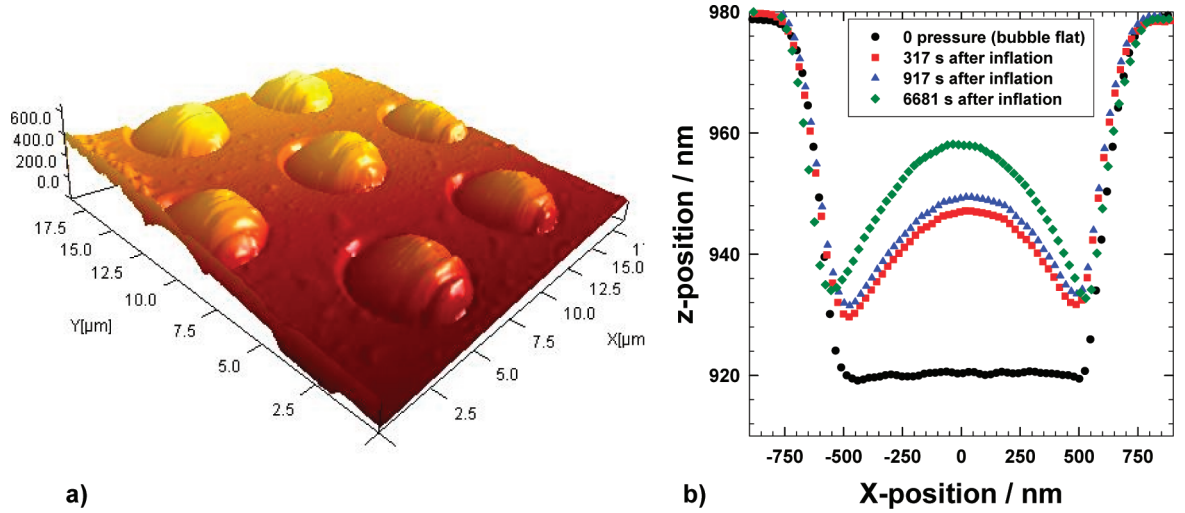


Figure 1. (a) Representative AFM image of 5 μm diameter bubbles for a 15 nm thick polycarbonate film. P = 3.5 kPa, inflated at 70 °C and imaged at room temperature. (b) Profiles of bubble shape for a 9.1 nm thick polycarbonate film at 60 °C for different creep times, as indicated. Bubble diameter was 1.2 μm. Pressure was 27.6 kPa.

understanding of the behavior of ultrathin polymer films. We finish with a set of conclusions.

MATERIALS AND METHODS

Materials. The prime material used in the present work was General Electric Lexan LS-2, which is a UV-stabilized, commercial grade bisphenol A polycarbonate[9] having a weight-average molecular weight of 47 kg/mol with a polydispersity of 2.55. The calorimetric T_g of this material is reported to be 414.2 K (141 °C)[9−11] after rapid cooling and heating at 10 K/min, and the T_g was taken as the midpoint of the measured heat flow signal in the transition region. Our current measurements give a glass transition from the limiting fictive temperature[12,13] T_f^i = 410.1 K (136.9 °C) after cooling at 10 K/min and reheating at 10 K/min. We use this latter value as the T_g throughout the paper. We also use a PVAc from our prior studies[1−3,5] that has a T_g = 303.8 K (30.6 °C) from cooling at 10 K/min.[1] The PVAc has a molecular weight of 157 kg/mol and M_w/M_n = 2.731.

The polycarbonate films were spin-cast from chloroform solution onto mica sheets at a speed of 2000 rpm for 30 s. The solution concentration determined the final film thickness, which was measured by a method developed in our laboratories[2] that involves scoring the films and determining the height change with the atomic force microscope. The films were floated from the mica onto a water surface and picked up onto a template containing through holes. The samples were then annealed at the reduced T_g + 15 K of the thin film for 15 min to ensure adhesion to the template. As in our in past work we used both 1.2 μm diameter and 5 μm diameter holes. Testing involves placing the templates with the films into a special device built for the purpose that fits into the AFM. By applying pressure across the film membrane at a controlled temperature, one can observe the bubble growth by scanning the template in the AFM. From the membrane approximation for the deformation of thin plates (films) we determine the biaxial creep compliance of the films. In all cases the membrane height was greater than 3 times the membrane thickness; hence, the membrane approximation is valid.[2,3,14]

Bubble Inflation Experiment. The TTU bubble inflation test method and methods of analysis have been described thoroughly in our prior publications.[1−8] Briefly, the creep measurements are made by placing a constant pressure across the thin polymer film (on the templates) and measuring the changing bubble height profile. Because the stress in the bubble decreases with increasing bubble height during the test, we apply Boltzmann superposition to the nonconstant stress history and the measured strain history to "back out" the creep compliance, as described previously (see ref 5).

The experiments in the present case were performed for film thicknesses of polycarbonate from 3 to 22 nm. The reason for the limited upper range of thickness is that the high glass transition temperature of polycarbonate in the bulk state, i.e., for thick films, is above the temperature capability of our instrument. However, as we will show, the 22 nm thickness films have a sufficiently reduced glass transition temperature that the creep experiments can be performed at below 112 °C even though the T_g of the PC is 136.9 °C. Time−temperature superposition was applied to all film thicknesses to obtain master curves of the creep response from the glassy state through to a rubbery plateau state. Temperature shift factors were obtained, and these are used in the determination of the glass transition reductions. The rubbery plateau compliances found are reported as a function of film thickness.

As part of the present investigation we also carried out creep experiments on films of poly(vinyl acetate) (PVAc) for very long times and at temperatures above the glass transition temperature to determine if we could obtain flow in this material, for reasons to be described below. Macroscopic measurements for the PVAc were obtained in our laboratories using a magnetic bearing torsional creep apparatus available in our laboratories and originally built and developed by Plazek.[15]

Importantly, the experiments are performed at stresses that are generally in the linear viscoelastic regime, though in some instances this may be slightly exceeded. Also, we have shown that measurements from bubble diameters of 1.2 and 5 μm give similar results. It is generally advantageous to perform experiments with the smaller diameter bubbles when the film thicknesses are small so that the pressures required to inflate the membranes can be larger, consistent with our bubble inflation pressure control being limited to a minimum of about 0.10 psi (0.4 kPa). We ran our experiments in the present work at conditions similar to the prior work[1−8] but with smaller strains. The stress levels are time-varying because they decrease as the bubble inflates. This has been discussed in the original publications, but we reiterate it here to emphasize that the stress values, by the time we can measure them, are always sub(macroscopic) yield, and the strains in this study were always less than 1%.

RESULTS AND DISCUSSION

PC Behavior: T_g Reduction and Rubbery Stiffening. Figure 1a shows a typical AFM bubble inflation image for a 15 nm PC film on a 5 μm hole diameter template. Figure 1b shows height profiles at different times for a 1.2 μm diameter bubble for a 9.1 nm thick film and illustrates how the film creeps. Figure 2 shows the derived creep response for a 22 nm thick

dx.doi.org/10.1021/ma300098h | Macromolecules 2012, 45, 2453−2459

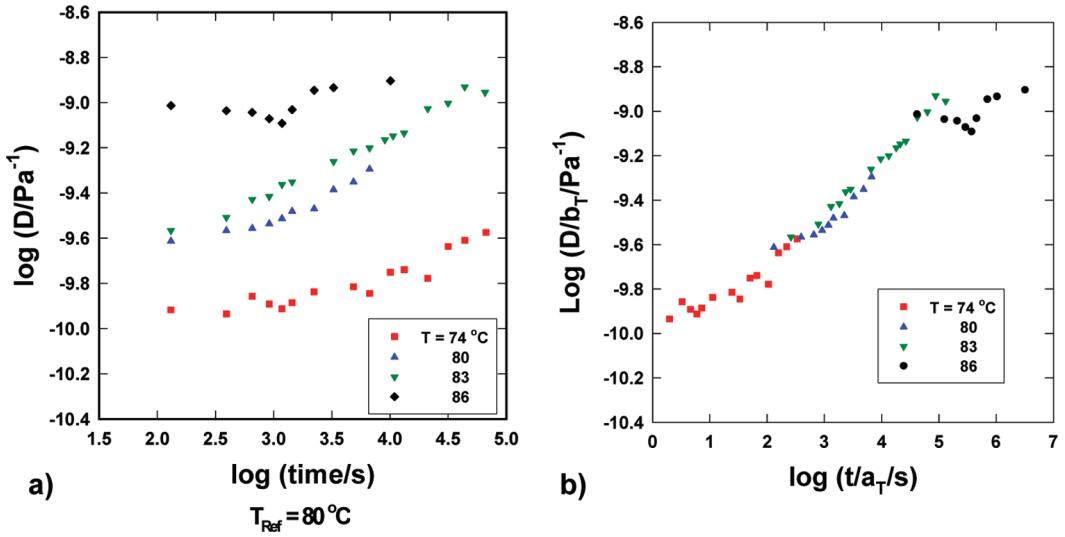


Figure 2. (a) Creep compliance for a 22 nm polycarbonate film at temperatures indicated. (b) Master curve for creep compliance of a 22 nm polycarbonate film with T_{ref} = 80 °C. Remark that the macroscopic rubbery plateau for polycarbonate is at log D = −7.1 (D in Pa^{-1}).

polycarbonate film at four temperatures as well as the corresponding master curve obtained by time−temperature superposition with a reference temperature of 80 °C. In the data we see that one achieves creep from the glassy regime to the rubbery regime at a temperature well below the macroscopic glass transition temperature of 136.9 °C. Figure 3 shows the creep master curves for the 22 nm film along with

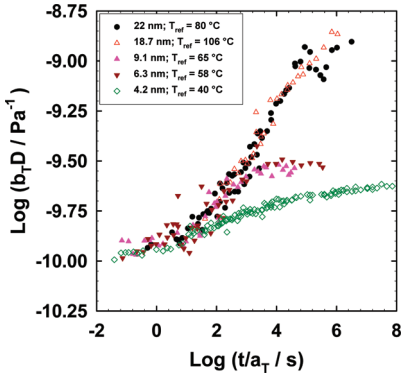


Figure 3. Creep master curves for polycarbonate ultrathin films having thicknesses from 4.2 to 22 nm. Reference temperatures are indicated in the figure.

those for 4 other film thicknesses from 4.2 to 18.7 nm. The temperatures of reference for each master curve are given in the figure. The data of Figure 3 show two clear trends. First, the glass transition temperature for the PC is considerably reduced relative to the bulk temperature, and the amount of reduction in the T_g increases as the films become thinner. We return to the quantitative measure of the reduction in T_g in a subsequent paragraph. The second trend that we see is that the rubbery regime stiffens significantly in these thin films and the compliance is significantly below the expected value for the rubbery plateau of polycarbonate. Neither of these results is *per se* surprising as the results are qualitatively similar to what we have reported previously for polystyrene for the reduction in the T_g as well as for the rubbery stiffening of both PS and PVAc. We will come back to the quantitative comparison subsequently. Perhaps more interesting is the observation we make that the films down to a thickness of 4.2 nm seem to behave consistently with what we have observed for the other polymers; i.e., they creep from the glass to a rubbery plateau but do not flow. We now turn to the problem of the flow of the ultrathin polymer films.

PC Behavior: Flow. In none of our prior work did we observe flow of our ultrathin polymer films, although the times of some of the experiments were long enough that the bulk material at the same distance above the glass transition temperature would have been well into the terminal flow regime. We see the same behavior in the data presented in Figure 3 for the polycarbonate and for films as thin as 4.2 nm. However, when we carried out our experiments for a film having a thickness of 3 nm, we obtained a surprising result. As shown in Figure 4, we observe flow of the film at the shortest

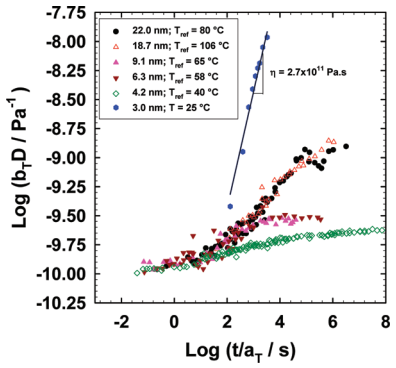


Figure 4. Creep master curves for polycarbonate ultrathin films having thicknesses from 4.2 to 22 nm, as in Figure 3. Hexagons with line show creep/flow response of the 3 nm polycarbonate film at T = 25 °C.

times we could measure (≈100 s) and at room temperature (T = 25 °C). The implications of the data are striking. First, we have a film of polycarbonate at ∼112 °C below the macroscopic glass transition temperature, and we observe viscous flow as evidenced by the slope of unity drawn through the data and the apparent viscosity of 2.7 × 10^{11} Pa s, close to what one might expect near to the glass transition temperature for such a low molecular weight, but entangled, polymer. We note that the

dx.doi.org/10.1021/ma300098h | *Macromolecules* 2012, 45, 2453−2459

molecular weight for entanglement in polycarbonate is ~2.5 kg/mol,[16] which gives an approximate entanglement density of M_w/M_e of 19/chain (M_n/M_e = 7.6). We also note that the flow is occurring at compliance values much below the rubbery plateau for the macroscopic material. In a sense, it is showing a liquidlike behavior if we did not know that there is a very stiff rubbery plateau compliance in these ultrathin films.

In order to further examine the problem and because we had not previously seen flow in our bubble inflation experiments, we repeated our measurements on the 9.1 nm thick PC film that had an approximate T_g of 65 °C (master curve reference temperature), but now at 75 °C. As we see in Figure 5, where

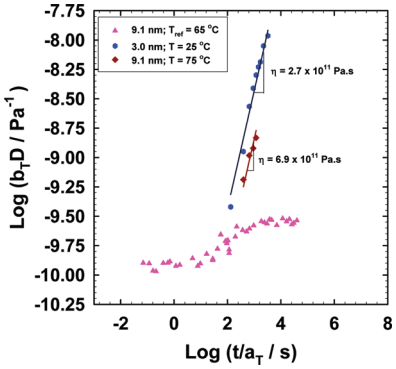


Figure 5. Comparison of flow of PC film of 3 nm thickness with the behavior of the 9.1 nm thickness film. The data for the test at 75 °C correspond to the same time scale as those obtained for the 3 nm film at 25 °C. The lines of slope unity are drawn to indicate that the samples have achieved steady state flow and biaxial viscosities are indicated.

we plot the data as creep compliance vs reduced time, the sample at 75 °C creeps to terminal flow at a similar time to the 3 nm thick film at 25 °C and with a viscosity of ~6.9 × 10^{11} Pa s, not greatly different from that of the room temperature viscosity of the 3 nm thick film. This suggests that the 3 nm film is ~10 °C above the glass transition temperature when it is at ambient conditions.

But, if the PC can flow, can we obtain conditions in which, e.g., the PVAc can flow? PVAc has an entanglement molecular weight of 9.1 kg/mol;[17] hence, the PVAc used in our experiments has an entanglement density of approximately M_w/M_e = 17/chain (M_n/M_e = 6.3), not dramatically different from the entanglement density for the polycarbonate. In Figure 6, we show the creep response of a 93 nm film of PVAc as a master curve created using temperatures up to 60 °C, which is 30 °C above the macroscopic glass transition of this material. For comparison, we show the creep response obtained from macroscopic rheology for the same material using a conventional rheometer.[15] As seen, the rubbery plateau region is stiffened and no flow occurs for times (reduced times) much longer than the time for which flow would be expected from the data for the macroscopic material. We did not perform further experiments due to issues at long times, such as film rupture, that limited our experimental time window. But it seems that the resistance to flow in the films is greatly enhanced relative to the bulk material. While the polystyrene used in our prior works had a molecular weight of ~10^3 kg/mol, hence an entanglement density of 55/chain, both the PVAc and the polycarbonate have much lower entanglement densities. Hence, it is unclear why the PC could flow and the PVAc could not. If

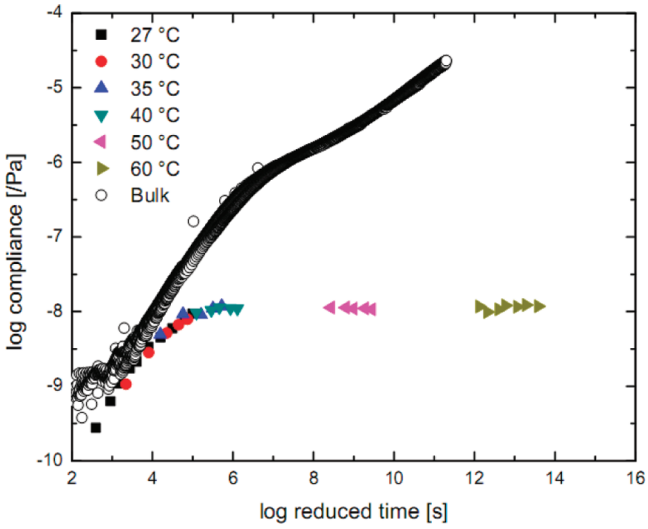


Figure 6. Comparison of creep master curves for poly(vinyl acetate) film having a thickness of of 93 nm with the macroscopic behavior of the same material. T_{ref} = 30 °C. Figure shows that even for extremely long reduced times the PVAc does not flow, though it is above its glass transition temperature.

the entanglement density is lowered by film confinement,[18] it may simply be that we are able to make thinner films with the PC (we were unable to make films thinner than 24 nm with the PVAc). It would be worth the effort to investigate the flow behavior of the PS thin films that have M_w/M_e similar to the polycarbonate investigated here, though we have not yet successfully made films of PS below 9 nm for the bubble inflation measurements and that was with the 10^3 kg/mol system. Lower molecular weight samples are harder to work with, and we also find that thinner films are prone to rupture. Finally, it is worth remarking that the studies of PBMA,[8] though all performed above the macroscopic glass transition temperature, also showed no evidence of flow.

PC Behavior: Glassy Compliance. In our prior work with polystyrene,[5] we reported that the glassy compliance was somewhat stiffened relative to the macroscopic glassy compliance. In the present work, we also find modest stiffening of the glassy compliance with the value being approximately D_g = 1 × 10^{-10} Pa^{-1}, which corresponds to a modulus of $E_{biax,g}$ = 10 GPa. From the known shear modulus at 30 °C,[11] assuming that E_{biax} = 6 G, we find a conservative value of the corresponding macroscopic modulus of 4.14 GPa. This is consistent with uniaxial moduli reported by Legrand[19] at 0 °C and 10 s of 2.25 GPa. This would give a biaxial modulus, assuming E_{biax} = 2E, of 5.5 GPa. Clearly, there is a stiffening of the glassy regime of ~2 in these ultrathin polycarbonate films.

Quantitative Analysis of T_g Reduction and Rubbery Stiffening of PC Ultrathin Films. In order to determine the reduction of the glass transition temperature of the ultrathin polycarbonate films, we plotted the temperature shift factors vs reciprocal temperature for each of the film thicknesses. Using the reference temperature as shift factor log a_T = 0 and simply comparing the ΔT_g required to shift the bulk VFT or WLF curve to the reference temperature, we obtain Figure 7. Assuming the macroscopic T_g to be 136.9 °C, we can determine the T_g reduction vs film thickness, as shown in Figure 8. We add that for the 3 nm thick film we have assumed that the T_g is 10 °C below room temperature (for the reasons explained above) in order to include that point on the figure.

dx.doi.org/10.1021/ma300098h | Macromolecules 2012, 45, 2453−2459

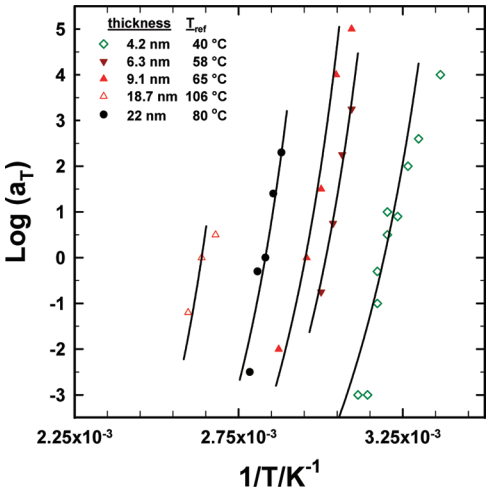


Figure 7. Time−temperature shift factors vs $1/T$ for polycarbonate ultrathin films of different thickness. Solid lines are calculated from the macroscopic VFT behavior shifted to the reference temperatures indicated. The reference temperatures determine the reduced glass transition temperatures.

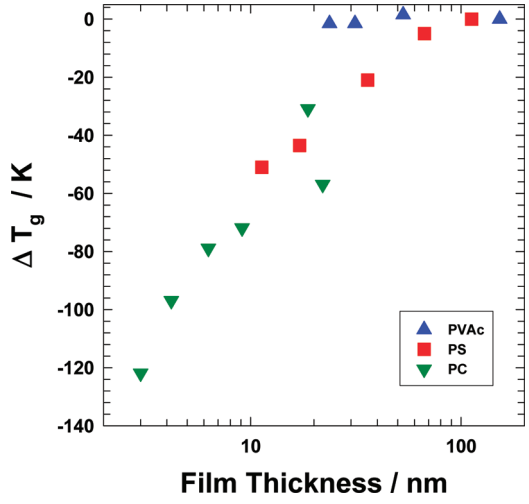


Figure 8. Reduction in the glass transition temperature as a function of film thickness in ultrathin films of polycarbonate (PC), polystyrene (PS), and poly(vinyl acetate) (PVAc).

For comparison, we show the T_g reductions obtained similarly for PS and PVAc from the TTU bubble inflation experiments. As seen, the T_g decreases for the polycarbonate are very large, perhaps the largest yet observed in polymer thin films. Furthermore, the large reductions become more surprising given that the molecular weight of the polycarbonate is relatively small, and in the seminal work on molecular weight effects in polystyrene,[20−22] there was no molecular weight effect on T_g reductions until above approximately M_w = 375 000 g/mol.

In the case of the film stiffening in the rubbery regime, it appears that the PC "rubbery plateau" compliance lies on the extrapolation of the compliance lines for PS or PVAc as shown in Figure 9. Hence, the rubbery stiffening is similar to the PS and PVAc[1,3,5−7] but differs from the poly(*n*-butyl methacrylate),[8] which has a weaker thickness dependence than the other polymers.

Placing the Results in Context. *Freely Standing Films.* There is a very broad range of literature on the behavior of

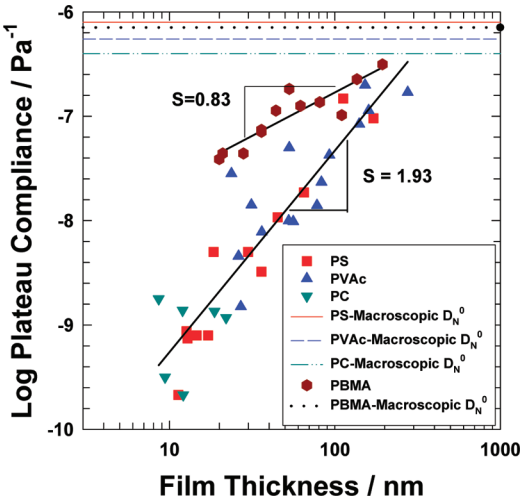


Figure 9. Comparison of the rubbery plateau compliance as a function of film thickness for polycarbonate (this study), polystyrene, and poly(vinyl acetate) (prior work). Also shown are results for poly(*n*-butyl methacrylate), which shows much less film stiffening than do the other polymers.

glass-forming materials, including polymers in film form, at the nanometer size scale.[21,23−25] Though there is much work in both small molecules in confinement and for supported polymer films, here we discuss the observations on freely standing polymer films as they are more limited and the purpose is to put the present work into that context first. In the next section we discuss briefly results from the supported polymer films and small molecules in confinement.

The first point of importance, then, is the observation of a reduction in the glass transition in freely standing films. The initial reports for polystyrene freely standing films[20,21] showed significant reductions in the glass transition temperature using Brillouin scattering and ellipsometry in the pseudothermodynamic mode[23] in which a material property is measured as temperature is scanned and an observed change in slope is interpreted as the glass transition temperature. In that work, it was found that the T_g decreased by up to ∼60 °C for film thicknesses that varied from 20 to 70 nm depending on molecular weight. For molecular weights from 120 to 378 kg/mol there was no molecular weight dependence. In the case of higher molecular weights, the thickness at which such a reduction in T_g was obtained increased, being ∼70 nm for films of 9100 kg/mol in molecular weight. Other polymers have generally been reported to show weaker reductions in T_g in freely standing films,[1,5,26,27] though there is not as great a set of measurements of the change in T_g in freely standing films as for supported films. Clearly, the polycarbonate results reported here show much greater reductions in the glass transition than do the polystyrene films (i.e., as much as 122 °C). Furthermore, this is for films having very low molecular mass. It is clear that it would be worth examining the molecular mass dependence of the T_g of polycarbonate. Unfortunately, this requires a synthesis program as readily available commercial PCs of varying molecular mass do not exist.

There are two other sets of measurement that are relevant vis-à-vis the reduction of the glass transition temperature in freely standing films. One is the recent work of Ediger and coworkers,[28−30] in which a photobleaching technique was used to monitor probe rotational relaxation as a function of temperature in freely standing films. Their results show that there is a

dx.doi.org/10.1021/ma300098h | *Macromolecules* 2012, 45, 2453−2459

mobile layer at the surface of most films studied and that this layer thickens as the glass transition temperature is approached. This work does not evidence a reduction in the glass transition based on the probe dynamics; rather, they find that there is a bulklike response and a liquid layer response, not a reduced glass transition temperature. Also, the liquid layer thickness varies from zero in the case of poly(α-methylstyrene) to about 10 nm in poly(*tert*-butylstyrene). Polycarbonate was not investigated, and the thickness of the liquid layer in polystyrene was about 6−7 nm at T_g. Such results seem to contradict what we have found for the viscoelastic response of the ultrathin films. If, for example, the PC had a liquid layer thickness the same as that of polystyrene, one would expect the thin film glassy compliance to be much higher for the thinner films as the liquid layer would be less stiff than the glass. The fact that the 4.2 nm thick film and the 9.1 nm thick film both have stiffened glassy compliance values seems to suggest that the surface layer must be much smaller than this. The flow of the 3 nm thick film, however, might suggest a layer thickness of order 1.5 nm; hence, two layers could traverse the film thickness. In the case of polystyrene measurements in prior studies, the smallest film thickness measured was ∼9 nm, which would still imply for polystyrene that the glassy compliance should be much higher than what was observed, especially since glassy stiffening was observed in that instance as well. The reasons for such discrepancies need further investigation.

The other reports of relevance to the response of freely standing films are those of Bodiguel and Fretigny[31−33] in which polystyrene thin films are floated onto a glycerol surface where they dewet spontaneously. Using the spreading parameter as the force causing a biaxial compression on the film, they were able to extract the creep compliance in the films for different temperatures. Unlike the bubble inflation measurements here, they observe only a modest increase in polymer mobility, i.e., a 3−4 °C reduction in the glass transition temperature for films ∼20 nm thick. Why these differences among experimental methods exist remains an open question.

The mechanical properties of ultrathin films that are freely standing have only been measured by ourselves with the nanobubble technique of this paper and by Bodiguel and Fretigny with their liquid dewetting method (assuming that the mobile glycerol/polymer interface is equivalent in that sense to the air/polymer interface). The results contrast significantly. In addition to the issue of the lack of a major reduction of the glass transition in the dewetting experiments, Bodiguel and Fretigny do not observe the rubbery stiffening in the polymer, and the flow behavior that they report is typical of the macroscopic polymer rheology. They do not observe the "rubbery" stiffening reported here, and we remark that other studies from this lab[3,6,8] have demonstrated fairly conclusively that the stiffening that we observe is not due to the surface tension acting at the film surface. The fact of flow in the 3 and 9.1 nm films evidenced here is further support that the surface tension is not the cause of the rubbery stiffening. Additionally, it is of interest to note that the pressures used to inflate the present 3 and 4.2 nm thickness films should have been too small to inflate the bubbles if the surface tension were the cause of the stiffening. Here, as reported, the polycarbonate seems to flow with a glass-like viscosity approximately 10 °C above the nominal glass transition temperature. These are the first reports of flow in the nanobubble inflation measurements. An interesting observation in recent work by Pye and Roth[34] gives an apparent double T_g in high molecular weight polystyrene films. The observation here of a reduced segmental dynamics followed by the "rubbery stiffening" and terminal flow may suggest that terminal flow dynamics is differently affected by the confinement than are the segmental dynamics. The case of the PVAc, where we did not observe flow even 30 °C above the macroscopic glass transition temperature, however, is not fully consistent with this interpretation, and further study is required. As for why the PVAc behaves differently from the PC, we speculate that the difference between the PVAc and the polycarbonate in this regard is related to the observation by Plazek[35] that the rubbery plateau for poly(vinyl acetate) "is too wide" for the molecular weight that he investigated. We postulate the possibility that this effect is magnified by the ultrathin film confinement.

As for the glassy compliance, the liquid dewetting method of measurement does not have sufficient resolution to measure the small deformations that occur in the glassy regime for the small stresses that result from the surface tension acting on the films.

Supported Films and Small Molecule Glass-Formers in Confinement. There is considerably more work on the behavior of supported polymer films and on small molecule glass formers in confinement than on freely standing films. Therefore, we need to be brief. However, it is worth noting that there is a general, but not universal, acceptance that the T_g decreases upon confinement when the interactions with the surface are weak. This is seen in works from the earliest in nanopores[36,37] in which only modest reductions in T_g were observed, in polymer films on weakly interacting substrates[38,39] where larger T_g reductions were seen, to the more recent works in pores[40] where very large reductions of T_g have been reported for large but nonpolymeric molecules. For the case of systems that interact with the confining surfaces,[23,41,42] such as hydrogen-bonding liquids, the T_g has been reported to either increase, remain the same or decrease modestly. In addition, some works have suggested that the mechanical constraints provided by the confining medium may contribute to observed changes in molecular mobility that lead to the reduced T_g observations.[43−45] The present work does not directly address these issues, but it is worth noting that the observations of T_g reductions in freely standing films are much stronger than those observed in supported films. Finally, one other work is worth considering in the context of the present study. Torkelson's work[46] using fluorescent probe intensity as a function of temperature to obtain the pseudothermodynamic T_g in supported films has led to the suggestion that the polymer chain backbone chemistry (is it rigid?) or how it relates to the macroscopic fragility of the glass-forming system may lead to very strong T_g dependence on film thickness. The limited set of data here comparing the T_g reductions of poly(vinyl acetate), polystyrene, and polycarbonate would fit into this framework. Further work is required to systematically explore this possibility.

SUMMARY AND CONCLUSIONS

The rheological response of a series of polycarbonate films having thicknesses from 3 to 22 nm has been measured using the TTU bubble inflation method. The results show exceptional property changes in the PC relative to those of the material at the macroscale. Reductions in the glass transition are observed that are greater than any previously observed, being ∼122 °C below the macroscopic T_g for the 3 nm thick film. Furthermore, for the first time we have been able to demonstrate flow in the ultrathin films in the nanobubble

experiment and we observe this flow at ~10 °C above the thin film glass transition and for deformations/compliance values well below the macroscopic rubbery plateau value. Also, we observe that the rubbery stiffening of these extremely thin polycarbonate films falls on an extrapolation of the stiffening observed previously for polystyrene and poly(vinyl acetate), suggesting that the observation of the reduced rubbery compliance follows the square of the thickness in these three materials to thicknesses at least as small as 4.2 nm. Finally, we also see an enhancement of the glassy stiffness as evidenced by a reduction of the glassy compliance. Insufficient data are available to provide a trend in the glassy stiffness with film thickness.

AUTHOR INFORMATION

Corresponding Author

*E-mail: greg.mckenna@ttu.edu.

Present Address

[†]The Dow Chemical Company, 2301 N. Brazosport Blvd., Freeport, TX 77541.

Notes

The authors declare no competing financial interest.

ACKNOWLEDGMENTS

The authors are grateful to the U.S. Army Research Office under Grant W911NF-07-1-0418, the National Science Foundation under Grant DMR-0804438, and the John R. Bradford Endowment at Texas Tech University each for partial support of this work.

REFERENCES

(1) O'Connell, P. A.; McKenna, G. B. *Science* **2005**, *307*, 1760−1763.
(2) O'Connell, P. A.; McKenna, G. B. *Rev. Sci. Instrum.* **2007**, *78*, 013901−1−013901−12.
(3) O'Connell, P. A.; McKenna, G. B. *Eur. Phys. J. E* **2006**, *20*, 143−150.
(4) O'Connell, P. A.; McKenna, G. B. *Scanning* **2008**, *30*, 184−196.
(5) O'Connell, P. A.; Hutcheson, S. A.; McKenna, G. B. *J. Polym. Sci., Part B: Polym. Phys.* **2008**, *46*, 1952−1965.
(6) O'Connell, P. A.; McKenna, G. B. *J. Polym. Sci., Part B: Polym. Phys.* **2009**, *47*, 2441−2448.
(7) O'Connell, P. A.; McKenna, G. B. ANTEC 2010 Proceedings of the 68th Annual Technical Conference & Exhibition, Orlando, FL, June 16−20; Society of Plastics Engineers, 2010; pp 365−368.
(8) Xu, S.; O'Connell, P. A.; McKenna, G. B. *J. Chem. Phys.* **2010**, *132*, 184902−1−184902−9.
(9) Niemiec, J. M.; Schultheisz, C. R.; Schutte, C.; McKenna, G. B. *SPE ANTEC Tech. Pap.* **1995**, *41*, 2402−2408.
(10) O'Connell, P. A.; McKenna, G. B. *J. Chem. Phys.* **1999**, *110*, 11054−11060.
(11) O'Connell, P. A.; McKenna, G. B. *Mech. Time-Depend. Mater.* **2002**, *6*, 207−229.
(12) Moynihan, C. T.; Lee, S. K.; Tatsumisago, M.; Minami, T. *Thermochim. Acta* **1996**, *280*, 153−162.
(13) McKenna, G. B.; Simon,S. L. In *Handbook of Thermal Analysis and Calorimetry*; Cheng,S. Z. D., Ed.; Elsevier: Amsterdam, 2002; Vol. 3, pp 50−109.
(14) Timoshenko, S. P.; Woinowsky-Krieger, S. *Theory of Plates and Shells*, 2nd ed.; McGraw-Hill: New York, 1959.
(15) Plazek, D. J. *J. Polym. Sci., Part A-2* **1968**, *6*, 621−638.
(16) Jordan, T. C.; Richards, W. D. In *Handbook of Polycarbonate Science and Technology*; LeGrand, D. G., Bendler, J. T., Eds.; Marcel Dekker: New York, 2000; pp 179−224.
(17) Ferry, J. D. *Viscoelastic Properties of Polymers*, 3rd ed.; J. Wiley and Sons: New York, 1980.
(18) Si, L.; Massa, M. V.; Dalnoki-Veress, K.; Brown, H. R.; Jones, R. A. L. *Phys. Rev. Lett.* **2005**, *94*, 127801−1−127801−4.
(19) LeGrand, D. G. In *Handbook of Polycarbonate Science and Technology*; LeGrand, D. G., Bendler, J. T., Eds.; Marcel Dekker: New York, 2000; pp 107−130.
(20) Dalnoki-Veress, K.; Forrest, J. A.; de Gennes, P. G.; Dutcher, J. R. *J. Phys. IV* **2000**, *10*, 221−226.
(21) Dalnoki-Veress, K.; Forrest, J. A.; Murray, C.; Gigault, C.; Dutcher, J. R. *Phys. Rev. E* **2001**, *63*, 031801−1−031801−10.
(22) Forrest, J. A.; Dalnoki-Veress, K. *Adv. Colloid Interface Sci.* **2001**, *94*, 167−196.
(23) Alcoutlabi, M.; McKenna, G. B. *J. Phys.: Condens. Matter* **2005**, *17*, R461−R524.
(24) McKenna, G. B. *Eur. Phys. J. Spec. Top.* **2010**, *189*, 285−302.
(25) Roth, C. B.; Dutcher, J. R. *J. Electroanal. Chem.* **2005**, *584*, 13−22.
(26) Sharp, J. S.; Forrest, J. A. *Eur. Phys. J. E* **2003**, *12*, S97−S101.
(27) Roth, C. B.; Dutcher, J. R. *Eur. Phys. J. E* **2003**, *12*, S103−S107.
(28) Paeng, K.; Swallen, S. F.; Ediger, M. D. *J. Am. Chem. Soc.* **2011**, *133*, 8444−8447.
(29) Paeng, K.; Lee, H.-N.; Swallen, S. F.; Ediger, M. D. *J. Chem. Phys.* **2011**, *134*, 024901−1−024901−10.
(30) Paeng, K.; Ediger, M. D. *Macromolecules* **2011**, *44*, 7034−7042.
(31) Bodiguel, H.; Fretigny, C. *Eur. Phys. J. E* **2006**, *19*, 185−193.
(32) Bodiguel, H.; Fretigny, C. *Phys. Rev. Lett.* **2006**, *97*, 266105−1−266105−4.
(33) Bodiguel, H.; Fretigny, C. *Macromolecules* **2007**, *40*, 7291−7298.
(34) Pye, J. E.; Roth, C. B. *Phys. Rev. Lett.* **2011**, *107*, 235701−1−235701−5.
(35) Plazek, D. J. *Polym. J.* **1980**, *12*, 43−53.
(36) Jackson, C. L.; McKenna, G. B. *J. Non-Cryst. Solids* **1991**, *131*, 221−224.
(37) Zhang, J.; Liu, G.; Jonas, J. *J. Phys. Chem.* **1992**, *96*, 3478−3480.
(38) Keddie, J. L.; Jones, R. A. L.; Cory, R. A. *Faraday Discuss.* **1994**, *98*, 219−230.
(39) Keddie, J. L.; Jones, R. A. L.; Cory, R. A. *Europhys. Lett.* **1994**, *27*, 59−64.
(40) Koh, Y. P.; Li, Q.; Simon, S. L. *Thermochim. Acta* **2009**, *492*, 45−50.
(41) Mel'nichenko, Y. B.; Schuller, J.; Richert, R.; Ewen, B.; Loong, C. K. *J. Chem. Phys.* **1995**, *103*, 2016−2024.
(42) Zheng, W.; Simon, S. L. *J. Chem. Phys.* **2007**, *127*, 194501−1−194501−11.
(43) McKenna, G. B. *J. Phys., IV* **2000**, *10*, 53−57.
(44) He, F.; Wang, L.-M.; Richert, R. *Phys. Rev. B* **2005**, *71*, 144205−1−144205−10.
(45) He, F.; Wang, L.-M.; Richert, R. *Eur. Phys. J. Spec. Top.* **2007**, *141*, 3−9.
(46) Torkelson, J. M. "Dramatic effects of confinement on glass transition temperature and dye diffusion coefficients in polymer films: Important roles of fragility and the distribution of alpha-relaxation times." Paper presented in the symposium Dynamics of Nano-structured Polymers, 242nd National Meeting of the American Chemical Society, Denver, CO, Aug 31, 2011.

Macromolecules

Article

pubs.acs.org/Macromolecules

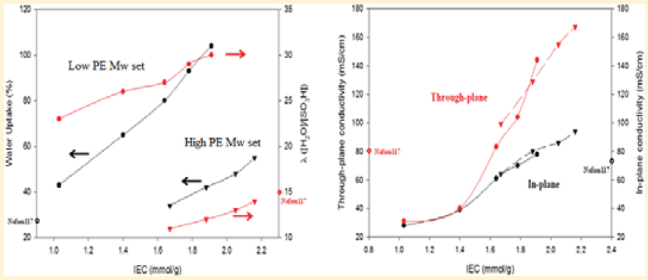
Synthesis of Polyethylene-Based Proton Exchange Membranes Containing PE Backbone and Sulfonated Poly(arylene ether sulfone) Side Chains for Fuel Cell Applications

Hyung Kyu Kim,[†] Min Zhang,[†] Xuepei Yuan,[†] Serguei N. Lvov,[†,‡,§] and T. C. Mike Chung[†,*]

[†]Department of Materials Science and Engineering, [‡]Department of Energy and Mineral Engineering, and [§]Electrochemical Technologies Program, EMS Energy Institute, The Pennsylvania State University, University Park, Pennsylvania 16802, United States

Supporting Information

ABSTRACT: This paper discusses a new class of proton exchange membranes (PEMs) that are based on a well-controlled polyolefin graft copolymer containing a polyethylene (PE) backbone and several sulfonated poly(arylene ether sulfone) (s-PAES) side chains. The chemistry involves a graft-onto reaction between high molecular weight PE with few pendent benzyl bromide groups and poly(arylene ether sulfone) (PAES) with two terminal phenol groups. The resulting PE-*g*-PAES graft copolymer, with predetermined backbone molecular weight, graft density, and graft length, was solution-cast into uniform film (thickness 20−40 μm), followed by a heterogeneous sulfonation reaction of PAES side chains to obtain the desired PE-*g*-s-PAES PEMs with a high sulfonation level. The unique combination of hydrophobicity, semicrystallinity, and high molecular weight of the PE backbone offers PEM with a stable (nonswellable) matrix. The embedded hydrophilic s-PAES proton-conductive domains show only moderate water uptake, even with a high ion exchange capacity (IEC >3 mmol/g in the s-PAES domains). Compared to Nafion 117, most PE-*g*-s-PAES PEMs show similar hydration numbers (λ <15) but higher proton conductivity (up to 160 mS/cm). More interestingly, all PE-*g*-s-PAES PEMs show higher through-plane conductivity than in-plane conductivity. Evidently, a thin hydrophobic PE layer is formed on the PEM surfaces due to the low surface energy of PE, resulting in anisotropic conductivity. Overall, this newly developed PE-*g*-s-PAES membrane offers a combination of desirable properties, including conductivity, water uptake, mechanical strength, and cost-effectiveness for fuel cell applications.



INTRODUCTION

Since the discovery of Nafion by DuPont in the 1960s, it has been extensively studied and applied in proton exchange membranes (PEMs).[1−8] Because of its high conductivity and good chemical and thermal stability, Nafion became a state-of-the-art material in fuel cell applications. However, Nafion also exhibits many shortfalls that hinder its large-scale, commercial adaptation, including high cost, limited processability, poor selectivity (methanol crossover), and reduced conductivity at high temperature and under low humidity conditions. As an alternative to Nafion, several sulfonated poly(arylene)-based engineering plastics, such as poly(arylene ether sulfone), poly(ether ketone), and poly(ether ether ketone), were extensively studied for PEMs in the past 2 decades.[7,9−14] These polymers offer many advantages due to ease of synthesis and fabrication, good thermal stability, high ion exchange capacity, and lower manufacturing costs. Because of the polycondensation mechanism, the synthesis requires high purity monomers with a precise functional group stoichiometry to obtain high molecular weight poly(arylene) polymers. Excessive water swelling and reduced selectivity in the highly sulfonated poly(arylene) polymers has prompted ample research activity by controlling its microstructures, including the introduction of some nonsulfonated monomer units. Several other polymers have also been intensely studied, including polystyrene (PS),[15,16] poly(vinylidene floride) (PVDF),[17−20] and composites.[21] Although sulfonated polystyrene with a cross-linked network is a traditional PEM material, the polymer exhibits some serious deficiencies, including weak mechanical strength and poor stability in fuel cell operation conditions due to free radical induced degradation.[22,23] Some PVDF/PS block and graft copolymers were synthesized and studied to help us understand the effects of the hydrophobic/hydrophilic phase separation in the PEM performance. Activities surrounding composites were focused on applications under high temperature and low humidity conditions. Overall, it is still a major scientific challenge and industrial importance to develop a PEM material that can fulfill a combination of key PEM properties, including conductivity, selectivity, mechanical strength, stability, and cost-effectiveness for fuel cell applications.

Polyolefins, such as polyethylene (PE) and polypropylene (PP), are the most widely used polymers in a broad range of commercial applications. They possess an excellent combina-

Received: November 12, 2011
Revised: February 3, 2012
Published: February 17, 2012

 © 2012 American Chemical Society dx.doi.org/10.1021/ma202492d | Macromolecules 2012, 45, 2460−2470

tion of chemical and physical properties along with low cost and good processability. Because of superior chemical and electrochemical stability and unique physical properties, including hydrophobicity and crystallinity, PE and PP polymers are commonly used as storage vessels for strong acids and bases. In electrochemical devices, microporous PE and PP films are extensively used as the separator between two electrodes, as well as supports for solid electrolytes.[24,25] In other words, the semicrystalline and highly hydrophobic PE and PP polymers are very stable under demanding (chemically, electrochemically, and mechanically) fuel cell environments. In the past, there had been several papers that discussed polyolefin-based PEMs.[26−30] Because of synthesis difficulties—catalyst poison[31,32] by a polar group in the direct Ziegler−Natta mediated α-olefin polymerization process—the most common functionalization routes have been based on the postpolymerization process, involving an irradiation-mediated free radical graft polymerization of a monomer-bearing ionic group or styrene followed by a sulfonation reaction of benzyl groups.[33−35] Unfortunately, the free radical process usually results in very complicated molecular structures.[36] The polymer structure and morphology have rarely been characterized. In this paper, we will discuss a new synthesis route to prepare PEMs with well-controlled PE-*g*-s-PAES graft copolymers that contain a high molecular weight PE backbone and several highly sulfonated poly(arylene ether sulfone) (s-PAES) side chains. The initial idea was to combine two stable and inexpensive polymers to perform a combination of separator and conductor functions.

EXPERIMENTAL SECTION

Materials and Instrumentation. All oxygen and moisture sensitive manipulations were carried out inside an argon-filled Vacuum Atmosphere drybox. Highly purified ethylene gas (Matheson) of chemical grade 3 was used as received. Toluene (Wiley Organics) was refluxed and distilled over Na under argon and kept in drybox before use. *p*-Methylstyrene (*p*-MS), *N*-methylpyrrolidinone (NMP), anisole, and 1,1,2,2-tetrachloroethane were distilled over CaH_2 under reduced pressure. Constrained geometric catalyst (CGC) was synthesized according to the published procedure.[37−39] Methylaluminoxane (MAO), benzoyl peroxide (BPO) and *n*-bromosuccinimide (NBS) were purchased from Sigma-Aldrich and used as received. Bisphenol A and dichlorodiphenyl sulfone (DCDPS) from Sigma-Aldrich were recrystallized in toluene and dried under vacuum at 100 °C before use. Potassium carbonate (Sigma-Aldrich) was dried at 330 °C under nitrogen before use.

All ^{1}H NMR spectra were recorded on a Bruker AM 300 instrument either in 1,1,2,2-tetrachloroethane-d_2 or dimethyl-d_6 sulfoxide (DMSO-d_6) at 110 °C. DSC thermograms were obtained by using TA Q100 instrument. Temperature range was from −30 to +230 °C with a heating rate of 10 °C/min. Second heating cycle was used to determine melting and crystallization temperatures, as well as heat of fusion. Thermal properties were investigated by using TA SDT Q600 instrument. Small amount of polymer was placed in ceramic cell and temperature was increased from 30 to 750 °C with a heating rate of 20 °C/min. Wide-angle X-ray scattering patterns (WAXS) were collected on a PANalytical X'Pert Pro MPD system using CuK_α radiation (λ = 0.15406 nm) and a PIXcel detector. Fourier transform infrared spectroscopy (FTIR) was recorded on a PE-1710 spectrometer from 4000 to 400 cm^{-1} with a 4 cm^{-1} resolution in 16 scans using polymer thin film. All mechanical properties were measured according to the ASTM D-1708 method. The membranes were investigated at 50% humidity at room temperature by pulling dumbbell shape thin polymer film in opposite direction at a rate of 2 mm/min using Instron 5866 Universal Test Instrument. All samples were tested at least three times to validate the results. In-plane and through-plane conductivity were measured by electrochemical impedance spectroscopy (EIS) with a Solartron 1260 frequency response analyzer (in-plane) or Gamry electrochemical measurement system (through-plane) in the frequency range from 10 to 1 MHz. Contact angle measurement was performed by using Perkin-Elmer contact angle goniometry.

Copolymerization of Ethylene and *p*-Methylstyrene. In a typical ethylene copolymerization condition, a Parr 450 mL stainless autoclave was predried under vacuum line and toluene, MAO (10 wt % in toluene), *p*-methylstyrene, and CGC were sequentially introduced into the autoclave under high pressure of ethylene gas. After the addition of CGC catalyst, copolymerization was conducted by extensive stirring at 60 °C for 20 min. Additional ethylene was fed continuously into the autoclave to maintain a constant ethylene pressure and copolymerization was terminated by stopping ethylene feed, followed by pouring polymer solution into acidic methanol solution. Polymer was filtered and washed with THF and methanol thoroughly and dried under vacuum at 70 °C for 12 h.

Bromination of PE-*co*-*p*-MS. Bromination was performed in heterogeneous condition using NBS and BPO as bromine source and free radical initiator, respectively. In a typical reaction condition (run II-3 in Table 2), 2 g of polymer was suspended in 100 mL of 1,1,2,2-tetrachlorethane and temperature was elevated up to 75 °C. With the protection of nitrogen gas and stirring, 2 g of NBS and 0.04 g of BPO were added, and the reaction took place at 75 °C for 3 h, leading to deep yellow solution. After bromination, the polymer solution was cooled down to room temperature and poured into large amount of acetone. Light yellow polymer was filtered, washed with water and acetone several times to remove any residual NBS and BPO and dried under vacuum at 50 °C for 12 h.

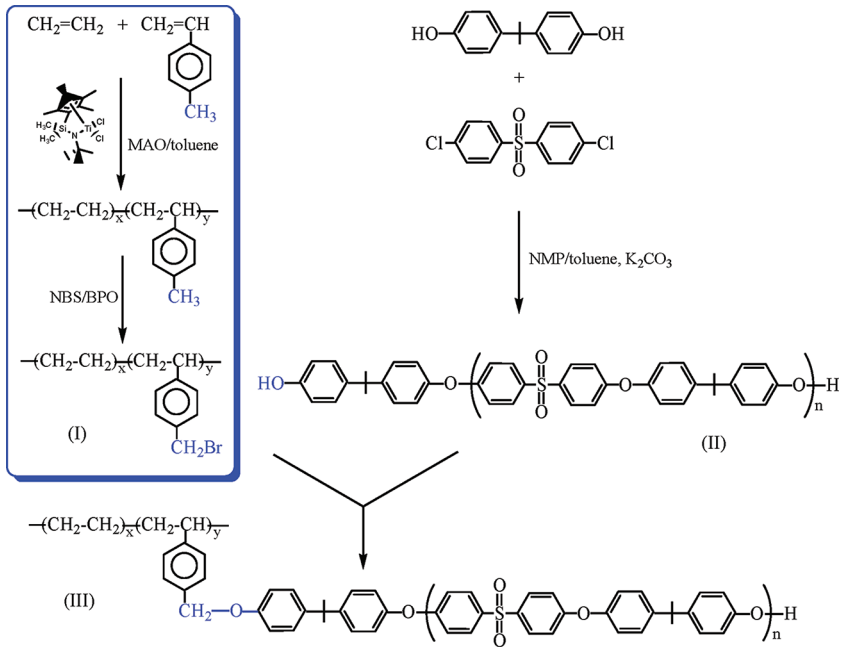
Synthesis of Poly(arylene ether sulfone) (PAES). In a typical polymerization reaction, 18 g of bisphenol A (78.85 mmol), 22.39 g of dichlorodiphenol sulfone (DCDPS, 77.98 mmol), and 13.08 g of potassium carbonate (94.62 mmol, 20 mol % excess to bisphenol A) were placed in 500 mL three neck round-bottom flask equipped with magnetic stirrer, condenser, argon inlet/outlet and dean stark trap. About 240 mL of dried NMP and 120 mL of toluene were injected into the flask at room temperature and kept for 1 h. Temperature was then elevated to 80 °C for 2 h and 150 °C for 4 h to dehydrate the solution. After most toluene was trapped into dean stark trap, reaction temperature was increased to 175 °C for carrying out polycondensation reaction. After a certain reaction time, viscous polymer solution was cooled down to room temperature, filtered, precipitated in isopropyl alcohol and filtered again. Resultant powdery polymer was washed with water and methanol, filtered again and dried at 110 °C for at least 24 h under vacuum to obtain PAES with 96% yield.

Graft-onto Reaction between Brominated PE-*co*-*p*-MS and Poly(arylene ether sulfone). Graft-onto reaction was carried out in a homogeneous solution. In a typical reaction, to a 500 mL three neck round-bottom flask equipped with magnetic stirrer and condenser, 3.6 g of PAES polymer (M_n = 20 kg/mol and OH content = 0.36 mmol) and 0.05 g of potassium carbonate were added at 150 °C. Anisole (200 mL) was then introduced into the flask with a syringe to dissolve PAES completely. In a 100 mL one neck round-bottom Schlenk flask with a magnetic stirrer, 0.5 g of brominated PE-*co*-*p*-MS (M_v: 320 kg/mol and Br content: 0.09 mmol) was dissolved into 50 mL of anisole at 120 °C. With the aid of a cannula, homogeneous brominated PE-*co*-*p*-MS/anisole solution was transferred into the reactor that contains PAES/anisole solution. The coupling reaction was carried out at 150 °C with agitation for a specific time. After cooling down to room temperature, the solution was centrifuged and washed with THF. Residual ungrafted PAES was completely removed by Soxhlet extraction with THF solvent. The resultant PE-*g*-PAES graft copolymer was washed with deionized water and methanol and then dried at 60 °C under vacuum for 12 h.

Membrane Preparation and Sulfonation. About 0.1 g of PE-*g*-PAES graft copolymer was dissolved in 6 mL of anisole at an elevated temperature. The homogeneous viscous solution was filtered through glass wool to remove any impurities (particles) and cast onto a clean glass plate. The cast solution was dried for 2 days at room temperature and another 12 h at 80 °C in vacuum. The resulting film (thickness: 20−40 μm) was annealed under pressure at 110 °C for 12 h in

dx.doi.org/10.1021/ma202492d | *Macromolecules* 2012, 45, 2460−2470

Scheme 1



vacuum. Sulfonation was then conducted on the PE-*g*-PAES thin film under heterogeneous condition. Typically, the film was immersed in 50 mL 1,1,2,2-tetrachloroethane solution in a sealed container. Trimethylsilyl chlorosulfonate (1 mL) was then added into the sealed container at room temperature. After 24 h of sulfonation, the resulting sulfonated film was washed with methylene chloride, acetone, and deionized water several times to remove any residual reagents. The film was then acidified by soaking it into 1 M HCl aqueous solution for 24 h at room temperature and then washed with deionized water thoroughly to remove any residual HCl before drying at 70 °C under vacuum for 12 h. The resulting PE-*g*-s-PAES membrane was usually kept in deionized water for use.

Measurements and Characterization. Water uptake (%) is calculated by $[(W_{wet} - W_{dry})/W_{dry}] \times 100\%$; wherein W_{wet} is the weight of fully hydrated membrane and W_{dry} is the weight of completely dried membrane. The membrane was dried under vacuum for 12 h at 70 °C and stored in a desiccator before measuring the weight in a "dry" state (W_{dry}). The membrane was then equilibrated in deionized water for 24 h at room temperature. After blotting the surface of the film quickly, the weight in "wet" state (W_{wet}) was measured. IEC was determined by back-titration using 0.01 N NaOH aqueous solution. The PE-*g*-s-PAES membrane was soaked into 1 M NaCl aqueous solution to release proton from the membrane. The solution was replaced every 4 h. After 24 h, the collected NaCl (aq) solution was titrated with 0.01 N NaOH (aq) using phenolphthalein as an indicator. Colorless NaCl (aq) solution was changed to purple when a certain amount (V_{NaOH}) of NaOH (aq) was added. As a reference, the pure 1 M NaCl aqueous solution was titrated using the same condition to obtain the reference amount (V_{pure}) of NaOH (aq). IEC (mmol/g) was calculated by $[NaOH] \times (V_{NaOH} - V_{pure})/W_{dry}$. With the obtained water uptake and IEC value, the hydration number (λ) was calculated by [water uptake (%) × 10]/[IEC value × 18].

In-plane conductivity was calculated by $l/(R \times \delta \times w)$, where l is the width between two electrodes (0.65 cm), R is the membrane resistance, δ is the thickness of the membrane (~40 μm), and w is the width of the membrane (~1.0 cm). Through-plane conductivity was determined by the same procedure described in the previous paper.[40] Nafion117 membrane was measured before all the conductivity measurements to confirm the validity of experimental condition. Measurement was conducted at least 5 times to obtain consistent impedance value over 2 h.

RESULTS AND DISCUSSION

As discussed, this paper shows a new class of PE-based proton exchange membranes that are based on new PE-*g*-s-PAES graft copolymers with a well-controlled molecular structure (i.e., backbone molecular weight, graft density, graft length, sulfonation level, etc.). They contain a high molecular weight PE backbone and several highly sulfonated poly(arylene ether sulfone) (s-PAES) side chains. With two extremely different polymer properties, the crystalline hydrophobic PE backbone and amorphous hydrophilic s-PAES side chains shall be microphase separated into a well-defined morphology that contains a robotic (water nonswellable) PE matrix and some stable embedded s-PAES continuous ion conductive channels through the PE film. The combination may provide a PEM with a high IEC value without water overswelling, therefore achieving high proton conductivity.[20] For a systematic study to identify suitable graft copolymer structures and compositions, the investigation involves several steps, including (i) the development of a chemical route to prepare a well-defined graft copolymer, (ii) utilizing the most suitable process to prepare PEM membranes, and (iii) a systematic comparison of structure−property relationships in conductivity, water-swelling, surface, and mechanical properties.

Synthesis of PE-*g*-PAES Graft Copolymer. Scheme 1 illustrates the synthesis steps in the preparation of PE-*g*-PAES graft copolymer (III), which involves a graft-onto reaction between poly(ethylene-*co*-*p*-bromomethylstyrene) (PE-*co*-*p*-MS−Br) (I) and poly(arylene ether sulfone) (PAES) (II). Both precursor polymer structures were predetermined before the coupling reaction. The synthesis of PAES polymers (II), with a varied range of molecular weights, were studied and reported in many papers.[11,41,42] In this study, we have prepared three PAES polymers with M_n = 13k, 20k, and 26k g/mol, respectively. Their molecular weights were determined by chain end analysis, discussed in the Supporting Information. In our prior research, we had investigated the copolymerization of ethylene and styrenic comonomers, including *p*-methylstyrene (*p*-MS), using various metallocene catalysts.[43−45] Several

dx.doi.org/10.1021/ma202492d | Macromolecules 2012, 45, 2460−2470

constrained geometry metallocene catalysts (CGC) showed comparative comonomer reactivity ratios, and we obtained various copolymers, including ethylene/*p*-MS copolymers, with narrow molecular weight and composition distributions.

Table 1 summarizes several ethylene/*p*-MS copolymerization conditions and results. They are prepared by the

Table 1. Summary of Metallocene-Mediated Copolymerization of Ethyelene and *p*-Methylstyrene

	reaction condition[a]		polymerization results			
run	ethylene (psi)	*p*-MS (mmol)	yield (g)	catalyst activity[b]	*p*-MS in PE (mol %)[c]	M_v (g/mol)[d]
I	125	7.6	3.4	2580	1.0	280 000
II	125	19	4.2	3180	1.8	220 000
III	125	38	4.4	3330	3.0	190 000
IV	125	76	4.8	3640	6.7	113 000
V	220	19	6.1	4620	1.4	320 000
VI	220	38	6.8	5150	2.0	260 000
VII	320	38	7.0	5300	1.5	390 000

[a]Reaction conditions: 75 mL of toluene, [Ti] = 4 × 10^{-6} mol, [MAO]/[Ti] = 2250, temp = 60 °C, and time =20 min. [b]Catalyst activity: kg of PE/mol of catalyst × hour. [c]Determined by ^{1}H NMR. [d]Determined by intrinsic viscosity in decalin at 135 °C with [η] = KM_v^a; K = 62 × 10^{-3} mL/g, and α= 0.7.[46]

[C_5Me_4($SiMe_2N^tBu$)]$TiCl_2$/MAO CGC−metallocene catalyst system. All resulting PE-*co*-*p*-MS copolymers show a sharp T_m transition and narrow molecular weight distribution (PDI ∼ 2). Comparing runs I to IV, the *p*-MS content in the PE-*co*-*p*-MS copolymer proportionately increases with the monomer feed, and a copolymer with more than 6 mol % of *p*-MS (run IV) was observed. Although the catalyst maintains high catalyst activity, the copolymer molecular weight systematically decreases with the *p*-MS content. However, the copolymer molecular weight is also strongly dependent on ethylene pressure. High molecular weight PE-*co*-*p*-MS copolymers (runs V and VII) can be easily obtained with high catalyst activity and desirable *p*-MS content. As will be discussed later, these PE-*co*-*p*-MS copolymers with [*p*-MS] <2 mol % were used in this study to maintain high PE crystallinity, melting temperature (T_m), and molecular weight.

Bromination of the PE-*co*-*p*-MS copolymer (fine powder) was carried out in a 1,1,2,2-tetrachloroethane suspension solution using benzoyl peroxide (BPO) as a free radical initiator and *N*-bromosuccinimide (NBS) as a bromination reagent. The heterogeneous reaction was performed at 75 °C under a nitrogen atmosphere in a dark environment, and the excess amount of NBS to *p*-MS in mol % was used. A light yellow polymer powder was obtained. Figure 1 compares the ^{1}H NMR spectra of a PE-*co*-*p*-MS copolymer (run VII) before and after the bromination reaction. The chemical shift at 2.35 ppm, corresponding to the benzyl proton Ph−C**H**$_3$ in PE-*co*-*p*-MS, significantly reduces its intensity, and a new split peak around 4.54 ppm, corresponding to the protons in benzyl bromide (Ph−C**H**$_2$Br), are observed. It clearly shows that the bromination reaction predominantly takes place at the *p*-CH_3 position. The degree of bromination estimated from the integrated peak areas between *p*-bromomethyl protons at 4.54 ppm and aromatic protons at 7.0−7.4 ppm is 53%.

Table 2 summarizes several comparative sets of the bromination reaction using three PE-*co*-*p*-MS copolymers (runs II, V, and VII in Table 1) with ∼1.5 mol % *p*-MS content and various molecular weights (220k, 320k, and 390 K

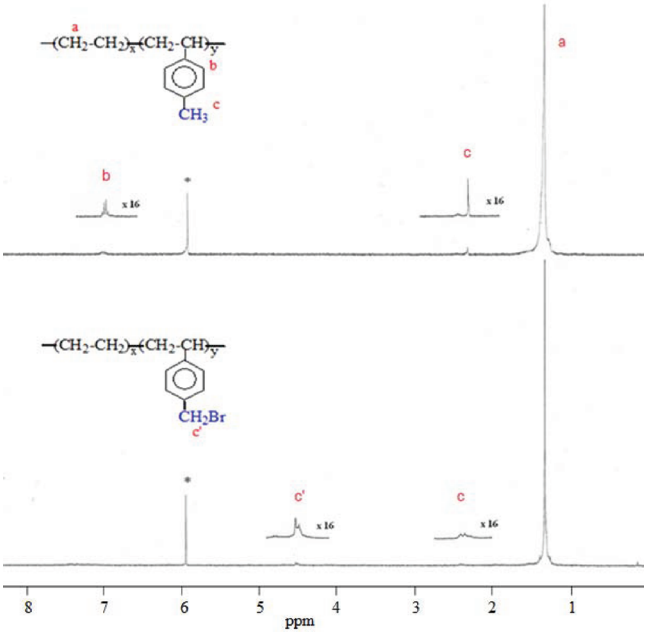


Figure 1. ^{1}H NMR spectra of (top) PE-*co*-*p*-MS and (bottom) PE-*co*-*p*-MS−Br.

Table 2. Summary of the Bromination Reaction[a] in Forming PE-co-*p*-MS−Br Copolymers

	starting PE-*co*-*p*-MS		reaction condition		PE-*co*-*p*-MS−Br product	
run	M_v (g/mol)	*p*-MS content (mol %)	[NBS]/[*p*-MS] (mole ratio)	reaction time (h)	Br content (mol %)[b]	Br efficiency (%)[c]
II-1	220k	1.8	10.5	1	0.6	33
II-2	220k	1.8	10.5	2	1.0	56
II-3	220k	1.8	10.5	3	1.2	67
II-4	220k	1.8	5.5	3	0.9	50
II-5	220k	1.8	2.6	3	0.5	28
V-1	320k	1.4	10.5	1	0.5	35
V-2	320k	1.4	10.5	2	0.7	50
VII-1	390k	1.5	10.5	2	0.5	33
VII-2	390k	1.5	10.5	3	0.8	53

[a]Reaction conditions: 100 mL of 1,1,2,2-tetrachloroethane, 2 g of PE-*co*-*p*-MS copolymer, 0.04 g of BPO, temp = 75 °C. [b]Determined by ^{1}H NMR. [c]Bromination efficiency: % of *p*-MS reacted to form *p*-MS−Br.

g/mol). The bromination reaction of PE-*co*-*p*-MS is very selective on *p*-MS moieties at 75 °C, and the efficiency of bromination is controlled by the reaction time and mole ratio of [NBS]/[*p*-MS], as well as by polymer molecular weight (kinetic reasons). With 3 h of reaction time at 75 °C, more than 50% of *p*-MS groups in the copolymer are brominated without showing any significant change in polymer molecular weight. However, with a further increase of the reaction temperature to 90 °C, we did observe some reduction in polymer molecular weight. It is interesting to note that the heterogeneous reaction condition may be beneficial to enhance this selective free-radical induced bromination reaction on *p*-MS moieties. The bulky *p*-MS groups in the PE-*co*-*p*-MS copolymer shall reside in the amorphous phase. With the solution swelling, the *p*-MS groups will have a good chance to come in contact with BPO/NBS reagents. On the other hand, the PE chains in the crystalline phase may have a lower chance of meeting the

dx.doi.org/10.1021/ma202492d | *Macromolecules* 2012, 45, 2460−2470

chemical reagent (solution), therefore delaying potential side reactions. Although there is a low Br concentration in the resulting PE-*co*-*p*-MS−Br, they provide more than sufficient coupling sites for the preparation of PE-*g*-PAES graft copolymers.

The graft-onto reaction between PE-*co*-*p*-MS−Br (I) and PAES polymers (II) was carried out under a similar condensation polymerization condition as was used in the preparation of PAES polymers, with the exception of applying a common anisole solvent to maintain both polymers in solution throughout the coupling reaction. After the coupling reaction, the unreactive PAES polymer was carefully removed by Soxhlet extraction. Figure 2 compares the ^{1}H NMR spectra between the

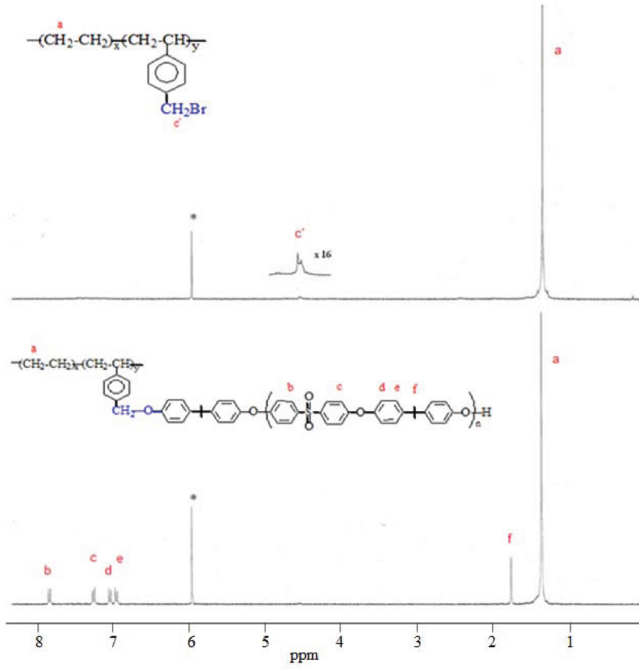


Figure 2. ^{1}H NMR spectra of (top) PE-*co*-*p*-MS−Br and (bottom) PE-*g*-PAES graft copolymer.

starting PE-*co*-*p*-MS−Br (run VII-2 in Table 2) and the resulting PE-*g*-PAES graft copolymer (run A-1 in Table 3). In addition to a major PE peak at 1.35 ppm, there are several new peaks shown in the PE-*g*-PAES graft copolymer, including a methyl peak at 1.67 ppm, corresponding to two methyl groups in bisphenol A units and several aromatic peaks between 6.9 and 7.9 ppm. The composition of the PE-*g*-PAES graft copolymer (i.e., the mole ratio between ether sulfone units in the side chains and ethylene units in the backbone) was determined by comparing the peak intensity between the 1.35 and 1.67 ppm peaks and the protons involved in each monomer unit. Since there is a huge difference between ethylene and arylene ether sulfone unit molecular weights (28 vs 442 g/mol), the mole ratio between these two cannot adequately reflect the structure of the graft copolymer (III). The PE-*g*-PAES graft copolymer in Figure 2 (bottom) contains only 2.7 mol % of ether sulfone units, but has 30 wt % and 25 vol. % to that of PAES in the graft copolymer. The FT-IR spectroscopy was also applied to confirm the graft copolymer. As shown in the Supporting Information (Figure S2), the PE-*g*-PAES graft copolymer exhibits several new absorption bands, including 1006 cm^{-1} for diphenyl ether, 1100 cm^{-1} for SO_2 (sym), and 1310 cm^{-1} for SO_2 (asym), corresponding to PAES side chains. After the sulfonation reaction, a new absorption band centered at 1030 cm^{-1} appears, which corresponds with sulfonic acid (sym).

Table 3 compares five sets of graft-onto reactions involving four PE-*co*-*p*-MS−Br copolymers with M_v= 220k, 250k, 320k, and 390k g/mol and three PAES polymers with M_n= 13k, 20k, and 26k g/mol, respectively. In each coupling (graft-onto) reaction, the mole ratio of two active sites ([*p*-MS−Br]/[phenol]) was maintained at 1/4, with excess PAES side chains. In sets A and B we compare two reaction temperatures (110 and 150 °C) and four reaction times (6, 9, 12, and 24 h), using the same PE-*co*-*p*-MS−Br (run VII-2 in Table 2 with molecular weight: 390 kg/mol and Br content: 0.8 mol %) and PAES (molecular weight: 20 kg/mol). The grafting efficiency significantly increases with the increase of both reaction temperature and time, and the gap between low and high temperature conditions become smaller with the sufficient reaction time. In run B-4 (under 150 °C and 24 h), the resulting PE-*g*-PAES graft copolymer contains about 18 PAES side chains along the PE backbone. In set C (runs C-1, C-2, and C-4), we investigated the molecular weight effect of PE-*co*-*p*-MS−Br using three PE-*co*-*p*-MS−Br copolymers (runs II-5, V-1, and VII-1 in Table 2) that have the same Br content (0.5 mol %) but different molecular weight (220k, 320k, and 390 K g/mol, respectively). The side-by-side coupling reactions were conducted under the same reaction condition (150 °C for 24 h) and PAES (molecular weight: 20 kg/mol). Evidently, high molecular weight PE-*co*-*p*-MS−Br (with high solution viscosity) clearly slowed down the coupling reaction with the PAES polymer. In set D, we focused on the effect of the poly(arylene ether sulfone) molecular weight to the coupling reaction. The comparative study involved three PAES polymers with molecular weights of 13k, 20k, and 26k g/mol, respectively, and the same PE-*co*-*p*-MS−Br copolymer (run V-1 in Table 2) at 150 °C for 24 h. The graft efficiency is strongly affected by the molecular weight of PAES—higher molecular weight means lower efficiency. This reverse molecular weight effect indicates the importance of PAES mobility to the coupling (graft-onto) reaction, due to the fact that the PAES polymer chain only contains two active terminal groups. Overall, the graft efficiency seems dependent on four factors: reaction temperature, reaction time, and the molecular weights of both PE-*co*-*p*-MS−Br (I) and PAES (II) polymers. High molecular weight polymers require higher temperatures and longer reaction times in the coupling reaction. With the proper selection of reaction conditions, there should be no problem to prepare a broad range of well-defined PE-*g*-PAES graft copolymers with controlled molecular structures (i.e., backbone molecular weight, graft density, and graft length).

Figure 3 compares DSC curves of a PE-*g*-PAES graft copolymer (run B-4 in Table 3) with the corresponding PE-*co*-*p*-MS−Br (run VII-2 in Table 2) and the starting PE-*co*-*p*-MS copolymer (run VII in Table 1). Both PE-*co*-*p*-MS and PE-*co*-*p*-MS−Br, having less than 2 mol % of comonomer units, show a sharp melting temperature peak (T_m) at 125 and 124 °C and heat of fusion (ΔH) of about 132.2 and 116.6 J/g, respectively. Both are slightly below those in high density polyethylene (HDPE). The low concentration of comonomer units (branch points) has only little effect on the PE chain crystallization. In Figure 3c, in addition to a melting peak at 118 °C and ΔH of about 47.5 J/g (41% of PE-*co*-*p*-MS−Br), the PE-*g*-PAES graft copolymer also exhibits a T_g at 175 °C, corresponding to the T_g

dx.doi.org/10.1021/ma202492d | *Macromolecules* 2012, 45, 2460−2470

Table 3. Summary of PE-*g*-PAES Graft Copolymers and Their Coupling Reaction Conditions

	coupling reaction condition[a]					PE-*g*-PAES graft copolymer				
run	M_v of PE (g/mol)	Br in PE (mol %)	M_n of PAES (g/mol)	reaction temperature (°C)	Reaction Time (h)	PAES (wt %)[b]	PAES (vol %)[c]	av. no. of PAES chains per PE	graft density[d]	graft efficiency (%)[e]
A-1	390k	0.8	20k	110	6	30	25	4.6	0.6	8
A-2	390k	0.8	20k	110	9	42	35	7.7	1.0	13
A-3	390k	0.8	20k	110	12	47	40	9.4	1.2	15
A-4	390k	0.8	20k	110	24	57	51	14.5	1.9	24
B-1	390k	0.8	20k	150	6	46	39	9.2	1.2	15
B-2	390k	0.8	20k	150	9	55	48	13.1	1.7	22
B-3	390k	0.8	20k	150	12	60	54	16.2	2.1	27
B-4	390k	0.8	20k	150	24	63	56	17.9	2.3	29
C-1	250k	0.5	20k	150	24	64	57	12.0	2.4	48
C-2	320k	0.5	20k	150	24	50	43	8.7	1.4	28
C-3	320k	0.8	20k	150	24	63	58	15.1	2.4	30
C-4	390k	0.5	20k	150	24	44	37	8.3	1.1	22
D-1	320k	0.5	13k	150	24	55	48	16.5	2.6	43
D-2	320k	0.5	20k	150	24	50	43	8.7	1.4	28
D-3	320k	0.5	26k	150	24	43	37	5.1	0.8	16
E-1	220k	1.2	20k	110	3	28	24	2.4	0.6	5
E-2	220k	1.2	20k	110	6	39	33	3.8	0.9	7
E-3	220k	1.2	20k	110	10	47	40	5.3	1.2	10
E-4	220k	1.2	20k	110	14	53	46	6.7	1.6	13
E-5	220k	1.2	20k	110	18	58	51	8.2	1.9	16

[a]Reaction conditions: 250 mL of anisole and mole ratio of [Br] in PE and [OH] in PAES = 1:4. [b]Determined by ^{1}H NMR. [c]Calculation based on PE density = 0.95 g/cm^3 and PAES density = 1.25 g/cm^3 [d]PAES side chains per 1000 ethylene units in the backbone. [e]% of Br in PE-*co*-*p*-MS−Br involved the coupling reaction with PAES.

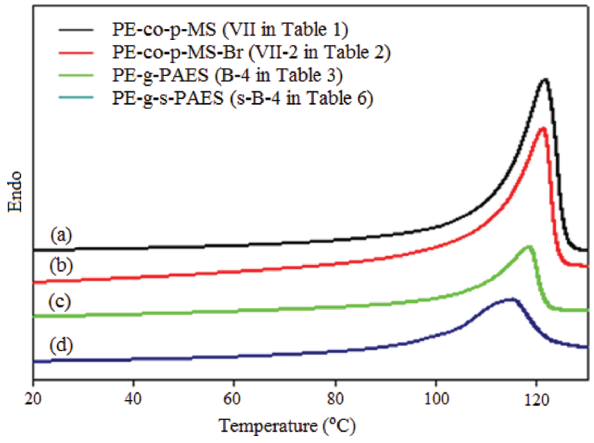


Figure 3. DSC curves of (a) PE-*co*-*p*-MS copolymer (with 1.5 mol % of *p*-MS units), (b) PE-*co*-*p*-MS−Br copolymer (with 0.8 mol % of Br units), (c) the corresponding PE-*g*-PAES graft copolymer containing 63 wt % of PAES, and (d) the corresponding PE-*g*-s-PAES graft copolymer.

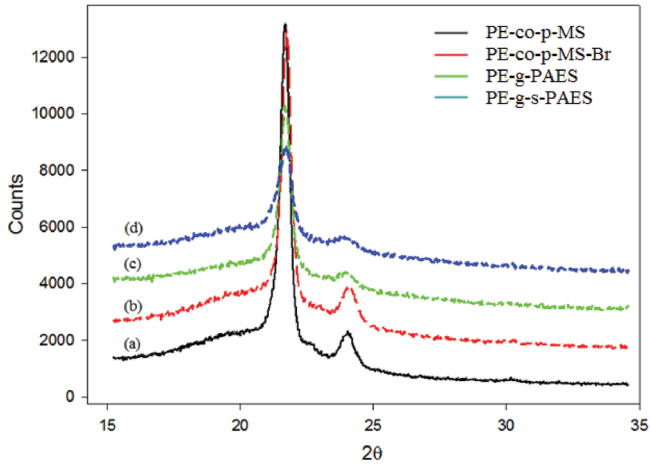


Figure 4. WAXS patterns of (a) PE-*co*-*p*-MS copolymer (with 1.5 mol % of *p*-MS units), (b) PE-*co*-*p*-MS−Br copolymer (with 0.8 mol % of Br units), (c) the corresponding PE-*g*-PAES graft copolymer containing 63 wt % of PAES, and (d) the corresponding PE-*g*-s-PAES graft copolymer.

of PAES homopolymer. The entire DSC curve that covers the high temperature range is shown in Figure S3 of the Supporting Information. Despite the incorporation of high molecular weight PAES side chains, the PE-*g*-PAES graft copolymer shows only a small decrease (~7 °C) in PE melting temperature and a decrease of heat of fusion (ΔH) mainly due to the dilution effect. Considering the PE backbone is only contributing to 43% of the weight to the PE-*g*-PAES graft copolymer, the PE backbone maintains its high crystallization ability despite the presence of the PAES side chains.

Figure 4 shows the WAXS patterns of the same set of PE copolymers (Figure 3). All samples exhibit two principal PE crystalline diffraction peaks at 2θ = 21.6°, 24.0°, corresponding to the 110 and 200 planes,[47] respectively, with the amorphous halo centered at 2θ = 19.8°. There is no detectable peak associated with amorphous polysulfone side chains in the graft copolymer. Comparing with the PE-*co*-*p*-MS copolymer, the reduction of the 110 peak height in the PE-*g*-PAES graft copolymer indicates a smaller PE crystal size, consistent with the DSC result showing a lower melting temperature. The quantitative determination of the degree of crystallinity (X_c) was estimated by Mandelkern's method,[47] based on an area ratio between crystalline (110 and 200) peaks and the sum of crystalline peaks and amorphous halo. Table 4 compares the X_c

dx.doi.org/10.1021/ma202492d | *Macromolecules* 2012, 45, 2460−2470

(%) values from DSC and WAXS results. Within the experimental error, there is very close agreement between

Table 4. Summary of DSC and WAXS Results for Various PE Copolymers during the Modification

sample	T_m (°C)	ΔH (J/g)	X_c (%) by DSC	X_c (%) by WAXS
PE-*co*-*p*-MS	125	132.2	67	64
PE-*co*-*p*-MS−Br	124	116.6	60	59
PE-*g*-PAES	118	47.5	24.2	26
PE-*g*-s-PAES	116.5	45.2	23.1	21

two methods. Evidently, in the PE-*g*-PAES graft copolymer with graft density <1 mol %, a clear microphase separation was developed in the morphology that includes a highly crystalline and hydrophobic PE phase and an amorphous (high T_g) and more hydrophilic PAES phase.

PE-*g*-s-PAES PEMs and Mechanical Properties. The resulting PE-*g*-PAES copolymers are completely soluble in organic solvents, such as anisole, at an elevated temperature. As illustrated in Scheme 2, the homogeneous viscous polymer solution was solution-cast into films, and then dried to form uniform membranes with thicknesses of 20−40 μm. The formed light brown transparent and ductile membranes, as shown in Figure 5 (left), were suspended in 1,1,2,2-tetrachloroethane solution for carrying out the sulfonation reaction using a trimethylsilyl chlorosulfonate reagent[42,48] under a heterogeneous condition. The films gradually deepen in color, maintaining their transparency. Figure 5 (right) shows a typical PE-*g*-s-PAES PEM with a higher sulfonation (DS) level, showing brown and transparent. It is interesting to note that the sulfonation level reported in the poly(arylene ether sulfone), including the commercial ones,[42,49,50] was usually less than 1 sulfonic acid per arylene ether sulfone unit. The higher sulfonation level leads to extensive swelling or dissolution by water and polar solvents. McGrath et al[9,11,51−54] reported the control of water swelling by direct copolymerization of bisulfonated sulfone monomers with the

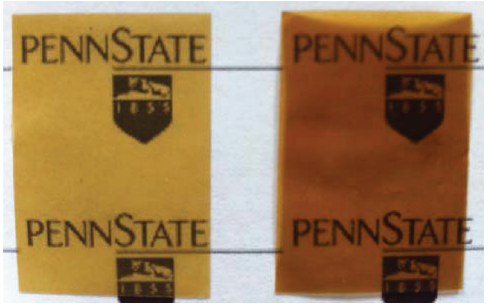
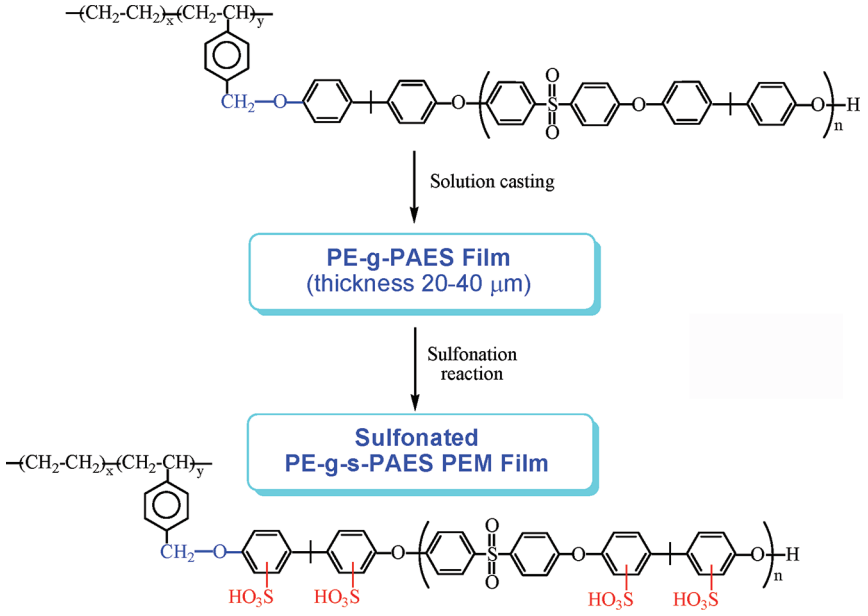


Figure 5. Photograph of (left) an unsulfonated PE-*g*-PAES membrane (run B-4) and (right) the corresponding sulfonated PE-*g*-s-PAES membrane (run s-B-4).

hydrophobic sulfone units in both random and block copolymers. As will be discussed later (Table 6), most PE-*g*-PAES graft copolymers achieved a higher degree of sulfonation with 1.6−1.7 sulfonic acid per arylene ether sulfone unit in this postsulfonation reaction, despite the heterogeneous reaction condition. In addition, the resulting PE-*g*-s-PAES PEMs still maintain very good mechanical properties and well-controlled water swelling. The DSC curve of PE-*g*-s-PAES PEM (curve d in Figure 3) reveals that PE crystalline phase remains intact during the sulfonation reaction. There were no significant change in melting temperature and heat of fusion. Evidently, the hydrophobic and crystalline PE backbone provides a stable matrix and allows the sulfonated PAES (s-PAES) side chains in forming highly hydrophilic (acidic) ion-conductive channels across the PEM film.

Figure 6 compares strain−stress curves of a set of polymers that are formed during the preparation of the PEM sequence, including the starting PE-*co*-*p*-MS, PE-*co*-*p*-MS−Br, PE-*g*-PAES (run B-4 in Table 3), and PE-*g*-s-PAES (run s-B-4 in Table 6). In general, the graft copolymers containing PAES (or s-PAES) side chains exhibit very different mechanical profiles than the starting PE-*co*-*p*-MS and PE-*co*-*p*-MS−Br copolymers, which behave like a typical PE thermoplastic with a yield curve showing relatively low tensile strength, low modulus, and high

Scheme 2



dx.doi.org/10.1021/ma202492d | *Macromolecules* 2012, 45, 2460−2470

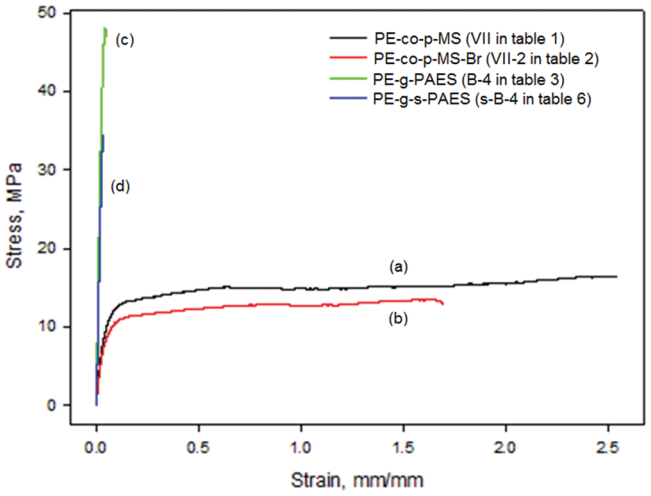


Figure 6. A comparison of strain–stress curves for a set of (a) PE-*co*-*p*-MS, (b) PE-*co*-*p*-MS–Br, (c) PE-*g*-PAES, and (d) PE-*g*-s-PAES during the PEM preparation.

elongation. The high T_g PAES in the PE-*g*-PAES graft copolymer abruptly increases tensile strength and modulus and decreases the elongation, resembling a high performance engineering plastic. After the subsequent heterogeneous sulfonation reaction, the sulfonated PE-*g*-s-PAES PEM film absorbs some water (discussed later), however it still maintains very good mechanical strength with similar stiffness with PE-*g*-PAES film and high tensile strength (~35 MPa).

Table 5 compares the mechanical properties of three graft copolymer sets, with various PE backbone molecular weights (390k, 320k, and 250k g/mol), before and after sulfonation.

Table 5. Summary of Mechanical Properties of the Polymers during the PEM Preparation

sample	structure information[a]	tensile strength [MPa]	Young's modulus [MPa]	elongation at break [%]
PE-*co*-*p*-MS	(390k/0/0/0)	16.7 ± 1.0	230 ± 40	256 ± 31
PE-*co*-*p*-MS–Br	(390k/0/0/0)	11.4 ± 0.6	150 ± 30	171 ± 19
Nafion117	–	13.7 ± 1.5	120 ± 10	208 ± 13
PE-*g*-PAES (run B-4)	(390k/20k/63/0)	48.0 ± 7.3	1750 ± 150	4.3 ± 0.2
PE-*g*-s-PAES (run s-B-4)	(390k/20k/63/1.54)	34.7 ± 5.0	1470 ± 130	5.8 ± 0.3
PE-*g*-PAES (run C-3)	(320k/20k/63/0)	34.5 ± 4.7	1320 ± 130	3.2 ± 0.2
PE-*g*-s-PAES (run s-C-3)	(320k/20k/63/1.56)	25.7 ± 2.3	1120 ± 120	6.6 ± 0.7
PE-*g*-PAES (run C-1)	(250k/20k/64/0)	27.4 ± 2.4	1090 ± 120	3.1 ± 0.2
PE-*g*-s-PAES (run s-C-1)	(250k/20k/64/1.60)	24.7 ± 2.3	960 ± 80	5.2 ± 0.3

[a](PE backbone molecular weight/PAES side chain molecular weight/PAES wt %/degree of sulfonation).

They have the same PAES side chains, similar high PAES content (63 wt %), and a degree of sulfonation (number of sulfonic acids per arylene ether sulfone unit in the s-PAES side chains). Three references, including PE-*co*-*p*-MS, PE-*co*-*p*-MS–Br, and Nafion 117 random copolymers, were also measured and compared side-by-side. In general, all PE-*g*-PAES and PE-*g*-s-PAES graft copolymers show a dramatic modulus increase and elongation reduction from the corresponding PE copolymers. They behave like rigid and strong engineering plastics. The higher the PE molecular weight in PE-*g*-PAES graft copolymers (before sulfonation), the higher the tensile strength and Young's modulus. However, the differences were reduced in the sulfonated PE-*g*-s-PAES graft copolymers. Sulfonic acids, with the associated water molecules (plasticizer) in the s-PAES phase (discussed later), somewhat reduce the overall mechanical strength. However, the high molecular weight PE-*g*-s-PAES graft copolymers (runs s-B-4 and s-C-3) still maintain very high tensile strength (~35 MPa) and Young's modulus (10 times that of Nafion 117). All mechanical results are consistent with a morphology that has continuous PAES domains imbedded in a highly crystalline PE matrix. In the fuel cell applications, high modulus PEM with low elongation is highly desirable, which provides long-term stability of MEA assemblies that are usually operated under harsh environments—strong acids, free radicals, and continuous fluctuation of pressure, temperature, humidity, etc. The weak PEMs also lead to the fuel crossover from anode to cathode or vice versa.[55] It is interesting to note that the combination of chemical and electrochemical stability with high crystallinity and hydrophobicity of the PE matrix may offer a unique (stable) framework for the water-swelled PEM containing many proton-conductive microchannels.

Proton Conductivity and Water Swelling. Table 6 shows ion exchange capacity (IEC), degree of sulfonation (DS), proton conductivity (in-plane and through-plane), water swelling (WS), and the hydration number (λ) for two sets of PE-s-PAES membranes that are prepared from two corresponding sets of PE-*g*-PAES graft copolymers (B and E sets in Table 3), with PE molecular weights of 390k and 220k g/mol, respectively, and the same PAES graft length (20k g/mol) but different graft density. All PE-*g*-PAES graft copolymers were sulfonated to a high degree of sulfonation (DS ranging from 1.48 to 1.62). As expected, both PEM sets show an increase in water uptake and proton conductivity proportional to the IEC value. Most of the PE-*g*-s-PAES membranes achieve high proton conductivity (in the same range or higher than Nafion 117). It is quite unexpected to see such a big effect on the PE backbone molecular weight to the water uptake and hydration number, as well as the significant higher through-plane conductivity than in-plane conductivity in all PE-s-PAES membranes, which is quite opposite to many reported PEMs.[56–58]

Figure 7 shows the side-by-side comparisons of water uptake and conductivity between two sets of PE-*g*-s-PAES PEMs (B and E samples in Table 6) and Nafion 117. Figure 7 (left) shows both water uptake (%) and hydration number (λ) vs IEC value (in s-PAES phase) for both sets of PE-*g*-s-PAES PEMs and Nafion 117. Considering the extensive water swelling (water uptake >160% and λ >50) in the sulfonated poly(arylene ether sulfone) with DS value ~1.2,[53] all PE-*g*-s-PAES PEMs (with DS value >1.4) show significantly smaller water swelling. In fact, the water uptake of PE-*g*-s-PAES PEM is strongly dependent on the PE backbone molecular weight, even in such a high molecular weight range (390k vs 220k g/mol). Comparing similar IEC values (s-B-1 vs s-E-3; 1.64 vs 1.67), the B set graft copolymers with a 390k g/mol PE backbone show less than half of the overall water swelling than those in the E set graft copolymers with a 220 K g/mol PE backbone. Evidently, the water pressure in the PE-*g*-s-PAES with a high

dx.doi.org/10.1021/ma202492d | *Macromolecules* 2012, 45, 2460–2470

Table 6. Summary of IEC, Water Uptake, Hydration Number, and the in-Plane and through-Plane Conductivities of Two Sets of PE-g-s-PAES PEMS and Nafion 117

sample	IEC [mmol/g of PE-*g*-s-PAES]	IEC [mmol/g of s-PAES]	DS value[a]	water uptake [%]	hydration number[b] [λ]	in-plane conductivity [mS/cm]	through-plane conductivity [mS/cm]
s-B-1	1.67	3.63	1.60	34	11	64	99
s-B-2	1.88	3.42	1.52	42	12	80	129
s-B-3	2.05	3.42	1.52	48	13	86	155
s-B-4	2.16	3.43	1.54	55	14	94	167
s-E-1	1.03	3.68	1.62	43	23	28	31
s-E-2	1.40	3.59	1.60	65	26	39	40
s-E-3	1.64	3.49	1.56	80	27	61	83
s-E-4	1.78	3.36	1.50	93	29	70	104
s-E-5	1.91	3.29	1.48	104	30	78	144
Nafion117	0.91	–	–	24	15	77	81

[a]Degree of sulfonation: no. of sulfonic acid per arylene ether sulfone unit in the s-PAES side chains. [b]Hydration number: no. of H_2O molecules per sulfonic acid by ^1H NMR.

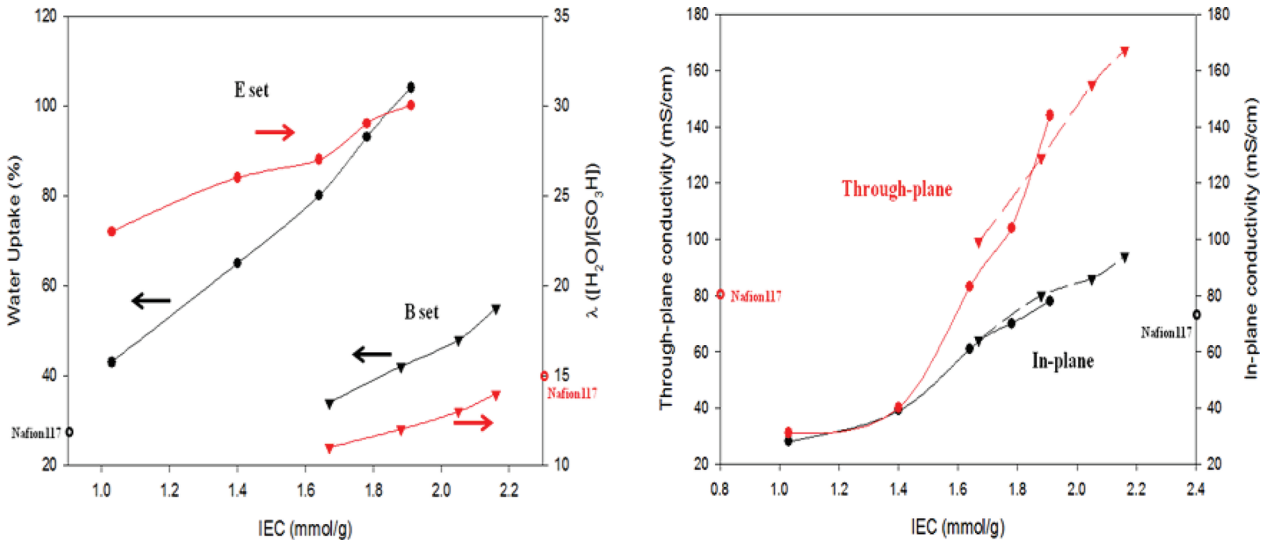


Figure 7. (Left) Comparison of water uptake (%) and hydration number (λ) and (right) in-plane and through-plane conductivities vs IEC values for two sets of PE-s-PAES PEMs (B and E) and Nafion117.

IEC value is so high that some extra high molecular weight and high crystallinity PE polymer is needed to contain the water overswelling. In set B (the 390k case), although the water uptake still linearly increases with the IEC value, the hydration number only shows a moderate increase. With regards to PE-*g*-s-PAES PEM (s-B-4) and its IEC value (more than double that of Nafion 117), the hydration number for each acid (λ = 14) in PE-*g*-s-PAES is nearly the same as that of Nafion 117 (λ = 15). The high molecular weight PE backbone, with the combination of high hydrophobicity and crystallinity, forms an exceptionally strong hydrophobic matrix (water prohibited zone) in PE-*g*-s-PAES PEM to resist water swelling in the hydrophilic phases even with very high acid content. It may form some well-protected (robotic) hydrophilic ion-conductive channels in PE-*g*-s-PAES PEMs, which are not very sensitive to acid contents. Therefore, it is possible to continuously increase the IEC value and proton conductivity (set B), without the penalty of the dilution effect, due to excessive water swelling that also weakens the membrane strength and stability.

Figure 7 (right) compares in-plane and through-plane conductivities for the same two sets of PE-*g*-s-PAES PEMs and Nafion 117. The conductivity essentially proportionately increases with the IEC value. The PE molecular weight appears to be not particularly sensitive to the conductivity. However, good control of water swelling in PE-*g*-s-PAES (set B), with higher PE molecular weight, allows the preparation of PEMs with higher IEC values while still maintaining high mechanical strength. Therefore, the PEMs in the high molecular weight B set can reach very high proton conductivity. After the IEC value reaches 1.4, both in-plane and through-plane conductivities accelerate with higher slopes. This turning point (from the s-E-2 sample in Table 6) implies that the morphology in PE-*g*-s-PAES changes from not fully connected ionic domains to a complete network structure with many ionic channels across the PEM film. In fact, this PEM sample was originated from the PE-*g*-PAES graft copolymer (run E-2 in Table 3) that contains 33 vol % of PAES, which is consistent with the expected percolation threshold.[59−61] It is a pleasant surprise to observe the through-plane conductivity of s-B-4 sample reaching 167 mS/cm (double that of Nafion 117) and significantly higher through-plane conductivity than in-plane conductivity in all PE-*g*-s-PAES graft copolymers with percolated ionic channels (IEC value >1.4). The difference becomes larger as the IEC increases. All results indicate a significantly improved connectivity between ion channels, especially in the through-plane direction. Since the through-plane conductivity is directly

dx.doi.org/10.1021/ma202492d | *Macromolecules* 2012, 45, 2460−2470

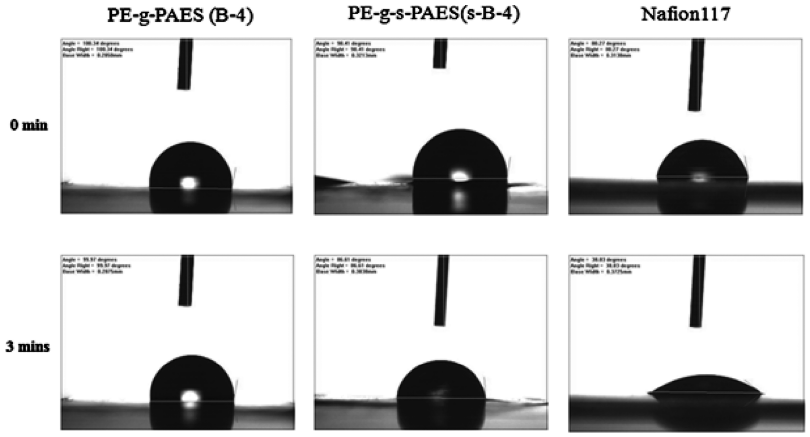


Figure 8. Comparison of water drops on PE-*g*-PAES, PE-*g*-s-PAES, and Nafion 117 PEMS.

relative to the fuel cell performance, this is a positive surprise, and it deserved a further study to understand the structure causing this anisotropy in conductivity.

Surface Properties of PE-*g*-s-PAES PEMs. The unusual phenomenon of higher through-plane conductivity than in-plane conductivity prompted us to investigate the surfaces of PE-*g*-s-PAES membranes. It is logical to speculate that the low surface energy of the PE chain in the graft structure may be favorable to diffuse and stay on the surface[62,63] of the PEM membrane. To verify this assumption, a contact angle measurement was performed using a water drop on PEM surfaces. Figure 8 shows the photographs of the water drop on the membrane surface (vs time) for both PE-*g*-PAES (run B-4 in Table 3) and PE-*g*-s-PAES (sample s-B-4 in Table 5), as well as for Nafion 117. Upon the water drop coming in contact with the Nafion 117 PEM surface, the water drop immediately diffused into the matrix. After 3 min, the water drop almost disappeared from the PEM surface, with the contact angle at 38.03°. On the contrary, the water drop was quite stable on the PE-*g*-PAES surface with the contact angle change less than 1 degree from 100.34° to 99.97°, which is significantly higher than the 83.84° of pure poly(arylene ether sulfone). The corresponding sulfonated PE-*g*-s-PAES PEM also retained the water drop very well, only allowing the water drop to slowly diffuse into the matrix. Its contact angle changed from 98.41° to 86.61° after 3 min. Evidently, the surfaces of both PE-*g*-PAES and PE-*g*-s-PAES are significantly more hydrophobic than the surface of Nafion 117. A very thin layer of PE must cover most of their surfaces. The detailed contact angle comparison is presented in the Supporting Information (Table S1).

■ CONCLUSION

We have developed a new class of polyethylene-based proton exchange membranes (PE−PEMs) for fuel cell applications. The systematic study of the graft-onto (coupling) reaction between brominated PE and poly(arylene ether sulfone) allows us to prepare a broad range of graft copolymers with well-controlled molecular structures, including the PE backbone and PAES side chain molecular weights, and graft density. With the combination of selective and efficient sulfonation reaction on PAES side chains, we have prepared PE-based PEMs with very high IEC values (>3 mmol/g in sulfonated PAES domains) in addition to well microphase separated morphology with a highly hydrophobic and crystalline PE matrix and the imbedded continuous proton conductive channels. The high molecular PE backbone in the graft copolymer provides the stable separator function, which allows the incorporation of a high concentration of sulfonic acids (high IEC value) in the conductive s-PAES domains for conduction function. In addition to the control of water swelling and maintaining good mechanical properties, the PE-based PEMs possess a thin PE hydrophobic surface layer that is reflected in the water contact angle and the anisotropic ion conductivity. Overall, this new class of PE-*g*-s-PAES PEMs offer a desirable set of properties, including conductivity, water uptake, mechanical strength, and cost-effectiveness for fuel cell applications.

■ ASSOCIATED CONTENT

Supporting Information

Determination of PAES molecular weight, TGA thermograms, FTIR spectra, DSC curves, and contact angle results. This material is available free of charge via the Internet at http://pubs.acs.org.

■ AUTHOR INFORMATION

Corresponding Author

*E-mail: chung@ems.psu.edu.

Notes

The authors declare no competing financial interest.

■ ACKNOWLEDGMENTS

The authors gratefully acknowledge the financial support of this work by an NSF Research Grant (CBET-1067554). S.N.L. expresses thanks for the support from the U.S. Department of Energy (Contract No. DE-FG07-07ID14886). We also would like to thank Albemarle Corp. and Solvay Polymers for their kind donation of MAO and high purity grade dichlorodiphenyl sulfone.

■ REFERENCES

(1) Steele, B. C. H.; Heinzel, A. *Nature* **2001**, *414* (6861), 345.
(2) Hickner, M. A.; Ghassemi, H.; Kim, Y. S.; Einsla, B. R.; McGrath, J. E. *Chem. Rev.* **2004**, *104* (10), 4587−4612.
(3) Mauritz, K. A.; Moore, R. B. *Chem. Rev.* **2004**, *104* (10), 4535−4586.
(4) Curtin, D. E.; Lousenberg, R. D.; Henry, T. J.; Tangeman, P. C.; Tisack, M. E. *J. Power Sources* **2004**, *131* (1−2), 41−48.
(5) Schmidt-Rohr, K.; Qiang, C. *Nat. Mater.* **2008**, *7* (1), 75−83.
(6) Lee, C. H.; Park, H. B.; Lee, Y. M.; Lee, R. D. *Ind. Eng. Chem. Res.* **2005**, *44* (20), 7617−7626.
(7) Kreuer, K. D. *J. Membr. Sci.* **2001**, *185* (1), 29−39.

(8) Smitha, B.; Sridhar, S.; Khan, A. A. *J. Membr. Sci.* **2005**, *259* (1−2), 10−26.
(9) Roy, A.; Hickner, M. A.; Yu, X.; Li, Y.; Glass, T. E.; McGrath, J. E. *J. Polym. Sci. B: Polym. Phys.* **2006**, *44* (16), 2226−2239.
(10) Bae, B.; Yoda, T.; Miyatake, K.; Uchida, H.; Watanabe, M. *Angew. Chem., Int. Ed.* **2010**, *49* (2), 317−320.
(11) Lee, H.-S.; Roy, A.; Lane, O.; Dunn, S.; McGrath, J. E. *Polymer* **2008**, *49* (3), 715−723.
(12) Choi, J.; Kim, D. H.; Kim, H. K.; Shin, C.; Kim, S. C. *J. Membr. Sci.* **2008**, *310* (1−2), 384−392.
(13) Kim, D. H.; Choi, J.; Hong, Y. T.; Kim, S. C. *J. Membr. Sci.* **2007**, *299* (1−2), 19−27.
(14) Kim, H. K. K., D. H.; Choi, J.; Kim., S. C. *Macromol. Res.* **2011**, *19* (9), 928−942.
(15) Chen, S.-L.; Krishnan, L.; Srinivasan, S.; Benziger, J.; Bocarsly, A. B. *J. Membr. Sci.* **2004**, *243* (1−2), 327−333.
(16) Kim, B.; Kim, J.; Jung, B. *J. Membr. Sci.* **2005**, *250* (1−2), 175−182.
(17) Cho, K.-Y.; Eom, J.-Y.; Jung, H.-Y.; Choi, N.-S.; Lee, Y. M.; Park, J.-K.; Choi, J.-H.; Park, K.-W.; Sung, Y.-E. *Electrochim. Acta* **2004**, *50* (2−3), 583−588.
(18) Zhang, Z.; Chalkova, E.; Fedkin, M.; Wang, C.; Lvov, S. N.; Komarneni, S.; Chung, T. C. *Macromolecules* **2008**, *41* (23), 9130−9139.
(19) Tsang, E. M. W.; Zhang, Z.; Shi, Z.; Soboleva, T.; Holdcroft, S. *J. Am. Chem. Soc.* **2007**, *129* (49), 15106−15107.
(20) Tsang, E. M. W.; Zhang, Z.; Yang, A. C. C.; Shi, Z.; Peckham, T. J.; Narimani, R.; Frisken, B. J.; Holdcroft, S. *Macromolecules* **2009**, *42* (24), 9467−9480.
(21) Tripathi, B. P.; Shahi, V. K. *Prog. Polym. Sci.* **2011**, *36* (7), 945−979.
(22) Sherazi, T. A.; Ahmad, S.; Kashmiri, M. A.; Guiver, M. D. *J. Membr. Sci.* **2008**, *325* (2), 964−972.
(23) Nasef, M. M.; Hegazy, E.-S. A. *Prog. Polym. Sci.* **2004**, *29* (6), 499−561.
(24) Arora, P.; Zhang, Z. *Chem. Rev.* **2004**, *104* (10), 4419−4462.
(25) Zhang, S. S. *J. Power Sources* **2007**, *164* (1), 351−364.
(26) Kostov, G. K.; Turmanova, S. C. *J. Appl. Polym. Sci.* **1997**, *64* (8), 1469−1475.
(27) Hiroshi Kawabe, M. Y. *Bull. Chem. Soc. Jpn.* **1969**, *42* (4), 1029−1036.
(28) Trochimczuk, W. M. *J. Polym. Sci.: Polym. Chem. Ed.* **1975**, *13* (2), 357−363.
(29) Kolhe, S. M.; Kumar, A. *Radiat. Phys. Chem.* **2005**, *74* (5), 384−390.
(30) Novoselova, L. Y. S., E. E. *Chem. Sustainable Dev.* **2006**, *14*, 199.
(31) Chung, T. C. *Functionalization of Polyolefins*; Academic Press: London, 2002.
(32) Chung, T. C. *Prog. Polym. Sci.* **2002**, *27* (1), 39−85.
(33) Gupta, B.; Büchi, F. N.; Scherer, G. G. *J. Polym. Sci. A: Polym. Chem.* **1994**, *32* (10), 1931−1938.
(34) Inoue, Y.; Matsugi, T.; Kashiwa, N.; Matyjaszewski, K. *Macromolecules* **2004**, *37* (10), 3651−3658.
(35) Kashiwa, N.; Matsugi, T.; Kojoh, S.-I.; Kaneko, H.; Kawahara, N.; Matsuo, S.; Nobori, T.; Imuta, J.-I. *J. Polym. Sci. A: Polym. Chem.* **2003**, *41* (22), 3657−3666.
(36) Ruggeri, G.; Aglietto, M.; Petragnani, A.; Ciardelli, F. *Eur. Polym. J.* **1983**, *19* (10−11), 863−866.
(37) Carpenetti, D. W.; Kloppenburg, L.; Kupec, J. T.; Petersen, J. L. *Organometallics* **1996**, *15* (6), 1572−1581.
(38) Canich, J. M. US Patent 5,026,798, 1991.
(39) Sullivan, J. M. US Patent 6,015,916, 2000.
(40) Wang, C.; Chalkova, E.; Lute, C.; Fedkin, M.; Komarneni, S.; Chung, T. C.; Lvov, S. *J. Electrochem. Soc.* **2010**, *157*, 1634.
(41) Kwon, Y. H.; Kim, S. C.; Lee, S.-Y. *Macromolecules* **2009**, *42* (14), 5244−5250.
(42) Baradie, B.; Poinsignon, C.; Sanchez, J. Y.; Piffard, Y.; Vitter, G.; Bestaoui, N.; Foscallo, D.; Denoyelle, A.; Delabouglise, D.; Vaujany, M. *J. Power Sources* **1998**, *74* (1), 8−16.
(43) Chung, T. C.; Lu, H. L. *J. Polym. Sci. A: Polym. Chem.* **1997**, *35* (3), 575−579.
(44) Lu, H. L.; Hong, S.; Chung, T. C. *Macromolecules* **1998**, *31* (7), 2028−2034.
(45) Dong, J. Y.; Chung, T. C. *Macromolecules* **2002**, *35* (5), 1622−1631.
(46) Brandrup, J., Immergut, E. H., Eds. *Polymer Handbook*, 2nd ed.,Wiley: New York, 1975.
(47) Gopalan, M. R.; Mandelkern, L. *J. Polym. Sci. B: Polym. Lett.* **1967**, *5* (10), 925−929.
(48) Genova-Dimitrova, P.; Baradie, B.; Foscallo, D.; Poinsignon, C.; Sanchez, J. Y. *J. Membr. Sci.* **2001**, *185* (1), 59−71.
(49) Lufrano, F.; Baglio, V.; Staiti, P.; Arico', A. S.; Antonucci, V. *J. Power Sources* **2008**, *179* (1), 34−41.
(50) Nolte, R.; Ledjeff, K.; Bauer, M.; Mülhaupt, R. *J. Membr. Sci.* **1993**, *83* (2), 211−220.
(51) Badami, A. S.; Lane, O.; Lee, H.-S.; Roy, A.; McGrath, J. E. *J. Membr. Sci.* **2009**, *333* (1−2), 1−11.
(52) Arnett, N. Y.; Harrison, W. L.; Badami, A. S.; Roy, A.; Lane, O.; Cromer, F.; Dong, L.; McGrath, J. E. *J. Power Sources* **2007**, *172* (1), 20−29.
(53) Wang, F.; Hickner, M.; Kim, Y. S.; Zawodzinski, T. A.; McGrath, J. E. *J. Membr. Sci.* **2002**, *197* (1−2), 231−242.
(54) Kim, Y. S.; Wang, F.; Hickner, M.; McCartney, S.; Hong, Y. T.; Harrison, W.; Zawodzinski, T. A.; McGrath, J. E. *J. Polym. Sci. B: Polym. Phys.* **2003**, *41* (22), 2816−2828.
(55) Patil, Y. P.; Jarrett, W. L.; Mauritz, K. A. *J. Membr. Sci.* **2010**, *356* (1−2), 7−13.
(56) Takamuku, S.; Takimoto, N.; Abe, M.; Shinohara, K. *J. Power Sources* **2010**, *195* (4), 1095−1098.
(57) Soboleva, T.; Xie, Z.; Shi, Z.; Tsang, E.; Navessin, T.; Holdcroft, S. *J. Electroanal. Chem.* **2008**, *622* (2), 145−152.
(58) Peckham, T. J.; Holdcroft, S. *Adv. Mater.* **2010**, *22* (42), 4667−4690.
(59) Gebel, G. *Polymer* **2000**, *41* (15), 5829−5838.
(60) Khandpur, A. K.; Foerster, S.; Bates, F. S.; Hamley, I. W.; Ryan, A. J.; Bras, W.; Almdal, K.; Mortensen, K. *Macromolecules* **1995**, *28* (26), 8796−8806.
(61) Hasegawa, H.; Tanaka, H.; Yamasaki, K.; Hashimoto, T. *Macromolecules* **1987**, *20* (7), 1651−1662.
(62) Gaines, G. L. Jr. *Macromolecules* **1981**, *14* (1), 208.
(63) Thomas, H. R.; O'Malley, J. J. *Macromolecules* **1979**, *12* (2), 323−329.

Macromolecules

Article

pubs.acs.org/Macromolecules

Order−Order Transition between Equilibrium Ordered Bicontinuous Nanostructures of Double Diamond and Double Gyroid in Stereoregular Block Copolymer

Che-Yi Chu,[†] Wen-Fu Lin,[‡] Jing-Cherng Tsai,[‡] Chia-Sheng Lai,[†] Shen-Chuan Lo,[§] Hsin-Lung Chen,*[,†] and Takeji Hashimoto*[,†,⊥]

[†]Department of Chemical Engineering and Frontier Research Center on Fundamental and Applied Sciences of Matters, National Tsing Hua University, Hsin-Chu 30013, Taiwan

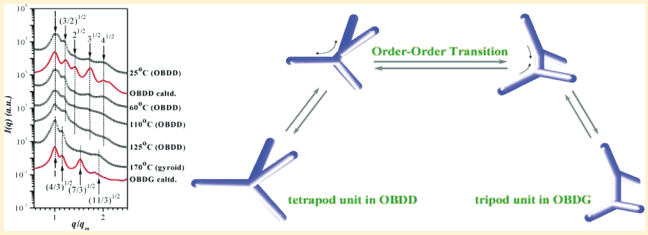
[‡]Department of Chemical Engineering, National Chung Cheng University, Chia-Yi 62102, Taiwan

[§]Material and Chemical Research Laboratories, Industrial Technology Research Institute, Chutung, Hsin-Chu, Taiwan

[⊥]Advanced Science Research Center, Japan Atomic Energy Agency, Naka-gun, Ibaraki Pref. 319-1195, Japan

Supporting Information

ABSTRACT: While ordered bicontinuous double diamond (OBDD) in block copolymers has always been considered as an unstable structure relative to ordered bicontinuous double gyroid (OBDG), here we report the existence of a thermodynamically stable OBDD structure in a diblock copolymer composed of a stereoregular block. A slightly asymmetric syndiotactic polypropylene-*block*-polystyrene (sPP-*b*-PS) as cast from xylene was found to display the OBDD morphology. When the OBDD-forming diblock was heated, this structure transformed to the OBDG phase at ca. 155 °C. Interestingly, OBDD was recovered upon cooling even in the temperature range above melting point of sPP, indicating that OBDD was a thermodynamically stable structure for sPP-*b*-PS melt, which was in contradiction to the conventional view. We propose that the larger free energy cost encountered in OBDD due to the larger packing frustration may be compensated sufficiently by the release of free energy due to local packing of the conformationally ordered segments of sPP blocks, which stabilizes the OBDD structure at the lower temperatures.



INTRODUCTION

Block copolymers have attracted great attention because of their capability of self-assembling into a series of long-range ordered nanostructures according to the block composition.[1] The lamellar and hexagonally packed cylindrical nanostructures constructed by block copolymers have been extensively used as nanoporous structure-directing agents,[3,2] templates for 1-D and 2-D photonic band gap materials,[4,5] and masks for nanolithography.[7−6] However, the nanopatterns translated from these nanostructures exhibit structural features such as low spatial continuity and less sustainability owing to the isolated microdomains. To reinforce further the potential application of block copolymers, the ordered bicontinuous structure, such as the double gyroid (OBDG) phase,[9] was introduced to fabricate nanostructured networks,[10,11] 3-D photonic crystals,[12] bulk heterojunction solar cells,[13,14] and low-refractive-index materials.[15]

The present study reports the existence of another thermodynamically stable bicontinuous structure, i.e., ordered bicontinuous double diamond (OBDD), in a diblock copolymer composed of a stereoregular block. Moreover, we clarify that the OBDD structure formed in this system underwent a thermally reversible transition to or from the OBDG phase upon heating or cooling, respectively, thereby representing the first instance of thermally induced order−order transition between the thermodynamically equilibrium bicontinuous structures of block copolymers. OBDD is constructed by 4-fold nodes connected with $Pn\bar{3}m$ symmetry and (6,4) nets.[16,17] This structure is different from OBDG, which is constructed by 3-fold nodes connected with $Ia\bar{3}d$ symmetry and (10,3) nets.[9] In complex fluids such as surfactants,[18] OBDD is known to be more common than OBDG within certain parameter space. However, the OBDD structure has always been considered to be unstable relative to OBDG for conventional block copolymers with van der Waals interactions only. The stability of OBDD relative to lamellae, OBDG, hexagonally packed cylinders, and bcc-packed spheres has been studied by theoretical calculations.[19−21] None of these studies provided a theoretical basis for considering OBDD as a thermodynamically stable structure in strongly segregated block copolymers. In the weakly segregated systems, the calculated

Received: September 9, 2011
Revised: December 11, 2011
Published: March 1, 2012

ACS Publications © 2012 American Chemical Society

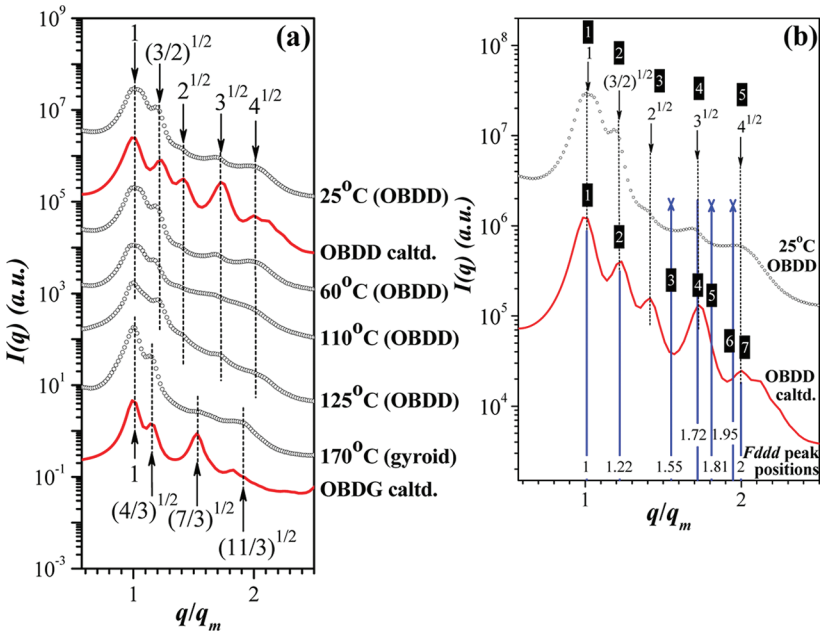


Figure 1. (a) Temperature-dependent SAXS profiles of the as-cast sPP-*b*-PS films obtained in a heating cycle, where each profile was collected after annealing at each temperature for 5 min, and followed by data acquisition for 5 min. The red solid curves represent the calculated SAXS curves of the OBDD and OBDG structures. The scattering profiles are presented as a function of q/q_m, with q_m being the position of the primary peak at each temperature. (b) Comparison of the peak-position ratios between the OBDD and *Fddd* structures. Blue lines indicate the peak-position ratios of *Fddd*.

free energy of OBDD was also never lower than that of OBDG.[22−24]

The issue regarding why OBDG is more stable than OBDD can be considered by the following two thermodynamic factors: (1) the interfacial free energy that favors the structure having the least interfacial area per unit volume[25] and (2) the packing frustration that favors microdomains with uniform thicknesses because the block chains do not have to be stretched excessively to fill space uniformly to attain the normal liquid density.[26] The calculated interfacial shape of OBDG has a lower standard deviation from the constant mean curvature (CMC) surface compared to that of OBDD; therefore, OBDG is more stable than OBDD in terms of minimization of packing frustration. This postulate was supported from the self-consistent mean-field theory (SCFT) calculations for the blends of A-*b*-B with homopolymer A (h-A), where the addition of h-A to the minority domains in the blend preferentially filled the space in the center of A domains, thereby relieving the packing frustration and stabilizing the OBDD structure over a very narrow range of composition.[26,27] Although both theoretical and experimental studies have predicted or reported the existence of the OBDD phase in A-*b*-B/h-A blends, the order−order transition (OOT) between equilibrium OBDD and OBDG has never been found thus far.

In this study, we disclose the formation of the OBDD morphology in the solvent-cast film of a slightly asymmetric diblock copolymer composed of a stereoregular block, syndiotactic polypropylene (sPP), and a conventional coil block, polystyrene (PS). This OBDD structure transformed to the OBDG phase upon heating the sPP-*b*-PS to ca. 155 °C, and the OBDG structure transformed back to OBDD on subsequent cooling even in the temperature range above melting temperature of sPP. The thermal reversibility of the morphological transformation indicated that OBDD is an equilibrium structure in the present diblock system. The stability of the OBDD phase in the present diblock melt will be discussed on the basis of the relief of the free energy cost of the packing frustration by local packing of conformationally ordered segments of sPP blocks in the melt, a new physical factor brought about by the stereoregularity of the block chain. Our finding presents a new scenario that the introduction of stereoregularity into the constituting block may release the packing free energy of diblock chains in the microdomain space, which in turn stabilizes the otherwise unstable nanostructure.

EXPERIMENTAL SECTION

Materials and Sample Preparation. The sPP-*b*-PS diblock copolymer ($M_{n,sPP}$ = 6800, $M_{n,PS}$ = 9400, PDI = M_w/M_n = 1.19) studied here was prepared in two steps according to the procedure reported in the literature.[28] First, 4-methylstyrene-capped sPP (M_n = 6800, PDI = 1.32), which served as an end-functionalized prepolymer, was prepared by syndiospecific polymerization of propylene conducted in the presence of 4-methylstyrene and hydrogen using $Me_2C(Cp)$-(Flu)$ZrCl_2$ as the catalyst. Second, the 4-methylstyrene-capped sPP was converted into silyl chloride-capped sPP, which was in situ treated with living anionic polystyrene (M_n = 9400 g/mol, PDI = 1.02) to yield the sPP-*b*-PS (the detailed synthetic and purification methods for sPP-*b*-PS can be found in the literature[28]). Figure S1 of the Supporting Information shows the ^{1}H NMR spectrum of the resulting sPP-*b*-PS. The successful preparation of a structurally well-defined sPP-*b*-PS sample can be further elucidated by the GPC analysis shown in Figure S2 (in the Supporting Information), which compares the GPC elution curves of the 4-methylstyrene-capped sPP (M_n = 6800, M_w/M_n = 1.32) and the living anionic polystyrene (M_n = 9400 g/mol, M_w/M_n = 1.02) with that of the sPP-*b*-PS (M_n = 16200 g/mol, M_w/M_n = 1.19). The symmetric GPC elution curve observed for the block copolymer rules out the possibility of the homopolymer contamination. The volume fraction of sPP block in this sample was 0.46 in the melt state.[29]

For the film preparation, the diblock copolymer was dissolved in xylene solvent at 50 °C, and the solution was subsequently cast on the Petri dish. The film was obtained after evaporating most of the solvent

quickly on the hot plate at ca. 140 °C (≅ boiling point of xylene). The film was further annealed at 100 °C (>T_g^{PS}) for 1 h followed by drying in vacuum at 70 °C for 24 h.

Small-Angle X-ray Scattering (SAXS) Measurement. The morphology of the sPP-*b*-PS was probed by SAXS performed at the Endstation BL23A1 of the National Synchrotron Radiation Research Center (NSRRC), Taiwan. The energy of X-ray source and the sample-to-detector distance were 8 keV and 1815 mm, respectively. The scattering signals were collected by a MarCCD detector of 512 × 512 pixel resolution. For the structure characterization, the sample was equilibrated at each temperature for 5 min followed by data acquisition for 5 min. The scattering intensity profile was output as the plot of the scattering intensity (I) vs the magnitude of the scattering vector, $q = (4\pi/\lambda)\ \sin(\theta/2)$ (θ = scattering angle). The SAXS profiles were corrected for the incident beam intensity, the detector sensitivity, and the background arising from the thermal diffuse scattering (TDS).

Fourier Transform Infrared Spectroscopy (FTIR) Measurement. The infrared spectra were recorded at a resolution of 1 cm^{-1} over 32 scans on a Nicolet AVATAR 320 FTIR spectrometer under a nitrogen atmosphere. The sPP-*b*-PS was cast directly onto a KBr pellet. The films were thin enough to be within the absorbance range where the Beer−Lambert law is obeyed. For the molecular conformation characterization, the sample was equilibrated at each temperature for 5 min prior to data acquisition.

RESULTS AND DISCUSSION

The theoretical scattering profiles of the OBDD and OBDG phase calculated by assuming *Pn*3*m* and *Ia*$\bar{3}$*d* space group symmetry, respectively, with the 3D network domain structure are shown in Figure 1a (the entire scattering profiles are shown in Figure S3 of the Supporting Information). The algorithm and model adopted were developed by Förster et al.,[33] which took into account the domain size distribution, distortion of domain spacing, grain size, and peak shape which varied analytically between Lorentzian and Gaussian functions. The OBDD structure exhibits a series of diffraction peaks with position ratio of $1:(3/2)^{1/2}:2^{1/2}:3^{1/2}:4^{1/2}$, corresponding to (110), (111), (200), (211), and (220) planes, respectively. The OBDG structure displays four diffraction peaks with position ratio of $1:(4/3)^{1/2}:(7/3)^{1/2}:(11/3)^{1/2}$, corresponding to (211), (220), (321), and (332) planes, respectively. The obvious difference between the position of the second-order peak relative to that of the primary peak (i.e., $(3/2)^{1/2}$ = 1.22 for OBDD vs $(4/3)^{1/2}$ = 1.15 for OBDG) can be used as the main index to distinguish these two structures from the SAXS profile.

Figure 1a also shows the temperature-dependent synchrotron-SAXS profiles of sPP-*b*-PS obtained in the heating process of the as-cast film (the entire scattering profiles are shown in Figure S4 of the Supporting Information), where each profile was collected after annealing at each temperature for 5 min, followed by data acquisition for 5 min. The scattering profiles are presented as a function of q/q_m, with q_m being the position of the primary peak (see Table 1) for clear identification of the change of the relative peak positions with temperature. The SAXS profile observed at 25 °C showed five peaks; the ratios of the higher-order peak positions to the primary peak position were not integral, indicating that the diblock did not exhibit lamellar morphology in spite of its rather symmetric composition. The observed peak-position ratios were indeed consistent with that predicted by the OBDD structure (the red curve).[33] The relative intensities of the observed peaks also agreed quite well with those of the calculated profile except for the fourth-order peak. This discrepancy may be attributed to the approximation of the form factor of the building block by the cylindrical form factor in calculating the theoretical SAXS pattern. When the copolymer was heated to 170 °C, the position of the second-order peak relative to that of the first-order peak shifted clearly from $(3/2)^{1/2}$ to $(4/3)^{1/2}$, and the scattering pattern became consistent with that associated with the OBDG phase. Therefore, a phase transition from OBDD to OBDG occurred upon the heating.

Table 1. Value of the Position of the Primary Peak (q_m) in Figure 1

T (°C)	25	60	110	125	170
q_m (nm^{-1})	0.26	0.26	0.26	0.25	0.27

The observed SAXS profiles at the low temperatures $T \leq 125$ °C were identified as the scattering from the OBDD symmetry with 4-fold nodes rather than the OBDG symmetry with 3-fold nodes, judging from the fact that the observed peak-position ratios matched with those predicted by the OBDD structure much better than those predicted by the OBDG phase. Since another ordered bicontinuous structure, *Fddd*, also has 3-fold nodes,[34] it is important to clearly distinguish the OBDD structure from the *Fddd* structure. For this purpose, the observed peak position ratios were further compared with those associated with the orthorhombic *Fddd* phase exhibiting the scattering peak position ratio of 1:1.22:1.55:1.72:1.81:1.95:2.00, etc.,[34] as shown by the solid blue vertical lines in Figure 1b. Except for the second-, fourth-, and seventh-order peaks (i.e., q/q_m = 1.22, 1.72, and 2) of the *Fddd* structure which were close to the observed second-, fourth-, and fifth-order peaks of OBDD, the third-, fifth-, and sixth-order ones (i.e., q/q_m = 1.55, 1.81 and 1.95) of *Fddd* were not identified in our observed SAXS profile. Moreover, the observed third-order peak at $q/q_m = 2^{1/2}$ is unidentified by *Fddd* but identified by OBDD. Consequently, we ruled out the formation of *Fddd* structure in the present diblock copolymer as well as the order−order phase transition from OBDD to *Fddd* as an order−order transition from 4-fold nodes to 3-fold nodes.

Since the equilibration time at each temperature was short in the synchrotron SAXS experiment despite the higher resolution for the scattering peaks, we conducted an in-house SAXS measurement to examine the thermodynamic stability of the phases and the thermal reversibility of the phase transition with much longer equilibration time at each temperature. Figure 2 shows the temperature-dependent SAXS profiles (focused on the first four scattering peaks) taken with the in-house SAXS measurements of the as-cast sPP-*b*-PS (the entire scattering profiles are shown in Figure S5 of the Supporting Information), where the sample was annealed at each temperature for 30 min followed by data acquisition for 1 h. Similar to that found in Figure 1, the as-cast sample exhibited the OBDD structure as evidenced by the scattering profile having a series of the peaks at the relative peak positions of $1:(3/2)^{1/2}:2^{1/2}:3^{1/2}:4^{1/2}$.

The OBDD structure experienced, to some extent, structural rearrangement caused by the melting of sPP crystallites (T_m^{sPP} ≅ 124 °C, the peak temperature of the melting endotherm; see the DSC thermogram in Figure S6 of the Supporting Information) and the gains of mobility of PS blocks and junction points upon heating to 110−135 °C, as manifested by the broadening of the scattering peaks. However, the scattering peaks of the OBDD structure became sharp and narrow again at $T \geq 140$ °C, where the effect of sPP crystallization completely disappeared (T_{mh}^{sPP} = 137 °C, the end temperature of melting of sPP crystallites; see the DSC thermogram in Figure S6). This result clarifies that the formation of the OBDD

dx.doi.org/10.1021/ma202057g | *Macromolecules* 2012, 45, 2471−2477

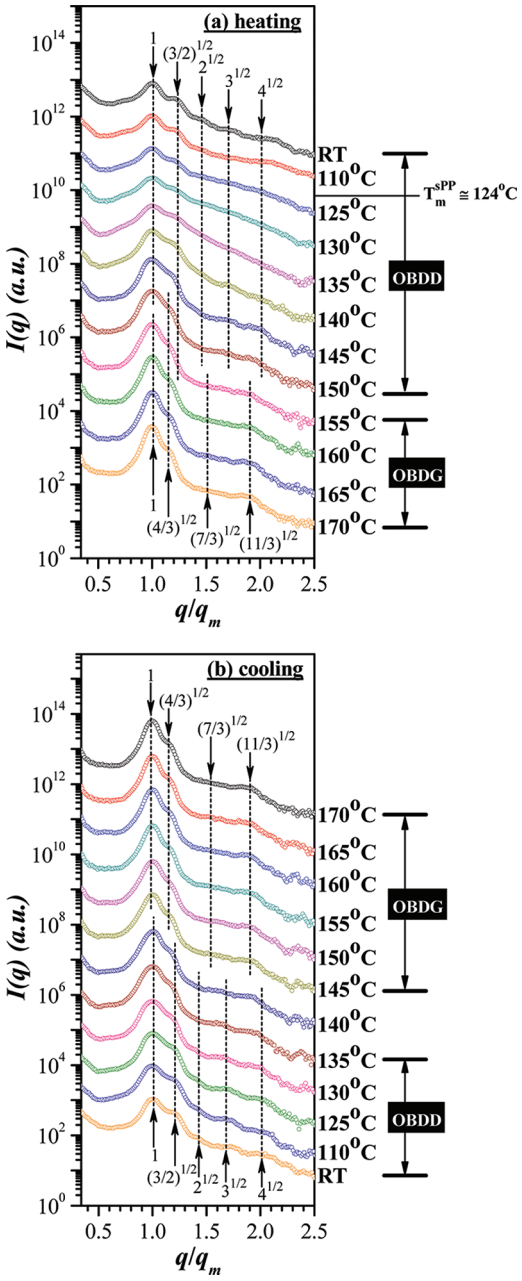


Figure 2. Temperature-dependent SAXS profiles of the as-cast sPP-*b*-PS: (a) a heating cycle and (b) a cooling cycle. Each profile was collected after annealing at each temperature for 30 min and followed by data acquisition for 1 h. The scattering profiles are presented as a function of q/q_m with q_m being the position of the primary peak at each temperature.

phase was not driven by the crystallization of sPP block. Upon further heating, a phase transition from the OBDD to OBDG structure took place between 150 and 155 °C. It is worth mentioning that both the OBDD and OBDG structures may coexist at 150 ≤ T (°C) < 155, possibly due to effects of random thermal noise, as in the case of the order-disorder coexistence in the very narrow temperature range around the order-disorder transition temperature,[35-37] and/or the kinetic effect (the slow transition). The latter effect is due to a very small degree of the superheating and supercooling from OOT in this temperature range. Interestingly, the OBDG structure transformed back to the OBDD structure upon subsequent cooling, as shown in Figure 2b. The thermal reversibility of the OOT attested that OBDD was the stable structure at the low temperatures. The OBDD structure became more ordered in the cooling process comparing with that found in the heating due to being less influenced by the crystallization of sPP.

The temperature dependence of the inverse of the primary scattering peak intensity (I_m^{-1}) above T_m^{sPP} is displayed in Figure 3. The peak intensity significantly increased at 125−140

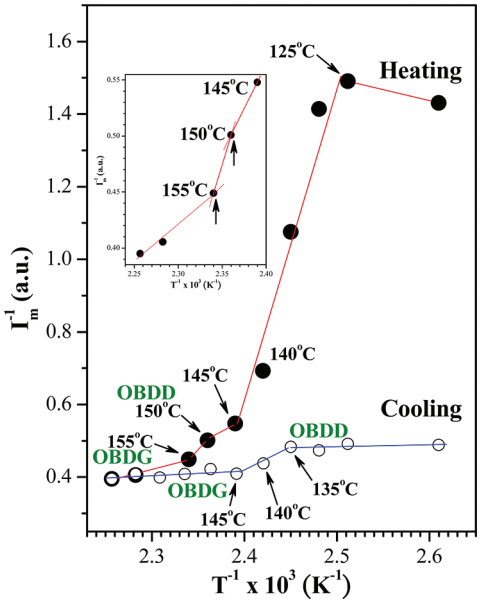


Figure 3. Temperature dependence of the inverse of the intensity of the primary scattering peak (I_m^{-1}) for the heating process of the as-cast sPP-*b*-PS and the subsequent cooling process. The inset shows the enlarged plot for the temperature ranging from 145 to 170 °C in the heating process.

°C in the heating process due to an increasing degree of ordering of the OBDD structure upon the melting of sPP crystallites. Contrarily, the intensity of scattering peak below 135 °C ($<T_{mh}^{sPP}$ = 137 °C) in the cooling process almost remained constant, due to pinning of the ordering process of OBDD via sPP crystallization. The large hysteresis in the temperature between 125 and 135 °C was attributed to the melting/crystallization of sPP blocks.

Let us further examine the data above T_{mh}^{sPP} where the kinetic effects of crystallization/melting were small or excluded. The transitions from OBDD to OBDG and OBDG to OBDD were clearly characterized by the discontinuity in I_m^{-1} in the heating (150−155 °C shown in the inset) and cooling (145−135 °C) process, respectively. A hysteresis was also found when comparing the peak intensity I_m in the heating and cooling process across the OOT. Both the discontinuity and the hysteresis observed here revealed that the order−order transition was the first-order phase transition in nature. These results evidenced that OBDD and OBDG were both thermodynamically stable structures in this system.

The stability of the OBDD structure was further demonstrated by a long-time annealing of the OBDD-forming sample to examine if the OBDD phase would transform into another more stable structure upon the annealing. Here the SAXS profile of sPP-*b*-PS was measured at room temperature after the sample has been isothermally annealed at 140 °C for 24 h, followed by quenching to liquid nitrogen to freeze the structure

dx.doi.org/10.1021/ma202057g | *Macromolecules* 2012, 45, 2471−2477

formed at 140 °C (see Figure S7 of the Supporting Information). It is obvious that the scattering profile still matched well with that prescribed by the OBDD phase, showing that OBDD in sPP-*b*-PS diblock copolymers is a stable structure.

To observe the OBDD structure in real space, the annealed sample was cut into the ultrathin section for observations under transmission electron microscopy (TEM). The formation of OBDD phase was evidenced by the micrograph displayed in Figure S8 of the Supporting Information, showing the image of the rhombus pattern. As indicated by Hasegawa et al.,[17] the projection from the [100] direction of a double-diamond (DD) lattice would give rise to a square-lattice image (see Figure S8 of the Supporting Information). The rhombus lattice image observed here should arise from a slight tilt of such a square lattice. The slight tilt made the projection vector slightly deviate from the [100] direction, so that the sequentially connected rods with an inclined angle were projected as an undulation pattern as observed in the image.

Our SAXS results have thus revealed the occurrence of a thermally induced OBDD−OBDG OOT in a sPP-*b*-PS diblock copolymer. Although such a phase transition has not been found for diblock copolymers previously, Benedicto et al. have mathematically described one possible transformation route from D surface (in the OBDD phase) into G surface (in the OBDG phase) on the basis of a continuous homotopic transformation through the minimal surfaces;[38] namely, the transformation from (6,4) net of D surface into (10,3) net of G surface can be achieved by "randomly pulling apart" a tetrahedral vertex to form two trigonal vertices. It is noted that pulling all vertices apart in one direction would result in the *Fddd*-type (10,3) net structure. However, the possibility of the *Fddd* structure has already been ruled out for the present diblock in conjunction with Figure 1b.

Here we would like to further discuss the thermodynamic driving forces that control the formation of the OBDD and OBDG phases in response to the temperature change. The main difference between the elementary units of the two bicontinuous structures lies in the degree of packing frustration associated with the stretching of the minority block chains (i.e., sPP blocks in our diblock), where the minority block chains have to be stretched more to fill the space at the center of the four-connector (in the OBDD structure) than that of the three-connector (in the OBDG structure). On the other hand, the four-connector domain in OBDD has a lower surface area per unit volume than that of the three-connector in gyroid[39] and should hence suffer a lower interfacial energy. Nevertheless, the enthalpy difference between surfaces "G" and "D" was calculated to be small when adopting an isometric mapping of minimal surface.[40,41] Since the theoretical works normally assume the block chains to obey Gaussian statistics, the relief of the entropic penalty arising from packing frustration can easily outweigh the reduction of interfacial free energy; as a result, OBDG is always predicted to be a more stable structure than OBDD for the conventional diblock copolymers even in the case of the larger segregation strength (or at lower temperatures).

Even in sPP-*b*-PS, the relief of packing frustration dominated the self-assembly, and hence the OBDG structure was favored at the high temperatures. Then why is OBDD favored for sPP-*b*-PS at the low temperatures? We may envision the following two possible physical factors: (1) a new factor involving the stereoregularity of sPP and (2) a physical factor associated with the polydispersity of sPP. We propose that factor (1) is primarily responsible for the stability of the OBDD structure; that is, the increasing degree of conformational order due to increasing amount of helical segments[42,43] of sPP block chains with lowering temperature increases the free energy release accompanied by the local packing of these segments and hence stabilizes the OBDD structure. Below we will first discuss factor (1) and then factor (2).

Stereoregular polymers such as iPP, sPP, iPS, and sPS adopt helical conformation in the crystalline state.[44−47] The helical segments however do not completely disappear even above the crystal melting point. In the case of sPP, the helical conformation of the segments in the noncrystalline state (H_A) gives rise to absorption peaks at 977, 844, and 836 cm^{-1} in the infrared spectrum.[48] Figure 4 displays the temperature-dependent FTIR spectra of the diblock to examine the existence of helical segments in sPP block and the temperature dependence of their population (the entire spectrum is shown in Figure S9 of the Supporting Information). Since the argument that the formation of the OBDD structure in the sPP-*b*-PS may be associated with the crystallization of sPP blocks could be precluded due to the existence of OBDD even in the melt state, we consider the conformation of sPP in the melt state only. As shown in Figure 4, the population of H_A decreased with raising temperature across the OBDD-to-OBDG transition temperature, as manifested by comparing the spectrum collected at 140 °C to that obtained at 175 °C, and this tendency was continuous to 200 °C. Upon cooling, the H_A signal was recovered.

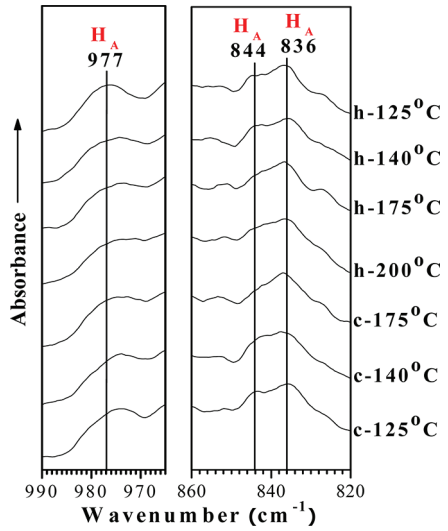


Figure 4. Temperature-dependent FTIR spectra of sPP-*b*-PS, in which "H_A" denotes the signals of helical chain conformation of sPP blocks at 977, 844, and 836 cm^{-1} in the noncrystalline state. "h" and "c" denote the spectra collected in the heating and cooling cycle, respectively. The spectra are vertically shifted to avoid overlaps.

The observed temperature dependence was analogous to that found in the previous temperature-dependent FTIR studies of the thermal stability of helical segments of sPP homopolymer in the melt state,[42,43] where the absorbance of the 977 cm^{-1} band was used as an index for the population of helical segments. It was postulated that the decrease of the helical segment population on heating was associated with the partial destruction of the longer helical segments into the shorter ones. The FTIR spectra hence confirmed that the amount of

dx.doi.org/10.1021/ma202057g | *Macromolecules* 2012, 45, 2471−2477

helical segments in sPP blocks in the OBDD phase is higher than that in the OBDG phase. When the population of helical segments was sufficiently high, their mutual interactions would allow sPP blocks to form locally ordered structures or mesomorphic packing of the helical segments. In this case, the entropic penalty associated with chain stretching was effectively compensated by the release of free energy on forming the mesomorphically ordered regions in the microdomains. The role of packing frustration, which is important for Gaussian chains, was hence greatly relaxed by locally ordered mesomorphic packing of the helical segments in the case of the block copolymer with the stereoregular block chain; as a consequence, OBDD became the favorable structure because of the lower interfacial free energy and lower free energy of the chain packing in the microdomain. The relief of packing frustration regained its dominant role when the population of helical segments was low at sufficiently high temperature, and thereby the OBDG phase became the more stable structure.

The issue for the relief of the packing frustration that dominated the self-assembly at the high temperatures of sPP-*b*-PS was further evidenced by blending with the corresponding constituent sPP homopolymer (see Figure S10 of the Supporting Information). It was found that the OBDD structure could also be formed in the sPP-*b*-PS/sPP blends. The OBDD-to-OBDG transition temperature of the blend was found to locate at ca. 10−20 °C higher than that of neat diblock, as the homopolymer chains were able to be segregated to fill the space at the center of the connectors to release the packing frustration. This thereby enhanced the stability of OBDD phase.

Let us now consider factor (2), i.e., the effect of the polydispersity of sPP (PDIs of sPP and PS blocks in our block copolymer are 1.32 and 1.02, respectively) on the stabilization of OBDD. If the polydispersity is caused by a contamination with sPP homopolymer, the sPP homopolymer can stabilize the OBDD as elucidated immediately above. However, we can rule out this possibility of the homopolymer contamination evidently from the symmetric GPC elution curve (see Figure S2 of the Supporting Information). Thus, we can focus on the issue whether the polydispersity of sPP-*b*-PS would stabilize the OBDD structure. Generally, the polydispersity of block copolymers varies the interface curvature and thereby the morphology of the microdomain primarily via the so-called "cosurfactant effect"[30] which is brought about by block chains having different chain lengths being packed in a given microdomain with their chemical junctions on the common interface. The effect was explored extensively for not only binary mixtures of diblock copolymers[49] but also block copolymers with polydispersity.[31,50,51] However, to our best knowledge, these copolymer systems having essentially random-coil conformation and van der Waals interactions never showed the OBDD structures; that is, their ordered bicontinuous structure reported so far is the OBDG phase. Thus, even in the block copolymers with relatively high molecular weight polydispersity, OBDG is still a selected equilibrium morphology but not OBDD, as long as the block chains adopt random-coil conformations and have van der Waals interactions only.

CONCLUSIONS

We have discovered that a slightly asymmetric sPP-*b*-PS as-cast from xylene displayed the OBDD structure. When the OBDD-forming copolymer was heated, this structure transformed into the gyroid (OBDG) phase at ca. 155 °C. Interestingly, OBDG transformed back to OBDD upon cooling. The thermal reversibility of the transformation indicated that OBDD was a thermodynamically stable structure for this system. This was in contradiction to the previous theoretical works which predicted that OBDD is unstable relative to OBDG for neat diblocks irrespective of the segregation strength, whereas OBDD may exist over a narrow window in the blend of A-*b*-B with homopolymer A. We propose that when the population of helical segments of sPP block in the melt was sufficiently high, their mutual interactions would allow sPP blocks to form locally ordered or mesomorphic packing of the helical segments. In this case, the entropic penalty associated with chain stretching was effectively compensated by the release of free energy on forming the ordered regions in the microdomains. The role of packing frustration was hence greatly relaxed and OBDD became the favorable structure.

ASSOCIATED CONTENT

Supporting Information

GPC elution curve and ^{1}H NMR spectrum of sPP-*b*-PS; theoretical SAXS profiles of the OBDD and OBDG phase; entire temperature-dependent SAXS profiles of sPP-*b*-PS; DSC heating scan of sPP-*b*-PS; SAXS profile of sPP-*b*-PS collected at room temperature after the sample has been isothermally annealed at 140 °C for 24 h; a transmission electron micrograph (TEM) of sPP-*b*-PS; entire temperature-dependent FTIR spectra of sPP-*b*-PS; SAXS profiles of neat sPP-*b*-PS and sPP-*b*-PS/sPP blends. This material is available free of charge via the Internet at http://pubs.acs.org.

AUTHOR INFORMATION

Corresponding Author

*E-mail: hlchen@che.nthu.edu.tw (H.-L.C.); hashi2@pearl.ocn.ne.jp (T.H.).

ACKNOWLEDGMENTS

We gratefully acknowledge the financial support from the National Science Council Taiwan under grant NSC 97-2221-E-007-034. We also thank the National Synchrotron Radiation Center for supporting us to carry out the SAXS experiments at beamline BL23A1 and BL17A1 under proposal 2010-3-059-1. We also thank Profs. Hirokazu Hasegawa and Mikihito Takenaka at Kyoto University for the insightful discussions and assistance in in-house SAXS experiment. The financial support from the Interchange Association Japan for sponsoring the visit of C. Y. Chu to Kyoto University to carry out the in-house SAXS experiment is also gratefully acknowledged.

REFERENCES

(1) Matsen, M. W.; Bates, F. S. *Macromolecules* **1996**, *29*, 1091.
(2) Zhao, D.; Feng, J.; Huo, Q.; Melosh, N.; Fredrickson, G. H.; Chmelka, B. F.; Stucky, G. D. *Science* **1998**, *279*, 548.
(3) Crepaldi, E. L.; Soler-lllia, Galo J. de A. A.; Grosso, D.; Cagnol, F.; Ribot, F.; Scanchez, C. *J. Am. Chem. Soc.* **2003**, *125*, 9770.
(4) Fink, Y.; Urbas, A. M.; Bawendi, B. G.; Joannopoulos, J. D.; Thomas, E. L. *J. Lightwave Technol.* **1999**, *17*, 1963.
(5) Edrington, A. C.; Urbas, A. M.; DeRege, P.; Chen, C. X.; Swager, T. M.; Hadjichristidis, N.; Xenidou, M.; Fetters, L. J.; Joannopoulos, J. D.; Fink, Y.; Thomas, E. L. *Adv. Mater.* **2001**, *13*, 421.
(6) Sundrani, D.; Sibener, S. J. *Macromolecules* **2002**, *35*, 8531.
(7) Kim, S. O.; Solak, H. H.; Stoykovich, M. P.; Ferrier, N. J.; dePablo, J. J.; Nealey, P. F. *Nature* **2003**, *424*, 411.

(8) Stoykovich, M. P.; Muller, M.; Kim, S. O.; Solak, H. H.; Edwards, E. W.; de Pablo, J. J.; Nrslry, P. F. *Science* **2005**, *308*, 1442.
(9) Hajduk, D. A.; Harper, P. E.; Gruner, S. M.; Honeker, C. C.; Kim, G.; Thomas, E. L.; Fetters, L. J. *Macromolecules* **1994**, *27*, 4063.
(10) (a) Hashimoto, T.; Tsutsumi, K.; Funaki, Y. *Langmuir* **1997**, *13*, 6869. (b) Hashimoto, T.; Nisikawa, Y.; Tsutsumi, K. *Macromolecules* **2007**, *40*, 1066.
(11) Okumura, A.; Nishikawa, Y.; Hashimoto, T. *Polymer* **2006**, *47*, 7805.
(12) Urbas, A. M.; Maldovan, M.; DeRege, P.; Thomas, E. L. *Adv. Mater.* **2002**, *14*, 1850.
(13) Crossland, E. J. W.; Kamperman, M.; Nedelcu, M.; Ducati, C.; Wiesner, U.; Smilgies, D.-M.; Toombes, G. E. S.; Hillmyer, M. A.; Ludwigs, S.; Steiner, U.; Snaith, H. J. *Nano Lett.* **2009**, *9*, 2807.
(14) Liu, Z.; Li, Y.; Zhao, Z.; Cui, Y.; Hara, K.; Miyauchi, M. *J. Mater. Chem.* **2010**, *20*, 492.
(15) Hsueh, H. Y.; Chen, H. Y.; She, M. S.; Chen, C. K.; Ho, R. M.; Gwo, S.; Hasegawa, H.; Thomas, E. L. *Nano Lett.* **2010**, *10*, 4994.
(16) Thomas, E. L.; Alward, D. B.; Kinning, D. J.; Martin, D. C.; Handlin, D. L. Jr.; Fetters, L. J. *Macromolecules* **1986**, *19*, 2197.
(17) Hasegawa, H.; Tanaka, H.; Yamasaki, K.; Hashimoto, T. *Macromolecules* **1987**, *20*, 1651.
(18) Larsson, K. *J. Phys. Chem.* **1989**, *93*, 7304.
(19) Anderson, D. M.; Thomas, E. L. *Macromolecules* **1988**, *21*, 3221.
(20) Olmsted, P. D.; Milner, S. T. *Phys. Rev. Lett.* **1994**, *72*, 936.
(21) Likhtman, A. E.; Semenov, A. N. *Macromolecules* **1994**, *27*, 3103.
(22) Matsen, M. W.; Schick, M. *Phys. Rev. Lett.* **1994**, *72*, 2660.
(23) Matsen, M. W.; Schick, M. *Macromolecules* **1994**, *27*, 7157.
(24) Matsen, M. W.; Schick, M. *Macromolecules* **1994**, *27*, 6761.
(25) Thomas, E. L.; Anderson, D. M.; Henkee, C. S.; Hoffman, D. *Nature* **1988**, *334*, 598.
(26) Matsen, M. W.; Bates, F. S. *Macromolecules* **1996**, *29*, 7641.
(27) Winey, K. I.; Thomas, E. L.; Fetters, L. J. *Macromolecules* **1992**, *25*, 422.
(28) Kuo, J. C.; Tsai, J. C.; Chung, T. M.; Ho, R. M. *Macromolecules* **2006**, *39*, 7520.
(29) OBDD and OBDG normally appear at volume fraction of 0.27−0.33 for the minority component for the conventional diblock copolymers such as those composed of PS and polyisoprene or polybutadiene. Thus, the observation of OBDD and OBDG for sPP-*b*-PS with volume fraction of sPP = 0.46 is rather unique, which may be attributed to the cosurfactant effect,[30] the polydispersity effect or dissimilarity of segmental volumes of the two kinds of block copolymer chains.[31] It is noted that a PS-*b*-poly(dimethylsiloxane) was found to exhibit OBDG structure at a rather symmetric volume fraction of 0.40−0.41.[32]
(30) Hasegawa, H.; Hashimoto, T. In *Comprehensive Polymer Science, Second Supplement*; Aggarwal, S., Russo, S., Eds.; Pergamon: New York, 1996; Chapter 14, pp 497−539.
(31) Lynd, N. A.; Hillmyer, M. A. *Macromolecules* **2005**, *38*, 8803.
(32) Politakos, N.; Ntoukas, E.; Avgeropoulos, A.; Krikorian, V.; Pate, B. D.; Thomas, E. L.; Hill, R. M. *J. Polym. Sci., Part B: Polym. Phys.* **2009**, *47*, 2419.
(33) Förster, S.; Timmann, A.; Schellbah, C.; Meyer, A.; Funari, S. S.; Mulvaney, P.; Knott, R. *J. Phys. Chem. B* **2005**, *109*, 1347.
(34) Takenaka, M.; Wakada, T.; Akasaka, S.; Nishitisuji, S.; Saijo, K.; Shimizu, H.; Kim, M. I.; Hasegawa, H. *Macromolecules* **2007**, *40*, 4399.
(35) Hashimoto, T.; Koga, T.; Koga, T.; Sakamoto, N.; In *The Physics of Complex Fluids*, Yonezawa, F., Tsuji, K., Kaji, K., Doi, M., Fujiwara, T.; Eds., World Scientific: Singapore, 1998, pp 291−308.
(36) Koga, T.; Koga, T.; Hashimoto, T. *Phys. Rev. E* **1999**, *60*, R1154−R1157.
(37) Koga, T.; Koga, T.; Hashimoto, T. *J. Chem. Phys.* **1999**, *110*, 11076.
(38) Benedicto, A. D.; O'Brien, D. *Macromolecules* **1997**, *30*, 3395.
(39) Schoen, A. H. *NASA Tech. Note* **1970**, *D-5541*, 1−98.
(40) Nitsche, J. C. C. *Lectures on Minimal Surfaces*; Cambridge University Press: Cambridge, England, 1989; Vol. 1.
(41) Dierkes, U.; Hildebrandt, S.; Kuster, A.; Wohlrab, O. *Minimal Surfaces I*; Springer-Verlag: Berlin, 1992.
(42) Sevegney, M. S.; Kannan, R. M.; Siedle, A. R.; Percha, P. A. *J. Polym. Sci., Part B: Polym. Phys.* **2005**, *43*, 439.
(43) Zheng, C. X.; Zhang, X. Q.; Dong, X.; Zhao, Y.; Wang, Z. G.; Zhu, S. N.; Xu, D. F.; Wang, D. J. *Polymer* **2006**, *47*, 7813.
(44) Kobayashi, M.; Tsumura, K.; Tadokoro, H. *J. Polym. Sci., Part A: Polym. Chem.* **1968**, *6*, 1493.
(45) Lotz, B.; Lovinger, A. J.; Cais, R. E. *Macromolecules* **1988**, *21*, 2375.
(46) Brookes, A.; Dyke, J. M.; Hendra, P. J.; Meehan, S. *Spectrochim. Acta, Part A* **1997**, *53*, 2313.
(47) Rizzo, P.; Lamberti, M.; Albunia, A. R.; Ruiz de Ballesteros, O.; Guerra, G. *Macromolecules* **2002**, *35*, 5854.
(48) Sevegney, M. S.; Parthasarthy, G.; Kannan, R. M.; Thurman, D. W.; Fernandez-Ballester, L. *Macromolecules* **2003**, *36*, 6472.
(49) See for example: (a) Court, F.; Hashimoto, T. *Macromolecules* **2001**, *34*, 2536−2545. (b) Court, F.; Hashimoto, T. *Macromolecules* **2002**, *35*, 2566−2575. (c) Court, F.; Yamaguchi, D.; Hashimoto, T. *Macromolecules* **2008**, *41*, 4828−4837. (d) Hashimoto, T.; Yamaguchi, D.; Court, F. *Macromol. Symp.* **2003**, *195*, 191−200. (e) Chen, F.; Kondo, Y.; Hashimoto, T. *Macromolecules* **2007**, *40*, 3714−3723.
(50) Sides., S. W.; Fredrickson, G. H. *J. Chem. Phys.* **2004**, *121*, 4974.
(51) Cooke, D. M.; Shi, A. C. *Macromolecules* **2006**, *39*, 6661.

Macromolecules

Article

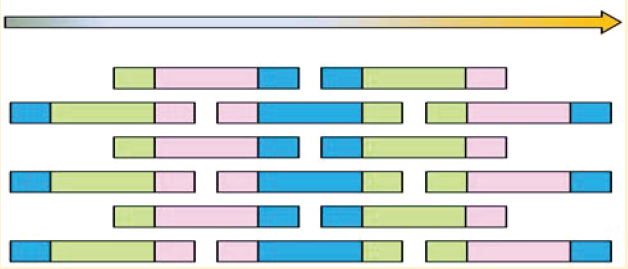
pubs.acs.org/Macromolecules

Ferrochemical Materials

Dominique Ausserré*

UMR CNRS 6087, "Molecular Landscapes, Biophotonic Horizons" Group, Université du Maine, Avenue Olivier Messiaen, BP 535, F-72085 Le Mans Cedex, France

ABSTRACT: Amphiphilic molecules such as phospholipids, smectic liquid crystals or diblock copolymers are chemical dipoles which, under appropriate conditions, spontaneously line up side by side in a ferro-like arrangement to form stable monolayers. In three dimensions, these monolayers stack in a head-to-tail or antiferro-like arrangement, which favors monopolar contact between similar species. It results in a symmetric bilayered lamellar material. Here we show that dipolar chemical interactions can be extended in the direction normal to the lamellae by the use of triphilic rather than amphiphilic molecules, so that stable self-assembled smectic stacks may be designed with a fully polar, hence noncentrosymmetric, ordering. We describe in details a generic model of such materials. It is made of a mixture of three triblock copolymers aBc, bCa, and cAb with their end blocks twice sorter than the corresponding middle block. Because each constitutive molecule extends over three different chemical layers, all pairs of adjacent layers are linked and oriented via dipolar interactions. As a consequence, a polar structure with remarkable thermodynamic and mechanical stabilities is expected. We name these materials "ferrochemicals" because any given triblock molecule of the blend is oriented the same way through the whole sample due to chemical dipole interactions with all neighboring molecules. In the polymer case, the polar lamellar stacks can also be used as organic matrices hosting and orienting inorganic Janus particles in order to get a large variety of hybrid polar materials with interesting nonlinear optical, ferromagnetic, or ferroelectric properties.



Self-assembled structures play an important part in the development of new nanostructured materials. Among them, materials formed spontaneously by block copolymers[1] are probably the simplest and the best defined. They are also easy to process because they adopt after simple annealing very regular periodic composite structures under the form of lamellae, cylinders or spheres[2] which are maintained in the solid state after being cooled back to normal temperature. The mechanisms that underlie this self-assembling are very independent of the precise chemical nature of the copolymers and the structure period can be adjusted between 10 and 100 nm through the length of the blocks. Block copolymers allow a wide range of applications and present a great chemical variety.[3,4] They are used, for instance as interfacial agents,[5] to make very tough plastics,[6] to structure surfaces at nanometer scales,[7] or to realize meso-porous materials[8] or photonic crystals.[9] However, some important applications, requiring noncentrosymmetric (NCS) structures, cannot benefit from their use because these block copolymers prefer to form self-assembled and centro-symmetric structures. For example, nonlinear optical components used in optical communications and integrated optics require a strong second-order nonlinear optical susceptibility, i.e., a strong χ^2, and thus a NCS structure. That is why research has been specifically engaged over the last 2 decades to imagine tricks that drive block copolymers to adopt spontaneous NCS structures,[10−13] unnatural for amphiphilic molecules. Different molecule compositions, blend formulations, and block sequences have been tried, yielding materials where symmetric and nonsymmetric domains coexist that show at best a weak NCS order preference, which means that it is brittle and that it cannot extend over a useful scale. These attempts have involved only lamellar structures. In this case, the expected NCS order is one-dimensional, i.e., simply polar. We stress that the term "polar" applies to the organization in its chemical composition, which is a first reason to call it "ferrochemical". In this article, we theoretically describe the composition and structure of a new self-assembled polar material that is expected to be mechanically and thermodynamically extremely stable, that is to say more stable than previous self-assembled lamellar materials by orders of magnitude. These structural properties, and the consequent physical properties, lie on the fact that all adjacent layers in it are linked via chemical dipoles. Two attached blocks in a copolymer chain may be viewed as a chemical dipole. Two adjacent molecules into a membrane layer are pair wise associated via chemical dipoles. In the new material described, composed of a blend of three complementary triblock copolymers, all neighboring molecules belonging to adjacent, hence different, layers are also pair wise associated via chemical dipoles. This original structural feature gives us another reason to call it "ferrochemical".

Received: October 9, 2011
Revised: January 27, 2012
Published: February 27, 2012

 © 2012 American Chemical Society

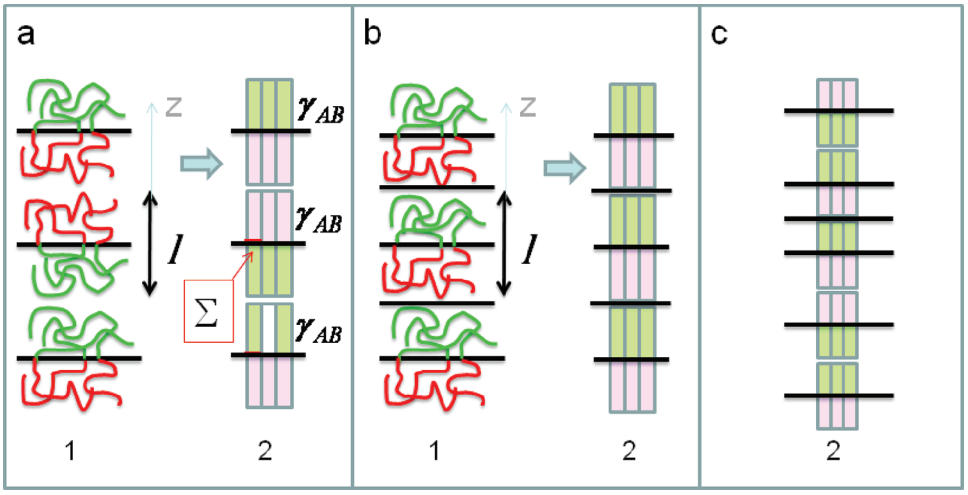


Figure 1. Bulk structure of a lamellar diblock copolymer. In the first two boxes (a and b), copolymer molecules are shown in a realistic way on the left (1) part of the box, where they are entangled, and in a simplified way on the right (2), where they are artificially split and compressed. Box a schematizes the symmetric order always observed in volume. Box b shows a hypothetical polar order, in practice never observed in the bulk; Box c shows a stack defect in the symmetric order, with the appearance of an additional AB interface, in the simplified representation (2).

RESULTS AND DISCUSSION

Figure.1a shows the lamellar structure of an AB diblock copolymer self-organized in the liquid state. We assume that the two blocks are immiscible, which is generally the case when two polymers are presenting a different chemical nature. Furthermore, we assume that they have the same length and the same volume. In order to form as few AB interfaces as possible, the lamellar structure is periodic and composed of bilayers. It is an AB/BA/AB/BA... symmetric structure. The free energy F per chain of this system, the minimum of which describes the equilibrium configuration, is the sum of two terms:[13−18] $F = \gamma_{AB}\Sigma + F_{el}$. The first term is the contact energy between A and B. It is the product of their interfacial tension and of the contact area per chain. It decreases when the chains stretch perpendicularly to the lamellae and this elastic stretching is expressed by the second term. At equilibrium, these two terms respect the rule of equipartition in the three directions of space. They represent respectively 2/3 and 1/3 of the total energy, so that $F = (3/2)\gamma_{AB}\Sigma$. If we divide the energy per chain by the molecular volume $l\Sigma$, where l is the height of an AB monolayer, we get a very simple expression of the free energy density of the material: $f = (3/2)\gamma_{AB}/l$. The free energy density of the rival nonsymmetric structure AB/AB/AB/AB..., shown in Figure 1b, is almost twice that of the symmetric one since it contains almost twice more AB interfaces per volume unit ("almost" because the lamellar equilibrium layer is bigger, which is not shown in Figure 1). Hence, f is proportional to the number of AB interfaces per unit volume. In more general terms, the sequences of block copolymers are organized as follows: two sequences that are chemically similar tend to gather and two sequences chemically different tend to split. The association of similar sequences happens both laterally (entangling two similar neighbor blocks) and longitudinally (similar end blocks interpenetrating each other). Notice that in lamellar structures of diblock copolymers, elementary bilayers are linked via monopolar block associations and hence are topologically disconnected from each other, which leads to bad resistance of the material to shearing.

Goldacker et al.[10] created the first material with block copolymers presenting a NCS structure. This structure is composed of a blend of ABC triblock and ac diblock copolymers, with small letters representing much shorter blocks than those written with capital letters. The interfacial tension between two similar species (γ_{AA} or γ_{aa}) is not strictly zero, though its value is always very low compared to that between immiscible species (γ_{AB}). For simplicity we will assume $\gamma_{AB} = \gamma_{AC} = \gamma_{BC} \equiv \gamma$. The interfacial tension between two blocks with the same chemistry, but different lengths (γ_{Aa}) is slightly lower than the average ($[\gamma_{AA} + \gamma_{aa}]/2$). As a consequence, the ABC/ca/ABC/ca... stacking is slightly better than the ABC/CBA/ac/ca/ABC/CBA/ac/ca... stack or any other stack composed of bilayers, and the NCS structure is predominant. Thus, in these materials, the NCS order only relies on a very slight preference among the various monopolar interactions. Furthermore, the insertion of a simple bilayer like ac/ca. in the structure is enough to change the ABC order in CBA, so that this solution cannot apply for the manufacturing of big NCS monodomains samples. An alternative has been recently suggested by Erukimovich and co-workers.[13] It consists in reinforcing the preference for the contact between similar chains with different lengths (like A and a) by the insertion of donor and acceptor interactions between long and short chains. However, there is no reason why the additional interaction would modify the ordering process of the material; consequently a lot of donor/acceptor pairs are likely to ignore each other indefinitely in a metastable structure containing many symmetric domains. Another example of a material with a NCS preference has been obtained by Takano et al.[11] The material is pure and composed of ABCA tetrablocks with two A blocks of the same length. It aligns preferably in a polar ABCA/ABCA/ABCA... lamellar sequence rather than in the symmetric ABCA/ACBA/ABCA... sequence. This is due to a slight dissymmetry between the lengths of B and C blocks, which leads the A end blocks respectively attached to B and C to adopt different stretching rates, and to behave as if they did not present the same length. The mechanism is thus very similar to the one described in the previous example, and the energy difference between the symmetric and the nonsymmetric structure is in the same range. In this case too, rival symmetric structures persist and the preference for the NCS order is very weak. In addition, in both situations the layers are disconnected

dx.doi.org/10.1021/ma202262m | Macromolecules 2012, 45, 2478−2484

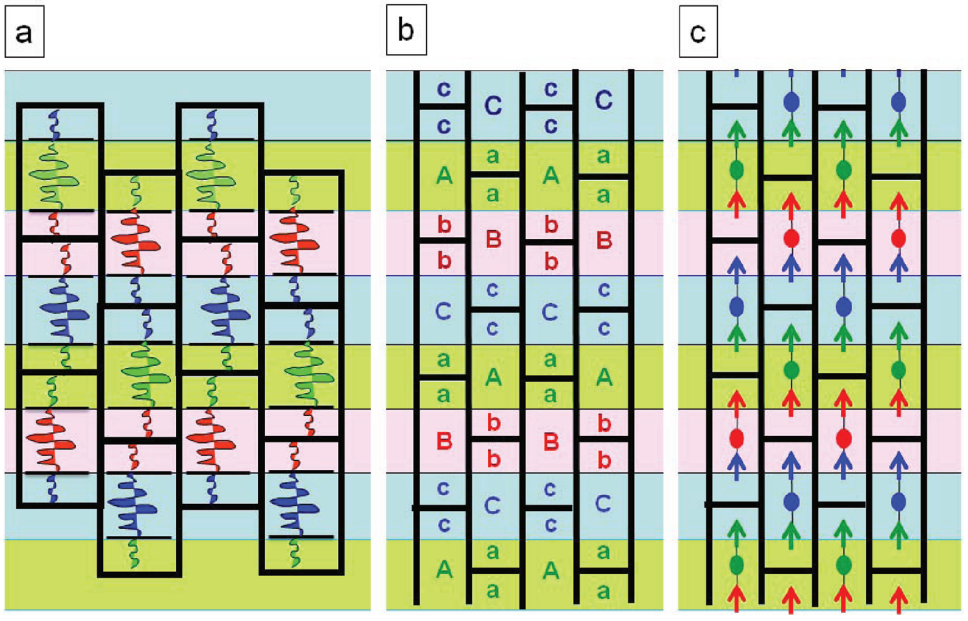


Figure 2. Nonsymmetric ternary blend of triblock copolymer chains. The most realistic picture in part a shows that each molecule is connected to its neighbors by a chemical dipole, including molecules located at an upper or a lower level. As a result, the orientation of the molecules in the blend is the same everywhere. In the topologic picture (b), molecules are compacted. The structure is that of a brick wall made with three colors and organized to maximize each color domain size. Each tricolor rectangle represents the volume of a chain. Picture c underlines the relative organization of the three kinds of chemical dipoles, which are attached in pairs along the z direction. The staggered arrangement of the rows insures a ferrochemical order between adjacent lamellae. Color dots at the center of rectangles represent the center of mass of the molecules.

and can slip easily, rendering the materials mechanically fragile. Abetz and co-workers[12] obtained a third type of material with a tendency NCS order by using a blend of two triblocks (or "terpolymers") ABC and AbC with the same composition but middle blocks with different lengths. The structure is lamellar but B and b blocks stretching rates differ widely. They become incompatible and the sequence ABC/CbA/ABC/CbA is locally observed. However, again this NCS order is delicate and coexists with symmetric stacks. Finally, a fourth solution was suggested by Stupp and co-workers[19−21] with a different approach, supra-molecular self-assembly. In these systems, the association of the molecules happens at different length scales. The diblock or triblock copolymers contain rigid sequences that associate into tight bundles. The other blocks are flexible, they do not easily cohabitate laterally, and the aggregate takes the form of a bunch of flowers that can receive only a finite number of molecules. Bunches then structure themselves in a head-to-tail fashion to fill the space homogeneously and the result is a NCS material. The chemical synthesis of this material is complex and does not allow many possibilities to host impurities, which, as we will discuss below, is essential in applications.

The material that we have imagined is based on self-assembly as were the systems just described. However, it is qualitatively different because it is made of triphilic rather than amphiphilic molecules and because all associations between molecules are dipolar in nature, in the sense explained previously. For instance, an ABC linear triblock copolymer and a CAB linear triblock copolymer can join together via their common AB dipole so that their orientation becomes linked. However, those molecules presenting different compositions, cannot take place on the same z level in a lamellar structure, the z axis being normal to the lamellae. As a consequence, adjacent lamellae become interconnected and we can talk of "dipolar interpenetration" between lamellae by contrast with the usual monopolar interpenetration. The triblock molecules that compose these lamellae may order themselves step by step in a three-dimensional way, each given molecule of the mixture finding always the same orientation, similar to the organization of the physical dipoles in ideal ferromagnetic or ferroelectric materials.[22] The model for the ferrochemical materials is composed of a blend of three triblock copolymers in equal proportions. The composition of each triblock is obtained thanks to a circular permutation of three immiscible species A, B, and C. To allow every molecule to form dipolar connections and avoid the appearance of constraints in the structure, end blocks are twice shorter than middle blocks, which we write as aBc, bCa, and cAb. During the annealing of this blend, copolymer chains can only order as shown in Figure 2. In this structure, the position of the chemical domains is decoupled from that of the copolymer's centers of mass. The whole material can be seen as a stacking of asymmetric bilayers (e.g., bAc/cBa) half filled with transmembrane middle molecules (e.g., aCb). In a plane perpendicular to the lamellae, the structure can also be viewed as the juxtaposition of similar columns composed of periodic linear arrangements aBc/cAb/bCa/aBc/cAb/bCa of copolymer chains ... that are shifted half a period with respect to each other like rows of bricks in a wall. Since each molecule acts as a staple for its neighbors, this system is expected to present very unusual mechanical properties for a lamellar structure. The material is very easy to obtain by mixing thoroughly the three components in the powder, and subsequently melt the system by heating. Self-assembly occurs spontaneously in the liquid state and the order is maintained after cooling back to room temperature. The only competing symmetric structure we could think of is that of a demixed state in which each species forms a bilayered monodomain (as aBc/cBa). From a static point of view, the

dx.doi.org/10.1021/ma202262m | *Macromolecules* 2012, 45, 2478−2484

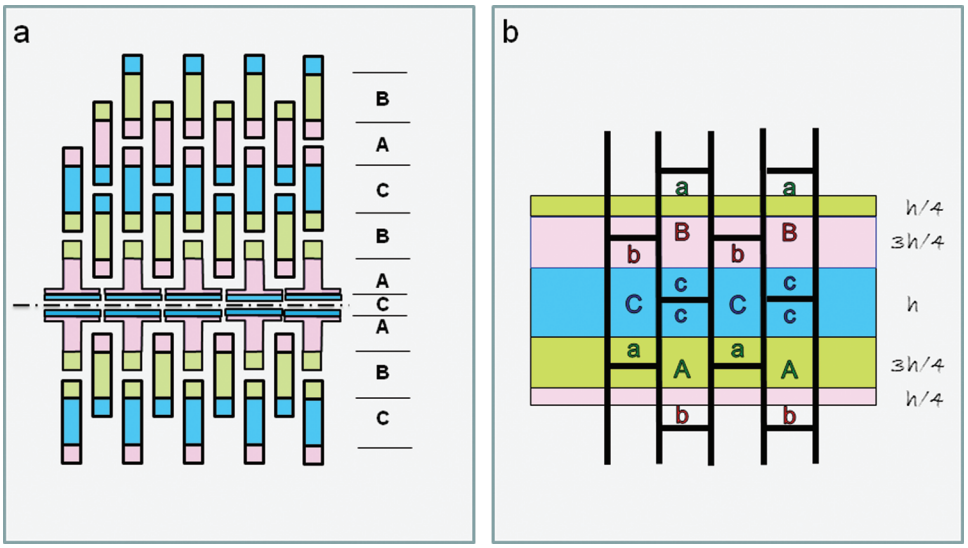


Figure 3. Homeotropic interfaces. Left panel: Polarity reversal. The bulk organization dictated by chemical dipolar combinations is polar, so the two z directions are not equivalent. The material polarity cannot be reversed unless a defect occurs in the stacking. The drawing shows the energetically cheapest defect with in-plane invariance that we could imagine. The dotted line at the middle of the perturbed area represents the plane of symmetry. Solid lines represent interfaces between immiscible polymer species. Considering the dashed dot line as the surface of a continuous medium, the upper (or lower) part of the same drawing illustrates how the material surface in the homeotropic material orientation can self-organize against a solid, the air, or an immiscible liquid. Right panel: Ferrochemical membrane. A ferrochemical membrane has two interfaces with similar topology; the drawing displays the thinnest stoichiometric membrane that can be formed by the ternary blend, with homeotropic orientation at both interfaces. It is worth noticing that the membrane is asymmetric. The bulk structure is recalled by the superimposed pattern of solid lines.

arrangement of the chains in each of these monodomains is expected to be the same as their arrangement in the blend. In addition, demixing decreases the entropy of the blend and thus increases the free energy. From a dynamical point of view, since the ordering mechanism of the lamellar structure takes place through the propagation of a local order, demixing is very unlikely to happen. We may conclude that the NCS structure of this system is particularly stable.

In the above description, we considered an ideal 3 × 1/3 mixture of perfect monodisperse terpolymer constituents, each block having an ideal relative length. When envisaging the synthesis of these materials, one must estimate how sensitive the structure will be toward a variation of the length ratio of the different blocks. Although any quantitative treatment remains beyond the scope of the present paper, we will give two arguments showing that a high margin of tolerance is expected in the system composition. The first argument is based on the property that two complementary tails such as two end blocks "a" of the aBc and bCa terpolymer chains with hypothetical lengths xN and $(1 - x)N$ behave exactly the same and contribute to space filling with the same monomer distribution as the central block A in the terpolymer chain cAb. As a consequence, the structure remains unperturbed as long as the sum of the lengths of two complementary end blocks in two given constituent triblock molecules equals the length of the corresponding central block in the third molecule. This property provides flexibility in the polymer synthesis. The second argument is obtained by considering the equilibrium energy of the main competing structure, which is the demixed lamellar state. A demixed state will result in confining one constituent terpolymer in a third of the available volume V. The associated energy penalty will be $-k_BT \ln[(V/3)/V]$, that is to say roughly k_BT per molecule. For long copolymer chains, where N is of order 100, this is typically 5 to 10% of the molecular free energy in the lamellar state. For shorter chains, it is even a higher fraction of it. Hence the secondary free energy minimum corresponding to the competing demixed state is well above that of the ideal mixture. It gives a lot of space for playing with chain lengths around their optimal values. Reminding that in a block copolymer system the relative increase of the free energy is one-third of the relative change of the total chain length, the same rule holding for each block, one expects the ferrochemical structure to accept deviations up to several 10% of the relative block lengths with respect to their targeted values without demixing. Hence, if chemically possible, the synthesis of the three constituent should not be too demanding. Finally, in order to proof that the synthesis of the three triblock permutations of three given A, B, and C components is feasible, we cite an example. It is taken from the work described in ref 23 by Hückstädt, Göpfert, and Abetz on one side, where the synthesis of polystyrene-*b*-polybutadiene-*b*-poly-2-vinylpyridine (SBV) and VSB terpolymers was reported, and from the work described in ref 24 by Watanabe, Shimura, Kotaka, and Tirrell on the other side, where the complementary synthesis of BVS terpolymers was reported.

Unusual physical properties for a lamellar structure derive from the absence of symmetry of the ferrochemical structure, especially a second-order nonlinear optical susceptibility that will be found interesting for optical telecommunication. These kinds of applications require the production of large NCS samples, which is made possible by the high thermodynamic stability of the ferrochemicals, but also the absence of any defect that could reverse the polarity within the NCS structure. We will now use the very simple rule of the minimum number of interfaces per unit volume explained at the beginning of this article to study the energetic cost of such a defect. This will be also useful in order to anticipate the behavior of this material at an interface with a solid.

Figure 3a shows in a simplified representation of the NCS structure the topology of the least energy consuming reversal

dx.doi.org/10.1021/ma202262m | *Macromolecules* 2012, 45, 2478–2484

defect that we could imagine. This defect is arbitrarily built around the C block. It leads the formation of three lamellae with deviant thickness. If h is the thickness of a chemical domain, hence $2h$ the height of a molecule, the thickness of a C domain in the middle of the interface is $h/2$ and the thickness of the domains located on each side of the interface is $3h/4$. So, the structure is perturbed over a total thickness of $2h$ that contains three interfaces between immiscible species while elsewhere the same thickness contains two such interfaces. In the defect, the excess free energy per unit area is γ and the averaged bulk free energy density of the defect is 1.5 times that of the bulk material. The difference is considerable and is comparable to the amount of free energy stored by a stack defect in the lamellar structure of symmetric diblock copolymers shown in Figure 1c, where an additional AB interface also appears in the defect area, which makes three interfaces in the perturbed thickness $2l$ instead of two elsewhere. It is well-known that this kind of stacking defect in diblock copolymers rarely happens and can easily be avoided. Given that the energy released by polarity reversal defects in ferrochemicals is rather similar, we can conclude that these materials are able to present faultless NCS order over large distances. The scheme on the left in Figure 3 also describes the structure of an interface between a ferrochemical and a solid surface if the dashed line represents the solid surface and we consider only one-half of the image. This structure corresponds to homeotropic anchorage of the material. The term "homeotropic" reminds us that, in a liquid state, the structure of the ferrochemical is that of a smectic A liquid crystal. This spontaneous polar smectic order is remarkable in that it is obtained with non chiral molecules that are orthogonal to the lamellae and moreover present a radial symmetry. With a ferroelectric order between adjacent layers, it corresponds to the $SmAP_F$ phase of the $C_{\infty V}$ symmetry group. Such a level of symmetry in smectic liquid crystals has never been obtained, even with bent-core ferroelectrics.[25] In a generic way, we show that this is made possible by introducing of a new kind of dipolar interactions, namely ferrochemical interactions, between adjacent layers. The scheme in Figure 3b illustrates that a very thin layer of the material will naturally form a nonsymmetric membrane. The example given in the figure is the thinnest membrane compatible with the material composition.

In polymer materials used for nonlinear optical applications, sought-after optical properties are improved by the presence of hyper-polarizable molecules. These molecules are introduced in the polymer matrix and oriented by annealing under electric or electromagnetic fields, the whole structure is then quenched to room temperature while maintaining the field (poling).[26] With the same method, permanent dipoles, whether magnetic or electric, can also be oriented.[27] In this way molecules are maintained in an out of equilibrium[28] arrangement, resulting in a material that is sensitive to heating and especially to aging.[29] Figure 4 shows how permanent dipoles can be oriented at equilibrium by a ferrochemical matrix. The three situations described by this scheme are also valid for induced dipoles, whether electric or magnetic. On the right, the dipole is placed chemically between two adjacent blocks of a copolymer in the blend. On the left, the dipole is inserted via a diblock composed of two of the three species constituting the matrix: it acts as a cosurfactant. In the center, the dipole is carried by a Janus grain covered with two different species on its two hemispheres,[30,31] both species being compatible with a component of the matrix.

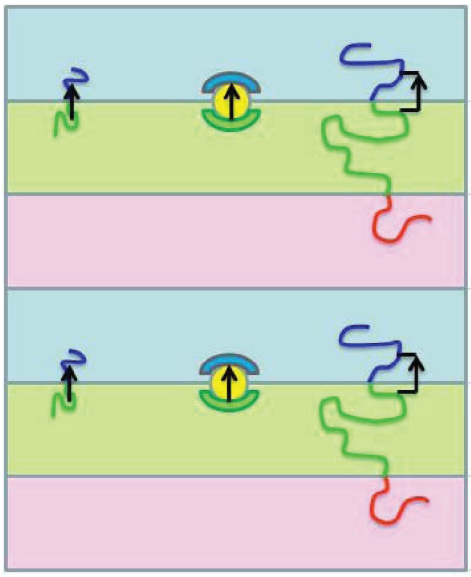


Figure 4. Nanocomposite hybrid material. A nanocomposite hybrid material at equilibrium is obtained by the introduction between two blocks of diblock surfactants (on the left), of Janus grains (in the middle), or of grafted bridges (on the right). The black arrows represent dipoles or hyperpolarizable molecules. The physical dipoles carried by the impurities are all parallel to the AC, CB and BA chemical dipoles.

In the latter example, the nanocomposite self-assembled material is different from materials containing isotropic particules,[32−38] because the nanoparticules prefer to settle at interfaces rather than in the center of the lamellae,[39,40] and because their orientation is now imposed by the polar chemical structure of the matrix. This structure appears sufficiently robust to sustain unfavorable interactions between parallel dipoles (by contrast with antiparallel), even at high dipole densities. Thus, the matrix organizes the dipoles in space, while the latter bring the sought-after physical properties. Therefore, ferrochemical interactions appear to be a powerful concept in order to design useful new materials.

To summarize, we predict that a blend of aBc, bCa and cAb triblock copolymers in equal proportions, with $a = A/2$ ..., will self- organize in a polar (NCS) lamellar structure. This material presents several unique features: dipolar interpenetration of juxtaposed layers, which couples their relative positions; dipolar association between the constituent molecules along their main axis, which confers on each constituent molecule a unique orientation in the entire sample; equal distribution of the molecule centers of mass among the lamellae filled with the three chemical species, which guarantees remarkable mechanical properties. We expect the total asymmetry of this self-assembled material to generate interesting physical properties such as second-order nonlinear optical susceptibility, ferroelectrics or piezoelectricity.[41] We use "ferrochemical" to qualify this material because of the ferro-like arrangement of identical molecules. We also use "ferrochemical" to qualify the pairwise association of chemical dipoles sustaining the polar structure. Other organic NCS materials can also be envisaged on the basis of the same principles with other blends of molecules, each of them being formed with at least three blocks. These molecules are for instance co-oligomers,[42,43] copolypeptides,[44] copolynucleotides[45−48] or comesogenic groups.[49] In particular, the latter might form ferroelectric smectic materials[23] with short

dx.doi.org/10.1021/ma202262m | *Macromolecules* 2012, 45, 2478−2484

switching times for display applications. In each of these families, there exists a great number of possible chemical species, and we expect the emergence of a broad range of new materials.[50] Making real examples of such materials certainly requires physicists and synthetic chemists working hand in hand.

AUTHOR INFORMATION

Corresponding Author

*E-mail: ausserre@univ-lemans.fr.

Notes

The authors declare no competing financial interest.

ACKNOWLEDGMENTS

This work is respectfully dedicated to the memory of P. G. de Gennes. We are indebted to Taco Nicolaï for critical reading of the manuscript.

REFERENCES

(1) Bates, F. S.; Fredrickson, G. H. Block Copolymer Thermodynamics: Theory and Experiment. *Annu. Rev. Phys. Chem.* **1990**, *41*, 525−557.

(2) Ruzette, A.-V.; Leibler, L. Block copolymers in tomorrow's plastics. *Nat. Mater.* **2005**, *4*, 19−31.

(3) Golas, P. L.; Matyjaszewski, K. Marrying click chemistry with polymerization: expanding the scope of polymeric materials. *Chem. Soc. Rev.* **2010**, *39*, 1338−1354.

(4) Hadjichristidis, N.; Iatrou, H.; Pitsikalis, M.; Pispas, S.; Avgeropoulos, A. Linear and non-linear triblock terpolymers. Synthesis, self-assembly in selective solvents and in bulk. *Prog. Polym. Sci.* **2005**, *30*, 725−782.

(5) Leibler, L. Nanostructured plastics: Joys of self-assembling. *Prog. Polym. Sci.* **2005**, *30*, 898−914.

(6) Kim, S. O.; Solak, H. H.; Stoykovich, M. P.; Ferrier, N. J.; de Pablo, J. J.; Nealey, P. F. Epitaxial self-assembly of block copolymers on lithographically defined nanopatterned substrates. *Nature* **2003**, *424*, 411−414.

(7) Lazzari, M.; Lopez-Quintela, M. A. Block Copolymers as a Tool for Nanomaterial Fabrication. *Adv. Mater.* **2003**, *15*, 1583−1594.

(8) Olson, D. A.; Chen, L.; Hillmyer, M. A. Templating Nanoporous Polymers with Ordered Block Copolymers. *Chem. Mater.* **2008**, *20*, 869−890.

(9) Erdington, A. C.; Urbas, A. M.; DeRege, P.; Chen, C. X.; Swager, T. M.; Hadjichristidis, N.; Xenidou, M.; Fetters, L. J.; Joannopoulos, J. D.; Fink, Y.; et al. Polymer-Based Photonic Crystals. *Adv. Mater.* **2001**, *13*, 421−425.

(10) Goldacker, T.; Abetz, V.; Stadler, R.; Erukhimovich, I.; Leibler, L. Non-centrosymmetric superlattices in block copolymer blends. *Nature* **1999**, *398*, 137−139.

(11) Takano, A.; Soga, K.; Suzuki, J.; Matsushita, Y. Non-centrosymmetric Structure from a Tetrablock Quarterpolymer of the ABCA Type. *Macromolecules* **2003**, *36*, 9288−9291.

(12) Abetz, V.; Goldacker, T. Formation of superlattices via blending of block Copolymers. *Macromol. Rapid Commun.* **2000**, *21*, 16−34.

(13) Erukhimovich, I. Y.; Belousov, M. V.; Govorun, E. N.; Abetz, V.; Tamm, M. V. Non-Centrosymmetric Lamellar Structures in the Associating Blends of Tri- and Diblock Copolymers. *Macromolecules* **2010**, *43*, 3465−3478.

(14) Helfand, E. Theory of inhomogeneous polymers − fundamentals of Gaussian random-walk model. *J. Chem. Phys.* **1975**, *62*, 999−1005.

(15) Alexander, S. *J. Phys. (Paris)* **1977**, *38*, 983.

(16) de Gennes, P. G. *Macromolecules* **1980**, *13*, 1069.

(17) Semenov, A. N. Contribution to the theory of microphase layering **in** block copolymer melts. *Zh. Eksp. Teor. Fiz.* **1985**, *88*, 1242−1256.

(18) Milner, S. T.; Witten, T. A.; Cates, M. E. *Macromolecules* **1988**, *21*, 2610.

(19) Stupp, S. I.; Lebonheur, V.; Walker, K.; Li, L. S.; Huggins, K. E.; Keser, M.; Amstutz, A. Positioning Janus Nanoparticles in Block Copolymer Scaffolds. *Science* **1997**, *276*, 384−389.

(20) Zubarev, E. R.; Pralle, M. U.; Li, L.; Stupp, S. I. Conversion of Supramolecular Clusters to Macromolecular Objects. *Science* **1999**, *283*, 523−526.

(21) Li, L.; Zubarev, E. R.; Acker, X.; E., R.; Stupp, S. I. Chemical Structure and Nonlinear Optical Properties of Polar Self-Assembling Films. *Macromolecules* **2002**, *35*, 2560−2565.

(22) Landau, L., Lifchitz, E. *Physique Théorique, Tome 8: Electrodynamique des Milieux Continus*; MIR: Moscow, 1990.

(23) Hückstädt, H.; Göpfert, A.; V. Abetz, V. Influence of the block sequence on the morphological behavior of ABCtriblock copolymers. *Polymer* **2000**, *41*, 9089−9094.

(24) Watanabe, H.; Shimura, T.; Tokata, T.; Tirrell, M. *Macromolecules* **1988**, *21*, 2610.

(25) Reddy, R. A.; Zhu, C.; Shao, R.; Korblova, E.; Gong, T.; Shen, Y.; Garcia, E.; Glaser, M. A.; Walba, D. M.; Clark, N. A. Spontaneous Ferroelectric Order in a Bent-Core Smectic Liquid Crystal of Fluid Orthorhombic Layers. *Science* **2011**, *332*, 72−77.

(26) Hubbard, S. F.; Singer, K. D.; Li, F.; Cheng, S. Z. D.; Harris, F. W. Nonlinear optical studies of a fluorinated poled polyimide guest host system. *Appl. Phys. Lett.* **1994**, *65*, 265.

(27) Qiu, X. Patterned piezo-, pyro-, and ferro-electricity of poled polymer electrets. *J. Appl. Phys.* **2010**, *108*, 011101.

(28) Dalton, L. R.; Harper, A. W.; Robinson, B. H. The role of London forces in defining noncentrosymmetric order of high dipole moment−high hyperpolarizability chromophores in electrically poled polymeric thin films. *Proc. Natl. Acad. Sci. U.S.A.* **1997**, *94*, 4842−4847.

(29) Gubbelmans, E.; Verbiest, T.; Beylen, M. V.; Persoons, A.; Samyn, C. Chromophore functionalized with high poling stabilities of the nonlinear optical effect at elevated temperature. *Polymer* **2002**, *43*, 1581.

(30) Wurm, F.; Kilbinger, A. Polymeric Janus Particles. *Angew. Chem., Int. Ed.* **2009**, *48*, 8412−8421.

(31) Walther, A.; Matussek, K.; Müller, A. H. Engineering Nanostructured Polymer Blends with Controlled Nanoparticle Location using Janus Particles. *ACS Nano* **2008**, *2*, 1167−1178.

(32) Hamdoun, B.; Ausserré, D.; Joly, S.; Gallot, Y.; Cabuil, V.; Clinard, C. New Nanocomposite Materials. *J. Phys. II Fr.* **1996**, *6*, 493−501.

(33) Fogg, D. E.; Radzilowski, L. H.; Blanski, R.; Schrock, R. R.; Thomas, E. L. Fabrication of Quantum Dot/Polymer Composites: Phosphine-Functionalized Block Copolymers as Passivating Hosts for Cadmium Selenide Nanoclusters. *Macromolecules* **1997**, *30*, 417−426.

(34) Thompson, R. B.; Ginzburg, V. V.; Matsen, M. W.; Balazs, A. C. Predicting the Mesophases of Copolymer-Nanoparticle Composites. *Science* **2001**, *292*, 2469−2472.

(35) Balazs, A. C.; Emrick, T.; Russell., T. P. Nanoparticle Polymer Composites: Where Two Small Worlds Meet. *Science* **2006**, *314*, 1107−1110.

(36) Bockstaller, M.; Mickiewicz, R. A.; Thomas, E. L. Perspectives for advanced tailored materials. *Adv. Mater.* **2005**, *17*, 1331−1349.

(37) Schultz, A. J.; Hall, C. K.; Genzer, J. Computer Simulation of Block Copolymer/Nanoparticle Composites. *Macromolecules* **2005**, *38*, 3007−3016.

(38) Pryamitsyn, V.; Ganesan, V. Strong Segregation Theory of Block Copolymer-Nanoparticle Composites. *Macromolecules* **2006**, *39*, 8499−8510.

(39) Yan, L.-T.; Popp, N.; Ghosh, S.-K.; Böker, A. Self-Assembly of Janus Nanoparticles in Diblock Copolymers. *ACS Nano* **2010**, *4*, 913−920.

(40) Kim, J. U.; Matsen., M. W. Positioning Janus Nanoparticles in Block Copolymer Scaffolds. *Phys. Rev. Lett.* **2009**, *102*, 078303.

(41) Samuel, P. Gido Asymmetry the easy way. *Nature* **1999**, *398*, 107−108.

(42) Bu, L.; Guo, X.; Yu, B.; Qu, Y.; Xie, Z.; Yan, D.; Geng, Y.; Wang, F. Monodisperse Co-oligomer Approach toward Nanostructured Films with Alternating Donor-Acceptor Lamellae. *J. Am. Chem. Soc.* **2009**, *131*, 13242−13243.
(43) Hancock, J. M.; Gifford, A. P.; Champion, R. D.; Jenekhe, S. A. Block Co-oligomers for Organic Electronics and Optoelectronics: Synthesis, Photophysics, Electroluminescence, and Field-Effect Charge Transport of Oligothiophene-*b*-oligoquinoline-*b*-oligothiophene Triblock Co-oligomers. *Macromolecules* **2008**, *41*, 3588−3597.
(44) Floudas, G.; Spiess, H. W. Self-Assembly and Dynamics of Polypeptides. *Macromol. Rapid Commun.* **2009**, *30*, 278−298.
(45) Winfree, E.; Liu, F.; Wenzler, L. A.; Seeman, N. C. Design and self-assembly of two-dimensional DNA crystals. *Nature* **1998**, *394*, 539−544.
(46) Douglas, S. M.; Dietz, H.; Liedl, T.; Högberg, B.; Graf, F.; Shih, W. M. Self-assembly of DNA into nanoscale three-dimensional shapes. *Nature* **2009**, *459*, 414−418.
(47) Reishus, D.; Shaw, B.; Brun, Y.; Chelyapov, N.; Adleman, L. Self-Assembly of DNA Double-Double Crossover Complexes into High-Density, Doubly Connected, Planar Structures. *J. Am. Chem. Soc.* **2005**, *127*, 17590−17591.
(48) Seeman, N. C. DNA in a material world. *Nature* **2003**, *421*, 427−431.
(49) Pensec, S.; Tournilhac, F.-G.; Bassoul, P.; Durliat, C. Synthesis and Structural Studies of Polyphilic Mesogens with Central or Terminal Perfluoroalkyl Chains. *J. Phys. Chem. B* **1998**, *102*, 52−60.
(50) D. Ausserré, D.; L. Fontaine, L. *French patent application* 2011, No. 11/55209, filed on June 15th.

Macromolecules

Article

pubs.acs.org/Macromolecules

Effects of Molar Mass of Poly(L-lactide acid) on the Crystallization of Poly[(*R*)-3-hydroxybutyrate] in Their Ultrathin Blend Films

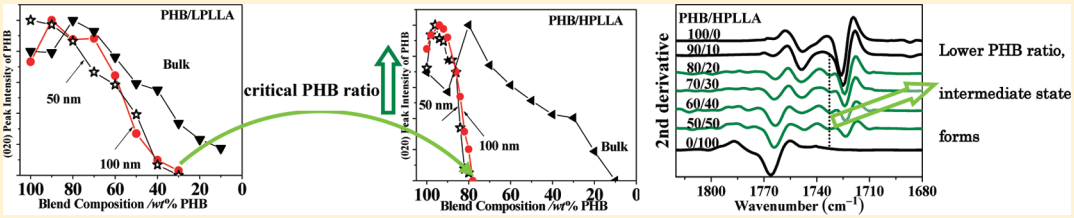
Xiaoli Sun,[†,§] Akihisa Tokuda,[§] Yusuke Oji,[§] Takashi Nakatani,[§] Hideto Tsuji,[‡] Yukihiro Ozaki,[§] Shouke Yan,*[,†] and Isao Takahashi*[,§]

[†]State Key Laboratory of Chemical Resource Engineering, Beijing University of Chemical Technology, Beijing 100029, China

[§]Faculty of Science and Technology, Kwansei Gakuin University, Sanda, Hyogo 669-1337, Japan

[‡]Department of Environmental and Life Sciences, Graduate School of Engineering, Toyohashi University of Technology, Tempaku-cho, Toyohashi, Aichi 441-8580, Japan

Supporting Information



ABSTRACT: Blends of poly[(*R*)-3-hydroxybutyrate] (PHB) with poly(L-lactide acid) (PLLA) were prepared to study the crystallization behavior of PHB in the blends. To investigate the effect of molar mass of PLLA on the crystallization of PHB, two types of PLLA with high and low molecular weight, HPLLA and LPLLA, were used. It was found that the crystallization behavior of PHB in PHB/HPLLA and PHB/LPLLA blends is essentially the same for thicker films, e.g., 1 μm thick films. The crystallization behavior of PHB within PHB/HPLLA and PHB/LPLLA blends in ultrathin films is, however, quite different. For PHB/LPLLA thin films, it was found that crystallization degree of PHB decreases first slightly with increasing LPLLA content, and then the crystallization stops when the weight ratio of PHB (w_{PHB}) decreases to 30 wt %. On the other hand, for the PHB/HPLLA thin films, the crystallization of PHB is inhibited even at extremely high weight ratio of PHB ($w_{PHB} \leq 78$ wt %). It was further found that thermal annealing does not enhance crystallization ability of PHB in PHB/HPLLA thin films with $w_{PHB} \leq 78$ wt %. Infrared reflection−absorption spectroscopy (IR-RAS) suggested the existence of an intermediate state of PHB. The transition from the intermediate state to crystalline phase is significantly slowed down in the thin film of PHB/HPLLA blend with $w_{PHB} \leq 78$ wt %.

INTRODUCTION

Poly[(*R*)-3-hydroxybutyrate] (PHB) is an environment-friendly biodegradable thermoplastic. Because of its chemical structure and physical properties that is similar to those of certain petroleum-based synthetic polymers, PHB has been extensively researched.[1−3] Poly(L-lactic acid) (PLLA) is another type of important environment-friendly polymeric material. It can be produced from renewable sources, such as corn, and readily degraded to lactic acid by hydrolysis under mild conditions, which is a common organic acid naturally present in the human body.[4−6]

The brittleness and poor processing properties of PHB have considerably limited its industrial application. To overcome these problems, several processes, e.g., copolymerization and blending, have been used.[7−11] With respect to the PHB/PLLA blends, the miscibility depends on the molecular weight of PLLA. It was reported that the PHB is miscible with low molecular weight PLLA ($M_w < 18\,000$)[8,9] in the melt over the entire composition range, whereas PHB blended with high molecular weight PLLA shows biphasic separation. Irrespective of a miscible or immiscible system, crystallization rate of PHB is decreased in the presence of PLLA.[12] In addition to crystallization kinetics of the PHB/PLLA blends, the molecular structures under mechanical elongation have also gained considerable attention because of the application potential of the polymer blends. The molecular orientation is closely related to the weight percent of components.[13,14] In the poly(lactic acid) (PLA)-rich PHB/PLLA blend films, the orientation of the PLA chains is in the direction of elongation, whereas that of the PHB chains is perpendicular to the drawing direction. On the other hand, the PHB/PLA blend films having weight ratio of PHB (w_{PHB}) higher than weight ratio of PLA (w_{PLA}) exhibit mechanical properties similar to those of PHB homopolymer, and both the components adopt a preferential chain alignment parallel to the drawing direction. Although previous studies provided considerable insights into blends of PHB and PLLA, most of them focused on bulk properties. The crystallization

Received: November 23, 2011
Revised: February 6, 2012
Published: February 22, 2012

 © 2012 American Chemical Society

behavior of the blends in thin films has not been widely reported.

Crystallization of polymers in thin films gained considerable attention in recent years. Although crystallization of polymer chains follows conventional habit whereby polymer chains fold back and forth to form crystalline lamellae, crystallization kinetics including nucleation and growth are significantly affected by nanoscale confinement. It has been found that, generally, the rate of crystallization sharply decreases on reducing the thickness, leading to an increase in the half-crystallization time ($t_{1/2}$) up to several orders of magnitude compared to that for the bulk conditions.[15−17] In addition to crystallization kinetics, lamellar orientations also change significantly for spatial confinement. The preference of the lamellar orientations is determined by the film thickness, crystallization temperature, and substrate surface energy.[18−23] The studies on crystallization in ultrathin films have been performed mainly for homopolymer films. In practice, however, many applications involve blending of polymers, which is an economical way to obtain materials with suitable characteristics. Therefore, investigation of polymer crystallization in the ultrathin films of polymer blends is beneficial for both a better understanding the thermal properties of nanoconfined thin films and developing new technologies for enhancing film performances.

Grazing incidence X-ray diffraction (GIXD) uses extremely small incident angles for incoming X-rays; therefore, diffraction can be made surface sensitive because of the total reflection of electromagnetic waves. By varying the incident angle, the penetration depth for measurements can be controlled from several nanometers to micrometers. Therefore, the measurement of Bragg reflections under GIXD conditions is a suitable approach for studying the crystallization behavior of the ultrathin polymer films. Infrared reflection−absorption spectroscopy (IR-RAS) provides additional useful information on the ultrathin films with respect to molecular organization and interaction. In previous studies, we have investigated the crystal structure of PHB in thin films via GIXD and found that the *b*-axis of the crystallites tend to align in a direction perpendicular to the film surface.[24] By comparing the relative intensity of the crystalline C═O stretching band with the corresponding amorphous band obtained by both IR-RAS and transmission spectra, the C═O group is confirmed to be oriented nearly parallel to the surface and along the direction of *a*-axis.[25]

This study aims to investigate the crystallization behavior of PHB in its blends with PLLA by using GIXD and Fourier transform infrared spectroscopy (FTIR). The blends of PHB with two types of PLLA having different molar masses were prepared to study the effect of PLLA molar mass on the crystallization behavior of PHB. Although both blends are miscible and PHB shows similar crystallization behavior in the bulk, the crystallization behavior of PHB in their ultrathin films is observed to be considerably different. Therefore, molar mass of PLLA and film thickness dependences of PHB crystallization are analyzed and discussed in detail.

EXPERIMENTAL SECTION

Material and Preparation Procedures. Two types of PLLA (M_w = 13 100 and 710 g mol^{-1}, M_w/M_n = 1.15 and 1.3, respectively) were purchased from the Polymer Source Co. Bacterially produced PHB with weight-averaged molecular weight of 6.0 × 10^5 g mol^{-1} was obtained from Procter & Gamble Co. To remove any impurities, the polymers were dissolved in hot chloroform, precipitated in methanol, and vacuum-dried at 60 °C.

Blends of PHB and PLLA were prepared by dissolving them together in hot chloroform. Bulk and ultrathin films for the GIXD measurements were respectively cast and spin-coated on silicon wafers. After most of the solvent had evaporated, the films were placed in low vacuum at room temperature for 1 week. For transmission IR measurement, solutions of the blends with a concentration of 1% (w/v) were cast on a KBr crystal. After casting, the samples were treated according to the aforementioned procedure. The thickness of such prepared polymer films was ca. 10 μm.

Thickness measurements of the thin polymer films were performed with a Nanoscope III MultiMode atomic force microscope (AFM) using Si cantilever tips (TESP) with a resonance frequency of 300 kHz and a spring constant of 40 N m^{-1}. The scan rate varied from 0.5 to 1.0 Hz. Film thicknesses were determined from AFM height profiles by partially removing the polymer films from the substrates and then evaluating the distance between the substrate surface and the average of all the heights measured through a linear scan across the sample surface. To minimize experimental error, several height profiles were recorded at different locations on the sample surface and then averaged. For GIXD measurements, the thin films with two different thickness values, which were 100 ± 15 and 50 ± 10 nm, were prepared. For IR-RAS measurement, solutions of the blends were spin-coated onto gold-coated glass substrates to prepare the ultrathin films having thickness of 50 ± 10 nm. To keep the similar thickness of different blend samples, the spin-coating speed has been changed slightly.

GIXD Measurement. GIXD measurements were conducted using a high-resolution four-circle diffractometer equipped with a rotating anode X-ray generator (SLX-2000 and UltraX, respectively, Rigaku Co., Ltd., λ = 0.154 05 nm). The size of the incident beam was defined by a 0.2 mm diameter collimator. A Soller slit was placed before a scintillation detector to collimate the scattered beam. The time fixed for data collection was 50 s per step, and the angular interval was 0.01°. In-plane and out-of-plane GIXD measurements were performed to detect the crystalline structure perpendicular and parallel to the substrate surface, respectively. The angle of incidence was set to be 0.19°, which corresponds to 1.14 θ_c.

IR Measurement. IR-RAS and transmission spectra were measured with a 2 cm^{-1} resolution using a Thermo Nicolet NEXUS 870 FTIR spectrometer with a liquid nitrogen cooled mercury−cadmium−telluride (MCT) detector. A total of 128 scans were coadded for each IR spectral measurement to ensure a high signal-to-noise ratio. For the IR-RAS measurement, a reflection attachment (Spectra-Tech, FT80 RAS) was employed at an incident angle of 80°, together with a rotatable wire grid polarizer of KRS5-substrate (ST Japan).

RESULTS AND DISCUSSION

Figure 1a shows GIXD out-of-plane profiles for 1 μm thick films of PHB blended with the lower molecular weight PLLA (710 g mol^{-1}) at different weight ratios, referred to as PHB/LPLLA. In the neat PHB film, the characteristic Bragg peaks of 020 and 110 are located at $2\theta \approx 13.58°$ and 16.67°, respectively. Moreover, a broad peak ranging from 18.65° to 24°, most likely attributed to the crystalline lattice planes of (021), (120), (111), and (101), is observed. The coexistence of several Bragg peaks suggests that the PHB crystals in the thick film are isotropic in orientation. After blending PHB with LPLLA, the peak intensity of PHB first increases markedly with the increase of LPLLA content and reaches a maximum value at the blend ratio of w_{PHB} = 80 wt % followed by a gradual decrease. It should be noted here that the in-plane profiles are similar to that of out-of-plane profiles for the 1 μm thick films of PHB and its blends, suggesting that there is no preferred orientation in the bulk samples, as has also been discussed by

dx.doi.org/10.1021/ma202543s | Macromolecules 2012, 45, 2485−2493

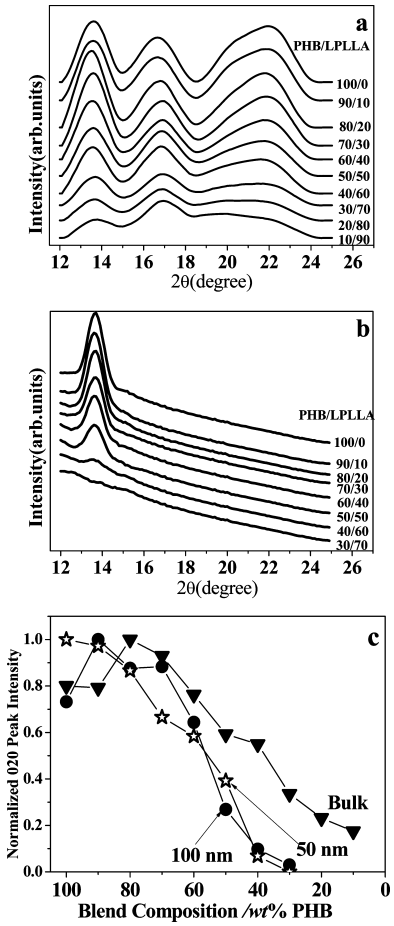


Figure 1. X-ray diffraction out-of-plane profiles for PHB/LPLLA blends having thickness of 1 μm (a) and 100 nm (b). The normalized 020 peak intensity as a function of blend composition is shown in (c).

our previous studies.[24] In addition, the volume of the sample illuminated by the X-ray beam is fixed in this study. Therefore, the change of the peak intensity in the out-of-plane profiles can be used to indicate the degree of crystallization. Moreover, since there is no Bragg peak of the PLLA crystals in the range of $12° < 2\theta < 15°$, the 020 Bragg peak of PHB is the most suitable peak for reflecting the changes of the degree of PHB crystallization. The 020 peak intensity of PHB as a function of w_{PHB} is plotted in Figure 1c. The increment of the 020 peak intensity with the addition of a small amount of PLLA implies that PLLA serves as a nucleating agent or nucleation-assisting or spherulite growth-accelerating agent.[26] The decrease in the 020 peak intensity with further increment of the PLLA weight ratio under the condition of $w_{PHB} < 80$ wt % may be caused by reduction in the total amount of PHB and/or the inhibition effect of PLLA on the crystallization of PHB. To distinguish between the two effects, the peak intensity has been normalized by the weight ratio. After normalization, the 020 peak intensity does not show a strong dependence on the weight ratio of PHB (Figure S1 in the Supporting Information), suggesting that the addition of LPLLA does not confine the crystallization of PHB in a wide weight ratio range.

Figure 1b shows the GIXD out-of-plane profiles for 100 nm thick PHB/LPLLA blend films; note that only one strong 020 Bragg reflection centered at $2\theta = 13.56°$ was observed. The presence of this unique 020 Bragg reflection and the absence of other reflections indicate that the *b*-axis of the PHB crystallites prefers to align in the direction normal to the film surface, resulting in an alignment of the *ac* planes parallel to the substrate surface. Note here that for the thin films the peak intensity in the in-plane profiles is very weak and not sensitive as that in the out-of-plane profiles. For example, there is no much difference between the in-plane profiles of thin films for neat PHB and PHB/LPLLA blend with $w_{PHB} = 70$ wt % (see Figure S2 in the Supporting Information). In this case, the in-plane data are not suitable for the estimation of crystallinity of PHB. Therefore, we have focused on the out-of-plane data because of their stronger reflection intensity and sensitivity. The 020 peak intensity obtained from out-of-plane profiles as a function of w_{PHB} is shown in Figure 1c. The crystallization behavior of PHB in the 100 nm thick film is slightly different from that of the thick film (e.g., 1 μm thick films shown in Figure 1a). The Bragg peaks of PHB crystallites disappear when $w_{PHB} \leq 30$ wt %. Comparison with the results showing that PHB can still crystallize at $w_{PHB} = 10$ wt % in the 1 μm thick film, one can realize that a thinner film tends to reduce crystallization of PHB. The films having a thickness of 50 nm exhibit the similar behavior as that of the 100 nm thick film (see Figure 1c). The crystallization of PHB is also completely inhibited at $w_{PHB} < 30$ wt %, suggesting that further decreasing the film thickness does not affect the crystallization behavior of PHB.

To investigate the effect of the molar mass of PLLA on the crystallization behavior of PHB in the blends, blends of PHB with higher molecular weight PLLA (PHB/HPLLA) were also studied. The GIXD profiles of the 1 μm thick PHB/HPLLA blend films with different blend ratios are displayed in Figure 2a. A Bragg peak at $2\theta \approx 13.58°$ and broad peaks ranging from 18.65° to 24° continuously decrease with the decrease in PHB content. In contrast, a Bragg peak centered at $2\theta = 16.8°$ first decreases with decreasing PHB when $w_{PHB} \geq 40$ wt %. Thereafter, a sharp Bragg peak at around $2\theta = 16.5°$ appears. It may be caused by crystallization of PLLA because the 200 and 110 Bragg peaks of PLLA are expected to be situated in the same range. This indicates that PLLA already crystallizes at room temperature during the preparation of sample although the glass transition temperature (T_g) of PLLA ($M_w = 13\,100$ g mol^{-1}) is around 39 °C (information supplied by the Polymer Source Co.). Here one can find that LPLLA does not crystallize in the blend at room temperature by comparing Figure 2a with Figure 1a. This is because a critical molecular weight for crystallizable PLA exists.[27] The molecular weight of LPLLA is lower than the critical molecular weight, and it can hardly crystallize. The intensity of the 020 peak as a function of weight ratio is shown in Figure 2c. The evolution of the Bragg peaks with the change of w_{PHB} for the thick films is almost the same as that in the PHB/LPLLA blends, indicating that the change in molar mass of PLLA from 710 to 13 100 g mol^{-1} does not significantly affect the crystallization behavior of PHB in the thick films.

In the 100 nm thick films of PHB/HPLLA blends with different blending ratios, the GIXD profiles only showed a 020 Bragg peak at $2\theta \approx 13.6°$ (see Figure 2b), which indicates that the preferred orientation of PHB crystals is the same as that in the PHB/LPLLA films. However, the plot of 020 peak intensity vs w_{PHB} remarkably differs from both the thick and thin PHB/LPLLA films. The intensity of the 020 Bragg peak considerably decreased and nearly dropped to zero for $w_{PHB} = 80$ wt %. In contrast, the 020 Bragg peak of PHB in the thick film with a similar ratio ($w_{PHB} = 80$ wt %) exhibits even a higher intensity

dx.doi.org/10.1021/ma202543s | *Macromolecules* 2012, 45, 2485−2493

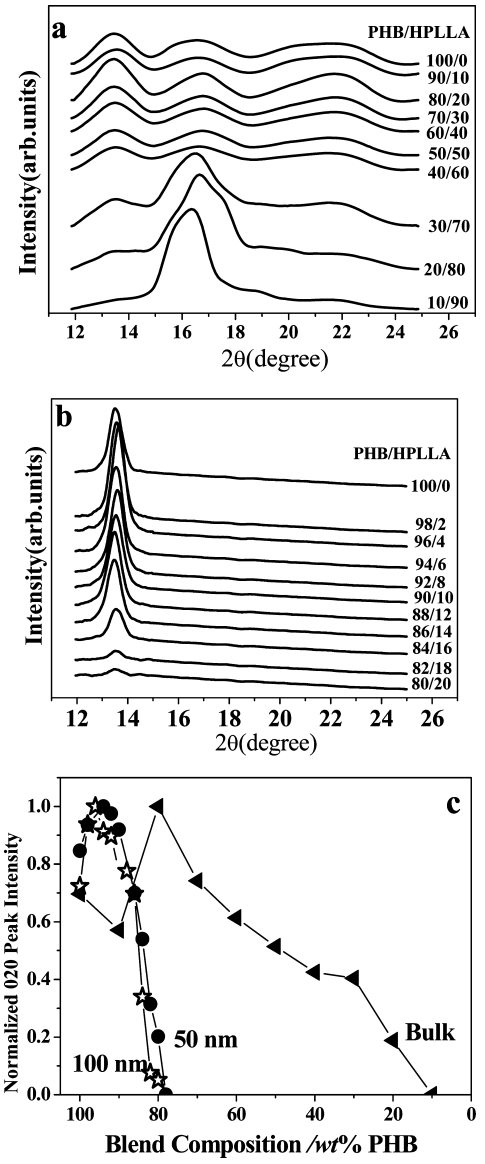


Figure 2. X-ray diffraction out-of-plane profiles for PHB/HPLLA blends having thickness of 1 μm (a) and 100 nm (b). The normalized 020 peak intensity as a function of blend composition is shown in (c).

than that of the neat PHB. The noticeable difference in the w_{PHB} dependence of PHB crystallization in the PHB/HPLLA films having thicknesses ranging from 1 μm to 100 nm suggests that in the ultrathin films crystallization of PHB is inhibited significantly in the presence of HPLLA. Further thinning of the film does not show any noticeable change (the peak intensity of the 50 nm thick film shown in Figure 2c). One may suggest the possibility of forming a layered structure consisting of PHB and HPLLA separating layers triggered by the phase separation. If this is true, the inhibition of the PHB crystallization should be then attributed to the geometrical confinement. However, considering the small amount of HPLLA where PHB crystallization is completely inhibited (w_{PLLA} < 22 wt %), even in a layered structures the thickness of the separated PHB layer should be still considerably larger than the critical thickness of the neat PHB film (<15 nm), below which PHB cannot crystallize.[28] Therefore, it can be concluded that the disappearance of the PHB crystallites in the PHB/HPLLA blend is not due to the effect of PHB thickness confinement, but that of HPLLA molecules. Because the crystallization behavior of PHB in the PHB/HPLLA blends shows the striking difference between the bulk and thin films, the PHB/HPLLA system should be focused to clarify the effect of longer PLLA chains in confined geometry.

Crystallization of polymers in the ultrathin films is known to be reduced when compared with that in the bulk. However, the results were not expected that crystallization of PHB in the ultrathin PHB/HPLLA blend is completely inhibited at a very high PHB ratio (w_{PHB} < 80 wt %). The shift of T_g may account for the increasing amorphous degree of PHB in the PHB/HPLLA blend because T_g of polymers is expected to shift to a higher temperature in the ultrathin film because of thickness confinement.[29−31] In the case of PHB/PLLA blends, in addition to the thickness confinement, the existence of PLLA is another factor that may promote the shift of T_g of PHB. Considering that the reduction in crystallization of PHB in the ultrathin PHB/LPLLA film is considerably less, it can be speculated that the existence of PLLA would play a more important role than film thickness in reducing the PHB crystallization. To determine whether the inhibition of PHB crystallization is caused mainly by the higher temperature shift of T_g, the ultrathin PHB/HPLLA films with w_{PHB} ranging from 100 to 20 wt % were subjected to a thermal annealing process. Figure 3 shows the 020 peak intensity as a function of annealing

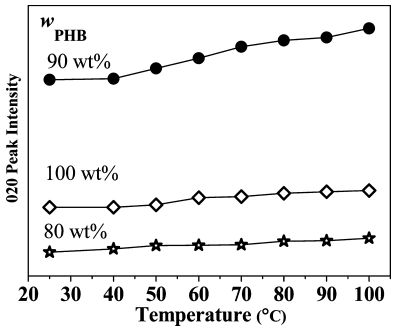


Figure 3. Annealing temperature dependence of 020 Bragg peak intensity for 100 nm thick films of PHB/HPLLA blends.

temperature. For the blend with w_{PHB} = 100, 90, and 80 wt %, the peak intensity increases gradually with temperature. However, there is no Bragg peak of PHB during the entire heating process for the blend with $w_{PHB} \leq$ 78 wt %. Figure 3 demonstrates that thermal annealing is ineffective to induce crystallization of PHB in the ultrathin films of the blend with $w_{PHB} \leq$ 78 wt % although it can enhance the degree of crystallization for PHB of the blend with $w_{PHB} \geq$ 80 wt %. Therefore, significant inhibition of PHB crystallization in the thin PHB/HPLLA film cannot be attributed to the shift of T_g.

To provide deeper insight into the inhibition of crystallization in the ultrathin PHB/HPLLA films, FTIR measurements were performed. FTIR is very sensitive to chain conformations including chain segment and chain packing features. Considering this ability, the FTIR spectra of the bulk and thin PHB/HPLLA films with different weight ratios were measured to obtain structural conformations at molecular level and length scales different from those of X-ray diffraction.

The crystallization behavior of PHB for the thick PHB/HPLLA blend films was investigated by transmitted FTIR. Figure 4 shows the FTIR spectra and their corresponding second derivative spectra in the carbonyl stretching vibration

dx.doi.org/10.1021/ma202543s | Macromolecules 2012, 45, 2485−2493

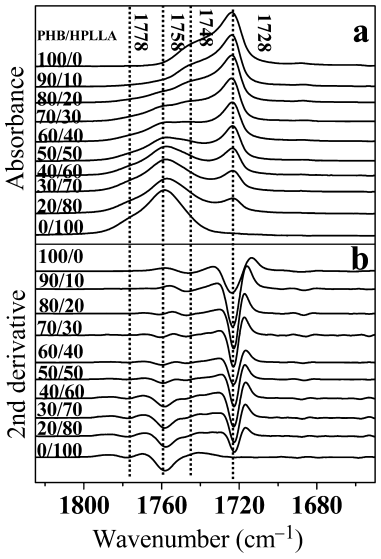


Figure 4. FTIR spectra obtained at room temperature in the C═O stretching region for the as-prepared 10 μm thick films of PHB/HPLLA blend (a) and their second derivatives (b).

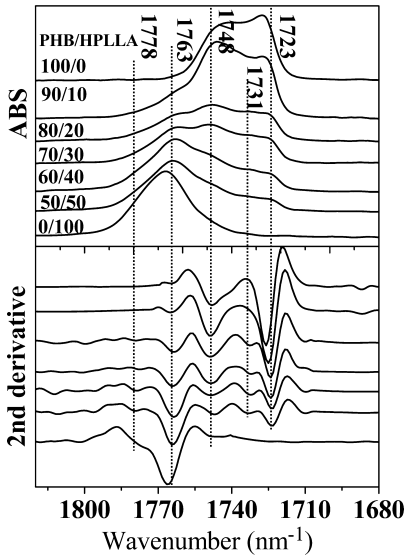


Figure 5. IR-RAS spectra obtained at room temperature in the C═O stretching region for the as-prepared 50 nm thick films of PHB/HPLLA blend (a) and their second derivatives (b).

region for the PHB/HPLLA solution-cast samples. For the neat PHB film, two bands centered at 1748 and 1728 cm^{-1}, which respectively correspond to the amorphous and crystalline states, are observed.[2] For the neat PLLA film, two additional bands at 1778 and 1758 cm^{-1} are clearly resolved in the second derivative spectra. The 1778 cm^{-1} band arises from structural defects of PLLA,[12] whereas the 1758 cm^{-1} band is assigned to the amorphous C═O stretching mode of PLLA.

The composition-dependent FTIR spectra of the as-prepared samples show the following trends with w_{PHB}: The intensity of the sharp and dominant crystalline band around 1728 cm^{-1} decreases smoothly with the decrease in w_{PHB} accompanied by a gradual increase in the amorphous band of PLLA at 1758 cm^{-1}. The sharp crystalline peak of PHB is still easily resolved in the IR spectrum at w_{PHB} = 20 wt %. In addition, the absorption intensity of the amorphous band at around 1748 cm^{-1} does not increase significantly with the decrease in w_{PHB}. These results imply that the molecular conformation and crystallinity of PHB in the thicker film is not significantly inhibited in the presence of PLLA, which is consistent with the results obtained by X-ray diffraction.

The IR results for the ultrathin films have been found to be significantly different from those for the bulk samples. Figure 5 shows the IR-RAS spectra in the C═O stretching vibration region obtained at room temperature for the 50 nm thick PHB/HPLLA films with different weight ratios. The spectrum of the neat PHB film exhibits two bands at 1728 and 1748 cm^{-1} attributed to the crystalline and amorphous states, respectively. By comparing the transmission spectrum of the neat PHB film with its IR-RAS spectrum, it is observed that the intensity ratio of the crystalline C═O stretching band at 1728 cm^{-1} to the amorphous one at 1748 cm^{-1} for the bulk film is significantly higher than that for the thin film. The difference may be attributed to the following two factors: (1) The degree of crystallization of PHB: in the ultrathin film, because of the size effect and/or the interface effect, the molecular mobility of PHB decreases, which leads to low degree of crystallization. Thus, the percentage of the crystalline band of PHB at 1728 cm^{-1} should be smaller. (2) The orientation of the PHB crystal, since the aforementioned GIXD results show that in the ultrathin film the *ac*-plane of the PHB crystallites is parallel to the surface. Combining with the previous results, this suggests that the C═O groups are parallel to the substrate and along the *a*-axis.[4] Considering the surface selection rule of IR-RAS spectroscopy in which the vibration modes whose transition dipole movements are parallel to the substrate surface appear faintly in an IR-RAS spectrum, it is reasonable that the intensity ratio of the two bands at 1728 and 1748 cm^{-1} is lower in the thin PHB film than in the bulk films.

The addition of PLLA significantly alters the spectra. When w_{PHB} = 90 wt %, in addition to the presence of a new peak at 1764 cm^{-1} ascribing to be the amorphous band of PLLA, the shape of the crystalline band of PHB around 1728 cm^{-1} becomes very blunt. The result is considerably different from that of bulk film where the sharp crystalline band around 1728 cm^{-1} can still be clearly resolved even when w_{PHB} = 20 wt %. When w_{PHB} = 80 wt %, the intensity of the crystalline band further weakens, and the shape of the band changes from peak to shoulder. Moreover, two unanticipated changes occur with decreasing w_{PHB}: the crystalline band of PHB shifts to lower wavenumbers from 1728 to 1723 cm^{-1}, and a new band appears at 1731 cm^{-1}. With further decrease in PHB content, the vibration bands related to PHB, including the 1748, 1731, and 1723 cm^{-1} bands, decrease gradually. Meanwhile, the intensity of the amorphous band of PLLA at 1764 cm^{-1} and the band at 1778 cm^{-1} ascribing to be the structural defect of PLLA increases with increasing PLLA weight ratio.

The present study focused on crystallization and molecular arrangement of PHB, the vibration spectra in the C═O stretching region of PHB affected by the weight ratio is discussed in detail from the following three viewpoints:

(1) The wavenumber shift for the crystalline C═O stretching band in the blend. From Figure 5, the crystalline C═O stretching band at 1728 cm^{-1} clearly shifted by 5 cm^{-1} to a lower wavenumber under the condition of $w_{PHB} \leq 80$ wt %. The PHB−PLLA interaction is most likely responsible for the shift of the C═O stretching band because the shift of the crystalline C═O stretching band of PHB is accompanied by

dx.doi.org/10.1021/ma202543s | *Macromolecules* 2012, 45, 2485−2493

the presence of PLLA. A weak $CH_3\cdots O{=}C$ interaction was recently reported to exist in the PHB crystals and PLLA/PDLA sterocomplex.[2,3,32] Considering the similar chemical structures of PHB and PLLA, the $CH_3\cdots O{=}C$ interaction of PHB and PLLA is also expected. Moreover, the interaction induced by dipolar interaction may also lead to the shift in the peak of the C=O stretching band.[33] It is not yet clear what type of interaction is specifically responsible for the PHB−PLLA interaction. Because the crystalline peak of PHB only shifts in the ultrathin blend film, it can be addressed that the potential intermolecular interaction between PHB and HPLLA is considerably stronger in thin or ultrathin films. Such kind of interaction is also expected to exist in the PHB/LPLLA blends and thick film. However, considering the higher extent of molecular entanglement of HPLLA and thickness confinement, the effect of the interaction between PHB and PLLA on inhibiting the crystallization of PHB is enlarged in the ultrathin films of PHB/HPLLA blends.

(2) The presence of 1731 cm^{-1} in the blend with $w_{PHB} \leq 80$ wt %. The band at 1731 cm^{-1} has been observed by several research groups in a specific process of PHB. It was found that the 1731 cm^{-1} band is only observed in the early stages of crystallization and reported to disappear at the end stages.[34,35] Therefore, it is preferred that this band is referred to as the "intermediate state" by adopting the concept proposed by Strobl.[36] In addition to the crystallization process, during the melting process of PHB, the 1731 cm^{-1} band is traced by 2D IR spectroscopy and assigned to the crystalline phase with a less ordered structure.[37,38] In this study, the 1731 cm^{-1} band is observed in the PHB/HPLLA blend thin film for the first time ($w_{PHB} \leq 80$ wt %). If one employs the concept of "intermediate state", it can be speculated that the existence of HPLLA in the ultrathin film hampers crystallization of PHB and traps the PHB molecules in the intermediate state.

(3) The controversy between GIXD and IR observations. GIXD suggests that no crystal exists in the thin films of the blends with $w_{PHB} \leq 78$ wt %. However, IR spectra exhibits the crystalline 1723 cm^{-1} band even in the film with $w_{PHB} = 50$ wt %. Following two possibilities explain these controversial results: First, the degree of crystallization is considerably too small to be detected by GIXD with the ultrathin polymer film. Second, the 1723 cm^{-1} is actually a conformation sensitive band corresponding to the C=O stretching vibration, which is not caused by intermolecular interaction of the chains packed in the crystalline unit cell. In this sense, the presence of the band at 1723 cm^{-1} suggests the existence of the C=O stretching vibration as that in the crystalline state, but not sufficient enough to suggest the formation of PHB crystals.

The GIXD results demonstrate that the degree of crystallization of PHB in the thin films of PHB/HPLLA blends with $w_{PHB} \geq 80$ wt % increases with the annealing temperature, whereas in the entire heating process, PHB remains in the amorphous state for the blend with $w_{PHB} \leq 78$ wt %. To better understand the effect of weight ratio on the molecular structure of PHB under thermal treatment, the temporal changes of the IR spectra of the blend are monitored. Figure 6 shows the spectra of the blend with $w_{PHB} = 90$ and 70 wt % in the C=O stretching vibration region. It can be observed that the amorphous band at 1748 cm^{-1} in both samples decreases with increasing temperature, while the crystalline band at 1728 cm^{-1} (1723 cm^{-1} for $w_{PHB} = 70$ wt %) strengthens. Moreover, for the blend with $w_{PHB} = 70$ wt %, in addition to the crystalline band at 1723 cm^{-1}, the 1731 cm^{-1} band is clearly observed and

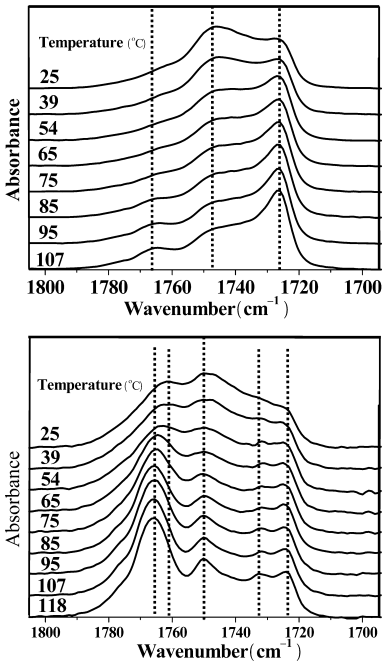


Figure 6. Annealing temperature dependence of IR-RAS spectra in the C=O stretching region for the as-prepared 50 nm thick films of PHB/HPLLA blend with $w_{PHB} = 90$ wt % (a) and $w_{PHB} = 70$ wt % (b).

increases with temperature. By comparing GIXD and IR results, it is realized that although the degree of crystallization does not increase under thermal treatment (see Figure 3), the amount of intermediate structure increases with the increasing of temperature.

Because several elemental C=O stretching vibration bands of PHB exist including two amorphous bands (1748 and 1739 cm^{-1}) arising from different conformations of the main chains, the crystalline band (1728 cm^{-1}) and the intermediate state band (1731 cm^{-1}), a curve-fitting procedure is employed to decompose the spectra in the C=O stretching region to quantitatively investigate the effects of the weight ratio and the temperature on the individual elemental C=O stretching vibration bands. Moreover, the amorphous band and structural defect of PLLA are also decomposed. For the decomposition, the peaks are assumed to be Gaussian in the spectrum. Figure 7 shows two typical curve fitting results of the thin film of PHB/HPLLA with $w_{PHB} = 90$ wt % (a) and 70 wt % (b).

The fractions of f_{1748}, f_{1739}, f_{1731}, and $f_{crystalline}$ were calculated on the basis of the Lambert−Beer law

$$f_i = \frac{A_i/\varepsilon_i}{\sum_i (A_i/\varepsilon_i)}$$

where A_i and ε_i are the absorbance and absorption coefficient of the elemental spectrum (i = 1748, 1739, 1731 cm^{-1}, and crystalline), respectively. We used the reported value[39,40] of $\varepsilon_{crystalline}/\varepsilon_{1748} = 1$ and assumed that $\varepsilon_{crystalline} = \varepsilon_{1731}$ and $\varepsilon_{1748} = \varepsilon_{1739}$. The results of the curve fitting analysis are summarized in Tables 1 and 2, and the fractions of each elemental vibration mode are shown as a function of annealing temperature in Figure 8. For the blend with $w_{PHB} = 90$ wt %, PHB is composed of three elemental spectra without the intermediate bands at 1731 cm^{-1}. The evolution of these spectra is displayed in Figure 8a. It can be seen that the amorphous band at 1748 cm^{-1} with the onset fraction of 63% decreases significantly with increasing

dx.doi.org/10.1021/ma202543s | Macromolecules 2012, 45, 2485−2493

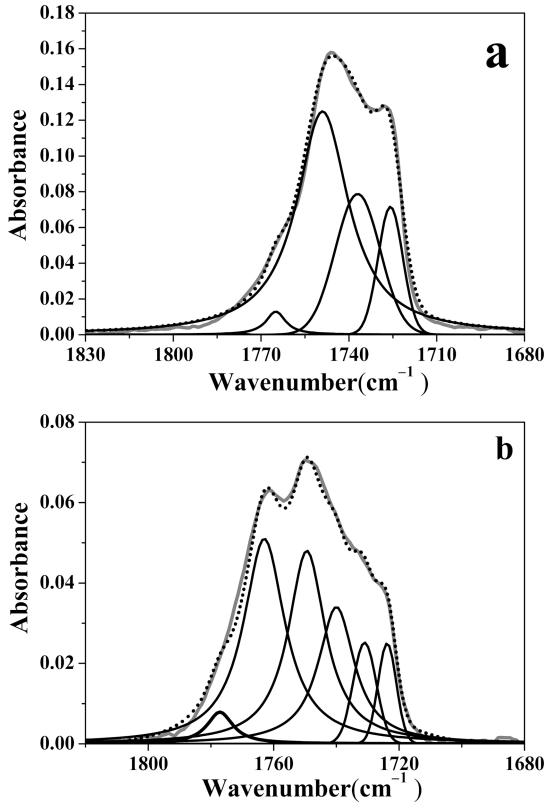


Figure 7. Decomposition of observed FTIR spectra in the C=O stretching region for 50 nm thick films of PHB/HPLLA blend with w_{PHB} = 90 wt % (a) and w_{PHB} = 70 wt % (b) (solid line) into crystalline component of PHB [1728 cm^{-1} for (a); 1723 cm^{-1} for (b)]; intermediate component of PHB [1731 cm^{-1} only for (b)]; amorphous component of PHB (1739 cm^{-1}); amorphous component of PHB (1748 cm^{-1}); amorphous component of PLLA (1764 cm^{-1}); and structure defects of PLLA (1778 cm^{-1}). The reconstructed absorbance (dotted line) was obtained by summing the absorbances of the elemental bands.

temperature. On the contrary, the amorphous band at 1739 cm^{-1} and the crystalline band at 1728 cm^{-1} increases with temperature. The crystalline band shows a trend that is similar to the amorphous band at 1739 cm^{-1}, and the fraction reaches 29% when the temperature is 118 °C. It can be seen that the thermal heating increases the crystallization degree of PHB, which is consistent with the GIXD results.

For the blend with w_{PHB} = 70 wt %, PHB is decomposed into four types of spectrum. The temperature dependence of the fractions for each component is displayed in Figure 8b. At 25 °C, the amorphous phase at 1748 cm^{-1} forms the largest fraction (49%), whereas, the crystalline band at 1723 cm^{-1} and the intermediate band at 1731 cm^{-1} account entirely for the fraction of 18%. During the heating process, the fraction for the amorphous band at 1748 cm^{-1} decreases with the gradual increase of the fraction for the crystalline band at 1723 cm^{-1} and the intermediate band at 1731 cm^{-1}. It is reasonable to expect that the amorphous phase transitions to the crystalline and intermediate phases. Note that the increase of the crystalline and intermediate phases are not as marked as that for the blend with w_{PHB} = 90 wt %, suggesting that the molecular structures of PHB in the blend prefer to stay in the amorphous state. Previously, the band at 1731 cm^{-1} is observed in the early stage of the melt-recrystallization process of PHB, and the intensity of this band first increases with time; thereafter, it tends to decrease with a rapid increase of the crystalline band at 1723 cm^{-1}.[34,35] The sequential changes of the bands at 1731 and 1723 cm^{-1} are strong indications of the transformation of the PHB structure from the amorphous state via the intermediate structure to the crystalline phase. In this study, the relationship between the bands at 1731 and 1723 cm^{-1} for the blend with w_{PHB} = 70 wt % has two features: first, they coexist instead of having a sequential appearance, and second, the fraction for the 1731 cm^{-1} band increases at a rate similar to that of the 1723 cm^{-1} band in the thermal annealing process. The decay of the 1731 cm^{-1} band with the increase of the 1723 cm^{-1} band is not evident. These two features may imply that the transition rate from intermediate structure to crystalline phase is slowed down in the blended form. Considering the absence of 1731 cm^{-1} in the thick film, thickness confinement may also play a role on changing the transition rate. Note that despite the increase in the fraction of the crystalline band at 1723 cm^{-1} during the heating process, the GIXD results suggest that no Bragg peaks of PHB crystals appear during the entire heating process. This controversy implies that the thermal treatment does not efficiently promote the degree of crystallization of PHB and favors only the development of the intermediate structure. In addition to the change in the PHB structures, the degree of crystallization of HPLLA increases significantly during the heating process, as suggested by the presence of the strong crystalline band of PLLA at 1766 cm^{-1}.

CONCLUSION

Two types of PHB/PLLA blends, PHB/HPLLA and PHB/LPLLA, were prepared for studying the crystallization behavior

Table 1. Curve Fitting Results for C=O Stretching Vibration Bands in the PHB/HPLLA Blend with w_{PHB} = 90 wt %

	1728 cm^{-1}		1739 cm^{-1}		1748 cm^{-1}		1764 cm^{-1}		1778 cm^{-1}	
temp (°C)	h^a	$w_{1/2}{}^b$	h	$w_{1/2}$	h	$w_{1/2}$	h	$w_{1/2}$	h	$w_{1/2}$
25	0.0716	5	0.0788	9	0.125	10.8	0.013	7	0.004	4
35	0.087	5.1	0.087	9.2	0.11	10.2	0.015	7	0.004	4
55	0.108	5.3	0.0799	9.5	0.0751	12	0.021	7	0.002	4
65	0.117	5.2	0.084	9.8	0.063	12	0.024	7.3	0.002	4
75	0.125	5.2	0.084	10	0.06	12	0.024	7.3	0.002	4
85	0.133	5.3	0.086	10.3	0.053	12	0.029	7.3	0.0024	4
95	0.138	5.1	0.082	10.5	0.048	12	0.034	7.3	0.004	4
105	0.146	5.1	0.083	10.5	0.046	12.4	0.0359	6.4	0.005	4
115	0.146	5.1	0.083	10.8	0.044	12.4	0.0379	6.4	0.005	4

[a]Peak height. [b]Full width at half-maximum.

dx.doi.org/10.1021/ma202543s | Macromolecules 2012, 45, 2485−2493

Table 2. Curve Fitting Results for C=O Stretching Vibration Bands in the PHB/HPLLA Blend with w_{PHB} = 70 wt %

	1723 cm^{-1}		1731 cm^{-1}		1739 cm^{-1}		1748 cm^{-1}		1764/1766 cm^{-1}		1778 cm^{-1}	
temp (°C)	h^a	$w_{1/2}{}^b$	h	$w_{1/2}$	h	$w_{1/2}$	h	$w_{1/2}$	h	$w_{1/2}$	h	$w_{1/2}$
25	0.025	3.46	0.0252	4.35	0.034	7	0.048	7.2	0.051	8	0.008	5
35	0.030	3.46	0.0252	4.35	0.033	7	0.043	7.2	0.050	8.4	0.009	5
55	0.032	3.46	0.0268	4.35	0.029	7	0.037	7.4	0.0515	8.5	0.009	5
65	0.034	3.46	0.0256	4.35	0.026	7	0.032	7.2	0.065	8.5	0.0062	5
75	0.034	3.46	0.0256	4.35	0.025	7	0.0349	6.8	0.0722	7.8	0.006	5
85	0.034	3.46	0.0256	4.35	0.026	6.8	0.034	6	0.077	7.5	0.004	5
95	0.034	3.46	0.0256	4.35	0.026	6.8	0.0349	5.5	0.085	7.5	0.004	5
105	0.034	3.46	0.0245	4.35	0.025	6.8	0.034	5.5	0.088	7.2	0.004	5
115	0.034	3.46	0.0248	4.35	0.024	6.8	0.0358	5.5	0.090	6.8	0.004	5

[a]Peak height. [b]Full width at half-maximum.

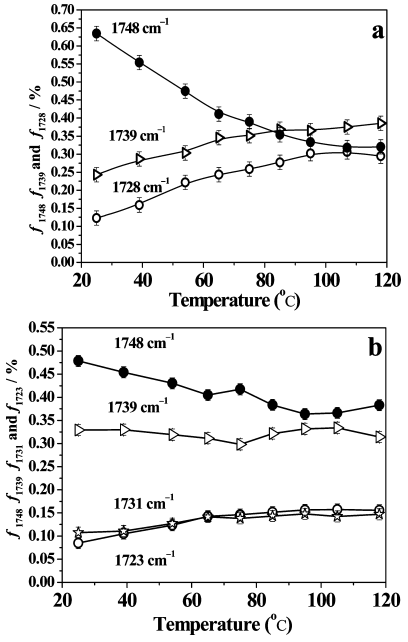


Figure 8. Annealing temperature dependence of the fraction of the elemental PHB-related bands for PHB/HPLLA with w_{PHB} = 90 wt % (a) and w_{PHB} = 70 wt % (b).

of PHB in the blends. The GIXD measurement focused on the characteristic 020 Bragg peak of PHB and revealed that for the thick films of the two types blends the crystallization behavior of PHB is almost the same. For the thin films, crystallization degree of PHB decreases slightly in the ultrathin film of PHB/LPLLA blend, and the crystallization stops when $w_{PHB} \leq 30$ wt %. In contrast, for the ultrathin film of PHB/HPLLA blend, crystallization of PHB is inhibited completely at a significantly high weight ratio of PHB ($w_{PHB} \leq 78$ wt %), and thermal annealing has no effect on the crystallization of PHB. Infrared reflection−absorption spectroscopy suggests that for the ultrathin PHB/HPLLA film the intensity of the crystalline band at 1728 cm^{-1} decreases drastically with decreasing w_{PHB}, and a new band appears at 1731 cm^{-1} with $w_{PHB} \leq 80$ wt %. The presence of the 1731 cm^{-1} band indicates that the existence of higher molar mass PLLA in the thin film changes the transition rate of PHB from its intermediate structure to crystalline structure. The amount of the intermediate structure increases with the annealing temperature. The key factor for the formation of the intermediate PHB structure found in the ultrathin film of PHB/HPLLA blend is still not clear. It may be induced by the interface effect and/or size effect strongly correlated with the size of molecular chains and the film thickness.

■ ASSOCIATED CONTENT

Supporting Information

The 020 peak intensity of PHB/LPLLA and PHB/HPLLA blends having thickness of 1 μm normalized by weight ratio of PHB, X-ray diffraction in-plane profiles for neat PHB and PHB/LPLLA blend with w_{PHB} = 70 wt % having thickness of 100 nm. This material is available free of charge via the Internet at http://pubs.acs.org.

■ AUTHOR INFORMATION

Corresponding Author

*E-mail: skyan@mail.buct.edu.cn (S.Y.); suikyo@kwansei.ac.jp (I.T.).

Notes

The authors declare no competing financial interest.

■ ACKNOWLEDGMENTS

This study was financially supported by the Kwansei Gakuin University (Kwansei Gakuin University Joint Research Fund, 2009) and the National Natural Science Foundations of China (No. 21004003).

■ REFERENCES

(1) Chiellini, E.; Solaro, R. *Recent Advances in Biodegradable Polymers and Plastics*; Wiley-VCH: Weinheim, 2003.
(2) Sato, H.; Nakamura, M.; Padermshoke, A.; Yamaguchi, H.; Terauchi, H.; Ekgasit, S.; Noda, I.; Ozaki, Y. *Macromolecules* **2004**, *37*, 3763.
(3) Sato, H.; Murakami, R.; Padermshoke, A.; Hirose, F.; Senda, K.; Noda, I.; Ozaki, Y. *Macromolecules* **2004**, *37*, 7203.
(4) Ikada, Y.; Tsuji, H. *Macromol. Rapid Commun.* **2000**, *21*, 117.
(5) Tsuji, H.; Ikada, Y. *Polymer* **1999**, *40*, 6699.
(6) Dorgan, J. R. *Poly(lactic acid) Properties and Prospects of an Environmentally Benign Plastic*; The American Chemical Society: Washington, DC, 1999; pp 145−149.
(7) Yoshie, N.; Saito, M.; Inoue, Y. *Macromolecules* **2001**, *34*, 8953.
(8) Koyama, N.; Doi, Y. *Polymer* **1997**, *38*, 1589.
(9) Owen, A. J.; Blumm, E. *Polymer* **1995**, *36*, 4077.
(10) Furukawa, T.; Sato, H.; Murakami, R.; Zhang, J. M.; Duan, Y. X.; Noda, I.; Ochiai, S.; Ozaki, Y. *Macromolecules* **2005**, *38*, 6445.
(11) Noda, I.; Satkowski, M. M.; Dowrey, A. E.; Marcott, C. *Macromol. Biosci.* **2004**, *4*, 269.
(12) Zhang, J.; Sato, H.; Furukawa, T.; Tsuji, H.; Noda, I.; Ozaki, Y. *J. Phys. Chem. B* **2006**, *110*, 24463.
(13) Vogel, C.; Wessel, E.; Siesler, H. *Biomacromolecules* **2008**, *9*, 523.
(14) Vogel, C.; Wessel, E.; Siesler, H. *Macromolecules* **2008**, *41*, 2975.

(15) Schultz, J. M. *Macromolecules* **1996**, *29*, 3022.
(16) Liu, Y.; Chen, E. *Coord. Chem. Rev.* **2010**, *254*, 1011.
(17) Despotopoulou, M.; Frank, C. W.; Miller, R. D.; Rabolt, J. F. *Macromolecules* **1996**, *29*, 5797.
(18) Basire, C.; Ivanov, D. A. *Phys. Rev. Lett.* **2000**, *85*, 5587.
(19) Wang, Y.; Ge, S.; Rafailovich, M.; Sokolov, J.; Zou, Y.; Ade, H.; Luening, J.; Lustiger, A.; Maron, G. *Macromolecules* **2004**, *37*, 3319.
(20) Lovinger, A. J.; Keith, H. D. *Macromolecules* **1979**, *12*, 919.
(21) Schonherr, H.; Frank, C. W. *Macromolecules* **2003**, *36*, 1188.
(22) Keith, H. D.; Padden, F. J.; Lotz, B.; Wittmann, J. C. *Macromolecules* **1989**, *22*, 2230.
(23) Wang, Y.; Chan, C. M.; Ng, K. M.; Li, L. *Macromolecules* **2008**, *41*, 2548.
(24) Mori, K.; Mukoyama, S.; Zhang, Y.; Sato, H.; Ozaki, Y.; Terauchi, H.; Noda, I.; Takahashi, I. *Macromolecules* **2008**, *41*, 1713.
(25) Sato, H.; Murakami, R.; Mori, K.; Ando, Y.; Takahashi, I.; Noda, I.; Ozaki, Y. *Vib. Spectrosc.* **2009**, *51*, 132.
(26) Tsuji, H.; Sawada, M.; Bouapao, L. *ACS Appl. Mater. Interfaces* **2009**, *1*, 1719.
(27) de Jong, S.; van Dijk-Wolthuis, W.; Kettenes-van den Bosch, J.; Schuyl, P.; Hennink, W. *Macromolecules* **1998**, *31*, 6397.
(28) Sun, X.; Guo, L.; Sato, H.; Ozaki, Y.; Yan, S.; Takahashi, I. *Polymer* **2011**, *52*, 3865.
(29) Ellison, C. J.; Torkelson, J. M. *Nature* **2003**, *2*, 695.
(30) DeMaggio, G. B.; Frieze, W. E.; Gidley, D. W.; Zhu, M.; Hristov., H. A.; Yee, A. F. *Phys. Rev. Lett.* **1997**, *78*, 1524.
(31) Priestley, R. D.; Ellison, C. J.; Broadbelt, L. J.; Torkelson, J. M. *Science* **2005**, *309*, 456.
(32) Zhang, J. M.; Sato, H.; Noda, I.; Ozaki, Y. *Macromolecules* **2005**, *38*, 4274.
(33) Painter, P. C.; Pehlert, J. G.; Hu, Y.; Coleman, M. M. *Macromolecules* **1999**, *32*, 2055.
(34) Zhang, J.; Sato, H.; Noda, I.; Ozaki, Y. *Macromolecules* **2005**, *38*, 4274.
(35) Suttiwijitpukdee, N.; Sato, H.; Zhang, J.; Hashimoto, T. *Macromolecules* **2011**, *44*, 3467.
(36) Strobl, G. *Eur. Phys. J. E* **2000**, *3*, 165.
(37) Yoshie, N.; Oike, Y.; Kasuya, K.; Doi, Y.; Inoue, Y. *Biomacromolecules* **2002**, *3*, 1320.
(38) Padermshoke, A.; Katsumoto, Y.; Sato, H.; Ekgasit, S.; Noda, I.; Ozaki, Y. *Spectrochim. Acta, Part A* **2005**, *61*, 541.
(39) Coleman, M. M.; Lichkus, A. M.; Painter, P. C. *Macromolecules* **1989**, *22*, 586.
(40) Iriondo, P.; Iruin, J. J.; Fernandez-Berridi, J. J. *Macromolecules* **1996**, *29*, 5605.

Macromolecules

Article

pubs.acs.org/Macromolecules

Guiding Block Copolymers into Sequenced Patterns via Inverted Terrace Formation

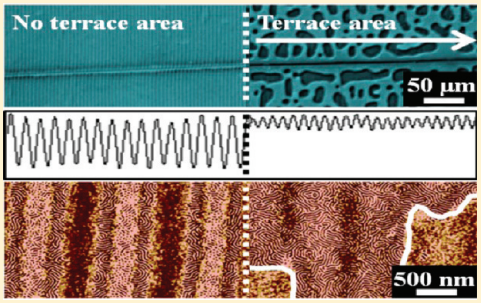
Sungjune Park,[†] Larisa Tsarkova,*[,†] Stephanie Hiltl,[†] Stefan Roitsch,[‡] Joachim Mayer,[‡] and Alexander Böker*[,†]

[†]DWI an der RWTH Aachen e. V., Lehrstuhl für Makromolekulare Materialien und Oberflächen, RWTH Aachen University, D-52056 Aachen, Germany

[‡]Gemeinschaftslabor für Elektronenmikroskopie, RWTH Aachen University, Ahornstr. 55, D-52074 Aachen, Germany

Supporting Information

ABSTRACT: Corrugated SiCN ceramic substrates fabricated by a facile replication process using nonlithographic PDMS masters were employed for the directed assembly of block copolymer microdomains. During thermal annealing of polystyrene-*b*-polybutadiene diblock copolymer, the material transport was guided by a wrinkled substrate to form regular modulations in the film thickness. As a consequence of the thickness-dependent morphological behavior of cylinder forming block copolymer, the film surface appears as sequenced patterns of alternative microphase-separated structures. The ordering process is attributed to the formation of inverted terraces which match the substrate topography, so that the resulting surface patterns are free from the surface relief structures within macroscopically large areas. The issues of the film thickness, the substrate surface energy, and the pattern geometry are addressed. Our approach demonstrates an effective synergism of external confinement and internal polymorphism of block copolymers toward complex hierarchically structured patterned surfaces.



INTRODUCTION

Self-assembly of block copolymers is a promising and low-cost route toward fabrication of hierarchically structured functional surfaces and patterns.[1−6] Depending on a number of well-established internal and external parameters,[7−11] block copolymers in thin films are guided to microphase separate into uniform microdomains with tunable dimensions and shapes including spheres,[12,13] cylinders,[14−16] lamellae,[17−19] hybrid structures,[20,21] or interconnected networks.[22,23] Along with ABC terblock polymers[24] and complexed block copolymers,[22,25] asymmetric cylinder-forming diblock copolymers exhibit structural polymorpohism in confined geometries.[11,26,27] The technological use of nanostructured block copolymer patterns depends decisively on our ability to ultimately manipulate their shape, the macroscopically uniform orientation, and long-range lateral order.

In the past years, intensive research convincingly demonstrated the possibility of precise registration of microphase-separated structures by using lithographically fabricated topographical[28] (known as graphoepitaxy)[13] or/and chemical patterns.[29−31] While chemical patterns take an advantage of a strong difference in the surface interactions of block copolymer component with the substrate patterns,[30] topographical graphoepitaxy in a form of regular[32−34] or irregular substrate corrugations[35] imposes an additional confinement to the system and thus affects the microphase separation mechanism.

A diversity of topographic geometries has been used for microdomain registration ranging from randomly roughened substrates,[35] trapezoidal shaped-Si grating substrates,[33] directional V-shaped grooves,[36] sawtoothed,[37] or channel topography[13,32,38] up to lithographically fabricated regular posts[28] or holes.[39] Different criteria of the substrate topography have been introduced, including the ratio of the characteristic lateral periodicity of the pattern λ_s to the microdomain dimension L_0,[34] the ratio of λ_s to the film thickness,[40] and the ratio of λ_s to the root-mean-square vertical displacement of the surface topography R[35] as well as the ratio of the grating height to L_0.[33] Ideal grating substrates (of $q_sR \sim 0.15$, where $q_s = 2\pi/\lambda_s$) gave rise to a lateral ordering of perforations in lamella along the peaks with corrugation amplitude of about $L_0/2$.[34] Sivaniah et al. demonstrated the appearance of perpendicular lamellae on rough substrates and found a critical surface roughness, below which the parallel orientation of lamella is favored.[35] Li et al. systematically studied modulations at the free surface in lamella-forming PS−P2VP diblock and triblock copolymer films supported by Si gratings with the heights which are comparable with the lamella period.[33] They determined topographical conditions for either in-phase (conformal) or out-of-phase (anticonformal) terrace formation. Relatively large aspect ratio grating substrates have been used to laterally align sphere-forming,[13] and cylinder-forming block copolymers,[41] and the mechanism of ordering in these cases was attributed to

Received: December 2, 2011
Revised: February 9, 2012
Published: February 22, 2012

ACS Publications © 2012 American Chemical Society

the coordinated surface-field-directed wetting of the base and of the side walls of the gratings. Grating substrates have been successfully used to generate micrometer-scale periodic structures from PS-*b*-PMMA block copolymer: the standing-up and lying-down cylinders assembled periodically as a result of the film thickness-dependent surface morphology.[32] The authors confirmed the importance of the compliance of the cylinder size to the trough width. However, uncontrolled dewetting and terracing of the film reduced the perfection of these patterns.[32] Another strategy for generating regions from microphase-separated block copolymer structures have been employed by Bosworth et al.,[42] who utilized a three-step approach based on selective solvent and block-selective solvent annealing with an intermediate UV cross-linking step to lock the structure at selectively masked areas.

Following the idea of Fasolka et al. on mediating sequenced patterns by substrate topography,[34] we take advantage of a macroscopic topographic parameter which matches the free surface profile of equilibrated block copolymer films. The phenomenon of spontaneous roughening of the film surface upon the equilibration of in-plane aligned microdomains (often referred to as "terrace formation") has been long studied in regards to the dynamics of microdomain evolution.[18,19,43] The shape of the transition region between the terraces depends greatly on the molecular weight and on the Flory−Huggins interaction parameter χ (i.e., on the chemical composition of the block copolymer as well as on the experimental variables which affect χ). From the practical point of view, the uncontrolled surface roughening of block copolmer films limits their applications in electronics, optics, and sensor technology.

In this work, we report a facile lithography-free method to overcome the problem of surface roughening and at the same time to generate ordered sequences from microphase-separated microdomains. Wrinkled SiCN (silicon carbon nitride) ceramic substrates have been fabricated by a replication process and were homogeneously covered with films of PS-*b*-PB diblock copolymer by floating. The corrugations dimensions of the substrates were in the range of the terrace shapes; i.e., they match the profile of the transition thickness between neighboring terraces of annealed PS-*b*-PB films. We first compare the morphological behavior of PS-*b*-PB films on flat and on corrugated substrates both under strong and under neutral surface fields. Further, the pattern formation as a function of the film thickness is discussed. Next, using grating substrates with a gradient in grating periodicity and amplitude, we demonstrate the importance of the compliance of the substrate corrugations with the characteristic roughness of the "terraced" film in order to eliminate the surface roughening on macroscopically large areas.

EXPERIMENTAL SECTION

Fabrication of Corrugated SiCN Ceramic Substrates. The nanostructured corrugated PDMS masters were prepared following an earlier described procedure.[44,45] Thermally cross-linked PDMS pieces were initially mounted on a custom-made stretching apparatus and subsequently stretched uniaxially to a strain of 5% of their original length. These stretched PDMS pieces were oxidized for 490 s in air plasma (0.2 mbar, 100 W, Plasma Activate Flecto 10 USB). A hard silicon oxide layer forms regularly corrugated patterns on the PDMS surface when the stress is relaxed. Poly(vinylsilazane) (PVSZ, HTT 1800, KiON Corp.) was used as a SiCN ceramic precursor. 1 wt % of photoinitiator (Irgarcure 500, Ciba specialty) and 0.5 wt % of thermal initiator (dicumyl peroxide, Aldrich) were added to the polymer and homogeneously mixed by stirring for 10 min. The corrugated PDMS surface was coated with trichloro(1*H*,1*H*,2*H*,2*H*-perfluorooctyl)silane ($CF_3(CF_2)_5CH_2CH_2SiCl_3$, Aldrich) to avoid adhesion between master and polymer by the evaporation method under vacuum. The PDMS master was placed on a PVSZ thin film spin-coated at 1500 rpm for 45 s. Prior to spin-coating the polymer on a Si wafer substrate (CrysTech Inc.), the polymer was diluted to 30 wt % with propylene glycol monomethyl ether acetate (PGMEA, Sigma-Aldrich) to prevent cracks in the patterned ceramic surface induced by anisotropic shrinkage behavior during pyrolysis. To intrude the polymer effectively into the grooves of the PDMS master, vacuum was applied for 10 min. The solidified PVSZ replica was created by UV curing for 15 min (Panacol UV-F 400 F, 450 W, λ = 325−380 nm) without pressure. After peeling of the PDMS master, the cured PVSZ replica was annealed in a furnace at 800 °C under a nitrogen atmosphere for 2 h at a heating rate of 2 °C min^{-1} to produce a SiCN ceramic material.[46] In order to prepare a neutral corrugated ceramic surface, a 29 ± 1 nm carbon layer was evaporated onto the ceramic substrate using a sputter coater (S150B, Edwards). To obtain the planar SiCN ceramic substrate, a 30 wt % polymer solution diluted with PGMEA was spin-coated onto Si wafer at 1500 rpm for 45 s. UV-cross-linking and pyrolysis were then applied as described above.

Fabrication of SiCN Ceramic Substrate with Gradient of the Corrugations. Cross-linked PDMS was cut in substrates of 0.5 × 3 cm^2. To induce the surface pattern, the substrate is clamped in a custom-made stretching apparatus and stretched to 130% of its original length. A rectangular silicon wafer (0.5 × 0.7 cm^2) with a spacer (glass slide with thickness of 1 mm) which is attached to one end was placed in the middle of the stretched sample. At one end, the wafer is resting directly on the sample, while at the opposite end a distance of 1 mm between the sample and the wafer is fixed. After exposure to the air plasma for 450 s at 0.2 mbar (Plasma Activate Flecto 10 USB, 100 W) the silicon wafer was removed prior to slow relaxation of the sample. For further use, the samples were placed on glass supports. Details of the preparation of the PDMS stamps with gradient of the corrugations and their characterization will be published elsewhere. To produce the SiCN ceramic replica from the gradient of the corrugations, fabrication steps including the UV-cross-linking and the pyrolysis were applied as mentioned above.

Preparation of Block Copolymer Thin Films. A poly(styrene-*b*-butadiene) (M_{nPS} = 13.6 kg/mol and M_{nPB} = 33.7 kg/mol) (PS-*b*-PB, Polymer source Inc.) block copolymer with a total molecular weight of 47.3 kg/mol and polydispersity index of 1.03 was used in this work. 1 wt % toluene solution was prepared with the addition of stabilizer (2,6-di-*tert*-butyl-*p*-cresol) in an amount of 0.03 wt % of the polymer weight to prevent cross-linking of PB during thermal annealing. Thin films on flat silicon wafers, SiCN ceramic films and mica substrates (Plano GmbH) have been prepared by spin-coating with 1000, 2000, and 4000 rpm to produce PS-*b*-PB films with 70, 40, and 24 nm thickness, respectively. Prior to use, Si wafers and SiCN ceramic substrates were cleaned in toluene for 1 day, followed by snow jet and air plasma for 1 min at 0.2 mbar. Mica was freshly cleaved before film deposition.

In order to prepare a homogeneous polymer film on a corrugated substrate, a spin-coated film was floated from mica onto water surface and then picked up by the corrugated ceramic substrate. To equilibrate the microphase-separated structures, films have been thermally annealed under vacuum at 120 °C for 18 h.

Characterization. The nanostructured corrugated ceramic substrates, microdomain morphologies, and absolute film thicknesses of PS-*b*-PB were characterized by scanning force microscopy (SFM) in TappingMode with Bruker Dimension ICON AFM using OTESPA tips with a resonance frequency in the range of 278−357 kHz and a spring constant of 12−103 N/m. The characteristic surface topography in annealed PS-*b*-PB films was investigated using an optical microscope (Axioplan 2 imaging, ZEISS). The PS-*b*-PB film thicknesses on corrugations were measured by cross-sectional transmission electron microscopy (TEM). Samples for cross-sectional TEM measurements were prepared on a dual-beam FIB workstation (FEI Helios Nanolab). Prior to inserting the sample in the FIB, a thin Au layer was sputter-deposited on the surface of the sample to protect the polymer in the subsequent preparation steps. In addition, a thicker

Pt layer was e-beam-deposited in the FIB on the areas from which cross-sectional lamellae were extracted. The FIB lamellae were extracted via in situ lift-out and attached to an Omniprobe grid via Pt deposition.

RESULTS AND DISCUSSION

Asymmetrical block copolymers in thin films are known to show a rich phase behavior with deviations from the bulk structures. Although it is a potentially useful property, the sequences of morphological structures are in most cases observed at the thickness gradients when the microdomains have to adjust to the changing thickness,[26] or phase transitions occur very locally under strong interactions with the substrate.[47] The phase behavior of cylinder-forming polystyrene (PS)-*block*-polybutadiene (PB) diblock copolymer (PS-*b*-PB) on flat strongly and weakly interacting substrates under both thermal[47] and solvent annealing[11] has been intensively studied before. Earlier it was shown that on freshly cleaned silicon oxide substrates (silicon wafers) the formation of the in-plane cylinder phase ($C_{\parallel}$) as well as of the nonbulk perforated lamella (PL) and lamella (L) phases in PS-*b*-PB melts depends on the local film thickness.

Figure 1 displays the macroscopic surface features (a) and microphase-separated domains (b) of PS-*b*-PB on a flat SiCN

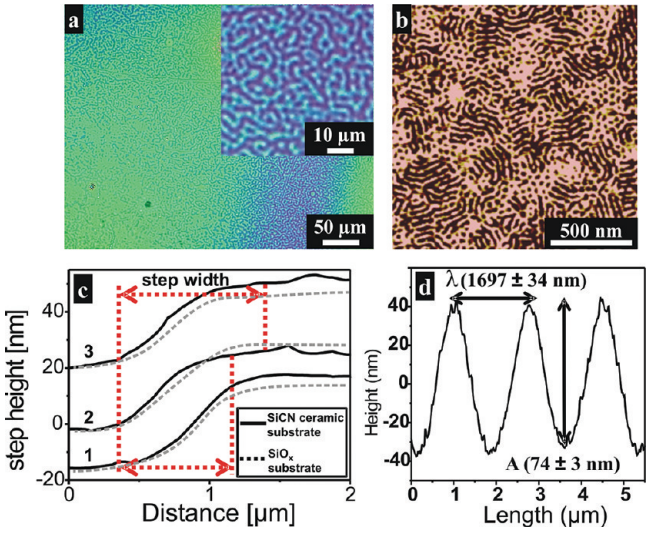


Figure 1. (a) Optical microscopy image of a 24 nm thick PS-*b*-PB film annealed on a flat SiCN ceramic substrate. The two colors correspond to two distinct film thicknesses. (b) SFM phase image of the same film. (c) Cross-section plot of SFM topography data, representing step height and step width between neighboring terraces in thermally annealed PS-*b*-PB films on flat silicon wafers (from ref 47) and on flat SiCN ceramic substrates. The number of a lower terrace (number of layers) is indicated. (d) SFM height profile of the corrugated SiCN ceramic substrate.

ceramic substrate after thermal annealing. The film shows a clear terrace formation behavior which is characteristic for strong surface fields at the substrate. Also, the microphase-separated pattern—a fine coexistence of C, PL, and L patches—confirms the strong pinning of the majority PB block to the SiCN ceramic surface and, consequently, reduced chain mobility in the bottom layer.[47] Both patterns—surface topography and microdomains—suffer from a low degree of order and small grain sizes. A detailed thickness-dependent morphological behavior of PS-*b*-PB on SiCN ceramic and silicon oxide substrates is presented in Figures S1 and S2 (Supporting Information).

Despite an apparent randomness, the surface relief structures in Figure 1a and Figure S1 can be characterized by a certain characteristic periodicity which is the repeated step height (ca. 24−30 nm) and the step width (ca. 0.6−1.2 μm) where the indicated ranges slightly depend on the number of layers and on the substrate chemistry (Figure 1c). In the following, we study the phase behavior of PS-*b*-PB films on corrugated SiCN substrates (Figures 1d and 2) with the surface undulations

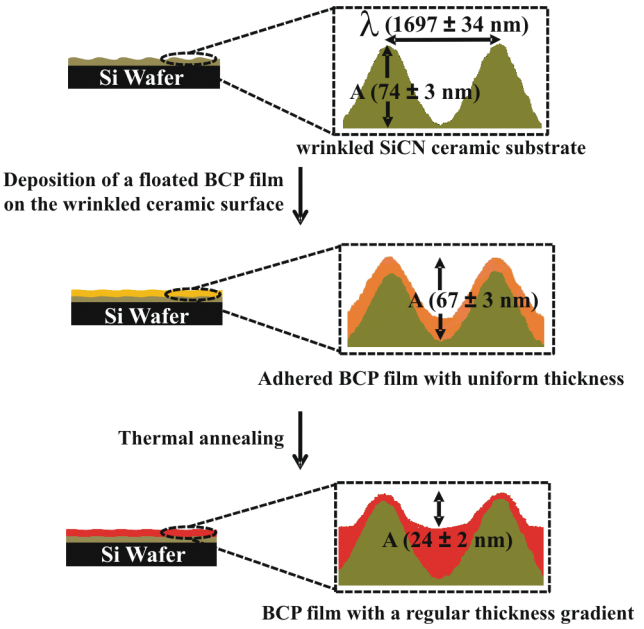


Figure 2. Schematic illustration of the substrate topography, the deposition of a homogeneous block copolymer film, and the development of thickness gradient in the film upon thermal annealing. Note that the height profiles on the right are measured cross sections from SFM height images.

which match the characteristic dimensions of the terraces (corrugation amplitude $A \sim$ tens of nm and corrugation wavelength λ (period) $\sim$ order of μm).

These SiCN substrates are obtained by a facile replication process using nonlithographic PDMS masters with regular periodic patterns on a several mm^2 scale and are resistible to high temperature and most of the solvents which enables block copolymer processing via thermal- or solvent-annealing. The dimensions of the corrugated ceramic structures depend on the dimensions of the PDMS master as wells as on unavoidable shrinkage of the precursor material during the pyrolysis step. A detailed characterization of corrugated SiCN ceramic substrates replicated using PDMS masters has been reported earlier.[46]

Phase Behavior on Strongly Interacting Corrugated Substrates. Figure 2 illustrates the sample preparation on corrugated substrates. The procedure includes a transfer of the spin-coated films via floating from mica to a water surface and then deposition onto the wrinkled ceramics followed by thermal annealing under vacuum. The floated block copolymer film completely adheres to the corrugated substrates so that the corrugations amplitude and wavelength exhibit no considerable changes. (Note that the height profiles in Figure 2 are real cross sections from SFM height images.) In contrast, thermal annealing significantly reduces the corrugations amplitude due

dx.doi.org/10.1021/ma202616w | *Macromolecules* 2012, 45, 2494−2501

to the flow of the polymer melt into the grooves (Figure 2). Such redistribution of polymer material is in agreement with earlier studies of block copolymers on corrugated patterned surfaces.[48−50]

The microphase-separated behavior of the samples prepared in the above way has been studied with SFM. Figure 3a,b displays the topography and phase images of a 24 nm thick PS-*b*-PB film (an initial spin-coating thickness on mica substrate) before the thermal annealing on the corrugated substrate. The initial corrugation amplitude (74 ± 3 nm) is slightly reduced after the adhesion of the film (67 ± 3 nm) (inset in Figure 3a) presumably due to a slight elastic deformation of the PS-*b*-PB material. The phase image in Figure 3b shows a disordered microphase separated structure which is a typical pattern after spin-coating. This confirms that the floating and adhesion steps do not affect the microphase separation.

Figure 3c−e presents the phase behavior after the annealing on the corrugated substrate. The corrugations in the height image (Figure 3c) have sharper edges as compared to the nonannealed film (Figure 3a) due to the flattening of the film in the valleys (as seen from the cross section of the corrugation profile in inset in Figure 3c). The amplitude of the profile is reduced to 24 ± 2 nm. As seen in Figure 3d, the initially disordered pattern developed after annealing into a sequence of distinct morphologies which follow the topography of the substrate. A featureless white pattern which is attributed to the PS sheet of the in-plane L phase (Figure 3e) is generated in the valleys of the corrugations, while the white (PS) lying cylinders ($C_{\parallel}$) are confined to the hills. This former cylinder phase is clearly distinguishable by the width of the white stripes from the stripped pattern at the curved side walls, i.e., at transition film thickness. The two striped structures (which have the same spacing between the next neighboring white stripes within the measurement resolution) are separated by a narrow region of the PL structures. We tentatively attribute the narrow white stripes to standing lamellae ($L_{\perp}$) or distorted cylinders ($DC_{\parallel}$) phases. The sketch in Figure 3e tentatively relates the observed morphologies to the thickness modulation in the annealed film. Remarkably, as a result of the sequencing, the topographic pattern appears on the phase image with a 2-fold multiplication (Figure. 3c,d), which implies the potential of our approach toward creating a chemically and topographically patterned surfaces.

Figure 3f shows an optical microscopy image of the annealed film where topographic features of the underlying substrate are visible. A striking result is the absence of the macroscopic patterning of the block copolymer film surface, i.e., the suppression of the terrace formation. This issue will be discussed in detail later.

Shown in Figure 4 is the morphological behavior of PS-*b*-PB films with a thickness of 40 nm (a, b) and 70 nm (c, d) which have been annealed on the corrugated substrates with similar characteristics as those in Figures 1d and 3. Both thicknesses are incompatible with the characteristic microdomain dimension. In both films basically the same sequence of structures (Figure 4b,d) as in the 24 nm thick film (Figure 3) is observed. The tiny differences in the morphological behavior, such as the precise position of the phase boundaries (the width of the stripes of each phase) and the phase identification ($L_{\perp}$ versus $DC_{\parallel}$), are currently under detailed investigation and go beyond the scope of the present work.

Insets in Figure 4a,c display the cross sections of the films after annealing. The corrugations amplitude is reduced from

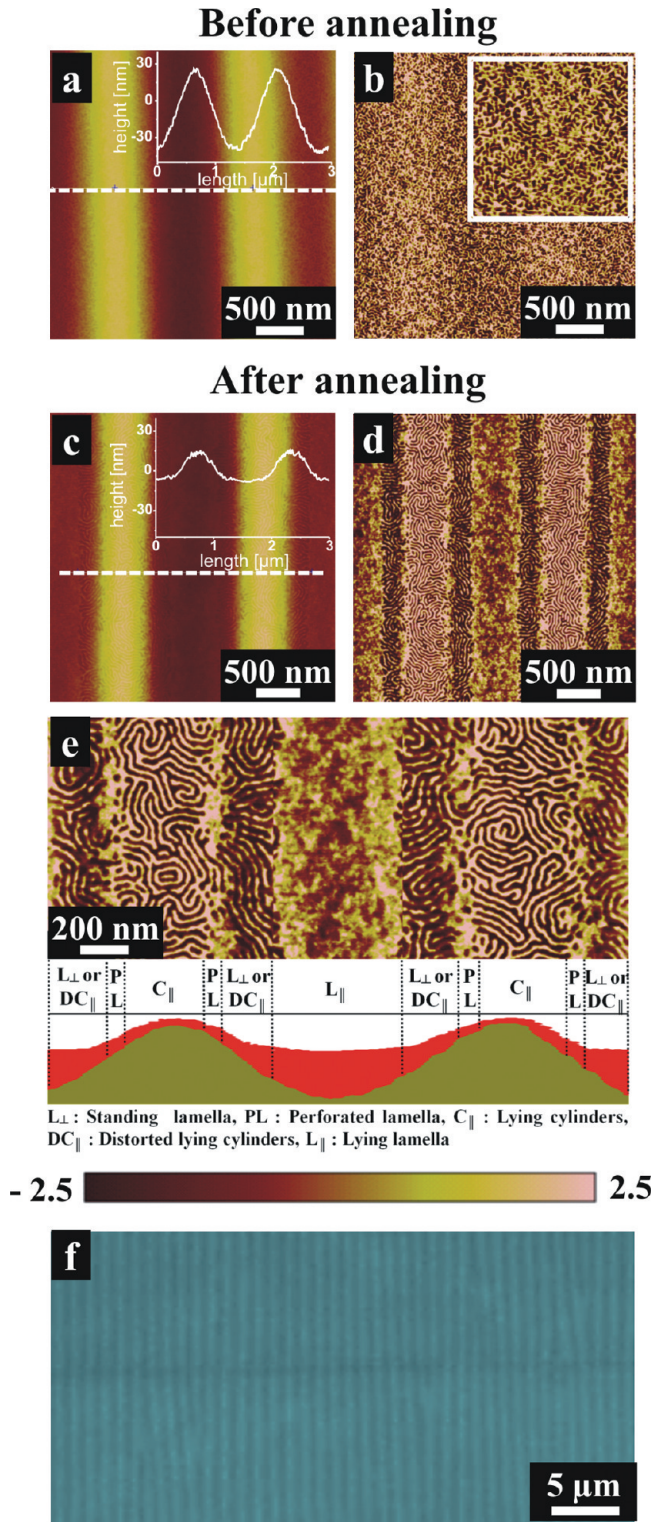


Figure 3. SFM height (a, c) and phase (b, d, e) images of a 24 nm thick PS-*b*-PB film (initial thickness after spin-coating on mica substrate): after deposition via floating onto a corrugated SiCN ceramic substrate (a, b) and after thermal annealing at 120 °C for 18 h (c−e) with the corresponding sketch showing a presumable assignment of the patterns to a particular morphology and film thickness. (f) Optical microscopy image of the film. Insets in (a) and (b) show cross-sectional height profiles along the indicated white dashed lines.

dx.doi.org/10.1021/ma202616w | *Macromolecules* 2012, 45, 2494−2501

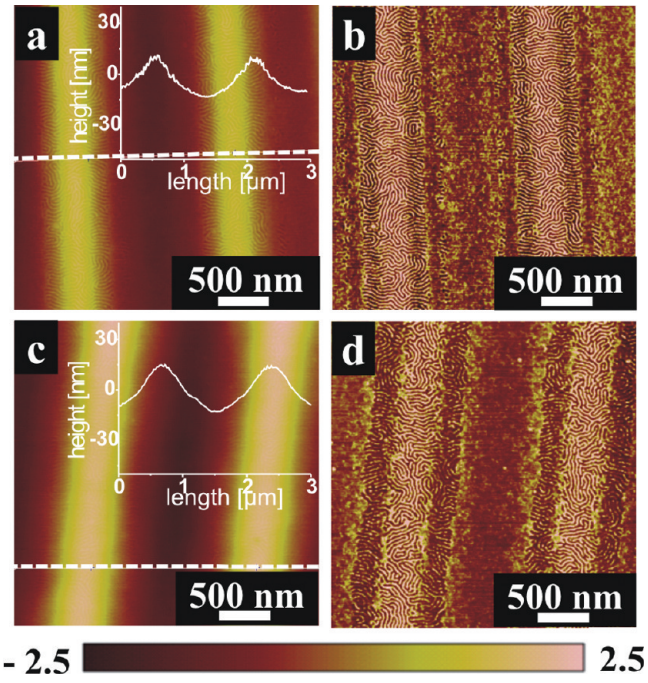


Figure 4. SFM topography (a, c) and phase (b, d) images of a 40 nm thick (a, b) and of a 70 nm thick (c, d) PS-*b*-PB film annealed on corrugated ceramic substrates at 120 °C for 18 h. Both thicknesses indicate the initial thickness of the films spin-coated on mica. Insets in (a) and (c) show cross-sectional height profiles along the indicated white dashed lines.

values of 64 ± 6 nm and 85 ± 6 nm after the films deposition to 24 ± 2 nm (Figure 4a) and to 28 ± 3 nm (Figure 4b), respectively. Importantly, the formation of terraces on corrugated substrates is also suppressed for these film thicknesses. We note that for all studied films the residual amplitude is in the range of 24−30 nm, which is very close to the intrinsic terrace step height in PS-*b*-PB films when they are thermally treated on flat substrates (Figure 1c).

Figure 5 shows a cross-sectional transmission electron microcopy (TEM) image of a thermally annealed PS-*b*-PB film with a nominal thickness of 70 nm (as in Figure 4c,d). It is clearly seen that the thickness of the film varies exactly between a minimum of 46 nm on the hills and a maximum of 86 nm in the valleys of the corrugations. However, the precise determination and assignment of the number of layers in the valleys and on the hills is only possible when the internal structure through the film is identified, since the interlayer period increases with the structure transformation from the cylinder phase to the PL phase and to the L phase.[47]

Phase Behavior on Weakly Interacting Corrugated Substrates. Neutrality of the block copolymer components to the substrate surface has been introduced by a thin carbon layer which was evaporated on the corrugated as well as on flat SiCN substrates. On weakly interacting carbon substrates, PS-*b*-PB exhibits asymmetric wetting conditions with the PB block at the free surface and no enthalpic preference for the components at the substrate. On flat carbon-coated substrates the morphological behavior is generally similar to that in bulk.[47] In order to satisfy the substrate neutrality, a bottom layer of half cylinders is stabilized on flat substrates, and all the following cylinder layers are aligned parallel to the film plane. The only phase transition from the bulk $C_{\parallel}$ morphology to the PL phase was observed around 1.5 layers thickness in the areas with the minor thickness variation.[47]

Figure 6 displays the microphase separation behavior of a 40 nm thick film which has been prepared on a carbon-coated corrugated SiCN substrate in accordance with the procedure shown in Figure 2. The initial corrugation amplitude of the SiCN substrate is insignificantly reduced after the coating with carbon layer and with the polymer film (inset in Figure 6a). The phase image in Figure 6b shows a disordered microphase-separated pattern before thermal annealing which is the same as after floating onto the bare SiCN surface.

The phase behavior of the annealed samples on corrugated carbon-coated substrates is presented in Figure 6c−f. The in-plane $C_{\parallel}$ phase is observed in thinned parts of the film on the hills. In addition, the nonbulk L phase appears in the valleys (Figure 6e,f). In this case, the pattern multiplication is not achieved in the phase image (Figure 6e,d). The phase behavior in a thinner film (with 24 nm thickness) on carbon-coated corrugations exhibits the same sequence of morphologies which consists of alternating $C_{\parallel}$ phase (with single PL patches) and lying lamellae L phase (Figure S3, Supporting Information). However, the development of the L phase on corrugations is a newly observed feature as compared to the behavior on flat carbon-coated substrates. Although the in-plane L phase with the PB sheet at the free surface satisfies the wetting condition, the nonbulk morphology is an excited state which presumably is a consequence of the confinement induced by the corrugations.

Figure 6g presents an optical microscopy image of the annealed film. Similar to the strongly interacting SiCN ceramic corrugated substrates, the terrace formation is suppressed by the carbon-coated corrugations. Following this low-cost procedure, macroscopically structured surfaces with chemically patterned topographical channels could be produced.

Guided Terrace Formation in Thin Films on Substrates with Gradient of the Corrugations. An important

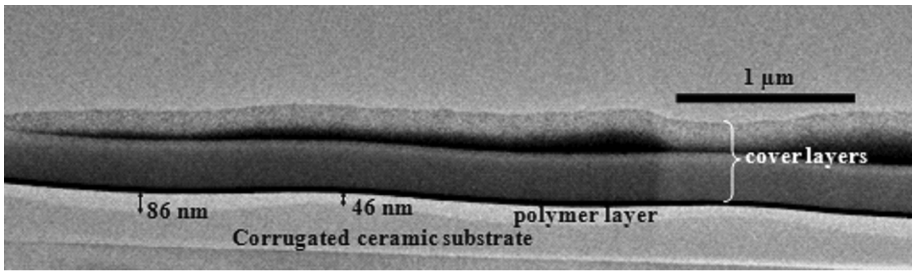


Figure 5. Cross-sectional TEM image of PS-*b*-PB film with 70 nm (initial spin-coating thickness on mica substrate) on corrugated SiCN ceramic substrate after thermal annealing at 120 °C for 18 h.

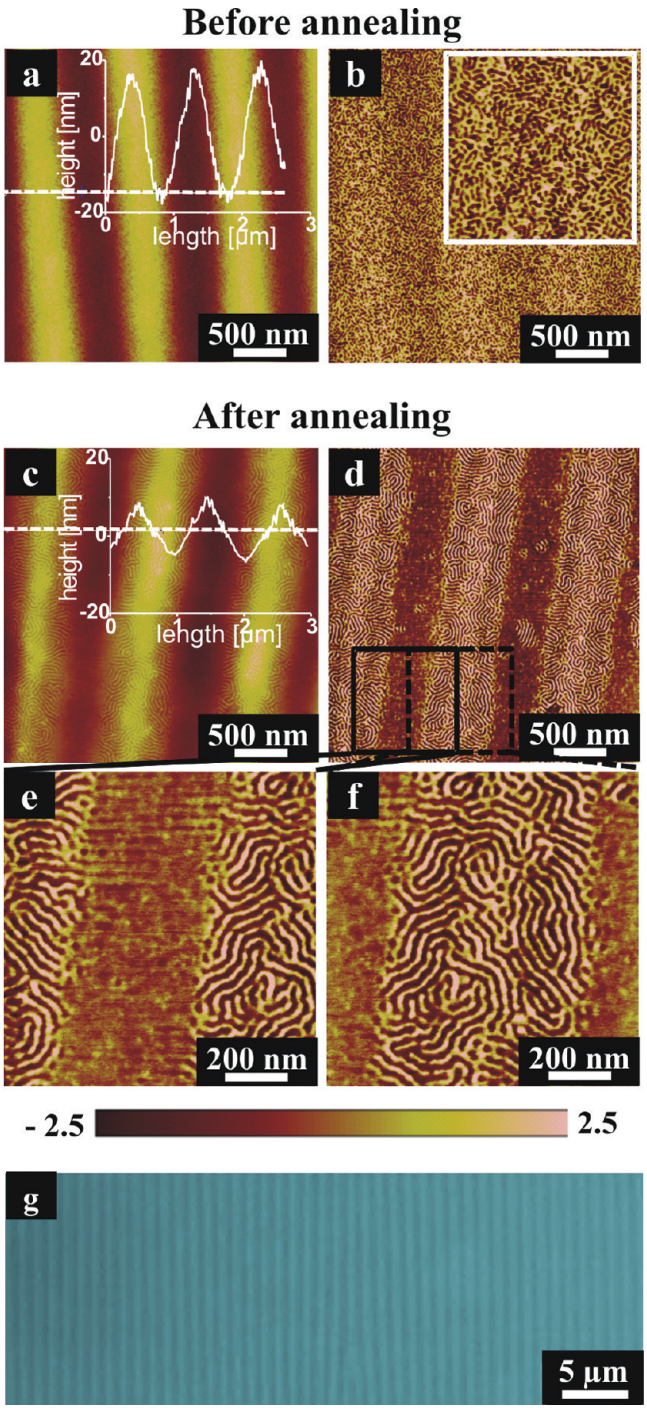


Figure 6. SFM topography (a, c) and phase (b, d, e, f) images of a 40 nm thick PS-*b*-PB film (initial spin-coating thickness on mica substrate): after floating onto a carbon-coated corrugated SiCN ceramic substrate (a, b); after thermal annealing at 120 °C for 18 h (c–f) and the optical microscopy image of the film (g). Insets in (a) and (c) show cross-sectional height profiles along the indicated white lines.

insight regarding the role of the corrugation geometry in suppressing the terrace formation was derived from the analysis of PS-*b*-PB films which have been annealed on ceramic substrates with gradient of the corrugations. Figure 7 presents optical microscopy and SFM images of a thermally annealed 24 nm thick PS-*b*-PB film on a wrinkled substrate with the corrugation amplitude A changing in the range from 55 to 16 nm and the corrugation wavelength λ changing in the range from ca. 1000 to ca. 700 nm (Figure 7a). We note that as the wrinkles are produced by relaxation of a stretched and surface-oxidized PDMS stamp where both the wrinkles' amplitude and the wrinkles' wavelength depend linearly on various parameters of the PDMS stamps (e.g., elastic moduli, silicon oxide film thickness), they cannot be varied independently from each other.[51] As seen in Figure 7b–g, both the ordering of the microphase-separated structures and terracing of the film surface are related to corrugations dimensions. As compared to well-structured and terrace-free PS-*b*-PB films on the corrugations with $A \approx 55$ nm and with $\lambda \approx 1010$ nm which have been extensively described above (Figures 3, 4, 6, and 7b,e), the directing effect of the corrugations diminishes with decreasing A and λ. As soon as the surface relief structures (terraces) are allowed to be formed (Figure 7c), the sequencing of the microphase-separated patterns is significantly less pronounced. As seen in Figure 7f, the $C_{||}$ phase and the PL phase alternate with interruptions, while the L phase has vanished completely. On smaller corrugations, terraces are built over the entire area (Figure 7d), and the microphase-separated structures are almost unaffected by the substrate topography (Figure 7g). We note that on the latter corrugations the PS-*b*-PB films still show a thickness-dependent morphological behavior since the microstructures in the neighboring terraces are different (highlighted by white border lines in Figure 7g). Since all gradient of the corrugations belong to one and the same substrate, we can exclude that the observed effects are affected by possible experimental perturbations related to the variations in the starting film thickness or the floating and annealing processes which may slightly differ from one to another experiment.

Since the variation in wavelength is inevitably accompanied by the variation in the amplitude, we used the roughness parameter $qA/2$, where $q = 2\pi/\lambda$ and A refers to the amplitude, to summarize the results. The corrugations in Figure 7b,c,d are characterized by roughness parameters of 0.16, 0.09, and 0.07, respectively. We believe that the near equality of the surface roughness parameter (0.16) of the perfectly guiding corrugations (Figure 7d,e) with that of the ideally grating substrates (0.15)[35] is accidental or a coincidence, since in earlier studies the roughness dimension were varied around the nanometer range. We rather use this value to compare it with the geometry of the intrinsic surface relief structures of PS-*b*-PB films on flat substrates,[47] i.e., with the step height H (ca. 25 nm) and the step width D (ca. 1 μm). The best fit to the perfectly guiding corrugations is obtained with $2\pi H/D$ (0.15). This result, on one side, gives a quantitative measure for the targeted fabrication of corrugations which eliminate the surface relief structures and, on the other side, suggests that the formation of sequenced patterns is a consequence of the "inverted terrace formation" under confinement by substrate corrugations.

■ CONCLUSIONS

We have demonstrated a facile and simple route to achieve sequenced patterns from microphase-separated structures in block copolymer films. For the guided block copolymer assembly we used structured corrugated SiCN ceramic substrates which were fabricated by a facile replication process using nonlithographic PDMS masters. Homogeneous block copolymer films have been floated onto to the corrugated substrate without significant changes to the corrugations topography. After thermal annealing, the polymer material is

dx.doi.org/10.1021/ma202616w | *Macromolecules* 2012, 45, 2494–2501

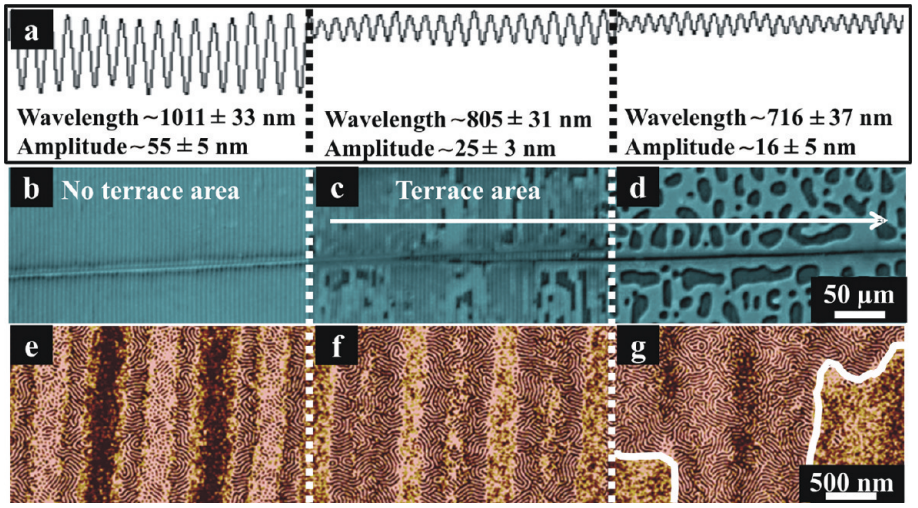


Figure 7. (a) Cross-sectional height profiles of the areas with gradient of the corrugations. (b, c) Optical microscopy and (c–g) SFM phase images of a 24 nm thick PS-*b*-PB film which has been floated onto the SiCN ceramic substrate with gradient of the corrugations and thermally annealed at 120 °C for 18 h.

redistributed between the hills and grooves of the corrugations. As a consequence of the thickness-dependent morphological behavior, the block copolymer is guided into sequenced patterns of alternative cylinder, perforated lamella, and lamella phases which follow the topography of the substrate. On strongly interacting corrugations, the phase pattern appears as a 2-fold multiplication of the initial topographic pattern. The position of the morphological boundaries as well as the stability of nonbulk morphologies is shown to be dependent on the film thickness, dimensions of the substrate corrugations, and the surface fields at the substrate. An important result is the suppression of the macroscopic roughening of the film surface (of terrace formation) so that the resulting microphase-separated patterns are free from the surface relief structures within macroscopically large areas. This phenomenon is attributed to the formation of inverted terraces when the substrate topography matches the dimensions of freely formed (on flat substrates) steps between neighboring terraces. Our approach demonstrates an effective synergism of external confinement and internal polymorphism of block copolymers toward complex hierarchically structured patterned surfaces.

■ ASSOCIATED CONTENT

Ⓢ Supporting Information

Optical images of surface topography and SFM phase images of PS-*b*-PB films thermally annealed on planar surfaces and carbon-coated corrugated SiCN ceramic substrate. This material is available free of charge via the Internet at http://pubs.acs.org.

■ AUTHOR INFORMATION

Corresponding Author

*E-mail: tsarkova@dwi.rwth-aachen.de (L.T.); boeker@dwi.rwth-aachen.de (A.B.).

Notes

The authors declare no competing financial interest.

■ ACKNOWLEDGMENTS

The authors thank Clemens Liedel for support during the AFM measurements. S.P. acknowledges RWTH Aachen for a PhD fellowship.

■ REFERENCES

(1) Park, C.; Yoon, J.; Thomas, E. L. *Polymer* **2003**, *44*, 6725–6760.
(2) Li, M.; Coenjarts, C. A.; Ober, C. K. *Adv. Polym. Sci.* **2005**, *190*, 183–226.
(3) Marencic, A. P.; Register, R. A. *Annu. Rev. Chem. Biomol. Eng.* **2010**, *1*, 277–297.
(4) Darling, S. B. *Prog. Polym. Sci.* **2007**, *32*, 1152–1204.
(5) Hamley, I. W. *Prog. Polym. Sci.* **2009**, *34*, 1161–1210.
(6) Park, S.; Russell, T. P. *Nano* **2010**, *5*, 1–11.
(7) Fredrickson, G. H.; Bates, F. S. *Annu. Rev. Mater. Sci.* **1996**, *26*, 501–550.
(8) Hamley, I. W. *The Physics of Block Copolymers*; Oxford University Press: New York, 1998.
(9) Matsen, M. W. *Curr. Opin. Colloid Interface Sci.* **1998**, *3*, 40–47.
(10) Fasolka, M. J.; Mayes, A. M. *Annu. Rev. Mater. Res.* **2001**, *31*, 323–355.
(11) Tsarkova, L.; Sevink, G. J. A.; Krausch, G. *Adv. Polym. Sci.* **2010**, *227*, 33–73.
(12) Segalman, R. A.; Hexemer, A.; Kramer, E. J. *Macromolecules* **2003**, *36*, 6831–6839.
(13) Segalman, R. A.; Yokoyama, H.; Kramer, E. J. *Adv. Mater.* **2001**, *13*, 1152–1155.
(14) Radzilowski, L. H.; Carvalho, B. L.; Thomas, E. L. *J. Polym. Sci., Part B: Polym. Phys.* **1996**, *34*, 3081–3093.
(15) Kim, H.-C.; Russell, T. P. *J. Polym. Sci., Part B: Polym. Phys.* **2001**, *39*, 663–668.
(16) Knoll, A.; Magerle, R.; Krausch, G. *J. Chem. Phys.* **2004**, *120*, 1105–1116.
(17) Collin, B.; Chatenay, D.; Coulon, G.; Ausserre, D.; Gallot, Y. *Macromolecules* **1992**, *25*, 1621–1622.
(18) Coulon, G.; Russell, T. P.; Deline, V. R.; Green, P. F. *Macromolecules* **1989**, *22*, 2581–2589.
(19) Maaloum, M.; Ausserre, D.; Chatenay, D.; Coulon, G.; Gallot, Y. *Phys. Rev. Lett.* **1992**, *68*, 1575–1578.
(20) Harrison, C.; Park, M.; Chaikin, P.; Register, R. A.; Adamson, D. H.; Yao, N. *Macromolecules* **1998**, *31*, 2185–2189.
(21) Elbs, H.; Drummer, C.; Abetz, V.; Krausch, G. *Macromolecules* **2002**, *35*, 5570–5577.
(22) Meuler, A. J.; Hillmyer, M. A.; Bates, F. S. *Macromolecules* **2009**, *42*, 7221–7250.
(23) Sperschneider, A.; Schacher, F. H.; Tsarkova, L.; Böker, A.; Müller, A. H. E. *Macromolecules* **2010**, *43*, 10213–10215.
(24) Krausch, G.; Magerle, R. *Adv. Mater.* **2002**, *14*, 1579–1583.
(25) van Zoelen, W.; ten Brinke, G. *Soft Matter* **2009**, *5*, 1568–1582.

(26) Knoll, A.; Horvat, A.; Lyakhova, K. S.; Krausch, G.; Sevink, G. J. A.; Zvelindovsky, A. V.; Magerle, R. *Phys. Rev. Lett.* **2002**, *89*, 035501/1−035501/4.
(27) Dobriyal, P.; Xiang, H.; Kazuyuki, M.; Chen, J.-T.; Jinnai, H.; Russell, T. P. *Macromolecules* **2009**, *42*, 9082−9088.
(28) Bita, I.; Yang, J. K. W.; Jung, Y. S.; Ross, C. A.; Thomas, E. L.; Berggren, K. K. *Science* **2008**, *321*, 939−943.
(29) Ruiz, R.; Kang, H.; Detcheverry, F. A.; Dobisz, E.; Kercher, D. S.; Albrecht, T. R.; de Pablo, J. J.; Nealey, P. F. *Science* **2008**, *321*, 936−939.
(30) Park, S.-M.; Stoykovich, M. P.; Ruiz, R.; Zhang, Y.; Black, C. T.; Nealey, P. F. *Adv. Mater.* **2007**, *19*, 607−611.
(31) Kim, S. O.; Solak, H. H.; Stoykovich, M. P.; Ferrier, N. J.; de Pablo, J. J.; Nealey, P. F. *Nature* **2003**, *424*, 411−414.
(32) Sundrani, D.; Sibener, S. J. *Macromolecules* **2002**, *35*, 8531−8539.
(33) Li, Z.; Qu, S.; Rafailovich, M. H.; Sokolov, J.; Tolan, M.; Turner, M. S.; Wang, J.; Schwarz, S. A.; Lorenz, H.; Kotthaus, J. P. *Macromolecules* **1997**, *30*, 8410−8419.
(34) Fasolka, M. J.; Harris, D. J.; Mayes, A. M.; Yoon, M.; Mochrie, S. G. J. *Phys. Rev. Lett.* **1997**, *79*, 3018−3021.
(35) Sivaniah, E.; Hayashi, Y.; Matsubara, S.; Kiyono, S.; Hashimoto, T.; Fukunaga, K.; Kramer, E. J.; Mates, T. *Macromolecules* **2005**, *38*, 1837−1849.
(36) Chuang, V. P.; Cheng, J. Y.; Savas, T. A.; Ross, C. A. *Nano Lett.* **2006**, *6*, 2332−2337.
(37) Park, S.; Lee, D. H.; Xu, J.; Kim, B.; Hong, S. W.; Jeong, U.; Xu, T.; Russell, T. P. *Science* **2009**, *323*, 1030−1033.
(38) Jung, Y. S.; Ross, C. A. *Adv. Mater.* **2009**, *21*, 2540−2545.
(39) Xiao, S.; Yang, X.; Park, S.; Weller, D.; Russell, T. P. *Adv. Mater.* **2009**, *21*, 2516−2519.
(40) Park, S.-M.; Berry, B. C.; Dobisz, E.; Kim, H.-C. *Soft Matter* **2009**, *5*, 957−961.
(41) Sundrani, D.; Darling, S. B.; Sibener, S. J. *Nano Lett.* **2004**, *4*, 273−276.
(42) Bosworth, J. K.; Black, C. T.; Obert, C. K. *ACS Nano* **2009**, *3*, 1761−1766.
(43) Horvat, A.; Knoll, A.; Krausch, G.; Tsarkova, L.; Lyakhova, K. S.; Sevink, G. J. A.; Zvelindovsky, A. V.; Magerle, R. *Macromolecules* **2007**, *40*, 6930−6939.
(44) Bowden, N.; Huck, W. T. S.; Paul, K. E.; Whitesides, G. M. *Appl. Phys. Lett.* **1999**, *75*, 2557−2559.
(45) Stafford, C. M.; Harrison, C.; Beers, K. L.; Karim, A.; Amis, E. J.; Vanlandingham, M. R.; Kim, H. −C.; Volksen, W.; Miller, R. D.; Simonyi, E. E. *Nature Mater.* **2004**, *3*, 545−550.
(46) Park, S.; Böker, A. *J. Mater. Chem.* **2011**, *21*, 11734−11736.
(47) Tsarkova, L.; Knoll, A.; Krausch, G.; Magerle, R. *Macromlecules* **2006**, *39*, 3608−3615.
(48) Jeong, S.-J.; Moon, H.-S.; Shin, J.; Kim, B. H.; Shin, D. O.; Kim, J. Y.; Lee, Y.-H.; Kim, J. U.; Kim, S. O. *Nano Lett.* **2010**, *10*, 3500−3505.
(49) Sundrani, D.; Darling, S. B.; Sibener, S. J. *Langmuir* **2004**, *20*, 5091−5099.
(50) Jung, Y. S.; Ross, C. A. *Nano Lett.* **2007**, *7*, 2046−2050.
(51) Cerda, E.; Mahadevan, L. *Phys. Rev. Lett.* **2003**, *90*, 074302/1−074302/4.

■ NOTE ADDED AFTER ASAP PUBLICATION

This article posted ASAP on February 22, 2012. Figure 5 has been revised. The correct version posted on February 23, 2012.

Macromolecules

Article

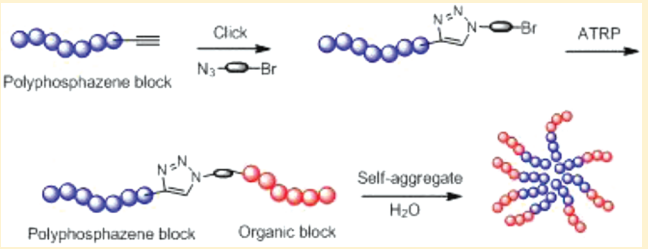
pubs.acs.org/Macromolecules

Synthesis and Micellar Behavior of Novel Amphiphilic Poly[bis(trifluoroethoxy)phosphazene]-*co*-poly[(dimethylamino)ethyl methacrylate] Block Copolymers

Zhicheng Tian, Xiao Liu, Chen Chen, and Harry R. Allcock*

Department of Chemistry, Pennsylvania State University, University Park, Pennsylvania 16802, United States

ABSTRACT: A number of amphiphilic diblock copolymers based on poly[bis(trifluoroethoxy)phosphazene] (TFE) as the hydrophobic block and poly[(dimethylamino)ethyl methacrylate] (PDMAEMA) as the hydrophilic block were developed. The TFE block was synthesized first by the controlled living cationic polymerization of a phosphoranimine, followed by replacement of all the chlorine atoms using sodium trifluoroethoxide. To allow for the growth of the PDMAEMA block, 3-azidopropyl-2-bromo-2-methylpropanoate, an atom transfer radical polymerization (ATRP) initiator, was grafted onto the end-cap of the TFE block via the "click" reaction followed by the ATRP of 2-(dimethylamino)ethyl methacrylate (DMAEMA). Once synthesized, micelles were formed by a standard method, and their characteristics were examined using fluorescence techniques, dynamic light scattering, and transmission electron microscopy. The critical micelle concentrations of the diblock copolymers as determined by fluorescence techniques using pyrene as a hydrophobic probe were between 3.47 and 9.55 mg/L, with the partition equilibrium constant of pyrene in these micelles ranging from 0.12×10^5 to 1.52×10^5. The diameters measured by dynamic light scattering were 100−142 nm at 25 °C with a narrow distribution, which were also confirmed by transmission electron microscopy.



INTRODUCTION

Amphiphilic diblock copolymers consisting of a hydrophobic and a hydrophilic segment have received considerable attention over the past few decades not only because of their unique self-aggregation properties in selective solvents to form micelles but also because of their potential applications in separation technologies, nanolithography, and drug/gene delivery.[1−6] In an aqueous environment the hydrophilic blocks will interact with the water and form the outer shell, allowing for the hydrophobic blocks to aggregate in the core to lower their interaction with the environment. By contrast, reverse micelles may be generated in an organic environment where the hydrophobic blocks form the shell and hydrophilic blocks form the core.[7] The cores of those micelles can then serve as microcontainers for various substances including drugs, dyes, and nanoparticles, while the outer shells determine the solubility and the interactions with the external environment.[8,9] Once formed, these micelles are thermodynamically stable with sizes that range from tens to a few hundreds of nanometers in diameter.[10] Therefore, it is important to develop new amphiphilic diblock copolymer structures with novel chemical and physical characteristics that can be easily tailored for specific applications.[11]

Polyphosphazenes are hybrid polymers consisting of an inorganic backbone of alternating phosphorus and nitrogen atoms with two side groups (usually organic) attached to each phosphorus.[12] These structures are synthesized via macromolecular substitutions, specifically by the replacement of chlorine atoms in poly(dichlorophosphazene) by various nucleophiles such as alkoxides,[13] aryloxides,[14] and primary or secondary amines.[15] The common synthetic route to poly(dichlorophosphazene) is through the thermal ring-opening polymerization of hexachlorocyclotriphosphazene at 250 °C in a sealed vacuum tube.[16] This route permits the facile synthesis of the poly(dichlorophosphazene), but it provides little control over molecular weight, polydispersity, and chain architecture.[17] These issues have been overcome by the recent development of an ambient-temperature living cationic via the PCl_5-induced polymerization of a phosphoranimine as reported by Allcock and Manners et al.[18] This polymerization allows for the production of a variety of polymeric phosphazene architectures with lower but controllable molecular weights and narrower polydispersities. This process has been used to synthesize a number of polyphosphazene-containing block copolymers.

Amphiphillic diblock copolyphosphazenes bearing two different side groups on two different polyphosphazene blocks, one hydrophobic and one hydrophilic, were first synthesized and their micelle properties tested in 1997 and 2001.[19,20] However, these initial diblock copolyphosphazenes had relative high critical micellar concentrations compared with other polymeric micelles.[8,9,11] To overcome these issues, unique hybrid block copolymers with a combination of polyphosphazene and organic polymer blocks were synthesized, and their ability to self-assemble into micelles in an aqueous environment was thoroughly studied. In previous work in our program, various organic blocks such as polystyrene,[21]

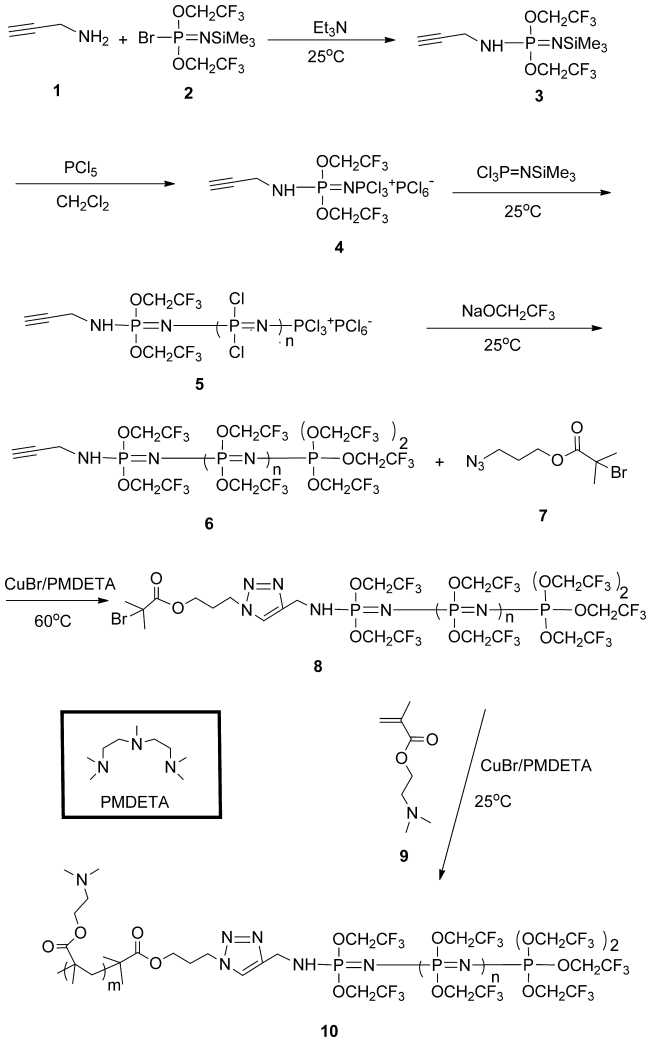
Received: January 18, 2012
Revised: February 15, 2012
Published: February 28, 2012

 © 2012 American Chemical Society dx.doi.org/10.1021/ma300139z | *Macromolecules* 2012, 45, 2502−2508

PPG,[22] and PEO[23] were linked to the polyphosphazene. These phosphazene−organic block copolymers showed advantageous micellar properties. However, they were synthesized following a "block-to" strategy, which involved the coupling two individual polymers via reaction sites at the polymer ends. Although this method was successful, it incurred disadvantages including low coupling efficiency, and the segment left unreacted after the coupling was hard to remove.[24]

In order to overcome the shortcomings of the "block-to" method, a new "block-from" approach has been widely utilized to synthesize diblock copolymers, especially after the development of atom transfer radical polymerization (ATRP).[25−28] In this approach, one block is synthesized first and the end-cap is modified to introduce a halogen-containing end group capable of acting as a macroinitiator to polymerize various monomers, including styrenes, acrylates, acrylamides, and acrylonitriles in the presence of Cu(I).[29] The resultant diblock copolymers usually have well-defined molecular weights and good chain uniformity.[25] In this present work, we report a new synthetic route to make polyphosphazene−organic amphiphilic diblock copolymers using the "block-from" method by combining the living cationic polymerization with ATRP (Scheme 1). The

Scheme 1. Synthetic Route of Diblock Copolymers



hydrophobic segment poly[bis(trifluoroethoxy)phosphazene] (TFE), which is produced via the living cationic polymerization, has been end-functionalized with an ATRP initiating site via an azide−alkyne "click" reaction. The subsequent macroinitiator was used to polymerize 2-(dimethylamino)ethyl methacrylate via ATRP to form the hydrophilic block. Once synthesized, the micellar behavior in an aqueous environment was investigated by fluorescence techniques, dynamic light scattering, and transmission electron microscopy.

EXPERIMENTAL SECTION

Materials. Lithium bis(trimethylsilyl)amide (Aldrich), propargylamine hydrochloride (TCI America), *N,N,N′,N″,N‴*-pentamethyldiethylenetriamine (PMDETA) (TCI America), CuBr (Aldrich), NaN_3 (Aldrich), 3-bromopropanol (Aldrich), and NaH (Aldrich) were used without further purification. Phosphorus pentachloride (Aldrich) was purified by sublimation under vacuum before use. 2,2,2-Trifluoroethanol was dried over calcium hydride and was distilled before use. Sulfuryl chloride (Aldrich) and phosphorus trichloride (Aldrich) were purified by distillation. Bromophosphoranime ($Br(CF_3CH_2O)_2P{=}NSiMe_3$) was synthesized and purified by literature procedures.[18,20] (Dimethylamino)ethyl methacrylate (DMAEMA) (Aldrich) was purified via an Al_2O_3 column to remove inhibitor. All the glassware was dried overnight at 120 °C before use. The synthesis reactions were carried out under an atmosphere of dry argon or nitrogen.

Equipment. ^1H and ^{31}P NMR spectra were recorded on a Bruker WM-360 NMR spectrometer operated at 360 and 145 MHz, respectively. ^1H NMR spectra were referenced to solvent signals while ^{31}P NMR chemical shifts were relative to 85% phosphoric acid as an external reference, with positive shift values downfield from the reference. Molecular weights were estimated using a Hewlett-Packard HP 1090 gel permeation chromatograph (GPC) equipped with an HP-1047A refractive index detector and American Polymer Standards AM gel 10 mm and AM gel 10 mm 104 Å columns and calibrated versus polystyrene standards (Polysciences). The samples were eluted at 40 °C with a 0.1 wt % solution of tetra-*n*-butylammonium nitrate (Aldrich) in tetrahydrofuran (THF).

Synthesis of Alkyne-Functionalized Trifluoroethoxyphosphoranimine (3). A mixture of propargylamine hydrochloride (0.10 g, 1.07 mmol) and triethylamine (0.11 g, 1.07 mmol) was suspended in THF (15 mL). The mixture was stirred under an inert atmosphere at 60 °C for 2 h while a white precipitate formed. The reaction mixture was then cooled to room temperature, and bromophosphoranime 2 (0.28 g, 0.71 mmol) and another 1 equiv of triethylamine (0.11 g, 1.07 mmol) were added to the mixture. The reaction mixture was then stirred at room temperature overnight. The white precipitate was filtered off, and all volatiles were removed under reduced pressure to give a colorless liquid **3**. Yield: 87%. ^1H NMR ($CDCl_3$): δ 4.23 (s, 4H), δ 3.45 (d, 2H), δ 2.26 (t, 1H), δ 0.13 (s, 9H). ^{31}P NMR ($CDCl_3$): δ −2.65.

Synthesis of Chlorophosphoranimine ($Cl_3P{=}NSiMe_3$). The synthesis of the chlorophosphoranimine monomer followed a previously reported procedures with some modifications.[18,20,30] Briefly, PCl_3 (46.25 g, 0.33 mol) was added dropwise to $LiN(SiMe_3)_2$ (56.93 g, 0.33 mol) in ether (500 mL) at 0 °C over 30 min. The mixture was allowed to remain at 0 °C and was stirred for another 1 h. SO_2Cl_2 (45.22 g, 0.33 mmol) was then added slowly over 30 min, and the reaction mixture was stirred at 0 °C for 2 h. After completion of the reaction, the salt was removed by filtration. The crude product was condensed to one-third of its volume and was purified by vacuum distillation at room temperature to yield a colorless liquid. Yield: 63%. ^1H NMR ($CDCl_3$): δ 0.16 (s, 9H). ^{31}P NMR ($CDCl_3$): δ −57.08.

Synthesis of Alkyne-Functionalized Poly[bis(trifluoroethoxy)phosphazene] (6). Compoud **3** (0.26 g, 0.71 mmol) was redissolved in CH_2Cl_2 (15 mL) along with PCl_5 (0.25 g, 1.19 mmol) to initiate polymerization, and the reaction mixture was stirred for 1 h. The chlorophosphoranime (4.00 g, 17.18 mmol) was then added rapidly, and the mixture was stirred for another 4 h under an inert atmosphere at room temperature. The solvent was removed under reduced pressure to yield a viscous liquid. The product was redissolved in THF (50 mL) and treated with an excess amount of CF_3CH_2ONa which was preprepared by treating CF_3CH_2OH (3.78 g, 37.80 mmol) with

dx.doi.org/10.1021/ma300139z | Macromolecules 2012, 45, 2502−2508

NaH (1.51 g, 37.80 mmol) in THF (20 mL). The reaction mixture was stirred at room temperature overnight, followed by concentration of the solution under reduced pressure and then precipitation of the polymer into water (500 mL × 3) and hexane (200 mL × 2) to isolate a white product **6**. Yield: 52%. ^{1}H NMR (acetone-d_6): δ 4.53 (180H). δ 3.60 (2H), δ 2.18 (1H). ^{31}P NMR (D_2O): δ −7.88

Synthesis of 3-Azidopropyl-2-bromo-2-methylpropanoate (7). Sodium azide (3.60 g, 55.40 mmol) was dissolved in water (80 mL), followed by the addition of 3-bromopropanol (3.84 g, 37.60 mmol) dropwise to the solution. The reaction mixture was stirred at 80 °C for 18 h. The solution was then extracted with ethyl acetate (100 mL × 3), and the organic layer was washed with saturated brine (100 mL × 3) and then dried over $MgSO_4$ overnight. The solvent was removed under reduced pressure to yield a colorless liquid. The liquid was then redissolved in CH_2Cl_2 (20 mL) and chilled to 0 °C before the addition of triethylamine (1.68 g, 16.61 mmol). In a second vial, 2-bromoisobutyl bromide was dissolved in CH_2Cl_2 (20 mL) before being added dropwise to the mixture at 0 °C over 1 h. The reaction mixture was then allowed to warm to room temperature and was stirred overnight. The precipitate was filtered off, and the solvent was removed under reduced pressure. The crude product was purified by passing through a silica column using CH_2Cl_2:hexane (2:1) as the mobile phase, and the sample was isolated as a light yellowish liquid **7**. Yield: 20.23%. ^{1}H NMR ($CDCl_3$): δ 4.23 (t, 2H), 3.41 (t, 2H), 1.93 (m, 2H), 1.89 (s, 6H).

Synthesis of Bromo-Functionalized Polyphosphazene Macroinitiator 8. Polymer **6** (1.13 g, 0.06 mmol) and 3-azidopropyl-2-bromo-2-methylpropanoate (**7**) (0.156 g, 0.63 mmol) were dissolved in THF (10 mL), along with PMDETA (0.04 g, 0.22 mmol). Nitrogen gas was bubbled through the solution for 20 min to remove any dissolved oxygen. A trace amount of CuBr (0.03 g, 0.22 mmol) was weighed in a vial, and the oxygen was removed by purging the system with nitrogen gas. Once the system was free from oxygen, the CuBr was added to the reaction solution rapidly, and the solution was stirred at 60 °C for 1 day under an inert atmosphere. The sample was forced through a silica plug using THF to remove the solids. The crude product was then precipitated from THF into water (500 mL × 3) and hexane (200 mL × 5) and was further purified by dialysis against acetone:methanol (2:1) for 2 days to remove any remaining compound **7**. The solvent was then removed under reduced pressure, and the resulting product was dried under vacuum overnight to yield a white powder (**8**). ^{1}H NMR (DMSO-d_6): δ 7.79 (1H), δ 4.45 (180H), δ 4.32 (2H), δ 4.20 (2H), δ 3.91 (2H), δ 2.41 (2H), δ 1.91 (6H). ^{31}P NMR (DMSO-d_6): δ −7.88.

Synthesis of Poly[bis(trifluoroethoxy)phosphazene]-*co*-poly[(dimethylamino)ethyl methacrylate] (10) (TFE-*b*-PDMAEMA). 2-(Dimethylamino)ethyl methacrylate (DMAEMA) was used as a monomer to grow a second block from the terminus of the polyphosphazene. Macroinitiator **8** (0.50 g, 0.03 mmol) was dissolved in THF (5 mL), followed by the addition of DMAEMA (1.97 g, 12.50 mmol) and PMDETA (0.017 g, 0.10 mmol) to the solution. Nitrogen gas was bubbled through the solution for 20 min to remove any dissolved oxygen. Copper(I) bromide (7.20 mg, 0.05 mmol) was weighed in a small vial and then purged with nitrogen to remove oxygen. It was then added to the solution, and the mixture was stirred for 6 h at room temperature (as an example for TFE-*b*-PDMAEMA-4). To terminate the polymerization, the catalysts were removed by passing the sample through a silica plug using THF as mobile phase, and the isolated crude product was dialyzed against acetone:methanol (2:1) for 2 days. All solvent was removed under reduced pressure to yield the diblock copolymer **10** as a yellowish powder. ^{1}H NMR (acetone-d_6): δ 4.55 ($-CH_2CF_3$), δ 4.09 ($-OCH_2-$), δ 2.62 ($-CH_2N$), δ 2.23 ($-N(CH_3)_2$), δ 1.88 ($-CH_2-$), δ 1.10 ($-CH_3$). ^{31}P NMR (acetone-d_6): δ −7.88.

Micelle Preparation. To prepare micellar solutions, nanopure water (20 mL) with a conductivity of 18.2 MΩ/cm was added dropwise to a mildly stirred solution of the diblock copolymer (200 mg) in THF (5 mL). Once the water was added, all the THF was removed under reduced pressure as monitored by ^{1}H NMR. The resulting solution was then diluted to obtain a micelle concentration in the range of 5 to 1 × 10^{-4} g/L. For fluorescence measurements, a pyrene solution in THF (1.2 × 10^{-3} M) was added to nanopure water to give a final pyrene concentration of 12 × 10^{-7} M. Following dilution, the THF was removed under reduced pressure, and its removal was confirmed by ^{1}H NMR spectroscopy. The pyrene solution was then mixed with the diblock copolymer solutions to obtain copolymer concentrations ranging from 2.5 to 5 × 10^{-5} g/L, while the pyrene concentration of the samples was maintained at 6 × 10^{-7} M. All the samples were sonicated for 10 min and were allowed to stand for 1 day before fluorescence measurements.

Fluorescence Measurements. Excitation spectra of pyrene were measured using a Photon Technology International (PTI) fluorescence spectrometer using an 814 photomultiplier detection system. For the excitation spectra, the emission wavelength was set at 391 nm. All the samples were measured in a 1 × 1 cm quartz cuvette at room temperature.

Light Scattering Measurements. The sizes and size distributions of the diblock copolymer micelles were evaluated by dynamic light scattering using a particle size analyzer (Zetasizer Nano S, Malvern Instruments Ltd.) at room temperature (25 °C) with a scattering angle of 90°. Samples were filtered through a 0.45 μm syringe filter before measurement of particle size for each sample. The hydrodynamic radius (R_h) of the micelles was calculated by using the Stokes−Einstein equation $R_h = k_BT/6\pi\eta D$, where k_B is the Boltzmann constant, T is the absolute temperature, η is the solvent viscosity, and D is the diffusion coefficient.[31] The polydispersity factor of micelles, represented as μ_2/Γ^2, where μ_2 is the second cumulant of the decay function and Γ is the average characteristic line width, was calculated by the cumulant method.[32]

Tranmission Electron Microscopy. Transmission electron microscopy (TEM) was performed using a KEOL 2010 unit, operated at an acceleration voltage of 200 kV. For observation of the size and distribution of the micellar particles, a drop of sample solution (concentration = 1 g/L) was placed onto a 400-mesh copper grid coated with carbon. About 1 min after deposition, the grid was tapped with a filter paper to remove surface water, followed by air-drying. Negative staining was performed by using a droplet of a 2.5 wt % uranyl acetate solution.[33] The samples were air-dried at room temperature overnight.

RESULTS AND DISCUSSION

Synthesis of Block Copolymers. Conventional free radical polymerization lacks control over the polymer structure due to the slow initiation, fast propagation, and subsequent transfer or termination and makes it unsuitable for synthesizing well-defined block copolymer structures.[34] The development of atom transfer radical polymerization (ATRP) is one of the most robust controlled/living radical polymerization techniques with a diversity of monomers, desirable molecular weight control, and narrow polydispersity. This comes about because the low radical concentrations present during the polymerization reduce the contribution of inter- and intramolecularly terminated chains.[26] In this work, ATRP was chosen to form the organic block linked to a polyphosphazene backbone, and it is the first report to apply ATRP to synthesize polyphosphazene-containing diblock copolymers. In order to introduce the ATRP initiation site to the end of polyphosphazene backbone, azide−alkyne "click" chemistry was applied due to its excellent reaction efficiency, high functional group tolerance, and solvent compatibility.[35,36] In this work, a small molecule linker (**7**), an ATRP initiation site, was "click" coupled onto the polyphosphazene block and used for subsequently growing the organic block at the end of the polymer chain ("block-from"). This avoids the preparation of two distinct polymers with azide or alkyne functionality on the two segments and then coupling them together ("block-to"). This "block-from" method showed a higher reaction efficiency than the "block-to" method due to the better diffusion of small molecules to the

dx.doi.org/10.1021/ma300139z | Macromolecules 2012, 45, 2502−2508

reaction site at the polymer end-cap in solution as compared to the reaction of two polymer chains.[24,26]

A series of phosphazene−organic block copolymers was prepared by the synthetic procedures illustrated in Scheme 1. The phosphoranimine readily underwent bromine replacement reactions in the presence of amines to produce an alkyne-functionalized initiator **3**. To produce the cationic species **4**, the initiator **3** was treated with 2 equiv of PCl_5 at room temperature in CH_2Cl_2. Once formed, the chloro monomer $Cl_3P{=}NSiMe_3$ was added to propagate the living cationic polymerization to give poly(dichlorophosphazene) with a predetermined chain length.[18,19,21] The resultant poly(dichlorophosphzene) was then treated with an excess amount of $NaOCH_2CF_3$ in THF to yield the hydrophobic poly[bis(trifluoroethoxy)phosphazene] block with a pendent triple bond attached to the end of the chain. The entire process was carried out in an inert anhydrous atmosphere to prevent uncontrollable cross-linking.[12,13]

Compound **7** with an azide and bromine at its opposing ends was prepared as both the linker between the phosphazene and organic blocks and the initiator for growing the organic block. Initial attempts with $CuSO_4{\cdot}5H_2O$/sodium ascorbate as the catalytic system for the "click" reaction in THF at room temperature were unsuccessful probably due to the poor solubility of the catalyst in THF and the donor coordinating nature of the polyphosphazene backbone. Thus, a stronger catalyst CuBr/PMDETA complex in THF was chosen at an elevated temperature of 60 °C for 1 day to yield the ATRP macroinitiator **8**.[37] Unlike the $CuSO_4{\cdot}5H_2O$/sodium ascorbate catalyst system, which is tolerant to limited amounts of oxygen in solution by *in situ* reduction of $CuSO_4$,[36] the CuBr/PMDETA catalyzed "click" reaction in this work required the careful removal of all the oxygen dissolved in the solution by exchanging it with nitrogen to prevent the oxidation of Cu^+. In order to remove all of the uncoupled initiator **7** from the polyphosphazene polymer, the sample was purified extensively by precipitation from THF into hexane 5 times, followed by dialysis against acetone:methol (2:1) for 2 days. DMAEMA was selected as the second monomer due to its high reactivity, and CuBr/PMDETA was used as the catalyst in this polymerization. ATRP is usually carried out by bulk polymerization by directly dissolving the initiators in the pure monomers without utilizing solvents.[25,29,38] However, in this work, THF was used as a solvent at a sacrifice of reaction efficiency due to the poor solubility of the macroinitiator **8** in DMAEMA.

The existence of both the trifluoroethoxyphosphazene block and PDMAEMA signals in the ^{1}H NMR (Figure 1) confirmed

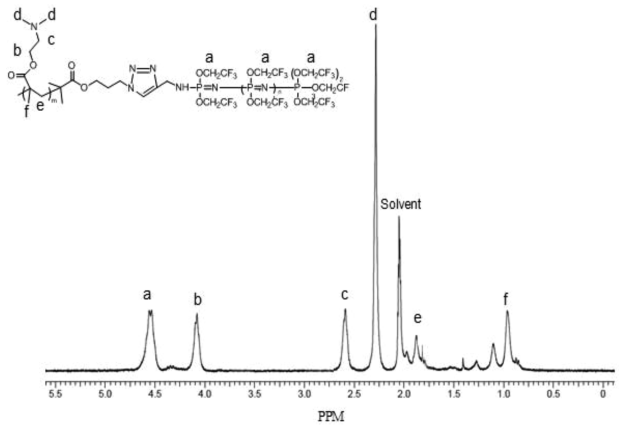


Figure 1. ^{1}H NMR of TFE-*b*-PDMAEMA-3 block copolymer at ambient temperature referenced to acetone-d_6.

the structure, together with the ^{31}P NMR (Figure 2) of the diblock copolymer. The molecular weight increased from 27

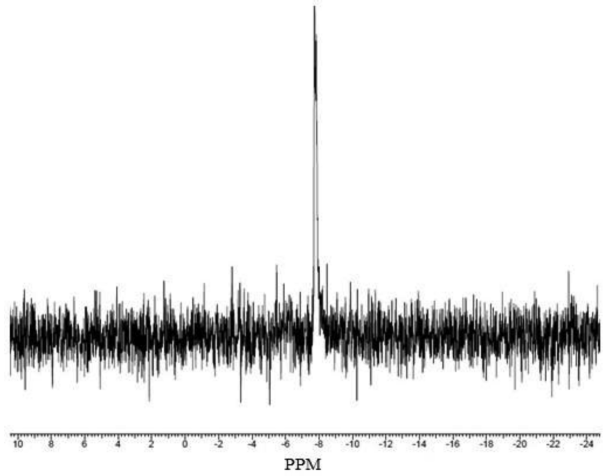


Figure 2. ^{31}P NMR of TFE-*b*-PDMAEMA-3 block copolymer at ambient temperature referenced to acetone-d_6.

900 to 42 300 (varying by ATRP reaction time) as determined by gel permeation chromatograph (GPC). All these items of evidence support the diblock copolymer structure. The length of both the hydrophobic and hydrophilic blocks can be tuned by controlling the ratio of initiator to monomer and the reaction time. In this work, the length of the hydrophobic block remained constant, and the length of the hydrophilic segment was controlled by the varying reaction times at the same monomer/initiator ratio. Table 1 shows the structural

Table 1. Characterization of TFE-*b*-PDMAEMA Block Copolymers

block copolymers	ATRP time (h)	block ratio (n:m)[a]	TFE (wt %)	M_n (g/mol) (GPC)[b]	M_n (g/mol) (NMR)[c]	PDI[d]
TFE-*b*-PDMAEMA-1	12	1:1.23	44	48 270	19 800	1.27
TFE-*b*-PDMAEMA-2	10	1:0.95	61	47 290	17 800	1.17
TFE-*b*-PDMAEMA-3	8	1:0.71	66	44 300	16 100	1.25
TFE-*b*-PDMAEMA-4	6	1:0.63	71	42 300	15 500	1.08

[a]The ratio of the hydrophobic block to the hydrophilic block was calculated from the integration obtained from ^{1}H NMR. [b]The number-average molecular weight (M_n) was calculated from ^{1}H NMR. [c]M_n was measured by gel-permeation chromatography (GPC). [d]Polydispersity index (PDI) = M_w/M_n.

characterization of a series of TFE-*b*-PDMAEMA diblock copolymers. The molecular weights calculated by ^{1}H NMR spectroscopy were estimated by comparing peak integration ratios of the end group on propargylamine (−CH_2−, 3.60 ppm), the trifluoroethoxy groups on the polyphosphazene (−CH_2−, 4.55 ppm), and the DMAEMA block (−CH_2−, 4.09 ppm). The significant difference of M_n between the GPC measurement and the ^{1}H NMR calculation as shown in Table 1 was attributed to (i) error caused by integration from the ^{1}H NMR peaks if the peak intensities of the end groups were too low and (ii) the difference of hydrodynamic radius between TFE-*b*-PDMAEMA and polystyrene standards which were used to calibrate the GPC. The final block copolymers were soluble in THF, acetone, DMSO, and DMF but were insoluble in hexane and toluene.

dx.doi.org/10.1021/ma300139z | *Macromolecules* 2012, 45, 2502−2508

Self-Association of Block Copolymers in the Aqueous Phase. The TFE-*b*-PDMAEMA block copolymer consists of the hydrophilic PDMAEMA and hydrophobic trfluoroethoxy-substituted polyphosphazene segments (TFE), which imparts the ability to form organized micellar structures in an aqueous environment. Generally, micelles can be formed in an aqueous environment by one of these three ways: (i) direct addition of block copolymers into stirred water; (ii) dissolution of the block copolymer in an organic solvent, followed by dialysis against water; or (iii) dissolution of the block copolymer in an organic solvent, followed by the addition of water dropwise to the solution using a mild stirring.[39,40] The last two methods are preferred, as the gradual exchange of the organic solvent with water can give more uniform micelle structures.[22] However, the organic solvent has to be removed completely from the aqueous medium to prevent it from influencing the micelle characterization. In this work, the third route was selected, and ^{1}H NMR was utilized to monitor for THF residues in the micelle solutions. The micellar behavior of the amphiphilic block copolymers was monitored by a fluorescence technique, dynamic light scattering, and TEM. The critical micelle concentrations (cmc's) of the diblock copolymers in an aqueous phase were determined by a fluorescence technique using pyrene as a probe. Previous studies have shown that pyrene has distinct fluorescence spectra depending on the environment utilized, aqueous or organic.[41,42] Figure 3 shows

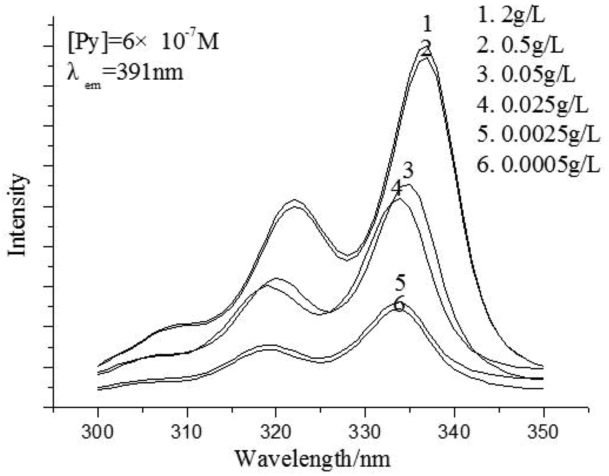


Figure 3. Excitation spectra of pyrene as a function of TFE-*b*-PDMAEMA-3 concentration in water.

the excitation fluorescence spectra of polymer and pyrene sample (TFE-*b*-PDMAEMA-3 as an example), in which the concentration of the pyrene was kept constant while varying the concentrations of the polymer. In the spectra, the symmetry-forbidden (0,0) band shifted from 332 to 337 nm, and the intensity gradually increased as the pyrene transferred from the aqueous environment to the hydrophobic micelle cores. Meanwhile, the pyrene fluorescence spectrum obtained in pure water is identical to the one obtained from a pyrene solution with low concentrations of block copolymers in Figure 3, and the block copolymers themselves give no fluorescence signals in this region. The ratios of the peak intensities at 337 and 332 nm were utilized to determine the cmc value.[41] Figure 4 shows the intensity ratios (I_{337}/I_{332}) of the pyrene excitation spectra versus the logarithm of concentrations of TFE-*b*-PDMAEMA-3 (log *C*). At low concentrations of the diblock copolymer, the change in the intensity ratio (I_{337}/I_{332}) was

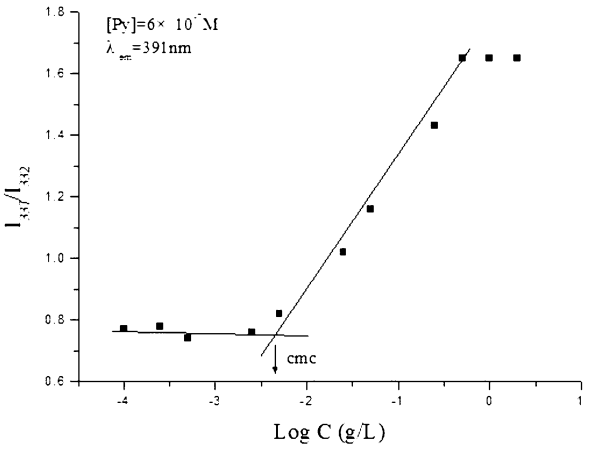


Figure 4. Plot of I_{337}/I_{332} (from pyrene excitation spectra) vs log *C* for TFE-*b*-PDMAEMA-3.

negligible since the concentrations of the block copolymer were insufficient to self-aggregate and form micelles. But at a threshold concentration of the diblock copolymer, the intensity ratios began to show a substantial increase with an increase in the concentration of the diblock copolymer. This reflects the shift of the pyrene probe from an aqueous environment to a hydrophobic one. This threshold indicated the minimum concentration of the diblock copolymer needed for the formation of micelles, the inner cores of which were able to act as hydrophobic containers to incorporate the pyrene. Using these data, the cmc values can be determined from the turning point of the curve as shown in Figure 4. The cmc values of the block copolymers were in the range 3.47–9.55 mg/L depending on the block composition (Table 2). The

Table 2. Properties of TFE-*b*-PDMAEMA Micelles

block copolymers	cmc (mg/L)	diam (nm)	μ_2/Γ^2	K_v ($\times 10^{-5}$)
TFE-*b*-PDMAEMA-1	9.55	100	0.29	0.12
TFE-*b*-PDMAEMA-2	6.31	130	0.29	0.40
TFE-*b*-PDMAEMA-3	5.46	134	0.16	0.48
TFE-*b*-PDMAEMA-4	3.47	142	0.20	1.52

results showed that the cmc values decreased with an increase in the proportion of the hydrophobic segment, which is in agreement with other studies on micelles.[11,42] These values are much lower than those of low molecular weight surfactants (e.g., 2.3 g/L for sodium dodecyl sulfate) and diblock copolyphosphazenes (e.g., 80 mg/L for methoxyethoxyethoxy and phenyl containing species)[20,41] but comparable to those of other polymeric amphiphiles.[1,5,39]

Dynamic light scattering (DLS) was carried out to determine the diameters of the micelles. Figure 5 shows an example of the size distribution of TFE-*b*-PDMAEMA-3 at 25 °C. The diameters of the micelles for the four polymers investigated were in the range of 100–142 nm with a narrow size distribution in an aqueous phase as summarized in Table 2. The diameters increased slightly with the increase in the proportion of the hydrophobic block. The polydispersity factors (μ_2/Γ^2) of the micelles are fairly low (0.16–0.29), which suggests a narrow size distribution.[31,32]

The size and shape of the micelles were also examined by TEM. In order to amplify the contrast of the micelles and background, negative staining was performed by using uranyl acetate solution to make the background dark gray.[33] Figure 6 shows the micelles formed from a solution with a polymer

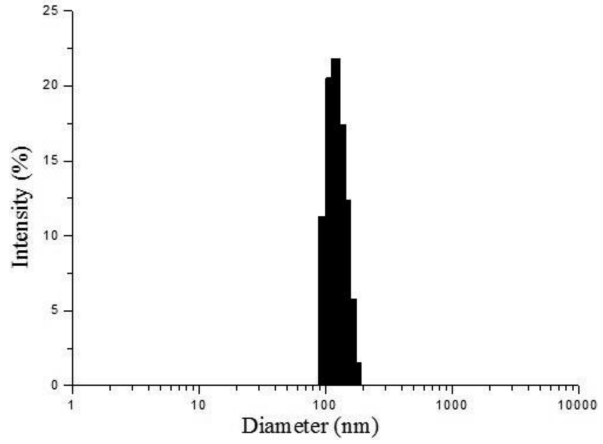


Figure 5. Diameters of TFE-*b*-PDMAEMA-3 from dynamic light scattering.

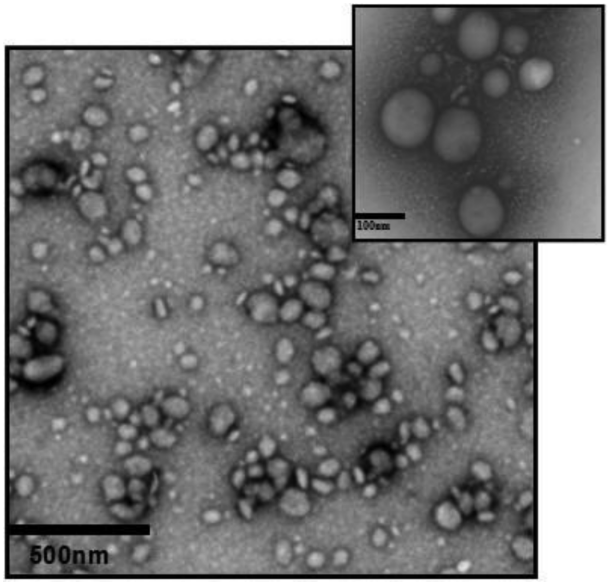


Figure 6. TEM image of TFE-*b*-PDMAEMA-3.

(TFE-*b*-PDMAEMA-3) concentration of 1 g/L. Although the average size of the micelles was about 100 nm, micelles with a size range of several hundreds of nanometers were often observed. This resulted from intermicellar aggregates that form a multicore structure through the association of individual micelles.[44,45] Most of the micelles had a spherical shape, and the average diameter from TEM was in agreement with the mean diameter measured from dynamic light scattering.

Partitioning of Pyrene in Micellar Solutions. The hydrophobicity of the micelle core was estimated by measuring the equilibrium constant K_v for the partitioning of pyrene between the micelle core and the aqueous media. A higher K_v indicates a higher hydrophobicity of the microdomain (micelle cores) constructed by the hydrophobic segments.[22,23] In this work, the equilibrium constant K_v was calculated following the approach reported by Wilhelm.[41] A simple equilibrium between pyrene in the bulk aqueous environment and pyrene incorporated into the micelle was assumed. The ratio of the pyrene concentration inside the micelle to that of pyrene dissolved in the bulk water phase ($[Py]_m/[Py]_w$) can be correlated to the ratio of the volumes of each phase as expressed in eq 1. The K_v here is the partition equilibrium constant of pyrene between the micelle core phase and water phase.

$$[Py]_m/[Py]_w = K_v V_m/V_w \quad (1)$$

Equation 1 can be rewritten as

$$[Py]_m/[Py]_w = K_v x(c - \mathrm{cmc})/1000\rho \quad (2)$$

where x is the weight fraction of the hydrophobic polyphosphazene block, c is the concentration of the block copolymer, and ρ is the density of the core of the micelles, which is assumed to be the bulk density of the poly[bis-(trifluoroethoxy)phosphazene] (1.10 g/mL). In the intermediate range of polymer concentration with a substantial increase of intensity ratio (I_{337}/I_{332}), $[Py]_m/[Py]_w$ can be written as

$$[Py]_m/[Py]_w = (F - F_{min})/(F_{max} - F) \quad (3)$$

where F_{max} and F_{min} correspond to the average magnitude of I_{337}/I_{332} in the flat region of the high and low concentration ranges, respectively, in Figure 4, and F is the intensity ratio (I_{337}/I_{332}) in the intermediate concentration range of the block copolymers. Combining eqs 2 and 3, K_v values for pyrene can be determined as the slope by using a plot of $(F - F_{min})/(F_{max} - F)$ versus block copolymer concentrations as shown in Figure 7.

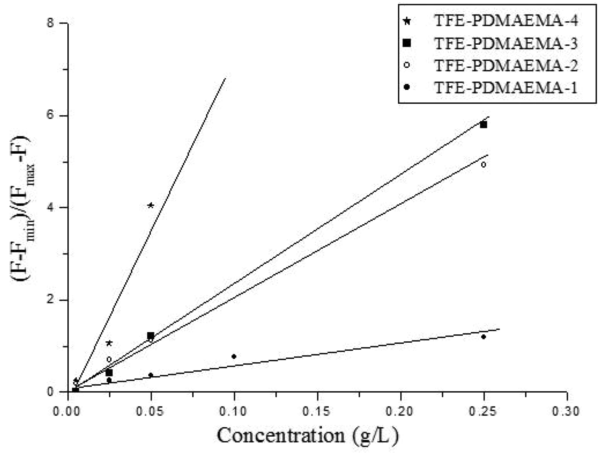


Figure 7. Plots of $(F - F_{min})/(F_{max} - F)$ vs concentration of block copolymers.

The K_v values, as summarized in Table 2, were in the range of 0.12×10^5 to 1.52×10^5 for the TFE-*b*-PDMAEMA system, which are much larger than those of amphiphillic diblock copolyphosphazenes (e.g., 7×10^3 for a methoxyethoxyethoxy and phenoxy containing copolyphosphazene).[20] The data also showed that, as the proportion of the hydrophobic blocks in the amphiphilic block copolymers increased, the K_v value also increased, suggesting an increase in the hydrophobic characteristic of the micelle cores.

CONCLUSION

A series of amphiphilic TFE-*b*-PDMAEMA diblock copolymers has been synthesized via the controlled living cationic polymerization of $Cl_3N{=}PSiMe_3$, azide−alkyne "click" chemistry, and atom transfer radical polymerization of DMAEMA. The length of each block was well controlled, and the polydispersity index was relatively low. The block copolymers self-aggregated into

dx.doi.org/10.1021/ma300139z | *Macromolecules* 2012, 45, 2502−2508

organized micelle structures in an aqueous environment. The micelles which were formed were characterized by the use of fluorescence techniques, dynamic light scattering, and transmission electron microscopy. The critical micelle concentrations of the block copolymers were determined from fluorescence spectra using pyrene as a probe. The cmc values depended on the proportion of the hydrophobic blocks in the copolymer and were in the range of 3.47−9.55 mg/L. TEM and dynamic light scattering results indicated that the spherical micelle aggregates were formed with an average diameter of 100−142 nm. The hydrophobicity of the micellar core was estimated by measurement of the partition equilibrium constant of pyrene in the micelle solution, and the values were in the range of 0.12×10^5 to 1.52×10^5. The combination of "click" reaction chemistry, and ATRP has opened a new facile route ("block-from") for synthesizing well-defined hybrid phosphazene−organic block copolymer structures with high synthetic tunability. The properties of the micelles can be tailored by changing either the phosphazene block or the organic block following the synthetic procedures described above. This can be achieved by varying the nucleophiles during the substitution of poly(dichlorophosphazene) or by varying the organic monomers during ATRP. For instance, to synthesize block copolymers containing biodegradable substituents, similar synthetic procedures can be followed except the side group nucleophiles used could be changed to amino acid esters instead of the trifluoroethoxy group to confer biodegradability to the micelles.[15]

AUTHOR INFORMATION

Corresponding Author

*E-mail: hra@chem.psu.edu.

Notes

The authors declare no competing financial interest.

REFERENCES

(1) Xu, R.; Winnik, M. A.; Hallett, F. R.; Riess, G.; Croucher, M. D. *Macromolecules* **1991**, *24*, 87−93.
(2) Kataoka, K.; Kwon, G. S.; Yokoyama, M.; Okano, T.; Sakurai, Y. *J. Controlled Release* **1993**, *24*, 119−132.
(3) Gref, R.; Minamitake, Y.; Peracchia, M. T.; Trubetskoy, V.; Torchilin, V.; Langer, R. *Science* **1994**, *263*, 1600−1603.
(4) Allen, C.; Yu, Y.; Maysinger, D.; Eisenberg, A. *Bioconjugate Chem.* **1998**, *9*, 564−572.
(5) Lee, Y.; Ishii, T.; Kim, H. J.; Nishiyama, N.; Hayakawa, Y.; Itaka, K.; Kataoka, K. *Angew. Chem., Int. Ed.* **2010**, *49*, 2552−2555.
(6) Han, D.; Tong, X.; Zhao, Y. *Macromolecules* **2011**, *44*, 437−439.
(7) Thurmond, K. B.; Kowalewski, T.; Wooley, K. L. *J. Am. Chem. Soc.* **1997**, *119*, 6656−6665.
(8) Qin, A.; Tian, M.; Tamireddy, C.; Webber, S. E.; Munk, P.; Tuzar, Z. *Macromolecules* **1994**, *27*, 120−126.
(9) Astafieva, I.; Zhong, X. F.; Eisenberg, A. *Macromolecules* **1993**, *26*, 7339−7352.
(10) Zhang, L.; Eisenberg, A. *Science* **1995**, *268*, 1728−1731.
(11) Lee, S. C.; Chang, Y.; Yoon, J. S.; Kim, C.; Kwon, I. C.; Kim, Y. H.; Jeong, S. Y. *Macromolecules* **1999**, *32*, 1847−1852.
(12) Allcock, H. R. *Chemistry and Applications of Polyphosphazenes*; John Wiley and Sons: Hoboken, NJ, 2003.
(13) Allcock, H. R.; Kugel, R. L. *J. Am. Chem. Soc.* **1965**, *87*, 4216−4217.
(14) Allcock, H. R.; Connolly, M. S.; Sisko, J. T.; Al-Shali, S. *Macromolecules* **1988**, *21*, 323−334.
(15) Allcock, H. R.; Pucher, S. R. *Macromolecules* **1994**, *27*, 1071−1075.
(16) Allcock, H. R.; Kugel, R. L. *J. Am. Chem. Soc.* **1965**, *87*, 4216−4217.
(17) Allcock, H. R. *J. Inorg. Organomet. Polym.* **2006**, *16*, 277−294.
(18) Honeyman, C. H.; Morrissey, C. T.; Manners, I.; Allcock, H. R. *J. Am. Chem. Soc.* **1995**, *117*, 7035−7036.
(19) Allcock, H. R.; Reeves, S. D.; Nelson, J. M.; Crane, C. A.; Manners, I. *Macromolecules* **1997**, *30*, 2213−2215.
(20) Chang, Y.; Lee, S. C.; Kim, K. T.; Scott, D. R.; Kim, C.; Allcock, H. R. *Macromolecules* **2001**, *34*, 269−274.
(21) Allcock, H. R.; Powell, E. S.; Chang, Y.; Kim, C. *Macromolecules* **2004**, *37*, 7163−7167.
(22) Cho, S. Y.; Steely, L. B.; Allcock, H. R. *Macromolecules* **2006**, *39*, 8334−8338.
(23) Chang, Y. K.; Prange, R.; Allcock, H. R. *Macromolecules* **2002**, *35*, 8556−8559.
(24) Sheiko, S. S.; Sumerlin, B. S.; Matyjaszewski, K. *Prog. Polym. Sci.* **2008**, *33*, 759−785.
(25) Matyjaszewski, K.; Xia, J. *Chem. Rev.* **2001**, *101*, 2921−2990.
(26) Patten, T. E.; Matyjaszewski, K. *Adv. Mater.* **1998**, *10*, 901−915.
(27) Li, C.; Buurma, N. J.; Haq, I.; Turner, C.; Armes, S. P.; Castelletto, V.; Hamley, I. W.; Lewis, A. L. *Langmuir* **2005**, *21*, 11026−11033.
(28) Dong, H.; Matyjaszewski, K. *Macromolecules* **2008**, *41*, 6868−6870.
(29) Coessens, V.; Pintauer, T.; Matyjaszewski, K. *Prog. Polym. Sci.* **2001**, *26*, 337−377.
(30) Wang, B.; Rivard, E.; Manners, I. *Inorg. Chem.* **2002**, *41*, 1690−1691.
(31) Harada, A.; Kataoka, K. *Macromolecules* **1998**, *31*, 288−294.
(32) Harada, A.; Kataoka, K. *Macromolecules* **1995**, *28*, 5294−5299.
(33) Zhang, L.; Eisenberg, A. *J. Am. Chem. Soc.* **1996**, *118*, 3168−3181.
(34) Wang, J. S.; Matyjaszewski, K. *Macromolecules* **1995**, *28*, 9701−9710.
(35) Kolb, H. C.; Finn, M. G.; Sharpless, K. B. *Angew. Chem., Int. Ed.* **2001**, *40*, 2004−2021.
(36) Johnson, J. A.; Finn, M. G.; Koberstein, J. T.; Turro, N. J. *Macromol. Rapid Commun.* **2008**, *29*, 1052−1072.
(37) Dirks, A. J. T.; van Berkel, S. S.; Hatzakis, N. S.; Opsteen, J. A.; van Delft, F. L.; Cornelissen, J. J. L. M.; Rowan, A. E.; van Hest, J. C. M.; Rutjes, F. P. J. T.; Nolte, R. J. M. *Chem. Commun.* **2005**, *33*, 4172−4174.
(38) Braunecker, W. A.; Matyjaszewski, K. *Prog. Polym. Sci.* **2007**, *32*, 93−146.
(39) Nagasaki, Y.; Okada, T.; Scholz, C.; Iijima, M.; Kato, M.; Kataoka, K. *Macromolecules* **1998**, *31*, 1473−1479.
(40) Tan, B. H.; Gudipati, C. S.; Hussain, H.; He, C.; Liu, Y.; Davis, T. P. *Macromol. Rapid Commun.* **2009**, *30*, 1002−1008.
(41) Wilhelm, M.; Zhao, C.; Wang, Y.; Xu, R.; Winnik, M. A.; Mura, J.; Riess, G.; Croucher, M. D. *Macromolecules* **1991**, *24*, 1033−1040.
(42) Kalyanasundaram, K.; Thomas, J. K. *J. Am. Chem. Soc.* **1977**, *99*, 2039−2044.
(43) Phillips, J. N. *Trans. Faraday Soc.* **1955**, *51*, 561−569.
(44) Kabanov, A. V.; Nazarova, I. R.; Astafieva, I. V.; Batrakova, W. V.; Alakhov, V. Y.; Yaroslavov, A. A.; Kabanov, V. A. *Macromolecules* **1995**, *28*, 2303−2314.
(45) Gao, Z.; Eisenberg, A. *Macromolecules* **1993**, *26*, 7353−7360.

Macromolecules

Article

pubs.acs.org/Macromolecules

From Brittle to Pliant Viscoelastic Materials with Solid State Linear Polyphosphonium–Carboxylate Assemblies

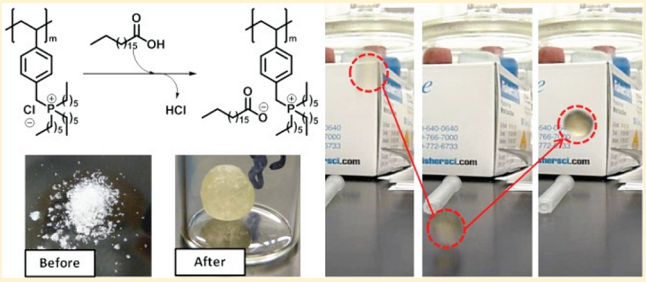
Guilhem Godeau,[†] Laurence Navailles,[§] Frédéric Nallet,[§] Xinrong Lin,[†] Thomas J. McIntosh,[‡] and Mark W. Grinstaff*,[†]

[†]Departments of Biomedical Engineering and Chemistry, Metcalf Center for Science and Engineering, Boston University, Boston, Massachusetts 02215, United States

[‡]Department of Cell Biology, Duke University Medical Center, Durham, North Carolina 27710, United States

[§]Université de Bordeaux, Centre de recherche Paul-Pascal–CNRS, 115 avenue du Docteur-Schweitzer, F-33600 Pessac, France

ABSTRACT: A polystyrenylphosphonium polymer was synthesized and complexed with various carboxylic acid derivatives to form new solid-state polyelectrolyte–surfactant assemblies. The properties of these ionic materials were highly dependent on the nature of the anion and included a brittle material, a rubbery ball that bounces, or a sticky fiber. The values for the equilibrium modulus, storage modulus, and loss modulus were dependent on the composition of the carboxylic acid and the number of electrostatic interactions. Small-angle X-ray scattering studies on the supramolecular assemblies confirmed a bilayer structure for two of the assemblies.



INTRODUCTION

Self-assembly methodologies are of significant utility as the use of noncovalent bonds such as H-bonding, van der Waals forces, or $\pi-\pi$ interactions enable the preparation of new materials notably different than their covalent analogues.[1−13] Recently, we reported the synthesis and properties of new ionic networks formed between a small molecular diphosphonium ionic liquid and a multivalent carboxylate anion (e.g., EDTA).[14,15] The electrostatic interactions between the cationic diphosphonium and the carboxylate anion are sufficient to afford supramolecular materials with defined shapes (e.g., fibers) and macroscopic properties (e.g., viscoelasticity). Building upon these results, we are investigating self-organizing ionic materials where the properties can not only be varied but also controlled based on discrete changes in the number of noncovalent interactions. In this work we report the synthesis of a linear polystyrenylphosphonium polymer (Figure 1) able to form several different supramolecular assemblies with mono- and dicarboxylates. Based on the nature of the anion, the properties of these ionic materials are found to be quite diverse, including (1) brittle, glass-like materials, (2) rubbery balls that bounce, and (3) sticky fibers that flow upon plucking.

As these materials are held together through ionic interactions they belong to a class of solid-state polyelectrolyte–surfactant complexes.[16−21] Although such complexes can also be formed via H-bonding[22−24] and metal–ligand bonds,[25] we will focus our attention on those complexes formed via electrostatic interactions. For example, Antonietti et al. have studied and characterized the structure of supramolecular assemblies formed between poly(styrenesulfonate) and alkyltrimethylammoniums of C12 to C20 in alkyl chain length or polyacrylates with cetyltrimethylammonium.[16,26] Likewise, Thünemann et al. have investigated cationic poly(dimethyldiallylammonium) and its structure with a sulfonated silicon surfactant or a soybean lecithin.[27,28] Structural studies using X-ray scattering have shown that poly(ethylenimine) and *n*-alkyl carboxylic acids form lamellar structures which are dependent on composition of the coordinating acid as well as the ratio of the two components.[29,30] Such polyelectrolyte–surfactant interactions can also be used to form small vesicles as found between the diblock copolymer of poly(ethylene oxide) and poly(sodium methacrylate) (PEO-*b*-PMANa) and a single-tail cationic surfactant like cetyltrimethylammonium bromide.[31] These interactions have been used to tune the optical properties of conjugated polyelectrolytes via coordination of a cationic[32] or zwitterion surfactant.[33] Finally, polyelectrolyte–surfactant complexes have been recently reported as thermoreversible organogelators.[34] As such, these solid-state polyelectrolyte–surfactant complexes are of interest for basic studies as well as for potential applications.

EXPERIMENTAL SECTION

General. All chemicals were purchased from Aldrich or Acros as highest purity grade and used without further purification. All reactions were performed under a nitrogen atmosphere. NMR spectra were recorded on Varian INOVA spectrometers [for ^{1}H (400 or 500 MHz), ^{13}C (101 or 126 MHz), and ^{31}P (161 MHz)]. Electrospray mass

Received: January 28, 2012
Revised: February 12, 2012
Published: February 23, 2012

ACS Publications © 2012 American Chemical Society

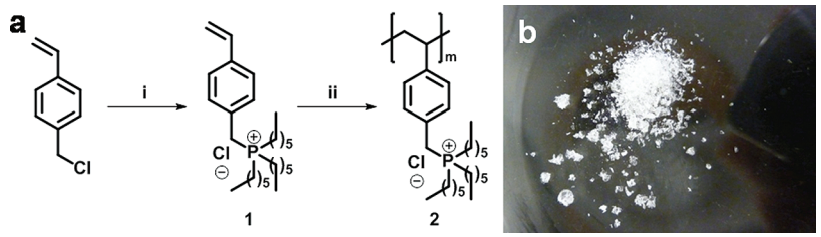


Figure 1. (a) Phosphonium polymer synthesis: (i) 1.1 equiv of trihexylphosphine, acetonitrile, 60 °C, 10 h; (ii) AIBN, dodecanthiol, anisole, 70 °C, overnight. (b) Photograph of the synthesized polymer.

spectra were obtained on an Agilent 1100 LC/MSD trap with ESI and APCI sources.

Synthesis of Trihexyl(4-vinylbenzyl)phosphonium Chloride (1). Under nitrogen, 4-chloromethylstyrene (3.4 g, 22.2 mmol, 1 equiv) and trihexylphosphine (7.02 g, 24.4 mmol, 1.1 equiv) were dissolved in 5 mL of acetonitrile. The mixture was stirred overnight at 60 °C. The solvent and excess of starting material were then removed under high vacuum overnight. The compound was used for the next step without further purification. 8.6 g of product was isolated (yield: 88%). R_f: 0.5 (DCM/methanol, 95/5). ^{1}H NMR (400 MHz, $CDCl_3$): 0.86−0.9 (m, 9H), 1.24−1.47 (m, 24H), 2.38−2.45 (m, 6H), 4.29 (s, 1H), 4.33 (s, 1H), 5.29 (d, J = 18 Hz, 1H), 5.76 (d, J = 18 Hz 1H), 6.69 (dd, J = 8 and 18 Hz, 1H), 7.38−7.43 (m, J = 8 Hz, 4H). ^{13}C NMR (101 MHz, $CDCl_3$): 13.7, 18.5, 19.0, 21.5, 22.1, 26.4, 26.8, 30.2, 30.4, 30.8, 114.5, 126.8, 128.2, 130.2, 135.7, 137.4. ^{31}P NMR (161 MHz, $CDCl_3$): 31.3. HRMS (ESI): $[M - Cl]^+$ calcd 403.3494; found 403.3487.

Synthesis of Poly(trihexyl(4-vinylbenzyl)phosphonium chloride). (2). In a Shlenck tube, compound **1** (2.89 g, 6.6 mmol) was dissolved in anisole (3 mL). The dodecanethiol (65 mg, 0.33 mmol, 0.05 equiv) and AIBN (1.6 mg, 0.01 mmol, 0.0015 equiv) were then added. The mixture was stirred overnight at 70 °C. The reaction was stopped by cooling the mixture to room temperature and exposing it to oxygen. The polymer was precipitated in hexane and filtered. 2.44 g of polymer was obtained (yield: 84%). All NMR signals appear as broad peak. ^{1}H NMR (500 MHz, $CDCl_3$): 0.84, 1.25, 1.43, 2.42, 6.41, 7.37. ^{13}C NMR (126 MHz, $CDCl_3$): 13.9, 18.7, 19.1, 21.7, 22.3, 30.2, 30.6, 31, 126.1−130.5. ^{31}P NMR (161 MHz, $CDCl_3$): 31.2. Size exclusion chromatography (SEC) was performed with dichloromethane as the solvent at a flow rate of 1 mL/min as eluent through an Agilent PLgel 3 μm Mixed-E 300 × 7.5 mm column. The molecular weights were measured against poly(ethylene glycol) standards. SEC studies gave a molecular weight: 60 000 g mol^{-1} (PDI: 1.83).

Synthesis of 15-Oxo-2,5,8,11,14-pentaoxaoctadecan-18-oic Acid (6). Anhydrous pyridine (2 mL) was added first at 0 °C to succinic anhydride (2 g, 20 mmol, 2.1 equiv). Tetraethylene glycolmonomethyl ether (2 g, 9.6 mmol, 1 equiv) was then added. The reaction mixture was stirred for 4 h at room temperature. 20 mL of ice cold 1 M HCl solution in water was added. The mixture was then extracted 3 times with 50 mL of DCM, and the organic layer was washed once with 20 mL of brine. The organic phase was dried with Na_2SO_4, and the solvent was removed under reduced pressure. 2.76 g of product was isolated after chromatography (95/5, DCM/methanol) (yield: 93%). R_f: 0.36 (90/10, DCM/methanol). ^{1}H NMR (400 MHz, $CDCl_3$): 2.66 (s, 4H), 3.38 (s, 3H), 3.55−3.57 (m, 2H), 3.64−3.71 (m, 12H), 4.24−4.27 (m, 2H). ^{13}C NMR (101 MHz, $CDCl_3$): 29.0, 29.3, 58.9, 63.8, 69.0, 70.4, 70.5, 70.6, 71.8, 172.2, 175.4. HRMS (ESI): $[M + Na]^+$ calcd 331.1369; found 331.1367.

General Procedure for Mixture Preparation. The polymer (300 mg) was added to the corresponding carboxylic acid (1 equiv per charge). The mixture was dissolved in organic solvent (DCM or THF) and mixed to give a homogeneous mixture. The solvent was then removed under high vacuum at 80 °C for 12 h.

General Procedure for Bounce Assays. A 90 mg ball was prepared by rolling the IL polymer 2. The ball was then left for 20 s at room temperature. The ball was then dropped onto a hard Bakelite surface, in front of a 12 in. ruler. The highest point to which the ball bounced back was measured. The experiment was performed 10 times, and the ball was left at room temperature for 10 s between each test.

General Procedure for Rheology Assays. A TA AR1000 rheometer equipped with a Peltier temperature controller and a 20 mm aluminum (plane−plane) geometry was used for creep recovery experiments, and a 12 mm steel geometry was used for G', E modulus, and delta angle determination. All rheological measurements were performed at 25 °C, and the viscosity data were reported at a frequency of 1 Hz. The samples were dried prior to the measurements.

Differential Scanning Calorimetry. Thermal transitions were measured using a differential scanning calorimeter (Q100, TA Instruments) at a heating rate of 20 °C/min and a cooling rate of 10 °C/min from −100 to 200 °C.

X-ray Diffraction. Two sets of X-ray diffraction experiments were performed. In one, specimens were prepared by drying a chloroform solution of the assembly onto a curved glass substrate, and patterns were recorded at ambient conditions using a line-focused X-ray camera with a flat plate film cassette loaded with Kodak BioMax film.[35] A second set of small-angle X-ray scattering (SAX) experiments were realized with a H.I. Nanostar device (from Bruker) with point collimation and wavelength of the radiation equal to λ = 1.5418 Å. Experiments were performed under vacuum at room temperature, and a 2D gas detector (HiStar, also from Bruker. 1024 × 1024 pixels with 100 μm pixel size) was used for recording the spectra. The sample-to-detector distance was 25.5 cm. Each sample was placed in the window of a metal cylinder inserted into a glass capillary with a diameter of 3 mm.

■ RESULTS AND DISCUSSION

In our system, we are interested in the solid-state polyelectrolyte−surfactant complexes formed between a polystyrenylphosphonium and four different carboxylates. The polystyrenylphosphonium polymer, **2**, was synthesized in two steps as shown in Figure 1. The monomer **1** was obtained by reacting 4-chloromethylstyrene with an excess of trihexylphosphine in acetonitrile at 60 °C for 10 h. The chlorophosphonium styrene derivative was isolated as a white powder by removing the remaining starting material under high vacuum (yield 88%). Polymer **2** was obtained using AIBN as the free radical initiator of **1** in anisole after 12 h. The M_w of **2** was controlled by the addition of 5% dodecanthiol as a chain transfer agent. Precipitation of the polymer in hexane gave **2** as a white powder (yield 84%; M_w 60 000; PDI 1.8; mp = 110−120 °C). The polymer is soluble in water, DMSO, DCM, and THF. As **1** is an ionic liquid monomer, the polymerization of ionic liquid monomers is also of general interest,[36−38] and recently, Long et al. have reported new phosphonium triblock copolymers using an ionic liquid monomer.[39]

The supramolecular ionic materials were prepared by dissolving **2** and either dodecandioic acid, stearic acid, oleic acid, or 15-oxo-2,5,8,11,14-pentaoxaoctadecan-18-oic acid in a volatile organic solvent (e.g., DCM) followed by removal of the solvent and volatiles under high vacuum at 80 °C. The samples were then cooled to room temperature. The resulting ionic materials exhibit strikingly different physical and rheological

dx.doi.org/10.1021/ma3002092 | Macromolecules 2012, 45, 2509−2513

properties depending on the carboxylate counteranion. Specifically, substituting the chloride counteranion of **2** for dodecandioic acid, while maintaining the charge ratio of 1:1, afforded a transparent and relatively hard and brittle material (Figure 2a). This ionic material, **2**−**3**, was a cross-linked

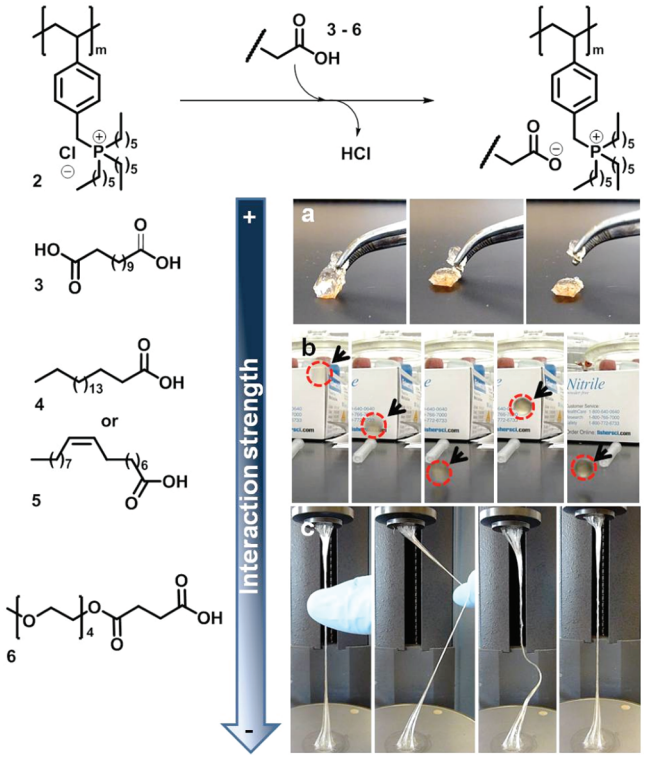


Figure 2. Preparation route for the solid-state linear polyphosphonium−alkyl carboxylate assemblies. (a) Photograph of a brittle ionic material formed with the dicarboxylate counteranion, **3**. (b) Photograph of an ionic material formed with the mono fatty carboxylate counteranion, **5**, that bounces. (c) Photograph of a sticky elastic ionic material formed with the tetraethylenglycol carboxylate, **6**, as the counteranion.

network with the diacid bridging between the phosphonium centers. Coordination of the carboxylate to the phosphonium was confirmed by IR as the C═O stretching frequency shifted from 1690 to 1719 cm^{-1} upon binding. **2**−**3** has an equilibrium modulus (E) of 21 MPa and a phase angle (δ) of 14° (Figure 3),

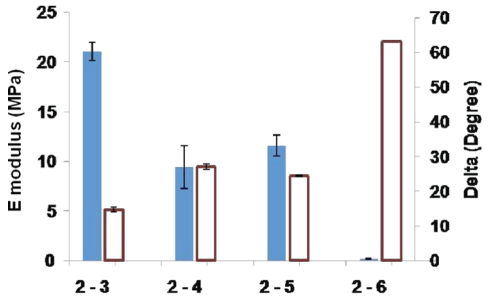


Figure 3. Equilibrium modulus (E) and phase angle (δ) for the ionic materials.

characteristic of a solid material. All rheological experiments were performed using an AR 1000 controlled strain rheometer (TA Instruments), and the data are reported at 25 °C.

In order to create a softer material that was less brittle with more viscoelastic character, we substituted dodecandioic acid for stearic acid, **4**, or oleic acid, **5**. The aliphatic acids coordinated with the phosphonium centers but were unable to cross-link the polymer chains of **2**. These ionic materials, **2**−**4** and **2**−**5**, were softer matter (Figure 2b). Specifically, ionic materials **2**−**4** and **2**−**5** had an E and δ of 9 MPa and 27° and 11 MPa and 24°, respectively (Figure 3). When shaped into a ball and dropped from a height of 30 cm, the **2**−**5** ionic material bounced back to about 45% of the original height. To further alter the mechanical properties of the ionic material, we used 15-oxo-2,5,8,11,14-pentaoxaoctadecan-18-oic acid, **6**, instead of oleic acid. The **2**−**6** ionic material was more fluidlike and sticky with more viscous character. It has an E of 0.2 MPa and δ of 63°. When stretched between two plates, the material gave a string that flowed upon plucking (Figure 2c). There have been only a few reports on the mechanical properties of polyelectrolyte−surfactant materials, notably the reports by Thünemann[27] and Antonietti,[40] who studied the mechanical properties of a poly(dimethyldiallylammonium)−isopropylammonium 6-(trimethylsilyl)-*n*-hexylsulfate complex and of a poly(acrylic acid)−didodecyldimethylammonium complex, respectively.

Because ionic materials, **2**−**4**, **2**−**5**, and **2**−**6** display interesting viscoelastic properties, we have performed creep and recovery experiments to further characterize and quantitate this viscoelasticity. In the creep part of the experiment, a constant stress (640 Pa) was applied on the sample for a duration of 10 min. The stress was then removed and the material was allowed to relax for an additional 10 min. As shown in Figure 4, the % recovery for **2**−**4**, **2**−**5**, and **2**−**6** was

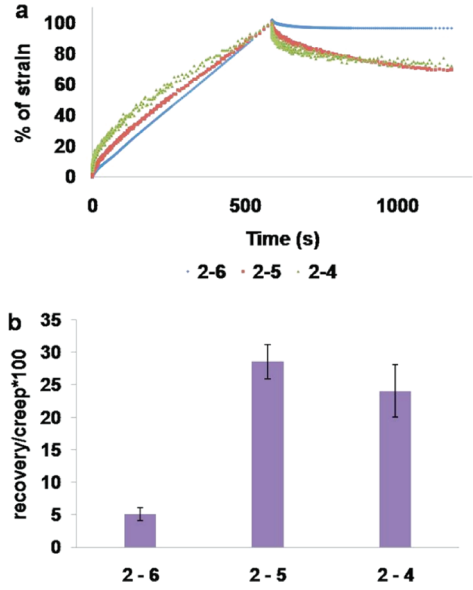


Figure 4. (a) Creep and recovery profiles for **2**−**4**, **2**−**5**, and **2**−**6** assemblies. (b) Percent recovery for **2**−**4**, **2**−**5**, and **2**−**6** assemblies.

24%, 28%, and 5%, respectively. The stearic (**2**−**4**) and oleic (**2**−**5**) acid based ionic materials absorb more energy while the **2**−**6** displays a higher strain response with low recovery similar to a liquid. To further investigate the phosphonium−carboxylate coordination on the viscoelastic properties, we replaced the oleic acid with oleyl alcohol, **7**. The resulting ionic material **2**−**7** was less viscous and more solidlike. This

dx.doi.org/10.1021/ma3002092 | *Macromolecules* 2012, 45, 2509−2513

observation was supported by the rheological measurements that showed going from **2**−**5** to **2**−**7** the *E* increased from 11 to 20.6 MPa and the phase angle decreased from 24° to 13.8°. In fact, a similar result was obtained by mixing **2** with DMSO at the same concentration. We attributed this change in material property to the oleyl alcohol acting as a solvent for **2** at high concentration. In contrast, when oleic or stearic acid is used, coordination to the phosphonium cation leads to a more organized state where the chains may be aligned imparting fluidity to the material. This type of structure has been previously observed with poly(acrylic acid)and alkylammonium[40] and poly(ethylenimine)−alkyl carboxylate[29] complexes that form lamellar bilayers with corresponding phase transitions.

Finally, the materials were investigated using differential scanning calorimetry (DSC) and small-angle X-ray scattering (SAXS). By DSC we observed a phase transition for **2**−**4** at 66 °C, which we attributed to packing of the stearic acid chains. However, no thermal transitions were observed for assemblies **2**−**3**, **2**−**5**, or **2**−**6**.

SAXS measurements for the **2**−**4** sample gave a lamellar structure with five sharp equally spaced Bragg reflections corresponding to a 3.9 nm lamellar repeat period (Figure 5).

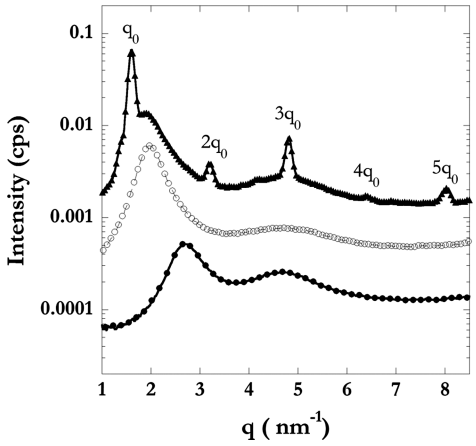


Figure 5. SAXS data for 2−4 (filled triangles), 2−5 (empty circles), and 2−3 (filled circles) assemblies. The initial scattered intensity was multiplied by a factor of 3 for the **2**−**5** sample and by a factor 9 for the **2**−**4** sample.

This lamellar repeat period, which was observed either at ambient humidity or under vacuum, was 0.5 nm greater than the lamellar repeat period previously observed for a PEI−stearic acid complex.[29] Since the polystrenyl polymer **2** should have a larger thickness than PEI, we propose that the structure of **2**−**4** is similar to the model reported for PEI:stearic acid,[29] with each layer composed of ionic sheets of **2** covering bilayers containing the highly tilted interdigited stearic chains of **4** (Figure 6). It is interesting to note that peak intensities of even order Bragg peaks ($2q_0$ and $4q_0$ peaks) were strongly reduced as compared to odd order peaks with the $5q_0$ peak being significantly more intense than the lower order $4q_0$ one. This feature, commonly observed in symmetrical block copolymer systems self-assembled into a lamellar structure,[41] can be attributed to a particular symmetry of the electron density profile in the periodic stacking, where the width of the electron-rich region ($\delta_H/2$), corresponding to benzyl phosphonium−carboxylate

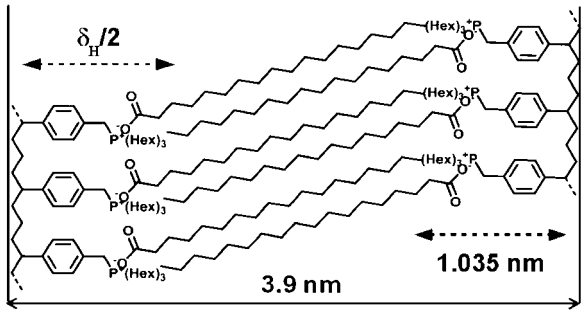


Figure 6. Illustration of the proposed lamellar structural model of **2**−**4** with each layer composed of ionic sheets of **2** containing the tilted hydrocarbon chains of **4**.

group, is close to half the stacking period (see structural model in Figure 6).

As evidenced in Figure 5, the SAXS data obtained for the **2**−**3** and **2**−**5** samples exhibited a diffuse scattering with **2**−**5** giving broad bands centered near q = 2 and 4.8 nm^{-1} and **2**−**3** giving broad bands near q = 2.7 and 4.8 nm^{-1}. The diffuse pattern from **2**−**5** was similar in shape to the diffuse scattering observed with system **2**−**4**. This diffuse scattering originates from the bilayer form factor contribution expected from the structural model proposed in Figure 6. That is, the characteristic shape of the diffuse scattering, including the low-angle intensity dip found at ca. 1 nm^{-1}, is accounted for by assigning a thickness of δ_H = 2.07 nm to the electron-rich domain of the bilayer and δ_T = 1.85 nm to the hydrocarbon region of the bilayer. We therefore propose that the **2**−**5** assembly has bilayers with similar geometric parameters as compared to the **2**−**4** assembly. As no Bragg reflections were observed, there was no long-range organization for the **2**−**5** assembly. Thus, we propose that **2**−**4** contains both well-ordered stacked arrays giving Bragg reflection as well as unordered bilayers giving diffuse diffraction, whereas **2**−**5** contains only unordered bilayers with no long-range organization so that only diffuse scattering is observed. The structure for **2**−**3** assembly is less clear, even though we did obtain a diffuse diffraction pattern. Unfortunately, it was not possible to obtain any structural information from the weak signal recorded with the **2**−**6** sample (data not shown).

■ CONCLUSION

In summary, we have synthesized a linear styrenylphosphonium polymer using free-radical polymerization. This polymer can be mixed with various anions to produce viscoelastic ionic assemblies or complexes with varying material properties. The mechanical properties of these ionic materials can be systematically varied through choice of the coordinating anion—an aliphatic dianion affords a more glassy-like, brittle material whereas an aliphatic monoanion gives a viscoelastic material. For one of the monoanion assemblies (stearic acid−polystyrenylphosphonium assembly), the SAXS data provide insight into the structure−property relationship as a lamellar-like structure is formed where the hydrocarbon chains are interdigitated but can flow past each other under an applied stress giving the viscoelastic properties. As this is the first report on these materials, additional studies are planned to better understand the trends in properties with composition (e.g., varying the M_w of the polymer) as well as the origins of the macroscopic mechanical properties. These results, in combination

dx.doi.org/10.1021/ma3002092 | *Macromolecules* 2012, 45, 2509−2513

with those reported by others, provide data that are critical to understanding these polyelectrolyte−surfactant materials as well as to manipulating the properties for a specific application. Continued research with new small molecule and macromolecular phosphoniums and their mixtures with mono- and multivalent anions will lead to new materials with interesting structural and rheological properties.

AUTHOR INFORMATION

Notes

The authors declare no competing financial interest.

ACKNOWLEDGMENTS

This work was supported by BU, the Advanced Energy Consortium http://www.beg.utexas.edu/aec/, NIH GM27278 (T.J.M.), and NSF CHE-1012464. L. Navailles and F. Nallet thank the Conseil général d'Aquitaine for financial support to purchase the X-ray diffraction device. The authors also thank Dr. M. Wathier for his discussions about these interesting materials.

REFERENCES

(1) Lehn, J. M. *Supramolecular Chemistry: Concepts and Perspectives*; VCH: Weinheim, 1995.
(2) Ikkala, O.; ten Brinke, G. *Science* **2002**, *295*, 2407−2409.
(3) Atwood, J. L.; Davies, J. E. D.; MacNicol, D. D.; Vögtle, F.; Lehn, J. M. *Comprehensive Supramolecular Chemistry*; Pergamon: Oxford, 1996.
(4) Brunsveld, L.; Folmer, B. J. B.; Meijer, E. W.; Sijbesma, R. P. *Chem. Rev.* **2001**, *101*, 4071.
(5) Serpe, M. J.; Craig, S. L. *Langmuir* **2007**, *23*, 1626−1634.
(6) Lehn, J. M. *Chem. Soc. Rev.* **2007**, *36*, 151−160.
(7) Corbin, P. S.; Zimmerman, S. C. In *Supramolecular Polymers*; Cifferi, A., Ed.; CRC Press: New York, 2005.
(8) Fouquey, C.; Lehn, J. M.; Levelut, A. M. *Adv. Mater.* **1990**, *2*, 254−257.
(9) Kato, T.; Kihara, H.; Kumar, U.; Uryu, T.; Frechet, J. M. J. *Angew. Chem., Int. Ed. Engl.* **1994**, *33*, 1644−1645.
(10) Zimmerman, N.; Moore, J. S.; Zimmerman, S. C. *Chem. Ind.* **1998**, *15*, 604−610.
(11) Pollino, J. M.; Weck, M. *Chem. Soc. Rev.* **2005**, *34*, 193−207.
(12) Sivakova, S.; Rowan, S. J. *Chem. Soc. Rev.* **2005**, *34*, 9−21.
(13) Lodge, T. P. *Science* **2008**, *321*, 50−51.
(14) Wathier, M.; Grinstaff, M. W. *J. Am. Chem. Soc.* **2008**, *130*, 9648−9649.
(15) Wathier, M.; Grinstaff, M. W. *Macromolecules* **2010**, *43*, 9529−9533.
(16) Antonietti, M.; Conrad, J.; Thünemann, A. F. *Macromolecules* **1994**, *27*, 6007−6011.
(17) MacKnight, W. J.; Ponomarenko, E. A.; Tirrell, D. A. *Acc. Chem. Res.* **1998**, *31*, 781−788.
(18) Goddard, E. D.; Ananthapadmanabhan, K. P. *Interactions of Surfactants with Polymers and Proteins*; CRC Press: Boca Raton, FL, 1993.
(19) Schmidt, M. *Polyelectrolytes with Defined Molecular Architecture II. Advances in Polymer Science*; Springer-Verlag: Berlin, 2004; Vol. *166*.
(20) Khandurina, Y. V.; Dembo, A. T.; Rogacheva, V. B.; Zezin, A. B.; Kabanov, V. A. *Polym. Sci. U.S.S.R.* **1994**, *36*, 189−194.
(21) Thünemann, A. F. *Prog. Polym. Sci.* **2002**, *27*, 1473−1572.
(22) Ruokolainen, J.; Torkkeli, M.; Serimaa, R.; Komanschek, E.; ten Brinke, G.; Ikkala, O. *Macromolecules* **1997**, *30*, 2002−2007.
(23) Ruokolainen, J.; Mäkinen, R.; Torkkeli, M.; Mäkelä, T.; Serimaa, R.; ten Brinke, G.; Ikkala, O. *Science* **1998**, *280*, 557−560.
(24) Valkama, S.; Ruotsalainen, T.; Nykanen, T.; Laiho, A.; Kosonen, H.; ten Brinke, G.; Ikkala, O.; Ruokolainen, J. *Macromolecules* **2006**, *39*, 9327−9336.
(25) Ruokolainen, J.; Tanner, J.; ten Brinke, G.; Ikkala, O.; Torkkeli, M.; Serimaa, R. *Macromolecules* **1995**, *28*, 7779−7784.
(26) Antonietti, M.; Maskos, M. *Macromolecules* **1996**, *29*, 4199−4205.
(27) Thünemann, A. F.; Lochhaas, K. H. *Langmuir* **1998**, *14*, 6220−6225.
(28) Antonietti, M.; Wenzel, A.; Thünemann, A. *Langmuir* **1996**, *12*, 2111−2114.
(29) Thunemann, A.; General, S. *Langmuir* **2000**, *16*, 9634−9638.
(30) Ren, B.; Cheng, Z.; Tong, Z.; Liu, X.; Wang, C.; Zeng, F. *Macromolecules* **2006**, *39*, 6552−6557.
(31) Kabanov, A. V.; Bronich, T. K.; Kabanov, V. A.; Yu, K.; Eisenberg, A. *J. Am. Chem. Soc.* **1998**, *120*, 9941−9942.
(32) Chen, L.; Xu, S.; McBranch, D.; Whitten, D. *J. Am. Chem. Soc.* **2000**, *122*, 9302−9303.
(33) Pace, G.; Tu, G. L.; Fratini, E.; Massip, S.; Huck, W. T. S.; Baglioni, P.; Friend, R. H. *Adv. Mater.* **2010**, *22*, 2073.
(34) Liu, Y.; Lloyd, A.; Guzman, G.; Cavicchi, K. A. *Macromolecules* **2011**, *44*, 8622−8630.
(35) Gandhavadi, M.; Allende, D.; Vidal, A.; Simon, S. A.; McIntosh, T. J. *Biophys. J.* **2002**, *82*, 1469−1482.
(36) Green, M. D.; Long, T. E. *Polym. Rev.* **2009**, *49*, 291−314.
(37) Chen, H.; Choi, J.-H.; Salas-de la Cruz, D.; Winey, K. I.; Elabd, Y. A. *Macromolecules* **2009**, *42*, 4809−4816.
(38) Matsumi, N.; Sugai, K.; Miyake, M.; Ohno, H. *Macromolecules* **2006**, *39*, 6924−6927.
(39) Cheng, S.; Beyer, F. L.; Mather, B. D.; Moore, R. B.; Long, T. E. *Macromolecules* **2011**, *44*, 6509−6517.
(40) Antonietti, M.; Neese, M.; Blum, G.; Kremer, F. *Langmuir* **1996**, *12*, 4436−4441.
(41) Hashimoto, T.; Shibayama, M.; Kawai, H. *Macromolecules* **1980**, *13*, 1237−1247.

Macromolecules

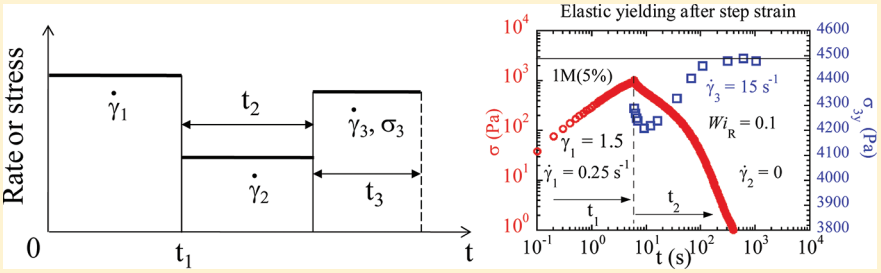
Article

pubs.acs.org/Macromolecules

Characterizing State of Chain Entanglement in Entangled Polymer Solutions during and after Large Shear Deformation

Yangyang Wang, Xin Li, Xiangyang Zhu, and Shi-Qing Wang*

Department of Polymer Science and Maurice Morton Institute of Polymer Science, University of Akron, Ohio 44325, United States



ABSTRACT: Using four entangled 1,4-polybutadiene solutions as model systems, we carry out rate-switching startup shear and elastic recovery tests to probe the state of chain entanglement during startup continuous shear and after shear cessation, respectively. Specifically, we apply a second startup shear of higher rate either during the first startup shear or after cessation of the first shear. The nonmonotonic response (overshoot) to the startup shear is evaluated to elucidate the effect of any preceding shear on the entanglement structure. In a second type of experiments, at different strains during and after shear or relaxing for a certain amount of time after shear cessation we set the shear stress free to determine the amount of elastic recoil, which can also reveal the status of chain entanglement interactions. Consistent with the emerging theoretical interpretations, these multistep rheometric procedures allow us to learn more about (a) elastic yielding during relaxation after cessation of shear that is produced at a low rate, (b) existence of a critical strain amplitude for the elastic yielding, (c) nonmonotonic evolution of the chain entanglement upon startup shear, and (d) yielding of the entanglement network at the point of shear stress overshoot.

I. INTRODUCTION

Entanglement interactions, arising from uncrossibility of chain backbone bonds, play a central role in governing dynamics and rheology of high-molecular-weight polymers. It has long been recognized that entangled polymers can be treated as transient elastic networks on short time scales.[1−3] It is also well-known from experiment that the flow state is reached more quickly for a higher imposed rate of shear. In the past five decades, various theoretical attempts have been made to rationalize the nonlinear responses of entangled polymers to fast large deformations. Some are based on continuum mechanical principles, and others are microscopic in origin. The most notable and successful molecular theory for entanglement dynamics is the tube model.[4−7]

Apart from conventional rheometric measurements, particle tracking velocimetric (PTV) measurements of polymer melts and solutions have recently proven very useful and insightful in the development of alternative interpretations of nonlinear responses of entangled polymers. In particular, the observed shear banding during startup shear[8,9] and nonquiescent relaxation after interrupted shear in well-entangled polymer solutions and melts[10−12] indicated that the entanglement network can suffer strain localization on time scales much shorter than the reptation time. In other words, upon startup shear, the samples showed inhomogeneous deformation after the shear stress maximum (overshoot), and after shear cessation the samples displayed macroscopic motions indicative of a massive breakdown of the entanglement network. Therefore, even entangled solutions and melts with an unimpressively short relaxation time appear to display nonlinear rheological behavior reminiscent of yielding phenomena widely observed of solids under large deformation. Upon continuous deformation of solids that has a practically infinitely long relaxation time, yielding often results in strain localization or failure. Thus, these PTV measurements of shear inhomogeneity have led us to suggest that the stress overshoot upon startup shear is a yield point, reflecting a moment of transition from elastic (recoverable) deformation to flow (irrecoverable deformation).

Yield is a phenomenological concept widely used to describe the transition from elastic defomation to plasticity in both hard and soft solids. Specifically, the notion of "yield" is frequently invoked in the literature[13] on colloidal dispersions, gels, and filled polymers. Rheologists rarely speak of yielding for unfilled polymeric liquids: Because of the existence of the terminal flow regime, nobody regards entangled polymer solutions and melts as yield-stress materials that are solidlike yet capable of flow at high enough stresses. But strongly viscoelastic liquids including well-entangled polymers actually do belong to the class of yield-stress materials if we broaden the definition to recognize the fact that these liquids can be forced to undergo flow on time

Received: November 10, 2011
Revised: February 8, 2012
Published: February 17, 2012

 © 2012 American Chemical Society dx.doi.org/10.1021/ma2024842 | *Macromolecules* 2012, 45, 2514−2521

scales much shorter than the dominant relaxation time (reptation time τ in the case of entangled polymers). In other words, the concept of yielding becomes relevant to non-cross-linked polymer liquids if they start to flow on time scales much shorter than τ. Macroscopic flow indeed takes place in entangled polymers beyond the stress overshoot at time $t_y \ll \tau$ upon startup shear (at $t = 0$)[14] when full elastic recovery is no longer possible.[15,16] Moreover, it is convenient to take a broad viewpoint that yielding does not have to result in strain localization. For many viscoelastic materials where the elastic state is not greatly different from the yielded state in terms of their mechanical characteristics, yielding, i.e., the transition from elastic deformation to flow, can take place homogeneously. Our present systems are such an example.

According to our picture,[17,18] yielding of the entanglement network upon fast startup deformation is plausibly due to an imbalance between the elastic retraction force and the intermolecular gripping force (arising from the chain uncrossability). On the other hand, after a large stepwise strain, the residual elastic retraction force, i.e., the tension within an entanglement strand, can be higher than the confining force (so-called entanglement force[17]) that keeps the strand localized in the network in quiescence. This force imbalance could also cause the network to rearrange on time scales shorter than the reptation time. In both cases, the yielding is caused by chain disentanglement via mutual chain sliding, in our view. The idea to associate chain disentanglement with the origin of stress decline beyond the overshoot deviates from the tube model description that could simply depicts the overshoot as a consequence of chain alignment. Thus, there are now at least two competing microscopic pictures for the macroscopic yielding phenomenon of stress overshoot. It is expected that future computer simulations may elucidate the molecular process in sufficient detail to differentiate the two scenarios.

Even before any proposal was made to suggest the overshoot as a yielding characteristic,[17,18,15,16] the features of stress overshoot have already been used[19] to probe the relaxation behavior following shear cessation from steady flow. Allowing different amounts of resting time before the same shear rate was reapplied, Menezes and Graessley[14] could identify the relaxation dynamics in terms of when the second startup shear produced the same overshoot stress as observed from an equilibrium sample. Double-step strain experiments[20] have also been carried out to test the then-relatively new Doi–Edwards tube model in absence of any PTV observations.[21] Along the line of Menezes and Graessley, Robertson et al.[22] associated the stress peak σ_y with the entanglement density and showed that it took a healing time much longer than the terminal relaxation time τ for the equilibrium entanglement structure to be restored after steady shear with Weissenberg number $Wi > 1$ (which is the product of nominal shear rate $\dot{\gamma}$ and τ, i.e., $Wi = \dot{\gamma}\tau$). These authors interpreted the weaker overshoot as indicating a less entangled state than the equilibrium state. It has also been shown that the elastic response to a suddenly superimposed step shear during steady shear weakens with increasing rate of the underlying steady shear.[23]

In the present work, we further study how the state of chain entanglement changes under different shearing conditions. In particular, the nonequilibrium state of entanglement will be probed by either measuring the overshoot response to a fast startup shear or determining the ability of the deformed sample to undergo elastic recovery. Unlike the previous PTV studies that focused on shear strain localization, the present experimental systems are designed to avoid shear inhomogeneity based on principles discussed elsewhere.[24,25]

II. EXPERIMENTAL SECTION

A. Protocol. Stress overshoot during startup shear is a salient feature of well-entangled polymer melts[16,26−29] and solutions.[14,30−34] In previous studies, upon a startup shear of an equilibrium sample, the stress maximum σ_y and the corresponding strain γ_y have been found to obey specific scaling laws.[15,16] Our experimental protocol is based on the observations that the stress overshoot has important characteristics. In particular, the magnitude of the overshoot σ_y correlates with the strength and degree of intermolecular interactions, i.e., the state of chain entanglement. In the past, interrupted-shear measurements have been widely used to investigate the time-dependent recovery of chain entanglement after steady shearing.[14,19,22] Specifically, after a certain period of relaxation from steady shear, the reapplied startup shear produces a stress overshoot whose magnitude approaches σ_y only when the relaxation period is sufficiently long, i.e., many times longer than the reptation time τ.[22]

We also note that the ability of entangled polymers to undergo elastic recoil toward its original un-deformed state after deformation[35−38] is another indicator of how much change has occurred in the structure of the entanglement network. In other words, the degree of elastic recovery reflects how much the entanglement network remembers its original state, which depends on how much relaxation has occurred and how much the network has been altered by the external straining.

The preceding discussion leads to the protocols of the present study that can be generically depicted as shown in Figure 1. After shearing at the first rate of $\dot{\gamma}_1$ for a period of t_1, which could represent either an interrupted startup shear or startup shear to steady state, the entanglement state of the sheared sample is immediately (setting $t_2 = 0$) probed by either another startup shear at rate $\dot{\gamma}_3$ that is higher or elastic recovery measurement with $\sigma_3 = 0$. In a second scenario, after shearing at $\dot{\gamma}_1$ for t_1, the sample is allowed to relax either in quiescence (setting $\dot{\gamma}_2 = 0$) or at a reduced rate $\dot{\gamma}_2 < \dot{\gamma}_1$ for a finite amount of time t_2 before this relaxing sample is probed in the third zone with either startup shear or elastic recovery.

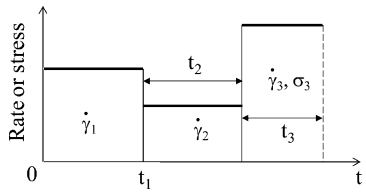


Figure 1. Schematic illustration of the generic protocol used in the present work, showing the first shear at rate $\dot{\gamma}_1$ is followed by either one (setting $t_2 = 0$) or two subsequent modes of shear, where the third stage can be an elastic recovery test upon setting $\sigma_3 = 0$.

The protocol depicted in Figure 1 can be readily implemented in a modern rheometer. Specifically, all the rheological measurements were carried out at 25 °C using a controlled-torque rheometer (Physica MCR-301, Anton Paar USA) in a cone–plate assembly involving a 25 mm diameter and 2° cone angle.

B. Materials. This investigation is based on four entangled 1,4-polybutadiene (PB) solutions. The parent PBs of these solutions were synthesized via anionic polymerization at the University of Akron and Bridgestone-Americas Center for Research and Technology. Their average molecular weights and distributions are presented in Table 1.

Table 1. Molecular Characteristics of High-MW Polybutadienes

sample	M_n (kg/mol)	M_w (kg/mol)	M_w/M_n	source
0.7M	0.74×10^3	0.75×10^3	1.01	Bridgestone
1M	1.01×10^3	1.05×10^3	1.04	University of Akron
2.6M	1.69×10^3	2.60×10^3	1.54	Bridgestone

dx.doi.org/10.1021/ma2024842 | Macromolecules 2012, 45, 2514−2521

Based on the three parent PBs, four entangled solutions were prepared using four different low-molecular-weight polybutadienes as "solvent" whose molecular characteristics are listed in Table 2.

Table 2. Molecular Characteristics of Low-MW Polybutadienes

sample	M_n (kg/mol)	M_w (kg/mol)	M_w/M_n	source	η_s (Pa·s)
1.8K	1.8			Sigma-Aldrich[a]	97[b]
9K	7.0	9.0		Bridgestone	8.7
10.5K	8.9	10.5	1.18	Bridgestone	14
18K	16.0	18.0	1.13	Bridgestone	96

[a]# 20,043-3. [b]This oligomeric polybutadiene has high vinyl content and, thus, much higher T_g and significantly greater viscosity.

The entangled solutions were prepared by first dissolving the parent ultrahigh molecular weight polybutadiene in a mixture of the low-MW polybutadiene solvent and toluene (cosolvent). Most of the toluene was evaporated slowly under a hood, and the rest was removed in a vacuum oven at room temperature. Table 3 summarizes the linear viscoelastic properties of these solutions, which were evaluated from small-amplitude oscillatory shear measurements, where the numbers in the parentheses of the samples' names indicate the weight fraction ϕ of the high-molecular-weight PBs and the numbers after the hyphens represent the types of polymeric solvents. The terminal relaxation time τ is taken as the reciprocal frequency where storage G' and loss G'' moduli are equal. We estimate the Rouse relaxation time τ_R according to the Osaki formula:[39]

Table 3. Properties of Entangled Solutions

sample	τ (s)	G_{pl} (Pa)	Z	η (kPa·s)	b (mm)
0.7M(5%)-1.8K	23	892	13	20	0.005
1M(5%)-10.5K	22	1000	18	18	0.03
2.6M(3%)-9K	190	180	26	10	0.04
1M(10%)-18K	59	4700	41	190	0.03

$$\tau_R = \frac{6M\eta}{\pi^2 cRT}\left(\frac{M_c}{M}\right)^{2.4} \quad (1)$$

where η is the zero-shear viscosity, c is the polymer concentration equal to $\rho\phi$, where ρ is the mass density of the pure polymer, and ϕ is the polymer weight fraction. Here M_c is the critical molecular weight for entanglement to be taken as twice the entanglement molecular weight $M_e(\phi)$, which can be estimated according to $M_e(\phi) = M_e\phi^{-1.2}$. Taking M_e = 1.5 kg/mol, we have $M_e(5\%)$ = 55 kg/mol, so that the Rouse relaxation time for the 1M(5%)-10.5K solution is estimated to be around τ_R = 0.45 s. The plateau modulus G_{pl} of the solution is either taken as the value of the storage modulus $G'(\omega)$ at the inflection point of the frequency sweep curve or using MAX method.[40] The number of entanglement per chain Z is estimated as $Z = M_w/M_e(\phi)$. The extrapolation (slip) length $b = l_{ent}(\eta/\eta_s)$ of these solutions is estimated to be on the order of 0.03 mm or lower, where the entanglement spacing $l_{ent}(\phi)$ is 17 nm for the 10% solution, 26 nm for the 5% solution, and 35 nm for the 3% solution. This value of b is small relative to the size of the rheometer gap around 1 mm because of the use of these polymeric solvents. As a consequence, wall slip and bulk shear banding are negligible both during startup shear and after shear interruption. In other words, homogeneous shear and quiescent relaxation would prevail in these samples. This expectation was indeed confirmed by our separate particle tracking velocimetric observations, in agreement with a recently published study.[24]

III. EXPERIMENTAL RESULTS

A. State of Entanglement Characterized by Stress Overshoot. *A.1. Startup Continuous Shear (t_2 = 0 in Figure 1).* We first probe the structure of an entangled solution during a startup shear at different stages by observing how the strained sample responds to imposition of a higher rate of shear. For example, we apply the protocol given in Figure 1 with $t_2 = 0$ and $\dot\gamma_3 \gg \dot\gamma_1$. Figure 2a shows the characteristic responses of a sheared 1M(5%) sample under the rate of 0.3 s^{-1} at different moments to a subsequent startup shear produced at 3.0 s^{-1}. There are 10 discrete rate-switching tests, expressed in Figure 2a. In Figure 2b, we show how the peak stress (σ_{3y}) as well as the elastic modulus level (G_{int}) first decreases during the first startup shear. Similar behavior is observed for the 2.6M(3%) solution as shown in a different representation in Figure 3. For completeness

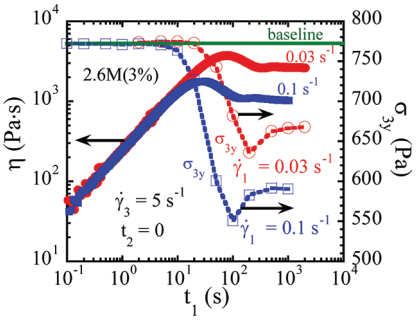


Figure 3. Plots of the peak shear stress σ_{3y} (*Y*-axis on the right-hand side) arising from the rate switching to 5 s^{-1} at the different times during startup shear at the two rates of 0.03 and 0.1 s^{-1} for 2.6M(3%). Shown against the left-hand-side *Y*-axis is the transient viscosity as a function of shearing time t_1. Here the horizontal straight baseline represents the peak stress resulting from a startup shear at 5.0 s^{-1} on a fully equilibrated sample.

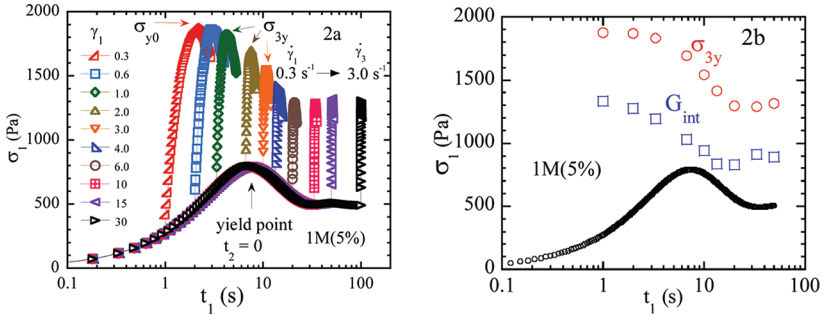


Figure 2. (a) Stress responses to the rate switch from 0.3 to 3.0 s^{-1} at different stages upon the startup shear with $\dot\gamma_1$ = 0.3 s^{-1} for the 1M(5%) solution, where σ_{y0} denotes the overshoot associated with startup shear on the equilibrium sample. (b) The peak stress σ_{3y} associated with the subsequent rate of 3.0 s^{-1}, along with the stress vs time curve due to the first startup at 0.3 s^{-1}. Also plotted is the initial modulus that characterizes the stress growth upon the rate switch, defined as $G_{int} = (d\sigma_3/d\gamma_3)|_{t_3\to 0}$, where $\gamma_3 = \dot\gamma_3 t_3$.

dx.doi.org/10.1021/ma2024842 | Macromolecules 2012, 45, 2514–2521

and to show universality, we summarize eight sets of such experiments in Figure 4. We note four features as follows.

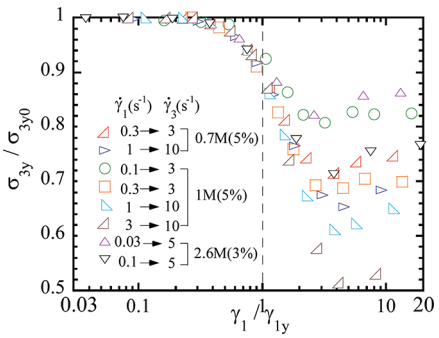


Figure 4. Eight plots of the normalized peak shear stress as a function of the normalized imposed strain, for three different samples sheared under the conditions specified in the figure.

(a) Up to the shear stress maximum γ_{1y}, labeled as "yield point"[17,18] in Figure 2a, the variation with the elapsed strain γ_1 of the overshoot σ_{3y} (associated with $\dot{\gamma}_3$) falls onto a master curve when represented by normalization with the overshoot σ_{3y0} measured from the equilibrium sample. The evidence to justify the use of the phrase "yield point" will be presented in a following subsection III.B.1. (b) The decline of σ_{3y} occurs steeply beyond γ_{1y} and stabilizes at strains typically more than ten times the yield strain γ_{1y}. (c) Many sets of the data show a minimum in the σ_{3y} vs γ_1 plot, which is also evident from Figure 3. (d) In the limit of high strain toward steady state, σ_{3y} decrease monotonically with the first rate $\dot{\gamma}_1$.

Probing the last feature in some more detail, Figure 5 describes the peak values of the stress overshoot upon the subsequent startup shear

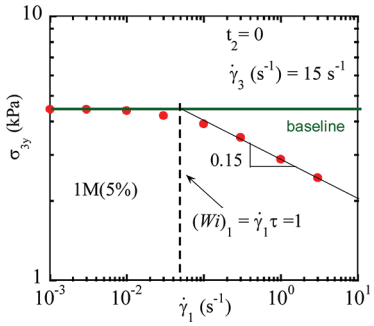


Figure 5. Peak shear stress upon the sudden rate switching to 5 s^{-1} from the various steady states corresponding to the various values of $\dot{\gamma}_1$.

at $\dot{\gamma}_3 = 15\ s^{-1}$ after the first shear at the various rate $\dot{\gamma}_1$ has reached the steady state. We note that the significant drop occurs only when $(Wi)_1$ is beyond unity. Since σ_{3y} probes the strength of the entanglement network, it is reasonable to expect it to be proportional to the effective plateau modulus $G_{pl}(\dot{\gamma}_1)$. The measurable drop of this modulus with the applied rate is consistent with the previous characterization of the steady state.[41] Assuming that the entanglement molecular weight $M_e(\dot{\gamma}_1)$ of the effective network is related to G_{pl} reciprocally, Figure 5 would indicate that $M_e(\dot{\gamma}_1) \sim \dot{\gamma}_1^{0.15}$.

A.2. Relaxation after Cessation from Steady Shear or Finite Shear ($t_2 \neq 0$ and $\dot{\gamma}_2 = 0$). The generic protocol of Figure 1 has also been applied to follow the evolution of a sheared sample toward recovery to equilibrium. Specifically, with $\dot{\gamma}_2 = 0$ for a finite t_2 in Figure 1, as a function of the time t_2 of relaxation or healing, we show in

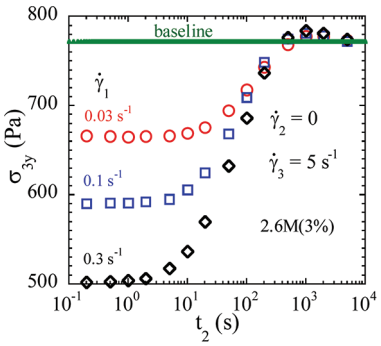


Figure 6. Peak shear stress as a function of the relaxation time t_2 from steady state produced at three respective values of $\dot{\gamma}_1$.

Figure 6 how the stress overshoot associated with $\dot{\gamma}_3 = 5\ s^{-1}$ for the sample of 2.6M(3%) improves as the sheared sample relaxes after shear cessation from steady state for three values of $\dot{\gamma}_1$. It is remarkable and unusual that during the recovery toward equilibrium the system attained a transient state of chain entanglement that responded to the startup shear of $\dot{\gamma}_3 = 5\ s^{-1}$ with an overshoot slightly higher than that produced from the equilibrium state.

After reaching steady state, if the applied rate is stepped down to a lower value, the system would take some time before re-establishing steady state corresponding to the new applied rate. As shown in Figure 7a, the shear stress actually shows a minimum after the rate switching at $t_2 = 0$. The nature of the stress dip can be clarified by applying the protocol of Figure 1. Figure 7b shows how the sample responds, during the different stages corresponding to the different values of t_2 in Figure 7a, to the third rate of $\dot{\gamma}_3 = 5\ s^{-1}$, where the case of shear cessation is also included for comparison. During the stress decline seen in Figure 7a, the state of chain entanglement only heals toward the equilibrium state as the chain retracts to reduce the elastic retraction force that is responsible for the measured stress.

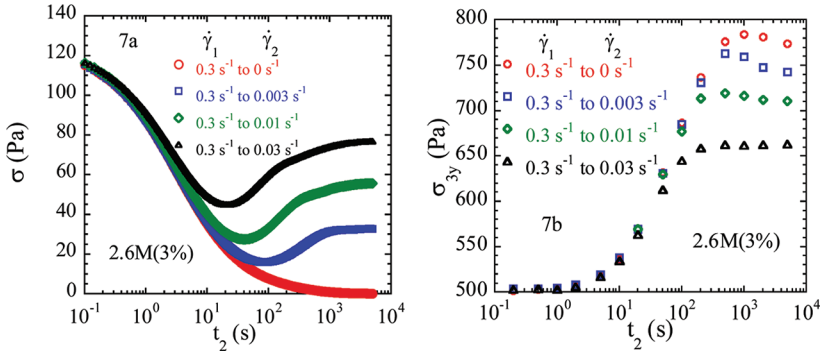


Figure 7. (a) Shear stress as a function of time t_2 after switching from steady state produced at $\dot{\gamma}_1$= 0.3 s^{-1} to the various lower rates of 0.03, 0.01, and 0.003 s^{-1} as well as 0 s^{-1}. (b) Peak shear stress σ_{3y} resulting from the sudden application of a high rate of 5 s^{-1} at the various moments during the "relaxation" depicted in (a).

dx.doi.org/10.1021/ma2024842 | Macromolecules 2012, 45, 2514–2521

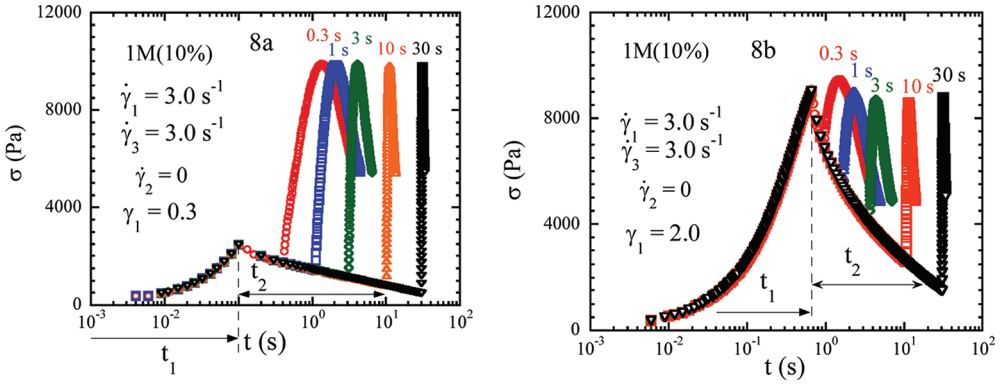


Figure 8. (a) Discrete stress overshoot resulting from application of a sudden startup shear at different relaxation stages after a stepwise strain of $\gamma_1 = 0.3$, where the time t_2 of relaxation is indicated to be 0.3, 1, 3, 10, and 30 s, respectively. Also plotted is the stress growth and relaxation during and after the step shear. The peak shear stress shows no dependence on t_2. (b) Discrete stress overshoot resulting from application of a sudden startup shear at different relaxation stages after a stepwise strain of $\gamma_1 = 2.0$. Also plotted is the stress growth and relaxation during and after the step shear. The peak stress σ_{3y} declines during relaxation before rising toward the baseline of σ_{y0} at long times.

The same protocol can be applied to learn about the relaxation behavior after a step shear. As a reference point, we first examine stress relaxation in the linear response regime. After a small stepwise strain of $\gamma_1 = 0.3$, the relaxation process is examined using five discrete sets of rate combination as shown in Figure 8a. The same overshoot values imply the entanglement structure is unchanged from that of the equilibrium state during the relaxation. The phenomenon is different upon a large step shear of $\gamma_1 = 2.0$: Figure 8b shows a drop in the stress overshoot during the quiescent relaxation. We verify that this is even true for a large (slow) stepwise strain that is produced at a rather low rate: Figure 9 shows a minimum in σ_{3y} during relaxation from a slow

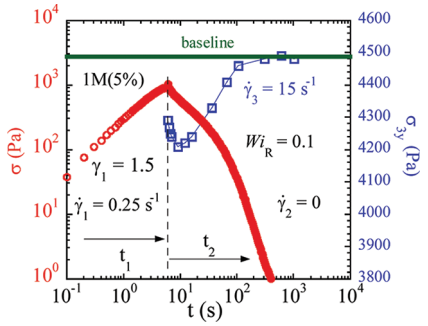


Figure 9. Stress growth and relaxation during and after a slow stepwise strain of $\gamma_1 = 1.5$, along with the stress overshoot values in squares against the right-hand-side *Y*-axis resulting from application of a high rate of 15 s^{-1} during the relaxation stage. Note that the rate used to produce the slow stepwise strain is only 0.25 s^{-1} corresponding to $Wi_R = 0.1$.

stepwise strain of $\gamma_1 = 1.5$ produced with $\dot{\gamma}_1 = 0.25\ s^{-1}$. Since the Rouse relaxation time τ_R for this 1M(5%) solution is 0.45 s, this rate corresponds to the Rouse–Weissenberg number $Wi_R = \dot{\gamma}\tau_R \sim 0.1$.

B. State of Entanglement Probed by Elastic Recovery Test. *B. 1. Startup Continuous Shear ($t_2 = 0$ and $\sigma_3 = 0$ in Figure 1).* We can probe in a different manner whether and how the state of polymer entanglement has been altered from the equilibrium state during startup shear. This involves setting the sheared sample stress free at different stages along the pathway during the startup shear as indicated in Figure 10a. The protocol can be characterized by setting $t_2 = 0$ and $\sigma_3 = 0$ in Figure 1. The ability of the strained sample to undergo elastic recovery is depicted in Figure 10b, where the strain $\gamma(t_3)$ denotes the position of the sample relative to the initial state ($t_1 = 0$) as a function of the recovery time t_3, so that the full recovery corresponds to $\gamma(t_3)$ approaching 0 at long times.

We can summarize such data as shown in Figures 10a,b for several different applied rates on two different samples. Specifically, Figure 11 shows that the elastic recovery is nearly complete as long as the applied shear has not reached the stress maximum located at the elapsed strain of γ_{1y}. Conversely, beyond the maximum, the level of elastic recovery drops sharply. Figure 11 is consistent with the previous conclusion[15] that irreversible deformation, i.e., flow, occurs, when the sample is sheared beyond the stress maximum with $\dot{\gamma}_1\tau_R > 1$ or when sheared at $\dot{\gamma}_1\tau_R < 1$ for a period longer than τ_R. Since no shear banding is observed during the startup shear either before or after the overshoot, Figure 11 shows that the yielding can occur without strain inhomogeneity for moderately entangled polymer solutions.

B. 2. Relaxation after Cessation from Step Shear ($t_2 \neq 0$, $\dot{\gamma}_2 = 0$, and $\sigma_3 = 0$ in Figure 1). We can apply the protocol of the elastic recovery to examine how the state of entanglement relaxes or changes after a stepwise strain. Instead of the setting $t_2 = 0$ as done in Figure 11, we allow the sheared sample to relax for different amounts of time t_2. In other words, we set $\dot{\gamma}_2 = 0$ for different values of t_2. Figure 12 shows the degree of elastic recovery for different levels of stepwise strain as a function of the resting time t_2, normalized by the reptation time τ. The ability to undergo elastic recovery declines with increasing resting time, as expected, although the particular quantitative dependence might have been unknown until now. It is clear that up to an imposed strain of unity ($\gamma \sim 1.0$) the samples show essentially the same level of elastic recovery independent of the strain amplitude for the various resting times. However, beyond $\gamma = 1.0$, the extent of elastic recovery suddenly drops as a function of the imposed strain γ_1.

IV. DISCUSSION

The present work aims to interrogate the state of polymer entanglement during or after a significant amount of shear. For well-entangled polymers, particle tracking velocimetric (PTV) observations revealed strain localization after shear cessation.[10−12] The phenomenon is challenging to describe within the framework of the tube theory.[42] The present samples have been carefully designed to avoid strain localization according to a well-understood rationale.[24] In other words, as confirmed by our PTV observations, only homogeneous deformation prevails upon startup shear and quiescent relaxation occurs after shear cessation in the present experimental systems. Therefore, it is hoped that theoretical calculations either based on the tube model or from first principles[43,44] can be made in the near future to compare with the current experimental data. Below we would like to offer our subjective explanations and comments regarding these new experimental results.

dx.doi.org/10.1021/ma2024842 | *Macromolecules* 2012, 45, 2514−2521

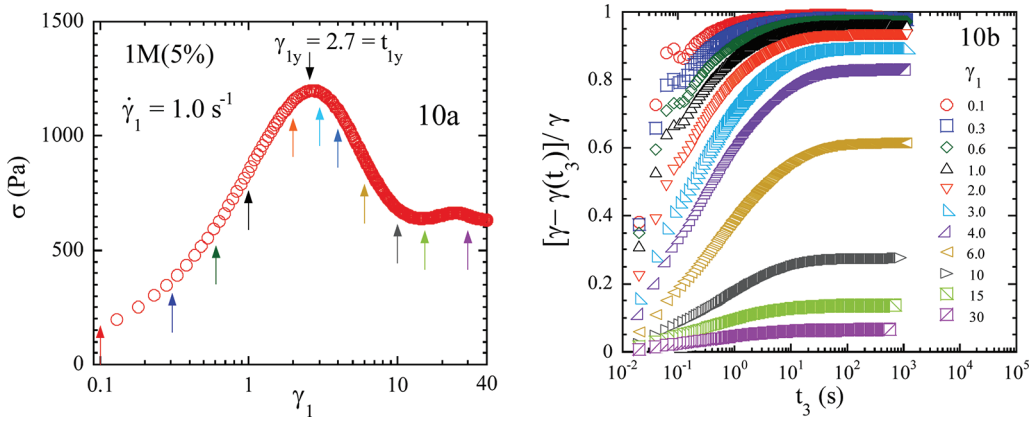


Figure 10. (a) Shear stress as a function of time during a startup shear at 1 s^{-1} for the 1M(5%) solution, where the vertical arrows indicate the different stages in the discrete elastic recovery experiments when the sample is set stress free. (b) Elastic recovery measurements after shearing for the different amounts of strain γ_1 as indicated in (a), following the protocol depicted in Figure 1 ($t_2 = 0$ and $\sigma_3 = 0$).

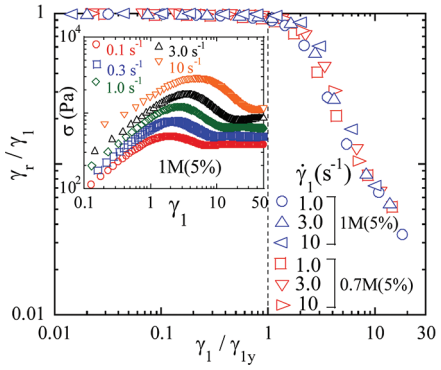


Figure 11. Summary of the elastic recovery measurements after startup shear for the 0.7M(5%) and 1M(5%) solutions, following the protocol of Figure 1 ($t_2 = 0$ and $\sigma_3 = 0$). The applied strain γ_1, at which the recovery experiment was performed, is normalized by the yield strain γ_{1y} corresponding to the shear stress peak produced by the startup shear of $\dot{\gamma}_1$. The inset shows in the case of 1M(5%) the shear stress as a function of the elapsed strain γ_1 for the five discretely applied rates.

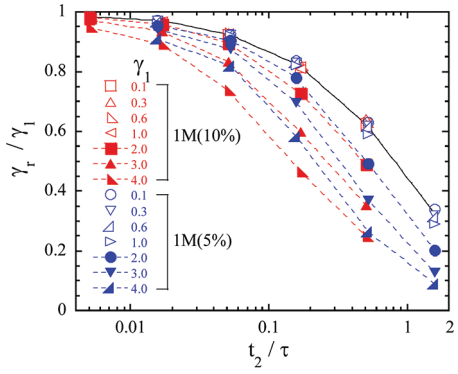


Figure 12. Summary of the ultimate elastic recovery as a function of the normalized resting time t_2/τ for the 1M(5%) and 1M(10%) solutions, where τ is the terminal relaxation time of each sample. Different symbols represent the various amplitudes γ_1 of step shear. The protocol is depicted by Figure 1 with $\dot{\gamma}_2 = 0$ and $\sigma_3 = 0$.

First, we note that the feature of reduced peak stress revealed systematically in Figure 4 may be numerically captured by sophisticated constitutive models such as the K-BKZ equation.[45,46] However, such a continuum mechanical model cannot describe the molecular origin of the declined peak stress. Just because the original Doi–Edwards theory[4] is of the same mathematical form as the K-BKZ equation, it does not mean we can be satisfied with the available molecular level theoretical description. In particular, the DE theory prescribes the stress maximum as originating from a monotonic increase in chain alignment leading to a nonmonotonic contribution to the shear stress. In contrast, we regard the stress overshoot as an indication of chain disentanglement and believe that the peak stress depends on the state of chain entanglement, i.e., specific topogical relationship among the flexible linear chains.

Most importantly, Figures 8b and 9 seem to suggest that there emerged a weaker state of chain entanglement after shear cessation. In other words, during the quiescent relaxation from a large stepwise strain, the entanglement network appeared to deteriorate because the relaxing sample responded to a subsequent startup shear of high rate with lower stress overshoots, before recovering at the later times the response corresponding to the equilibrium state. This behavior contrasts sharply with the essentially monotonic rise of σ_{3y} after shear cessation from steady state as shown in Figure 7b. Such a nonmonotonic change in the state of entanglement during relaxation even occurs as shown in Figure 9 when the stepwise strain is produced at a rate too low to cause chain stretching (according to the tube model). In our view, even such a slowly imposed strain can produce a sufficiently high elastic retraction force attributable to chain stretching so that the confining entanglement force can be overcome. Chain disentanglement can occur in the sense that the strands would slide past one another after shear cessation to cause rearrangement of the entanglement network on time scales much shorter than the terminal relaxation time τ. This process of elastic yielding[17] may produce a temporarily weaker state of chain entanglement.

Figure 12 also reveals something remarkable about the relxation behavior after a large stepwise strain. Here we evaluate the ability of the sample to undergo elastic recoil, which is a indicator to show how a strained sample remembers its initial state. Up to a strain of amplitude equal to 100%, the strained system retains its ability to undergo elastic recoil (ER), as indicated by the open symbols in Figure 12. The degree of ER of course drops with longer resting time t_2. At a fixed time t_2 after shear cessation, a significantly reduced elastic recovery appears only when the imposed stepwise strain γ_1 is higher than 1.0 as shown by the filled symbols in Figure 12. In other words, the sample appears to remain essentially intact as long as the imposed

dx.doi.org/10.1021/ma2024842 | Macromolecules 2012, 45, 2514–2521

strain is not high enough. We interpret this as another piece of evidence that offers support for the idea of finite cohesion associated with an entanglement network.[17]

Furthermore, the change in the topological chain packing during a startup shear is apparently nonmonotonic as shown in Figures 3 and 4: For example, reading from the open blue squares in Figure 3 (corresponding to $\dot{\gamma}_1 = 0.1\ s^{-1}$), we see that after shearing for $t_2 = 100$ s, near the end of the stress decline, the sample responded to the startup shear of $\dot{\gamma}_2 = 5\ s^{-1}$ with the lowest level of overshoot.

Finally, the fact that a signficant overshoot emerges upon the rate switching after steady shear of the first rate to a higher value in Figure 2a elucidates an important concept: In the steady shear state of $\dot{\gamma}_1 = 0.3\ s^{-1}$ there is no chain entanglement in the sense that chains are constantly sliding past one another on the time scale comparable to the reciprocal shear rate as evidenced by superimposed SOAS and small stepwise strain tests.[41] On the other hand, the emergence of a stress maximum (right-hand-side pointed black triangles) due to the application of the higher rate of $3.0\ s^{-1}$ in steady state ($t_1 \sim 100$ s) in Figure 2a confirms that chain entanglement is present when probed in the manner described herein, i.e., when explored using a much higher rate. Therefore, the concepts of chain entanglement and disentanglement must be generalized: they are defined relative to a given rate on a given time scale. To reiterate, in steady state, any given chain would constantly slide past its surrounding chains over a time scale on the order of the reciprocal shear rate. Unless this steady state is examined on much shorter time scales, the system would no longer appear to be a network. In passing, we note, as shown in Figure 2b, that the state of chain entanglement gradually deteriorates as the system is brought past the stress overshoot, with the weakest point located around where the first stress nears the completion of its decline. The change in the entanglement network by the imposed shear is also reflected in the characteristic that the response of the sheared sample is softer to the sequent high rate of shear as shown in Figure 2b by the squares.

V. CONCLUSION

The rate switching and elastic recovery tests allow us probe the state of chain entanglement during startup shear and after step shear. Specifically, (a) there is evidence to support the idea that elastic yielding, i.e., chain disentanglement after step shear, would only occur for a stepwise strain of sufficient amplitude, consistent with the concept that there is a finite level of cohesion associated with chain entanglement.[17] (b) The level of chain entanglement interactions can decline during relaxation from a large stepwise strain even though the slow stepwise strain is produced with a rate satisfying $Wi_R \ll 1$. (c) The physical origin of stress overshoot may correspond to chain disentanglement[17,18] because the entanglement network shows significantly reduced elastic recovery only after getting sheared beyond the shear stress maximum. While we look forward to future tube-model-based calculations to compare with the present data, we note that a molecular level treatment of entangled rigid rods has emerged and claimed to have identified the mechanisms for dynamic yielding and chain delocalization upon large shear deformation.[43,44]

AUTHOR INFORMATION

Corresponding Author

*E-mail: swang@uakron.edu.

Notes

The authors declare no competing financial interest.

ACKNOWLEDGMENTS

This work is supported, in part, by a grant (DMR-0821697) from the National Science Foundation. We are grateful to Xiaorong Wang and Chris Robertson at Bridgestone-Americas for providing some of the polybutadiene melts used in this work.

REFERENCES

(1) Green, M. S.; Tobolsky, A. V. *J. Chem. Phys.* **1946**, *14*, 80.
(2) Lodge, A. S. *Trans. Faraday Soc.* **1956**, *52*, 120.
(3) Yamamoto, M. *J. Phys. Soc.* **1956**, *11*, 413.
(4) Doi, M.; Edwards, S. F. *The Theory of Polymer Dynamics*; Oxford University Press: Oxford, 1986.
(5) Watanabe, H. *Prog. Polym. Sci.* **1999**, *24*, 1253.
(6) McLeish, T. C. B. *Adv. Phys.* **2002**, *51*, 1379.
(7) Graham, R. G.; Likhtman, A. E.; McLeish, T. C. B.; Milner, S. T. *J. Rheol.* **2003**, *47*, 1171.
(8) Ravindranath, S.; Wang, S. Q. *Macromolecules* **2008**, *41*, 2663.
(9) Ravindranath, S.; Wang, S. Q. *J. Rheol.* **2008**, *52*, 957.
(10) Wang, S. Q.; Ravindranath, S.; Boukany, P. E.; Olechnowicz, M.; Quirk, R. P.; Halasa, A.; Mays, J. *Phys. Rev. Lett.* **2006**, *97*, 187801.
(11) Ravindranath, S.; Wang, S. Q. *Macromolecules* **2007**, *40*, 8031.
(12) Boukany, P. E.; Wang, S. Q.; Wang, X. R. *Macromolecules* **2009**, *42*, 6261.
(13) Mason, T. G.; Bibette, J.; Weitz, D. A. *J. Colloid Interface Sci.* **1996**, *179*, 439.
(14) Menezes, E.; Graessley, W. *J. Polym. Sci., Polym. Phys. Ed.* **1982**, *20*, 1817.
(15) Ravindranath, S.; Wang, S. Q. *J. Rheol.* **2008**, *52*, 681.
(16) Boukany, P. E.; Wang, S. Q.; Wang, X. R. *J. Rheol.* **2009**, *53*, 617.
(17) Wang, S. Q.; Ravindranath, S.; Wang, Y. Y.; Boukany, P. E. *J. Chem. Phys.* **2007**, *127*, 064903.
(18) Wang, Y. Y.; Wang, S. Q. *J. Rheol.* **2009**, *53*, 1389.
(19) Dealy, J. M.; Tsang, W. K. W. *J. Appl. Polym. Sci.* **1981**, *26*, 1149.
(20) Osaki, K.; Kimura, S. *J. Rheol.* **1981**, *25*, 549.
(21) Liu, G. X.; Wang, S. Q., manuscript in preparation. The unpublished work shows based on PTV observations that these entangled polystyrene solutions actually undergo nonquiescent relaxation after shear cessation. Such results have significant implications regarding the past agreement between experiment and the Doi–Edwards tube theory.
(22) Robertson, C. G.; Warren, S.; Plazek, D. J.; Roland, C. M. *Macromolecules* **2004**, *37*, 10018.
(23) Archer, L. A. *J. Rheol.* **1999**, *43*, 1617.
(24) Ravindranath, S.; Wang, S. Q.; Olechnowicz, M.; Chavan, V.; Quirk, R. P. *Rheol. Acta* **2011**, *50*, 97.
(25) Wang, S. Q.; Ravindranath, S.; Boukany, P. E. *Macromolecules* **2011**, *44*, 183.
(26) Vinogradov, G. V.; Belkin, I. M. *J. Polym. Sci., Part A: Polym. Chem.* **1965**, *3*, 917.
(27) Schweizer, T. *Rheol. Acta* **2002**, *41*, 337.
(28) Collis, M. W.; Lele, A. K.; Mackley, M. R.; Graham, R. G.; Groves, D. J.; Likhtman, A. E.; Nicholson, T. M.; Harlen, O. G.; McLeish, T. C. B.; Hutchings, L. R.; Fernyhough, C.; Young, R. N. *J. Rheol.* **2005**, *49*, 501.
(29) Auhl, D.; Ramirez, J.; Likhtman, A. E.; Chambon, P.; Fernyhough, C. *J. Rheol.* **2008**, *52*, 801.
(30) Huppler, J. D.; MacDonald, I. F.; Ashare, E.; Spriggs, T. W.; Bird, R. B.; Holmes, L. A. *Trans. Soc. Rheol.* **1967**, *11*, 181.
(31) Pearson, D.; Kiss, A. D.; Fetters, L. J.; Doi, M. *J. Rheol.* **1989**, *33*, 517.
(32) Osaki, K.; Inoue, T.; Isomura, T. *J. Polym. Sci., Part B: Polym. Phys.* **2000a**, *38*, 1917.
(33) Osaki, K.; Inoue, T.; Isomura, T. *J. Polym. Sci., Part B: Polym. Phys.* **2000b**, *38*, 2043.
(34) Osaki, K.; Inoue, T.; Uematsu, T. *J. Polym. Sci., Part B: Polym. Phys.* **2000c**, *38*, 3271.

(35) Graessley, W. W. *Adv. Polym. Sci.* **1974**, *16*, 1.
(36) Bird, R. B.; Armstrong, R. C.; Hassager, O. *Dynamics of Polymeric Liquids: Fluid Dynamics*; Wiley: New York, 1987.
(37) Lodge, A. S. *Rheol. Acta* **1989**, *28*, 351.
(38) Lodge, T. P.; Rotstein, N. A.; Prager, S. *Adv. Chem. Phys.* **1990**, *79*, 1.
(39) Osaki, K.; Uematsu, T.; Yamashita, Y. *J. Polym. Sci., Part B: Polym. Phys.* **2001**, *39*, 1704.
(40) Liu, C.; He, J.; Ruymbeke, E.; Keunings, R.; Bailly, C. *Polymer* **2006**, *47*, 4461.
(41) Boukany, P. E.; Wang, S. Q. *J. Rheol.* **2009**, *53*, 1425. Li, X.; Wang, S. Q. *Macromolecules* **2010**, *43*, 5904.
(42) An attempt to depict nonquiescent relaxation after shear cessation was recently made. See Adams and Olmsted*Phys. Rev. Lett.* **2009**, *102*, 067801, where it was asserted that the nonquiescent relaxation could arise from a monotonic constitutive equation. In the reply (*Phys. Rev. Lett.* **2009**, *103*, 219802) to our Comment (*Phys. Rev. Lett.* **2009**, *103*, 219801) they still had to involve a nonuniform deformation field in order to produce nonquiescence after shear cessation. See Figure 2 which shows a varying slope. Thirty years ago, the report of ultrastrain-softening behavior of polybutadiene melts by Vrentas and Graessley (Vrentas, C. M.; Graessley, W. W *J. Rheol.* **1982**, *26*, 359) led to the following tube-model-based study to suggest that strain inhomogeneity could occur: Marrucci, G.; Gruizzuti, N. *J. Rheol.* **1983**, *27*, 433.
(43) Sussman, D. M.; Schweizer, K. S. *Phys. Rev. Lett.* **2011**, *107*, 078102.
(44) Sussman, D. M.; Schweizer, K. S. *J. Chem. Phys.* **2011**, *135*, 131104.
(45) Kaye, A. *Non-Newtonian Flow in Incompressible Fluids*; College of Aeronautics Press: Cranford, UK, 1962.
(46) Bernstein, B.; Kearsley, E. A.; Zapas, L. J. *Trans. Soc. Rheol.* **1963**, *7*, 391.

Macromolecules

Article

pubs.acs.org/Macromolecules

Neutron Scattering and X-ray Investigation of the Structure and Dynamics of Poly(ethyl methacrylate)

A.-C. Genix,*[,†] A. Arbe,[‡] J. Colmenero,[‡,§,∥] J. Wuttke,[⊥] and D. Richter[○]

[†]Laboratoire Charles Coulomb, UMR 5221, CNRS, Université Montpellier 2, 34095 Montpellier, France

[‡]Centro de Física de Materiales (CSIC, UPV/EHU) and Materials Physics Center MPC, Paseo Manuel de Lardizabal 5, E-20018 San Sebastián, Spain

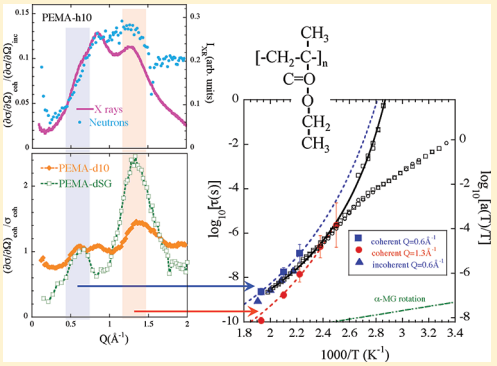
[§]Departamento de Física de Materiales (UPV/EHU), Apartado 1072, 20080 San Sebastián, Spain

[∥]Donostia International Physics Center, Paseo Manuel de Lardizabal 4, 20018 San Sebastián, Spain

[⊥]Outstation at FRM II, Jülich Center for Neutron Science JCNS 1, Forschungszentrum Jülich GmbH, Lichtenbergstraße 1, 85747 Garching, Gemany

[○]Jülich Center for Neutron Science (JCNS 1) and Institut for Complex Systems (ICS 1), Forschungszentrum Jülich GmbH, D-52425 Jülich, Germany

ABSTRACT: We present a study on the structure and dynamics of poly(ethyl methacrylate) (PEMA), one of the polymers with shortest side-group in the poly(*n*-alkyl methacrylate)s (PnMAs) series. The contributions to the structure factor have been unveiled by combining *T*-dependent X-ray and neutron diffraction with polarization analysis on samples with different deuteration labelings, accessing thereby different partial structure factors of PEMA. We find clear hints for strong structural ordering with anticorrelated side-groups and main-chain locations, fitting thus in the general scenario of nanosegregation of main chains and side groups found in higher order PnMAs members. Backscattering measurements on a PEMA sample with deuterated side-group have revealed the dynamics of main-chain and α-methyl group hydrogens. The characterization of the rotations of the latter indicates highly disordered environments in the glassy state. Above the glass transition, the incoherent scattering function related to segmental relaxation shows stretching and clear deviations from Gaussian behavior in the accessed window. We also present results on the dynamic structure factor (collective dynamics) at the peaks characteristic (i) for the intermain-chain and interside-group-domain correlations and (ii) for the side-group/side-group atomic correlations within the domains. Viscosity dictates the temperature dependence in both cases, and also that of the dielectric spectroscopy results at high temperatures. However, the α-process followed by dielectric relaxation deviates from the rheological behavior when approaching the calorimetric glass-transition, indicating a strong influence of the faster side-group motions on the dynamics of the dielectric probes.



I. INTRODUCTION

To relate the structural and dynamical features of polymers is a great challenge in order to understand and optimize their macroscopic properties. In particular, the poly(*n*-alkyl methacrylate) (PnMA) series has attracted a lot of interest over the past decades,[1−24] as these polymers display a complex molecular structure coupled with a variety of relaxational processes. In this series, a heterogeneous nanostructure has been found. On the basis of X-ray diffraction coupled to calorimetric, dielectric and shear measurements, it was suggested that the alkyl parts of different side groups tend to aggregate forming self-assembled nanodomains—called polyethylene-like nanodomains—in the higher members. In parallel, the existence of two distinct glass transitions was proposed: the one at low temperature presumably corresponds to the freezing of the motions within the alkyl nanodomains and the second one relates to main-chain dynamics.[14,15,19] For the main chains, an additional slowest process was also detected by advanced solid state NMR and associated with the isotropization of backbone orientation.[22,23]

More insight into these complex systems was recently gained using neutron scattering combined with isotopic labeling.[25,26] Such technique allowed us to selectively follow the different molecular groups, namely main chain (MC) and side groups (SG), thanks to the difference in scattering lengths of hydrogen and deuteron in partially deuterated samples. Neutron diffraction experiments provided strong support to the nanosegregated structure in PnMAs and the temperature dependence of the diffraction peak related to the SG/SG correlations revealed the occurrence of a glass transition within the polyethylene-like nanodomains. Note that already in the shortest polymer of the series, i.e., poly(methyl methacrylate) (PMMA),

Received: December 7, 2011
Revised: February 13, 2012
Published: February 29, 2012

 © 2012 American Chemical Society dx.doi.org/10.1021/ma202653k | *Macromolecules* 2012, 45, 2522−2536

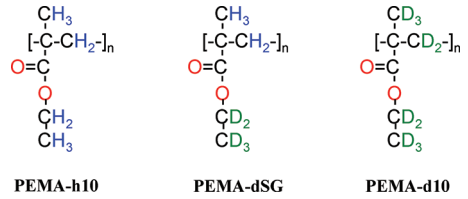
the existence of strong local order was evidenced with the help of fully atomistic molecular dynamics (MD) simulations.[27,28] Regarding the dynamical properties, the collective dynamics at the SG- and MC-levels and the self-motions of hydrogen atoms in the side groups were selectively followed using the neutron spin echo technique. The structural relaxation of the main chains displays standard features, whereas an anomalous behavior is obtained for the dynamics of the side groups in higher order members. It is characterized by extremely stretched functional forms, Arrhenius-like behavior and much faster time scales for self-motions than for collective-motions. A length increase of the flexible side groups results in the development of a strong dynamic asymmetry with a complete decoupling of side groups dynamics from the main-chain motions, as observed in the case of poly(*n*-hexyl methacrylate) (PHMA).[26] All these results are supported by a recent MD simulations work[29] on a bead−spring model for copolymers with comb-like architecture. It appears that the qualitative features observed in methacrylates with large side groups are not specific but can be generalized to side-chain polymers with strong dynamic asymmetry.

In the present work, we focus on poly(ethyl methacrylate) (PEMA) in order to determine how the local ordering and the dynamical properties evolves in this *intermediate* polymer of the series, located between PMMA and higher order PnMAs previously investigated. We have first combined X-ray and neutron diffraction exploiting isotopic labeling to disentangle the different contributions to the diffraction peaks in PEMA. Such strategy was previously used by Wind et al.[24] in PEMA, where they could demonstrate that local ordering exists. Here, we are going one step further in the interpretation of the diffraction peaks thanks to an additional labeled sample (the fully deuterated one) and the comparison with previous structural results on higher order members based on neutron diffraction. Moreover, the consideration of the recently published simulations on comb-like polymers above-mentioned[29] as well as the study on PMMA structure[27] based on a fully atomistic model has illuminated the interpretation of the experimental data. As observed in PMMA, PEMA exhibits a strong local order with a strong anticorrelation between the main chain and the side groups, that hints a precursor effect of the proposed nanophase separation. In a second part, quasielastic neutron scattering measurements reveals the dynamics of main-chain and α-methyl group hydrogens. Above the glass transition, stretching of the self-correlation function and strong deviation from Gaussian behavior are observed, that can be rationalized invoking a distribution of elementary jumps underlying the anomalous diffusion. The collective dynamics at the length scales characteristic for both the interdomain correlations and the correlations between side groups whithin the nanodomains are also investigated. The temperature dependence of the different relaxation processes is finally discussed in comparison with viscosity results.

The paper is organized as follows. Section II deals with the experimental aspects, describing the samples, the neutron scattering and X-ray techniques used, as well as the quantities they allow to access. In section III the obtained results are presented, first regarding the structure, then the dynamics. The data analysis is performed in section IV, and the different results are discussed in section V where we propose different interpretations. Finally, the conclusions are summarized.

II. EXPERIMENTAL SECTION

A. Samples. PEMA samples (Polymer Source, Inc.) with different deuteration levels were investigated (see Figure 1): fully protonated



PEMA-h10 **PEMA-dSG** **PEMA-d10**

Figure 1. Chemical formulas of the different samples investigated in this work.

(PEMA-h_{10}), fully deuterated (PEMA-d_{10}), and partially deuterated sample where only the side group is deuterated (main chain and α-methyl group are protonated) (PEMA-dSG). Their characteristics can be found in Table 1.

B. Neutron Scattering. Neutron diffraction measures differential scattering cross sections, i.e., the number of neutrons scattered into a solid angle comprised between Ω and $\Omega + d\Omega$ with respect to the total number of incident neutrons.[30−33] The modulus of the momentum transfer Q ($\vec{Q} = \vec{k}_f - \vec{k}_i$) is determined by the scattering angle θ and the wavelength of the incoming neutrons λ as $Q = 4\pi \sin(\theta/2)/\lambda$. The differential scattering cross section contains a coherent and an incoherent term. The coherent term is related to the relative position of pairs of atoms and gives information on the structural organization of the sample:

$$\left(\frac{\partial\sigma}{\partial\Omega}\right)_{coh} = \frac{1}{N}\langle \sum_{i,j=1}^{N} \bar{b}_i \bar{b}_j e^{i\vec{Q}\vec{r}_{ij}} \rangle \quad (1)$$

where b_i is the neutron coherent scattering length of atom i, N is the number of atoms, $\vec{r}_{ij} = \vec{r}_i - \vec{r}_j$ is the vector distance between atom i and j and the brackets express the thermal average. In the limit of $Q \to \infty$, the differential coherent cross section is determined by the total coherent cross section σ_{coh}:

$$\left(\frac{\partial\sigma}{\partial\Omega}\right)_{coh} = \frac{1}{N}\sum_{i=1}^{N} \bar{b}_i^2 = \frac{\sigma_{coh}}{4\pi} \quad (2)$$

The incoherent contribution is related to the fluctuations of scattering lengths in the sample, is Q-independent, and is determined by the total incoherent cross section:

$$\left(\frac{\partial\sigma}{\partial\Omega}\right)_{inc} = \frac{1}{4\pi N}\sum_{i=1}^{N} \sigma_{inc}^{i} = \frac{\sigma_{inc}}{4\pi} \quad (3)$$

The values of the scattering lengths, coherent and incoherent scattering cross sections of the different atoms composing the samples here investigated are reported in Table 2. The cross sections of the monomers can be found in Table 1.

Information on the *dynamics* of a sample can be obtained by analyzing the change in energy ($\hbar\omega$) experienced by the scattered neutrons, i.e., through the double differential scattering cross sections (which integrals over all the possible energy transfers are the above-described differential cross sections). The momentum- and energy transfer dependence of the incoherent contribution is determined by the incoherent scattering function, $S_{inc}(Q,\omega)$, which is related via Fourier transformation with the intermediate incoherent scattering function, $S_s(Q,t)$. The double Fourier transform of $S_{inc}(Q,\omega)$ is the self-part of the Van Hove correlation function, $G_s(r,t)$. In the classical limit, $G_s(r,t)$ is the probability of a given nucleus to be at a distance r from the position where it was located at a time t before. Thus, incoherent scattering looks at correlations between the positions of the same nucleus at different times. On the other hand, the coherent scattering reveals the dynamic structure factor $S_{coh}(Q,t)$ dealing with the time-dependent relative positions of atomic pairs, i.e., the collective dynamics.

dx.doi.org/10.1021/ma202653k | *Macromolecules* 2012, 45, 2522−2536

Table 1. Molecular Weight M_w, Polydispersity, Tacticity (Syndiotactic Diads), and Glass-Transition Temperature (Midpoint) of the Samples Investigated, Coherent and Incoherent Cross Sections of the Monomers, and their Ratio

polymer	M_w(g/mol)	M_w/M_n	syndio (%)	T_g (K)	σ_{coh}(barns/mon)	σ_{inc}(barns/mon)	$\sigma_{coh}/\sigma_{inc}$
PEMA-h_{10}	515 000	–	76 ± 1	345	59.35	802.61	0.074
PEMA-d_{10}	18 000	1.06	87 ± 2	350	97.74	20.50	4.77
PEMA-dSG	12 100	1.05	87 ± 2	345	78.57	411.6	0.19

Table 2. Coherent Scattering Lengths, and Coherent and Incoherent Cross Sections for Neutrons of the Nuclei Composing the Samples

nucleus	b (fm)	σ_{coh} (barns/atom)	σ_{inc} (barns/atom)
H	−3.7406	1.7583	80.27
D	6.671	5.592	2.05
C	6.6511	5.559	0
O	5.803	4.232	0

We note that, as neutron scattering spectrometers offer a limited energy resolution, the measured functions are affected by the instrumental resolution function, $R(Q,\omega)$. $R(Q,\omega)$ is the obtained spectrum when purely elastic ($\hbar\omega = 0$) scattering events take place in the sample [i.e., it is the "image" of $\delta(\omega)$]. It can usually be determined from the scattering of the sample at very low temperature, where all the dynamical processes are frozen. Thus, the experimentally accessed quantity has to be compared with the convolution of the model function and the resolution, $I_{exp}(Q,\omega) \leftrightarrow S^{theo}(Q,\omega)\otimes R(Q,\omega)$.

1. Structure: Neutron Diffraction. The differential cross section of PEMA-d_{10} was investigated by means of the neutron diffractometer D16 at the Institute Laue-Langevin (ILL, Grenoble, France) with incoming wavelength λ = 4.54 Å. Thereby, the Q-range covered was between 0.2 and 1.9 Å^{-1}. The sample was investigated at different temperatures ranging from 100 to 420 K.

In order to separate the coherent and incoherent contributions to the scattered intensity, we performed diffraction measurements with polarization analysis on the same PEMA-d_{10} sample at 300 and 500 K and also on the fully protonated sample PEMA-h_{10} and the partially deuterated sample PEMA-dSG at 300 K. The fundamentals of this technique can be found elsewhere.[31,33] The instrument D7 at the ILL was used for the measurements on PEMA-d_{10}, while PEMA-dSG was investigated by means of DNS instrument of JCNS at FRM II (Forschungsneutronenquelle Heinz Maier-Leibnitz at Garching, Germany). Using λ = 4.81 Å (D7) and λ = 4.75 Å (DNS), the Q-ranges 0.12 ≤ 2.52 Å^{-1} and 0.15 ≤ 2.34 Å^{-1} were respectively covered.

In all cases the correction for background scattering was done by properly subtracting the intensity scattered by the empty cell.

2. Backscattering. In this work, we used the high-flux backscattering spectrometer SPHERES of JCNS at FRM II to investigate the PEMA-dSG sample. In this instrument, the resolution is optimized by using single crystal diffraction of cold neutrons with Bragg angles close to 180° for monochromatization and energy analysis.[34] Using a neutron wavelength of 6.271 Å, a Q-range between 0.6 and 1.9 Å^{-1} was accessed and an energy window of ±20 μeV was explored. The energy resolution, with nearly Gaussian shape, was δE(fwhm) ≈0.65 μeV. The sample was placed in an Aluminum flat container at 45° with respect to the incident beam. The thickness was such that a transmission of ≈0.9 was calculated. QENS spectra were recorded at 255, 270, 295, 320, 350, 375, 400, 420, 440, 460, 480, 500, 525, and 545 K, with measuring times of about 16 h. The experimental resolution function was obtained from measurement on the sample at 4 K. Empty cell measurements at 3 temperatures (4, 295, and 545 K) were also carried out to correct the spectra. The measurement was carried out in 2007 as one of the very first user experiments on SPHERES. Since then, the spectrometer underwent further development, resulting in a much better flux and signal-to-noise ratio. By now, measurements of comparable quality can be obtained in much shorter time (about 6 h/scan instead of 16 h).

3. Neutron Spin Echo. NSE directly accesses the scattering functions in the time domain, i.e., the intermediate scattering functions, through the following function:[35]

$$\tilde{S}_{NSE}(Q,t) = \frac{I_{coh}(Q,t) - \frac{1}{3}I_{inc}(Q,t)}{I_{coh}(Q,0) - \frac{1}{3}I_{inc}(Q,0)} \quad (4)$$

$I_{coh}(Q,t)$ and $I_{inc}(Q,t)$ are related via Fourier transformation to the coherent and incoherent scattering functions, respectively.

We used the IN11 spectrometer at the ILL to investigate the fully deuterated sample. With λ = 5.5 Å the accessed time range was 0.04 ns ≤ t ≤ 8 ns. The Q-values investigated were 0.6 and 1.3 Å^{-1}. The sample was placed into an Aluminum flat container. We performed measurements at 400, 420 (only for 1.3 Å^{-1}), 450, 480, and 520 K with measuring times of about 5 h per Q and temperature. As NSE works in the time domain, the deconvolution of the measured spectra from resolution can be realized dividing by a measurement on the sample at 120 K, which is representative of the instrumental response to a purely elastic process.

C. X-ray Diffraction. X-ray diffraction experiments were performed on the fully protonated sample using a Rigaku PSAXS-L system located at the Centro de Física de Materiales (CSIC, UPV/EHU) in San Sebastian, Spain. The MicroMax-002+ X-ray generator system is composed by a microfocus sealed tube source module and an integrated X-ray generator unit which produces Cu Kα transition photons of λ = 1.54 Å. The two-dimensional multiwire detector 2D-200X offering a 200 mm diameter active area with ca. 200 μm resolution was placed at 50 cm from the sample. In this way we measured diffraction patterns in a Q-range from ≈0.1 to 0.9 Å^{-1} in the temperature range between 175 and 500 K (measurements each 25 K). Measurements at RT covering a larger Q-range (0.1 to 2.1 Å^{-1}) were performed in the Laboratoire Charles Coulomb (UMR 5221), Université Montpellier 2, France. We used a Cu-rotating anode X-ray source with a multilayer focusing monochromator giving high flux and punctual collimation, and an image plate 2D detector. In both diffractometers a transmission configuration was used. Contrarily to the case of neutron diffraction, in the patterns obtained by X-rays, eq 1, the atomic scattering length does not only depend on the nature of the atom (for X-rays, it is proportional to the atomic number) but also on the Q-value.

III. EXPERIMENTAL RESULTS

A. Diffraction. Figure 2a shows the coherent differential cross section normalized to the incoherent scattering for PEMA-d_{10} at 300 and 500 K. In this way, the coherent data may be put in an absolute scale (see below) and also corrected for the Debye–Waller factor. In this sample, the coherent contribution dominates and this ratio is larger than 1 in the whole Q-range investigated. We note however that the theoretical value of $\sigma_{coh}/\sigma_{inc}$ is close to 5 (see Table 1), i.e., about two times larger than the value expected from the high-Q limit of the D7 measurements. This discrepancy is easily explainable by a slightly deficient deuteration of the sample. Assuming 3.5% of protons, the value of $\sigma_{coh}/\sigma_{inc}$ decreases to 2, which would be perfectly compatible with the experimental results. This deuteration level in fact agrees with that given by Polymer Source. On the other hand, since the incoherent cross section is isotropic, the Q-dependence of this curve is due to the coherent cross section.

dx.doi.org/10.1021/ma202653k | Macromolecules 2012, 45, 2522–2536

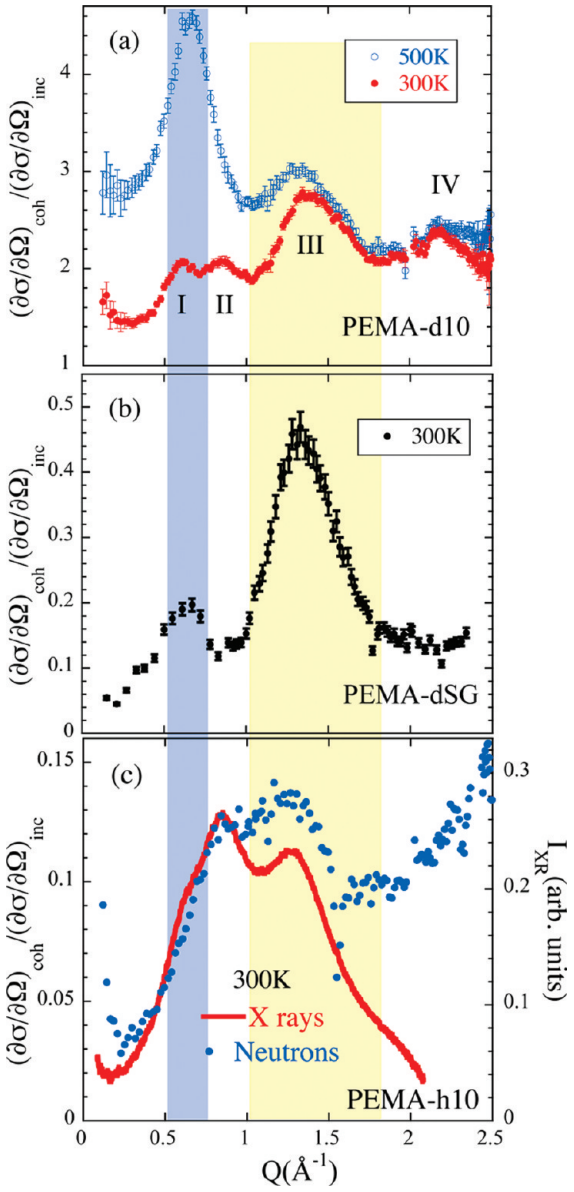


Figure 2. Ratio between the coherent and incoherent scattering cross sections measured at 300 and 500 K on PEMA-d_{10} by D7 (a), on PEMA with deuterated side group at 300 K by DNS (b) and on PEMA-h_{10} at 300 K by D7 (c). In part c, the X-ray result is also included for comparison (line).

In the case of this fully deuterated sample, all the different atomic pair correlations contribute practically with the same weight to the coherent cross section (see Tables 2 and 3), and therefore the latter directly reveals the "true" or total static structure factor $S(Q)$ of PEMA. At 300 K, $S(Q)$ shows four peaks in the Q-range accessed by D7, centered at about 0.6 Å^{-1} (peak I), 0.85 Å^{-1} (peak II), 1.3 Å^{-1} (peak III), and 2.2 Å^{-1} (peak IV). At 500 K instead, only one very intense peak appears in the region below 1 Å^{-1}. The detailed temperature dependence of $S(Q)$ was followed through the differential cross section accessed by D16 (dominated, as above demonstrated, by the coherent contribution) (see Figure 3). The most striking effect is the increase of the intensities of the peaks labeled as I and II with respect to peak III until they finally merge in a strong maximum. In addition, at high temperatures the D16 patterns resolve the emergence of a peak (IIIa) in the

Table 3. Relative Weights of the Contributions Involving Molecular Groups A and B (A, B: MC, SG, COO) to the Coherent Scattering in the Sample Defined[a] as $f_{coh}^{A/B} = \Sigma_{\alpha A\in A,\beta B\in B} b_{\alpha A} b_{\beta B}/\Sigma_{\alpha,\beta} b_\alpha b_\beta/F$, $F = \Sigma_{A,B} f_{coh}^{A/B}$

groups	PEMA-d_{10}	PEMA-dMC	PEMA-dSG
MC/MC	0.27	0.68	0.12
SG/SG	0.22	0.09	0.54
MC/SG	0.31	−0.09	0.02
COO/COO	0.03	0.08	0.08
MC/COO	0.09	0.23	0.05
SG/COO	0.08	0.01	0.20

[a]We note that this neglects the possibly slightly different local densities of the various considered monomer subgroups.

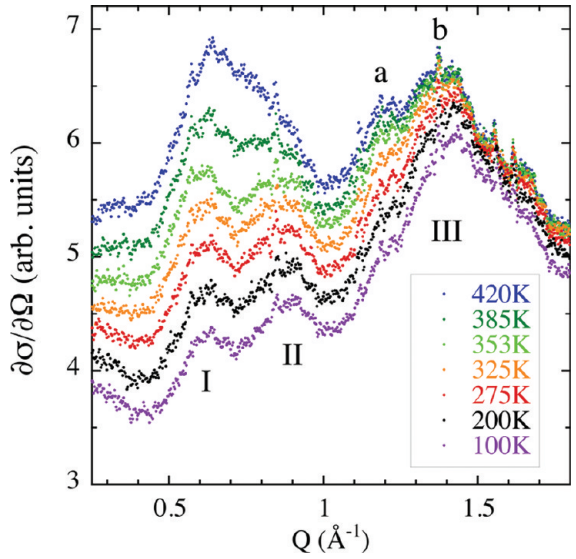


Figure 3. Scattering cross section of PEMA-d_{10} determined by D16 at the different temperatures indicated.

low-Q flank of peak III. At low temperatures, peak IIIa is present only as a kind of shoulder. The positions of all these peaks show slight shifts with varying temperature above the glass transition (see Figure 4). Peak IV was not accessible by D16.

The partial structure factor revealed by the coherent cross section of the PEMA-dSG sample (Figure 2b), where the correlations involving protons along the main chain are differently weighted, displays only two peaks in the positions corresponding to peaks I and III. The intensity scattered by this sample is, as expected (see Table 1), mainly of incoherent nature and is dominated by the contribution of the protons (see Table 2).

The relative incoherent contribution to the neutron diffraction patterns is largest in the fully protonated sample PEMA-h_{10} (see Figure 2c). In the corresponding partial structure factor, all cross-correlations of atomic pairs involving a proton are negatively weighted. Peak I disappears, while peaks II and III are well visible, though with different relative intensities with respect to the other samples. In this figure, the X-ray diffraction pattern obtained on the same sample is shown for comparison. A kind of shoulder is reminiscent of peak I. Peaks II and III are the major features in this pattern. The Q-dependence of the atomic form factors for X-rays leads to the marked decrease of the scattered intensity with increasing Q in this pattern. Focusing on the low-Q region, Figure 5 shows the temperature dependence of the X-ray patterns. At low T, the presence of two peaks becomes evident, while their evolution with

dx.doi.org/10.1021/ma202653k | Macromolecules 2012, 45, 2522−2536

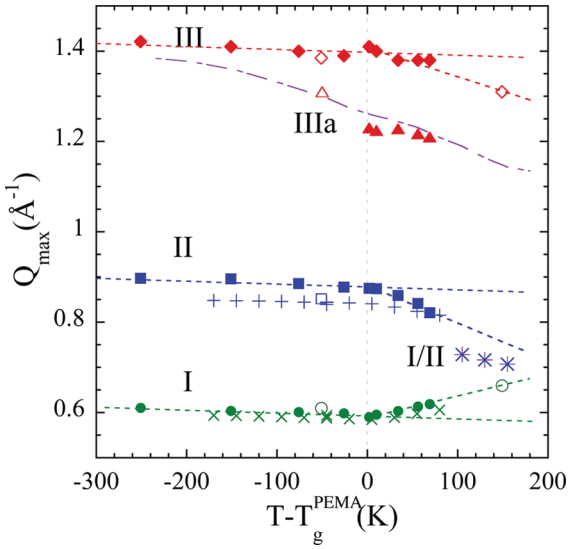


Figure 4. Temperature dependence of the positions of the maxima corresponding to the $S(Q)$-peaks identified in Figure 2a (empty diamonds, empty square and empty circles), Figure 2b (empty triangle: peak III), Figure 3 (filled symbols) and Figure 5 (crosses, pluses, and stars). Dotted lines are guides for the eye. The dashed−dotted line through the high-T data of peak III displays the temperature dependence observed for the peak in PHMA attributed to interside-group correlations.[26]

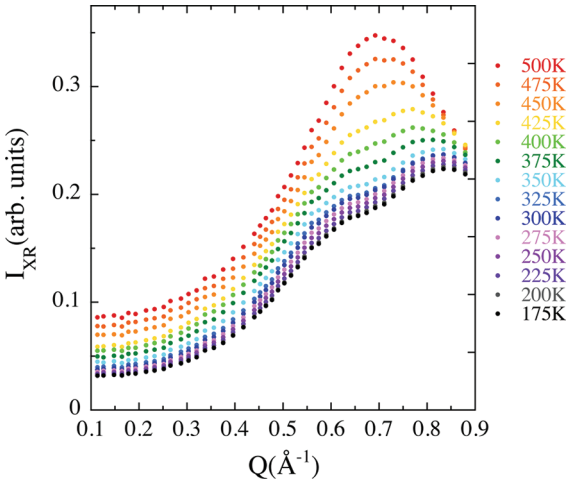


Figure 5. X-ray diffraction patterns obtained on a fully protonated PEMA sample at the different temperatures indicated.

increasing T leads to a unique broad peak well above T_g. The positions of these peaks are also included in Figure 4.

B. Backscattering. Figure 6 based on the D7 results on PEMA-dSG clearly shows that the signal measured by SPHERES on this sample is highly dominated by the incoherent contribution, revealing the self-correlation function of main-chain and α-methyl group hydrogens. As examples, Figure 7 shows spectra obtained for $Q = 1.7$ Å^{-1} at different temperatures below T_g. With increasing temperature, the intensity of the spectra diminishes in the elastic region while it increases in the quasielastic region. In the glassy state, it is expected that backbone motions are basically frozen. Therefore, the quasielastic broadening could be attributed to the α-methyl group rotations.

Figure 8 shows SPHERES spectra measured at the same Q-value in the melt. They significantly broaden with increasing temperature and finally at 500 K most of the quasielastic intensity is outside the backscattering (BS) dynamic window.

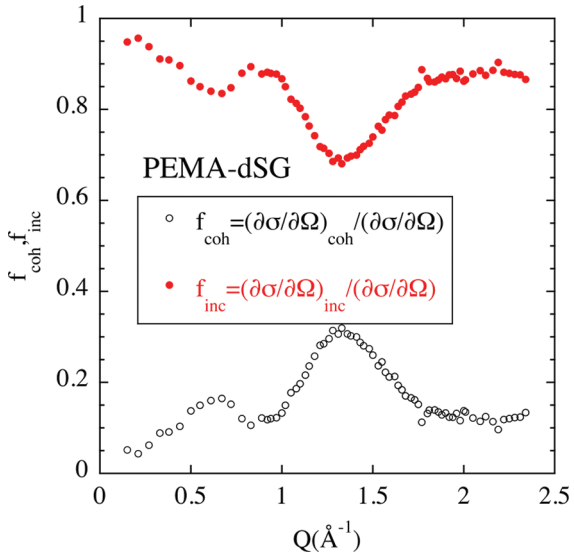


Figure 6. Incoherent (solid circles) and coherent (empty circles) relative contributions to the intensity scattered by PEMA-dSG obtained from the D7 data shown in Figure 2b.

On the other hand, Figure 9 shows the Q-dependence of the BS spectra for an intermediate temperature in the range investigated above T_g, namely 480 K. As can be seen, the broadening -which is determined by the inverse of the characteristic time- increases with increasing Q-value. This implies some kind of diffusive-like behavior taking place in this temperature range well above T_g.

C. Neutron Spin Echo. Since the intensity scattered by PEMA-d_{10} is basically coherent and reveals the equally weighted atomic pair correlations, the NSE signal (eq 4) directly delivers the normalized dynamic structure factor, $S(Q,t)/S(Q)$. Parts a and b of Figure 10 present this function measured at $Q = 0.63$ and 1.3 Å^{-1} (peaks I and III respectively, see Figure 3). The curves show the typical stretching characterizing this function in glass-forming liquids. For a given temperature, the decay of the correlations at peak I is slower and the amplitude is larger than at peak III. With decreasing temperature, the characteristic time of the decay increases in both cases, hinting the freezing of the structure toward the glass transition.

IV. DATA ANALYSIS

1. Backscattering. *Dynamics in the Glassy State: α-Methyl Group Rotations.* We have assumed that below T_g the only dynamical processes leading to quasielastic signal in the SPHERES window is the rotation of the α-CH_3 group. In our analysis of the spectra of PEMA-dSG, we have considered the total incoherent scattering function (i. e., from all the protons in the system) as

$$S_{inc}^{H,\alpha MG-rot}(Q,\omega) = [n_{MC}\delta(\omega) + n_{\alpha MG}S_{inc}^{rot}(Q,\omega)] \quad (5)$$

where n_{MC} and $n_{\alpha MG}$ are the relative abundances of hydrogens in the main chain and α-methyl, respectively. $S_{inc}^{rot}(Q,\omega)$ is the incoherent scattering function for the rotational motion. For rotational motion with characteristic rate Γ, it can be written as

$$S_{inc}^{\Gamma}(Q,\omega) = EISF\,\delta(\omega) + (1-EISF)\frac{1}{\pi}\frac{\Gamma}{\Gamma^2+\omega^2} \quad (6)$$

dx.doi.org/10.1021/ma202653k | Macromolecules 2012, 45, 2522−2536

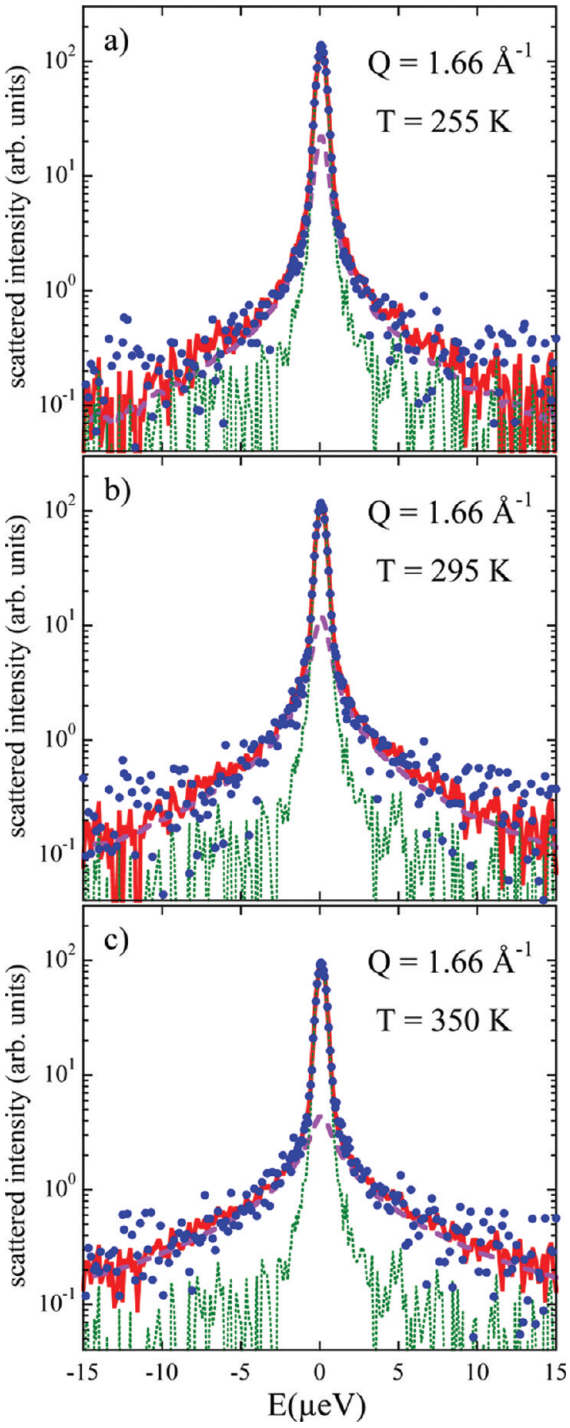


Figure 7. SPHERES results on PEMA-dSG (filled circles) at Q = 1.66 Å^{-1} in the glassy state: 255 (a), 295 (b), and 350 K (c). The continuous red line is the fitting curve modeling the methyl-group rotation (eq 12), which quasielastic contribution is depicted by the dashed purple line. The dotted line shows the resolution function.

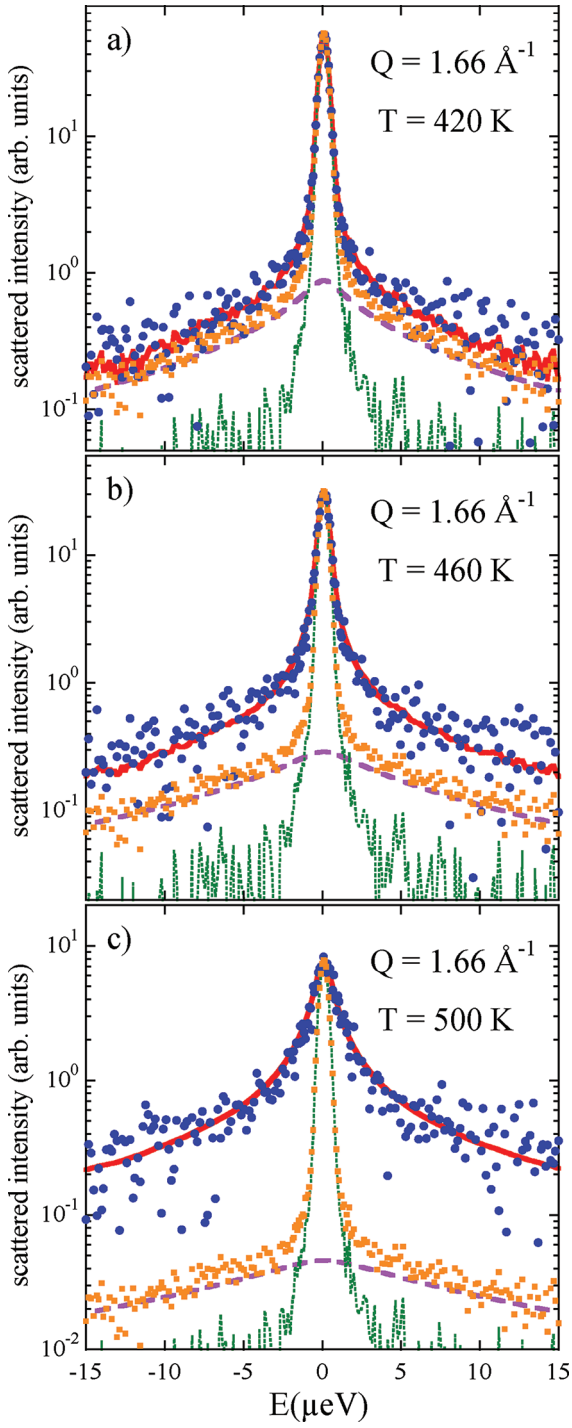


Figure 8. SPHERES results on PEMA-dSG (filled circles) at Q = 1.66 Å^{-1} in the supercooled liquid state: 420 (a), 460 (b), and 500 K (c). The continuous red line is the fitting curve constructed by eq 14 with the effective resolution (eq 15) shown as orange squares. As in Figure 7, the quasielastic contribution corresponding to the rotational motion of α-MG hydrogens is depicted by the dashed purple line. The dotted line shows the resolution function.

where the elastic incoherent structure factor *EISF* carries the information about the geometry of the particular motion involved. In the case of CH_3 rotation, it is given by

$$EISF = \frac{1}{3}\left(1 + 2\frac{\sin(Qr_{HH})}{Qr_{HH}}\right) \quad (7)$$

where r_{HH} = 1.78 Å is the distance between the hydrogens in the methyl group. It is well-known that the disorder inherent to the amorphous state leads to distributions of rates in glassy systems. This aspect was introduced by the rotation rate distribution model (RRDM),[36−40] that considers

dx.doi.org/10.1021/ma202653k | *Macromolecules* 2012, 45, 2522−2536

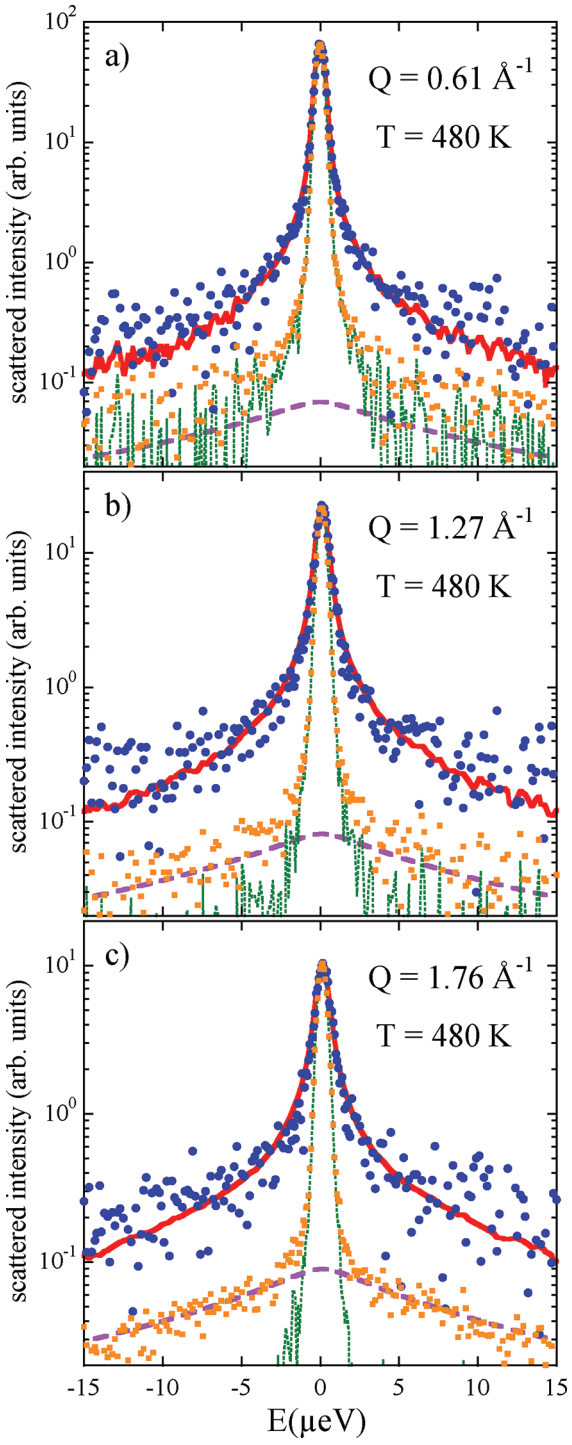


Figure 9. SPHERES results on PEMA-dSG (filled circles) at 480 K and Q = 0.61 (a), 1.27 (b), and 1.76 Å^{-1} (c). Symbols and lines like in Figure 8.

as a first approximation a log-normal distribution of hopping rates

$$H(\log\Gamma) = \frac{1}{\sqrt{2\pi}\,\sigma_\Gamma}\exp\left[-\frac{(\log\Gamma - \log\Gamma_o)^2}{2{\sigma_\Gamma}^2}\right] \quad (8)$$

σ_Γ is the width of the distribution centered at Γ_o. For the hopping rate we expect an Arrhenius temperature dependence

$$\Gamma = \Gamma_\infty \exp\left[-\frac{E_A}{k_B T}\right] \quad (9)$$

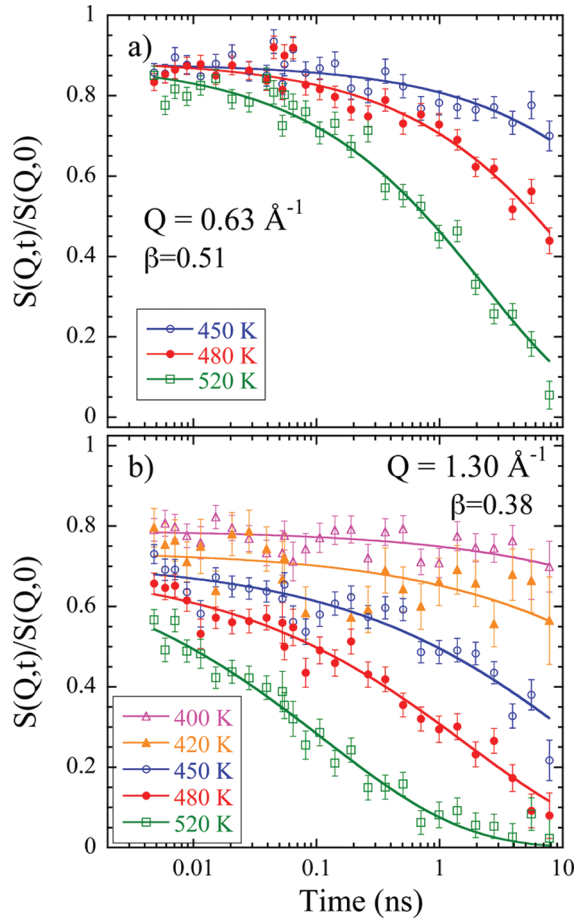


Figure 10. NSE results on fully deuterated PEMA at Q = 0.63 (a) and 1.30 Å^{-1} (b) at the temperatures written. Lines are KWW fits with the β-parameters indicated.

where Γ_∞ is a pre-exponential factor and E_A the activation energy for the rotation. If $H(\log\Gamma)$ is a consequence of an underlying Gaussian distribution of activation energies E_A of width σ_E, the widths of both distributions are related via

$$\sigma_\Gamma = \frac{\sigma_E \log(e)}{k_B T} \quad (10)$$

Thus, the final scattering function for methyl-group hydrogens undergoing rotation in a glass-forming system, $S_{inc}^{rot}(Q,\omega)$, is built by adding the scattering functions of the hydrogens located in the different environments, i.e., weighted by the distribution function:

$$S_{inc}^{rot}(Q,\omega) = \int_{-\infty}^{+\infty} H(\log\Gamma) S_{inc}^{\Gamma}(Q,\omega)\, \mathrm{d}(\log\Gamma) \quad (11)$$

The final fitting function to be compared with the experimental data for PEMA-dSG was

$$I(Q,\omega) = A(Q)R(Q,\omega) \otimes [f_{inc}(Q) S_{inc}^{H,\alpha MG-rot}(Q,\omega) + f_{coh}(Q)\delta(\omega)] \quad (12)$$

where $A(Q)$ is an amplitude. Equation 12 also takes into account the coherent contribution originated mainly from the deuterated side-group. In the glassy state this contribution was assumed to be elastic (represented by the $\delta(\omega)$ function). This is justified by the following arguments: (i) the contribution of

dx.doi.org/10.1021/ma202653k | Macromolecules 2012, 45, 2522–2536

the CD_2 group is expected to be mainly of vibrational origin—other kind of motions should be frozen in the glassy state—and therefore not to give rise to quasielastic scattering in the BS window and (ii) the coherent signal of the ester methyl group rotation should be elastic in any case since the rotation involves transitions between identical configurations of the atomic pairs. The values of the relative contributions f_{coh} and f_{inc} (Figure 6) were calculated from the DNS results (Figure 2). In eq 12, we are assuming that the vibrational contribution parametrized by the amplitude $A(Q)$ is the same for all kinds of atoms and type of scattering. Apart from this amplitude, the only free parameters in this model are Γ_o and σ_Γ. In a first approach, the experimental scattering curves in the temperature range between 255 and 350 K were fitted with free Γ_o and σ_Γ parameters. Within the experimental uncertainty, we observed that the width parameter σ_Γ did not depend on Q, as expected for such a localized process. Then, this parameter was kept constant to the average values obtained at each temperature for the 3 highest Qs, i.e., where the quasielastic broadening is most pronounced (small values of the EISF). The same procedure was used for the Γ_o parameter, which also did not show any significant Q-dependence. The temperature dependence of both parameters is shown in Figure 11, together with the fit of eq 9 for Γ_o and of eq 10 for σ_Γ. In the fit of σ_Γ the highest temperature was not considered, since the low value obtained for this parameter could indicate already a softening of the structure. We obtained an average activation energy E_{Ao} = 195 meV, Γ_∞ = 3.1 meV, and σ_E = 41.4 meV. The final description of the experimental spectra was done with eq 12 fixing the values of Γ_o and σ_Γ at each temperature to the fitted lines in Figure 11, parts a and b, respectively. Figure 7 shows the good quality of the descriptions obtained in this way.

2. Dynamics above the Glass Transition. At 375 K (30 K above T_g), the description of the spectra by eq 5 fails. From this temperature, it becomes clear that an additional dynamical process has to be taken into account. In the dynamic and Q windows covered by the BS instrument, the main process contributing to the spectra above T_g should relate to the structural or α-relaxation. By now it is well-established that the intermediate scattering function describing the hydrogen motions in this regime is well represented by a stretched exponential or Kohlrausch–Williams–Watts (KWW) function

$$S^{KWW}(Q, t) = \exp\left[-\left(\frac{t}{\tau_w}\right)^{\beta}\right] \tag{13}$$

Here β is the stretching parameter describing the shape of the relaxation function ($0 < \beta \leq 1$, and close to 0.5 for most polymers) and τ_w the relaxation time which may depend on Q and T. This function also describes the coherent structure factor, as we will see below. Thus, we have assumed eq 13 for the intermediate incoherent scattering function of the motions involved in the structural relaxation of main-chain and α-methyl hydrogens and also for the coherent contributions. In the case of α-methyl hydrogens, a quasielastic broadening of the spectra due to their simultaneous rotation is also expected. As already shown for PMMA in a blend with PEO,[41] or for polyisoprene[42] a good approximation to describe the dynamics of these hydrogens is to consider that both kinds of motions are statistically independent. Then, the total intermediate scattering function is given by the product of the respective intermediate scattering functions, which translates into a convolution in the frequency domain. Under this assumption, the spectra are described by means of

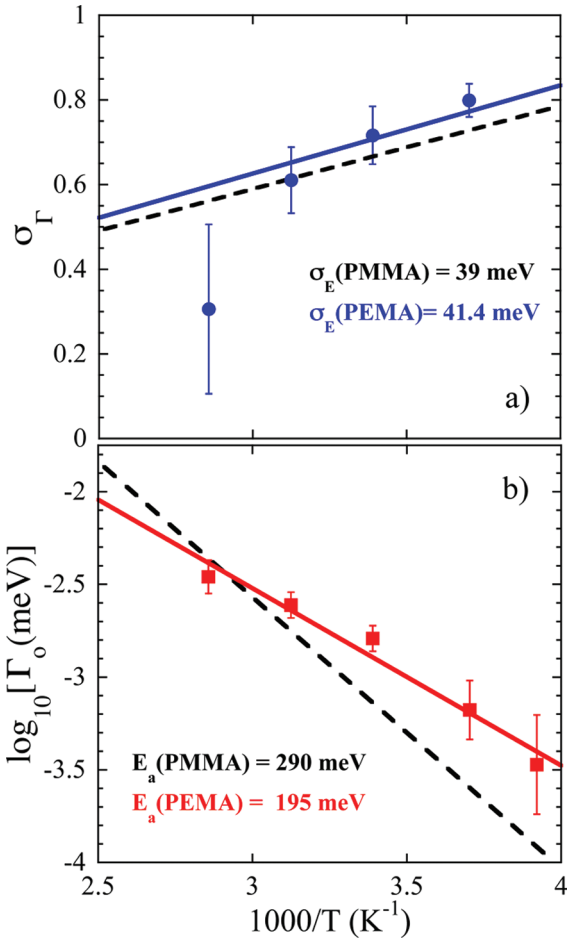


Figure 11. Temperature dependence of the width (a) and mean value (b) of the distributions of rotation rates for methyl groups obtained for the α-methyl group of PEMA. The solid line in part a shows the expected widths in the case of a unique distribution of activation energies of width σ_E = 41.4 meV (best fit). At the lowest temperature investigated, the value of σ_Γ presented a large uncertainty and has not been plotted. Solid line in part b is an Arrhenius fit with E_a = 195 meV; dashed lines correspond to the values obtained for the α-methyl group of PMMA.[41]

$$I_{\exp}(Q, \omega) \leftrightarrow A(Q)R_{eff}(Q, \omega) \otimes S_{inc}^{KWW}(Q, \omega) \tag{14}$$

where we have defined the "effective resolution function" $R_{\text{eff}}(Q,\omega)$ as

$$R_{eff}(Q, \omega) = R(Q, \omega) \otimes [f_{inc}(Q)S_{inc}^{H,\alpha MG-rot}(Q, \omega) + f_{coh}(Q)\delta(\omega)] \tag{15}$$

that represents the expected experimental result in the case of the frozen system with exception of α-methyl group rotations. $R_{\text{eff}}(Q,\omega)$ was constructed with the Γ_o and σ_Γ values extrapolated at each temperature using their T-dependence as obtained in the previous part. We have thereby implicitely assumed that the energy barrier distribution function is not appreciably sensitive to the glass transition, as shown by MD-simulations in polyisoprene.[42] The resulting $R_{\text{eff}}(Q,\omega)$ curves are plotted as filled squares in Figures 8 and 9. As can be seen in Figure 8, at Q = 1.7 Å^{-1} the quasielastic contribution

dx.doi.org/10.1021/ma202653k | *Macromolecules* 2012, 45, 2522–2536

corresponding to the rotations (dashed line) constitutes a large part of the measured spectra at 420 K, while at 500 K it is so broad that it could be well approximated by a weak flat background. In the fitting procedure the β-value was fixed to 0.5, which is the typical value observed for the stretching parameter in polymers and is also compatible with the data obtained for coherent scattering (see below). We note that we have implicitly assumed that all parameters in the KWW description are identical for both kinds of hydrogens in the sample (MC and α-MG) as well as for the coherent contribution. We note that the latter is only noticeable (larger than ≈20%) in the neighborhood of peak III (see Figure 6). There, as we will see below, the coherent scattering function shows very similar characteristic times as the incoherent scattering function of hydrogens in PEMA-dSG. As can be seen in Figures 8 and 9, this approach allows a very good description of the experimental curves. The such obtained Q- and T-dependent characteristic times, τ_w, are displayed in Figure 12.

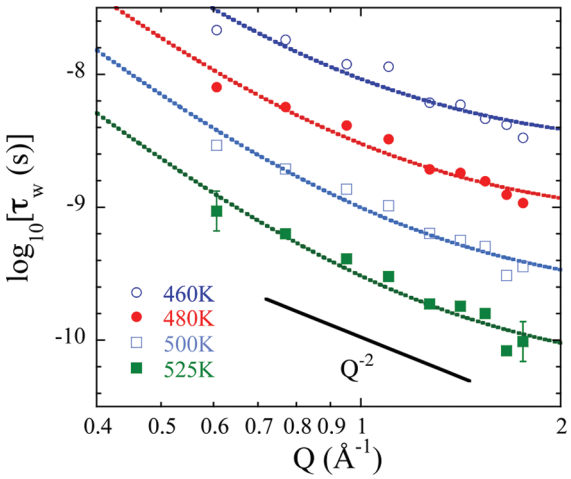


Figure 12. Momentum-transfer dependence of the characteristic time for segmental relaxation obtained on PEMA-dSG at the temperatures indicated. The dotted lines correspond to the anomalous jump diffusion model (fits of eq 16 with β = 0.5) with l_0-values continuously decreasing from 1.1 Å at 460 K to 0.84 Å at 525 K. Representative error bars are shown for the lowest and highest-Q results at 525 K.

In Figure 13, the characteristic times obtained at the same Q-values investigated by NSE are represented as a function of temperature in a compiling relaxation map of PEMA.

B. Neutron Spin Echo. As already commented in the previous section, the KWW functional form is usually assumed to describe the time-dependence of the dynamic structure factor (coherent scattering) of glass-forming polymers above the glass transition. Individual fits of KWW functions (eq 13) to the NSE results on PEMA-d_{10} were first made in order to determine the β-value. The free parameters involved were β, τ_w, and a prefactor accounting for the decrease of the amplitude due to the vibrational contributions (Debye–Waller factor). The fits leaded to a β-value of 0.5 ± 0.08 for Q = 0.63 Å^{-1} and of 0.38 ± 0.04 for Q = 1.3 Å^{-1}. In the latter case, only the three highest temperatures were considered due to the large uncertainties involved in this fit for $T \leq 420$ K. The solid lines in Figure 10 are fitting curves with β fixed to the obtained values. The corresponding characteristic times are represented as filled squares and circles in Figure 13.

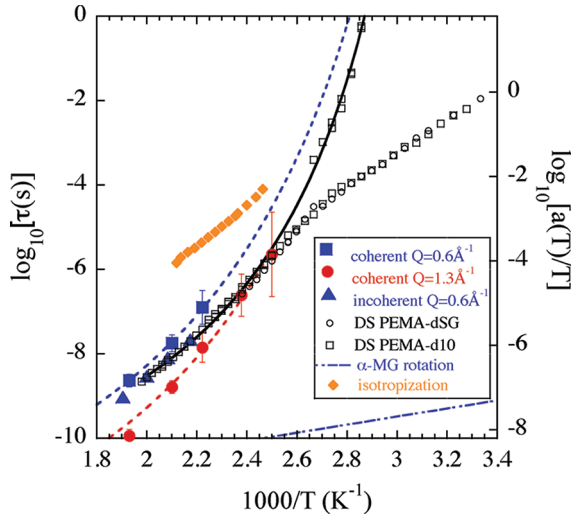


Figure 13. (a) Temperature dependence of the derivative of the specific heat of PEMA-d_{10}. (b) Relaxation map of PEMA including neutron scattering and dielectric spectroscopy results of this work. Diamonds represent the isotropization process reported by Spiess et al.[23] Dotted lines show the temperature dependence expected from mechanical measurements (see text). Solid line: see text. Dashed–dotted line shows the characteristic time for α-methyl group rotation.

V. DISCUSSION

A. Structure Factor. Unraveling the origin of the different peaks of $S(Q)$ in polymers with relatively complex microstructure like PEMA is not an easy task without the aid of simulations. Nevertheless, the access to the total structure factor from the fully deuterated sample and to different partial structure factors through H/D labeling and/or employing X-ray diffraction can provide deep insights to compose a global picture. Of special interest is the availability of the coherent cross sections in absolute units provided by neutron diffraction with polarization analysis. Moreover, in the particular case of PEMA, comparison with existing information on PMMA obtained from combined neutron diffraction and simulation results[27] and on higher-order members of the family of PnMAs by neutron scattering[25,26] can also help to put the results into a context. The latter works have shown clear evidence for the nanosegregation of main chains and alkyl side groups, and for the existence of alkyl nanodomains in high-order PnMAs[25,26] that was previously suggested by Beiner.[14,15,19] The neutron diffraction patterns of high-order PnMA members display two peaks below 2 Å^{-1}. The peak centered at lower Q-values contains correlations from main-chain atoms and its position depends on the side-group length. It has been identified as an interdomain peak. The second peak is centered around 1.3 Å^{-1}. Its T-dependent position in poly(n-hexyl methacrylate) (PHMA) is depicted as a dashed-dotted line in Figure 4. The similarity of this peak with the intermolecular peak of molten bulk PE[43] allowed its identification as originating from atoms of different alkyl groups within the PE-like environment of the side groups nanodomains.[25,26]

PMMA exhibits a strong local order leading to a characteristic correlation peak at 0.73 Å^{-1}, hinting the existence of a precursor effect of such nanophase separation already in the polymer with shortest side groups.[27] A recent computational investigation[29] of a simple bead–spring model for comb-like polymers mimicking

dx.doi.org/10.1021/ma202653k | Macromolecules 2012, 45, 2522–2536

polymers with long side groups ("arms") like PnMAs has shown that nanosegregation of main chains and arms can arise as a purely entropic effect, provided that the density of branch points is large enough. The main manifestation of this nanosegregation is the presence of coinciding well-defined correlation peaks for main-chain/main-chain correlations and arm/arm correlations (both positive). They are characteristic for the size of the nanodomains and thereby arm-length dependent. Furthermore, the cross-correlations between main chains and arms exhibit a strong negative contribution in the same range that is a proof of anticorrelated main-chain and arm positions. This feature was also revealed by the MD-simulations of PMMA. In the following, we disentangle the origin of the different peaks observed in the structure factor of PEMA and address the question whether these features can also be identified in the structure of PEMA.

Deuterium substitution changes the relative weight of the contributions involving H atoms to the measured cross sections (see eq 1). In our analysis we will distinguish three different molecular groups in PEMA: MC (main-chain and α-methyl group), SG (alkyl side group [CH_2−CH_3]) and COO group. Table 3 lists the relative weights of the different partial structure factors corresponding to these molecular groups for the PEMA samples with different deuterium substitutions. These weights are based on the different scattering lengths involved and the relative abundance of the atomic pairs. We will also consider in this discussion the results previously reported by Meier et al.[44] on a PEMA sample with only the main-chain deuterated, PEMA-dMC (inverse labeling as the one here investigated). In that sample, the overwhelming contribution to the coherent cross section is that of main-chain correlations. Those results are reproduced in Figure 14. They show a unique strong peak centered at 0.63 $Å^{-1}$, univocally demonstrating that peak I contains MC/MC correlations. These should be attributed to intermain-chain correlations, with an associated average distance in the Bragg approximation of 10 Å.

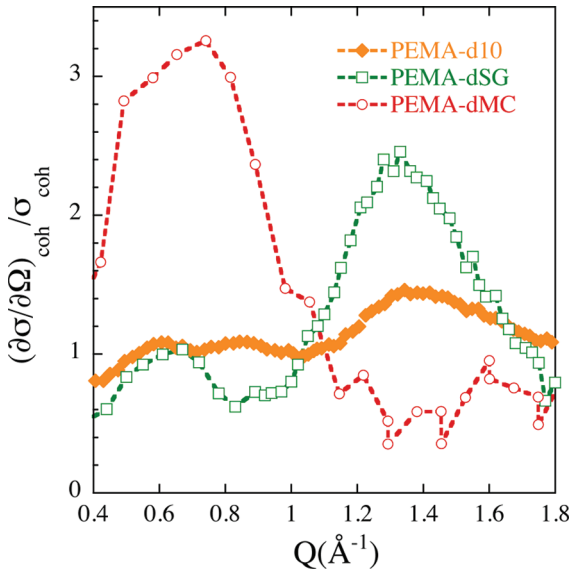


Figure 14. Coherent differential scattering cross-section normalized to the total coherent scattering cross section for fully deuterated PEMA-d_{10} (yellow diamonds) and main-chain protonated/side group deuterated (green squares) PEMA-dSG obtained in this work at 300 K. The PEMA-d_{10} results have been corrected for the observed deficiency in the deuteration level. Data on main-chain deuterated/side group protonated (red circles) PEMA (PEMA-dMC) at 8 K published in ref 44 are also plotted for comparison.

Contrarily, in PEMA-dSG the coherently scattered intensity is dominated by the correlations involving atoms of the deuterated alkyl side-group (SG). The prominence of Peak III in this case (and its absence in the PEMA-dMC results) hints that peak III has to contain to a large extent SG/SG correlations. In addition, we observe also the presence of peak I in the PEMA-dSG pattern, indicating that peak I has to contain also SG/SG correlations. Thus, the same characteristic length of ≈10 Å emerges when SG/SG correlations are followed, supporting the extensibility of the nanophase scenario to the PEMA case. The same conclusion was drawn by Wind et al.[24] based on the interpretation of the first peak of $S(Q)$. Additional information on Peak I can be obtained by considering the PEMA-d_{10} results. In PEMA-d_{10}, all correlations are approximately equivalently weighted. Peak I in PEMA-d_{10} would then contain MC/MC, SG/SG, and also MC/SG correlations. From Figure 14, we realize that the intensity of this peak is much weaker than that expected from the addition of the MC/MC and SG/SG contributions as observed in the partially deuterated samples. This must mean that an important negative contribution from the MC/SG cross-correlations is present that would be the signature of the anticorrelation of MCs and SGs, i.e., of the nanosegregated microstructure. The presence of such a pronounced anticorrelation peak for main-chain and side groups correlations was also revealed in the decomposition of the structure factor facilitated by the MD-simulations on PMMA.[27]

Furthermore, in PEMA-dSG the contributions from MC atoms are small as compared to PEMA-d_{10}, while the contributions of SG/SG correlations are just the same as in PEMA-d_{10}. Then, the vanishing of Peak II in the PEMA-dSG data (Figures 2 and 14) indicates that this peak must be produced by correlations involving the backbone (main chain and α-MG) atoms. We also note that in PEMA-h_{10} the partial structure factor still displays peaks II and III, while the first low-Q peak is not visible (only a shoulder in the X-ray spectrum of Figure 2c). It would mean that the backbone correlations related to peaks I and II have different origins. In particular, we note that peak II is clearly dominating the X-ray diffraction pattern, pointing to the presence of correlations involving the carbonyl group and the ether oxygen. Taking into account that this peak becomes more pronounced in the PEMA-d_{10} sample and disappears in the PEMA-dSG sample, we suggest that it could be mainly due to COO/MC cross-correlations.

From the above discussion we have attributed the origin of peak III to SG-correlations. Supporting this identification, there is absolutely no indication for this peak in the PEMA-dMC results previously reported[44](see Figure 14). This point was initially commented by Wind et al.[24] based on a similar comparison between X-ray and neutron data of main-chain or side-chain deuterated PEMA. We note that the position of peak III in the PEMA-dSG data is located at a slightly smaller Q-value than in PEMA-d_{10}. This could mean that peak III in PEMA-d_{10} would contain contributions beyond the SG/SG correlations. The position of peak IIIa resolved in the D16 experiments on PEMA-d_{10} corresponds to the SG/SG correlation peak that is isolated in the PEMA-dSG sample (see Figure 4). Thus, peak IIIa relates to the SG/SG also. In the PHMA work, this peak was shown to originate from the correlations from atoms of different alkyl groups within the PE-like environment of the side

dx.doi.org/10.1021/ma202653k | Macromolecules 2012, 45, 2522−2536

groups nanodomains. Thus, we assign the same origin to peak IIIa in PEMA. Table 4 summarizes the origin of the correlations

Table 4. Correlations Contributing to the Structure Factor Peaks

peak	correlations involved
I	MC/MC, SG-domain/SG-domain, MC/SG-domain (anticorrelation)
II	correlations involving backbone atoms, mainly MC/COO
III	correlations involving SGs, in particular SG/SG at IIIa

leading to the different peaks, according to the present discussion.

The thermal evolution of $S(Q)$ (Figures 2a and 3) suggests that the correlations below ≈1.5 Å^{-1} have a predominantly intermolecular character. As shown in Figure 4, the positions of peaks I, II, and III display a smooth T-dependence below T_g while they sensitively shift above T_g. A decrease in the peak position Q-value with increasing T, as observed for peaks II and III, is the expected behavior reflecting an expansion of the structure (more pronounced in the supercooled liquid state than in the glassy state) leading to an increase of the intermolecular distances. In this sense, the opposite tendency displayed by peak I could be puzzling at a first sight. We can interpret this peculiar feature as a signature of the complexity of this peak which contains the contributions from MC/MC and SG/SG correlations reflecting the overall periodicity of the system but also the MC/SG cross-correlations reflecting their anticorrelation.

From the T-dependence of the diffraction peak positions, it is possible in principle to calculate[24] the linear coefficient of thermal expansion, α, which describes the relative change in length of a material per degree temperature change. Below T_g, from the D16 data on PEMA-d_{10} we obtain similar thermal coefficients for the three peaks, namely $\alpha = 3 \times 10^{-4}$ K^{-1}. This value is compatible with our X-ray results for peaks I and II, very similar to that reported by Wind et al.[24] from the T-dependence of their X-ray data for peaks II and III and in very good agreement with results from dilatometric methods.[45]

Above T_g, it is difficult to discuss the temperature dependence of peaks I and II, as both peaks are merged at high temperature (about 100 K above T_g). The dramatic increase of the intensity of the low-Q peaks would indicate a more pronounced order in nanodomains at high temperatures. Focusing on the behavior of peak III, based mainly on the highest temperature result from D7 we can estimate $\alpha = 10.6 \times 10^{-4}$ K^{-1} (see Figure 4). Within the uncertainties, peak IIIa from PEMA-d_{10} also follows this temperature dependence, but in this case the same expansion coefficient seems to persist even below T_g (see the PEMA-dSG result at 300 K). This behavior is analogous to that found for PBMA and PHMA.[26] In those samples, the change of slope in the temperature dependence of the peak position does not occur at the calorimetric glass transition but at a much lower temperature, that was identified with the glass transition within the nanodomains, T_g^{SG}. As can be seen in Figure 4, PEMA and PHMA show a quite similar expansion coefficient ($\alpha^{PHMA} = 18.6 \times 10^{-4}$ K^{-1}), close to that reported for PE ($\alpha^{PE} = 20.2 \times 10^{-4}$ K^{-1}). α^{PE} was obtained from the temperature dependent position of the intermolecular peak of a fully deuterated PE sample above the melting point. The reported dilatometric values for the PnMA series turn out to be lower (from 6 to 7 $\times 10^{-4}$ K^{-1}).[45] Dilatometry is sensitive to the total change of volume, that should be mainly determined by the expansion of the main chains (i. e., of the overall structure). At the SG/SG peak instead, we are following the expansion of the side-group distances within the nanodomains. In this direction, we comment that the Q-value of the intermolecular peak in PE is larger than in PBMA and PHMA. E.g., at $T \approx 420$ K, Q_{max}^{PE}=1.285 Å^{-1} vs Q_{max}^{PHMA} = 1.213 Å^{-1}, leading to average distances between alkyl chains of $d^{PE} \approx 4.9$ Å vs d^{PHMA}≈5.2 Å. This suggests a less compact structure within the nanodomains, allowing for a "generous" thermal expansion independent of the main-chain expansion in the glassy state.

We finally note that our results provide experimental support to the prediction made on the basis of a generic coarse-grained model,[29] namely that in the partial structure factor accessible on samples with protonated main chains and deuterated side groups the interdomain peak should also remain. This feature can in fact already been inferred from the work on PMMA,[27] where the diffraction pattern of the sample with deuterated ester methyl group shows a small peak in the position of the intermain chain peak. In PEMA, this effect is more evident due to the larger difference between the characteristic lengths involved in the two kinds of correlations.

B. α-Methyl Group Dynamics. The widths of the distribution functions of hopping rates used to describe the α-MG rotation of PEMA are very similar to those found for the equivalent group in PMMA.[28,41] The deduced values of the width of the underlying distribution of activation energies (σ_E(PEMA) = 41.4 meV, σ_E(PMMA) = 39 meV) are relatively large compared to those reported for other amorphous polymers, like e. g., for poly(vinyl acetate) (PVAc) (σ_E(PVAc) = 21.8 meV), PI (σ_E(PI) = 30 meV) or poly(vinyl methyl ether) (PVME) (σ_E(PVME) = 23.8 meV).[39] MD-simulations results[46] have suggested that σ_E is mainly controlled by the very local nonbonded interactions. Thus, broad distributions hint to particularly heterogeneous local environments for the MGs in PMMA and PEMA. On the other hand, the average value of the barrier in PEMA is sensitively reduced with respect to that in PMMA (E_{Ao}(PEMA) = 195 meV vs E_{Ao}(PMMA) = 290 meV) and is similar to those found in, e.g., poly(ethylene propylene) (PEP), or in atactic and head-to-head polypropylene (PP). Methyl group rotational barriers are determined by both intra- and intermolecular interactions. For α-MGs in PMMA and PEMA the intramolecular contribution to the potential are expected to be very similar. The larger value of E_a found for PMMA can be attributed to stronger contributions of intermolecular origin, probably related to a more densely packed structure. At 25 °C, the density of PEMA is 1.119 g/cm^3, while PMMA has 1.22 g/cm^3.[47] The data of the density at 25 °C for PnMAs from PMMA (number of carbons in the side-group n_C = 1) to PHMA (n_C = 6)[47] obey very well the law ρ(g/cm^3) = 1.2133$n_C^{-0.105}$. We thus would expect a continuous decrease on the value of E_{Ao} for α-methyl group rotations with increasing side-group length in this family of polymers.

C. Hydrogen Dynamics in the α-Region. The relatively low barriers for α-MG dynamics and the plasticization effect of the side groups on the α-process (reduction of T_g with respect to that of PMMA) lead to the simultaneous observation in the BS window of both dynamics, the MG-rotation and the segmental relaxation, in the supercooled liquid state of PEMA. Under the assumption of statistical independence of the two processes, we have characterized the segmental-relaxation component. The Q-dependence of the characteristic times for segmental motions appears to show a unique law $\tau_w \propto Q^{-2}$ in the whole Q- and temperature range investigated (see Figure 12). This dependence is much weaker than that expected in the case

dx.doi.org/10.1021/ma202653k | Macromolecules 2012, 45, 2522−2536

of a Gaussian intermediate scattering function. For a Gaussian self-correlation function the stretching exponent β and the Q-dispersion of the characteristic times[48] are related by: $\tau_w \propto Q^{-2/\beta}$ (with β = 0.5, the exponent would be 4 in our case). Deviations from Gaussian behavior at high Q-values (above $\approx$1 Å^{-1}) have been observed in various polymers.[28,49−57] In those cases, a crossover from heterogeneous dynamics at local scales to the expected Gaussian regime at larger scales was found at a crossover momentum transfer, Q_c, which is located between about 0.65 and 1.3 Å^{-1}, depending on the sample. Thanks to the combination of quasielastic neutron scattering and molecular dynamics simulation,[28] in the case of PMMA a broad and smooth crossover could be identified for the dynamics of the main-chain and α-methyl hydrogens around $Q\approx$0.7 Å^{-1}. Here, in the restricted Q-range of our measurements such a crossover is not observed and one can only assume that in PEMA it could occur below $Q_c \leq$ 0.6 Å^{-1}. We also note that a correlation has been proposed between the location of Q_c and the position of the first maximum of $S(Q)$.[50] Supporting this hypothesis, in a recent work combining BS and MD-simulations on the poly(vinylpyrrolidone) system, Gaussian behavior has only been found in the Q-range below the intermain-chain correlation peak. That system is of particular interest in this framework because it possesses relatively bulky side groups and displays peculiar behavior attributed to the large dynamic asymmetry existing between main-chain and side-group subsystems − analogous to the case of PnMAs.[25] With the present data at hand we cannot proof that below the intermolecular peak -in this case, peak I/II is around 0.7 Å^{-1} in the temperature range under consideration- the dynamics of PEMA's protons is Gaussian. Nevertheless, we may assume that the model proposed to explain this kind of deviations from Gaussian behavior in other polymers (see, e.g., refs 51 and 52 for polyisoprene (PI) and ref 28 for PMMA) is also extensible to the case of PEMA. This model is a generalization of the well-known jump diffusion model to the case of anomalous diffusion (sublinear increase of the mean-squared displacement, $\langle r^2\rangle \propto t^{\beta}$). The jump diffusion model assumes the superposition of discrete jumps of different lengths l with a most probable value l_0 as the origin of the diffusive motion. In the case of anomalous diffusion, the characteristic time of the intrinsically stretched intermediate scattering function can be written as

$$\tau_w = \tau_0\left[1 + \frac{1}{Q^2 {l_0}^2}\right]^{1/\beta} \qquad (16)$$

which in the asymptotic low-Q limit yields the Gaussian law $\tau_w \propto Q^{-2/\beta}$. This equation accounts approximately for the dispersion of the segmental characteristic times for PEMA (see dotted lines in Figure 12), assuming rather large values of the jump lengths ($l_0 \approx$ 1 Å). For example, for PMMA and PI, values of l_0 = 0.6 and 0.4 Å respectively are found. If this scenario applies also for PEMA, we suggest that the process of escaping from the local environment for the PEMA monomer with its longer side group would involve larger length scales than in the case of PMMA, shifting the crossover to lower Q-values.

D. Temperature Dependence. Time−temperature superposition is a universal feature of the structural relaxation[58] that has been revealed by direct measurements of the dynamic structure factor at the intermolecular level in different glass-forming systems.[59] This scaling universality is usually checked with the shift factors based on viscosity measurements, that allow a fairly accurate superposition of the microscopic data. The temperature dependence of the characteristic time associated with the viscosity η(T) is related to the temperature-dependent rheological shift factors $a(T)$ through $\tau_\eta(T) \propto a(T)/T$. For the both investigated Q-values, Figure 15 shows

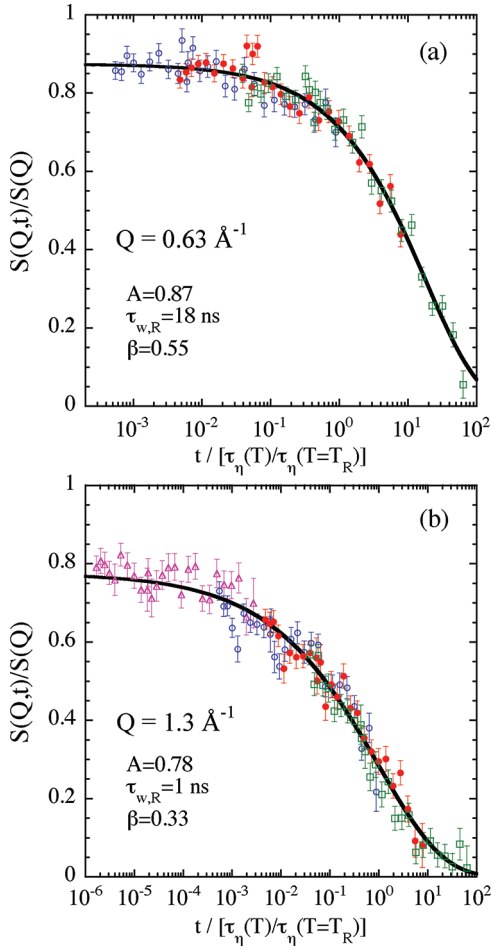


Figure 15. Master curves obtained from the NSE results on PEMA-d_{10} at Q = 0.63 (a) and 1.30 Å^{-1} (b). The time has been scaled with the temperature-dependent shift factors obtained from mechanical measurements[60] considering 480 K as reference temperature. Symbols as in Figure 10. Lines are KWW fits with the parameter values indicated.

the master curves obtained from the temperature dependent dynamic structure factor from the PEMA-d_{10} sample. Thereby the time was scaled according to $\tau_\eta(T)$, taking 480 K as reference temperature T_R. We have used results from dynamic shear compliance $J^*(\omega)$ obtained in the interval from 352.7 to 428 K,[60] $\log_{10}a(T) = -C_1(T - T_o)/(C_2 + T - T_o)$, with C_1 = 11.18, C_2 = 103.5 K, and T_o = 373 K. According to our structural analysis, at Q = 0.63 Å^{-1} the NSE data reveal the decay of (i) main-chain/main-chain correlations (ii) domain−domain correlations, and (iii) MC/SG cross-correlations that would add in a negative way. We observe perfect scaling (Figure 15a), with a resulting stretching of the master curve that can be described by a KWW exponent of 0.55. This is in the typical range found for the structural relaxation in chemically more simple glass-forming polymers like the main-chain polymer polybutadiene[61] or polymers with small side groups like polyisobutylene.[49] This behavior indicates a similar functional form and characteristic time for the decay of the

dx.doi.org/10.1021/ma202653k | Macromolecules 2012, 45, 2522−2536

three correlation functions contributing to the dynamic structure factor, and, obviously, the same temperature dependence. Such observation is in perfect agreement with the MD-simulation results on the generic comb model.[29] The NSE results at Q = 1.3 Å^{-1} reveal the decay of the SG/SG intermolecular correlations within the nanodomains. They also show a nice scaling with $\tau_\eta(T)$ (see Figure 15b). Thus, at least in the high temperature range that is explored by neutron scattering techniques, the time−temperature superposition seems to hold at both Q-values and the viscosity controls not only the relaxation of the interdomain and inter-MC/MC correlations but also the dynamics within the domains. In this case, we note however a smaller value of the stretching parameter (0.33) than that found for the domain/domain and MC/MC correlations. We could consider this enhancement of the stretching as a precursor for the extreme stretching found for higher order members of the PnMAs series, where even logarithmic-like decays are observed for the dynamic structure factor within the domains.[25,26]

For comparative purposes, Figure 13 compiles results obtained for PEMA from different techniques. Starting with the collective times in Figure 13b, we note a 10-fold faster relaxation of the correlations within the domains than those between domains (and between main chains), indicating a substantial dynamic asymmetry in the system. Underlining the similar viscosity-driven character of the dynamics at both levels, the dashed lines depict the T-dependence of the characteristic time associated with the viscosity, properly scaled to match the corresponding absolute values of the NSE relaxation times. For the lowest Q-value, this law has been extended down to the glass-transition region. In a consistent way, the such extrapolated characteristic times for the domain−domain and MC/MC relaxation would reach the typical values of 1...100 s in the temperature range where the calorimetric measurements reveal the loss of equilibrium of the system (peak in the derivative of the specific heat, see Figure 13a). Considering now the characteristic times for the incoherent scattering function of MC atoms, they follow, as expected, the same temperature dependence as the collective times. At Q_I, the self-motions are faster than the collective ones, suggesting a kind of de Gennes narrowing.[62] De Gennes predicted that for simple diffusion the collective times are related with the self-correlation times via multiplication by the static structure factor. This relationship has been experimentally checked in a simple monatomic liquid.[30] Because of such modulation, the values of the collective times in the neighborhood of the first amorphous halo (where $S(Q) > 1$) are larger than the corresponding values of the self-times. A semiquantitative agreement with the de Gennes narrowing prediction has also been reported for more simple polymers like polyethylene[43] and poly(ethylene propylene),[63] and also in PMMA.[28] It is indicative for diffusive-like motions. The self-times corresponding to the atomic correlations giving rise to the peak at Q_{II} = 1.3 Å^{-1} would be those characteristic for the side-group atoms, that are not accessed by our BS experiments on PEMA-dSG. They would be measurable on a PEMA-dMC sample, instead. Therefore, in this work we cannot address the question of the extensibility of the de Gennes narrowing to the case of the correlations within the nanodomains.

Figure 13b also shows the characteristic times obtained from dielectric measurements on our samples (further experimental details can be found elsewhere[26]). They perfectly agree with the results published by other authors on PEMA.[7,9] In the neighborhood of the glass transition, the contributions of the α and β-relaxations can be resolved, the latter being much more intense. At higher temperatures, a single peak corresponding to the merged α and β-relaxations is observed. In the overlapping range with the neutron scattering results the dielectric characteristic times perfectly match the incoherent relaxation times of the main-chain hydrogens at $Q = Q_I$. This coincidence has also been reported for, e.g., PVAc,[55] and within the uncertainties, could also apply for PMMA. At those high temperatures, the temperature dependence observed by dielectric spectroscopy is thus the same as that of the magnitudes followed by neutron scattering, namely that dictated by the viscosity. There, the β-contribution is not important and the spectra are dominated by the structural relaxation. However, with decreasing temperature the dielectric characteristic times clearly deviate from this behavior. In order to describe the temperature dependence of the dielectric α-relaxation we have considered the results close to T_g, where it can be isolated, together with those in the overlapping range with neutron scattering. A Vogel−Fulcher dependence $\tau=\tau_\infty\exp[B/(T - T_{VF})]$ with τ_∞ = 1.2 ps, B = 1649.4 K, and T_{VF} = 288.2 K is obtained (see solid line in Figure 13). This global T-dependence displayed by the dielectric results is different from that observed for the characteristic time of the viscosity. The reorientational process of the carbonyl group leading to the dielectric signal does not follow the rheological behavior. We also note that the maximum of the specific heat derivative is very close to the temperature where the MC/MC (equivalently, domain−domain) correlations freeze, while the dynamic glass-transition temperature deduced from the dielectric results is lower. This indicates that the carbonyl groups carrying the main dipole moment in the sample relax faster than the domain (respectively, MC) structure. Their enhanced mobility at low temperatures shall be attributed to a strong coupling with the side-group dynamics within the domains. A similar observation is made in PBMA and PHMA.[26] Finally, we comment that none of the processes identified here can be directly related with the isotropization process reported from NMR experiments,[22,23] that occurs in a much slower fashion.

VI. CONCLUSIONS

The combination of different H/D labeling enhancing different partial structure factors has allowed a deeper understanding of the static features of PEMA previously investigated by Wind et al.[24] Of great help has been the exploitation of analogies with previously identified structural properties of PMMA[27] and high-order PnMAs.[25,26] The PEMA results also show clear hints for strong structural ordering with nanosegregated side-group domains in agreement with Wind et al.[24] We have identified the contributions to peak I (≈0.6 Å^{-1}) as originating from (i) main-chain/main-chain correlations, (ii) inter side-group domain correlations, and (iii) anticorrelations between main-chains and side groups domains. Peak II, dominating X-ray patterns, mainly contains backbone correlations, being probably the main-chain/carbonyl correlations the most prominently contributing. The peak at around 1.3 Å^{-1} is largely determined by side-group correlations. In particular, the 'sub-Peak' IIIa seems to be due to SG/SG correlations and thereby analogous to the PE-like peak in high-order PnMAs, that has been attributed to correlations from atoms of the different alkyl side groups within the nanodomains. The same position and T-dependence in both peaks (IIIa in PEMA and PE-like peak in higher order members) also suggests a decoupling from the main-chain and side-groups T_gs, and larger expansion coefficient within the nanodomains than between them. We also emphasize that the

dx.doi.org/10.1021/ma202653k | Macromolecules 2012, 45, 2522−2536

structural results on PEMA perfectly fit in the frameworks deduced from fully atomistic MD-simulations on PMMA[27] as one extreme of the PnMAs series and also from MD-simulations on a generic coarse-grained model capturing the peculiar architecture induced by more or less long side groups in the polymer chains.[29]

Regarding the dynamics, the α-MG rotations reveal highly disordered environments in the glassy state, as well as a less densely packed structure than in PMMA. Above the glass transition, the main-chain hydrogen self-correlation function related to segmental relaxation shows stretching and clear deviations from Gaussian behavior in the accessed window. They could be rationalized invoking an underlying distribution of relatively large elementary jumps as compared with those found in other polymers. This scenario implicitly assumes a crossover to Gaussian behavior that would occur at lower Q-values than those accessed in this work. It would be very plausible that this crossover would be located around Q_I, i.e., determined by the main-chain/main-chain correlations. On the other hand, the temperature dependence of the characteristic times for backbone hydrogen self-motions is the same as that observed for the collective dynamics at peaks I and III. Viscosity dictates not only the domain/domain and main-chain/main-chain relaxation but also for the dynamics within the nanodomains and the dielectric spectroscopy results at high temperatures. With decreasing temperature, nevertheless, the α-process as followed by dielectric spectroscopy shows a different T-dependence than the rheological law, indicating a strong influence of the side-group faster motions on the dynamics of the dipole-carrying moeity.

AUTHOR INFORMATION

Notes

The authors declare no competing financial interest.

ACKNOWLEDGMENTS

We are thankful to W. Schweika from Forschungszentrum Jülich, and to the Institut Laue Langevin (ILL, Grenoble, France) scientists P. Fouquet, M. Maccarini, B. Deme, and P. P. Deen for experimental help. The ILL is acknowledged for neutron scattering facilities. We thank support by the "Donostia International Physics Center", the European Commission NoE SoftComp, Contract NMP3-CT-2004-502235, FP7-PEOPLE-2007-1-1-ITN (DYNACOP, EU), Projects MAT2007-63681 and IT-436-07 (GV) and the Spanish Ministerio de Educacion y Ciencia (Grant No. CSD2006-53). The European Commission, NMI3 Contract RII3-CT-2003-505925, supported the experiments at the Forschungsreaktor in Jülich, Germany. The authors acknowledge P. Dieudonné for the X-ray measurements in Montpellier, France.

REFERENCES

(1) Heijboer, J. In *Physics of Non-Crystalline Solids*; Prins, J. A., Ed.; North-Holland: Amsterdam, 1965; pp 231−254.
(2) McCrum, N. G.; Read, B. E., Williams, G. *Anelastic, Dielectric Effects in Polymeric Solids*; Wiley: London, 1967.
(3) Cowie, J. M. G. *J. Macromol. Sci.—Phys. B* **1980**, *18*, 569−623.
(4) Miller, R. L.; Boyer, R. F.; Heijboer, J. *J. Polym. Sci., Polym. Phys. Ed.* **1984**, *22*, 2021.
(5) Meier, G.; Fytas, G.; Dorfmüller, T. *Macromolecules* **1984**, *17*, 957−961.
(6) Giebel, L.; Meier, G.; Fytas, G.; Fischer, E. W. *J. Polym. Sci., Part B: Polym. Phys.* **1992**, *30*, 1291−1297.
(7) Garwe, F.; Schönhals, A.; Lockwenz, H.; Beiner, M.; Schröter, K.; Donth, E. *Macromolecules* **1996**, *29*, 247−253.
(8) Kuebler, S. C.; Schaefer, D. J.; Boeffel, C.; Pawelzik; Spiess, H. W. *Macromolecules* **1997**, *30*, 6597−6609.
(9) Schröter, K.; Unger, R.; Reissig, S.; Garwe, F.; Kahle, S.; Beiner, M.; Donth, E. *Macromolecules* **1998**, *31*, 8966−8972.
(10) Floudas, G.; Stepanek, P. *Macromolecules* **1998**, *31*, 6951−6957.
(11) Mpoukouvalas, K.; Floudas, G.; Williams, G. *Macromolecules* **2009**, *42*, 4690−4700.
(12) Dudognon, E.; Bernès, A.; Lacabanne, C. *Macromolecules* **2001**, *34*, 3988−3992.
(13) Dudognon, E.; Bernès, A.; Lacabanne, C. *Macromolecules* **2002**, *35*, 5927−5931.
(14) Beiner, M.; Schröter, K.; Hempel, E.; Reissig, S.; Donth, E. *Macromolecules* **1999**, *32*, 6278−6282.
(15) Beiner, M. *Macromol. Rapid Commun.* **2001**, *22*, 869−895.
(16) Beiner, M.; Kabisch, O.; Reichl, S.; Huth, H. *J. Non-Cryst. Solids* **2002**, *307*, 658−666.
(17) Hempel, E.; Beiner, M.; Huth, H.; Donth, E. *Thermochim. Acta* **2002**, *391*, 219−225.
(18) Pascui, O.; Beiner, M.; Reichert, D. *Macromolecules* **2003**, *36*, 3992−4003.
(19) Beiner, M.; Huth, H. *Nat. Mater.* **2003**, *2*, 595−599.
(20) Hiller, S.; Pascui, O.; Kabisch, O.; Reichert, D.; Beiner, M. *New J. Phys.* **2004**, *6*, 10.
(21) Beiner, M. *CP832, Flow Dynamics, The Second International Conference on Flow Dynamics*; Tokuyama, M., Maruyama, S., Eds.; American Institute of Physics: College Park, MD, 2006; pp 134−140.
(22) Wind, M.; Graf, R.; Heuer, A.; Spiess, H. W. *Phys. Rev. Lett.* **2003**, *91*, 155702.
(23) Wind, M.; Graf, R.; Renker, S.; Spiess, H. W. *Macromol. Chem. Phys.* **2005**, *206*, 142−156.
(24) Wind, M.; Graf, R.; Renker, S.; Spiess, H. W.; Steffen, W. *J. Chem. Phys.* **2005**, *122*, 014906.
(25) Arbe, A.; Genix, A.-C.; Colmenero, J.; Richter, D.; Fouquet, P. *Soft Matter* **2008**, *4*, 1792−1795.
(26) Arbe, A.; Genix, A.-C.; Arrese-Igor, S.; Colmenero, J.; Richter, D. *Macromolecules* **2010**, *43*, 3107−3119.
(27) Genix, A.-C.; Arbe, A.; Alvarez, F.; Colmenero, J.; Schweika, W.; Richter, D. *Macromolecules* **2006**, *39*, 3947−3958.
(28) Genix, A.-C.; Arbe, A.; Alvarez, F.; Colmenero, J.; Farago, B.; Wischnewski, A.; Richter, D. *Macromolecules* **2006**, *39*, 6260−6272.
(29) Moreno, A. J.; Arbe, A.; Colmenero, J. *Macromolecules* **2011**, *44*, 1695−1706.
(30) Springer, T. *Quasielastic Neutron Scattering for the Investigation of Diffusive Motions in Solids, Liquids*; Springer Tracts in Modern Physics 64; Springer-Verlag: Berlin, Heidelberg, Germany, and New York, 1972; Vol. *64*.
(31) Lovesey, S. W. *Theory of Neutron Scattering from Condensed Matter*; Clarendon Press: Oxford, U.K., 1984.
(32) Bée, M. *Quasielastic Neutron Scattering*; Adam Hilger: Bristol, U.K., 1988.
(33) Squires, G. L. *Introduction to the Theory of Thermal Neutron Scattering*; Dover Publication Inc.: New York, 1996).
(34) Häussler, W.; Holderer, O.; Unruh, T.; Wuttke, J. *Neutron News* **2011**, *22*, 24.
(35) Mezei, F. *Neutron Spin Echo*; Lecture Notes in Physics 28; Springer-Verlag: Heidelberg, Germany, 1980.
(36) Chahid, A.; Alegría, A.; Colmenero, J. *Macromolecules* **1994**, *27*, 3282−3288.
(37) Colmenero, J.; Mukhopadhyay, R.; Alegría, A.; Frick, B. *Phys. Rev. Lett.* **1998**, *80*, 2350.
(38) Colmenero, J.; Alegría, A. *Adv. Funct. Molecules Polym.* **2001**, *2*, 271−293.
(39) Colmenero, J.; Moreno, A.; Alegría, A. *Prog. Polym. Sci.* **2005**, *30*, 1147−1184.
(40) Moreno, A. J.; Alegría, A.; Colmenero, J.; Frick, B. *Macromolecules* **2001**, *34*, 4886−4896.
(41) Genix, A.-C.; Arbe, A.; Alvarez, F.; Colmenero, J.; Willner, L.; Richter, D. *Phys. Rev. E* **2005**, *72*, 031808.

(42) Alvarez, F.; Arbe, A.; Colmenero, J. *Chem. Phys.* **2000**, *261*, 47−59.
(43) Arbe, A.; Colmenero, J. *Phys. Rev. E* **2009**, *80*, 041805.
(44) Meier, G.; Pawelzik, U.; Schweika, W.; Kockelmann, W. *Physica B* **2000**, *369*, 276−278.
(45) Rogers, S. S.; Mandelkern, L. *J. Phys. Chem.* **1957**, *61*, 985−990.
(46) Alvarez, F.; Alegría, A.; Colmenero, J.; Nicholson, T. M.; Davis, G. R. *Macromolecules* **2000**, *33*, 8077−8084.
(47) *Physical Properties of Polymers Handbook*; Mark, J. E., Eds.; AIP Press: New York, 1996.
(48) Colmenero, J.; Alegría, A.; Arbe, A.; Frick, B. *Phys. Rev. Lett.* **1992**, *69*, 478.
(49) Farago, B.; Arbe, A.; Colmenero, J.; Faust, R.; Buchenau, U.; Richter, D. *Phys. Rev. E* **2002**, *65*, 051803.
(50) Colmenero, J.; Alvarez, F.; Arbe, A. *Phys. Rev. E* **2002**, *65*, 041804.
(51) Arbe, A.; Colmenero, J.; Alvarez, F.; Monkenbusch, M.; Richter, D.; Farago, B.; Frick, B. *Phys. Rev. Lett.* **2002**, *89*, 245701.
(52) Arbe, A.; Colmenero, J.; Alvarez, F.; Monkenbusch, M.; Richter, D.; Farago, B.; Frick, B. *Phys. Rev. E* **2003**, *67*, 051802.
(53) Narros, A.; Alvarez, F.; Arbe, A.; Colmenero, J.; Richter, D.; Farago, B. *J. Chem. Phys.* **2004**, *121*, 3282.
(54) Pérez Aparicio, R.; Arbe, A.; Colmenero, J.; Frick, B.; Willner, L.; Richter, D.; Fetters, L. J. *Macromolecules* **2006**, *39*, 1060−1072.
(55) Tyagi, M.; Arbe, A.; Alvarez, F.; Colmenero, J.; Gonzalez, M. A. *J. Chem. Phys.* **2008**, *129*, 224903.
(56) Capponi, S.; Arbe, A.; Alvarez, F.; Colmenero, J.; Frick, B.; Embs, J. P. *J. Chem. Phys.* **2009**, *131*, 204901.
(57) Arbe, A.; Colmenero, J.; Monkenbusch, M.; Richter, D. *Phys. Rev. Lett.* **1998**, *81*, 590.
(58) Götze, W. In *Liquids, Freezing, Glass Transition*; Hansen, J. P., Levesque, D.; Zinn-Justin, J., Eds.; North-Holland: Amsterdam, 1991; p 287.
(59) Richter, D.; Monkenbusch, M.; Arbe, A.; Colmenero, J. *Neutron Spin Echo Investigations on Polymer Dynamics*; Advances in Polymer Science 174; Springer Verlag: Berlin, Heidelberg, Germany, and New York, 2005.
(60) Ferry, J. D.; Child, W. C.; Zand, R.; Stern, D. M.; Williams, M. L.; Landel, R. F. *J. Colloid Sci* **1957**, *12*, 53−67.
(61) Arbe, A.; Richter, D.; Colmenero, J.; Farago, B. *Phys. Rev. E* **1996**, *54*, 3853.
(62) de Gennes, P. G. *Physica* **1959**, *25*, 825−839.
(63) Perez-Aparicio, R.; Arbe, A.; Alvarez, F.; Colmenero, J.; Willner, L. *Macromolecules* **2009**, *42*, 8271−8285.

Macromolecules

Article

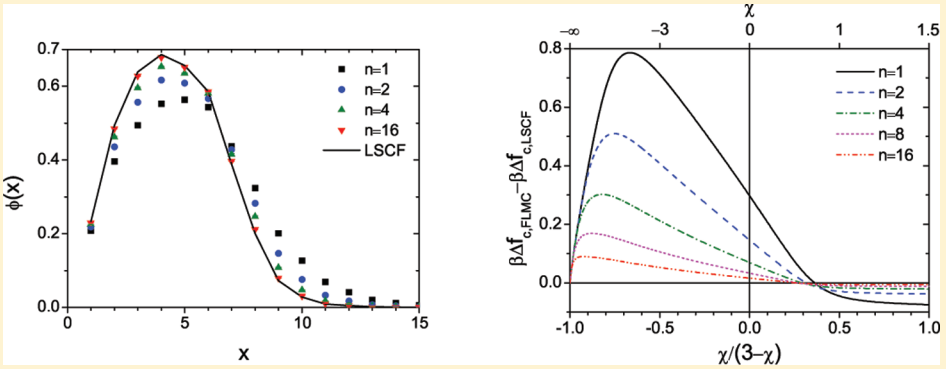
pubs.acs.org/Macromolecules

Quantitative Study of Fluctuation Effects by Fast Lattice Monte Carlo Simulations. III. Homopolymer Brushes in an Explicit Solvent

Pengfei Zhang,[†,‡] Baohui Li,[†] and Qiang Wang*[,‡]

[†]School of Physics, Nankai University, Tianjin, P. R. China 300071

[‡]Department of Chemical and Biological Engineering, Colorado State University, Fort Collins, Colorado 80523-1370, United States



ABSTRACT: Using fast lattice Monte Carlo (FLMC) simulations both in a canonical ensemble and with Wang-Landau−transition-matrix sampling, we have studied a model system of laterally homogeneous homopolymer brushes in an explicit solvent. Direct comparisons of the simulation results with those from the corresponding lattice self-consistent field (LSCF) theory, both of which are based on the *same* Hamiltonian (thus without any parameter-fitting between them), unambiguously and quantitatively reveal the fluctuations and correlations in the system. We have examined in detail how the Flory−Huggins interaction parameter χ between polymer segments and solvent molecules and the number of grafted chains n affect both the brush structures and thermodynamics. For our model system, the LSCF theory is exact in the limit of $\chi \to -\infty$, except that it neglects the correlations among solvent molecules caused by the incompressibility constraint (thus overestimating the solvent entropy). At finite n and χ, the segmental density profile in the direction perpendicular to the grafting substrate obtained from FLMC simulations is flatter than the LSCF prediction, and the free-end density from FLMC simulations is also lower than the LSCF prediction close to the substrate. At finite n and $\chi > 0$, the LSCF theory overestimates the internal energy. In addition, at small $\chi \geq 0$ it underestimates the difference in free energy but overestimates that in entropy from the reference state in the limit of $\chi \to -\infty$, and at larger χ the opposite occurs. At large n, FLMC results approach LSCF predictions at a rate of $1/n$ in most cases.

1. INTRODUCTION

This is the third paper in our series of study,[1,2] where fast lattice Monte Carlo (FLMC) simulations[3] are directly compared with the corresponding lattice polymer field theories based on the same model system (Hamiltonian), thus without any parameter-fitting, to unambiguously and quantitatively reveal the effects of fluctuations and correlations either neglected or treated approximately in the theories. In the second paper in this series (referred to as paper II hereafter), we studied monodisperse, uncharged and flexible homopolymer brushes on a planar and nonadsorbing substrate in an implicit, good solvent.[2] Here we extend that study to the case of an explicit solvent.

As explained in paper II, in the most widely used self-consistent field (SCF) theory,[4] an implicit solvent is described by the second virial coefficient v (with the third virial coefficient w also needed for a poor solvent), and an explicit solvent is described by the Flory−Huggins χ parameter for the interactions between polymer segments and solvent molecules along with the incompressibility constraint requiring the total volume fraction of polymer and solvent be 1 everywhere, which includes all the higher-order terms neglected in the theoretical treatment of an implicit solvent. As shown below, the incompressibility constraint may limit the allowed chain conformations in a brush, which makes such cases more difficult to analyze. It also leads to correlations among solvent molecules; SCF theory neglects such correlations, thus overestimating the entropy of solvent molecules. We refer readers to the Introduction of paper II for an overview of some previous SCF studies on the brushes in an explicit solvent.[5−22]

The meaning of implicit/explicit solvent is somewhat different in molecular simulations. The vacancies (unoccupied lattice sites)

Received: November 7, 2011
Revised: December 20, 2011
Published: February 8, 2012

ACS Publications © 2012 American Chemical Society

in conventional lattice Monte Carlo (MC) simulations of the brushes[9,23−31] can be considered as an explicit solvent due to the self- and mutual-avoiding walk (i.e., the incompressibility constraint) used. On the other hand, in off-lattice simulations of the brushes,[32−44] an explicit (or implicit) solvent simply means that solvent molecules are explicitly (or not) included in the system; in such simulations, the above incompressibility constraint clearly cannot be enforced and v (and w) is rarely used (except in refs 43 and 44).

As explained in detail in the Introduction of paper II, while various forms of SCF theory have been compared with molecular simulations[9,23,25,26,31−33,35−37,43,45] (for example, Pépin and Whitmore compared their lattice MC simulations with continuum SCF calculations both in an explicit and good solvent[9]), which provided important insights and greatly furthered our understanding of polymer brushes, none of these comparisons was done using exactly the same model system in both SCF theories and molecular simulations. They therefore could not unambiguously distinguish the model differences from the consequences of the mean-field approximation inherent in all SCF theories. In addition, only structures (e.g., segmental distributions, brush height, and bond orientation) but not thermodynamics (e.g., internal energy, free energy, and entropy) of the brushes have been examined. This motivated our study presented in paper II and here, which are the prerequisite for developing more accurate theories for polymer brushes.

One complication for the brushes in a poor solvent is the possible formation of laterally inhomogeneous structures, which requires both FLMC simulations and LSCF calculations be performed in 3D. The Wang-Landau−transition-matrix sampling[46−48] we use to study the brush thermodynamics, however, is computationally very expensive for multichain systems in 3D due to the large number of micro/macrostates. We therefore limit this work to laterally homogeneous brushes in 1D, which is justified by the lateral instability analysis as shown in section 3 below, and report our 3D study of phase transitions of grafted chains in an explicit, poor solvent in another paper.[49] Our 2D and 3D canonical-ensemble FLMC simulations of the brushes in an implicit, good solvent reported in Paper II further indicate that, while the differences between FLMC and LSCF results caused solely by the system fluctuations/correlations are smaller in higher dimensions, most qualitative features can be studied in 1D.

2. MODEL AND METHODS

2.1. Model System. We consider an incompressible polymer brush system consisting of n chains of homopolymer A each having N segments and n_S solvent molecules on a lattice having $L = N$ lattice layers in the x direction; for the 1D lattice, the total number of lattice sites $V = L$. Each homopolymer segment or solvent molecule occupies one lattice site, and each lattice site is occupied by totally $\rho_0 \equiv (nN + n_S)/V$ segments and solvent molecules. The first segment of all chains is grafted at $x = 1$ (i.e., in the first layer), and an impenetrable wall is placed at $x = 0$, which cannot be occupied by either polymer segments or solvent molecules. The canonical-ensemble partition function is

$$\mathcal{Z} = \frac{1}{n!n_S!}\prod_{k=1}^{n}\prod_{s=1}^{N}\sum_{X_{k,s}}\cdot\prod_{k=1}^{n_S}\sum_{x_k}\cdot\exp\left\{-\beta\sum_{k=1}^{n}h_k^C - \beta\mathcal{H}^E\right\}\cdot\prod_{x}\delta_{\hat{\rho}(x)+\hat{\rho}_S(x),\rho_0} \quad (1)$$

where $X_{k,s}$ denotes the spatial position of the sth segment on the kth chain, x_k denotes the position of the kth solvent molecule, the summations are over all possible positions of all polymer segments and solvent molecules, respectively, "·" means that the products before it do not apply to the terms after it but the summations before it do, and $\beta \equiv 1/k_BT$ with k_B being the Boltzmann constant and T the absolute temperature. h_k^C is the Hamiltonian of the kth chain due to its chain connectivity; $\beta h_k^C = 0$ if the chain connectivity is maintained and ∞ otherwise. Finally, the Hamiltonian due to nonbonded interactions is given by

$$\beta\mathcal{H}^E[\hat{\rho},\hat{\rho}_S] = \frac{\chi}{\rho_0}\sum_{x}[\hat{\rho}(x)\hat{\rho}_S(x) - n(\rho_0 - n)] \quad (2)$$

where χ is the Flory−Huggins parameter characterizing the interaction between polymer segments and solvent molecules, the microscopic number density of polymer segments and solvent molecules at lattice site x is given by $\hat{\rho}(x) \equiv \sum_{k=1}^{n}\sum_{s=1}^{N}\delta_{x,X_{k,s}}$ and $\hat{\rho}_S(x) \equiv \sum_{k=1}^{n_S}\delta_{x,x_k}$, respectively, and $\delta_{x,X_{k,s}}$ denotes the Kronecker δ-function. The last term in eq 2 is included such that $\beta\mathcal{H}^E = 0$ for a *homogeneous* system.

With the incompressibility constraint imposed by the last term in eq 1, we can rewrite $\beta\mathcal{H}^E[\hat{\rho}] = -C\chi NE/\rho_0^2$, where $C \equiv n/\bar{\phi}V$ with the average polymer volume fraction $\bar{\phi} \equiv nN/(nN + n_S)$, $E[\hat{\rho}] \equiv \sum_x[\hat{\rho}(x) - \bar{\phi}\rho_0]^2$ is defined as the energy level of our system, and we have used $V = N$. The partition function in eq 1 can then be rewritten as

$$\mathcal{Z} = \frac{1}{n!n_S!}\prod_{k=1}^{n}\prod_{s=1}^{N}\sum_{X_{k,s}}\cdot\frac{n_S!}{\prod_x[\rho_0 - \hat{\rho}(x)]!}\times\exp\left\{-\beta\sum_{k=1}^{n}h_k^C + C\chi N\frac{E}{\rho_0^2}\right\}\cdot\prod_{x}\theta(\rho_0 - \hat{\rho}(x)) \quad (3)$$

where $\theta(x) = 1$ if $x \geq 0$ and 0 otherwise. Here we have eliminated the dependence on the spatial positions of all solvent molecules $\{x_k\}$ in the summation, and $n_S!/\prod_x[\rho_0 - \hat{\rho}(x)]!$ is the number of different ways of arranging these solvent molecules for a given configuration $\{X_{k,s}\}$ of all chains. In Appendix A, we give an approximate correspondence between this model system for brushes in an explicit solvent and that for brushes in an implicit solvent studied in paper II.[2]

2.2. Fast Lattice Monte Carlo Simulations. *2.2.1. Canonical-Ensemble Simulations.* Some of our FLMC simulations are performed in a canonical ensemble, where n, $V = L = N$, n_S, and χ are fixed. We use the same configurationally biased trial moves as in paper II. To take into account the entropy of solvent molecules, however, the Rosenbluth weight[50] R used in the acceptance criterion in paper II must be multiplied by $W \equiv \prod_x[\rho_0 - \hat{\rho}(x)]!$ for the corresponding configuration, i.e., $R \rightarrow WR$ for both the trial and old configurations. About $(4−20) \times 10^6$ Monte Carlo steps (MCS) are performed in each simulation, where one MCS is defined as nN trial moves. The error bar of each ensemble-averaged quantity is estimated in the same way as in the first paper[1] in our series (referred to as paper I hereafter).

2.2.2. Wang-Landau−Transition-Matrix (WL-TM) Sampling. As in papers I and II, we use the combined WL-TM sampling[46−48] to estimate the density of states (DoS) within a chosen E-range. The partition function in eq 3 can be rewritten as

$$\mathcal{Z} = \sum_E \Omega(E)\exp\left(C\chi N\frac{E}{\rho_0^2}\right) \quad (4)$$

with DoS $\Omega(E)$ defined as

$$\Omega(E) \equiv \frac{1}{n!}\prod_{k=1}^{n}\prod_{s=1}^{N}\sum_{X_{k,s}}\frac{\delta_{E,E[\hat{\rho}]}}{\prod_x[\rho_0 - \hat{\rho}(x)]!}\times\exp\left\{-\beta\sum_{k=1}^{n}h_k^C\right\}\cdot\prod_{x}\theta(\rho_0 - \hat{\rho}(x)) \quad (5)$$

dx.doi.org/10.1021/ma202454s | Macromolecules 2012, 45, 2537−2550

Note that $\Omega(E) = 0$ for odd E in our simulations, and such macrostates are not included here. We use the same trial moves as in our canonical-ensemble simulations, and the details of our WL-TM sampling are given in paper II. As explained above, however, R used in paper II now needs to be replaced by WR for both the trial and old configurations.

Note that the normalized DoS $g(E)$ obtained from WL-TM simulations gives $g(E = 0) = 1$. Since DoS of the ground state of our n-chain system (where all chains are fully stretched) is $\Omega(E = 0) = 1/n![(\rho_0 - n)!]^V$, we have $\Omega(E) = g(E)/n![(\rho_0 - n)!]^V$ (for conciseness, the explicit dependence of $\Omega(E)$ and $g(E)$ on n is omitted in our notation).

Once $g(E)$ is obtained, we can compute the Helmholtz free energy per chain of length N (i.e., per N lattice sites)

$$\beta f_{c,\mathrm{FLMC}}(\chi) \equiv -N\frac{\ln \mathcal{Z}(\chi)}{\rho_0 V} = -\frac{\bar{\phi}}{n}\ln \sum_E \frac{g(E)}{n![(\rho_0 - n)!]^V} \times \exp\left(C\chi N\frac{E}{{\rho_0}^2}\right) \quad (6)$$

and any canonical-ensemble average as a function of χ. For the latter, we define the normalized probability distribution of E at given χ as

$$P(E,\chi) = \frac{g(E)}{n![(\rho_0 - n)!]^V}\exp\left(C\chi N\frac{E}{{\rho_0}^2}\right)\Big/\mathcal{Z}(\chi) \quad (7)$$

The internal energy per chain is then

$$\beta u_{c,\mathrm{FLMC}}(\chi) \equiv N\frac{\langle \beta \mathcal{H}^E(\chi)\rangle}{\rho_0 V} = -\frac{\chi N}{V}\frac{\langle E(\chi)\rangle}{{\rho_0}^2} = -\frac{\chi N}{V}\sum_E \frac{E}{{\rho_0}^2}P(E,\chi) \quad (8)$$

and the entropy per chain can be obtained from the thermodynamic relation

$$s_c(\chi)/k_B = \beta u_c(\chi) - \beta f_c(\chi) \quad (9)$$

The specific heat per chain is

$$C_{v,\mathrm{FLMC}}(\chi)/k_B \equiv \frac{N}{\rho_0 V}\left[\langle(\beta\mathcal{H}^E(\chi))^2\rangle - \left\langle \beta\mathcal{H}^E(\chi)\right\rangle^2\right] = \frac{C(\chi N)^2}{V{\rho_0}^4}\left[\langle E(\chi)^2\rangle - \langle E(\chi)\rangle^2\right] \quad (10)$$

Finally, the canonical-ensemble averages of the mean-square chain end-to-end distance ${R_{e,\mathrm{FLMC}}}^2(\chi)$, the mean-square chain radius of gyration ${R_{g,\mathrm{FLMC}}}^2(\chi)$ and the brush height $h_{\mathrm{FLMC}}(\chi)$ are calculated in the same way as in paper II, except that the parameter N/κ there is replaced by χ.

2.2.3. Enumeration. One advantage of working in 1D is that we can use enumeration to obtain the exact DoS $\Omega_{\mathrm{exact}}(E)$ for the single-chain system; all of our FLMC results shown for $n = 1$ are actually obtained from enumeration and thus exact. These are further used in our error estimation as discussed in detail later.

2.3. Lattice Self-Consistent Field Theory. Here we start with the *same* Hamiltonian as in our FLMC simulations, and insert in eq 1 the identity $1 = (\rho_0/2\pi)^{2L}\int \mathrm{d}\boldsymbol{\phi}\ \mathrm{d}\boldsymbol{\omega}\ \mathrm{d}\boldsymbol{\phi}_S\ \mathrm{d}\boldsymbol{\omega}_S\ \exp[i\boldsymbol{\omega}\cdot(\rho_0\boldsymbol{\phi} - \hat{\boldsymbol{\rho}})] \times \exp[i\boldsymbol{\omega}_S\cdot(\rho_0\boldsymbol{\phi} - \hat{\boldsymbol{\rho}}_S)]$, where vectors $\hat{\boldsymbol{\rho}} \equiv \{\hat{\rho}(x)\}$ and $\hat{\boldsymbol{\rho}}_S \equiv \{\hat{\rho}_S(x)\}$ have L elements, $\boldsymbol{\phi} \equiv \{\phi(x)\}$ and $\boldsymbol{\phi}_S \equiv \{\phi_S(x)\}$ are the normalized density (volume fraction) fields of polymer segments and solvent molecules, respectively, constrained to $\hat{\boldsymbol{\rho}}/\rho_0$ and $\hat{\boldsymbol{\rho}}_S/\rho_0$, and $\boldsymbol{\omega} \equiv \{\omega(x)\}$ and $\boldsymbol{\omega}_S \equiv \{\omega_S(x)\}$ are the conjugate fields imposing these constraints, respectively. We then substitute the following integral form of the δ-function into eq 1

$$\prod_x \delta_{\hat{\rho}(x)+\hat{\rho}_S(x),\rho_0} = \frac{1}{(2\pi)^L}\int \mathrm{d}\boldsymbol{\eta}\ \exp[-\rho_0 i\boldsymbol{\eta}\cdot(\boldsymbol{\phi} + \boldsymbol{\phi}_S - \mathbf{1})] \quad (11)$$

where the vector $\boldsymbol{\eta} \equiv \{\eta(x)\}$ is the conjugate field imposing the incompressibility constraint and $\mathbf{1}$ has L elements of 1. We finally have $\mathcal{Z} = [\rho_0^{2L}/(2\pi)^{3L}]\int \mathrm{d}\boldsymbol{\phi}\ \mathrm{d}\boldsymbol{\omega}\ \mathrm{d}\boldsymbol{\phi}_S\ \mathrm{d}\boldsymbol{\omega}_S\ \mathrm{d}\boldsymbol{\eta}\ \exp\{-(n/\bar{\phi})\beta f_c[\boldsymbol{\phi},i\boldsymbol{\omega},\boldsymbol{\phi}_S,i\boldsymbol{\omega}_S,i\boldsymbol{\eta}]\}$ with

$$\beta f_c = \chi\boldsymbol{\phi}\cdot\boldsymbol{\phi}_S - \frac{1}{N}\boldsymbol{\phi}\cdot i\boldsymbol{\omega} - \frac{1}{N}\boldsymbol{\phi}_S\cdot i\boldsymbol{\omega}_S + \frac{1}{N}i\boldsymbol{\eta}\cdot(\boldsymbol{\phi} + \boldsymbol{\phi}_S - \mathbf{1}) - \chi N\bar{\phi}(1 - \bar{\phi}) - \bar{\phi}\ln Q[i\omega] - N(1 - \bar{\phi})\ln Q_S[i\omega_S] + \beta f_c^{id} \quad (12)$$

where the single-chain partition function $Q[i\omega] \equiv \prod_{s=1}^N \sum_{X_s} \exp[-\beta h^C - i\sum_{s=1}^N \omega(X_S)/N]/G$ with $G \equiv \prod_{s=1}^N \sum_{X_s}\exp(-\beta h^C) = z^{N-1}L$ and the lattice coordination number $z = 2$ in our 1D case, the single-particle partition function $Q_S[i\omega_S] \equiv \sum_x \exp[-i\omega_S(x)/N]/L$, the free energy per chain of length N for an ideal system of n *ungrafted* chains and n_S solvent molecules (which is noninteracting and *not* subject to the incompressibility constraint)

$$\beta f_c^{id} \equiv -\frac{\bar{\phi}}{n}\ln\frac{G^n}{n!n_S!} - N(1 - \bar{\phi})\ln V = -\frac{s_c^{id}}{k_B} \quad (13)$$

with s_c^{id} denoting the entropy per chain for the ideal system, and we have rescaled variables according to $N\boldsymbol{\omega} \to \boldsymbol{\omega}$, $N\boldsymbol{\omega}_S \to \boldsymbol{\omega}_S$, and $N\boldsymbol{\eta} \to \boldsymbol{\eta}$.

The SCF equations are obtained by setting $\delta\beta f_c/\delta\phi(x) = \delta\beta f_c/\delta i\omega(x) = \delta\beta f_c/\delta\phi_S(x) = \delta\beta f_c/\delta i\omega_S(x) = \delta\beta f_c/\delta i\eta(x) = 0$ (i.e., the mean-field approximation[4]) and given by

$$i\omega(x) = \chi N\phi_S(x) + i\eta(x) \quad (14)$$

$$i\omega_S(x) = \chi N\phi(x) + i\eta(x) \quad (15)$$

$$\phi(x) = \sum_{s=1}^N \phi_s(x) \quad (16)$$

$$\phi_s(x) = \frac{\bar{\phi}\ \exp[i\omega(x)/N]}{q^*_N(x = 1)}q_s(x)q^*_{N+1-s}(x) \quad (17)$$

$$\phi_S(x) = \frac{1 - \bar{\phi}}{Q_S[i\omega_S]}\exp\left[-\frac{i\omega_S(x)}{N}\right] \quad (18)$$

$$\phi(x) + \phi_S(x) = 1 \quad (19)$$

where $\phi_s(x)$ is the volume fraction of the sth segment of all chains at x, $q_s(x)$ is the probability of finding a partial chain of s segments starting from the grafted end and ending at position x in the system, and $q^*_t(x)$ is the probability of finding a partial chain of $t \equiv N + 1 - s$ segments starting from the free end and ending at x in the system. According to the chain connectivity, we have the recursive relations

$$q^*_{t+1}(x) = \exp\left[-\frac{i\omega(x)}{N}\right]\frac{q^*_t(x - 1) + q^*_t(x + 1)}{2},\quad q^*_{t=1}(x) = \exp\left[-\frac{i\omega(x)}{N}\right] \quad (20)$$

$$q_{s+1}(x) = \exp\left[-\frac{i\omega(x)}{N}\right]\frac{q_s(x - 1) + q_s(x + 1)}{2},\quad q_{s=1}(x) = \exp\left[-\frac{i\omega(x)}{N}\right]\delta_{x,1} \quad (21)$$

It is worthy to note that, if $\{i\boldsymbol{\omega},i\boldsymbol{\omega}_S,i\boldsymbol{\eta}\}$ is a solution of the SCF equations, $\{i\boldsymbol{\omega} + c,i\boldsymbol{\omega}_S + c,i\boldsymbol{\eta} + c\}$ is also a solution with c being an arbitrary constant; the corresponding $\{\boldsymbol{\phi},\boldsymbol{\phi}_S\}$ and $\beta f_{c,\mathrm{LSCF}}$ remain

dx.doi.org/10.1021/ma202454s | Macromolecules 2012, 45, 2537−2550

unchanged. We therefore set $Q_S = 1 - \bar{\phi}$ to obtain a unique solution. Then from eqs 14, 15, 18, and 19 we obtain

$$i\omega(x) = -N \ln[1 - \phi(x)] + \chi N[1 - 2\phi(x)] \tag{22}$$

This, along with eq 16, is solved using the Broyden method combined with a globally convergent strategy,[51] where the maximum residual error at all x is less than 10^{-12}.

Once the SCF equations are solved, we calculate the free energy per chain as

$$\begin{aligned}\beta(f_{c,\mathrm{LSCF}} - f_c^{id}) &= \sum_x \{\chi\phi^2(x) + \ln[1 - \phi(x)]\} - \chi N\bar{\phi}(1 - \bar{\phi}) \\ &\quad - \bar{\phi} \ln Q - N(1 - \bar{\phi}) \ln(1 - \bar{\phi})\end{aligned} \tag{23}$$

with $Q = q^*_N(x = 1)/L$ (where eq 22 is used), the internal energy per chain as

$$\beta u_{c,\mathrm{LSCF}} = -\frac{\chi N}{V}\frac{E_{\mathrm{LSCF}}}{{\rho_0}^2} \tag{24}$$

with

$$\frac{E_{\mathrm{LSCF}}}{{\rho_0}^2} \equiv \sum_x [\phi(x) - \bar{\phi}]^2 \tag{25}$$

and the entropy per chain $s_{c,\mathrm{LSCF}}/k_B$ through eq 9. The LSCF predictions of the mean-square chain end-to-end distance ${R_{e,\mathrm{LSCF}}}^2$ and radius of gyration ${R_{g,\mathrm{LSCF}}}^2$ are calculated in the same way as in paper II, and the brush height $h_{\mathrm{LSCF}} \equiv 2\sum_{x=1}^{L}(x - 1)\phi(x)/\bar{\phi}L$.

It is easy to show that, for a *homogeneous* incompressible system of *ungrafted* chains and solvent molecules, our LSCF theory with Kronecker δ-function interactions reduces to the standard Flory–Huggins theory as expected. On the other hand, Appendix A gives the correspondence between our brushes in an explicit solvent and those in an implicit solvent studied in paper II; that is, when $\phi(x) \ll 1$, $(1-2\chi)N\bar{\phi}$ and $\phi(x)/\bar{\phi}$ here correspond to N/κ and $\phi(x)$ in paper II, respectively.

2.3.1. LSCF Predictions in the Limits of $\chi \to \pm\infty$. In the limit of $\chi \to -\infty$, the system is in the ground state with no fluctuations, where all chains are fully stretched with no correlations among them, and the LSCF predictions of $\phi(x) = \bar{\phi}$ for $x \in [1,N]$, $\phi_{s=N}(x) = 1$ at $x = N$ (and 0 otherwise), $E = \beta u_c = 0$, ${R_e}^2 = (N-1)^2$, ${R_g}^2 = (N^2 - 1)/12$, and $h = N - 1$ are exact. LSCF theory further gives $GQ = 1$ in this limit; thus, $\beta(f_{c,\mathrm{LSCF}} - f_c^{id}) = -(s_{c,\mathrm{LSCF}} - s_c^{id})/k_B = \bar{\phi} \ln G$.[52] The latter, however, is not exact for any finite n_S-value due to the correlations among solvent molecules caused by the incompressibility constraint.

To understand this, let us consider the entropy of solvent s_c^S in the general case where n_S solvent molecules are arranged for a given $\{\phi(x)\}$ according to the incompressibility constraint. The exact microcanonical-ensemble partition function for the solvent is $\Omega^S = 1/\prod_{x=1}^{L}[\rho_0\phi_S(x)]!$ with $\phi_S(x) \equiv 1 - \phi(x)$, leading to the exact solvent entropy per chain

$$\frac{s^S_{c,\mathrm{exact}}}{k_B} \equiv \frac{N \ln \Omega^S}{\rho_0 V} = -\frac{N}{\rho_0 V}\sum_x \ln[\rho_0\phi_S(x)]! \tag{26}$$

LSCF theory, however, neglects the correlations among solvent molecules caused by the incompressibility constraint and gives[52]

$$\frac{s^S_{c,\mathrm{LSCF}}}{k_B} = \frac{1}{\rho_0}\ln\frac{V^{n_S}}{n_S!} + N(1 - \bar{\phi}) \ln(1 - \bar{\phi}) - \sum_x \phi_S(x) \ln \phi_S(x) \tag{27}$$

Using the Stirling approximation, it is easy to show that $s^S_{c,\mathrm{exact}} - s^S_{c,\mathrm{LSCF}} \to 0$ as $n_S \to \infty$ (i.e., $\rho_0 \to \infty$ at constant $\bar{\phi}$).

In the limit of $\chi \to \infty$, the system is in the "ceiling" state with the largest $E/{\rho_0}^2$, and it is clear that $\beta u_c \to -\infty$ and thus $\beta f_c \to -\infty$ for $N \geq 3$. Two cases need to be considered separately:

(1) When $\bar{\phi} \leq \lfloor (N+1)/2 \rfloor^{-1}$ (where $\lfloor a \rfloor$ denotes the integer part of a non-negative number a), the incompressibility constraint does not limit chain conformations. In the limit of $\chi \to \infty$, all chains are fully collapsed (i.e., $X_s = 1$ for odd s and 2 for even s), and LSCF theory gives $GQ = 1$, which corresponds to the total number of chain conformations of a single grafted chain.[52] For odd N, LSCF theory gives the following exact results: $\phi(x) = [(N+1)/2]\bar{\phi}$ at $x = 1$, $[(N-1)/2]\bar{\phi}$ at $x = 2$, and 0 otherwise; $\phi_{s=N}(x) = 1$ at $x = 1$, and 0 otherwise; $E/{\rho_0}^2 = [(N-1)^2/2]\bar{\phi}^2$; $h = 1 - 1/N$, ${R_e}^2 = 0$, and ${R_g}^2 = 1/4 - 1/4N^2$. As shown above, its prediction[52] of $(s_{c,\mathrm{LSCF}} - s_c^{id})/k_B = -\bar{\phi} \ln G - (1 - (N+1)\bar{\phi}/2) \ln(1 - (N+1)\bar{\phi}/2) - (1 - (N-1)\bar{\phi}/2) \ln(1 - (N-1)\bar{\phi}/2) + N(1 - \bar{\phi}) \ln(1 - \bar{\phi})$ is not exact for any finite n_S-value due to the correlations among solvent molecules. For even N, LSCF theory gives the following exact results: $\phi(x) = N\bar{\phi}/2$ at $x = 1$ and 2, and 0 otherwise; $\phi_{s=N}(x) = 1$ at $x = 2$, and 0 otherwise; $E/{\rho_0}^2 = (N^2 - 2N)\bar{\phi}^2/2$; $h = 1$, ${R_e}^2 = 1$, and ${R_g}^2 = 1/4$. Its prediction[52] of $(s_{c,\mathrm{LSCF}} - s_c^{id})/k_B = -\bar{\phi} \ln G - 2(1 - N\bar{\phi}/2) \ln(1 - N\bar{\phi}/2) + N(1 - \bar{\phi}) \ln(1 - \bar{\phi})$ is again not exact for any finite n_S-value.

(2) When $\bar{\phi} > \lfloor (N+1)/2 \rfloor^{-1}$, the incompressibility constraint limits chain conformations. In the limit of $\chi \to \infty$, chains are therefore in the most collapsed states as permitted by the incompressibility. The "ceiling" state is in general degenerated (i.e., $GQ > 1$[52]) with $E/{\rho_0}^2 = -A\bar{\phi}(1 - A\bar{\phi}) - B\bar{\phi}(1 - B\bar{\phi}) + N\bar{\phi}(1 - \bar{\phi})$, where $A = \lfloor N/2 - \lfloor N\bar{\phi}/2 \rfloor/\bar{\phi} \rfloor$ and $B = N - 2\lfloor N\bar{\phi}/2 \rfloor/\bar{\phi} - A$. These values of A and B can be found in the following way: Let us first consider the single-chain system. One of the allowed chain conformations in the most collapsed state gives $\phi(x) = 1$ for $x \leq x_0 \equiv 2\lfloor N\bar{\phi}/2 \rfloor$, < 1 at both $x_1 \equiv x_0 + 1$ and $x_2 \equiv x_0 + 2$, and 0 otherwise. That is, there are totally $2\lfloor N\bar{\phi}/2 \rfloor\rho_0 = 2\lfloor N\bar{\phi}/2 \rfloor/\bar{\phi}$ segments at lattice sites $1 \leq x \leq x_0$, $\lfloor (N - 2\lfloor N\bar{\phi}/2 \rfloor/\bar{\phi})/2 \rfloor = A$ segments at x_2, and B segments at x_1. For multichain systems, this chain conformation can be applied to all the chains, leading to the above $E/{\rho_0}^2$, which is independent of n. This exact result is therefore also the LSCF prediction (i.e., in the limit of $n \to \infty$). When $N\bar{\phi}/2$ is an integer, LSCF theory gives the exact result of $\phi(x) = 1$ for $x \in [1,N\bar{\phi}]$ and 0 otherwise, thus the exact result of $h = N\bar{\phi} - 1$; $\phi_{s=N}(x)$, however, depends on n and its exact result therefore cannot be predicted by LSCF theory, so are ${R_e}^2$ and ${R_g}^2$. When $N\bar{\phi}/2$ is not an integer, the exact results of $\phi(x)$ and $\phi_{s=N}(x)$ cannot be predicted by LSCF theory, so are h, ${R_e}^2$, and ${R_g}^2$. Finally, since GQ is in general not known analytically,[52] we do not have an expression for $s_{c,\mathrm{LSCF}}$, which cannot be exact for any finite n_S-value as explained above.

From the above analysis, it is clear that the limit of $\chi \to -\infty$ provides a well-understood reference state, which is used in the following.

3. RESULTS AND DISCUSSION

Our model system of brushes in an explicit solvent is specified by a few physical parameters: the chain length N,

the average polymer volume fraction $\bar{\phi} = n/\rho_0$, the Flory–Huggins interaction parameter χ between polymer segments and solvent molecules, and the number of grafted chains n; the first three completely determine the LSCF results, and the last one controls system fluctuations in FLMC simulations, the results of which approach LSCF predictions in the limit of $n \to \infty$. Different from the compressible polymer melts studied in paper I or the brushes in an implicit solvent studied in paper II, here N characterizes both the chain discretization and the polymer/solvent size ratio; it is therefore a physical parameter instead of a model parameter. Unless specified otherwise, our results presented here are for $N = 40$ and $\bar{\phi} = 0.1$; similar results are found for other values of N and $\bar{\phi}$.

In this 1D study, we are mainly interested in the range of $0 \le \chi \le 1.5$; both LSCF calculations and FLMC simulations at much larger χ-values are found to be challenging. To justify our 1D study of brushes in a poor solvent, we have analyzed the lateral instability of our LSCF results obtained under the assumption of lateral homogeneity, following refs 53 and 54; our approach is similar to that in ref 54, except that we use lattice polymers (instead of continuous Gaussian chains) and equal bulk number density for polymer segments and solvent molecules. For $N = 40$ and $\bar{\phi} = 0.1$, the laterally homogeneous brush is found to be stable for $\chi < 1.575$ on any 2D and 3D lattices having $z_0 = 0$ as the 1D lattice (thus the same LSCF results for the laterally homogeneous brush), where z_0 denotes the fraction of the nearest-neighbor lattice sites that are at the same x of a given lattice site; one example of such 3D lattice is the body-centered cubic lattice. Finally, to show the bridging to our reference system in the limit of $\chi \to -\infty$, some of our results are presented below as a function of $\chi/(3-\chi)$ in the range of $[-1,1]$.

3.1. Density of States and Error Estimation. Figure 1a shows $g(E)$ obtained from our WL-TM simulations for systems of various $n \ge 2$; the exact $g(E)$ obtained from enumeration for $n = 1$ is also shown. We see that $g(E)$ increases with increasing E at small E and decreases at large E, and that $g(E)$ oscillates slightly at large E due to the use of a lattice. In addition, the E-range is broader for systems with larger n, as expected. The normalized probability distribution $P(E,\chi)$ is shown in Figure 1b for systems with $n = 1$ and 16 at $\chi = 0$ and 1.5. We see that E of those states contributing significantly to canonical-ensemble averages increases with increasing χ and n, and that the E-ranges we choose are broad enough for computing canonical-ensemble averages in the range of χ from $-\infty$ to 1.5.

Following paper I, for the single-chain system we define the error in ln $g(E)$ per macrostate as $\varepsilon \equiv (\sum_E[\ln g(E) - \ln g_{\text{exact}}(E)]^2/N_E)^{1/2}$, where N_E denotes the total number of even E-macrostates contained in the E-window, and the (related) error in $\beta f_{c,\text{FLMC}}(\chi)$ as

$$\varepsilon_f(\chi) \equiv \left|\beta f_{c,\text{FLMC}} - \beta f_{c,\text{exact}}\right| = \frac{\bar{\phi}}{n}\left|\ln \sum_E g(E)\exp\left(C\chi N\frac{E}{\rho_0^2}\right) - \ln \sum_E g_{\text{exact}}(E)\exp\left(C\chi N\frac{E}{\rho_0^2}\right)\right| \quad (28)$$

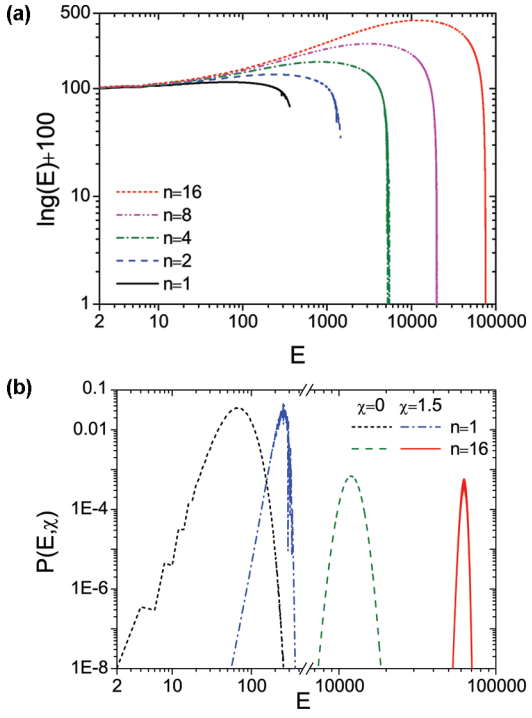


Figure 1. (a) Density of states $g(E)$ estimated by WL-TM simulations for $n \ge 2$ and the exact $g(E)$ for $n = 1$ obtained by enumeration; (b) the normalized probability distribution function $P(E,\chi)$ at $\chi = 0$ and 1.5 for $n = 1$ and 16 . Note that $g(E) = 0$ for odd E and we omit such points, as well as those points at large E where $g(E) = 0$. $L = N = 40$ and $\bar{\phi} = 0.1$ are used here.

where $g(E)$ is obtained from WL-TM simulations and $g_{\text{exact}}(E) \equiv \Omega_{\text{exact}}(E)/\Omega_{\text{exact}}(E=0)$ obtained by enumeration. Figure 2a shows that ε and ε_f (at $\chi = 0$, 1 and 1.5) decrease gradually with increasing number of MCS in TM simulations (TM MCS), and that $\varepsilon_f < 0.006$ in our single-chain simulation at 4×10^7 TM MCS. Figure 2b shows $\beta f_{c,\text{FLMC}} - \beta f_{c,\text{exact}}$ as a function of χ at 4×10^7 TM MCS for the single-chain systems with $N = 20$ and 40; note that eq 28 gives $\varepsilon_f(\chi \to -\infty) = 0$. While $\varepsilon_f(\chi)$ exhibits a maximum as χ varies in both cases, its location is outside the χ-range that we are interested in. At large χ, $\beta f_{c,\text{FLMC}} - \beta f_{c,\text{exact}}$ approaches a constant, the value of which is mainly determined by the error of our $g(E)$ for the "ceiling" state (i.e., $E = 180$ for $N = 20$ and 360 for $N = 40$).

Different from the brushes in an implicit solvent studied in paper II (i.e, the application of eq 28 there), there is no *finite* χ-value at which chains are uncorrelated for the brushes in an explicit solvent (even at $\chi = 0.5$, where only the second virial coefficient vanishes). To estimate the error in βf_c for our multichain systems with $n \ge 2$, where $g_{\text{exact}}(E)$ is not known, we follow paper I and plot in Figure 2c $\beta f_{c,\text{FLMC}}$ as a function of the number of TM MCS for systems with $n = 2$ and 16 at $\chi = 0$ and 1.5. We see that in all the cases $\beta f_{c,\text{FLMC}}$ increases toward an asymptotic value with increasing number of TM MCS, and that 4×10^7 TM MCS give an error in $\beta f_{c,\text{FLMC}}$ (difference from the value at 2×10^7 TM MCS) of less than 0.003 and 0.00012 at $\chi = 0$ for $n = 2$ and 16, respectively, and less than 0.002 and 0.00003 at $\chi = 1.5$ for $n = 2$ and 16, respectively. As found in paper I, the error in $\beta f_{c,\text{FLMC}}$ from our WL-TM simulations decreases with increasing n. Hereafter we use the simulation results at 4×10^7 TM MCS for $n \ge 2$.

dx.doi.org/10.1021/ma202454s | Macromolecules 2012, 45, 2537–2550

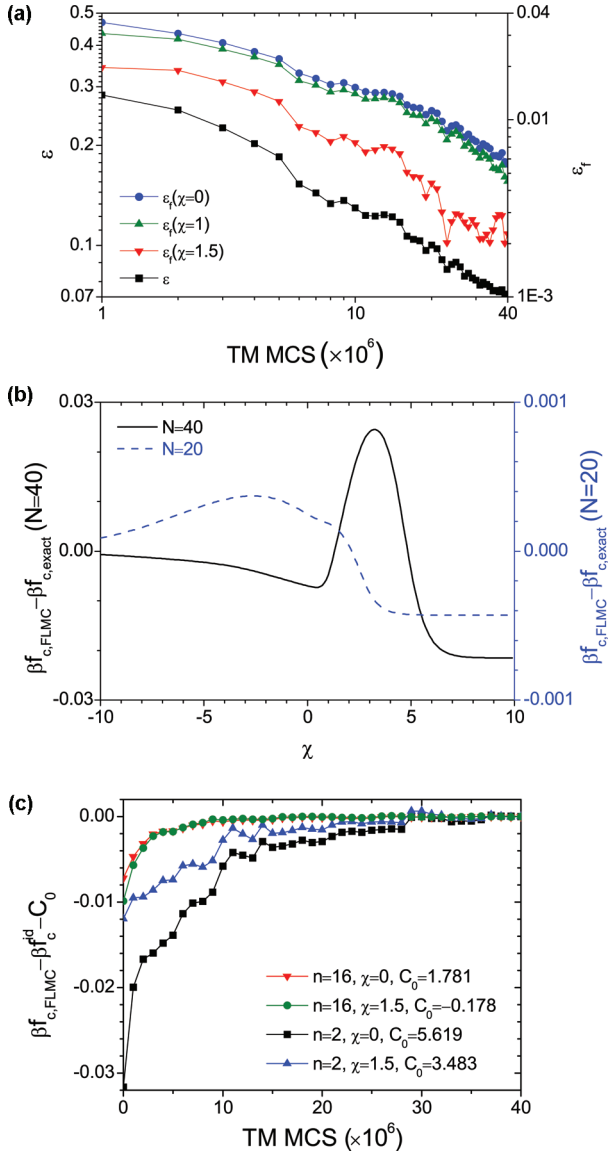


Figure 2. (a) Log–log plot of the error per energy level ε and the related error in the free energy per chain, ε_f, as a function of the number of Monte Carlo steps of the transition-matrix sampling, TM MCS, in our WL-TM simulations of the single-chain system. $L = N = 40$ and $\overline{\phi} = 0.1$ are used here. (b) Difference of free energy per chain between the WL-TM algorithm and the enumeration for the single-chain system as a function of χ, where the WL-TM simulation results are obtained at 40×10^6 TM MCS. $\overline{\phi} = 0.1$ is used here. (c) Free energy per chain at $\chi = 0$ and 1.5 for the multichain systems with $n = 2$ and 16, where the curves are shifted by C_0 such that their value is 0 at 4×10^7 TM MCS. $L = N = 40$ and $\overline{\phi} = 0.1$ are used here.

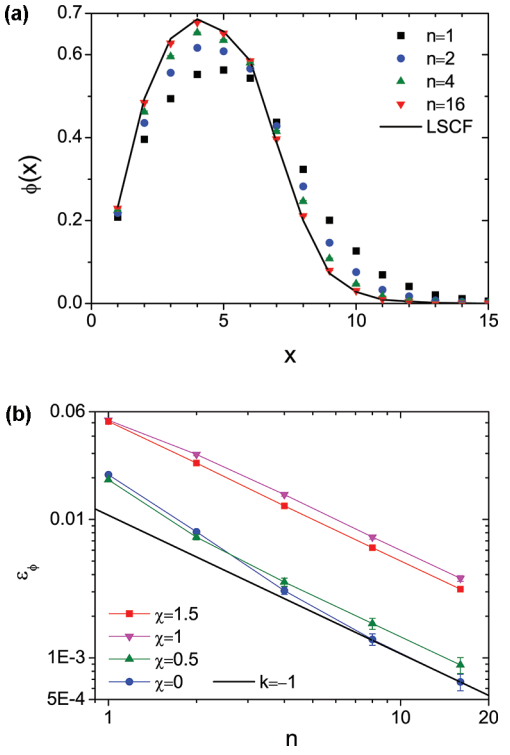


Figure 3. (a) Polymer segmental density profiles $\phi(x)$ obtained from canonical-ensemble simulations on the 1D lattice with various n and the corresponding LSCF predictions at $\chi = 1$. Part b shows how the difference in $\phi(x)$ between FLMC and LSCF results, ε_ϕ, varies with n, where "$k = -1$" denotes a straight line of slope −1. $L = N = 40$ and $\overline{\phi} = 0.1$ are used here.

3.2. Brush Structures. *3.2.1. Segmental Density Profile and Brush Height.* Figure 3a shows $\phi(x)$ obtained from canonical-ensemble simulations (denoted by $\phi_{\mathrm{FLMC}}(x)$) with various n at $\chi = 1$, along with the corresponding LSCF predictions (denoted by $\phi_{\mathrm{LSCF}}(x)$). In such a poor solvent, polymer segments collapse near the substrate. As found in Paper II, $\phi_{\mathrm{FLMC}}(x)$ is flatter than $\phi_{\mathrm{LSCF}}(x)$ due to the system fluctuations, and the largest deviation in $\phi(x)$, defined as $\max_{\{x\}}|\phi_{\mathrm{FLMC}}(x) - \phi_{\mathrm{LSCF}}(x)|$, occurs at $x = 3$ in all the cases, very close to the location (at $x = 4$) of the maximum of $\phi_{\mathrm{LSCF}}(x)$. Similar results are found at other χ-values.

On the other hand, the FLMC results approach the LSCF predictions with increasing n at a given χ, as expected. To quantitatively analyze the n-dependence of $\phi(x)$, we define $\varepsilon_\phi \equiv (\sum_{x=1}^{L}[\phi_{\mathrm{FLMC}}(x) - \phi_{\mathrm{LSCF}}(x)]^2/L)^{1/2}$ as in paper II. Figure 3b shows ε_ϕ as a function of n at various χ. We see that ε_ϕ is larger in a poor solvent (i.e., at $\chi = 1$ and 1.5) than in a good or θ-solvent (i.e., at $\chi = 0$ and 0.5), and that $\varepsilon_\phi \propto n^{-1}$ at large n for all the χ-values.

The brush height is directly related to $\phi(x)$, i.e., $h = 2\sum_{x=1}^{L}(x - 1)\phi(x)/\overline{\phi}L$. In the limit of $\chi \to -\infty$, all chains are fully stretched and LSCF theory gives the exact value of $h = 39$ (for $N = 40$). Figure 4a shows that h_{LSCF} monotonically decreases with increasing χ.

Figure 4b shows that LSCF theory underestimates the brush height at any finite $\chi \leq 1.5$; this is different from the brushes in an implicit, good solvent studied in paper II, where LSCF theory overestimates h near the θ-point.[2] We further see that $h_{\mathrm{FLMC}} - h_{\mathrm{LSCF}}$ varies nonmonotonically within the range of $0 < \chi < 1$. Similar to ε_ϕ, we also find that $h_{\mathrm{FLMC}} - h_{\mathrm{LSCF}} \propto n^{-1}$ at large n for all the χ-values (data not shown).

3.2.2. Free-End Distribution and Chain Dimensions. Parts a and b of Figure 5 show $\phi_{s=N}(x)$ obtained from canonical-ensemble simulations (denoted by $\phi_{s=N,\mathrm{FLMC}}(x)$) at $\chi = 0$ and 1, respectively, along with the corresponding LSCF predictions (denoted by $\phi_{s=N,\mathrm{LSCF}}(x)$); note that $\phi_{s=N}(x) = 0$ at odd x for chains of even N on the 1D lattice, and we omit such points in the figures. At $\chi = 0$, we see that $\phi_{s=N,\mathrm{FLMC}}(x) \propto \exp(kx/L)$ at small x and for small n. This exponential distribution of the free ends is also found in the 1D brushes in an implicit, good

dx.doi.org/10.1021/ma202454s | Macromolecules 2012, 45, 2537–2550

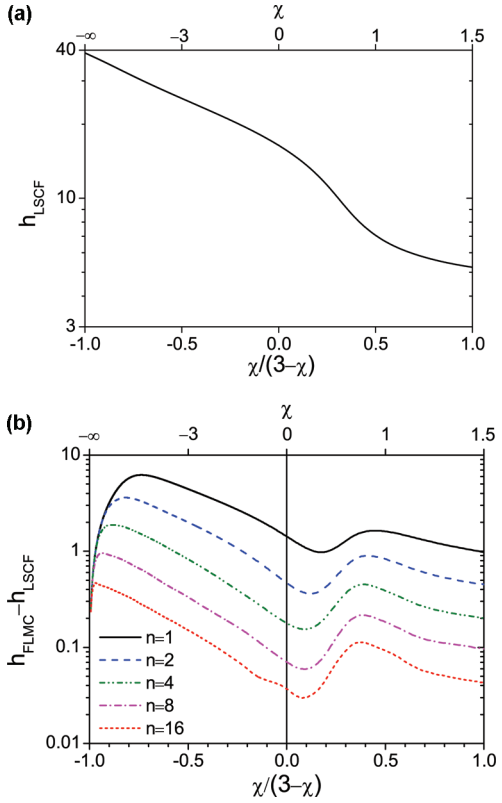


Figure 4. (a) Brush height obtained from LSCF theory, h_{LSCF} and (b) the difference between the brush height obtained from WL-TM simulations, h_{FLMC}, and h_{LSCF} as functions of χ. $L = N = 40$ and $\overline{\phi} = 0.1$ are used here.

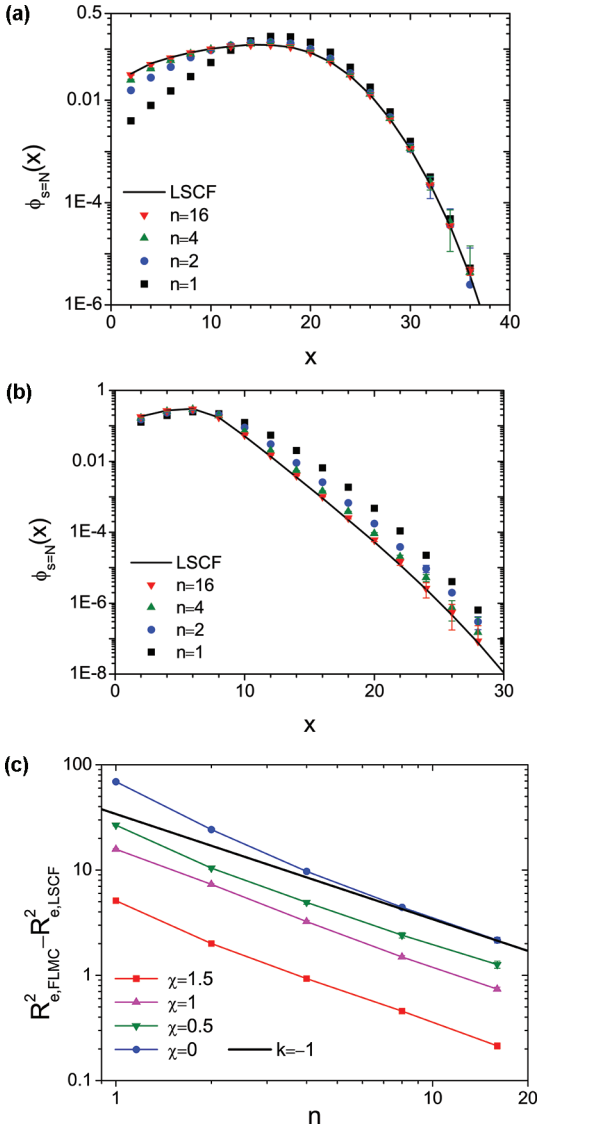


Figure 5. Free-end distributions $\phi_{s=N}(x)$ obtained from canonical-ensemble simulations on the 1D lattice with various n and the corresponding LSCF predictions at (a) $\chi = 0$ and (b) $\chi = 1$. (c) Difference in the mean-square chain end-to-end distance between FLMC and LSCF results, $R_{e,FLMC}^2 - R_{e,LSCF}^2$, as a function of n, where "$k = -1$" denotes a straight line of slope −1. $L = N = 40$ and $\overline{\phi} = 0.1$ are used here.

solvent studied in Paper II, and can be explained accordingly with an effective value of $(1-2\chi)N\overline{\phi} = 4$ for the parameter N/κ used in that paper, although at such a small value we cannot quantitatively predict k.[2] As also found in Paper II, $\phi_{s=N,FLMC}(x) < \phi_{s=N,LSCF}(x)$ close to the substrate in all the cases. On the other hand, we find that $(\sum_{x=1}^{L}[\phi_{s=N,FLMC}(x) - \phi_{s=N,LSCF}(x)]^2/L)^{1/2} \propto n^{-1}$ at large n for all the χ-values (data not shown), as in the case of $\phi(x)$.

The mean-square chain end-to-end distance R_e^2 is directly related to $\phi_{s=N}(x)$, i.e., $R_e^2 = \sum_{x=1}^{L}(x-1)^2\phi_{s=N}(x)$. We find that both R_e^2 and the mean-square chain radius of gyration R_g^2 exhibits qualitatively the same behavior as h. That is, LSCF theory gives exact $R_e^2 = 1521$ and $R_g^2 = 133.25$ (for $N = 40$) in the limit of $\chi \to -\infty$. With increasing χ, both $R_{e,LSCF}^2$ and $R_{g,LSCF}^2$ monotonically decrease; note, however, that in the case of $N = 40$ and $\overline{\phi} = 0.1$ LSCF theory does not give the exact R_e^2 and R_g^2 in the limit of $\chi \to \infty$ for finite n due to the chain correlations. On the other hand, LSCF theory underestimates R_e^2 and R_g^2 at any finite $\chi \le 1.5$, and both $R_{e,FLMC}^2 - R_{e,LSCF}^2$ and $R_{g,FLMC}^2 - R_{g,LSCF}^2$ vary similarly to $h_{FLMC} - h_{LSCF}$ shown in Figure 4b. Finally, Figure 5c shows that $R_{e,FLMC}^2 - R_{e,LSCF}^2 \propto n^{-1}$ at large n for all the χ-values, and similar results are also found for R_g^2 (data not shown).

3.3. Thermodynamic Quantities. *3.3.1. Internal energy and specific heat.* From eqs 8 and 10, we see that the internal energy per chain βu_c and the specific heat per chain C_v/k_B are directly related to $\langle E\rangle/\rho_0^2$ and $(\langle E^2\rangle - \langle E\rangle^2)/\rho_0^4$, respectively. Figure 6a shows how E_{LSCF}/ρ_0^2 and $\beta u_{c,LSCF}$ vary with χ. In the limit of $\chi \to -\infty$, the system is in the ground state with all chains fully stretched, and LSCF theory gives exact $E = \beta u_c = 0$. With increasing χ, E_{LSCF}/ρ_0^2 monotonically increases and $\beta u_{c,LSCF}$ exhibits a maximum around $\chi = -6.3$.

Figure 6b shows $(\langle E\rangle - E_{LSCF})/\rho_0^2$ as a function of χ for systems of various n, where $\langle E\rangle$ is obtained from WL-TM simulations. In all the cases, $(\langle E\rangle - E_{LSCF})/\rho_0^2$ exhibits with increasing χ a negative minimum followed by a positive maximum located at a χ-value slightly larger than 0.5, and approaches 0 in the limit of $\chi \to \infty$. Following paper II, we split $(\langle E\rangle - E_{LSCF})/\rho_0^2$ into two parts: $\Delta\phi_1 \equiv \sum_{x=1}^{L}[\langle\hat{\rho}_{FLMC}^2(x)\rangle/\rho_0^2 - \phi_{FLMC}^2(x)]$ is the fluctuations of local segmental densities around their average in FLMC simulations, and $\Delta\phi_2 \equiv \sum_{x=1}^{L}[\phi_{FLMC}^2(x) - \phi_{LSCF}^2(x)]$ is the difference between the square of the ensemble-averaged density profile in FLMC simulations and the corresponding LSCF prediction. Both parts are due to the fluctuation effects neglected in LSCF theory.

dx.doi.org/10.1021/ma202454s | Macromolecules 2012, 45, 2537−2550

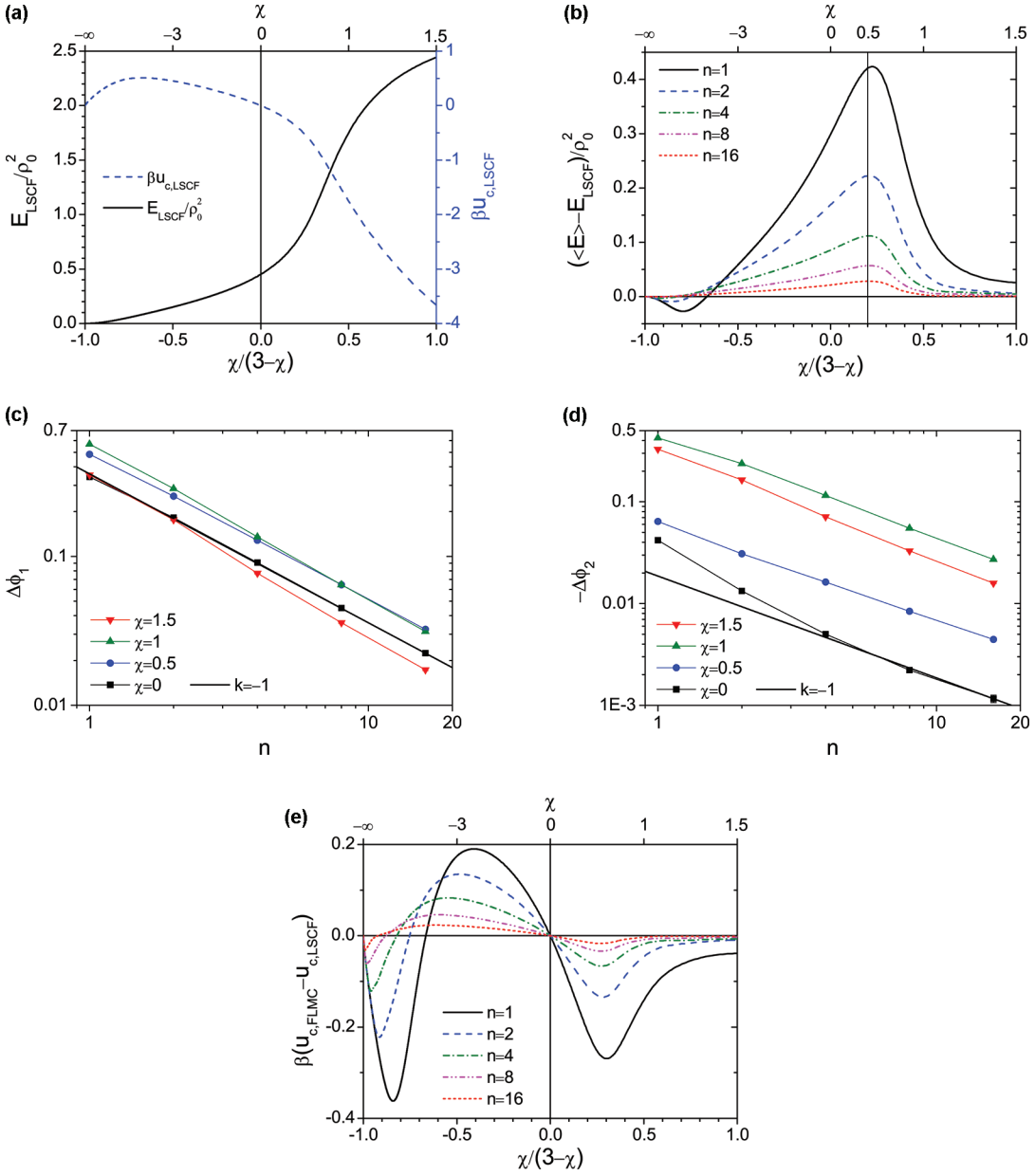


Figure 6. (a) LSCF predictions of the energy level E_{LSCF}/ρ_0^2 and the internal energy per chain $\beta u_{c,LSCF}$ as a function of χ. (b) Difference in the ensemble-averaged energy level $\langle E\rangle/\rho_0^2$ between WL-TM and LSCF results. (c) Fluctuations of local segmental densities around their average in canonical-ensemble simulations, $\Delta\phi_1$, where "$k = -1$" denotes a straight line of slope −1. (d) Difference between the square of the ensemble-averaged density profile in canonical-ensemble simulations and the corresponding LSCF prediction, $\Delta\phi_2$, where "$k = -1$" denotes a straight line of slope −1. (e) Difference in the internal energy per chain between WL-TM and LSCF results, $\beta(u_{c,FLMC} - u_{c,LSCF})$. $L = N = 40$ and $\bar{\phi} = 0.1$ are used here.

Parts c and d of Figure 6 show that $\Delta\phi_1 > 0$ and $\Delta\phi_2 < 0$ at finite n and $\chi \geq 0$, which can be compared with parts c and d of Figure 7 in paper II, respectively. In fact, with the mapping of $N/\kappa = (1-2\chi)N\bar{\phi}$, the behavior of $(\langle E\rangle - E_{LSCF})/\rho_0^2$ for $-\infty < \chi \leq 0.5$ shown in Figure 6b is qualitatively the same as Figure 7b in paper II. On the other hand, as revealed in parts c and d of Figure 6, the decrease of $(\langle E\rangle - E_{LSCF})/\rho_0^2$ from $\chi = 0.5$ to 1 is due to the large decrease of $\Delta\phi_2$, which is similar to ε_ϕ shown in Figure 3b since both measure the difference between $\phi_{FLMC}(x)$ and $\phi_{LSCF}(x)$, and that from $\chi = 1$ to 1.5 is due to the large decrease of $\Delta\phi_1$. Finally, parts c and d of Figure 6 also show that both $\Delta\phi_1$ and $\Delta\phi_2$ are proportional to n^{-1} at large n for all the χ-values, which leads to $(\langle E\rangle - E_{LSCF})/\rho_0^2 \propto n^{-1}$ at large n.

With eq 8, we therefore have $\beta u_{c,FLMC} - \beta u_{c,LSCF} = 0$ at $\chi = 0$ and in the limits of $\chi \to \pm\infty$. Figure 6e shows $\beta u_{c,FLMC} - \beta u_{c,LSCF}$ as a function of χ for systems of various n, which can be easily understood based on the above analysis. In particular, at finite $\chi > 0$, LSCF theory overestimates the internal energy per chain and its prediction is approached by FLMC results at a rate of $1/n$ at large n.

Figure 7a shows $(\langle E^2\rangle - \langle E\rangle^2)/\rho_0^4$ as a function of χ for systems of various n obtained from FLMC simulations; note that the LSCF prediction is 0 regardless of χ. We see that $(\langle E^2\rangle - \langle E\rangle^2)/\rho_0^4$ exhibits a maximum at $\chi \approx 0.9$. In the limits of $\chi \to -\infty$ and ∞, the system is in the ground state of $E = 0$ and the "ceiling" state of $E = 360n^2$ (for $\bar{\phi} = 0.1$ and $N = 40$), respectively, with no fluctuations, thus $(\langle E^2\rangle - \langle E\rangle^2)/\rho_0^4 = 0$.

dx.doi.org/10.1021/ma202454s | Macromolecules 2012, 45, 2537−2550

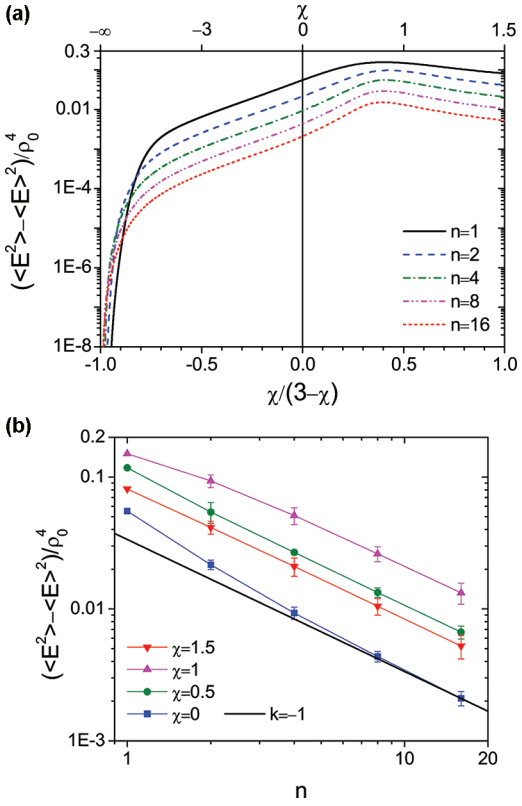


Figure 7. (a) Fluctuations of energy level $(\langle E^2\rangle - \langle E\rangle^2)/\rho_0{}^4$ obtained from WL-TM simulations as a function of χ for different n; the LSCF prediction is 0. (b) $(\langle E^2\rangle - \langle E\rangle^2)/\rho_0{}^4$ obtained from canonical-ensemble simulations as a function of n, where "$k = -1$" denotes a straight line of slope -1. $L = N = 40$ and $\bar{\phi} = 0.1$ are used here.

Figure 7b shows the n-dependence of $(\langle E^2\rangle - \langle E\rangle^2)/\rho_0{}^4$ at various χ obtained from canonical-ensemble simulations, where we see that $(\langle E^2\rangle - \langle E\rangle^2)/\rho_0{}^4 \propto n^{-1}$ at large n for all the χ-values.

With eq 10, we therefore have $C_v/k_B = 0$ at $\chi = 0$ and in the limits of $\chi \to \pm\infty$, and >0 at other χ-values. LSCF theory gives $C_v/k_B = 0$ regardless of χ, which, for any finite $\chi > 0$, is approached by FLMC results at a rate of $1/n$ at large n (data not shown).

3.3.2. Free Energy and Entropy. Similar to papers I and II, here we compare the differences in free energy per chain, $\Delta f_c \equiv f_c(\chi) - f_c(\chi \to -\infty)$, and in entropy per chain, $\Delta s_c \equiv s_c(\chi) - s_c(\chi \to -\infty)$, from the reference state in the limit of $\chi \to -\infty$, where all chains are fully stretched. Note that, for any finite n_S-value, while LSCF theory does not give the exact f_c and s_c in this reference state due to the correlations among solvent molecules caused by the incompressibility constraint, the deviations from the exact value are known analytically (see eqs 26 and 27).

Figure 8a shows how the LSCF predictions of $\beta\Delta f_{c,\mathrm{LSCF}}$ and $\Delta s_{c,\mathrm{LSCF}}/k_B$ vary with χ. With increasing χ, $\beta\Delta f_{c,\mathrm{LSCF}}$ monotonically decreases but $\Delta s_{c,\mathrm{LSCF}}/k_B$ exhibits a maximum at $\chi = 0$; the latter is a general feature, as shown in Appendix B. In the limit of $\chi \to \infty$, $\beta\Delta f_{c,\mathrm{LSCF}}$ approaches $-\infty$ but $\Delta s_{c,\mathrm{LSCF}}/k_B$ approaches a finite value.

Figure 8b shows that $\beta(\Delta f_{c,\mathrm{FLMC}} - \Delta f_{c,\mathrm{LSCF}})$ exhibits a maximum at a negative χ-value (which decreases with increasing n), crosses 0 at a χ-value between 0.5 and 0.8, and seems to approach a negative constant in the limit of $\chi \to \infty$ at any finite n. LSCF theory therefore underestimates Δf_c at small $\chi \geq 0$ and overestimates it at larger χ at finite n. Figure 8c shows that, while $\beta|\Delta f_{c,\mathrm{FLMC}} - \Delta f_{c,\mathrm{LSCF}}| \propto n^{-1}$ seems to hold at large n for $\chi = 0$ and large χ-values (e.g., 1.5), it may not hold even at large n for intermediate χ-values (e.g., 0.5 and 1) near which $\Delta f_{c,\mathrm{FLMC}}$ coincides with $\Delta f_{c,\mathrm{LSCF}}$.

With eq 9, the behavior of $-(\Delta s_{c,\mathrm{FLMC}} - \Delta s_{c,\mathrm{LSCF}})/k_B$ shown in Figure 8d can be readily understood. We see that, with increasing χ, $-(\Delta s_{c,\mathrm{FLMC}} - \Delta s_{c,\mathrm{LSCF}})/k_B$ exhibits two maxima, one at a negative χ-value (which decreases with increasing n) and the other at a χ-value slightly larger than 0.5; these locations coincide with the corresponding extremum of $(\langle E\rangle - E_{\mathrm{LSCF}})/\rho_0{}^2$ in Figure 6b, which is a general feature as shown in Appendix C. $-(\Delta s_{c,\mathrm{FLMC}} - \Delta s_{c,\mathrm{LSCF}})/k_B$ then crosses 0 at a larger χ, and approaches the same negative constant as $\beta(\Delta f_{c,\mathrm{FLMC}} - \Delta f_{c,\mathrm{LSCF}})$ does in the limit of $\chi \to \infty$ at any finite n. LSCF theory therefore overestimates Δs_c at small $\chi \geq 0$ and underestimates it at larger χ at finite n. In addition, $-(\Delta s_{c,\mathrm{FLMC}} - \Delta s_{c,\mathrm{LSCF}})/k_B$ exhibits a local minimum at $\chi = 0$, which is a general feature of the brushes in an explicit solvent as shown in Appendix C but not seen in the brushes in an implicit solvent studied in paper II.

Finally, Figure 8e shows that, while $|\Delta s_{c,\mathrm{FLMC}} - \Delta s_{c,\mathrm{LSCF}}|/k_B \propto n^{-1}$ seems to hold at large n for $\chi = 0$ and 0.5, it may not hold even at large n for χ-values (e.g., 1 and 1.5) near which $\Delta s_{c,\mathrm{FLMC}}$ coincides with $\Delta s_{c,\mathrm{LSCF}}$.

4. SUMMARY

Using fast lattice Monte Carlo (FLMC) simulations[3] both in a canonical ensemble and with Wang-Landau−transition-matrix (WL-TM) sampling,[46−48] we have studied a 1D model system of laterally homogeneous homopolymer brushes in an explicit solvent with Kronecker δ-function interactions. The fluctuations and correlations in this system are controlled by a few physical parameters: the chain length N, the average polymer volume fraction $\bar{\phi}$, the Flory−Huggins interaction parameter χ between polymer segments and solvent molecules, and the number of grafted chains n. Direct comparisons of the simulation results with those from the corresponding lattice self-consistent field (LSCF) theory, both of which are based on the *same* Hamiltonian (thus without any parameter-fitting between them), unambiguously and quantitatively reveal the fluctuations and correlations in the system. This is the third paper in our series of studies with similar methodology and purpose, and extends our previous work on the brushes in an implicit, good solvent reported in the preceding paper in this series[2] (referred to as paper II). Such direct comparisons distinguish our work from all previously reported comparisons between SCF theories and molecular simulations of homopolymer brushes,[9,23,25,26,31−33,35−37,43,45] where different models were used in the theories and simulations.

We have examined in detail how χ and n affect both the brush structures (including the ensemble-averaged segmental density profile $\phi(x)$ and free-end distribution $\phi_{s=N}(x)$, where x denotes the direction perpendicular to the grafting substrate, as well as the related brush height h, mean-square chain end-to-end distance R_e^2 and radius of gyration R_g^2) and various thermodynamic quantities (including the canonical-ensemble average of energy level $\langle E\rangle$ and the related internal energy per chain of length N (i.e., per N lattice sites) u_c, the fluctuations of energy level $\langle E^2\rangle - \langle E\rangle^2$ and the related specific heat per chain C_v, the difference in free-energy per chain $\Delta f_c \equiv f_c(\chi) - f_c(\chi \to -\infty)$ and that in entropy per chain $\Delta s_c \equiv s_c(\chi) - s_c(\chi \to -\infty)$ from the reference state in the limit of $\chi \to -\infty$, where all chains are

dx.doi.org/10.1021/ma202454s | *Macromolecules* 2012, 45, 2537−2550

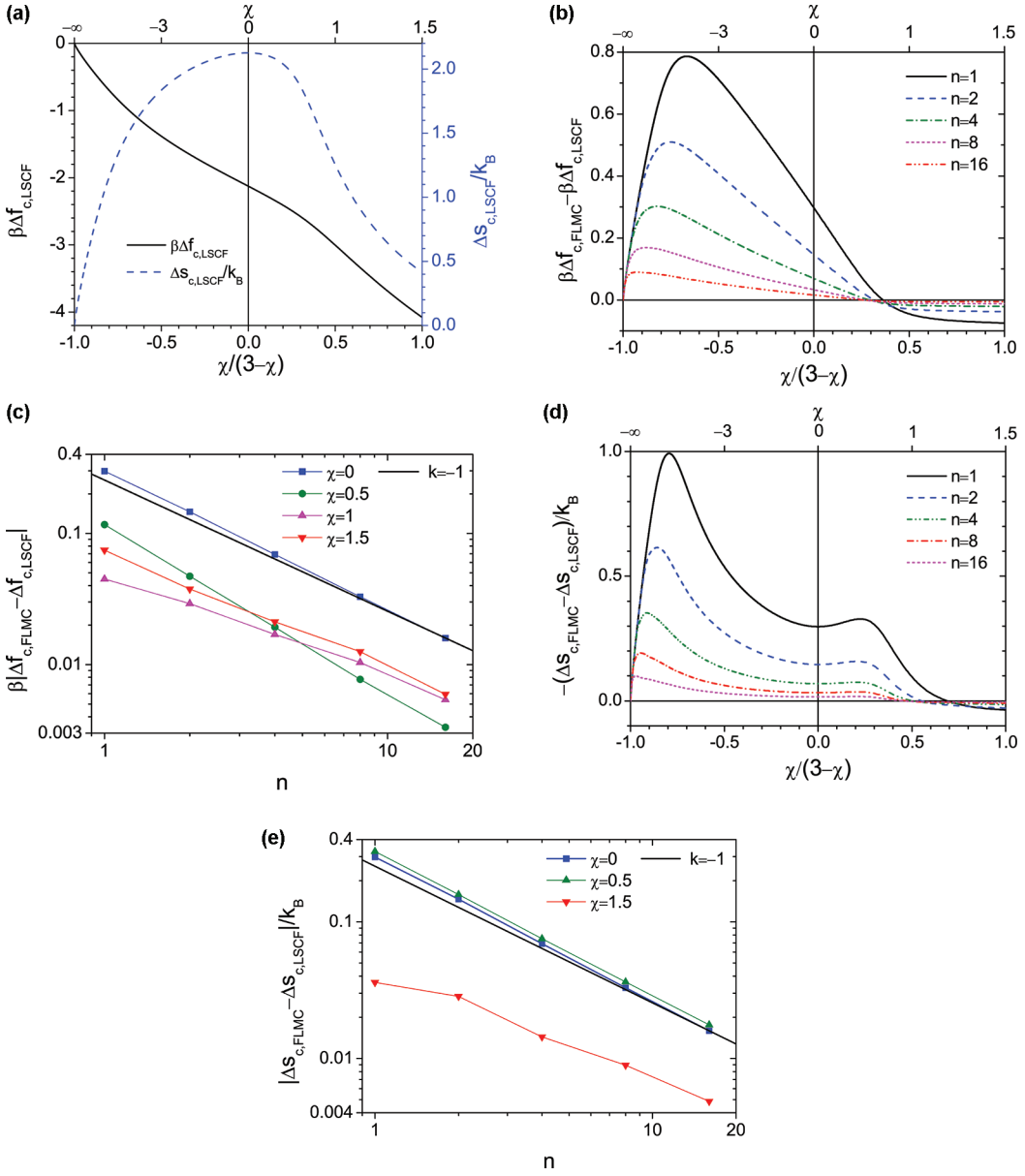


Figure 8. (a) LSCF predictions of the difference in free energy per chain, $\beta\Delta f_c$, and that in entropy per chain, $\Delta s_c/k_B$, from the ideal reference state in the limit of $\chi \to -\infty$. (b) The difference in free energy per chain between WL-TM and LSCF results, $\beta(\Delta f_{c,\mathrm{FLMC}} - \Delta f_{c,\mathrm{LSCF}})$, as a function of χ. (c) $\beta|\Delta f_{c,\mathrm{FLMC}} - \Delta f_{c,\mathrm{LSCF}}|$ as a function of n, where "$k = -1$" denotes a straight line of slope -1. (d) The difference in entropy per chain between WL-TM and LSCF results, $(\Delta s_{c,\mathrm{FLMC}} - \Delta s_{c,\mathrm{LSCF}})/k_B$, as a function of χ. (e) $|\Delta s_{c,\mathrm{FLMC}} - \Delta s_{c,\mathrm{LSCF}}|/k_B$ as a function of n, where $k = -1$ denotes a straight line of slope -1.

fully stretched). Such thermodynamic quantities were not examined in previous comparisons of homopolymer brushes. While most results presented here are for $N = 40$ and $\bar{\phi} = 0.1$, similar results are found for other values of N and $\bar{\phi}$.

For systems at finite n, we find that LSCF theory gives exact results for all the above quantities in the limit of $\chi \to -\infty$, where the system is in the ground state of $E = 0$ (i.e., no fluctuations) with all chains having the same conformation (i.e., no chain correlations). LSCF theory, however, neglects the correlations among solvent molecules caused by the incompressibility constraint, thus overestimating the solvent entropy; this is different from the brushes in an implicit, good solvent studied in paper II.

At finite n and χ, the segmental density profile obtained from FLMC simulations $\phi_{\mathrm{FLMC}}(x)$ is flatter than the LSCF prediction $\phi_{\mathrm{LSCF}}(x)$. The largest deviation between the two profiles occurs close to the grafting substrate where $\phi_{\mathrm{LSCF}}(x)$ is almost at its maximum, and the mean-square difference between them is larger in a poor solvent than in a good or θ-solvent. Close to the substrate, the free-end density from FLMC simulations $\phi_{s=N,\mathrm{FLMC}}(x)$ is lower than the LSCF prediction $\phi_{s=N,\mathrm{LSCF}}(x)$. LSCF theory underestimates h, R_e^2, and R_g^2 at any finite $\chi \leq 1.5$, different from the brushes in an implicit, good solvent studied in paper II.

Regarding the thermodynamic quantities, since $\langle E\rangle/\rho_0^2 \equiv \sum_x[\phi(x) - \bar{\phi}]^2 = -\beta u_c/(\chi N/V)$ and $C_v/k_B = [(\chi N)^2\rho_0/VN](\langle E^2\rangle - \langle E\rangle^2)/\rho_0^4$, where $\rho_0 = nN/\bar{\phi}V$ is the average number density of polymer segments and solvent molecules and V the total number of lattice sites (=N for our 1D brushes), understanding the behavior of $\langle E\rangle$ and $\langle E^2\rangle - \langle E\rangle^2$ is crucial for

dx.doi.org/10.1021/ma202454s | Macromolecules 2012, 45, 2537−2550

understanding that of u_c and C_v. As expected, E_{LSCF} monotonically increases while $\beta u_{c,\mathrm{LSCF}}$ monotonically decreases with increasing $\chi \geq 0$. We find that $(\langle E\rangle - E_{\mathrm{LSCF}})/{\rho_0}^2$ exhibits with increasing χ a negative minimum followed by a positive maximum located at a χ-value slightly larger than 0.5, and approaches 0 in the limit of $\chi \to \infty$. Following paper II, we split it into two parts: $\Delta\phi_1$ is the fluctuations of local segmental densities around their average in FLMC simulations, and $\Delta\phi_2$ is the difference between the square of the ensemble-averaged density profile in FLMC simulations and the corresponding LSCF prediction. Both parts are due to fluctuations neglected in LSCF theory, and $\Delta\phi_2$ is unique for inhomogeneous systems. We find that $\Delta\phi_1 > 0$ and $\Delta\phi_2 < 0$ at finite n and $\chi \geq 0$. We also see that $(\langle E^2\rangle - \langle E\rangle^2)/{\rho_0}^4$ exhibits a maximum at $\chi \approx 0.9$. It is trivial that LSCF theory gives exact results of $\beta u_c = 0$ and $C_v/k_B = 0$ at $\chi = 0$ and in the limit of $\chi \to -\infty$, as well as that of $C_v/k_B = 0$ in the limit of $\chi \to \infty$. At finite $\chi > 0$, LSCF theory overestimates βu_c and underestimates C_v/k_B.

On the other hand, while $\beta\Delta f_{c,\mathrm{LSCF}}$ monotonically decreases with increasing χ, $\Delta s_{c,\mathrm{LSCF}}/k_B$ exhibits a maximum at $\chi = 0$ as proved in Appendix B. In the limit of $\chi \to \infty$, $\beta\Delta f_{c,\mathrm{LSCF}}$ approaches $-\infty$ but $\Delta s_{c,\mathrm{LSCF}}/k_B$ approaches a finite value. At finite n, while $\beta(\Delta f_{c,\mathrm{FLMC}} - \Delta f_{c,\mathrm{LSCF}})$ monotonically decreases with increasing $\chi \geq 0$, $-(\Delta s_{c,\mathrm{FLMC}} - \Delta s_{c,\mathrm{LSCF}})/k_B$ exhibits a local minimum at $\chi = 0$ and a local maximum at a χ-value slightly larger than 0.5; the location of the latter coincides with the corresponding extremum of $(\langle E\rangle - E_{\mathrm{LSCF}})/{\rho_0}^2$, as proved in Appendix C. Both $\beta(\Delta f_{c,\mathrm{FLMC}} - \Delta f_{c,\mathrm{LSCF}})$ and $-(\Delta s_{c,\mathrm{FLMC}} - \Delta s_{c,\mathrm{LSCF}})/k_B$ then cross 0 at a larger χ, and approach the same constant in the limit of $\chi \to \infty$. At finite n, LSCF theory therefore underestimates Δf_c but overestimates Δs_c at small $\chi \geq 0$, and the opposite occurs at larger χ.

At finite $\chi \geq 0$, FLMC results approach LSCF predictions at a rate of $1/n$ at large n. This scaling has also been found in our previous work.[1−3] As expected, LSCF theory is exact in the limit of $n \to \infty$, where there are no fluctuations or correlations. For the homopolymer brushes studied here, however, this scaling does not hold for certain quantities close to the finite χ-values at which the FLMC results concide with LSCF predictions, e.g., Δf_c and Δs_c at χ-values somewhat larger than 0.5 (see parts b and d of Figure 8).

Finally, when $\phi(x) \ll 1$ for all x, there is an approximate correspondence between brushes in an explicit solvent studied here and those in an implicit, good solvent studied in paper II, where a parameter κ inversely proportional to the second virial coefficient was used to characterize the solvent quality. Most results for $\chi \leq 0.5$ reported here can therefore be qualitatively understood based on paper II, with $(1 - 2\chi)\bar{\phi}$ and $\phi(x)/\bar{\phi}$ here corresponding to κ and $\phi(x)$ in that work. This correspondence is independent of the system dimensionality and whether or not the chains are grafted, as shown in Appendix A.

APPENDIX

A. Correspondence between Brushes in Explicit and Implicit Solvents

When $\hat{\rho}(x) \ll \rho_0$ (i.e., $\phi(x) \ll 1$) for all x, there is an approximate correspondence between brushes in explicit and implicit solvents. In this case, eq 3 can be re-written as

$$\begin{aligned}\mathcal{Z} &= \frac{1}{n!}\prod_{k=1}^{n}\prod_{s=1}^{N}\sum_{X_{k,s}}\cdot\exp\left\{-\beta\sum_{k=1}^{n}h_k^C + \frac{\chi}{\rho_0}E - \sum_x \ln[\rho_0 - \hat{\rho}(x)]!\right\}\\ &\sim \frac{1}{n!}\prod_{k=1}^{n}\prod_{s=1}^{N}\sum_{X_{k,s}}\cdot\exp\left\{-\beta\sum_{k=1}^{n}h_k^C + \frac{\chi}{\rho_0}E - \sum_x [\rho_0 - \hat{\rho}(x)]\ln[\rho_0 - \hat{\rho}(x)]\right\}\\ &\sim \frac{1}{n!}\prod_{k=1}^{n}\prod_{s=1}^{N}\sum_{X_{k,s}}\cdot\exp\left\{-\beta\sum_{k=1}^{n}h_k^C + \frac{\chi}{\rho_0}E + \sum_x [\rho_0 - \hat{\rho}(x)]\left[\frac{\hat{\rho}(x)}{\rho_0} + \frac{\hat{\rho}^2(x)}{2\rho_0^2}\right]\right\}\\ &\sim \frac{1}{n!}\prod_{k=1}^{n}\prod_{s=1}^{N}\sum_{X_{k,s}}\cdot\exp\left\{-\beta\sum_{k=1}^{n}h_k^C - \left(\frac{1}{2} - \chi\right)\bar{\phi}\frac{E}{\bar{\phi}\rho_0}\right\}\end{aligned} \tag{29}$$

where we have used the Stirling approximation and the Taylor expansion $\ln(1 - a) \approx -a - a^2/2$ for small a, "$\sim$" indicates that a constant in the Hamiltonian is further neglected, and to obtain the last line the $O(\hat{\rho}^3(x))$-term is also neglected. Comparing the above to eqs 1 and 2 in paper II and noting that $\bar{\phi}\rho_0 = nN/V$ here corresponds to ρ_0 in paper II, we see that $(1 - 2\chi)N\bar{\phi}$ and $\tilde{\phi}(x) \equiv \phi(x)/\bar{\phi}$ here correspond to N/κ and $\phi(x)$ in paper II, respectively. We note that this correspondence is actually independent of the system dimensionality and whether or not the chains are grafted.

This correspondence can also be seen in LSCF calculations. Using the Taylor expansion in eq 22 and defining $i\tilde{\omega}(x) \equiv i\omega(x) + \chi N(2\bar{\phi} - 1) - N\bar{\phi}$, we have

$$i\tilde{\omega}(x) \approx (1 - 2\chi)N\bar{\phi}[\tilde{\phi}(x) - 1] \tag{30}$$

With the definitions of $\tilde{q}^*_t(x) \equiv q^*_t(x)\exp[-\chi(2\bar{\phi} - 1)t + \bar{\phi}t]$ and $\tilde{q}_s(x) \equiv q_s(x)\exp[-\chi(2\bar{\phi} - 1)s + \bar{\phi}s]$, which satisfy the same recursive relations as eqs 20 and 21 with $i\omega(x)$ there replaced by $i\tilde{\omega}(x)$, eq 17 becomes

$$\tilde{\phi}_s(x) = \frac{\exp[i\tilde{\omega}(x)/N]}{\tilde{q}^*_N(x = 1)}\tilde{q}_s(x)\tilde{q}^*_{N+1-s}(x) \tag{31}$$

with $\tilde{\phi}_s(x) \equiv \phi_s(x)/\bar{\phi}$. Comparing eqs 30 and 31 with eqs 12 and 14 in paper II, we see that, in addition to the aforementioned correspondence, $i\tilde{\omega}(x)$, $\tilde{q}^*_t(x)$, $\tilde{q}_s(x)$, and $\tilde{\phi}_s(x)$ here correspond to $i\omega(x)$, $q^*_t(x)$, $q_s(x)$, and $\phi_s(x)$ in paper II, respectively.

To quantify the difference in polymer segmental density profile between brushes in an implicit and an explicit solvent, Figure 9 shows $\Delta\phi \equiv (\sum_x[\phi^{\mathrm{Ex}}(x)/\bar{\phi} - \phi^{\mathrm{Im}}(x)]^2/L)^{1/2}$ as a function of $\bar{\phi}$ for $N = 40$, where $\phi^{\mathrm{Ex}}(x)$ and $\phi^{\mathrm{Im}}(x)$ denote,

dx.doi.org/10.1021/ma202454s | Macromolecules 2012, 45, 2537−2550

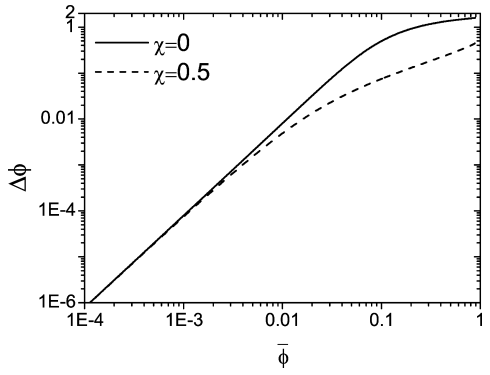


Figure 9. Difference in polymer segmental density profile between brushes in an implicit and an explicit solvent, $\Delta\phi$, as a function of $\bar{\phi}$ for $N = 40$ obtained from LSCF calculations; see text for details.

respectively, the polymer segmental density profile obtained from LSCF calculations of brushes in an explicit and an implicit solvent on the 1D lattice, with $N/\kappa = (1-2\chi)N\bar{\phi}$ used in the latter.[2] We see that $\Delta\phi$ increases with increasing $\bar{\phi}$ as expected, and that $\Delta\phi \propto \bar{\phi}^2$ at small $\bar{\phi}$. In addition, $\Delta\phi$ is larger in a solvent of better quality.

Finally, the shift of $i\omega(x)$ to $i\tilde{\omega}(x)$ gives $\tilde{Q} \equiv \tilde{q}^*_N(x=1)/L = Q\exp[-\chi N(2\bar{\phi} - 1) + N\bar{\phi}]$. With this and the Taylor expansion, eq 23 gives

$$\beta f_{c,\mathrm{LSCF}} = \frac{\bar{\phi}}{2L}(1-2\chi)N\bar{\phi}\sum_x[1-\tilde{\phi}^2(x)] - \bar{\phi}\ln\tilde{Q}[i\tilde{\omega}] - \bar{\phi}\frac{\ln(G^n/n!)}{n} + \frac{\bar{\phi}}{n}\ln n_S! - N(1-\bar{\phi})\ln V \tag{32}$$

For homopolymer brush in an implicit, good solvent, eqs 19 and 28 in paper II give

$$\beta f_{c,\mathrm{LSCF}} = \frac{1}{2L}\frac{N}{\kappa}\sum_{x=1}^{L}[1-\phi^2(x)] - \ln Q[i\omega] - \frac{\ln(G^n/n!)}{n} \tag{33}$$

Comparing these two equations, we see that $\beta f_c/\bar{\phi}$ in an explicit solvent corresponds to βf_c in an implicit, good solvent; the last two terms in eq 32 correspond to the solvent entropy.

Our FLMC and LSCF results for brushes in an explicit, good solvent reported here can therefore be qualitatively understood based on those for brushes in an implicit, good solvent reported in paper II. Note, however, that the reference state used for Δf_c and Δs_c here (i.e., the limit of $\chi \to -\infty$) is different from that used in paper II (i.e., $N/\kappa = 0$); for our model system studied in paper II, $\beta[f_c(N/\kappa \to \infty) - f_c(N/\kappa = 0)] = -[s_c(N/\kappa \to \infty) - s_c(N/\kappa = 0)]/k_B = 24.956$ for chains of $N = 40$.

B. The Maximum of $\Delta s_{c,\mathrm{LSCF}}/k_B$ at $\chi = 0$

At given N and $\bar{\phi}$, $s_{c,\mathrm{LSCF}}$ can be obtained from eqs 9 and 23 as

$$\frac{s_{c,\mathrm{LSCF}} - s_c^{id}}{k_B} = \chi N\bar{\phi} - 2\chi\sum_x\phi^2(x) - \sum_x\ln[1-\phi(x)] + N(1-\bar{\phi})\ln(1-\bar{\phi}) + \bar{\phi}\ln Q \tag{34}$$

which gives

$$\frac{\mathrm{d}}{\mathrm{d}\chi}\left(\frac{s_{c,\mathrm{LSCF}} - s_c^{id}}{k_B}\right) = \bar{\phi}N - \sum_x\left[2\phi^2(x) + \left(4\chi\phi(x) - \frac{1}{1-\phi(x)}\right)\frac{\mathrm{d}\phi(x)}{\mathrm{d}\chi}\right] + \bar{\phi}\frac{\mathrm{d}\ln Q}{\mathrm{d}\chi} \tag{35}$$

With $\delta\ln Q/\delta i\omega = -\phi(x)/N\bar{\phi}$ (i.e., eqs 16 and 17) and eq 22, we have

$$\bar{\phi}\frac{\mathrm{d}\ln Q}{\mathrm{d}\chi} = \bar{\phi}\sum_x\frac{\delta\ln Q}{\delta i\omega(x)}\frac{\mathrm{d}i\omega(x)}{\mathrm{d}\chi} = \sum_x\left[-\frac{\phi(x)}{1-\phi(x)}\frac{\mathrm{d}\phi(x)}{\mathrm{d}\chi} + 2\phi^2(x) + 2\chi\phi(x)\frac{\mathrm{d}\phi(x)}{\mathrm{d}\chi}\right] - \bar{\phi}L \tag{36}$$

We therefore obtain

$$\frac{\mathrm{d}}{\mathrm{d}\chi}\left(\frac{s_{c,\mathrm{LSCF}} - s_c^{id}}{k_B}\right) = -2\chi\sum_x\phi(x)\frac{\mathrm{d}\phi(x)}{\mathrm{d}\chi} \tag{37}$$

which gives

$$\left.\frac{\mathrm{d}}{\mathrm{d}\chi}\left(\frac{s_{c,\mathrm{LSCF}} - s_c^{id}}{k_B}\right)\right|_{\chi=0} = 0 \tag{38}$$

and

$$\left.\frac{\mathrm{d}^2}{\mathrm{d}\chi^2}\left(\frac{s_{c,\mathrm{LSCF}} - s_c^{id}}{k_B}\right)\right|_{\chi=0} = -2\sum_x\phi(x)\left.\frac{\mathrm{d}\phi(x)}{\mathrm{d}\chi}\right|_{\chi=0} = -\left.\frac{\mathrm{d}}{\mathrm{d}\chi}\sum_x[\phi(x)-\bar{\phi}]^2\right|_{\chi=0} < 0 \tag{39}$$

where the last inequality results from the fact that $\sum_x[\phi(x) - \bar{\phi}]^2$ is a monotonically increasing function of χ. $(s_{c,\mathrm{LSCF}} - s_c^{id})/k_B$ therefore exhibits a maximum at $\chi = 0$, so does $\Delta s_{c,\mathrm{LSCF}}/k_B$.

C. Extrema of $-(\Delta s_{c,\mathrm{FLMC}} - \Delta s_{c,\mathrm{LSCF}})/k_B$ and $(\langle E\rangle - E_{\mathrm{LSCF}})/\rho_0^2$

From eqs 6–9, we have at given n, N and $\bar{\phi}$

$$\frac{s_{c,\mathrm{FLMC}}(\chi)}{k_B} = -\frac{\chi}{\rho_0}\frac{\mathrm{d}\ln\mathcal{Z}}{\mathrm{d}\chi} + \frac{1}{\rho_0}\ln\mathcal{Z} \tag{40}$$

and

$$\frac{\langle E(\chi)\rangle}{\rho_0^2} = \frac{1}{\rho_0}\frac{\mathrm{d}\ln\mathcal{Z}}{\mathrm{d}\chi} \tag{41}$$

dx.doi.org/10.1021/ma202454s | Macromolecules 2012, 45, 2537–2550

With eq 37 we therefore obtain

$$\frac{\mathrm{d}}{\mathrm{d}\chi}\left[-\frac{s_{c,\mathrm{FLMC}}-(s_{c,\mathrm{LSCF}}-s_c^{id})}{k_B}\right] = \chi\frac{\mathrm{d}}{\mathrm{d}\chi}\left(\frac{\langle E\rangle - E_{\mathrm{LSCF}}}{\rho_0^2}\right) = -\frac{\chi}{\rho_0}\frac{\mathrm{d}^2\ln\mathcal{Z}}{\mathrm{d}\chi^2} + 2\chi\sum_x \phi(x)\frac{\mathrm{d}\phi(x)}{\mathrm{d}\chi} \quad (42)$$

which indicates that the extrema of $(\langle E\rangle - E_{\mathrm{LSCF}})/\rho_0^2$ have the same location as those of $-[s_{c,\mathrm{FLMC}} - (s_{c,\mathrm{LSCF}} - s_c^{id})]/k_B$ (or equivalently $-(\Delta s_{c,\mathrm{FLMC}} - \Delta s_{c,\mathrm{LSCF}})/k_B$), and that the latter has an additional extremum at $\chi = 0$. Furthermore, at the extrema of $(\langle E\rangle - E_{\mathrm{LSCF}})/\rho_0^2$

$$\frac{\mathrm{d}^2}{\mathrm{d}\chi^2}\left[-\frac{s_{c,\mathrm{FLMC}}-(s_{c,\mathrm{LSCF}}-s_c^{id})}{k_B}\right] = \chi\frac{\mathrm{d}^2}{\mathrm{d}\chi^2}\left(\frac{\langle E\rangle - E_{\mathrm{LSCF}}}{\rho_0^2}\right) \quad (43)$$

which indicates that both $(\langle E\rangle - E_{\mathrm{LSCF}})/\rho_0^2$ and $-[s_{c,\mathrm{FLMC}} - (s_{c,\mathrm{LSCF}} - s_c^{id})]/k_B$ (or equivalently $-(\Delta s_{c,\mathrm{FLMC}} - \Delta s_{c,\mathrm{LSCF}})/k_B$) reach either local maximum or local minimum at $\chi > 0$, but one of them reaches local maximum while the other reaches local minimum at $\chi < 0$. Because of the $\ln\mathcal{Z}$-term involved, however, it is difficult to tell whether these extrema are local maxima or minima.

AUTHOR INFORMATION

Corresponding Author

*E-mail: q.wang@colostate.edu.

ACKNOWLEDGMENTS

We thank Mr. Delian Yang for the lateral instability analysis of our LSCF results. B.L. acknowledges the financial support for this work provided by the National Science Fund for Distinguished Young Scholars of China (No. 20925414), and Q.W. acknowledges the financial support provided by NSF CAREER Award CBET-0847016.

REFERENCES

(1) Zhang, P.; Zhang, X.; Li, B.; Wang, Q. *Soft Matter* **2011**, *7*, 4461.
(2) Zhang, P.; Li, B.; Wang, Q. *Macromecules* **2011**, *44*, 7837.
(3) Wang, Q. *Soft Matter* **2009**, *5*, 4564; **2010**, *6*, 6206.
(4) Fredrickson, G. H. *The Equilibrium Theory of Inhomogeneous Polymers*; Oxford University Press: London, 2006.
(5) Whitmore, M. D.; Noolandi, J. *Macromolecules* **1990**, *23*, 3321.
(6) Baranowski, R.; Whitmore, M. D. *J. Chem. Phys.* **1995**, *103*, 2343.
(7) Baranowski, R.; Whitmore, M. D. *J. Chem. Phys.* **1998**, *108*, 9885.
(8) Whitmore, M. D.; Baranowski, R. *Macromol. Theory Simul.* **2005**, *14*, 75.
(9) Pepin, M. P.; Whitmore, M. D. *J. Chem. Phys.* **1999**, *111*, 10381.
(10) Skvortsov, A. M.; Pavlushkov, I. V.; Gorbunov, A. A.; Zhulina, E. B.; Borisov, O. V.; Pryamitsyn, V. A. *Polym. Sci. USSR* **1988**, *30*, 1706.
(11) Zhulina, E. B.; Borisov, O. V.; Pryamitsyn, V. A.; Birshtein, T. M. *Macromolecules* **1991**, *24*, 140.
(12) Shim, D. F. K.; Cates, M. E. *J. Phys.-Paris* **1989**, *50*, 3535.
(13) Amoskov, V. M.; Pryamitsyn, V. A. *J. Chem. Soc., Faraday Trans.* **1994**, *90*, 889.
(14) Amoskov, V. M.; Pryamitsyn, V. A. *Polym. Sci. Ser. A* **1995**, *37*, 731.
(15) Amoskov, V. M.; Pryamitsyn, V. A. *Macromol. Theory Simul.* **2003**, *12*, 223.
(16) Cosgrove, T.; Heath, T.; Vanlent, B.; Leermakers, F.; Scheutjens, J. *Macromolecules* **1987**, *20*, 1692.
(17) Gorbunov, A. A.; Pavlushkov, I. V.; Skvortsov, A. M. *Polym. Sci. USSR* **1988**, *30*, 414.
(18) Skvortsov, A. M.; Pavlushkov, I. V.; Gorbunov, A. A. *Polym. Sci. USSR* **1988**, *30*, 487.
(19) Hirz, S. J. Masters Thesis, University of Minnesota, 1986.
(20) Huang, K. L.; Balazs, A. C. *Macromolecules* **1993**, *26*, 4736.
(21) Martin, J. I.; Wang, Z. G. *J. Phys. Chem.* **1995**, *99*, 2833.
(22) Wijmans, C. M.; Scheutjens, J.; Zhulina, E. B. *Macromolecules* **1992**, *25*, 2657.
(23) Chakrabarti, A.; Toral, R. *Macromolecules* **1990**, *23*, 2016.
(24) Milik, M.; Kolinski, A.; Skolnick, J. *J. Chem. Phys.* **1990**, *93*, 4440.
(25) Lai, P. Y.; Binder, K. *J. Chem. Phys.* **1991**, *95*, 9288.
(26) Lai, P. Y.; Binder, K. *J. Chem. Phys.* **1992**, *97*, 586.
(27) Pakula, T. *Macromol. Symp.* **1999**, *139*, 49.
(28) Huh, J.; Ahn, C. H.; Jo, W. H.; Bright, J. N.; Williams, D. R. M. *Macromolecules* **2005**, *38*, 2974.
(29) Ohno, K.; Sakamoto, T.; Minagawa, T.; Okabe, Y. *Macromolecules* **2007**, *40*, 723.
(30) Coluzza, I.; Hansen, J. P. *Phys. Rev. Lett.* **2008**, *100*, 016104.
(31) Karaiskos, E.; Bitsanis, I. A.; Anastasiadis, S. H. *J. Polym. Sci., Part B: Polym. Phys.* **2009**, *47*, 2449.
(32) Murat, M.; Grest, G. S. *Macromolecules* **1989**, *22*, 4054.
(33) Grest, G. S.; Murat, M. *Macromolecules* **1993**, *26*, 3108.
(34) Grest, G. S. *Macromolecules* **1994**, *27*, 418.
(35) Seidel, C.; Netz, R. R. *Macromolecules* **2000**, *33*, 634.
(36) Kreer, T.; Metzger, S.; Muller, M.; Binder, K.; Baschnagel, J. *J. Chem. Phys.* **2004**, *120*, 4012.
(37) He, G. L.; Merlitz, H.; Sommer, J. U.; Wu, C. X. *Macromolecules* **2007**, *40*, 6721.
(38) Dimitrov, D. I.; Milchev, A.; Binder, K. *J. Chem. Phys.* **2007**, *127*, 084905.
(39) He, G. L.; Merlitz, H.; Sommer, J. U.; Wu, C. X. *Eur. Phys. J. E* **2007**, *24*, 325.
(40) Neelov, I. M.; Binder, K. *Macromol. Theory Simul.* **1995**, *4*, 119.
(41) Pal, S.; Seidel, C. *Macromol. Theory Simul.* **2006**, *15*, 668.
(42) Weinhold, J. D.; Kumar, S. K. *J. Chem. Phys.* **1994**, *101*, 4312.
(43) Laradji, M.; Guo, H.; Zuckermann, M. J. *Phys. Rev. E* **1994**, *49*, 3199.
(44) Soga, K. G.; Guo, H.; Zuckermann, M. J. *Europhys. Lett.* **1995**, *29*, 531.
(45) Lai, P. Y.; Zhulina, E. B. *J. Phys. II* **1992**, *2*, 547.
(46) Shell, M. S.; Debenedetti, P. G.; Panagiotopoulos, A. Z. *J. Chem. Phys.* **2003**, *119*, 9406.
(47) Ghulghazaryan, R. G.; Hayryan, S.; Hu, C. *J. Comput. Chem.* **2007**, *28*, 715.
(48) Chapter 3 in *Free Energy Calculations: Theory and Applications in Chemistry and Biology*; Chipot, C., Pohorille, A., Eds., Springer: Berlin, 2007.
(49) Yang, D.; Wang, Q. *J. Chem. Phys.* **2012**, to be submitted.
(50) Frenkel, D.; Smit, B. *Understanding Molecular Simulation — From Theory to Applications*; Academic Press: San Diego, CA, 2002
(51) Press, W. H.; Teukolsky, S. A.; Vetterling, W. T.; Flannery, B. P. *Numerical Recipes in FORTRAN: the Art of Scientific Computing*; Cambridge University Press: London, 2002.
(52) Different from eq 22, this is the case when $\boldsymbol{\phi}\cdot i\boldsymbol{\omega}$ is set to be 0, as can be seen from eq 11.

(53) Yeung, C.; Balazs, A. C.; Jasnow., D. *Macromolecules* **1994**, *26*, 1914.
(54) Roderick, C.; Guo, H.; Zuckermann, M. J. *Phys. Rev. E* **2000**, *63*, 012501.

■ NOTE ADDED AFTER ASAP PUBLICATION

This article posted ASAP on February 8, 2012. Due to a production error, the paper was published before final corrections were made. The correct version posted on February 27, 2012.

Macromolecules

Article

pubs.acs.org/Macromolecules

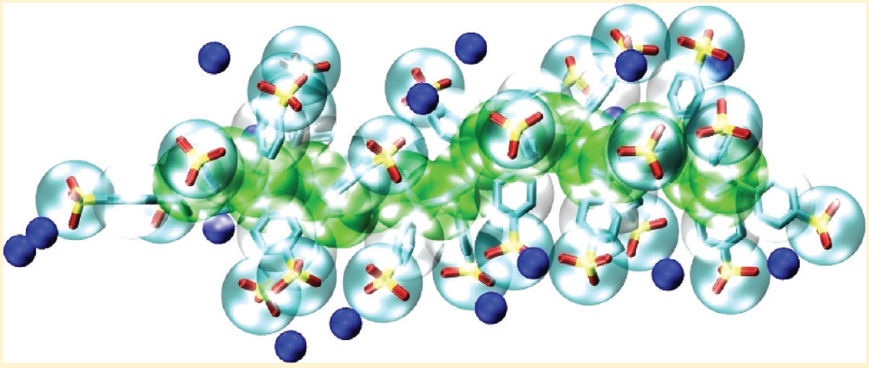
A Chemically Accurate Implicit-Solvent Coarse-Grained Model for Polystyrenesulfonate Solutions

Chunli Li,[†] Jiawei Shen,[‡] Christine Peter,[‡] and Nico F. A. van der Vegt*,[†]

[†]Center of Smart Interfaces, Technische Universität Darmstadt, Petersenstrasse 32, D-64287 Darmstadt, Germany

[‡]Max Planck Institute for Polymer Research, Ackermannweg 10, D-55128 Mainz, Germany

Supporting Information



ABSTRACT: A systematic molecular coarse-graining (CG) approach for aqueous polyelectrolyte solutions is presented with sodium polystyrenesulfonate (NaPSS) with different chain tacticities as example systems. The styrenesulfonate repeat unit is mapped on a three-site CG representation with the counterion being modeled explicitly while the solvent is modeled implicitly. The CG force field discriminates between bonded and nonbonded forces, which have been developed independently. The bonded interactions correspond to the potentials of mean force of CG bond, angle, and torsion degrees of freedom obtained from sampling isolated chains with an atomistic force field that includes only the local interactions along the chain. The nonbonded interactions correspond to bead−bead potentials of mean force, obtained from simulations of small molecule or ion pairs in explicit water. The CG model reproduces the local and global conformations of polyelectrolyte chains in good agreement with the parent atomistic chains in aqueous solution. By using a relative dielectric permittivity based on the local concentration of counterions around the polyelectrolyte chain, the quality of our CG models can be further improved substantially. The effect of added salt (NaCl) on the radius of gyration of PSS chains with different tacticities has also been studied and results show the transferability of the CG NaPSS model to regimes with different electrostatic conditions. We furthermore show that the CG procedure presented here can easily be extended to CG models for partially sulfonated polystyrene systems.

1. INTRODUCTION

The structures and properties of polyelectrolyte systems are of great research interests due to their important role in biological systems and materials science.[1−7] In particular, many biopolymers such as proteins, DNA, and RNA are polyelectrolytes. Polyelectrolytes differ from low molecular weight electrolytes as well as from neutral polymers. They dissociate charges in polar solvents such as water and result in charged polymer chains and small mobile counterions.[8] The interplay between backbone hydrophobicity and electrostatic interactions from ionized groups results in an impressive variety of phenomena, which makes these systems very interesting from a fundamental point of view.

A considerable number of both experimental and theoretical studies have been performed to investigate the structure and dynamics of polyelectrolyte systems. For example, light scattering techniques have been widely used to study polyelectrolyte solutions, revealing properties such as the molecular weight, charge density, and concentrations of polyelectrolyte, along with the ionic strength and the pH of the solution,[9−14] as well as the formation of large multichain domains,[15,16] aggregates,[17] or clusters.[18] Detailed atomistic molecular dynamics (MD) studies of polyelectrolytes include investigations of poly(ethylene oxide) sulfonic acid in water,[19] the influences of counterions on DNA solvation in water,[20] simulations of poly(acrylic acid)with calcium counterions,[21] complex formations of PSS/PAA chains in water,[22] and surface effects on polyelectrolyte adsorption[23] etc. However, these simulations are rather expensive computationally due to the fact that polyelectrolyte chains, counterions, and/or water molecules in the systems are modeled explicitly. Limitations in terms of system sizes and time scales result in exhaustive sampling of

Received: November 11, 2011
Revised: February 2, 2012
Published: February 28, 2012

ACS Publications © 2012 American Chemical Society

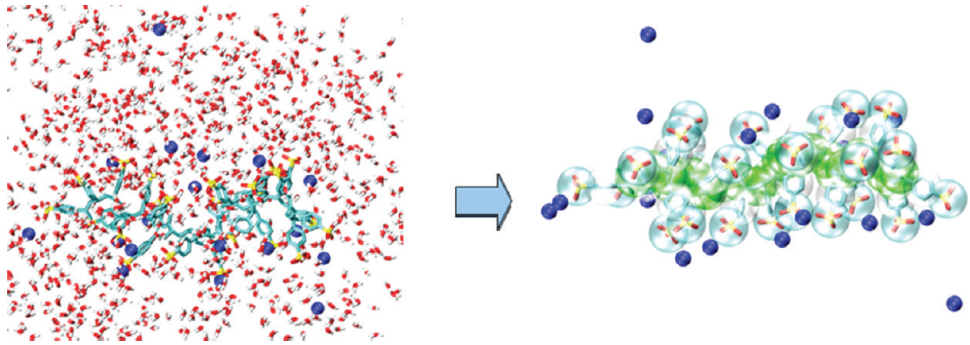


Figure 1. Implicit solvent CG model of a PSS chain with its counterions (Na^+) compared with its atomistic model. Left figure is the atomistic model, and right figure is the CG model. Small blue beads are counterions.

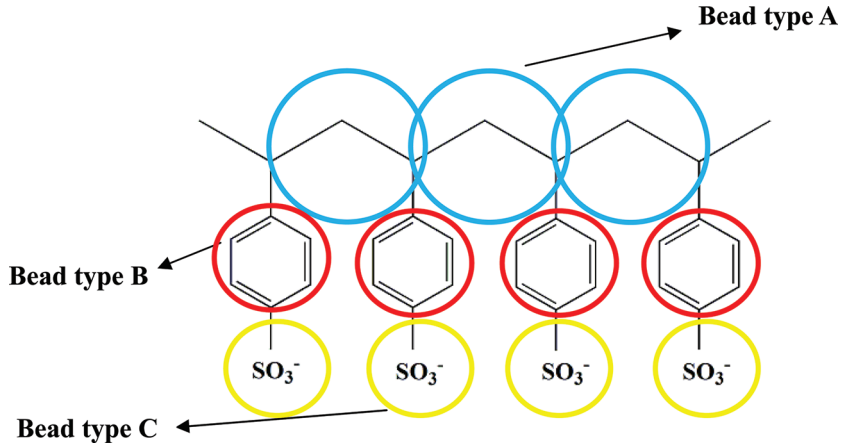


Figure 2. Mapping scheme of PSS chain.

polymer conformations only for short chains and/or few chains. On the other hand, coarse grained (CG) models have also been developed for polyelectrolyte solutions. However, some of these CG models use generic force fields, where polyelectrolytes with different chemical structures, counterions and co-ions, solvents and salt ions cannot be distinguished, ion specific effects and ion pairing with polymer side chains etc. cannot be indicated,[1,6,24] while in other CG models both water and counterions are represented implicitly; therefore, it is not possible to investigate ion correlation effects, such as the distributions of counterions along the polymer chain.[3]

In this work, a novel implicit solvent CG model was developed for a polyelectrolyte system containing a polystyrenesulfonate (PSS) chain with its counterions (Na^+) solvated in water. NaPSS was chosen due to its important applications in biomimetic materials research. In the development of synthetic bioinspired materials, NaPSS is widely used as the organic layer where nanometer-sized mineral particles are attached to generate hierarchically structured mesocrystal composites.[25] However, it is worth noting that the coarse graining strategy presented in this work can be easily extended to other polyelectrolyte systems as well.

In the CG model described here, the polymer chain and its counterions are both modeled explicitly while water molecules are modeled implicitly. Bonded and nonbonded CG potentials are obtained separately from independent atomistic level simulations. Furthermore, bonded interactions for NaPSS chains with different tacticities (isotactic, syndiotactic, atactic) are modeled differently in the CG description in analogy to a previously developed PS model.[26] Figure 1 depicts the resulting implicit solvent CG model compared with the parent atomistic model. By applying this strategy, we aim at developing a transferable CG model for polyelectrolyte solutions. In the results and discussion, the local and global conformational properties of CG isotactic, syndiotactic, atactic NaPSS chain in solutions are presented. The effects of added salt (NaCl) to the NaPSS solutions are also discussed and compared with atomistic level simulations. We point out that the CG models developed here can also be extended to systems containing NaPSS chains with various degrees of sulfonation.

2. COARSE GRAINING MODELS

2.1. Mapping Scheme. Each monomer of the PSS chain is mapped on three different CG bead types. The mapping scheme is shown in Figure 2. Bead A contains the CH_2 group in the backbone and half of its two neighboring CH groups to which the phenyl rings are attached; bead B contains all the atoms of the phenyl ring; and bead C contains all the atoms in the sulfonate group. All three beads are located at the center of mass of the group of atoms they contain. This mapping scheme leads to a CG PSS chain with alternating bead type A and B as backbone. CG bonds provide a "backbone" connectivity −A−B−A−B−. Bead C is attached to bead B as side group.

In the development of our CG model, PSS chains with different tacticities are distinguished by differentiating between two different scenarios of the stereochemistry in the subsequent monomers (diads) in the polymer chain. As shown in Figure 3, assuming the polymer backbone is in all-trans configuration, in a meso diad both phenyl rings point in the same direction while in a racemic diad phenyl rings point in opposite directions.

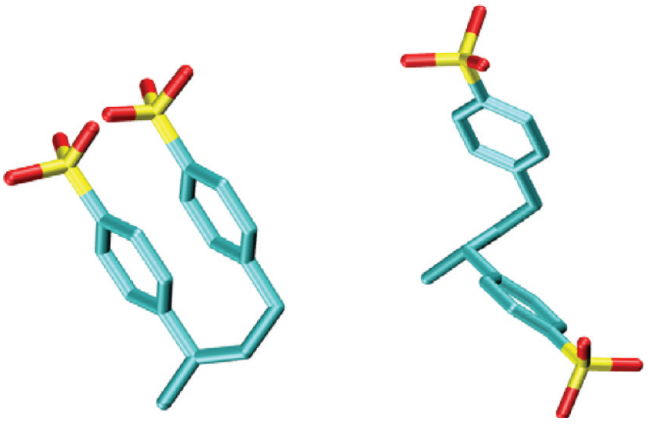


Figure 3. Diads in polystyrene: in meso diads (left), the subsequent side groups point in the same direction; in racemic diads (right), they point in opposite directions.

Correspondingly, a chain consisting of only meso diads is isotactic; a chain containing only racemic diads is syndiotactic; while in an atactic chain different types of diads are randomly distributed. More details about symmetry equivalent or analogous potentials (dihedrals) are discussed in the Supporting Information.

2.2. Coarse-Graining Procedure. Following the previous studies on the development of CG models for polystyrene (PS) chains,[26] our coarse-graining procedure is based on the same assumption that the total potential energy of a CG chain, U^{CG}, contains additive contributions of bonded, U^{CG}_{bonded}, and nonbonded, $U^{CG}_{nonbonded}$, terms:

$$U^{CG} = \sum U^{CG}_{bonded} + \sum U^{CG}_{nonbonded} \quad (1)$$

In this way, the CG bonded and nonbonded interaction potentials can be developed independently. In this work, the bonded potentials are derived from the atomistic sampling of an isolated PSS chain in vacuum,[26] while the nonbonded interactions are obtained by calculating the potentials of mean force (PMF) between two small molecules or ions in water representing the corresponding CG mapping beads in the polymer chain.[27]

2.2.1. Bonded Potentials. For the development of bonded potentials, atomistic MD simulations of isolated random walks in vacuum are performed at a selected temperature T. These simulations take into account the local bonded and nonbonded interactions between neighboring monomers on the chain while all nonbonded interactions between distant monomers are excluded.[26] The probability distributions of the CG bond lengths, $P^{CG}(r,T)$, bending angles, $P^{CG}(\theta,T)$ and dihedral angles, $P^{CG}(\phi,T)$, are obtained from the sampled trajectories and subsequently Boltzmann inverted to get the corresponding CG bond, angle and dihedral potentials of mean force:

$$U^{CG}(r, T) = -k_B T \ln(P^{CG}(r, T)/r^2) + C_r \quad (2)$$

$$U^{CG}(\vartheta, T) = -k_B T \ln(P^{CG}(\vartheta, T)/\sin\vartheta) + C_\vartheta \quad (3)$$

$$U^{CG}(\phi, T) = -k_B T \ln P^{CG}(\phi, T) + C_\phi \quad (4)$$

The probability distribution functions for the bond length and bond angle are normalized by taking into account the corresponding volume elements r^2 and sin θ. By means of this procedure we assume that the probability distributions $P^{CG}(r,\theta,\phi,T)$ obtained by the atomistic sampling of a single PSS chain random walk can be factorized as:

$$P^{CG}(r, \vartheta, \phi, T) = P^{CG}(r, T)P^{CG}(\vartheta, T)P^{CG}(\phi, T) \quad (5)$$

This assumption holds provided that the internal CG degrees of freedom are uncorrelated. However, previous studies show that correlations among internal CG degrees of freedom do exist in polystyrene models.[26,28,29] But by carefully choosing the range of local interactions along the backbone in the atomistic vacuum sampling and a suitable set of bonded interactions, correlations present in the atomistic models can be preserved in the CG models. Besides, the choice of CG mapping scheme is also crucial.

The distribution functions of the bonded degrees of freedom do not depend on long-range nonbonded interactions along the chain (or with other chains), nor on interactions with the solvent molecules or with counterions and salt ions. The net effect of these interactions on the chain conformations in solution depends on the thermodynamic conditions (concentration, temperature, *etc.*) and will be accounted for with independently developed nonbonded interactions that will be described in the next section.

It has been found that the interaction cutoff used in the single-chain sampling procedure critically determines whether the CG model is capable of reproducing conformational properties of the parent atomistic system down to the level of a few neighboring repeat units. This aspect will be discussed in greater detail below. The atomistic sampling run was performed with a single PSS chain (one isotactic and one syndiotactic chain) with 25 repeats units in vacuum at 298 K by using the stochastic dynamics integrator of GROMACS[30] with time coupling constant of 2 ps. By doing this we obtain all distribution functions necessary to model all tacticities. Force field parameters were taken from a united atom model presented by Hoda et al.[22] During the vacuum sampling, the electrostatic contributions to the potentials have been switched off. The effects of electrostatic interactions on the chain rigidity and conformations are separately accounted for through the nonbonded CG interactions discussed below.

2.2.2. Nonbonded Potentials. CG nonbonded potentials are obtained by calculating pair potentials of mean force as a function of distance between the mass centers of two small molecules or ions (representative of a CG bead) in a box of pure water. In this way, the molecules' internal degrees of freedom and the solvent degrees of freedom are accounted for implicitly in the effective bead−bead interactions. The resulting potentials thus depend explicitly on distance, but, as for the case of the bonded potentials, also contain an implicit dependence on state which limits the transferability of the model.

The potential of mean force between two molecules or groups in a box of pure water can be calculated from n distance constraint simulations by using the following equation:[27,31,32]

$$V_{PMF}(r) = \int_r^{r_m} \left[\langle f_c \rangle_s + \frac{2k_B T}{s} \right] ds + C \quad (6)$$

Here k_B is the Boltzmann constant, T is the temperature, f_c is the constraint force between the chosen centers of two molecules, and r_m is the maximum distance between the above two centers of molecules. For all PMF simulations in this

dx.doi.org/10.1021/ma202490h | *Macromolecules* 2012, 45, 2551−2561

research, the distance r varies from 0.2 to 1.2 nm in steps of 0.02 nm.

Previous studies[31] show that the effective potential between two ions in water is very close to a Coulomb interaction at distances greater than 1.0 nm. Therefore, we assume that beyond 1.2 nm, the PMF between two ions can be approximated with a Coulomb potential:

$$V_{PMF}(r) = \frac{q_1 q_2}{4\pi\varepsilon_0\varepsilon_r r}, \quad r > 1.2 \text{ nm} \tag{7}$$

where q_1 and q_2 are the charges of the ions, ε_0 is the dielectric permittivity of vacuum and ε_r is the relative dielectric permittivity of the solvent with a value of 72 for the SPC/E water model used in this work.[33] The constant C in eq 6 is equal to the Coulomb potential at 1.2 nm for the ion−ion interactions, and is chosen as identical zero for interactions between electrically neutral species. Furthermore, for the implementation of $V_{PMF}(r)$ in eq 6 and 7 in GROMACS, a short-range contribution $V_{short}(r)$ is obtained by subtracting the long-range Coulomb interaction between different molecules or ions from $V_{PMF}(r)$:

$$V_{short}(r) = V_{PMF}(r) - \frac{q_1 q_2}{4\pi\varepsilon_0\varepsilon_r r} \tag{8}$$

In our CG simulation, this short-range (non-Coulomb) contribution $V_{short}(r)$ is implemented in GROMACS in tabulated form, while the remaining long-ranged Coulomb interactions are computed using the particle mesh Ewald (PME) algorithm[34] with $\varepsilon_r = 72$.

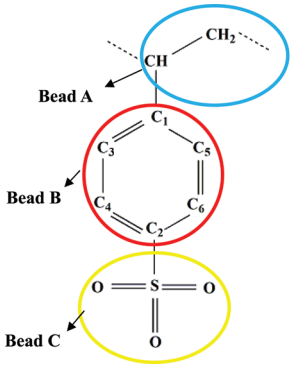
In our PSS CG model, there are three different types of beads. Together with the counterions and co-ions, used to model effects of added salt, a total number of 15 bead−bead nonbonded pair potentials need to be constructed. Each of these potentials is obtained by calculating the PMF between a single pair of small molecules or ions in explicit water by means of eq 6. These small molecules or ions are chosen to represent the corresponding CG beads. Propane, benzene, and the methylsulfonate ion model the CG beads A, B, and C, respectively. The molecular centers used to define the distances in the constraint simulations were chosen to correspond to the mapping points of the CG PSS beads.

3. METHODS/COMPUTATIONAL DETAILS

The molecular dynamics package GROMACS 4.0.7 was used to perform all the simulations reported in this research.[30]

3.1. Atomistic MD Simulations. For the atomistic modeling of the NaPSS chain and sodium *p*-toluene sulfonate salt (the osmotic coefficient of this salt in water was later on calculated in order to validate the atomistic model), a united atom model based on the TraPPE force field was used.[5,22,35−37] The partial charges assigned on a PSS monomer are shown in Table 1. The force field parameters for the counterions (Na^+) and co-ions (Cl^-) was taken from ref 38. The SPC/E model[33] was used to model water molecules. All the bond lengths were constrained using the LINCS method[39] except those of water molecules, where the SETTLE algorithm[40] was used. For nonbonded interactions, a cutoff value of 1.0 nm was used for the van der Waals interaction. The PME method[40] was employed to treat Coulomb interactions, with a real space cutoff distance of 1.0 nm. A long-range dispersion correction was applied for energy and pressure. All atomistic simulations were performed under isothermal−isobaric (*NPT*) conditions. The Berendsen thermostat and barostat[41] was used to couple the system to an external bath at 1 bar and 298 K, with time coupling constants of 1 and 0.1 ps, respectively. The integration time step was 1 fs. We simulated NaPSS solutions of isotactic,

Table 1. Partial Charges Assigned on a PSS Monomer in the Atomistic Models and CG Models



Atomistic		CG	
Group	Charge (e)	Group	Charge (e)
CH2/CH	0	A	0
C1	-0.03		
C2	-0.23	B	-0.505
C3/C5	-0.02		
C4/C6	-0.1025		
S	1.755	C	-0.495
O	-0.75		

syndiotactic, and atactic chains, respectively. Each system contained a single PSS chain with a degree of polymerization (DP) of 25 monomers, 25 Na^+ ions, and 13890 water molecules, which corresponds to a concentration of the polyions of 0.1 *m* (monomer). For systems where the effect of added salt was investigated, corresponding number of Na^+ and Cl^- ions were added.

The combination of the united atom PSS force field, ion and water models used in this work are validated by calculating the osmotic pressure of sodium *p*-toluene sulfonate solutions at different concentrations. The simulation system set up is depicted in Figure 4.[32,42] Two semipermeable walls are imposed perpendicular to the long axis z direction in a three-dimensional periodic simulation box, where salt ions are restricted in the central regions between two walls and water molecules can pass freely through the walls. A shifted 10−4 potential is set up so that ions experience repulsive forces as they start to diffuse out of the central region. By setting the simulation box to be semi-isotropic (*i.e.*, side length x and y are fixed while z is allowed to change) and performing *NPT* simulations, the osmotic pressure of the salt solutions can be calculated from the average forces exerted by the walls on the salt ions divided by the surface areas of two walls. In the above osmotic pressure calculations, 22224 water molecules were contained in each system; while 40, 80, 120, 160, and 200 ion pairs were used in the simulations for concentrations of sodium p-toluene sulfonate at 0.2, 0.4, 0.6, 0.8, and 1 *m* (molality) respectively. In each, 30 ns of *NPT* simulations were performed and the block average of the last 10 ns was used to calculate the osmotic pressure. Osmotic coefficients of the solutions were also calculated by using the following equation:

$$\phi = \frac{\pi}{CRT} \tag{9}$$

where φ is the osmotic coefficient, π is the osmotic pressure, C is twice the salt concentration in unit of mol/L, R is the universal gas constant, and T is the temperature, respectively.

3.2. Coarse-Grained MD Simulations. For all CG simulations presented in this work, bonded and nonbonded (short-range non-Coulomb) potentials are presented in tabulated forms implemented in GROMACS 4.0.7.[30] All CG simulations were performed in canonical (*NVT*) ensembles at 298 K by using stochastic dynamics with a time coupling constant of 2 ps.[30] Volumes of the CG systems were taken from the average volumes of their corresponding (*NPT*) atomistic systems. The integration time step is 4 fs and simulation time is 400 ns. In each CG system, a single PSS chain with DP = 25 or DP = 200 and the corresponding number of counterions (Na^+) were simulated. In systems investigating effects of added salt, certain numbers of salt ions (Na^+ and Cl^-) were added according to the salt concentrations. The mapping of atomistic models into CG beads was done by using the VOTCA toolkit.[43] The initial configurations of each CG system were taken from the mapping of the equilibrated structures from its corresponding atomistic simulations.

dx.doi.org/10.1021/ma202490h | *Macromolecules* 2012, 45, 2551−2561

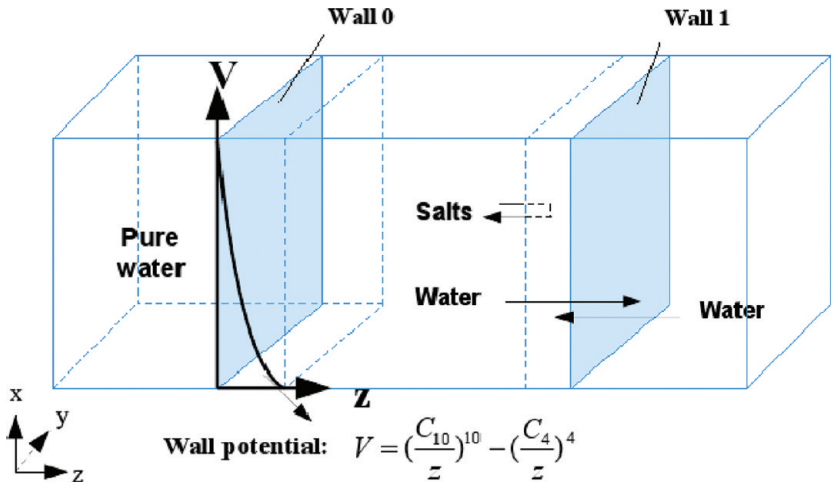


Figure 4. Simulation system set up[42] to calculate osmotic pressure of sodium *p*-toluene sulfonate solutions.

4. RESULTS AND DISCUSSION

4.1. Validation of Atomistic Models. Osmotic pressures and osmotic coefficients of sodium *p*-toluene sulfonate solutions were calculated at various concentrations, from 0.2 to 1 m, respectively. These results are compared with the experimental results and are shown in Figure 5. It can be seen

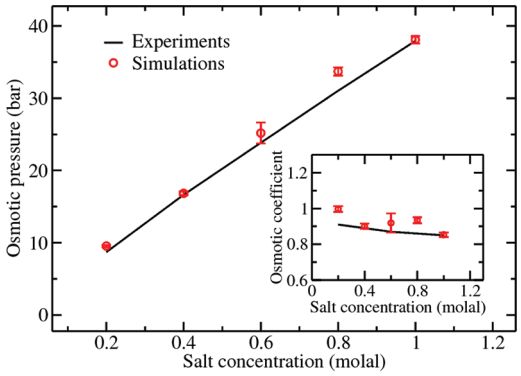


Figure 5. Comparison of simulation and experimental results for osmotic pressure and osmotic coefficient (inset) of sodium *p*-toluene sulfonate solutions at different concentrations (298 K).

that the united atom model we used here reproduces the experimental osmotic pressures[44] well at these concentrations. Therefore, the model has not been further refined and has been used as parent atomistic model for constructing the CG model by systematic coarse graining.

4.2. Development of CG Potentials. *4.2.1. Bonded Potentials.* The distributions of CG bond lengths, angles and dihedral angles depend on the "interaction range" used in the atomistic sampling of a single PSS chain in vacuum. Here, the "interaction range" refers to the number of neighboring beads (in terms of the CG mapping) that are included in evaluating the nonbonded pair interactions between atoms in atomistic vacuum simulations. The BAB angle distributions in fully isotactic and syndiotactic chains are shown in Figure 6 for different interaction ranges. We can see that in both cases the peak positions in the BAB angle distribution curves shift when local interactions up to 1−5 neighbors (the counting is done on the basis of CG beads) are included. With the inclusion of 1−6 interactions and beyond, the positions of the peaks always stay

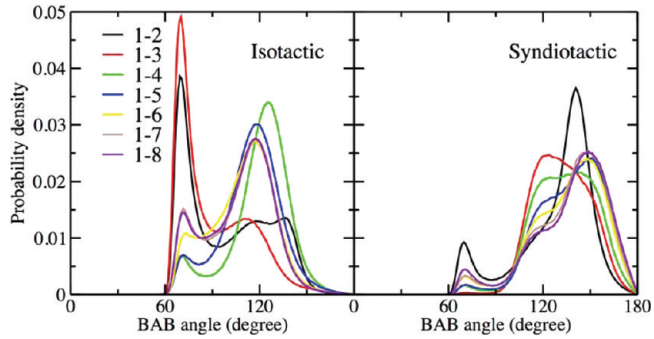


Figure 6. Distributions of BAB angles in a fully isotactic (left) and fully syndiotactic (right) single chain in vacuum at 298 K. The interaction range in these atomistic runs was varied from 1−2 to 1−8 in the CG description. All distributions are normalized.

the same, although their heights slightly change. By including the 1−5 interactions, the pentane effect in the polymer backbone is taken into account.

In order to further determine which range of intramolecular nonbonded interactions is required to fully represent the configurational sampling of the polymer chain, we looked at correlations between the probability distributions of two subsequent CG dihedral angles as shown in Figure 7. These plots show that more combinations of subsequent dihedral angles are suppressed as longer interaction ranges are included in the atomistic sampling of a single PSS chain in vacuum. But as 1−7 interactions are included, the correlation plot converges; i.e., no further changes are seen upon extending the range to 1−8 and beyond. This means that the interactions up to 1−7 determine the correlations and local conformations of a single PSS chain. Therefore, we performed the atomistic sampling of a single chain with all interactions included up to the 1−7 CG level for the derivation of the CG bond, angle, and dihedral angle potentials. However, we need to keep in mind that in this way, contributions from 1−5, 1−6, and 1−7 interactions are double counted since the final CG model uses additional nonbonded potentials for these interactions. The bonded potentials of the CG PSS model are summarized in the Supporting Information.

4.2.2. Nonbonded Effective Potentials. Figure 8 depicts the nonbonded potentials between different CG beads obtained from calculations of PMFs between molecules and/or ion pairs

dx.doi.org/10.1021/ma202490h | *Macromolecules* 2012, 45, 2551−2561

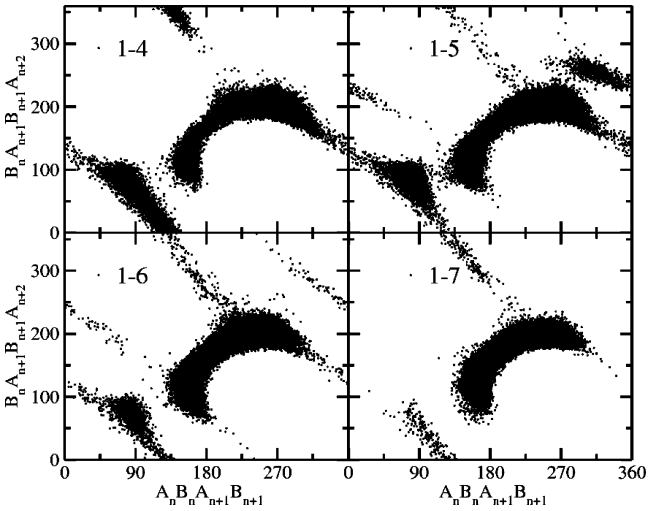


Figure 7. Conformation space sampled by two subsequent CG dihedral angles along the backbone in a single, isotactic chain obtained from atomistic sampling in vacuum (298 K). The two dihedrals share three beads, which form a BAB angle. Combinations with varied interaction ranges are shown.

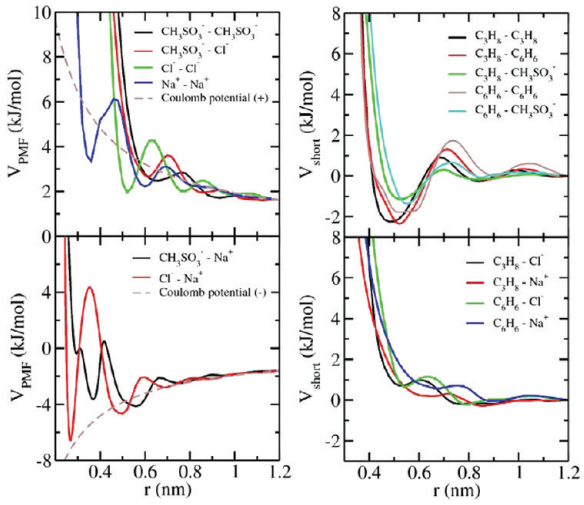


Figure 8. CG effective potentials obtained from PMF calculations: the left panel shows the $V_{PMF}(r)$ between ion pairs (compared with analytical Coulomb potentials), and the right panel shows the $V_{short}(r)$ between molecules/ion pairs without Coulomb interactions.

in water. The left panel in Figure 8 shows PMFs between ion pairs (compared with analytical Coulomb potentials), the right panel shows short-range potentials between molecules/ion pairs where Coulomb interactions are not involved. In this work, the obtained effective potentials, $V_{PMF}(r)$, are used to describe intermolecular interactions between CG beads, as well as for intramolecular interactions between beads that are separated by more than three CG bonds along the polymer chain. The nonbonded bead−bead pair potentials in Figure 8 include not only the effective, direct bead−bead interactions but also any changes in bead−solvent and solvent−solvent interactions as the two beads approach each other. As the beads perturb the local solvent structure in a way that may vary with the distance between them, the effective pair potentials contain solvation (or structural) contributions that give rise to the typical oscillations of the potentials at short-range. The effective interaction between oppositely charged beads (e.g., Na^+ with bead C or Na^+ with Cl^-) at contact distance corresponds to an energy minimum which is typically a factor 2 up to 3 times deeper than the effective (hydrophobic) interaction between the noncharged beads (A−A, B−B, or A−B) of the PSS chain.

We note that the short-range potentials involving the B bead have been obtained using benzene as a representative molecule, which, however, is electrically neutral unlike the phenyl unit of PSS, which carries a partial electronic charge of −0.505e (Table 1). The short-range potentials involving the C bead have in turn been obtained using methylsulfonate as a representative molecule, which carries a −1.0e charge, which compares to a −0.495e partial charge on the sulfonate group of PSS. While the coarse grained B and C beads both carry partial charges identical to those of the corresponding chemical groups of the polymer (giving rise to correct long-range electrostatic interactions), differences in the hydration structure of the small molecules and the chain fragments may give rise to deviations in the effective short-range interactions.

It is straightforward to extend the CG procedure presented here to PSS systems with varying degree of sulfonation. By virtue of the fact that the PMF calculations were performed between small molecules or ions instead of polymer segments, the development of CG potentials for partially sulfonated PS chains only requires the validation of the CG bonded part. In the Supporting Information, we compare the CG bonded potentials obtained from vacuum sampling of isolated atomistic chain of PSS, alternating styrenesulfonate and styrene groups, and PS respectively.

4.3. Comparison of Atomistic and CG Conformations.

As described in section 2.2, our CG bonded potentials are developed based on the random walk sampling of an isolated PSS atomistic chain in vacuum instead of that of PSS chain conformations in solution. Therefore, it is necessary to know how well the above CG potentials represent the atomistically sampled local conformations of the polyelectrolyte chain in aqueous solution. Our final CG model combines the bonded and nonbonded potentials discussed in the previous sections. Nonbonded interactions between beads on different chains and beads separated by more than three coarse grained bonds along the chain are described with the potentials summarized in Figure 8. Figure 9 shows the comparison of angle and dihedral

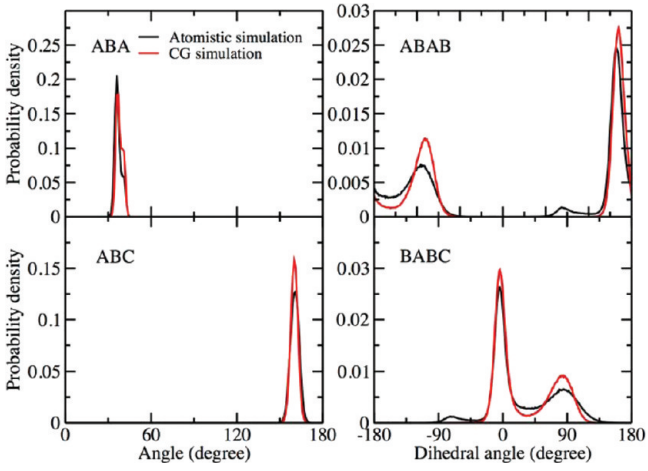


Figure 9. Distributions of selected CG degrees of freedom from atomistic (black curves) and CG (red curves). All figures shown here are calculations of a single isotactic PSS chain (DP = 25) with its counterions in water (298 K).

dx.doi.org/10.1021/ma202490h | *Macromolecules* 2012, 45, 2551−2561

distributions of an isotactic PSS chain in water with Na^+ counterions from atomistic and CG simulations, respectively. Bond distributions are always in perfect agreement and therefore not shown here. The simulation results of syndiotactic and atactic PSS solutions are reported in the Supporting Information. The agreement between the CG and atomistically sampled distributions is good; all major peaks observed in atomistic simulations are also shown in the CG simulations. Although some discrepancies can be observed in the dihedral distributions, the overall chain conformations are accurately reproduced as will be shown below. The BAB angle distributions (shown in the Supporting Information) of the CG atactic and isotactic systems show peak heights that deviate from the atomistic reference distributions. Introduction of a special 1−5 interaction results in better agreement (see Supporting Information).

Another important way to validate the CG model is to check to which extent the assumption of uncorrelated intramolecular degrees of freedom is realistic, and whether the CG model can preserve the correlations found in the atomistic sampling. To do this, correlations between two subsequent backbone dihedral angles were calculated and compared with the atomistic sampling in Figure 10. The comparison shows that

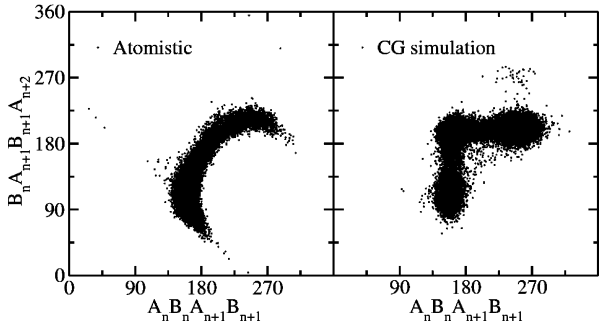


Figure 10. Conformation space of two subsequent CG dihedral angles along the backbone of an isotactic PSS chain in a system with its counterions in aqueous solution (298 K). Shown are results from atomistic and CG simulations.

the conformation space sampled by the atomistic and CG chains is quite similar, except for the regions around (160°, 200°). Most importantly, however, the CG model does not sample the region (270°, 90°) forbidden by the atomistic simulations. Hence, CG model reproduces the local correlations between adjacent torsional degrees of freedom along the PSS backbone in satisfactory agreement with the parent atomistic model.

The PSS chain conformations in CG and atomistic solutions can be compared by looking at $\langle R^2(n)\rangle$, the mean square distance between two monomers separated by n carbon−carbon bonds (two per monomer) along the backbone. To this end, the atomistic and CG simulation trajectories were analyzed using the mapping points of the A and B beads. Figure 11 shows $\langle R^2(n)\rangle$ of a single isotactic, syndiotactic and atactic PSS chain (DP = 25) in water. It can be seen that our CG model reproduces the mean square distance between internal monomers on chains with different tacticities in very good agreement with the atomistic model. In particular, the differences in $\langle R^2(n)\rangle$ for chains with different tacticities suggest that the stiffness of the isotactic, syndiotactic, and atactic chains is well reproduced in the CG model.

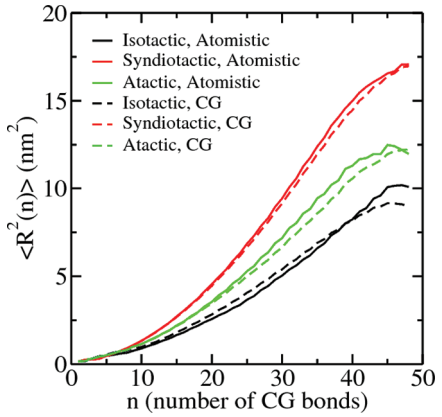


Figure 11. $\langle R^2(n)\rangle$, the mean square distance between two monomers separated by n bonds (two per monomer) along the backbone of a single isotactic, syndiotactic, and atactic PSS chain with DP = 25 monomers in salt free solution (298 K).

4.4. Counterion Distributions in Salt Free Solution. Primitive models for polyelectrolytes replace the aqueous solvent by a dielectric medium and introduce a constant dielectric permittivity in the description of electrostatic interactions. The resulting, attenuated Coulomb interaction is assumed to provide a realistic description independent of the separation distance between the charges. Hydration (or structural) forces, which start playing a role at the length scale of a few solvent diameters, are ignored in primitive models but accounted for in this work in the short-range part of the nonbonded interaction potential. Despite this sophistication, the *representability* and *transferability* of the new model needs to be investigated. Here, we investigate the counterion distribution around the PSS chain. Figure 12 shows that this quantity is not represented correctly by direct comparison with the explicit solvent atomistic model. The primitive CG model with $\varepsilon_r = 72$ does not reproduce the local structural features of the electrolyte in the atomistic explicit solvent system and shows an overall underprediction of the local counterion density. Because of the high negative charge density of the polyelectrolyte chain, the dielectric properties of its hydration water differ from bulk water as well as water molecules involved in mediating ionic interactions at the pair level. In previous, alternative developments of CG implicit solvent models, the representation of counterion distributions around the polyelectrolyte has been obtained with coarse graining procedures that iteratively improve a set of effective potentials until counterion distribution functions obtained from detailed atomistic simulations of polyelectrolyte solutions are reproduced.[46,47] Here, we follow a different route and investigate if representative and transferable potentials can be obtained by means of including a concentration dependent dielectric permittivity in the electrostatic pair forces as was introduced earlier by Hess et al.[31] Figure 12 compares the RDFs between the centers of mass of CG bead A, bead B, bead C, and Na^+ calculated from atomistic and CG simulations, respectively. The CG model, which uses a Na^+-chain interaction potential based on pair PMFs obtained at infinite dilution of ions (eqs 6−8) and a dielectric constant of 72, reproduces the positions of the peaks in the RDF curve, but underestimates the heights of the peaks. Because of the strong electrostatic interactions between the polyelectrolyte charges and its counterions, the local concentration of Na^+ close to PSS chain is much higher than at

dx.doi.org/10.1021/ma202490h | *Macromolecules* 2012, 45, 2551−2561

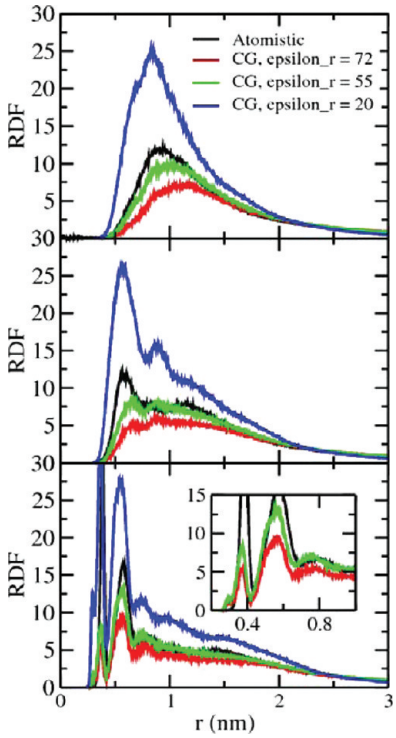


Figure 12. Comparison of RDFs between the center of mass of CG bead A (top panel), bead B (middle panel), bead C (lower panel), and Na^+ obtained from atomistic simulation, CG simulation with ε_r = 72, CG simulation with ε_r = 55, and CG simulation with ε_r = 20.

infinite dilution of ions where the pair potential was developed. This large, local increase of charge concentration leads to significant electrostriction of water, a resulting decrease of the local dielectric permittivity and increase of the electrostatic forces. To estimate the reduction of the dielectric permittivity, we evaluated the local concentration of Na^+ ions around a PSS chain by counting the total number of Na^+ ions in the first and second peaks of atomistic RDF between bead C and Na^+ and dividing it by the volume occupied by these Na^+ ions. In this case, the concentration is about 1 *m*. The resulting dielectric permittivity (ε_r = 55) was obtained by calculating the fluctuations of the total solvent dipole moment[45] in atomistic simulations of a 1 *m* of sodium *p*-toluene sulfonate solution. CG simulations were performed with a dielectric permittivity of 55 and the resulting RDF between different CG beads and Na^+ ions are shown in Figure 12. It shows that by using a concentration dependent relative dielectric permittivity, the CG RDF curves are substantially improved. In particular, the second peak and the long-range tail of the RDF curve between bead C and Na^+ agree very well with the atomistic curves. However, the improvement in the first peaks of all curves is still limited, which may be owing to limitations of the short-range potentials (see section 4.2.2). To see if further improvement could be achieved, we performed CG simulations with even smaller values of relative dielectric permittivity. The bottom graph in Figure 12 shows the RDF between bead C and Na^+ ions with ε_r = 20. It can be seen that with ε_r = 20, the height of the first peak is reproduced. However, the RDF of the coarse grained system is overstructured everywhere else, and moreover shows a shoulder at small distance before the first peak in the atomistic RDF. The A−Na^+ (Figure 12, top) and B−Na^+ (Figure 12, middle) RDFs obtained with ε_r = 20 are also severely overstructured. This leads us to the conclusion that the physically motivated ε_r = 55 indeed gives a very good representation of the screened electrostatics of the polyelectrolyte/counterion system.

The approach followed here provides a good representation of the counterion distribution at all distances except direct ion-polyelectrolyte contact. Although perfect agreement with atomistic simulation data has not been reached, the use of a concentration dependent dielectric constant bears a significant advantage, since it offers a route to ensure transferability of the effective pair potential to systems with different electrostatic conditions (*e.g.*, added salt) as was illustrated in our previous work on simple electrolyte solutions.[32] The comparison with atomistic simulation data in Figure 12 clearly demonstrates that the polyelectrolyte chain-counterion interactions obtained from the primitive CG model with ε_r = 72 are significantly too weak.

4.5. Effective Charges. In polyelectrolyte solutions, condensation of oppositely charged counterions on the polyelectrolyte chain can greatly affect the conformations of the chains. To describe the local distribution of Na^+ ions along the PSS chain, effective charges on beads of the PSS chain were calculated.[24] To this end, we calculated the distributions of distances between each monomer and the counterions:

$$n_q(r, j) = \langle \sum_{i \in C_j} \upsilon_i \delta(r - d_i(j)) \rangle \tag{10}$$

Here, $n_q(r,j)$ is the canonical average (over the simulation trajectory) of ion charge located at distance r from the charged monomer j. For each simulation configuration the counterions are attributed to their respective closest monomer j; C_j denotes the set of all counterions i to which monomer j is the closest monomer of the chain; ν_i is the charge on counterion i; $d_i(j)$ is the distance between the counterion i and its closest charged monomer j; and $\delta(x)$ is the Dirac delta function.

The local effective charge is then defined as

$$q_{eff}(r, j) = \nu(j) + P(r, j) \tag{11}$$

where ν_j is the charge on monomer j, and $P(r,j)$ is the local ion charge contained in the interval $[0, r]$ by integrating $n_q(r,j)$ from zero to r:

$$P(r, j) = \int_0^r \mathrm{d}r' n_q(r', j) \tag{12}$$

In our systems, due to the fact that CG bead B and C both carry charges, effective charges were calculated relative to beads B and C. Figure 13 shows the effective charges on bead B and C along the contour length of the PSS chain (DP=25) with ε_r = 55. The effects of ε_r values on the results of effective charges will be discussed later. For the effective charges on bead B, the cutoff radius for the integration in eq 12 was chosen to be the distance corresponding to the minimum between the first and second peak in the B - Na^+ RDF (0.76 nm); while for the effective charges on bead C, the minimum between the first and second, and between the second and third peak of C−Na^+ RDF curve were chosen as the cutoff distances (0.42 and 0.66 nm), respectively. In agreement with the observation of Limbach et al.[24] on a generic model of polyelectrolyte solution, the choice of the cutoff radius does not affect the qualitative form of the effective charge curves. The effective charges on beads C and B, obtained from CG simulations, are in very good agreement with the corresponding data from the detailed atomistic simulations for cutoff radii of 0.66 and 0.76 nm, respectively.

dx.doi.org/10.1021/ma202490h | *Macromolecules* 2012, 45, 2551−2561

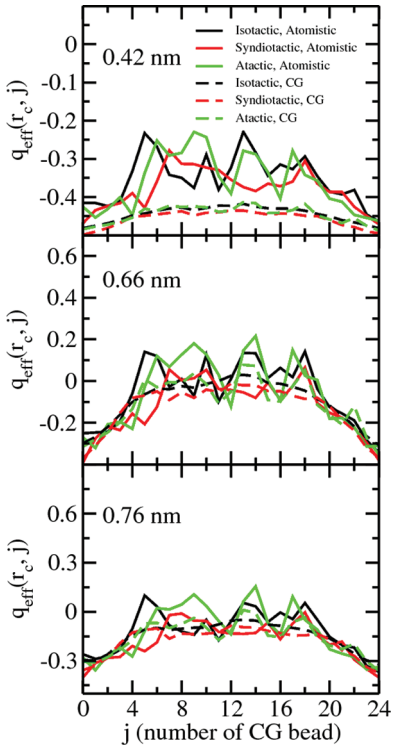


Figure 13. Effective charges on bead C (top and middle panel with cutoff radii 0.42 and 0.66 nm, respectively) and bead B (lower panel, cutoff radius 0.76 nm) of PSS chains (DP = 25) in water obtained from simulations (298 K) with ε_r = 55.

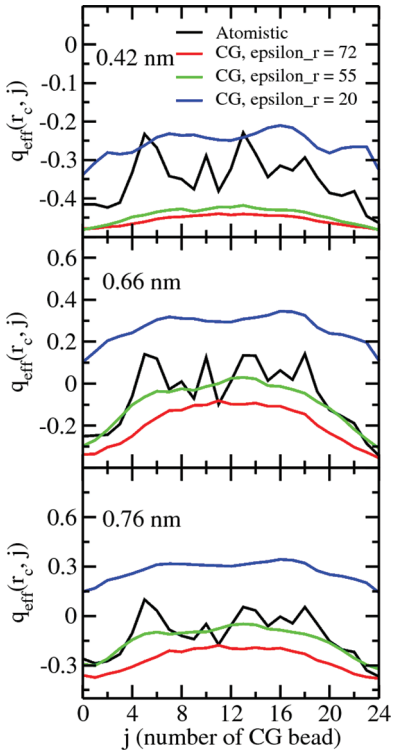


Figure 14. Effective charges of the isotactic PSS chain (DP = 25) obtained from atomistic simulations and CG simulations (298 K) with relative dielectric permittivities of 72, 55, and 20. The data in the top and middle panels correspond to the effective charge on bead C, the data in the lower panel corresponds to the effective charge on bead B.

Only for the short cutoff radius of 0.42 nm (bead C), the effective charge is overpredicted which is due to the discrepancy in the local electrolyte structure (see Figure 12). Inhomogeneity of effective charges along the contour length is observed both in atomistic and CG simulations, with beads in the central part of the backbone being stronger screened than those at the chain ends. This is due to the higher charge density of the central part of the polyelectrolyte backbone. Atomistic effective charge curves show rather big fluctuations due to the poor statistics, and no obvious differences can be identified among PSS chain with different tacticities. Comparing with atomistic simulation results, CG simulation curves are much smoother, except that the atactic chain exhibits relatively larger fluctuations. These larger fluctuations may derive from the inhomogeneous distributions of meso and racemic diads along the atactic PSS chain.

In Figure 14, it is again shown that the agreement of the effective charge is strongly dependent on the value of the concentration dependent dielectric permittivity. The different lines represent the effective charges on beads of the isotactic PSS chain obtained from atomistic simulations and CG simulations with relative dielectric permittivity of 72, 55, and 20 respectively. The dielectric permittivity of 55 gives the best agreement (except for bead C at very short cutoff radius, due to the deviation of the local structure as discussed above). Note that the difference between ε_r = 20 and ε_r = 55 and larger is qualitative. At ε_r = 20 the system is overcharged and the absolute sign of the charge is inverted, i.e. the beads appears to be positively charged instead of negatively.

4.6. PSS Conformations in Solution with Added Salt. In salt free solution, the PSS chain is expanded due to electrostatic repulsion among negatively charged groups on different monomers. On the other hand, counterions prefer to condense on the chain thereby reducing its net charge and consequently facilitating chain contraction. The presence of small molecular monovalent salts has long been known to enhance this condenstation effect.[48,49] Therefore, by adding salt (for example NaCl) to the polyelectrolyte solution, we expect a shrinkage of the polyelectrolyte chain dimension.

We characterize the polyelectrolyte conformation by its radius of gyration (R_g) and compare R_g of the PSS chains calculated from atomistic and CG simulations. In the CG simulations, the relative dielectric permittivity ε_r was chosen to be 72, 57.50, and 50.70 for systems with NaCl concentration of 0, 1, and 2 *m*, respectively. These values were obtained by calculating the fluctuations of the total solvent dipole moment of NaCl solutions at corresponding concentrations. Here, in order to identify the effects of added salt only, the above ε_r values were not further adjusted according to the local concentrations of Na^+ ions around the PSS chain in each atomistic system. In fact, we also investigated the effects of changing ε_r on the change of R_g of the isotactic PSS chain in salt free solution. We found that by decreasing ε_r, R_g of the isotactic PSS chain slightly decreases (shown in Figure 15), in agreement with the observations in the RDF curves in Figure 12.

The radius of gyration of PSS chains with different tacticities obtained from both atomistic and CG simulations are shown in Figure 15. The atomistic and CG simulations both show the order R_g (syndiotactic) > R_g (atactic) > R_g (isotactic) in solutions with or without added salt. With the addition of salt, R_g of PSS chains with different tacticities decreases, showing the trend of the polymer chain contraction due to salt-induced

dx.doi.org/10.1021/ma202490h | *Macromolecules* 2012, 45, 2551–2561

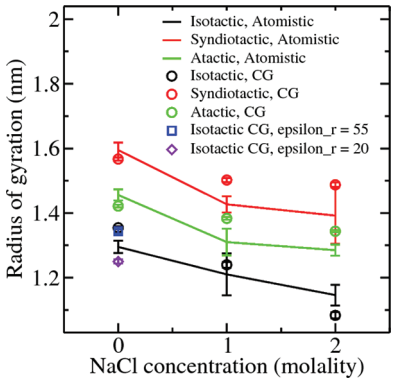


Figure 15. Effect of added salt on the radius of gyration (R_g) of the polyelectrolyte chain (DP = 25) with different tacticities solvated in water with its counterions (298 K).

screening of the electrostatic interactions. As mentioned above, in the systems with added NaCl, salt concentration dependent dielectric permittivity parameters were used to take into account different multibody effects in polyelectrolyte solutions with different salt concentrations. Without having to derive a new model at each salt concentration, our CG model can reasonably reproduce R_g values of PSS chains with different tacticities over a range of salt concentrations, showing the transferability of the CG model upon salt conditions.

4.7. Chemical Accuracy of the CG Model: Counterion Distributions around Isotactic and Syndiotactic NaPSS Chains (DP = 200). The PSS coarse grained model has been developed with an eye to chemical and thermodynamic transferability. The model allows for variation of the chain length, tacticity, degree of sulfonation and electrolyte concentration. A detailed study of how polyelectrolyte properties depend on such variations goes beyond the scope of the present work. Here, we examine one aspect of the chemical accuracy of the CG model, which is not represented by generic polyelectrolyte models. Figure 16 (upper panel) shows the effective charges of the C beads (within 0.66 nm radius) of isotactic and syndiotactic PSS chains with DP=200 in salt-free and 0.1 *m* salt (NaCl) solutions. In agreement with the data for shorter chains in Figure 13, the central beads of the chain are always screened more strongly by the counterions than the outer beads. In 0.1 *m* NaCl solution, the effective charges of all C beads on the isotactic chain are further screened, leading to an almost complete charge neutralization of these beads. Interestingly, the effective charges of inner C beads of the syndiotactic chain are hardly affected by salt, while the outer beads' effective charges increase (becomes more strongly negative)—rather than decrease − in 0.1 *m* salt solution. The Cl^- co-ions do not play a role in the observed effect, as they were found to always stay far away from the polyelectrolyte chain. In moving from salt free conditions to 0.1 *m* NaCl, the Na^+ counterions however redistribute around the polyelectrolyte chain in a decisively different manner for the two stereoregular polyelectrolytes. Figure 16 (lower panel) shows the Na^+ ion concentration vicinal to C beads of the isotactic and syndiotactic PSS chains in salt free solution and in 0.1 *m* NaCl. For the isotactic system, the Na^+ ion concentration vicinal to C beads increases monotonically relative to the salt free system over the entire distance range. This is in agreement with the observed charge screening of the C beads in the upper panel of Figure 16. We however observe that the local Na^+ ion

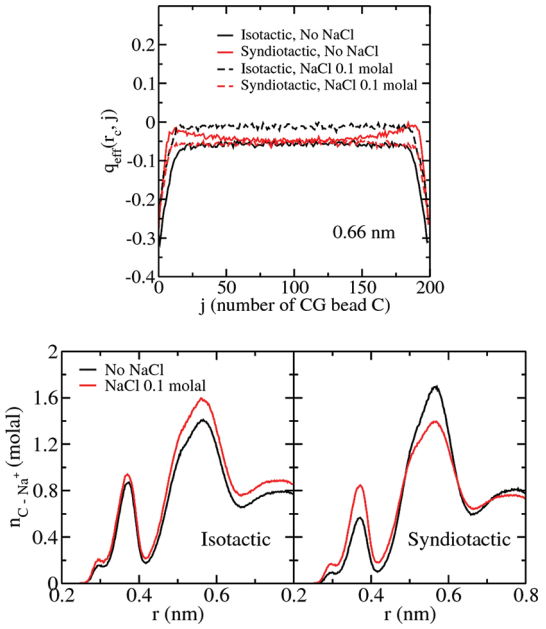


Figure 16. Effective charges within cutoff radius of 0.66 nm on the C bead of PSS (DP = 200) in salt-free and 0.1 *m* NaCl salt solution (upper panel). Comparison of the local number density of Na^+ ions at the distance *r* from beads C on isotactic and syndiotactic polyelectrolyte chains (lower panel).

concentration around C beads on the syndiotactic chain increases at small distances (<0.47 nm) but decreases at larger distances (>0.50 nm) with the addition of NaCl. Thus, upon increasing salt, the effective negative charge of the C bead increases within the range of 0.66 nm, despite stronger *direct* charge screening through Na^+ contact pair interactions (<0.47 nm) with the C beads on the syndiotactic chain. It is furthermore noteworthy that comparison of the local Na^+ ion concentration for isotactic and syndiotactic PSS in salt free solution clearly indicates that the counterions around syndiotactic PSS have stronger preference to accumulate in the second peak (~0.57 nm) while a larger fraction of the counterions around the isotactic chain accumulate in the first peak and form direct contact interactions with the C beads. This behavior is likely caused by a larger charge density of the isotactic chain. The BAB angle of the isotactic chain is smaller than the corresponding angle of the syndiotactic chain (see Figures S5 and S6 in the Supporting Information), which causes smaller distances among adjacent C beads in the isotactic chain and a correspondingly larger charge density. Consequently, both the chemically accurate representation of the chain conformations and the locally specific and transferable behavior of the ion−ion interaction are crucial to observe such an effect in the CG model.

5. CONCLUSIONS

In conclusion, we have developed a chemically and thermodynamically transferable coarse grained PSS model allowing for systematic variation of chain length, tacticity, electrolyte concentration and degree of sulfonation with high chemical accuracy and a close link to the parent atomistic model. The model features an implicit solvent (water) representation, while both the polyelectrolyte chain and its counterions are modeled explicitly. The short-range chemical forces related to ionic solvation are taken into account and

dx.doi.org/10.1021/ma202490h | *Macromolecules* 2012, 45, 2551−2561

specific-ion phenomena can therefore be investigated. CG bonded and nonbonded potentials are developed separately, where bonded potentials are obtained from atomistic sampling of random walks of a single polyelectrolyte chain in vacuum and nonbonded potentials are developed from the calculation of pair PMFs between two small molecules or ions in water representing corresponding CG beads. Comparison of distributions of CG bonded degrees of freedom and internal distances along the polymer chain show that the resulting CG model reproduces the atomistically sampled local conformation of a PSS chain (with 25 monomers) in solution with different tacticities. Our CG model also reproduces the positions of the peaks in the atomistic radial distribution function (RDF) curve between PSS chain beads and Na^+, although the heights of the peaks are underestimated. Furthermore, by adjusting the dielectric permittivity based on the local concentration of counterions around the polyelectrolyte chain, the CG RDF curve is substantially improved and reproduces the counterion structure around the chain (except for very local effects) very well. This observation shows that with primitive polyelectrolyte model (solvent dielectric permittivity $\varepsilon_r = 72$), the interactions between counterions and the polyelectrolyte chain calculated by CG models are too weak compared with atomistic models. Effects of adding salt on the change of radius of gyration of PSS chains with different tacticities were also studied. The agreement of CG model and atomistic simulations on R_g values show the transferability of our CG model upon salt conditions, even without having to rederive new potentials at each different salt concentration.

■ ASSOCIATED CONTENT

Ⓢ Supporting Information

Coarse graining models, polyelectrolyte solution simulations, and partially sulfonated polystyrene CG models. This material is available free of charge via the Internet at http://pubs.acs.org.

■ AUTHOR INFORMATION

Corresponding Author

*E-mail: vandervegt@csi.tu-darmstadt.de.

Notes

The authors declare no competing financial interest.

■ ACKNOWLEDGMENTS

We would like to thank Dominik Fritz and Kurt Kremer for many helpful discussions. This project has been carried out as part of the priority program SPP 1420 by the German Science Foundation. C.P. gratefully acknowledges financial support by the German Science Foundation within the Emmy Noether program (grant PE 1625/1).

■ REFERENCES

(1) Limbach, H. J.; Holm, C. *J. Phys. Chem. B* **2003**, *107*, 8041.
(2) Carrillo, J. M. Y.; Dobrynin, A. V. *J.Phys.Chem. B* **2010**, *114*, 9391.
(3) Reith, D.; Mueller, B.; Mueller-Plathe, F.; Wiegand, S. *J. Chem. Phys.* **2002**, *116*, 9100.
(4) Essafi, W.; Lafuma, F.; Baigl, D.; Williams, C. E. *Europhys. Lett.* **2005**, *71*, 938.
(5) Vishnyakov, A.; Neimark, A. V. *J. Chem. Phys.* **2008**, *128*, 164902.
(6) Kalyuzhnyi, Y. V.; Vlachy, V.; Cummings, P. T. *Chem. Phys. Lett.* **2007**, *438*, 238.
(7) Stevens, M. J.; Plimpton, S. J. *Eur. Phys. J. B* **1998**, *2*, 341.
(8) Barrat, J. L.; Joanny, J. F. *Adv. Chem. Phys.* **1996**, *94*, 1.
(9) Sedlak, M. *Langmuir* **1999**, *15*, 4045.
(10) Xia, J.; Dubin, P. L.; Edwards, S.; Havel, H. *J. Polym. Sci., Part B: Polym. Phys.* **1995**, *33*, 1117.
(11) Tanahatoe, J. J.; Kuil, M. E. *J. Phys. Chem. B* **1997**, *101*, 9233.
(12) Chisaka, S.; Norisuye, T. *J. Polym. Sci., Part B: Polym. Phys.* **2001**, *39*, 2071.
(13) Pohlmeier, A.; Haber-Pohlmeier, S. *J. Colloid Interface Sci.* **2004**, *273*, 369.
(14) Zhou, K.; Li, J.; Lu, Y.; Zhang, G.; Xie, Z.; Wu, C. *Macromolecules* **2009**, *42*, 7146.
(15) Sedlak, M. *J. Chem. Phys.* **2002**, *116*, 5236.
(16) Sedlak, M. *J. Chem. Phys.* **2005**, *122*, 151102.
(17) Michel, R. C.; Reed, W. F. *Biopolymers* **2000**, *53*, 19.
(18) Smits, R. G.; Kuil, M. E.; Mandel, M. *Macromolecules* **1994**, *27*, 5599.
(19) Ennari, J.; Elomaa, M.; Sundholm, F. *Polymer* **1999**, *40*, 2001.
(20) Lyubartsev, A. P.; Laaksonen, A. *J. Biomol. Struct. Dyn.* **1998**, *16*, 579.
(21) Duca, J. S.; Hopfinger, A. J. *Comput. Theor. Polym. Sci.* **1999**, *9*, 227.
(22) Hoda, N.; Larson, R. G. *Macromolecules* **2009**, *42*, 8851.
(23) Qiao, B. F.; Cerda, J. J.; Holm, C. *Macromolecules* **2011**, *44*, 1707.
(24) Limbach, H. J.; Holm, C. *J. Chem. Phys.* **2001**, *114*, 9674.
(25) Coelfen, H.; Antonietti, M. *Angew. Chem., Int. Ed.* **2005**, *44*, 5576.
(26) Fritz, D.; Harmandaris, V. A.; Kremer, K.; van der Vegt, N. F. A. *Macromolecules* **2009**, *42*, 7579.
(27) Villa, A.; Peter, C.; van der Vegt, N. F. A. *Phys. Chem. Chem. Phys.* **2009**, *11*, 2077.
(28) Harmandaris, V. A.; Adhikari, N. P.; van der Vegt, N. F. A.; Kremer, K. *Macromolecules* **2006**, *39*, 6708.
(29) Harmandaris, V. A.; Reith, D.; van der Vegt, N. F. A.; Kremer, K. *Macromol. Chem. Phys.* **2007**, *208*, 2109.
(30) Hess, B.; Kutzner, C.; van der Spoel, D.; Lindahl, E. *J. Chem. Theory Comput.* **2008**, *4*, 435.
(31) Hess, B.; Holm, C.; van der Vegt, N. F. A. *Phys. Rev. Lett.* **2006**, *96*, 147801.
(32) Shen, J.; Li, C.; van der Vegt, N. F. A.; Peter, C. *J. Chem. Theory Comput.* **2011**, *7*, 1916.
(33) Berendsen, H. J. C.; Grigera, J. R.; Straatsma, T. P. *J. Phys. Chem.* **1987**, *91*, 6269.
(34) Darden, T.; York, D.; Pedersen, L. *J. Chem. Phys.* **1993**, *98*, 10089.
(35) Wick, C. D.; Martin, M. G.; Siepmann, J. I. *J. Phys. Chem. B* **2000**, *104*, 8008.
(36) Martin, M. G.; Siepmann, J. I. *J. Phys. Chem. B* **1999**, *103*, 4508.
(37) Vishnyakov, A.; Neimark, A. *J. Phys. Chem. B* **2000**, *104*, 4471.
(38) Hess, B.; van der Vegt, N. F. A. *Proc. Natl. Acad. Sci. U.S.A.* **2009**, *106*, 13296.
(39) Hess, B.; Bekker, H.; Berendsen, H. J. C.; Fraaije, J. G. E. M. *J. Comput. Chem.* **1997**, *18*, 1463.
(40) Miyamoto, S.; Kollman, P. A. *J. Comput. Chem.* **1992**, *13*, 952.
(41) Berendsen, H. J. C.; Postma, J. P. M.; van Gunsteren, W. F.; DiNola, A.; Haak, J. R. *J. Chem. Phys.* **1984**, *81*, 3684.
(42) Luo, Y.; Roux, B. *J. Phys. Chem. Lett.* **2010**, *1*, 183.
(43) Ruehle, V.; Junghans, C.; Lukyanov, A.; Kremer, K.; Andrienko, D. *J. Chem. Theory Comput.* **2009**, *5*, 3211.
(44) Robinson, R. A.; Stokes, R. H. *Trans. Faraday Soc* **1949**, *45*, 612.
(45) Neumann, M. *Mol. Phys.* **1983**, *50*, 841.
(46) Savelyev, A.; Papoian, G. A. *J. Phys. Chem. B* **2009**, *113*, 7785.
(47) Savelyev, A.; Papoian, G. A. *Proc. Natl. Acad. Sci. U.S.A.* **2010**, *107*, 20340.
(48) Manning, G. S. *J. Chem. Phys.* **1969**, *51*, 924.
(49) Kundagrami, A.; Muthukumar, M. *J. Chem. Phys.* **2008**, *128*, 244901.

Macromolecules

Article

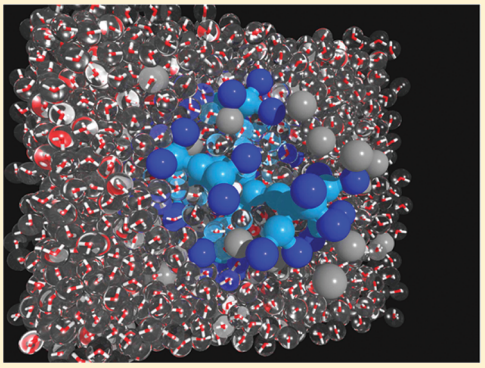
pubs.acs.org/Macromolecules

Explicit vs Implicit Water Simulations of Charged Dendrimers

Sebastian Huißmann,† Christos N. Likos, and Ronald Blaak*

Faculty of Physics, University of Vienna, Boltzmanngasse 5, A-1090 Vienna, Austria

ABSTRACT: Charged dendrimers with terminal or full charge of the nodes, single- or double-spacer, are simulated and a comparison is made between implicit and explicit water results. The main conclusion is that modeling the solvent with a continuum (dielectric constant $\varepsilon_r = 80$) and ignoring its discrete nature results into a surprisingly accurate description of their properties. Sizes, density profiles and spacer dependence are reproduced within 10% at most. The counterion intake is overestimated by the implicit water model because in reality water intrudes all the way to the center and locally expels some counterions. The amount of water absorbed increases rapidly with charging the dendrimer.



1. INTRODUCTION

Dendrimers[1,2] are very versatile macromolecules with a large number of technical and pharmaceutical applications. They are of great technological importance due to their role in for instance gene-delivery experiments,[3] cancer treatment,[4] or their use as contrast agents in biomedical imaging.[5] Dendrimers are also interesting from a fundamental aspect.[6−10] Their compactness and flexibility can be tuned by changing generation number and/or spacer length, which makes them an ideal model system, capable of bridging the gap between flexible polymers and hard spheres.[11]

Advances in synthesis techniques have led to a large variety of dendritic architectures with many different key structural features.[12] Nowadays, the most commonly studied dendrimers are of the poly(amidoamine) (PAMAM) or poly(propyleneimine) (PPI) type. Dendrimers with acidic functional groups, synthesized by Newkome et al., were the first for which large size changes with pH variance have been observed for generation three (G3) dendrimers.[12] The change of the solution's pH value induces dissociation of ions into the solution, thereby charging the remaining molecule, which results in the electrostatic swelling of the latter. In a more systematic study, Young et al. compared dendrimers with acidic, neutral, or basic terminal functionality.[13] They reported a maximum swelling of the hydrodynamic radius of 35% for the carboxylic acid- and amine-terminated dendrimers. However, alcohol-terminated dendrimers displayed no swelling or shrinking at all under pH change. Their results are consistent with the assumption that size variation arises from Coulombic repulsions between the charged monomers. Furthermore, they concluded that the finding of size variation as a function of pH should be general, provided the interior branches of the dendrimers are relatively flexible.[13] The aforementioned discoveries formed the basis for experimental and simulation studies regarding the conformation of charged dendrimers and their possible use as encapsulation agents.

For polyelectrolyte chains and stars, it is well-known that charging them leads to dramatic changes in their size and conformations.[11,14,15] It is therefore surprising that some controversy arose regarding the electrostatic swelling of high-generation dendrimers. Nisato et al. found in small angle neutron scattering (SANS) experiments that the size of a G8 PAMAM dendrimer is independent of charge density and ionic strength.[16] On the contrary, Chen et al. found in their experiments on G6 dendrimers clear evidence for conformational changes and attributed the size invariance found by Nisato et al. to the dense packing of the G8 dendrimer.[17] Moreover, pioneering simulation studies of dendrimers under varying ionic strength predicted a conformational change from dense-core to dense-shell.[18] These contradictory observations led to many conjectures and debates on whether a charge-induced dendrimer swelling is completely absent or only diminished due to the very high steric crowding.[11,16,17,19−24] A recent combined SANS and X-ray scattering study performed by Liu et al. clarified the microscopic behavior of charged polyelectrolyte dendrimers.[25] They provided conclusive evidence of the fact that high-generation PAMAM dendrimers undergo electrostatic swelling and conformational changes toward a denser-shell conformation upon protonation. A MD-simulation study of stiff and flexible dendritic polyelectrolytes not only confirmed their observations, but also showed that the flexibility of the dendrimer is of high importance for the understanding of conformational changes.[26] In line with these results is also the common use of dendrimers in gene-delivery experiments to make high generational PAMAM dendrimers more flexible by hydrolytic removal of some of their branches, which is necessary to maximize transfection efficiency.[3] In recent small-angle neutron scattering experiments,[27] contrast variation was

Received: November 16, 2011
Revised: February 8, 2012
Published: February 22, 2012

ACS Publications © 2012 American Chemical Society

employed to measure the monomer, counterion and water profiles of hydrophilic neutral and charged dendrimers. Once again, the growth of the dendrimer upon charging was confirmed, whereas at the same time the monomers maintain the dense-core configuration, i.e., significant back-folding exists also in the case of charging. Moreover, considerable water intake was found for the neutral dendrimer, which is further enhanced at low pH-values, for which the molecule is charged. The increase in size and water intake upon charging was also found in the simulation studies of Maiti et al.[28] and of Wu.[29]

The size of the dendrimers being on the order of a few nanometers, is much smaller than that of a typical colloidal particle. The dendrimer's building blocks, the monomeric units consisting of, e.g., hydrocarbons, are of the same order of magnitude in size as water molecules. This makes a theoretical/computational treatment very time-consuming, since a large number of monomeric units and water molecules are involved. So what is required here, is an efficient computational technique that takes into account both the charge and the screening by the solvent—which is, in this case, water. It is therefore tempting to follow an implicit solvent approach. However, the granular nature of the solvent cannot always be neglected, since the formation of hydrogen bonds, the electrostatic interactions and hydrophobic attractions between nonpolar molecules might result in nontrivial effects. For example, Dzubiella et al. pointed out that taking into account the water molecules explicitly can cause the effect known as like-charge attractions between colloids.[30] Moreover, the very idea of screening via an effective dielectric constant ε requires averaging over *many* water molecules intervening between charges, which is not a priori guaranteed to be accurate at the microscopic scale.[31]

Previous MD-simulations have focused on charged PAMAM dendrimers in either implicitly or explicitly simulated water.[22,28,29,32−37] However, a direct comparison of explicit vs implicit water simulation of charged dendrimers at different pH conditions is lacking up to now. In this work, we therefore examine the effects explicit/implicit water has on the conformational properties of a G4 dendrimer. The focus lies on the question of whether the screening character of water can be well approximated by an implicit solvent. We employ MD-simulations with the SPC/E model for water at ambient conditions and compare the results with the simulations of dendrimers in which the water is treated as an implicit continuum by means of the appropriate relative permittivity for the electrostatic interactions. Apart from a minor discrepancy of the counterion density in the core region of the dendrimer that can be attributed to steric interactions, we find that the static properties related to the conformational characterization of the dendrimers, can be accurately described by the implicit solvent approach.

The rest of this paper is organized as follows: The simulation model is described in section 2. We present our results in section 3 for dendrimers with and without spacer monomers between their branching nodes as a means of tuning their flexibility. A direct comparison shows that for charged dendrimers essentially the same behavior can be seen for implicit and explicit water. We summarize and draw our conclusions in section 4.

2. SIMULATION MODEL

We examine the conformations of 4th generation (G4) dendrimers and number of spacer segments P between the branching points, in solvents of varying pH by means of monomer-resolved MD simulations.[38,39] A bead−spring model is used for the dendrimers, where the monomers are modeled as beads in a united-atom approximation. The model dendrimers used in this work commence with two central beads that form the core, the so-called generation 0. By repeatedly linking two beads at each site, a new generation is formed. A dendrimer constructed this way has thus 2^{g+1} monomers or nodes per generation g, and since there are no spacer monomers between the nodes present this corresponds to having $P = 1$ spacer segments. When one spacer monomer is inserted between each of the nodes of the dendrimer, the number of spacer segments is $P = 2$. A G4-dendrimer has therefore 32 terminal monomers, a total of 62 nodes, and in the case of a dendrimer with $P = 2$ spacer segments, a total number of 123 monomers is present.

Dendrimers can be synthesized in such a fashion that the nodes become ionized at low pH values of the solution and remain neutral at high pH.[11] Furthermore, when monomeric units like primary and secondary amines are incorporated, a dendrimer can be obtained, such that only its terminal beads are charged at intermediate pH values.[40] A change in the pH value of the solution can therefore be modeled by charging the dendrimers in different fashions. Here, we restrict ourselves to terminally charged dendrimers, $Z = 32$, and fully charged dendrimers, $Z = 62$, with either $P = 1$ or $P = 2$ spacer segments.

We assume good solvent conditions for the monomers of the dendrimer. To this end, we employ a model of intermonomer interactions, in which each pair of beads at a relative distance r interacts via the purely repulsive, truncated and shifted Lennard-Jones[41] potential:

$$V_{\mathrm{LJ}}(r) = \begin{cases} 4\varepsilon\left[\left(\frac{\sigma}{r}\right)^{12} - \left(\frac{\sigma}{r}\right)^{6} + \frac{1}{4}\right], & r \le 2^{1/6}\sigma \\ 0, & r > 2^{1/6}\sigma \end{cases} \quad (1)$$

where the interaction strength ε and the diameter σ fix the units of energy and length, respectively. A value of $\sigma = 4$ Å has been chosen for the monomer diameter and $\varepsilon = 0.19$ kcal/mol for the interaction parameter, which are reasonable values for hydrocarbons in a united-atom approximation.[42,43]

The connectivity in the dendrimer, which is typically maintained by covalent chemical bonds, can be described by the so-called finite extensible nonlinear elastic (FENE) potential:[44]

$$V_{\mathrm{FENE}}(r) = \begin{cases} -U_0\left(\frac{R_0}{\sigma}\right)^2 \ln\left[1 - \left(\frac{r}{R_0}\right)^2\right], & r \le R_0 \\ \infty, & r > R_0 \end{cases} \quad (2)$$

Here, U_0 is a measure for the spring constant and R_0 is the maximal bond-length between two monomers, for which we have chosen $U_0 = 15\varepsilon$ and $R_0 = 1.5\sigma$, respectively.

The effective solvent simulations were performed using the Ewald summation method for the long-range Coulomb interactions between charged particles, given by

$$V_{\mathrm{Coulomb}}(r) = \frac{e^2}{\varepsilon_{\mathrm{r}}}\frac{Z_i Z_j}{r} \quad (3)$$

with Z_i and Z_j the charge numbers, e the elementary charge, and ε_{r} the relative permittivity. The monomers are chosen to be either neutral or carrying positive monovalent charges. Overall charge neutrality is guaranteed by adding oppositely charged

dx.doi.org/10.1021/ma202520d | Macromolecules 2012, 45, 2562−2569

counterions to the solution, which otherwise have the same steric interactions as neutral monomers. For the solvent, water at room temperature (T = 293 K) is chosen. Only the screening of the electrostatic interactions caused by water is modeled in the implicit solvent simulations, by imposing ε_r = 80.

A large number of effective models have been used for the simulation of liquid water. The computational cost rises with the number of charged sites that is included in the various models. Moreover, a distinction can be made between rigid[45,46] and flexible[47,48] models, where the OH-bond interaction in the latter case is described by a harmonic or anharmonic potential. A frequently used three-site model is the extended simple point charge (SPC/E) model.[48] This model is easy to implement; it consists of only three sites, and has therefore a relatively low computational cost as compared to other more complex ones. Nevertheless, it reproduces many of the properties of liquid water at ambient conditions with reasonable accuracy. For example, the dielectric constant is found to be 75 ± 7 for SPC/E under ambient conditions.[49]

A single SPC/E water molecule is represented by a spherical particle with three charged sites, one oxygen (O) atom in the center and two hydrogen (H) atoms. The H atoms are bound to the O-site by an anharmonic interaction with equilibrium length l_0 and interaction constants k_l and k_{cub}. The OH-bond potential is given by

$$V_{OH}(l) = k_l(l - l_0)^2 + k_l k_{cub}(l - l_0)^3 \tag{4}$$

where l is the distance between an O and either of the H atoms of the same molecule. The H−O−H angle θ is constraint via a harmonic angle potential,

$$V_{HOH}(\theta) = k_\theta(\theta - \theta_0)^2 \tag{5}$$

where θ_0 is the equilibrium bond angle and spring constant k_θ.

The non-Coulombic intermolecular interaction between SPC/E water molecules consists only of a Lennard-Jones interaction between two O-sites at a relative distance r,

$$V_{OO}(r) = \frac{A}{r^{12}} - \frac{B}{r^6} \tag{6}$$

The dipolar nature of the water molecules is modeled with partial charges for the O and H atoms, given by q_O and q_H, respectively. Coulomb interactions between charged sites are calculated between distinct water molecules only. All Coulomb interactions in the explicit water simulations are modeled via eq 3 with ε_r = 80. For completeness, the full parameter set of the SPC/E model by Ferguson[49] is given in Table 1.

From a comparison of eq 6 with the form of the Lennard-Jones potential,

$$V_{LJ}(r) = 4\varepsilon\left[\left(\frac{\sigma}{r}\right)^{12} - \left(\frac{\sigma}{r}\right)^{6}\right] \tag{7}$$

one obtains a diameter σ_w = 3.183 Å and an interaction strength ε_w = 0.166 kcal/mol for the water molecule. All neutral and charged particles interact with the O atom of a water molecule via the Lennard-Jones potential eq 7. The corresponding parameters are calculated from the Lorentz−Berthelot mixing rules,

$$\varepsilon_{\alpha\beta} = \sqrt{\varepsilon_\alpha \varepsilon_\beta} \tag{8}$$

for the interaction strength, and

$$\sigma_{\alpha\beta} = 0.5(\sigma_\alpha + \sigma_\beta) \tag{9}$$

for the molecular diameter, where α and β correspond to any type of particle in the system, being a neutral or charged monomers, counterion or the O-site of a SPC/E water molecule.

A word of caution should be mentioned regarding the modeling of the monomer−monomer interactions in the implicit- and explicit water simulations. In our work, we have taken *the same* monomer−monomer interaction potential for both cases, namely the truncated-and-shifted (purely repulsive) Lennard-Jones potential of eq 1. Strictly speaking, this is not correct. The purely repulsive monomer−monomer potential employed in the implicit water simulation is itself an effective interaction with results from the combined effect of the bare monomer−monomer potential $\tilde{v}_{mm}(r)$ and the water molecules, which have been traced out. The bare potential $\tilde{v}_{mm}(r)$, which is not purely repulsive but rather of the Lennard-Jones type, should be the one to be employed in the explicit water simulations. However, we do not know which precise form of this potential would give rise, upon tracing out the solvent, to the truncated-and-shifted Lennard-Jones potential which is commonly employed in almost all implicit-water simulations. We argue here that the precise form of $\tilde{v}_{mm}(r)$ should not be important, though. As far as the charged monomers are concerned, the unscreened (ε_r = 1) Coulomb interaction is strongly repulsive and thus renders the weak, short-range attractions between monomers irrelevant. Concerning the neutral monomers, which are found in the interior of terminally charged dendrimers, we argue that their strong hydrophilicity will result into substantial water intake, as it has been confirmed both by previous simulations[28,29] and in experiments.[27] Under these conditions, and given the tendency of water molecules to form clusters and connected groups, any two neutral monomers will almost always be found to be separated by intervening water molecules, so that the attractions present in $\tilde{v}_{mm}(r)$ will not be relevant. Accordingly, we adopt the simplest possible approach by assuming pure steric repulsions between monomers, modeled in an identical way in both the implicit and the explicit water approaches. This is also similar to the approach of Gurtovenko et al.,[35] who performed simulations of charged dendrimers in explicit, nonpolar solvents, employing also a truncated-and-shifted Lennard-Jones interaction between the monomers. A proper, microscopic, and substance-specific treatment of this coarse-graining step is also possible by means of *ab initio* techniques that commence at a quantum-mechanical level and proceed to the derivation of molecular-mechanical (MM) force fields.[50−52] However, this is beyond the scope of our work, which focuses on more generic aspects. Besides, the form of the MM-force is not uniquely determined but it rather depends on the original,

Table 1. Parameter Set[a] for the SPC/E Model Taken from Ferguson et al.[49]

k_l	k_{cub}	l_0	k_θ	θ_0	A	B	q_H	q_O	m_H	m_O	m_M
547.5	−1.65	1.0	49.9	109.5	650 000	625.47	0.413	−0.826	1	16	14

[a]Energies are given in kcal/mol, lengths in Å, angles in radians, masses in u, and the partial charges in electron units. The symbol m_M denotes the monomer mass.

dx.doi.org/10.1021/ma202520d | *Macromolecules* 2012, 45, 2562−2569

quantum-mechanical quantities that should be matched by this field, see ref 50 for details.

For bulk water at room temperature and normal pressure, the nonpolarizable SPC/E model reproduces many of the properties of water with similar accuracy as other very good rigid and more complex models.[46,53] Moreover, simulation studies of polarizable water models have shown that polarization effects are of secondary importance at hydrophobic and other surfaces.[54−56] A temperature of $T = 293$ K has been maintained by applying the Berendsen thermostat[47] to the explicitly simulated solvent only, in order to avoid artifacts such as the hot-solvent/cold-solute problem.[57] For the implicit solvent simulation, the Andersen thermostat[58] has been used. The simulation box was chosen to be a cube with sides $L = 48$ Å and periodic boundary conditions. For the explicit water simulations 3678 water molecules have been used, a choice which corresponds to assuming normal pressure at the imposed water temperature. In the case of the $P = 1$ dendrimers, this is sufficient to guarantee that they do not interact with their own image. For the $P = 2$ dendrimers the same box size is used for computational reasons, but it should be noted that it is now comparable to the maximum extension of the dendrimers. Consequently, these dendrimers are simulated at a non-negligible, finite density. The MD equations of motion were integrated with a time step of $\delta t = 1.25$ fs. Initial configurations have been equilibrated for about $t_{eq} = 400$ ps, which is sufficiently long for the counterions to diffuse into the core of the dendrimer and to reach a steady state for the in- and out-flux. After equilibration, the simulations were run for $t_{run} = 1.25$ ns to obtain good statistics for the measurements. In terms of the natural time unit in the implicit water simulations, $\tau = (m_M\sigma^2/\varepsilon)^{1/2}$, introducing the values $\varepsilon = 0.19$ kcal/mol, $\sigma = 4$ Å, and $m_M = 14$u employed here, $\tau = 1.68$ ps obtains, yielding $\delta t = 7.5 \times 10^{-4}\tau$, and subsequent times $t_{eq} = 240\tau$ for equilibration, as well as $t_{run} = 750\tau$ for measurements.

3. RESULTS

Simulation snapshots of $P = 1$ dendrimers with charged endgroups, $Z = 32$, and with all nodes charged, $Z = 62$, are shown in Figure 1 for explicitly and implicitly simulated water. In all cases, the charged dendrimers have a more open conformation as compared to a neutral dendrimer that looks rather compact (not shown). This is mainly due to the Coulombic interaction between the charged monomers. At the same time, counterions are absorbed by the dendrimers, thereby screening the electrostatic repulsion to some extent. Although the fractions of neutral and charged particles are almost the same, the water molecules are found also within the terminally charged dendrimer structure, as illustrated in Figure 1a. This suggests that these dendrimers are soluble in aqueous solutions. The formation of hydrogen-bonds between the dendrimer's terminal moieties and the water molecules, however, results in a larger energy gain than the formation of bonds between water molecules in the bulk. Consequently, the water density at their periphery is increased with respect to that of hydrophobic solutes.[30] This effect leads to an enlarged separation between the charged monomers, in addition to the one already caused by the electrostatic repulsions. Similar considerations hold for the fully charged dendrimer, shown in Figure 1 (c), (d) for explicitly and implicitly simulated water, respectively. Here of course, no hydrophobic core is involved, since all monomers are charged.

Because no differences in the dendrimer's conformations can be discerned from the snapshots, a more detailed analysis is necessary. Information about the size changes can be obtained by considering the radius of gyration, R_g, of the dendrimers, which can be measured by SANS, X-ray, or static-light scattering experiments, and is given by

$$R_g^2 = \left\langle \frac{1}{N}\sum_{i=1}^{N} (\mathbf{r}_i - \mathbf{r}_c)^2 \right\rangle \tag{10}$$

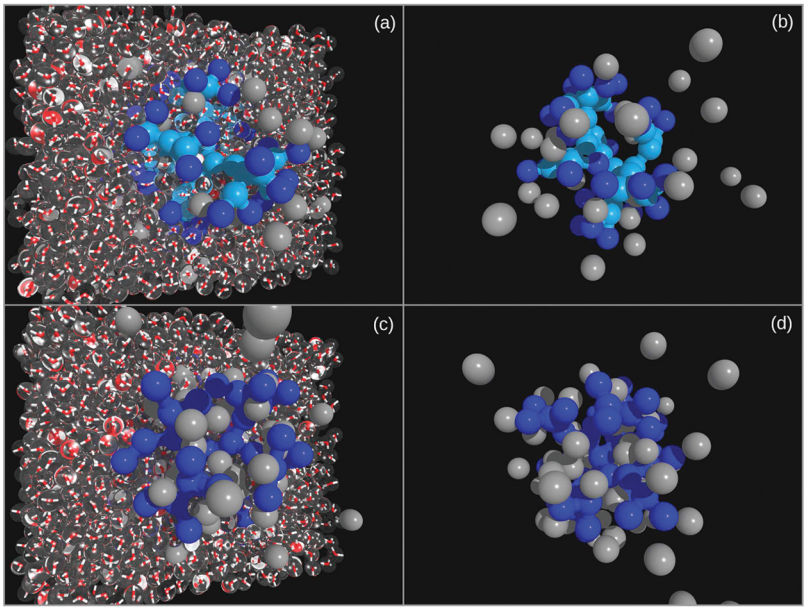


Figure 1. Snapshots from simulations of $P = 1$ dendrimers with $Z = 32$ (a, b), and $Z = 62$ (c, d) in explicitly and implicitly simulated water, respectively. Charged monomers of the dendrimer are shown in dark blue, neutral monomers in light blue and counterions in gray color. The water molecules are shown as transparent spheres, where the oxygen position is indicated by red and that of the hydrogens by white colors. The diameter of the spheres are σ and σ_w for the monomer/ions and water molecules, respectively.

dx.doi.org/10.1021/ma202520d | Macromolecules 2012, 45, 2562−2569

where N is the number of monomers, $\mathbf{r}_i$ the position of the ith monomer, and $\mathbf{r}_c$ the position vector of the center of mass of the dendrimer. Simulation results are shown in Table 2. The

Table 2. Radius of Gyration, R_g, Measured in Units of the Monomer Diameter σ for Dendrimers with $P = 1$ and $P = 2$ Spacer Segments in Explicitly and Implicitly Simulated Water[a]

	explicit water		implicit water	
Z	$P = 1$	$P = 2$	$P = 1$	$P = 2$
32	2.80	3.87	2.72	4.14
62	3.23	4.57	2.95	4.44

[a]The error is on the order of 0.01σ in all cases.

size of the $P = 1$ dendrimers is larger for explicitly simulated water than for implicit water, for both the terminally charged and fully charged dendrimers. The increase in the number of neutral monomers by the insertion of spacers diminishes the growth in size of the dendrimers upon charging, because of the additional effective attractions between them that are induced by the solvent. The relative size increase of the dendrimers upon lowering the pH, is in good quantitative agreement with experiments.[12,13,24,25,27] This illustrates that although an oversimplified simulation model without detailed atomistic information is employed here, it is sufficient to capture the essential features and understand the basic conformational properties of dendrimers.

In order to gain a better understanding of the intramolecular structure the density profiles of the node monomers and of the counterions have been measured with respect to the center of mass $\mathbf{r}_c$,

$$\rho(r) = \langle \sum_{i=1}^{N} \delta(\mathbf{r} - \mathbf{r}_i + \mathbf{r}_c) \rangle \tag{11}$$

where $\mathbf{r}_i$ denotes the position of the ith particle from the total number of particles N, which can be either nodes or counterions.

The density profiles of the node monomers, $\rho_n(r)$, and of the counterions, $\rho_c(r)$, are shown in Figure 2 for the $P = 1$ dendrimer. For the terminally charged dendrimers, see Figure 2 (a), the density distributions of the monomers with explicitly and implicitly simulated water almost coincide. However, in the case of explicit water the shell structure of the dendrimer is more pronounced. This is also the case for the fully charged dendrimers, as shown in Figure 2c. In addition, the peaks are shifted outward with respect to the center, which is explained by water molecules being absorbed into the core of the dendrimer. This is in fact a simple scaling, which becomes apparent from the inset where both profiles are shown as a function of the distance $x = r/R_g$ to the center in terms of the radius of gyration R_g. The fact that the monomer density profiles stemming from the implicit and explicit water simulations collapse onto the same curve for either dendrimer, illustrates that the implicit simulations are capable of reproducing the salient characteristics of (partially) charged dendrimers.

The counterion distributions are shown in Figure 2, parts b and d, for the terminally and fully charged dendrimers, respectively. These profiles are slightly more structured when the water molecules are simulated explicitly. The open dendrimer structure allows counterions to diffuse into the center of the molecule, only to be expelled from a small region near the center of mass due to its closeness to the central pair of generation 0 monomers. Since the monomer density profiles are very similar, the fact that counterion density in the case of explicit water is somewhat lower as well as more structured can only be attributed to the presence of water molecules.

The measured density distributions of node monomers and counterions for the $P = 2$ dendrimer are shown in Figure 3. The overall structure in these profiles is less pronounced compared to those of the $P = 1$ dendrimers, which is caused by the additional freedom and flexibility by the additional spacer. The terminally charged dendrimer in Figure 3a is more compact in

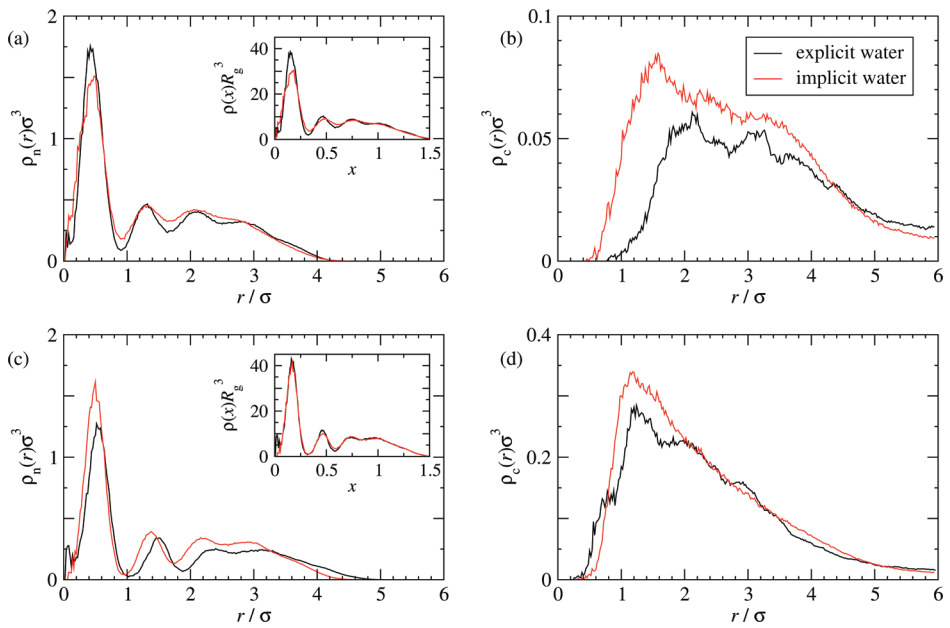


Figure 2. Radial density distribution of node monomers, $\rho_n(r)$, (a, c) and counterions, $\rho_c(r)$, (b, d) as a function of the distance, r, from the center of mass for the $P = 1$ dendrimer. The dendrimer's and counterion's total charge is $Z = 32$ (a, b) and $Z = 62$ (c, d). The insets show the distribution of node monomers but with the radius of gyration, R_g, as the reference length scale.

dx.doi.org/10.1021/ma202520d | Macromolecules 2012, 45, 2562–2569

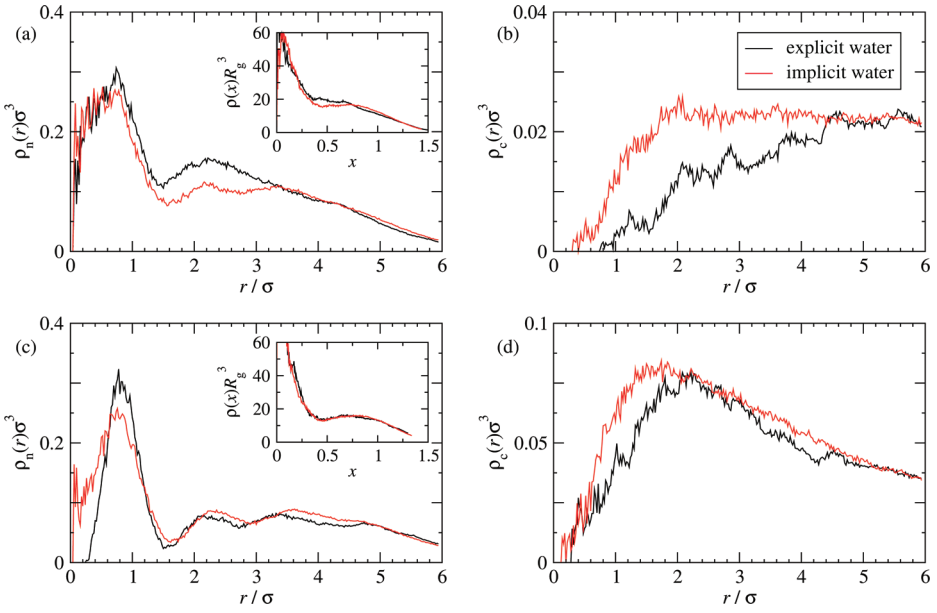


Figure 3. Radial density distribution of node monomers, $\rho_n(r)$, (a, c) and counterions, $\rho_c(r)$, (b, d) as a function of the distance, r, from the center of mass for the $P = 2$ dendrimer. The dendrimer's and counterion's total charge is $Z = 32$ (a, b) and $Z = 62$ (c, d). The insets show the combined distribution of node monomers and spacers as a function of the scaled distance $x = r/R_g$. Note that the insets show the total monomer profile, including the spacers, whereas the main plots only the nodes, thus the two are not scaled versions of one another.

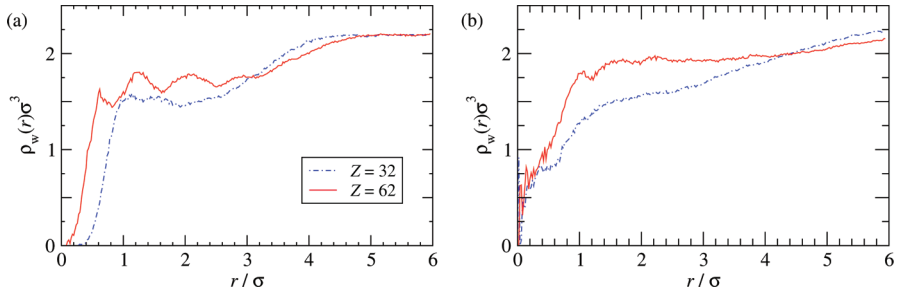


Figure 4. Radial distribution of water molecules, $\rho_w(r)$, as a function of the distance, r, from the center of mass for dendrimers with (a) $P = 1$ and (b) $P = 2$ spacer segments.

explicit water, which is due to the hydrophobically induced attraction between the neutral monomers of the lower generations, which is missing in the implicit water simulation. At the same time the counterions, as shown in Figure 3b, are expelled from the dendrimer's interior. The leveling off of these profiles is caused by the finite dendrimer density that is being used. The nodes of the fully charged dendrimer, Figure 3c, show good agreement between explicit and implicit water both with respect of the position of the peaks and their heights. However, the structure-stabilizing effect of the water, absorbed into the dendrimer is clearly visible here, as indicated by expulsion of monomers from the region around the center of mass. The combined density profiles of node monomers and spacers are shown in the insets with the radius of gyration as the reference length scale. Similar as in the case of the $P = 1$ dendrimers, the scaled profiles coincide.

A quantity that is experimentally accessible is the number of water molecules absorbed by the dendrimer.[59] The water distributions, $\rho_w(r)$, of the $P = 1$ and $P = 2$ dendrimers in the explicit water simulations are shown in Figure 4, parts a and b, respectively. In both cases, more water is absorbed the higher the charge of the dendrimers. Combined with the observation that the shell structure of the fully charged dendrimer without spacer is imposed on the water distribution, this supports the picture sketched above that it is preferential for the water molecules to bind to the charged monomers. The additional steric interactions between charged monomers and water provide the basis for the anticorrelation between the profiles in the interior. In the periphery of the molecule, the distance between charged sites is large enough to avoid the necessity of following that shell structure. For the dendrimers with an additional spacer this is even the case for the lower generation nodes, because of the additional available volume they provide. Also note that they facilitate the diffusion of water and counterions to the core and allow them to reach the center of mass for the $P = 2$ dendrimers. Our findings are consistent with experimental results from SANS measurements,[27] where very substantial water intake within the interior of neutral dendrimers was found, and which was further enhanced by charging the molecules. Though we have not simulated a completely neutral dendrimer in our case but rather terminally charged (as well as fully charged) ones, the trend is the same: upon additional charging, more water molecules are absorbed to the interior of the dendrimer. The same feature was also seen in the simulations of Maiti et al.,[28] who employed explicit water models, as well as in the work of Gurtovenko et al.[35] In the latter case, however, the solvent particles were modeled as apolar beads and the charging

dx.doi.org/10.1021/ma202520d | Macromolecules 2012, 45, 2562−2569

by modification of the Bjerrum length, which has no direct correspondence with our approach.

In order to quantify the amount of absorbed water the number of water molecules within a sphere of radius R_g around the center of mass have been measured, see Table 3. The

Table 3. Water Intake Obtained by integrating the radial water distribution up to R_g

Z	$P = 1$	$P = 2$
32	137	412
62	242	779

amount of absorbed water is almost doubled upon going from a terminally to a fully charged dendrimer for the $P = 1$ as well as the $P = 2$ case. This illustrates again that the water intake is strongly correlated with the total charge of the dendrimer. However, due to the relatively small amount of free space within the $P = 1$ dendrimer the density of water is somewhat lower than that of the dendrimer with $P = 2$ spacer segments.

4. DISCUSSION AND CONCLUSIONS

We investigated the effect that the discrete nature and the dielectric properties of an aqueous solution have on the conformations of dendrimers. Electrostatic interactions between charged entities constitute the main contribution to the conformation of the dendrimers in all studied cases here. The absorbed water molecules do result in some additional steric interactions, which cause the dendrimers to swell more than one might expect on the basis of their screened Coulomb interactions. In addition, it causes minor rearrangements of the counterions internally. These differences are however small, hence simulating the water molecules explicitly is only of secondary importance for the terminally or fully charged dendrimers considered here. We have shown that the equilibrium properties of charged dendrimers are very weakly sensitive on the explicit water against continuum water modeling of the solvent. This holds for the monomer and the counterion density profiles, for the ordering of the generations and the existence of voids in the structure (as witnessed by the minima in the density profiles). In addition, we have shown that when the density profiles are scaled on the gyration radius, i.e., when the dendrimers are seen at a mesoscopic scale, the profiles from the two approaches collapse onto one another. Given the known fact that a further coarse-graining of the dendrimers, i.e., the derivation of a dendrimer−dendrimer effective interaction[60,61] crucially depends on the form of these profiles, it can be asserted that the latter will be insensitive to the modeling of the aqueous solvent as a dielectric continuum although there is no *a priori* guarantee for this to be the case. Therefore, there are reasons to believe that a host of equilibrium properties of dendrimers or concentrated solutions of the same can be calculated in continuum solvent simulation models, which are much faster than their explicit water counterparts.

The usage of the implicit water model for athermal solvents is well suited for the description of (partially) charged dendrimers and can be controlled via the adjustment of the relative permittivity. A very good agreement between implicit and explicit water simulation, as seen by the collapse of the density profiles when suitably scaled, is found. However, the deviations increase when more neutral monomers are included into the dendrimer, i.e., when hydrophobic effects start playing an increasingly important role. Finally, we emphasize that the work presented here is focused on the static properties, related to dendrimer conformations. In previous works employing explicit solvent models,[33,35] the dynamics of water and/or the dendrimer branches was also studied. Although it would have been possible to do the same here and provide a comparison with the previous results, this would lie clearly outside the scope of this work, which is to provide a comparison between implicit and explicit solvent models. Such a comparison makes little sense when dynamical quantities are concerned, since the whole dynamics changes when solvent is eliminated: the Newtonian equations of motion at the solvent-resolved level turn into a Langevin dynamics, including friction and possible hydrodynamic effects when the solvent is integrated out. Otherwise, if one employs the same dynamics at both scales, an enormous acceleration of the dynamics results at the coarse-grained level, as is well-known also for other soft systems.[62] A study of the effects of multivalent counterions on the internal dynamics of dendrimers, which has direct connections with recent simulations[36] and experiments[63] will be the subject of future work.

AUTHOR INFORMATION

Corresponding Author

*E-mail: ronald.blaak@univie.ac.at.

Notes

The authors declare no competing financial interest.

Present Address

[†]Institute for Computational Molecular Science and Department of Chemistry, Temple University, Philadelphia, Pennsylvania 19122, United States.

ACKNOWLEDGMENTS

This work has been supported by the CMS Vienna and by the Marie Curie Training Network ITN-COMPLOIDS, FP7-PEOPLE-ITN-2008, Project No. 234810.

REFERENCES

(1) Buhleier, G. E.; Wehner, W.; Vögtle, F. *Synthesis (Stuttgart)* **1978**, *2*, 155.

(2) Tomalia, D. A.; Naylor, A. M.; Goddard, W. A. *Angew. Chem., Int. Ed. Engl.* **1990**, *29*, 138−175.

(3) Dennig, J. *Dendrimers V*; Springer: Berlin and Heidelberg, Germany, 2003; Vol. *228*; pp 621−672.

(4) Choi, Y. S.; Thomas, T.; Kotlyar, A.; Islam, M. T.; Baker, J. R. Jr. *Chem. Biol.* **2005**, *12*, 35−43.

(5) Stiriba, S. E.; Frey, H.; Haag, R. *Angew. Chem., Int. Ed. Engl.* **2002**, *41*, 1329−1334.

(6) Harreis, H. M.; Likos, C. N.; Ballauff, M. *J. Chem. Phys.* **2003**, *118*, 1979−1988.

(7) Rosenfeldt, S.; Dingenouts, N.; Ballauff, M.; Lindner, P.; Likos, C. N.; Werner, N.; Vögtle, F. J. *Macromol. Chem. Phys.* **2002**, *203*, 1995−2004.

(8) Pötschke, D.; Ballauff, M.; Lindner, P.; Fischer, M.; Vögtle, F. *Macromolecules* **1999**, *32*, 4079.

(9) Pötschke, D.; Ballauff, M.; Lindner, P.; Fischer, M.; Vögtle, F. *Macromol. Chem. Phys.* **2000**, *201*, 330.

(10) Rissanou, A. N.; Economou, I. G.; Panagiotopoulos, A. Z. *Macromolecules* **2006**, *39*, 6298−6305.

(11) Ballauff, M.; Likos, C. N. *Angew. Chem., Int. Ed. Engl.* **2004**, *43*, 2998−3020.

(12) Newkome, G. R.; Young, J. K.; Baker, G. R.; Potter, R. L.; Audoly, L.; Cooper, D.; Weis, C. D. *Macromolecules* **1993**, *26*, 2394−2396.

(13) Young, J. K.; Baker, G. R.; Newkome, G. R.; Morris, K. F.; Johnson, C. S. Jr. *Macromolecules* **1994**, *27*, 3464−3471.

(14) Jusufi, A.; Likos, C. N. *Rev. Mod. Phys.* **2009**, *81*, 1753−1772.

(15) Likos, C. N. *Phys. Rep.* **2001**, *348*, 267−439.
(16) Nisato, G.; Ivkov, R.; Amis, E. J. *Macromolecules* **2000**, *33*, 4172.
(17) Chen, W.; Tomalia, D. A.; Thomas, J. L. *Macromolecules* **2000**, *33*, 9169−9172.
(18) Welch, P.; Muthukumar, M. *Macromolecules* **1998**, *31*, 5892−5897.
(19) Likos, C. N.; Ballauff, M. *Functional Molecular Nanostructures*; Topics in Current Chemistry 245; Springer: Berlin and Heidelberg, Germany, 2005; pp 239−252.
(20) Chen, W.-R.; Porcar, L.; Liu, Y.; Butler, P. D.; Magid, L. J. *Macromolecules* **2007**, *40*, 5887−5898.
(21) Giupponi, G.; Buzza, D. M. A.; Adolf, D. B. *Macromolecules* **2007**, *40*, 5959−5965.
(22) Liu, Y.; Bryantsev, V. S.; Diallo, M. S.; Goddard, W. A. III. *J. Am. Chem. Soc.* **2009**, *131*, 2798−2799.
(23) Blaak, R.; Lehmann, S.; Likos, C. N. *Macromolecules* **2008**, *41*, 4452−4458.
(24) Porcar, L.; Hong, K.; Butler, P. D.; Herwig, K. W.; Smith, G. S.; Liu, Y.; Chen, W.-R. *J. Phys. Chem. B* **2010**, *114*, 1751−1756.
(25) Liu, Y.; Chen, C.-Y.; Chen, H.-L.; Hong, K.; Shew, C.-Y.; Li, X.; Liu, L.; Melnichenko, Y. B.; Smith, G. S.; Herwig, K. W.; Porcar, L.; Chen, W.-R. *J. Phys. Chem. Lett.* **2010**, *1*, 2020−2024.
(26) Huißmann, S.; Likos, C. N.; Blaak, R. *J. Mater. Chem.* **2010**, *20*, 10486−10494.
(27) Wu, B.; Li, X.; Do, C.; Kim, T.-H.; Shew, C.-Y.; Liu, Y.; Yang, J.; Hong, K.; Porcar, L.; Chen, C.-Y.; Liu, E.; Smith, G.; Herwig, K.; Chen, W.-R. *J. Chem. Phys.* **2011**, *135*, 144903.
(28) Maiti, P. K.; Çağin, T.; Lin, S.-T.; Goddard, W. A. III. *Macromolecules* **2005**, *38*, 979.
(29) Wu, C. *Mol. Simulat.* **2010**, *36*, 1164.
(30) Dzubiella, J.; Hansen, J.-P. *J. Chem. Phys.* **2003**, *119*, 12049.
(31) Dzubiella, J.; Swanson, J. M. J.; McCammon, J. A. *J. Chem. Phys.* **2006**, *124*, 084905.
(32) Lee, I.; Athey, B. D.; Wetzel, A. W.; Meixner, W.; Baker, J. R. Jr. *Macromolecules* **2002**, *35*, 4510−4520.
(33) Lin, S.-T.; Maiti, P. K.; Goddard, W. A. III. *J. Phys. Chem. B* **2005**, *109*, 8663.
(34) Maiti, P. K.; Goddard, W. A. III. *J. Phys. Chem. B* **2006**, *110*, 25628−25632.
(35) Gurtovenko, A. A.; Lyulin, S. V.; Karttunen, M.; Vattulainen, I. *J. Chem. Phys.* **2006**, *124*, 8.
(36) Tian, W.-D.; Ma, Y.-Q. *Soft Matter* **2010**, *6*, 1308.
(37) Zhong, T.; Ai, P.; Zhou, J. *Fluid Phase Equilib.* **2010**, *302*, 43.
(38) Frenkel, D.; Smit, B. *Understanding Molecular Simulation*; Academic Press: San Diego, CA, 1996.
(39) Allen, M. P.; Tildesley, D. J. *Computer Simulation of Liquids*; Clarendon Press: Oxford, U.K., 1989.
(40) Cakara, D.; Kleinmann, J.; Borkovec, M. *Macromolecules* **2003**, *36*, 4201−4207.
(41) Weeks, J.; Chandler, D.; Andersen, H. *J. Chem. Phys.* **1971**, *54*, 5237.
(42) Jorgensen, W. L.; Madura, J. D.; Swenson, C. J. *J. Am. Chem. Soc.* **1984**, *106*, 6638−6646.
(43) Götze, I. O.; Harreis, H. M.; Likos, C. N. *J. Chem. Phys.* **2004**, *120*, 7761−7771.
(44) Grest, G. S.; Kremer, K.; Witten, T. A. *Macromolecules* **1987**, *20*, 1376−1383.
(45) Jorgensen, W. L.; Chandrasekhar, J.; Madura, J. D.; Impey, R. W.; Klein, M. L. *J. Chem. Phys.* **1983**, *79*, 926.
(46) Bagchi, K.; Balasubramanian, S.; Klein, M. L. *J. Chem. Phys.* **1997**, *107*, 8561−8567.
(47) Berendsen, H. J. C.; Postma, J. P. M.; van Gunsteren, W. F.; DiNola, A.; Haak, J. R. *J. Chem. Phys.* **1984**, *81*, 3684.
(48) Berendsen, H. J. C.; Grigera, J. R.; Straatsma, T. P. *J. Phys. Chem.* **1987**, *91*, 6269−6271.
(49) Ferguson, D. M. *J. Comput. Chem.* **1995**, *16*, 501−511.
(50) Lyubartsev, A.; Mirzoef, A.; Chen, L.-J.; Laaksonen, A. *Faraday Discuss.* **2010**, *144*, 43.
(51) Lyubatsev, A. P.; Laaksonen, A. *J. Chem. Phys.* **1999**, *111*, 11207.
(52) Lyubatsev, A. P.; Laaksonen, A. *Phys. Rev. E* **1995**, *52*, 3730.
(53) Kusalik, P. G.; Svishchev, I. M. *Science* **1994**, *265*, 1219.
(54) Wallqvist, A. *Chem. Phys. Lett.* **1990**, *165*, 437.
(55) Kohlmeyer, A.; Witschel, W.; Spohr, E. *Chem. Phys.* **1996**, *213*, 211−216.
(56) Bresme, F.; Wynveen, A. *J. Chem. Phys.* **2007**, *126*, 044501.
(57) Lingenheil, M.; Denschlag, R.; Reichold, R.; Tavan, P. *J. Chem. Theory Comput.* **2008**, *4*, 1293−1306.
(58) Andersen, H. C. *J. Chem. Phys.* **1980**, *72*, 2384.
(59) Li, T. K.; Hong, K.; Porcar, L.; Verduzco, R.; Butler, P. D.; Smith, G. S.; Liu, Y.; Chen, W.-R. *Macromolecules* **2008**, *41*, 8916−8920.
(60) Tian, W.-D.; Ma, Y.-Q. *Soft Matter* **2011**, *7*, 500.
(61) Huißmann, S.; Blaak, R.; Likos, C. N. *Soft Matter* **2011**, *7*, 8419.
(62) Lopez, C. F.; Moore, P. B.; Shelley, J. C.; Shelley, M. Y.; Klein, M. L. *Comput. Phys. Commun.* **2002**, *147*, 1.
(63) Li, X.; Zamponi, M.; Hong, K.; L.; Porcar, C.-Y. S.; Jenkins, T.; Liu, E.; Smith, G. S.; Herwig, K. W.; Liu, Y.; Chen, W.-R. *Soft Matter* **2011**, *7*, 618−622.

Macromolecules

Article

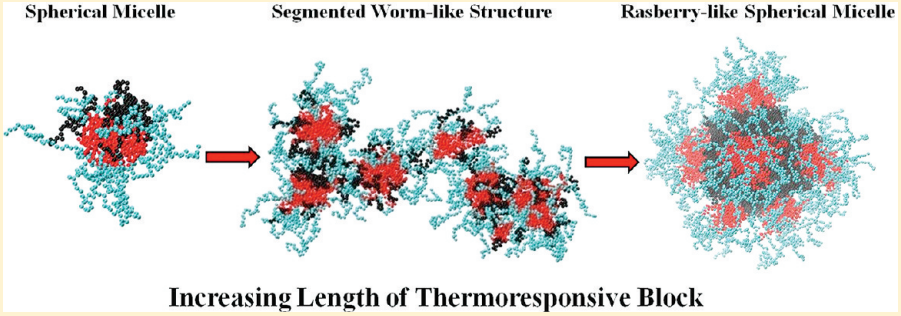
pubs.acs.org/Macromolecules

Self-Assembly Behavior of Thermoresponsive Bis-Solvophilic Linear Block Terpolymers: A Simulation Study

Othonas Moultos,[†] Leonidas N. Gergidis,[‡] and Costas Vlahos[†,*]

[†]Department of Chemistry, University of Ioannina, 45110 Ioannina, Greece

[‡]Department of Materials Science & Engineering, University of Ioannina, 45110 Ioannina, Greece



ABSTRACT: The micellization behavior of linear ABC terpolymers containing a solvophobic block in the middle, accompanied by solvophilic and thermoresponsive blocks at the ends, is studied by means of Brownian dynamics simulations. The effects of the length of the thermoresponsive moiety on the shape and size of aggregates, formed as the temperature of the solution reduces and solvent progressively becomes bad for the thermoresponsive block, are studied in detail. Two crossover temperatures, $T^* = 2.4$ and $T^* = 2.0$, were found. The first one corresponds to the formation of loose aggregates and the second one to regular micelles. At both solution temperatures, as the thermoresponsive block length increases, a shape transition from spherical to segmented worm-like and back to spherical loose aggregates or micelles was observed. Our results are compared with recent experimental findings of similar systems.

1. INTRODUCTION

The self-assembly of amphiphilic AB diblock copolymers in solution into spherical or cylindrical micelles, has attracted much attention in recent years due to their potential applications in nanotechnology, cosmetics, paints and drug delivery systems.[1,2] The effects of architecture, molecular weight, and the stiffness of the blocks on the micelle's shape and size as well as the ones of the chemical mismatch between the blocks have been studied extensively by theory and experiments in the past few years and are relatively well understood.[3−8]

As the number of distinct blocks increases from two to three, for example, ABA linear triblock copolymers and ABC linear terpolymers, both the complexity and the variety of self-assembled structures significantly increase. In the case of linear ABA terpolymers built from two solvophobic A blocks on the sides and a solvophilic B block in the middle, flower-like micelles are obtained at low copolymer concentration while thermodynamic geletion is observed at higher concentrations.[9,10] Linear amphiphilic ABC terpolymers, containing two different solvophilic A, C blocks at the sides and a solvophobic B block, form a plethora of complex vesicle shapes or spherical micelles with mixed, patchy or Janus-like corona depending on the tuning of interaction parameters between the different blocks and their relative lengths.[11,12] Linear terpolymers of the opposite nature, containing a solvophilic A block at the one end and two successive solvophobic blocks B and C, form multicompartment core, raspberry-like, worm-like, or comb-like micelles.[13,14]

An interesting category of ABC terpolymers are those containing an environmentally sensitive polymeric block. These terpolymers exhibit large, sharp changes in response to physical stimuli (such as temperature, solvent, or light) or to chemical stimuli (such as pH, ions in solution, or chemical recognition). Responses differ depending on the stimulus applied and may include changes in shape, volume or mechanical properties among others. These terpolymers involved in a variety of interesting applications for encapsulation, for controlled delivery, or as "intelligent" switches among them.[15−18]

Walther et al.[19] have synthesized and studied a series of bishydrophilic block terpolymers, with a poly(*n*-butyl acrylate) (PnBuA) as hydrophobic middle block and poly(ethylene oxide) (PEO) and poly(*N*-isopropylacrilamide) (PNiPAAm) as outer blocks. PNiPAAm is a thermoresponsive polymer with lower critical solution temperature (LCST), behavior exhibiting cloud points just below the human body temperature (32 °C). Cryo-TEM and light scattering measurements showed that the collapse of PNiPAAm block triggers the clustering of micelles

Received: November 23, 2011
Revised: February 2, 2012
Published: February 22, 2012

 © 2012 American Chemical Society dx.doi.org/10.1021/ma2025573 | *Macromolecules* 2012, 45, 2570−2579

into superstructures when the contour length of the thermoresponsive block is longer than the one of the hydrophilic PEO polymer. Several heating cycles from 25 to 45 °C showed an increase in the amount of micelles from mainly mixed micelles into micelles with preferentially two opposing sticky patches. This gives rise to a linear assembly of segmented worms and comb like micelles. A full transition to the Janus-like micelles and consequently to spherical superstructures does not take place.

At temperatures higher than the LCST of PNiPAAm the micellization behavior of the aforementioned terpolymer should be more or less similar to an ABC terpolymer's composed of solvophilic−solvophobic−solvophobic blocks when the interactions between different units are similar. Li et al.[20] studied ABC miktoarm star terpolymers composed of two hydrophobic (poly(ethylethylene), poly(methylcaprolactone)) and one hydrophilic (poly(ethylene oxide)) branches. In contrast, they found that when the poly(methylcaprolactone) arm increases results in a transition from spherical micelles to segmented worms and to spherical superstructures. The latter transition can be attributed on the assembly of sticky patchy Janus type segments.

Despite the aforementioned potential of thermoresponsive ABC terpolymers in applications the theoretical and experimental studies reported in the literature are restricted. We employed Brownian dynamics simulations in order to elucidate the effects of the thermoresponsive block and the system temperature on the micellization behavior. Brownian dynamics has successfully been used in the study of self- assembly of various copolymers and it is expected to be also appropriate for the study of linear ABC terpolymers.[6−8,21] The properties of interest are the preferential aggregation number (N_{ag}) and the shape of the micelle which is expressed by the shape anisotropy parameter (κ^2) and the mean square radius of gyration ($\langle R_g^2 \rangle$) of the solvophobic core, of the corona, and of the whole micelle. In addition, we report direct comparisons of our simulation results with experimental findings of similar systems existing in the literature.[19,20]

2. MODEL

We employed a coarse-grained model in order to study the amphiphilic terpolymers. A group of atoms was modeled as a bead (with diameter σ), while different beads were connected with flexible finitely extended elastic bonds (FENE). The FENE potential is expressed as

$$U_{Bond}(r_{ij}) = \begin{cases} -0.5kR_0^2 \ln\left[1 - \left(\frac{r_{ij}}{R_0}\right)^2\right], & r_{ij} \le R_0 \\ \infty, & r_{ij} > R_0 \end{cases} \quad (1)$$

where r_{ij} is the distance between beads i and j, $k = 25T\varepsilon/\sigma^2$, and R_0 is the maximum extension of the bond ($R_0 = 1.5\sigma$). These parameters[21,22] prevent chain crossing by ensuring an average bond length of 0.97σ. Monomer−monomer interactions were calculated by means of a truncated and shifted Lennard-Jones potential

$$U_{LJ}(r_{ij}) = \begin{cases} 4\varepsilon_{ij}\left[\left(\frac{\sigma}{r_{ij}}\right)^{12} - \left(\frac{\sigma}{r_{ij}}\right)^{6} - \left(\frac{\sigma}{r_{cij}}\right)^{12} + \left(\frac{\sigma}{r_{cij}}\right)^{6}\right] \\ \quad + \varepsilon_{ij}, \quad r_{ij} \le r_{cij} \\ 0, \quad r_{ij} > r_{cij} \end{cases} \quad (2)$$

where ε_{ij} is the well-depth and r_{cij} is the cutoff radius. The solvent molecules are considered implicitly. The short time-steps needed to model solvent's behavior (the fast motion) restrict the time scales that maybe sampled, thereby limiting the information that can be obtained for the slower motion of the copolymer. Brownian dynamics simulation method allows the statistical treatment of the solvent, incorporating its influence on the copolymer by a combination of random forces and frictional terms. The friction coefficient and the random force couple the simulated system to a heat bath and therefore the simulation has canonical ensemble (NVT) constraints. The equation of motion of each bead i of mass m in the simulation box follows the Langevin equation:

$$m_i\ddot{\boldsymbol{r}}_i(t) = -\nabla \sum_j [U_{LJ}(r_{ij}) + U_{Bond}(r_{ij})] - m_i\xi\dot{\boldsymbol{r}}_i(t) + \mathbf{F}_i(t) \quad (3)$$

where m_i, $\boldsymbol{r}_i$, and ξ are the mass, the position vector, and the friction coefficient of the i bead, respectively. The friction coefficient is equal to ξ=0.5τ^{-1}, with $\tau = \sigma(m/\varepsilon)^{1/2}$. The random force vector $\boldsymbol{F}_i$ is assumed to be Gaussian, with zero mean, and satisfies the equation

$$\langle \mathbf{F}_i(t)\cdot\mathbf{F}_j(t')\rangle = 6k_BTm\xi\delta_{ij}\delta(t - t') \quad (4)$$

k_B is the Boltzmann constant and T is the temperature.

We constructed linear ABC terpolymers of the type $A_{NA}B_{30}A_{NC}$, with solvophilic A units, solvophobic B and thermoresponsive C units as typically shown in Figure 1. In



Figure 1. Cartoon representation of $A_5B_5C_5$ terpolymer.

all conducted simulations both the solvophobic part B and the solvophilic part A of terpolymers contained 30 beads, while the length of the thermoresponsive block varied containing N_c = 3, 5, 10, 15, 30, and 45. The Brownian dynamics simulations were performed in a cubic box with periodic boundary conditions, using the open-source massive parallel simulator LAMMPS.[23,24] Previous works have proved the high efficiency of LAMMPS in the study of amphiphilic copolymers.[6−8,21] The reduced temperature of the simulation $T^* = k_BT/\varepsilon$ varied from T^* = 4.0 (good solvent) to T^* = 3.0 (Θ solvent), 2.8, 2.6, 2.4, 2.2, 2.0 (bad solvent) and T^* = 1.8 (deep inside the biphasic area). Different cutoff distances and epsilon parameters (ε_{BB}= T^*/1.8, $\varepsilon_{ij} = \varepsilon$, for i,j ≠ B) in the Lennard-Jones potential were used[21,22] to describe the interactions between copolymer units. The A−A, A−B, A−C, and B−C interactions were considered repulsive

dx.doi.org/10.1021/ma2025573 | Macromolecules 2012, 45, 2570−2579

and have cutoff radii $r_{cij} = 2^{1/6}\sigma$ while the B−B interaction had an attractive potential with cutoff radius $r_{cij} = 2.5\sigma$. With the chosen interaction parameters the A units will remain under good solvent conditions and the B under bad solvent conditions despite the temperature changes. The solvent conditions for the thermoresponsive block C (C−C interactions) varied from good to Θ and progressively to bad solvent. For the sake of simplicity, all types of beads were considered to have the same mass ($m = 1$) and diameter ($\sigma = 1$).

In the present work, systems with 1000 polymeric chains were simulated. Amphiphiles at reduced temperatures T^* higher than the order−disorder transition temperature of the thermoresponsive moiety (UCST in the simulations) were assumed to reside to the same micelle if the distance between any two nonbonded solvophobic beads B, belonging to different chains, was found within 1.5σ. The aforementioned criterion has been adopted by the literature for the description of the micellization process where this distance corresponds to the maximum extension of the FENE bonds.[21] At reduced temperatures T^* close to or smaller than the order−disorder transition temperature of the thermoresponsive block we have secondary aggregation and different micelles are connected to form larger aggregates. Thus, the 1.5σ criterion were also applied for the distance between any two nonbonded C type units, belonging to different terpolymer chains. The choice of $\varepsilon_{BB} = T^*/1.8$ allows the studied systems to have both micelles and free molecules[21] at the reduced temperatures where no secondary aggregation due to thermoresponsive moieties is observed. If the ε_{BB} value is very high, the studied system contains only aggregates and no free molecules; while if it is very low, the studied system contains only free molecules and no aggregates. The system size was chosen so to prevent the largest micelles from having a radius of gyration greater than the one-fourth of the box side length. The use of the one-quarter of the simulation box side proved to be a sufficient condition to avoid interaction of chains and micelles with their images. In all simulations, we set $\varepsilon = 1$.

In order to avoid bond crossing at the desired concentration, the ABC terpolymer molecule was arranged on a lattice box. The energy of the chain was minimized and then the small system was replicated $N_{Polymer}$ times, equal to the number of polymer chains. We performed 1 million time steps with time step 0.008τ setting all cutoff radii equal to $r_{cij} = 2^{1/6}\sigma$ in order to eliminate any bias introduced from the initial conformation. The system then was allowed to equilibrate for 5 million steps. The simulation subsequently conducted for 100 million steps with time step 0.001τ to 0.006τ. This run time corresponds to 0.1−0.6 μs. The length of the simulation was evaluated by calculating the tracer autocorrelation function

$$C(t) = \frac{\langle N(t_o + t)N(t_o)\rangle - \langle N(t_o)\rangle^2}{\langle N^2(t_o)\rangle - \langle N(t_o)\rangle^2} \quad (5)$$

where $N(t)$ is the number of molecules in the micelle in which the copolymer resides at time t. We took all copolymers as tracers, and every time step as a time origin t_0. The characteristic relaxation time t_{relax} is defined as the required time for $C(t)$ to reach the value of e^{-1}. Each simulation was conducted for at least $10t_{relax}$ in order to have 10 independent conformations. Every production run was submitted on 14 processors in a parallel machine with Opteron 2.2 GHz CPU's, and needed about 3−4 weeks time to be completed. The properties of interest were calculated as averages from 1000 snapshots,[7,8] at the concentration [X] = 0.12 where most aggregates are formed.

3. RESULTS AND DISCUSSION

The simulated systems in the present study consisted of a series of ABC terpolymers with one inner solvophobic (B) and two outer solvophilic (A) and thermoresponsive (C) blocks. The terpolymers were of the type $A_{30}B_{30}C_{Nc}$ with 30 solvophilic, 30 solvophobic and a varied number of thermoresponsive units (N_c = 3, 5, 10, 15, 30 and 45). Thus, the lengths of the thermoresponsive block are shorter, comparable to or longer than the solvophilic block, respectively. Consequently the terpolymer systems mentioned above allow a systematic study of the effect of the thermoresponsive block length on the aggregation and the shape of the resulting micelles. According to our calculations of the Kuhn lengths presented in section 4 (Comparison with Experiments) micelles with larger sizes were obtained experimentally in terpolymers with half the thermoresponsive block length compared to the respective solvophilic which is similar to our $A_{30}B_{30}C_{15}$ terpolymers.

3.1. $A_{30}B_{30}C_{15}$ Terpolymer. Our simulation results for the mass distribution of micelles formed by the $A_{30}B_{30}C_{15}$ terpolymers are illustrated in Figure 2 for different solution

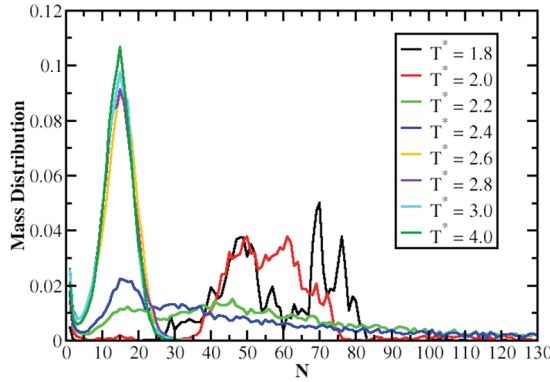


Figure 2. Mass distribution of aggregates for $A_{30}B_{30}C_{15}$ terpolymer at various solution temperatures T^*.

temperatures T^*. The radii of gyration, the shape anistotropy parameter κ^2, of the core, the thermoresponsive units and the whole micelle are presented in Table 1. In every solution temperature examined, the cross interactions between A−B, A−C, and B−C were always considered repulsive while the B−B, with chosen $\varepsilon_{BB} = T^*/1.8$, were very attractive deep inside the biphasic area where the B polymer melts. At $T^* = 4.0$, both solvophilic A and thermoresponsive C units are under good solvent conditions, forming micelles with mixed corona, while the solvophobic B units form the core. In Figure 2, one can observe that the mass distribution of micelles is bell-shaped with most probable aggregation number N_{ag}=15. The shape of the most probable micelle is spherical with shape anisotropy parameter $\kappa^2 = 0.0319$.

Lowering the solution temperature to $T^* = 3.0$, which is Θ for the thermoresponsive block C, the chemical mismatch between A and C units, expressed by the Flory χ_{AC} parameter, increases. This increase is not adequate to change the most probable aggregation number of micelles which remains equal to 15. However, the mean square radius of gyration of the whole micelle is slightly affected and increases from 70.5 to

dx.doi.org/10.1021/ma2025573 | Macromolecules 2012, 45, 2570−2579

Table 1. Shape Characteristic Properties for $A_{30}B_{30}C_{15}$ Terpolymer Aggregates[a]

	T^*	$\langle R_g^2\rangle_{mic}$	$\langle R_g^2\rangle_{solvophobic}$	$\langle R_g^2\rangle_{thermoresponsive}$	$\langle \kappa^2\rangle_{mic}$	$\langle \kappa^2\rangle_{solvophobic}$	$\langle \kappa^2\rangle_{thermoresponsive}$
N_{ag} = 15	4.0	70.5 (0.2)	22.8 (0.2)	69.3 (0.1)	0.0319 (0.0008)	0.098 (0.003)	0.078 (0.002)
	3.0	72.2 (0.3)	23.9 (0.3)	68.5 (0.4)	0.0340 (0.0007)	0.105 (0.002)	0.089 (0.002)
	2.8	72.3 (0.2)	23.9 (0.1)	67.5 (0.3)	0.0345 (0.0008)	0.106 (0.003)	0.093 (0.002)
N_{ag} = 16	2.6	75.0 (0.5)	25.4 (0.4)	68.7 (0.6)	0.035 (0.001)	0.113 (0.004)	0.097 (0.003)
N_{ag} = 29	2.4	153.0 (3.8)	102.4 (4.4)	129.3 (5.0)	0.24 (0.02)	0.50 (0.02)	0.29 (0.02)
	2.2	147.6 (6.3)	96.6 (6.2)	113.4 (6.2)	0.21 (0.01)	0.47 (0.02)	0.27 (0.02)
	2.0	131.4 (5.6)	79.3 (4.3)	65.8 (11.9)	0.16 (0.03)	0.39 (0.06)	0.18 (0.06)
N_{ag} = 47	2.4	245.3 (7.9)	192.5 (8.5)	216.0 (10.0)	0.28 (0.01)	0.46 (0.03)	0.35 (0.02)
	2.2	204.4 (15.3)	148.1 (16.2)	155.5 (19.7)	0.21 (0.04)	0.39 (0.05)	0.29 (0.05)
	2.0	150.4 (1.1)	93.4 (0.7)	63.9 (4.0)	0.09 (0.01)	0.22 (0.03)	0.11 (0.02)
N_{ag} = 50	2.0	155.2 (1.7)	97.7 (2.1)	65.8 (3.7)	0.08 (0.01)	0.18 (0.03)	0.11 (0.01)
N_{ag} = 61	2.0	173.8 (6.9)	113.3 (7.5)	73.8 (10.6)	0.08 (0.02)	0.16 (0.04)	0.12 (0.05)
N_{ag} = 70	1.8	172.8 (8.3)	112.6 (9.2)	48.1 (8.9)	0.04 (0.03)	0.07 (0.04)	0.10 (0.04)
N_{ag} = 76	2.4	420.5 (33.3)	365.7 (33.6)	387.2 (31.8)	0.31 (0.06)	0.41 (0.06)	0.36 (0.06)
	2.2	380.2 (33.1)	323.2 (34.4)	327.8 (38.2)	0.32 (0.06)	0.43 (0.06)	0.41 (0.05)
	2.0	302.1 (63.9)	243.5 (68.3)	210.6 (79.3)	0.3 (0.1)	0.4 (0.1)	0.5 (0.2)
	1.8	195.1 (37.3)	133.4 (38.5)	69.7 (45.7)	0.10 (0.05)	0.10 (0.05)	0.20 (0.05)

[a]Standard deviation is inside the parentheses.

72.2. The respective shape anisotropy parameter κ^2 increases from 0.0319 to 0.0340. Similar trends are also obtained at the solution temperature $T^* = 2.8$. A small increase in the micelles' most probable aggregation number (N_{ag} = 16) is observed in lower solution temperature $T^* = 2.6$. The Flory χ_{AC} parameter increases further and this results in a small increase in the total micelles mean square radius of gyration ($\langle R_g^2\rangle$ = 75.0) and on the respective shape anisotropy parameter κ^2= 0.035.

There are some interesting experimental studies on the aggregation behavior of thermoresponsive PEO−PNIPAAm diblock copolymers in aqueous solutions below the critical micelle temperature (CMT).[25] Since water is a good solvent for both moieties, at lower temperatures (LCST) PEO−PNIPAAm were usually considered to exist as single chains. However, aggregation of PEO−PNIPAAm in aqueous solution at temperatures below its cloud point (32 °C) was observed. This aggregation started at 15 °C, which is 17 °C below the cloud point. The formation of such loose aggregates decreases the free energy of the system since the PNIPAAm blocks get closer, reducing the interaction strength with the solvent and thus increasing the more favored homointeractions.

In Figure 3, we present our Brownian dynamics simulation results for the mean square radius of gyration of thermoresponsive block for a single ABC terpolymer chain at various solution temperatures. All the interaction parameters were the same with the respective parameters of the more concentrated systems. Three different regimes, with two crossover solutions temperatures at $T^* = 2.4$ and $T^* = 2.0$, can be observed. A possible explanation for the regime started at $T^* = 2.4$ could be the end-group effect. It is known that the hydrophobic end group could decrease the solubility and induce the aggregation of the solvophilic polymer, especially in the case that the overall molecular weight of the amphiphilic polymer is relatively low. In the current study we consider that the loose aggregates started to form at this temperature. Thus, for solution temperatures equal to or lower than $T^* = 2.4$, we modified the micellization criterion used for higher solution temperatures. According to the new criterion, two chains reside to the same micelle if the distance between any two nonbonded solvophobic beads B or the distance between any two nonbonded thermoresponsive beads C, belonging to different

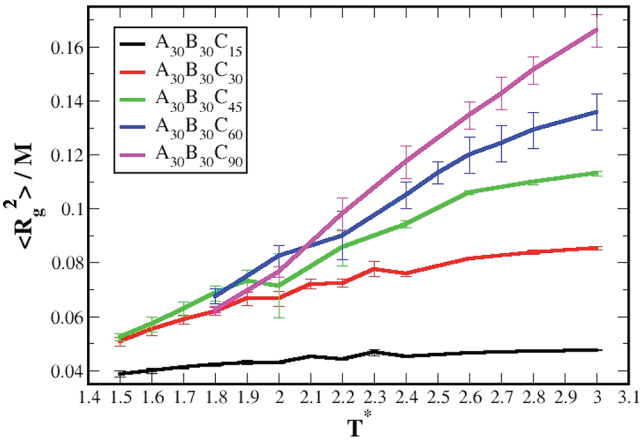


Figure 3. Mean square radius of gyration $\langle R_g^2\rangle$ normalized with the molecular weight M of the thermoresponsive block for various ABC single chain terpolymers with respect to the solution temperatures T^*.

chains, was found within 1.5σ. At $T^* = 2.4$ (Figure 2) the decrease in solubility of the thermoresponsive block triggers the clustering of a significant part of initial micelles (Figure 4a) into new hyper-structures. Snapshot analysis presented in Figure 4 shows the formation of segmented worm-like (Figure 4b, c, d) and comb-like (Figure 4e) loose aggregates connected through thermoresponsive stickers with a wide range of aggregation numbers. The radius of gyration and the shape anisotropy parameter confirm these conclusions. The mean square radius of gyration (Table 1) of hyper-structures with aggregation numbers N_{ag} = 29, 47, 76 are $\langle R_g^2\rangle$ = 153, 245, 420 which are 2, 3, and 5 times higher than the respective radius of gyration of the initial micelle ($\langle R_g^2\rangle$ = 76) with aggregation number N_{ag} = 15. The shape anisotropy parameter κ^2 of the whole aggregate has values 0.046, 0.236, 0.285, and 0.313 for aggregates with N_{ag} = 15, 29, 47, and 76 respectively, indicating a non spherical conformation. In solution temperature $T^* = 2.2$ more of the initial micelles were connected to form hyper-structures. For comparison purposes we have calculated the conformational properties of loose aggregates with the same aggregation numbers as before (N_{ag} = 29, 47, and 76). Both, mean square radius of gyration ($\langle R_g^2\rangle$ = 148, 204, 380) and shape anisotropy

dx.doi.org/10.1021/ma2025573 | Macromolecules 2012, 45, 2570−2579

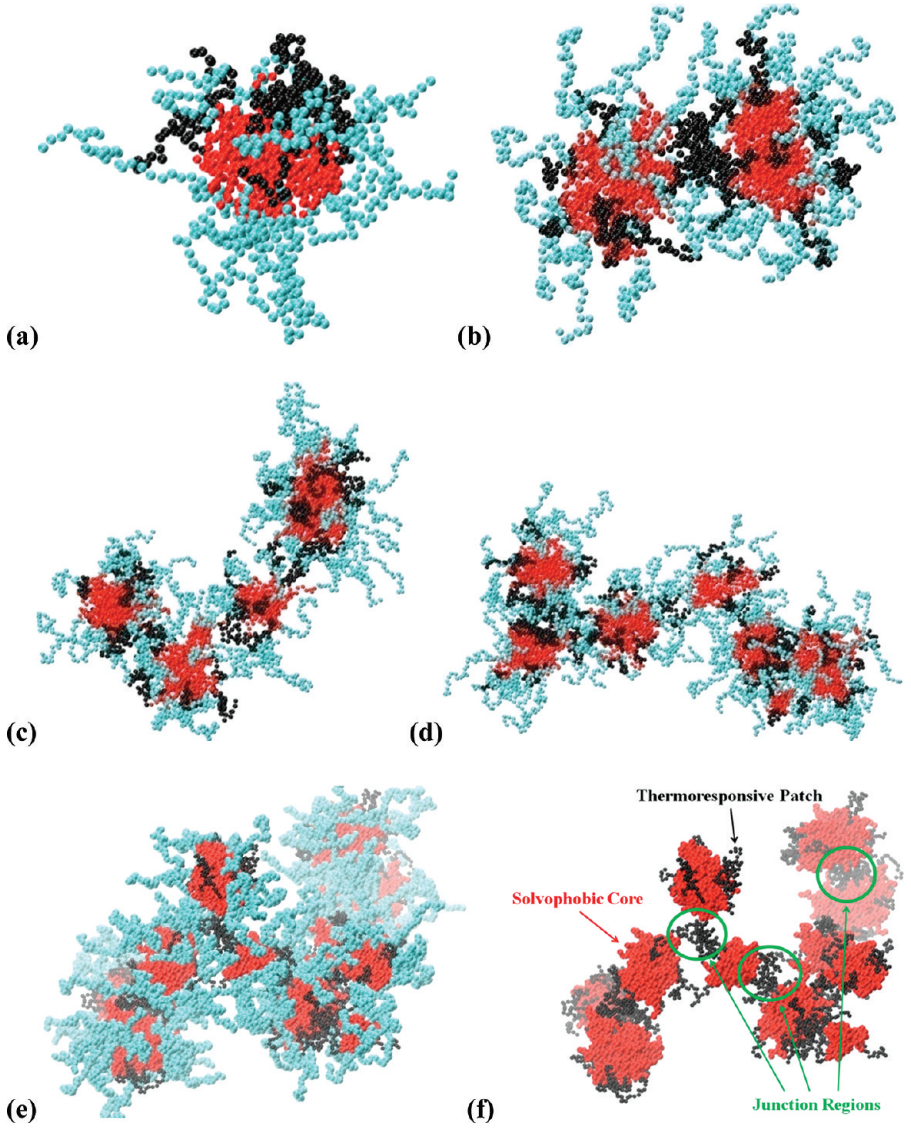


Figure 4. Snapshots of aggregates formed by $A_{30}B_{30}C_{15}$ terpolymer, at $T^* = 2.4$, with aggregation numbers (a) $N_{ag} = 15$, (b) $N_{ag} = 31$, (c) $N_{ag} = 62$, (d) $N_{ag} = 92$, (e) $N_{ag} = 171$, and (f) $N_{ag} = 171$ with solvophilic beads excluded for clarity.

parameter values (κ^2 = 0.211, 0.210, 0.319) were slightly smaller compared to the respective ones at temperature $T^* = 2.4$.

At temperature $T^* = 2.0$, the thermoresponsive block starts to melt and micelles with raspberry-like core (thermoresponsive units in the interior with hydrophobic patches attached on the periphery as shown in Figure 5a,b) are obtained with preferential aggregation numbers N_{ag} = 50 and 61. Snapshot analysis initially revealed the formation of segmented worm like hyper-structures connected through thermoresponsive stickers. Then with the evolution of time these segmented worm-like micelles were wrapped and new spherical micelles with raspberry-like cores were obtained. This shape transition takes place due to the rearrangement of the thermoresponsive blocks which form the interior part of micelles' core. In this mixed core the outer patches are formed by the solvophobic blocks surrounded by the solvophilic corona. The shape anisotropy parameter values for the micelles with the preferential aggregation numbers N_{ag} = 50 and 61 are κ^2= 0.077, 0.077 respectively, clearly indicating a spherical conformation. At the lowest solution temperature examined in the present study ($T^* = 1.8$) all micelles formed were spherical with raspberry-like core, similar to the ones presented in Figure 5c. We should notice here that there was significant population of micelles with aggregation numbers N_{ag}= 70, 76 higher than the ones in the previous temperature $T^* = 2.0$.

3.2. $A_{30}B_{30}C_{30}$ Terpolymer. Next we studied the amphiphilic terpolymers $A_{30}B_{30}C_{30}$ where the thermoresponsive C block contained the same number of beads with the solvophilic A block. Our results for the micelles mass distribution are illustrated in Figure 7 while the values of their size and shape are presented in Table 2. At solution temperature $T^* = 4.0$, where the thermoresponsive block is under good solvent conditions, only spherical micelles (κ^2 = 0.028, $\langle R_g^2 \rangle$ = 74.17) with mixed corona, containing both solvophilic and thermoresponsive units, with preferential aggregation number N_{ag} = 12 are obtained. One can observe that this aggregation number is smaller than the respective N_{ag} of $A_{30}B_{30}C_{15}$ terpolymers. The reason is the higher steric interactions in the micelle's corona in the case of $A_{30}B_{30}C_{30}$ due to the longer thermoresponsive block. At $T^* = 3.0$ the size of the thermoresponsive block decreases and the Flory χ_{AC}

dx.doi.org/10.1021/ma2025573 | *Macromolecules* 2012, 45, 2570–2579

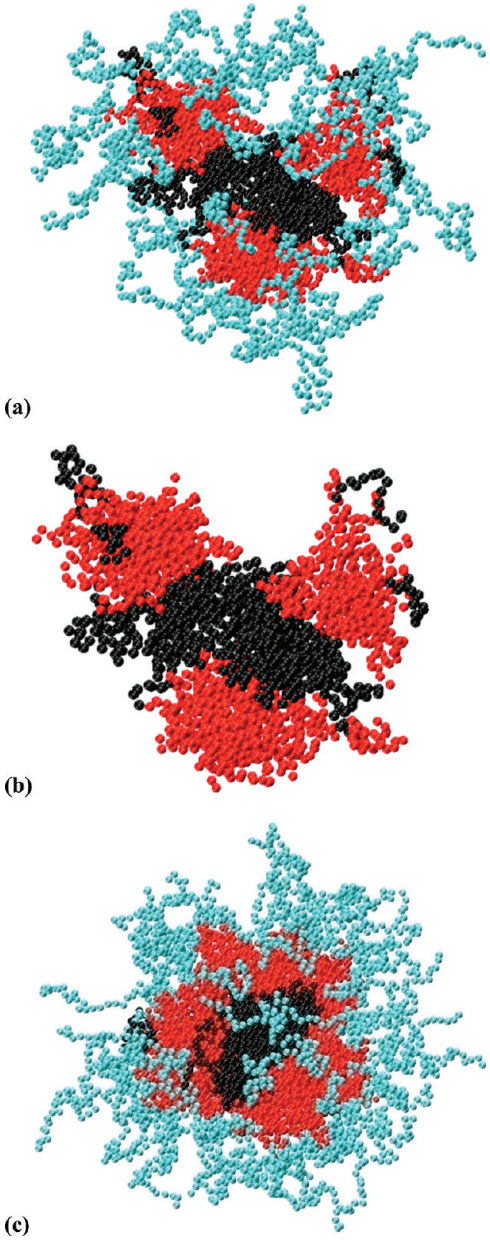


Figure 5. Snapshots of micelles formed by $A_{30}B_{30}C_{15}$ terpolymer with aggregation numbers (a) N_{ag} = 50 at T^* = 2.0, (b) N_{ag} = 50 at T^* = 2.0 with solvophilic beads excluded for clarity and (c) N_{ag} = 76 at T^* = 1.8.

parameter, describing the strength of A-C heterointeractions, increases. However, this increase is not high enough to change both the preferential aggregation number and the total size of micelles ($\langle R_g^2 \rangle$ = 74.31).

At solution temperatures T^* = 2.8 and 2.6 the preferential aggregation number increases to N_{ag} = 13 and 15 respectively, where the A-C heterointeractions become stronger. At this temperatures the thermoresponsive blocks occupy less space due to the decrease of their size but a small increase in the mean square radii of gyration of the whole micelle ($\langle R_g^2 \rangle_{mic}$) is observed ($\langle R_g^2 \rangle$ = 76.47, 80.32) due to the higher number of terpolymer chains involved in the aggregates. Temperature T^* = 2.4 triggers the aggregation of the thermoresponsive units as described in the $A_{30}B_{30}C_{15}$ case, driving the majority of terpolymer chains to form loose aggregates with N_{ag} varying

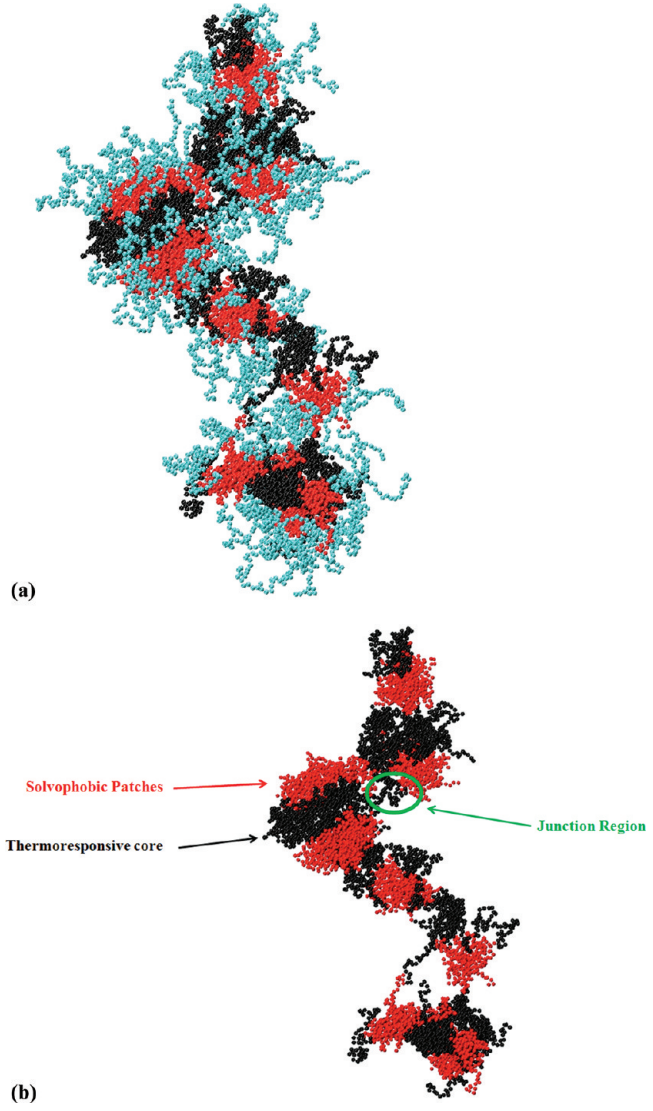


Figure 6. Snapshots of aggregates formed by $A_{30}B_{30}C_{30}$ terpolymer with N_{ag} = 122 at T^* = 2.4.

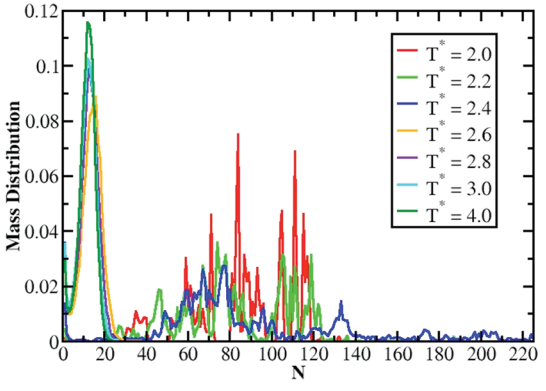


Figure 7. Mass distribution of aggregates for $A_{30}B_{30}C_{30}$ terpolymer at various solution temperatures T^*.

from 60 to 77. The shape of these micelles is spherical as indicated from the shape anisotropy parameter (κ^2 = 0.033 and 0.030) while the snapshot analysis revealed a raspberry-like mixed core with the thermoresponsive units lying in the interior and the solvophobic units residing, as patches, at the periphery

dx.doi.org/10.1021/ma2025573 | *Macromolecules* 2012, 45, 2570–2579

Table 2. Shape Characteristic Properties for $A_{30}B_{30}C_{30}$ Terpolymer Aggregates[a]

T^*	N_{ag}	$\langle R_g^2\rangle_{mic}$	$\langle R_g^2\rangle_{solvophobic}$	$\langle R_g^2\rangle_{thermoresponsive}$	$\langle \kappa^2\rangle_{mic}$	$\langle \kappa^2\rangle_{solvophobic}$	$\langle \kappa^2\rangle_{thermoresponsive}$
4.0	12	74.17 (0.09)	19.87 (0.08)	89.1 (0.3)	0.0279 (0.0007)	0.097 (0.002)	0.097 (0.002)
3.0	12	74.3 (0.2)	20.7 (0.1)	83.0 (0.5)	0.0298 (0.0007)	0.104 (0.003)	0.127 (0.003)
2.8	13	76.5 (0.1)	21.8 (0.1)	81.8 (0.7)	0.0282 (0.0004)	0.106 (0.003)	0.137 (0.003)
2.6	15	80.3 (0.5)	24.1 (0.2)	75.7 (1.3)	0.026 (0.001)	0.116 (0.004)	0.152 (0.005)
2.4	67	212.2 (21.5)	172.3 (20.4)	109.3 (33.3)	0.04 (0.04)	0.07 (0.05)	0.12 (0.09)
2.4	77	221.0 (15.6)	180.5 (14.9)	106.8 (21.9)	0.03 (0.03)	0.05 (0.04)	0.11 (0.07)
2.2	74	198.6 (1.6)	162.4 (2.0)	73.3 (1.5)	0.017 (0.005)	0.030 (0.009)	0.054 (0.007)
2.2	119	258.6 (21.8)	220.7 (21.9)	108.3 (25.8)	0.020 (0.005)	0.030 (0.005)	0.09 (0.03)
2.0	84	221.6 (33.20)	187.7 (33.9)	86.3 (38.7)	0.10 (0.05)	0.10 (0.05)	0.10 (0.05)
2.0	111	235.6 (1.0)	199.9 (1.0)	80.7 (1.1)	0.008 (0.002)	0.013 (0.002)	0.041 (0.008)

[a]Standard deviation is inside the parentheses.

of the core. A significant part of amphiphilic chains, around 29%, forms segmented worm like aggregates with $N_{ag} > 100$. The difference with the respective segmented worm like aggregates formed by the $A_{30}B_{30}C_{15}$ (Figure 4) terpolymers at the same solution temperature is found in the segmented worm-like structure (Figure 6a).

The building blocks of the segmented worm like structures are spherical micelles having raspberry-like mixed core with the thermoresponsive units lying in the interior and the solvophobic units residing, as patches, at the periphery of the core. These segments are connected to each other via thermoresponsive moieties as can be observed in Figure 6b. In the case of the $A_{30}B_{30}C_{15}$ terpolymers each segment core is composed by solvophobic units with two thermoresponsive stickers at the opposite sites of the periphery (Figure 4).

At $T^* = 2.2$, 2.0, and 1.8 only spherical micelles with similar raspberry-like core structure to the ones at $T^* = 2.4$ were obtained. At the solution temperature $T^* = 2.2$ the preferential aggregates contain 74 and 119 terpolymer chains, while when the temperature decreases at $T^* = 2.0$, N_{ag} becomes 84 and 111 respectively. At $T^* = 1.8$ all terpolymer chains were associated in micelles and no free chains were present in the solution. The lack of free chains is reflected on the shape of the mass distribution curve (not shown in the Figure 7) which becomes discontinuous with Dirac δ function type artifact peaks.

In order to study in detail the effects of the length of the thermoresponsive block on micelles hyper structures we are concentrated on the two different solution temperatures, $T^* = 2.4$ and 2.0 in which loose aggregates and normal micelles are formed, respectively.

3.3. Solution Temperature $T^* = 2.4$. Terpolymers $A_{30}B_{30}C_3$, $A_{30}B_{30}C_5$, $A_{30}B_{30}C_{10}$, and $A_{30}B_{30}C_{45}$ were also simulated at the solution temperature $T^* = 2.4$ and our results for the micelles mass distributions are illustrated in Figure 8, while the micelles' shape results are presented in Table 3. From Table 3, we can observe that the $A_{30}B_{30}C_3$ terpolymers form single spherical micelles ($\kappa^2 = 0.037$, $\langle R_g^2\rangle = 81$) with preferential aggregation number $N_{ag} = 21$ (Figure 8). Snapshot analysis indicated that the thermoresponsive blocks are located at the periphery of the solvophobic core segregated from each other forming very few aggregative domains. The thermoresponsive units are very well protected from the solvent by the solvophilic blocks and no secondary aggregation takes place. By increasing the length of thermoresponsive moiety ($A_{30}B_{30}C_5$ and $A_{30}B_{30}C_{10}$) we obtained similar results. The micelles aggregation number decreases to N_{ag} =20 and 17 respectively while a small decrease in the size of the spherical micelles ($\kappa^2 = 0.040$, $\kappa^2 = 0.040$) is also observed ($\langle R_g^2\rangle = 80$, $\langle R_g^2\rangle = 77$). In

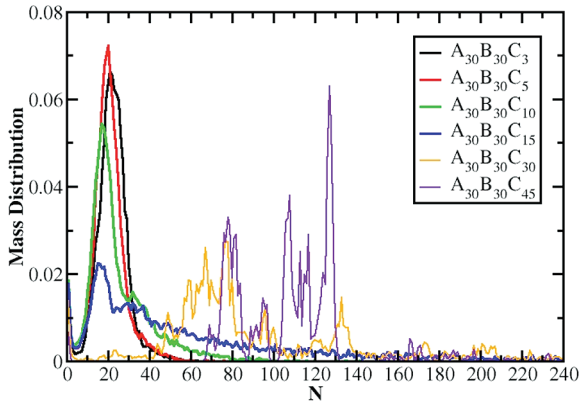


Figure 8. Mass distribution of aggregates for various ABC terpolymers at solution temperature $T^* = 2.4$.

micelles formed by $A_{30}B_{30}C_5$ terpolymers we observed an increased number of domains containing thermoresponsive units belonging to different terpolymers chains in the periphery of solvophobic core. Further increase of the thermoresponsive length ($A_{30}B_{30}C_{15}$) triggers the secondary aggregation of the single micelles as we have mentioned in the respective section and segmented worm-like hyper structures were obtained. In the case of $A_{30}B_{30}C_{30}$ terpolymers, the case analyzed in detail previously, spherical micelles with raspberry-like mixed core occupied the 70% of the total aggregation mass along with a 30% of segmented worms.

Terpolymers with longer thermoresponsive block ($A_{30}B_{30}C_{45}$) formed spherical micelles with aggregation numbers N_{ag} =78, 108, and 127 and only a 3% of segmented worms with segment structure similar to the one obtained in the case of $A_{30}B_{30}C_{30}$ terpolymers. Simulations of terpolymers with higher thermoresponsive content ($A_{30}B_{30}C_{60}$, $A_{30}B_{30}C_{90}$) suffered from the absence of free terpolymers chains. Nevertheless, snapshot analysis (Figure 9) indicates the formation of spherical micelles with raspberry-like core similar to the ones obtained in the case of the $A_{30}B_{30}C_{30}$, $A_{30}B_{30}C_{45}$ but with much greater aggregation numbers.

3.4. Solution Temperature $T^* = 2.0$. Our results for the $A_{30}B_{30}C_3$, $A_{30}B_{30}C_5$, $A_{30}B_{30}C_{10}$, $A_{30}B_{30}C_{15}$, and $A_{30}B_{30}C_{30}$ terpolymers are presented in Figures 10 and 11 and Tables 1, 2, and 3. From snapshot analysis and the values of shape anisotropy parameter κ^2, we observed a similar transition in the shape of micelles from spherical to segmented worm-like hyperstructures and back to spherical micelles, when the length of the thermoresponsive block increases. The difference with $T^* = 2.4$ is that the decrease of the solution temperature down

dx.doi.org/10.1021/ma2025573 | Macromolecules 2012, 45, 2570–2579

Table 3. Shape Characteristic Properties for Various Terpolymer Systems[a]

terpolymer	T^*	N_{ag}	$\langle R_g^2\rangle_{mic}$	$\langle R_g^2\rangle_{solvophobic}$	$\langle R_g^2\rangle_{thermoresponsive}$	$\langle \kappa^2\rangle_{mic}$	$\langle \kappa^2\rangle_{solvophobic}$	$\langle \kappa^2\rangle_{thermoresponsive}$
$A_{30}B_{30}C_3$	2.0	22	84.3 (0.5)	32.5 (0.5)	53.8 (0.5)	0.039 (0.002)	0.125 (0.009)	0.079 (0.006)
$A_{30}B_{30}C_3$	2.4	21	81.0 (0.4)	30.5 (0.3)	52.0 (0.2)	0.037 (0.002)	0.114 (0.006)	0.075 (0.003)
$A_{30}B_{30}C_5$	2.4	20	80.1 (0.5)	30.2 (0.4)	56.7 (0.4)	0.040 (0.003)	0.123 (0.007)	0.078 (0.003)
$A_{30}B_{30}C_5$	2.0	21	83.5 (0.5)	32.1 (0.5)	58.2 (0.4)	0.041 (0.002)	0.129 (0.008)	0.080 (0.004)
$A_{30}B_{30}C_{10}$	2.0	20	85.7 (1.4)	34.6 (1.4)	65.5 (0.9)	0.052 (0.007)	0.16 (0.02)	0.105 (0.007)
$A_{30}B_{30}C_{10}$	2.4	17	76.9 (1.2)	28.6 (1.2)	62.6 (1.3)	0.041 (0.003)	0.126 (0.009)	0.091 (0.004)
$A_{30}B_{30}C_{45}$	2.4	78	226.3 (7.3)	212.8 (8.0)	103.8 (7.0)	0.019 (0.009)	0.03 (0.01)	0.06 (0.03)
$A_{30}B_{30}C_{45}$	2.4	108	266.0 (5.1)	256.3 (5.4)	123.9 (6.8)	0.012 (0.005)	0.016 (0.006)	0.05 (0.02)
$A_{30}B_{30}C_{45}$	2.4	127	287.1 (10.3)	278.3 (10.5)	137.6 (11.4)	0.030 (0.005)	0.030 (0.005)	0.12 (0.09)

[a]Standard deviation is inside the parentheses.

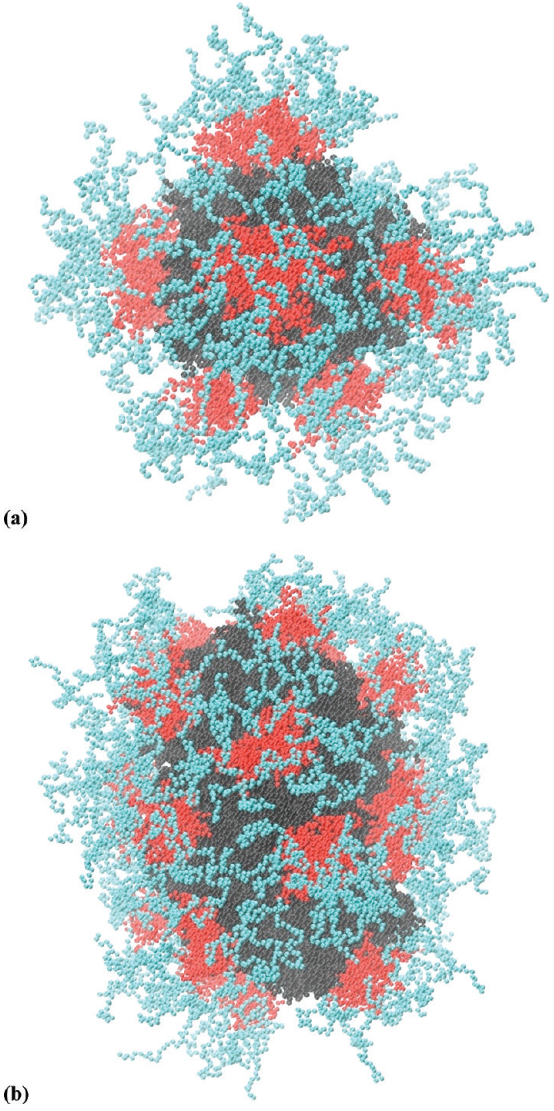


Figure 9. Snapshots of micelles formed by (a) $A_{30}B_{30}C_{60}$ terpolymer with aggregation number N_{ag} = 144 and (b) $A_{30}B_{30}C_{90}$ terpolymer with N_{ag} = 66 at T^* = 2.0.

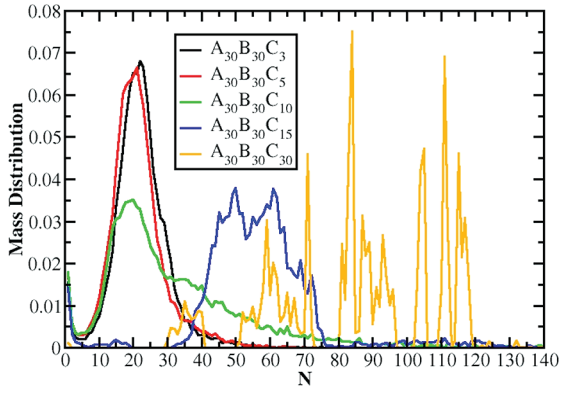


Figure 10. Mass distribution of aggregates for various ABC terpolymers at solution temperature T^* = 2.0.

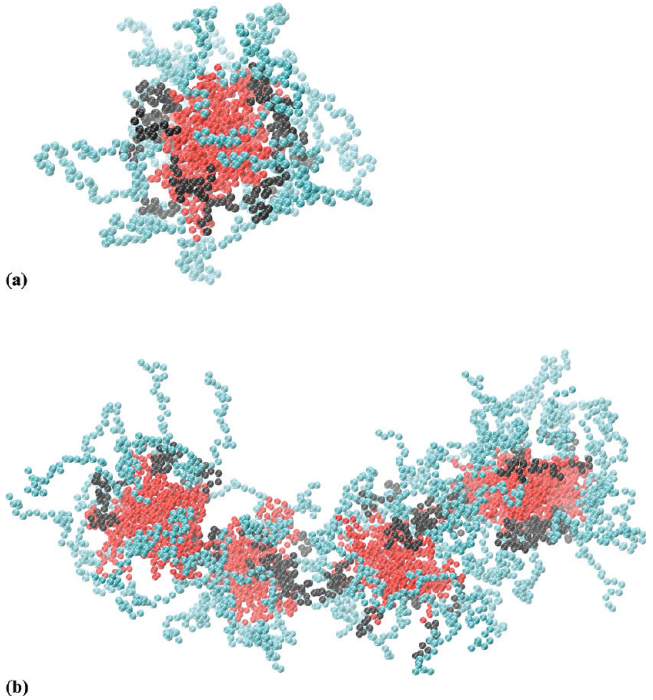


Figure 11. Snapshots of micelles formed by $A_{30}B_{30}C_{10}$ terpolymer with aggregation numbers (a) N_{ag} = 20 and (b) N_{ag} = 66 at T^* = 2.0.

to T^* = 2.0 triggers the formation of segmented worm hyperstructures in terpolymers with shorter thermoresponsive block ($A_{30}B_{30}C_{10}$). The comparison of the size of spherical micelles formed by terpolymers with short thermoresponsive length (smaller than the critical length that triggers the formation of segmented worm hyperstructures), e.g., $A_{30}B_{30}C_5$ with the same aggregation number N_{ag} = 20 at temperatures T^* = 2.4 and T^* = 2.0 showed a marginal decrease in the radius of gyration from $\langle R_g^2\rangle$ = 81.5 to $\langle R_g^2\rangle$ = 80.11 respectively. For terpolymers with thermoresponsive block greater than the aforementioned critical length, the differences in the size of micelles are much greater ($A_{30}B_{30}C_{30}$

dx.doi.org/10.1021/ma2025573 | Macromolecules 2012, 45, 2570−2579

in $T^* = 2.4$ has $N_{ag} = 49$, $\langle R_g^2 \rangle = 178$ and $\kappa^2 = 0.07$ while in $T^* = 2.0$ has $N_{ag} = 49$, $\langle R_g^2 \rangle = 159$ and $\kappa^2 = 0.05$) as expected. Hence, one can observe that the micelles obtained in $T^* = 2.0$ are smaller and more spherical.

4. COMPARISON WITH THE EXPERIMENTS

As we have mentioned in the Introduction, the micellization properties of PEO−PnBuA−PNiPAAm terpolymers were studied experimentally by Walther et al.[19] at the solution temperature of 45 °C. At this temperature, water is good solvent for the PEO block and bad solvent for PnBuA and the thermoresponsive PNiPAAm blocks. In all samples PEO blocks contained 114 monomers while the PNiPAAm blocks contained a varying number of monomers equal to 65, 82, 116, 165, 178, 197, and 350. By straightforward calculations we have determined the number of segments and the Kuhn length of PEO block using the characteristic ratio value $C_\infty = 4.055$.[26,27] Similarly we have calculated the number of PNiPAAm segments using the PNiPAAm Kuhn length value of 0.7 nm, obtained from the literature.[28] We found that the terpolymers studied by Walther et al.[19] contained 20 PEO segments having Kuhn length equal to 1.339 nm and 10, 21, 30, 32, 35, and 63 PNiPAAm segments with almost half the Kuhn length. Thus, the experimental terpolymers would be equivalent to our $A_{40}B_xC_{10}$, $A_{40}B_xC_{21}$, $A_{40}B_xC_{30}$, $A_{40}B_xC_{32}$, $A_{40}B_xC_{35}$, and $A_{40}B_xC_{63}$ which contains the longer thermoresponsive block with contour length 1.5 times larger than the respective length of the hydrophilic block. For the $A_{40}B_xC_{10}$ terpolymer they found that the temperature induced aggregation was clearly absent due to long PEO block that sufficiently shielded the collapsed PNiPAAm patches from aggregation. The $A_{40}B_{30}C_{21}$ and $A_{40}B_{30}C_{30}$ formed spherical or elongated sphere aggregates and appeared to have an increased total radius of gyration by 15% in comparison with the one at $T = 25$ °C (good solvent for the thermoresponsive block). For the $A_{40}B_{30}C_{32}$, $A_{40}B_{30}C_{35}$, and $A_{40}B_{30}C_{63}$ terpolymers, with long thermoresponsive block, segmented worm-like hyperstructures were formed. The authors[19] considering the size of the PEO and PNiPAAm monomers instead of the Kuhn lengths concluded that the thermoresponsive block was 3 times longer than the hydrophilic one. Consequently they concluded that Janus type aggregation (with one aggregative thermoresponsive patch) does not take place in the case of thermoresponsive terpolymers because for such long thermoresponsive blocks spherical micelles were not observed (see Figure 6e of ref 29).

Our simulation results for both solution temperatures $T^* = 2.0$ and 2.4 clearly indicate a micelle shape transition from spheres to segmented worms and to spheres again. Our results are in qualitative agreement with the experimental results for ABC miktoarm star terpolymers composed by two hydrophobic (poly(ethylethylene), poly(methylcaprolactone)) and one hydrophilic (poly(ethylene oxide)) branches, studied by Li et al.[20] According to our experience the micelle shape obtained from linear and three arm star copolymers[6,8] (consist of one or two solvophobic blocks) are quite similar, differ in the preferential aggregation number (micelle size). The linear ABC terpolymer contains two successive blocks under bad solvent conditions behave as a linear diblock copolymer with a solvophilic and solvophobic block. Thus, the micellization of linear ABC terpolymers should be similar to respective star ABC terpolymers.

As we have mentioned in the introduction, Li et al.[20] found that when the poly(methylcaprolactone) arm increases, a transition from spherical micelles to segmented worm hyperstructures and back to spherical micelles takes place. Since both experimental systems are very similar in bad solvent conditions we suppose that PEO−PnBuA−PNiPAAm terpolymers with even larger PNiPAAm blocks should form spherical micelles as we found in our simulations. Further experimental studies are needed to clarify this issue.

5. OTHER APPROACHES IN MODELING OF THERMORESPONSIVE POLYMERS

The coil to globule transition of a single PNIPAM homopolymer chain was studied experimentally by laser light scattering techniques in an extremely dilute aqueous solution.[30] The radius of gyration of the PNIPAM chain indicates a sharp coil to globule transition, reaching its fully collapsed globule state before demixing. Our simulations for the coil to globule transition of a single polymer chain, using a typical Lennard-Jones potential predict a gradual shrinking of the polymer chain even after the solution enters inside the binodal region, as shown in Figure 12. Similar results are also obtained by other existing models using the typical Lennard-Jones potential.

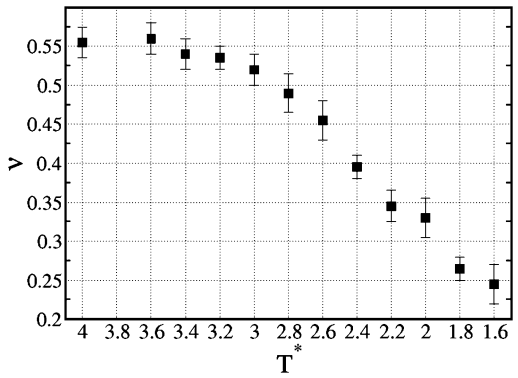


Figure 12. Critical exponent, ν, of the mean radius of gyration ($\langle S^2 \rangle \sim N^{2\nu}$) for a single polymer chain versus the reduced solution temperature, T^*.

Anderson et al.[31] separated thermal effects into kinetic temperature and solvation effects, which has allowed parametrizing of the temperature by a single parameter α in an implicit solvent coarse grained model. The potential used is a modified Lennard-Jones to describe the interactions between units

$$U(r_{ij}) = 4\varepsilon_{ij}\left[\left(\frac{\sigma}{r_{ij}}\right)^{12} - a\left(\frac{\sigma}{r_{ij}}\right)^{6}\right] \quad (6)$$

The parameter α varies between $0 \leq \alpha \leq 1$. This way the variation of the radius of gyration critical exponent ν (Figure 4 of ref 31), for long polymer chains, mimics better the experimental findings (more abrupt coil to globule transition and constant values of ν inside the binodal region) and should be efficient for the study of the thermoresponsive polymers.

6. CONCLUSIONS

The micellization behavior of linear ABC terpolymers containing a solvophobic block in the middle, accompanied by solvophilic and thermoresponsive blocks at the ends, was studied by means of Brownian dynamics simulations. The

dx.doi.org/10.1021/ma2025573 | Macromolecules 2012, 45, 2570−2579

effects of the length of the thermoresponsive moiety on the shape and size of aggregates, formed as the temperature of the solution reduces and solvent progressively becomes bad for the thermoresponsive block, were studied in detail. Analysis of the radius of gyration of the thermoresponsive block of single chain terpolymers revealed the existence of different crossover solution temperatures, $T^* = 2.4$ and $T^* = 2.0$, corresponding to the formation of loose aggregates and regular micelles. At both temperatures, as the length of thermoresponsive block increases, we found a shape transition from spherical to segmented worm-like and back to spherical loose aggregates or micelles.

Our results are in qualitative agreement with the experimental findings on star ABC terpolymers with one hydrophilic and two hydrophobic branches. Walther et al. studied similar linear ABC terpolymers and observed a shape transition of micelles from spherical to segmented worm-like, as the length of thermoresponsive block increases. Our analysis on their terpolymer Kuhn lengths, and our simulation results, may suggest that in order the PEO−PnBuA−PNiPAAm terpolymers to reach the full shape transition from spherical to segmented worm-like and back to spherical micelles, longer thermoresponsive length PNiPAAm blocks are needed.

AUTHOR INFORMATION

Corresponding Author

*E-mail: cvlahos@cc.uoi.gr.

Notes

The authors declare no competing financial interest.

ACKNOWLEDGMENTS

The Research Center for Scientific Simulations (RCSS) of the University of Ioannina is gratefully acknowledged for providing the computer resources used in this work. We thank the reviewer who brought to our notice ref 31.

REFERENCES

(1) Rodriguez-Hernandez, J.; Checot, F.; Gnanou, Y.; Lecommandoux, S. *Prog. Polym. Sci.* **2005**, *30*, 691−724.
(2) Hadjichristidis, N.; Pispas, S.; Floudas, G. Block Copolymers, Synthetic Strategies. In *Physical Properties and Applications*; Wiley-Interscience: Hoboken, NJ, 2003.
(3) Iatrou, H.; Willner, L.; Hadjichristidis, N.; Halperin, A.; Richter, D. *Macromolecules* **1996**, *29*, 581−591.
(4) Mountrichas, G.; Mpiri, M.; Pispas, S. *Macromolecules* **2005**, *38*, 940−947.
(5) Nguyen, P.; Hammond, P. *Langmuir* **2006**, *22*, 7825−7832.
(6) Cheng, L.; Cao, D. *Langmuir* **2009**, *25*, 2749−2756.
(7) Moultos, O.; Gergidis, L. N.; Vlahos, C. *Macromolecules* **2010**, *43*, 6903−6911.
(8) Georgiadis, C.; Moultos, O.; Gergidis, L. N.; Vlahos, C. *Langmuir* **2011**, *27*, 835−842.
(9) Taribagil, R. R.; Hillmyer, M. A.; Lodge, T. P. *Macromolecules* **2010**, *43*, 5396−5404.
(10) Charbonneau, C.; Chassenieux, C.; Colombani, O.; Nicolai, T. *Macromolecules* **2011**, *44*, 4487−4495.
(11) Cui, J.; Jiang, W. *Langmuir* **2010**, *26*, 13672−13676.
(12) Charlaganov, M.; Borisov, O. V.; Leermarkers, F. A. M. *Macromolecules* **2008**, *41*, 3668−3677.
(13) Eisenberg, A.; Yu, G. E. *Macromolecules* **1998**, *31*, 5546−5549.
(14) Berlpsch, H.; Bottcher, C.; Skrabania, K.; Laschewsky, A. *Chem. Commun.* **2009**, 2290−2292.
(15) Zhang, L.; Bernard, J.; Davis, T. P.; Barner-Kowollik, C.; Stenzel, M. H. *Macromol. Rapid Commun.* **2008**, *29*, 123−129.
(16) Gu, J.; Cheng, W. P.; Liu, J.; Lo, S. Y.; Smith, D.; Qu, X.; Yang, Z. *Biomacromolecules* **2008**, *9*, 255−262.
(17) Sfika, V.; Tsitsilianis, C.; Kiriy, A.; Gorodyska, G.; Stamm, M. *Macromolecules* **2004**, *37*, 9551−9560.
(18) Zhao, J.; Zhang, G.; Pispas, S. *J. Polym. Sci., Part A: Polym. Chem* **2009**, *47*, 4099−4110.
(19) Walther, A.; Barner-Kowollik, C.; Müller, A. H. E. *Langmuir* **2010**, *26*, 12237−12246.
(20) Li, Z.; Hillmyer, M. A.; Lodge, T. P. *Langmuir* **2006**, *22*, 9409−9417.
(21) Suek, N.; Lamm, M. *Langmuir* **2008**, *24*, 3030−3036.
(22) Murat, M.; Grest, G. *Macromolecules* **1996**, *29*, 1278−1285.
(23) LAMMPS Molecular Dynamics Simulator http://lammps.sandia.gov. Accessed 11/2011.
(24) Plimpton, S. J. *Comput. Phys.* **1995**, *117*, 1−19.
(25) Yan, J.; Ji, W.; Chen, E.; Li, Z.; Liang, D. *Macromolecules* **2008**, *41*, 4908−4913.
(26) Zhang, W.; Zou, S.; Wang, C.; Zhang, X. *J. Phys. Chem. B* **2000**, *104*, 10258−10264.
(27) Lee, H.; Venable, R. M.; MacKerell, A. D. Jr.; Pastor, R. W. *Biophys. J.* **2008**, *95*, 1590−1599.
(28) Rodd, L. E.; Scott, T. P.; Cooper-White, J. J.; McKinley, G. H. *Appl. Rheol.* **2005**, *15*, 12−27.
(29) Sheng, Y.-J.; Nung, C.-H.; Tsao, H.-K. *J. Phys. Chem. B* **2006**, *110*, 21643−21650.
(30) Wang, X.; Qiu, X.; Wu, C. *Macromolecules* **1998**, *31*, 2972−2976.
(31) Anderson, A. J.; Travesset, A. *Macromolecules* **2006**, *39*, 5143−5151.

Macromolecules

Article

pubs.acs.org/Macromolecules

Stretching of Free Chains Confined in Concave Brush-Coated Nanocylinders

Rong Wang,[†,‡] Sergei A. Egorov,[†,§] Andrey Milchev,*[,†,⊥] and Kurt Binder[†]

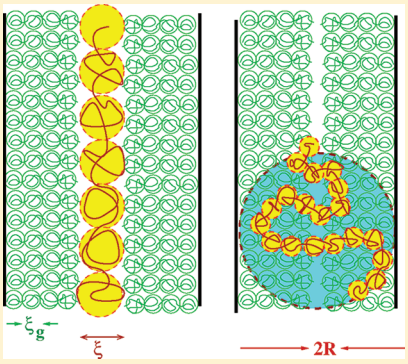
[†]Institut für Physik, Johannes Gutenberg-Universität Mainz, Staudinger Weg 7, D-55099 Mainz, Germany

[‡]Department of Polymer Science and Engineering, State Key Laboratory of Coordination Chemistry, Nanjing National Laboratory of Microstructures, School of Chemistry and Chemical Engineering, Nanjing University, Nanjing 210093, China

[§]Department of Chemistry, University of Virginia, Charlottesville, Virginia 22901, United States

[⊥]Institute of Physical Chemistry, Bulgarian Academy of Sciences, 1113 Sofia, Bulgaria

ABSTRACT: The structure of a free flexible macromolecule confined in a cylindrical nanopore whose wall is coated by a polymer brush is studied by Monte Carlo simulation, varying the grafting density as well as the radius of the cylindrical pore. Because of this confinement, the free chain is stretched in axial direction; while for small grafting densities of the brush the end-to-end distance increases monotonously with decreasing pore radius, a nonmonotonic variation occurs for larger grafting densities. We show that this effect is due to strong interpenetration of the free chain and the brush chains; for very narrow pores a strong layering of cylindrical shells is found, and comparison with self-consistent field calculations (SCF) shows that the latter can predict the nonmonotonic variation in qualitative accord with the simulation. The robustness of the SCF approach is then used to demonstrate the occurrence of the observed "*penetration transition*" in a broader range of chain lengths and grafting densities.



I. INTRODUCTION

Polymer brushes[1−7] are formed by grafting flexible macromolecules via a special end group on a nonadsorbing substrate surface, covering this substrate by a dense layer of chains stretched away from the substrate (under good solvent conditions). The thickness of these soft layers can be controlled by various external stimuli (temperature, pH-value of the solution, etc.) and polymer brushes on flat substrates allow numerous applications[8−11] and have been studied extensively (see, e.g., refs 11 and 12 for recent reviews).

Recently also brushes on concave surfaces in cylindrical surfaces have been considered[13−20] since such systems can possibly be used to control flow in nanocylindric channels,[21−25] to modify electroosmotic flow,[26,27] control transport of macromolecules through nanopores,[28−32] and to allow applications such as reversed phase[33] and size-exclusion[34,35] chromatography. Also in a biological context (biopolymer translocation through pores[36]) applications are conceivable.

While macromolecules confined in cylinders with bare repulsive walls have been considered for a long time,[37−44] the behavior of a macromolecule inside a brush-coated cylindrical pore has only been considered very recently.[20] Results obtained with self-consistent mean field (SCFT) calculations suggested a nonmonotonic dependence of the end-to-end distance of the confined macromolecule with the pore radius. This is in contrast to the behavior of polymers confined in tubes with bare repulsive walls where the variation is monotonic. Since the accuracy of mean field methods is doubtful in such a context (note also that the predicted minimum of the end-to-end distance occurs at a radius of about three lattice spacings of the SCFT scheme used[20]), it is rather desirable to clarify whether such nonmonotonic behavior also occurs, when one goes beyond mean field theory, and uses off-lattice models. Such a task can be performed by Monte Carlo simulation, as done in the present paper. Of course, the delicate structural changes of the macromolecule confined in such a cylindrical brush-coated pore have important implications on the transport of the polymer through the pore, but this latter problem will not be considered here. In section II, we describe the model that we study, and briefly comment on our simulation methods. Section III describes our simulation results, and section IV discusses the comparison with the SCFT results. Section V then summarizes our conclusions.

II. MODEL AND SIMULATION METHOD

We choose a cylinder with radius R and axial length L, orienting the cylinder axis along the z-direction, and applying periodic boundary conditions in the z-direction. The interaction between the wall and an effective monomer (irrespective of whether it belongs to the free chain or the grafted chains) is chosen to be purely repulsive, $U_w(r') = \varepsilon_w r'^{-9}$, where $r' = R - r$, $\varepsilon_w = 0.1$, r being the radial coordinate relative to the cylinder axis. In order to realize the conditions that the first monomer of

Received: December 3, 2011
Revised: February 4, 2012
Published: February 27, 2012

 © 2012 American Chemical Society dx.doi.org/10.1021/ma202620z | *Macromolecules* 2012, 45, 2580−2587

each grafted chain is tightly bound to the grafting surface, we choose a different potential for the first monomer, namely

$$U_{w,1}(r') = \varepsilon_w(r'^{-9} - fr'^{-9}), \quad f = 100 \tag{1}$$

We recall that the motivation for the choice of this particular form of the potential is the assumption of Lennard-Jones (6/12) interactions between any atom in the solid forming the wall and the effective monomers; integrating then these interactions over a (semi-infinite) half-space with a free (flat) surface, an interaction of the form eq 1 results. However, if one took such an argument literally, for the curved surface of a nanopore the actual potential clearly would be R-dependent. This complication is disregarded here, and we take eq 1 just as a generic model assumption, since we do not wish to address a specific system.

As is usually done, the arrangement of grafting sites is not chosen at random, but according to a regular pattern. The interaction between any pairs of monomers is chosen as a truncated and shifted Lennard-Jones (LJ) potential, while bonded monomers interact also with the standard FENE ("finitely extensible nonlinear elastic") potential. Thus, our potentials are of the same type as are standard for molecular dynamics simulations of polymer brushes.[5,12]

Specifically, we use

$$U_{LJ}(r) = \begin{cases} 4\varepsilon[(\sigma_{LJ}/r)^{12} - (\sigma_{LJ}/r)^6] + C, \\ \quad r < r_c = 2.2^{1/6}\sigma_{LJ} \\ 0, \quad r > r_c \end{cases} \tag{2}$$

Here $r = |\vec{r}_i - \vec{r}_j|$ is the distance between beads at positions $\vec{r}_i$ and $\vec{r}_j$. The constant C is chosen such that the potential $U_{LJ}(r)$ is continuous at the cutoff distance r_c. We use the LJ diameter $\sigma_{LJ} = 1$ as our length unit throughout. Similarly, we also take $\varepsilon = 1$ and Boltzmann's constant $k_B = 1$. The spring potential between two neighboring monomers then is

$$U_{FENE}(r) = \begin{cases} -\frac{1}{2}kr_0^2 \ln[1 - (r/r_0)^2], & r \le r_0 \\ \infty, & r > r_0 \end{cases} \tag{3}$$

with the usual choice $r_0 = 1.5$, $k = 20$. Remember that the total potential between two neighboring beads, $U_{LJ}(r) + U_{FENE}(r)$, has a minimum at $r_{min}^{(b)} \approx 0.96$, while the minimum of the LJ potential (acting between nonbonded monomers) occurs at $r_{min}^{(nb)} = 2^{1/6} \approx 1.12$. Because of this mismatch between $r_{min}^{(b)}$ and $r_{min}^{(nb)}$, this model has little tendency to form regularly ordered (crystalline) arrangements of the monomers at high density and/or low temperatures, respectively. In the present work, however, we wish to investigate the properties of the system only in the good solvent regime. Since for this model the Θ-temperature has been estimated to occur at $\Theta \approx 3.3$,[45,46] we work at $T = 4.0$, a case for which brush properties at flat substrates has already been studied.[47]

The simulations were carried out with standard Monte Carlo methods[48] but adopting several kinds of moves:[49] Local moves are done by choosing a position in the neighborhood. This neighborhood is a cube of linear dimension δ centered around the previous position of the chosen monomer. The magnitude of δ is chosen such that the average acceptance rate is close to 50%. For the grafted chains, also pivot rotations around the y-axis (an axis that is perpendicular to the grafting wall and goes through the position of a randomly chosen monomer i of a randomly chosen brush chain) are attempted. Choosing an angle φ uniformly distributed between 0 and 2π, the outer part of the grafted chain (i.e., the part of the chain from monomer i to N, if one labels the monomers consecutively from the grafted monomer to the free chain end) is rotated around this z-axis like a rigid object.[43,49] Of course, any such Monte Carlo move is only accepted if the standard Metropolis test is passed.[48,49] For the free chain, standard slithering snake moves are performed,[49] while no pivot moves were then attempted. Only a single choice of chain lengths is studied ($N = 8$ for the grafted chains, $N_f = 50$ for the free chains), which corresponds to the choice made in the previous[20] self-consistent field calculations. Of course, these chain lengths are extremely short, but one must consider that every bead of the simulated chains corresponds to $n \approx 3-5$ chemical monomers of a real polymer.[49] In our simulations, N local move attempts of a grafted chain are followed by 100 pivot move attempts, and one reptation move attempt is followed by N_f local move attempts for the free chain. We refer to this sequence of moves as "one Monte Carlo step". Typically 10^7 MCS were performed, and the first half of the run (5×10^6 MCS) is omitted to avoid any influence of the initial configuration.

III. SIMULATION RESULTS

We consider free chains with chain length $N_f = 50$ in brush-coated nanocylinders (choosing $N = 8$ for the brush chains) as a function of the pore radius R, for the four grafting densities $\sigma = 0.05$, 0.08, 0.10, and 0.12. The length of the cylinder then was chosen (remember that we work with a regular arrangement of grafting sites) $L = 35.77$, 38.89, 37.95, and 37.53, respectively. Here and in what follows, the monomer concentration in the tube is taken as particle number density.

Figure 1 presents the end-to-end distance of the free chain along the cylindrical axis as a function of the cylinder radius for

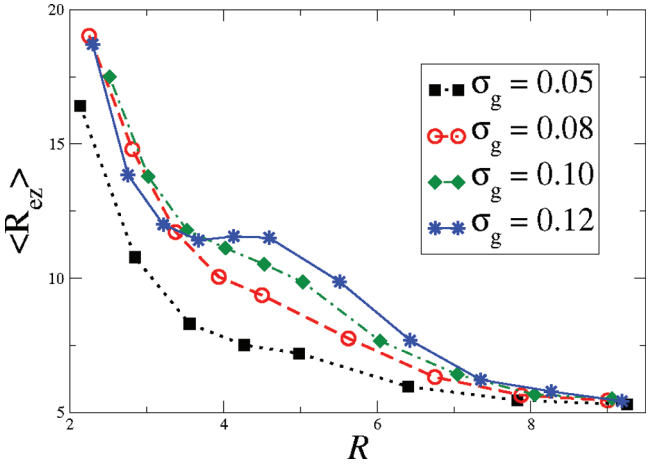


Figure 1. End to end distance of the free chain along the cylinder axis as a function of the cylinder radius R, for four grafting densities, as indicated.

the grafting densities that were studied. One can see that the end-to-end distance is almost constant when R is large. When the cylinder radius R decreases, the end-to-end distance of the free chain starts to increase, i.e. the chain stretches out along the cylinder axis. For the two smallest grafting densities ($\sigma = 0.05$ and 0.08) the variation of $\langle R_{ez} \rangle$ with R is monotonic, while for $\sigma = 0.10$ a flat plateau near $R = 4$ starts to develop, and for

dx.doi.org/10.1021/ma202620z | Macromolecules 2012, 45, 2580–2587

still larger σ (such as $\sigma = 0.12$) the variation is nonmonotonic. Note that the average end-to-end distance $\langle R_{ez} \rangle$ always is much smaller than the chosen cylinder length L, so there are no finite size effects due to the finite value of L to be expected.

Qualitatively, such a nonmonotonic variation of the end-to-end distance with the cylinder radius was predicted by self-consistent field calculations,[20] and hence, we confirm this result. The interpretation that can be given[20] is that for small grafting densities the grafted chains form a rather dense polymer layer at the cylinder wall, but near the cylinder axis there is a cylindrical region effectively free from the monomers of the grafted chains. The free chain then occupies the region of this inner cylinder, in which significant overlap with the monomers of the grafted chains can be avoided. The free chain then forms a rather long string of blobs in this region of the inner cylinder. However, when the cylinder radius is still smaller, the region near the cylinder axis then is also occupied by monomers of the grafted chains. Then there is no possibility for the free chain to avoid overlap with the grafted chains; and if the monomers of the grafted chains fill the cylinder more or less uniformly,[16,17] for entropic reasons it becomes advantageous for the free chain to form a string of blobs which have a radius comparable to the full cylinder radius. One might call appropriately the observed phenomenon, which is driven by osmotic pressure inside the brush coating, a *penetration transition*, given its universality and similarity to other cases of parameter-driven configurational changes in polymers. Indeed, one deals here with a *reversible* transformation in equilibrium that comes about due to free energy minimization. One should note, however, that this is a gradual rather than an abrupt transition and is, therefore, not a genuine "phase transition" in the sense of thermodynamics.

Regarding our methods of investigation, one should be aware that the self-consistent field results[20] may suffer from the mean field approximation inherent in the theory, and moreover, they were based on a rather crude discretization (using a lattice spacing of unity even though cylinder radii down to $R = 2$ were considered). Thus, it is of significant interest that the present off-lattice Monte Carlo simulations confirm this finding.

An advantage of the simulation, of course, is that very detailed information on the chain conformations can be extracted. Figure 2 therefore correlates typical snapshot pictures of the chain conformation at various conditions with the behavior of the end-to-end distance. Compare, e.g., the snapshots at $R = 3.6$ and $R = 6.4$: The projections on the *xy*-plane are rather similar in both cases, filling an almost circular region of a diameter of about 6. For the smaller value of R, this diameter is almost as large as $2R$, i.e., the free chain occupies space everywhere in the tube, while for the large value of R, D is much less than $2R$, so indeed the chain then avoids overlap with the brush chains to a large extent. For the largest value of R, the *xz*- and *xy*-projections of the free chain are already rather similar: now there is so much space available that the anisotropy of the conformation gets greatly reduced, and a crossover to the structure of a free unconfined chain in a solution occurs. In the regime of intermediate R, where the end-to-end distance depends most strongly on the grafting density, one notes also a corresponding effect on the radial distribution (Figure 3).

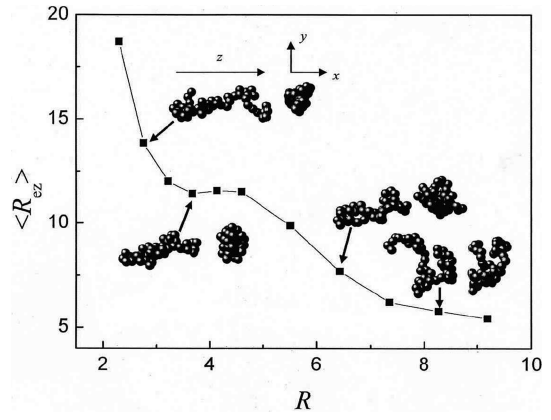


Figure 2. End to end distance of the free chain plotted vs R for $\sigma = 0.12$. The insert snapshots show typical conformations of the free chain showing projections on the *xz*-plane containing hence the axis of the cylinder (left) and on the perpendicular *xy*-plane (right).

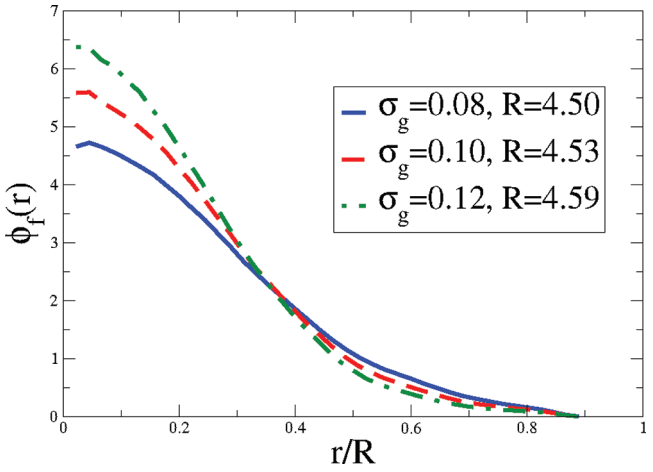


Figure 3. Radial distribution function $\phi_f(r)$ vs r/R of the free chain in the brush coated cylinder at three grafting densities for comparable values of R (the values of R slightly differ because of the requirement of putting a regular arrangement of grafting sites on the cylindrical surface at given grafting density). Note that with increasing σ the half width of the distributions decrease, consistent with the increase of $\langle R_{ez} \rangle$. The normalization has been chosen as $\pi \int_0^R \phi_f(r) r \, dr \, N_f = 50$.

A subtle aspect of the behavior shown in Figures 1, 2 is the fact that the total monomer concentration (that is, the number of particles per unit volume) in the cylinder varies from almost dilute ($c = 0.1$) to melt conditions ($c = 1.0$), see Figure 4. So, while for large R (where the concentration is small) the free chain will almost exhibit self-avoiding walk statistics ($\langle R_{ez} \rangle \propto N_f^{\nu}$ with $\nu \approx {}^3/_5$), for small R all correlations due to excluded volume are screened, and instead the monomers of the free chain and of the grafted chains are expected to share the available volume, as it happens in a typical polymer melt. However, the dense packing of monomers will lead to a considerable slowing down of the chain motions, and ultimately glassy freezing in of the free chain in the brush may be expected. However, molecular dynamics methods[16−18] would be more appropriate to study such aspects of the problem than Monte Carlo simulation, and hence we do not elaborate on this aspect further here.

To study the interpenetration of the free chain and the brush chains in more detail, we focus on the radial density profiles of the monomers (Figure 5). When the radius of the cylinder is very small, such as $R = 2.76$, the grafted chains show a very pronounced layering effect: actually there occur then three

dx.doi.org/10.1021/ma202620z | *Macromolecules* 2012, 45, 2580−2587

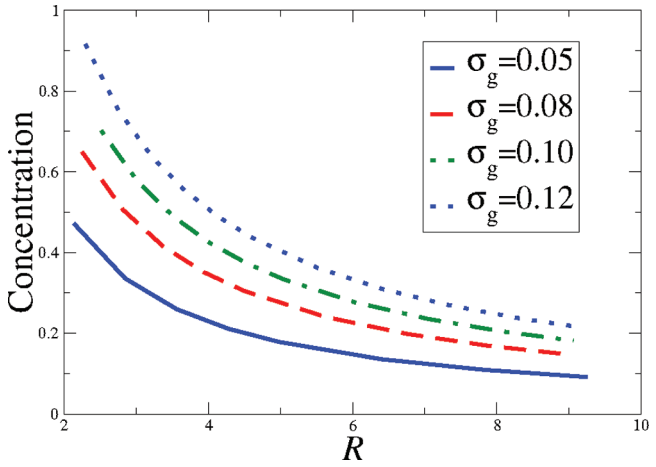


Figure 4. Total monomer concentration of the model (grafted chains plus one free chain) as a function of the cylinder radius R for the different grafting densities σ_g studied, as indicated. Here the concentration is normalized on the number of monomers per unit volume in the pore (remember the choice of length with $\sigma_{LJ} = 1$ for this model).

pronounced density maxima, for $r = 0$ (the cylinder axis), near $r = 1$ and near $r = 2$, respectively. It is remarkable that also the density distribution of the monomers of the free chain exhibits peaks at the same locations: the monomers of the free chain are incorporated into the layered structure enforced by this strong cylindrical confinement in a "democratic" fashion, together with the monomers of the grafted chains. For $R = 3.68$, on the other hand, the density distribution of the grafted monomers near the cylinder axis is almost flat, the maxima at $r = 0$ and near $r = 1$ are no longer clearly distinguished, while near $r = 2$ and $r = 3$ well-developed peaks do occur. $\phi_f(r)$ now is clearly largest in the center, although it still extends throughout the pore. For $R = 4.59$, however, $\phi_f(r \geq 2.5) \approx 0$, and while there is still considerable overlap of $\phi_f(r)$ with $\phi(r)$, the free chain now is confined near the cylinder axis.This segregation continues for larger R: even for $R = 8.27$ the monomer density of the grafted chains exhibits two pronounced layering peaks close to the wall, but only in an intermediate regime of r, $3 \leq r \leq 4$, there is still a bit of overlap between $\phi_g(r)$ and $\phi_f(r)$.

To quantify the overlap, we define the quantity

$$\varphi_{fg} = \int_0^\infty \varphi_g(r)\varphi_f(r) r\, dr / \int_0^\infty \varphi_f(r) r\, dr \quad (4)$$

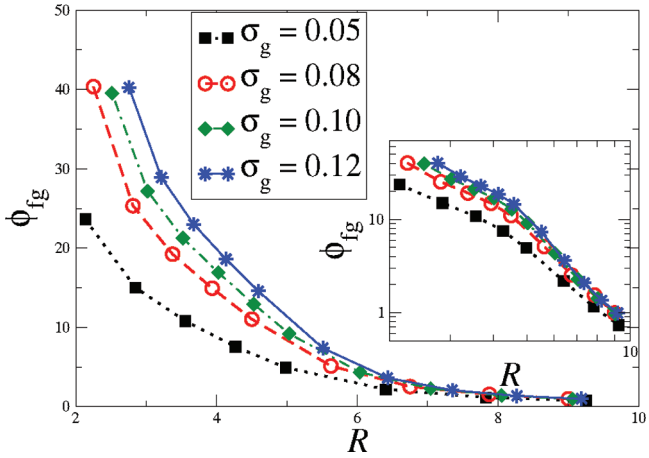


Figure 6. Overlap ϕ_{fg} between the monomer density distributions of the free chain and the grafted chains plotted vs R for several choices of σ_g, as indicated. Inset shows the same data on a log–log plot.

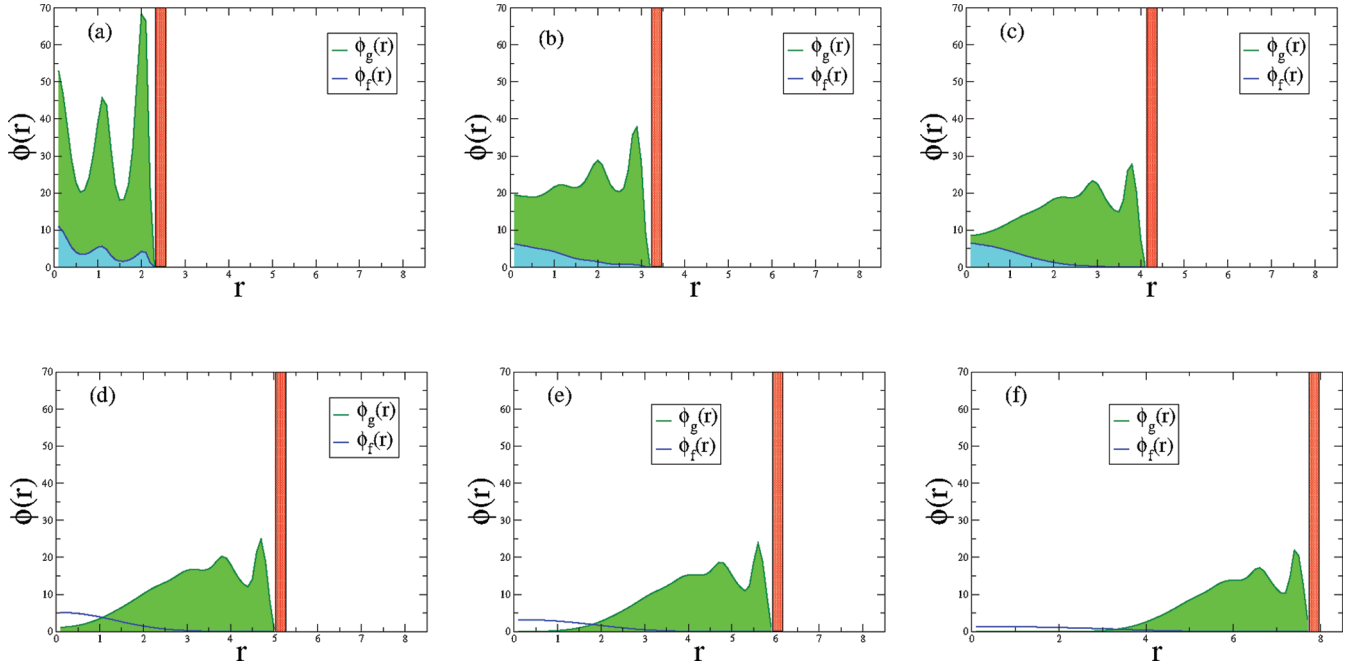


Figure 5. Radial density distribution of the monomers of the grafted chains $\phi_g(r)$, and of the free chain $\phi_f(r)$, plotted as a function of the distance r from the cylinder axis at grafting density $\sigma = 0.12$ and various choices of R: $R = 2.76$ (a), 3.68 (b), 4.59 (c), 5.51 (d), 6.43 (e) and 8.27 (f). The tube wall is also indicated. Note that normalizations have been chosen such that $2\pi\int_0^R \phi_g(r) r\, dr = N_g$, the total number of monomers in grafted chains in the system, and $2\pi\int_0^R \phi_f(r) r\, dr = N_f = 50$, the total number of monomers in the free chain.

dx.doi.org/10.1021/ma202620z | Macromolecules 2012, 45, 2580–2587

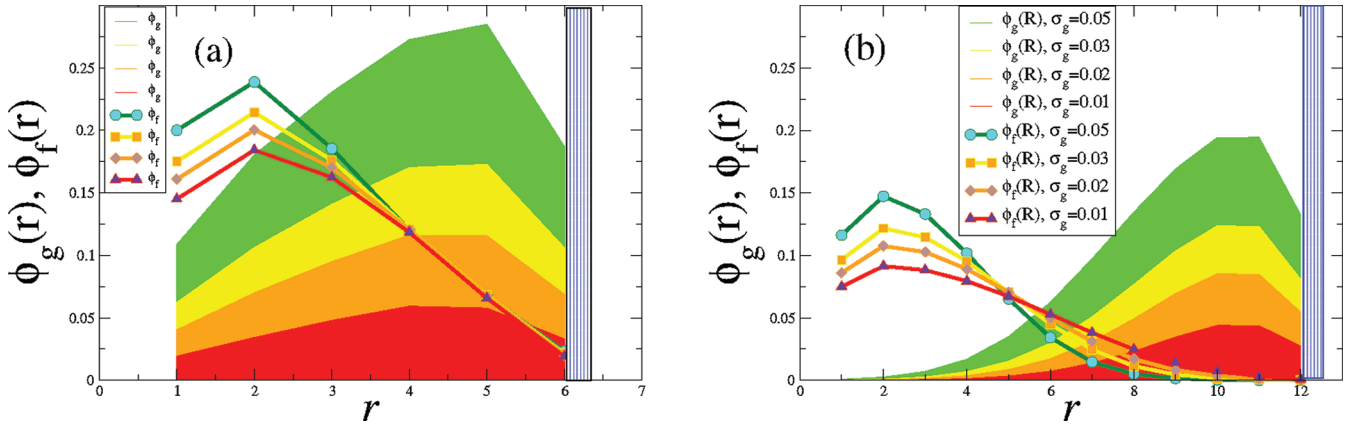


Figure 7. Monomer radial density profiles $\rho_g(r)$ and $\rho_f(r)$ of grafted (g) and free (f) chains for the case $N_f = 200$, $N = 16$, $R = 6$ (a), and $R = 12$ (b). In each case, four grafting densities are shown, $\sigma_g = 0.01$, 0.02, 0.03, and 0.05, as indicated in part a. Note that densities are defined at integer values of r only, and the boundary condition at $r = 0$, $n_g(0) = n_f(0) = 0$ has the consequence that the maximum of $\rho_f(r)$ occurs at $r = 2$ rather than at $r = 1$ (in contrast to what one expects from the continuum calculations, cf. Figure 3 and 5). Straight lines connecting points at integer values of r are guides to the eye only. Vertical bars beyond $R = 12$ (a) and $R = 6$ (b) indicate the confining cylindrical wall.

This quantity is plotted in Figure 6.[50] Again the behavior of the overlap indicates clearly two regimes with different slopes on the log–log plot, as in ref 20.

IV. COMPARISON WITH SELF-CONSISTENT FIELD RESULTS

The advantage of the self-consistent field theory (SCFT) is that it easily allows a generalization to longer chain lengths of both grafted chains (N) and of free chains (N_f), which would be more difficult to consider via Monte Carlo simulation. On the other hand, there are two approximations made, namely (i) the mean-field approximation inherent in all formulations of SCFT[3,51] (ii) The spatial discretization in terms of a cylindrical lattice. The latter leads to a somewhat different normalization of local densities than in the continuum, which we discuss first.

In the continuum, the grafted chains are localized in a volume $V_g = \pi R^2 L$, and the total number of monomers of grafted chains in the system is $\mathcal{N}_g = 2\pi RL\sigma_g N$, remembering that the grafting density σ_g refers to the surface $2\pi RL$ of the confining cylinder. The average monomer density due to grafted chains in the cylinders is

$$\bar{\rho}_g = \mathcal{N}_g/V_g = 2\sigma N/R \tag{5}$$

Introducing then a local density $\rho_g(r,z)$ per unit volume (z is the coordinate along the cylinder axis) we also have

$$\bar{\rho}_g = V_g^{-1} 2\pi \int_0^R r\,\mathrm{d}r \int_0^L \mathrm{d}z\, \rho_g(r,z) \approx (2/R^2) \int_0^R \rho_g(r) r\,\mathrm{d}r \tag{6}$$

where in the last step we have assumed that $\rho_g(r,z)$ is independent of z, $\rho_g(r,z) \approx \rho_g(r)$, even if a free chain is present in part of the cylinder. The free chain is present only in a piece of the cylinder of length R_{ez} with $V_f = \pi R^2 R_{ez}$, R_{ez} being the end-to-end distance of the chain, from $z = z_1$ to $z = z_1 + R_{ez}$. In this region, we have an average density of monomers of the free chain given by

$$\bar{\rho}_f = N_f/(\pi R^2 R_{ez}) \tag{7}$$

which alternatively can be written as an average over the local density $\rho_f(r,z)$

$$\bar{\rho}_f = V_f^{-1} 2\pi \int_{z_1}^{z_1+R_{ez}} \mathrm{d}z \int_0^R \rho_f(z,r) r\,\mathrm{d}r \approx \frac{2}{R^2} \int_0^R \rho_f(r) r\,\mathrm{d}r \tag{8}$$

Here again the approximation is made that $\rho_f(z,r)$ does not depend on z, in the regime $z_1 \le z \le z_1 + R_{ez}$, while outside of this regime $\rho_f(z,r) = 0$, of course. This approximation is certainly doubtful near the chain ends of the free chain, of course, but then $\rho_f(r)$ still can be interpreted as an average along z, $R_{ez}^{-1} \int_{z1}^{z1+Rez} \mathrm{d}z\, \rho_f(r,z)$. In fact, data shown in Figures 3 and 5 have to be understood in this way. With these normalizations, $\rho_g(r)$ and $\rho_f(r)$ can be compared on an absolute scale, denoting both numbers of monomeric units per volume element.

These considerations can be carried over the SCFT treatment, where one introduces planes equidistant perpendicular to the z-axis ($\Delta z = 1$), and in each plane one has concentric circles around the z-axis, with radii $r = 1, 2, 3, R$.[52] The number of occupied sites at each circle (integrated over z) is defined as $2\pi n(r)$. Thus, the total number of monomers due to grafted chains in the system is

$$\mathcal{N}_g = 2\pi \sum_{r=1}^{R} n_g(r) = 2\pi RL\sigma_g N \tag{9}$$

and hence the local density of monomers from grafted chains and per length Δl=1 along the circle of radius r and per $\Delta z = 1$ simply is

$$\rho_g(r) = n_g(r)/(rL) \tag{10}$$

since the area of the cylinder surface at radius r is $2\pi rL$ (and the factor 2π has been written explicitly in eq 9. The density $\rho_g(r)$ of eq 10 becomes identical to $\rho_g(r)$ as used in eq 6 in the continuum limit (when $r \gg \Delta r = 1$ and $z \gg \Delta z = 1$ is considered).

dx.doi.org/10.1021/ma202620z | Macromolecules 2012, 45, 2580–2587

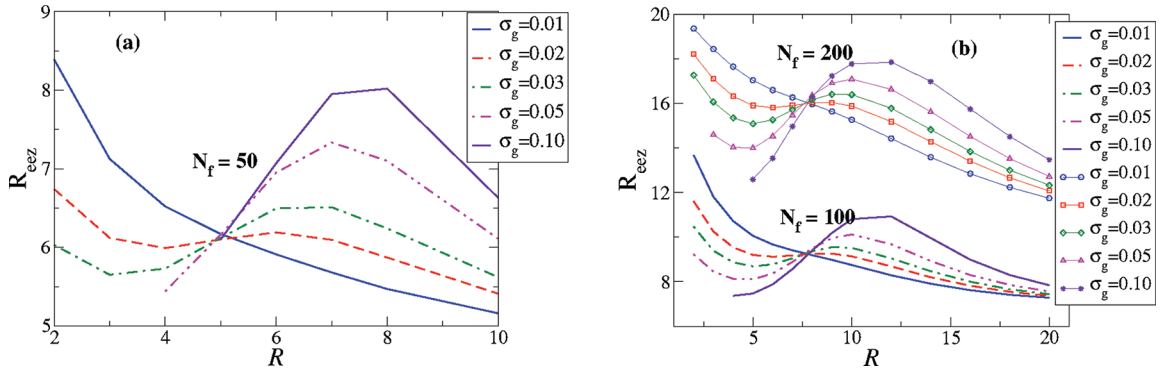


Figure 8. SCFT results for the end-to-end distance $\langle R_{ez}\rangle$ of a free chain along the cylinder axis plotted vs the cylinder radius R, for several grafting densities (as indicated) and the cases (a) $N = 8$, $N_f = 50$, and (b) $N = 16$, $N_f = 100$, and $N_f = 200$. A single intersection point is observed at $R^{is} \approx 5.01R$ (a), and $R^{is} \approx 7.74R$ (b).

For the free chains, we have analogously

$$\mathcal{N}_f = 2\pi \sum_{r=1}^{R} n_f(r),\ \rho_f(r) = n_f(r)/(rR_{ez}) \tag{11}$$

While along the z-axis monomers of grafted chains occur over the full length L, monomers of the free chain occur only over a distance R_{ez}, the end-to-end distance in z-direction. Equation 11 directly corresponds to $\rho_f(r)$ as considered in the continuum theory (eq 8).

Now SCFT provides a numerical recursion scheme,[20,52] from which $n_g(r,z)$, $n_f(r,z)$, the corresponding monomer numbers on a circle at radius r in plane z, can be constructed.[20,52] Of course, one has the sum rules $n_f(r) = \sum_z n_f(r,z)$ and $n_g(r) = \sum_z n_g(r,z)$. Indeed the calculation shows that the z-dependence of $n_g(r,z)$ can be neglected completely, and also the z-dependence of $n_f(r,z)$ is not important in the regime of z in between the two chain ends, as assumed above. Figure 7 shows typical results for $\rho_g(r)$ and $\rho_f(r)$ as obtained from the SCFT calculations. Recall that in this figure the normalization of densities is such that $\rho_g(r) + \rho_f(r) = \rho_{tot}(r)$, so one sees that in the case of strong interpenetration ($R = 6$, Figure 7b) the total density $\rho_{tot}(r)$ varies less than the individual contributions $\rho_g(r)$, $\rho_f(r)$, and reaches a broad maximum ($\rho_{tot}^{max} \approx 0.4$) in between $r = 2$ and $r = 4$. Note that $\rho_f(r \geq 3)$ is almost independent of σ_g: it would cost too much entropy for the free chain to use only the space close to the cylinder axis, and hence interpenetration between the brush and the free chain is inevitable. For $R = 12$, on the other hand, grafted chains do not extend toward the region of the cylinder axis. Of course, the lattice SCFT model cannot reveal details of the simulation of the continuum model, such as the pronounced layering of the local density (Figure 5). But the bonus of the lattice SCFT model is that much longer chains can be handled, and a comprehensive variation of parameters is much easier. Thus, we can make sure that the nonmonotonic variation of $\langle R_{ez}\rangle$ with R (for large enough grafting densities) is a generic effect; see Figure 8. Note that in Figure 8 data are only available at integer R (highlighted by points which are connected by straight lines to guide the eye). Because of this discretization, we cannot say with certainty whether or not SCFT strictly predicts a unique intersection point for different σ_g (as the curves seem to suggest). At present, we are not aware of a convincing theoretical argument as to why such a single intersection point should exist either. In any case, the location of this apparent intersection can be taken as an estimate for the location of the "penetration transition" where the blobs of the free chain penetrate into the brush.

Finally, Figure 9 presents a log–log plot of the overlap (defined in analogy to eq 4) vs R. Note that for a given choice

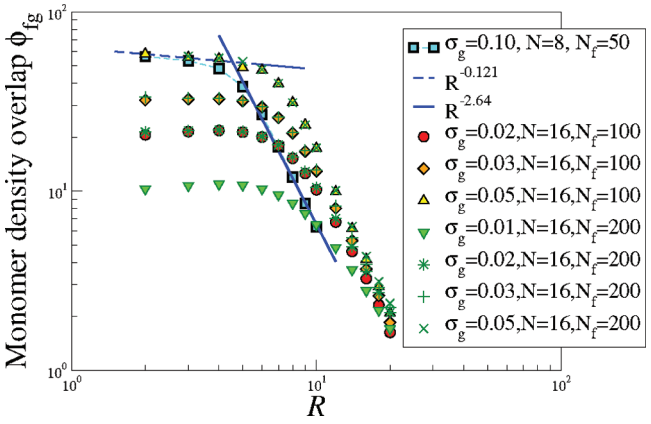


Figure 9. Overlap ϕ_{fg} (eq 4) between the density profiles of free and grafted chains, shown as log–log plot vs R. Various choices of N, N_f, and σ_g are included.

of σ_g and N it does not matter how large N_f is chosen: if we take $N_f = 200$ instead of $N_f = 100$, R_{ez} is twice as large, of course. But $\rho_f(r)$ does not change, due to the homogeneity of $\rho_f(r,z)$ with respect to z (in the regime $z_1 \leq z \leq z_{Nf} = z_1 + R_{ez}$). Thus, such data sets superimpose precisely. We also very clearly recognize that there always occur two regimes: (i) a regime of significant overlap, almost independent of R. The value of the overlap in this regime is roughly proportional to σ_g, while (ii) for large R, where the overlap is small, the overlap is almost independent of σ_g. The overlap for large R decays with an apparent power law, but we do not have a theoretical explanation for this behavior. The value of R where the onset of this power law occurs roughly agrees with the position where the R_{ez} vs R curves for different σ_g intersect. This crossover occurs at larger R when N increases but does not depend on N_f.

V. CONCLUSIONS

In this paper, the conformation of flexible polymer chains confined in nanotubes coated with polymer brushes formed from very short chains has been studied by Monte Carlo simulations and by numerical lattice SCFT calculations. We have shown that there is a delicate interplay between a possible

dx.doi.org/10.1021/ma202620z | Macromolecules 2012, 45, 2580–2587

interpenetration of the free chain with the brush chains and the axial stretching of the free chains, for the case of good solvent conditions that is studied throughout. For very narrow nanotubes, the monomers arrange in the tube in concentric cylindrical shells, reminiscent of the layering of particles in dense fluids adjacent to hard walls; these shells are shared by monomers of the free and grafted chains. This layering effect can be described by off-lattice models. The lattice SCF theory (or other lattice models where polymers are described by self-avoiding walks on the simple cubic lattice) is not suited for a description of this effect. However, the SCFT calculations provide a rather reliable description for the dependence of the end-to-end distance of the free chains and the overlap between free and grafted chains. As the radius of the nanotube decreases, first the free chain gets more and more stretched. Then a 'penetration' transition takes place when the free energy cost of further confinement gets too unfavorable in comparison with the free energy cost of the strong interpenetration.

In our previous work,[20] we have interpreted this effect qualitatively in terms of a blob picture, however, one should not take the blob picture too seriously. One can see from the present numerical results, that the overlap between free and grafted chains starts already when the free chain is only weakly confined and its conformation is only weakly perturbed, cf. Figure 2, in comparison with the conformation of a free chain in solution. The snapshot pictures shown in Figure 2 clearly indicate that one must not take the description of confined polymers in terms of linear cigar-like strings of blobs literally. Also the numerical lattice SCFT results presented in section IV demonstrates that the behavior of the system changes rather gradually when parameters such as pore diameter, grafting density, chain length of the grafted chains, etc. are varied, even though this method does not give as many details on the chain conformation as the simulation.

Of course, there are still open questions regarding the possible effects of solvent quality variation, chemical mismatch between the grafted and free chains, chain stiffness, etc. The dynamics of the confined free chain is a problem that could be of interest for applications too. Therefore, we hope that the present work will stimulate further research in this area.

AUTHOR INFORMATION

Notes

The authors declare no competing financial interest.

ACKNOWLEDGMENTS

R.W. and S.A.E. acknowledge partial support both by the Alexander von Humboldt foundation and by the Deutsche Forschungsgemeinschaft (DFG) under grant No SFB625/A3. A.M. and K.B. acknowledge the support from the DFG under Grant No. Bi 314/23. S.A.E is grateful to Prof. F. Leermakers for his sharing and help with using the software package *sfbox* which was employed for the calculations presented in section IV. R.W. is indebted to Dr. P. Virnau and Dr. H.-P. Hsu for useful discussions, and thanks the National Natural Science Foundation of China (Grant Nos 20874046, 21074053) and National Basic Research Program of China (Grant No 2010CB923303) for financial support and thanks to the Institut für Physik at the Johannes Gutenberg Universität Mainz for its hospitality.

REFERENCES

(1) Alexander, S. *J. Phys. (Paris)* **1977**, *38*, 983.
(2) De Gennes, P. G. *Macromolecules* **1980**, *13*, 1069.
(3) Milner, S. T. *Science* **1991**, *251*, 905.
(4) Halperin, A.; Tirrell, M.; Lodge, T. P. *Adv. Polym. Sci.* **1992**, *100*, 33.
(5) Grest, G. S.; Murat, M. In *Monte Carlo and Molecular Dynamics Simulations in Polymer Science*; Binder, K., Ed.; Oxford Univ. Press: New York, 2005.
(6) Szleifer, I.; Carignano, M. A. *Adv. Chem. Phys.* **1996**, *94*, 165.
(7) Leger, L.; Raphael, E.; Hervet, H. *Adv. Polym. Sci.* **1999**, *138*, 185.
(8) Napper., D. H,. *Polymeric Stabilization of Colloidal Dispersions*; Academic: London, 1983.
(9) Klein, J. *Annu. Rev. Mater. Sci.* **1996**, *26*, 581.
(10) Mansky, P.; Liu, Y.; Huang, T. P.; Russell, T. P.; Hawker, C. *Science* **1997**, *275*, 1485.
(11) Advincula, R. C.; Brittain, W. J.; Caster, K. C.; Rühe, J. (Eds.) *Polymer Brushes*: Wiley-VCH: Weinheim, Germany, 2004.
(12) Binder, K.; Kreer, T.; Milchev, A. *Soft Matter* **2011**, *7*, 7159.
(13) Sevick, E. M. *Macromolecules* **1996**, *29*, 6952.
(14) Manghi, M.; Aubouy, M.; Gay, C.; Ligoure, C. *Eur. Phys. J. E., Soft Matter, Biol. Phys.* **2001**, *5*, 519.
(15) (a) Viduna, D.; Limpouchova, Z.; Prochazka, K. *J. Chem. Phys.* **2001**, *115*, 7309. (b) *Macromol. Theory Simul.* **2001**, *10*, 165.
(16) Dimitrov, D. I.; Milchev, A.; Binder, K. *J. Chem. Phys.* **2006**, *125*, 034905.
(17) Dimitrov, D. I.; Milchev, A.; Binder, K.; Heermann, D. I. *Macromol. Theory Simul.* **2006**, *15*, 573.
(18) Dimitrov, D. I.; Milchev, A.; Binder, K. *Macromol. Symp.* **2007**, *252*, 47.
(19) Koutsioukas, A. G.; Spiliopoulos, N.; Anastassopoulos, D. L.; Vradis, A. A.; Toprakcioglu, C. *J. Chem. Phys.* **2009**, *131*, 044901.
(20) Egorov, S. A.; Milchev, A.; Klushin, L.; Binder, K. *Soft Matter* **2011**, *7*, 5669.
(21) Adiga, S. P.; Brenner, D. W. *Nano Lett.* **2005**, *5*, 2509.
(22) Adiga, S. P.; Brenner, D. W. *Macromolecules* **2007**, *40*, 1342.
(23) Dimitrov, D. I.; Klushin, L. I.; Milchev, A.; Binder, L. *Phys. Fluids* **2008**, *20*, 092107.
(24) Dimitrov., D. I.; Milchev, A.; Binder, K. *Ann. N.Y. Acad. Sci.* **2009**, *1161*, 537.
(25) Tagliazucchi, M.; Azzaroni, O.; Szleifer, I. *J. Am. Chem. Soc.* **2010**, *132*, 12404.
(26) Tessier, F.; Slater, G. W. *Macromolecules* **2006**, *38*, 6752.
(27) Tessier, F.; Slater, G. W. *Macromolecules* **2006**, *39*, 1250.
(28) Meller, A. *J. Phys.: Condes. Matter* **2003**, *15*, R581.
(29) Reisner, W.; Morton, K. J.; Riehn, R.; Wang, Y. M.; Yu., Z.; Rosen, M.; Sturm, J. C.; Chou, S. Y.; Frey, E.; Austen, R. H. *Phys. Rev. Lett.* **2005**, *94*, 196101.
(30) Krasilnikov, O. V.; Rodriguez, C. G.; Bezrukhov, S. M. *Phys. Rev. Lett.* **2006**, *97*, 018301.
(31) Klushin, L. I.; Skvortsov, A. M.; Hsu, H.-P.; Binder, K. *Macromolecules* **2008**, *41*, 5890.
(32) Milchev, A.; Klushin, L. I.; Skvortsov, A. M.; Binder, K. *Macromolecules* **2010**, *43*, 6877.
(33) Rafferty, J. L.; Siepmann, J. I.; Schure, M. R. *J. Chromatrogr. A* **2009**, *1216*, 1182.
(34) Boyd, R. H.; Chance, R. R.; Strate, G. V. *Macromolecules* **1996**, *29*, 1182.
(35) Wang, Y.; Teraoka, I.; Hansen, F. Y.; Peters, G. H.; Hassager, O. *Macromolecules* **2010**, *43*, 1651.
(36) Kasianowicz, J. J.; Brandin, E.; Branton, D.; Deamer, D. *Proc. Natl. Acad. U.S.A.* **1996**, *93*, 13770.
(37) Daoud, M.; De Gennes, P. G. *J. Phys. (Paris)* **1977**, *38*, 85.
(38) Kremer, K.; Binder, K. *J. Chem. Phys.* **1984**, *81*, 6381.
(39) Milchev, A.; Paul, W.; Binder, K. *Macromol. Theory Simul.* **1994**, *3*, 305.
(40) Morrison, G.; Thirumalai, D. *J. Chem. Phys.* **2005**, *122*, 194907.
(41) Cifra, P.; Benkova, Z.; Bleha, T. *Faraday Discuss.* **2008**, *139*, 377.
(42) Cifra, P. *J. Chem. Phys.* **2009**, *131*, 224903.

(43) Wang, R.; Virnau, P.; Binder, K. *Macromol. Theory Simul.* **2010**, *19*, 258.
(44) Tegenfeldt, I. O.; Prinz, C.; Cao, H.; Chou, S.; Renner, W. W.; Rieches, R.; Wang, Y. M.; Cox, E. C.; Sturm, J. C.; Silberzan, P.; Austin, R. H. *Proc. Natl. Acad. Sci. U.S.A.* **2004**, *59*, 5833.
(45) MacDowell, L. G.; Müller, M.; Vega, C.; Binder, K. *J. Chem. Phys.* **2000**, *113*, 219.
(46) Müller, M.; MacDowell, L. G. *Macromolecules* **2000**, *33*, 3902.
(47) Kreer, T.; Metzger, S.; Müller, M.; Binder, K. *J. Chem. Phys.* **2004**, 4012.
(48) Landau, D. P.; Binder, K. *A Guide to Monte Carlo Simulation in Statistical Physics*, 3rd ed.; Cambridge Univ. Press: Cambridge, U.K., 2009.
(49) Binder, K., Ed. *Monte Carlo and Molecular Dynamics Simulations in Polymer Science*; Oxford Univ. Press: New York, 1995.
(50) Egorov et al.[20] also did consider an overlap but it was normalized differently. We feel that the present choice is more useful, however. Note also that "densities $\phi_f(r)$, $\phi_g(r)$ in ref 20 already did include the extra factor r, which in eq 4 appears explicitly.
(51) Fleer, G. J.; Stuart, M. A. C.; Scheutjens, J. M. H. M.; Cosgrove, T.; Vincent, B. *Polymers at Interfaces*; Chapman and Hall: London, 1993.
(52) Huinink, H. P.; de Keizer, A.; Leermakers, F. A. M.; Lyklema, J. *Langmuir* **1997**, *13*, 6618.

Macromolecules

Article

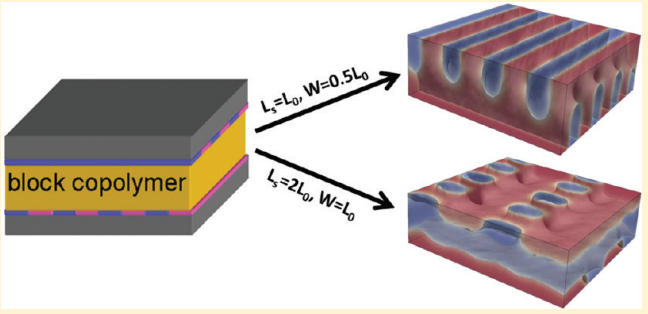
pubs.acs.org/Macromolecules

Symmetric Diblock Copolymers Confined by Two Nanopatterned Surfaces

Abelardo Ramírez-Hernández, Guoliang Liu, Paul F. Nealey, and Juan J. de Pablo*

Department of Chemical and Biological Engineering, University of Wisconsin—Madison, Madison, Wisconsin 53706, United States

ABSTRACT: Using Monte Carlo simulations of a coarse-grained model, we explore the equilibrium morphologies of symmetric diblock copolymers between two chemically patterned surfaces. The chemical patterns on the surfaces consist of periodic stripes of width W with a periodicity L_s. The stripes on the two chemical patterns are oriented orthogonally. By systematically varying the width of the stripes, the interaction strength between the patterns and block copolymers, and the thickness of the block copolymer films, we investigate complex three-dimensional morphologies that are not available in the bulk and that could be useful in a wide array of applications. The results of simulations are shown to be in quantitative agreement with experimental observations.



INTRODUCTION

The self-assembly of soft materials provides a means to create well-defined morphologies with applications in nanoscale science and engineering.[1,2] In particular, recent reports have shown that self-assembly of copolymers can be used in advanced technologies found in the microelectronics and high-density memory device industries.[2,3]

Traditional patterning methods such as photolithography and electron beam lithography are well suited for fabrication of well-defined two-dimensional features. However, the creation of three-dimensional structures requires repeated photoresist patterning and pattern transfer processes.[4] The use of self-assembling soft materials such as supramolecules, colloids or block copolymers promises to enable fabrication of complex three-dimensional structures with fewer steps.[5,6]

Block copolymer melts have the ability to self-assemble into a variety of periodic structures whose scales range from 5 to 100 nm.[7−9] The complexity of these structures depends on the architecture (linear, branched, etc.) and composition of the macromolecules. Furthermore, by using blends of homopolymers and block copolymers, one can increase the variety of morphologies available for use in various technologies. One disadvantage of these materials can be defect formation, which impedes the long-range order necessary in many applications. This problem can be avoided through the use of external fields. In that regard, a particular promising nanofabrication approach relies on the directed assembly of block copolymer thin films, where chemically patterned surfaces act as external fields that direct the assembly of the block copolymers on the nanoscale.[10−12] These chemical patterns provide the thermodynamic forces needed to achieve the assembly with registration, perfection, resolution and improved quality.[10−12] In the context of high-density storage media, it has been demonstrated that this approach can lead to defect-free arrays of copolymer domains at densities of 1 terabit per square inch.[3]

The directed assembly of block copolymers has been used to fabricate periodic structures, including spherical, cylindrical, and lamellar morphologies[13−15] and nonperiodic structures such as bends, jogs, and T-junctions.[16−19] While most of these features are inherently two-dimensional, it has been demonstrated that it is possible to create a variety of complex three-dimensional structures under specific chemical patterning conditions.[20,21] It has also been shown that block copolymers can be used to localize nanoparticles in specific positions dictated by the block copolymer morphologies.[22,23]

Work to date has largely focused on the use of only one patterned surface; therefore, it is of interest to explore the possible structures created when block copolymers are confined by two patterned surfaces. The interplay between the entropic penalty due the one-dimensional confinement and the energetic contributions of both patterns attempting to induce, locally, a specific symmetry, opens the possibility for creation of complex three-dimensional structures, even in the simple case of an AB diblock copolymer.

Several theoretical approaches, ranging from lattice Monte Carlo simulations to self-consistent field theory (SCFT) calculations and Landau−Ginzburg descriptions, have been used to explore the morphologies that arise when one patterned surface is used to induce order in block copolymers. Wang et al.[24−26] used a lattice model to explore the influence of the patterned surface on the morphologies of symmetric block copolymer thin films by Monte Carlo simulations. In those studies, the conditions for long-range order of perpendicular

Received: December 8, 2011
Revised: January 31, 2012
Published: February 22, 2012

ACS Publications © 2012 American Chemical Society

dx.doi.org/10.1021/ma2026594 | *Macromolecules* 2012, 45, 2588−2596

lamellae were indentified, obtaining good agreement with experimental data. Petera et al.[27,28] performed 2D SCFT calculations to investigate the ordering of diblock copolymer thin films in the presence of one chemically patterned surface and one homogeneous surface; the studies were perfomed both above and below the order−disorder transition (ODT). They found a dependence of the orientation of the lamellae on the ratio of the natural bulk period to the pattern period, and observed that for strong surface interactions the lamellae comply with the surface pattern. Tsori et al.[29,30] used a phenomenological Landau−Ginzburg free energy approach to investigate the effect of a chemically patterned surface on the morphology of symmetric diblock copolymer thin films. It was found that periodically patterned surfaces could induce a tilt of the lamellae in order to match the surface periodicity, and also identified the conditions required to obtain lamellae in other orientations. These past studies have improved our understanding of surface-induced ordering and its propagation in thin block copolymer melts. However, few reports considered the influence of two patterned surfaces confining block copolymer thin films. In particular, in ref 31, Tsori and Andelman used a Landau−Ginzburg free energy functional to investigate the morphology of diblock copolymers between two patterned surfaces in the weak segregation limit, above the ODT transition. Wang[33] performed lattice Monte Carlo simulations of symmetric diblock copolymers confined between stripe patterned surfaces. Both studies revealed that by using two patterned surfaces interesting morphologies could emerge as a result of the confinement and the pattern's properties.[31−33]

Here we also focus on the specific case where the assembly of a symmetric AB block copolymer is directed by two patterned surfaces. The patterns on both surfaces are identical but have different relative orientations. Our study builds on that presented in ref 31, where a more coarse-grained approach was employed. We perform a screening of the different morphologies that arise as a function of the size of confinement, the strength of the copolymer interaction with the patterned surface, and the geometric properties of the patterns. We resort to Monte Carlo simulations with a recently introduced theoretically informed coarse-grained model of block copolymers, which has been successfully used to predict the structures created in the directed assembly of these materials.[3,21,34−38] The results of simulations are compared to experimental data for diblocks between lithographically nanopatterned surfaces.

METHODS

The Model. The calculations presented here rely on a coarse-grained model that describes the universal properties of multipolymeric systems and, in particular, block copolymer melts. It is based on the standard Hamiltonian used in polymeric field theory.[39,40] It has been successfully used to predict equilibrium morphologies of block copolymers by resorting to Monte Carlo simulations in arbitrary ensembles,[23,41−43] and to describe the behavior of homopolymer melts and solutions under strong confinement or in the presence of solid contacts.[44,45] We focus on an AB block copolymer melt, but the generalization to more complex architectures or blends does not introduce additional complications.[23,42] The system comprises n chains of AB block copolymer in a volume V at temperature T. The block copolymers are represented by a discretized Gaussian chain model, in which each chain is made of N beads and the mean-squared bond length is b^2. The position of the sth bead in the ith chain is given by $\mathbf{r}_i(s)$. The bonded interactions, $\mathcal{H}_b$, acting along the chains are given by

$$\frac{\mathcal{H}_b}{k_BT} = \frac{3}{2}\sum_{i=1}^{n}\sum_{s=1}^{N-1}\frac{N-1}{R_e^2}[\mathbf{r}_i(s+1)-\mathbf{r}_i(s)]^2 \quad (1)$$

where $R_e^2 = (N-1)b^2$ is the mean squared end-to-end distance of an ideal chain and k_B is the Boltzmann constant. The nonbonded interactions, $\mathcal{H}_{nb}$, are expressed as a functional of the local densities of the beads and take into account the repulsion between unlike monomers and the finite compressibility of the melt. Explicitly, it is given by

$$\frac{\mathcal{H}_{nb}}{k_BT} = \sqrt{\bar{N}}\int_V \frac{\mathrm{d}\mathbf{r}}{R_e^3}\left[\chi N\varphi_A\varphi_B + \frac{\kappa N}{2}(\varphi_A+\varphi_B-1)^2\right] \quad (2)$$

where $\phi_\gamma(\mathbf{r})$ is the local dimensionless density of beads of type γ (=A,B) and $\bar{N} = (\rho_0 R_e^3/N)^2$, with ρ_o being the bead number density. The repulsion between unlike monomers is represented by the first term in eq 2 and its strength is given by the Flory−Huggins parameter χ. The second term is based on Helfand's quadratic approximation[46] and it gives a finite compressibility to the melt. The parameter κ is related to the inverse isothermal compressibility of the melt.[43]

In the presence of chemical patterns used to direct the assembly of block copolymer thin films, the chains are confined by two impenetrable hard surfaces located in the planes $z = 0$ and $z = L_z$. In this work, we consider two chemically patterned confining surfaces. The chemical pattern on each is represented by a one-body potential, $\mathcal{U}$, acting on each bead that depends explicitly on the position and type of the bead. Thus, we need to add the potential $\mathcal{H}_S = \Sigma_j \mathcal{U}(\mathbf{r}_j,\gamma_j)$ to the total Hamiltonian for each surface contribution, the sum runs over all beads and γ_j is the type of particle j. The system behavior is well described by the total Hamiltonian $\mathcal{H} = \mathcal{H}_b + \mathcal{H}_{nb} + \mathcal{H}_{Stop} + \mathcal{H}_{Sbottom}$. Following previous studies,[3,47] the potential used is

$$\frac{\mathcal{U}(\mathbf{r},\gamma)}{k_BT} = -\frac{\Lambda^\gamma(x,y)}{\xi/R_e}\mathrm{e}^{-z^2/2\xi^2} \quad (3)$$

This potential decays over a short distance ξ. Λ^γ determines the strength of the interaction between the beads of type γ and the pattern and depends on the coordinates (x,y). The explicit dependence on these variables is defined by the geometry of the pattern. The variable z is the distance with respect to the corresponding surface. In this work, the patterns on both surfaces consists of repeated stripes of width W and period L_s. The areas between the stripes are referred to as background (Figure 1). Because of the simple geometry of the patterns, the interactions between the blocks (A or B) with the patterned surfaces are specified by four parameters: Λ^A_{stripe}, Λ^A_{backg}, Λ^B_{stripe}, and Λ^B_{backg}. In general, there will be eight parameters (four parameters associated with each surface) describing both chemical patterns, but for simplicity we have assumed that both surfaces have the same characteristics, thus only four parameters are required. Also, we assume that for striped and background areas, the attraction for the preferred block is equal in magnitude to the repulsion for the nonpreferred block, i.e. $\Lambda^A_{stripe}N = -\Lambda^B_{stripe}N = \Lambda_S$ and $\Lambda^B_{backg}N = -\Lambda^A_{backg}N = \Lambda_b$. In this work,

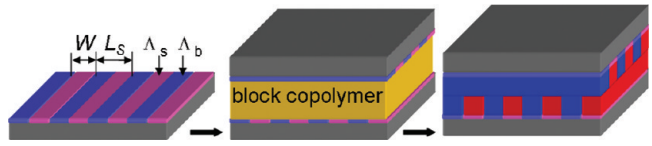


Figure 1. Schematic representation of the directed assembly of a block copolymer between two chemically patterned surfaces. The patterns consist of periodic stripes of width W and period L_s. Thin films of block copolymer equilibrate into three-dimensional structures between the confining surfaces.

dx.doi.org/10.1021/ma2026594 | Macromolecules 2012, 45, 2588−2596

the stripes exhibit a preference for the block A ($\Lambda_s > 0$) and the background for the block B ($\Lambda_b > 0$).

The exploration of equilibrium morphologies is performed by Monte Carlo simulations. The local densities are defined in a lattice with a spacing ΔL and computed from the beads' positions by a particle-to-mesh interpolation.[23,41] We sample configurations according to a Metropolis criterion,[48] $P_{acc} = \min[1,\exp(-\beta\Delta\mathcal{H})]$, where $\Delta\mathcal{H}$ is the energy change between two configurations. It includes both bonded and nonbonded contributions as well as the change of the one-body potentials related to the patterns. The trial moves considered include reptation-like movements, local displacements of the beads, switching the order of blocks and translation of an entire chain. For additional details concerning the simulations readers are referred to the literature.[23] To visualize the 3*D* structures after the directed assembly, we compute the local composition scalar field, $\psi(r)$, defined by

$$\psi(\mathbf{r}) = \left\langle \frac{\varphi_A(\mathbf{r}) - \varphi_B(\mathbf{r})}{\varphi_A(\mathbf{r}) + \varphi_B(\mathbf{r})} \right\rangle \tag{4}$$

The regions where $\psi = -1$, 0, or +1 represent the B-rich domains, the interface between the A and B regions, and the A-rich domains, respectively. It has been shown that rapid deep quenches of block copolymer thin films, can trap the system in metastable states; this problem can be avoided by using a gradual annealing process.[49−51] While we have used aggressive MC trial moves to achieve better sampling, it is still important to determine whether one is trapped in local minima. To that end, we have also performed simulations starting from different disordered initial conditions. In most of calculations the final morphology was independent of the initial configuration; in some isolated cases, however, a different morphology was formed. For those cases, we report the morphology that appears in the majority of simulations.

We consider a symmetric AB diblock copolymer, where A and B represent PMMA (poly methyl-methacrylate) and PS (polystyrene), respectively. The majority of work was performed using the following parameter values: $\kappa N = 35$, $\chi N = 25$ and $\sqrt{\bar{N}} = 110$; for these values the natural period of the lamellae in the bulk is $L_0 = 1.66\ R_e$, and we fixed R_e as our unit length scale. This set of values correspond to a PS-*b*-PMMA block copolymer with a molecular weight around 74 kg/mol.[21] To compare with experiments, further simulations were performed using $\kappa N = 85$, $\chi N = 63$ and $\sqrt{\bar{N}} = 167$, the computed natural period of the lamellae in the bulk for this case is $L_0 = 1.935R_e$. These parameters correspond to a PS-*b*-PMMA block copolymer with a molecular weight $M_n = 176$ kg/mol. We discretize the chain into $N = 32$ beads and the lattice spacing is chosen such that each bead interacts with $n_{int} = 14$ particles on average. For the interaction potential with the patterns, we have chosen a short-range function for which $\xi = 0.15R_e$. The stripe affinity was fixed at $\Lambda_s = 2$. The simulation box has lateral dimensions: $L_x = L_y = 4L_0$, and we applied periodic boundary conditions along these directions. We study the effect of the confinement (by changing L_z), the background affinity Λ_b, the period of the patterns L_s and the width of the stripes W on the equilibrium morphologies. The patterns on both surfaces have the same properties but are orthogonal to each other.

Experiments. Hydroxyl-terminated polystyrene (PS−OH, num PDI = 1.07) homopolymer and polystyrene-*block*-poly(methyl methacrylate) (PS-*b*-PMMA, M_n = 85−91 kg/mol, PDI = 1.12) block copolymer were purchased from Polymer Source, Inc., and used as received. The block copolymer formed lamellae with a natural period of L_0 = 75.8 nm, as characterized with small-angle X-ray scattering (SAXS) of the bulk sample and fast Fourier transform (FFT) of the top-down SEM image of thin film sample. Poly(methyl methacrylate) (PMMA, M_n = 950 kg/mol) photoresist was purchased from MicroChem, Corp. Polished, test grade silicon ⟨100⟩ wafers were purchased from Montco Silicon Technologies, Inc. Toluene, chlorobenzene, methyl isobutyl ketone, and isopropanol were purchased from Sigma-Aldrich, Milwaukee, WI, and used as received.

The silicon wafers were exposed to oxygen plasma for 5 min to remove any possible organic residue and ensure a thin layer of silicon oxide present on the surface. PS−OH was dissolved in toluene (1.5 wt %) and spin-coated onto the silicon substrates. The initial polymer films had thicknesses of approximately 50 nm. The PS−OH was grafted onto the substrates by annealing at 160 °C for 24 h under vacuum and reached a sufficient brush grafting density. To minimize the potential degradation by residual oxygen, the vacuum chamber was purged with argon repeatedly before annealing. The substrates were then cooled to room temperature and repeatedly sonicated in toluene for 5 min by 3 times to remove the ungrafted polymer. The grafted polymer formed a brush layer on the substrate and had a thickness of 4 nm, as characterized previously.

The PS−OH brush layers on the substrates were then covered with a ∼ 40 nm thick layer of PMMA photoresist and subsequently patterned with electron beam lithography (EBL) using the Nanometer Pattern Generation System (NPGS, Nabity Lithography Systems) on a LEO 1550VP field emission scanning electron microscope (FE-SEM). After the exposure, the photoresist was developed in a mixture of methyl isobutyl ketone and isopropanol (1:3 v/v) and then dried in a nitrogen stream. The resulting topographic pattern had a period, L_s, of 76 nm (∼ L_0), an exposed line width, W, of ∼38 nm (∼ $L_0/2$), and the patterned area was about 2.0 mm by 1.0 mm, sufficiently large for SAXS measurement. The topographic photoresist pattern was exposed to oxygen plasma for 10 s to chemically modify the exposed regions so that they preferentially wet the PMMA domain of the block copolymer. Afterward, the PMMA photoresist was removed by sonication in chlorobenzene for 5 min for 3 times, resulting in chemical patterns of alternating PS brush (preferentially wet the PS block of PS-*b*-PMMA) and chemically modified regions (preferentially wet the PMMA block of PS-*b*-PMMA). A 152 nm-thick ($2L_0$) film of PS-*b*-PMMA was spin-coated on the film was covered with another substrate with the same chemical pattern as described above. The top chemical pattern was rotated approximately 90° (within 3 degree error) with respect to the bottom chemical pattern. The two substrates were clamped between two steel surfaces to ensure full contact. On the basis of the clamping process that was reported previously in ref 52, the block copolymer films should experience little, if any, distortion. The sandwiched block copolymer film was loaded into the vacuum chamber and annealed again for 72 h at 230 °C. After annealing, the top substrate was peeled-off mechanically; while the mechanical peeling represents a rather crude method to recover the polymer film, SEM images do not reveal any appreciable damage to the samples. SAXS was used to characterize the morphology inside the film.

SAXS of the PS-*b*-PMMA thin film samples was performed on the SAXS station at the Swiss Light Source (SLS) of the Paul Scherrer Institut (PSI), Switzerland. The samples were mounted onto a copper stage, which had a hole in the center to allow scattered X-rays to pass through. The scattering was performed in transmission mode with the incoming coherent X-rays from the synchrotron source oriented perpendicular to the substrate. The scattered X-rays traveled through a 7 m flight tube and were collected by a PILATUS detector.

■ RESULTS AND DISCUSSION

Figure 1 illustrates the directed assembly of block copolymer films between two chemically patterned surfaces. The chemical pattern contains periodic stripes with a periodicity of L_s. The width of a chemically patterned stripe is W. The interaction strengths between the block copolymers and the chemically patterned stripes or the unmodified stripes (background) are Λ_s or Λ_b, respectively. Block copolymers are equilibrated between two orthogonally oriented chemically patterned surfaces. When only one chemically patterned surface is present, the block copolymers form a lamellar morphology perpendicular to the substrate in registration with the patterned stripes. Between two chemically patterned surfaces, the block copolymers are expected to form complex morphologies at equilibrium.

dx.doi.org/10.1021/ma2026594 | *Macromolecules* 2012, 45, 2588−2596

$L_s = L_0$ and Scherk's First Surface. In a recent report we have provided evidence, through comparison to experimental data, that the model employed here is able to capture the physics of copolymers confined by two patterned surfaces. That work was limited to a specific case in which $L_s = L_0$, $W = L_0/2$, and $L_z = 2L_0$; only the case with strong affinities both for A and B blocks for stripes and background regions, respectively, was considered.[53] Figure 2c shows the morphology that arises between two chemically patterned surfaces; the morphology is bicontinuous, with the majority of the lamellae aligned with the top or bottom surfaces and a thin connecting interface in the region where the orthogonal lamellae come together. Two-dimensional SAXS patterns show two sets of scattering peaks along the x and y directions after directed assembly (Figure 2a); the angle between the x and y directions is ≈87°, as measured from the SAXS pattern. The experiments show that two lamellar-shaped structures are present in the film, as predicted by the simulations. In terms of concepts used to describe bulk properties, the two chemical patterns on the top and bottom surfaces induce the nucleation of a *grain* of lamellae oriented along the chemically patterned stripes. The two grains meet inside the film at a *grain boundary*. In this particular configuration, the two lamellae grains were twisted in the middle of the film and the two grains met at the twist grain boundary (TGB). On the basis of the intensity of the scattering peaks along the two directions, the lamellar domains near the top- and the bottom-substrate were of approximately the same domain size, and the two lamellar grains met in the middle of the film.

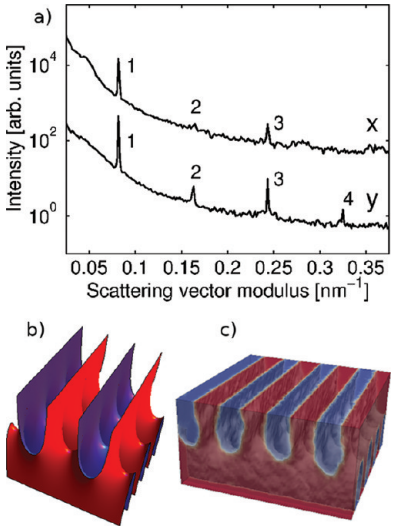


Figure 2. (a) SAXS spectrum along the two orthogonal directions of the block copolymer thin film after directed assembly between two chemical patterns. (b) Scherk's surface obtained by the analytical expression (eq 5). (c) Three-dimensional morphology obtained by Monte Carlo simulations. The color map shows the scalar field ψ, eq 4. Red represents the PS-rich domains, blue the PMMA-rich domains, and the surface is the interface between these two domains.[59] The parameters $\chi N = 63$ and $\sqrt{N} = 167$ were chosen such that the model represents a block copolymer with a molecular weight $M_n = 176$ kg/mol. (see text for details).

Thomas et al.[54,55] investigated the geometric properties of these grain boundaries for block copolymers in the bulk. They suggested that the TGB has the following interesting properties: (1) the block copolymer domains are bicontinuous and (2) the domains of the diblock copolymers are separated by a minimal surface. By using a Ginzburg–Landau free energy approach for surfactant systems, Gompper et al.[56] showed that the TGB in those systems is a minimal surface.

The results of simulations show that each domain of the block copolymer forms a cross-bar-like network through the entire film, and the interface between the two domains resembles Scherk's first minimal surface, as was proposed for the bulk in ref 54. The Scherk surface is defined by doubly periodic arranged saddle points, all of which are localized on a plane. In our particular case, where the relative orientation of the lamellar grains is $\pi/2$, the implicit expression defining the Scherk surface (Figure 2b) is given by

$$e^z \cos y - \cos x = 0 \tag{5}$$

We have therefore shown that by using two nanopatterned surfaces, it is possible to direct the assembly, at a large scale, of this bicontinuous morphology. The good agreement between experimental data and simulations serves to underscore the validity of the model, and it gives us confidence in the predictions presented in what follows for a wide array of conditions.

To examine our results we have used concepts taken from the bulk description, namely grains and TGB. However, it is necessary to point out that the structure and the associated interface correspond to a thermodynamic equilibrium state, instead of a metastable state as in the bulk. For block copolymer thin films in the presence of chemically patterned surfaces, interfacial and bulk-like contributions to the free energy have comparable magnitudes. Thus, a simple description in terms of a bulk morphology perturbed by the patterns is not valid anymore. For thin block copolymer films in the presence of patterned surfaces, the equilibrium morphologies arise from an interplay between the breaking of translational symmetry (due to one-dimensional confinement), energetic contributions of the patterns (attempting to induce, locally, a specific morphology), the incompatibility between the blocks and the entropic force associated with chain elasticity. Moreover, the structural frustration due to the incompatibility between the natural periodicity of the bulk morphology and film thickness can play an important role.

We next consider the effect of various system parameters on the equilibrium morphology. It is expected that for thick films, the influence of the patterned surfaces becomes less pronounced; in that case lamellar grains can grow in any orientation inside the film and induce irregular structures. Another important parameter is the affinity of the pattern to the blocks of the block copolymers. Similarly, the width of the patterned stripes can play an important role in determining the possible morphologies. We next screen all these parameters to understand the block copolymer morphologies that one can induce.

For the case of patterns with exactly the same geometric properties as the lamellar morphology in the bulk, we find that the background affinity has little influence on the morphologies. Although MC simulations do not give dynamical information, we find that for stronger affinities, it is easier (or faster, in terms of MC steps) to attain equilibrium. The effect of the background affinity is limited for low-affinity values, where a slight asymmetry between two contiguous domains occurs, resulting in a lamellar grain with one domain slightly larger than the other one. Globally, the structure has the same geometric properties as the perfect lamellae with the TGB described by the Scherk's surface, except that the saddle points are located

dx.doi.org/10.1021/ma2026594 | *Macromolecules* 2012, 45, 2588–2596

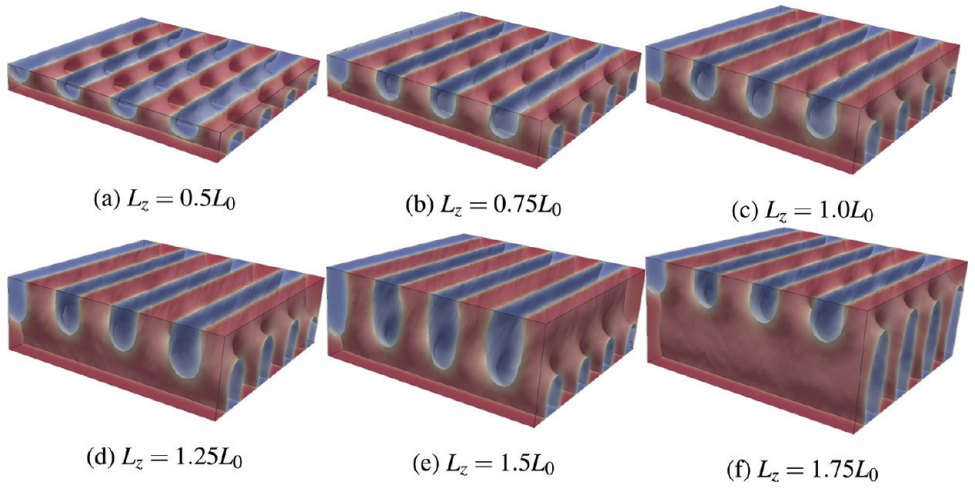


Figure 3. Three-dimensional morphologies of block copolymers between two chemical patterns with $L_s = L_0$, $W = 0.5L_0$, $\Lambda_b = 0.4$, $\Lambda_s = 2.0$ for various film thicknesses, L_z, obtained from Monte Carlo simulations. The corresponding film thickness is shown in the figure. The patterned stripes on the top and bottom surfaces are orthogonal to each other. The twist grain boundary delocalizes from the middle of the film for block copolymer films with a thickness larger than $1.0L_0$. The color map shows the scalar field ψ. Red represents the A-rich domains, blue the B-rich domains, and the surface indicates the interface between these two domains.[59] $\chi N = 25$ and $\sqrt{\bar{N}} = 110$.

in a thin layer whose thickness decreases as the background affinity increases (where the asymmetry between two contiguous domains disappears), thereby localizing all the saddle points in a plane, as expected for perfect symmetric lamellar domains.

In contrast, the film thickness has a significant effect on the final morphology for the values considered here (going from $L_z = 0.5L_0$ to $L_z = 2.0L_0$). The final morphology consists of two grains meeting in the TGB, whose localization, as expected, exhibits a strong dependence on thickness. Here TGB localization means the thin layer position were all the saddle points are located. In Figure 3, we show the morphologies obtained for different thickness for an intermediate value of $\Lambda_b = 0.4$. All of them show the two grains induced by the patterns and the TGB.[60] We can observe the delocalization of the twist grain boundary away from the middle of the film for thicknesses larger than $1.0L_0$. The influence of the twist grain boundary is not restricted to the small region where the saddle points are located but, in fact, it propagates far from it. One can assign a size to that boundary; from our results, it has a value around $1.0L_0$, consistent with the expected value in the bulk.[55] For smaller values of L_z, we can say that the complete sample basically consists of a single interface spanning the entire film. For thicker films, the kinetics of morphology formation plays an important role in the localization of the TGB: if one pattern starts the nucleation faster that the other, then the grain induced by the first one is going to be larger than the second one. Thus, the TGB is going to be located near the second surface. However, there exists a minimum distance from the surfaces where the TGB can be localized. The entropy penalty due to being near the surface and the requirement to satisfy the boundary conditions on the patterns compete with the frustration induced by the nonflat interfaces of the TGB, causing the minimum distance of the TGB from a surface to be around half of the TGB thickness; once the TGB is far enough from a wall, it can be localized anywhere. Parts e and f of Figure 3 show representative configurations where the TGB appears near different surfaces, illustrating the mechanism outlined above.

$L_s = 2L_0$ and Complex Morphologies. As mentioned above, for block copolymer thin films confined by chemically patterned surfaces, different contributions to the total free energy (the interfacial and bulk terms), have comparable magnitudes. In particular, the pattern's properties (periodicity, affinities, geometry, etc.) have a profound influence over the block copolymer morphology, and small changes (for example, weak or strong interactions with the background) can drastically affect the equilibrium morphology. In contrast, for thick films, the bulk contributions to the free energy will have a dominant role over the interfacial terms.

The patterns studied above have the same periodicity as the lamellar morphology of the block copolymer in the bulk. By changing the pattern periodicity and geometry, however, one can create more complex morphologies. The symmetry of the local structures induced by the patterns will compete with that of the block copolymer in the bulk (in this case the lamellae). It is therefore of interest to explore how this interplay affects the final morphology. To do that, we focus on $L_s = 2L_0$ and $\Lambda_s = 2.0$. We choose this value of L_s because in previous studies we found that when only one chemically patterned surface is used, a lamellae-forming block copolymer can multiply the feature density of the chemical patterns.[21] The morphology interpolates the lamellar domains in the background areas when these regions are slightly attractive to one block of the block copolymer or neutral to both blocks of the block copolymer.[57] We consider two cases: (i) weak Λ_b ($\Lambda_b = 0.2$) and (ii) strong Λ_b ($\Lambda_b = 2.0$). We explore the block copolymer morphologies as a function of W and L_z. We find that the block copolymers equilibrate into structures that do not arise in the bulk.

$\Lambda_b = 0.2$: Block Copolymers on Background with Weak Interaction Strength. When $W = L_0/2$, the tendency to form perpendicular lamellae (because of the strong stripe affinity to the A component of the block copolymer) competes with the influence of the background to be wet by block B, trying to form, locally, parallel lamellae. The film thickness plays an important role in defining which influence dominates the behavior: as the thickness increases, the influence of the weak background decreases compared with that of the bulk free energy. In thicker films, it is expected that there exists a

dx.doi.org/10.1021/ma2026594 | *Macromolecules* 2012, 45, 2588−2596

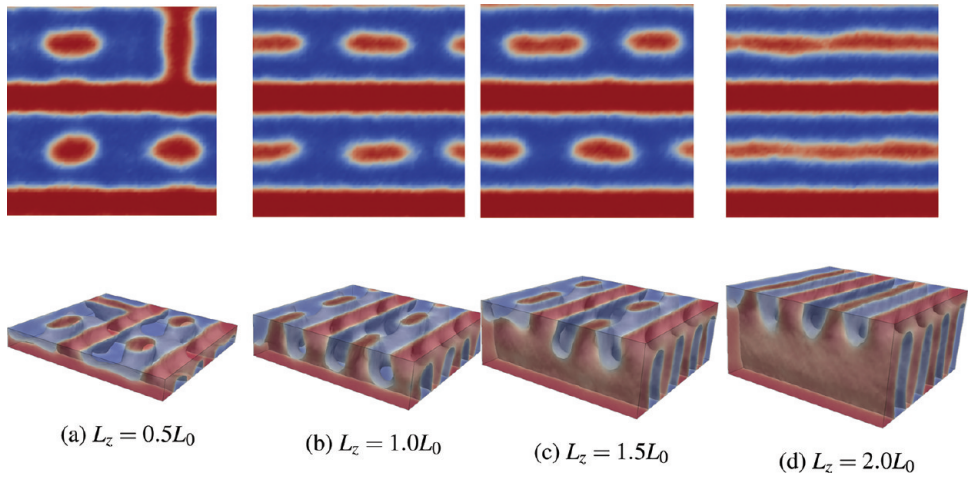


Figure 4. (Top) Top-down views and (bottom) three-dimensional snapshots of block copolymer morphologies between two chemical patterns with $L_s = 2L_0$, $W = 0.5L_0$, $\Lambda_b = 0.2$, and $\Lambda_s = 2.0$ for various film thicknesses, L_z, obtained from Monte Carlo simulations. The corresponding film thickness is shown in the figure. The patterned stripes on the top and bottom surfaces are orthogonal to each other. The color map shows the scalar field ψ. Red represents the A-rich domains, blue the B-rich domains, and the surface indicates the interface between these two domains.[59] $\chi N = 25$ and $\sqrt{\bar{N}} = 110$.

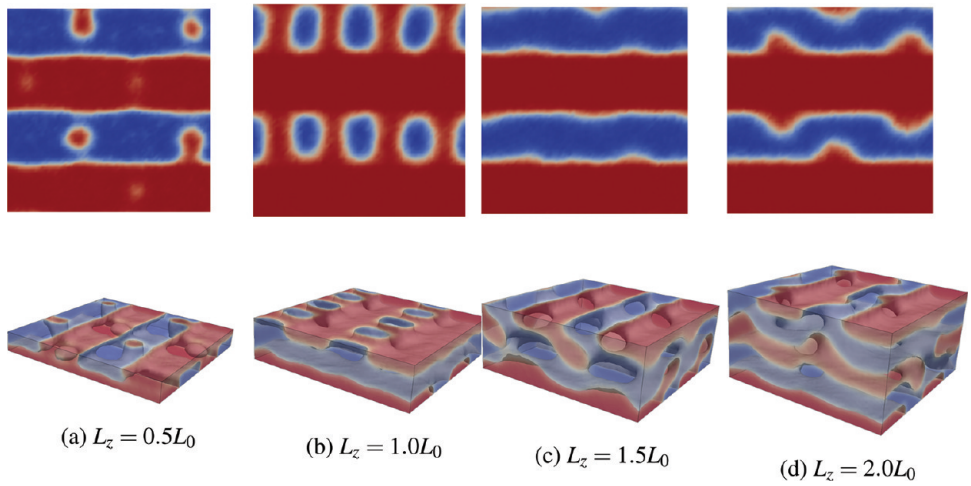


Figure 5. (Top) Top-down views and (bottom) three-dimensional snapshots of block copolymer morphologies between two chemical patterns with $L_s = 2L_0$, $W = L_0$, $\Lambda_b = 0.2$, $\Lambda_s = 2.0$, and various film thicknesses, L_z, obtained from Monte Carlo simulations. The corresponding L_z is shown in the figure. The patterned stripes on the top and bottom surfaces are orthogonal to each other. The color map shows the scalar field ψ. Red represents the A-rich domains, blue the B-rich domains, and the surface indicates the interface between these two domains.[59] $\chi N = 25$ and $\sqrt{\bar{N}} = 110$.

tendency to form perpendicular lamellar-shaped domains, because the energetic penalty for having the A component wet the background can be compensated by the minimization of the A−B interfaces in the lamellar-shaped domains and the favorable wetting of the stripes by the A blocks. How weak the background needs to be in order for bulk-like terms to become dominant depends on the value of χN. This example provides an illustration of the subtle balance between the different factors involved in the assembly of block copolymer thin films in the presence of chemically patterned surfaces.

Figure 4 shows the equilibrium morphologies of block copolymers as a function of film thickness, when $W = L_0/2$. In all cases, the block copolymer morphologies are bicontinuous. For stronger confinement ($L_z = 0.5L_0$), the block A (red) wets the chemically patterned stripes and forms orthogonal tubular domains with a spacing of $2L_0$. These domains are connected with each other, similar to how the Scherk's surface connects the two domains. In the background areas, the nonpreferred blocks (block A) try to interpolate, but the interpolated regions are limited to small spots that wet the background surface. Occasionally, these spots create an orthogonal bridge between two parallel domains. As the thickness increases to $L_z = 1.0L_0$, the interpolating spots start to grow in the background areas and form a dashed line pattern near the surfaces. In other words, the morphologies consist of alternating continuous lines and dashed lines near the surfaces, as can be seen in the top-down views in Figure 4. The lines at the top and bottom surfaces are orthogonal to each other, and they join inside the film in a continuous manner. As the thickness increases further to $L_z = 1.5L_0$, the size of the dashed lines increases. For $L_z = 2.0L_0$, the dashed lines become continuous and the pattern at the surfaces consists of periodic lines with a period of L_0. The morphology resembles the one found in the case with $L_s = L_0$.

The morphologies of block copolymers as a function of film thickness on wide chemically patterned stripes ($W = L_0$) and backgrounds having a weak interaction strength ($\Lambda_b = 0.2$) are

dx.doi.org/10.1021/ma2026594 | Macromolecules 2012, 45, 2588−2596

shown in Figure 5. Because of the wide chemically patterned stripes, perpendicular lamellae are not consistent with the boundary conditions, and parallel lamellae dominate locally, near the surfaces. For small film thickness, $L_z = 0.5L_0$, the confinement is strong and, to satisfy the local ordering induced by the patterns and to decrease the A-B interfacial area, the block copolymers arrange in a manner in which A and B blocks wet the stripes and background, respectively, to form equally spaced, orthogonally arranged bands near the two surfaces (Figure 5a). The bands are joined continuously inside the film. In addition, some features appear inside the bands: small ellipsoidal-shapes of block B appear in the matrix of A domains. Similarly, small perpendicular cylinders of A block appear in the matrix of B domains. However, contrary to the ellipsoidal B domains in the A matrix, the cylindrical A domains are not isolated in the B matrix, and they form bridges connecting them to the large A domains.

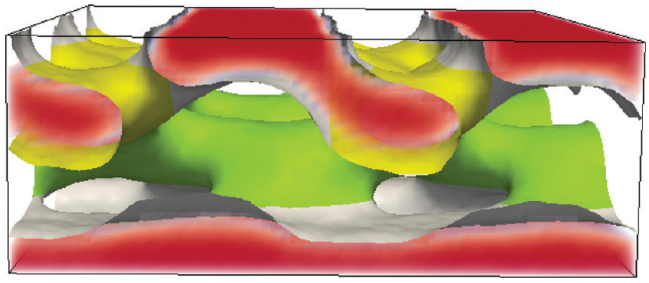
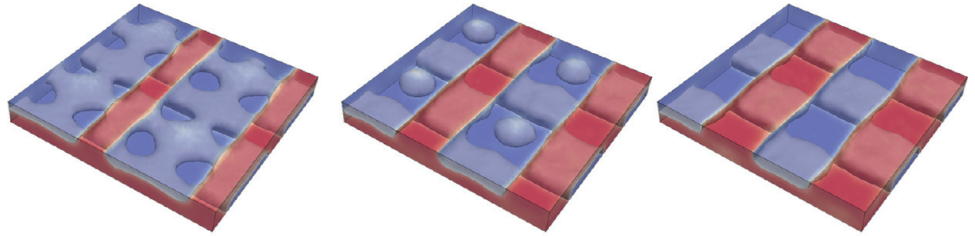


Figure 6. Iso-surface of the composition scalar parameter $\psi = 0$ corresponding to the interface between the A and B domains (gray). The red regions correspond to the A domains. In green and yellow we highlight the tubular regions induced by the bottom and top patterns. $\Lambda_b = 0.2$ (see text for details). $\chi N = 25$, and $\sqrt{\bar{N}} = 110$.

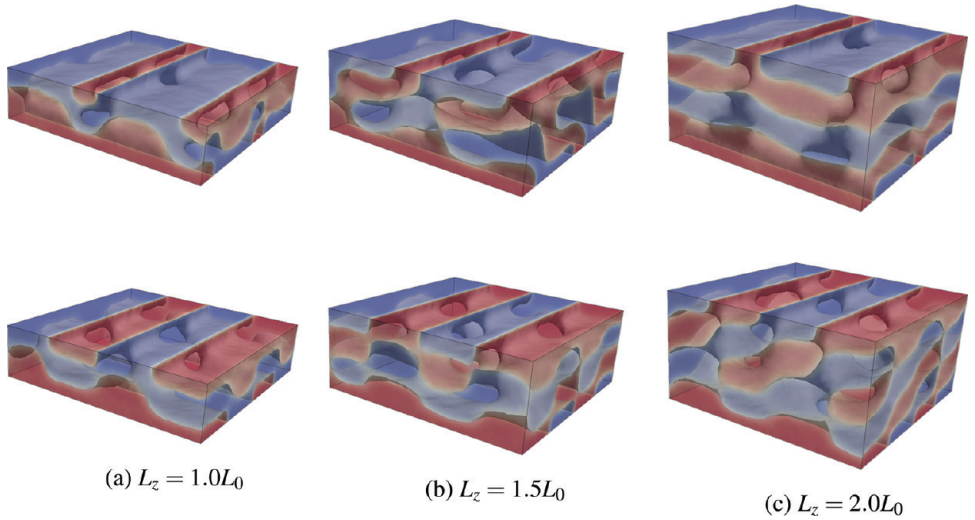
When the film thickness increases to $L_z = 1.0L_0$, symmetric parallel lamellae are entropically and energetically favorable. Because of the weak background affinity for block B, a linear array of necks of B domains in contact with the background is formed on both surfaces. This disrupts the perfect symmetric parallel lamellae morphology (Figure 5b).

For a film thickness of $L_z = 1.5L_0$, the block copolymer morphology is more complex (Figure 5c). The chemically patterned stripes and the background areas induce the formation of orthogonal bands of A domains and B domains. The tendency to phase separate induces the formation of tubular A regions just above/below the bottom/top background areas. The tubes associated with the bottom surface are orthogonal to those induced by the top surface and they merge



(a) $W = 0.5L_0$ (b) $W = 0.8L_0$ (c) $W = 1.0L_0$

Figure 7. Three-dimensional morphologies of block copolymers between two chemical patterns with $L_s = 2L_0$, $L_z = 0.5L_0$, $\Lambda_b = 2.0$, $\Lambda_s = 2.0$ for various width of stripes, W, obtained from Monte Carlo simulations. The corresponding W is shown in the figure. The patterned stripes on the top and bottom surfaces are orthogonal to each other. The color map shows the scalar field ψ. Red represents the A-rich domains, blue the B-rich domains, and the surface indicates the interface between the two domains.[59] $\chi N = 25$ and $\sqrt{\bar{N}} = 110$.



(a) $L_z = 1.0L_0$ (b) $L_z = 1.5L_0$ (c) $L_z = 2.0L_0$

Figure 8. Three-dimensional morphologies of block copolymers between two chemical patterns with $L_s = 2L_0$, $\Lambda_b = 2.0$, $\Lambda_s = 2.0$ for various widths of stripes, W, and various film thicknesses, L_z, obtained from Monte Carlo simulations. (Top) $W = 0.5L_0$ and (bottom) $W = 1.0L_0$. The corresponding L_z are shown in the figure. The patterned stripes on the top and bottom surfaces are orthogonal to each other. The color map shows the scalar field ψ. Red represents the A-rich domains, blue the B-rich domains, and the surface indicates the interface between the two domains.[59] $\chi N = 25$ and $\sqrt{\bar{N}} = 110$.

dx.doi.org/10.1021/ma2026594 | Macromolecules 2012, 45, 2588–2596

in the middle of the film forming a network of connected tubes. They also connect with the bands wetting the stripes, resulting in a global network spanning the entire film. Figure 6 shows the interface between the A and B domains (gray surface), and in green and yellow we highlight the tubular regions induced by the bottom and top patterns, respectively. The zigzag shape of the tubes occurs where two orthogonal tubes merge, bending toward the middle of the film. From the figure we can see the structure of the network mentioned above.

For the case with $L_z = 2.0L_0$, the larger film thickness allows the domains to adopt a sheet-like shape that resembles the parallel lamellae morphology (see Figure 5d). These sheet-like domains are merged by bridges to the bands and small tubular domains as in the case $L_z = 1.5L_0$.

Λ_b = 2.0: Block Copolymers on Background with Strong Interaction Strength. By increasing the affinity of the background areas to its preferred block ($\Lambda_b = 2.0$), the interaction strength avoids the wetting of nonpreferential blocks and attracts completely the preferential blocks. The morphologies of block copolymers as a function of the width of the chemically patterned stripes are shown in Figure 7 for small film thickness ($L_z = 0.5L_0$). For $W = 0.5L_0$, small A domains appear immersed in the B domains; these small domains are connected to the large A domains by bridges (Figure 7a). As W increases to $W = 0.8L_0$, these small domains become isolated and appear to be spherical (Figure 7b). The morphology consists of bicontinuous, orthogonal, and band-like A or B domains and a square array of A spheres in the matrix of B domains. For $W = 1.0L_0$, the spherical domains disappear and the morphology consists of simple orthogonal bands only (Figure 7c).

For larger film thicknesses, the tendency to form lamellae starts to have more influence, particularly when the confinement size is a multiple of the lamellar period in the bulk. Figure 8 shows the block copolymer morphologies as a function of the film thickness on a background with a strong interaction strength ($\Lambda_b = 2.0$), and two different widths of chemically patterned stripes, $W = 0.5L_0$ and $W = 1.0L_0$. In this scenario, although the film thickness increases, the overall film structures are very similar and consist of networks connecting the full sample.

CONCLUSION

A series of new three-dimensional morphologies for block copolymers have been identified through their directed assembly between two chemically nanopatterned surfaces. Even in the simplest case, that of a symmetric lamellae-forming diblock copolymer, the system can form a series of intricate morphologies that could find applications in advanced technologies. For example, they could be useful in photovoltaic devices where it is required that the interfaces where the charge separation occurs be separated by only a few nanometers.[58] Additionally, photovoltaic devices require straight paths to transport the electrons and holes without loses due to irregular paths,[58] a condition that is also met by the morphologies presented in this work.

By changing the symmetry of the patterns with respect to the block copolymer morphology, the geometric properties and affinities of the chemically patterned stripes, and the thickness of the polymer films, block copolymers form complex three-dimensional structures that are not accessible in the bulk, or through the use of a single chemically patterned surface in thin films. It is expected that through more elaborate architectures and through use of blends it will be possible to increase the range of morphologies available.

AUTHOR INFORMATION

Corresponding Author

*E-mail: depablo@engr.wisc.edu.

Notes

The authors declare no competing financial interest.

ACKNOWLEDGMENTS

This work is supported by the National Science Foundation through the Nanoscale Science and Engineering Center at the University of Wisconsin under Grant No. DMR-0832760, and by the Semiconductor Research Corporation.

REFERENCES

(1) Hamley, I. W. *Angew. Chem., Int. Ed.* **2003**, *42*, 1692.
(2) Hamley, I. W. *Nanotechnology* **2003**, *14*, R39.
(3) Ruiz, R.; Kang, H.; Detcheverry, F. A.; Dobisz, E.; Kercher, D. S.; Albrecht, T. R.; de Pablo, J. J.; Nealey, P. F. *Science* **2008**, *321*, 936.
(4) Mirkin, C. A.; Rogers, J. A. *MRS Bull.* **2001**, *26*, 506.
(5) Whitesides, G. M.; Grzybowski, B. *Science* **2002**, *295*, 2418.
(6) Xia, Y. D.; et al. *Polymer* **2008**, *49*, 5596.
(7) Bates, F. S.; Fredrickson, G. H. *Annu. Rev. Phys. Chem.* **1999**, *41*, 525.
(8) Bates, F. S.; Fredrickson, G. H. *Phys. Today* **1999**, *52*, 32.
(9) Hamley, I. W., *The Physics of Block Copolymers*: Oxford University Press: Oxford, U.K., 1998.
(10) Kim, S. O.; et al. *Nature* **2003**, *424*, 411.
(11) Stoykovich, M. P.; Müller, M.; Kim, S. O.; Solak, H. H.; Edwards, E. W.; de Pablo, J. J.; Nealey, P. F. *Science* **2005**, *308*, 5727.
(12) Stoykovich, M.; Nealey, P. *Mater. Today* **2006**, *9*, 20.
(13) Park, M.; et al. *Science* **1997**, *276*, 1401.
(14) Cheng, J. Y.; Ross, C. A.; Thomas, E. L.; Smith, H. I.; Vancso, G. J. *Appl. Phys. Lett.* **2002**, *81*, 3657.
(15) Park, C.; Yoon, J.; Thomas, E. L. *Polymer* **2003**, *44*, 6725.
(16) Stoykovich, M. P.; et al. *Science* **2005**, *308*, 1442.
(17) Wilmes, G. M.; et al. *Macromolecules* **2006**, *39*, 2435.
(18) Stoykovich, M. P.; et al. *ACS Nano* **2007**, *1*, 168.
(19) Liu, G.; et al. *Adv. Funct. Mater.* **2010**, *20*, 1251.
(20) Ch. Daoulas, K.; et al. *Phys. Rev. Lett.* **2006**, *96*, 036104.
(21) Detcheverry, F. A.; Liu, G.; Nealey, P. F.; de Pablo, J. J. *Macromolecules* **2010**, *43*, 3446.
(22) Kang, H.; Detcheverry, F. A.; Mangham, A. N.; Stoykovich, M. P.; Ch. Daoulas, K.; Hamers, R. J.; Müller, M.; de Pablo, J. J.; Nealey, P. F. *Phys. Rev. Lett.* **2008**, *100*, 148303.
(23) Detcheverry, F. A.; Kang, H.; Ch. Daoulas, K.; Müller, M.; Nealey, P. F.; de Pablo, J. J. *Macromolecules* **2008**, *41*, 4989.
(24) Wang, Q.; Yan, Q.; Nealey, P. F.; de Pablo, J. J. *Macromolecules* **2000**, *33*, 4512.
(25) Wang, Q.; Nath, S. K.; Graham, M. D.; Nealey, P. F.; de Pablo, J. J. *J. Chem. Phys.* **2000**, *112*, 9996.
(26) Wang, Q.; Nealey, P. F.; de Pablo, J. J. *Macromolecules* **2002**, *35*, 9563.
(27) Petera, D.; Muthukumar, M. *J. Chem. Phys.* **1997**, *107*, 9640.
(28) Petera, D.; Muthukumar, M. *J. Chem. Phys.* **1998**, *109*, 5101.
(29) Tsori, Y.; Andelman, D. *J. Chem. Phys.* **2001**, *115*, 1970.
(30) Tsori, Y.; Andelman, D. *Europhys. Lett.* **2001**, *53*, 722.
(31) Tsori, Y.; Andelman, D. *Macromolecules* **2001**, *34*, 2719.
(32) Tsori, Y.; Andelman, D. *J. Polym. Sci., Part B: Polym. Phys.* **2006**, *44*, 2725.
(33) Wang, Q. *Macromol. Theory Simul.* **2005**, *14*, 96.
(34) Detcheverry, F. A.; Nealey, P. F.; de Pablo, J. J. *Macromolecules* **2010**, *43*, 6495.
(35) Stuen, K. O.; Detcheverry, F. A.; Craig, G. S. W.; Thomas, C. S.; Farrell, R. A.; Morris, M. A.; de Pablo, J. J.; Nealey, P. F. *Nanotechnology* **2010**, *21*, 495301.

(36) Nagpal, U.; Detcheverry, F. A.; Nealey, P. F.; de Pablo, J. J. *Macromolecules* **2011**, *44*, 5490.
(37) Nagpal, U.; Kang, H.; Craig, G. S. W.; Nealey, P. F.; de Pablo, J. J. *ACS Nano* **2011**, *5*, 5673.
(38) Ji, S.; Nagpal, U.; Liao, W.; Liu, C.-C.; de Pablo, J. J.; Nealey, P. F. *Adv. Mater.* **2011**, *23*, 3692.
(39) Matsen, M. W. *J. Phys.: Condens. Matter* **2002**, *14*, R21.
(40) Fredrickson, G. H., *The Equilibrium Theory of Inhomogeneous Polymers*; Oxford University Press: Oxford, U.K., 2006.
(41) Detcheverry, F. A.; Pike, D. Q.; Nagpal, U.; Nealey, P. F.; de Pablo, J. J. *Soft Matter* **2009**, *5*, 4858.
(42) Detcheverry, F. A.; Pike, D. Q.; Nealey, P. F.; Müller, M.; de Pablo, J. J. *Phys. Rev. Lett.* **2009**, *102*, 197801.
(43) Pike, D. Q.; Detcheverry, F. A.; Müller, M.; de Pablo, J. J. *J. Chem. Phys.* **2009**, *131*, 084903.
(44) Ramírez-Hernández, A.; Detcheverry, F. A.; de Pablo, J. J. *J. Chem. Phys.* **2010**, *133*, 064905.
(45) Müller, M.; Steinmüller, B.; Ch. Daoulas, K.; Ramírez-Hernández, A.; de Pablo, J. J. *Phys. Chem. Chem. Phys.* **2011**, *13*, 10491.
(46) Helfand, E. *J. Chem. Phys.* **1975**, *62*, 999.
(47) Ch. Daoulas, K.; Müller, M.; de Pablo, J. J.; Nealey, P. F.; Smith, G. *Soft Matter* **2006**, *2*, 573.
(48) Frenkel, D.; Smit, B., *Understanding Molecular Simulations*, 2nd ed.; Academic Press: San Diego, CA, 2002.
(49) Wu, X.-F.; Dzenis, Y. *J. Chem. Phys.* **2006**, *125*, 174707.
(50) Man, X.; Andelman, D.; Orland, H. *Macromolecules* **2010**, *43*, 7261.
(51) Hur, S.-H.; Frischknecht, A. L.; Huber, D. L.; Fredrickson, G. H. *Soft Matter* **2011**, *7*, 8776.
(52) Ji, S.; Liu, C.-C.; Liu, G.; Nealey, P. F. *ACS Nano* **2010**, *4*, 599.
(53) Liu, G.; Ramírez-Hernández, A.; Yoshida, H.; Nygård, K.; Satapathy, D. K.; Bunk, O.; de Pablo, J. J.; Nealey, P. F. *Phys. Rev. Lett.* **2012**, *108*, 065502.
(54) Thomas, E. L.; et al. *Nature* **1988**, *334*, 598.
(55) Gido, S. P.; et al. *Macromolecules* **1993**, *26*, 4506.
(56) Belushkin, M.; Gompper, G. *J. Chem. Phys.* **2009**, *130*, 134712.
(57) Liu, C. C.; A. Ramírez-Hernández, Han, E.; Tada, Y.; Yoshida, H.; Kang, H.; Gopalan, P.; J. J. de Pablo Nealey, P. F.; to be published.
(58) Darling, S. B. *Energy Environ. Sci. 2* **2009**, 1266.
(59) Images created using Paraview, an Open-Source Scientific Visualization Software, http://www.paraview.org/.
(60) Only when $L_Z = mL_0$, where m is an integer and the background is neutral, do we observe a parallel symmetric lamellar morphology.

Macromolecules

Article

pubs.acs.org/Macromolecules

Simulation of Semiflexible Cyclic and Linear Chains Moderately and Strongly Confined in Nanochannels

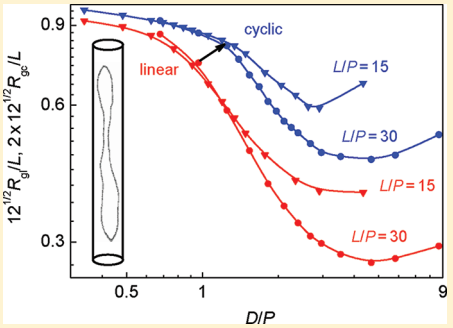
Zuzana Benková*[,†,‡] and Peter Cifra[†]

[†]Polymer Institute, Slovak Academy of Sciences, Dúbravská cesta 9, 845 41 Bratislava, Slovakia

[‡]REQUIMTE, Chemistry Department, University of Porto, Rua do Campo Alegre 687, 4169-007 Porto, Portugal

Supporting Information

ABSTRACT: The constraints due to the chain closure in combination with the geometrical constraints of a DNA molecule are inevitable for many biological processes. In this work, structural properties of flexible and semiflexible cyclic chains and their linear analogues confined in cylindrical channels were studied using the coarse-grained Metropolis Monte Carlo simulations. The radius of gyration satisfactorily represents the longitudinal stretching of both chain topologies. Transition between the moderate and strong confinement regime of semiflexible cyclic chains is described for the first time. Qualitatively similar response of the chain elongation to the confinement strength variation $R_g(D)$ is obtained in the case of cyclic chains. However, the relative chain extension is stronger, the Odijk strong confinement regime is extended to larger channel diameters D, and under moderate confinement the chain extension declines less steeply for cyclic chains. All three findings are explained in terms of the strong self-avoidance of confined chains relative to their linear analogues and the last finding is consistent with the reported experimental measurements. In the Odijk regime, the relative chain extension is governed by the same analytical functions provided half of the contour length for a cyclic chain is considered at the full extension. The orientation correlations for a cyclic chain in narrow channels are characterized by a typical sharp central minimum. Upon increasing the channel cross-sectional area, the minimum is broadened, turns into a negative maximum and, ultimately, the orientation correlations merge with those for a free cycle. Confined flexible and less stiff chains resemble their linear analogues more readily. The static structure factor for tightly confined chains provides better differentiation between the chain architecture than for free chains.



1. INTRODUCTION

In biological systems, biomacromolecules usually adopt conformations perturbed by the constraints invoked by a crowded cellular environment. Because of the reduced conformational freedom, the structure of a confined chain appreciably differs from the structure of a free chain in bulk. Exploring the structural changes triggered by confinement is inevitable for understanding biological properties and functions of DNA and other biomacromolecules as well as for manufacturing nanopores and nanochannels used to investigate and manipulate DNA. The free space achievable for a confined biomacromolecule is usually of micro- or nanoscale dimensions, which often means orders of magnitude smaller dimensions than the unperturbed size of a free biomacromolecule. Depending on the dimensionality of the confining object, classified according to the number of dimensions in which a chain is prevented from relaxation as uni-, bi-, or triaxial geometries (in fully symmetric approximation being slit, channel, or sphere, respectively), the structural and dynamic properties of confined macromolecules are substantially modified.

Recent advances in visualization and manipulation of semiflexible biopolymers in experimental techniques dealing with the macromolecular systems have recorded a great improvement in providing information on single-chain systems. Of special relevance to nanotechnology are the experimental approaches based on the chip-based micro- and nanofluidic devices combined with the florescence microscopy.[1−7] In these experimental setups, the extensions and Brownian dynamics of solvated chains, for example, DNA molecules being very often scrutinized, are affected.

The significant elongation of a DNA molecule was attained at the experimental level in cylindrical nanochannels, as high as 88% of the entirely stretched DNA backbone.[7] The average chain extension dependence on its molecular weight achieved in these experiments are consistent with the blob-theory predictions worked out by de Gennes.[8,9] Accordingly, under the biaxial constraints, a chain is viewed as a linear sequence of self-avoiding impenetrable blobs. The size of a particular blob is equivalent to the diameter of the channel cross-section. A fragment of the chain conforming to each blob obeys statistics of an unconfined chain. Assuming the excluded volume (EV) interactions among segments within each blob, the linear array

Received: December 19, 2011
Revised: February 16, 2012
Published: March 1, 2012

 © 2012 American Chemical Society dx.doi.org/10.1021/ma202730c | *Macromolecules* 2012, 45, 2597−2608

of such a blob determines the average chain extension along the channel axis

$$R \approx L\left(\frac{Pw}{D^2}\right)^{1/3} \quad (1)$$

where L is the contour length of a chain, P and w are its effective persistence length and width, respectively, and D stands for the diameter of a channel. Validity of eq 1 requires a sufficiently long chain comprising enough blobs for good statistics as well as sufficient number of segments in a blob for the EV interactions. The latter condition is controlled by the persistence length and width of the chain backbone (for a given polymer being a function of the ionic strength) and by the diameter of the channel cross-section since $D \approx (gl)^{3/5}(Pw)^{1/5}$, g is a number of segments constituting one blob and l is a bond length between two consecutive segments.

In the context of the channel cross-section dimension, it should be pointed out that the de Gennes moderate-confinement regime is restricted to $P \ll D \ll R_{g0}$; R_{g0} is the radius of gyration of a corresponding free chain. Beyond the upper boundary, a chain retrieves the conformation of a free chain. Once the channel width drops approximately below the Kuhn statistical segment ($2P$), the EV interactions fade away and the conformation of a confined chain is governed by the interplay of the confinement strength and intrinsic chains stiffness. In this strong-confinement regime, a polymer becomes preferentially directed and thus the contour length is stored solely in deflections of a chain from channel boundaries. The new characteristic length scale, the deflection length λ, introduced by Odijk for this regime,[10] scales as $\lambda \approx (D^2P)^{1/3}$ and represents the average distance along the chain contour between two consecutive deflection points. Using these arguments leads to the following relation for the chain extension

$$R = L\left[1 - A\left(\frac{D}{P}\right)^{2/3}\right] \quad (2)$$

where A is a constant dependent solely on the geometry of a cross-section.[11] The transition between the moderate-confinement (de Gennes) regime and the strong-confinement (Odijk) regime occurs at the channel width of the order of the persistence length.[2,12,13] Notice that in both regimes, the chain elongation is linear in the chain contour length as is clear from eqs 1 and 2. This is an advantageous phenomenon in sizing of DNA fragments in nanofluidic arrays.

Experimental measurements gave support to the linear dependence of the chain extension on the chain contour length and point out the importance of this relation in one-to-one mapping between genomic order and measured position along the stretched chains.[1] However, scaling of the chain extension with the strength of moderate confinement $R \sim D^x$ yields the exponent x slightly departing from the predicted value $-2/3$.[2,6] The steeper decrease in chain extension with increasing cross-section dimensions was reported.[2,6] This exponent appeared to be a nonuniversal quantity[6] as a consequence of the transition regime at which the reported experiments were conducted. We found similar scaling relation, performing the Metropolis Monte Carlo (MC) simulations on single linear coarse-grained DNA chains confined in a channel and explained the steeper decrease by the tendency of semiflexible chains to ideality.[13,14] However, the recent mean-field analysis shows that, except for very wide channels, there is no power-law dependence of the axial chain extension on the channel diameter even for the infinitely long chain limit.[15] In agreement with computer simulations and experimental measurements, this analysis predicts rather steeper decay in this regime.[15]

Among the experimental and theoretical works focused on linear chains trapped in a constrained space, special attention is paid to the semiflexible biopolymers such as DNA molecules or actin filaments.[16−19] Nevertheless, in comparison with a relatively great deal of results achieved for biaxially confined linear macromolecules, the number of works aimed at their cyclic analogues is relatively scarce.[6,20,21] This means an inadequate imbalance in regard to the widespread occurrence of prokaryotic genomes and plasmids which are of circular topology and play an important role in manifold biochemical processes.[22] It is the ring topology of biomacromolecules which is essential to many biological and biochemical processes.

In order to shed light into the response of cyclic chains to the biaxial geometrical confinement in addition to the topological circularity constraints, we have carried out simulations using the Metropolis MC method. Since the majority of biopolymers are stiff on the length scale comparable to their persistence length, we have studied flexible as well as semiflexible chains. We have investigated the moderate chain contour length corresponding to a few persistence lengths representing the contour length-persistence length ratio intrinsic to many biopolymers relevant to biological regulatory functions or to a gene therapy based on plasmids. The conformations of closed semiflexible chains induced by the cylindrical constraints were compared with the open chain analogues as well as with the unconfined counterparts in order to address the effects arising from the topological and biaxial geometric constraints. The influence of backbone stiffening was investigated through the comparison with analogous flexible chains.

This study is aimed to fill the gap in investigation of cyclic flexible and semiflexible chains confined in a cylindrical channel and to compare their behavior with corresponding linear counterparts. The response of the chain elongation to the confinement strength is scrutinized and regimes close to the original Odijk and de Gennes regimes are investigated for cyclic macromolecules. The existence, behavior and location of a confinement transition from the weak to strong confinement for cyclic chains are intriguing issues. Under the strong confinement, $D/P < 1$, a linear chain can be trapped fully extended in a narrow channel of the width D almost as small as the chain thickness. The question that emerges is whether a semiflexible cyclic chain with two natural loops stemming from the chain closure can be trapped in such a narrow channel. Apart from the chain extension-confinement strength curves, the orientation correlations and static structure factor are examined as the quantities differentiating both chain architectures.

The rest of the paper is organized as follows. The details of the simulations including the simulation technique, the potential functions and polymer model systems are outlined in the next section. Section 3 divided into four subsections presents the results obtained in this study. In section 4, our main conclusions are summarized based on the results presented in previous discussion.

2. METHODOLOGY

The semiflexible chains were represented by a bead−spring worm-like chain (WLC) model which has been adopted in previous studies of chains threading between inter connected cavities[23] and the structural properties of confined semiflexible polymers.[24,25] This model differs from the classical WLC model in the discretization of the chain backbone into N effective monomers (beads) connected along a chain by the fluctuating effective bonds (springs) of an average length $\langle l \rangle$. Since the bonds were allowed to vibrate around a preferred value, the contour length $L = (N - 1)\langle l \rangle$ in the case of open chains and $L = N\langle l \rangle$ in the case of closed chains underwent small fluctuations.

Molecular simulations were carried out using the Metropolis Monte Carlo technique. The total potential energy of a system was composed of contributions due to the effective bond stretching, nonbonded pair interactions between beads, and bending of two consecutive effective bonds from their collinear arrangement. Since we focused on the behavior associated with the topological effects we truncated detailed local conformation properties for simplicity reasons. In the future refinements especially the torsion rigidity could be included together with the bending rigidity.[26] The role of torsion, however, has not been well established yet. It was shown that at viral packaging the torsion can be omitted from the simulations without alteration of DNA conformation or the free energy of packaging even at low volume fraction or at early stages of filling the bacteriophage.[27] The MC simulations of a DNA molecule confined in a nanochannel using primitive model of DNA which did not consider torsion interactions also produced results in a good agreement with the experimental observations and theoretical prediction.[7] However, for a circular dsDNA chain, the assumption of the neglected torsional effects is adequate only provided it is in a torsionally released, nicked state. In addition, one should not resort to this model in the case the short-range DNA self-interactions, especially dehydration and cholesteric effects are present.

We adopted the established model used previously for bond stretching and nonbonded interactions.[28] The lengths of effective bonds were determined by the finitely extensible, nonlinear elastic potential (FENE)

$$\frac{U_{\mathrm{FENE}}(l)}{k_{\mathrm{B}}T} = -\kappa(l_{\max} - l_{\mathrm{o}})^2 \ln\left[1 - \left(\frac{l - l_{\mathrm{o}}}{l_{\max} - l_{\mathrm{o}}}\right)^2\right] \tag{3}$$

The bond vibrations were considered to be temperature independent with the spring constant $\kappa = 20$. The bond length was restricted to the preferred value $l_0 = 0.7$ and allowed to oscillate by the increment $l_{\max} - l_0 = 0.3$. The maximum allowable bond distance $l_{\max} = 1$ was identified with the length unit.

The nonbonded interactions were characterized by a Morse potential[28] which contains repulsive and attractive terms.

$$U_{\mathrm{M}}(r) = \varepsilon\{\exp[-2\alpha(r - r_{\min})] - 2\exp[-\alpha(r - r_{\min})]\} \tag{4}$$

where the energy at minimum ε, the distance at minimum $r_{\min}$ and the steepness of the potential energy function α were set to 1 $k_{\mathrm{B}}T$, 0.8 and 24, respectively. This combination yields the core radius of a bead $w/2 \approx 0.38$. As the core diameter w exceeded the effective bond length $\langle l \rangle \approx l_0$ by a factor of about 1.08 the utilized approach belonged to partially fused-spheres molecular models in contrast to the tangent sphere model, where $w = \langle l \rangle$. The nonbonded interactions were marginally small for $r > l_{\max}$.

The bending energy was quantified by the bending potential[29]

$$U_{\mathrm{b}}(\gamma) = b^*(1 + \cos\gamma) \tag{5}$$

where γ was the valence angle made by the two consecutive effective bonds. The stiffness of chains was considered to be temperature dependent through the bending parameter $b = b^*/k_BT$ since b^* was proportional to the pair-contact interaction energy ε entering eq 4, $b^* = C\varepsilon$. Except for the bending stiffness of a rod the bending parameter also includes the effect from the nonbonded interactions between chain segments, it leads to the orientation correlation between chains and to the chain stiffening by interactions or by lowering the temperature. Coupling of parameters of the interaction potentials is common in the coarse-grained simulations and allows for a reliable prediction of the polymer−solvent phase diagram.[30] The simulations were performed, however, at constant reduced temperature $T^* = k_{\mathrm{B}}T/\varepsilon = 1$ representing good solvents, since the reduced theta temperature of the model flexible linear chain is at $T_\theta^* = 0.62$. As was shown and explained at theoretical and experimental level,[31] the topological constraints ensuing from the chain closure are responsible for entropy reduction and for increase of the excluded volume effect.[32] This leads to a drop of the T_θ value for circular chains and thus the good solvent conditions used in these simulations apply for cyclic polymers as well.

The investigated closed and open polymers comprised $N = 300$ effective monomers. The bending parameter b introduced in the expression for the bending energy 5 quantified the rigidity of chains. For linear infinitely long WLC chains the elasticity theory of semiflexible rods relates the parameter b directly to the persistence length P, defined as the average projection of the end-to-end vector on the direction of the first bond, through $b = P/\langle l \rangle$. The validity of this relation for the discretized WLC model used in this work was confirmed in previous simulations.[33] This value of persistence length can be extracted from the initial exponential decay of the orientation correlations. Recently, it has become clear that for real polymer chains the standard definition of persistence length as a measure of the local chain stiffness should be modified mainly due to an increased flexibility of chain ends.[34,35] In ring polymers, however, we are in more favorable situation since we do not need to subtract the effect of more flexible chain ends when evaluating the orientation correlations along the chain backbone. In addition to simulations of semiflexible chains of the stiffness $b = 10$ and 20, corresponding to $L/P = 30$ and 15, respectively, we examined fully flexible ($b = 0$) chains.

At this point it is instructive to show the mapping of the presented model to a double stranded DNA chain.[36] First, the bond length l_0 is set equal to the effective diameter $d = 2.5$ nm of a dsDNA chain (notice that the bond length in model is very close to the diameter of a bead core). The commonly accepted persistence length of about $P = 50$ nm, i.e., $P/l_0 = b = 20$, represents the intrinsic stiffness of DNA at physiological conditions. However, this value is length-scale dependent and might not necessarily characterize the true stiffness of a confined DNA chain. Rather it might be altered across cells, cellular states, as well as locally within any given cell depending on its biological state. This type of parametrization of the

dx.doi.org/10.1021/ma202730c | Macromolecules 2012, 45, 2597−2608

coarse-grained bead−spring model was used previously and performed well in describing the extension of linear DNA molecules in channels and of toroidal packing of DNA in viral capsids.[37−39] Comparison of the results obtained with the two different stiffness parameters might supply the effect of increased ionic strength responsible for diminishing of the backbone stiffness.[40,41]

The confinement effect of a channel was modeled through the cylindrical hard-wall potential. The transverse dimension accessible for the bead centers in a channel was characterized by the diameter D^*. However, to consider the space reachable for all the bead volume, the diameter of the channel was assigned as $D = D^* + w$. Such a width for the bead volume was used in other simulation studies of confined polymers.[42,43] Periodic boundary conditions were applied along the channel axis. The lumen of a channel covered the range $D/l_0 = 6.80-86.80$.

For the simulations of linear chains the procedure of the reptation chain updates with 3×10^7 MC cycles of trial moves was used to obtain the ensemble averages. The initial conformations for the simulations were a straight rod and a prolate ellipse aligned with the channel axis, for a linear and for a circular chain, respectively. The conformations of closed chains were generated by small trial random displacements of beads. The amplitude of small displacements (kinks) was 0.125 l_0. In order to prevent circles from opening the quasi-terminal segments 1 and N were excluded from these motions. After a predefined number of kinks, corresponding to the number of chain segments allowed for the random displacement $(N - 2)$, new quasi-terminal segments were selected randomly and the chain was subject to respective renumbering. The number of described MC cycles varied between 2×10^8 to 4×10^8. The equilibrium of the simulated systems was judged from the smoothness of the distribution function of the radius of gyration evaluated from the histograms (Figures S1−S6, Supporting Information). The estimated errors of ensemble averages in the chain extensions were typically within the size of figure symbols.

3. RESULTS AND DISCUSSION

3.1. Chain Extension. It has been well established that a linear chain confined to a sufficiently long and narrow channel is significantly extended along the channel axis. Figure 1 compares the logarithmic plots of the chain extension-channel diameter functions obtained for linear flexible ($b = 0$) and semiflexible ($b = 10, 20$) chains of the length $N = 300$ with their cyclic analogues. Because of the absence of terminal monomers in cyclic chains, the extension is quantified using the radius of gyration

$$R_g = \langle R_g^2 \rangle^{1/2} = \frac{1}{N}\left(\frac{1}{2}\sum_{i=1}^{N}\sum_{j=1}^{N}\langle R_{ij}^2\rangle\right)^{1/2} \quad (6)$$

where R_{ij} denotes the distance between the effective monomers i and j and the angle brackets stand for averaging over all equilibrated chain conformations.

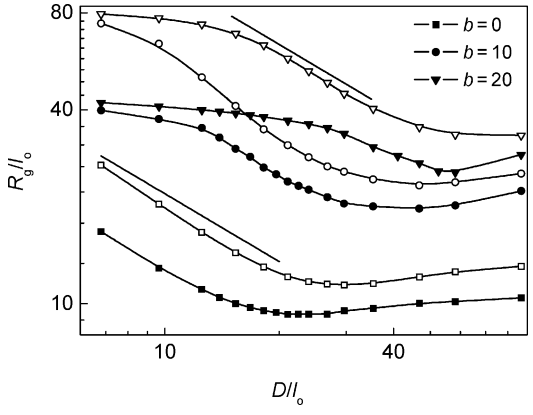


Figure 1. Logarithmic plot of the radius of gyration R_g/l_0 for cyclic (solid symbols) and linear (open symbols) chains of indicated stiffness parameters b as a function of the channel diameter D/l_0. The solid lines illustrate the slope of $1 - 1/\nu = -0.701$ with $\nu = 0.588$.

In Figure 1, the curves for flexible chains of both topologies and of the same contour length are very similar displaying a typical nonmonotonous pattern. Upon reduction of the channel cross-section size, starting from the weak confinement, chains are slightly squeezed and, after a shallow minimum, their radius of gyration follows an increasing trend with further reduction of D under the moderate and strong confinement. The scaling exponents in this linear part are -0.65 ± 0.03 and -0.76 ± 0.02 for cyclic and linear chains, respectively. No evidence for the Odijk regime has been detected for flexible chains of both architectures, in line with the absence of bending energy penalty.

For chains of both topologies and of $b = 10$, the behavior in the weak confinement is akin to that of flexible chains. However, in the narrow channels there is a small curvature found in the plot for a linear chain while the Odijk regime is already recognizable in the plot for a cyclic chain. For both nonzero stiffness parameters the radius of gyration for both chain architectures tends to the same limit as $D \to 0$ (Figure 1). In the moderate-confinement regime, the scaling exponents gained by fitting of the linear section of the curves are -0.69 ± 0.02 and -0.85 ± 0.02, respectively, for cyclic and linear chains of $b = 10$. In fact, the extension-confinement strength function $R_g(D)$ for a chain of the linear topology and of the stiffness $b = 20$ more or less parallels the plot for a cyclic chain of $b = 10$. The linear regime is again characterized by faster decrease for the open chain analogues. The respective exponents are -0.47 ± 0.02 and -0.71 ± 0.01 for cyclic and linear chains of $b = 20$, the former value should be taken only roughly because of a very short interval of the linear part. These findings are qualitatively consistent with the experimental results obtained for circular and linear DNA molecules[6] where the authors reported the corresponding exponents of -0.65 ± 0.01 and -0.85 ± 0.01 for a circular and linear DNA.

In the present simulations, the chain length in the number of segments is below the limit P^3/l_0w^2 roughly corresponding to approximately 850 and 6800 monomers for chains of $b = 10$ and 20, respectively, which is prerequisite for the existence of the classic de Gennes regime for linear chains.[12] In this regime, a chain is represented by an array of the impenetrable isometric blobs with the EV statistics inside each blob. Nevertheless, even the shorter contour length of a chain might be sufficient for the appearance of the de Gennes regime extended toward narrower channels, in which a chain is envisioned as an array of the anisometric blobs each containing $c(D^4P)^{1/3}/l_0w^{2/3}$ monomers obeying Gaussian statistics with a corresponding longitudinal length $(2NPl_o)^{1/2} = (2c)^{1/2}(DP)^{2/3}/w^{1/3}$ (c is a constant of the order of unity).[12] However, the extension of a chain is given by eq 1 in both the isometric and anisometric blob regimes. In the

dx.doi.org/10.1021/ma202730c | Macromolecules 2012, 45, 2597−2608

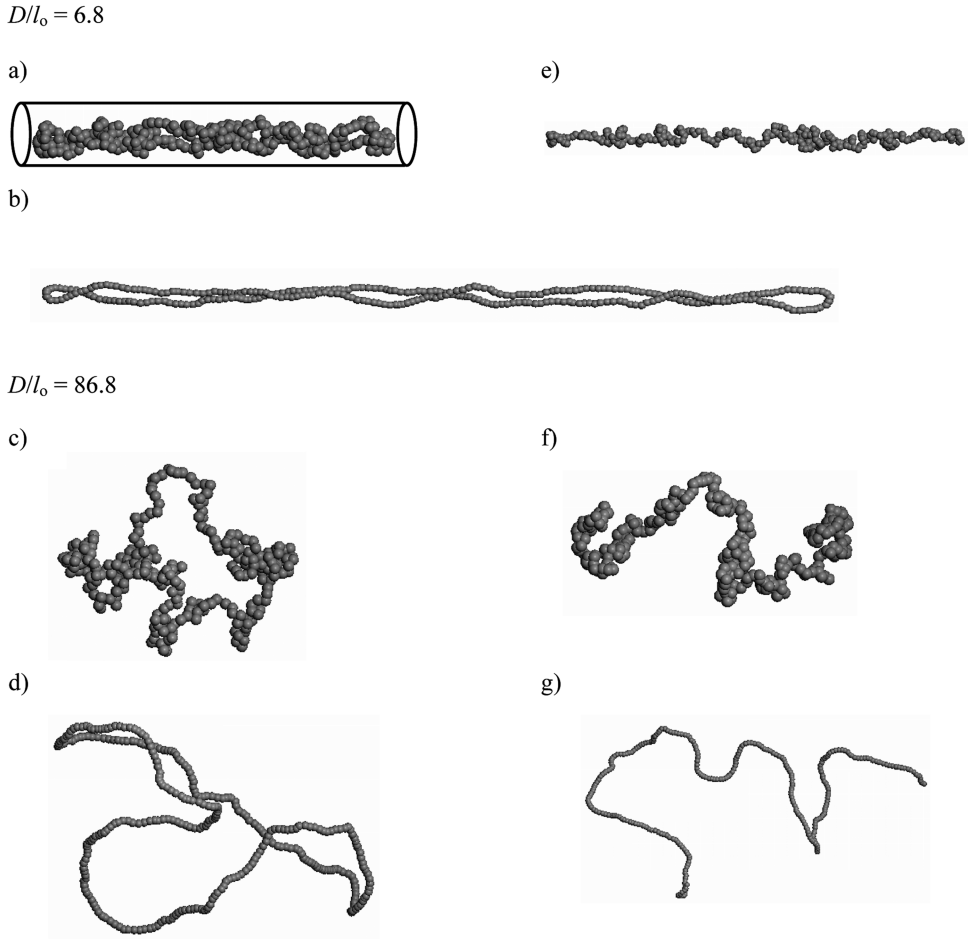


Figure 2. Snapshots illustrating the instantaneous conformations of cyclic (a–d) and linear chains (e–g) confined to a cylindrical channel of indicated diameter D/l_0. Snapshots a, c, e, f depict flexible chains ($b = 0$) and snapshots b, d, and g depict semiflexible chains ($b = 20$). The real size of the effective monomers is assumed to be the same in all snapshots.

later regime assuming $c = 1$, from 2 ($b = 20$, $D/l_0 = 20$) to 7 ($b = 10$, $D/l_0 = 10$) anisometric blobs can be formed within investigated chains of the length $N = 300$ monomers. For comparison, in the experimental study on linear (48.5 kbp) and circular (42.2 kbp) DNA[6] using the persistence length of 50 nm and the effective width of 2.5 nm the contour lengths of the investigated chain backbones were amenable to accommodate only about 5 to 18 anisometric blobs in channels of the geometrically averaged diameter of about 240 and 97 nm, respectively, however the chains were too short for even one isometric blob.

The slightly less pronounced decreasing tendency of the axial extension with the increasing channel width for a cyclic chain when compared with the extension of a linear analogue might be explained in terms of the chain extension dependence on the channel diameter scaling as $D^{1-(1/\nu)}$, where ν is the Flory exponent. As has been highlighted by the direct renormalization theory[44] and confirmed at the experimental level[45] the constraints due to the chain closure do not affect the Flory exponent for a free chain. However, in Figure 1 the scaling in the region of moderate confinement suggests a larger effective value of ν for cyclic chains ($\nu_c = 0.592 \pm 0.013$ vs $\nu_l = 0.541 \pm 0.036$ for $b = 10$). This discrepancy might be attributed to a more compact organization of monomers in a cyclic chain under the biaxial confinement caused by the doubled appearance of the monomers along the channel axis within the closed backbone. The denser segment arrangement follows also from the pattern of the structure factor-wavevector dependence discussed below. Consequently, monomers of a cyclic chain are slightly more susceptible to self-avoidance under the confinement and the effectively higher Flory exponent for the cyclic polymers diminishes the absolute value of exponent $x < 0$ in the D^x-dependent extension. Similar interpretation has been already offered by the experiments of Persson et al.[6] The same effect was observed also for linear chains.[46] Partly folded DNA chains confined in nanochannels were reported to have the extension of folded fragments greater by 30% as opposed to unfolded fragments. This was attributed to a greater self-exclusion in these folded fragments induced by a channel.

The deviation from the predicted $R_g(D)$ dependence of the chain extension is most likely due to the short-range of the extended de Gennes regime and thus due to a relatively large contamination ensuing from the intermediate regime between the Odijk regime and the de Gennes regime.[12] The range of the de Gennes regime becomes even shorter for cyclic chains because of the more striking apparent stiffening induced by the geometrical and topological constraints, which expands the Odijk regime toward larger channels. In order to achieve the quantitative agreement with the theoretically predicted $x = -0.701$ for $\nu = 0.588$, as well as to discern all predicted regimes,[12] one should rather resort to much longer chains,

dx.doi.org/10.1021/ma202730c | *Macromolecules* 2012, 45, 2597–2608

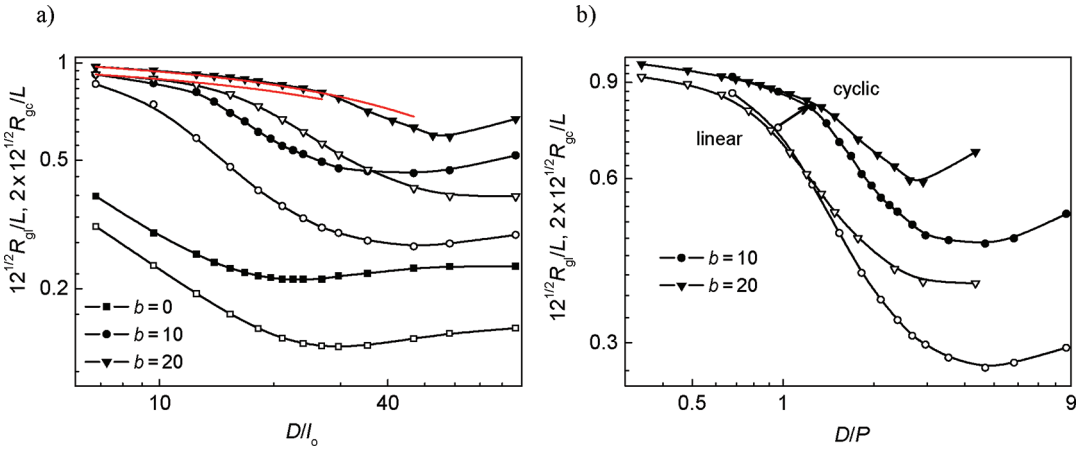


Figure 3. Logarithmic plot of the radius of gyration R_g reduced by the corresponding maximal feasible extension $L/(2\sqrt{12})$ and $L/\sqrt{12}$ for cyclic (solid symbols) and linear chains (open symbols), respectively, as a function of the channel diameter D/l_0 (a) and D/P (b). Stiffness parameters b are indicated in the legend. The solid lines in part a are fits based on eq 7.

which is beyond the scope of the present study. Considering the length and width of commonly used DNA molecules in experimental studies of confinement effects, it appears to be difficult to achieve the de Gennes regime for semiflexible chains even at the experimental level.[2,6]

The snapshots in Figure 2 outline the instantaneous conformations of flexible and semiflexible, open and closed chains trapped in a channel of $D < P$ as well as in a channel of $D > 2R_{g0}$.

In order to compare the relative extension of cyclic and linear chains the plots of the radius of gyrations reduced by the maximal achievable extension, being $L/\sqrt{12}$ for a linear chain and $L/(2\sqrt{12})$ for a cyclic chain, are presented in Figure 3a. These plots confirm the enhanced tendency of closed chains to the elongation in a biaxially confined space. Especially, in the weak and moderate confinement regimes (not too small D), the relative elongation of cyclic chains non-negligibly exceeds the relative elongation of linear chains. Since the circular chain architecture imposes back folding of a chain at both extreme positions of monomers in a channel, the monomers become more prevented from local back folding. In order to release the overcrowding caused by the enhanced monomer density, a cyclic chain becomes stretched along the channel axis. In very narrow channels the difference in the relative extension between semiflexible chains of both architectures diminishes as the plots approach unity, i.e., the limit value of reduced R_g characteristic for the maximally extended conformations.

On the contrary, the plots for flexible chains are getting closer in relative extension as the confinement strength increases but are still far from being merged. Since there is no correlation between monomers along the flexible chain backbone arising from bending interactions, the conformation is dictated exclusively by the EV interactions. Thus, in the case of flexible chains, one might expect a great deal of the chain extension in channels of the diameter comparable to the two effective widths of the monomer segments, i.e., $\sim 2.18l_0$. However, as the simulations revealed, even in such a narrow channel the ratio of $2\sqrt{12}R_g/L = 0.80$ and $\sqrt{12}R_g/L = 0.73$ for a cyclic and linear chain, respectively, is still less than unity approaching by semiflexible chains (Figure 3a). This finding along with the absence of the Odijk regime for flexible chains are evidence for presence of the coiled backbone sections instead of the locally stiff segments bouncing against channel walls.

Figure 3a also involves an analogue of eq 2 for the relative elongation of chains of both architectures and of the stiffness $b = 20$. Though this equation is derived for the longitudinal end-to-end distance, one may see that it applies to the radius of gyration as well. What is more striking, it applies also to cyclic chains and one might use the following equation in the analysis of cyclic chains in microfluidic devices

$$R_{gc} = \frac{L}{2\sqrt{12}}\left[1 - A\left(\frac{D}{P}\right)^{2/3}\right] \tag{7}$$

Only A parameter was fitted using eq 7, while the value of the persistence length was kept fixed at the value determined by the stiffness parameter b. The fitting procedure yields $A = 0.21$ and 0.20 for a cyclic and linear chain, respectively; both values are virtually equal within the error bar. These estimates are slightly higher than the estimate 0.1701 obtained by simulations for a channel with the cylindrical cross-section[11,47] and agree very well with the prefactor of 0.2 derived analytically when the confinement effect was represented by a parabolic potential.[48] While for a linear chain of $b = 20$ the onset of the Odijk regime might be assigned for a channel of the diameter around $12.51l_0$, the topological constraints due to the circularity shift this value to $D \approx 29.66l_0$. This statement is well supported by the plot of the reduced radius of gyration against the channel diameter reduced by the persistence length D/P (Figure 3b). According to eqs 2 and 7, such plots are anticipated to collapse onto one master curve in the Odijk regime. A satisfactory single curve is obtained for cyclic chains in this region, while for linear chains the coalescence is more shifted to the moderate-confinement regime. However, the expansion of the Odijk regime for cycles beyond $D/P = 1$, characteristic for linear chains, up to $D/P \approx 1.5$ is clearly seen. This is in line with the above discussion of the enhanced local density of monomers caused by the closed chain topology. The strong confinement regime becomes thus wider for semiflexible cyclic chains than for their linear counterparts.

dx.doi.org/10.1021/ma202730c | *Macromolecules* 2012, 45, 2597–2608

The relative mean square extension of a worm-like chain under a strong confinement is often described by the following relation[16]

$$\frac{\langle R^2\rangle}{L^2} = 1 - \frac{\lambda}{2P}\left\{1 + \frac{\lambda^2}{L^2}\left[1 - \sqrt{2}\,e^{-L/\lambda}\sin\left(\frac{L}{\lambda} + \frac{\pi}{4}\right)\right]\right\} \quad (8)$$

from which one may extract λ, or alternatively, the geometry-dependent prefactor a in relation $\lambda = aD^{2/3}P^{1/3}$ when plotted the relative chain extension against D. We have applied this relation to fit $\langle R_g\rangle^2/(12L^2)$ in Figure 4. The half circumference

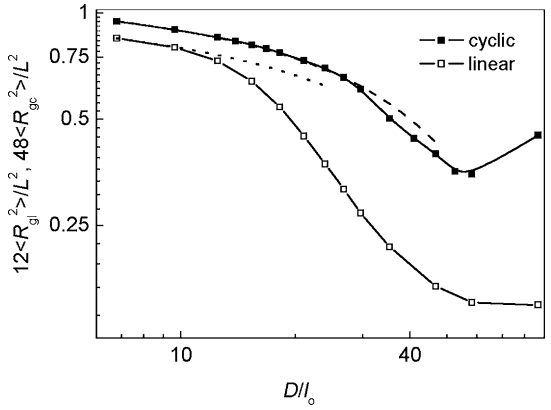


Figure 4. Logarithmic plot of the square radius of gyration R_g^2 reduced by the corresponding maximal feasible square extension $L^2/48$ and $L^2/12$ for cyclic (solid symbols) and linear (open symbols) chains, respectively, as a function of the channel diameter D/l_0. The stiffness parameter is $b = 20$. The dashed and dotted lines are the corresponding fits to eq 8.

length $L/2$ for the contour length of a cyclic chain was used in this relation. These plots are shown in Figure 4 along with their respective best fits which render the numerical prefactor $a = 0.69$. This value agrees fairly well with the value of 0.68 obtained by a two-parameter fit of the orientation correlation data for a linear chain of $b = 20$ to the prediction derived for a worm-like chain model similar to eq 8.[36] Köster et al. obtained the value of 0.76 by fitting the MC results using the same procedure.[49] The difference is most likely caused by the parabolic potential used to mimic the interactions between a chain and a channel wall in ref 49 while hard-wall potential was used in the present study. Nevertheless, our estimate is within the experimental bar of values 0.65−0.8.[49]

3.2. Radius of Gyration to Hydrodynamic Radius Ratio. An important quantity differentiating the ring conformation from the open-chain conformation is the radius of gyration to the hydrodynamic radius ratio R_g/R_h. The hydrodynamic radius was calculated as follows

$$\langle R_h\rangle = N^2\left(2\sum_{i=1}^{N}\sum_{j>i}^{N}\langle R_{ij}^{-1}\rangle\right)^{-1} \quad (9)$$

For free flexible cyclic and linear Gaussian chains, respectively, these analytic values read $(\pi/2)^{1/2}$ and $8/(3\pi^{1/2})$.[32] The excluded volume effects are accounted for through the cluster expansions.[32] The evolution of R_g/R_h ratio with the confinement strength is displayed in Figure 5. The theoretical predictions for free flexible Gaussian chains are also included.

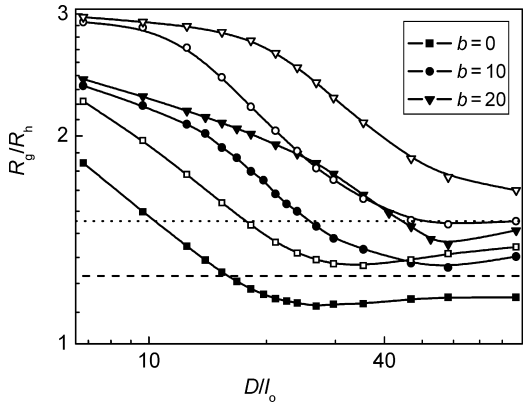


Figure 5. Logarithmic plot of the radius of gyration to the hydrodynamic radius ratio R_g/R_h for cyclic (solid symbols) and linear (open symbols) chains of indicated stiffness parameters b as a function of the channel diameter D/l_0. The dashed and dotted lines, respectively, depict the analytical predictions of $(\pi/2)^{1/2}$ and $8/(3\pi^{1/2})$ for flexible cyclic and linear Gaussian chains.

One should take into account that the results presented in Figure 5 contain contributions due to the EV, local chain stiffness, geometrical and in the case of cyclic chains also topological constraints. Moreover, the chain length is far from the saturation limit where the finite-chain-length correction for both R_g and R_h is negligible. Since the accurate estimation of the hydrodynamic radius is more sensitive to the finite chain length than the radius of gyration,[50] this correction is supposed not to be canceled in the R_g/R_h ratio. To determine the exact value computationally is a challenging task.

As is seen in Figure 5, the R_g/R_h ratio for semiflexible chains of both investigated stiffness parameters tends to the same value in a very strong confinement. This limit is larger for linear chains. In intermediate channels the stiffer chains exhibit larger R_g/R_h ratio. In the case of flexible chains the curves for both chain architectures are more or less parallel. The trend in the plots is qualitatively akin to the trend of corresponding R_g plots (Figure 1) but the shallow minima are slightly shifted toward the larger channel diameters.

3.3. Orientation Correlation Function. Now, we continue this study by investigation of the orientation correlation function $\langle \boldsymbol{u}_i\boldsymbol{u}_j\rangle = \langle\cos\theta_{ij}\rangle = \exp[(-|i-j|\langle l\rangle)/P]$, where $\boldsymbol{u}_i$ and $\boldsymbol{u}_j$ hold for the unit vectors tangent to the chain contour at positions of the ith and jth segments, respectively, θ_{ij} is the angle formed by these vectors and the exponential terms is the WLC representation of the orientation correlations. The averaging runs over all equilibrated MC steps and all pairs of indices i and j separated along the chain backbone by the same section $|i-j|\langle l\rangle$ of the contour length L. This property is applicable to distinguish a cyclic chain from its linear analogue.

The orientation correlations as a function of the segment separation for flexible and semiflexible closed chains of $b = 10$ and 20 confined in channels of different cross-sectional diameters are compared with the respective functions for open counterparts in Figure 6. In the orientation correlations, the closed topology manifests itself by a fundamental difference which is the symmetric shape around $n = N/2$ with a negative minimum, or a negative local maximum in the center of the chain backbone discussed in more detail below.

For a linear chain the deflection from a channel wall demonstrates itself by the local minimum followed by the horizontal line.[36,49] The reduced $\langle \boldsymbol{u}_i\boldsymbol{u}_j\rangle$ value around the

dx.doi.org/10.1021/ma202730c | Macromolecules 2012, 45, 2597−2608

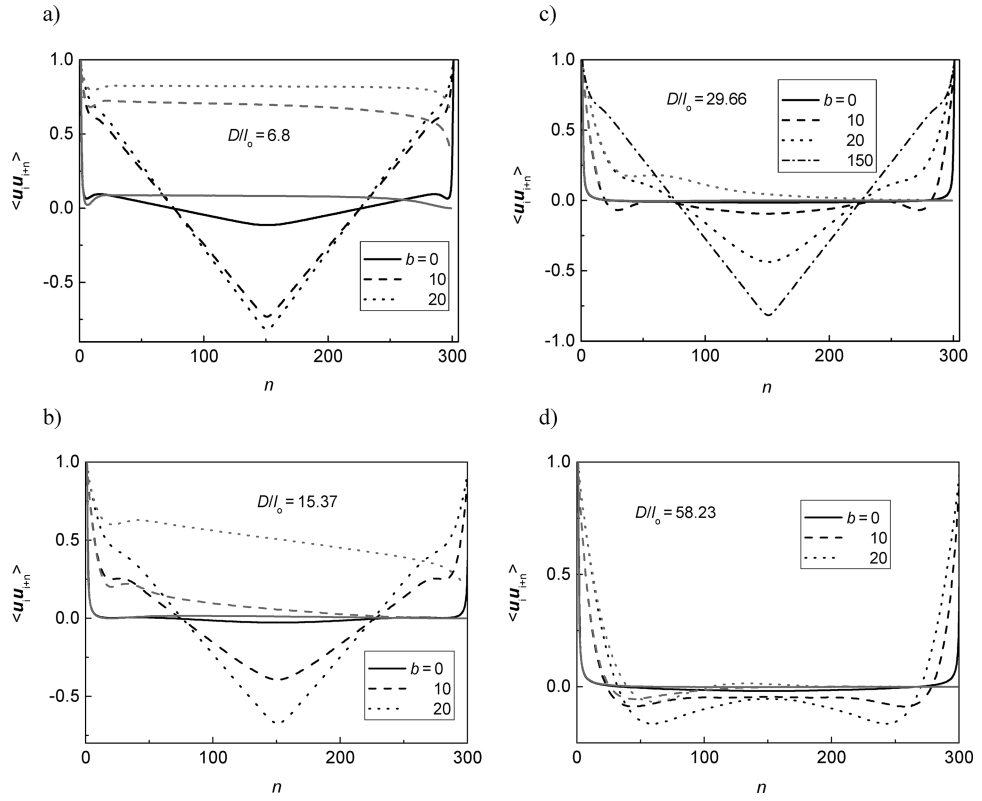


Figure 6. Dependence of the orientation correlations $\langle u_i u_j \rangle$ on the segment separation n along the chain backbone for cyclic (black lines) and linear (gray lines) chains of indicated stiffness parameters b confined in a cylindrical channel of diameter D/l_0 = 6.80 (a), 15.37 (b), 29.68 (c), and 58.23 (d).

deflection point for semiflexible cyclic chains with respect to their linear counterparts implies that the first collision of the cyclic chain backbone with a channel wall is realized at slightly larger angle for closed than for open chains (Figure 6a). This is brought about by a U-turn at the end of a stretched cyclic chain in a channel. The initial decay turns out to be identical for both architectures of a free chain[51] or moderately confined and not too stiff chains (Figure 6b–d). After the initial decay of $\langle u_i u_j \rangle$ followed by a less steeply declining part (Figure 6a, b = 10, 20; Figure 6b,c, b = 20) or a plateau after the local minimum (Figure 6b,c, b = 10) in narrow channels, the plots of the orientation correlations of closed semiflexible chains decrease in a linear fashion toward the central sharp minimum, representing the U-turn, while open chains are characterized by only slightly decreasing orientation correlations. Such a linear behavior of the orientation correlations is a compromise between the correlations of monomers induced by the geometrical and topological constraints combined with the local rigidity of semiflexible cyclic chains. Interestingly, similar pattern of the initial decay of the orientation correlation functions consisting of two regimes has been found for two-dimensional polymer rings in the Langevin dynamics study and confirmed by the experimental measurements.[52] For a flexible chain no plateau evolves and in very narrow channels the linear decrease follows immediately after the local minimum (Figure 6a) in the first half of x abscissa. In wider channels, the orientation correlations for a flexible chain of both architectures are more or less identical, except for the tailing part of the orientation correlations (Figure 6b–d). This implies that the excluded volume and local correlations are more important than the circularity constraint.

While the difference in the orientation correlations appears to be marginal between semiflexible cyclic chains of both b values in the channel of D/l_0 = 6.80 (Figure 6a), the orientation correlations for a flexible chain decrease more slowly in the linear part, since the topological constraints are less severe. As the channel is widened the orientation correlations of a stiffer cyclic chain (b = 20) are getting steeper and deeper around the central minimum than those of a chain of b = 10 (Figure 6b) and thus the differentiation between cyclic chains of different stiffness becomes more pronounced. On the other hand, the channel widening is accompanied by attenuating differences in the orientation correlations between cyclic and linear chains. This trend, however, is least noticeable for a chain of b = 20 (Figure 6c).

Interestingly, in a wide channel of $D/l_0 \approx 60$ a local maximum replaces a central minimum for chains of b = 10 and 20. The shape of the orientation correlations for investigated semiflexible cyclic chains confined in the channel of D/l_0 = 58.23 might be interpreted in terms of loop formation (Figure 6d). Generation of such locked entities is expected for a certain combination of the chain persistence length and channel diameter ratio[53] analogously to the hairpin formation found along the biaxially confined linear chain backbone.[36] The similar orientation correlations were obtained in MC simulations of semiflexible cyclic chains in a confinement of spherical symmetry.[54] After the first collision of a linear chain with the channel wall the oscillations of the chain backbone along the wall is feasible. Averaging of these oscillations over all equilibrated chain conformations damps their amplitudes and ultimately leads to a plateau followed by declining tailing part or, in wider channels, it decreases without any flat region.[15,55,56]

dx.doi.org/10.1021/ma202730c | Macromolecules 2012, 45, 2597–2608

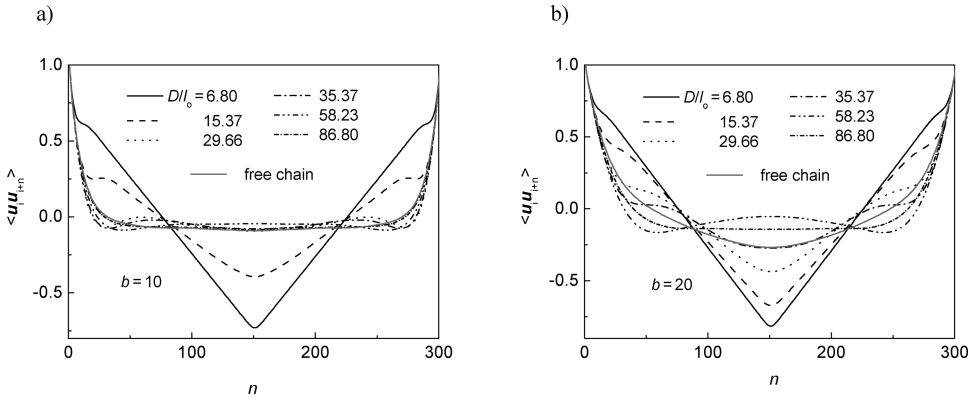


Figure 7. Dependence of the orientation correlations $\langle u_i u_j \rangle$ on the segment separation n along the chain backbone for cyclic chains of the stiffness parameter b = 10 (a) and 20 (b) confined in a cylindrical channel of indicated diameters D/l_0. For comparative purposes, the orientation correlation function of a free chain is also comprised for both stiffness parameters.

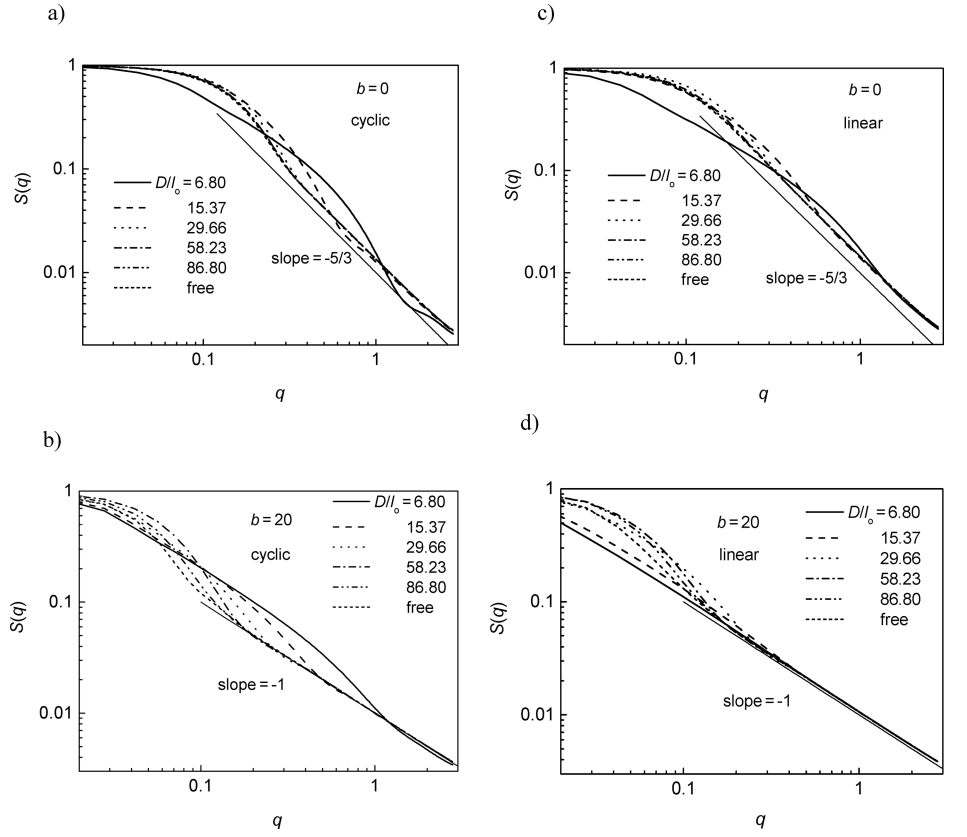


Figure 8. Logarithmic plot of the static structure factor $S(q)$ vs the wavevector q for cyclic (a, b) and linear (c, d) chains of the stiffness parameter b = 0 (a, c) and b = 20 (b, d) in the channel of indicated diameters D/l_0. The plot for a corresponding free chain is also included and the solid straight line in each graph is a guide for the eye representing the slope of −5/3 (a, c) and −1 (b, d), i.e., $q^{-1/\nu}$ type of behavior discussed in the text for the coil and rod-like regime, respectively.

Parts a and b of Figure 7 provide the evolution of the orientation correlation functions with the channel dimensions for a cyclic chain of b = 10 and 20, respectively. Increase of the channel diameter is reflected on the gradual plateau formation between the initially decaying part and linear part of the plot. As mentioned above, in the case of a semiflexible chain of b = 10 the plateau is preceded by a local minimum. Upon channel widening the linear part of the orientation correlation function is simultaneously shortened and reduced in the steepness which shifts the minimum upward along the y axis. As aforementioned, in the channel of D/l_0 = 58.23, the central minimum turns to a local maximum for semiflexible cyclic chains of both stiffness parameters. In the channel of $D > 2R_{g0}$, the geometrical constraints are less important and the orientation correlation functions tend to those of free cyclic chains, faster for more flexible chains. Comparison between orientation correlations for chains of b = 10 and 20 (Figure 7a vs 7b) shows that the orientation behavior of both chains follows the same trend but more flexible chains undergo the particular changes in spacial organization already at stronger confinement. To demonstrate this observation, the orientation correlations for a cycle of b = 150 is added in Figure 6c as well.

dx.doi.org/10.1021/ma202730c | *Macromolecules* 2012, 45, 2597−2608

Worth noting is that the orientation correlation functions for both semiflexible chains confined in channels of various diameters conforming to the Odijk regime intersect in the same narrow region symmetrically distributed around $N/2$. At these points, being $n = 75$ and 226, the orientation correlations essentially attain zero value. The orientation correlations of free semiflexible up to very stiff cyclic chains of the length $N = 300$ were shown to cross each other exactly at these points.[51] As one can see in Figure 2a−d, the restricted space along with the topological constraints is responsible for the enhanced formation of loops. The looping structures are prerequisite to many important biological processes involved, e.g., in the genome-wide coordination of gene expression.[57] Nevertheless, as inferred from the missing regular oscillations in the orientation correlations (Figures 6 and 7) the loops do not possess any defined size upon biaxial confinement as opposed to the oscillatory orientation correlations behavior found for a triaxial confinement using the MC bond-fluctuation model.[58] The authors of this study calculated also the orientation correlations for cyclic chains trapped in the rectangular confinement of a squared base and of a width-to-height ratio 1:8.[58] For the shortest chain they obtained results similar to ours with no central maximum. In other simulation studies, the toroidal structure of a semiflexible chain confined to a spherical cavity produced regular oscillations in the orientation correlations.[59] In other two-dimensional MC study of a linear semiflexible chain exposed to a square confinement, the orientation correlations of the spiral chain conformation possess a similar trend.[60] Since the chain investigated in the present study is free to relax in the longitudinal directions of a channel the same applies to its loops.

3.4. Static Structure Factor. The other quantity which might provide information on polymer topology and conformation is the single-chain static structure factor $S(q)$ plotted against the wavevector q

$$S(q) = \frac{1}{N^2}\left\langle \sum_{i=1}^{N}\sum_{j=1}^{N} \sin(qR_{ij})/qR_{ij} \right\rangle \tag{10}$$

This quantity is accessible through experimental measurements exploiting neutron and light scattering techniques. The behavior of a chain on different length scales is reflected on the behavior of the single-chain static structure factor. The most coarse-grained length scale, the Guinier regime, at $q \ll 1/R_g$ contains only information on the size of a chain. The length scales of the coil and rod regimes, in turn, correspond to the wavevector intervals $1/R_g \ll q \ll 1/P$ and $q \gg 1/P$, respectively. In both regimes, the structure factor is a power-law function of the wavevector $S(q) \sim q^{-1/\nu}$.

The effect of channel diameter on the structure factor for flexible and semiflexible chains of closed and open topology is seen in Figure 8. The behavior of $S(q)$ for a flexible cyclic chain confined in the channel of diameter down to $21.09l_0$ (not shown) is identical with that for a free flexible cyclic chain (Figure 8a). The peculiarity discerning a cyclic chain from its linear analogue is the "hump" pattern in $S(q)$ plot after the Guinier regime. Because of the increased compactness of monomers originating from the tight arrangement of two strands of a cyclic chain along a narrow channel this "hump" becomes even more apparent and consequently the coil regime with the characteristic exponent −5/3 is identified only for a flexible cyclic chain in channels of $D/l_0 \geq 12.51$. In contrast to a flexible cyclic chain, the coil regime in the $S(q)$ plot for a flexible linear chain, though shortened, remains also in very narrow channels (Figure 8c). In wider channels the $S(q)$ for both chain architectures become very similar and one should rather employ the Kratky representation of $S(q)$ to discern between both architectures.[51]

The coil regime is completely suppressed in Figure 8b,d illustrating the structure factor for confined semiflexible cyclic and linear chains of $b = 20$. Such a behavior is expectable on the basis of the enhanced backbone rigidity when the condition $R_g \gg P$ is not met. Similarly to a flexible cyclic chain, the "hump", though less noticeable, occurs also in the $S(q)$ plot for a strongly confined semiflexible cyclic chain (Figure 8b). In very narrow channels, it is the straight line stipulating the rod regime and covering whole interval of the q values for a semiflexible linear chain (Figure 8d) which discerns between both chain topologies. One can infer from Figure 8b,d that on smaller length scales, the impact of confinement on the structure of a confined semiflexible cyclic chain is more substantial when compared with the impact on a confined linear counterpart.

Shown in Figure 9 is the structure factor for a cyclic chain of different stiffness parameters contained in the channel of D/l_o = 29.66. Even for a very stiff cyclic chain of $b = 150$ ($L/P = 2$, $D/P = 0.2$) the typical gradually ceasing oscillations of $S(q)$ found for an unconfined chain of this stiffness[51] are vanishing under strong confinement and only a small sign of the periodic behavior is preserved for such a stiff chain in the channel of $D/l_o = 29.66$. This is expected since the periodicity of $S(q)$ indicates a rigid-ring conformation.

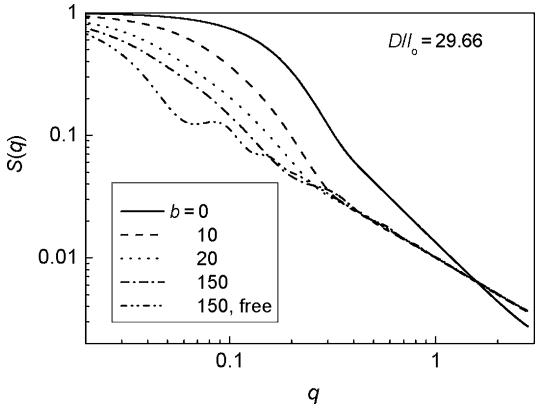


Figure 9. Logarithmic plot of the static structure factor $S(q)$ vs the wavevector q for cyclic chains of indicated stiffness parameters b in the channel of diameter $D/l_0 = 29.66$.

4. CONCLUSIONS

The significance of a circular DNA molecule in constrained spaces encountered in plenty of biological and biophysical phenomena is well-known. However, only a little attention has been paid to such systems so far. Inspired by the experimental measurements conducted on a circular DNA molecule in a tapered nanochannel leading to intriguing confrontation with a linear analogue,[6] we performed the Metropolis Monte Carlo simulations of biaxially confined flexible and semiflexible cyclic chains and their linear analogues. Semiflexible chains of two stiffness parameters corresponding to the ratio $L/P \approx N/b$ of 15 and 30 were investigated.

dx.doi.org/10.1021/ma202730c | Macromolecules 2012, 45, 2597−2608

The chain extension-channel diameter functions for both chain architectures exhibit a qualitative concordance. Nevertheless, the relative extension of cyclic chains is larger than that of linear chains. Under confinement, the densification of segment organization within the closed chains on the intermediate length scale is capable of larger repulsion which effectively raises the Flory exponent ν with respect to linear chains. Thus, the extension-confinement function $R_g \sim D^x$ in the de Gennes regime renders exponent $x = 1 - 1/\nu$ in absolute values lower for cyclic chains and we arrive at the same conclusion as reported in the experimental study.[6] The disagreement with the theoretical prediction of x is ascribed to the short interval of the de Gennes regime, mainly for cyclic chains, and to the stronger self-avoidance in cycles. Because of the stronger self-avoidance of the cycle in a channel its relative extension is enhanced and the Odijk-like strong confinement regime appears already at a weaker confinement $D/P \approx 1.5$ compared to the linear chain where the respective onset is at $D/P \approx 1$.

The Odijk theory for strong biaxial confinement seems to work not only for linear chains and the end-to-end distance but also for cyclic chains assuming the radius of gyration with respect to the halved and whole radius of gyration of a rigid rod for cyclic and linear chains, respectively, as a measure of the relative chain extension. Despite some doubts about existence of the Odijk regime for macrocycles, emerging because semiflexible closed chains can not be stretched to their full contour lengths as linear chains do in narrow channels, it was shown that this approach applies also to cycles. A qualitatively very similar trend in the mean chain extension vs the confinement strength is achieved for the radius of gyration to the hydrodynamic radius ratio, a property characterizing polymer topology and connecting static and dynamic quantity.

In order to pinpoint the difference between chains of both investigated architectures the orientation correlation function and static structure factor are also analyzed.

The symmetric shape around $N/2$th segment in the orientation correlations plotted against the segment contour position along with the negative values around this point found for free cycles remain as the principal discerning features also in constraining space. Besides, however, geometrical constraints combined with the translational invariance (cyclic topology) are reflected also on the shape of the orientation correlations which is now the interplay of the EV effect, conformational entropy, and bending energy (semiflexible chains). The strong confinement gives rise to orientation correlations with a sharp minimum in the middle. This global minimum is broadened upon releasing the confinement strength and before the behavior of the orientation correlations starts reminding the correlations of a free semiflexible cyclic chain it evolves into a broad maximum. This maximum and the two minima are explained by the formation of a locked single loop conformation. A deeper analysis is needed to shed light into this phenomenon which is beyond the scope of the present study.

The logarithmic plot of the structure factor vs the wavevector resolves better the topology of semiflexible chains confined in narrow channels than the topology of free or more loosely confined chains. The oscillations characterizing a stiff ring conformation are suppressed upon the confinement.

The differences in static properties between chains of the closed and open architectures signify interesting comparison of dynamical behavior between both chain architectures. Such information is crucial for comprehension of dynamical processes in biological systems. Therefore, our next focus is on the molecular dynamics simulations of dynamical properties of cyclic vs linear chains of various stiffness parameters.

■ ASSOCIATED CONTENT

Supporting Information

Distribution functions of the radius of gyration (Figures S1−S6) evaluated from the histograms for cyclic and linear chains of the stiffness parameter. This material is available free of charge via the Internet at http://pubs.acs.org.

■ AUTHOR INFORMATION

Corresponding Author

*E-mail: upolzben@savba.sk.

Notes

The authors declare no competing financial interest.

■ ACKNOWLEDGMENTS

This work was supported by the FCT postdoc Grant SFRH/BPD/63568/2009 cofinanced by the European Social Found and VEGA Grant 2/0093/12.

■ REFERENCES

(1) Tegenfeldt, J. O.; Prinz, C.; Cao, H.; Chou, S.; Reisner, W. W.; Riehn, R.; Wang, Y. M.; Cox, E. C.; Sturm, J. C.; Silberzan, P.; Austin, R. H. *Proc. Natl. Acad. Sci. U.S.A.* **2004**, *101*, 10979−10983.

(2) Reisner, W.; Morton, K. J.; Riehn, R.; Wang, Y. M.; Yu, Z.; Rosen, M.; Sturm, J. C.; Chou, S. Y.; Frey, E.; Austin, R. H. *Phys. Rev. Lett.* **2005**, *94*, 196101.

(3) Choi, M. C.; Santangelo, C. D.; Pelletier, O.; Kim, J. H.; Kwon, S. Y.; Wen, Z.; Li, Y.; Pincus, P. A.; Safinya, C. R.; Kim, M. W. *Macromolecules* **2005**, *38*, 9882−9884.

(4) Jo, K.; Dhingra, D. M.; Odijk, T.; de Pablo, J. J.; Graham, M. D.; Runnheim, R.; Forrest, D.; Schwartz, D. C. *Proc. Natl. Acad. Sci. U.S.A.* **2007**, *104*, 2673−2678.

(5) Reisner, W.; Beech, J. P.; Larsen, N. B.; Flyvbjerg, H.; Kristensen, A.; Tegenfeldt, J. O. *Phys. Rev. Lett.* **2007**, *99*, 058302.

(6) Persson, F.; Utko, P.; Reisner, W.; Larsen, N. B.; Kristensen, A. *Nano Lett.* **2009**, *9*, 1382−1385.

(7) Kim, Y.; Kim, K. S.; Kounovsky, K. L.; Chang, R.; Jung, G. Y.; de Pablo, J. J.; Jo, K.; Schwartz, D. C. *Lab Chip* **2011**, *11*, 1721−1729.

(8) de Gennes, P.-G. *Scaling Concepts in Polymer Physics*; Cornell University: Ithaca, NY, 1979.

(9) Brochard-Wyart, F.; Tanaka, T.; Borghi, N.; de Gennes, P.-G. *Langmuir* **2005**, *21*, 4144−4148.

(10) Odijk, T. *Macromolecules* **1983**, *16*, 1340−1344.

(11) Yang, Y.; Burkhardt, T. W.; Gompper, G. *Phys. Rev. E* **2007**, *76*, 011804.

(12) Odijk, T. *Phys. Rev. E* **2008**, *77*, 060901(R).

(13) Cifra, P.; Benková, Z.; Bleha, T. *J. Phys. Chem. B* **2009**, *113*, 1843−1851.

(14) Cifra, P. *J. Chem. Phys.* **2009**, *131*, 224903.

(15) Werner, E.; Persson, F.; Westerlund, F.; Tegenfeldt, J. O.; Mehling, B. *cond-mat.soft* 2012, arXiv:1201.2961v1201.

(16) Wagner, F.; Lattanzi, G.; Frey, E. *Phys. Rev. E* **2007**, *75*, 050902(R).

(17) Jun, S.; Thirumalai, D.; Ha, B.-Y. *Phys. Rev. Lett.* **2008**, *101*, 138101.

(18) Wang, Y.; Tree, D. R.; Dorfman, K. D. *Macromolecules* **2011**, *44*, 6594−6604.

(19) Jones, J. J.; van der Maarel, J. R. C.; Doyle, P. S. *Nano Lett.* **2011**, *11*, 5047−5053.

(20) Micheletti, C.; Marenduzzo, D.; Orlandini, E. *Phys. Rep.* **2011**, *504*, 1−73.

(21) Jung, Y.; Jeon, C.; Kim, J.; Jeoung, H.; Jun, S.; Ha, B.-Y. *Soft Matter* **2011**, DOI: 10.1039/c1031sm05706e.
(22) Semlyen, J. A. *Cyclic polymers*; Elsevier: London, 1986.
(23) Cifra, P. *J. Chem. Phys.* **2006**, *124*, 024706.
(24) Cifra, P.; Benková, Z.; Bleha, T. *J. Phys. Chem. B* **2008**, *112*, 1367−1375.
(25) Cifra, P.; Benková, Z.; Bleha, T. *Faraday Discuss.* **2008**, *139*, 377−392.
(26) Bulacu, M.; van der Giessen, E. *J. Chem. Phys.* **2005**, *123*, 114901.
(27) Rollins, G. C.; Petrov, A. S.; Harvey, S. C. *Biophys. J.* **2008**, *94*, L38−L40.
(28) Milchev, A.; Binder, K. *Macromolecules* **1996**, *29*, 343−354.
(29) Fynewever, H.; Yethiraj, A. *J. Chem. Phys.* **1998**, *108*, 1636−1644.
(30) Sheng, Y.-J.; Panagiotopoulos, S. K.; Kumar, S. K. *Macromolecules* **1996**, *29*, 4444−4446.
(31) Jang, S. S.; Çağin, T.; Goddard, W. A. *J. Chem. Phys.* **2003**, *119*, 1843−1854.
(32) Burkchard, W.; Schmidt, M. *Polymer* **1980**, *21*, 745−749.
(33) Cifra, P.; Bleha, T. *Polymer* **2007**, *48*, 2444−2452.
(34) Hsu, H.-P.; Paul, W.; Binder, K. *Macromolecules* **2010**, *43*, 3094−3102.
(35) Hsu, H.-P.; Paul, W.; Binder, K. *Europhys. Lett.* **2010**, *92*, 28003.
(36) Cifra, P.; Benková, Z.; Bleha, T. *Phys. Chem. Chem. Phys.* **2010**, *12*, 8934−8942.
(37) Ali, I.; Marenduzzo, D.; Yeomans, J. M. *Phys. Rev. Lett.* **2006**, *96*, 208102.
(38) Locker, C. R.; Harvey, S. C. *Multiscale Model. Simul.* **2006**, *5*, 1264−1279.
(39) Ali, I.; Marenduzzo, D.; Yeomans, J. M. *Biophys. J.* **2008**, *94*, 4159−4164.
(40) Skolnick, J.; Fixman, M. *Macromolecules* **1977**, *10*, 944−948.
(41) Odijk, T. *J. Polym. Sci., Part B: Polym. Phys* **1977**, *15*, 477−483.
(42) Teraoka, I.; Cifra, P.; Wang, Y. *Colloid. Surface. A* **2002**, *206*, 299−303.
(43) Dimitrov, D. I.; Milchev, A.; Binder, K.; Klushin, L. I.; Skvortsov, A. M. *J. Chem. Phys.* **2008**, *128*, 234902.
(44) Prentis, J. J. *J. Chem. Phys.* **1982**, *76*, 1574−1583.
(45) Robertson, R. M.; Laib, S.; Smith, D. E. *Proc. Natl. Acad. Sci. U.S.A.* **2006**, *103*, 7310−7314.
(46) Levy, S. L.; Mannion, J. T.; Cheng, J.; Reccius, C. H.; Craighead, H. G. *Nano Lett.* **2008**, *8*, 3839−3844.
(47) Burkhardt, T. W.; Yang, Y.; Gompper, G. *Phys. Rev. E* **2010**, *82*, 041801.
(48) Su, T.; Das, S. K.; Xiao, M.; Purohit, P. K. *PLoS ONE* **2011**, *6*, e16890.
(49) Köster, S.; Stark, H.; Pfohl, T.; Kierfeld, J. *Biophys. Rev. Lett* **2007**, *2*, 155−166.
(50) Dünweg, B.; Reith, D.; Steinhauser, M.; Kremer, K. *J. Chem. Phys.* **2002**, *117*, 914−924.
(51) Benková, Z.; Cifra, P. *Macromol. Theory Simul.* **2011**, *20*, 65−74.
(52) Sakaue, T.; Witz, G.; Dietler, G.; Wada, H. *Europhys. Lett.* **2010**, *91*, 68002.
(53) Dolgushev, M.; Berezovska, G.; Blumen, A. *J. Chem. Phys.* **2011**, *135*, 094901.
(54) Ostermeir, K.; Alim, K.; Frey, E. *Soft Matter* **2010**, *6*, 3467−3471.
(55) Köster, S.; Steinhauser, D.; Pfohl, T. *J. Phys.: Condens. Matter* **2005**, *17*, S4091−4104.
(56) Köster, S.; Kierfeld, J.; Pfohl, T. *Eur. Phys. J. E* **2008**, *25*, 439−449.
(57) Junier, I.; Martin, O.; Képès, F. *PLoS Comput. Biol.* **2010**, *6*, e1000678.
(58) Fritsche, M.; Heermann, D. W. *Soft Matter* **2011**, *7*, 6906−6913.
(59) Cifra, P.; Bleha, T. *Eur. Phys. J. E* **2010**, *32*, 273−279.
(60) Liu, Y.; Chakraborty, B. *Phys. Biol.* **2008**, *5*, 026004.

Macromolecules

Note

pubs.acs.org/Macromolecules

Synthesis of Well-Defined Poly(2-alkoxypyridine-3,5-diyl) via Ni-Catalyst-Transfer Condensation Polymerization

Yutaka Nanashima, Akihiro Yokoyama, and Tsutomu Yokozawa*

Department of Material and Life Chemistry, Kanagawa University, Rokkakubashi, Kanagawa-ku, Yokohama 221-8686, Japan

Supporting Information

ABSTRACT: Ni-catalyzed Kumada−Tamao coupling polymerization of 5-bromo-3-chloromagnesio-2-(2-(2-methoxyethoxy)-ethoxy)pyridine (**1**) was investigated. Monomer **1**, which was obtained quantitatively by treatment of the corresponding bromoiodopyridine **3** with 1.0 equiv of ^{i}PrMgCl at 0 °C, was polymerized with Ni(dppp)Cl_2 (dppp = 1,3-bis(diphenylphospino)propane)) in the presence of 2.0 equiv of LiCl in THF at room temperature to yield poly(2-(2-(2-methoxyethoxy)ethoxy)pyridine-3,5-diyl) (*m*-PMEEOPy) with narrow polydispersity. The M_n value was controlled by the feed ratio of the monomer precursor **3** to Ni(dppp)Cl_2. MALDI-TOF mass spectra showed that *m*-PMEEOPy uniformly had a bromine atom at one end and a hydrogen atom at the other. Both end groups could be converted to aryl groups by addition of an excess of aryl magnesium chloride to the reaction mixture after completion of the polymerization. These results indicate that the polymerization of **1** with Ni(dppp)Cl_2 involves the intramolecular catalyst-transfer polymerization mechanism.

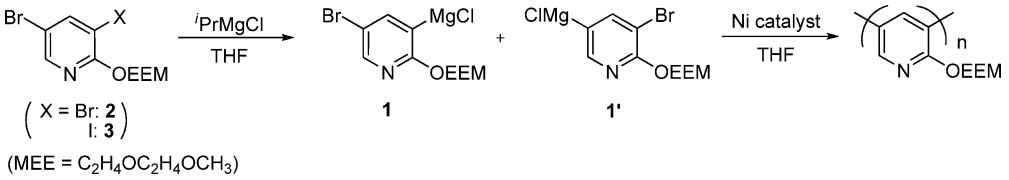
π-Conjugated polymers are an increasingly important class of materials because of their widespread application in electronic devices, such as thin film transistors (TFTs),[1] organic light-emitting diodes (OLEDs),[2] and photovoltaic cells.[3] Many π-conjugated polymers have been conventionally synthesized by means of polycondensation involving transition-metal-catalyzed cross-coupling reaction, but they did not have well-defined structures, owing to the involvement of the step-growth polymerization mechanism.[4,5] However, development of catalyst-transfer condensation polymerization, which proceeds in chain-growth polymerization manner, has made it feasible to control the molecular weight, polydispersity, and end groups of π-conjugated polymers.[6,7] Ni-catalyzed Kumada−Tamao catalyst-transfer condensation polymerization (KTCTCP) of AB-type monomers yields well-defined poly(alkylthiophene)s,[8−10] polyfluorenes,[11,12] polyphenylenes,[13] and poly(*N*-alkylpyrrole)-s[12,14] as well as block copolymers[7] and gradient copolymers.[15] Furthermore, external Ni initiators[16−22] were applied to the production of π-conjugated polymer brushes from a substrate surface.[16,18,21,22] However, most of KTCTCP has been limited to the polymerization of donor monomers for the synthesis of p-type π-conjugated polymers. Intramolecular catalyst transfer would be assisted by the π-electron-rich character of the p-type π-conjugated polymers on the basis of the fact that well-defined π-conjugated block copolymers were obtained by the successive polymerization from a monomer with low π-donor ability to a monomer with high π-donor ability,[23,14] but on the other hand, the KTCTCP of acceptor monomers would be a challenge owing to the weaker π-donation of the n-type polymer backbone to a Ni(0) catalyst. Kiriy and Huck have recently reported the synthesis of well-defined π-conjugated copolymers containing acceptor monomer units by Suzuki−Miyaura coupling polymerization of a fluorene−benzothiadiazole monomer with a Pd catalyst[24] and by unusual coupling polymerization of an anion radical of a thiophene−naphthalenediimide−thiophene monomer with a Ni catalyst.[25] To the best of our knowledge, however, the KTCTCP of acceptor monomer consisting of single arene has not been reported. We have set out to explore the KTCTCP of simple acceptor monomers by focusing on the polymerization of pyridine monomers. We have recently reported the polymerization of a Grignard pyridine monomer, 2-bromo-5-chloromagnesio-3-(2-(2-methoxyethoxy)ethoxy)pyridine, with Ni(dppp)Cl_2 (dppp = 1,3-bis(diphenylphospino)propane)) to yield head-to-tail poly(3-(2-(2-methoxyethoxy)ethoxy)-pyridine-2,5-diyl) (HT-*p*-PMEEOPy), but we could not investigate the chain-growth polymerization behavior because the polymer was precipitated during polymerization.[26] Only if the polymer is soluble in the reaction solvent would we be able to establish whether this acceptor monomer unit undergoes KTCTCP. Therefore, we changed the polymerization position of this monomer unit from the 2,5-position (para type) to the 3,5-position (meta type) while retaining the same side chain (MEEO group), although the obtained polypyridine is not conjugated between the repeat units in the polymer. However, Geng et al.[27] and Ueda et al.[28] recently reported that the Ni catalyst can be transferred on the backbone of nonconjugated polymers. In this paper, we report KTCTCP of a meta-type pyridine acceptor monomer, 5-bromo-3-chloromagnesio-2-(2-(2-methoxyethoxy)ethoxy)pyridine (**1**) with Ni(dppp)Cl_2, yielding poly(2-(2-(2-methoxyethoxy)ethoxy)pyridine-3,5-diyl) (*m*-PMEEOPy) with defined molecular weight and narrow polydispersity (Scheme 1).

We first used 3,5-dibromo-2-(2-(2-methoxyethoxy)ethoxy)-pyridine (**2**) as a monomer precursor, which was converted to a Grignard-type monomer by treatment with 1.0 equiv of ^{i}PrMgCl[29] in THF at 0 °C for 1 h (83% conversion of **2** based on analytical GC). A small aliquot of the reaction mixture

Received: December 21, 2011
Revised: February 13, 2012
Published: February 27, 2012

ACS Publications © 2012 American Chemical Society

Scheme 1. KTCTCP of 1 for the Synthesis of *m*-PMEEOPy



was quenched with water, and the products were analyzed by ^{1}H NMR spectroscopy (Figure S1). It turned out that **1** and regioisomer **1′** were formed in a ratio of 95:5,[30] and therefore the bromine of **2** at the 3-position was highly selectively converted to a chloromagnesio group; chelation of the oxygens of the MEEO group to magnesium would be responsible for high regioselectivity at the 3-position. Polymerization of Grignard monomer **1** and **1′** was then carried out by addition of 1.8 mol % Ni(dppp)Cl_2 to the reaction mixture, as in the case of the polymerization of Grignard alkylthiophene monomers[8] (Scheme 1). The gel permeation chromatography (GPC) profile of the product showed a relatively narrow peak in the high-molecular-weight region accompanied by low-molecular-weight oligomers (total polymers and oligomers in the higher-molecular-weight region than monomer: M_n = 5100, M_w/M_n = 2.37), and the crude product was washed with diethyl ether to afford high-molecular-weight *m*-PMEEOPy (M_n = 11 500, M_w/M_n = 1.30) (Figure S2). The obtained *m*-PMEEOPy was readily soluble in common organic solvents, such as ethyl acetate, THF, CH_2Cl_2, and $CHCl_3$. This good solubility can probably be attributed to the kinked structure of the meta-linked main chain, in addition to the MEEO side chain, and is in contrast to the low solubility of *p*-PMEEOPy. The end groups of *m*-PMEEOPy were analyzed by matrix-assisted laser desorption ionization time-of-flight (MALDI-TOF) mass spectrometry with dithranol as a matrix in the presence of sodium trifluoroacetate as a cationizing salt. The observed molecular weight values of major peaks correspond to *m*-PMEEOPy with an isopropyl group at one end and a bromine atom at the other (designated as ^{i}Pr/Br) (Figure S3). These results imply that the polymerization proceeded in a chain-growth polymerization manner and that the propagating polymer–Ni complex reacted with residual ^{i}PrMgCl used for generation of Grignard monomer **1** and **1′** from dibromo monomer precursor **2**.

We next used 5-bromo-3-iodo-2-(2-(2-methoxyethoxy)-ethoxy)pyridine (**3**) as a monomer precursor, hoping for quantitative generation of Grignard monomer **1** via more facilitated magnesium–iodo exchange reaction. Indeed, the reaction of **3** with 1.0 equiv of ^{i}PrMgCl smoothly proceeded at 0 °C for 1 h to quantitatively afford Grignard monomer **1** (100% conversion of **3** based on analytical GC).[31] The polymerization of **1** was then carried out by addition of 1.8 mol % of Ni(dppp)Cl_2. However, the polymerization proceeded slowly (69% conversion in 63 h), and the GPC profiles of the products showed a broad molecular weight distribution, although the peak shifted toward the higher-molecular-weight region with time (Figure S4). This polymerization behavior presumably arises from aggregation of Grignard monomer **1** due to coordination of the nitrogen of the pyridine ring to the magnesium.

Accordingly, the polymerization of **1** with Ni(dppp)Cl_2 was carried out in the presence of LiCl (2 equiv to **1**) in a similar manner to the KTCTCP of *p*-phenylene monomer.[13] As a result, the polymerization proceeded much faster (Figure 1A), and the GPC chromatogram peak became narrow (Figure 1B).

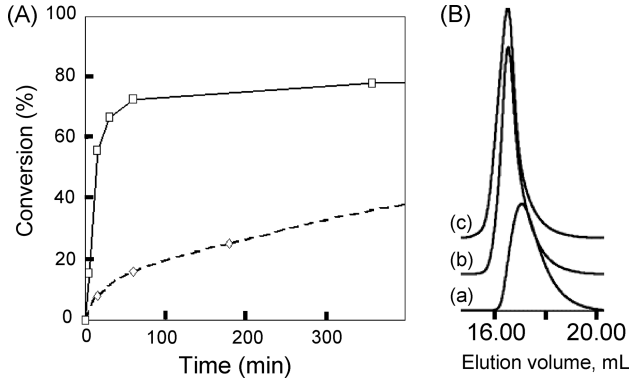


Figure 1. (A) Time–conversion curves for the polymerization of **1** with 1.8 mol % of Ni(dppp)Cl_2 in the absence of LiCl (dashed line) and in the presence of 2.0 equiv of LiCl (solid line) in THF ($[3]_0$ = 0.1 mol/L) at room temperature. (B) GPC profiles of *m*-PMEEOPy obtained by the polymerization of **1** with 1.8 mol % of Ni(dppp)Cl_2 in the presence of 2.0 equiv of LiCl in THF at room temperature for (a) 5 min (conversion of **1** = 25%, M_n = 4000, M_w/M_n = 1.34), (b) 15 min (conversion of **1** = 52%, M_n = 6690, M_w/M_n = 1.26), and (c) 60 min (conversion of **1** = 70%, M_n = 8000, M_w/M_n = 1.24).

When the M_n and M_w/M_n values of the crude *m*-PMEEOPy (without purification by precipitation or fractionation) were plotted against monomer conversion, the M_n value increased in proportion to conversion, and the M_w/M_n ratio was 1.34 or below over the whole conversion range (Figure 2A), indicating chain-growth polymerization behavior. Furthermore, the M_n value also linearly increased in proportion to the feed ratio of monomer precursor **3** to the Ni catalyst (Figure 2B). The MALDI-TOF mass spectrum of *m*-PMEEOPy obtained by polymerization for 5 min (conversion of **1** = 25%, M_n = 4000, M_w/M_n = 1.34) contained one major series of peaks and one minor series of peaks (Figure 3). The major peaks correspond to the Na^+ adducts of *m*-PMEEOPy with bromine at one end and hydrogen at the other (designated as Br/H). For example, the 21-mer of this distribution is expected to produce a signal at m/z 195.2 × 21 (repeat unit) + 79.9 (Br) + 1.0 (H) + 23.0 (Na^+) = 4203.1, and indeed, a signal is observed at 4202.5. The minor peaks correspond to *m*-PMEEOPy with Br/H ends. The polymerization behavior and the MALDI-TOF mass spectrum strongly support the involvement of a catalyst-transfer polymerization mechanism.[32]

Functionalization of the polymer end groups was conducted by using Grignard reagent. Thus, **1** was polymerized with 1.99 mol % Ni(dppp)Cl_2 in the presence of 2.0 equiv of LiCl in THF at room temperature for 1 h (conversion of **1** = 80%, M_n = 7800, M_w/M_n = 1.22), and then an excess of 3,4-dimethylphenylmagnesium chloride **4** (3,4-$Me_2C_6H_3MgCl$) was added to the reaction mixture (Scheme 2). The mixture

dx.doi.org/10.1021/ma202756y | *Macromolecules* 2012, 45, 2609–2613

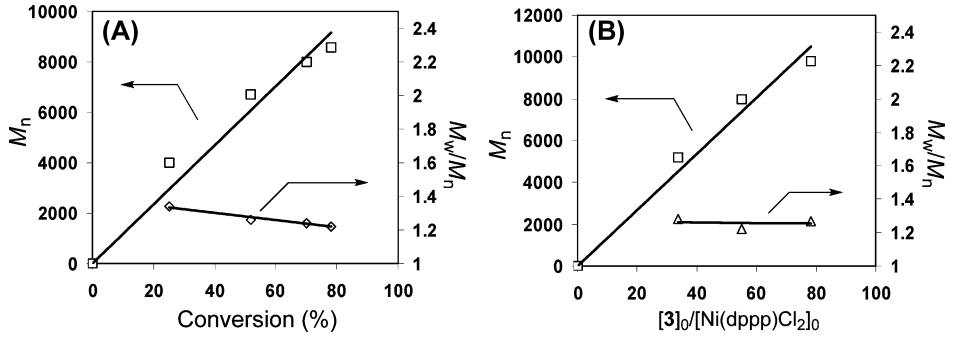


Figure 2. (A) M_n and M_w/M_n values of *m*-PMEEOPy as a function of monomer conversion in the polymerization of **1** with 1.8 mol % of Ni(dppp)Cl_2 in the presence of 2.0 equiv of LiCl in THF ($[3]_0$ = 0.1 mol/L) at room temperature. (B) M_n and M_w/M_n values of *m*-PMEEOPy as a function of the feed ratio of **3** to Ni(dppp)Cl_2.

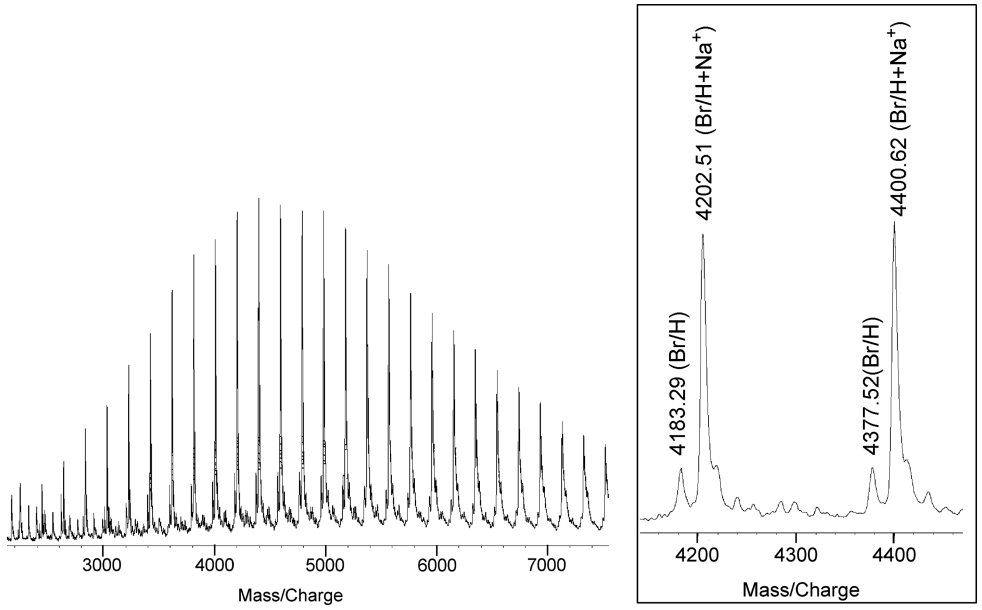
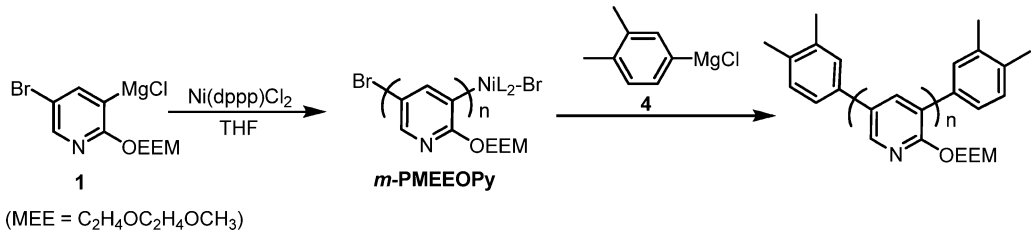


Figure 3. MALDI-TOF mass spectra of *m*-PMEEOPy obtained by the polymerization of **1** with 1.8 mol % of Ni(dppp)Cl_2 in the presence of 2.0 equiv of LiCl in THF at room temperature for 5 min (conversion of **1** = 25%, M_n = 4000, M_w/M_n = 1.34).

Scheme 2. Functionalization of Polymer Chain Ends



was stirred for a further 3 h, and then the reaction was quenched with 5 M HCl. End-group analysis of the obtained polymer (M_n = 7870, M_w/M_n = 1.23) was performed by MALDI-TOF mass spectrometry (Figure 4). The spectrum of an aliquot taken before addition of the Grignard reagent showed the peaks of the Na^+ cation adduct of *m*-PMEEOPy with Br/H end groups and the noncation adducts (Figure 4A), whereas after the reaction with the Grignard reagent, the spectrum showed a new series of peaks, the values of which corresponded to Na^+ adducts of *m*-PMEEOPy with $Me_2C_6H_3$/$Me_2C_6H_3$ end groups. Consequently, it turns out that aryl groups can be introduced at both ends of *m*-PMEEOPy by using the aryl Grignard reagent, as in the case of end-functionalization of poly(3-alkylthiophene)s with Grignard reagents.[8c,9c]

Polymerization with other Ni catalysts with different bidendate ligands (1.8 mol %) was studied. When Ni(dppe)Cl_2 (dppe = 1,2-bis(diphenylphospino)ethane) was used, the polymerization proceeded more slowly than the polymerization with Ni(dppp)Cl_2 to afford a polymer with broader polydispersity (M_n = 7040, M_w/M_n = 1.52) (Figure S5A,C). The MALDI-TOF mass spectrum contains one series of major peaks, which correspond to the Na^+ adducts of *m*-PMEEOPy with Br/H end groups, as well as two series of minor peaks

dx.doi.org/10.1021/ma202756y | *Macromolecules* 2012, 45, 2609–2613

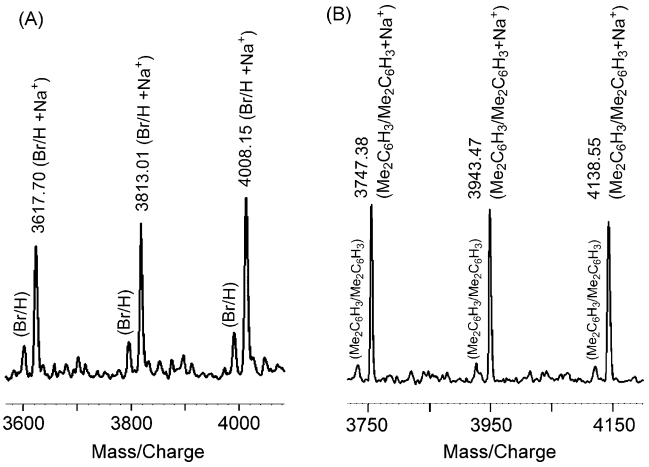


Figure 4. MALDI-TOF mass spectra of *m*-PMEEOPy obtained by (A) the polymerization of **1** with 1.99 mol % of Ni(dppp)Cl_2 in the presence of 2 equiv of LiCl in THF at room temperature for 1 h (conversion of **1** = 80%, M_n = 7800, M_w/M_n = 1.22) and (B) subsequent reaction with 3,4-dimethylphenylmagnesium chloride (M_n = 7870, M_w/M_n = 1.23).

(Figure S6). The minor peaks are due to the Na^+ adducts of *m*-PMEEOPy with Br/Br and H/H end groups. These results imply that the polymerization of **1** with Ni(dppe)Cl_2 proceeds mainly via the intramolecular catalyst-transfer polymerization mechanism but is accompanied by intermolecular transfer of the catalyst to afford the polymers with H/H and Br/Br ends in a similar manner to that reported by Geng et al. in the KTCTCP of fluorene monomer.[11] On the other hand, the polymerization with Ni(dppf)Cl_2 was faster than the polymerization with Ni(dppp)Cl_2; it was completed within 10 min. The molecular weight was higher and the polydispersity was narrower (M_n = 10 430, M_w/M_n = 1.17) than those of the polymers obtained with Ni(dppp)Cl_2 (Figure S5B,C). The MALDI-TOF mass spectrum showed one series of major peaks, which correspond to the Na^+ adducts of *m*-PMEEOPy with Br/H end groups, and two series of minor peaks. One of the minor peaks stems from the Na^+ adducts of *m*-PMEEOPy with Br/Br end groups, and the other could not be assigned (Figure S7). On the basis of the results that the GPC elution curve of the obtained polymer showed a leading peak in the higher-molecular-weight region and that peaks due to *m*-PMEEOPy with H/H end groups were not observed, we speculated that *m*-PMEEOPy with Br/Br ends might be formed in this case via disproportionation reaction of *m*-PMEEOPy with Br/Ni(II)Br end groups, followed by reductive elimination to afford the coupled *m*-PMEEOPy with Br/Br ends, as in the case of the products obtained in the KTCTCP of thiophene monomer, followed by quenching with water.[8b] Therefore, we concluded that Ni(dppp)Cl_2 is an excellent catalyst for KTCTCP of *m*-pyridine monomer **1**.

In conclusion, we have demonstrated that Ni-catalyzed Kumada–Tamao coupling polymerization of Grignard-type pyridine **1** as an acceptor monomer proceeds via a catalyst-transfer chain-growth polymerization mechanism to yield well-defined *m*-PMEEOPy. Ni(dppp)Cl_2 is an effective catalyst and addition of LiCl is crucial for this polymerization. The molecular weight was controlled by the feed ratio of monomer precursor **3** to the Ni catalyst, and the polymer end groups were defined as a bromine atom at one end and a hydrogen atom at the other. Both end groups were converted to aryl groups by reaction of aryl Grignard reagent with *m*-PMEEOPy formed in the reaction mixture. Further experiments are in progress to evaluate catalyst-transfer polymerization of other pyridine monomers.

■ ASSOCIATED CONTENT

Supporting Information

Procedures for synthesis and polymerization of the monomer and the GPC profiles, ^{1}H NMR spectra, and MALDI-TOF mass spectra of *m*-PMEEOPy. This material is available free of charge via the Internet at http://pubs.acs.org.

■ AUTHOR INFORMATION

Corresponding Author

*E-mail: yokozt01@kanagawa-u.ac.jp.

Notes

The authors declare no competing financial interest.

■ ACKNOWLEDGMENTS

This work was partially supported by a Grant-in-Aid (No. 21350067) for Scientific Research from Japan Society for the Promotion of Science and a Scientific Frontier Research Project from the Ministry of Education, Culture, Sports, Science and Technology, Japan.

■ REFERENCES

(1) Arias, A. C.; MacKenzie, J. D.; McCulloch, I.; Rivnay, J.; Salleo, A. *Chem. Rev.* **2010**, *110*, 3–24.
(2) Grimsdale, A. C.; Chen, K. L.; Martin, R. E.; Jokisz, P. G.; Holmes, A. B. *Chem. Rev.* **2010**, *109*, 897–1091.
(3) Li, C.; Liu, M.; Pschirer, N. G.; Baumgarten, M.; Müllen, K. *Chem. Rev.* **2010**, *110*, 6817–6855.
(4) Babudri, F.; Farinola, G. M.; Naso, F. *J. Mater. Chem.* **2004**, *14*, 11–34.
(5) Yamamoto, T. *Bull. Chem. Soc. Jpn.* **2010**, *83*, 431–455.
(6) Yokozawa, T.; Yokoyama, A. *Chem. Rev.* **2009**, *109*, 5595–5619.
(7) Yokozawa, T. Catalyst-Transfer Condensation Polymerization for Precision Synthesis of π-Conjugated Polymers. In *Conjugated Polymer Synthesis*; Chujo, Y., Ed.; Wiley-CH: Weinheim, 2010; pp 35–58.
(8) (a) Yokoyama, A.; Miyakoshi, R.; Yokozawa, T. *Macromolecules* **2004**, *37*, 1169–1171. (b) Miyakoshi, R.; Yokoyama, A.; Yokozawa, T. *Macromol. Rapid Commun.* **2004**, *25*, 1663–1666. (c) Miyakoshi, R.; Yokoyama, A.; Yokozawa, T. *J. Am. Chem. Soc.* **2005**, *127*, 17542–17547. (d) Adachi, I.; Miyakoshi, R.; Yokoyama, A.; Yokozawa, T. *Macromolecules* **2006**, *39*, 7793–7795.
(9) (a) Sheina, E. E.; Liu, J.; Iovu, M. C.; Laird, D. W.; McCullough, R. D. *Macromolecules* **2004**, *37*, 3526–3528. (b) Iovu, M. C.; Sheina, E. E.; Gil, R. R.; McCullough, R. D. *Macromolecules* **2005**, *38*, 8649–8656. (c) Jeffries-El, M.; Sauve, G.; McCullough, R. D. *Macromolecules* **2005**, *38*, 10346–10352. (d) Osaka, I.; McCullough, R. D. *Acc. Chem. Res.* **2008**, *41*, 1202–1214.
(10) (a) Beryozkina, T.; Senkovskyy, V.; Kaul, E.; Kiriy, A. *Macromolecules* **2008**, *41*, 7817–7823. (b) Tkachov, R.; Senkovskyy, V.; Komber, H.; Sommer, J.-U.; Kiriy, A. *J. Am. Chem. Soc.* **2010**, *132*, 7803–7810.
(11) Huang, L.; Wu, S.; Qu, Y.; Geng, Y.; Wang, F. *Macromolecules* **2008**, *41*, 8944–8947.
(12) Stefan, M. C.; Javier, A. E.; Osaka, I.; McCullough, R. D. *Macromolecules* **2009**, *42*, 30–32.
(13) Miyakoshi, R.; Shimono, K.; Yokoyama, A.; Yokozawa, T. *J. Am. Chem. Soc.* **2006**, *128*, 16012–16013.
(14) Yokoyama, A.; Kato, A.; Miyakoshi, R.; Yokozawa, T. *Macromolecules* **2008**, *41*, 7271–7273.
(15) Locke, J. R.; McNeil, A. J. *Macromolecules* **2010**, *43*, 8709–8710.

(16) Senkovskyy, V.; Khanduyeva, N.; Komber, H.; Oertel, U.; Stamm, M.; Kuckling, D.; Kiriy, A. *J. Am. Chem. Soc.* **2007**, *129*, 6626−6636.
(17) Bronstein, H. A.; Luscombe, C. K. *J. Am. Chem. Soc.* **2009**, *131*, 12894−12895.
(18) Senkovskyy, V.; Tkachov, R.; Beryozkina, T.; Komber, H.; Oertel, U.; Horecha, M.; Bocharova, V.; Stamm, M.; Gevorgyan, S. A.; Krebs, F. C.; Kiriy, A. *J. Am. Chem. Soc.* **2009**, *131*, 16445−16453.
(19) Smeets, A.; Van den Bergh, K.; De Winter, J.; Gerbaux, P.; Verbiest, T.; Koeckelberghs, G. *Macromolecules* **2009**, *42*, 7638−7641.
(20) Senkovskyy, V.; Sommer, M.; Tkachov, R.; Komber, H.; Huck, W. T. S.; Kiriy, A. *Macromolecules* **2010**, *43*, 10157−10161.
(21) (a) Khanduyeva, N.; Senkovskyy, V.; Beryozkina, T.; Bocharova, V.; Simon, F.; Nitschke, M.; Stamm, M.; Grotzschel, R.; Kiriy, A. *Macromolecules* **2008**, *41*, 7383−7389. (b) Khanduyeva, N.; Senkovskyy, V.; Beryozkina, T.; Horecha, M.; Stamm, M.; Uhrich, C.; Riede, M.; Leo, K.; Kiriy, A. *J. Am. Chem. Soc.* **2009**, *131*, 153−161. (c) Tkachov, R.; Senkovskyy, V.; Horecha, M.; Oertel, U.; Stamm, M.; Kiriy, A. *Chem. Commun.* **2010**, *46*, 1425−1427.
(22) Sontag, S. K.; Marshall, N.; Locklin, J. *Chem. Commun.* **2009**, 3354−3356.
(23) (a) Miyakoshi, R.; Yokoyama, A.; Yokozawa, T. *Chem. Lett.* **2008**, *37*, 1022−1023. (b) Yokozawa, T.; Kohno, H.; Ohta, Y.; Yokoyama, A. *Macromolecules* **2010**, *43*, 7095−7100. (c) Yokozawa, T.; Suzuki, R.; Nojima, M.; Ohta, Y.; Yokoyama, A. *Macromol. Rapid Commun.* **2011**, *32*, 801−806.
(24) Elmalem, E.; Kiriy, A.; Huck, W. T. S. *Macromolecules* **2011**, *44*, 9057−9061.
(25) Senkovskyy, V.; Tkachov, R.; Komber, H.; Sommer, M.; Heuken, H.; Voit, B.; Huck, W. T. S.; Kataev, V.; Petr, A.; Kiriy, A. *J. Am. Chem. Soc.* **2011**, *133*, 19966−19970.
(26) Nanashima, Y.; Yokoyama, A.; Yokozawa, T. *J. Polym. Sci., Part A: Polym. Chem.* **2012**, *50*, 1054−1061.
(27) Wu, S.; Sun, Y.; Huang, L.; Wang, J.; Zhou, Y.; Geng, Y.; Wang, F. *Macromolecules* **2010**, *43*, 4438−4440.
(28) Ohimizu, K.; Takahashi, A.; Higashihara, T.; Ueda, M. *J. Polym. Sci., Part A: Polym. Chem.* **2011**, *49*, 2709−2714.
(29) (a) Fukumoto, H.; Kimura, R.; Sasaki, S.; Kubota, K.; Yamamoto, T. *J. Polym. Sci., Part B: Polym. Phys.* **2005**, *43*, 215−222. (b) Kobayashi, N.; Sasaki, S.; Abe, M.; Watanabe, S.; Fukumoto, H.; Yamamoto, T. *Macromolecules* **2004**, *37*, 7986−7991.
(30) A model compound **6**, which is identical with quenched **1**, was synthesized, and the structure of the major product after quenching was confirmed: see Figure S1 and the synthetic procedure for **6** in Supporting Information.
(31) If the solution became yellow to orange in color during addition of ^{i}PrMgCl to a solution of **3** in THF, instead of almost colorless in the usual case, the polymerization of **1** with the Ni catalyst became sluggish; it seems likely that an inhibitor of the catalyst was formed as a byproduct, though the structure of the putative inhibitor has not been identified yet. However, the reverse addition of **3** to 1.0 equiv of ^{i}PrMgCl was found to provide greater reproducibility of the polymerization of **1** after the data presented here had been obtained.
(32) Exclusive production of 3,5-diphenylpyridine in the reaction of 3,5-dibromopyridine with 0.5 equiv of phenylmagnesium chloride in the presence of 0.5 mol % of Ni(dppp)Cl_2 also supports intramolecular transfer of the catalyst on the pyridine ring: see Supporting Information.

Macromolecules

Note

pubs.acs.org/Macromolecules

Hybrids by Cluster Complex-Initiated Polymerization

Xiaoyan Tu, Gary S. Nichol, Pei Keng, Jeffrey Pyun, and Zhiping Zheng*

Department of Chemistry and Biochemistry, University of Arizona, Tucson, Arizona 85721, United States

Supporting Information

Inorganic−organic hybrids offer great opportunities to integrate the desirable properties of the two distinct realms and to create entirely new properties not exhibited by either due to the compositional, functional, and organizational synergism between the inorganic and organic components.[1] An intriguing example is the superparamagnetic hybrid obtained by copolymerizing ethyl acrylate with $Mn_{12}O_{12}$(acrylate)$_{16}$,[2] a complex featuring the celebrated superparamagnetic metal cluster core of $Mn_{12}O_{12}$. This work provides an encouraging example of how the properties of an inorganic component with interesting properties may be integrated with the propitious characteristics of organics to develop useful and processable materials. Another example is the cluster-cored metallodendrimer emanating from the biologically significant $[Fe_4S_4]^{2+}$ cluster core.[3] The kinetics and potential of the cluster-based redox processes have been found to be tunable by the dendritic ligands (dendrons), suggesting potential applications of such hybrids for information storage.

Great potentials notwithstanding, there exist a number of issues.[4] First, oxide or oxoalkoxide clusters are generally sensitive to water and other types of nucleophiles, thus limiting the choice of polymerization methods including reaction conditions, in addition to the concern of their structural integrity. Second, most of these clusters possess multiple reactive groups, leading to high degree of cross-linking and complicating the characterization of the resulting hybrids. Lastly, in terms of realizing functional materials, the high expectation is still limited by the small number of available clusters with useful electronic, optical, or magnetic properties.

The use of hexanuclear clusters of the general formula $[M_6X_n]^z$ (M, transition metal; X, halide or chacogenide; n = 6 or 12; z, charge of the cluster core) potentially addresses the aforementioned issues as these clusters, typically synthesized by high-temperature solid-state reactions, maintain their structural integrity under conventional reaction conditions yet quite amenable to synthetic manipulations.[5] The existence of multiple metal sites allows for site-specific functionalization, facilitating the systematic modification of properties by varying the number and type of the ligands. Hybrids featuring clusters of this type include $[Mo_6Cl_8]^{4+}$/poly(4-vinylpyridine) and poly(vinylimidazole),[6,7] $[Mo_6S_8]$ and $[W_6S_8]$/polystyrene,[8] $[Mo_6Cl_8]^{4+}$ cored-metallodendrimers,[9] and the more recent mesogenic hybrids containing the cluster cores of $[Mo_6Br_8]^{4+}$ and $[Re_6Se_8]^{2+}$.[10]

Our own efforts along this line of interest have relied on the use of the $[Re_6Se_8]^{2+}$ cluster core (Figure 1).[11] The 24-electron face-capped hexanuclear core can be viewed as an octahedron of rhenium enclosed in a cube formed by the eight face-capping Se ligands, with six additional terminal ligands. The cluster core

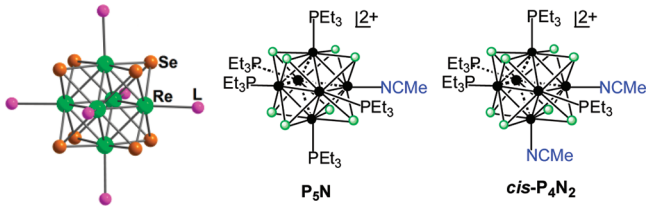


Figure 1. From left to right: structure of the $[Re_6Se_8]^{2+}$ cluster core shown with terminal ligands L and the molecular structures of cationic cluster solvates[12] $[Re_6Se_8(PEt_3)_5(CH_3CN)]^{2+}$ (P_5N) and *cis*-$[Re_6Se_8(PEt_3)_4(CH_3CN)_2]^{2+}$ (*cis*-P_4N_2).

undergoes a reversible, one-electron oxidation event, with the potential dependent upon the nature and number of the terminal ligands.[12] The parent and oxidized clusters exhibit markedly different absorption characteristics, and more intriguingly, both are luminescent; the luminescence is dependent on both the oxidation state and coordination environment of the cluster.[13] These findings suggest the possibility of altering the absorption and emission characteristics of the clusters by changing electrochemical conditions. Electrochromic and electroluminescent materials may thus be envisioned.

The initial success of utilizing this cluster system has been demonstrated by the cluster-cored metallodendrimers using Fréchet-type dendrons derived from gallic acid.[14] We found that the nature of the focal coordinating group of the dendron profoundly affects the electronic structure of the cluster core, giving rise to intriguing photophysical properties of the hybrids. In principle, it should be possible to tune such properties via the use of various combinations of dendrons. This effort would require the cluster precursors be modified to accommodate the different numbers and types of polymeric ligands. In other words, the availability of appropriately designed and systematically altered cluster building blocks is key to establishing the relationship between the structure of the building blocks and the property of the hybrids. Materials with controlled structure, composition, dimension, and properties can thus be realized.

Toward the goal of synthesizing compositionally and structurally tunable cluster-containing hybrids, we have previously prepared a cluster complex $[Re_6Se_8(PEt_3)_5$(4-vinylpyridine)$](SbF_6)_2$ in which a bifunctional 4-vinylpyridine ligand coordinates the cluster core via Re−N (pyridyl) bonding while leaving the vinyl group available for further chemical transformations.[15] Copolymerization of the complex with

Received: January 5, 2012
Revised: February 9, 2012
Published: February 22, 2012

ACS Publications © 2012 American Chemical Society

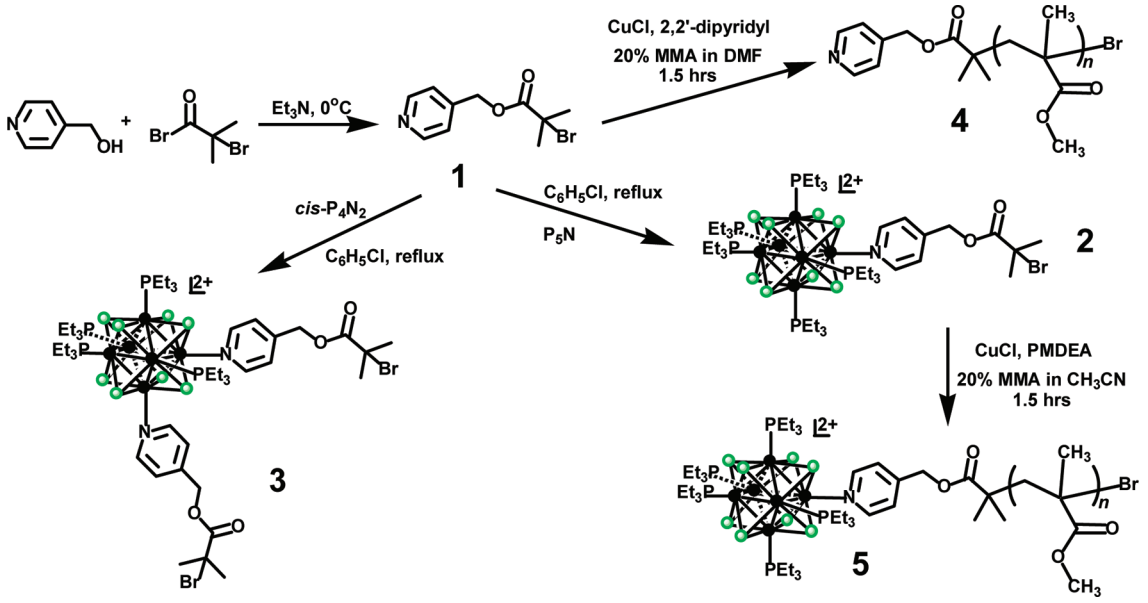


Figure 2. Syntheses of cluster complexes (**2** and **3**) with polymerization-initiating ligand **1** and the polymerization of methyl methacrylate (MMA) initiated by **2** with the pure organic initiator **1** in a control experiment.

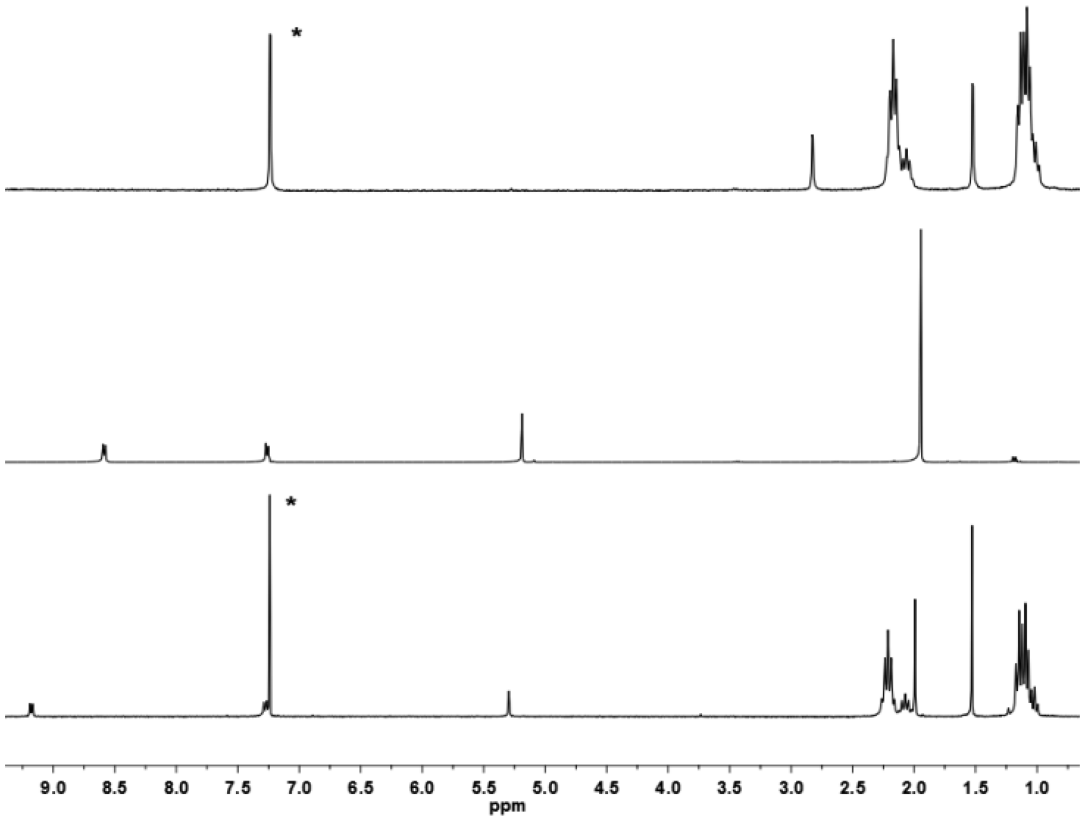


Figure 3. Comparative ^{1}H NMR studies of complexes P_5N, **1**, and **2** (from top to bottom; *$CDCl_3$ solvent peak).

styrene resulted in a waxy solid, displaying an orange color characteristic of the parent cluster but contrasting morphologically with the highly crystalline precursor complex. In this Note, we report our preliminary studies by employing site-differentiated cluster complexes as initiators for controlled radical polymerization.[16] Two cluster complexes featuring respectively one and two potentially polymerization-initiating ligands, pyridin-4-ylmethyl 2-bromo-2-methylpropanoate (**1**, PyBr), $[Re_6Se_8(PEt_3)_5(PyBr)](SbF_6)_2$ (**2**) and *cis*-$[Re_6Se_8(PEt_3)_4(PyBr)_2](SbF_6)_2$ (**3**), have been prepared, and polymerization of methyl methacrylate (MMA) using **2** as the initiator has been studied (Supporting Information).

The synthesis of the organic initiator **1** was achieved by acylation of pyridine-4-methanol with α-bromoisobutyryl bromide (Figure 2). Originally obtained using CH_2Cl_2 as solvent produced a complex mixture, from which pure product was obtained by chromatographic separation. Characterization by ^{1}H NMR spectroscopy was straightforward: Upon acylation

dx.doi.org/10.1021/ma300024a | *Macromolecules* 2012, 45, 2614−2618

the broad −OH signal of the starting pyridine-4-methanol at 3.32 ppm disappeared, while the $-CH_2-$ proton resonance sizably shifted from 4.72 to 5.19 ppm of the product. The product yield was significantly improved when the reaction was carried in a hexanes/THF mixture, but chromatographic separation was still necessary. Compound **1** can be stabilized up to 6 months as a 20% solution in hexanes when stored under dry N_2 at 4 °C; gradual decomposition was observed upon standing as a solid under ambient conditions.

Subsequent ligand substitution reaction of site-differentiated nitrile solvates[12] $[Re_6Se_8(PEt_3)_5(CH_3CN)](SbF_6)_2$ (P_5N) and *cis*-$[Re_6Se_8(PEt_3)_4(CH_3CN)_2](SbF_6)_2$ (*cis*-P_4N_2) with **1** was unexceptional, affording cluster-complex initiators **2** and **3** in essentially quantitative yields. The formation of the targeted complex **2** is clearly revealed by comparative NMR studies: The ^{1}H NMR spectrum of **2** shows significant downfield shift of the pyridyl α-H from 8.59 ppm in **1** to 9.18 ppm upon coordination to the Lewis acidic cluster core, but shifts of other signals are not as obvious due to their remoteness to the cluster core (Figure 3). The distinct relative integration of 4:1 in the ^{31}P NMR indicates that the pentakis substitution of the cluster core was maintained upon ligand exchange (Figure 4).

The identity of complex **2** was further verified by using X-ray diffraction analysis. Its crystal structure is shown in Figure 5.

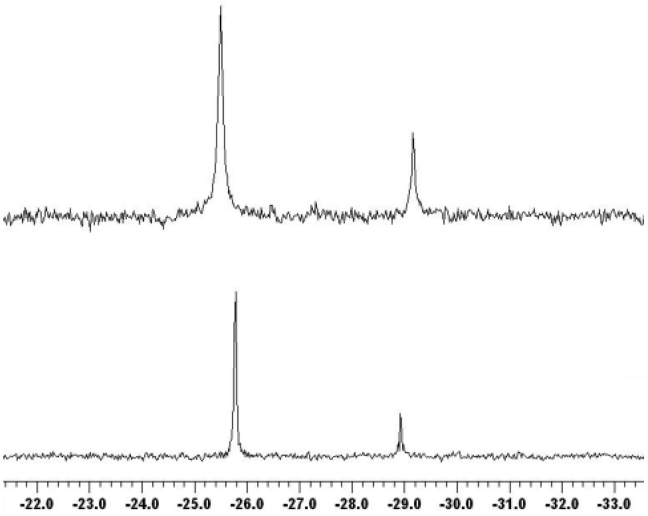


Figure 4. Comparative ^{31}P NMR studies of P_5N (top) and **2** (bottom).

The metric values of bond distances and angles (Supporting Information) defining the $Re_6Se_8(PEt_3)_5$ moiety are comparable to its precursor $[Re_6Se_8(PEt_3)_5(CH_3CN)](SbF_6)_2$ and other structurally characterized cluster complexes containing the same structural motif.[11c,12] The Re−N bond of 2.211(17) Å and the pyridyl C−C bond distances averaged at 1.39 Å fall in the respective ranges reported for analogous cluster complexes with pyridyl coordination.[12]

The ability of **1** to initiate controlled radical polymerization was first tested in order to generate a reference point for the evaluation of the cluster complex **2** in a similar capacity. Under conditions typically applied for atom transfer radical polymerization,[16] a mixture containing **1** and MMA in a molar ratio of 1:100 and 1.1 equiv of Cu(I)-2,2′-bipyridyl catalyst in dimethylformamide (DMF) was heated at 70 °C for 90 min. Isolation and purification of the polymeric product (**4**) were

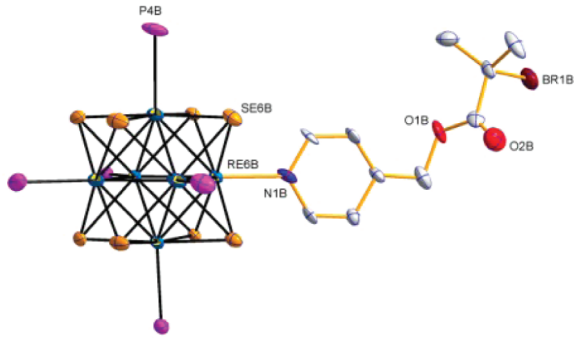


Figure 5. Crystal structure of **2** with partial labelings. Counterions, ethyl groups of PEt_3 ligands, and H atoms are omitted for clarity. Anisotropic displacement ellipsoids at the 50% probability level.

carried out by following standard procedures. Analysis by size-exclusion chromatography showed that the number-averaged molecular weight (M_n) of the polymer is 10 309 amu with a polydipersity of 1.18 (Figure 6). Integration of the ^{1}H NMR of **4** yielded an averaged initiator-to-monomer ratio of 1:88; the initiator efficiency is thus 94% (based on 97% conversion).

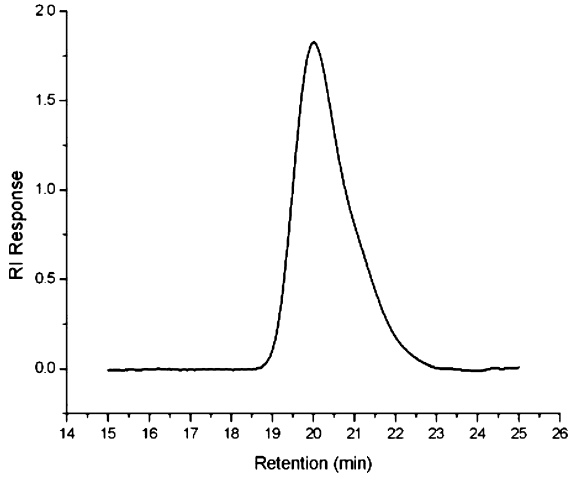


Figure 6. SEC analysis of polymer **4** using THF as mobile phase and with a RI detector. The SEC molar masses were calibrated against low polydispersity linear polystyrene standards.

These values suggested that the initiation by **1** was effective and that the polymerization was nicely controlled.

The polymerization of MMA using the cluster-based initiator **2** was then carried out under otherwise the same conditions as when the organic initiator **1** was used. SEC analysis of the product mixture showed two fractions, one with M_n of 24 716 amu and the other, 7930 amu (Figure 7a). Since the cluster absorbs at ca. 240 nm, a UV detector was also used to monitor the presence of cluster in the product. It has been found that only the lower molecular weight fraction has noticeable UV absorption at 240 nm. These observations may suggest that (1) the initiating power of **1** is mitigated when bound to the cluster and (2) decomposition of cluster-complex initiator **2** may have occurred under the polymerization conditions. The former may be rationalized in terms of the electronic influences upon coordination to the Lewis acidic core. As for the latter, both 2,2′-dipyridyl and DMF are potentially competing for coordination with the cluster, thus destabilizing the cluster-

dx.doi.org/10.1021/ma300024a | *Macromolecules* 2012, 45, 2614−2618

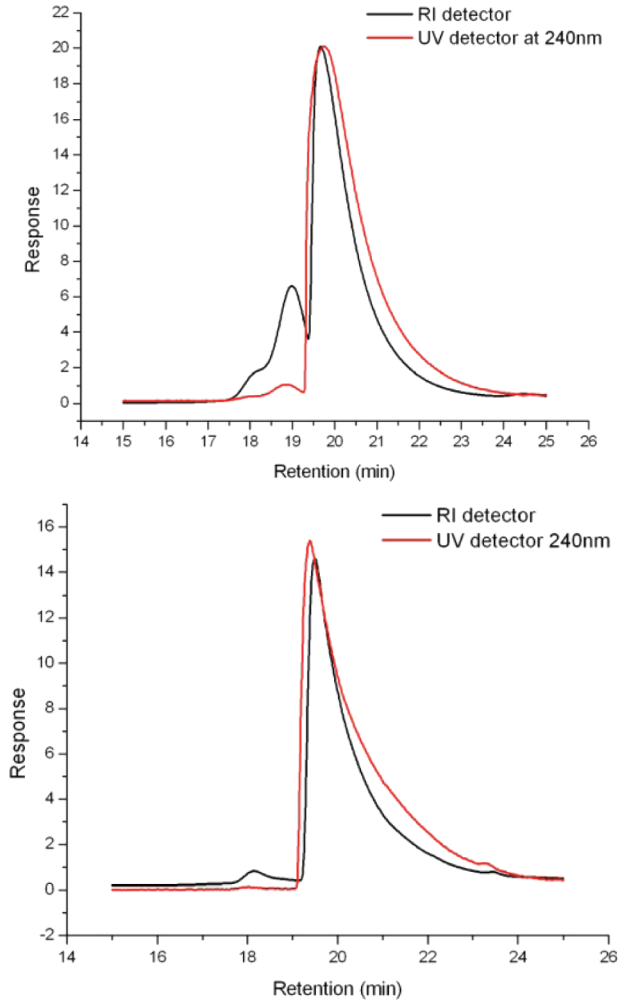


Figure 7. SEC analyses of hybrids obtained by using **2** as initiator and under two different sets of conditions: (a) ratio [**2**]:[CuCl]:[2,2′-bipy]:[MMA] = 1:1:2:200; 20% DMF, 70 °C, 6 h (top); (b) ratio [**2**]:[CuCl]:[PMDEA]:[MMA] = 1:1.5:2:200; 30% CH_3CN, 70 °C, 1.5 h (bottom; hybrid **5** in Figure 2).

complex initiator and effectively reducing its effectiveness in polymerizing MMA.

As a possible solution to minimize competitive coordination of the cluster core and thus the decomposition of **2**, pentamethyldiethylenetriamine (PMDEA) was used in place of 2,2′-dipyridyl as ligand for the Cu(I) catalyst. For the same consideration, CH_3CN was used in place of DMF as solvent. Polymerization under such conditions reached the viscous state after 1.5 h with a monomer conversion of 81% compared to 6 h when the combination of 2,2′-dipyridyl/DMF was used. The SEC trace showed a predominant product with M_n of 11 366 amu and a polydispersity index of 1.21, accompanied by a minor fraction (about 1.6%) with M_n of 44 822 amu and a PDI of 1.02 (Figure 7b). The lower-molecular-weight fraction displays a strong UV absorption at 240 nm, characteristic of the $[Re_6Se_8]^{2+}$ core, whereas the higher-molecular-weight fraction does not show any significant absorption associated with the presence of the cluster. On the basis of these results, it is reasonable to conclude that with a less competitive ligand for Cu(I) and a less coordinating solvent, the polymerization reaction can be improved.

In summary, two $[Re_6Se_8]^{2+}$ core-containing cluster complexes with a ligand capable of initiating controlled radical polymerization have been prepared, and the potential of using such cluster complexes to create cluster-containing hybrids was demonstrated by the polymerization of MMA with one of these complexes as initiator. The present results validate our original goal of using such cluster complexes in making functional hybrid materials, but the performance of the cluster complex initiator is somewhat compromised when compared with the initiator ligand itself, possibly due to the decomposition of the complex as a result of the competitive coordination by the solvent and the ancillary ligand of the Cu(I) catalysts used in the ATRP process. Indeed, significant improvement was achieved by substituting 2,2′-dipyridyl for pentamethyldiethylenetriamine (PMDEA) as ligand for the Cu(I) catalysts and dimethylformamide (DMF) for acetonitrile (CH_3CN) as solvent; both are less coordinating toward the cluster core. We will extend this chemistry with the use of other complexes equipped with different types, numbers, and/or spatial arrangement of the initiator groups for the generation of polymeric hybrids with structurally distinct architectures.[16b] The potential applications of such hybrids, for example, as radiographic contrast agents,[17] redox-active liquid crystals,[18] and phosphorescent organic light-emitting materials,[19] will also be pursued.

■ ASSOCIATED CONTENT

Ⓢ Supporting Information

Synthesis and characterization details and crystal data and structure refinement parameters of compound **2**. This material is available free of charge via the Internet at http://pubs.acs.org.

■ AUTHOR INFORMATION

Corresponding Author

*E-mail zhiping@u.arizona.edu; Tel (520) 626-6495; Fax (520) 621-8407.

Notes

The authors declare no competing financial interest.

■ ACKNOWLEDGMENTS

We thank the NSF (CHE-0750530) for financial support of this work.

■ REFERENCES

(1) Gomez-Romero, P.; Sanchez, C. *New J. Chem.* **2005**, *29*, 57.
(2) Palacio, F.; Oliete, P.; Schubert, U.; Mijatovic, I.; Hüsing, N.; Peterlik, N. *J. Mater. Chem.* **2004**, *14*, 1873.
(3) Gorman, C. B.; Parkhurst, B. L.; Su, W. Y.; Chen, K.-Y. *J. Am. Chem. Soc.* **1997**, *119*, 1141.
(4) Schubert, U.; Völkel, T.; Moszner, N. *Chem. Mater.* **2001**, *13*, 3811.
(5) (a) Gray, T. G. *Coord. Chem. Rev.* **2003**, *243*, 213. (b) Welch, E. J.; Long, J. R. *Prog. Inorg. Chem.* **2005**, *54*, 1.
(6) Robinson, L. M.; Lu, H.; Hupp, J. T.; Shriver, D. F. *Chem. Mater.* **1995**, *7*, 43.
(7) Golden, H. H.; Deng, H.; DiSalvo, F. J.; Fréchet, J. M. J.; Thompson, P. M. *Science* **1995**, *268*, 1463.
(8) Sogah, D. Y.; Weimer, M. W.; Jin, S.; DiSalvo, F. J.; Vemkataraman, D. *Polym. Mater. Sci. Eng.* **2001**, *84*, 845.
(9) Gorman, C. B.; Su, W. Y.; Jiang, H.; Watson, C. M.; Boyle, P. *Chem. Commun.* **1999**, 877.
(10) (a) Molard, Y.; Ledneva, A.; Amela-Cortes, M.; Circu, V.; Naumov, N. G.; Meriadec, C.; Artzner, F.; Cordier, S. *Chem. Mater.* **2011**, *23*, 5122. (b) Molard, Y.; Dorson, F.; Brylev, K. A.; Shestopalov,

M. A.; Le Gal, Y.; Cordier, S.; Mironov, Y. V.; Kitamura, N.; Perrin, C. *Chem.—Eur. J.* **2010**, *16*, 5613. (c) Mocanu, A. S.; Amela-Cortes, M.; Molard, Y.; Circu, V.; Cordier, S. *Chem. Commun.* **2011**, *47*, 2056. (d) Molard, Y.; Dorson, F.; Circu, V.; Roisnel, T.; Artzner, F.; Cordier, S. *Angew. Chem., Int. Ed.* **2010**, *49*, 3351.

(11) For reviews on the $[Re_6Q_8]^{2+}$ (Q = S, Se) clusters, see: (a) Gabriel, J.-C. P.; Boubekeur, K.; Uriel, S.; Batail, P. *Chem. Rev.* **2001**, *101*, 2037. (b) Oilet, G.; Perrin, A. *C. R. Chim.* **2005**, *8*, 1728. (c) Selby, H. D.; Roland, B. K.; Zheng, Z. *Acc. Chem. Res.* **2003**, *36*, 933. (d) Sasaki, Y. *J. Nucl. Radiochem. Sci.* **2005**, *6*, 145. (e) Naumov, N. G.; Virovets, A. V.; Fedorov, V. E. *J. Struct. Chem.* **2000**, *41*, 499. (f) Saito, T. *J. Chem. Soc., Dalton Trans.* **1999**, 97.

(12) Zheng, Z.; Long, J. R.; Holm, R. H. *J. Am. Chem. Soc.* **1997**, *119*, 2163.

(13) (a) Long, J. R.; McCarty, L. S.; Holm, R. H. *J. Am. Chem. Soc.* **1996**, *118*, 4603. (b) Arratia-Pérez, R; Hernández-Acevedo, L. *J. Chem. Phys.* **1999**, *111*, 168. (c) Arratia-Perez, R.; Hernandez-Acevedo, L. *J. Chem. Phys.* **1999**, *110*, 2529. (d) Gray, T. G.; Rudzinski, C. M.; Meyer, E. E.; Holm, R. H.; Nocera, D. G. *J. Am. Chem. Soc.* **2003**, *125*, 4755. (e) Gray, T. G.; Rudzinski, C. M.; Nocera, D. G.; Holm, R. H. *Inorg. Chem.* **1999**, *38*, 5932.

(14) Wang, R.; Zheng, Z. *J. Am. Chem. Soc.* **1999**, *121*, 3549.

(15) Roland, B. K.; Flora, W. H.; Carducci, M. D.; Armstrong, N. R.; Zheng, Z. *J. Cluster Sci.* **2004**, *14*, 449.

(16) (a) Matyjaszewski, K.; Xia, J. *Chem. Rev.* **2001**, *101*, 2921. (b) Pyun, J.; Matyjaszewski, K. *Chem. Mater.* **2001**, *13*, 3436.

(17) Yu, S.; Watson, A. *Chem. Rev.* **1999**, *99*, 2353.

(18) Zhang, C.; Bunning, T.; Laine, R. M. *Chem. Mater.* **2001**, *13*, 3653.

(19) Baldo, M. A.; Thompson, M. E.; Forrest, S. R. *Nature* **2000**, *403*, 750.